

World Journal of *Radiology*

World J Radiol 2015 January 28; 7(1): 1-27





Editorial Board

2014-2017

The *World Journal of Radiology* Editorial Board consists of 365 members, representing a team of worldwide experts in radiology. They are from 36 countries, including Afghanistan (1), Argentina (2), Australia (5), Austria (7), Belgium (2), Brazil (8), Canada (6), Chile (1), China (43), Croatia (1), Denmark (4), Egypt (6), France (5), Germany (22), Greece (10), India (12), Iran (6), Ireland (2), Israel (3), Italy (47), Japan (13), Netherlands (1), New Zealand (1), Pakistan (1), Poland (2), Portugal (1), Serbia (1), Singapore (3), Slovakia (1), South Korea (18), Spain (4), Sweden (2), Switzerland (4), Thailand (1), Turkey (26), United Kingdom (11), and United States (82).

EDITORS-IN-CHIEF

Kai U Juergens, *Bremen*
Edwin JR van Beek, *Edinburgh*
Thomas J Vogl, *Frankfurt*

GUEST EDITORIAL BOARD MEMBERS

Wing P Chan, *Taipei*
Chung-Huei Hsu, *Taipei*
Chin-Chang Huang, *Taipei*
Tsong-Long Hwang, *Taoyuan*
Jung-Lung Hsu, *Taipei*
Chia-Hung Kao, *Taichung*
Yu-Ting Kuo, *Tainan*
Hon-Man Liu, *Taipei*
Hui-Lung Liang, *Kaohsiung*
Chun Chung Lui, *Kaohsiung*
Sen-Wen Teng, *Taipei*
Yung-Liang (William) Wan, *Taoyuan*

MEMBERS OF THE EDITORIAL BOARD



Afghanistan

Takao Hiraki, *Okayama*



Argentina

Patricia Carrascosa, *Vicente Lopez*
Maria C Ziadi, *Rosario*



Australia

Lourens Bester, *Sydney*
Gemma A Figtree, *Sydney*



Austria

Herwig R Cerwenka, *Graz*
Gudrun M Feuchtnner, *Innsbruck*
Benjamin Henninger, *Innsbruck*
Rupert Lanzenberger, *Vienna*
Shu-Ren Li, *Vienna*
Veronika Schopf, *Vienna*
Tobias De Zordo, *Innsbruck*



Belgium

Steve Majerus, *Liege*
Kathelijne Peremans, *Merelbeke*



Brazil

Clerio F Azevedo, *Rio de Janeiro*
Patrícia P Alfredo, *São Paulo*
Eduardo FC Fleury, *São Paulo*
Edward Araujo Júnior, *São Paulo*
Wellington P Martins, *Ribeirao Preto*
Ricardo A Mesquita, *Belo Horizonte*
Vera MC Salemi, *São Paulo*
Claudia Szobot, *Porto Alegre*
Lilian YI Yamaga, *São Paulo*



Canada

Marie Arsalidou, *Toronto*
Otman A Basir, *Waterloo*

Tarik Zine Belhocine, *Toronto*
James Chow, *Toronto*
Tae K Kim, *Toronto*
Anastasia Oikonomou, *Toronto*



China

Hong-Wei Chen, *Wuxi*
Feng Chen, *Hangzhou*
Jian-Ping Chu, *Guangzhou*
Guo-Guang Fan, *Shenyang*
Bu-Lang Gao, *Shijiazhuang*
Qi-Yong Gong, *Chengdu*
Ying Han, *Beijing*
Xian-Li Lv, *Beijing*
Yi-Zhuo Li, *Guangzhou*
Xiang-Xi Meng, *Harbin*
Yun Peng, *Beijing*
Jun Shen, *Guangzhou*
Ze-Zhou Song, *Hangzhou*
Wai Kwong Tang, *Hong Kong*
Gang-Hua Tang, *Guangzhou*
Jie Tian, *Beijing*
Lu-Hua Wang, *Beijing*
Xiao-bing Wang, *Xi'an*
Yi-Gen Wu, *Nanjing*
Kai Wu, *Guangzhou*
Hui-Xiong Xu, *Shanghai*
Zuo-Zhang Yang, *Kunming*
Xiao-Dan Ye, *Shanghai*
David T Yew, *Hong Kong*
Ting-He Yu, *Chongqing*
Zheng Yuan, *Shanghai*
Min-Ming Zhang, *Hangzhou*
Yudong Zhang, *Nanjing*
Dong Zhang, *Chongqing*
Wen-Bin Zeng, *Changsha*

Yue-Qi Zhu, *Shanghai*



Croatia

Goran Kusec, *Osijek*



Denmark

Poul E Andersen, *Odense*

Lars J Petersen, *Aalborg*

Thomas Z Ramsøy, *Frederiksberg*

Morten Ziebell, *Copenhagen*



Egypt

Mohamed F Bazeed, *Mansoura*

Mohamed Abou El-Ghar, *Mansoura*

Reem HA Mohamed, *Cairo*

Mohamed R Nouh, *Alexandria*

Ahmed AKA Razek, *Mansoura*

Ashraf A Zytoon, *Shebin El-Koom*



France

Sabine F Bensamoun, *Compiègne*

Romarc Loffroy, *Dijon*

Stephanie Nougaret, *Montpellier*

Hassane Oudadesse, *Rennes*

Vincent Vinh-Hung, *Fort-de-France*



Germany

Henryk Barthel, *Leipzig*

Peter Bannas, *Hamburg*

Martin Beeres, *Frankfurt*

Ilja F Ciernik, *Dessau*

A Dimitrakopoulou-Strauss, *Heidelberg*

Peter A Fasching, *Erlangen*

Andreas G Schreyer, *Regensburg*

Philipp Heusch, *Duesseldorf*

Sonja M Kirchhoff, *Munich*

Sebastian Ley, *Munich*

Adel Maataoui, *Frankfurt am Main*

Stephan M Meckel, *Freiburg*

Hans W Muller, *Duesseldorf*

Kay Raum, *Berlin*

Dirk Rades, *Luebeck*

Marc-Ulrich Regier, *Hamburg*

Alexey Surov, *Halle*

Martin Walter, *Magdeburg*

Axel Wetter, *Essen*

Christoph Zilkens, *Düsseldorf*



Greece

Panagiotis Antoniou, *Thessaloniki*

Nikos Efthimiou, *Athens*

Dimitris Karnabatidis, *Patras*

George Latsios, *Athens*

Stylianios Megremis, *Iraklion*

Alexander D Rapidis, *Athens*

Kiki Theodorou, *Larissa*

Ioannis A Tsalafoutas, *Athens*

Evanthia E Tripoliti, *Ioannina*

Athina C Tsili, *Ioannina*



India

Ritesh Agarwal, *Chandigarh*

Chandan J Das, *New Delhi*

Prathamesh V Joshi, *Mumbai*

Naveen Kalra, *Chandigarh*

Chandrasekharan Kesavadas, *Trivandrum*

Jyoti Kumar, *New Delhi*

Atin Kumar, *New Delhi*

Kaushala P Mishra, *Allahabad*

Daya N Sharma, *New Delhi*

Binit Sureka, *New Delhi*

Sanjay Sharma, *New Delhi*

Raja R Yadav, *Allahabad*



Iran

Majid Assadi, *Bushehr*

SeyedReza Najafizadeh, *Tehran*

Mohammad Ali Oghabian, *Tehran*

Amir Reza Radmard, *Tehran*

Ramin Sadeghi, *Mashhad*

Hadi Rokni Yazdi, *Tehran*



Ireland

Tadhg Gleeson, *Wexford*

Frederik JAI Vernimmen, *Cork*



Israel

Dafna Ben Bashat, *Tel Aviv*

Amit Gefen, *Tel Aviv*

Tamar Sella, *Jerusalem*



Italy

Adriano Alippi, *Rome*

Dante Amelio, *Trento*

Michele Anzidei, *Rome*

Filippo F Angileri, *Messinas*

Stefano Arcangeli, *Rome*

Roberto Azzoni, *San Donato milanese*

Tommaso V Bartolotta, *Palermo*

Tommaso Bartalena, *Imola*

Livia Bernardin, *San Bonifacio*

Federico Boschi, *Verona*

Sergio Casciaro, *Lecce*

Emanuele Casciani, *Rome*

Musa M Can, *Napoli*

Alberto Cuocolo, *Napoli*

Michele Ferrara, *Coppito*

Mauro Feola, *Fossano*

Giampiero Francica, *Castel Volturno*

Luigi De Gennaro, *Rome*

Giulio Giovannetti, *Pisa*

Francesca Iacobellis, *Napoli*

Formato Invernizzi, *Monza Brianza*

Francesco Lassandro, *Naples*

Lorenzo Livi, *Florence*

Pier P Mainenti, *Napoli*

Laura Marzetti, *Chieti*

Giuseppe Malinverni, *Crescentino*

Enrica Milanese, *Turin*

Giovanni Morana, *Treviso*

Lorenzo Monti, *Milan*

Silvia D Morbelli, *Genoa*

Barbara Palumbo, *Perugia*

Cecilia Parazzini, *Milan*

Stefano Pergolizzi, *Messina*

Antonio Pinto, *Naples*

Camillo Porcaro, *Rome*

Carlo C Quattrocchi, *Rome*

Alberto Rebonato, *Perugia*

Giuseppe Rizzo, *Rome*

Roberto De Rosa, *Naples*

Domenico Rubello, *Rovigo*

Andrea Salvati, *Bari*

Sergio Sartori, *Ferrara*

Luca M Sconfienza, *Milano*

Giovanni Storto, *Rionero*

Nicola Sverzellati, *Parma*

Alberto S Tagliafico, *Genova*

Nicola Troisi, *Florence*



Japan

Yasuhiko Hori, *Chiba*

Hidetoshi Ikeda, *Koriyama*

Masahito Kawabori, *Sapporo*

Tamotsu Kamishima, *Sapporo*

Hiro Kiyosue, *Yufu*

Yasunori Minami, *Osaka-sayama*

Yasuhiro Morimoto, *Kitakyushu*

Satoru Murata, *Tokyo*

Shigeki Nagamachi, *Miyazaki*

Hiroshi Onishi, *Yamanashi*

Morio Sato, *Wakayama Shi*

Yoshito Tsushima, *Maebashi*

Masahiro Yanagawa, *Suita*



Netherlands

Willem Jan van Rooij, *Tilburg*



New Zealand

W Howell Round, *Hamilton*



Pakistan

Wazir Muhammad, *Abbottabad*



Poland

Maciej S Baglaj, *Wroclaw*

Piotr Czauderna, *Gdansk*



Portugal

Joao Manuel RS Tavares, *Porto*



Serbia

Olivera Ciraj-Bjelac, *Belgrade*



Singapore

Gopinathan Anil, *Singapore*

Terence KB Teo, *Singapore*

Cher Heng Tan, *Singapore*



Slovakia

Stefan Sivak, *Martin*



South Korea

Ki Seok Choo, *Busan*

Seung Hong Choi, *Seoul*

Dae-Seob Choi, *Jinju*

Hong-Seok Jang, *Seoul*

Yong Jeong, *Daejeon*

Chan Kyo Kim, *Seoul*

Se Hyung Kim, *Seoul*

Joong-Seok Kim, *Seoul*

Sang Eun Kim, *Seongnam*

Sung Joon Kwon, *Seoul*

Jeong Min Lee, *Seoul*

In Sook Lee, *Busan*

Noh Park, *Goyang*

Chang Min Park, *Seoul*

Sung Bin Park, *Seoul*

Deuk Jae Sung, *Seoul*

Choongsoo Shin, *Seoul*

Kwon-Ha Yoon, *Iksan*



Spain

Miguel A De Gregorio, *Zaragoza*

Antonio Luna, *Jaén*

Enrique Marco de Lucas, *Santander*

Fernando Ruiz Santiago, *Granada*



Sweden

Dmitry Grishenkov, *Stockholm*

Tie-Qiang Li, *Stockholm*



Switzerland

Nicolau Beckmann, *Basel*

Christian Boy, *Bern*

Giorgio Treglia, *Bellinzona*

Stephan Ulmer, *Kiel*



Thailand

Sirianong Namwongprom, *Chiang Mai*



Turkey

Kubilay Aydin, *Istanbul*

Ramazan Akdemir, *Sakarya*

Serhat Avcu, *Ankara*

Ayşe Aralasmak, *Istanbul*

Oktay Algin, *Ankara*

Nevbahar Akcar, *Meselik*

Bilal Battal, *Ankara*

Zulkif Bozgeyik, *Elazig*

Nazan Ciledag, *Aakara*

Fuldem Y Donmez, *Ankara*

Gulgun Engin, *Istanbul*

Ahmet Y Goktay, *Izmir*

Oguzhan G Gumustas, *Bursa*

Kaan Gunduz, *Ankara*

Pelin Ozcan Kara, *Mersin*

Kivanc Kamburoglu, *Ankara*

Ozgur Kilickesmez, *Istanbul*

Furuzan Numan, *Istanbul*

Cem Onal, *Adana*

Ozgur Oztekin, *Izmir*

Seda Ozbek (Boruban), *Konya*

Selda Sarikaya, *Zonguldak*

Figen Taser, *Kutahya*

Baran Tokar, *Eskisehir*

Ender Uysal, *Istanbul*

Ensar Yekeler, *Istanbul*



United Kingdom

Indran Davagnanam, *London*

M DC Valdés Hernández, *Edinburgh*

Alan Jackson, *Manchester*

Suneil Jain, *Belfast*

Long R Jiao, *London*

Miltiadis Krokidis, *Cambridge*

Pradesh Kumar, *Liverpool*

Peter D Kuzmich, *Derby*

Georgios Plataniotis, *Brighton*

Vanessa Sluming, *Liverpool*



United States

Garima Agrawal, *Saint Louis*

James R Brasic, *Baltimore*

Rajendra D Badgaiyan, *Buffalo*

Ulas Bagci, *Bethesda*

Anat Biegon, *Stony Brook*

Ramon Casanova, *Winston Salem*

Wenli Cai, *Boston*

Zheng Chang, *Durham*

Corey J Chakarun, *Long Beach*

Kai Chen, *Los Angeles*

Hyun-Soon Chong, *Chicago*

Marco Cura, *Dallas*

Ravi R Desai, *Bensalem*

Delia DeBuc, *Miami*

Carlo N De Cecco, *Charleston*

Timm-Michael L Dickfeld, *Baltimore*

Subba R Digumarthy, *Boston*

Huy M Do, *Stanford*

Todd A Faasse, *Grand Rapids*

Salomao Faintuch, *Boston*

Girish M Fatterpekar, *New York*

Dhakshinamoorthy Ganesan, *Houston*

Robert J Griffin, *Little Rock*

Andrew J Gunn, *Boston*

Sandeep S Hedgire, *Boston*

Timothy J Hoffman, *Columbia*

Mai-Lan Ho, *San Francisco*

Juebin Huang, *Jackson*

Abid Irshad, *Charleston*

Matilde Inglese, *New York*

El-Sayed H Ibrahim, *Jacksonville*

Paul R Julsrud, *Rochester*

Pamela T Johnson, *Baltimore*

Ming-Hung Kao, *Tempe*

Sunil Krishnan, *Houston*

Richard A Komoroski, *Cincinnati*

Sandi A Kwee, *Honolulu*

King Kim, *Ft. Lauderdale*

Guozheng Liu, *Worcester*

Yiyan Liu, *Newark*

Venkatesh Mani, *New York*

Lian-Sheng Ma, *Pleasanton*

Rachna Madan, *Boston*

Zeyad A Metwalli, *Houston*

Yilong Ma, *Manhasset*

Hui Mao, *Atlanta*

Feroze B Mohamed, *Philadelphia*

Gul Moonis, *Boston*

John L Noshier, *New Brunswick*

Rahmi Oklu, *Boston*

Aytekun Oto, *Chicago*

Bishnuhari Paudyal, *Philadelphia*

Rajul Pandya, *Youngstown*

Chong-Xian Pan, *Sacramento*

Jay J Pillai, *Baltimore*

Neal Prakash, *Duarte*

Reza Rahbar, *Boston*

Ali S Raja, *Boston*

Gustavo J Rodriguez, *El Paso*

David J Sahn, *Portland*

Steven Schild, *Scottsdale*

Ali R Sepahdari, *Los Angeles*

Li Shen, *Indianapolis*

JP Sheehan, *Charlottesville*

Atul B Shinagare, *Boston*

Sarabjeet Singh, *Boston*

Charles J Smith, *Columbia*

Kenji Suzuki, *Chicago*

Monvadi Srichai-Parsia, *Washington*

Sree H Tirumani, *Boston*

Hebert A Vargas, *New York*

Sachit Verma, *Philadelphia*

Yoichi Watanabe, *Minneapolis*

Li Wang, *Chapel Hill*

Carol C Wu, *Boston*

Shoujun Xu, *Houston*

Min Yao, *Cleveland*

Xiaofeng Yang, *Atlanta*

Qingbao Yu, *Albuquerque*

Aifeng Zhang, *Chicago*

Chao Zhou, *Bethlehem*

Hongming Zhuang, *Philadelphia*

**EDITORIAL**

- 1 Treatment assessment of radiotherapy using MR functional quantitative imaging
Chang Z, Wang C

TOPIC HIGHLIGHT

- 7 Conventional radiological strategy of common gastrointestinal neoplasms
Li YZ, Wu PH

MINIREVIEWS

- 17 Fetal brain tumors: Prenatal diagnosis by ultrasound and magnetic resonance imaging
Milani HJ, Araujo Júnior E, Cavalcheiro S, Oliveira PS, Hisaba WJ, Barreto EQS, Barbosa MM, Nardozza LM, Moron AF

ORIGINAL ARTICLE**Retrospective Study**

- 22 Comparison of conventional radiography and MDCT in suspected scaphoid fractures
Behzadi C, Karul M, Henes FO, Laqmani A, Catala-Lehnen P, Lehmann W, Nagel HD, Adam G, Regier M

ABOUT COVER

Editorial Board Member of *World Journal of Radiology*, Jian-Ping Chu, MD, PhD, Associate Professor, Diagnostic Radiology, the First Affiliated Hospital, Sun Yat-sen University, Guangzhou 510080, Guangdong Province, China

AIM AND SCOPE

World Journal of Radiology (*World J Radiol*, *WJR*, online ISSN 1949-8470, DOI: 10.4329) is a peer-reviewed open access academic journal that aims to guide clinical practice and improve diagnostic and therapeutic skills of clinicians.

WJR covers topics concerning diagnostic radiology, radiation oncology, radiologic physics, neuroradiology, nuclear radiology, pediatric radiology, vascular/interventional radiology, medical imaging achieved by various modalities and related methods analysis. The current columns of *WJR* include editorial, frontier, diagnostic advances, therapeutics advances, field of vision, mini-reviews, review, topic highlight, medical ethics, original articles, case report, clinical case conference (clinicopathological conference), and autobiography.

We encourage authors to submit their manuscripts to *WJR*. We will give priority to manuscripts that are supported by major national and international foundations and those that are of great basic and clinical significance.

INDEXING/ABSTRACTING

World Journal of Radiology is now indexed in PubMed Central, PubMed, Digital Object Identifier, and Directory of Open Access Journals.

FLYLEAF

I-III Editorial Board

EDITORS FOR THIS ISSUE

Responsible Assistant Editor: *Xiang Li*
Responsible Electronic Editor: *Su-Qing Liu*
Proofing Editor-in-Chief: *Lian-Sheng Ma*

Responsible Science Editor: *Fang-Fang Ji*
Proofing Editorial Office Director: *Xiu-Xia Song*

NAME OF JOURNAL
World Journal of Radiology

ISSN
ISSN 1949-8470 (online)

LAUNCH DATE
December 31, 2009

FREQUENCY
Monthly

EDITORS-IN-CHIEF
Kai U Juergens, MD, Associate Professor, MRT und PET/CT, Nuklearmedizin Bremen Mitte, ZEMODI - Zentrum für morphologische und molekulare Diagnostik, Bremen 28177, Germany

Edwin JR van Beek, MD, PhD, Professor, Clinical Research Imaging Centre and Department of Medical Radiology, University of Edinburgh, Edinburgh EH16 4TJ, United Kingdom

Thomas J Vogl, MD, Professor, Reader in Health Technology Assessment, Department of Diagnostic and Interventional Radiology, Johann Wolfgang

Goethe University of Frankfurt, Frankfurt 60590, Germany

EDITORIAL OFFICE
Jin-Lei Wang, Director
Xiu-Xia Song, Vice Director
World Journal of Radiology
Room 903, Building D, Ocean International Center, No. 62 Dongsihuan Zhonglu, Chaoyang District, Beijing 100025, China
Telephone: +86-10-59080039
Fax: +86-10-85381893
E-mail: editorialoffice@wjnet.com
Help Desk: <http://www.wjnet.com/esps/helpdesk.aspx>
<http://www.wjnet.com>

PUBLISHER
Baishideng Publishing Group Inc
8226 Regency Drive,
Pleasanton, CA 94588, USA
Telephone: +1-925-223-8242
Fax: +1-925-223-8243
E-mail: bpgoffice@wjnet.com
Help Desk: <http://www.wjnet.com/esps/helpdesk.aspx>
<http://www.wjnet.com>

PUBLICATION DATE
January 28, 2015

COPYRIGHT
© 2015 Baishideng Publishing Group Inc. Articles published by this Open-Access journal are distributed under the terms of the Creative Commons Attribution Non-commercial License, which permits use, distribution, and reproduction in any medium, provided the original work is properly cited, the use is non commercial and is otherwise in compliance with the license.

SPECIAL STATEMENT
All articles published in journals owned by the Baishideng Publishing Group (BPG) represent the views and opinions of their authors, and not the views, opinions or policies of the BPG, except where otherwise explicitly indicated.

INSTRUCTIONS TO AUTHORS
Full instructions are available online at http://www.wjnet.com/1949-8470/g_info_20100316162358.htm.

ONLINE SUBMISSION
<http://www.wjnet.com/esps/>

Treatment assessment of radiotherapy using MR functional quantitative imaging

Zheng Chang, Chunhao Wang

Zheng Chang, Chunhao Wang, Department of Radiation Oncology, Duke University, Durham, NC 27710, United States
Author contributions: Chang Z and Wang C wrote the paper; Chang Z approved the version to be published.

Conflict-of-interest: The authors have no conflict of interest related to the manuscript.

Open-Access: This article is an open-access article which was selected by an in-house editor and fully peer-reviewed by external reviewers. It is distributed in accordance with the Creative Commons Attribution Non Commercial (CC BY-NC 4.0) license, which permits others to distribute, remix, adapt, build upon this work non-commercially, and license their derivative works on different terms, provided the original work is properly cited and the use is non-commercial. See: <http://creativecommons.org/licenses/by-nc/4.0/>

Correspondence to: Zheng Chang, PhD, Associate Professor, Department of Radiation Oncology, Duke University, Duke University Rd, Durham, NC 27710, United States. zheng.chang@duke.edu
Telephone: +1-919-6812608
Fax: +1-919-6817183

Received: October 31, 2014

Peer-review started: October 31, 2014

First decision: November 14, 2014

Revised: November 24, 2014

Accepted: December 29, 2014

Article in press: December 31, 2014

Published online: January 28, 2015

Abstract

Recent developments in magnetic resonance (MR) functional quantitative imaging have made it a potentially powerful tool to assess treatment response in radiation therapy. With its abilities to capture functional information on underlying tissue characteristics, MR functional quantitative imaging can be valuable in assessing treatment response and as such to optimize therapeutic outcome. Various MR quantitative imaging techniques, including diffusion weighted imaging, diffusion tensor imaging, MR spectroscopy and dynamic contrast

enhanced imaging, have been investigated and found useful for assessment of radiotherapy. However, various aspects including data reproducibility, interpretation of biomarkers, image quality and data analysis impose challenges on applications of MR functional quantitative imaging in radiotherapy assessment. All of these challenging issues shall be addressed to help us understand whether MR functional quantitative imaging is truly beneficial and contributes to future development of radiotherapy. It is evident that individualized therapy is the future direction of patient care. MR functional quantitative imaging might serve as an indispensable tool towards this promising direction.

Key words: MR functional quantitative imaging; Radiation therapy; Treatment assessment

© The Author(s) 2015. Published by Baishideng Publishing Group Inc. All rights reserved.

Core tip: Treatment assessment using magnetic resonance (MR) functional quantitative imaging is the process of using such technique before and/or during and/or after the treatment course to evaluate the changes of functional information. In the area of radiation oncology, MR functional quantitative imaging can be used to quantify radiation-induced functional changes of both radiotherapy targets and critical organs. This article briefly reviews and discusses the basic principles of MR functional quantitative imaging, recent status, critical challenges and future perspectives on radiotherapy assessment. Future clinical trials and research works are needed to further develop MR functional quantitative imaging, towards the goal of individualized radiation therapy.

Chang Z, Wang C. Treatment assessment of radiotherapy using MR functional quantitative imaging. *World J Radiol* 2015; 7(1): 1-6 Available from: URL: <http://www.wjgnet.com/1949-8470/full/>

INTRODUCTION

Recent developments in magnetic resonance imaging (MRI) have substantially improved its performance, making it a potentially powerful tool for not only diagnosis but also treatment planning and assessment. Being an advanced MRI technique, MR functional quantitative imaging offers an approach to extract functional information from MR images. Compared with other functional imaging methods including positron emission tomography (PET) and single photon emission computed tomography on the nuclear medicine basis, MR functional quantitative imaging has a distinguished feature of estimating anatomical and functional information jointly in a single imaging session with potentially improved spatial resolution^[1]. In addition, the zero ionizing radiation risk enables MR functional quantitative imaging a good candidate for longitudinal *in vivo* studies, which require repeated acquisitions within a short period of time. In the past few years, MR functional quantitative imaging has been found valuable in treatment assessment.

Treatment assessment using MR functional quantitative imaging is the process of using such technique before, during and after the treatment course to evaluate the changes of functional information. In the area of radiation oncology, MR functional quantitative imaging can be used to quantify the radiation-induced functional changes of both radiotherapy targets and critical organs. For the optimal therapeutic outcome, the captured early functional change can be utilized to optimize the radiotherapy plan along the treatment course in aspect of fractionation altering, treatment target refinement and dose escalation^[2]. Thus, as an key component in the generalized concept of MR image-guided radiotherapy^[3,4], MR functional quantitative imaging might serve as an indispensable tool towards individualized radiotherapy^[5].

MR FUNCTIONAL QUANTITATIVE IMAGING

Conventional MRI techniques generally provide morphological information of tissue structure, with the superior soft tissue contrast in the anatomical scale. These techniques have demonstrated their effectiveness in the context of oncologic diagnosis and staging. Despite their popularity, the lack of quantitative approach limits conventional MR techniques' capacity in the derivation of biological processes that occur in the sub-anatomical scale. From radiotherapy perspective in oncologic treatment, it is important to recognize that functional properties, such as tumor cells density, tissue oxygenation, acidosis and microvessel activities, are important factors that influence the radiotherapy outcome *via* changing cell radiosensitivity^[6]. Thus, reliable functional information

is in demand to ensure the quality of radiotherapy. Over the past few decades, various MR quantitative methodologies have been developed for functional information assessment: Diffusion weighted imaging (DWI) reflects the cellular density *via* imaging the random motion of water molecules in the microscopic cellular environment. Under the same concept of capturing water mobility, diffusion tensor imaging (DTI) measures the anisotropic water diffusion process to characterize the tissue's microstructural organization. MR spectroscopy utilizes its sensitivity to chemical shift and measures the concentration of metabolites of interest. Functional MRI uses blood-oxygen-level-dependent signal variation to quantify local neuronal activity changes. Dynamic contrast-enhanced (DCE) and dynamic susceptibility contrast (DSC) imaging acquires the rapid dynamics of the intravenously administered low molecular-weight contrast agents to depict the process of microvessel kinetics. For easy appreciation, Figures 1-3 show the examples of brain DWI, DTI and DCE data before and after radiotherapy. Previous works have proved MR functional quantitative imaging as a valuable tool to assess radiotherapy response^[7-12]. However, various aspects including data reproducibility, interpretation of biomarkers, image quality and novel image analysis methodology all impose challenges on applications of MR functional quantitative imaging in radiotherapy assessment.

FUTURE PERSPECTIVES

Reproducibility of quantitative data

As defined by the Toward Quantitative Imaging task force of the Radiological Society of North America: Quantitative imaging is the extraction of quantitative information from clinical images, which can be used to assess change or status of an acute or chronic disease condition relative to normal^[13]. In reality, various imaging protocols, scanners and data analysis methods may compromise the reproducibility of data, especially when it comes to multiple center clinical trials. To achieve this goal, standardized acquisition protocols, data analysis and assessment shall be promoted for MR quantitative imaging. As part of these initiatives, the Quantitative Imaging Biomarkers Alliance was established in 2007. The mission of this initiative was to promote and achieve useful and cost-effective standardization across the community on a large scale^[13]. All of these efforts are to ensure that quantitative anatomical and physiological information can be accurately and precisely obtained from clinical images and as such can be applied to research and patient care.

Interpretation of biomarker

Though functional biomarkers serve as metrics for functional information evaluation, the physiologic meanings of the selected imaging biomarkers need to be fully examined towards the future clinical application. The interpretation of functional biomarkers quantitative

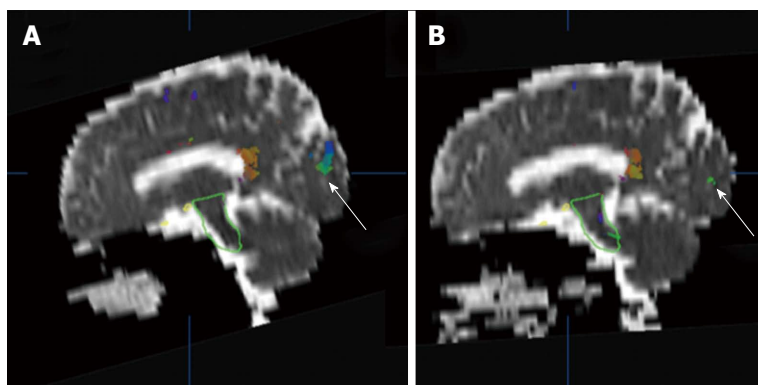


Figure 1 An example of brain apparent diffusion coefficient maps calculated from diffusion weighted images ($b = 500 \text{ mm}^2/\text{s}$) in a sagittal plane before (A) and after (B) radiotherapy. The white arrows indicate a comparison of superimposed colored maps of neural fiber bundles derived from diffusion tensor imaging data ($b = 500 \text{ mm}^2/\text{s}$).

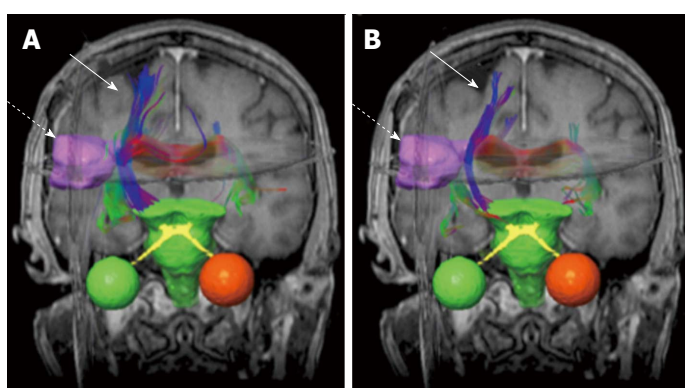


Figure 2 An example of brain neural fiber bundles (solid arrows) derived from diffusion tensor imaging data ($b = 500 \text{ mm}^2/\text{s}$). The pre-treatment (A) and post-treatment (B) results are superimposed on coronal T1-weighted magnetic resonance images. The dashed arrows indicate gross tumor volume (pink boundary).

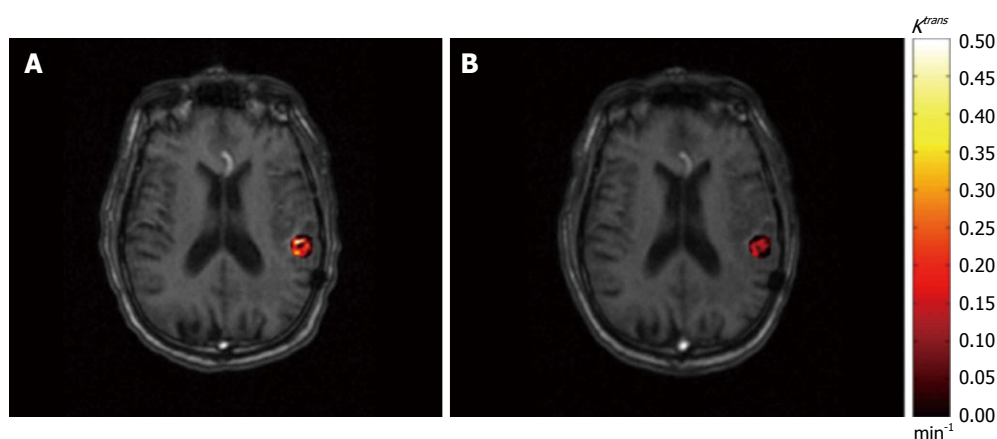


Figure 3 An example of permeability rate constant K^{trans} map derived from dynamic contrast-enhanced imaging. The pre-treatment (A) and post-treatment (B) K^{trans} results within gross tumor volume are superimposed on axial T1-weighted magnetic resonance images.

results may depend on the image technical parameters, imaging site, physiologic model selection, and patient's physiologic variability. For example, as the reported imaging biomarker in DWI, apparent diffusion coefficient (ADC) calculation is affected by the amplitude, duration and spacing of diffusion weighted gradient (jointly expressed as b value) in the pulse sequence. Studies have revealed that different selection of b value had influence on white

matter ADC value in brain analysis, and the variation of ADC value showed the potential effect in long-term assessment results^[14,15]. In addition, the varying size and location of tumor in different patients with rectal cancer have been shown to have a considerable effect on tumor ADC values^[16]. In DCE imaging, the nomenclature of tracer kinetics has been standardized. Nevertheless, when different pharmacokinetics (PK) model are adopted for

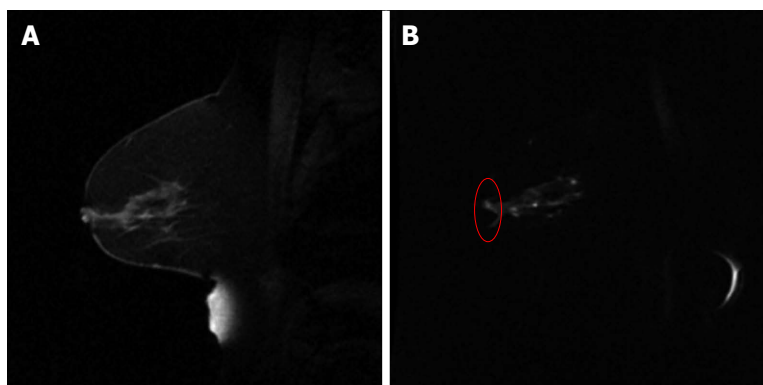


Figure 4 An example of sagittal breast T1w image (A) and the diffusion weighted image ($b = 500 \text{ mm}^2/\text{s}$) using echo planar imaging sequence (B). The red circle in (B) highlights the distorted breast boundary.

analysis, the parameters' may needs to be understood in different ways. Even when same PK model was used, large differences have been reported in the value of contrast agent transfer constant K^{trans} in tissue^[17,18]. Thus, for the accurate interpretation of functional biomarkers, the correlation of these biomarkers with histological markers shall be validated through rigorous and comprehensive studies. It is crucial to understand how and why these biomarkers can be correlated with clinical outcome.

It is also important to point out that the data consistency between results from MR functional quantitative imaging and those from other imaging modalities may also affect the validity of MR biomarkers' interpretation. For example, DSC imaging was developed for perfusion study and has been identified by the American Heart Association as a priority for acute stroke treatment^[19]. In the brain perfusion quantification, noticeable discrepancies of cerebral blood flow and cerebral blood volume were reported between DSC and gold standard PET measurements^[20,21]. Such discrepancies render the quantitative DSC study challenging and elusive. While some studies investigated methods correcting the data discrepancy in DSC studies^[22], the issue is not yet completed resolved. The recently emerging PET/MRI modality provides simultaneous MR and PET measurements and might be a valuable tool to help resolve the long standing issue^[23]. Future works on PET/MR perfusion research are needed to improve interpretation and quantification of MR perfusion biomarkers.

Image quality improvement

For the radiotherapy assessment purpose, it is important to recognize that image quality of MR functional quantitative imaging may potentially affect the quantitative assessment outcome. Of the factors that contribute to the image quality, spatial resolution is crucial for the precise delineation of target volume. In current state-of-art advanced radiation treatments such as stereotactic radiosurgery and stereotactic body radiotherapy, the target volume is often small while high radiation dose is delivered in a limited number of fractions. Therefore, the target volume needs to be accurately delineated with high spatial resolution to ensure the highly conformal

dose distribution. Therefore, clinical needs demand high spatial resolution MR functional quantitative imaging, which has not yet been well developed. Geometrical accuracy is another matter of concern for radiotherapy. As a commonly used imaging technique for clinical investigations, DWI suffers from geometrical deformations that are generally associated with the field inhomogeneity problem using echo-planar imaging sequence^[24] (Figure 4). In Brachytherapy, this deformation may have a prominent effect on treatment assessment, where the dose from radiation sources falls quadratically with the distance.

As another key factor of MR functional quantitative imaging quality, temporal resolution may affect the accuracy of the dynamics analysis. To assess the permeability and perfusion information using DCE imaging, the arterial input function (AIF) depicting the dynamics of tracers in arterial blood needs to be determined *via* imaging a major arterial structure in the imaged volume, and the fast acquisition of a second per volume is in demand for the reliable capture of rapid wash-in and wash-out features of AIF^[25]. However, because the current imaging time for a 3D volume is often not fast enough (to capture AIF information from a qualified arterial structure for such measurement), population-derived mathematical AIF models are widely used for DCE analysis instead. As simple approaches ignoring the individual physiologic features, these AIF models may introduce errors to the functional parameter results^[26]. Parallel imaging techniques have been proposed to accelerate the image acquisition, but the tradeoff of signal-to-noise ratio limits the reliability of the derived quantitative results^[27]. Recently, iterative MR reconstruction using undersampled image data with newly-developed mathematical concepts has been proposed. Though shown promising, the reproducibility of functional quantitative results needs to be validated with comprehensive studies.

Novel image analysis methodology

In treatment assessment, it is always critical to accurately interpret and analyze the functional data to reveal underlying context of a tumor or a specific critical organ.

Currently, metrics including the average/median value of a certain functional parameter within the region-of-interest and the target volume identified by thresholding the parametric map are widely reported in radiotherapies studies. Focusing on the absolute quantity, these approaches may miss the underlying morphological information hidden in the functional images. As an emerging topic in treatment assessment, image texture features have been investigated for their feasibilities of monitoring treatment assessment^[28-30]. As some of the texture features, especially the grey-tone spatial-dependence matrix (GTSDM) features, are defined independent of the parameter's absolute values, these texture features may be preferred in the case when the quantitative parameter values are not fully reliable. Another promising and interesting topic in the field is to use multiparametric functional MR for assessment purpose. With statistical approaches, multiparametric MR including both anatomical and functional images have been studied in tumor localization and staging^[31-33]. Since the mechanisms of some of the functional changes in response to radiotherapy have not been fully understood yet, the creditability of multiparametric MR study results in radiotherapy response may be undermined. With an ultimate goal of individualized radiotherapy, the imaging modalities, imaging parameters, statistical packages and other factors in multiparametric functional MR study need to be standardized and optimized to ensure adequate application to radiotherapy assessment.

CONCLUSION

Further development and research is needed to understand and validate whether MR quantitative imaging is truly beneficial to future radiotherapy treatment. Being a promising imaging modality, MRI not only plays a critical role in diagnosis, but also may lead the future directions of radiotherapy.

ACKNOWLEDGMENTS

The authors would like to thank Kevin Kelly in our department for his help with DCE-MRI data acquisition. We would also like to thank Taylor Richards for his comments and language improvements.

REFERENCES

- 1 Choyke PL, Dwyer AJ, Knopp MV. Functional tumor imaging with dynamic contrast-enhanced magnetic resonance imaging. *J Magn Reson Imaging* 2003; **17**: 509-520 [PMID: 12720260 DOI: 10.1002/jmri.10304]
- 2 van der Heide UA, Houweling AC, Groenendaal G, Beets-Tan RG, Lambin P. Functional MRI for radiotherapy dose painting. *Magn Reson Imaging* 2012; **30**: 1216-1223 [PMID: 22770686 DOI: 10.1016/j.mri.2012.04.010]
- 3 Crijs SP, Bakker CJ, Seevinck PR, de Leeuw H, Lagendijk JJ, Raaymakers BW. Towards inherently distortion-free MR images for image-guided radiotherapy on an MRI accelerator. *Phys Med Biol* 2012; **57**: 1349-1358 [PMID: 22349351 DOI: 10.1088/0031-9155/57/5/1349]
- 4 Verellen D, De Ridder M, Linthout N, Tournel K, Soete G, Storme G. Innovations in image-guided radiotherapy. *Nat Rev Cancer* 2007; **7**: 949-960 [PMID: 18034185 DOI: 10.1038/nrc2288]
- 5 Yaromina A, Krause M, Baumann M. Individualization of cancer treatment from radiotherapy perspective. *Mol Oncol* 2012; **6**: 211-221 [PMID: 22381063 DOI: 10.1016/j.mol-onc.2012.01.007]
- 6 Hall EJ, Giaccia AJ. Radiobiology for the Radiologist. Wolters Kluwer Health, 2006
- 7 Yankeelov TE, Lepage M, Chakravarthy A, Broome EE, Niernann KJ, Kelley MC, Meszoely I, Mayer IA, Herman CR, McManus K, Price RR, Gore JC. Integration of quantitative DCE-MRI and ADC mapping to monitor treatment response in human breast cancer: initial results. *Magn Reson Imaging* 2007; **25**: 1-13 [PMID: 17222711 DOI: 10.1016/j.mri.2006.09.006]
- 8 Haider MA, Chung P, Sweet J, Toi A, Jhaveri K, Ménard C, Warde P, Trachtenberg J, Lockwood G, Milosevic M. Dynamic contrast-enhanced magnetic resonance imaging for localization of recurrent prostate cancer after external beam radiotherapy. *Int J Radiat Oncol Biol Phys* 2008; **70**: 425-430 [PMID: 17881141 DOI: 10.1016/j.ijrobp.2007.06.029]
- 9 Kim S, Loevner L, Quon H, Sherman E, Weinstein G, Kilger A, Poptani H. Diffusion-weighted magnetic resonance imaging for predicting and detecting early response to chemoradiation therapy of squamous cell carcinomas of the head and neck. *Clin Cancer Res* 2009; **15**: 986-994 [PMID: 19188170 DOI: 10.1158/1078-0432.CCR-08-1287]
- 10 Lee SC, Poptani H, Pickup S, Jenkins WT, Kim S, Koch CJ, Delikatny EJ, Glickson JD. Early detection of radiation therapy response in non-Hodgkin's lymphoma xenografts by in vivo 1H magnetic resonance spectroscopy and imaging. *NMR Biomed* 2010; **23**: 624-632 [PMID: 20661875 DOI: 10.1002/nbm.1505]
- 11 Chang Z, Kirkpatrick JP, Wang Z, Cai J, Adamson J, Yin FF. Evaluating radiation-induced white matter changes in patients treated with stereotactic radiosurgery using diffusion tensor imaging: a pilot study. *Technol Cancer Res Treat* 2014; **13**: 21-28 [PMID: 23862743 DOI: 10.7785/tcrt.2012.500358]
- 12 White D, Mason RP. Non-invasive pre-clinical MR imaging of prostate tumor hypoxia for radiation therapy prognosis. *Int J Cancer Ther Oncol* 2014; **2**: 020243 [DOI: 10.14319/ijcto.0202.43]
- 13 Buckler AJ, Bresolin L, Dunnick NR, Sullivan DC. A collaborative enterprise for multi-stakeholder participation in the advancement of quantitative imaging. *Radiology* 2011; **258**: 906-914 [PMID: 21339352 DOI: 10.1148/radiol.10100799]
- 14 Ben Bashat D, Ben Sira L, Graif M, Pianka P, Hendler T, Cohen Y, Assaf Y. Normal white matter development from infancy to adulthood: comparing diffusion tensor and high b value diffusion weighted MR images. *J Magn Reson Imaging* 2005; **21**: 503-511 [PMID: 15834918 DOI: 10.1002/jmri.20281]
- 15 Zhou XJ, Gao Q, Abdullah O, Magin RL. Studies of anomalous diffusion in the human brain using fractional order calculus. *Magn Reson Med* 2010; **63**: 562-569 [PMID: 20187164 DOI: 10.1002/mrm.22285]
- 16 Lambregts DM, Beets GL, Maas M, Curvo-Semedo L, Kessels AG, Thywissen T, Beets-Tan RG. Tumour ADC measurements in rectal cancer: effect of ROI methods on ADC values and interobserver variability. *Eur Radiol* 2011; **21**: 2567-2574 [PMID: 21822946 DOI: 10.1007/s00330-011-2220-5]
- 17 Kozlowski P, Chang SD, Meng R, Mädler B, Bell R, Jones EC, Goldenberg SL. Combined prostate diffusion tensor imaging and dynamic contrast enhanced MRI at 3T--quantitative correlation with biopsy. *Magn Reson Imaging* 2010; **28**: 621-628 [PMID: 20392586 DOI: 10.1016/j.mri.2010.03.011]
- 18 Langer DL, van der Kwast TH, Evans AJ, Plotkin A, Trachtenberg J, Wilson BC, Haider MA. Prostate tissue composition and MR measurements: investigating the relationships between ADC, T2, K(trans), v(e), and corresponding histologic

- features. *Radiology* 2010; **255**: 485-494 [PMID: 20413761 DOI: 10.1148/radiol.10091343]
- 19 **Latchaw RE**, Yonas H, Hunter GJ, Yuh WT, Ueda T, Sorensen AG, Sunshine JL, Biller J, Wechsler L, Higashida R, Hademenos G. Guidelines and recommendations for perfusion imaging in cerebral ischemia: A scientific statement for healthcare professionals by the writing group on perfusion imaging, from the Council on Cardiovascular Radiology of the American Heart Association. *Stroke* 2003; **34**: 1084-1104 [PMID: 12677088 DOI: 10.1161/01.STR.0000064840.99271.9E]
- 20 **Calamante F**. Bolus dispersion issues related to the quantification of perfusion MRI data. *J Magn Reson Imaging* 2005; **22**: 718-722 [PMID: 16261569 DOI: 10.1002/jmri.20454]
- 21 **Xu G**, Rowley HA, Wu G, Alsop DC, Shankaranarayanan A, Dowling M, Christian BT, Oakes TR, Johnson SC. Reliability and precision of pseudo-continuous arterial spin labeling perfusion MRI on 3.0 T and comparison with 15O-water PET in elderly subjects at risk for Alzheimer's disease. *NMR Biomed* 2010; **23**: 286-293 [PMID: 19953503 DOI: 10.1002/nbm.1462]
- 22 **Shin W**, Horowitz S, Ragin A, Chen Y, Walker M, Carroll TJ. Quantitative cerebral perfusion using dynamic susceptibility contrast MRI: evaluation of reproducibility and age- and gender-dependence with fully automatic image postprocessing algorithm. *Magn Reson Med* 2007; **58**: 1232-1241 [PMID: 17969025 DOI: 10.1002/Mrm.21420]
- 23 **Wehrl HF**, Judenhofer MS, Wiehr S, Pichler BJ. Pre-clinical PET/MR: technological advances and new perspectives in biomedical research. *Eur J Nucl Med Mol Imaging* 2009; **36** Suppl 1: S56-S68 [PMID: 19194703 DOI: 10.1007/s00259-009-1078-0]
- 24 **Wu M**, Chang LC, Walker L, Lemaitre H, Barnett AS, Marenco S, Pierpaoli C. Comparison of EPI distortion correction methods in diffusion tensor MRI using a novel framework. *Med Image Comput Comput Assist Interv* 2008; **11**: 321-329 [PMID: 18982621 DOI: 10.1007/978-3-540-85990-1_39]
- 25 **Henderson E**, Rutt BK, Lee TY. Temporal sampling requirements for the tracer kinetics modeling of breast disease. *Magn Reson Imaging* 1998; **16**: 1057-1073 [PMID: 9839990 DOI: 10.1016/S0730-725x(98)00130-1]
- 26 **Wang CH**, Yin FF, Horton J, Chang Z. Review of treatment assessment using DCE-MRI in breast cancer radiation therapy. *World J Methodol* 2014; **4**: 46-58 [PMID: 25332905 DOI: 10.5662/wjm.v4.i2.46]
- 27 **Deshmane A**, Gulani V, Griswold MA, Seiberlich N. Parallel MR imaging. *J Magn Reson Imaging* 2012; **36**: 55-72 [PMID: 22696125 DOI: 10.1002/jmri.23639]
- 28 **Li KL**, Wilmes LJ, Henry RG, Pallavicini MG, Park JW, Hu-Lowe DD, McShane TM, Shalinsky DR, Fu YJ, Brasch RC, Hylton NM. Heterogeneity in the angiogenic response of a BT474 human breast cancer to a novel vascular endothelial growth factor-receptor tyrosine kinase inhibitor: assessment by voxel analysis of dynamic contrast-enhanced MRI. *J Magn Reson Imaging* 2005; **22**: 511-519 [PMID: 16161072 DOI: 10.1002/Jmri.20387]
- 29 **Karahaliou A**, Vassiou K, Arikidis NS, Skiadopoulos S, Kanavou T, Costaridou L. Assessing heterogeneity of lesion enhancement kinetics in dynamic contrast-enhanced MRI for breast cancer diagnosis. *Br J Radiol* 2010; **83**: 296-309 [PMID: 20335440 DOI: 10.1259/bjr/50743919]
- 30 **Alic L**, van Vliet M, van Dijke CF, Eggermont AM, Veenland JF, Niessen WJ. Heterogeneity in DCE-MRI parametric maps: a biomarker for treatment response? *Phys Med Biol* 2011; **56**: 1601-1616 [PMID: 21335648 DOI: 10.1088/0031-9155/56/6/006]
- 31 **Turkbey B**, Pinto PA, Mani H, Bernardo M, Pang Y, McKinney YL, Khurana K, Ravizzini GC, Albert PS, Merino MJ, Choyke PL. Prostate cancer: value of multiparametric MR imaging at 3 T for detection--histopathologic correlation. *Radiology* 2010; **255**: 89-99 [PMID: 20308447 DOI: 10.1148/radiol.09090475]
- 32 **Franiel T**, Stephan C, Erbersdobler A, Dietz E, Maxeiner A, Hell N, Huppertz A, Miller K, Strecker R, Hamm B. Areas suspicious for prostate cancer: MR-guided biopsy in patients with at least one transrectal US-guided biopsy with a negative finding--multiparametric MR imaging for detection and biopsy planning. *Radiology* 2011; **259**: 162-172 [PMID: 21233291 DOI: 10.1148/radiol.10101251]
- 33 **Hoeks CM**, Barentsz JO, Hambroek T, Yakar D, Somford DM, Heijmink SW, Scheenen TW, Vos PC, Huisman H, van Oort IM, Witjes JA, Heerschap A, Fütterer JJ. Prostate cancer: multiparametric MR imaging for detection, localization, and staging. *Radiology* 2011; **261**: 46-66 [PMID: 21931141 DOI: 10.1148/radiol.11091822]

P- Reviewer: Azevedo CF, Latsios G, Storto G, Wan YL

S- Editor: Song XX **L- Editor:** A **E- Editor:** Liu SQ



WJR 6th Anniversary Special Issues (2): Gastrointestinal imaging

Conventional radiological strategy of common gastrointestinal neoplasms

Yi-Zhuo Li, Pei-Hong Wu

Yi-Zhuo Li, Pei-Hong Wu, Imaging Diagnosis and Interventional Center, State Key Laboratory of Oncology in Southern China, Cancer Center, Sun Yat-sen University, Collaborative Innovation Center for Cancer Medicine, Guangzhou 510060, Guangdong Province, China

Author contributions: Li YZ and Wu PH both contributed to this paper.

Conflict-of-interest: The authors declare that they have no conflicting interests, commercial, personal, political, intellectual or religious.

Open-Access: This article is an open-access article which was selected by an in-house editor and fully peer-reviewed by external reviewers. It is distributed in accordance with the Creative Commons Attribution Non Commercial (CC BY-NC 4.0) license, which permits others to distribute, remix, adapt, build upon this work non-commercially, and license their derivative works on different terms, provided the original work is properly cited and the use is non-commercial. See: <http://creativecommons.org/licenses/by-nc/4.0/>

Correspondence to: Pei-Hong Wu, MD, Imaging Diagnosis and Interventional Center, State Key Laboratory of Oncology in Southern China, Cancer Center, Sun Yat-Sen University, Collaborative Innovation Center for Cancer Medicine, 651 Dongfeng Road East, Guangzhou 510060, Guangdong Province, China. wupeihong56@126.com

Telephone: +86-20-87343272

Fax: +86-20-87343272

Received: May 18, 2014

Peer-review started: May 19, 2014

First decision: June 27, 2014

Revised: November 21, 2014

Accepted: December 3, 2014

Article in press: December 10, 2014

Published online: January 28, 2015

or not at all invasive. A neoplasm may be manifested as various imaging findings, including mucosal disruption, soft mass, ulcer, submucosal invasion and lumen stenosis on barium studies. Benign tumors typically appear as smoothly marginated intramural masses. Malignant neoplasms most often appear as irregular infiltrative lesions on barium examination. Tumor extension to adjacent GI segments may be indistinct on barium images. Cross-sectional images such as computed tomography and magnetic resonance imaging may provide more accurate details of the adjacent organ invasion, omental or peritoneal spread.

Key words: Gastrointestinal; Barium enema; Computed tomography; Magnetic resonance imaging; Neoplasm

© The Author(s) 2015. Published by Baishideng Publishing Group Inc. All rights reserved.

Core tip: Gastrointestinal neoplasms are very common diseases. A neoplasm may be manifested as a wide spectrum of imaging findings. Barium studies are readily available for displaying primary malignancies in a short time and at low cost. Malignant neoplasms most often appear as irregular infiltrative lesions on barium examination. Cross-sectional imaging such as computed tomography or magnetic resonance imaging may provide more accurate details of the adjacent organ invasion, omental or peritoneal spread.

Li YZ, Wu PH. Conventional radiological strategy of common gastrointestinal neoplasms. *World J Radiol* 2015; 7(1): 7-16 Available from: URL: <http://www.wjgnet.com/1949-8470/full/v7/i1/7.htm> DOI: <http://dx.doi.org/10.4329/wjr.v7.i1.7>

Abstract

This article summarizes the clinical characteristics and imaging features of common gastrointestinal (GI) neoplasms in terms of conventional radiological imaging methods. Barium studies are readily available for displaying primary malignancies and are minimally

INTRODUCTION

The techniques of gastrointestinal (GI) radiology have



Figure 1 A 60-year-old male patient with squamous cell carcinoma in the first third section of esophagus. Polypoid-type lesions, presented as a filling defect with luminal narrowing and without ulceration.



Figure 2 A 60-year-old male with squamous cell carcinoma. On barium esophagography, infiltration in the upper third of esophageal carcinoma, with irregular luminal narrowing, mucosal destruction, dilatation and abrupt proximal borders. Prestenotic dilatation is also present.



Figure 3 A 59-year-old male with advanced esophageal carcinoma. Asymmetric stenosis of the first third esophagus, with central, large irregular ulceration, surrounded by a radiolucent rim of neoplastic infiltration.

changed dramatically in the last three decades. The basic mission of modern GI radiology is earlier diagnosis, a better avenue to evidence-based treatment options, to predict tumor response to treatment and non-invasive follow-up^[1].

Barium enema can provide valuable information. multislice computed tomography (CT) has proven to provide more valuable information for abdominal imaging. High-resolution magnetic resonance imaging (MRI) with its high soft tissue contrast has documented its clinical application in abdominal imaging. Positron emission tomography (PET) has excellent tissue penetration. However, apart from conventional imaging such as barium enema and multi-slice CT, the other options should increase their specificity and sensitivity using exogenous tracers or contrast agents.

The objective of this paper is to review the conventional radiological imaging of common GI neoplasms.

ESOPHAGEAL DISEASE

Esophageal carcinoma

About 80% of esophageal neoplasms are malignant and more than 90% of these are squamous cell carcinomas

(SCCs) or adenocarcinomas^[2].

SCC is the most common malignant esophageal neoplasm worldwide. It arises from epithelial cells with stratified squamous differentiation, which develops from precursor lesions of intraepithelial neoplasia^[3]. Alcohol and tobacco use are the most important risk factors for SCC of the esophagus. Most SCCs occur in the middle third of the esophagus, then the upper and lower third of the esophagus^[4,5]. Pathologically, SCCs appear as a variety of gross morphological types, polypoid mass, flat or ulcerated lesions. About 65% of SCC patients are men and the peak age range is from 60 to 74 years^[6]. Adenocarcinomas are the second common malignant tumor of the esophagus. The majority of esophageal adenocarcinomas develop from malignant degeneration of underlying Barrett epithelium, which are located in the distal esophagus, and the gastroesophageal junction, and these tumors have a tendency to invade the stomach^[7]. About 85% of esophageal adenocarcinoma patients are men^[2].

On barium esophagography, most SCCs show an infiltrative irregular luminal stricture, filling defect, with or without areas of ulceration (Figures 1-3).

On CT, esophageal cancer shows a soft tissue mass or localized irregular esophageal wall thickening, with irregular luminal narrowing. The located wall thickening may be asymmetrical in the early stage and concentric thickening in the advanced stage. The lesions usually show moderate enhancement (Figure 4). CT plays very important roles in evaluating the primary tumor, mediastinal invasion, lymph node involvement, distant metastases, such as liver, lungs and bones, and the complications of esophageal obstruction.

On MRI, esophageal carcinoma reveals an irregular soft tissue mass with low T1 weighted signal intensity and intermediate T2 weighted signal intensity. MRI was reported to be comparable to CT in evaluating the tumor's features, including local spread, distant metastases and lymph node involvement^[8,9].

On ¹⁸F-fluorodeoxyglucose-PET, esophageal carcinoma

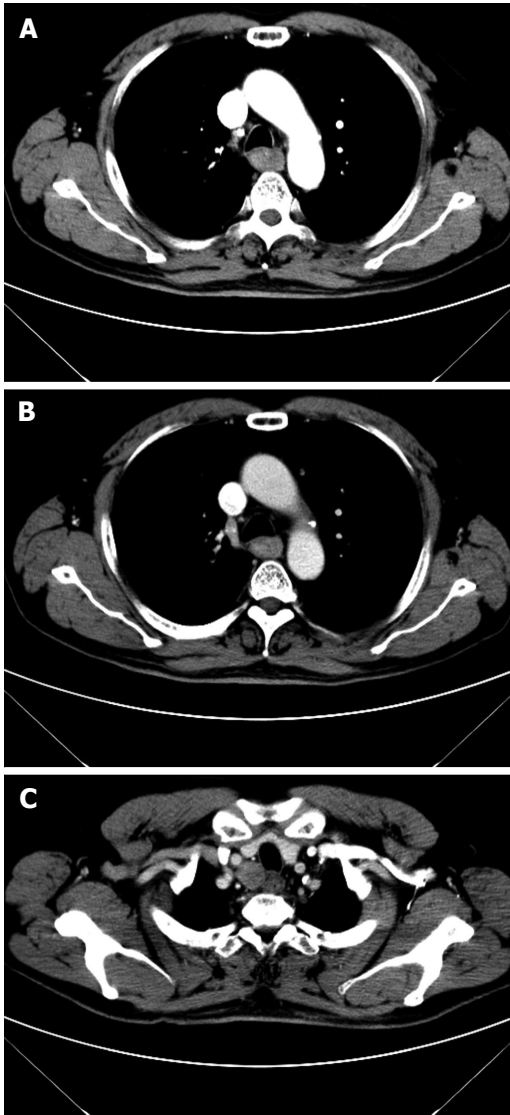


Figure 4 A 61-year-old male with squamous cell carcinoma in the first third section of esophagus. At computed tomography, esophageal cancer shows a soft tissue mass, with irregular luminal narrowing. The located wall thickening was asymmetric. The lesion shows moderate arterial phase enhancement (A) and slight venous phase enhancement (B). The enlarged lymph node metastasis is shown in the upper right paratracheal (C).

and its metastases show avid uptake value. However, the regional lymph nodes may be obscured by the high uptake tissue of primary tumor^[10].

Other malignant esophageal neoplasms

Leiomyosarcoma is a relatively more common malignant tumor of esophagus than the others, apart from esophageal carcinoma. On esophagography, this tumor shows intramural mass with large exophytic parts, with or without calcification and tracking areas. On CT images, they reveal heterogeneous mass with exophytic edge^[11]. On MRI, they appear as an intermediate signal intensity heterogeneous mass with exophytic edge on T1W images and slightly high signal intensity on T2W images.

The lesions usually show moderate arterial phase enhancement both on CT and MR images.

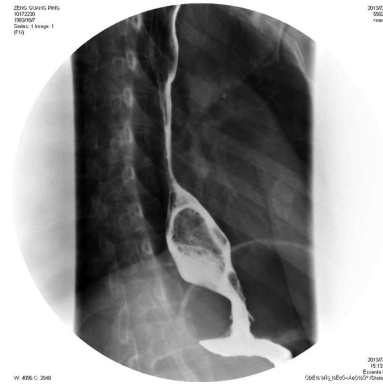


Figure 5 A 29-year-old female with leiomyoma. A large exophytic submucosal mass with a sharply defined, smooth filling defect is shown in the distal esophagus.

Benign esophageal neoplasms

Benign tumors are usually small and without ulceration, peritumoral invasion or distant metastases and do not cause symptoms, so less than 1% of esophageal tumors gain clinical attention^[12]. General imaging features of these tumors show a smooth intramural or intraluminal homogeneous mass, without necrosis or peritumoral spread.

Leiomyomas are the commonest benign esophageal neoplasm. They arise in the mature smooth muscle cells of the esophagus. Most patients with esophageal leiomyomas are asymptomatic, the rest may develop dysphagia or pain, depending on the lesion's size and the amount of encroachment on the esophageal lumen. On barium examination, an intramural mass with a sharply defined, smooth or lobulated filling defect forms the typical findings^[13] (Figure 5). On CT, esophageal leiomyomas show a sharply marginated homogeneous mass in the mid to lower third esophagus. These tumors show isoattenuating of slight hypoattenuating to muscle at nonenhanced CT and moderate enhancement, occasionally with coarse calcification (Figure 6). On MRI, slightly hyperintense at T2 weighted, slightly hypointense at T1 weighted images, and with moderate homogeneous enhancement without necrosis are shown^[14].

GASTRIC DISEASE

Gastric cancer

Most primary gastric cancers are adenocarcinoma. Adenocarcinoma represents over 95% of malignant tumors of the stomach^[15]. Common risk factors relating to the development of gastric adenocarcinoma include *Helicobacter pylori* infection^[16], chronic gastritis, pernicious anemia and adenomatous polyps^[17]. Gastric primary adenocarcinoma most often occurs in the gastric antrum, followed by the lesser curvature and cardia of the stomach.

Early gastric cancer: Radiologically, early gastric cancer is identified as a superficial lesion that is confined to the gastric mucosa and has not spread to the muscularis

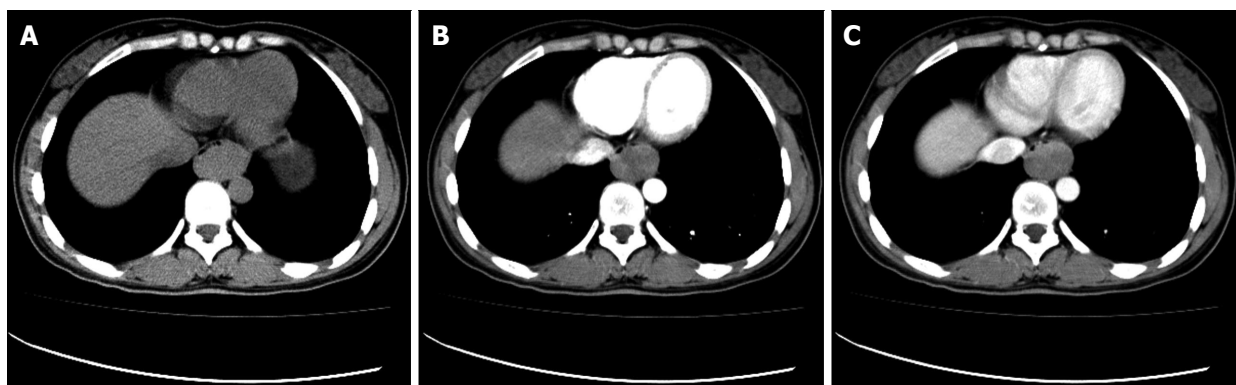


Figure 6 A 29-year-old female with leiomyoma. Esophageal leiomyoma shows sharply margined homogeneous mass in the lower third esophagus. These tumors show isoattenuating or slight hypoattenuating to muscle at non-enhanced computed tomography (A), moderate arterial (B) and venous (C) phase enhancement.

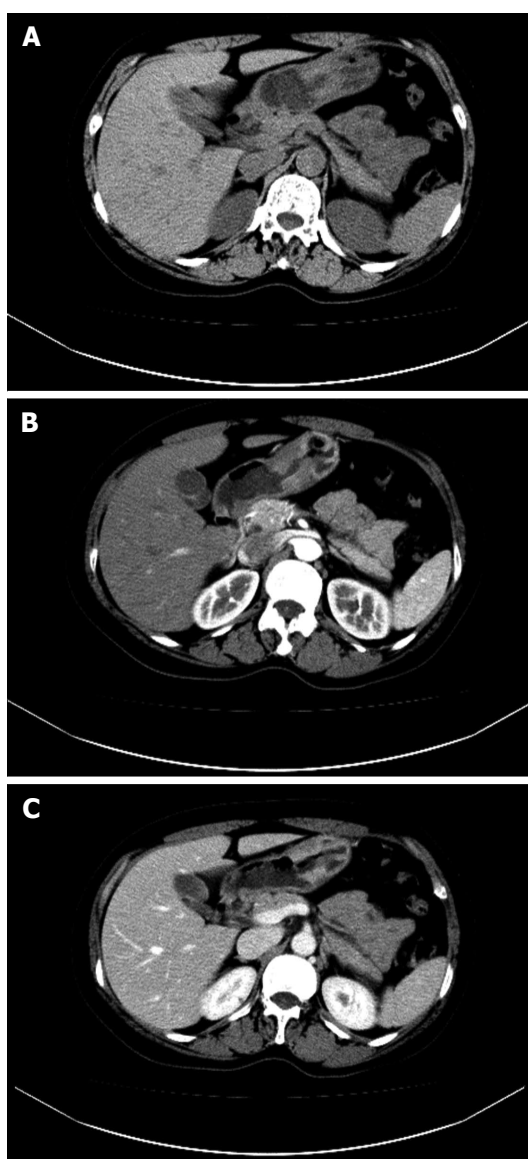


Figure 7 A 56-year-old female patient with early gastric carcinoma. Computed tomography scans showing thickening wall and narrowing antrum of stomach (A), moderate arterial (B) and venous (C) phase enhancement.

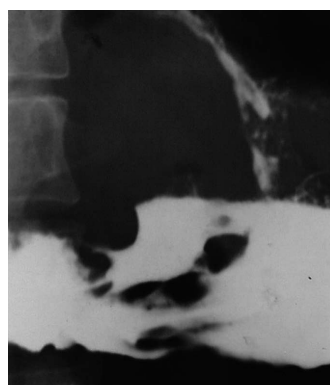


Figure 8 A 62-year-old male with ulcerated gastric carcinoma: a huge ulcerated mass is seen in the gastric antrum. The margins of the neoplasm's tissue surrounding the irregular ulcer are also seen.

propria. It may feature as polypoid, superficial or depressed lesions^[18]. The folds entering the center of the lesion are often irregular, nodular or club-shaped, or it may be manifested by a plaque-like elevation^[19]. On CT scans, gastric cancer is shown as thickening of the gastric wall (Figure 7). The major benefits of CT scanning in patients with gastric cancer are preoperative staging, treatment planning, prognosis evaluation and recurrence detection.

Advanced carcinoma: Advanced gastric carcinomas may be classified as polypoid, ulcerative or infiltrative lesions according to their gross morphological appearance. Imaging feature overlapping may occur in this classification^[17]. Polypoid-type tumors usually appear as a large mass lesion. The surface of the lesion may be highly irregular. Large lesions may protrude into the lumen^[20]. There may be a distinct angular demarcation or “shelf” at the tumor margins. When the lesion is located in the antrum, the tumor may obstruct the outlet of the stomach. Ulcerated-type carcinoma reveals an irregular ulcer crater. Radiating folds are irregular, converging at the edge of the ulcer crater^[20] (Figure 8). Infiltrative lesions display



Figure 9 A 56-year-old male. Diffuse, marked gastric narrowing, with irregular contour and thickened spiculated folds due to primary scirrhous carcinoma.

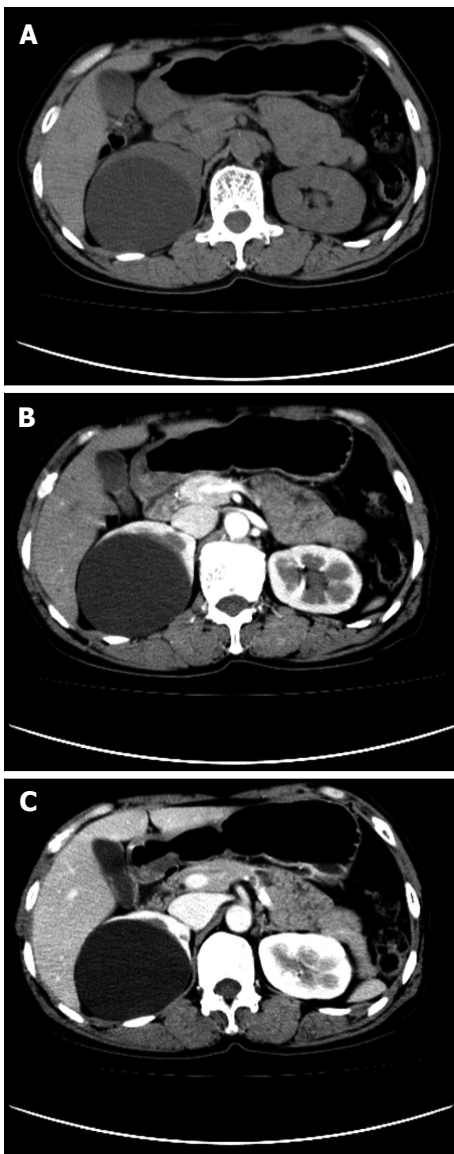


Figure 10 A 60-year-old female patient with mucosa-associated lymphoid tissue in gastric antrum. The tumor reveals as segmental, smooth homogeneous wall thickening on non-contrast computed tomography (A), minimal enhancement on arterial (B) and venous (C) phase enhancement.

a diffuse, predominantly submucosal infiltrative tumor, with irregular narrowing of the lumen and rigidity of the majority or the whole gastric wall due to the desmoplastic reaction, the so-called linitis plastica^[21] (Figure 9).

Gastric lymphoma

In adults, the stomach is the most frequent organ of GI tract lymphomas. Non-Hodgkin's lymphoma is more common than Hodgkin's disease^[22]. Much of this tumor spread is submucosal. The invasion of the gastric wall by the lymphoma is with relative flexibility. Findings of enlargement of the spleen and involvement of retrogastric and other regional lymph nodes are suggestive of lymphoma. On barium studies, gastric lymphoma reveals a nodular polypoid mass. The marked sign is thickened gastric folds^[23,24]. Its findings may mimic other tumors, such as adenocarcinoma and leiomyosarcoma.

On CT, gastric lymphoma reveals a segmental or diffuse, smooth homogeneous, isoattenuated (minimal enhancement), wall thickening or mass (Figure 10). Lymphoma usually involves more than one site of the stomach. It seldom leads to gastric outlet obstruction, unlike gastric adenocarcinoma, because lymphoma is a "soft" tumor^[25]. In contrast, gastric adenocarcinoma usually appears with more focal wall thickening, more enhancement, direct infiltration beyond the gastric wall, mural rigidity and luminal narrowing (linitis plastica), which may result in gastric outlet obstruction^[26].

Gastrointestinal stromal tumors

Gastrointestinal stromal tumors (GISTs) are the most frequent mesenchymal tumors of the GI tract which arise from the interstitial cells of Cajal. Previously, mesenchymal tumors of the GI tract were classified as leiomyosarcomas or leiomyomas^[27,28]. However, more and more evidence has suggested that GISTs are a unique entity and so GISTs were separated from leiomyomas and leiomyosarcomas. GISTs are now defined as spindle cell, epithelioid and pleomorphic mesenchymal tumors of the GI tract. GISTs express the KIT protein (CD117, stem cell factor receptor) detected at immunohistochemistry^[29-31]. This finding differentiates GISTs from leiomyomas, leiomyosarcomas, schwannomas and neurofibromas which do not express the KIT protein^[32]. The prolonged survival of GIST patients and the progress in the recognition of GISTs have made imaging more and more important for diagnosis and monitoring the treatment outcome. CT is the preferred option of imaging modality for these purposes^[33]. There are three important factors in determining the malignancy of GISTs: mitotic rate, tumor size and site^[34].

On CT, the frequent imaging findings of GISTs are of a round, exophytic, well-circumscribed heterogeneously enhancing tumor appearing as a mass extrinsic to the wall of the stomach (Figure 11). Central fluid attenuation indicative of necrosis is common in larger lesions. Smaller lesions may be homogeneous in density. The liver is the

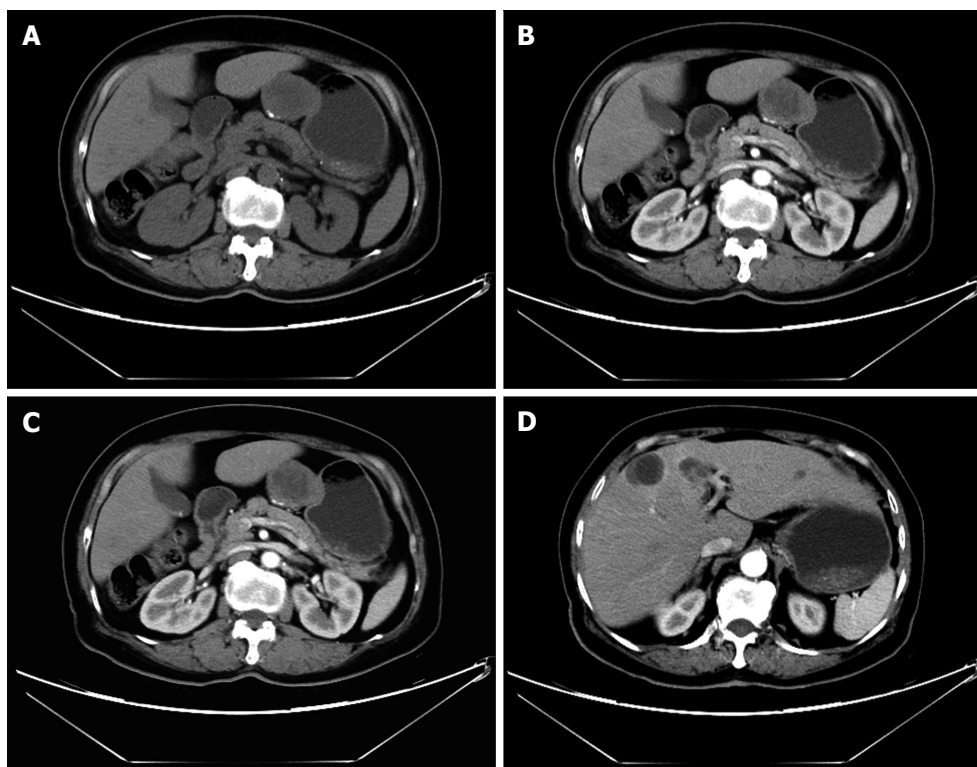


Figure 11 A 76-year-old female with gastrointestinal stromal tumors. Axial plain (A) shows an round, exophytic soft tissue mass, appearing as a dominant mass extrinsic to the wall of the stomach, contrast-enhanced computed tomography arterial (B) and venous phase (C) scan shows slightly enhancing, occasionally with coarse calcification. Liver metastases were shown (D).

most common site for metastasis^[35]. CT may display spreading to the adjacent organ, ascites and omental or peritoneal infiltrate. Associated lymphadenopathy is more infrequent than gastric adenocarcinoma or lymphoma^[28].

SMALL INTESTINAL NEOPLASMS

Primary neoplasms of the small intestine are rare. Primary tumors of the small intestine are less than 2% of primary GI tumors^[36,37]. They may occur in association with genetic diseases and chronic intestinal inflammatory disorders. The frequent benign tumors of the small intestine are leiomyoma, lipoma, hamartoma and desmoid tumors. These tumors are usually asymptomatic. The frequent small intestinal primary malignancies are adenocarcinoma, leiomyosarcoma and lymphoma. These tumors may lead to intestinal obstruction, jaundice and bleeding. Extraintestinal tumors may lead to peritoneal metastasis^[38].

Malignant neoplasms

Adenocarcinoma of the small intestine is frequent, approximately 30% to 50% of all malignant tumors in the small intestine^[39,40]. Proximal duodenum and jejunum is the usual site of primary small intestinal adenocarcinoma, except in the setting of Crohn's disease^[38,41]. Predisposing risk factors include villous adenomas, adenomatous polyps, celiac disease and long-standing Crohn's disease^[42,43]. The most frequent clinical features of small intestinal adenocarcinomas are obstruction, overt or occult GI

bleeding, weight loss and jaundice. Enteroclysis is a reliable sensitive diagnostic means for depicting intracavity small intestinal disease^[44,45]. The presence of extracavity spread or metastases can be evaluated with CT scan; in some instances, magnetic resonance imaging, EUS or angiography may also be useful^[38].

On barium examination, the general radiological appearances are filling defects, annular narrowing, polypoid and/or ulcerated masses, or a combination of these. Infiltrating adenocarcinomas are the most frequent type^[46,47]. These are almost revealed as short, sharply demarcated, annular constricting lesions with mucosal disruption. Polypoid-type adenocarcinomas may be displayed as large, irregular, polypoid-filling defects. Ulceration is common in adenocarcinomas. Mixed radiological features such as infiltrating, polypoid and ulcerating lesions indicate an advanced lesion. CT is used for demonstrating the intestine, mesentery, lymph nodes and liver metastases in a single examination and for staging the tumor, as well as follow-up after the treatment.

Lymphoma

Lymphoma is one of the most frequent tumors of the small intestine. Intestinal lymphomas are considered to be primary when the lesion is found in the small intestine and the clinical symptoms are related to intestinal invasion^[48]. The majority of small intestine lymphomas are non-Hodgkin's lymphomas (NHL)^[49] coming from mucosa-associated lymphoid tissue. This tumors are

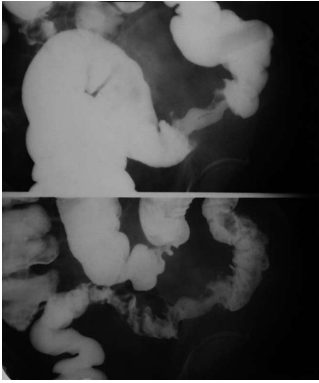


Figure 12 A 59-year-old female patient with sigmoid carcinoma. An annular stenosis of the sigmoid colon, with an irregular mucosal surface with contour deformity.

mostly located in the ileum. The lymphoid follicles of the submucosa are the site of origin of lymphoma as these are more numerous in the ileum than in the jejunum^[50].

On barium examination, the general radiological signs include luminal narrowing, cavitation, ulceration, valvulae conniventes thickening, discrete intraluminal filling defects and intramural masses^[48]. The frequent finding of NHL is the lumen narrowing without intestinal obstruction. A discrete, broad-based mass are characteristic radiological features of lymphomas^[48,51]. The valvulae conniventes thickening is a relatively less frequent finding of lymphoma^[20]. Focal aneurysmal dilatation is highly suggestive of lymphoma^[48].

CT and MRI can reveal the sites and extent of the tumor involvement, such as abdominal lymph nodes and solid viscera, and staging at a single examination. The lymphoma may be displayed as a homogeneous soft tissue mass with only a small intraluminal component. The tumors have only slight or moderate enhancement after the intravenous injection of contrast medium^[50].

Leiomyosarcoma

Leiomyosarcoma is the fourth most frequent primary small intestine tumor. It is equally distributed in the jejunum and ileum. Leiomyosarcomas are predominantly extraluminal and eccentric. Acute bleeding is the most common presenting symptom. Necrosis and hemorrhage are also frequent. Occasionally, less frequent signs may be seen: calcification, fistula formations and secondary infection^[46,47].

The most common radiological feature is a large irregular exophytic mass with or without ulceration, cavitation or fistula formation^[17]. There is marked enhancement of the solid component of the tumor following intravenous contrast medium^[52]. Less frequently, leiomyosarcoma may be displayed as a large irregular cavity filled with barium^[17].

Benign neoplasms

Leiomyomas are the most common primary benign tumors in the small bowel. The jejunum, ileum and duodenum are the most frequent locations^[53]. Leiomyomas

are usually single, firm soft tissue masses with well-defined margins. It is reported that there are four different types: intraluminal, intramural, extraluminal and dumbbell shaped^[54]. Microscopically, leiomyomas consist of bundles of well-differentiated smooth muscle with no evidence of mitosis. The absence of mitosis is a critical parameter in differentiating it from leiomyosarcoma^[38]. Leiomyomas are shown as regular smooth intramural filling defects on barium studies or regular homogenous soft tissue mass on CT scans. There is moderate enhancement of the tumor following intravenous contrast medium.

Adenomas are the most frequent asymptomatic small intestinal benign tumors. Histologically, there are three types: villous, tubular and tubulovillous. Villous with atypia and/or large size increase the risk for malignancy^[55]. Because of their potential for malignant transformation, these tumors should be resected or ablated endoscopically^[38]. The general radiological findings show adenomas as round smooth intraluminal filling defects on barium examination or smooth well-defined regular soft tissue mass on CT scans and with moderate enhancement after intravenous contrast medium.

COLORECTAL NEOPLASMS

Colorectal carcinoma

Colorectal carcinoma is an extremely common malignancy of the large bowel and in developed countries, it is one of the most frequent causes of death from cancer^[56]. Other types of malignant tumors, such as primary lymphoma and leiomyosarcoma are relatively rare^[17]. About 69% of carcinomas occur in the colon and only 31% of them are in the rectum and rectosigmoid junction^[57,58]. Usually, colorectal carcinomas are not diagnosed until they are relatively advanced.

Barium enema examination has been proven safe and accurate for detecting colorectal tumors. Early carcinoma usually presents as a polypoid lesion. Polyps show as filling defects in the barium column or as soft tissue densities coated with barium within the air-filled lumen. Larger polypoid lesions generally reveal an irregular and/or ulcerated mucosal surface^[17,59] (Figure 12). A flat ulcerating type of carcinoma is more frequent in the transverse and descending colon^[60]. Infiltrating type of carcinoma is featured by thickened bowel wall due to infiltrated submucosal and muscular layers^[61].

CT can be used for assessing the extension areas of the tumor, such as locoregional spreading and distant metastases^[62]. On CT scanning, the polypoid type reveals a bulky mass with lobulated margins. An infiltrating type appears with an eccentric or concentric thickening wall. The density of the lesion increases markedly after injection of contrast medium^[62] (Figure 13). CT may be used in assessing the extramural spread of tumor when extraintestinal infiltration is diagnosed in the presence of irregularity and dense stripes in the peri-intestinal adipose tissue. CT may also be used in assessment of the extension of any locoregional spread and distant



Figure 13 Sigmoid colon cancer in a 59-year-old female. Contrast-enhanced spiral computed tomography scan shows luminal narrowing and marked wall thickening. There is adjacent stranding of the serosa and mesenteric fat, a small lymph node anterior to the irregular thickening wall.

metastases, such as spreading to the adjacent or distant organs (bladder, vagina and abdominal and pelvic muscles). The liver is the most commonly infiltrated organ by metastases from colorectal cancer and CT has more than 90% sensitivity in diagnosing lesions larger than 1 cm^[63,64]. Complications of colorectal carcinoma include obstruction, perforation, pericolic abscess, ischemic colitis and intussusception.

Lymphoma

Other malignancies that invade the colon are rare. Primary lymphomas of the colon often involve the cecum and rectum and are non-Hodgkin in type. The tumors may appear as localized, large, extraluminal masses or constricting. Diffuse infiltration is the most frequent form of colonic lymphoma and is featured by nodules with intact mucosal surface and diffuse or segmental distribution^[17,23,24]. The local complications of lymphoma include perforation, pneumatosis coli and intussusception.

Polyps

A “polyp” is a raised mucosal lesion. This term does not imply any histological features. Metaplastic polyps are relatively more common in the rectum and less common in the colon. These have no malignant potential. Most adenomas are polyps. Adenomas are well-defined circumscribed areas of dysplastic epithelium. The overall pattern of the epithelium and stroma may be classified as tubular, villous or mixed. The significance of adenoma is its malignant potential. The imaging features created by a polyp depend on the angle at which it is viewed and its relationship to the barium pool. Several signs are described on the radiological features: (1) meniscus sign: en face view showing a clearly defined inner and outer margin of the meniscus; (2) increased density sign: on barium enema, polyps are intraluminal lesions coated with barium. The incident X-ray beam may pass through four layers of barium. These factors may increase the density. A localized area of “increased density” may also be drawn; and (3) filling defect: a polyp on the dependent wall

creates a “shadow” (low density area) in the barium pool. This feature is helpful in differentiating that the lesion is intraluminal. If the polyp is on the non-dependent wall, it may be hidden by the dense barium pool. To confirm the relationship between the lesions and the intestinal wall, it is helpful to turn the patients from side to side with the table flat and view the lesions at different angles.

In general, the radiological features of a polyp may be noted as six “S’s”: its site, size, shape (regular/irregular), surface texture (smooth, lobulated, very nodular), symmetry of the base (smooth/irregular, indrawn) and singularly or otherwise^[65]. Although polyposis syndrome is generally rare, it plays important roles in relation to cancer prevention, screening and genetic counseling.

CONCLUSION

Conventional radiographs can provide valuable information on detection, characterization, staging and prediction of treatment response of GI malignancies. However, barium imaging has some limited roles in staging GI tract tumors. Tumors spreading to adjacent GI segments and accompanying complications may not be disclosed by barium imaging. Cross-sectional imaging may provide more accurate details of the adjacent organ invasion, omental or peritoneal spread.

REFERENCES

- 1 **Hoeffel C**, Mulé S, Romaniuk B, Ladam-Marcus V, Bouché O, Marcus C. Advances in radiological imaging of gastrointestinal tumors. *Crit Rev Oncol Hematol* 2009; **69**: 153-167 [PMID: 18674926 DOI: 10.1016/j.critrevonc]
- 2 **Lewis RB**, Mehrotra AK, Rodriguez P, Levine MS. From the radiologic pathology archives: esophageal neoplasms: radiologic-pathologic correlation. *Radiographics* 2013; **33**: 1083-1108 [PMID: 23842973 DOI: 10.1148/rg.334135027]
- 3 **Glickman JN**. Section II: pathology and pathologic staging of esophageal cancer. *Semin Thorac Cardiovasc Surg* 2003; **15**: 167-179 [PMID: 12838487]
- 4 **Levine MS**, Laufer I, Yamada A. Tumors of the esophagus. In Laufer I, Levine MS (eds). *Double contrast radiology of the gastrointestinal tract*. Philadelphia: WB Saunders, 157-190
- 5 **Meyers MA**. Carcinoma of the esophagus: Imaging, staging and management. In Meyers MA (ed). *Neoplasms of the digestive tract: imaging, staging and management*. Philadelphia: Lippincott-Raven, 1998: 9-19
- 6 **Trivers KF**, Sabatino SA, Stewart SL. Trends in esophageal cancer incidence by histology, United States, 1998-2003. *Int J Cancer* 2008; **123**: 1422-1428 [PMID: 18546259 DOI: 10.1002/ijc.23691]
- 7 **Bosch A**, Frias Z, Caldwell WL. Adenocarcinoma of the esophagus. *Cancer* 1979; **43**: 1557-1561 [PMID: 445351]
- 8 **Riddell AM**, Hillier J, Brown G, King DM, Wotherspoon AC, Thompson JN, Cunningham D, Allum WH. Potential of surface-coil MRI for staging of esophageal cancer. *AJR Am J Roentgenol* 2006; **187**: 1280-1287 [PMID: 17056917]
- 9 **Takashima S**, Takeuchi N, Shiozaki H, Kobayashi K, Morimoto S, Ikezoe J, Tomiyama N, Harada K, Shogen K, Kozuka T. Carcinoma of the esophagus: CT vs MR imaging in determining resectability. *AJR Am J Roentgenol* 1991; **156**: 297-302 [PMID: 1898802]
- 10 **Bruzzi JF**, Munden RF, Truong MT, Marom EM, Sabloff BS,

- Gladish GW, Iyer RB, Pan TS, Macapinlac HA, Erasmus JJ. PET/CT of esophageal cancer: its role in clinical management. *Radiographics* 2007; **27**: 1635-1652 [PMID: 18025508]
- 11 Levine MS, Buck JL, Pantongrag-Brown L, Buetow PC, Hallman JR, Sobin LH. Leiomyosarcoma of the esophagus: radiographic findings in 10 patients. *AJR Am J Roentgenol* 1996; **167**: 27-32 [PMID: 8659399]
 - 12 Rice TW. Benign esophageal tumors: esophagoscopy and endoscopic esophageal ultrasound. *Semin Thorac Cardiovasc Surg* 2003; **15**: 20-26 [PMID: 12813685]
 - 13 Levine MS. Benign tumors of the esophagus: radiologic evaluation. *Semin Thorac Cardiovasc Surg* 2003; **15**: 9-19 [PMID: 12813684]
 - 14 Yang PS, Lee KS, Lee SJ, Kim TS, Choo IW, Shim YM, Kim K, Kim Y. Esophageal leiomyoma: radiologic findings in 12 patients. *Korean J Radiol* 2001; **2**: 132-137 [PMID: 11752983]
 - 15 Fishman EK, Urban BA, Hruban RH. CT of the stomach: spectrum of disease. *Radiographics* 1996; **16**: 1035-1054 [PMID: 8888389]
 - 16 Parsonnet J, Friedman GD, Vandersteen DP, Chang Y, Vogelstein JH, Orentreich N, Sibley RK. Helicobacter pylori infection and the risk of gastric carcinoma. *N Engl J Med* 1991; **325**: 1127-1131 [PMID: 1891020]
 - 17 Gourtsoyiannis N, Grammatikakis J, Prassopoulos P. Role of conventional radiology in the diagnosis and staging of gastrointestinal tract neoplasms. *Semin Surg Oncol* 2001; **20**: 91-108 [PMID: 11398203]
 - 18 Farley DR, Donohue JH. Early gastric cancer. *Surg Clin North Am* 1992; **72**: 401-421 [PMID: 1549800]
 - 19 White RM, Levine MS, Enterline HT, Laufer I. Early gastric cancer. Recent experience. *Radiology* 1985; **155**: 25-27 [PMID: 3975406]
 - 20 Levine MS, Megibow AJ. Carcinoma. In Gore RM, Levine MS, Laufer I (eds). Textbook of gastrointestinal radiology. Philadelphia: WB Saunders, 1994: 660-683
 - 21 Levine MS, Kong V, Rubesin SE, Laufer I, Herlinger H. Scirrhus carcinoma of the stomach: radiologic and endoscopic diagnosis. *Radiology* 1990; **175**: 151-154 [PMID: 2156284]
 - 22 Papadimitriou CS, Papacharalampous NX, Kittas C. Primary gastrointestinal malignant lymphomas. A morphologic and immunohistochemical study. *Cancer* 1985; **55**: 870-879 [PMID: 3917844]
 - 23 Dodd GD. Lymphoma of the hollow abdominal viscera. *Radiol Clin North Am* 1990; **28**: 771-783 [PMID: 2190270]
 - 24 Zornoza J, Dodd GD. Lymphoma of the gastrointestinal tract. *Semin Roentgenol* 1980; **15**: 272-287 [PMID: 7001640]
 - 25 Horton KM, Fishman EK. Current role of CT in imaging of the stomach. *Radiographics* 2003; **23**: 75-87 [PMID: 12533643]
 - 26 Gollub MJ. Imaging of gastrointestinal lymphoma. *Radiol Clin North Am* 2008; **46**: 287-312, ix [PMID: 18619382 DOI: 10.1016/j.rcl.2008.03.002]
 - 27 Clark RA, Alexander ES. Computed tomography of gastrointestinal leiomyosarcoma. *Gastrointest Radiol* 1982; **7**: 127-129 [PMID: 7084594]
 - 28 Pannu HK, Hruban RH, Fishman EK. CT of gastric leiomyosarcoma: patterns of involvement. *AJR Am J Roentgenol* 1999; **173**: 369-373 [PMID: 10430139]
 - 29 Miettinen M, Lasota J. Gastrointestinal stromal tumors-definition, clinical, histological, immunohistochemical, and molecular genetic features and differential diagnosis. *Virchows Arch* 2001; **438**: 1-12 [PMID: 11213830]
 - 30 Kindblom LG, Remotti HE, Aldenborg F, Meis-Kindblom JM. Gastrointestinal pacemaker cell tumor (GIPACT): gastrointestinal stromal tumors show phenotypic characteristics of the interstitial cells of Cajal. *Am J Pathol* 1998; **152**: 1259-1269 [PMID: 9588894]
 - 31 Fletcher CD, Berman JJ, Corless C, Gorstein F, Lasota J, Longley BJ, Miettinen M, O'Leary TJ, Remotti H, Rubin BP, Shmookler B, Sobin LH, Weiss SW. Diagnosis of gastrointestinal stromal tumors: A consensus approach. *Hum Pathol* 2002; **33**: 459-465 [PMID: 12094370]
 - 32 Hersh MR, Choi J, Garrett C, Clark R. Imaging gastrointestinal stromal tumors. *Cancer Control* 2005; **12**: 111-115 [PMID: 15855894]
 - 33 Bano S, Puri SK, Upreti L, Chaudhary V, Sant HK, Gondal R. Gastrointestinal stromal tumors (GISTs): an imaging perspective. *Jpn J Radiol* 2012; **30**: 105-115 [PMID: 22190071 DOI: 10.1007/s11604-011-0020-0]
 - 34 Miettinen M, El-Rifai W, H L Sobin L, Lasota J. Evaluation of malignancy and prognosis of gastrointestinal stromal tumors: a review. *Hum Pathol* 2002; **33**: 478-483 [PMID: 12094372]
 - 35 Burkill GJ, Badran M, Al-Muderis O, Meirion Thomas J, Judson IR, Fisher C, Moskovic EC. Malignant gastrointestinal stromal tumor: distribution, imaging features, and pattern of metastatic spread. *Radiology* 2003; **226**: 527-532 [PMID: 12563150]
 - 36 Landis SH, Murray T, Bolden S, Wingo PA. Cancer statistics, 1998. *CA Cancer J Clin* 1998; **48**: 6-29 [PMID: 9449931]
 - 37 Barclay TH, Schapira DV. Malignant tumors of the small intestine. *Cancer* 1983; **51**: 878-881 [PMID: 6821853]
 - 38 Gill SS, Heuman DM, Mihos AA. Small intestinal neoplasms. *J Clin Gastroenterol* 2001; **33**: 267-282 [PMID: 11588539]
 - 39 Brucher BL, Roder JD, Fink U, Stein HJ, Busch R, Siewert JR. Prognostic factors in resected primary small bowel tumors. *Dig Surg* 1998; **15**: 42-51 [PMID: 9845562]
 - 40 Ojha A, Zacherl J, Scheuba C, Jakesz R, Wenzl E. Primary small bowel malignancies: single-center results of three decades. *J Clin Gastroenterol* 2000; **30**: 289-293 [PMID: 10777190]
 - 41 Miller TL, Skucas J, Gudex D, Listinsky C. Bowel cancer characteristics in patients with regional enteritis. *Gastrointest Radiol* 1987; **12**: 45-52 [PMID: 3792758]
 - 42 Swinson CM, Slavin G, Coles EC, Booth CC. Coeliac disease and malignancy. *Lancet* 1983; **1**: 111-115 [PMID: 6129425]
 - 43 Collier PE, Turowski P, Diamond DL. Small intestinal adenocarcinoma complicating regional enteritis. *Cancer* 1985; **55**: 516-521 [PMID: 3965106]
 - 44 Maglinte DD, Kelvin FM, O'Connor K, Lappas JC, Chernish SM. Current status of small bowel radiography. *Abdom Imaging* 1996; **21**: 247-257 [PMID: 8661560]
 - 45 Bessette JR, Maglinte DD, Kelvin FM, Chernish SM. Primary malignant tumors in the small bowel: a comparison of the small-bowel enema and conventional follow-through examination. *AJR Am J Roentgenol* 1989; **153**: 741-744 [PMID: 2672733]
 - 46 Gourtsoyiannis NC, Nolan DJ. Primary malignant neoplasms: "Imaging of small intestinal tumours". Amsterdam: Elsevier, 1997: 105-189
 - 47 Gourtsoyiannis N, Makó E. Imaging of primary small intestinal tumours by enteroclysis and CT with pathological correlation. *Eur Radiol* 1997; **7**: 625-642 [PMID: 9166558]
 - 48 Gourtsoyiannis NC, Nolan DJ. Lymphoma of the small intestine: radiological appearances. *Clin Radiol* 1988; **39**: 639-645 [PMID: 3243056]
 - 49 Lewin KJ, Ranchod M, Dorfman RF. Lymphomas of the gastrointestinal tract: a study of 117 cases presenting with gastrointestinal disease. *Cancer* 1978; **42**: 693-707 [PMID: 354774]
 - 50 Grainger RG, Allison DJ, Baert A. Diagnostic radiology: A text book of medical imaging: Third edition, Volume two. 995-996
 - 51 Sartoris DJ, Harell GS, Anderson MF, Zboralske FF. Small-bowel lymphoma and regional enteritis: radiographic similarities. *Radiology* 1984; **152**: 291-296 [PMID: 6739786]
 - 52 Grainger RG, Allison DJ, Baert A. Diagnostic radiology: A text book of medical imaging: 3rd ed. Volume two. 996
 - 53 Blanchard DK, Budde JM, Hatch GF, Wertheimer-Hatch L, Hatch KF, Davis GB, Foster RS, Skandalakis JE. Tumors of the small intestine. *World J Surg* 2000; **24**: 421-429 [PMID: 10777190]

- 10706914]
- 54 **Starr GF**, Dockerty MB. Leiomyomas and leiomyosarcomas of the small intestine. *Cancer* 1955; **8**: 101-111 [PMID: 13231039]
- 55 **Bjork KJ**, Davis CJ, Nagorney DM, Mucha P. Duodenal villous tumors. *Arch Surg* 1990; **125**: 961-965 [PMID: 2378560]
- 56 **Padhani AR**. Advances in imaging of colorectal cancer. *Crit Rev Oncol Hematol* 1999; **30**: 189-199 [PMID: 10439064]
- 57 **Coates RJ**, Greenberg RS, Liu MT, Correa P, Harlan LC, Reynolds P, Fenoglio-Preiser CM, Haynes MA, Hankey BF, Hunter CP. Anatomic site distribution of colon cancer by race and other colon cancer risk factors. *Dis Colon Rectum* 1995; **38**: 42-50 [PMID: 7813344]
- 58 **Devesa SS**, Chow WH. Variation in colorectal cancer incidence in the United States by subsite of origin. *Cancer* 1993; **71**: 3819-3826 [PMID: 8508350]
- 59 **Laufer I**. Double contrast enema: technical aspects. In Laufer I, Levine MS (eds). Double contrast gastrointestinal radiology. Philadelphia: WB Saunders, 1992: 423-445
- 60 **Boland CR**. Malignant tumors of the colon. In Yamada T (ed). Textbook of gastroenterology. Philadelphia: Lippincott-Raven, 1995: 1967-2026
- 61 **Kelvin FM**. Diagnosis of colorectal cancer by conventional radiology. In Meyers MA (ed). Neoplasms of the digestive tract: imaging, staging and management. Philadelphia: Lippincott-Raven, 1998: 219-235
- 62 **Angelelli G**, Ianora AA, Scardapane A, Pedote P, Memeo M, Rotondo A. Role of computerized tomography in the staging of gastrointestinal neoplasms. *Semin Surg Oncol* 2001; **20**: 109-121 [PMID: 11398204]
- 63 **Leen E**, Angerson WJ, Wotherspoon H, Moule B, Cook TG, McArdle CS. Detection of colorectal liver metastases: comparison of laparotomy, CT, US, and Doppler perfusion index and evaluation of postoperative follow-up results. *Radiology* 1995; **195**: 113-116 [PMID: 7892449]
- 64 **Horton KM**, Abrams RA, Fishman EK. Spiral CT of colon cancer: imaging features and role in management. *Radiographics* 2000; **20**: 419-430 [PMID: 10715340]
- 65 **Grainger RG**, Allison DJ, Baert A. Diagnostic radiology: A text book of medical imaging: 3rd ed. Volume two. 1016-1021

P- Reviewer: Chiu KW, Tsushima Y, Verma S

S- Editor: Song XX **L- Editor:** Roemmele A **E- Editor:** Liu SQ



Fetal brain tumors: Prenatal diagnosis by ultrasound and magnetic resonance imaging

Hérbene José Milani, Edward Araujo Júnior, Sérgio Cavalheiro, Patrícia Soares Oliveira, Wagner Jou Hisaba, Enoch Quinderé Sá Barreto, Maurício Mendes Barbosa, Luciano Marcondes Nardozza, Antonio Fernandes Moron

Hérbene José Milani, Edward Araujo Júnior, Wagner Jou Hisaba, Enoch Quinderé Sá Barreto, Maurício Mendes Barbosa, Luciano Marcondes Nardozza, Antonio Fernandes Moron, Department of Obstetrics, Paulista School of Medicine-Federal University of São Paulo (EPM-UNIFESP), São Paulo 05303-000, Brazil

Sérgio Cavalheiro, Discipline of Neurosurgery, Paulista School of Medicine - Federal University of São Paulo (EPM-UNIFESP), São Paulo 05303-000, Brazil

Patrícia Soares Oliveira, Department of Diagnostic Imaging, Paulista School of Medicine - Federal University of São Paulo (EPM-UNIFESP), São Paulo 05303-000, Brazil

Author contributions: Milani HJ, Cavalheiro S, Oliveira PS and Barreto EQS designed and collected data; Milani HJ and Araujo Júnior E written of the article; Hisaba WJ and Barbosa MM reviewed the manuscript; Nardozza LM and Moron AF reviewed and supervised the manuscript.

Conflict-of-interest: The authors declare no conflict of interests.

Open-Access: This article is an open-access article which was selected by an in-house editor and fully peer-reviewed by external reviewers. It is distributed in accordance with the Creative Commons Attribution Non Commercial (CC BY-NC 4.0) license, which permits others to distribute, remix, adapt, build upon this work non-commercially, and license their derivative works on different terms, provided the original work is properly cited and the use is non-commercial. See: <http://creativecommons.org/licenses/by-nc/4.0/>

Correspondence to: Edward Araujo Júnior, PhD, Professor, Department of Obstetrics, Paulista School of Medicine-Federal University of São Paulo (EPM-UNIFESP), Rua Carlos Weber, 956, apto. 113 Visage, São Paulo 05303-000, Brazil. araujojred@terra.com.br

Telephone: +55-11-37965944
 Fax: +55-11-37965944

Received: August 20, 2014
 Peer-review started: August 20, 2014

First decision: November 3, 2014
 Revised: December 5, 2014

Accepted: December 18, 2014
 Article in press: December 19, 2014

Published online: January 28, 2015

Abstract

Congenital central nervous system tumors diagnosed during pregnancy are rare, and often have a poor prognosis. The most frequent type is the teratoma. Use of ultrasound and magnetic resonance image allows the suspicion of brain tumors during pregnancy. However, the definitive diagnosis is only confirmed after birth by histology. The purpose of this mini-review article is to describe the general clinical aspects of intracranial tumors and describe the main fetal brain tumors.

Key words: Fetus; Brain tumors; Teratoma; Ultrasound; Magnetic resonance imaging

© The Author(s) 2015. Published by Baishideng Publishing Group Inc. All rights reserved.

Core tip: Congenital central nervous system tumors diagnosed during pregnancy are rare, and often have a poor prognosis. The prenatal diagnosis is possible by ultrasound; however, the magnetic resonance imaging is important to demonstrate the relationship among the tumor and the adjacent structures. Although definitive diagnosis is realized after the birth, the prenatal diagnosis is very important to counseling of parents.

Milani HJ, Araujo Júnior E, Cavalheiro S, Oliveira PS, Hisaba WJ, Barreto EQS, Barbosa MM, Nardozza LM, Moron AF. Fetal brain tumors: Prenatal diagnosis by ultrasound and magnetic resonance imaging. *World J Radiol* 2015; 7(1): 17-21 Available from: URL: <http://www.wjgnet.com/1949-8470/full/v7/i1/17.htm>

INTRODUCTION

Congenital central nervous system (CNS) tumors are rare^[1]. The incidence of brain tumors in newborns is 0.34 per million live births and they represent 0.5%-1.5% of all pediatric CNS tumors^[2]. Many of the congenital brain tumors often result in intrauterine fetal demise, thus making the accurate assessment of the true incidence difficult^[3]. The literature primarily includes single case reports^[4].

In 1980 Hoff *et al*^[5] were the first to describe a brain teratoma diagnosed by ultrasound (US) in a fetus with 28 wk of gestation. Since then, other cases of congenital brain tumors have been reported during pregnancy. Teratomas and gliomas are the most frequent of them^[1].

Modern US machines and routine US scanning during pregnancy allows early diagnoses of these tumors during fetal period^[6]. The association among US and magnetic resonance image (MRI) has permitted more precise diagnoses of the congenital CNS tumors during pregnancy^[1]. However, the definitive diagnosis is only confirmed after birth by histology^[4]. In majority of cases their prognosis is poor. Neonates generally die shortly after birth, being the survival rate about 28%^[7,8]. Congenital brain tumors are usually sporadic and are not associated with other malformations^[3]. The purpose of this mini-review article is to describe the general clinical aspects of intracranial tumors and describe the main fetal brain tumors.

CLINICAL FEATURES OF FETAL BRAIN TUMORS

The clinical aspects of congenital CNS tumors are entirely different from those found in older children or adults. Large studies on fetal intracranial tumors have provided data about the different histologic subtypes^[3]. Congenital CNS tumors are divided into teratomas (most frequent described), and nonteratomatous tumors, including neuroepithelial tumors (choroid plexus papilloma, medulloblastoma, astrocytoma), mesenchymal tumors (such as craniopharyngioma), and others of different origin (such as lipoma of the corpus callosum and tuberous sclerosis, which may be found in cases of cardiac rhabdomyoma)^[9].

The cause of malignancies that occur in early life are unknown. Fetal and/or maternal exposure to exogenous factors, including drugs, viruses, and ionizing irradiation, may initiate the biological mechanisms responsible for tumor formation^[10]. Developmental errors during embryonic and fetal maturation may also result in congenital tumors^[11].

US imaging is the main method used to establish a correct diagnosis during pregnancy, once a solid, cystic, or calcified lesion has been observed. It is also the best

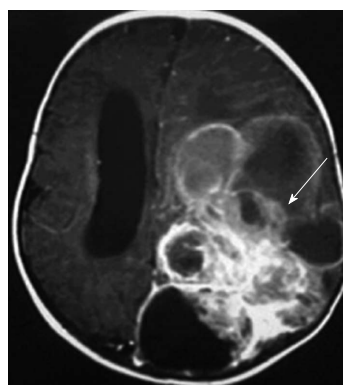


Figure 1 Case of anaplastic astrocytoma. Magnetic resonance imaging (T1 Fast Spin Echo, axial plane) 7 d after birth showing large parieto-occipital lesion with solid and cystic components (white arrow).

modality for evaluating fetal macrocrania^[12]. The contribution of MRI is relatively limited, but it may help in determining the remaining brain structures and exact localization of the tumor, as well as in differentiating between tumors and hemorrhages^[13]. The sequences performed in MRI in cases of congenital CNS tumors are: T2, T1 Fast Spin Echo, T1 and T2 gradient.

The main finding in prenatal diagnosis is an intracranial mass with solid, cystic or mixture pattern with or without visualization of hypervascularity by US and fetal MRI (Figure 1). The associated abnormalities include macrocrania or local skull swelling, secondary hydrocephalus, intracranial hemorrhage, epignathus, polyhydramnios, heart failure by high-cardiac output, and hydrops^[14]. Hydrocephaly is caused by either compression of the ventricular system or intracranial hemorrhage from the tumor^[3]. Unlike in older children, 70% of congenital fetal brain tumors are supratentorial and only 30% are infratentorial^[14].

During fetal period the skull has the remarkable ability to expand, so some congenital CNS tumors can expand enormously in utero (Figure 2), probably leading to dystocia and stillbirths. Large tumors are responsible for fetal hydrops and may necessitate decompression of the cranium to permit vaginal delivery^[15,16]. Cesarean section is necessary in approximately 60% of these cases^[17].

Some brain tumors are often large lesions, so it is important to assess tumoral extension by US or MRI. Precisely determining the extension of the tumor and the degree of involvement of adjacent structures is very important to determine the prognosis, the potential of the lesion for surgical resection, and the possible sequels of surgery^[4]. Karyotyping is not necessary to be performed in all cases of congenital CNS tumors, however it should be discussed if other malformations are present^[18]. Congenital brain tumors can mimic other brain pathologies, and main differential diagnoses are arachnoid cyst, vein of Galen aneurysm, porencephaly, schizencephaly, periventricular leukomalacia, and subdural hemorrhage^[14].

Prognosis in neonates is generally poor, but depends

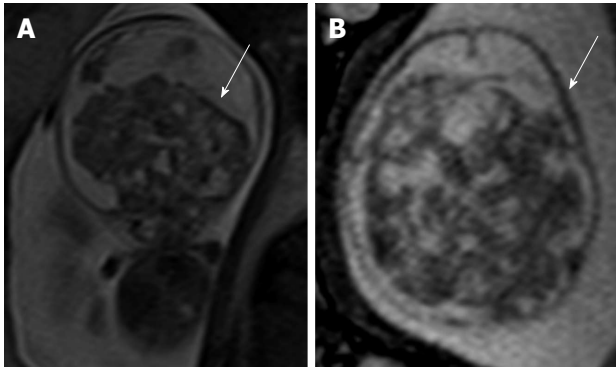


Figure 2 Fetus at 15 wk of gestation. Magnetic resonance imaging (T2 haste), (A) coronal plane, and (B) axial plane, showing a large lesion with solid and cystic components involving the whole brain (white arrows), and a severe macrocrania (cranial biometry for 30 wk). Histology confirmed immature teratoma.

on the timing of diagnosis and on the histological type of the tumor^[14]. Teratomas are the most frequent brain tumor found in fetuses, but their prognosis is very poor^[1]. Issacs *et al*^[7,8] reviewing 250 cases of brain tumor diagnosed during perinatal period concluded that choroid plexus papillomas, gliomas, and astrocytomas of a low degree have a better prognosis. On the other hand, teratomas and primitive neuroectoderms tumors have a bad prognosis (survival rate about 28%).

When an intracranial tumor is suspected, the option for termination of pregnancy should be offered, if legally possible. If termination of pregnancy is not allowed, cesarean section may be considered. In patients with severe hydrocephaly and/or macrocephaly, the possibility of dystocia should be contemplated and cephalocentesis considered for maternal reasons. However, obstetric management should not be modified in patients with choroid plexus papilloma and lipomas^[3]. Neurosurgical tumor resection and chemotherapy are possible treatments for neonatal tumors; instead, radiotherapy is not recommended in neonates^[14].

Intracranial teratoma

Teratomas are the most frequent type of congenital CNS tumors. They represent approximately 62% of all types of brain tumors diagnosed during pregnancy^[17]. The majority of fetal brain teratomas is histologically benign and generally contains both mature components from all three germ layers and immature neuroglial elements. Since the first US description by Hoff *et al*^[5] in 1980, approximately 100 reports on the prenatal diagnosis of fetal intracranial teratomas have been published^[3].

Their diagnoses are usually performed by US during the second or third trimester of gestation, being very rare the early diagnoses. The sonographic and MRI appearance of the intracranial teratoma is usually that of an irregular solid mass, in some cases with cystic and/or calcified components, distorting brain anatomy. MRI can help in determining the remaining brain structures and exact localization of the tumor (Figure 3). They

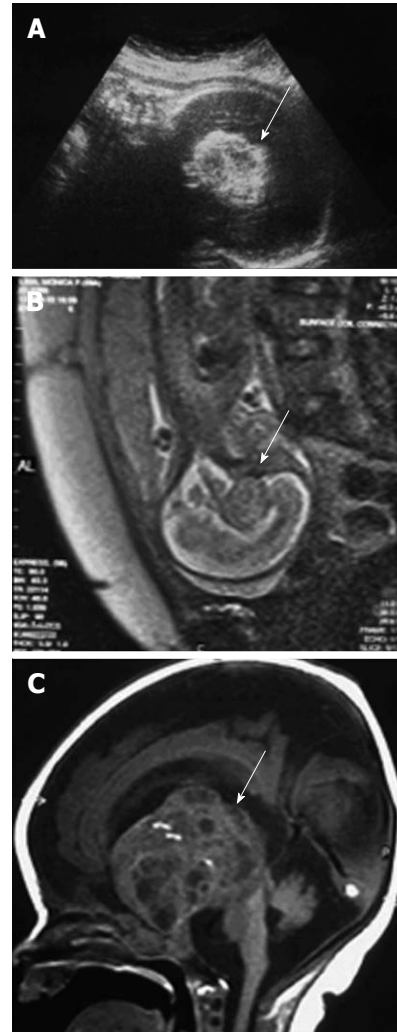


Figure 3 Teratoma. A: Ultrasound (US) at 29 wk of gestation (median sagittal plane) showing heterogeneous and hyperechogenic lesion in the suprasellar region (white arrow); B: Fetal magnetic resonance imaging (T2 haste, sagittal plane) at 29 wk of gestation confirming aspects observed on US (white arrow); C: Magnetic resonance imaging (T1 Fast Spin Echo, sagittal plane) 3 d after birth showing suprasellar lesion with solid and cystic components distorting brain anatomy (white arrow). Histology confirmed teratoma.

appear as a heterogeneous mass with hyperechogenic and hypoechogenic features. Color Doppler imaging may be useful to show vascularization in the tumor and helps to confirm the diagnosis. Brain teratoma presents rapidly growing, and may be associated with progressive hydrocephalus and polyhydramnios. Hydrocephalus may be responsible for macrocephaly and secondary dystocia by cephalopelvic disproportion^[19].

The prognosis for intracranial teratomas is generally poor, and the survival rate, which is dependent on the time of diagnosis and on the size of the teratoma, is low (under 10%)^[17,19].

Choroid plexus papilloma

Choroid plexus papilloma (CPP) is a rare and benign tumor composed of epithelial cells that line the ventricular choroid plexus, and correspond to 0.4%-0.6% of fetal intracranial tumors. The incidence is inversely

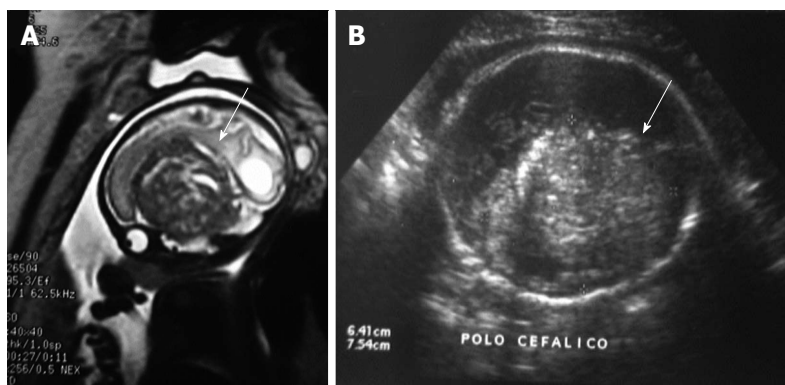


Figure 4 Craniopharyngioma. (A) Fetal magnetic resonance imaging (T2 hASTE, sagittal plane) and (B) ultrasound (axial plane) at 28 wk of gestation showing a heterogeneous and hyperechogenic suprasellar lesion and hydrocephalus (white arrows). Histology confirmed craniopharyngioma.

correlated with age, and 50% of patients in the pediatric age group are diagnosed during the first year of life^[20].

CPP may develop in the lateral ventricle, third ventricle, and fourth ventricle. It is generally diagnosed during the third trimester and is always associated with unilateral or bilateral ventriculomegaly^[3]. CPP has slow growth and noninvasive behavior; however, because of its specific location, CPP can block the drainage of cerebrospinal fluid and cause hydrocephalus.

An echogenic mass involving the choroid plexus is visualized on US and MRI. Color Doppler imaging may be useful to show vascularization in the lesion, facilitating the differential diagnosis of intraventricular hemorrhage^[3]. MRI is also useful in differentiating between hemorrhage and CPP.

CPP may be associated with Aicardi syndrome, a dominant X-linked chromosome syndrome, defined by a triad: partial or complete agenesis of the corpus callosum, lacunar chorioretinitis, and spasms^[21].

CPP has a good prognosis, but can become a carcinoma in 20% of cases, thus increasing the rate of mortality and morbidity.

Craniopharyngioma

Craniopharyngiomas are benign and represent 2%-5% of all congenital CNS tumors. They develop from remnants of squamous cells originating from Rathke's pouch (ectodermal diverticulum originating from the upper limit of the oropharynx) and are most commonly found in the suprasellar region^[22]. Although histologically benign, tumor expansion can cause significant destruction of the brain parenchyma and hydrocephalus.

An intracranial large echogenic mass (basically indistinguishable from teratomas) is diagnosed by US. MRI can help in determining the remaining brain structures and exact localization of the tumor (Figure 4). The head circumference may be increased because of the size of the tumor, and hydrocephalus may be present because of secondary obstruction of cerebrospinal fluid drainage^[4,21]. Differential diagnoses include: teratomas, astrocytomas, and hamartomas^[21].

In countries where termination of pregnancy is

permitted, it may be suggested in cases of early diagnosis, especially with progressive hydrocephalus^[23]. If the parents refuse to terminate the pregnancy or in countries where the law does not permit it, follow-up and elective delivery should be offered (according to the degree of macrocephaly and hydrocephalus)^[24].

CONCLUSION

Fetal brain tumors are very rare and their diagnosis during the prenatal period is challenging. The suspicion of this kind of lesion arises when it is observed a space-occupying mass in the fetal brain. Modern US machines and routine US scanning during pregnancy permit early detection of these tumors during fetal period. However, definitive diagnosis is only confirmed after birth by histology. Progress in technology has contributed to early diagnosis of congenital CNS tumors, but the same is not observed with fetal surgery, perhaps because the prognosis of fetal brain tumors remains poor. Fetal medicine centers should be composed of a multidisciplinary team acting together to provide better assistance for fetuses with congenital CNS tumors and to develop new methods of treatment.

REFERENCES

- 1 **Cavalheiro S**, Moron AF, Hisaba W, Dastoli P, Silva NS. Fetal brain tumors. *Childs Nerv Syst* 2003; **19**: 529-536 [PMID: 12908112 DOI: 10.1007/s00381-003-0770-9]
- 2 **Stiller CA**, Bunch KJ. Brain and spinal tumours in children aged under two years: incidence and survival in Britain, 1971-85. *Br J Cancer Suppl* 1992; **18**: S50-S53 [PMID: 1503926]
- 3 **Meizner I**. Tumors of the Brain. In: *Ultrasonography of the prenatal brain*. 3rd ed. McGraw-Hill: New York, 2012: 393-406
- 4 **Cassart M**, Bosson N, Garel C, Eurin D, Avni F. Fetal intracranial tumors: a review of 27 cases. *Eur Radiol* 2008; **18**: 2060-2066 [PMID: 18458906 DOI: 10.1007/s00330-008-0999-5]
- 5 **Hoff NR**, Mackay IM. Prenatal ultrasound diagnosis of intracranial teratoma. *J Clin Ultrasound* 1980; **8**: 247-249 [PMID: 6769967 DOI: 10.1002/jcu.1870080313]
- 6 **Palo P**, Penttinen M, Kalimo H. Early ultrasound diagnosis of fetal intracranial tumors. *J Clin Ultrasound* 1994; **22**: 447-450 [PMID: 7962593 DOI: 10.1002/jcu.1870220707]
- 7 **Isaacs H. I**. Perinatal brain tumors: a review of 250 cases. *Pediatr Neurol* 2002; **27**: 249-261 [PMID: 12435562 DOI: 10.1007/s00381-003-0770-9]

- 10.1016/S0887-8994(02)00459-9]
- 8 **Isaacs H. II.** Perinatal brain tumors: a review of 250 cases. *Pediatr Neurol* 2002; **27**: 333-342 [PMID: 12504200 DOI: 10.1016/S0887-8994(02)00472-1]
- 9 **Volpe JJ.** Brain tumors and vein of Galen malformation. In: *Neurology of the newborn*. 4th ed. WB Saunders: Philadelphia, 2001: 841-856
- 10 **Court brown WM, Doll R, Hill RB.** Incidence of leukaemia after exposure to diagnostic radiation in utero. *Br Med J* 1960; **2**: 1539-1545 [PMID: 13695977 DOI: 10.1136/bmj.2.5212.1539]
- 11 **Becker LE.** Central neuronal tumors in childhood: relationship to dysplasia. *J Neurooncol* 1995; **24**: 13-19 [PMID: 8523068 DOI: 10.1007/BF01052652]
- 12 **D'Addario V, Pinto V, Meo F, Resta M.** The specificity of ultrasound in the detection of fetal intracranial tumors. *J Perinat Med* 1998; **26**: 480-485 [PMID: 10224606 DOI: 10.1515/jpme.1998.26.6.480]
- 13 **Garel C.** MRI of the Fetal Brain: normal development and cerebral pathologies. Berlin: Springer, 2004: 267 [DOI: 10.1007/978-3-642-18747-6]
- 14 **Pooh RK, Pooh K.** Antenatal assessment of CNS anomalies, including neural tube defects. In: *Fetal and neonatal neurology and neurosurgery*. 4th ed. Philadelphia: Elsevier, 2009: 291-338 [DOI: 10.5005/jp/books/10305]
- 15 **Bolat F, Kayaselcuk F, Tarim E, Kilicdag E, Bal N.** Congenital intracranial teratoma with massive macrocephaly and skull rupture. *Fetal Diagn Ther* 2008; **23**: 1-4 [PMID: 17934288 DOI: 10.1159/000109216]
- 16 **Vibert-Guigue C, Gonzales M, Gouellet N, Zirah C, Milliez J, Carbonne B.** Vaginal delivery using cranioclasia following prenatal diagnosis of a giant fetal intracranial teratoma. *Fetal Diagn Ther* 2008; **23**: 222-227 [PMID: 18417982 DOI: 10.1159/000116745]
- 17 **Schlembach D, Bornemann A, Rupprecht T, Beinder E.** Fetal intracranial tumors detected by ultrasound: a report of two cases and review of the literature. *Ultrasound Obstet Gynecol* 1999; **14**: 407-418 [PMID: 10658280 DOI: 10.1046/j.1469-0705.1999.14060407.x]
- 18 **Schwartz S, Raffel LJ, Sun CC, Waters E.** An unusual mosaic karyotype detected through prenatal diagnosis with duplication of 1q and 19p and associated teratoma development. *Teratology* 1992; **46**: 399-404 [PMID: 1384156 DOI: 10.1002/tera.1420460410]
- 19 **Saada J, Enza-Razavi F, Delahaye S, Martinovic J, Macaleese J, Benachi A.** Early second-trimester diagnosis of intracranial teratoma. *Ultrasound Obstet Gynecol* 2009; **33**: 109-111 [PMID: 18991328 DOI: 10.1002/uog.6231]
- 20 **Galassi E, Godano U, Cavallo M, Donati R, Nasi MT.** Intracranial tumors during the 1st year of life. *Childs Nerv Syst* 1989; **5**: 288-298 [PMID: 2804999 DOI: 10.1007/BF00274516]
- 21 **Severino M, Schwartz ES, Thurnher MM, Rydland J, Nikas I, Rossi A.** Congenital tumors of the central nervous system. *Neuroradiology* 2010; **52**: 531-548 [PMID: 20428859 DOI: 10.1007/s00234-010-0699-0]
- 22 **Kawamata T, Kubo O, Hori T.** Histological findings at the boundary of craniopharyngiomas. *Brain Tumor Pathol* 2005; **22**: 75-78 [PMID: 18095108 DOI: 10.1007/s10014-005-0191-4]
- 23 **Lonjon M, Dran G, Casagrande F, Vandenbos F, Mas JC, Richelme C.** Prenatal diagnosis of a craniopharyngioma: a new case with radical surgery and review. *Childs Nerv Syst* 2005; **21**: 177-180 [PMID: 15290187 DOI: 10.1007/s00381-004-1019-y]
- 24 **Joó JG, Rigó J, Sápi Z, Timár B.** Foetal craniopharyngioma diagnosed by prenatal ultrasonography and confirmed by histopathological examination. *Prenat Diagn* 2009; **29**: 160-163 [PMID: 19180629 DOI: 10.1002/pd.2202]

P-Reviewer: Chu JP, Murai T, Pillai JJ, Shen J **S-Editor:** Ji FF
L-Editor: A **E-Editor:** Liu SQ



Retrospective Study

Comparison of conventional radiography and MDCT in suspected scaphoid fractures

Cyrus Behzadi, Murat Karul, Frank Oliver Henes, Azien Laqmani, Philipp Catala-Lehnen, Wolfgang Lehmann, Hans-Dieter Nagel, Gerhard Adam, Marc Regier

Cyrus Behzadi, Murat Karul, Frank Oliver Henes, Azien Laqmani, Gerhard Adam, Marc Regier, Center for Radiology and Endoscopy, Department of Diagnostic and Interventional Radiology, University Medical Center Hamburg-Eppendorf, 20246 Hamburg, Germany

Philipp Catala-Lehnen, Wolfgang Lehmann, Department of Hand-, Trauma-, and Reconstructive Surgery, University Medical Center Hamburg-Eppendorf, 20246 Hamburg, Germany

Hans-Dieter Nagel, Science and Technology for Radiology, 21244 Buchholz, Germany

Author contributions: Behzadi C and Karul M collected and analyzed the data equally; Henes FO and Laqmani A provided analytical oversight; Lehmann W and Catala-Lehnen P revised the manuscript; Adam G and Regier M designed and supervised the study; Nagel HD provided technical support, dose calculation and statistical analysis; all authors had taken part in literature research and manuscript preparation and had read and approved the final version.

Ethics approval: The study was reviewed and approved by the local ethics committee (WF-061/13).

Informed consent: Due to the retrospective study design exclusively involving data sets from past examinations taken from the local PACS system, no written informed consent was assessable.

Conflict-of-interest: None of the authors has to declare any conflict of interest in the presented study.

Data sharing: Technical appendix, statistical code, and dataset available from the corresponding author at c.bhezadi@uke.de. Informed consent was not obtained but the presented data are anonymized and risk of identification is low.

Open-Access: This article is an open-access article which was selected by an in-house editor and fully peer-reviewed by external reviewers. It is distributed in accordance with the Creative Commons Attribution Non Commercial (CC BY-NC 4.0) license, which permits others to distribute, remix, adapt, build upon this work non-commercially, and license their derivative works on different terms, provided the original work is properly cited and the use is non-commercial. See: <http://creativecommons.org/licenses/by-nc/4.0/>

Correspondence to: Cyrus Behzadi, MD, Center for Radiology and Endoscopy, Department of Diagnostic and Interventional Radiology, University Medical Center Hamburg-Eppendorf, Martinistrasse 52, 20246 Hamburg, Germany. c.bhezadi@uke.de

Telephone: +49-40-741054029

Fax: +49-40-741053802

Received: September 24, 2014

Peer-review started: September 24, 2014

First decision: November 19, 2014

Revised: November 28, 2014

Accepted: December 29, 2014

Article in press: December 31, 2014

Published online: January 28, 2015

Abstract

AIM: To determine the diagnostic accuracy and radiation dose of conventional radiography and multidetector computed tomography (MDCT) in suspected scaphoid fractures.

METHODS: One hundred twenty-four consecutive patients were enrolled in our study who had suffered from a wrist trauma and showed typical clinical symptoms suspicious of an acute scaphoid fracture. All patients had initially undergone conventional radiography. Subsequent MDCT was performed within 10 d because of persisting clinical symptoms. Using the MDCT data as the reference standard, a fourfold table was used to classify the test results. The effective dose and impaired energy were assessed in order to compare the radiation burden of the two techniques. The Wilcoxon test was performed to compare the two diagnostic modalities.

RESULTS: Conventional radiography showed 34 acute fractures of the scaphoid in 124 patients (42.2%). Subsequent MDCT revealed a total of 42 scaphoid fractures. The sensitivity of conventional radiography for scaphoid fracture detection was 42.8% and its specificity was 80% resulting in an overall accuracy of 59.6%. Conventional radiography was significantly inferior to MDCT ($P < 0.01$) concerning scaphoid

fracture detection. The mean effective dose of MDCT was 0.1 mSv compared to 0.002 mSv of conventional radiography.

CONCLUSION: Conventional radiography is insufficient for accurate scaphoid fracture detection. Regarding the almost negligible effective dose, MDCT should serve as the first imaging modality in wrist trauma.

Key words: Musculoskeletal imaging; Scaphoid fracture; Multidetector computed tomography; Biplane radiography; Emergency radiology; Diagnostic accuracy; Wrist trauma; Dose calculation

© The Author(s) 2015. Published by Baishideng Publishing Group Inc. All rights reserved.

Core tip: Correct diagnosis of acute wrist trauma with suspected scaphoid fractures is a challenging topic in every emergency department. Based on our data, conventional radiography has to be considered as insufficient for accurate scaphoid fracture detection. Regarding the high diagnostic accuracy and low effective dose of multidetector computed tomography, it should be implemented as the imaging modality of first choice in suspected fractures of the scaphoid.

Behzadi C, Karul M, Henes FO, Laqmani A, Catala-Lehnen P, Lehmann W, Nagel HD, Adam G, Regier M. Comparison of conventional radiography and MDCT in suspected scaphoid fractures. *World J Radiol* 2015; 7(1): 22-27 Available from: URL: <http://www.wjgnet.com/1949-8470/full/v7/i1/22.htm> DOI: <http://dx.doi.org/10.4329/wjr.v7.i1.22>

INTRODUCTION

Acute wrist trauma with suspected fracture of the scaphoid is a common presentation in an emergency department (ED) around the world. It is considered as the most common fracture of the carpal bones^[1-3].

Acute scaphoid fractures are widely seen in young, active adults^[1-5] or sportsmen^[6,7] who have experienced a fall on the outstretched hand. Usually, clinical examination and biplane radiography are the first diagnostic steps^[8]. Although snuffbox tenderness, limited range of motion and swelling are 3 any evidence of an acute fracture^[5,9,10].

Conversely, in a patient with only mild symptoms subsequent diagnostic imaging may demonstrate a dislocated fracture^[11].

In clinical practice, following a negative standard radiography patients are initially treated with immobilization using a plaster cast and an appointment is scheduled 7-14 d later including repeated biplane radiography^[12,13].

In a recent review study, Brookes-Fazakerley *et al*^[14] compared the imaging protocols between 130 institutions within the United Kingdom and demonstrated a huge inconsistency concerning the imaging practice in suspected

scaphoid fractures^[14]. Thirty-one percent of the institutions tend to perform a repeat radiograph at the first clinic review, within two weeks post-injury, although the limited value of this approach has been underlined before^[11,15].

In contrast to the international treatment, the German society of trauma (DGU) supports early cross-sectional imaging [multidetector computed tomography (MDCT)] in their guidelines^[8,16,17].

During the last decade, cross-sectional imaging has gained in prominence in the detection of scaphoid fractures. In particular, MDCT has achieved acceptance due to its high resolution, diagnostic accuracy and comparatively low cost^[18,19]. Further, due to consistent technical development the radiation burden of MDCT can be limited to a minimum, enhancing the use of MDCT in trauma imaging even in younger adults.

The purpose of the present study was to assess the diagnostic accuracy of standard radiography in patients with suspected scaphoid fracture in an intra-individual comparison to MDCT. Depending on these results, we intended to re-evaluate the diagnostic algorithm applied in acute wrist trauma with regard to time to recovery, radiation dose and financial cost estimation.

MATERIALS AND METHODS

Patient population

In this retrospective study the data sets of all patients admitted to the ED of our university medical center after acute wrist trauma and suspected scaphoid fracture between January 2011 and January 2013 were included. The local institutional review board approved this study, and informed consent was waived owing to the retrospective nature of the study.

The inclusion criteria were defined as follows: (1) Acute wrist trauma with suspected scaphoid fracture; (2) Snuffbox tenderness in the clinical examination; and (3) Initial biplane projection radiography and a MDCT scan of the wrist within an interval of less than 10 d. The exclusion criteria were set as follows: (1) Prior history of scaphoid fracture; and (2) Follow-up imaging after surgical intervention.

Applying this approach, a total of 124 patients were identified who met all inclusion criteria. Their mean age was 49 years \pm 21 (range 16-91 years) to a high extent representing working population. Sixty-six patients were male and fifty-eight patients were female.

Biplane radiography

Within the ED, biplane radiography was performed using a commercially available flat detector direct digital system (Digital Diagnost; Philips, Best, The Netherlands). Anterior-posterior, lateral and oblique projections were conducted. The central ray was centered on the proximal carpal bones. The imaging parameters were set as follows: tube current 1.9 mAs, 115 cm film-focus distance and voltage 50 kVp. Imaging was performed with the patient seated on a chair, placing his hand on the bucky table in

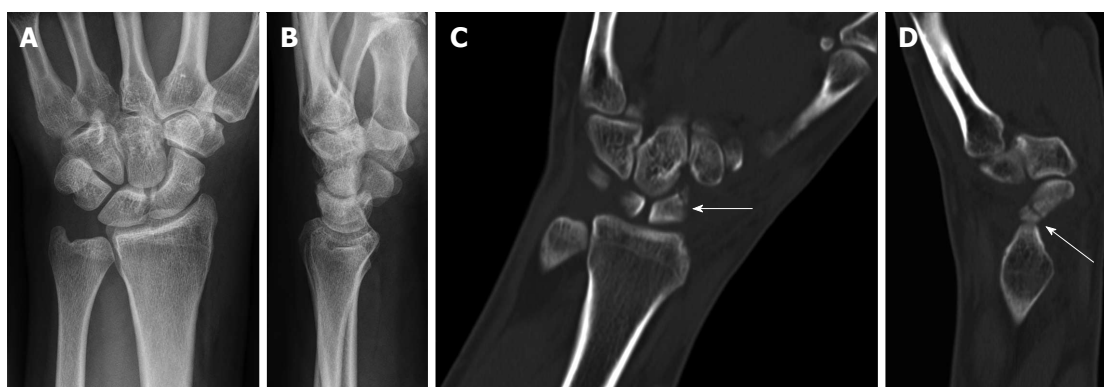


Figure 1 Non-dislocated fissural fracture of the scaphoid that had not been detected by initial conventional radiography (A and B). Cross-sectional multidetector computed tomography clearly depicted the oblique fissural fracture line in the middle third of the scaphoid with coronal (C) and sagittal (D) reformation on the same day.

three to four different positions. If present, casts were removed by a trauma surgeon for the imaging procedure.

MDCT

A 256-slice MDCT (Brilliance iCT; Philips Healthcare, Best, the Netherlands) was performed (voltage, 120 kVp; eff. current-time product, 70 mAs) on each patient, who was placed in the swimmer's position. Transverse images were reconstructed with a 1 mm slice thickness and an increment of 0.5 mm, creating an overlap of 50%. Further, coronal and sagittal reconstructions were post-processed with a slice thickness of 2 mm in standard bone window settings (Center, 1000 HU; Width, 2500 HU).

Key findings for scaphoid fractures at biplane radiography and MDCT: In the anterior-posterior and lateral view the three arcs of Gilula were analyzed searching for signs of carpal instability^[20]. The bone pattern, discontinuity of the cortex, avulsion fracture and subluxation of any carpal bone were examined.

The scapholunate joint space was analyzed as well as the soft tissues surrounding the scaphoid bone. In an acute scaphoid fracture the para scaphoid fat stripe can be obliterated and dorsal swelling can be observed^[21,22].

Dose calculation

For all MDCT data sets the dose length product ($\text{mGy} \times \text{cm}$) was determined. In biplane radiography we recorded the dose field product ($\text{dGy} \times \text{cm}^2$). For comparative reasons, as in imaging studies of the wrist only skin and bones contribute to the effective dose, other organs can be seen as irrelevant due to their distance from the cone-beam. Hence, the effective dose (Sv) of biplane radiography was assessed by calculating the impaired energy.

Image analysis

A maximum of ten days between the two imaging modalities was defined. All conventional radiographs and MDCT images were examined during daily practice by resident radiologists with two to five years of experience

in musculoskeletal radiology. Afterwards, all images were reviewed and confirmed by an attending radiologist with 10 years of experience in musculoskeletal Radiology. Finally, the consensus of the clinical examination and MDCT data was defined as the reference standard and the conventional reports were compared to these.

The focus of this study was to assess the relative sensitivities and specificities of the two modalities in a biased population i.e. those who in retrospect had both investigations within 10 d of each other.

A classification of the detected scaphoid fractures was not part of this investigation and therefore not analyzed.

Statistical analysis

A fourfold table was used to appraise the test results. The statistical analysis included sensitivity, specificity, positive and negative predictive value and the Wilcoxon test.

The authors confirm that the statistical analysis has been carried out with the help of a biomedical statistician prior to the initiation of the study as well as after image readout and final manuscript preparation.

RESULTS

Biplane radiography *vs* MDCT in patients who were analyzed in both modalities within 10 d because of a suspected scaphoid fracture:

Reading the conventional radiographs, 34 acute fractures of the scaphoid were diagnosed in 124 patients (42.2%, Figure 1). Sixteen fractures were classified as false positive in adjacent MDCT. A total of 42 scaphoid fractures were diagnosed in subsequent MDCT. The sensitivity of conventional radiography for scaphoid fracture detection was therefore 42.8% (18/42) with a specificity of 80.5% (66/82). Hence, the positive predictive value was 52.9% (18/34) whereas the negative predictive value was 73.3% (66/90), resulting in an overall accuracy of 59.6%.

In this intra-individual comparison, the statistical analysis revealed a distinct inferiority of scaphoid fracture detection by biplane radiography compared to the



Figure 2 Diagonal fracture line of the scaphoid detected by conventional radiography (A and B) and subsequently confirmed by multidetector computed tomography (C and D) for preoperative planning.

reference standard of MDCT ($P < 0.01$).

Secondary findings

Apart from 42 scaphoid fractures, MDCT revealed 66 further fractures in other locations in our patient population. MDCT depicted three fractures of the lunate, 11 fractures of the triquetrum, six of the trapezoid, three fractures of the capitate, three of the hamate, seven fractures of the metacarpals, 27 fractures of the distal radius and six fractures of the distal ulna.

In 27 patients a total of 33 additional fractures apart from a scaphoid fracture were diagnosed. Three fractures of the lunate, two fractures of the triquetrum, four fractures of the trapezoid, three fractures of the capitate, three of the hamate, two fractures of the metacarpals, 12 fractures of the distal radius and four fractures of the distal ulna were accompanied by a scaphoid fracture.

Biplane radiography depicted 41 of these 66 fractures. Twenty-five fractures were misdiagnosed as false negatives, including two lunate, seven triquetrum, four trapezoid, two capitate, three hamate (Figure 2), two metacarpal, four radius and one ulnar fracture. Twenty fractures were treated conservatively with a plaster cast and ambulatory treatment. One capitate, two hamate and two metacarpal fractures underwent subsequent surgery at the trauma department of our university medical center.

Estimation of radiation doses from radiography and MDCT

The mean effective dose at MDCT was 0.1 mSv. Conventional radiography included only 0.2% of the impaired energy compared to MDCT. Therefore, the effective dose of radiography was determined to be distinctly lower at 0.002 mSv.

DISCUSSION

The results of this study underline the limited diagnostic value of conventional radiography in acute scaphoid fractures. Investigating 124 subjects who underwent conventional radiography and MDCT within 10 d we determined a sensitivity of radiography for scaphoid

fracture detection of only 42.8%. The positive predictive value was as low as 52.9%. Moreover, in 24 patients conventional radiography suggested no fracture although subsequent MDCT could clearly demonstrate a fracture line (Figure 3). Therefore, it can be assumed that early diagnosis and treatment planning cannot be assured if diagnosis relies on biplane radiography only.

This is in concordance with recent reports supporting MDCT as a diagnostic modality of high diagnostic accuracy in scaphoid fracture detection^[23-26] whereas in these reports radiography also was of limited value^[23,25,27]. Stevenson *et al.*^[24] showed that using initial MDCT an occult scaphoid fracture can be ruled out with the patient returning to regular activity immediately. Acute scaphoid fractures are typically seen in young adults who fall on the outstretched hand^[7,25]. Patients who suffer from an acute scaphoid fracture are almost always part of the working population^[25,28]. Therefore an early identification of the injury can help to enable a fast return to work and therefore reduce the injury related socioeconomic impact.

The rate of late complications such as osteonecrosis, pseudarthrosis or chronic pain can be decreased. For example, the blood supply to the scaphoid is predominantly provided by dorsal branches of the radial artery which enter at the waist of the scaphoid^[29]. Therefore, dislocated and proximal pole fractures in particular need surgical treatment within a narrow time frame in order to prevent osteonecrosis. In concordance with other investigators, we therefore underline the shortcomings of relying on radiography exclusively^[23] and postulate the broad application of MDCT in the acute trauma setting of the wrist. The gains of a rapidly initialized therapy prevail over the possibility of any missed fracture and possible consequences. Based on the German medical fee schedule, comparing the costs of the diagnostic modalities, MDCT is about six times more expensive than conventional radiography (110.75 € *vs* 17.48 €). Concerning the adverse impact of severe complications and a delayed healing process on medical care expenses and socioeconomic ramifications, these costs can be considered as irrelevant.

There are many factors contributing to the poor results of conventional radiography: First of all, the

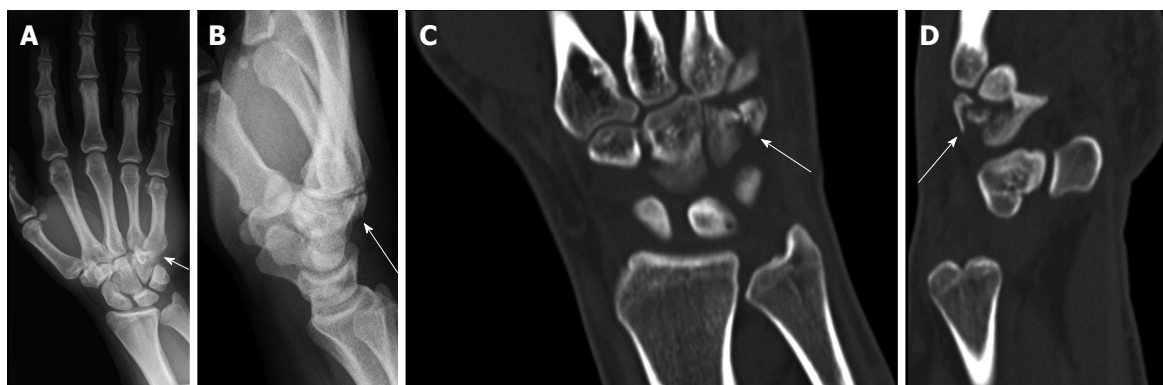


Figure 3 Conventional radiography (A and B) and multidetector computed tomography (C and D) revealed an acute hamate fracture as a secondary finding.

geometric structure of the scaphoid is complex and fractures are difficult to assess^[27,30]. Low inter-observer agreement^[7,31] is a known problem and even experienced radiologists may overlook scaphoid fractures^[30].

Taking the radiation burden into account, we investigated the impaired energy and effective dose values of radiography and MDCT in the diagnostic workup of the wrist. Indeed, the impaired energy of MDCT exceeded conventional radiography by far. Nevertheless, the effective dose of MDCT was calculated to be approximately 0.1 mSv. Compared to the yearly natural background radiation of approximately 2 mSv in Germany, the radiation dose of an MDCT of the wrist can be considered negligible as evaluated in a recent report^[32]. In addition to that, the common issue of radiation exposure from MDCT has been countered by the implementation of iterative reconstruction techniques which allow for a significant dose reduction of up to 75% without loss of anatomical information^[6,7,33].

We have not included magnetic resonance imaging^[11,15] or bone scintigraphy^[8,16,17] into our study design. Both modalities represent complementary imaging approaches which can be used to assess mid-hand fractures with a sensitivity comparable to MDCT^[11,15-17], but their availability within the emergency room setup is clearly limited. Therefore, the approach of image acquisition at 256 slice MDCT resembles the optimum most practical setting that can routinely be applied in daily trauma care.

Certain limitations of the presented study have to be addressed. First, the selection bias based on the exclusive investigation of patients with aggravated symptoms who underwent initial conventional radiography prior to MDCT has to be considered. Second, the retrospective study design has to be considered as a further limitation. Hence, a prospective evaluation of MDCT may be required to prospectively underline the presented findings of our study.

In conclusion, the results of the presented study underline the exceeding value of 256 slice MDCT in the diagnostic workup of acute wrist trauma in suspected scaphoid fractures. If trauma and clinical presentation are suggestive of any fracture, conventional radiography

should be ignored and replaced by MDCT as the diagnostic imaging approach of first choice and any hesitation due to elevated costs or radiation dose should no longer be sustained.

COMMENTS

Background

Scaphoid fractures are a challenging topic in every emergency department. In daily routine, initial X-ray often does not securely rule out a fracture and consequent multidetector computed tomography (MDCT) is added. In the presented study the authors analyzed the diagnostic accuracy of both entities and tried to formulate a new algorithm for daily clinical routine.

Research frontiers

Scaphoid fractures occur mainly in young and active people. They need an accurate and early diagnosis in order to minimize days of absence from work. Undetected or delayed diagnosed scaphoid fractures can lead to pseudarthrosis and prolonged pain.

Innovations and breakthroughs

Based on the authors' data, initial X-ray, which is requested in almost every patient suspected of a scaphoid fracture, is not necessary. The diagnostic accuracy of conventional radiography in scaphoid fractures is very poor. Many fractures are missed and not securely ruled out. MDCT is clearly superior and should be considered as necessary in every patient.

Applications

To the authors' opinion, MDCT should serve as the imaging modality of first choice in the diagnostic workup of suspected fractures of the scaphoid. The effective doses of MDCT of the wrist can be regarded as negligible and the patients benefit clearly supports the implementation.

Terminology

To knowledge, all unusual terms or abbreviations are explained in the context and should be understandable to the reader.

Peer review

This is a good paper suitable for publication.

REFERENCES

- 1 Munk PL, Lee MJ, Logan PM, Connell DG, Janzen DL, Poon PY, Worsley DF, Coupland D. Scaphoid bone waist fractures, acute and chronic: imaging with different techniques. *AJR Am J Roentgenol* 1997; **168**: 779-786 [PMID: 9057534]
- 2 Dunn AW. Fractures and dislocations of the carpus. *Surg Clin North Am* 1972; **52**: 1513-1538 [PMID: 4564432]
- 3 Brøndum V, Larsen CF, Skov O. Fracture of the carpal scaphoid: frequency and distribution in a well-defined population. *Eur J Radiol* 1992; **15**: 118-122 [PMID: 1425745 DOI: 10.1016/0720-048X(92)90135-V]

- 4 **Ring D**, Jupiter JB, Herndon JH. Acute fractures of the scaphoid. *J Am Acad Orthop Surg* 1999; **8**: 225-231 [PMID: 10951111]
- 5 **Parvizi J**, Wayman J, Kelly P, Moran CG. Combining the clinical signs improves diagnosis of scaphoid fractures. A prospective study with follow-up. *J Hand Surg Br* 1998; **23**: 324-327 [PMID: 9665518 DOI: 10.1016/S0266-7681(98)80050-8]
- 6 **Geyer LL**, Körner M, Hempel R, Deak Z, Mueck FG, Linsenmaier U, Reiser MF, Wirth S. Evaluation of a dedicated MDCT protocol using iterative image reconstruction after cervical spine trauma. *Clin Radiol* 2013; **68**: e391-e396 [PMID: 23537577 DOI: 10.1016/j.crad.2012.11.025]
- 7 **Barton N**. Sports injuries of the hand and wrist. *Br J Sports Med* 1997; **31**: 191-196 [PMID: 9298551 DOI: 10.1136/bjsm.31.3.191]
- 8 **Stürmer KMH**. Leitlinie Skaphoidfraktur. S1 Leitlinie, Deutsche Gesellschaft für Unfallchirurgie, 2008: 1-17
- 9 **Waizenegger M**, Barton NJ, Davis TR, Wastie ML. Clinical signs in scaphoid fractures. *J Hand Surg Br* 1994; **19**: 743-747 [PMID: 7706878 DOI: 10.1016/0266-7681(94)90249-6]
- 10 **Kozin SH**. Incidence, mechanism, and natural history of scaphoid fractures. *Hand Clin* 2001; **17**: 515-524 [PMID: 11775464]
- 11 **Hunter JC**, Escobedo EM, Wilson AJ, Hanel DP, Zink-Brody GC, Mann FA. MR imaging of clinically suspected scaphoid fractures. *AJR Am J Roentgenol* 1997; **168**: 1287-1293 [PMID: 9129428 DOI: 10.2214/ajr.168.5.9129428]
- 12 **Mulkens TH**, Marchal P, Daineffe S, Salgado R, Bellinck P, te Rijdt B, Kegelaers B, Termote JL. Comparison of low-dose with standard-dose multidetector CT in cervical spine trauma. *AJNR Am J Neuroradiol* 2007; **28**: 1444-1450 [PMID: 17846188 DOI: 10.3174/ajnr.A0608]
- 13 **Steinmann SP**, Adams JE. Scaphoid fractures and nonunions: diagnosis and treatment. *J Orthop Sci* 2006; **11**: 424-431 [PMID: 16897211 DOI: 10.1007/s00776-006-1025-x]
- 14 **Brookes-Fazakerley SD**, Kumar AJ, Oakley J. Survey of the initial management and imaging protocols for occult scaphoid fractures in UK hospitals. *Skeletal Radiol* 2009; **38**: 1045-1048 [PMID: 19194702 DOI: 10.1007/s00256-008-0640-3]
- 15 **Tiel-van Buul MM**, Roolker W, Broekhuizen AH, Van Beek EJ. The diagnostic management of suspected scaphoid fracture. *Injury* 1997; **28**: 1-8 [PMID: 9196618]
- 16 **Beeres FJ**, Rhemrev SJ, den Hollander P, Kingma LM, Meylaerts SA, le Cessie S, Bartlema KA, Hamming JF, Hogervorst M. Early magnetic resonance imaging compared with bone scintigraphy in suspected scaphoid fractures. *J Bone Joint Surg Br* 2008; **90**: 1205-1209 [PMID: 18757961 DOI: 10.1302/0301-620X.90B9.20341]
- 17 **Rhemrev SJ**, Ootes D, Beeres FJ, Meylaerts SA, Schipper IB. Current methods of diagnosis and treatment of scaphoid fractures. *Int J Emerg Med* 2011; **4**: 4 [PMID: 21408000]
- 18 **Kusano N**, Churei Y, Shiraishi E, Kusano T. Diagnosis of occult carpal scaphoid fracture: a comparison of magnetic resonance imaging and computed tomography techniques. *Tech Hand Up Extrem Surg* 2002; **6**: 119-123 [PMID: 16520609 DOI: 10.1097/00130911-200209000-00004]
- 19 **Hindman BW**, Kulik WJ, Lee G, Avolio RE. Occult fractures of the carpals and metacarpals: demonstration by CT. *AJR Am J Roentgenol* 1989; **153**: 529-532 [PMID: 2763950 DOI: 10.2214/ajr.153.3.529]
- 20 **Gilula LA**. Carpal injuries: analytic approach and case exercises. *AJR Am J Roentgenol* 1979; **133**: 503-517 [PMID: 111512 DOI: 10.2214/ajr.133.3.503]
- 21 **Terry DW**, Ramin JE. The navicular fat stripe: a useful roentgen feature for evaluating wrist trauma. *Am J Roentgenol Radium Ther Nucl Med* 1975; **124**: 25-28 [PMID: 1147160 DOI: 10.2214/ajr.124.1.25]
- 22 **Banerjee B**, Nashi M. Abnormal scaphoid fat pad: is it a reliable sign of fracture scaphoid. *Injury* 1999; **30**: 191-194 [PMID: 10476265 DOI: 10.1016/S0020-1383(98)00240-X]
- 23 **Welling RD**, Jacobson JA, Jamadar DA, Chong S, Caoili EM, Jebson PJ. MDCT and radiography of wrist fractures: radiographic sensitivity and fracture patterns. *AJR Am J Roentgenol* 2008; **190**: 10-16 [PMID: 18094287 DOI: 10.2214/AJR.07.2699]
- 24 **Stevenson JD**, Morley D, Srivastava S, Willard C, Bhoora IG. Early CT for suspected occult scaphoid fractures. *J Hand Surg Eur Vol* 2012; **37**: 447-451 [PMID: 22086787 DOI: 10.1177/1753193411428993]
- 25 **Hove LM**. Epidemiology of scaphoid fractures in Bergen, Norway. *Scand J Plast Reconstr Surg Hand Surg* 1999; **33**: 423-426 [PMID: 10614752 DOI: 10.1080/02844319950159145]
- 26 **Cruickshank J**, Meakin A, Breadmore R, Mitchell D, Pincus S, Hughes T, Bently B, Harris M, Vo A. Early computerized tomography accurately determines the presence or absence of scaphoid and other fractures. *Emerg Med Australas* 2007; **19**: 223-228 [PMID: 17564689 DOI: 10.1111/j.1742-6723.2007.00959.x]
- 27 **Puopolo SM**, Rettig ME. Management of acute scaphoid fractures. *Bull Hosp Jt Dis* 2003; **61**: 160-163 [PMID: 15156820]
- 28 **Krasin E**, Goldwirth M, Gold A, Goodwin DR. Review of the current methods in the diagnosis and treatment of scaphoid fractures. *Postgrad Med J* 2001; **77**: 235-237 [PMID: 11264484 DOI: 10.1136/pmj.77.906.235]
- 29 **Filan SL**, Herbert TJ. Herbert screw fixation of scaphoid fractures. *J Bone Joint Surg Br* 1996; **78**: 519-529 [PMID: 8682813]
- 30 **Gale SC**, Gracias VH, Reilly PM, Schwab CW. The inefficiency of plain radiography to evaluate the cervical spine after blunt trauma. *J Trauma* 2005; **59**: 1121-1125 [PMID: 16385289 DOI: 10.1097/01.ta.0000188632.79060.ba]
- 31 **Dorsay TA**, Major NM, Helms LA. Cost-effectiveness of immediate MR imaging versus traditional follow-up for revealing radiographically occult scaphoid fractures. *AJR Am J Roentgenol* 2001; **177**: 1257-1263 [PMID: 11717059]
- 32 **Biswas D**, Bible JE, Bohan M, Simpson AK, Whang PG, Grauer JN. Radiation exposure from musculoskeletal computerized tomographic scans. *J Bone Joint Surg Am* 2009; **91**: 1882-1889 [PMID: 19651945 DOI: 10.2106/JBJS.H.01199]
- 33 **Laqmani A**, Buhk JH, Henes FO, Klink T, Sehner S, von Schultendorff HC, Hammerle D, Nagel HD, Adam G, Regier M. Impact of a 4th generation iterative reconstruction technique on image quality in low-dose computed tomography of the chest in immunocompromised patients. *Rofo* 2013; **185**: 749-757 [PMID: 23749649 DOI: 10.1055/s-0033-1335577]

P- Reviewer: Pinto A S- Editor: Ji FF

L- Editor: A E- Editor: Liu SQ





Published by **Baishideng Publishing Group Inc**

8226 Regency Drive, Pleasanton, CA 94588, USA

Telephone: +1-925-223-8242

Fax: +1-925-223-8243

E-mail: bpgoffice@wjgnet.com

Help Desk: <http://www.wjgnet.com/esps/helpdesk.aspx>

<http://www.wjgnet.com>



World Journal of *Radiology*

World J Radiol 2015 February 28; 7(2): 28-56





Editorial Board

2014-2017

The *World Journal of Radiology* Editorial Board consists of 365 members, representing a team of worldwide experts in radiology. They are from 36 countries, including Afghanistan (1), Argentina (2), Australia (5), Austria (7), Belgium (2), Brazil (8), Canada (6), Chile (1), China (43), Croatia (1), Denmark (4), Egypt (6), France (5), Germany (22), Greece (10), India (12), Iran (6), Ireland (2), Israel (3), Italy (47), Japan (13), Netherlands (1), New Zealand (1), Pakistan (1), Poland (2), Portugal (1), Serbia (1), Singapore (3), Slovakia (1), South Korea (18), Spain (4), Sweden (2), Switzerland (4), Thailand (1), Turkey (26), United Kingdom (11), and United States (82).

EDITORS-IN-CHIEF

Kai U Juergens, *Bremen*
Edwin JR van Beek, *Edinburgh*
Thomas J Vogl, *Frankfurt*

GUEST EDITORIAL BOARD MEMBERS

Wing P Chan, *Taipei*
Chung-Huei Hsu, *Taipei*
Chin-Chang Huang, *Taipei*
Tsong-Long Hwang, *Taoyuan*
Jung-Lung Hsu, *Taipei*
Chia-Hung Kao, *Taichung*
Yu-Ting Kuo, *Tainan*
Hon-Man Liu, *Taipei*
Hui-Lung Liang, *Kaohsiung*
Chun Chung Lui, *Kaohsiung*
Sen-Wen Teng, *Taipei*
Yung-Liang (William) Wan, *Taoyuan*

MEMBERS OF THE EDITORIAL BOARD



Afghanistan

Takao Hiraki, *Okayama*



Argentina

Patricia Carrascosa, *Vicente Lopez*
Maria C Ziadi, *Rosario*



Australia

Lourens Bester, *Sydney*
Gemma A Figtree, *Sydney*



Austria

Herwig R Cerwenka, *Graz*
Gudrun M Feuchtnner, *Innsbruck*
Benjamin Henninger, *Innsbruck*
Rupert Lanzenberger, *Vienna*
Shu-Ren Li, *Vienna*
Veronika Schopf, *Vienna*
Tobias De Zordo, *Innsbruck*



Belgium

Steve Majerus, *Liege*
Kathelijne Peremans, *Merelbeke*



Brazil

Clerio F Azevedo, *Rio de Janeiro*
Patrícia P Alfredo, *São Paulo*
Eduardo FC Fleury, *São Paulo*
Edward Araujo Júnior, *São Paulo*
Wellington P Martins, *Ribeirao Preto*
Ricardo A Mesquita, *Belo Horizonte*
Vera MC Salemi, *São Paulo*
Claudia Szobot, *Porto Alegre*
Lilian YI Yamaga, *São Paulo*



Canada

Marie Arsalidou, *Toronto*
Otman A Basir, *Waterloo*

Tarik Zine Belhocine, *Toronto*
James Chow, *Toronto*
Tae K Kim, *Toronto*
Anastasia Oikonomou, *Toronto*



China

Hong-Wei Chen, *Wuxi*
Feng Chen, *Hangzhou*
Jian-Ping Chu, *Guangzhou*
Guo-Guang Fan, *Shenyang*
Bu-Lang Gao, *Shijiazhuang*
Qi-Yong Gong, *Chengdu*
Ying Han, *Beijing*
Xian-Li Lv, *Beijing*
Yi-Zhuo Li, *Guangzhou*
Xiang-Xi Meng, *Harbin*
Yun Peng, *Beijing*
Jun Shen, *Guangzhou*
Ze-Zhou Song, *Hangzhou*
Wai Kwong Tang, *Hong Kong*
Gang-Hua Tang, *Guangzhou*
Jie Tian, *Beijing*
Lu-Hua Wang, *Beijing*
Xiao-bing Wang, *Xi'an*
Yi-Gen Wu, *Nanjing*
Kai Wu, *Guangzhou*
Hui-Xiong Xu, *Shanghai*
Zuo-Zhang Yang, *Kunming*
Xiao-Dan Ye, *Shanghai*
David T Yew, *Hong Kong*
Ting-He Yu, *Chongqing*
Zheng Yuan, *Shanghai*
Min-Ming Zhang, *Hangzhou*
Yudong Zhang, *Nanjing*
Dong Zhang, *Chongqing*
Wen-Bin Zeng, *Changsha*

Yue-Qi Zhu, *Shanghai*



Croatia

Goran Kusec, *Osijek*



Denmark

Poul E Andersen, *Odense*

Lars J Petersen, *Aalborg*

Thomas Z Ramsøy, *Frederiksberg*

Morten Ziebell, *Copenhagen*



Egypt

Mohamed F Bazeed, *Mansoura*

Mohamed Abou El-Ghar, *Mansoura*

Reem HA Mohamed, *Cairo*

Mohamed R Nouh, *Alexandria*

Ahmed AKA Razek, *Mansoura*

Ashraf A Zytoon, *Shebin El-Koom*



France

Sabine F Bensamoun, *Compiègne*

Romarc Loffroy, *Dijon*

Stephanie Nougaret, *Montpellier*

Hassane Oudadesse, *Rennes*

Vincent Vinh-Hung, *Fort-de-France*



Germany

Henryk Barthel, *Leipzig*

Peter Bannas, *Hamburg*

Martin Beeres, *Frankfurt*

Ilja F Ciernik, *Dessau*

A Dimitrakopoulou-Strauss, *Heidelberg*

Peter A Fasching, *Erlangen*

Andreas G Schreyer, *Regensburg*

Philipp Heusch, *Duesseldorf*

Sonja M Kirchhoff, *Munich*

Sebastian Ley, *Munich*

Adel Maataoui, *Frankfurt am Main*

Stephan M Meckel, *Freiburg*

Hans W Muller, *Duesseldorf*

Kay Raum, *Berlin*

Dirk Rades, *Luebeck*

Marc-Ulrich Regier, *Hamburg*

Alexey Surov, *Halle*

Martin Walter, *Magdeburg*

Axel Wetter, *Essen*

Christoph Zilkens, *Düsseldorf*



Greece

Panagiotis Antoniou, *Thessaloniki*

Nikos Efthimiou, *Athens*

Dimitris Karnabatidis, *Patras*

George Latsios, *Athens*

Stylianios Megremis, *Iraklion*

Alexander D Rapidis, *Athens*

Kiki Theodorou, *Larissa*

Ioannis A Tsalafoutas, *Athens*

Evanthia E Tripoliti, *Ioannina*

Athina C Tsili, *Ioannina*



India

Ritesh Agarwal, *Chandigarh*

Chandan J Das, *New Delhi*

Prathamesh V Joshi, *Mumbai*

Naveen Kalra, *Chandigarh*

Chandrasekharan Kesavadas, *Trivandrum*

Jyoti Kumar, *New Delhi*

Atin Kumar, *New Delhi*

Kaushala P Mishra, *Allahabad*

Daya N Sharma, *New Delhi*

Binit Sureka, *New Delhi*

Sanjay Sharma, *New Delhi*

Raja R Yadav, *Allahabad*



Iran

Majid Assadi, *Bushehr*

SeyedReza Najafizadeh, *Tehran*

Mohammad Ali Oghabian, *Tehran*

Amir Reza Radmard, *Tehran*

Ramin Sadeghi, *Mashhad*

Hadi Rokni Yazdi, *Tehran*



Ireland

Tadhg Gleeson, *Wexford*

Frederik JAI Vernimmen, *Cork*



Israel

Dafna Ben Bashat, *Tel Aviv*

Amit Gefen, *Tel Aviv*

Tamar Sella, *Jerusalem*



Italy

Adriano Alippi, *Rome*

Dante Amelio, *Trento*

Michele Anzidei, *Rome*

Filippo F Angileri, *Messinas*

Stefano Arcangeli, *Rome*

Roberto Azzoni, *San Donato milanese*

Tommaso V Bartolotta, *Palermo*

Tommaso Bartalena, *Imola*

Livia Bernardin, *San Bonifacio*

Federico Boschi, *Verona*

Sergio Casciaro, *Lecce*

Emanuele Casciani, *Rome*

Musa M Can, *Napoli*

Alberto Cuocolo, *Napoli*

Michele Ferrara, *Coppito*

Mauro Feola, *Fossano*

Giampiero Francica, *Castel Volturno*

Luigi De Gennaro, *Rome*

Giulio Giovannetti, *Pisa*

Francesca Iacobellis, *Napoli*

Formato Invernizzi, *Monza Brianza*

Francesco Lassandro, *Naples*

Lorenzo Livi, *Florence*

Pier P Mainenti, *Napoli*

Laura Marzetti, *Chieti*

Giuseppe Malinverni, *Crescentino*

Enrica Milanese, *Turin*

Giovanni Morana, *Treviso*

Lorenzo Monti, *Milan*

Silvia D Morbelli, *Genoa*

Barbara Palumbo, *Perugia*

Cecilia Parazzini, *Milan*

Stefano Pergolizzi, *Messina*

Antonio Pinto, *Naples*

Camillo Porcaro, *Rome*

Carlo C Quattrocchi, *Rome*

Alberto Rebonato, *Perugia*

Giuseppe Rizzo, *Rome*

Roberto De Rosa, *Naples*

Domenico Rubello, *Rovigo*

Andrea Salvati, *Bari*

Sergio Sartori, *Ferrara*

Luca M Sconfienza, *Milano*

Giovanni Storto, *Rionero*

Nicola Sverzellati, *Parma*

Alberto S Tagliafico, *Genova*

Nicola Troisi, *Florence*



Japan

Yasuhiko Hori, *Chiba*

Hidetoshi Ikeda, *Koriyama*

Masahito Kawabori, *Sapporo*

Tamotsu Kamishima, *Sapporo*

Hiro Kiyosue, *Yufu*

Yasunori Minami, *Osaka-sayama*

Yasuhiro Morimoto, *Kitakyushu*

Satoru Murata, *Tokyo*

Shigeki Nagamachi, *Miyazaki*

Hiroshi Onishi, *Yamanashi*

Morio Sato, *Wakayama Shi*

Yoshito Tsushima, *Maebashi*

Masahiro Yanagawa, *Suita*



Netherlands

Willem Jan van Rooij, *Tilburg*



New Zealand

W Howell Round, *Hamilton*



Pakistan

Wazir Muhammad, *Abbottabad*



Poland

Maciej S Baglaj, *Wroclaw*

Piotr Czauderna, *Gdansk*



Portugal

Joao Manuel RS Tavares, *Porto*



Serbia

Olivera Ciraj-Bjelac, *Belgrade*



Singapore

Gopinathan Anil, *Singapore*

Terence KB Teo, *Singapore*

Cher Heng Tan, *Singapore*



Slovakia

Stefan Sivak, *Martin*



South Korea

Ki Seok Choo, *Busan*

Seung Hong Choi, *Seoul*

Dae-Seob Choi, *Jinju*

Hong-Seok Jang, *Seoul*

Yong Jeong, *Daejeon*

Chan Kyo Kim, *Seoul*

Se Hyung Kim, *Seoul*

Joong-Seok Kim, *Seoul*

Sang Eun Kim, *Seongnam*

Sung Joon Kwon, *Seoul*

Jeong Min Lee, *Seoul*

In Sook Lee, *Busan*

Noh Park, *Goyang*

Chang Min Park, *Seoul*

Sung Bin Park, *Seoul*

Deuk Jae Sung, *Seoul*

Choongsoo Shin, *Seoul*

Kwon-Ha Yoon, *Iksan*



Spain

Miguel A De Gregorio, *Zaragoza*

Antonio Luna, *Jaén*

Enrique Marco de Lucas, *Santander*

Fernando Ruiz Santiago, *Granada*



Sweden

Dmitry Grishenkov, *Stockholm*

Tie-Qiang Li, *Stockholm*



Switzerland

Nicolau Beckmann, *Basel*

Christian Boy, *Bern*

Giorgio Treglia, *Bellinzona*

Stephan Ulmer, *Kiel*



Thailand

Sirianong Namwongprom, *Chiang Mai*



Turkey

Kubilay Aydin, *Istanbul*

Ramazan Akdemir, *Sakarya*

Serhat Avcu, *Ankara*

Ayşe Aralasmak, *Istanbul*

Oktay Algin, *Ankara*

Nevbahar Akcar, *Meselik*

Bilal Battal, *Ankara*

Zulkif Bozgeyik, *Elazig*

Nazan Ciledag, *Aakara*

Fuldem Y Donmez, *Ankara*

Gulgun Engin, *Istanbul*

Ahmet Y Goktay, *Izmir*

Oguzhan G Gumustas, *Bursa*

Kaan Gunduz, *Ankara*

Pelin Ozcan Kara, *Mersin*

Kivanc Kamburoglu, *Ankara*

Ozgur Kilickesmez, *Istanbul*

Furuzan Numan, *Istanbul*

Cem Onal, *Adana*

Ozgur Oztekin, *Izmir*

Seda Ozbek (Boruban), *Konya*

Selda Sarikaya, *Zonguldak*

Figen Taser, *Kutahya*

Baran Tokar, *Eskisehir*

Ender Uysal, *Istanbul*

Ensar Yekeler, *Istanbul*



United Kingdom

Indran Davagnanam, *London*

M DC Valdés Hernández, *Edinburgh*

Alan Jackson, *Manchester*

Suneil Jain, *Belfast*

Long R Jiao, *London*

Miltiadis Krokidis, *Cambridge*

Pradesh Kumar, *Liverpool*

Peter D Kuzmich, *Derby*

Georgios Plataniotis, *Brighton*

Vanessa Sluming, *Liverpool*



United States

Garima Agrawal, *Saint Louis*

James R Brasic, *Baltimore*

Rajendra D Badgaiyan, *Buffalo*

Ulas Bagci, *Bethesda*

Anat Biegon, *Stony Brook*

Ramon Casanova, *Winston Salem*

Wenli Cai, *Boston*

Zheng Chang, *Durham*

Corey J Chakarun, *Long Beach*

Kai Chen, *Los Angeles*

Hyun-Soon Chong, *Chicago*

Marco Cura, *Dallas*

Ravi R Desai, *Bensalem*

Delia DeBuc, *Miami*

Carlo N De Cecco, *Charleston*

Timm-Michael L Dickfeld, *Baltimore*

Subba R Digumarthy, *Boston*

Huy M Do, *Stanford*

Todd A Faasse, *Grand Rapids*

Salomao Faintuch, *Boston*

Girish M Fatterpekar, *New York*

Dhakshinamoorthy Ganesan, *Houston*

Robert J Griffin, *Little Rock*

Andrew J Gunn, *Boston*

Sandeep S Hedgire, *Boston*

Timothy J Hoffman, *Columbia*

Mai-Lan Ho, *San Francisco*

Juebin Huang, *Jackson*

Abid Irshad, *Charleston*

Matilde Inglese, *New York*

El-Sayed H Ibrahim, *Jacksonville*

Paul R Julsrud, *Rochester*

Pamela T Johnson, *Baltimore*

Ming-Hung Kao, *Tempe*

Sunil Krishnan, *Houston*

Richard A Komoroski, *Cincinnati*

Sandi A Kwee, *Honolulu*

King Kim, *Ft. Lauderdale*

Guozheng Liu, *Worcester*

Yiyan Liu, *Newark*

Venkatesh Mani, *New York*

Lian-Sheng Ma, *Pleasanton*

Rachna Madan, *Boston*

Zeyad A Metwalli, *Houston*

Yilong Ma, *Manhasset*

Hui Mao, *Atlanta*

Feroze B Mohamed, *Philadelphia*

Gul Moonis, *Boston*

John L Noshier, *New Brunswick*

Rahmi Oklu, *Boston*

Aytekun Oto, *Chicago*

Bishnuhari Paudyal, *Philadelphia*

Rajul Pandya, *Youngstown*

Chong-Xian Pan, *Sacramento*

Jay J Pillai, *Baltimore*

Neal Prakash, *Duarte*

Reza Rahbar, *Boston*

Ali S Raja, *Boston*

Gustavo J Rodriguez, *El Paso*

David J Sahn, *Portland*

Steven Schild, *Scottsdale*

Ali R Sepahdari, *Los Angeles*

Li Shen, *Indianapolis*

JP Sheehan, *Charlottesville*

Atul B Shinagare, *Boston*

Sarabjeet Singh, *Boston*

Charles J Smith, *Columbia*

Kenji Suzuki, *Chicago*

Monvadi Srichai-Parsia, *Washington*

Sree H Tirumani, *Boston*

Hebert A Vargas, *New York*

Sachit Verma, *Philadelphia*

Yoichi Watanabe, *Minneapolis*

Li Wang, *Chapel Hill*

Carol C Wu, *Boston*

Shoujun Xu, *Houston*

Min Yao, *Cleveland*

Xiaofeng Yang, *Atlanta*

Qingbao Yu, *Albuquerque*

Aifeng Zhang, *Chicago*

Chao Zhou, *Bethlehem*

Hongming Zhuang, *Philadelphia*

**REVIEW**

- 28 Imaging and interventions in hilar cholangiocarcinoma: A review
Madhusudhan KS, Gamanagatti S, Gupta AK

ORIGINAL ARTICLE**Basic Study**

- 45 Evaluation of changes of intracranial blood flow after carotid artery stenting using digital subtraction angiography flow assessment
Wada H, Saito M, Kamada K

Retrospective Study

- 52 Transcranial Doppler screening in sickle cell disease: The implications of using peak systolic criteria
Naffaa LN, Tandon YK, Irani N

ABOUT COVER

Editorial Board Member of *World Journal of Radiology*, Alexey Surov, MD, PhD, N/A, Department of Radiology, Martin-Luther-University Halle-Wittenberg, Halle D-06097, Germany

AIM AND SCOPE

World Journal of Radiology (*World J Radiol*, *WJR*, online ISSN 1949-8470, DOI: 10.4329) is a peer-reviewed open access academic journal that aims to guide clinical practice and improve diagnostic and therapeutic skills of clinicians.

WJR covers topics concerning diagnostic radiology, radiation oncology, radiologic physics, neuroradiology, nuclear radiology, pediatric radiology, vascular/interventional radiology, medical imaging achieved by various modalities and related methods analysis. The current columns of *WJR* include editorial, frontier, diagnostic advances, therapeutics advances, field of vision, mini-reviews, review, topic highlight, medical ethics, original articles, case report, clinical case conference (clinicopathological conference), and autobiography.

We encourage authors to submit their manuscripts to *WJR*. We will give priority to manuscripts that are supported by major national and international foundations and those that are of great basic and clinical significance.

INDEXING/ABSTRACTING

World Journal of Radiology is now indexed in PubMed Central, PubMed, Digital Object Identifier, and Directory of Open Access Journals.

FLYLEAF

I-III Editorial Board

EDITORS FOR THIS ISSUE

Responsible Assistant Editor: *Xiang Li*
Responsible Electronic Editor: *Huan-Liang Wu*
Proofing Editor-in-Chief: *Lian-Sheng Ma*

Responsible Science Editor: *Xue-Mei Gong*
Proofing Editorial Office Director: *Xin-Xia Song*

NAME OF JOURNAL
World Journal of Radiology

ISSN
ISSN 1949-8470 (online)

LAUNCH DATE
December 31, 2009

FREQUENCY
Monthly

EDITORS-IN-CHIEF
Kai U Juergens, MD, Associate Professor, MRT und PET/CT, Nuklearmedizin Bremen Mitte, ZEMODI - Zentrum für morphologische und molekulare Diagnostik, Bremen 28177, Germany

Edwin JR van Beek, MD, PhD, Professor, Clinical Research Imaging Centre and Department of Medical Radiology, University of Edinburgh, Edinburgh EH16 4TJ, United Kingdom

Thomas J Vogl, MD, Professor, Reader in Health Technology Assessment, Department of Diagnostic and Interventional Radiology, Johann Wolfgang

Goethe University of Frankfurt, Frankfurt 60590, Germany

EDITORIAL OFFICE
Jin-Lei Wang, Director
Xiu-Xia Song, Vice Director
World Journal of Radiology
Room 903, Building D, Ocean International Center, No. 62 Dongsihuan Zhonglu, Chaoyang District, Beijing 100025, China
Telephone: +86-10-59080039
Fax: +86-10-85381893
E-mail: editorialoffice@wjnet.com
Help Desk: <http://www.wjnet.com/esps/helpdesk.aspx>
<http://www.wjnet.com>

PUBLISHER
Baishideng Publishing Group Inc
8226 Regency Drive,
Pleasanton, CA 94588, USA
Telephone: +1-925-223-8242
Fax: +1-925-223-8243
E-mail: bpgoffice@wjnet.com
Help Desk: <http://www.wjnet.com/esps/helpdesk.aspx>
<http://www.wjnet.com>

PUBLICATION DATE
February 28, 2015

COPYRIGHT
© 2015 Baishideng Publishing Group Inc. Articles published by this Open-Access journal are distributed under the terms of the Creative Commons Attribution Non-commercial License, which permits use, distribution, and reproduction in any medium, provided the original work is properly cited, the use is non commercial and is otherwise in compliance with the license.

SPECIAL STATEMENT
All articles published in journals owned by the Baishideng Publishing Group (BPG) represent the views and opinions of their authors, and not the views, opinions or policies of the BPG, except where otherwise explicitly indicated.

INSTRUCTIONS TO AUTHORS
Full instructions are available online at http://www.wjnet.com/1949-8470/g_info_20100316162358.htm.

ONLINE SUBMISSION
<http://www.wjnet.com/esps/>

Imaging and interventions in hilar cholangiocarcinoma: A review

Kumble Seetharama Madhusudhan, Shivanand Gamanagatti, Arun Kumar Gupta

Kumble Seetharama Madhusudhan, Shivanand Gamanagatti, Arun Kumar Gupta, Department of Radiodiagnosis, All India Institute of Medical Sciences, New Delhi, Delhi 110029, India

Author contributions: All the authors equally contributed to this work.

Conflict-of-interest: The authors declare that they have no competing interests.

Open-Access: This article is an open-access article which was selected by an in-house editor and fully peer-reviewed by external reviewers. It is distributed in accordance with the Creative Commons Attribution Non Commercial (CC BY-NC 4.0) license, which permits others to distribute, remix, adapt, build upon this work non-commercially, and license their derivative works on different terms, provided the original work is properly cited and the use is non-commercial. See: <http://creativecommons.org/licenses/by-nc/4.0/>

Correspondence to: Shivanand Gamanagatti, Additional Professor, Department of Radiodiagnosis, All India Institute of Medical Sciences, Ansari Nagar East, Gautam Nagar, New Delhi, Delhi 110029, India. shiv223@rediffmail.com

Telephone: +91-11-26594567

Fax: +91-11-26588660

Received: October 8, 2014

Peer-review started: October 8, 2014

First decision: November 1, 2014

Revised: November 14, 2014

Accepted: December 16, 2014

Article in press: December 17, 2014

Published online: February 28, 2015

form of biliary drainage and/or portal vein embolization. In inoperable cases, palliative interventions include biliary drainage, biliary stenting and intra-biliary palliative treatment techniques. Complete knowledge of application of various imaging modalities available and about the possible radiological interventions is important for a radiologist to play a critical role in appropriate management of such patients. We review the various imaging techniques and appearances of hilar cholangiocarcinoma and the possible radiological interventions.

Key words: Cholangiocarcinoma; Biliary malignancy; Imaging; Biliary intervention; Computed tomography; Magnetic resonance imaging

© The Author(s) 2015. Published by Baishideng Publishing Group Inc. All rights reserved.

Core tip: Poor prognosis of hilar cholangiocarcinoma mandates early diagnosis. The article outlines the performance of various imaging modalities in making a diagnosis and allows the readers to decide the appropriately modality in a given case. Further, the brief descriptions of a wide range of radiological interventions in hilar cholangiocarcinoma educate the readers about the available options and choose them judiciously.

Abstract

Hilar cholangiocarcinoma is a common malignant tumor of the biliary tree. It has poor prognosis with very low 5-year survival rates. Various imaging modalities are available for detection and staging of the hilar cholangiocarcinoma. Although ultrasonography is the initial investigation of choice, imaging with contrast enhanced computed tomography scan or magnetic resonance imaging is needed prior to management. Surgery is curative wherever possible. Radiological interventions play a role in operable patients in the

Madhusudhan KS, Gamanagatti S, Gupta AK. Imaging and interventions in hilar cholangiocarcinoma: A review. *World J Radiol* 2015; 7(2): 28-44 Available from: URL: <http://www.wjgnet.com/1949-8470/full/v7/i2/28.htm> DOI: <http://dx.doi.org/10.4329/wjr.v7.i2.28>

INTRODUCTION

Cholangiocarcinoma (CC) is a malignant tumor of the biliary tree, originating from the bile duct epithelium. It is the second most common biliary

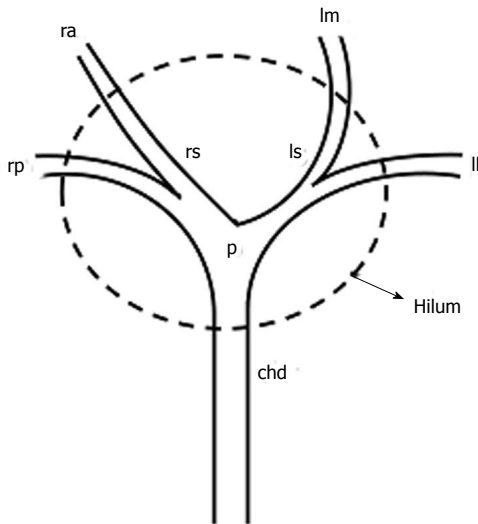


Figure 1 Schematic diagram showing structures forming hilum. chd: Common hepatic duct; ll: Left lateral segmental duct; lm: Left medial segmental duct; ls: Left secondary confluence; p: Primary biliary confluence; ra: Right anterior segmental duct; rp: Right posterior segmental duct; rs: Right secondary confluence.

tract malignancy, after carcinoma of gall bladder and second most common primary hepatic malignancy after hepatocellular carcinoma. The occurrence of the disease is increasing worldwide with an incidence of 1-2/100000^[1]. The symptoms at presentation are mostly non-specific and occur late in the course of the disease. Further, hilar masses invade adjacent vascular structures early and curative surgery is possible in less than half of the cases^[2]. The tumor has very poor prognosis with 5-year survival of about 5%^[3]. Hence, early diagnosis and curative surgery is needed to improve survival in these patients. We describe the various imaging modalities used in the diagnosis of CC and its appearances in these modalities. We further discuss various interventional radiological procedures playing role in management of patients with CC.

Cholangiocarcinoma can arise from any part of the biliary tree and depending on the location, they have been classified into three types - peripheral CC (or intrahepatic CC), hilar CC (or Klatskin tumor) and distal CC^[4]. Hilar CC is the most common variety forming about 40%-60% of all cases; distal CC forms 30%-42% and intrahepatic CC forms 5%-10%^[5,6]. Intrahepatic CC typically arise from beyond second order bile ducts whereas distal CC arise from extrahepatic common bile duct. Bismuth has classified hilar cholangiocarcinoma into four types depending on the location and extent of involvement bile ducts^[7]. Involvement of common hepatic duct (CHD) alone is defined as type 1, involvement of CHD and primary biliary confluence (PBC) as type 2, involvement of CHD, PBC and right or left hepatic ducts as type 3a or 3b respectively and involvement of CHD, PBC and both hepatic ducts or multifocal tumor as type 4.

Hilar cholangiocarcinoma (HiCC) is the most common anatomical type of CC. Although it can involve both intrahepatic and extrahepatic bile ducts, it is considered as a type of extrahepatic CC according to WHO classification^[8]. The tumor may arise from primary biliary confluence, right or left hepatic ducts, secondary biliary confluence or distal second order bile ducts (which together form the hilum) (Figure 1)^[9]. Although, the lesion is mostly extrahepatic, it may also extend intrahepatically and thus some use the term perihilar CC for the same. Macroscopically, HiCC has been classified into three types based on the growth pattern on gross specimen^[10]. They include nodular, periductal infiltrating and papillary types, of which the periductal infiltrating variety is the most common type (Figure 2). The nodular type begins as a small mucosal nodule and grows beyond the walls of the bile ducts to form a mass^[11]. The bile duct is obstructed at an early stage. Periductal-infiltrating type grows along the walls of the bile ducts causing its thickening and irregular luminal narrowing. Associated desmoplastic reaction may show smooth stenosis of the bile ducts adjacent to the tumor. Papillary tumor arises as a mucosal polypoidal or sessile lesion remains limited to the bile duct wall till late stages. This variety has better prognosis compared to the other two types. Histologically, about 90% of HiCC are adenocarcinomas, which range from well differentiated to poorly differentiated glands^[9]. Microscopically, the tumor consists of glands or tubules with fibrous stroma and inflammatory cells. Perineural, perilymphatic and perivenous invasion may be seen, of which the former is characteristic.

CLINICAL FEATURES

Due to the location of the tumor, even small masses produce biliary obstruction at an early stage and most patients present with obstructive jaundice. Other symptoms at presentation include anorexia, weight loss, right upper quadrant pain and pruritus. Patients may present with high-grade fever associated with chills and rigors due to cholangitis. Various risk factors predispose to the development of CC. These include primary sclerosing cholangitis, hepatolithiasis, liver fluke infection (*Opisthorchis viverrini* and *Clonorchis sinensis*), choledochal cyst and inflammatory bowel disease^[12]. Hepatitis B and C viruses have also been associated with increased risks of CC.

RADIOLOGICAL IMAGING

Imaging evaluation of HiCC is very important for accurate staging of the tumor and possible curative surgical resection. Assessment of longitudinal and extra-ductal extent of the tumor is critical as it defines treatment planning. However, varying

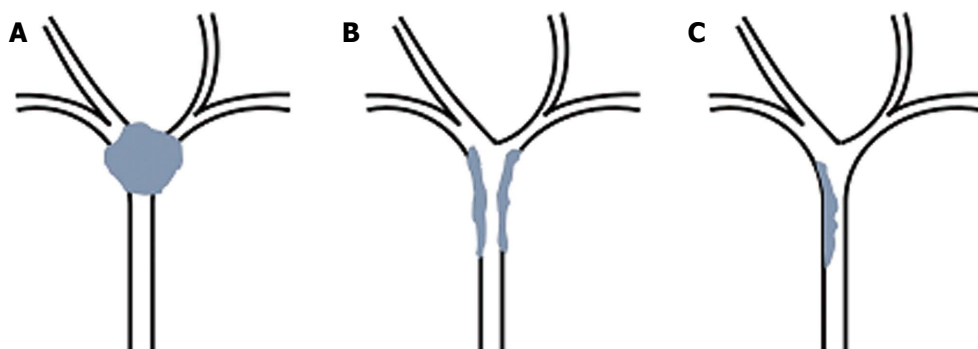


Figure 2 Schematic diagram showing three morphological types of hilar cholangiocarcinoma. A: Nodular variety; B: Periductal infiltrating; C: Intraductal papillary.

morphologies of HiCC may result in over or under-estimation of the tumor extent along the ducts and result in failure of curative treatment^[13]. Local extension of the tumor which suggest non-resectability on imaging include involvement of bilateral secondary biliary confluence, portal vein of one lobe and hepatic artery of other lobe, proper hepatic artery, main portal vein, hepatic artery or portal vein of one lobe with atrophy of other lobe. Ultrasonography, computed tomography (CT) and magnetic resonance imaging (MRI) are the most common non-invasive imaging modalities which are used in the diagnosis and staging of HiCC. Other less commonly used techniques are invasive and include percutaneous transhepatic cholangiography (PTC) and endoscopic retrograde cholangiography (ERC).

ULTRASONOGRAPHY

Sonography is the initial investigation which is performed in most patients presenting with obstructive jaundice or abdominal pain. In addition to detection of CC, it helps in excluding other causes of obstructive jaundice, primarily gall stones. The most common finding is dilatation of intrahepatic bile ducts^[14]. The union of right and left hepatic ducts is usually not visualized. At the site of obstruction, tumor may be seen with the currently available equipments. The primary tumor is most commonly isoechoic on ultrasonography (USG) (65%), but may be hypoechoic (21%) or hyperechoic (15%) (Figure 3)^[15]. Thenodular and papillary varieties can be seen as ill-defined lesions at the primary biliary confluence. The infiltrating variety may be seen as irregular isoechoic wall thickening of the right or left hepatic or proximal common hepatic ducts (Figure 3C). Lobar atrophy is a less common finding and is suggested by crowding of the dilated ducts and smaller size of the lobe (Figure 3D). This occurs when there is dominant involvement of one duct than the other. Lobar atrophy is seen in about 14% of patients with CC^[16]. Sonography also helps in evaluation of vascular structures, regional nodes and liver. The accuracy of lesion detection

on USG is about 82% and the sensitivity and specificity of portal vein involvement is 75%-83% and 93%-100%, respectively^[15,17]. USG has low accuracy for hepatic artery involvement. Contrast enhanced USG is an additional technique which can be performed in arterial, venous and delayed phases for better visualization and characterization of the tumor^[18,19]. Administration of USG contrast agents variably improves detection of primary lesion, the sensitivity of which may reach up to 100%^[20].

Endoscopic ultrasonography (EUS) is a technique where a high-frequency ultrasound probe is attached to the end of the endoscope. This helps in better visualization of hilar masses through stomach or duodenum^[21]. The benefits of EUS include no interference due to bowel gas (as seen with trans-abdominal USG), better visualization of mass and loco-regional lymph nodes and ability to obtain fine needle aspiration (FNA) or biopsy from the mass and nodes. The sensitivity and specificity of EUS in diagnosing and staging cholangiocarcinoma is 94% and 85% respectively^[22]. The diagnostic sensitivity and specificity of EUS with the use of FNAC for suspected HiCC is 89% and 100% respectively^[23]. Intraductal USG (IDUS) is another technique of using a high-resolution USG probe through either ERC or percutaneous transhepatic biliary drainage (PTBD) route^[24]. Hilar lesions are seen as hypoechoic masses around the biliary channels with irregular outline. This technique, when used with ERC has a sensitivity and specificity of 90% and 93%^[25]. However, visualization of deeper structures like vessels and nodes is difficult.

CT

CT scan is the most common widely used modality used for detection and staging of HiCC. Multidetector CT (MDCT) scan offers excellent spatial resolution and fast scanning and optimally depicts relation of the tumor with hepatic artery and portal vein^[26,27]. Multiplanar reformats (MPR) and maximum and minimum intensity projections are useful in accurately demonstrating ductal and vascular invasion (Figure 4).

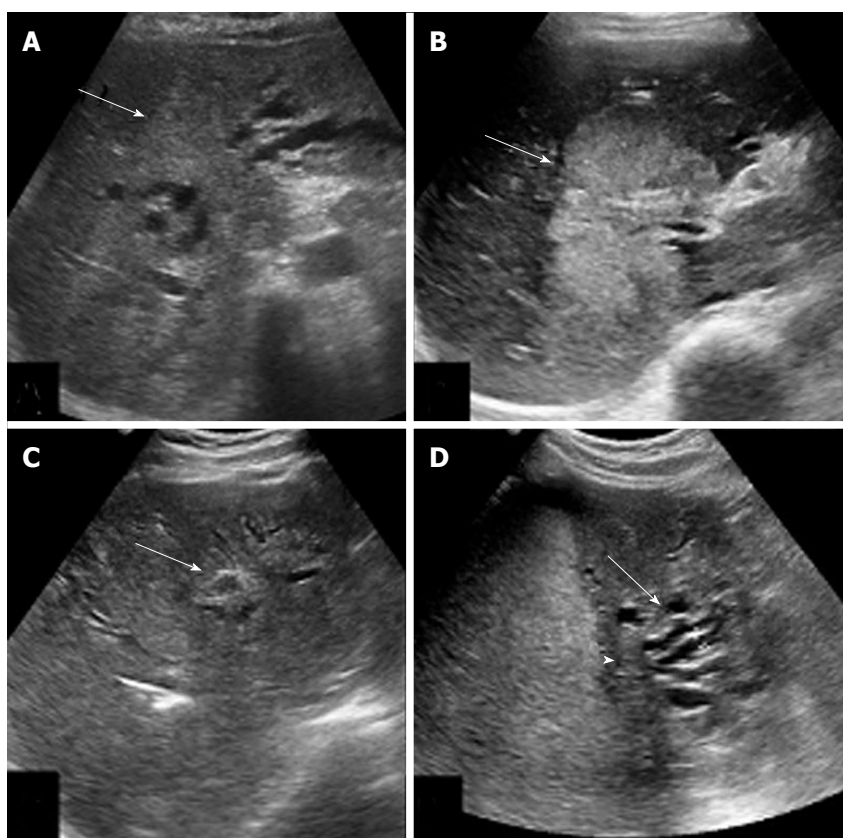


Figure 3 Ultrasonographic appearances of hilar cholangiocarcinoma. A: Isoechoic lesion (arrow) involving primary biliary confluence; B: Hyperechoic mass (arrow) involving hilum; C: Infiltrative lesion (arrow) with periductal wall thickening; D: Atrophy of left lobe with crowding of bile ducts (arrow) due to isoechoic hilar mass (arrow head).

MDCT has an accuracy of about 86% in assessment of ductal extent of HiCC^[28]. The sensitivity and specificity of MDCT in evaluation of portal vein, hepatic artery and lymph node involvement are 89% and 92%, 84% and 93%, and 61% and 88%, respectively.

The routine protocol for performing a CT scan in patients with suspected HiCC includes an arterial phase (25-35 s after beginning of contrast injection), portal venous phase (70-80 s) and delayed phase (180 s). Oral contrast is usually neutral or negative. Positive oral contrast is not given as it interferes with formation of MPRs. The arterial phase, demonstrates involvement of arteries (importantly main, right or left hepatic artery) by the tumor and also any variations in the arterial anatomy, which is useful for the surgeon. Portal venous phase reveals involvement of main portal vein or its first order branches. Further, this phase also better demonstrates primary tumor, liver metastases and extrahepatic spread (nodes, peritoneum) (Figure 5)^[29]. Delayed phase is useful in demonstration of primary mass which shows enhancement in delayed phase due to its scirrhous nature (Figure 6)^[30]. Oblique and curved MPRs show involvement of biliary tree and vessels better than the axial images and improve diagnostic accuracy^[29]. An additional and

important role of MDCT is in assessment of volume of future liver remnant (FLR) prior to surgery. The volume of FLR can be calculated either automatically or manually (Figure 7). Depending on the FLR volume in relation to body weight, either surgery can be planned directly or portal vein embolization may be performed to increase its volume. MDCT cholangiography without administration of biliary contrast agent can be done with volume rendering after adjusting the rendering parameters^[26]. This technique has a sensitivity and specificity of about 94% each in diagnosis of malignant biliary obstruction.

Nodular or mass-forming CC typically show thick irregular peripheral or heterogeneous enhancement in the arterial phase images with gradual centripetal enhancement in portal venous and delayed phase images (Figure 8)^[31]. However, very often the mass is small and may be difficult to visualize. Periductal infiltrating lesions typically show wall thickening and enhancement, which may completely obliterate the lumen. The lesion is usually hypoenhancing and may show enhancement in the delayed phase (Figure 9); occasionally it can enhance in arterial phase^[30]. Intraductal papillary lesions show single or multiple intraluminal polypoidal soft tissue which show contrast enhancement and distend the lumen of the

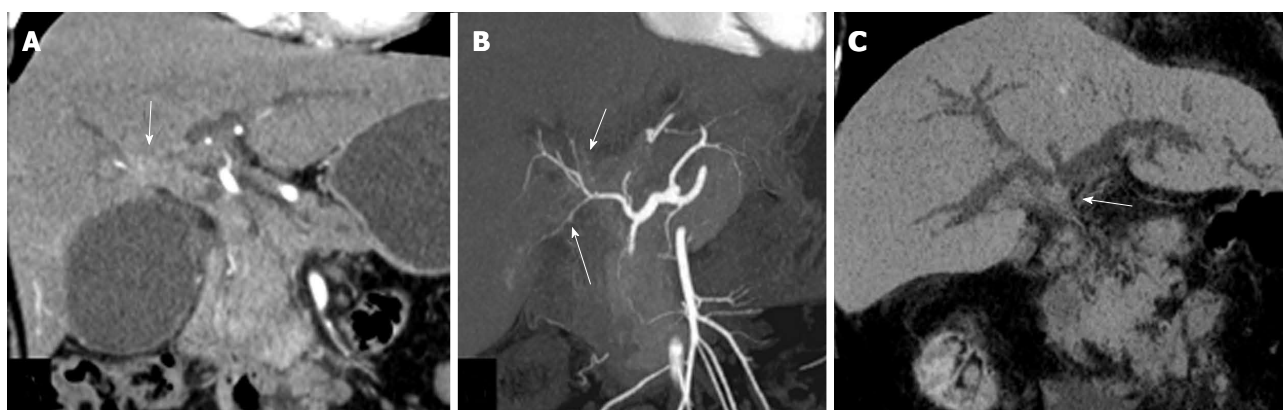


Figure 4 Post processing of computed tomography scan. A: Coronal reformat showing ill-defined enhancing mass (arrow) in relation to hilum and common hepatic duct; B: Coronal thick maximum intensity projection showing same mass as in A (short arrow) with irregularity of right posterior hepatic artery (long arrow); C: Minimum intensity projection showing the extent of biliary involvement by the mass (arrow).

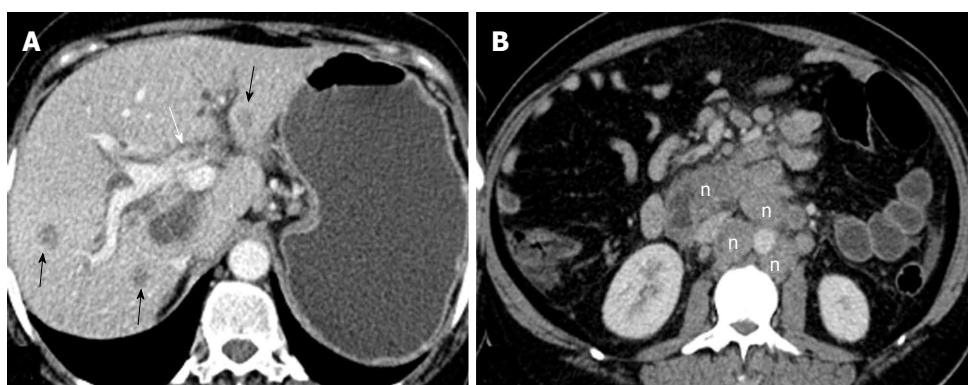


Figure 5 Axial contrast enhanced venous phase images. A: Showing hilar mass (white arrow) with multiple liver metastases (black arrows); B: Showing multiple metastatic retroperitoneal nodes (n).

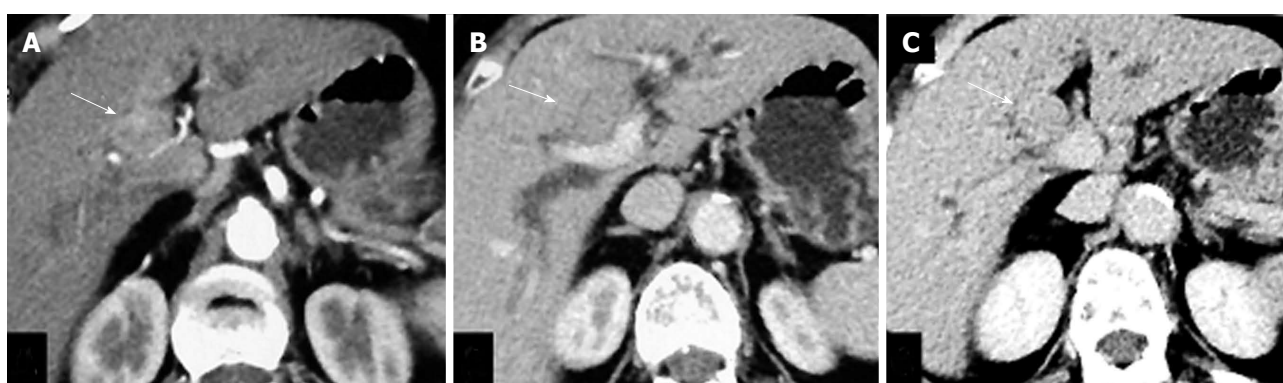


Figure 6 Axial contrast enhanced computed tomography scan in arterial (A), venous (B) and delayed (C) phases showing mild enhancement of the lesion (arrow) in arterial phase with persistence of enhancement in venous and delayed phases suggesting scirrhus nature of the lesion.

bile duct (Figure 10). Extension beyond the bile duct wall and lymph node involvement is uncommon. In addition to the primary lesion, CT scan also shows dilatation of the bile ducts upto the lesion and atrophy or hypertrophy of the lobes or segments (Figure 11). As with any other malignant tumors, vascular invasion is suggested by the presence of soft tissue encasing the vessel, large area of contact, narrowing of the calibre and complete luminal

obstruction (Figure 12).

MRI

Magnetic resonance cholangio-pancreatography (MRCP) is a heavily T2-weighted sequence used for demonstration of biliary channels and is as accurate as ERCP^[32]. Its advantages over ERCP include its non-invasiveness, its ability to visualize ducts

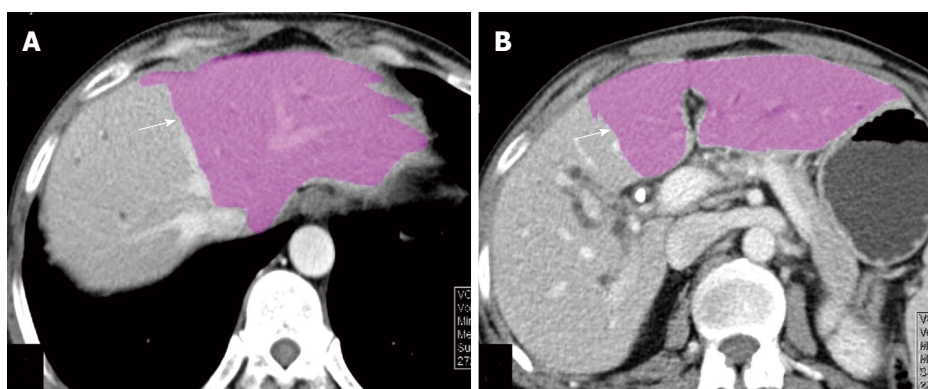


Figure 7 Axial venous phase computed tomography images (A and B) showing automated volumetry map with colour coding indicating the volume of future liver remnant (arrow).



Figure 8 Axial contrast enhanced computed tomography scan in arterial (A), venous (B) and delayed (C) phases of nodular variety of hilar cholangiocarcinoma (arrow) showing mildly enhancing ill-defined mass lesion in arterial phase with increasing enhancement in venous and delayed phases.



Figure 9 Axial (A) and coronal (B) images of venous phase of computed tomography scan of periductal infiltrating type of hilar cholangiocarcinoma showing wall thickening and enhancement of proximal common hepatic duct (arrow) causing luminal obstruction.

proximal to the obstruction and better visualization of the mass and non-requirement of contrast. Thin sections of MRCP and 3D-MRCP sequence further improve accuracy of lesion demonstration. MRI with gadolinium based contrast agents accurately depicts the mass, local extension, vascular involvement and regional metastases^[13,33]. The benefits of MRI over CT scan include no radiation, higher soft tissue contrast which helps in better demonstration of

tumor extent and better demonstration of biliary tree. MRI has its own share of limitations including longer acquisition times, motion artifacts, lower spatial resolution and lower accuracy in the presence of stents^[29]. The accuracy of MRI with MRCP in the prediction of involvement of biliary confluence, hepatic artery, portal vein and lymph node is 89%, 86%, 96% and 74%, respectively^[13].

Routine evaluation requires MRCP and MRI

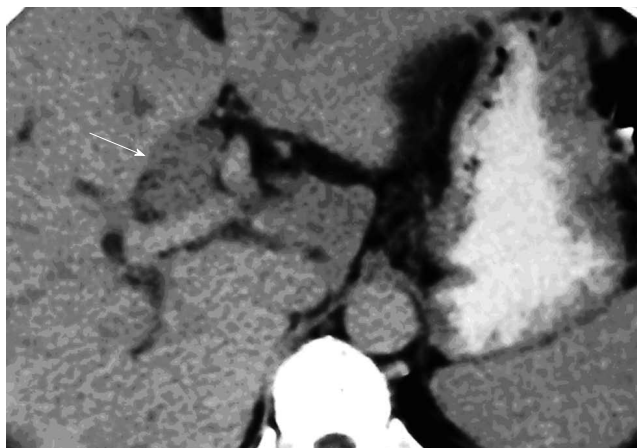


Figure 10 Axial contrast enhanced computed tomography scan in venous phase of papillary type of hilar cholangiocarcinoma showing minimally enhancing intraductal polypoidal lesion (arrow) causing distension of the duct.

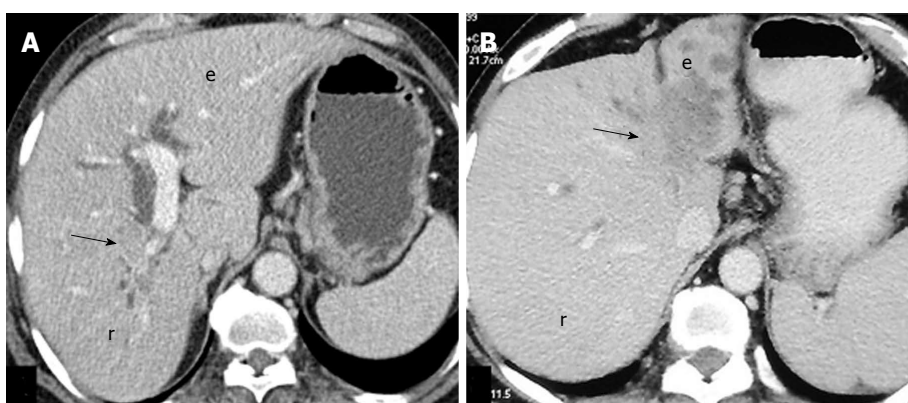


Figure 11 Axial computed tomography images showing atrophy of right lobe (r) due to hilar mass (arrow) in A, and atrophy of left lobe (l) caused by a mass (arrow) in B.

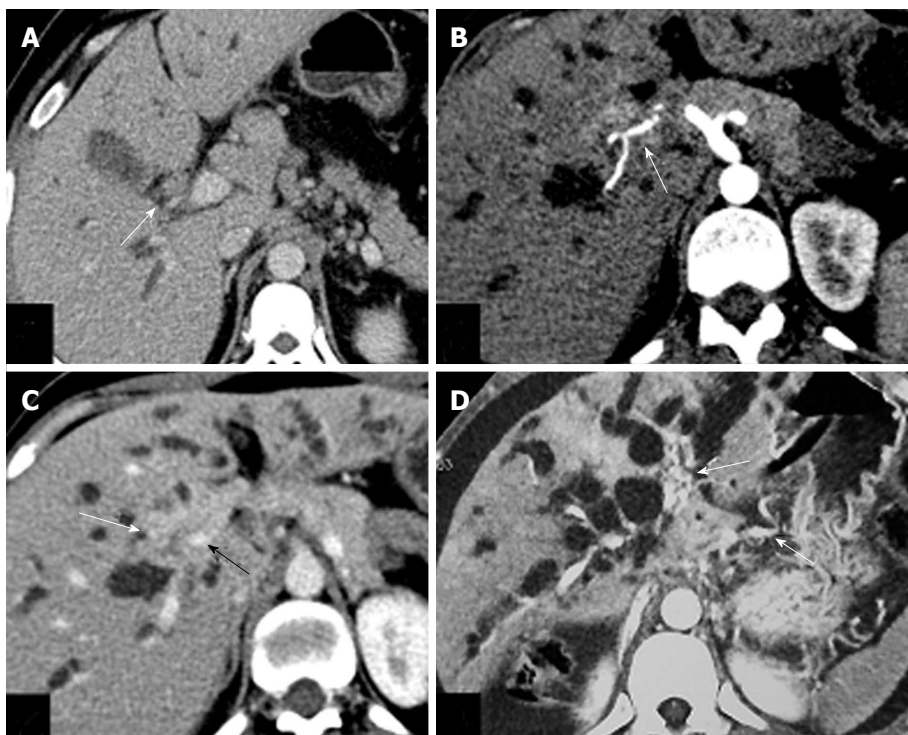


Figure 12 Axial computed tomography scan images showing vascular invasion. A: Small hilar mass (white arrow) abutting right hepatic artery posteriorly; B: Hilar mass (white arrow) encasing right hepatic artery causing irregularity in outline; C: Ill-defined hilar mass (white arrow) encasing portal vein and causing its narrowing (black arrow); D: Multiple collaterals (white arrows) seen in periportal and perigastric location due to portal vein obstruction.

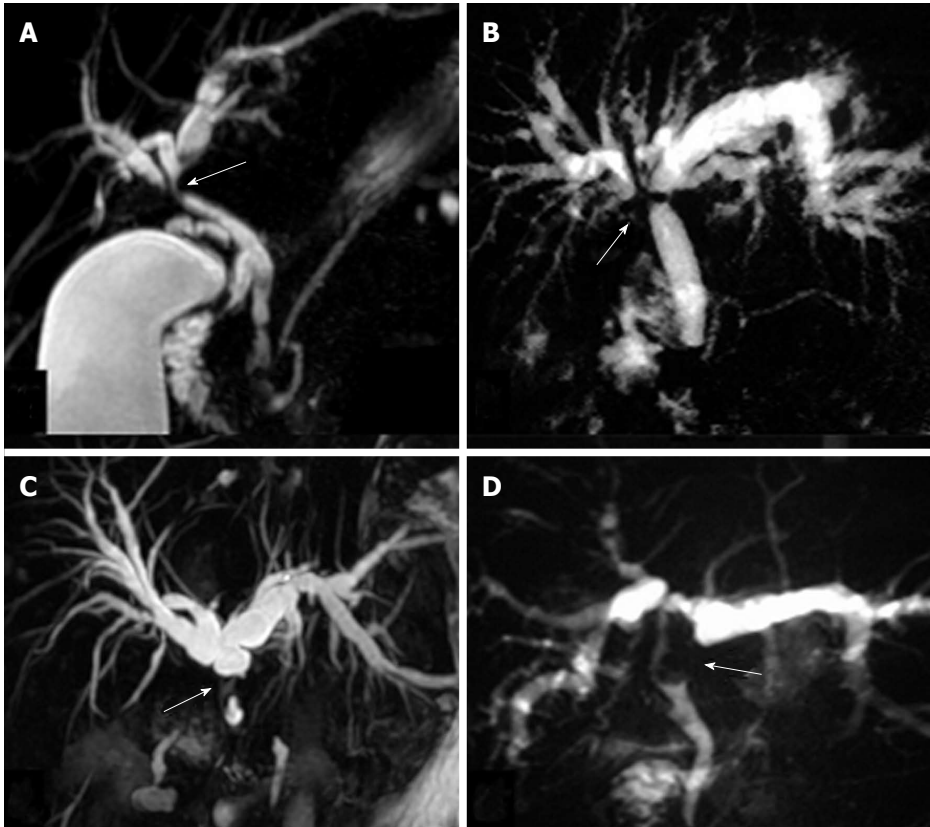


Figure 13 Magnetic resonance cholangio-pancreatography images showing various appearances of hilar cholangiocarcinoma. A: Smooth luminal narrowing (arrow); B: Complete hilar obstruction (arrow); C: Irregular asymmetric complete obstruction (arrow); D: Intraluminal filling defect (arrow).

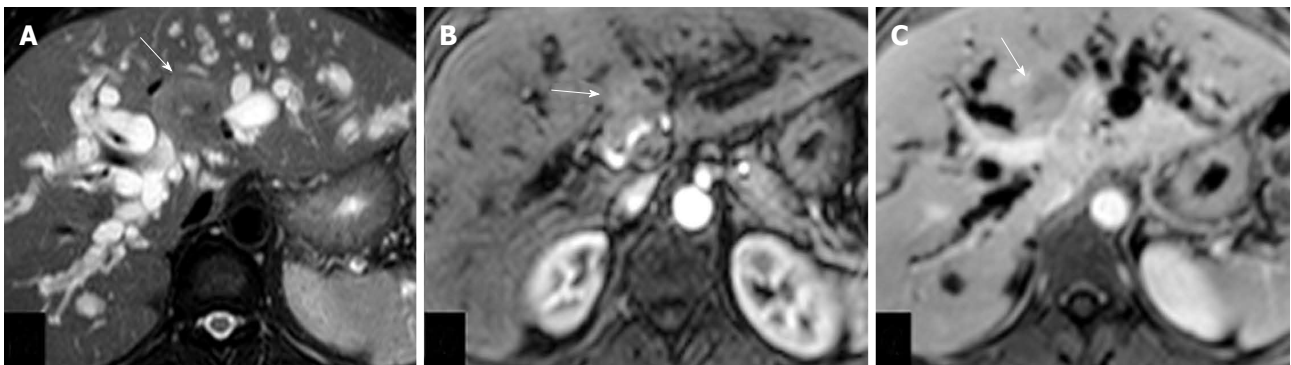


Figure 14 Case of nodule type of hilar cholangiocarcinoma. A: Axial T2-weighted magnetic resonance image show hypointense hilar mass (arrow) with biliary dilatation; B and C: Axial T1-weighted magnetic resonance images in arterial (B) and venous (C) phases showing mildly enhancing ill-defined mass lesion (arrow) encasing right hepatic artery and left portal vein.

with contrast in multiple phases, similar to that of multiphase CT scan. On MRCP, the lesions cause irregular narrowing of the bile ducts, with or without obstruction, asymmetric luminal narrowing, abrupt luminal narrowing and as intraluminal filling defects (Figure 13). The appearance of the three morphological types of HiCC on contrast enhanced MRI is similar to that seen on CT scan (Figures 14 and 15). As in CT scan, the lesion shows peripheral or heterogeneous arterial enhancement with gradually increasing enhancement in the venous and delayed phases. Enhancement of ductal wall and

periductal infiltration is often better seen on MRI than on CT scan due to inherent higher contrast resolution of MRI. Diffusionweighted imaging (DWI) is useful in detecting smaller lesions (Figure 16). The b-values routinely used are 0, 500 and 800 s/mm². The technique has higher sensitivity and accuracy than MRI in detection of lesions and has high positive predictive value^[34]. Some inflammatory and benign lesions may mimic HiCC on MRI, but short segment involvement, irregular margins, asymmetric narrowing and diffusion restriction on DWI may point towards HiCC^[35]. The presence of stent affects

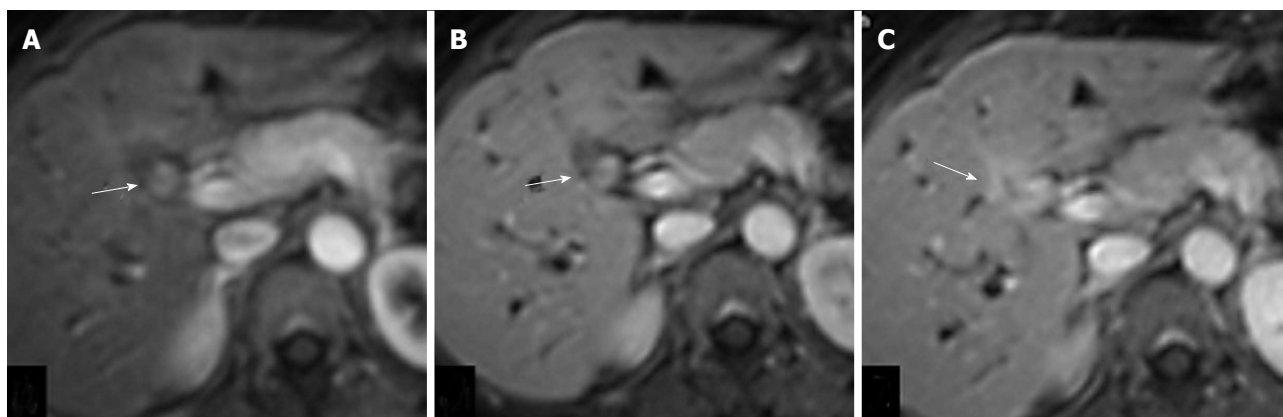


Figure 15 Axial contrast enhanced T1-weighted magnetic resonance images in arterial (A), venous (B) and delayed (C) phases of periductal infiltrating variety of hilar cholangiocarcinoma showing mildly enhancing thick walled proximal hepatic duct in arterial phase (arrow) with increasing contrast enhancement in venous and delayed phases.

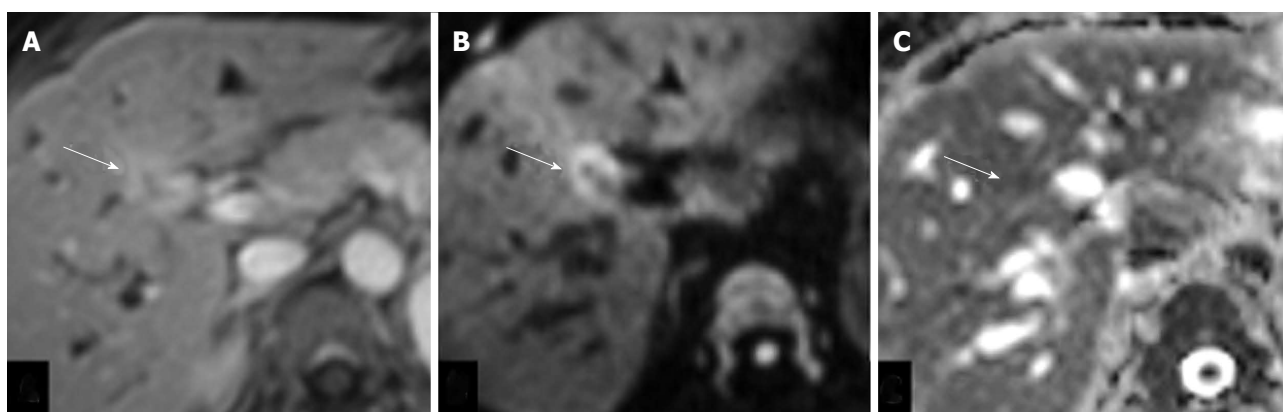


Figure 16 A case of periductal type of hilar cholangiocarcinoma. A: Axial T1-weighted contrast enhanced magnetic resonance (MR) image in delayed phase showing enhancing periductal lesion (arrow); B and C: Axial diffusion weighted b=800 MR images (B) and ADC map (C) showing diffusion restriction of the lesion.

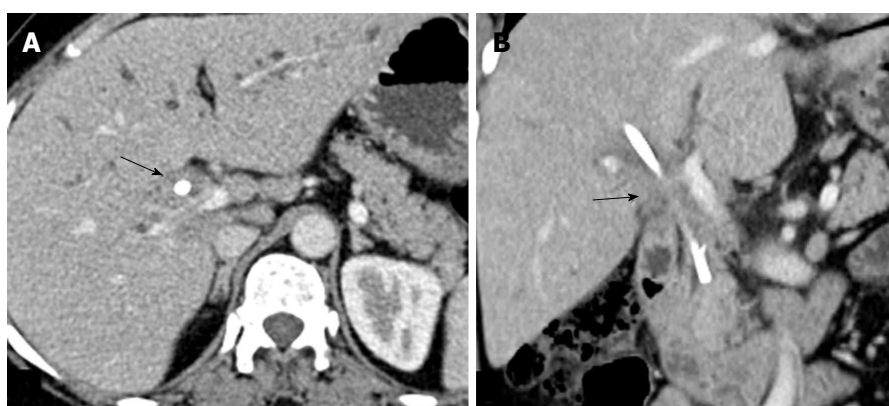


Figure 17 Axial (A) and coronal (B) computed tomography scan of a case of hilar cholangiocarcinoma after endoscopic stenting showing circumferential wall thickening of common hepatic duct around the stent. It would be difficult to differentiate this from reactive thickening.

evaluation of the tumor due to difficulty in assessing the level of obstruction as the bile ducts are decompressed after stenting and due to secondary sub-clinical cholangitis which cause wall thickening (Figure 17). Thus, imaging should be done prior to biliary decompression for accurate evaluation of the tumor.

POSITRON EMISSION TOMOGRAPHY CT

Cholangiocarcinomas express glucose transporter in higher concentration and take up ^{18}F Fluoro-deoxy Glucose (FDG). The sensitivity of detection depends on the morphological type and location of the tumor with lower rates of sensitivity seen in infiltrating

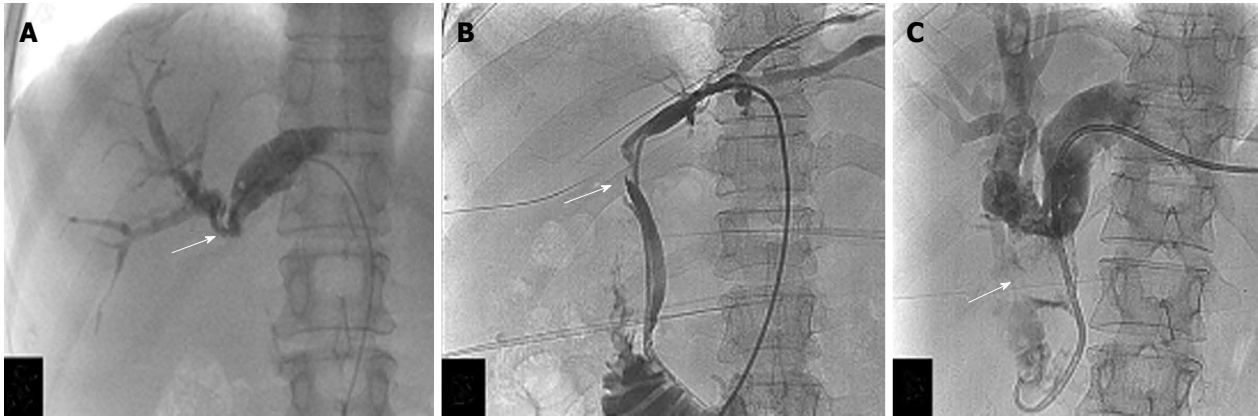


Figure 18 Percutaneous cholangiograms showing complete obstruction of common hepatic duct with patent primary biliary confluence (arrow, A), blocked primary biliary confluence with irregular outline (arrow, B) and intraluminal polypoidal filling defect (arrow, C).

Table 1 Bismuth-Corlette classification of hilar cholangiocarcinoma

Stage	Description
I	Tumor involving common hepatic duct without involvement of primary biliary confluence (confluence of right and left hepatic ducts) (Figure 19)
II	Tumor involving primary biliary confluence (Figure 20)
IIIa	Tumor involving primary biliary confluence and right secondary biliary confluence (confluence of right anterior and posterior sectoral ducts) (Figure 21)
IIIb	Tumor involving primary biliary confluence and left secondary biliary confluence (confluence of left medial and lateral sectoral ducts) (Figure 22)
IV	Tumor involving primary and both secondary biliary confluence (Figure 23)

types and extrahepatic cholangiocarcinoma^[36]. Nodular lesions show better uptake but infiltrating lesions are seen as streak-like uptake, which is sometimes difficult to detect. In the detection of primary tumor, FDG positron emission tomography CT (PET-CT) has a sensitivity, specificity and accuracy of 84%, 79% and 83%, respectively^[37]. However, for HiCC, sensitivity of PET-CT is lower than CT scan^[38]. Hence, routine use of PET-CT does not offer advantage over CT scan or MRI in the detection of HiCC. However, it has higher accuracy in the detection of metastatic regional lymph nodes and distant sites than other imaging modalities.

DIRECT CHOLANGIOGRAPHY

PTC and ERC are invasive techniques which involve injection of contrast directly into the bile ducts^[29]. In PTC, the dilated bile ducts are directly punctured under fluoroscopic or USG guidance through transhepatic route and contrast is injected antegradely to define the level and type of obstruction (Figure 18). In ERC, the duodenal ampulla is cannulated endoscopically and contrast is injected retrogradely to fill the bile ducts distal to the obstruction; proximal ducts may be visualized if obstruction is partial. Presence of short segment involvement, irregular stricture, asymmetric narrowing and nodularity suggests malignancy. Nodular type is usually seen as complete obstruction at primary biliary confluence^[39]. Short segment irregular or smooth narrowing is seen in case of periductal infiltrating variety and polypoidal or plaque

like filling defect in case of papillary type of HiCC. Additional benefits of PTC and ERCP include drainage of the obstructed system and ability to obtain brush cytology/biopsy.

Cholangioscopy is a technique of direct visualization of the tumor either through ERC route or PTBD route. It can help in differentiation of benign and malignant biliary strictures on the basis of presence of nodularity and irregularity of the mucosa and mucosal vessels^[40]. It has good accuracy in detection and evaluation of extent of HiCC which can be improved with the use of biopsy.

CLASSIFICATION AND STAGING

Bismuth-Corlette classified cholangiocarcinoma based on the longitudinal extent of the tumor^[41]. MRCP has high accuracy in classification of HiCC with an accuracy of 95% when compared to findings at surgery^[42]. The classification has been described in Table 1. This classification alone is not sufficient for assessing resectability of the tumor as it does not define lateral extension and it has little prognostic value^[43].

American Joint Committee on Cancer uses TNM classification for staging HiCC which is useful for selecting surgical candidates^[44]. "T" stands for primary tumor stage, "N" for nodal disease and "M" for metastases. The classification is as follows: (1) T stage: T1 - Tumor confined to bile duct, T2 - Tumor extending beyond the bile duct, this is further divided into T2a where there is involvement of



Figure 19 Schematic diagram and magnetic resonance cholangio-pancreatography image of type 1 hilar cholangiocarcinoma.

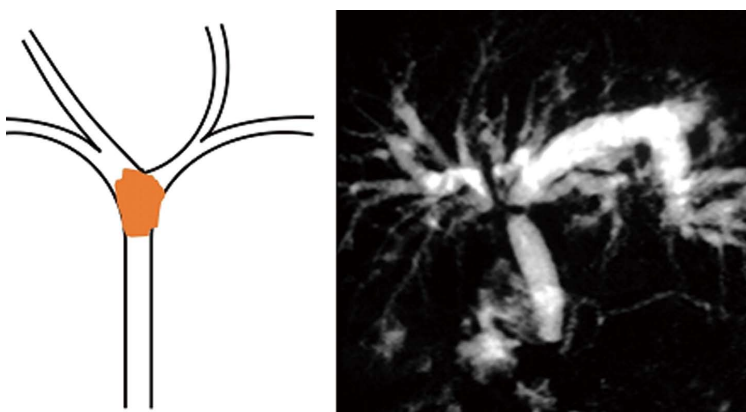


Figure 20 Schematic diagram and magnetic resonance cholangio-pancreatography image of type 2 hilar cholangiocarcinoma.

periductal fat and T2b where there is involvement of adjacent liver, T3 - Tumor involving unilateral portal vein or hepatic artery branches, T4 - Tumor involving one lobar portal vein branch and other lobar hepatic artery branch, main portal vein or common hepatic artery, second order bile ducts; (2) N stage: N0 - No lymph node involvement, N1 - Regional lymph nodes involvement (periductal or periportal nodes), N2 - Retroperitoneal nodes involvement; (3) M stage: M0 - No distant metastasis, M1 - Distant metastasis; and (4) Stages: I - T1 N0 M0, II - T2a-b N0 M0, III A - T3 N0 M0, III B - T1-3 N1 M0, IVA - T4 N0-1 M0, IVB - Any T N2 M0 or Any T Any N M1.

Imaging with multiphase CT scan and/or contrast enhanced MRI is helpful in accurately staging HiCC^[28]. Staging laparoscopy may rarely be needed when imaging findings are inconclusive.

RADIOLOGICAL INTERVENTIONS

Various radiological interventions are available in the management of HiCC, which could be either pre-operative (prior to definitive surgery) or palliative (in inoperable cases). Often the tumors are unresectable at the time of presentation and palliation is the only treatment possible to improve patients' quality of life^[2]. The main aim of palliation is to create a communication between the biliary system and small intestine to allow physiological drainage. This procedure reduces pain and relieves biliary obstruction and thus significantly decreases the

incidence of cholangitis and prepares the patient to receive chemotherapy. If it is done as a pre-operative procedure, it improves the liver function so that the patient can be treated surgically^[45].

Several safe and effective percutaneous radiological interventions are available in the management of HiCC. Although endoscopic drainage has the advantages of causing less pain, absence of an uncomfortable external drainage tube and less risk of biliary peritonitis, its success rate in too high obstructions is less and hence percutaneous technique is preferred^[46]. Cholangitis is seen in significantly higher number of patients as compared to percutaneous intervention as some of the obstructed ducts may not be drained^[45]. Various radiological interventional procedures include PTBD, biliary stenting (BS), intrabiliary tumor therapy and portal vein embolization (PVE). After the initial imaging, optimal further management is planned at the gastrointestinal-radiology meeting involving surgeons, gastroenterologists and radiologists.

PTBD

PTBD is the most common and well established interventional procedure performed in the management of HiCC. This is done either as a pre-operative procedure to improve liver functions or as a palliative procedure. Drainage of a single lobe (or at least 20% of liver parenchyma) is sufficient to relieve jaundice and improve liver functions^[47]. The



Figure 21 Schematic diagram and magnetic resonance cholangiopancreatography image of type 3A hilar cholangiocarcinoma.

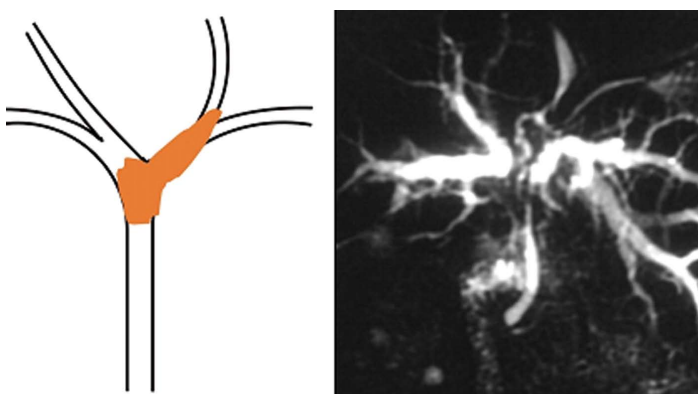


Figure 22 Schematic diagram and magnetic resonance cholangiopancreatography image of type 3B hilar cholangiocarcinoma.

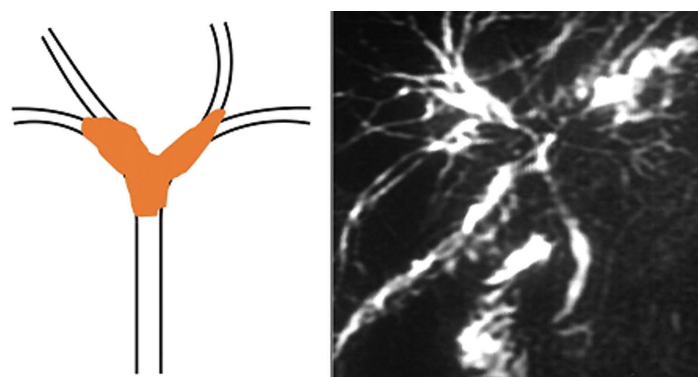


Figure 23 Schematic diagram and magnetic resonance cholangiopancreatography image of type 4 hilar cholangiocarcinoma.

primary biliary confluence is most often blocked in patients with HiCC and draining either the right or left lobe is adequate. The factors determining the selection of lobe to be drained are the size of the lobe and involvement of secondary biliary confluence. Prior imaging plays a crucial role in assessing the extent and severity of biliary dilatation and location of stricture. The larger lobe and one with patent secondary biliary confluence is preferred to allow maximum drainage. However, any dilated system could be a source of infection due to stasis and an attempt must be made to drain it, especially if it is infected. When unilateral drainage, which has lower incidence of complications, is planned, cholangiogram must be carefully done to avoid filling of the non-drainable biliary system and thus subsequent infection^[48]. If the primary biliary confluence is patent, either left or right

sided drainage can be done depending on the local practice, patient comfort and radiologist's expertise. Bilobar or multiple system drainage may also be done. In cases where there is atrophy of a lobe due to chronic biliary obstruction, the system may not need drainage as improvement in liver function is unlikely^[49]. But it needs drainage if this lobe is the source of cholangitis. No absolute contraindication exists for PTBD. Relative contraindications include bleeding diathesis, contrast allergies and ascites.

Prior to the procedure, patient preparation is needed. This includes correction of coagulation profile, if deranged and administration of a dose of broad spectrum antibiotic. Ascites should be drained before PTBD. The segmental duct (preferably segment 3 for left sided and segment 6 for right sided drainage) is punctured, using ultrasonography as guidance. The puncture needle is exchanged for

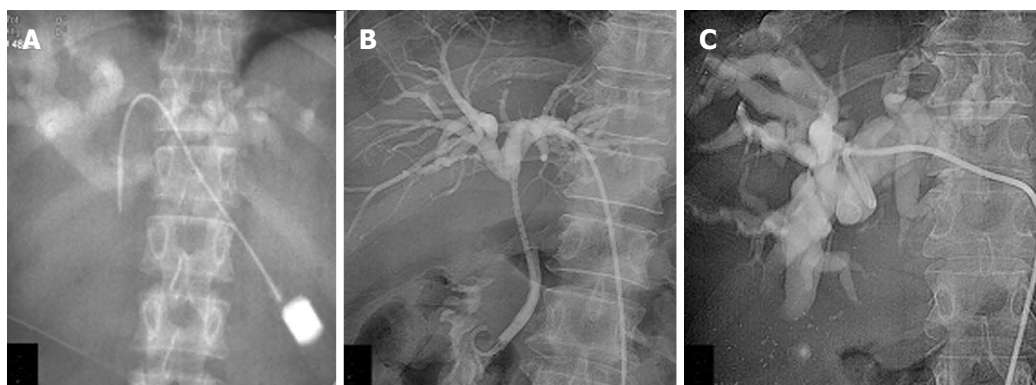


Figure 24 Types of biliary drainages. A: Initial cholangiogram showing dilated intrahepatic bile ducts with hilar obstruction; B: Cholangiogram after placement of ring biliary catheter (Internal-External drainage) showing opacification of bile ducts and duodenum; C: Cholangiogram after placement of external drainage pig-tail catheter.

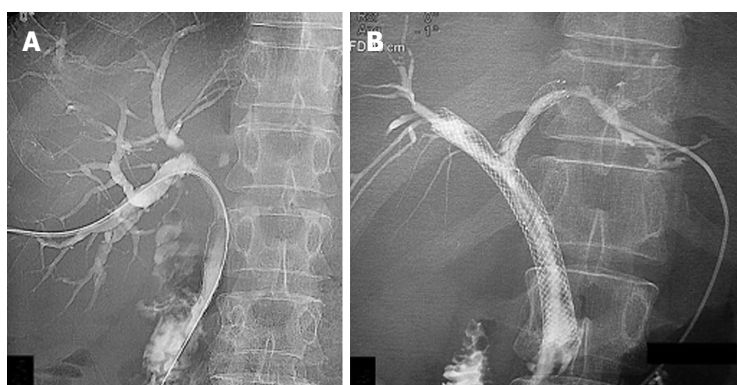


Figure 25 Types of biliary stenting. A: Cholangiogram after placement of unilobar (right sided) biliary metallic stent; B: Cholangiogram after bilobar stent placement showing free flow of contrast into duodenum across the stricture.

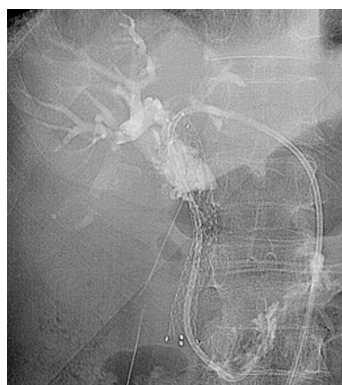


Figure 26 Percutaneous biliary drainage through ring biliary catheter after obstruction of biliary metallic stent due to tumor ingrowth.

a dilator over a guidewire, and check cholangiogram is performed to define the biliary anatomy (Figure 24A). Subsequently a guidewire is manipulated across the stricture following which the tract is dilated and an 8.3 F internal-external drainage catheter (Ring biliary catheter, Cook, Bloomington, IN) is placed across the stricture (Figure 24B). In cases where there is difficulty in crossing the stricture, an external drainage catheter is placed *in situ* (Figure 24C) and internal drainage is attempted two-four days later. This approach often helps in reducing the inflammation and edema and increases the chances of negotiating the stricture. Küçükay *et*

al^[50], in their study ($n = 256$) on percutaneous treatment of malignant biliary obstructions found that suprahilar lesions and lesions with flat or ovoid shape had higher failure rates. They suggested that an external drainage should be done after five unsuccessful attempts of internal drainage. Mueller *et al*^[51], reported easier catheterization of a stricture in a delayed second session due to straightened course of the guide wire directing into the lumen by decreased duct calibre above the obstruction, resolution of reactive edema at the site of obstruction and development of a tract around the catheter enabling the use of large-caliber catheters. An additional advantage of PTBD is the ability to obtain endobiliary tissue sample for histopathology using brush (for cytology) or forceps (for biopsy)^[52].

BILIARY STENTING

Biliary stenting is done in inoperable cases as a palliative measure. It can be done as a primary procedure or after PTBD. In primary stenting, once the stricture is crossed with guide-wire, stent can be deployed over the guide-wire across the obstruction. This reduces the incidence of procedure related complications compared to stenting done after PTBD^[53]. Self-expandablemetallic stents are preferred. Metallic stents have higher patency rates, lower overall cost and shorter hospital stay

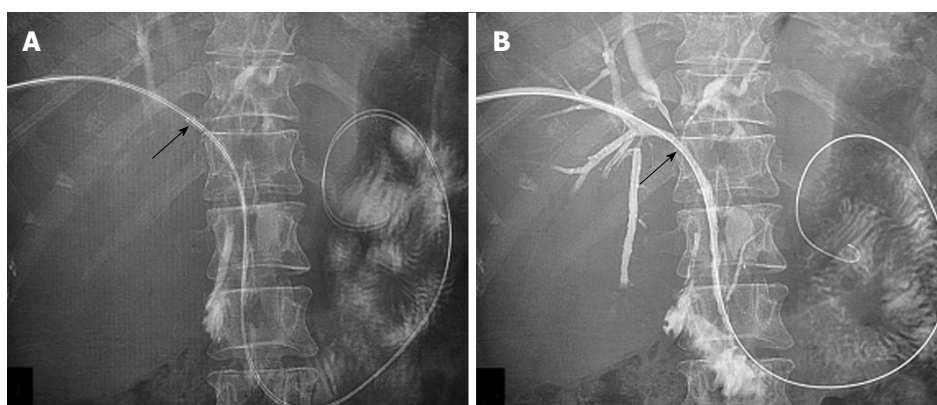


Figure 27 Percutaneous radiofrequency ablation for hilar cholangiocarcinoma. A: Pre-radiofrequency ablation (RFA) image with probe *in situ* (arrow); B: Cholangiogram after RFA showing opening of obstruction (arrow).

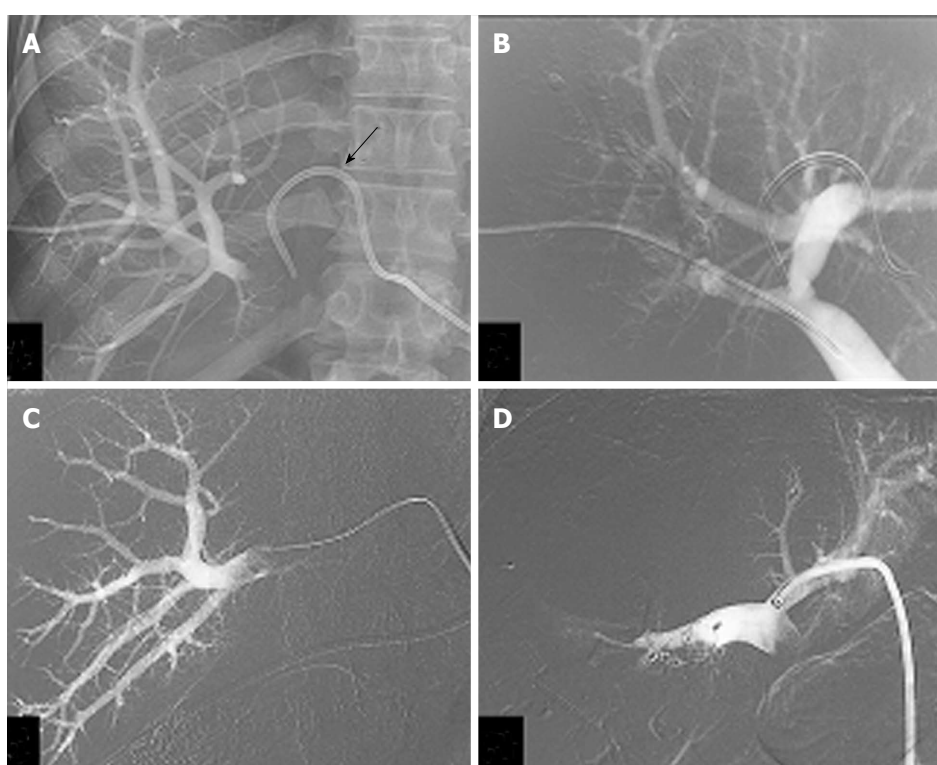


Figure 28 Right portal vein embolization with ipsilateral (A and B) and contralateral (C and D) approaches. A: Right portal venogram with ipsilateral approach. percutaneous transhepatic biliary drainage catheter is seen (arrow); B: Portal venogram after embolization of right portal vein with PVA and glue; C: Right portal venogram with contralateral approach; D: Portal venogram after embolization of right portal vein with glue and vascular plug.

than plastic stents (Figure 25)^[54]. Pre-stent balloon dilatation is usually avoided as it increases the risk of bleeding^[53]. The stent usually expands completely within 24-48 h and allows decompression of the biliary tree. If it does not adequately expand after 48 h, balloon dilatation of the stent may be done subsequently for adequate drainage. For masses involving the primary biliary confluence, two metallic stents (right and left side) can be placed in “Y” shape to drain both the systems (Figure 25B).

The biliary stent may get blocked by internal biliary sludge or by the tumor. Tumor ingrowth occurs when the tumor grows into the stent lumen through

the gaps between the struts of the stent. This may be dealt with endoscopically or percutaneously. Endoscopic placement of plastic stent through the blocked primary stent is often successful^[55]. Otherwise, percutaneous intervention in the form of balloon dilatation or placement of a smaller calibre coaxial stent or ring biliary catheter is done (Figure 26)^[55]. Use of covered metallic stents prevents tumor ingrowth and thus improves stent patency rates and reduces the incidence of re-intervention^[56]. Progression of the tumor may result in involvement of more proximal ducts and the stent may become ineffective. Such cases may need further drainage

which is often difficult to achieve. Stent migration, a very rare complication, may require repeat procedure.

INTRA-BILIARY PALLIATIVE THERAPY

Intra-biliary brachytherapy or photodynamic therapy prior to stenting improves the life expectancy of patients with HiCC and also stent patency^[57]. The primary advantage of intraluminal brachytherapy over external beam radiotherapy is that higher doses of irradiation can be given without damaging adjacent normal tissues^[58]. This procedure is usually done through PTBD route, preferably after metallic stent placement. The iridium-192 strands are intraluminally placed at the site of the tumor or stricture through PTBD catheter. Chen *et al.*^[59], found 98% success rate of intraluminal brachytherapy using Iridium-192 in 34 patients of malignant biliary obstruction and concluded that intraluminal brachytherapy is a safe palliative therapy and improves patient survival. In photodynamic therapy, a photosensitizer is injected intravenously followed by application of light to the tumor, endoscopically or through PTBD route. The photosensitizer interacts with the light releasing free radicals and causing cell death. Lee *et al.*^[60] in their study ($n = 33$) found that photodynamic treatment prior to metallic stenting resulted in significantly longer stent patency and longer survival, with low risk of complications (17%).

RADIOFREQUENCY ABLATION

Radiofrequency ablation (RFA), a technique which causes coagulation necrosis of tissue, is well known in the treatment of hepatic tumors. Its use as a palliative procedure in unresectable HiCC has produced promising results^[61]. The procedure can be done either through transhepatic route with routine probes used for liver tumors or through endoscopic or PTBD route with the use of special endobiliary probe (Figure 27)^[62,63]. RFA in unresectable cases is a safe procedure and it improves stent patency and survival.

PVE

This procedure is done to induce hypertrophy of non-involved lobe of liver by HiCC if the remnant liver volume is insufficient to maintain normal body function. Although it is not specific for HiCC, it is done in a few such patients so that a curative surgery can be performed. Embolization of the portal vein branch of the lobe which is involved by the lesion and which would be subsequently resected is done to induce hypertrophy of the other lobe^[64,65]. Hypertrophy normally occurs in 2-4 wk after which surgery can be done. Various embolizing materials

are used including polyvinyl alcohol particles, gelatin sponge (gelfoam) and n-butyl cyanoacrylate (glue)^[66]. Vascular plugs can also be used in addition to these materials to increase the chance of hypertrophy.

The procedure can be performed puncturing either ipsilateral or contralateral portal vein branch under USG guidance. Once within the system, the puncture needle is exchanged for a catheter over a guide-wire. With the tip of the catheter sufficiently distal to the bifurcation, the embolizing material is injected till the flow slows down significantly (Figure 28). After embolization, the needle tract either can be left alone or can be embolized with a coil or gelatin sponge. Imaging is then usually performed after 3-4 wk and the volume of future liver remnant is measured. If it is adequate, curative surgery can be performed. The procedure has a technical success rate of 99.3%, clinical success rate of 96.1% and mean liver hypertrophy rate of 38%^[66].

CONCLUSION

HiCC is a common malignancy of the biliary tract and imaging with various modalities play an important role planning appropriate management. Selection of appropriate imaging modality is important to obtain complete information needed for management. Multiphase CT scan and MRI are comparable in pre-operative diagnosis and staging. Additional modalities like EUS, IDUS, cholangioscopy and DWI are complementary. Surgery, wherever possible, is the only curative treatment available. Various percutaneous interventions are available including PTBD, stenting, intra-biliary palliation and PVE as either pre-operative or palliative procedure in such patients.

REFERENCES

1. **Friman S.** Cholangiocarcinoma—current treatment options. *Scand J Surg* 2011; **100**: 30-34 [PMID: 21491796]
2. **Bold RJ,** Goodnight JE. Hilar cholangiocarcinoma: surgical and endoscopic approaches. *Surg Clin North Am* 2004; **84**: 525-542 [PMID: 15062660 DOI: 10.1016/S0039-6109(03)00232-9]
3. **Patel T.** Worldwide trends in mortality from biliary tract malignancies. *BMC Cancer* 2002; **2**: 10 [PMID: 11991810 DOI: 10.1186/1471-2407-2-10]
4. **Suarez-Munoz MA,** Fernandez-Aguilar JL, Sanchez-Perez B, Perez-Daga JA, Garcia-Albiach B, Pulido-Roa Y, Marin-Camero N, Santoyo-Santoyo J. Risk factors and classifications of hilar cholangiocarcinoma. *World J Gastrointest Oncol* 2013; **5**: 132-138 [PMID: 23919107 DOI: 10.4251/wjgo.v5.i7.132]
5. **Nakeeb A,** Pitt HA, Sohn TA, Coleman J, Abrams RA, Piantadosi S, Hruban RH, Lillemoe KD, Yeo CJ, Cameron JL. Cholangiocarcinoma. A spectrum of intrahepatic, perihilar, and distal tumors. *Ann Surg* 1996; **224**: 463-473; discussion 473-475 [PMID: 8857851 DOI: 10.1097/0000658-199610000-00005]
6. **DeOliveira ML,** Cunningham SC, Cameron JL, Kamangar F, Winter JM, Lillemoe KD, Choti MA, Yeo CJ, Schulick RD. Cholangiocarcinoma: thirty-one-year experience with 564 patients at a single institution. *Ann Surg* 2007; **245**: 755-762 [PMID: 17457168 DOI: 10.1097/01.sla.0000251366.62632.d3]

- 7 **Bismuth H**, Corlette MB. Intrahepatic cholangioenteric anastomosis in carcinoma of the hilus of the liver. *Surg Gynecol Obstet* 1975; **140**: 170-178 [PMID: 1079096]
- 8 **Bosman FT**, Carneiro F, Hruban RH, Theise ND. WHO classification of tumors of the digestive system. 4th ed. IARC: Lyon, 2010: 195-278
- 9 **Castellano-Megías VM**, Ibarrola-de Andrés C, Colina-Ruizdelgado F. Pathological aspects of so called "hilar cholangiocarcinoma". *World J Gastrointest Oncol* 2013; **5**: 159-170 [PMID: 23919110 DOI: 10.4251/wjgo.v5.i7.159]
- 10 **Liver Cancer Study Group of Japan**. The general rules for the clinical and pathological study of primary liver cancer, 4th ed. Tokyo: Kanehara, 2000
- 11 **Lim JH**, Park CK. Pathology of cholangiocarcinoma. *Abdom Imaging* 2004; **29**: 540-547 [PMID: 15383897 DOI: 10.1007/s00261-004-0187-2]
- 12 **Shin HR**, Oh JK, Masuyer E, Curado MP, Bouvard V, Fang YY, Wiangnon S, Sripa B, Hong ST. Epidemiology of cholangiocarcinoma: an update focusing on risk factors. *Cancer Sci* 2010; **101**: 579-585 [PMID: 20085587 DOI: 10.1111/j.1349-7006.2009.01458.x]
- 13 **Park HS**, Lee JM, Choi JY, Lee MW, Kim HJ, Han JK, Choi BI. Preoperative evaluation of bile duct cancer: MRI combined with MR cholangiopancreatography versus MDCT with direct cholangiography. *AJR Am J Roentgenol* 2008; **190**: 396-405 [PMID: 18212225 DOI: 10.2214/AJR.07.2310]
- 14 **Bloom CM**, Langer B, Wilson SR. Role of US in the detection, characterization, and staging of cholangiocarcinoma. *Radiographics* 1999; **19**: 1199-1218 [PMID: 10489176 DOI: 10.1148/radiographics.19.5.g99se081199]
- 15 **Hann LE**, Greatrex KV, Bach AM, Fong Y, Blumgart LH. Cholangiocarcinoma at the hepatic hilus: sonographic findings. *AJR Am J Roentgenol* 1997; **168**: 985-989 [PMID: 9124155 DOI: 10.2214/ajr.168.4.9124155]
- 16 **Choi BI**, Lee JH, Han MC, Kim SH, Yi JG, Kim CW. Hilar cholangiocarcinoma: comparative study with sonography and CT. *Radiology* 1989; **172**: 689-692 [PMID: 2549565 DOI: 10.1148/radiology.172.3.2549565]
- 17 **Neumaier CE**, Bertolotto M, Perrone R, Martinoli C, Loria F, Silvestri E. Staging of hilar cholangiocarcinoma with ultrasound. *J Clin Ultrasound* 1995; **23**: 173-178 [PMID: 7730463 DOI: 10.1002/jcu.1870230305]
- 18 **Xu HX**. Contrast-enhanced ultrasound in the biliary system: Potential uses and indications. *World J Radiol* 2009; **1**: 37-44 [PMID: 21160719 DOI: 10.4329/wjrv.v1.i1.37]
- 19 **Xu HX**, Chen LD, Xie XY, Xie XH, Xu ZF, Liu GJ, Lin MX, Wang Z, Lu MD. Enhancement pattern of hilar cholangiocarcinoma: contrast-enhanced ultrasound versus contrast-enhanced computed tomography. *Eur J Radiol* 2010; **75**: 197-202 [PMID: 19464836 DOI: 10.1016/j.ejrad.2009.04.060]
- 20 **Khalili K**, Metser U, Wilson SR. Hilar biliary obstruction: preliminary results with Levovist-enhanced sonography. *AJR Am J Roentgenol* 2003; **180**: 687-693 [PMID: 12591675 DOI: 10.2214/ajr.180.3.1800687]
- 21 **Aljiffry M**, Walsh MJ, Molinari M. Advances in diagnosis, treatment and palliation of cholangiocarcinoma: 1990-2009. *World J Gastroenterol* 2009; **15**: 4240-4262 [PMID: 19750567 DOI: 10.3748/wjg.15.4240]
- 22 **Mohamadnejad M**, DeWitt JM, Sherman S, LeBlanc JK, Pitt HA, House MG, Jones KJ, Fogel EL, McHenry L, Watkins JL, Cote GA, Lehman GA, Al-Haddad MA. Role of EUS for preoperative evaluation of cholangiocarcinoma: a large single-center experience. *Gastrointest Endosc* 2011; **73**: 71-78 [PMID: 21067747 DOI: 10.1016/j.gie.2010.08.050]
- 23 **Brugge WR**. Advances in the endoscopic management of patients with pancreatic and biliary malignancies. *South Med J* 2006; **99**: 1358-1366 [PMID: 17233192 DOI: 10.1097/01.smj.0000251324.81191.cd]
- 24 **Chak A**, Catanzaro A. Innovative methods of biliary tract diagnosis: intraductal ultrasound and tissue acquisition. *Gastrointest Endosc Clin N Am* 2003; **13**: 609-622 [DOI: 10.1016/S1052-5157(03)00068-0]
- 25 **Farrell RJ**, Agarwal B, Brandwein SL, Underhill J, Chuttani R, Pleskow DK. Intraductal US is a useful adjunct to ERCP for distinguishing malignant from benign biliary strictures. *Gastrointest Endosc* 2002; **56**: 681-687 [PMID: 12397276 DOI: 10.1016/S0016-5107(02)70117-X]
- 26 **Ahmetoğlu A**, Koşucu P, Kul S, Dinç H, Sari A, Arslan M, Alhan E, Gümele HR. MDCT cholangiography with volume rendering for the assessment of patients with biliary obstruction. *AJR Am J Roentgenol* 2004; **183**: 1327-1332 [PMID: 15505298 DOI: 10.2214/ajr.183.5.1831327]
- 27 **Cha JH**, Han JK, Kim TK, Kim AY, Park SJ, Choi BI, Suh KS, Kim SW, Han MC. Preoperative evaluation of Klatskin tumor: accuracy of spiral CT in determining vascular invasion as a sign of unresectability. *Abdom Imaging* 2000; **25**: 500-507 [PMID: 10931985 DOI: 10.1007/s002610000081]
- 28 **Ruys AT**, van Beem BE, Engelbrecht MR, Bipat S, Stoker J, Van Gulik TM. Radiological staging in patients with hilar cholangiocarcinoma: a systematic review and meta-analysis. *Br J Radiol* 2012; **85**: 1255-1262 [PMID: 22919007 DOI: 10.1259/bjr/88405305]
- 29 **Choi JY**, Kim MJ, Lee JM, Kim KW, Lee JY, Han JK, Choi BI. Hilar cholangiocarcinoma: role of preoperative imaging with sonography, MDCT, MRI, and direct cholangiography. *AJR Am J Roentgenol* 2008; **191**: 1448-1457 [PMID: 18941084 DOI: 10.2214/AJR.07.3992]
- 30 **Ramiah JM**. Hilar cholangiocarcinoma. *World J Gastrointest Oncol* 2013; **5**: 113-114 [PMID: 23919104 DOI: 10.4251/wjgo.v5.i7.115]
- 31 **Lim JH**. Cholangiocarcinoma: morphologic classification according to growth pattern and imaging findings. *AJR Am J Roentgenol* 2003; **181**: 819-827 [PMID: 12933488 DOI: 10.2214/ajr.181.3.1810819]
- 32 **Lee MG**, Lee HJ, Kim MH, Kang EM, Kim YH, Lee SG, Kim PN, Ha HK, Auh YH. Extrahepatic biliary diseases: 3D MR cholangiopancreatography compared with endoscopic retrograde cholangiopancreatography. *Radiology* 1997; **202**: 663-669 [PMID: 9051013 DOI: 10.1148/radiology.202.3.9051013]
- 33 **Kim HJ**, Lee JM, Kim SH, Han JK, Lee JY, Choi JY, Kim KH, Kim JY, Lee MW, Kim SJ, Choi BI. Evaluation of the longitudinal tumor extent of bile duct cancer: value of adding gadolinium-enhanced dynamic imaging to unenhanced images and magnetic resonance cholangiography. *J Comput Assist Tomogr* 2007; **31**: 469-474 [PMID: 17538298 DOI: 10.1097/01.rct.0000238011.42060.b5]
- 34 **Cui XY**, Chen HW. Role of diffusion-weighted magnetic resonance imaging in the diagnosis of extrahepatic cholangiocarcinoma. *World J Gastroenterol* 2010; **16**: 3196-3201 [PMID: 20593506 DOI: 10.3748/wjg.v16.i25.3196]
- 35 **Li N**, Liu C, Bi W, Lin X, Jiao H, Zhao P. MRCP and 3D LAVA imaging of extrahepatic cholangiocarcinoma at 3 T MRI. *Clin Radiol* 2012; **67**: 579-586 [PMID: 22137873 DOI: 10.1016/j.crad.2011.10.016]
- 36 **Jadvar H**, Henderson RW, Conti PS. [F-18]fluorodeoxyglucose positron emission tomography and positron emission tomography: computed tomography in recurrent and metastatic cholangiocarcinoma. *J Comput Assist Tomogr* 2007; **31**: 223-228 [PMID: 17414758 DOI: 10.1097/01.rct.0000237811.88251.d7]
- 37 **Kim JY**, Kim MH, Lee TY, Hwang CY, Kim JS, Yun SC, Lee SS, Seo DW, Lee SK. Clinical role of 18F-FDG PET-CT in suspected and potentially operable cholangiocarcinoma: a prospective study compared with conventional imaging. *Am J Gastroenterol* 2008; **103**: 1145-1151 [PMID: 18177454 DOI: 10.1111/j.1572-0241.2007.01710.x]
- 38 **Moon CM**, Bang S, Chung JB, Park SW, Song SY, Yun M, Lee JD. Usefulness of 18F-fluorodeoxyglucose positron emission tomography in differential diagnosis and staging of cholangiocarcinomas. *J Gastroenterol Hepatol* 2008; **23**: 759-765 [PMID: 17931372 DOI: 10.1111/j.1440-1746.2007.05173.x]
- 39 **Han JK**, Choi BI, Kim AY, An SK, Lee JW, Kim TK, Kim SW. Cholangiocarcinoma: pictorial essay of CT and cholangiographic findings. *Radiographics* 2002; **22**: 173-187 [PMID: 11796906 DOI: 10.1148/radiographics.22.1.g02ja15173]
- 40 **Nimura Y**. Staging cholangiocarcinoma by cholangioscopy. *HPB (Oxford)* 2008; **10**: 113-115 [PMID: 18773067 DOI: 10.1080/13651820801992658]
- 41 **Bismuth H**, Castaing D, Traynor O. Resection or palliation: priority of surgery in the treatment of hilar cancer. *World J Surg* 1988; **12**: 39-47

- [PMID: 2449769 DOI: 10.1007/BF01658484]
- 42 **Vogl TJ**, Schwarz WO, Heller M, Herzog C, Zangos S, Hintze RE, Neuhaus P, Hammerstingl RM. Staging of Klatskin tumours (hilar cholangiocarcinomas): comparison of MR cholangiography, MR imaging, and endoscopic retrograde cholangiography. *Eur Radiol* 2006; **16**: 2317-2325 [PMID: 16622690 DOI: 10.1007/s00330-005-0139-4]
 - 43 **Jarnagin WR**, Fong Y, DeMatteo RP, Gonen M, Burke EC, Bodniewicz BS J, Youssef BA M, Klimstra D, Blumgart LH. Staging, resectability and outcome in 225 patients with hilar cholangiocarcinoma. *Annals of Surgery* 2001; **234**: 507-519 [PMID: 11573054]
 - 44 **Edge SB**, Byrd DR, Compton CC, Fritz AG, Greene FL, Trotti A, editors. Perihilar bile ducts. AJCC Cancer Staging Manual. 7th ed. New York, NY: Springer, 2010: 219-222
 - 45 **Kloek JJ**, van der Gaag NA, Aziz Y, Rauws EA, van Delden OM, Lameris JS, Busch OR, Gouma DJ, van Gulik TM. Endoscopic and percutaneous preoperative biliary drainage in patients with suspected hilar cholangiocarcinoma. *J Gastrointest Surg* 2010; **14**: 119-125 [PMID: 19756881 DOI: 10.1007/s11605-009-1009-1]
 - 46 **Indar AA**, Lobo DN, Gilliam AD, Gregson R, Davidson I, Whittaker S, Doran J, Rowlands BJ, Beckingham IJ. Percutaneous biliary metal wall stenting in malignant obstructive jaundice. *Eur J Gastroenterol Hepatol* 2003; **15**: 915-919 [PMID: 12867803 DOI: 10.1097/00042737-200308000-00013]
 - 47 **George C**, Byass OR, Cast JE. Interventional radiology in the management of malignant biliary obstruction. *World J Gastrointest Oncol* 2010; **2**: 146-150 [PMID: 21160822 DOI: 10.4251/wjgo.v2.i3.146]
 - 48 **Chang WH**, Kortan P, Haber GB. Outcome in patients with bifurcation tumors who undergo unilateral versus bilateral hepatic duct drainage. *Gastrointest Endosc* 1998; **47**: 354-362 [PMID: 9609426 DOI: 10.1016/S0016-5107(98)70218-4]
 - 49 **van Delden OM**, Laméris JS. Percutaneous drainage and stenting for palliation of malignant bile duct obstruction. *Eur Radiol* 2008; **18**: 448-456 [PMID: 17960388 DOI: 10.1007/s00330-007-0796-6]
 - 50 **Küçükay F**, Oken RS, Yurdakul M, Ozdemir E, Parlak E, Olçer T, Cumhur T. Percutaneous management of malignant biliary disease: factors influencing the ability to overcome the stricture. *Diagn Interv Radiol* 2011; **17**: 169-173 [PMID: 20698007]
 - 51 **Mueller PR**, van Sonnenberg E, Ferrucci JT. Percutaneous biliary drainage: technical and catheter-related problems in 200 procedures. *AJR Am J Roentgenol* 1982; **138**: 17-23 [PMID: 6976698 DOI: 10.2214/ajr.138.1.17]
 - 52 **Xing GS**, Geng JC, Han XW, Dai JH, Wu CY. Endobiliary brush cytology during percutaneous transhepatic cholangiodrainage in patients with obstructive jaundice. *Hepatobiliary Pancreat Dis Int* 2005; **4**: 98-103 [PMID: 15730930]
 - 53 **Inal M**, Akgül E, Aksungur E, Demiryürek H, Yağmur O. Percutaneous self-expandable uncovered metallic stents in malignant biliary obstruction. Complications, follow-up and reintervention in 154 patients. *Acta Radiol* 2003; **44**: 139-146 [PMID: 12694096 DOI: 10.1034/j.1600-0455.2003.00049.x]
 - 54 **Lammer J**, Hausegger KA, Flückiger F, Winkelbauer FW, Wildling R, Klein GE, Thumher SA, Havelec L. Common bile duct obstruction due to malignancy: treatment with plastic versus metal stents. *Radiology* 1996; **201**: 167-172 [PMID: 8816539 DOI: 10.1148/radiology.201.1.8816539]
 - 55 **Cho JH**, Jeon TJ, Park JY, Kim HM, Kim YJ, Park SW, Chung JB, Song SY, Bang S. Comparison of outcomes among secondary covered metallic, uncovered metallic, and plastic biliary stents in treating occluded primary metallic stents in malignant distal biliary obstruction. *Surg Endosc* 2011; **25**: 475-482 [PMID: 20602138 DOI: 10.1007/s00464-010-1196-6]
 - 56 **Hatzidakis A**, Krokidis M, Kalbakis K, Romanos J, Petrakis I, Gourtsoyannis N. ePTFE/FEP-covered metallic stents for palliation of malignant biliary disease: can tumor ingrowth be prevented? *Cardiovasc Intervent Radiol* 2007; **30**: 950-958 [PMID: 17508236 DOI: 10.1007/s00270-007-9049-y]
 - 57 **Killeen RP**, Harte S, Maguire D, Malone DE. Achievable outcomes in the management of proximal cholangiocarcinoma: an update prepared using "evidence-based practice" techniques. *Abdom Imaging* 2008; **33**: 54-57 [PMID: 17874306 DOI: 10.1007/s00261-007-9312-3]
 - 58 **Andrašina T**, Válek V, Pánek J, Kala Z, Kiss I, Tuček S, Slampa P. Multimodal oncological therapy comprising stents, brachytherapy, and regional chemotherapy for cholangiocarcinoma. *Gut Liver* 2010; **4** Suppl 1: S82-S88 [PMID: 21103300 DOI: 10.5009/gnl.2010.4.S1.S82]
 - 59 **Chen Y**, Wang XL, Yan ZP, Cheng JM, Wang JH, Gong GQ, Qian S, Luo JJ, Liu QX. HDR-192Ir intraluminal brachytherapy in treatment of malignant obstructive jaundice. *World J Gastroenterol* 2004; **10**: 3506-3510 [PMID: 15526374]
 - 60 **Lee TY**, Cheon YK, Shim CS, Cho YD. Photodynamic therapy prolongs metal stent patency in patients with unresectable hilar cholangiocarcinoma. *World J Gastroenterol* 2012; **18**: 5589-5594 [PMID: 23112552 DOI: 10.3748/wjg.v18.i39.5589]
 - 61 **Steel AW**, Postgate AJ, Khorsandi S, Nicholls J, Jiao L, Vlavianos P, Habib N, Westaby D. Endoscopically applied radiofrequency ablation appears to be safe in the treatment of malignant biliary obstruction. *Gastrointest Endosc* 2011; **73**: 149-153 [PMID: 21184881 DOI: 10.1016/j.gie.2010.09.031]
 - 62 **Fan WJ**, Wu PH, Zhang L, Huang JH, Zhang FJ, Gu YK, Zhao M, Huang XL, Guo CY. Radiofrequency ablation as a treatment for hilar cholangiocarcinoma. *World J Gastroenterol* 2008; **14**: 4540-4545 [PMID: 18680236 DOI: 10.3748/wjg.14.4540]
 - 63 **Alis H**, Sengoz C, Gonenc M, Kalayci MU, Kocatas A. Endobiliary radiofrequency ablation for malignant biliary obstruction. *Hepatobiliary Pancreat Dis Int* 2013; **12**: 423-427 [PMID: 23924501 DOI: 10.1016/S1499-3872(13)60066-1]
 - 64 **Giraud G**, Greget M, Oussoultzoglou E, Rosso E, Bachellier P, Jaeck D. Preoperative contralateral portal vein embolization before major hepatic resection is a safe and efficient procedure: a large single institution experience. *Surgery* 2008; **143**: 476-482 [PMID: 18374044 DOI: 10.1016/j.surg.2007.12.006]
 - 65 **May BJ**, Madoff DC. Portal vein embolization: rationale, technique, and current application. *Semin Intervent Radiol* 2012; **29**: 81-89 [PMID: 23729977 DOI: 10.1055/s-0032-1312568]
 - 66 **van Lienden KP**, van den Esschert JW, de Graaf W, Bipat S, Lameris JS, van Gulik TM, van Delden OM. Portal vein embolization before liver resection: a systematic review. *Cardiovasc Intervent Radiol* 2013; **36**: 25-34 [PMID: 22806245 DOI: 10.1007/s00270-012-0440-y]

P- Reviewer: Cerwenka HR, Verma S, Vinh-Hung V
S- Editor: Tian YL **L- Editor:** A **E- Editor:** Wu HL



Basic Study

Evaluation of changes of intracranial blood flow after carotid artery stenting using digital subtraction angiography flow assessment

Hajime Wada, Masato Saito, Kyousuke Kamada

Hajime Wada, Masato Saito, Kyousuke Kamada, Department of Neurosurgery, Asahikawa Medical University, Asahikawa, Hokkaido 0788510, Japan

Author contributions: All authors contributed to this work.

Ethics approval: The study was reviewed and approved.

Institutional animal care and use committee: This study has been approved by institutional ethical committee (No. 132).

Conflict-of-interest: The authors report no conflict of interest regarding the manuscript.

Data sharing: The authors accept the data sharing.

Open-Access: This article is an open-access article which was selected by an in-house editor and fully peer-reviewed by external reviewers. It is distributed in accordance with the Creative Commons Attribution Non Commercial (CC BY-NC 4.0) license, which permits others to distribute, remix, adapt, build upon this work non-commercially, and license their derivative works on different terms, provided the original work is properly cited and the use is non-commercial. See: <http://creativecommons.org/licenses/by-nc/4.0/>

Correspondence to: Kyousuke Kamada, MD, PhD, Department of Neurosurgery, Asahikawa Medical University, 2-1, 1-1, Midorigaoka-Higashi, Asahikawa, Hokkaido 078-8510, Japan. hjwada@asahikawa-med.ac.jp

Telephone: +81-166-682594

Fax: +81-166-682599

Received: October 28, 2014

Peer-review started: October 29, 2014

First decision: December 12, 2014

Revised: December 25, 2014

Accepted: January 15, 2015

Article in press: January 19, 2015

Published online: February 28, 2015

METHODS: Twenty patients treated by CAS participated in this study. We analyzed the change in concentration of the contrast media at the anterior-posterior and profile view image with the flow assessment application "Flow-Insight". And we compared the results with N-isopropyl-p-[123I] iodoamphetamine-single-photon emission computed tomography (IMP SPECT) performed before and after the treatment.

RESULTS: From this study, 200% of the parameter "blood flow" change in the post/pre-treatment is suggested as the critical line of the hyperperfusion syndrome arise. Although the observed blood flow increase in the digital subtraction angiography system did not strongly correlate with the rate of increase of SPECT, the "Flow-Insight" reflected the rate of change of the vessels well. However, for patients with reduced reserve blood flow before CAS, a highly elevated site was in agreement with the site analysis results.

CONCLUSION: We concluded that the cerebral angiography flow assessment application was able to more finely reveal hyperperfusion regions in the brain after CAS compared to SPECT.

Key words: Intracranial blood flow; Cerebral angiography; Carotid artery stenting; Single-photon emission computed tomography

© **The Author(s) 2015.** Published by Baishideng Publishing Group Inc. All rights reserved.

Abstract

AIM: To evaluate the changes of intracranial blood flow after carotid artery stenting (CAS), using the flow assessment application "Flow-Insight", which was developed in our department.

Core tip: Hyperperfusion syndrome is a relatively rare, but potentially serious, complication of carotid revascularization procedures. It is important to detect the excessive increase blood flow after treatment as soon as possible. We found that, although the observed blood flow increase in the digital subtraction

angiography system did not strongly correlate with the rate of increase of single-photon emission computed tomography before and after carotid artery stenting, the digital subtraction angiography flow assessment application more finely reflected the rate of change of the vessels well.

Wada H, Saito M, Kamada K. Evaluation of changes of intracranial blood flow after carotid artery stenting using digital subtraction angiography flow assessment. *World J Radiol* 2015; 7(2): 45-51 Available from: URL: <http://www.wjgnet.com/1949-8470/full/v7/i2/45.htm> DOI: <http://dx.doi.org/10.4329/wjr.v7.i2.45>

INTRODUCTION

Cerebral hyperperfusion after carotid revascularization treatment is defined as a major increase in ipsilateral cerebral blood flow (CBF) well above the metabolic demands of the brain tissue. Cerebral hyperperfusion syndrome is characterized by a unilateral headache, face and eye pain, seizures, and focal symptoms secondary to cerebral edema or intracerebral hemorrhage. The pathological mechanisms of the irreversible changes have been theorized to involve organic dysautoregulation of maximally dilated cerebral vessels. Although the incidence of intracerebral hemorrhage is relatively low, the prognosis for patients with this condition is poor^[1,2]. Schroeder *et al*^[3] reported that CBF on N-isopropyl-p-[123I] iodoamphetamine-single-photon emission computed tomography ([123I] IMP-SPECT) postoperatively is increased beyond that in the preoperative state^[3]; and, in cases of marked hypoperfusion, hyperperfusion after surgical revascularization is known to occur^[4].

In this study, we aimed to evaluate the change of intracranial blood flow after carotid artery stenting (CAS) using the flow assessment application "Flow-Insight," which was developed in our department; and to compare the results with those of IMP-SPECT, which is currently commonly used in clinical practice^[5].

MATERIALS AND METHODS

A total of 20 patients (18 men and 2 women), aged 56-82 years (mean, 70.0 ± 5.9 years), without large cortical infarction on conventional magnetic resonance imaging, who underwent CAS between October 2012 and April 2014 were enrolled in the present study. The mean degree of internal carotid artery stenosis was 75.3% ± 15.8% (range, 59%-93%), according to the method of the North American Symptomatic Carotid Endarterectomy Trial^[6]. Three patients had symptomatic stenosis and 4 patients had occlusion or stenosis greater

than 50% in the contralateral internal carotid artery. All cases of CAS were performed under general anesthesia, using a proximal balloon, distal filter protection, and flow reverse to the femoral vein. Using the location memory of the digital subtraction angiography (DSA) suit Artis zee (Siemens AG Healthcare, Erlangen, Germany), intracranial angiography acquisitions were evaluated in the same position before and after treatment. We analyzed the changes in the concentration of the contrast media as changes in brightness using the novel flow assessment application "Flow-Insight" (Infocom, Tokyo, Japan). The result images were created as an anterior-posterior (AP) view and a profile image. The software converts DSA DICOM image data to 8 bit digital data. It utilizes a mutual information method and phase correction of the two-dimensional Fourier transformation as a motion artifact correction method, and can calculate the integral value of the luminance change of each pixel in the converted data and the peak periods to examine. The calculated parameters include the calculation amount arrival time, time to peak, and mean transit time, with a focus on the time and blood volume, as determined by the accumulated amount of brightness and blood flow. In the result images, the rate of the blood flow is displayed by a color bar representing changes of 50%-200%. In this study, we used paired *t* test for parameter changes before and after CAS and statistical significance was less than 0.05. We determined the region of interest (ROI) in the result images, and compared the results by the ARG method with one 123I-IMP SPECT before and after CAS, using Spearman's rank correlation coefficient and simple regression analyses.

Statistical analysis

The study protocol was performed in accordance with the Declaration of Helsinki and its later amendments. All participants provided written informed consent.

RESULTS

Our results show that the novel "Flow-Insight" application was capable of determining a qualitative value of the blood flow, which was defined as the blood volume divided by the mean transit time (Figure 1B and C) using a central volume principle as previously described^[7]. The blood volume and mean transit time were determined using a time density curve (Figure 1A). We next created an ROI and calculated the cerebral blood flow before and after treatment, and compared the increased rate with the corresponding rate evaluated by IMP SPECT. The increased rate was calculated by taking the ratio of the cerebellum and the left and right blood flow communication. We found that the "Flow-Insight" blood flow increase rate of the middle cerebral artery

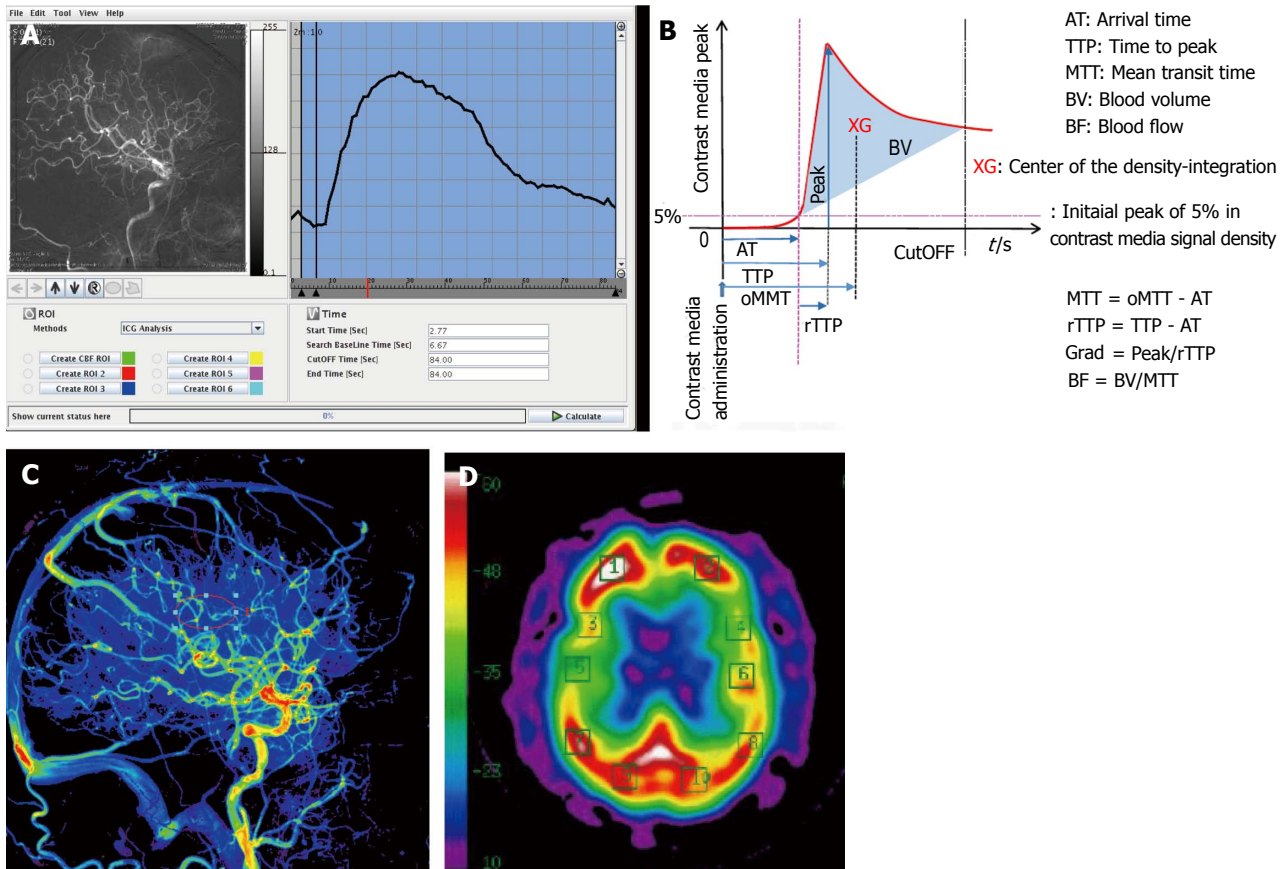


Figure 1 Digital subtraction angiography. A: Time-density curve of digital subtraction angiography lateral view. The change in the concentration of the contrast media, visualized as a change in brightness, was calculated; B: The parameters calculable by the "Flow-Insight" application; C: Lateral view of a pre-operative qualitative image of cerebral blood flow in Case 2; D: Pre-operative N-isopropyl-p-[123I] iodoamphetamine-single-photon emission computed tomography image.

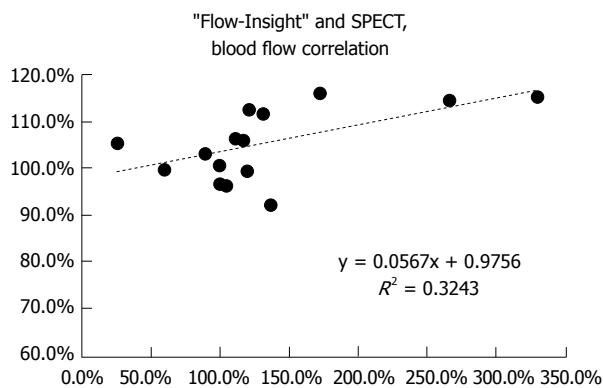


Figure 2 Horizontal axis: Rate of change of the "Flow-Insight" (%); Vertical axis: Rate of the rise of the ipsilateral cerebellum ratio as determined postoperatively by N-isopropyl-p-[123I] iodoamphetamine-single-photon emission computed tomography. SPECT: Single-photon emission computed tomography.

territory correlated with the increase ratio of the same SPECT territory in the cerebellum (Figure 2). The distribution with "Flow-Insight" was close to the 50%-200% range in all patients.

Because of the nature of DSA, it is generally difficult to capture the brain tissue blood perfusion changes. However, the images obtained using the "Flow-Insight" application were found to reflect the

changes in the vessels well. To avoid the vessels, we set the ROI as the motor and premotor cortex in the frontal lobe, just above the Sylvian fissure (Figure 1C and D). "Flow-Insight" successfully showed the highly elevated blood flow increase rate areas of patients with reduced vascular reserve areas.

In order to detect the actual increasing area in the human brain, we next created images based on the DSA blood flow increase ratio in the AP and lateral views, by dividing the post-operative CAS images by the pre-operative images (Figures 2 and 3). The result images showed the rate of blood flow, as defined by the color bar at 50%-200%. This range was chosen based on the range from the correlation of blood flow with SPECT. We reduced the image matrix settings to 100 × 100, because the displacement of high-resolution image calculations may lead to overestimation of the results.

It should be noted that the increased distribution observed after CAS was variable. For example, while Cases 1 and 2 did not show any blood flow from the contra-lateral *via* the anterior communicating artery, differences in the increased area and in the degree of the increase were noted upon DSA (Figure 3). Conversely, Cases 3 and 4 suffered severe right cervical internal carotid artery stenosis, and our

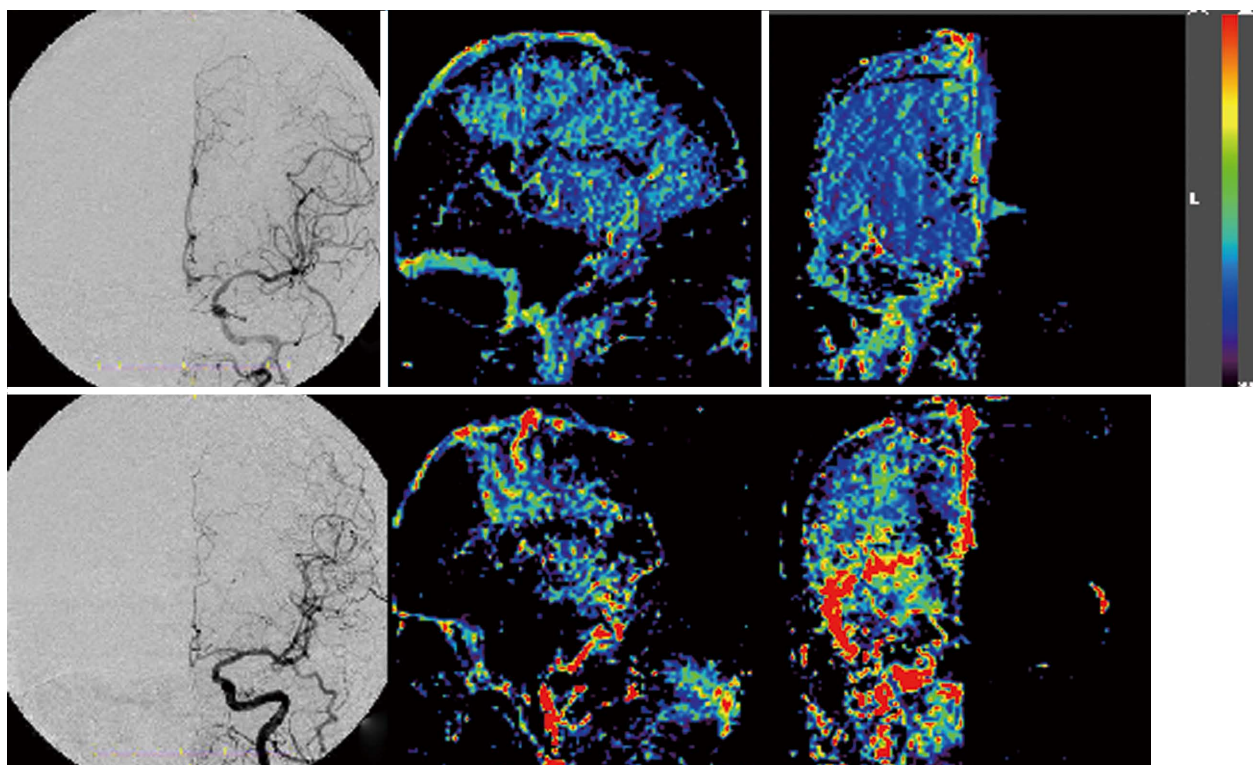


Figure 3 Upper panel: Digital subtraction angiography anterior-posterior view, lateral view showing the blood flow increase ratio, and the anterior-posterior view in Case 1; and Lower panel: Case 2, same series. Pre-operative digital subtraction angiography in Cases 1 and 2 did not reveal blood flow to the operative side *via* the anterior communicating artery. In Case 1, a wide and slight increase was noted in the area in the middle cerebral artery territory. In Case 2, the increase was only noted in a part of the middle cerebral artery perfusion area; the rate of increase was high.

analyses revealed blood flow from the contra-lateral side *via* the anterior communicating artery at the preoperative DSA (Figure 4). However, while the SPECT for case 4 showed a 114.2% increase ratio, the “Flow-Insight” showed a 265% increase ratio. The patient suffered mild delirium symptoms for 2 d after CAS. On the other hand, Case 3 also showed blood flow *via* the anterior communicating artery. However, in this case, the “Flow-Insight” blood flow increase ratio was only 131%, while the SPECT also showed a relatively low ratio, at 111.3%, suggesting that the patient did not suffer hyper-perfusion syndrome *per se*. The fact that the distribution of the intracranial blood flow increase rate after CAS showed quite different results in each case, not only in terms of the presence or absence of the left and right or anterior-posterior communication, but also in terms of the diameter and length, may be due to differences in the degree and area of the increased blood flow. The “Flow-Insight” application successfully revealed the presence of increased blood flow regions, which were not evident upon conventional SPECT.

DISCUSSION

In the case of carotid endarterectomy, the presence or absence of collateral flow *via* the anterior or posterior communicating artery deeply affects the

risk of intraoperative ischemic complications^[8,9]. Moreover, intraoperative measurement of distal internal carotid artery pressure reflects the intracranial vascular reserve, and is important in predicting postoperative hyperperfusion^[4]. Reduced blood flow due to internal carotid artery stenosis results in decreased blood flow reserves intracranially, and this has been demonstrated to be significantly influenced by the microscopic vascular bed and the left and right or anterior and posterior communication^[10]. Local increases of blood flow after treatment and blood flow buffering through the left-right or anterior-posterior communication may lead to hyperperfusion syndrome. Therefore, hyperperfusion syndrome cannot completely be predicted by the presence or absence of blood flow communication only. Furthermore, local variations at the site of the blood flow increase may cause different symptoms of hyperperfusion syndrome, such as headaches, intracranial hemorrhage (subarachnoid hemorrhage, subcortical hemorrhage, or basal ganglia hemorrhage), delirium, or convulsions^[1,2,11].

IMP-SPECT is currently the conventional modality for measuring intracranial blood flow. In this study, when comparing the SPECT and the “Flow-Insight” blood flow increase rates in the whole treated area, no clear correlation was observed. However, when evaluating the correlation restricted to the MCA territory, which is devoid of major vessels and which

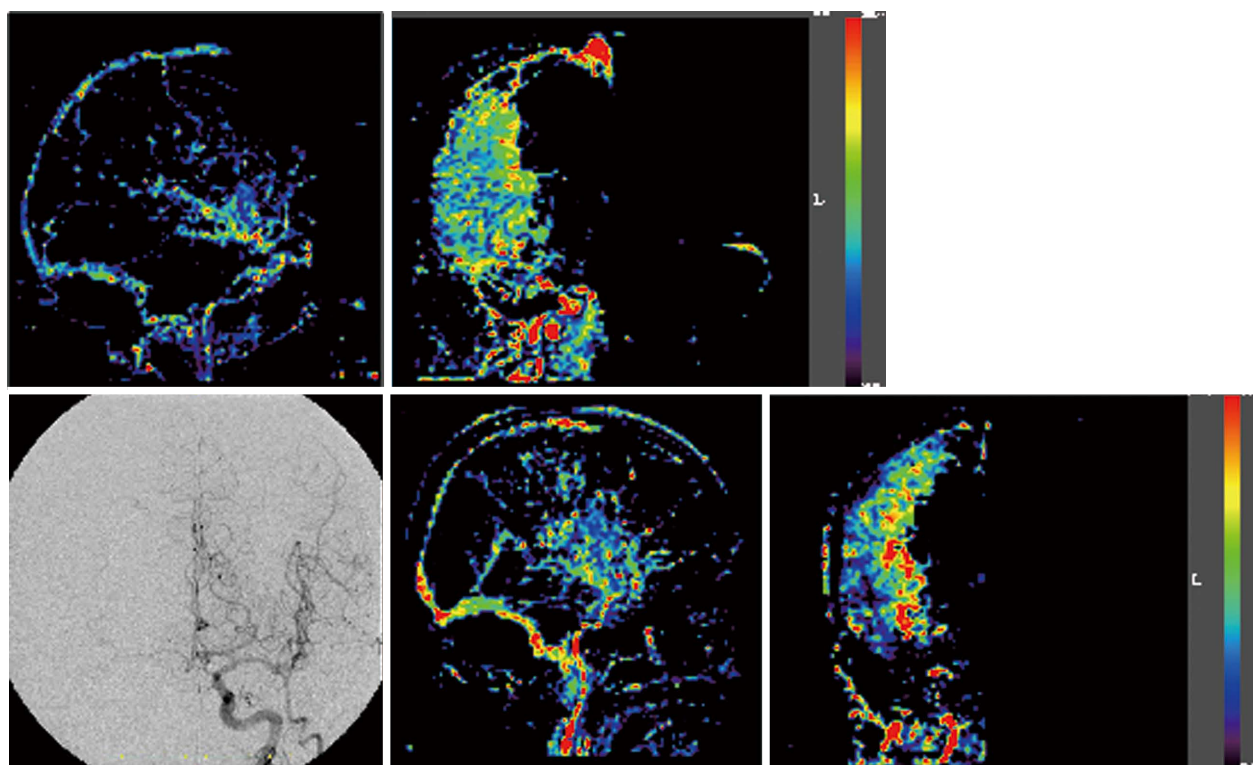


Figure 4 Upper panel: Digital subtraction angiography anterior-posterior view, lateral view showing the blood flow increase ratio, and the anterior-posterior view in Case 3; and Lower panel: Case 4, same series. Pre-operative digital subtraction angiography in Cases 3 and 4 revealed blood flow to the operative side via the anterior communicating artery. A wide and uniform increase in the area in the middle cerebral artery territory was noted in Case 3. In Case 4, the increase was only noted in a part of the middle cerebral artery perfusion area, especially in the basal ganglia; the rate of increase was high.

is the perfusion area of the internal carotid artery, we detected a good correlation. We moreover found that increased blood flow after treatment of internal carotid artery stenosis is not confined to a uniform territory. However, we were unable to draw any firm and conclusions regarding this observation because of the limited size of the study, since only one patient presented with typical hyperperfusion syndrome. This novel evaluation method revealed the increase ratio and its intracranial distribution, and because it strongly reflected the local vascular reserve, as well as the left and right or anterior-posterior artery communication, we believe that it has the potential to predict the presence of hyperperfusion syndrome.

At this time, quantification of cerebral blood flow is not available from the "Flow-Insight". However, we hypothesized that if there was a high correlation with the results of the post-operative blood flow achieved from the "Flow-Insight" and that obtained from SPECT, the "Flow-Insight" would be able to predict post-operative hyperperfusion syndrome. Accordingly, we found that the "Flow-Insight" blood flow increase rate correlated with the increase ratio of SPECT. However, the correlation, R^2 , was 0.324, which suggests that the correlation was only moderate. One reason for why no strong correlation was observed could be that the "Flow-Insight" is performed immediately after treatment, whereas SPECT is usually performed approximately 24 h

post-operation. After CAS, normalization of cerebral blood flow may spontaneously be initiated. Thus, the results of the flow assessment using DSA will be different from the blood flow measured by SPECT in the following points: first, contrast medium is a non-diffusible tracer. The contrast medium is injected just proximal of the lesion in "Flow-Insight," indicating that this evaluation method is highly focal. Moreover, it is based on processing of an image acquired by the inhibition of the radiation translucency and subtraction of an X-ray image. Accordingly, "Flow-Insight" reveals slightly different blood flow from that evaluated by conventional SPECT or computed tomography perfusion. In terms of the terminology of this novel method, it should be pointed out that "Flow-Insight" is the flow assessment software used, while cerebral angiography is simply a method used to obtain the black-and-white 2D image, and is used only to evaluate the appearance of the vascular system, such as the form of aneurysms or continuity of vessels. However, a major advantage of DSA is that it has a time scale, which computed tomography angiography and magnetic resonance angiography do not.

It has been previously reported that the right and left venous phase appearance times are symmetrical in the internal carotid artery occlusion test (balloon occlusion test)^[12], and this method has been proposed as an alternative to angiographic imaging.

However, it was due to the statistical processing taking a partial ROI.

By using the "Flow-Insight" software, it is easy to visualize the intracranial blood flow changes using the color bar, despite the 2D nature of the images. It is hence a useful indicator to understand the entire brain, unlike focal methods evaluating only the ROI. Moreover, the fact that it can be used immediately after treatment unlike other post-operative evaluations such as SPECT or computed tomography perfusion is a great advantage.

Application of flow assessment angiography with indocyanine green in bypass surgery has been previously reported^[13-15], and cerebral blood flow assessment using the latest DSA system may also be applied for these patients^[16]. The "Flow-Insight" application is based on the same principle as flow assessment angiography and is easy to use with the proper equipment. However, the method of analysis could be improved further, and the application is currently inconvenient to apply in other ways. DSA flow assessment is also associated with a number of issues related to certain factors, such as the head position during data acquisition, the velocity and amount of contrast media used, and the diameter of the catheter. Moreover, it is a direct injection of contrast media, which may cause increased pressure in the arteries, rather than a systemic intravenous administration into the physiological blood flow. Furthermore, since it is based on two-dimensional images, the accumulated value of the 2D images are greatly affected by the three-dimensional volume, such as for example the intracranial venous phase overlapping with the arterial phase, and the image accumulated by subtraction images can be easily affected by motion artifacts. However, the risk of this can be minimized by using general anesthesia to keep the patients stationary, and by the angle and position of the table being memorized by a specialized device during the treatment. In the future, if it becomes possible to perform 3D assessment analyses, it can be expected that the accuracy of this application will dramatically improve.

In the present study, using flow assessment application we were able to reveal more finely hyperperfusion regions in the brain after CAS. Flow assessment application was useful for understanding the pathology of the brain post-CAS. Further studies to determine the optimal angiographic conditions, such as the optimal contrast agent concentration and amount, are warranted.

COMMENTS

Background

Flow assessment study derived from digital subtraction angiography (DSA) for the cerebral arterial flow in clinical settings have been proposed, but no exist so much. Hyperperfusion syndrome is a relatively rare, but potentially serious, complication of carotid artery stenting. Therefore, the authors applied to detect the excessive increase blood flow after treatment.

Research frontiers

In the present study, using flow assessment application of cerebral angiography the authors were able to reveal more finely hyperperfusion regions in the brain after carotid artery stenting. Then it suggests that any hyperperfusion syndrome variation is come from which brain area of excessive increased flow.

Innovations and breakthroughs

Just after treatment, only usual cerebral angiography, without using other modality, can predict the occurrence of serious complications. Furthermore, it reveals that flow assessment application was aim to be a useful clinical application.

Applications

From this study, 200% of the parameter "blood flow" change in the post/pre-treatment is suggested as the critical line of the hyperperfusion syndrome arise. By using the "Flow-Insight" software, it is easy to visualize the intracranial blood flow changes using the color bar, despite the 2D nature of the images. It is hence a useful indicator to understand the entire brain, unlike focal methods evaluating only the region of interest.

Terminology

Flow assessment application: It analyze focal blood flow and derive parametric imaging maps from DSA. The origin is from Indocyanine green video angiography at the open micro-surgery. Cerebral hyperperfusion syndrome: It is a rare, serious complication either after carotid endarterectomy or carotid stent placement. Impaired cerebral autoregulation. The syndrome is characterized by a unilateral headache, face and eye pain, seizures, and focal symptoms secondary to cerebral edema or intracerebral hemorrhage. It may be fatal once an intracranial hemorrhage occurs.

Peer-review

The paper is well written.

REFERENCES

- 1 **Bernstein M**, Fleming JF, Deck JH. Cerebral hyperperfusion after carotid endarterectomy: a cause of cerebral hemorrhage. *Neurosurgery* 1984; **15**: 50-56 [PMID: 6472594]
- 2 **Piegras DG**, Morgan MK, Sundt TM, Yanagihara T, Mussman LM. Intracerebral hemorrhage after carotid endarterectomy. *J Neurosurg* 1988; **68**: 532-536 [PMID: 3351580 DOI: 10.3171/jns.1988.68.4.0532]
- 3 **Schroeder T**, Sillesen H, Sørensen O, Engell HC. Cerebral hyperperfusion following carotid endarterectomy. *J Neurosurg* 1987; **66**: 824-829 [PMID: 3572512]
- 4 **Yoshimoto T**, Shirasaka T, Yoshizumi T, Fujimoto S, Kaneko S, Kashiwaba T. Evaluation of carotid distal pressure for prevention of hyperperfusion after carotid endarterectomy. *Surg Neurol* 2005; **63**: 554-557; discussion 557-558 [DOI: 10.1016/j.surneu.2004.06.016]
- 5 **Iida H**, Itoh H, Nakazawa M, Hatazawa J, Nishimura H, Onishi Y, Uemura K. Quantitative mapping of regional cerebral blood flow using iodine-123-IMP and SPECT. *J Nucl Med* 1994; **35**: 2019-2030 [PMID: 7989987]
- 6 **North American Symptomatic Carotid Endarterectomy Trial Collaborators**. Beneficial effect of carotid endarterectomy in symptomatic patients with high-grade carotid stenosis. *N Engl J Med* 1991; **325**: 445-453 [PMID: 1852179 DOI: 10.1056/NEJM199108153250701]
- 7 **Meier P**, Zierler KL. On the theory of the indicator-dilution method for measurement of blood flow and volume. *J Appl Physiol* 1954; **6**: 731-744 [PMID: 13174454]
- 8 **Lopez-Bresnahan MV**, Kears LA, Yanez P, Young TI. Anterior communicating artery collateral flow protection against ischemic change during carotid endarterectomy. *J Neurosurg* 1993; **79**: 379-382 [PMID: 8360734 DOI: 10.3171/jns.1993.79.3.0379]
- 9 **Schwartz RB**, Jones KM, LeClerc GT, Ahn SS, Chabot R, Whittemore A, Mannick JA, Donaldson MC, Gugino LD. The value of cerebral angiography in predicting cerebral ischemia during carotid endarterectomy. *AJR Am J Roentgenol* 1992; **159**: 1057-1061 [PMID: 1414775 DOI: 10.2214/ajr.159.5.1414775]
- 10 **Kuroda H**, Ogasawara K, Hirooka R, Kobayashi M, Fujiwara S, Chida K, Ishigaki D, Otawara Y, Ogawa A. Prediction of cerebral hyperperfusion after carotid endarterectomy using middle cerebral

- artery signal intensity in preoperative single-slab 3-dimensional time-of-flight magnetic resonance angiography. *Neurosurgery* 2009; **64**: 1065-1071; discussion 1071-1072 [PMID: 19487885 DOI: 10.1227/01.NEU.0000345941.99443.99]
- 11 **Solomon RA**, Loftus CM, Quest DO, Correll JW. Incidence and etiology of intracerebral hemorrhage following carotid endarterectomy. *J Neurosurg* 1986; **64**: 29-34 [PMID: 3941347 DOI: 10.3171/jns.1986.64.1.0029]
 - 12 **Abud DG**, Spelle L, Pötting M, Mounayer C, Vanzin JR, Moret J. Venous phase timing during balloon test occlusion as a criterion for permanent internal carotid artery sacrifice. *AJNR Am J Neuroradiol* 2005; **26**: 2602-2609 [PMID: 16286409]
 - 13 **Li J**, Lan Z, He M, You C. Assessment of microscope-integrated indocyanine green angiography during intracranial aneurysm surgery: a retrospective study of 120 patients. *Neurol India* 2009; **57**: 453-459 [PMID: 19770547 DOI: 10.4103/0028-3886.55607]
 - 14 **Oda J**, Kato Y, Chen SF, Sodhiya P, Watabe T, Imizu S, Oguri D, Sano H, Hirose Y. Intraoperative near-infrared indocyanine green-videoangiography (ICG-VA) and graphic analysis of fluorescence intensity in cerebral aneurysm surgery. *J Clin Neurosci* 2011; **18**: 1097-1100 [PMID: 21715173 DOI: 10.1016/j.jocn.2010.12.045]
 - 15 **Uchino H**, Nakamura T, Houkin K, Murata J, Saito H, Kuroda S. Semiquantitative analysis of indocyanine green videoangiography for cortical perfusion assessment in superficial temporal artery to middle cerebral artery anastomosis. *Acta Neurochir (Wien)* 2013; **155**: 599-605 [PMID: 23287901 DOI: 10.1007/s00701-012-1575-y]
 - 16 **Struffert T**, Deuerling-Zheng Y, Engelhorn T, Kloska S, Göllitz P, Bozzato A, Kapsreiter M, Strother CM, Doerfler A. Monitoring of balloon test occlusion of the internal carotid artery by parametric color coding and perfusion imaging within the angio suite: first results. *Clin Neuroradiol* 2013; **23**: 285-292 [PMID: 23525670 DOI: 10.1007/s00062-013-0208-z]

P- Reviewer: Rodriguez GJ, Spalice A, Shen J **S- Editor:** Ji FF
L- Editor: A **E- Editor:** Wu HL



Retrospective Study

Transcranial Doppler screening in sickle cell disease: The implications of using peak systolic criteria

Lena N Naffaa, Yasmeen K Tandon, Neville Irani

Lena N Naffaa, Department of Radiology, Akron Children's Hospital, Akron, OH 44308, United States

Yasmeen K Tandon, Department of Radiology, Case Western Reserve University-Metro Health Medical Center, Cleveland, OH 44109, United States

Neville Irani, Radiology, Kansas University Medical Center, Kansas City, KS 66160, United States

Author contributions: Naffaa LN, Tandon YK and Irani N contributed equally to this work; Naffaa LN and Irani N interpreted images in this study; Naffaa LN, Tandon YK and Irani N collected the patient's clinical data; Naffaa LN, Tandon YK and Irani N analyzed the data and wrote the paper; Naffaa LN, Tandon YK and Irani N gave final approval of the version to be published.

Ethics approval: The study was reviewed and approved by the Akron Children's Hospital Institutional Review Board.

Informed consent: Informed consent was not required for this study as it was a retrospective study and the presented data are anonymized and risk of identification is low.

Conflict-of-interest: The authors have no conflicts of interest to declare.

Data sharing: Technical appendix, statistical code, and dataset available from the corresponding author at lnaffaa@chmca.org.

Open-Access: This article is an open-access article which was selected by an in-house editor and fully peer-reviewed by external reviewers. It is distributed in accordance with the Creative Commons Attribution Non Commercial (CC BY-NC 4.0) license, which permits others to distribute, remix, adapt, build upon this work non-commercially, and license their derivative works on different terms, provided the original work is properly cited and the use is non-commercial. See: <http://creativecommons.org/licenses/by-nc/4.0/>

Correspondence to: Lena N Naffaa, MD, Radiologist, Department of Radiology, Akron Children's Hospital, 1 Perkins Square, Akron, OH 44308, United States. lnaffaa@chmca.org

Telephone: +1-330-5438275

Fax: +1-330-5433760

Received: October 14, 2014

Peer-review started: October 15, 2014

First decision: December 17, 2014

Revised: December 25, 2014

Accepted: January 18, 2015

Article in press: January 20, 2015

Published online: February 28, 2015

Abstract

AIM: To compare time average maximum mean velocity (TAMV) and peak systolic velocity (PSV) criteria of Trans Cranial Doppler (TCD) in their ability to predict abnormalities on magnetic resonance imaging (MRI)/magnetic resonance angiogram (MRA) in patients with sickle cell disease.

METHODS: A retrospective evaluation was performed of the outcomes in all patients with a Transcranial Doppler examination at our institution since the implementation of the hospital picture archiving and communication system (PACS) system in January 2003 through December 2012. All ultrasound imaging exams were performed by the same technologist with a 3 MHz transducer. Inclusion criteria was based upon the Transcranial Doppler procedure code in our PACS which had an indication of sickle cell disease in the history. The patient's age and gender along with the vessel with the highest time averaged mean velocity as well as the highest peak systolic velocity was recorded for analysis. A subset of the study cohort also had subsequent MR imaging and Angiograms performed within 6 mo of the TCD examination. MRI results were categorized as having a disease related abnormality (vessel narrowing, collateral formation/moya-moya, or abnormal fluid attenuation inversion recovery signal in parenchyma indicative of prior stroke) or normal. The MRI results formed the comparison standards for TCD exams in evaluating intracranial injury. Sensitivity and specificity for the two TCD criteria (TAMV and PSV) were calculated to determine which could be a better predictor for intracranial vasculopathy /clinically occult strokes.

RESULTS: The study cohort for our institution was 110

patients with a total of 291 TCD examinations. These patients had a mean age of 7.6 years with a range from 2-18 years of age. Sixty-two of the 110 patients (56%) had two or more TCD exams. Thirty-seven patients (34%) had at least one MRI following a TCD examination. Of the 291 TCD examinations, 46 (16%) were conditional or abnormal by TAMV criteria. One hundred and sixteen (40%) were conditional or abnormal by PSV criteria. All studies that were abnormal by TAMV were also abnormal by PSV criteria. Seventy of the 116 (60%) studies which were conditional or abnormal by peak systolic criteria would not have been identified by time averaged mean maximum velocity criteria. The most frequent location of highest velocity measurement was noted to be in the middle cerebral artery regardless of whether it was measured by PSV or TAMV. From the 37 patients having one or more MRIs, 43 MRI exams were performed within 6 mo of a TCD examination. Twenty two (51%) MRIs had a disease related abnormality reported. When evaluating conditional or abnormal exams by PSV criteria against follow-up MRI/MRA, the sensitivity was 73% [16/(16 + 6)] and specificity was 81% [17/(4 + 17)]. When evaluating conditional or abnormal exams by TAMV criteria by follow-up MRI/MRA as the gold standard, the sensitivity was 41% [9/(9 + 13)] and the specificity was 100% [21/(21 + 0)]. In using conditional or abnormal criteria from PSV and TAMV to predict abnormalities on follow-up MRI/MR Angiogram, PSV was more sensitive (73% *vs* 41%) while TAMV was more specific (100% *vs* 81%).

CONCLUSION: Based on the data obtained at our institution and using the assumption that the best screening test is the one with the highest sensitivity, the peak systolic velocity could be the measurement of choice for TCD screening.

Key words: Sickle; Ischemic; Stroke; Trans Cranial Doppler; Average maximum mean velocity; Peak systolic velocity; Magnetic resonance imaging

© **The Author(s) 2015.** Published by Baishideng Publishing Group Inc. All rights reserved.

Core tip: To the best of our knowledge, there has been no direct comparison between peak systolic velocity and time average maximum mean velocity in their ability to predict abnormalities on magnetic resonance imaging (MRI)/magnetic resonance angiogram in children with sickle cell disease. With the growing clinical use of MR Angiography to assess sickle cell patients, the sensitivity of Trans Cranial Doppler (TCD) should be maximized if it is to maintain its role as a screening test in the sickle cell population. Based on the data obtained at our institution and using the assumption that the best screening test is the one with the highest sensitivity, the peak systolic velocity could be the measurement of choice for TCD screening.

Naffaa LN, Tandon YK, Irani N. Transcranial Doppler screening in sickle cell disease: The implications of using peak systolic criteria. *World J Radiol* 2015; 7(2): 52-56 Available from: URL:

INTRODUCTION

Over the past 20 years, there has been a significant increase in understanding the cerebrovascular consequences of sickle cell disease. Without treatment, 11% of children with sickle cell disease will have an ischemic stroke by 20 years of age^[1]. It is also well documented that children with an ischemic stroke are at high risk for recurrence unless treated with repeated transfusions with a goal of maintaining the level of sickle hemoglobin below 30%^[2]. By treating the patients with abnormal time average maximum mean velocity (TAMV) with transfusion, the 10% per year risk of stroke is reduced to less than 1%^[3].

The Stroke Prevention Trial in Sickle Cell Anemia (STOP) was a significant advance in screening for this complication of sickle cell disease as it demonstrated the efficacy of Trans Cranial Doppler (TCD) in identifying patients at high risk for ischemic brain injury. The trial involved correlating the TAMV in the internal carotid artery (ICA) and proximal middle cerebral artery (MCA) on an annual Doppler waveform tracing with the clinical outcome of stroke. A TAMV of 200 cm/s was indicative of a 10% stroke risk over the ensuing year, while a level of 170 cm/s was considered conditional, requiring shorter interval follow-up^[3].

The thresholds that carried forward into the STOP trial grew from a post hoc analysis of potential cutoff values for TAMV which looked to minimize false positives and yield the highest relative risk. The analysis did not maximize sensitivity as would be assumed if the intent were to utilize this test to screen asymptomatic patients with sickle cell disease. This fundamental oversight in selecting the TAMV criteria ultimately undercuts TCD's potential as a screening test. The reference standard in evaluating thresholds in the 1992 analysis was cerebral angiography and not MRI; the latter is now the current standard of care for stroke detection. Indeed, in many centers, MRI is now ordered more frequently than TCD for sickle cell patients as reporting of TCD results based upon TAMV criteria do not satisfy the criteria of an optimal screening test. If we look back at the original data, the highest sensitivity for patients with stroke was not at 170 cm/s, but rather, at a much lower level of 140 cm/s. A final consideration in how this cutoff determination process ultimately limits TCD's applicability is the relatively small cohort of seven patients with clinically evident stroke that was included in the original analysis^[4].

In 2005, the results from the STOP trial were revisited to determine if another, equally predictive,

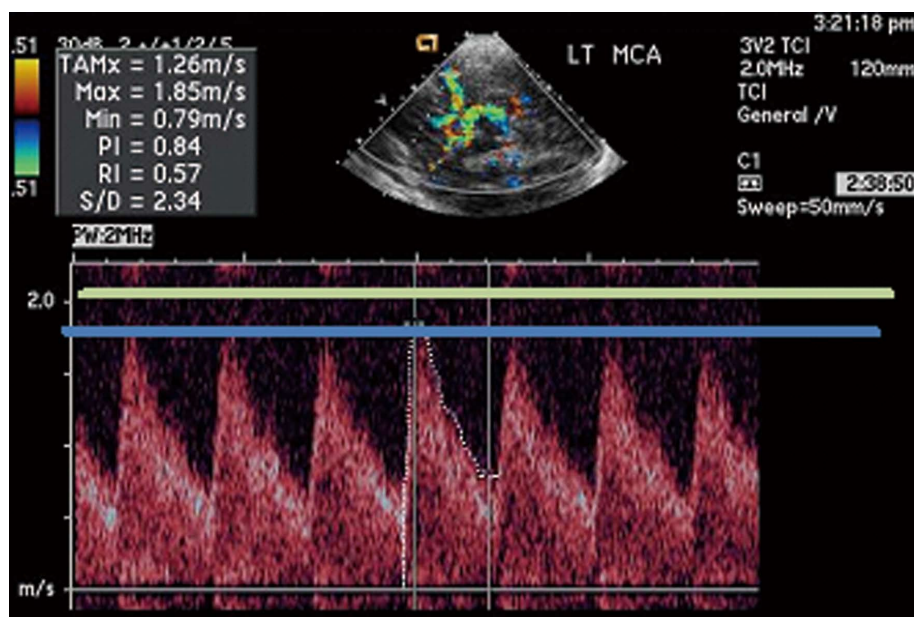


Figure 1 Example of time averaged mean maximum velocity measurement in the left middle cerebral artery. The green line represents the cutoff for PSV (200 cm/s) which was considered conditional requiring increased surveillance. The blue line represents the cutoff for TAMV (170 cm/s) which was considered conditional requiring increased surveillance. This study did not result in a conditional interpretation by either criteria (TAMV = 126 cm/s and PSV = 185 cm/s). MCA: Middle cerebral artery; TAMV: Time average maximum mean velocity; PSV: Peak systolic velocity.

criterion for clinically apparent stroke could be found for TCD with imaging acquisition (the more common TCD method utilized in practice for sickle cell patients). Peak systolic velocity (PSV) was one of the measures evaluated as it has long been a metric for determining stenosis in other important vascular distributions^[5]. A comparison of PSV and TAMV revealed that the PSV appeared to predict stroke as well as TAMV albeit with different velocity cutoffs. From this analysis, came the recommendation of using a PSV of 250 cm/s being as abnormal (high risk) and a PSV of 200 cm/s or greater considered conditional requiring increased surveillance^[6].

Following this analysis, there are now two possible criteria (PSV and TAMV) which validated against the same data set, as being equally predictive of a clinically apparent stroke. In practice, it would seem that the sensitivity of the TCD evaluation in predicting the more proximate cause of sickle cell stroke (intracranial vasculopathy) should depend upon which of these criteria were utilized to identify "normal". To our knowledge, there has been no comparison of these two criteria in their ability to predict abnormalities on MRI/MRA.

With the growing clinical use of magnetic resonance imaging (MRI)/magnetic resonance angiogram (MRA) to assess sickle cell patients, the sensitivity of TCD should be maximized if it is to maintain its role as a screening test in the sickle cell population. Our retrospective analysis of eight years of TCD data at our institution aims to provide this correlation.

MATERIALS AND METHODS

Our Institutional Review Board approved a retro-

spective evaluation of the outcomes in all patients with a Transcranial Doppler examination at our institution since the implementation of the hospital PACS system in January 2003 through December 2012. All ultrasound imaging exams were performed by the same technologist with a 3 MHz transducer. Inclusion criteria was based upon the Transcranial Doppler procedure code in our PACS which had an indication of sickle cell disease in the history. Indications other than sickle cell disease were excluded (e.g., ancillary brain death evaluation, vasospasm). The patient age and gender along with the vessel with the highest time averaged mean velocity as well as the highest peak systolic velocity was recorded for analysis (Figure 1).

A subset of the study cohort also had subsequent MR imaging and Angiograms performed within 6 mo of the TCD examination on a 1.5 Tesla MRI. MRI results were categorized as having a disease related abnormality (vessel narrowing, collateral formation/moya-moya, or abnormal fluid attenuation inversion recovery signal in parenchyma indicative of prior stroke) or normal. The MRI results formed the comparison standards for TCD exams in evaluating intracranial injury.

Sensitivity and specificity for the two TCD criteria (TAMV and PSV) were calculated to determine which could be a better predictor for intracranial vasculopathy /clinically occult strokes.

Statistical analysis

The statistics were reviewed and analyzed by the authors. Determinations of sensitivity and specificity were made based upon data collected and public domain information. No biostatistician was involved

Table 1 Evaluating Peak Systolic Criteria by follow-up magnetic resonance imaging/magnetic resonance angiogram

		MRI/MRA	
		Condition/ abnormal	Normal
Peak systolic criteria	Conditional/ abnormal	16	4
	Normal	6	17

The sensitivity was 73% [16/(16 + 6)] and specificity was 81% [17/(4 + 17)].
MRI: Magnetic resonance imaging; MRA: Magnetic resonance angiogram.

with this project due to resource constraints.

RESULTS

The study cohort for our institution was 110 patients with a total of 291 TCD examinations. These patients had a mean age of 7.6 years with a range from 2-18 years of age. Sixty-two of the 110 patients (56%) had two or more TCD exams. Thirty-seven patients (34%) had at least one MRI following a TCD examination. The subset of patients with an MRI exam following the TCD exam had a higher age, as expected, with a mean of 8.6 years with a range of 3-18 years.

Of the 291 TCD examinations, 46 (16%) were conditional or abnormal by TAMV criteria. One hundred and sixteen (40%) were conditional or abnormal by PSV criteria. All studies that were abnormal by TAMV were also abnormal by PSV criteria. Seventy of the 116 (60%) studies which were conditional or abnormal by peak systolic criteria would not have been identified by time averaged mean maximum velocity criteria.

The most frequent location of highest velocity measurement was noted to be in the MCA regardless of whether it was measured by PSV or TAMV. This accounted for over 80% of all exams during our study period. For TAMV measurement, the ACA demonstrated the highest velocity in 19% of exams. The highest PSV was found in the ACA in 16% of exams. One exam demonstrated the highest velocity within the PCA, although the TAMV and PSV were both less than 100 cm/s. No exams (using either criteria) found the highest velocity to be within the ICA.

From the 37 patients having one or more MRIs, 43 MRI exams were performed within 6 mo of a TCD examination. Twenty two (51%) MRIs had a disease related abnormality reported. When evaluating conditional or abnormal exams by PSV criteria against follow-up MRI/MRA (Table 1), the sensitivity was 73% [16/(16 + 6)] and specificity was 81% [17/(4 + 17)]. When evaluating conditional or abnormal exams by TAMV criteria by follow-up MRI/MRA as the gold standard (Table 2), the sensitivity was 41% [9/(9 + 9 + 13)] and the specificity

Table 2 Evaluating mean velocity criteria by follow-up magnetic resonance imaging/magnetic resonance angiogram

		MRI/MRA	
		Condition/ abnormal	Normal
Mean velocity criteria	Conditional/ abnormal	9	0
	Normal	13	21

The sensitivity was 41% [9/(9 + 9 + 13)] and the specificity was 100% [21/(21 + 0)]. MRI: Magnetic resonance imaging; MRA: Magnetic resonance angiogram.

was 100% [21/(21 + 0)]. In using conditional or abnormal criteria from PSV and TAMV to predict abnormalities on follow-up MRI/MR Angiogram, PSV was more sensitive (73% vs 41%) while TAMV was more specific (100% vs 81%).

DISCUSSION

Since the original STOP trial publication, there has been a significant increase in utilization of TCD with imaging in asymptomatic sickle cell patients to identify increased stroke risk^[7]. A finding of elevated velocities requires further monitoring or transfusion intervention. The use of TCD in this manner is that of a screening test. A good screening test is one with maximum sensitivity, so that if the test is negative, the condition is not present. In this case, the condition was "clinically evident stroke". The threshold for TCD velocities was set in the STOP trial to detect 97% of all patients with clinically evident stroke. The trial did not measure TCD sensitivity against the presence or progression of intracranial vasculopathy, which is a more proximate cause of stroke in these patients. While nearly all patients with an abnormal TCD by STOP criteria will have vasculopathy, not all patients with vasculopathy will have an abnormal TCD by the STOP TAMV criteria.

It has been further documented that clinically silent strokes in sickle cell patients with normal neurologic and TCD exam are detectable by MR Imaging^[8]. This observation is also concordant with data indicating that patients with silent infarcts on MRI and normal TCD results by the original STOP criteria are more than twice as likely as the unscreened sickle cell population to develop a clinically apparent stroke^[9]. Indeed, even though patients with abnormalities only on MRI frequently have a "normal" neurologic exam, it is becoming more apparent that neuropsychological deficits exist^[10].

In order for TCD screening to maintain its role as an adequate screening test, it must perform close to the level of MRI at least in predicting the presence or progression of intracranial vasculopathy. To this purpose, a number of studies have compared TCD velocity measurements with the presence of

stenosis at MR Angiography. Lowering the TAMV threshold to 165 cm/s could yield a sensitivity of 92% in predicting stenosis on MRI^[11]. Adult studies, however, indicate that the threshold for TAMV would have to be set at 123 cm/s for 100% sensitivity^[12].

The restricted availability of the exam with only a single trained technologist ensured uniformity throughout the study period. The limitations of our study include the small sample size given the relative underutilization of sickle cell services and difficulty of follow-up. While the ultrasound technical exam factors remain well controlled, variations in MRI technique over the 10-year time period could have influenced uniformity of the gold standard. We also did not have the ability to correlate clinical outcomes given the relatively recent transition to an electronic medical record (2010) at our institution. A larger prospective study with the ability to correlate TCD TAMV, PSV, MRI and MRA findings, neuropsychological exam results, and clinically apparent stroke could provide a useful follow-up to the STOP trial to update best practice recommendations for what is one of the leading causes of stroke in pediatric patients.

Based on the data obtained at our institution and using the assumption that the best screening test is the one with the highest sensitivity, the peak systolic velocity could be the measurement of choice for TCD screening. A more specific test with MRI or neuropsychological evaluation should follow in those patients who may have suffered clinically silent ischemic brain injury.

COMMENTS

Background

Without treatment, 11% of children with sickle cell disease will have an ischemic stroke by 20 years of age. Trans Cranial Doppler (TCD) is used as a screening test to prevent this complication in the sickle cell population. A finding of elevated velocities requires further monitoring or transfusion intervention. Velocities can be measured using the time average maximum mean velocity (TAMV) or the peak systolic velocity (PSV) criteria.

Research frontiers

With the growing clinical use of magnetic resonance imaging (MRI)/magnetic resonance angiogram (MRA) to assess sickle cell patients, the sensitivity of TCD should be maximized if it is to maintain its role as a screening test in the sickle cell population.

Innovations and breakthroughs

To the best of our knowledge, there has been no comparison of PSV and TAMV criteria in their ability to predict abnormalities on MRI/MRA.

Applications

Based on the data obtained at our institution and using the assumption that the best screening test is the one with the highest sensitivity, the peak systolic velocity

could be the measurement of choice for TCD screening.

Terminology

The STOP trial is the acronym for Stroke Prevention Trial in Sickle Cell Anemia. It was a significant advance in screening for the complication of ischemic stroke in sickle cell disease as it demonstrated the efficacy of TCD in identifying patients at high risk for ischemic brain injury.

Peer review

It is a very good article.

REFERENCES

- 1 **Ohene-Frempong K**, Weiner SJ, Sleeper LA, Miller ST, Embury S, Moohr JW, Wethers DL, Pegelow CH, Gill FM. Cerebrovascular accidents in sickle cell disease: rates and risk factors. *Blood* 1998; **91**: 288-294 [PMID: 9414296]
- 2 **Pegelow CH**, Adams RJ, McKie V, Abboud M, Berman B, Miller ST, Olivieri N, Vichinsky E, Wang W, Brambilla D. Risk of recurrent stroke in patients with sickle cell disease treated with erythrocyte transfusions. *J Pediatr* 1995; **126**: 896-899 [PMID: 7776091]
- 3 **Adams RJ**, McKie VC, Hsu L, Files B, Vichinsky E, Pegelow C, Abboud M, Gallagher D, Kutlar A, Nichols FT, Bonds DR, Brambilla D. Prevention of a first stroke by transfusions in children with sickle cell anemia and abnormal results on transcranial Doppler ultrasonography. *N Engl J Med* 1998; **339**: 5-11 [PMID: 9647873]
- 4 **Adams R**, McKie V, Nichols F, Carl E, Zhang DL, McKie K, Figueroa R, Litaker M, Thompson W, Hess D. The use of transcranial ultrasonography to predict stroke in sickle cell disease. *N Engl J Med* 1992; **326**: 605-610 [PMID: 1734251]
- 5 **Alexandrov AV**, Brodie DS, McLean A, Hamilton P, Murphy J, Burns PN. Correlation of peak systolic velocity and angiographic measurement of carotid stenosis revisited. *Stroke* 1997; **28**: 339-342 [PMID: 9040686]
- 6 **Jones A**, Granger S, Brambilla D, Gallagher D, Vichinsky E, Woods G, Berman B, Roach S, Nichols F, Adams RJ. Can peak systolic velocities be used for prediction of stroke in sickle cell anemia? *Pediatr Radiol* 2005; **35**: 66-72 [PMID: 15517239]
- 7 **Armstrong-Wells J**, Grimes B, Sidney S, Kronish D, Shiboski SC, Adams RJ, Fullerton HJ. Utilization of TCD screening for primary stroke prevention in children with sickle cell disease. *Neurology* 2009; **72**: 1316-1321 [PMID: 19365052 DOI: 10.1212/WNL.0b013e3181a110da]
- 8 **Siegel MJ**, Luker GD, Glauser TA, DeBaun MR. Cerebral infarction in sickle cell disease: transcranial Doppler US versus neurologic examination. *Radiology* 1995; **197**: 191-194 [PMID: 7568822]
- 9 **Pegelow CH**, Macklin EA, Moser FG, Wang WC, Bello JA, Miller ST, Vichinsky EP, DeBaun MR, Guarini L, Zimmerman RA, Younkin DP, Gallagher DM, Kinney TR. Longitudinal changes in brain magnetic resonance imaging findings in children with sickle cell disease. *Blood* 2002; **99**: 3014-3018 [PMID: 11929794]
- 10 **Platt OS**. Prevention and management of stroke in sickle cell anemia. *Hematology Am Soc Hematol Educ Program* 2006; **Abstract**: 54-57 [PMID: 17124040]
- 11 **Arkuszewski M**, Krejza J, Chen R, Kwiatkowski JL, Ichord R, Zimmerman R, Ohene-Frempong K, Melhem ER. Sickle cell disease in children: accuracy of imaging transcranial Doppler ultrasonography in detection of intracranial arterial stenosis. *Neuroradiol J* 2012; **25**: 402-410 [PMID: 24029032]
- 12 **Silva GS**, Vicari P, Figueiredo MS, Carrete H, Idagawa MH, Massaro AR. Brain magnetic resonance imaging abnormalities in adult patients with sickle cell disease: correlation with transcranial Doppler findings. *Stroke* 2009; **40**: 2408-2412 [PMID: 19443807]

P- Reviewer: Al-Haggag M S- Editor: Ji FF L- Editor: A
E- Editor: Wu HL





Published by **Baishideng Publishing Group Inc**

8226 Regency Drive, Pleasanton, CA 94588, USA

Telephone: +1-925-223-8242

Fax: +1-925-223-8243

E-mail: bpgoffice@wjgnet.com

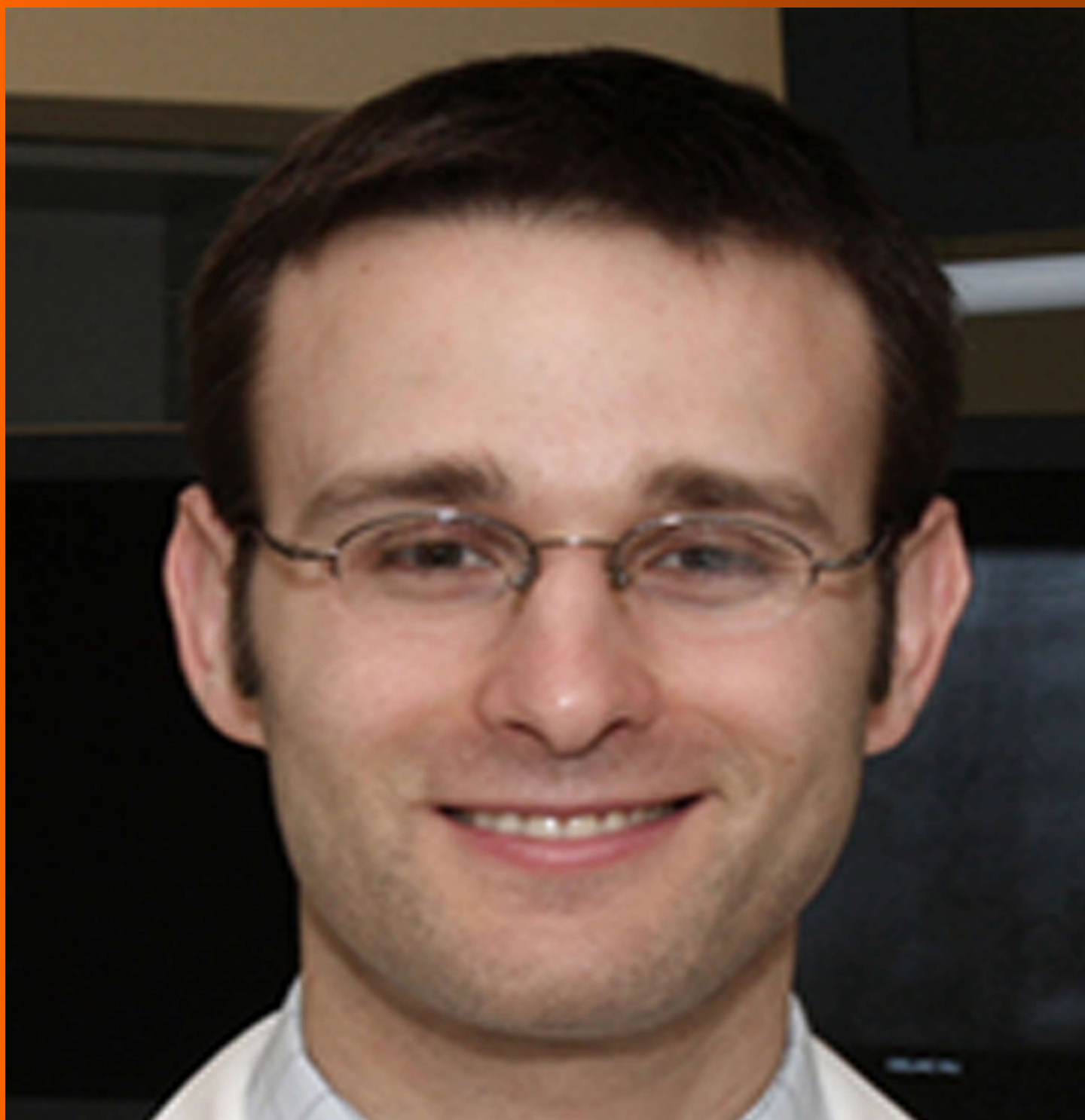
Help Desk: <http://www.wjgnet.com/esps/helpdesk.aspx>

<http://www.wjgnet.com>



World Journal of *Radiology*

World J Radiol 2015 March 28; 7(3): 57-69





Editorial Board

2014-2017

The *World Journal of Radiology* Editorial Board consists of 365 members, representing a team of worldwide experts in radiology. They are from 36 countries, including Afghanistan (1), Argentina (2), Australia (5), Austria (7), Belgium (2), Brazil (8), Canada (6), Chile (1), China (43), Croatia (1), Denmark (4), Egypt (6), France (5), Germany (22), Greece (10), India (12), Iran (6), Ireland (2), Israel (3), Italy (47), Japan (13), Netherlands (1), New Zealand (1), Pakistan (1), Poland (2), Portugal (1), Serbia (1), Singapore (3), Slovakia (1), South Korea (18), Spain (4), Sweden (2), Switzerland (4), Thailand (1), Turkey (26), United Kingdom (11), and United States (82).

EDITORS-IN-CHIEF

Kai U Juergens, *Bremen*
Edwin JR van Beek, *Edinburgh*
Thomas J Vogl, *Frankfurt*

GUEST EDITORIAL BOARD MEMBERS

Wing P Chan, *Taipei*
Chung-Huei Hsu, *Taipei*
Chin-Chang Huang, *Taipei*
Tsong-Long Hwang, *Taoyuan*
Jung-Lung Hsu, *Taipei*
Chia-Hung Kao, *Taichung*
Yu-Ting Kuo, *Tainan*
Hon-Man Liu, *Taipei*
Hui-Lung Liang, *Kaohsiung*
Chun Chung Lui, *Kaohsiung*
Sen-Wen Teng, *Taipei*
Yung-Liang (William) Wan, *Taoyuan*

MEMBERS OF THE EDITORIAL BOARD



Afghanistan

Takao Hiraki, *Okayama*



Argentina

Patricia Carrascosa, *Vicente Lopez*
Maria C Ziadi, *Rosario*



Australia

Lourens Bester, *Sydney*
Gemma A Figtree, *Sydney*



Austria

Herwig R Cerwenka, *Graz*
Gudrun M Feuchtnner, *Innsbruck*
Benjamin Henninger, *Innsbruck*
Rupert Lanzenberger, *Vienna*
Shu-Ren Li, *Vienna*
Veronika Schopf, *Vienna*
Tobias De Zordo, *Innsbruck*



Belgium

Steve Majerus, *Liege*
Kathelijne Peremans, *Merelbeke*



Brazil

Clerio F Azevedo, *Rio de Janeiro*
Patrícia P Alfredo, *São Paulo*
Eduardo FC Fleury, *São Paulo*
Edward Araujo Júnior, *São Paulo*
Wellington P Martins, *Ribeirao Preto*
Ricardo A Mesquita, *Belo Horizonte*
Vera MC Salemi, *São Paulo*
Claudia Szobot, *Porto Alegre*
Lilian YI Yamaga, *São Paulo*



Canada

Marie Arsalidou, *Toronto*
Otman A Basir, *Waterloo*

Tarik Zine Belhocine, *Toronto*
James Chow, *Toronto*
Tae K Kim, *Toronto*
Anastasia Oikonomou, *Toronto*



China

Hong-Wei Chen, *Wuxi*
Feng Chen, *Hangzhou*
Jian-Ping Chu, *Guangzhou*
Guo-Guang Fan, *Shenyang*
Bu-Lang Gao, *Shijiazhuang*
Qi-Yong Gong, *Chengdu*
Ying Han, *Beijing*
Xian-Li Lv, *Beijing*
Yi-Zhuo Li, *Guangzhou*
Xiang-Xi Meng, *Harbin*
Yun Peng, *Beijing*
Jun Shen, *Guangzhou*
Ze-Zhou Song, *Hangzhou*
Wai Kwong Tang, *Hong Kong*
Gang-Hua Tang, *Guangzhou*
Jie Tian, *Beijing*
Lu-Hua Wang, *Beijing*
Xiao-bing Wang, *Xi'an*
Yi-Gen Wu, *Nanjing*
Kai Wu, *Guangzhou*
Hui-Xiong Xu, *Shanghai*
Zuo-Zhang Yang, *Kunming*
Xiao-Dan Ye, *Shanghai*
David T Yew, *Hong Kong*
Ting-He Yu, *Chongqing*
Zheng Yuan, *Shanghai*
Min-Ming Zhang, *Hangzhou*
Yudong Zhang, *Nanjing*
Dong Zhang, *Chongqing*
Wen-Bin Zeng, *Changsha*

Yue-Qi Zhu, *Shanghai*



Croatia

Goran Kusec, *Osijek*



Denmark

Poul E Andersen, *Odense*

Lars J Petersen, *Aalborg*

Thomas Z Ramsøy, *Frederiksberg*

Morten Ziebell, *Copenhagen*



Egypt

Mohamed F Bazeed, *Mansoura*

Mohamed Abou El-Ghar, *Mansoura*

Reem HA Mohamed, *Cairo*

Mohamed R Nouh, *Alexandria*

Ahmed AKA Razek, *Mansoura*

Ashraf A Zytoon, *Shebin El-Koom*



France

Sabine F Bensamoun, *Compiègne*

Romarc Loffroy, *Dijon*

Stephanie Nougaret, *Montpellier*

Hassane Oudadesse, *Rennes*

Vincent Vinh-Hung, *Fort-de-France*



Germany

Henryk Barthel, *Leipzig*

Peter Bannas, *Hamburg*

Martin Beeres, *Frankfurt*

Ilja F Ciernik, *Dessau*

A Dimitrakopoulou-Strauss, *Heidelberg*

Peter A Fasching, *Erlangen*

Andreas G Schreyer, *Regensburg*

Philipp Heusch, *Duesseldorf*

Sonja M Kirchhoff, *Munich*

Sebastian Ley, *Munich*

Adel Maataoui, *Frankfurt am Main*

Stephan M Meckel, *Freiburg*

Hans W Muller, *Duesseldorf*

Kay Raum, *Berlin*

Dirk Rades, *Luebeck*

Marc-Ulrich Regier, *Hamburg*

Alexey Surov, *Halle*

Martin Walter, *Magdeburg*

Axel Wetter, *Essen*

Christoph Zilkens, *Düsseldorf*



Greece

Panagiotis Antoniou, *Thessaloniki*

Nikos Efthimiou, *Athens*

Dimitris Karnabatidis, *Patras*

George Latsios, *Athens*

Stylianios Megremis, *Iraklion*

Alexander D Rapidis, *Athens*

Kiki Theodorou, *Larissa*

Ioannis A Tsalafoutas, *Athens*

Evanthia E Tripoliti, *Ioannina*

Athina C Tsili, *Ioannina*



India

Ritesh Agarwal, *Chandigarh*

Chandan J Das, *New Delhi*

Prathamesh V Joshi, *Mumbai*

Naveen Kalra, *Chandigarh*

Chandrasekharan Kesavadas, *Trivandrum*

Jyoti Kumar, *New Delhi*

Atin Kumar, *New Delhi*

Kaushala P Mishra, *Allahabad*

Daya N Sharma, *New Delhi*

Binit Sureka, *New Delhi*

Sanjay Sharma, *New Delhi*

Raja R Yadav, *Allahabad*



Iran

Majid Assadi, *Bushehr*

SeyedReza Najafizadeh, *Tehran*

Mohammad Ali Oghabian, *Tehran*

Amir Reza Radmard, *Tehran*

Ramin Sadeghi, *Mashhad*

Hadi Rokni Yazdi, *Tehran*



Ireland

Tadhg Gleeson, *Wexford*

Frederik JAI Vernimmen, *Cork*



Israel

Dafna Ben Bashat, *Tel Aviv*

Amit Gefen, *Tel Aviv*

Tamar Sella, *Jerusalem*



Italy

Adriano Alippi, *Rome*

Dante Amelio, *Trento*

Michele Anzidei, *Rome*

Filippo F Angileri, *Messinas*

Stefano Arcangeli, *Rome*

Roberto Azzoni, *San Donato milanese*

Tommaso V Bartolotta, *Palermo*

Tommaso Bartalena, *Imola*

Livia Bernardin, *San Bonifacio*

Federico Boschi, *Verona*

Sergio Casciaro, *Lecce*

Emanuele Casciani, *Rome*

Musa M Can, *Napoli*

Alberto Cuocolo, *Napoli*

Michele Ferrara, *Coppito*

Mauro Feola, *Fossano*

Giampiero Francica, *Castel Volturno*

Luigi De Gennaro, *Rome*

Giulio Giovannetti, *Pisa*

Francesca Iacobellis, *Napoli*

Formato Invernizzi, *Monza Brianza*

Francesco Lassandro, *Naples*

Lorenzo Livi, *Florence*

Pier P Mainenti, *Napoli*

Laura Marzetti, *Chieti*

Giuseppe Malinverni, *Crescentino*

Enrica Milanese, *Turin*

Giovanni Morana, *Treviso*

Lorenzo Monti, *Milan*

Silvia D Morbelli, *Genoa*

Barbara Palumbo, *Perugia*

Cecilia Parazzini, *Milan*

Stefano Pergolizzi, *Messina*

Antonio Pinto, *Naples*

Camillo Porcaro, *Rome*

Carlo C Quattrocchi, *Rome*

Alberto Rebonato, *Perugia*

Giuseppe Rizzo, *Rome*

Roberto De Rosa, *Naples*

Domenico Rubello, *Rovigo*

Andrea Salvati, *Bari*

Sergio Sartori, *Ferrara*

Luca M Sconfienza, *Milano*

Giovanni Storto, *Rionero*

Nicola Sverzellati, *Parma*

Alberto S Tagliafico, *Genova*

Nicola Troisi, *Florence*



Japan

Yasuhiko Hori, *Chiba*

Hidetoshi Ikeda, *Koriyama*

Masahito Kawabori, *Sapporo*

Tamotsu Kamishima, *Sapporo*

Hiro Kiyosue, *Yufu*

Yasunori Minami, *Osaka-sayama*

Yasuhiro Morimoto, *Kitakyushu*

Satoru Murata, *Tokyo*

Shigeki Nagamachi, *Miyazaki*

Hiroshi Onishi, *Yamanashi*

Morio Sato, *Wakayama Shi*

Yoshito Tsushima, *Maebashi*

Masahiro Yanagawa, *Suita*



Netherlands

Willem Jan van Rooij, *Tilburg*



New Zealand

W Howell Round, *Hamilton*



Pakistan

Wazir Muhammad, *Abbottabad*



Poland

Maciej S Baglaj, *Wroclaw*

Piotr Czauderna, *Gdansk*



Portugal

Joao Manuel RS Tavares, *Porto*



Serbia

Olivera Ciraj-Bjelac, *Belgrade*



Singapore

Gopinathan Anil, *Singapore*

Terence KB Teo, *Singapore*

Cher Heng Tan, *Singapore*



Slovakia

Stefan Sivak, *Martin*



South Korea

Ki Seok Choo, *Busan*

Seung Hong Choi, *Seoul*

Dae-Seob Choi, *Jinju*

Hong-Seok Jang, *Seoul*

Yong Jeong, *Daejeon*

Chan Kyo Kim, *Seoul*

Se Hyung Kim, *Seoul*

Joong-Seok Kim, *Seoul*

Sang Eun Kim, *Seongnam*

Sung Joon Kwon, *Seoul*

Jeong Min Lee, *Seoul*

In Sook Lee, *Busan*

Noh Park, *Goyang*

Chang Min Park, *Seoul*

Sung Bin Park, *Seoul*

Deuk Jae Sung, *Seoul*

Choongsoo Shin, *Seoul*

Kwon-Ha Yoon, *Iksan*



Spain

Miguel A De Gregorio, *Zaragoza*

Antonio Luna, *Jaén*

Enrique Marco de Lucas, *Santander*

Fernando Ruiz Santiago, *Granada*



Sweden

Dmitry Grishenkov, *Stockholm*

Tie-Qiang Li, *Stockholm*



Switzerland

Nicolau Beckmann, *Basel*

Christian Boy, *Bern*

Giorgio Treglia, *Bellinzona*

Stephan Ulmer, *Kiel*



Thailand

Sirianong Namwongprom, *Chiang Mai*



Turkey

Kubilay Aydin, *Istanbul*

Ramazan Akdemir, *Sakarya*

Serhat Avcu, *Ankara*

Ayşe Aralasmak, *Istanbul*

Oktay Algin, *Ankara*

Nevbahar Akcar, *Meselik*

Bilal Battal, *Ankara*

Zulkif Bozgeyik, *Elazig*

Nazan Ciledag, *Aakara*

Fuldem Y Donmez, *Ankara*

Gulgun Engin, *Istanbul*

Ahmet Y Goktay, *Izmir*

Oguzhan G Gumustas, *Bursa*

Kaan Gunduz, *Ankara*

Pelin Ozcan Kara, *Mersin*

Kivanc Kamburoglu, *Ankara*

Ozgur Kilickesmez, *Istanbul*

Furuzan Numan, *Istanbul*

Cem Onal, *Adana*

Ozgur Oztekin, *Izmir*

Seda Ozbek (Boruban), *Konya*

Selda Sarikaya, *Zonguldak*

Figen Taser, *Kutahya*

Baran Tokar, *Eskisehir*

Ender Uysal, *Istanbul*

Ensar Yekeler, *Istanbul*



United Kingdom

Indran Davagnanam, *London*

M DC Valdés Hernández, *Edinburgh*

Alan Jackson, *Manchester*

Suneil Jain, *Belfast*

Long R Jiao, *London*

Miltiadis Krokidis, *Cambridge*

Pradesh Kumar, *Liverpool*

Peter D Kuzmich, *Derby*

Georgios Plataniotis, *Brighton*

Vanessa Sluming, *Liverpool*



United States

Garima Agrawal, *Saint Louis*

James R Brasic, *Baltimore*

Rajendra D Badgaiyan, *Buffalo*

Ulas Bagci, *Bethesda*

Anat Biegon, *Stony Brook*

Ramon Casanova, *Winston Salem*

Wenli Cai, *Boston*

Zheng Chang, *Durham*

Corey J Chakarun, *Long Beach*

Kai Chen, *Los Angeles*

Hyun-Soon Chong, *Chicago*

Marco Cura, *Dallas*

Ravi R Desai, *Bensalem*

Delia DeBuc, *Miami*

Carlo N De Cecco, *Charleston*

Timm-Michael L Dickfeld, *Baltimore*

Subba R Digumarthy, *Boston*

Huy M Do, *Stanford*

Todd A Faasse, *Grand Rapids*

Salomao Faintuch, *Boston*

Girish M Fatterpekar, *New York*

Dhakshinamoorthy Ganesan, *Houston*

Robert J Griffin, *Little Rock*

Andrew J Gunn, *Boston*

Sandeep S Hedgire, *Boston*

Timothy J Hoffman, *Columbia*

Mai-Lan Ho, *San Francisco*

Juebin Huang, *Jackson*

Abid Irshad, *Charleston*

Matilde Inglese, *New York*

El-Sayed H Ibrahim, *Jacksonville*

Paul R Julsrud, *Rochester*

Pamela T Johnson, *Baltimore*

Ming-Hung Kao, *Tempe*

Sunil Krishnan, *Houston*

Richard A Komoroski, *Cincinnati*

Sandi A Kwee, *Honolulu*

King Kim, *Ft. Lauderdale*

Guozheng Liu, *Worcester*

Yiyan Liu, *Newark*

Venkatesh Mani, *New York*

Lian-Sheng Ma, *Pleasanton*

Rachna Madan, *Boston*

Zeyad A Metwalli, *Houston*

Yilong Ma, *Manhasset*

Hui Mao, *Atlanta*

Feroze B Mohamed, *Philadelphia*

Gul Moonis, *Boston*

John L Noshier, *New Brunswick*

Rahmi Oklu, *Boston*

Aytekun Oto, *Chicago*

Bishnuhari Paudyal, *Philadelphia*

Rajul Pandya, *Youngstown*

Chong-Xian Pan, *Sacramento*

Jay J Pillai, *Baltimore*

Neal Prakash, *Duarte*

Reza Rahbar, *Boston*

Ali S Raja, *Boston*

Gustavo J Rodriguez, *El Paso*

David J Sahn, *Portland*

Steven Schild, *Scottsdale*

Ali R Sepahdari, *Los Angeles*

Li Shen, *Indianapolis*

JP Sheehan, *Charlottesville*

Atul B Shinagare, *Boston*

Sarabjeet Singh, *Boston*

Charles J Smith, *Columbia*

Kenji Suzuki, *Chicago*

Monvadi Srichai-Parsia, *Washington*

Sree H Tirumani, *Boston*

Hebert A Vargas, *New York*

Sachit Verma, *Philadelphia*

Yoichi Watanabe, *Minneapolis*

Li Wang, *Chapel Hill*

Carol C Wu, *Boston*

Shoujun Xu, *Houston*

Min Yao, *Cleveland*

Xiaofeng Yang, *Atlanta*

Qingbao Yu, *Albuquerque*

Aifeng Zhang, *Chicago*

Chao Zhou, *Bethlehem*

Hongming Zhuang, *Philadelphia*

**EDITORIAL**

- 57 Metformin and cancer: Technical and clinical implications for FDG-PET imaging
Capitanio S, Marini C, Sambuceti G, Morbelli S

CASE REPORT

- 61 Transarterial chemoembolization for liver metastases from solid pseudopapillary epithelial neoplasm of pancreas: A case report
Prasad TV, Madhusudhan KS, Srivastava DN, Dash NR, Gupta AK
- 66 Gastrointestinal manifestations of Henoch-Schonlein purpura: A report of two cases
Prathiba Rajalakshmi P, Srinivasan K

ABOUT COVER

Editorial Board Member of *World Journal of Radiology*, Salomao Faintuch, MD, MSc, Assistant Professor, Department of Radiology, Harvard Medical School-Beth Israel Deaconess Medical Center, Boston, MA 02215, United States

AIM AND SCOPE

World Journal of Radiology (*World J Radiol*, *WJR*, online ISSN 1949-8470, DOI: 10.4329) is a peer-reviewed open access academic journal that aims to guide clinical practice and improve diagnostic and therapeutic skills of clinicians.

WJR covers topics concerning diagnostic radiology, radiation oncology, radiologic physics, neuroradiology, nuclear radiology, pediatric radiology, vascular/interventional radiology, medical imaging achieved by various modalities and related methods analysis. The current columns of *WJR* include editorial, frontier, diagnostic advances, therapeutics advances, field of vision, mini-reviews, review, topic highlight, medical ethics, original articles, case report, clinical case conference (clinicopathological conference), and autobiography.

We encourage authors to submit their manuscripts to *WJR*. We will give priority to manuscripts that are supported by major national and international foundations and those that are of great basic and clinical significance.

INDEXING/ABSTRACTING

World Journal of Radiology is now indexed in PubMed Central, PubMed, Digital Object Identifier, and Directory of Open Access Journals.

FLYLEAF

I-III Editorial Board

EDITORS FOR THIS ISSUE

Responsible Assistant Editor: *Xiang Li*
Responsible Electronic Editor: *Ya-Jing Lu*
Proofing Editor-in-Chief: *Lian-Sheng Ma*

Responsible Science Editor: *Xue-Mei Gong*
Proofing Editorial Office Director: *Xin-Xia Song*

NAME OF JOURNAL
World Journal of Radiology

ISSN
ISSN 1949-8470 (online)

LAUNCH DATE
December 31, 2009

FREQUENCY
Monthly

EDITORS-IN-CHIEF
Kai U Juergens, MD, Associate Professor, MRT und PET/CT, Nuklearmedizin Bremen Mitte, ZEMODI - Zentrum für morphologische und molekulare Diagnostik, Bremen 28177, Germany

Edwin JR van Beek, MD, PhD, Professor, Clinical Research Imaging Centre and Department of Medical Radiology, University of Edinburgh, Edinburgh EH16 4TJ, United Kingdom

Thomas J Vogl, MD, Professor, Reader in Health Technology Assessment, Department of Diagnostic and Interventional Radiology, Johann Wolfgang

Goethe University of Frankfurt, Frankfurt 60590, Germany

EDITORIAL OFFICE
Jin-Lei Wang, Director
Xiu-Xia Song, Vice Director
World Journal of Radiology
Room 903, Building D, Ocean International Center, No. 62 Dongsihuan Zhonglu, Chaoyang District, Beijing 100025, China
Telephone: +86-10-59080039
Fax: +86-10-85381893
E-mail: editorialoffice@wjnet.com
Help Desk: <http://www.wjnet.com/esps/helpdesk.aspx>
<http://www.wjnet.com>

PUBLISHER
Baishideng Publishing Group Inc
8226 Regency Drive,
Pleasanton, CA 94588, USA
Telephone: +1-925-223-8242
Fax: +1-925-223-8243
E-mail: bpgoffice@wjnet.com
Help Desk: <http://www.wjnet.com/esps/helpdesk.aspx>
<http://www.wjnet.com>

PUBLICATION DATE
March 28, 2015

COPYRIGHT
© 2015 Baishideng Publishing Group Inc. Articles published by this Open-Access journal are distributed under the terms of the Creative Commons Attribution Non-commercial License, which permits use, distribution, and reproduction in any medium, provided the original work is properly cited, the use is non commercial and is otherwise in compliance with the license.

SPECIAL STATEMENT
All articles published in journals owned by the Baishideng Publishing Group (BPG) represent the views and opinions of their authors, and not the views, opinions or policies of the BPG, except where otherwise explicitly indicated.

INSTRUCTIONS TO AUTHORS
Full instructions are available online at http://www.wjnet.com/1949-8470/g_info_20100316162358.htm.

ONLINE SUBMISSION
<http://www.wjnet.com/esps/>

Metformin and cancer: Technical and clinical implications for FDG-PET imaging

Selene Capitanio, Cecilia Marini, Gianmario Sambuceti, Silvia Morbelli

Selene Capitanio, Gianmario Sambuceti, Silvia Morbelli, Nuclear Medicine Unit, IRCCS AOU San Martino-IST, Department of Health Sciences, University of Genoa, 16132 Genoa, Italy

Cecilia Marini, CNR Institute of Bioimages and Molecular Physiology, Milan, Section of Genoa, 16132 Genoa, Italy

Author contributions: Morbelli S designed the study; Capitanio S performed literature search and draft the manuscript; Marini C, Sambuceti G and Morbelli S made critical revisions related to important intellectual content of the manuscript; Morbelli S have given final approval of the version of the article to be published; all authors read and approved the final manuscript.

Conflict-of-interest: The authors have no conflict of interest to declare.

Open-Access: This article is an open-access article which was selected by an in-house editor and fully peer-reviewed by external reviewers. It is distributed in accordance with the Creative Commons Attribution Non Commercial (CC BY-NC 4.0) license, which permits others to distribute, remix, adapt, build upon this work non-commercially, and license their derivative works on different terms, provided the original work is properly cited and the use is non-commercial. See: <http://creativecommons.org/licenses/by-nc/4.0/>

Correspondence to: Silvia Morbelli, Full Staff, Nuclear Medicine Unit, IRCCS AOU San Martino-IST, Department of Health Sciences, University of Genoa, L.go R. Benzi, 10, 16132 Genova, Italy. silviadaniela.morbelli@hsanmartino.it

Telephone: +39-10-5552025

Fax: +39-10-5556911

Received: November 7, 2014

Peer-review started: November 9, 2014

First decision: December 12, 2014

Revised: January 15, 2015

Accepted: February 4, 2015

Article in press: February 9, 2015

Published online: March 28, 2015

to involve the interference with key pathways in cellular proliferation and glycolysis. To date, many clinical trials implying the use of metformin in cancer treatment are on-going. The increasing use of ^{18}F -2-fluoro-2-deoxy-d-glucose positron emission tomography (FDG-PET) in cancer evaluation raises a number of questions about the possible interference of the biguanide on FDG distribution. In particular, the interferences exerted by metformin on AMP-activated protein kinase pathway (the cellular energy sensor), on insulin levels and on Hexokinase could potentially have repercussion on glucose handling and thus on FDG distribution. A better comprehension of the impact of metformin on FDG uptake is needed in order to optimize the use of PET in this setting. This evaluation would be useful to ameliorate scans interpretation in diabetic patients under chronic metformin treatment and to critically interpret images in the context of clinical trials. Furthermore, collecting prospective data in this setting would help to verify whether FDG-PET could be a valid tool to appreciate the anticancer effect of this new therapeutic approach.

Key words: Metformin; Cancer; ^{18}F -2-fluoro-2-deoxy-d-glucose positron emission tomography; Diabetes; Glucose metabolism

© The Author(s) 2015. Published by Baishideng Publishing Group Inc. All rights reserved.

Core tip: Given the recent increasing number of clinical trials involving the use of metformin as anticancer agent and with the widespread use of ^{18}F -2-fluoro-2-deoxy-d-glucose positron emission tomography (FDG-PET), this editorial deals with a critical evaluation of the main variables regulating FDG uptake that could be potentially influenced by the biguanide. This analysis could optimize not only the interpretation of PET images in diabetic patients but could also help to verify whether FDG-PET could be a valid tool to appreciate anticancer potential of this new therapeutic approach thus opening a new window on clinical trials.

Abstract

Metformin is the most widely used hypoglycemic agent. Besides its conventional indications, increasing evidence demonstrate a potential efficacy of this biguanide as an anticancer drug. Possible mechanisms of actions seem to be independent from its hypoglycemic effect and seem

Capitanio S, Marini C, Sambuceti G, Morbelli S. Metformin and cancer: Technical and clinical implications for FDG-PET imaging. *World J Radiol* 2015; 7(3): 57-60 Available from: URL: <http://www.wjgnet.com/1949-8470/full/v7/i3/57.htm> DOI: <http://dx.doi.org/10.4329/wjrv.7.i3.57>

INTRODUCTION

Due to its safety, tolerability, and a very low incidence of lactic acidosis^[1], metformin is the most widely prescribed oral hypoglycemic agent and exerts this effect by reducing hepatic glucose production and by increasing insulin sensitivity as well as glucose use by peripheral tissues^[2,3]. Besides diabetes and other established indications for metformin^[4,5], increasing evidence demonstrate a possible efficacy of this agent as an anticancer drug^[6].

METFORMIN AND CANCER

The hypothesized beneficial actions of metformin against cancer involve different and not yet fully clarified mechanisms. A key role is believed to be mediated by AMP-activated protein kinase (AMPK), a major player in the regulation of metabolism and growth, for both normal and cancer cells^[7]. The activation of this molecule results from a decrease in mitochondrial ATP production due to the direct inhibition of metformin on respiratory complex I^[8] and consequently of the mammalian target of rapamycin. This effect induces cell cycle arrest and inhibits protein synthesis in cancer cells. However, more recent data have suggested that metformin can also regulate cancer cell biology in an AMPK-independent manner through the inhibition of the unfolded protein response with a consequent apoptosis, preventing angiogenesis and exerting toxicity on cancer stem cells^[9].

Several recent epidemiological, animal, and cellular studies support these findings and a recent meta-analysis has highlighted a correlation between decreased incidence of cancer and treatment with metformin in type II diabetes patients^[10-12].

Taken together these findings have encouraged more than 100 clinical trials on the effect of this drug in cancer patients, including prevention, adjuvant treatment and palliative treatment (cfr. on the NIH ClinicalTrials.gov web site^[13]).

METFORMIN AND FDG-PET IMAGING: TECHNICAL AND CLINICAL IMPLICATIONS

The increasing widespread use of ¹⁸F-2-fluoro-2-deoxy-d-glucose positron emission tomography (FDG-PET) for the imaging of neoplastic disease^[14] raises a number of questions about the possible technical and

clinical implication of metformin on this technique.

In particular, can metformin interfere with FDG distribution in the whole body or in cancer tissue? And, if so, how should we interpret FDG PET scans in diabetic patients under chronic treatment with the biguanide? Finally, can this tracer be used to test and assess the antineoplastic effect of metformin on cancer?

In clinical practice, the use of FDG-PET to non-invasively diagnose, monitor, and evaluate treatment response of cancers is well established from many years^[15]. This concept was extended from the observation by Di Chiro *et al.*^[16] who firstly demonstrated that FDG was more avidly accumulated in human brain tumors than in surrounding brain as well as in tumor recurrence.

The evaluation of gastro-intestinal tract is a well-known pitfall in FDG-PET imaging interpretation. Actually, metformin leads to intense, diffusely increased intestinal FDG in the colon, and to a lesser extent in the small bowel^[17]. This effect can limit the diagnostic capabilities of FDG-PET/CT scanning and may mask gastrointestinal malignancies potentially resulting in incorrect cancer staging, inability to detect second primary cancers and inability to assess response to therapy^[18,19]. To solve this problem, some authors proposed drug discontinuation before imaging with different schemes^[20,21], in order to improve image analysis. However, to date there is no agreement about which is the best approach and feasibility and washout duration still have to be verified in the clinical setting.

Our group^[22] has tried to elucidate the determinants of high intestinal ¹⁸F-FDG radioactivity content in a mouse model, treated with long- or short-term metformin administration. We showed that this phenomenon, appearing after a relatively long period of treatment and persisting soon after drug washout, was related to biguanide-induced modifications in the gut cell phenotype and was characterized by an ATP-depletion with the consequent increased phosphorylated-AMPK levels and reduced *TXNIP* gene expression.

With these premises, it is evident that the consequences of metformin treatment on FDG-PET scans are difficult to predict. On one side, as a drug with anti-proliferative activity metformin should decrease FDG uptake; on the other side, by activating AMPK in tumors, it would be expected to increase their glucose metabolism.

A further factor that has to be taken into account when we use FDG in cancer evaluation during metformin treatment is insulin asset^[23]. As mentioned before, some recent experimental models have reported that one of the possible mechanism by which metformin could exert an antineoplastic activity, is its capability to lower both glucose and insulin levels in type II diabetes patients^[24,25]. In order to examine this aspect, Mashhedi *et al.*^[26] studied FDG distribution in an example of insulin-responsive tumor. In a murine colon

cancer model, they found that metformin exposure did not affect insulin levels nor tumor FDG uptake in normo-insulinemic mice while decreased insulin levels and FDG uptake in hyper-insulinemic mice suggesting that, at least in this model, in neoplastic tissue the effect of this compound on insulin levels was more important than any AMPK activation.

This observation would imply carefulness in the evaluation of clinical trials using metformin in cancer treatment because its effect could be limited to hyper-insulinemic subjects with insulin sensitive neoplasms. As a consequence, it has also important implications on for the interpretation of FDG-PET images and on for understanding influences of exerted by host metabolism and metformin on tumor behavior.

Another important role of metformin that could be involved in antineoplastic activity and thus can interfere with FDG uptake, is its capability to directly and selectively inhibit the enzymatic function of hexokinase (HK) I and II as demonstrated by Marini *et al.*^[27]. This work extended previous evidence about metformin *in vitro* effect in different cancer models such as CALU-1 cells as a model of non-small cell lung cancer^[28] and in MDA-MB231 as a model of triple negative breast cancer. In all these cells metformin determined a dose- and time-dependent reduction in FDG uptake, in agreement with the expected effect of the biguanide on AMPK phosphorylation. Interestingly, this molecular mechanisms rely on the dislocation of HK from outer mitochondrial membrane with a consequent loss of enzymatic functional properties.

By interfering with HK activity, a rate limiting step of glucose consumption, metformin could influence FDG uptake. In fact, even if unquestionable evidence attesting that it is the exact surrogate and has the same metabolic fate of glucose is still lacking, we know that this tracer enters within the cell through the same facilitative transporters of glucose, is then phosphorylated by HK to FDG6P and remains trapped within cytosol, preventing all further glycolytic reactions.

Obviously, all these findings cannot be easily transferred in clinical practice due to the high doses needed to induce this response (750 mg/kg per day) in mice. However, they rise up some interesting reflections. Metformin could influence some important determinants of FDG uptake in the different tissue: by lowering serum glucose and insulin levels it could modify tracer availability in the blood, reducing the usual competition between glucose and FDG for GLUT-1 receptor and other glucose transport proteins. This could lead to an increase in tracer availability for lesion uptake making the simple measurement of lesion tracer uptake (the so called SUV) a suboptimal index of lesion metabolism.

Even more complex is to establish whether FDG-PET could represent a correct technique in for the assessment of the potential antineoplastic effect of metformin in the clinical setting.

In this line, it is of primary importance to understand how metformin could modulate PET signal in order to correctly verify whether this technique is useful to assess any therapeutic response.

This task is particularly relevant when metformin is used as adjuvant with other conventional therapy such as chemotherapeutic agents able to alter FDG distribution *per se*.

In apparent disagreement with other evidence^[27], Habibollahi *et al.*^[29] showed that, in two colon cancer models, metformin increased ¹⁸F-FDG uptake soon after initiation of treatment. However, as the cells die from the effects of the biguanide and other chemotherapies, ¹⁸F-FDG uptake should eventually decrease. But this possible biphasic response on ¹⁸F-FDG PET scans could confound the evaluation of therapeutic efficacy leading to an incorrect classification of patients as non-responders on the basis of an earlier scan.

To date, present available clinical trial results on the use of metformin as anticancer agent involve intermediate or surrogate outcome measurements, such as changes in cellular proliferation or hormone levels, rather than direct measures of clinical benefit and thus do not allow definitive conclusions. Furthermore, with respect to the colon, available data deal with the effects of metformin, at least in non-diabetic subjects, on normal epithelial cells rather than cancer cells and thus hypotheses concerning the use of this drug for prevention rather than for treatment are more feasible^[30].

FUTURE DIRECTIONS

Prospective trials in diabetic patients submitted to routine FDG-PET scans are mandatory to verify if FDG-PET can be used as an early marker of response or if metformin interference with FDG distribution is significant enough to prevent its use in this setting and, in this case, if the use of proliferation markers would be preferable as appropriate choice to image the response of tumors.

To this purpose, a possible approach could be the use of compartmental analysis of tracer through dynamic PET acquisition in order to measure cancer glucose consumption in absolute terms (micromole/min/g) and to obtain information about the possible relationship with lesion progression and therapeutic response.

CONCLUSION

FDG PET is useful to evaluate cancer metabolism in response to the different interventions. In order to establish if this technique could be a valid tool to appreciate anticancer potential of new therapeutic approach such as metformin, a better comprehension of all the variables that could interfere with FDG uptake is needed and further studies in this field are required.

REFERENCES

- 1 **Lalau JD**, Race JM. Lactic acidosis in metformin therapy. *Drugs* 1999; **58** Suppl 1: 55-60; discussion 75-82 [PMID: 10576527 DOI: 10.2165/00003495-199958001-00013]
- 2 **Shaw RJ**, Lamia KA, Vasquez D, Koo SH, Bardeesy N, Depinho RA, Montminy M, Cantley LC. The kinase LKB1 mediates glucose homeostasis in liver and therapeutic effects of metformin. *Science* 2005; **310**: 1642-1646 [PMID: 16308421 DOI: 10.1126/science.1120781]
- 3 **Kozka IJ**, Clark AE, Reckless JP, Cushman SW, Gould GW, Holman GD. The effects of insulin on the level and activity of the GLUT4 present in human adipose cells. *Diabetologia* 1995; **38**: 661-666 [PMID: 7672486 DOI: 10.1007/BF00401836]
- 4 **Nestler JE**. Metformin for the treatment of the polycystic ovary syndrome. *N Engl J Med* 2008; **358**: 47-54 [PMID: 18172174 DOI: 10.1056/NEJMct0707092]
- 5 **Chen CH**, Huang MC, Kao CF, Lin SK, Kuo PH, Chiu CC, Lu ML. Effects of adjunctive metformin on metabolic traits in nondiabetic clozapine-treated patients with schizophrenia and the effect of metformin discontinuation on body weight: a 24-week, randomized, double-blind, placebo-controlled study. *J Clin Psychiatry* 2013; **74**: e424-e430 [PMID: 23759461 DOI: 10.4088/JCP.12m08186]
- 6 **Pollak MN**. Investigating metformin for cancer prevention and treatment: the end of the beginning. *Cancer Discov* 2012; **2**: 778-790 [PMID: 22926251 DOI: 10.1158/2159-8290.CD-12-0263]
- 7 **Long YC**, Zierath JR. AMP-activated protein kinase signaling in metabolic regulation. *J Clin Invest* 2006; **116**: 1776-1783 [PMID: 16823475 DOI: 10.1172/JCI29044]
- 8 **El-Mir MY**, Nogueira V, Fontaine E, Avéret N, Rigoulet M, Leverve X. Dimethylbiguanide inhibits cell respiration via an indirect effect targeted on the respiratory chain complex I. *J Biol Chem* 2000; **275**: 223-228 [PMID: 10617608 DOI: 10.1074/jbc.275.1.223]
- 9 **Kourelis TV**, Siegel RD. Metformin and cancer: new applications for an old drug. *Med Oncol* 2012; **29**: 1314-1327 [PMID: 21301998 DOI: 10.1007/s12032-011-9846-7]
- 10 **Decensi A**, Puntoni M, Goodwin P, Cazzaniga M, Gennari A, Bonanni B, Gandini S. Metformin and cancer risk in diabetic patients: a systematic review and meta-analysis. *Cancer Prev Res (Phila)* 2010; **3**: 1451-1461 [PMID: 20947488 DOI: 10.1158/1940-6207.CAPR-10-0157]
- 11 **Zhang P**, Li H, Tan X, Chen L, Wang S. Association of metformin use with cancer incidence and mortality: a meta-analysis. *Cancer Epidemiol* 2013; **37**: 207-218 [PMID: 23352629 DOI: 10.1016/j.canep.2012.12.009]
- 12 **Noto H**, Goto A, Tsujimoto T, Noda M. Cancer risk in diabetic patients treated with metformin: a systematic review and meta-analysis. *PLoS One* 2012; **7**: e33411 [PMID: 22448244 DOI: 10.1371/journal.pone.0033411]
- 13 **National Institutes of Health**. NIH Clinical Research Trials and You. Available from: URL: <http://www.nih.gov/health/clinicaltrials/index.htm>
- 14 **Gambhir SS**. Molecular imaging of cancer with positron emission tomography. *Nat Rev Cancer* 2002; **2**: 683-693 [PMID: 12209157 DOI: 10.1038/nrc882]
- 15 **Conti PS**, Lilien DL, Hawley K, Keppler J, Grafton ST, Bading JR. PET and [18F]-FDG in oncology: a clinical update. *Nucl Med Biol* 1996; **23**: 717-735 [PMID: 8940714 DOI: 10.1016/0969-8051(96)00074-1]
- 16 **Di Chiro G**, DeLaPaz RL, Brooks RA, Sokoloff L, Kornblith PL, Smith BH, Patronas NJ, Kufta CV, Kessler RM, Johnston GS, Manning RG, Wolf AP. Glucose utilization of cerebral gliomas measured by [18F] fluorodeoxyglucose and positron emission tomography. *Neurology* 1982; **32**: 1323-1329 [PMID: 6983044 DOI: 10.1212/WNL.32.12.1323]
- 17 **Gontier E**, Fourme E, Wartski M, Blondet C, Bonardel G, Le Stanc E, Mantzarides M, Foehrenbach H, Pecking AP, Alberini JL. High and typical 18F-FDG bowel uptake in patients treated with metformin. *Eur J Nucl Med Mol Imaging* 2008; **35**: 95-99 [PMID: 17786437 DOI: 10.1007/s00259-007-0563-6]
- 18 **Steenkamp DW**, McDonnell ME, Meibom S. Metformin may be Associated with False-Negative Cancer Detection in the Gastrointestinal Tract on PET/CT. *Endocr Pract* 2014; **20**: 1079-1083 [PMID: 25100379 DOI: 10.4158/EP14127.RA]
- 19 **Bybel B**, Greenberg ID, Paterson J, Ducharme J, Leslie WD. Increased F-18 FDG intestinal uptake in diabetic patients on metformin: a matched case-control analysis. *Clin Nucl Med* 2011; **36**: 452-456 [PMID: 21552023 DOI: 10.1097/RLU.0b013e318217399e]
- 20 **Ozülker T**, Ozülker F, Mert M, Özpaçacı T. Clearance of the high intestinal (18)F-FDG uptake associated with metformin after stopping the drug. *Eur J Nucl Med Mol Imaging* 2010; **37**: 1011-1017 [PMID: 20107796 DOI: 10.1007/s00259-009-1330-7]
- 21 **Oh JR**, Song HC, Chong A, Ha JM, Jeong SY, Min JJ, Bom HS. Impact of medication discontinuation on increased intestinal FDG accumulation in diabetic patients treated with metformin. *AJR Am J Roentgenol* 2010; **195**: 1404-1410 [PMID: 21098202 DOI: 10.2214/AJR.10.4663]
- 22 **Massollo M**, Marini C, Brignone M, Emionite L, Salani B, Riondato M, Capitanio S, Fiz F, Democrito A, Amaro A, Morbelli S, Piana M, Maggi D, Cilli M, Pfeffer U, Sambuceti G. Metformin temporal and localized effects on gut glucose metabolism assessed using 18F-FDG PET in mice. *J Nucl Med* 2013; **54**: 259-266 [PMID: 23287574 DOI: 10.2967/jnumed.112.106666]
- 23 **Pollak M**. Insulin and insulin-like growth factor signalling in neoplasia. *Nat Rev Cancer* 2008; **8**: 915-928 [PMID: 19029956 DOI: 10.1038/nrc2536]
- 24 **Buzzai M**, Jones RG, Amaravadi RK, Lum JJ, DeBerardinis RJ, Zhao F, Viollet B, Thompson CB. Systemic treatment with the antidiabetic drug metformin selectively impairs p53-deficient tumor cell growth. *Cancer Res* 2007; **67**: 6745-6752 [PMID: 17638885 DOI: 10.1158/0008-5472.CAN-06-4447]
- 25 **Algire C**, Amrein L, Bazile M, David S, Zakikhani M, Pollak M. Diet and tumor LKB1 expression interact to determine sensitivity to anti-neoplastic effects of metformin in vivo. *Oncogene* 2011; **30**: 1174-1182 [PMID: 21102522 DOI: 10.1038/ncr.2010.483]
- 26 **Mashhedi H**, Blouin MJ, Zakikhani M, David S, Zhao Y, Bazile M, Birman E, Algire C, Aliaga A, Bedell BJ, Pollak M. Metformin abolishes increased tumor (18)F-2-fluoro-2-deoxy-D-glucose uptake associated with a high energy diet. *Cell Cycle* 2011; **10**: 2770-2778 [PMID: 21811094 DOI: 10.4161/cc.10.16.16219]
- 27 **Marini C**, Salani B, Massollo M, Amaro A, Esposito AI, Orenco AM, Capitanio S, Emionite L, Riondato M, Bottoni G, Massara C, Boccardo S, Fabbi M, Campi C, Ravera S, Angelini G, Morbelli S, Cilli M, Cordera R, Truini M, Maggi D, Pfeffer U, Sambuceti G. Direct inhibition of hexokinase activity by metformin at least partially impairs glucose metabolism and tumor growth in experimental breast cancer. *Cell Cycle* 2013; **12**: 3490-3499 [PMID: 24240433 DOI: 10.4161/cc.26461]
- 28 **Salani B**, Marini C, Rio AD, Ravera S, Massollo M, Orenco AM, Amaro A, Passalacqua M, Maffioli S, Pfeffer U, Cordera R, Maggi D, Sambuceti G. Metformin impairs glucose consumption and survival in Calu-1 cells by direct inhibition of hexokinase-II. *Sci Rep* 2013; **3**: 2070 [PMID: 23797762 DOI: 10.1038/srep02070]
- 29 **Habibollahi P**, van den Berg NS, Kuruppu D, Loda M, Mahmood U. Metformin--an adjunct antineoplastic therapy--divergently modulates tumor metabolism and proliferation, interfering with early response prediction by 18F-FDG PET imaging. *J Nucl Med* 2013; **54**: 252-258 [PMID: 23376854 DOI: 10.2967/jnumed.112.107011]
- 30 **Pollak M**. Potential applications for biguanides in oncology. *J Clin Invest* 2013; **123**: 3693-3700 [PMID: 23999444 DOI: 10.1172/JCI67232]

P- Reviewer: Juergens KU, Salemi VMC S- Editor: Tian YL

L- Editor: A E- Editor: Lu YJ



Transarterial chemoembolization for liver metastases from solid pseudopapillary epithelial neoplasm of pancreas: A case report

TV Prasad, KS Madhusudhan, Deep N Srivastava, Nihar R Dash, Arun K Gupta

TV Prasad, KS Madhusudhan, Deep N Srivastava, Arun K Gupta, Department of Radiology, All India Institute of Medical Sciences, New Delhi 110029, India

Nihar R Dash, Department of Gastrointestinal Surgery, All India Institute of Medical Sciences, Ansari Nagar, New Delhi 110029, India

Author contributions: All authors contributed to this manuscript.

Ethics approval: The study was reviewed and approved.

Informed consent: This is to state that all the details revealing the identity of the patient are omitted from the manuscript. Informed consent was waived off because of the retrospective nature of the case report.

Conflict-of-interest: None.

Open-Access: This article is an open-access article which was selected by an in-house editor and fully peer-reviewed by external reviewers. It is distributed in accordance with the Creative Commons Attribution Non Commercial (CC BY-NC 4.0) license, which permits others to distribute, remix, adapt, build upon this work non-commercially, and license their derivative works on different terms, provided the original work is properly cited and the use is non-commercial. See: <http://creativecommons.org/licenses/by-nc/4.0/>

Correspondence to: Dr. KS Madhusudhan, MD, Department of Radiology, All India Institute of Medical Sciences, Ansari Nagar, New Delhi 110029, India. drmadhuks@gmail.com

Telephone: +91-98-68398826

Fax: +91-11-26588663

Received: November 15, 2014

Peer-review started: November 16, 2014

First decision: December 26, 2014

Revised: January 23, 2015

Accepted: February 10, 2015

Article in press: February 12, 2015

Published online: March 28, 2015

extensive liver metastasis from SPEN of pancreatic body for which she was operated four years ago. Due to the extensive nature of metastatic disease she was offered Transarterial chemoembolisation (TACE) using gemcitabine as chemotherapeutic agent. Short term follow up after a month of TACE with multiphase computed tomography showed > 90% resolution in the viable tumor with significant clinical improvement. TACE ensures targeted delivery of chemotherapeutic drugs in higher doses with least systemic toxicity and is more effective and safe than systemic chemotherapy. TACE with gemcitabine was found to be very effective in our patient with numerous liver metastasis.

Key words: Solid pseudopapillary epithelial neoplasm; Liver metastases; Transarterial chemoembolization; Gemcitabine

© **The Author(s) 2015.** Published by Baishideng Publishing Group Inc. All rights reserved.

Core tip: Solid pseudo-papillary epithelial neoplasm (SPEN) is a rare epithelial tumor of pancreas which is generally less aggressive and patients rarely present with liver metastasis. Our patient is a middle aged lady presented with extensive liver metastasis several years after the removal of primary tumor. Transarterial chemoembolisation (TACE) is a recognized treatment modality for inoperable hepatocellular carcinoma and metastasis from certain tumors. However, this novel technique is reported to be used only once for a patient with SPEN metastasis. In our patient, we performed TACE with gemcitabine as chemotherapeutic agent with encouraging short term results.

Abstract

Solid pseudo-papillary epithelial neoplasm (SPEN) is a rare epithelial tumor of pancreas with a low malignant potential occurs most commonly in young females. We report a case of 40 years old woman presented with

Prasad TV, Madhusudhan KS, Srivastava DN, Dash NR, Gupta AK. Transarterial chemoembolization for liver metastases from solid pseudopapillary epithelial neoplasm of pancreas: A case report. *World J Radiol* 2015; 7(3): 61-65 Available from: URL:

INTRODUCTION

Solid pseudo-papillary epithelial neoplasm (SPEN) is a rare epithelial tumor of pancreas with a low malignant potential^[1]. After the first description of the entity in 1959, more cases are reported in literature in the last decades^[2]. Local aggressiveness and metastasis are reported in less than 15% cases^[3]. Surgical resection is optimal in localized disease. Surgery is also frequently offered in locally aggressive tumors and oligo-metastatic lesions in liver because of indolent nature of the disease and younger ages of presentation. There are sporadic reports in literature discussing chemo-radiotherapy in disseminated disease^[4-7]. We present a case of multiple hepatic metastasis from SPEN, developing four years after primary treatment of pancreatic lesion, treated with transarterial chemoembolization (TACE).

CASE REPORT

A 40-year-old woman presented to the gastrointestinal surgery clinic with abdominal pain for one month duration. Clinical examination was unremarkable except for hepatomegaly. She had a past history of surgery (Distal pancreatectomy) for pancreatic tumor (Figure 1) four years ago which was histopathologically proven as SPEN. Presently, she was evaluated with ultrasonography which showed multiple hypoechoic focal lesions in both lobes of liver with fatty infiltration (Figure 2). Subsequently multiphase contrast enhanced computed tomography (CT) was done, which showed multiple arterial enhancing lesions in both lobes of liver with no significant washout in venous and delayed phases (Figure 3). No capsule was seen. There was no recurrent or residual lesion at the primary site. Fine needle aspiration cytology of the new liver lesions was suggestive of metastases from pancreatic SPEN.

Due to the presence of numerous liver metastasis involving both lobes, chemotherapy was planned. After a detailed discussion with the gastroenterologist, gastrointestinal surgeons and oncologists it was decided to treat the patient with TACE using gemcitabine as the chemotherapeutic drug. Through the transfemoral route, both hepatic arteries were catheterized selectively and the drug was injected. Gemcitabine (dose 1 g) was mixed with 20 mL of lipiodol (Lipiodol ultra-fluid, Guerbet, United States) and saline was mixed to make a solution of about 80 mL. About 40 mL each was injected into right and left hepatic arteries separately followed by embolisation of the arteries with gelfoam slurry. Post embolization images showed significant retention of lipiodol within the lesions (Figure 4). Patient did not experience any procedure

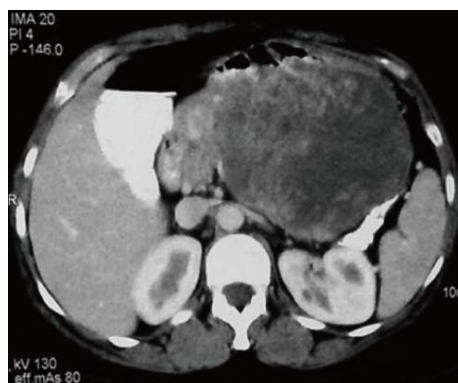


Figure 1 Axial computed tomography scan shows a well defined heterogeneous mass lesion arising from body and tail of pancreas with marked central necrosis which was proven as solid pseudo-papillary epithelial neoplasm after surgery.



Figure 2 Ultrasonography image showing multiple well defined hypoechoic lesions in the background of fatty liver, suggestive of metastases.

related complications. The patient was subsequently followed up with CT scan after one month of TACE. It showed significant (> 90%) reduction in the size and enhancement of the lesions suggesting marked necrosis and complete response (Figure 5). The patient is currently (after 6 mo of TACE) asymptomatic and is on regular follow up.

DISCUSSION

SPEN accounts for less than 2% of exocrine tumors of pancreas with a low malignant potential and has high incidence in young females. Metastasis from SPEN is seen in 10%-15% of cases with liver being the commonest target organ^[2]. Although the mean interval for liver metastasis from initial diagnosis of primary tumor is 8.5 years, it is reported as late as 15.8 years after the resection of primary neoplasm^[8,9]. Most of the patients of SPEN present with abdominal pain and lump. Incidental detection of cases during imaging for other purposes is also not infrequent. Ultrasonography, CT scan and Magnetic Resonance Imaging are the imaging modalities used in assessing the primary lesion and in staging the tumor. These tumors have solid and cystic areas on imaging with frequent detection of haemorrhage.

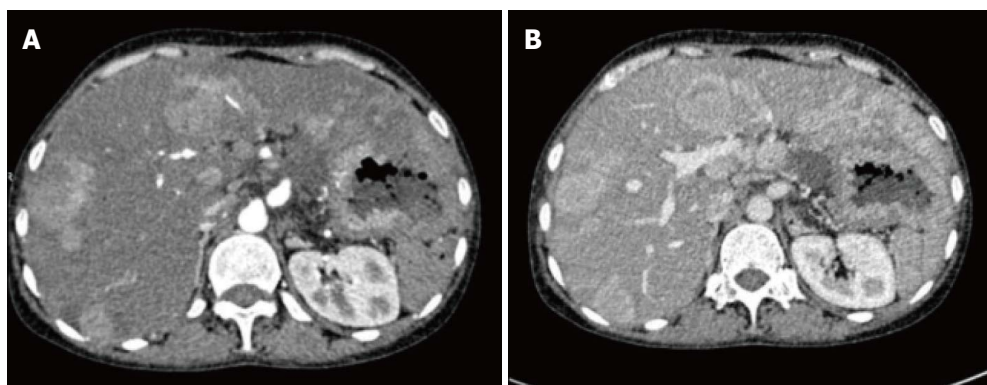


Figure 3 Arterial (A) and venous (B) phases of multiphase contrast enhanced axial computed tomography images showing multiple arterial enhancing focal lesions in liver with no significant wash out in venous phase.

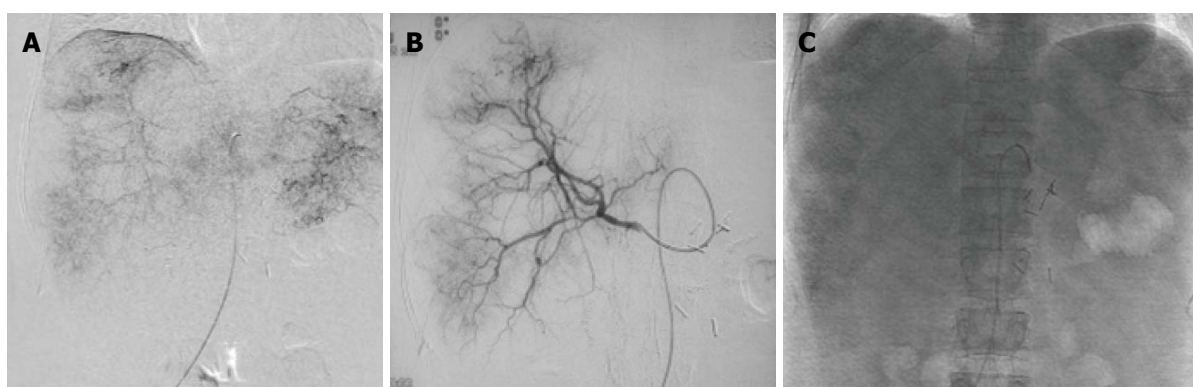


Figure 4 DSA: (A) Common hepatic artery and (B) right hepatic artery angiography showing multiple tumor blush in the liver, (C) post embolisation spot image showing lipiodol retention within the lesions.

Localised SPEN is usually managed by surgical resection. Solitary and resectable metastatic lesions are also managed by surgery. Patients with aggressive tumors and multiple metastasis are offered chemotherapy or radiotherapy. Although no guidelines could be found in literature regarding chemotherapy for metastatic SPEN, the various drugs used are mitomycin, cisplatin, gemcitabine and 5-fluorouracil in different combinations^[4,5]. Most of the reports have managed liver metastases with systemic chemotherapy. Hormone therapy has also been tried in patients with tumors positive for estrogen-progesterone receptors with varying results^[7].

TACE is an accepted method of palliative chemotherapy in unresectable primary and secondary malignant neoplasms of liver. Apart from hepatic metastasis from colorectal malignancies, it also has been found useful in metastatic pancreatic cancers^[10]. TACE is preferred over systemic chemotherapy due to the fact that the preferential hepatic arterial supply of the metastatic lesions allow delivery of higher doses of chemotherapeutic drugs, ensuring targeted delivery of drug in optimal doses with less chances of systemic toxicity. Administration of chemotherapeutic drugs with lipiodol during TACE allows optimal retention of agents in the tumor, increasing the contact period. Degree of

lipiodol retention is used as an indicator of treatment adequacy on follow up. Gelfoam embolisation of the feeding vessel causes ischemia in tumor cells increasing the efficacy of chemotherapy apart from facilitating the contact period of drug with the tumor. Gemcitabine is an established chemotherapeutic agent used for palliation in extensive disease of pancreatic adenocarcinoma. Gemcitabine is often used in combination with 5-fluorouracil in advanced pancreatic malignancies^[10].

Only one case report of TACE in the management of liver metastasis from pancreatic SPEN was found in English literature by Matsuda *et al*^[6]. They performed intraarterial chemoinfusion of doxorubicin followed by gelfoam embolization of only right hepatic artery. On follow up, there was 28% and 15% shrinkage in the size of the lesions in right lobe and left lobe respectively, signifying the role of gel foam embolization. In our case, TACE with gemcitabine and lipiodol followed by gelfoam embolization gave optimum short term results.

In conclusion, liver metastasis is unusual in pancreatic SPEN. Although solitary metastasis is managed by surgery, extensive liver lesions require palliative chemotherapy. TACE ensures targeted delivery of chemotherapeutic drugs in higher doses with least systemic toxicity and is more effective and safe than systemic chemotherapy. TACE with gemcitabine was

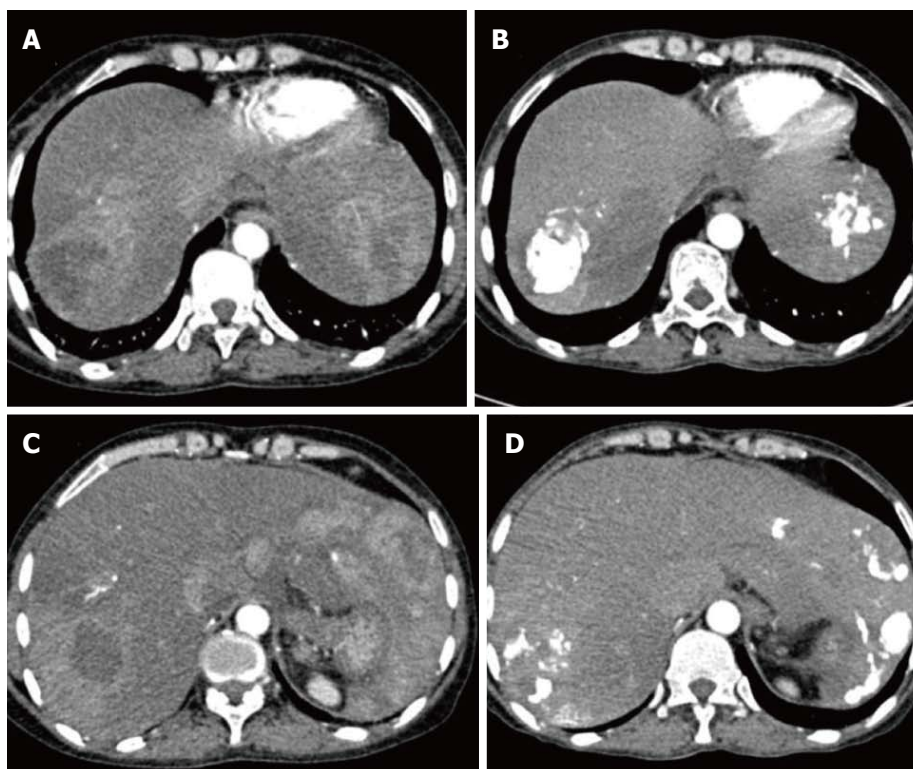


Figure 5 Pre and Post transarterial chemoembolization. A and C showing arterial enhancing lesions in pre transarterial chemoembolisation (TACE) images; B and D are corresponding post TACE images showing lipiodol retention with significant reduction in enhancing component of the lesions.

found to be very effective in our patient with numerous liver metastasis. However further large and long term studies are required to establish this technique in liver metastasis from SPEN.

COMMENTS

Case characteristics

Middle aged lady with history of distal pancreatectomy for solid pseudo-papillary epithelial neoplasm (SPEN) four years ago, presented with abdominal pain for one month.

Clinical diagnosis

On physical examination she had tender hepatomegaly.

Differential diagnosis

Malignant tumors (metastatic tumors, hepatocellular carcinoma), benign neoplasms (focal nodular hyperplasia, hemangioma and adenoma), and abscess.

Laboratory diagnosis

Lab investigations revealed normal findings.

Imaging diagnosis

USG and enhanced spiral computerized tomography showed multiple focal liver lesions.

Pathological diagnosis

FNAC from liver lesions suggested liver metastasis from pancreatic SPEN.

Treatment

Transarterial chemoembolisation (TACE) using gemcitabine as chemotherapeutic agent.

Related reports

Only one case report of TACE in the management of liver metastasis from pancreatic SPEN was found in English literature by Matsuda *et al.*

Term explanation

SPEN is a rare epithelial tumor of pancreas with a low malignant potential.

Experiences and lessons

TACE with gemcitabine is found to be very effective in patients with inoperable liver metastasis from SPEN.

Peer-review

Well written case report.

REFERENCES

- 1 Yu PF, Hu ZH, Wang XB, Guo JM, Cheng XD, Zhang YL, Xu Q. Solid pseudopapillary tumor of the pancreas: a review of 553 cases in Chinese literature. *World J Gastroenterol* 2010; **16**: 1209-1214 [PMID: 20222163 DOI: 10.3748/wjg.v16.i10.1209]
- 2 Papavramidis T, Papavramidis S. Solid pseudopapillary tumors of the pancreas: review of 718 patients reported in English literature. *J Am Coll Surg* 2005; **200**: 965-972 [PMID: 15922212 DOI: 10.1016/j.jamcollsurg.2005.02.011]
- 3 Mao C, Guvendi M, Domenico DR, Kim K, Thomford NR, Howard JM. Papillary cystic and solid tumors of the pancreas: a pancreatic embryonic tumor? Studies of three cases and cumulative review of the world's literature. *Surgery* 1995; **118**: 821-828 [PMID: 7482268 DOI: 10.1016/S0039-6060(05)80271-5]
- 4 Strauss JF, Hirsch VJ, Rubey CN, Pollock M. Resection of a solid and papillary epithelial neoplasm of the pancreas following treatment with cis-platinum and 5-fluorouracil: a case report. *Med Pediatr Oncol* 1993; **21**: 365-367 [PMID: 8492753 DOI: 10.1002/mpo.2950210511]
- 5 Das G, Bhuyan C, Das BK, Sharma JD, Saikia BJ, Purkayastha J. Spleen-preserving distal pancreatectomy following neoadjuvant chemotherapy for papillary solid and cystic neoplasm of pancreas. *Indian J Gastroenterol Off J Indian Soc Gastroenterol* 2004; **23**: 188-189
- 6 Matsuda Y, Imai Y, Kawata S, Nishikawa M, Miyoshi S, Saito R, Minami Y, Tarui S. Papillary-cystic neoplasm of the pancreas with multiple hepatic metastases: a case report. *Gastroenterol Jpn* 1987; **22**: 379-384 [PMID: 2442059]

- 7 **Sclafani LM**, Reuter VE, Coit DG, Brennan MF. The malignant nature of papillary and cystic neoplasm of the pancreas. *Cancer* 1991; **68**: 153-158 [PMID: 2049737 DOI: 10.1002/1097-0142(19910701)68:1<153::AID-CNCR2820680128>3.0.CO;2-N]
- 8 **Vollmer CM**, Dixon E, Grant DR. Management of a solid pseudopapillary tumor of the pancreas with liver metastases. *HPB* (Oxford) 2003; **5**: 264-267 [PMID: 18333000 DOI: 10.1080/13651820310001397]
- 9 **Gomez P**, Yorke R, Ayala AG, Ro JY. Solid-pseudopapillary neoplasm of pancreas with long delayed liver metastasis. *Ann Diagn Pathol* 2012; **16**: 380-384 [PMID: 21641841 DOI: 10.1016/j.anndiagpath.2011.02.008]
- 10 **Tajima H**, Kitagawa H, Tsukada T, Okamoto K, Nakanuma SI, Sakai S, Makino I, Furukawa H, Hayashi H, Oyama K, Inokuchi M, Nakagawara H, Miyashita T, Itoh H, Fujita H, Takamura H, Ninomiya I, Fushida S, Fujimura T, Ohta T, Koda W, Minami T, Ryu Y, Sanada J, Gabata T, Matsui O, Sai Y. Hepatic arterial infusion chemotherapy with gemcitabine and 5-fluorouracil or oral S-1 improves the prognosis of patients with postoperative liver metastases from pancreatic cancer. *Mol Clin Oncol* 2013; **1**: 869-874 [PMID: 24649263]

P- Reviewer: Bester L, Bhosale P, Smart NJ **S- Editor:** Ji FF

L- Editor: A **E- Editor:** Lu YJ



Gastrointestinal manifestations of Henoch-Schonlein purpura: A report of two cases

Parameswaran Prathiba Rajalakshmi, Kalyanasundaram Srinivasan

Parameswaran Prathiba Rajalakshmi, Department of Radiology, Sree Balaji Medical College and Hospital, Chromepet, Chennai 600044, Tamil Nadu, India

Kalyanasundaram Srinivasan, Global Hospital, Chennai 600100, Tamil Nadu, India

Author contributions: Prathiba Rajalakshmi P prepared the manuscript and analyzed the data, approval of final version to be published; Srinivasan K collected the patient's clinical data and radiological images.

Informed consent: All study participants, or their legal guardian, provided informed written consent prior to study enrolment.

Conflict-of-interest: The authors have no personal or financial conflict of interest to disclose.

Open-Access: This article is an open-access article which was selected by an in-house editor and fully peer-reviewed by external reviewers. It is distributed in accordance with the Creative Commons Attribution Non Commercial (CC BY-NC 4.0) license, which permits others to distribute, remix, adapt, build upon this work non-commercially, and license their derivative works on different terms, provided the original work is properly cited and the use is non-commercial. See: <http://creativecommons.org/licenses/by-nc/4.0/>

Correspondence to: Parameswaran Prathiba Rajalakshmi, MD, Assistant Professor, Department of Radiology, Sree Balaji Medical College and Hospital, No 7, Works Road, Chromepet, Chennai 600044, Tamil Nadu, India. prathibaaaiims@gmail.com

Telephone: +91-44-22415600

Fax: +91-44-22416676

Received: August 18, 2014

Peer-review started: August 18, 2014

First decision: September 28, 2014

Revised: December 22, 2014

Accepted: February 10, 2015

Article in press: February 12, 2015

Published online: March 28, 2015

by palpable purpura, arthritis, glomerulonephritis and gastrointestinal manifestations and commonly occurs in children and young adults. The patients with gastrointestinal involvement usually present with colicky abdominal pain, vomiting and melena. The imaging findings include multifocal bowel thickening with mucosal hyperenhancement, presence of skip areas, mesenteric vascular engorgement, with involvement of unusual sites like stomach, duodenum and rectum. These imaging findings in a child or young adult with appropriate clinical findings could suggest HSP.

Key words: Henoch-Schonlein purpura; Vasculitis; Skip areas; Bowel thickening

© The Author(s) 2015. Published by Baishideng Publishing Group Inc. All rights reserved.

Core tip: The gastrointestinal involvement in Henoch-Schonlein purpura produces typical imaging findings. In an appropriate clinical setting, these findings often suggest the diagnosis.

Prathiba Rajalakshmi P, Srinivasan K. Gastrointestinal manifestations of Henoch-Schonlein purpura: A report of two cases. *World J Radiol* 2015; 7(3): 66-69 Available from: URL: <http://www.wjgnet.com/1949-8470/full/v7/i3/66.htm> DOI: <http://dx.doi.org/10.4329/wjr.v7.i3.66>

INTRODUCTION

Vasculitides are characterized by inflammation of walls of the blood vessels and their clinical manifestations depend on size and location of the involved vessels. Large vessel vasculitis (e.g., Takayasu arteritis) affects aorta and its largest branches and its gastrointestinal manifestations in the absence of systemic involvement

Abstract

Henoch-Schonlein purpura (HSP) is a small vessel vasculitis mediated by type III hypersensitivity with deposition of IgA immune complex in the walls of vessels. It is a multi-system disorder characterized

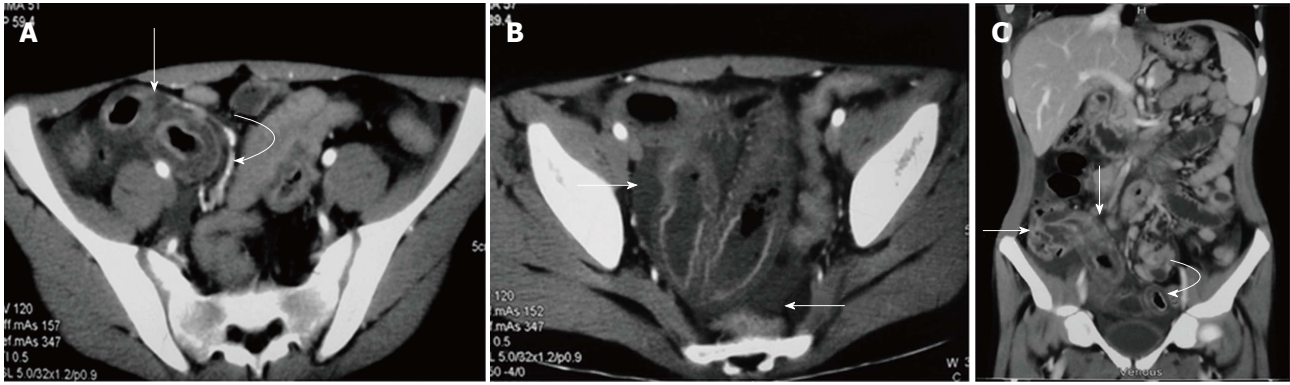


Figure 1 Bowel involvement in Henoch-Schonlein purpura in a 15-year-old male. A: Contrast enhanced axial computed tomography (CT) image in the arterial phase shows circumferential wall thickening involving a distal ileal loop (arrow) with mural stratification. Engorged mesenteric vessels are seen adjacent to the thickened bowel (curved arrow); B: Axial CT image at the level of pelvis shows free fluid (arrows) and thickening of ileal loops; C: Coronal multiplanar reformatted image shows long segment thickening involving terminal ileum and ascending colon (straight arrows). Another segment of distal ileal loop also shows wall thickening (curved arrow).

are usually indistinguishable from mesenteric thromboembolic disease. Medium vessel vasculitis (*e.g.*, polyarteritis nodosa) affects main visceral arteries and its branches and may lead to aneurysm formation with consequent gastrointestinal/intra-abdominal hemorrhage. Small vessel vasculitis involves arterioles, venules and capillaries and its bowel involvement is characterised by ulceration and stricture formation. Henoch-Schonlein purpura (HSP) is a type III hypersensitivity mediated small vessel vasculitis presenting with skin rashes, arthritis involving large joints, colicky abdominal pain, gastrointestinal hemorrhage and hematuria. In this article, we report two cases of gastrointestinal involvement of HSP and discuss its imaging features and radiological differential diagnoses.

CASE REPORT

Case 1

A 15-year-old male presented with history of skin rashes and joint pain for nearly a week. The skin rashes initially appeared in bilateral thighs which then progressed to bilateral hands and face. The patient also gave history of abdominal pain and melena. On clinical examination, the skin lesions were symmetrical, non-blanching and erythematous in nature. He was afebrile and his vitals were pulse rate 82/min and blood pressure 130/80 mmHg. Stool examination for occult blood was negative. Laboratory investigations were unremarkable (blood urea 43 mg%; serum creatinine 0.8 mg%; sodium 137 mg%; potassium 4.9 mg%). Computed tomography (CT) angiography of abdomen was performed which showed multifocal areas of symmetric small bowel wall thickening with intervening normal segments. Mural stratification was observed in the thickened bowel loops with enhancing mucosa/serosa and hypodense submucosa. The mesenteric vessels were engorged and mild free fluid was noted in pelvis. Biopsy from the skin lesions showed features

of leukocytoclastic vasculitis. The diagnosis of HSP was made based on clinical features and biopsy findings. The patient was administered a short course of intravenous steroids followed by oral steroids. Abdominal symptoms resolved in a few days and the skin lesions disappeared by third week of initiation of treatment (Figure 1).

Case 2

An 8-year-old male presented with 4 d history of skin rashes and 2 d history of severe abdominal pain. Skin rashes were erythematous in nature and were seen over bilateral gluteal regions. The child did not give any history of vomiting, altered bowel habits or melena. Laboratory investigations were unremarkable except for mild leucocytosis. Contrast enhanced CT of the abdomen was performed which showed long segment circumferential symmetric thickening of a mid-ileal loop with mural stratification. The adjacent mesenteric vessels were engorged and a few subcentimetric mesenteric lymph nodes were noted. Punch biopsy from skin lesions revealed granulocytes in vessel walls suggestive of leukocytoclastic vasculitis. The patient was treated with short course of oral steroids and supportive care. Abdominal pain subsided completely with initiation of steroids and skin lesions disappeared by second week (Figure 2).

DISCUSSION

HSP is an acute systemic small vessel vasculitis characterized by a classic palpable purpura, arthritis, gastrointestinal and renal manifestations^[1]. It is the most common vasculitis of childhood and commonly occurs in children between 3 and 10 years of age; however it is known to affect young adults also. Many patients have a strong history of atopy and though the exact etiology is unknown, the disease is thought to result from an exaggerated immune response to a preceding, usually upper respiratory tract infection. There is consequent IgA and C3 containing immune complex deposition in

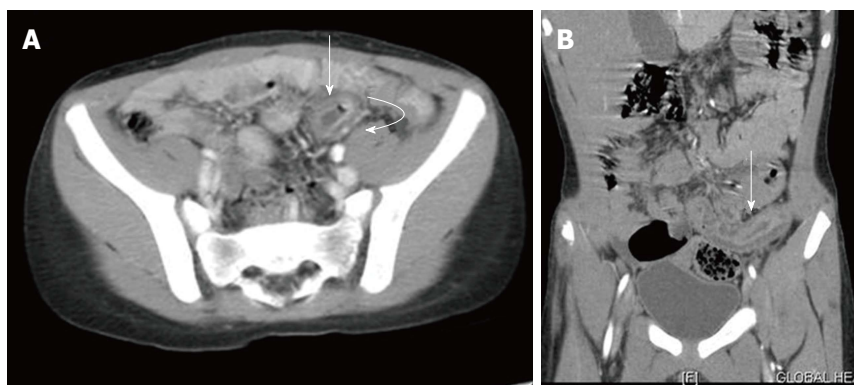


Figure 2 Bowel involvement in Henoch-Schonlein purpura in an 8-year-old child. A: Axial contrast-enhanced computed tomography image shows circumferential wall thickening in a mid-ileal loop with target like appearance (straight arrow) with adjacent engorged mesenteric vessels (curved arrow); B: Coronal reformatted images shows long segment thickening of the mid-ileal loop (straight arrow).

small vessels of skin, joints, gastrointestinal tract and kidneys. Skin lesions are the earliest manifestation in majority of patients (approximately 70%) and typically develop in dependent locations like lower extremities and gluteal regions. These lesions start as erythematous papules which mature into purpura. Punch biopsy from skin lesions shows the presence of granulocytes in walls of small vessels which is termed as leukocytoclastic vasculitis. In about 75% of patients, transient arthritis involving large joints of lower limbs is seen^[2].

Gastrointestinal involvement is seen in 50% to 75% patients and is often the most debilitating manifestation of HSP characterised by colicky abdominal pain, vomiting and gastrointestinal hemorrhage. Intramural hemorrhage and edema are the contributing factors to these symptoms. Gastrointestinal manifestations precede the appearance of skin lesions in 10%-15% patients and under such circumstances, differentiating from other numerous causes of acute abdomen is difficult^[3,4]. On CT imaging, bowel involvement is seen as multifocal symmetric, circumferential wall thickening with target appearance. The target pattern is appreciable after administration of intravenous contrast and consists of enhancing mucosal and serosal layers due to hyperaemia with intervening hypodense submucosal layer due to edema. Associated findings include free intraperitoneal fluid, ileus of affected loop, vascular engorgement in the adjoining mesentery and non-specific lymphadenopathy^[5].

The target sign is not specific for vasculitis and can be seen in many other conditions including ischemic bowel disease, idiopathic inflammatory bowel disease, infectious enterocolitis, radiation enteritis, *etc.* Common causes of mesenteric ischemia in children include cardioembolic occlusions, hypercoagulable states and venous obstruction secondary to midgut volvulus and incarcerated hernias. The imaging findings in early phase of mesenteric ischemia which is characterised by mucosal hyperaemia and edema are indistinguishable from those in HSP. CT angiography can be used to visualize the site of the arterial or venous occlusion; however a normal angiogram does not rule out the possibility of mesenteric ischemia^[6]. The presence of skip lesions with intervening normal segments (as seen in Case 1), involvement of unusual sites like stomach, duodenum and rectum and bowel

involvement not confining to a single vascular territory help in differentiating HSP from mesenteric ischemia^[7]. Although the peak age of occurrence of Crohn's disease is second and third decades of life, approximately 25% cases occur in pediatric population (pediatric Crohn). Wall thickening in active Crohn's disease can be circumferential or eccentric involving the mesenteric border. Mesenteric vascular engorgement and skip areas are also seen in Crohn's disease. However, terminal ileal involvement, fibrofatty proliferation, formation of stricture, sinus, fistula and abscess would favour Crohn's disease over other conditions^[8]. Infectious enteritis or colitis usually has mild wall thickening and less commonly, target appearance. Significant fat streakiness in the surrounding mesentery with presence of lymphadenopathy and ascites can point to infectious etiology; however correlation with laboratory investigations is essential for diagnosis.

Since the intramural hemorrhages are confined to mucosa and submucosa, HSP spontaneously resolves with conservative management in about 94% of children^[9,10]. However in nearly 5% patients, there may be development of gastrointestinal complications including ileo-ileal intussusception, massive gastrointestinal hemorrhage, ileal perforation, stricture and protein losing enteropathy^[11].

Renal involvement in HSP is seen in 40%-50% patients and in most cases occurs by first month. However, it may develop months to years after initial presentation and the manifestations may range in severity from asymptomatic hematuria to progressive glomerulonephritis. Other less frequent complications of HSP include pulmonary hemorrhage, myocardial infarction, orchitis, *etc.*

Uncomplicated HSP is usually managed with supportive care and steroids. Patients with renal involvement are treated with high dose pulsed steroids and immunosuppressive drugs to prevent progressive renal damage^[2].

HSP generally has a self-limiting course; however recurrence has been reported in about 33% cases. Patients with renal involvement have a greater chance for disease recurrence and the long term outcome is determined predominantly by the severity of renal involvement^[12].

To conclude, imaging findings in bowel involvement of HSP are typical and in the appropriate clinical setting, can

corroborate to the diagnosis of HSP. Even when seen as an isolated manifestation, it can aid in narrowing down the possible differential diagnosis and in arriving at an early diagnosis.

COMMENTS

Case characteristics

The two young aged male patients presented with similar symptoms: skin rashes and abdominal pain.

Clinical diagnosis

In the first patient, erythematous skin rashes with melena and in the second patient, erythematous rashes with abdominal pain.

Differential diagnosis

Ischemic bowel disease, idiopathic inflammatory bowel disease, infectious enterocolitis, radiation enteritis.

Laboratory diagnosis

Case 1: Blood urea 43 mg%; serum creatinine 0.8 mg%; sodium 137 mg%; potassium 4.9 mg%; Case 2: Mild leukocytosis.

Imaging diagnosis

In both patients, computed tomography showed multifocal symmetric, circumferential wall thickening with target appearance and vascular engorgement in the adjoining mesentery.

Pathological diagnosis

Biopsy from skin lesions revealed granulocytes in vessel walls suggestive of leukocytoclastic vasculitis.

Treatment

Both patients received steroids and supportive care.

Experiences and lessons

The case report shows that imaging findings in Henoch-Schonlein purpura (HSP) are typical and in an appropriate clinical setting can suggest the diagnosis.

Peer-review

The authors present a very good review of a rather rare disease HSP. Both cases are very "academic", and images provide a clear view of the diagnostic radiological findings.

REFERENCES

1 Ha HK, Lee SH, Rha SE, Kim JH, Byun JY, Lim HK, Chung

- JW, Kim JG, Kim PN, Lee MG, Auh YH. Radiologic features of vasculitis involving the gastrointestinal tract. *Radiographics* 2000; **20**: 779-794 [PMID: 10835128 DOI: 10.1148/radiographics.20.3.g00mc02779]
- 2 Sinclair P. Henoch-Schonlein purpura- a review. *Curr Allergy Clin Immunol* 2010; **23**: 116-120
- 3 Mills JA, Michel BA, Bloch DA, Calabrese LH, Hunder GG, Arend WP, Edworthy SM, Fauci AS, Leavitt RY, Lie JT. The American College of Rheumatology 1990 criteria for the classification of Henoch-Schönlein purpura. *Arthritis Rheum* 1990; **33**: 1114-1121 [PMID: 2202310 DOI: 10.1002/art.1780330809]
- 4 Agha FP, Nostrant TT, Keren DF. Leucocytoclastic vasculitis (hypersensitivity angiitis) of the small bowel presenting with severe gastrointestinal hemorrhage. *Am J Gastroenterol* 1986; **81**: 195-198 [PMID: 3485374]
- 5 Jeong YK, Ha HK, Yoon CH, Gong G, Kim PN, Lee MG, Min YI, Auh YH. Gastrointestinal involvement in Henoch-Schönlein syndrome: CT findings. *AJR Am J Roentgenol* 1997; **168**: 965-968 [PMID: 9124151]
- 6 Moschetta M, Telegrafo M, Rella L, Stabile Ianora AA, Angelelli G. Multi-detector CT features of acute intestinal ischemia and their prognostic correlations. *World J Radiol* 2014; **6**: 130-138 [PMID: 24876917 DOI: 10.4329/wjr.v6.i5.130]
- 7 Fernandes T, Oliveira MI, Castro R, Araújo B, Viamonte B, Cunha R. Bowel wall thickening at CT: simplifying the diagnosis. *Insights Imaging* 2014; **5**: 195-208 [PMID: 24407923 DOI: 10.1007/s13244-013-0308-y]
- 8 d'Almeida M, Jose J, Oneto J, Restrepo R. Bowel wall thickening in children: CT findings. *Radiographics* 2008; **28**: 727-746 [PMID: 18480481 DOI: 10.1148/rg.283065179]
- 9 Chung DJ, Park YS, Huh KC, Kim JH. Radiologic findings of gastrointestinal complications in an adult patient with Henoch-Schönlein purpura. *AJR Am J Roentgenol* 2006; **187**: W396-W398 [PMID: 16985111]
- 10 Sohagia AB, Gunturu SG, Tong TR, Hertan HI. Henoch-schonlein purpura-a case report and review of the literature. *Gastroenterol Res Pract* 2010; **2010**: 597648 [PMID: 20508739 DOI: 10.1155/2010/597648]
- 11 Chen SY, Kong MS. Gastrointestinal manifestations and complications of Henoch-Schönlein purpura. *Chang Gung Med J* 2004; **27**: 175-181 [PMID: 15148994]
- 12 Tizard EJ, Hamilton-Ayres MJ. Henoch Schonlein purpura. *Arch Dis Child Educ Pract Ed* 2008; **93**: 1-8 [PMID: 18208978 DOI: 10.1136/adc.2004.066035]

P- Reviewer: Monclova JL S- Editor: Gong XM L- Editor: A
E- Editor: Lu YJ





Published by **Baishideng Publishing Group Inc**

8226 Regency Drive, Pleasanton, CA 94588, USA

Telephone: +1-925-223-8242

Fax: +1-925-223-8243

E-mail: bpgoffice@wjgnet.com

Help Desk: <http://www.wjgnet.com/esps/helpdesk.aspx>

<http://www.wjgnet.com>



World Journal of *Radiology*

World J Radiol 2015 April 28; 7(4): 70-86





Editorial Board

2014-2017

The *World Journal of Radiology* Editorial Board consists of 365 members, representing a team of worldwide experts in radiology. They are from 36 countries, including Afghanistan (1), Argentina (2), Australia (5), Austria (7), Belgium (2), Brazil (8), Canada (6), Chile (1), China (43), Croatia (1), Denmark (4), Egypt (6), France (5), Germany (22), Greece (10), India (12), Iran (6), Ireland (2), Israel (3), Italy (47), Japan (13), Netherlands (1), New Zealand (1), Pakistan (1), Poland (2), Portugal (1), Serbia (1), Singapore (3), Slovakia (1), South Korea (18), Spain (4), Sweden (2), Switzerland (4), Thailand (1), Turkey (26), United Kingdom (11), and United States (82).

EDITORS-IN-CHIEF

Kai U Juergens, *Bremen*
Edwin JR van Beek, *Edinburgh*
Thomas J Vogl, *Frankfurt*

GUEST EDITORIAL BOARD MEMBERS

Wing P Chan, *Taipei*
Chung-Huei Hsu, *Taipei*
Chin-Chang Huang, *Taipei*
Tsong-Long Hwang, *Taoyuan*
Jung-Lung Hsu, *Taipei*
Chia-Hung Kao, *Taichung*
Yu-Ting Kuo, *Tainan*
Hon-Man Liu, *Taipei*
Hui-Lung Liang, *Kaohsiung*
Chun Chung Lui, *Kaohsiung*
Sen-Wen Teng, *Taipei*
Yung-Liang (William) Wan, *Taoyuan*

MEMBERS OF THE EDITORIAL BOARD



Afghanistan

Takao Hiraki, *Okayama*



Argentina

Patricia Carrascosa, *Vicente Lopez*
Maria C Ziadi, *Rosario*



Australia

Lourens Bester, *Sydney*
Gemma A Figtree, *Sydney*



Austria

Herwig R Cerwenka, *Graz*
Gudrun M Feuchtnner, *Innsbruck*
Benjamin Henninger, *Innsbruck*
Rupert Lanzenberger, *Vienna*
Shu-Ren Li, *Vienna*
Veronika Schopf, *Vienna*
Tobias De Zordo, *Innsbruck*



Belgium

Steve Majerus, *Liege*
Kathelijne Peremans, *Merelbeke*



Brazil

Clerio F Azevedo, *Rio de Janeiro*
Patrícia P Alfredo, *São Paulo*
Eduardo FC Fleury, *São Paulo*
Edward Araujo Júnior, *São Paulo*
Wellington P Martins, *Ribeirao Preto*
Ricardo A Mesquita, *Belo Horizonte*
Vera MC Salemi, *São Paulo*
Claudia Szobot, *Porto Alegre*
Lilian YI Yamaga, *São Paulo*



Canada

Marie Arsalidou, *Toronto*
Otman A Basir, *Waterloo*

Tarik Zine Belhocine, *Toronto*
James Chow, *Toronto*
Tae K Kim, *Toronto*
Anastasia Oikonomou, *Toronto*



China

Hong-Wei Chen, *Wuxi*
Feng Chen, *Hangzhou*
Jian-Ping Chu, *Guangzhou*
Guo-Guang Fan, *Shenyang*
Bu-Lang Gao, *Shijiazhuang*
Qi-Yong Gong, *Chengdu*
Ying Han, *Beijing*
Xian-Li Lv, *Beijing*
Yi-Zhuo Li, *Guangzhou*
Xiang-Xi Meng, *Harbin*
Yun Peng, *Beijing*
Jun Shen, *Guangzhou*
Ze-Zhou Song, *Hangzhou*
Wai Kwong Tang, *Hong Kong*
Gang-Hua Tang, *Guangzhou*
Jie Tian, *Beijing*
Lu-Hua Wang, *Beijing*
Xiao-bing Wang, *Xi'an*
Yi-Gen Wu, *Nanjing*
Kai Wu, *Guangzhou*
Hui-Xiong Xu, *Shanghai*
Zuo-Zhang Yang, *Kunming*
Xiao-Dan Ye, *Shanghai*
David T Yew, *Hong Kong*
Ting-He Yu, *Chongqing*
Zheng Yuan, *Shanghai*
Min-Ming Zhang, *Hangzhou*
Yudong Zhang, *Nanjing*
Dong Zhang, *Chongqing*
Wen-Bin Zeng, *Changsha*

Yue-Qi Zhu, *Shanghai*



Croatia

Goran Kusec, *Osijek*



Denmark

Poul E Andersen, *Odense*

Lars J Petersen, *Aalborg*

Thomas Z Ramsøy, *Frederiksberg*

Morten Ziebell, *Copenhagen*



Egypt

Mohamed F Bazeed, *Mansoura*

Mohamed Abou El-Ghar, *Mansoura*

Reem HA Mohamed, *Cairo*

Mohamed R Nouh, *Alexandria*

Ahmed AKA Razek, *Mansoura*

Ashraf A Zytoon, *Shebin El-Koom*



France

Sabine F Bensamoun, *Compiègne*

Romarc Loffroy, *Dijon*

Stephanie Nougaret, *Montpellier*

Hassane Oudadesse, *Rennes*

Vincent Vinh-Hung, *Fort-de-France*



Germany

Henryk Barthel, *Leipzig*

Peter Bannas, *Hamburg*

Martin Beeres, *Frankfurt*

Ilja F Ciernik, *Dessau*

A Dimitrakopoulou-Strauss, *Heidelberg*

Peter A Fasching, *Erlangen*

Andreas G Schreyer, *Regensburg*

Philipp Heusch, *Duesseldorf*

Sonja M Kirchhoff, *Munich*

Sebastian Ley, *Munich*

Adel Maataoui, *Frankfurt am Main*

Stephan M Meckel, *Freiburg*

Hans W Muller, *Duesseldorf*

Kay Raum, *Berlin*

Dirk Rades, *Luebeck*

Marc-Ulrich Regier, *Hamburg*

Alexey Surov, *Halle*

Martin Walter, *Magdeburg*

Axel Wetter, *Essen*

Christoph Zilkens, *Düsseldorf*



Greece

Panagiotis Antoniou, *Thessaloniki*

Nikos Efthimiou, *Athens*

Dimitris Karnabatidis, *Patras*

George Latsios, *Athens*

Stylianios Megremis, *Iraklion*

Alexander D Rapidis, *Athens*

Kiki Theodorou, *Larissa*

Ioannis A Tsalafoutas, *Athens*

Evanthia E Tripoliti, *Ioannina*

Athina C Tsili, *Ioannina*



India

Ritesh Agarwal, *Chandigarh*

Chandan J Das, *New Delhi*

Prathamesh V Joshi, *Mumbai*

Naveen Kalra, *Chandigarh*

Chandrasekharan Kesavadas, *Trivandrum*

Jyoti Kumar, *New Delhi*

Atin Kumar, *New Delhi*

Kaushala P Mishra, *Allahabad*

Daya N Sharma, *New Delhi*

Binit Sureka, *New Delhi*

Sanjay Sharma, *New Delhi*

Raja R Yadav, *Allahabad*



Iran

Majid Assadi, *Bushehr*

SeyedReza Najafizadeh, *Tehran*

Mohammad Ali Oghabian, *Tehran*

Amir Reza Radmard, *Tehran*

Ramin Sadeghi, *Mashhad*

Hadi Rokni Yazdi, *Tehran*



Ireland

Tadhg Gleeson, *Wexford*

Frederik JAI Vernimmen, *Cork*



Israel

Dafna Ben Bashat, *Tel Aviv*

Amit Gefen, *Tel Aviv*

Tamar Sella, *Jerusalem*



Italy

Adriano Alippi, *Rome*

Dante Amelio, *Trento*

Michele Anzidei, *Rome*

Filippo F Angileri, *Messinas*

Stefano Arcangeli, *Rome*

Roberto Azzoni, *San Donato milanese*

Tommaso V Bartolotta, *Palermo*

Tommaso Bartalena, *Imola*

Livia Bernardin, *San Bonifacio*

Federico Boschi, *Verona*

Sergio Casciaro, *Lecce*

Emanuele Casciani, *Rome*

Musa M Can, *Napoli*

Alberto Cuocolo, *Napoli*

Michele Ferrara, *Coppito*

Mauro Feola, *Fossano*

Giampiero Francica, *Castel Volturno*

Luigi De Gennaro, *Rome*

Giulio Giovannetti, *Pisa*

Francesca Iacobellis, *Napoli*

Formato Invernizzi, *Monza Brianza*

Francesco Lassandro, *Naples*

Lorenzo Livi, *Florence*

Pier P Mainenti, *Napoli*

Laura Marzetti, *Chieti*

Giuseppe Malinverni, *Crescentino*

Enrica Milanese, *Turin*

Giovanni Morana, *Treviso*

Lorenzo Monti, *Milan*

Silvia D Morbelli, *Genoa*

Barbara Palumbo, *Perugia*

Cecilia Parazzini, *Milan*

Stefano Pergolizzi, *Messina*

Antonio Pinto, *Naples*

Camillo Porcaro, *Rome*

Carlo C Quattrocchi, *Rome*

Alberto Rebonato, *Perugia*

Giuseppe Rizzo, *Rome*

Roberto De Rosa, *Naples*

Domenico Rubello, *Rovigo*

Andrea Salvati, *Bari*

Sergio Sartori, *Ferrara*

Luca M Sconfienza, *Milano*

Giovanni Storto, *Rionero*

Nicola Sverzellati, *Parma*

Alberto S Tagliafico, *Genova*

Nicola Troisi, *Florence*



Japan

Yasuhiko Hori, *Chiba*

Hidetoshi Ikeda, *Koriyama*

Masahito Kawabori, *Sapporo*

Tamotsu Kamishima, *Sapporo*

Hiro Kiyosue, *Yufu*

Yasunori Minami, *Osaka-sayama*

Yasuhiro Morimoto, *Kitakyushu*

Satoru Murata, *Tokyo*

Shigeki Nagamachi, *Miyazaki*

Hiroshi Onishi, *Yamanashi*

Morio Sato, *Wakayama Shi*

Yoshito Tsushima, *Maebashi*

Masahiro Yanagawa, *Suita*



Netherlands

Willem Jan van Rooij, *Tilburg*



New Zealand

W Howell Round, *Hamilton*



Pakistan

Wazir Muhammad, *Abbottabad*



Poland

Maciej S Baglaj, *Wroclaw*

Piotr Czauderna, *Gdansk*



Portugal

Joao Manuel RS Tavares, *Porto*



Serbia

Olivera Ciraj-Bjelac, *Belgrade*



Singapore

Gopinathan Anil, *Singapore*

Terence KB Teo, *Singapore*

Cher Heng Tan, *Singapore*



Slovakia

Stefan Sivak, *Martin*



South Korea

Ki Seok Choo, *Busan*

Seung Hong Choi, *Seoul*

Dae-Seob Choi, *Jinju*

Hong-Seok Jang, *Seoul*

Yong Jeong, *Daejeon*

Chan Kyo Kim, *Seoul*

Se Hyung Kim, *Seoul*

Joong-Seok Kim, *Seoul*

Sang Eun Kim, *Seongnam*

Sung Joon Kwon, *Seoul*

Jeong Min Lee, *Seoul*

In Sook Lee, *Busan*

Noh Park, *Goyang*

Chang Min Park, *Seoul*

Sung Bin Park, *Seoul*

Deuk Jae Sung, *Seoul*

Choongsoo Shin, *Seoul*

Kwon-Ha Yoon, *Iksan*



Spain

Miguel A De Gregorio, *Zaragoza*

Antonio Luna, *Jaén*

Enrique Marco de Lucas, *Santander*

Fernando Ruiz Santiago, *Granada*



Sweden

Dmitry Grishenkov, *Stockholm*

Tie-Qiang Li, *Stockholm*



Switzerland

Nicolau Beckmann, *Basel*

Christian Boy, *Bern*

Giorgio Treglia, *Bellinzona*

Stephan Ulmer, *Kiel*



Thailand

Sirianong Namwongprom, *Chiang Mai*



Turkey

Kubilay Aydin, *Istanbul*

Ramazan Akdemir, *Sakarya*

Serhat Avcu, *Ankara*

Ayşe Aralasmak, *Istanbul*

Oktay Algin, *Ankara*

Nevbahar Akcar, *Meselik*

Bilal Battal, *Ankara*

Zulkif Bozgeyik, *Elazig*

Nazan Ciledag, *Aakara*

Fuldem Y Donmez, *Ankara*

Gulgun Engin, *Istanbul*

Ahmet Y Goktay, *Izmir*

Oguzhan G Gumustas, *Bursa*

Kaan Gunduz, *Ankara*

Pelin Ozcan Kara, *Mersin*

Kivanc Kamburoglu, *Ankara*

Ozgur Kilickesmez, *Istanbul*

Furuzan Numan, *Istanbul*

Cem Onal, *Adana*

Ozgur Oztekin, *Izmir*

Seda Ozbek (Boruban), *Konya*

Selda Sarikaya, *Zonguldak*

Figen Taser, *Kutahya*

Baran Tokar, *Eskisehir*

Ender Uysal, *Istanbul*

Ensar Yekeler, *Istanbul*



United Kingdom

Indran Davagnanam, *London*

M DC Valdés Hernández, *Edinburgh*

Alan Jackson, *Manchester*

Suneil Jain, *Belfast*

Long R Jiao, *London*

Miltiadis Krokidis, *Cambridge*

Pradesh Kumar, *Liverpool*

Peter D Kuzmich, *Derby*

Georgios Plataniotis, *Brighton*

Vanessa Sluming, *Liverpool*



United States

Garima Agrawal, *Saint Louis*

James R Brasic, *Baltimore*

Rajendra D Badgaiyan, *Buffalo*

Ulas Bagci, *Bethesda*

Anat Biegon, *Stony Brook*

Ramon Casanova, *Winston Salem*

Wenli Cai, *Boston*

Zheng Chang, *Durham*

Corey J Chakarun, *Long Beach*

Kai Chen, *Los Angeles*

Hyun-Soon Chong, *Chicago*

Marco Cura, *Dallas*

Ravi R Desai, *Bensalem*

Delia DeBuc, *Miami*

Carlo N De Cecco, *Charleston*

Timm-Michael L Dickfeld, *Baltimore*

Subba R Digumarthy, *Boston*

Huy M Do, *Stanford*

Todd A Faasse, *Grand Rapids*

Salomao Faintuch, *Boston*

Girish M Fatterpekar, *New York*

Dhakshinamoorthy Ganesan, *Houston*

Robert J Griffin, *Little Rock*

Andrew J Gunn, *Boston*

Sandeep S Hedgire, *Boston*

Timothy J Hoffman, *Columbia*

Mai-Lan Ho, *San Francisco*

Juebin Huang, *Jackson*

Abid Irshad, *Charleston*

Matilde Inglese, *New York*

El-Sayed H Ibrahim, *Jacksonville*

Paul R Julsrud, *Rochester*

Pamela T Johnson, *Baltimore*

Ming-Hung Kao, *Tempe*

Sunil Krishnan, *Houston*

Richard A Komoroski, *Cincinnati*

Sandi A Kwee, *Honolulu*

King Kim, *Ft. Lauderdale*

Guozheng Liu, *Worcester*

Yiyan Liu, *Newark*

Venkatesh Mani, *New York*

Lian-Sheng Ma, *Pleasanton*

Rachna Madan, *Boston*

Zeyad A Metwalli, *Houston*

Yilong Ma, *Manhasset*

Hui Mao, *Atlanta*

Feroze B Mohamed, *Philadelphia*

Gul Moonis, *Boston*

John L Noshier, *New Brunswick*

Rahmi Oklu, *Boston*

Aytekun Oto, *Chicago*

Bishnuhari Paudyal, *Philadelphia*

Rajul Pandya, *Youngstown*

Chong-Xian Pan, *Sacramento*

Jay J Pillai, *Baltimore*

Neal Prakash, *Duarte*

Reza Rahbar, *Boston*

Ali S Raja, *Boston*

Gustavo J Rodriguez, *El Paso*

David J Sahn, *Portland*

Steven Schild, *Scottsdale*

Ali R Sepahdari, *Los Angeles*

Li Shen, *Indianapolis*

JP Sheehan, *Charlottesville*

Atul B Shinagare, *Boston*

Sarabjeet Singh, *Boston*

Charles J Smith, *Columbia*

Kenji Suzuki, *Chicago*

Monvadi Srichai-Parsia, *Washington*

Sree H Tirumani, *Boston*

Hebert A Vargas, *New York*

Sachit Verma, *Philadelphia*

Yoichi Watanabe, *Minneapolis*

Li Wang, *Chapel Hill*

Carol C Wu, *Boston*

Shoujun Xu, *Houston*

Min Yao, *Cleveland*

Xiaofeng Yang, *Atlanta*

Qingbao Yu, *Albuquerque*

Aifeng Zhang, *Chicago*

Chao Zhou, *Bethlehem*

Hongming Zhuang, *Philadelphia*

**ORIGINAL ARTICLE****Retrospective Study**

- 70 Accuracy of magnetic resonance cholangiography compared to operative endoscopy in detecting biliary stones, a single center experience and review of literature

Polistina FA, Frego M, Bisello M, Manzi E, Vardanega A, Perin B

- 79 100 classic papers of interventional radiology: A citation analysis

Crockett MT, Browne RFJ, MacMahon PJ, Lawler L

Contents

World Journal of Radiology
Volume 7 Number 4 April 28, 2015

ABOUT COVER

Editorial Board Member of *World Journal of Radiology*, Antonio Pinto, MD, PhD, Doctor, Department of Radiology, Cardarelli Hospital, I-80123 Naples, Italy

AIM AND SCOPE

World Journal of Radiology (*World J Radiol*, *WJR*, online ISSN 1949-8470, DOI: 10.4329) is a peer-reviewed open access academic journal that aims to guide clinical practice and improve diagnostic and therapeutic skills of clinicians.

WJR covers topics concerning diagnostic radiology, radiation oncology, radiologic physics, neuroradiology, nuclear radiology, pediatric radiology, vascular/interventional radiology, medical imaging achieved by various modalities and related methods analysis. The current columns of *WJR* include editorial, frontier, diagnostic advances, therapeutics advances, field of vision, mini-reviews, review, topic highlight, medical ethics, original articles, case report, clinical case conference (clinicopathological conference), and autobiography.

We encourage authors to submit their manuscripts to *WJR*. We will give priority to manuscripts that are supported by major national and international foundations and those that are of great basic and clinical significance.

INDEXING/ABSTRACTING

World Journal of Radiology is now indexed in PubMed Central, PubMed, Digital Object Identifier, and Directory of Open Access Journals.

FLYLEAF

I-III Editorial Board

EDITORS FOR THIS ISSUE

Responsible Assistant Editor: *Xiang Li*
Responsible Electronic Editor: *Xiao-Kang Jiao*
Proofing Editor-in-Chief: *Lian-Sheng Ma*

Responsible Science Editor: *Fang-Fang Ji*
Proofing Editorial Office Director: *Xiu-Xia Song*

NAME OF JOURNAL
World Journal of Radiology

ISSN
ISSN 1949-8470 (online)

LAUNCH DATE
December 31, 2009

FREQUENCY
Monthly

EDITORS-IN-CHIEF
Kai U Juergens, MD, Associate Professor, MRT und PET/CT, Nuklearmedizin Bremen Mitte, ZEMODI - Zentrum für morphologische und molekulare Diagnostik, Bremen 28177, Germany

Edwin JR van Beek, MD, PhD, Professor, Clinical Research Imaging Centre and Department of Medical Radiology, University of Edinburgh, Edinburgh EH16 4TJ, United Kingdom

Thomas J Vogl, MD, Professor, Reader in Health Technology Assessment, Department of Diagnostic and Interventional Radiology, Johann Wolfgang

Goethe University of Frankfurt, Frankfurt 60590, Germany

EDITORIAL OFFICE
Jin-Lei Wang, Director
Xiu-Xia Song, Vice Director
World Journal of Radiology
Room 903, Building D, Ocean International Center, No. 62 Dongsihuan Zhonglu, Chaoyang District, Beijing 100025, China
Telephone: +86-10-59080039
Fax: +86-10-85381893
E-mail: editorialoffice@wjnet.com
Help Desk: <http://www.wjnet.com/esps/helpdesk.aspx>
<http://www.wjnet.com>

PUBLISHER
Baishideng Publishing Group Inc
8226 Regency Drive,
Pleasanton, CA 94588, USA
Telephone: +1-925-223-8242
Fax: +1-925-223-8243
E-mail: bpgoffice@wjnet.com
Help Desk: <http://www.wjnet.com/esps/helpdesk.aspx>
<http://www.wjnet.com>

PUBLICATION DATE
April 28, 2015

COPYRIGHT
© 2015 Baishideng Publishing Group Inc. Articles published by this Open-Access journal are distributed under the terms of the Creative Commons Attribution Non-commercial License, which permits use, distribution, and reproduction in any medium, provided the original work is properly cited, the use is non commercial and is otherwise in compliance with the license.

SPECIAL STATEMENT
All articles published in journals owned by the Baishideng Publishing Group (BPG) represent the views and opinions of their authors, and not the views, opinions or policies of the BPG, except where otherwise explicitly indicated.

INSTRUCTIONS TO AUTHORS
Full instructions are available online at http://www.wjnet.com/1949-8470/g_info_20100316162358.htm.

ONLINE SUBMISSION
<http://www.wjnet.com/esps/>

Retrospective Study

Accuracy of magnetic resonance cholangiography compared to operative endoscopy in detecting biliary stones, a single center experience and review of literature

Francesco A Polistina, Mauro Frego, Marco Bisello, Emy Manzi, Antonella Vardanega, Bortolo Perin

Francesco A Polistina, Mauro Frego, Department of General Surgery, Suor Maria Teresa di Calcutta, Padova sud Hospital, 35043 Monselice, Italy

Marco Bisello, Department of General Surgery and Service of Endoscopy, Suor Maria Teresa di Calcutta, Padova sud Hospital, 35043 Monselice, Italy

Emy Manzi, School of Surgery, La Sapienza University, 00185 Rome, Italy

Antonella Vardanega, Bortolo Perin, Department of Radiology, Suor Maria Teresa di Calcutta, Padova sud Hospital, 35043 Monselice, Italy

Author contributions: Polistina FA designed the report, drafted and edited the manuscript; Vardanega A and Perin B revised radiologic imaging and drafted the manuscript; Bisello M and Manzi E revised EUS/ERCP procedures and selected articles for review from literature; Frego M performed the literature search discussed literature and edited the manuscript.

Ethics approval: The present article has been approved by the Suor M. T. di Calcutta, Padova sud Hospital Advisory board.

Informed consent: Since the present study is retrospective there was no specific written informed consent. However, all involved subjects gave their verbal consent to the use of their own data for research purposes given the anonymity guarantee for each one from the study designer.

Conflict-of-interest: All authors declare: no support from any organization for the submitted work; authors declare no conflict of interests nor other relationships or activities that could appear to have influenced the submitted work.

Data sharing: No data will be available on public repository for the present study.

Open-Access: This article is an open-access article which was selected by an in-house editor and fully peer-reviewed by external reviewers. It is distributed in accordance with the Creative Commons Attribution Non Commercial (CC BY-NC 4.0) license, which permits others to distribute, remix, adapt, build upon this work non-commercially, and license their derivative works on different terms, provided the original work is properly cited and the use is non-commercial. See: <http://creativecommons.org/licenses/by-nc/4.0/>

Correspondence to: Francesco A Polistina, MD, Department of General Surgery, Suor Maria Teresa di Calcutta, Padova sud Hospital, Via Albere 1, SP8, 35043 Monselice,

Italy. francescopolistina@hotmail.it

Telephone: +39-42-715883

Fax: +39-42-715886

Received: June 18, 2014

Peer-review started: June 19, 2014

First decision: July 10, 2014

Revised: February 17, 2015

Accepted: March 16, 2015

Article in press: March 18, 2015

Published online: April 28, 2015

Abstract

AIM: To compare diagnostic sensitivity, specificity and accuracy of magnetic resonance cholangiopancreatography (MRCP) without contrast medium and endoscopic ultrasound (EUS)/endoscopic retrograde cholangiopancreatography (ERCP) for biliary calculi.

METHODS: From January 2012 to December 2013, two-hundred-sixty-three patients underwent MRCP at our institution, all MRCP procedure were performed with the same machinery. In two-hundred MRCP was done for pure hepatobiliary symptoms and these patients are the subjects of this study. Among these two-hundred patients, one-hundred-eleven (55.5%) underwent ERCP after MRCP. The retrospective study design consisted in the systematic revision of all images from MRCP and EUS/ERCP performed by two radiologist with a long experience in biliary imaging, an experienced endoscopist and a senior consultant in Hepatobiliopancreatic surgery. A false positive was defined an MRCP showing calculi with no findings at EUS/ERCP; a true positive was defined as a concordance between MRCP and EUS/ERCP findings; a false negative was defined as the absence of images suggesting calculi at MRCP with calculi localization/extraction at EUS/ERCP and a true negative was defined as a patient with no

calculi at MRCP and at least 6 mo of asymptomatic follow-up. Biliary tree dilatation was defined as a common bile duct diameter larger than 6 mm in a patient who had an *in situ* gallbladder. A third blinded radiologist who examined the MRCP and ERCP data reviewed misdiagnosed cases. Once obtained overall data on sensitivity, specificity, accuracy, positive predictive value (PPV) and negative predictive value (NPV) we divided patients in two groups composed of those having concordant MRCP and EUS/ERCP (Group A, 72 patients) and those having discordant MRCP and EUS/ERCP (Group B, 20 patients). Dataset comparisons had been made by the Student's *t*-test and χ^2 when appropriate.

RESULTS: Two-hundred patients (91 men, 109 women, mean age 67.6 years, and range 25-98 years) underwent MRCP. All patients attended regular follow-up for at least 6 mo. Morbidity and mortality related to MRCP were null. MRCP was the only exam performed in 89 patients because it did show only calculi into the gallbladder with no signs of the presence of calculi into the bile duct and symptoms resolved within a few days or after colecistectomy. The patients remained asymptomatic for at least 6 mo, and we assumed they were true negatives. One hundred eleven (53 men, 58 women, mean age 69 years, range 25-98 years) underwent ERCP following MRCP. We did not find any difference between the two groups in terms of race, age, and sex. The overall median interval between MRCP and ERCP was 9 d. In detecting biliary stones MRCP Sensitivity was 77.4%, Specificity 100% and Accuracy 80.5% with a PPV of 100% and NPV of 85%; EUS showed 95% sensitivity, 100% specificity, 95.5% accuracy with 100% PPV and 57.1% NPV. The association of EUS with ERCP performed at 100% in all the evaluated parameters. When comparing the two groups, we did not find any statistically significant difference regarding age, sex, and race. Similarly, we did not find any differences regarding the number of extracted stones: 116 stones in Group A (median 2, range 1 to 9) and 27 in Group B (median 2, range 1 to 4). When we compared the size of the extracted stones we found that the patients in Group B had significantly smaller stones: 14.16 ± 8.11 mm in Group A and 5.15 ± 2.09 mm in Group B; 95% confidence interval = 5.89-12.13, standard error = 1.577; $P < 0.05$. We also found that in Group B there was a significantly higher incidence of stones smaller than 5 mm: 36 in Group A and 18 in Group B, $P < 0.05$.

CONCLUSION: Major finding of the present study is that choledocholithiasis is still under-diagnosed in MRCP. Smaller stones (< 5 mm diameter) are hardly visualized on MRCP.

Key words: Biliary strictures; Magnetic resonance cholangiopancreatography; Biliary stones; Endoscopic retrograde cholangiopancreatography; Endoscopic ultrasound;

© The Author(s) 2015. Published by Baishideng Publishing Group Inc. All rights reserved.

Core tip: The present paper is the report on a series of patients evaluated for biliary disease. Particularly the study is focused on performance of magnetic resonance cholangiopancreatography performance as the upfront examination tool for this group of diseases as compared to endoscopic ultrasounds and endoscopic retrograde cholangiopancreatography. Furthermore we did an extensive revision of the worldwide literature on the issue and discuss results of the review comparing them to our own.

Polistina FA, Frego M, Bisello M, Manzi E, Vardanega A, Perin B. Accuracy of magnetic resonance cholangiography compared to operative endoscopy in detecting biliary stones, a single center experience and review of literature. *World J Radiol* 2015; 7(4): 70-78 Available from: URL: <http://www.wjgnet.com/1949-8470/full/v7/i4/70.htm> DOI: <http://dx.doi.org/10.4329/wjrr.v7.i4.70>

INTRODUCTION

Despite continuing technological progress and the increasing availability of imaging tests, such as endoscopic ultrasound (EUS), computed tomography (CT), and magnetic resonance imaging (MRI), accurately detecting hepatobiliary and pancreatic diseases remains a challenge for clinicians and radiologists.

Magnetic resonance cholangiopancreatography (MRCP) is the most accurate, noninvasive imaging study for the hepatobiliary system^[1-3]. However, endoscopic retrograde cholangiopancreatography (ERCP) combined with EUS is the gold standard for evaluating hepatobiliary and pancreatic ducts morphology, moreover it allows many therapeutic interventions that carry a greater morbidity and mortality^[4-7].

The advantages of MRCP include the lack of invasiveness, ionizing radiation, and/or contrast media in the biliary and pancreatic ducts and general feasibility with no need for anesthesia. Furthermore, MRCP helps detect clinical relevant extrabiliary ductal diseases, which may also be responsible for a patient's symptoms^[3].

Several studies have compared MRCP and ERCP, and most suggested patients should be examined with ERCP without prior MRCP when laboratory values or other imaging studies strongly suggest an abnormal hepatobiliary process such as a stone, stricture, or obstruction^[8,9]. However, for patients who complain of right upper quadrant abdominal pain, without laboratory values or imaging studies that suggest an obstructive hepatobiliary or pancreatic process, many studies suggest using MRCP to determine whether ERCP is necessary in order to avoid useless morbidity^[1,2,11].

We retrospectively reviewed the medical records of patients evaluated for cholestasis and/or right upper quadrant abdominal pain without imaging studies that suggested overt biliary obstruction. We assumed ERCP

was the gold standard (100% sensitivity and specificity in the hands of an experienced provider). We studied MRCP for sensitivity, specificity, positive predictive value (PPV), and negative predictive value (NPV) in diagnosing choledocholithiasis and stricture of the hepatobiliary system.

The aim of the study was to obtain data for MRCP and EUS/ERCP related to outcome in patients evaluated for cholestasis and/or right upper quadrant abdominal pain without images indicating biliary obstruction.

MATERIALS AND METHODS

From January 2012 to December 2013, two-hundred-sixty-three patients underwent MRCP at our institution. In two-hundred MRCP was done for pure hepatobiliary symptoms and these patients are the subjects of this study. Among these two-hundred patients, one-hundred-eleven (55.5%) underwent ERCP after MRCP. All MRCP images were retrospectively reviewed from three experienced radiologists in the field of hepatobiliary diseases. EUS/ERCP procedures were all conducted by experienced endoscopist. Data from both MRCP and EUS/ERCP were finally reviewed and compared by the radiologists, the endoscopist and an experienced hepatobiliary surgeon. We retrospectively reviewed all clinical records and images of these latter patients. Bile duct dilatation was defined as choledocus larger than 6 mm in a patient whose gallbladder was *in situ*. Gamma glutamyl transpeptidase was considered changed at a twofold normal value (0-31 mg/dL).

Patient consent for processing of personal data was acquired according to our institution's protocol.

MRCP procedures

All scans were performed on a 1.5 Tesla Magnetic Resonance (Intera 1.5 T Pulsar; Philips, Amsterdam, the Netherlands) according to our institutional standardized MRCP protocol. All patients were examined in the supine position. A channel-phased array body coil was used. Before the scan, pineapple juice, a negative oral contrast agent, was taken orally by all patients^[12]. The scans were performed as follows: The first scan was T2/TSE/HR: TR 3024, TE 115 Flip Angle 90° slices thickness 7 mm. The second scan was T1/Proset GR FFE: TR 230, TE4.6 Flip Angle 85° slices thickness 7 mm. The third scan was MRCP/3D/HR triggered: TR1800, TE650 Flip Angle 90° slices thickness 1 mm. The fourth scan was MRCP/MS breath hold: TR8000, TE800, Flip Angle 90° slice thickness 40 mm with MIP retro-reconstruction. No drug administration or contrast medium was required.

ERCP procedures

The indications for ERCP were persistent cholestasis and right upper quadrant abdominal pain, with a positive MRCP for stones or stricture, independent of bile duct dilatation. Written informed consent was obtained from all patients before the procedures were performed.

Combined EUS and ERCP were performed under sedation using intravenous Propofol and Ramifentanyl. EUS was performed with a radial echoendoscope (GF-UE 160; Olympus Medical Systems Co., Tokyo, Japan). Subsequent ERCP-related procedures were performed following EUS during the same session using a duodenoscope (JF-Q-180W; Olympus Medical Systems Co.). Papillotomies were performed with either a Cook-DASH-1 or a Cook DASH-21 Papillotome (Cook Medical, Limerick, Ireland). Biliary cannulation was done using a guide wire (Cook MET-35-480 coupled to the Dash-1 Papillotome and Cook MET II21-480 coupled to the DASH-21 Papillotome; Cook Medical). Calculi were extracted with either a Dormia Basket (Memory Soft Wire Basket: MSB 1.5 × 3.5 G22136; MSB 2.5 × 5 G22019; MSB 2 × 4 G21525; MSB 3 × 6 - 6 G 21913 (six wires); MSB 2 × 4 - 6 G21544 (six wires); Cook Medical) or an extraction balloon (Cook TXR-8.5-12-15-A; Cook Medical).

Data re-evaluation

All MRCP and ERCP images were retrospectively reviewed by two radiologists who had experience in hepatobiliary diseases. Previous reports were re-examined paying attention to choledocholithiasis, strictures, extra luminal compressions, and dilatation. Hepatobiliary and pancreatic tree obstruction was defined as any obstruction in the system secondary to a mass, stone, or stricture. Biliary tree dilatation was defined as a common bile duct diameter larger than 6 mm in a patient who had an *in situ* gallbladder. A third blinded radiologist who examined the MRCP and ERCP data reviewed misdiagnosed cases.

Statistical analysis

Dataset comparisons had been made by the Student's *t*-test and chi-square when appropriate. An independent biostatistician reviewed the whole dataset and approved it.

All the data were blinded reviewed by an independent biostatistician.

RESULTS

From January 2012 to December 2013, we evaluated 263 patients with confirmed colelithiasis and symptoms suggesting the presence of stones in the biliary tract. Table 1 shows the criteria we used for first evaluation of patient to be addressed towards further examination. Patients showing a low risk were addressed to MRCP, patients showing high risk were addressed to upfront EUS/ERCP. Moreover, patients showing signs of cancer at ultrasound (US) and/or CT scan were excluded from the study. Two-hundred patients (91 men, 109 women, mean age 67.6 years, and range 25-98 years) underwent MRCP. All patients attended regular follow-up for at least 6 mo. Morbidity and mortality related to MRCP were null. MRCP was the only exam performed

Table 1 Criteria for stratifying risk for choledocholithiasis

Age > 55 yr
Evidence/suspicion of calculi at US
Cholelith larger than 6 mm at US (in patients having gallbladder)
Conjugated bilirubin higher than 51 micromoles/L
Persistence of cholestasis 72 h after the acute episode
All criteria present: Biliary tree lithiasis probability > 90%
All but one criteria: Biliary tree lithiasis probability about 20%

US: Ultrasound.

Table 2 General features of magnetic resonance cholangiopancreatography performance on biliary stones detection

	ERCP+	ERCP-	
MRCP+	102	0	PPV 100%
MRCP-	8	90	NPV 91.8 %
	Sensitivity 92.7%	Specificity 100%	Accuracy 96%

MRCP: Magnetic resonance cholangiopancreatography; ERCP: Endoscopic retrograde cholangiopancreatography; PPV: Positive predictive value; NPV: Negative predictive value.

in 89 patients because it did show only calculi into the gallbladder with no signs of the presence of calculi into the bile duct and symptoms resolved within a few days or after colecistectomy. The patients remained asymptomatic for at least 6 mo, and we assumed they were true negatives.

Seventy-two patients with calculi into the biliary tree diagnosed at MRCP (Figures 1, 2 and 3) were scheduled to receive EUS/ERCP within no more than 1 wk as well as patients who showed persistence or recurrence of symptoms even with a negative MRCP scan. Furthermore, patients who showed recurrence of symptoms at some point during follow-up were also provided EUS/MRC even if they had an MRCP scan reported as non-diagnostic exam. One hundred eleven (53 men, 58 women, mean age 69 years, range 25-98 years) underwent ERCP following MRCP. We did not find any difference between the two groups in terms of race, age, and sex. The overall median interval between MRCP and ERCP was 9 d.

One hundred eight patients (97.3%) underwent a therapeutic intervention during ERCP such as stone/sludge extraction, stricture dilatation, or papillotomy. The median number of extracted stones was 2.6 (mean 2.4, range 1-12). The extracted stones had a median diameter of 7.8 mm (mean 8.1, range 2-36). ERCP-related complications included 3 acute cases of pancreatitis, in 1 case severe requiring surgical debridement; 1 duodenal microperforation resolved conservatively within 1 wk, and 4 patients bled from the papillotomy that in 2 cases required endoscopic hemostasis. Perioperative mortality was 0.9% (1 patient died of myocardial infarction during the procedure).

MRCP diagnosis of biliary stone was correct in 72

patients confirmed and removed with EUS/ERCP with 100% concordance between the two methods, no false positives were reported at MRCP.

In 21 cases, MRCP did not show the presence of calculi. In 9 of these cases, radiologic diagnosis was biliary stricture (Figure 4), in 2 cases MRCP was negative, and in 10 cases only microlithiasis of the gallbladder was diagnosed. All 21 patients underwent EUS/ERCP, in 9 cases due to the MRCP diagnosis of biliary stricture (Figure 5), in 3 cases for persistent cholestasis, and in the latter 9 for recurrence of symptoms during follow-up. Among these cases, 16 were found at EUS to have biliary microstones or sludge that was removed by ERCP during the same procedure, in 6 cases EUS did not show stones but after papillotomy and choledochus exploration microcalculi or sludge were extracted. In 1 case, even EUS and ERCP did not show any significant biliary disease, and the patient was diagnosed with sclerosing cholangitis. In 2 cases, the ERCP confirmed the associated presence of a choledochal stenosis. At this point, we divided patients into two groups. The first group (Group A) consisted of 72 patients who had concordant MRCP and EUS/ERCP (44 women and 28 men, median age 67 years, range 29-81); the second group consisted of 20 patients who had discordant MRCP and EUS/ERCP (14 women and 7 men, median age 59 years, range 25-98).

When we compared the two groups, we did not find any statistically significant difference regarding age, sex, and race. Similarly, we did not find any differences regarding the number of extracted stones: 116 stones in Group A (median 2, range 1 to 9) and 27 in Group B (median 2, range 1 to 4). When we compared the size of the extracted stones we found that the patients in Group B had significantly smaller stones: 14.16 ± 8.11 mm in Group A and 5.15 ± 2.09 mm in Group B; 95% confidence interval = 5.89-12.13, standard error = 1.577; $P < 0.05$. We also found that in Group B there was a significantly higher incidence of stones smaller than 5 mm: 36 in Group A and 18 in Group B, $P < 0.05$. MRCP also diagnosed 35 biliary strictures, 9 of which on EUS/ERCP were revealed to be microstones; therefore, we correctly diagnosed 26 biliary strictures on MRCP, and conversely, all the ERCP confirmed biliary stenoses were previously correctly defined by MRCP. In detecting biliary stones MRCP Sensitivity was 77.4%, Specificity 100% and Accuracy 80.5% with a PPV of 100% and NPV of 85%; EUS showed 95% sensitivity, 100% specificity, 95.5% accuracy with 100% PPV and 57.1% NPV. The association of EUS with ERCP performed at 100% in all the evaluated parameters.

Table 2 shows the general data on MRCP performance, and Table 3 gives details on MRCP features for biliary strictures and stones. On the subsequent blinded review performed on the false-negative patients, in only 3 of the 9 cases with previous diagnosis of stenosis, reviewers suspected the presence of microcalculi but without unanimity in each case.

Table 3 Performance of magnetic resonance cholangiopancreatography on most common biliary diseases

Diagnosis	Sensitivity	Specificity	Accuracy	PPV	NPV
Choledocholithiasis	77.40%	100%	80.50%	100%	85%
Hepatobiliary/pancreatic stricture	100%	95%	57.50%	79%	100%

PPV: Positive predictive value; NPV: Negative predictive value.

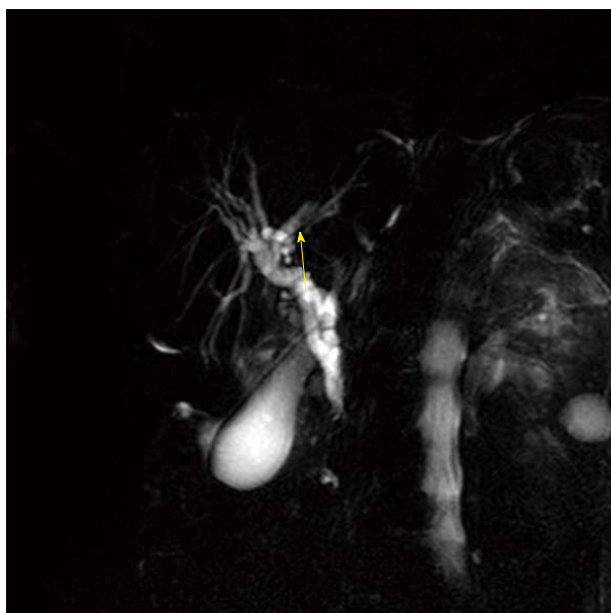


Figure 1 Little stones in left branch of biliary tree (arrow).

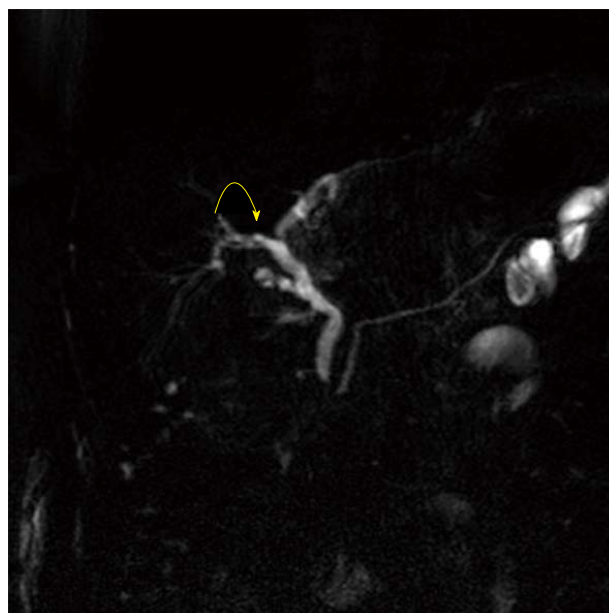


Figure 3 (Same patient of Figure 2) next image shows the fake stone as biliary branches crossing (curved arrow).

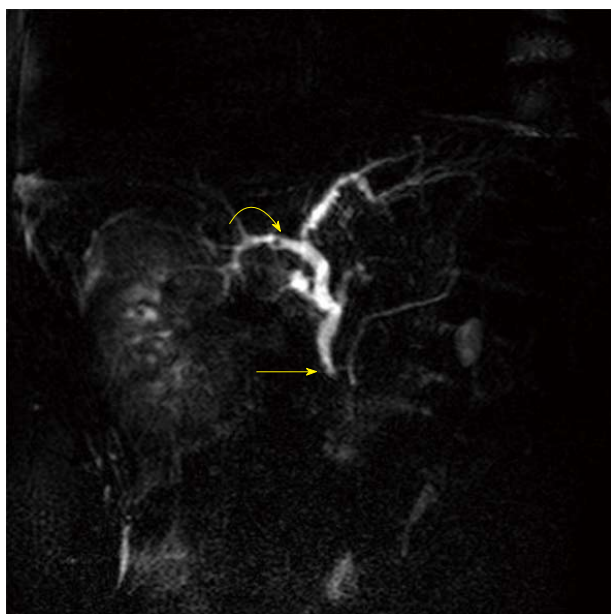


Figure 2 Pre-papillary micro stones (arrow) fake stone in right branch of biliary tree (curved arrow).

DISCUSSION

Various types of lesions can cause biliary obstruction; the most frequent are calculi. MRCP is an abdominal MR imaging method that allows noninvasive visualization

of the intra- and extrahepatic tree and requires no contrast administration. Recent studies reported that administration of gadoxetic disodium acid or gadobenate dimeglumine improves the sensitivity and specificity of the tool^[13,14]. A more recent paper from Choi and Colleagues showed no difference in performance of MRCP with or without contrast medium in detecting biliary stones^[15]. Gadoxetic disodium acid (Primovist, Schering Co., Berlin, Germany) and gadobenate dimeglumine (MultiHance, Bracco, Milan, Italy) are both hepatocyte-selective T1-weighted MR agents that are administered intravenously and excreted primarily through the biliary system thus allowing the direct visualization of the biliary tree. Visualization starts after 20 to 100 min following injection, depending on the agent, and lasts for 1-2 h. Use of these contrast agents should provide anatomic information and functional data and should have detected the misdiagnosed stones in our series. We investigated patients with T2-weighted TSE scans that assessed the main sign of biliary tree obstruction: dilatation of extrahepatic or intrahepatic bile ducts. We found that the thin slices provided by this TSE technique may display ductal filling defects as areas of signal void surrounded by bright bile; they provide an optimal contrast between the hyperintense signal of the bile and the hypointense signal of the pathology. The secondary imaging signs of suspected

Table 4 Previous studies data on magnetic resonance cholangiopancreatography as compared to the present study

Ref.	Sensitivity (%)	Specificity (%)	Accuracy (%)	PPV (%)	NPV (%)	Cohort numerosity
De Waele <i>et al</i> ^[17]	82.6	97.5	94.2	90.5	95.2	104 pts
Shanmugam <i>et al</i> ^[18]	97.98	84.4				374 pts
Moon <i>et al</i> ^[19]	80					32 pts
Kondo <i>et al</i> ^[20]	88					28 pts
Norero <i>et al</i> ^[21]	97	74	90	89	90	125 pts
Scaffidi <i>et al</i> ^[22]	88	72	83	87	72	140 pts
Rahaman <i>et al</i> ^[23]	84.5	87.4				165 pts
Li <i>et al</i> ^[24]	64.09	80	66.27	95.27	26.17	255 pts
	80.41 ¹	79.41 ¹	69.23 ¹	94.44 ¹	48.21 ¹	
Bilgin <i>et al</i> ^[13]	82.3	96	91.7			108 pts
Present study	100	95	57.5	100	85	200 pts

¹Microstones. PPV: Positive predictive value; NPV: Negative predictive value.

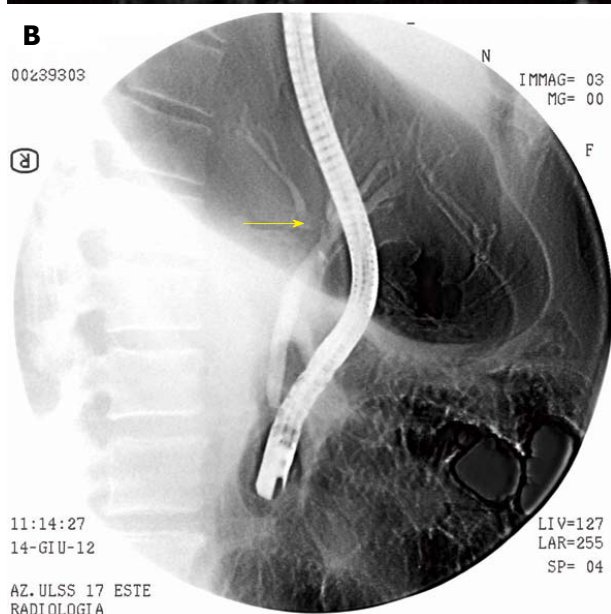
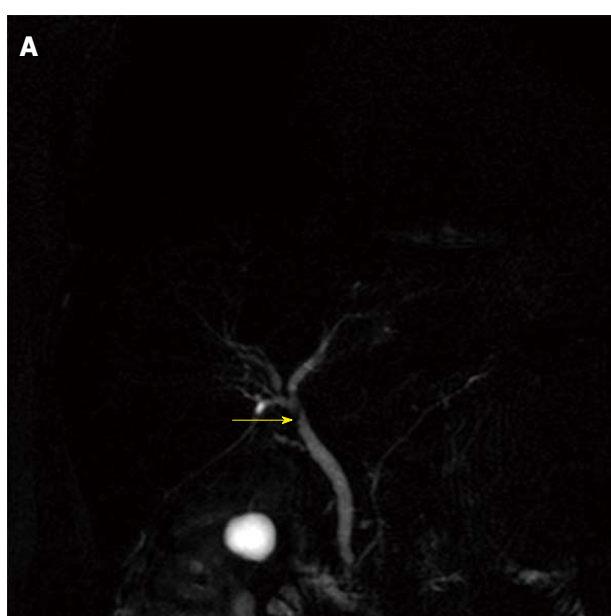


Figure 4 Stricture or stones (arrow) at origin of common bile duct (A) and stricture (arrow) confirmed at endoscopic retrograde cholangiopancreatography but the balloon-catheter pulled out micro stones and no stricture was confirmed at control (B).

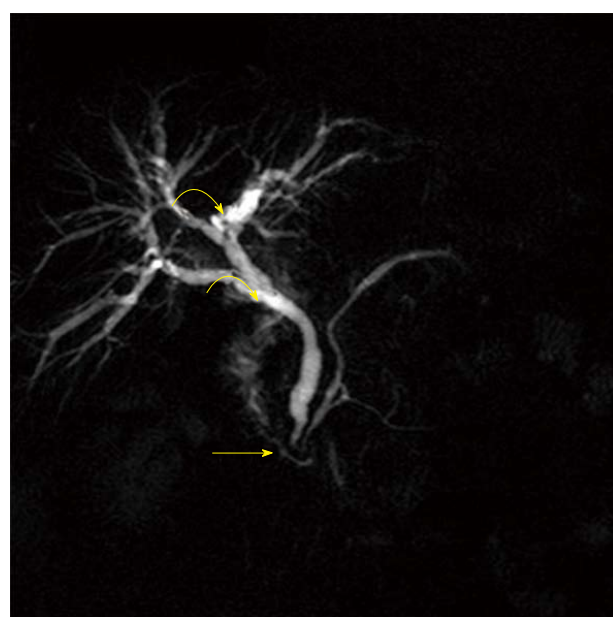


Figure 5 Pre-papillary stricture (arrow) microstones in right and left branch (curved arrows, confirmed at endoscopic retrograde cholangiopancreatography).

obstruction include hypointense signal defects caused by gallstones or irregularly shaped defects of contours or border in the biliary tree^[16]. In our series, stone size was the primary factor that determined efficacy of MRI scans. The hugest limitation of this MRCP technique in detecting lithiasis is that the slices are thicker than 5 mm and this requires partial volume averaging in T2 and T1 series. This can lead to false-negative results when stones are smaller than 5 mm in diameter. The best stone detection was due to the 3D series, in most reviewed cases.

Our data do not differ significantly from those reported in literature^[17-24] (Table 4). In detail, we found MRCP had slightly higher sensitivity and PPV than other reported series and slightly lower accuracy in diagnosing biliary calculi when the calculi were smaller than 5 mm (Figure 6). We believe that this may at least partially depend upon the decision not to use a biliary specific contrast. All but one of the missed calculi were smaller

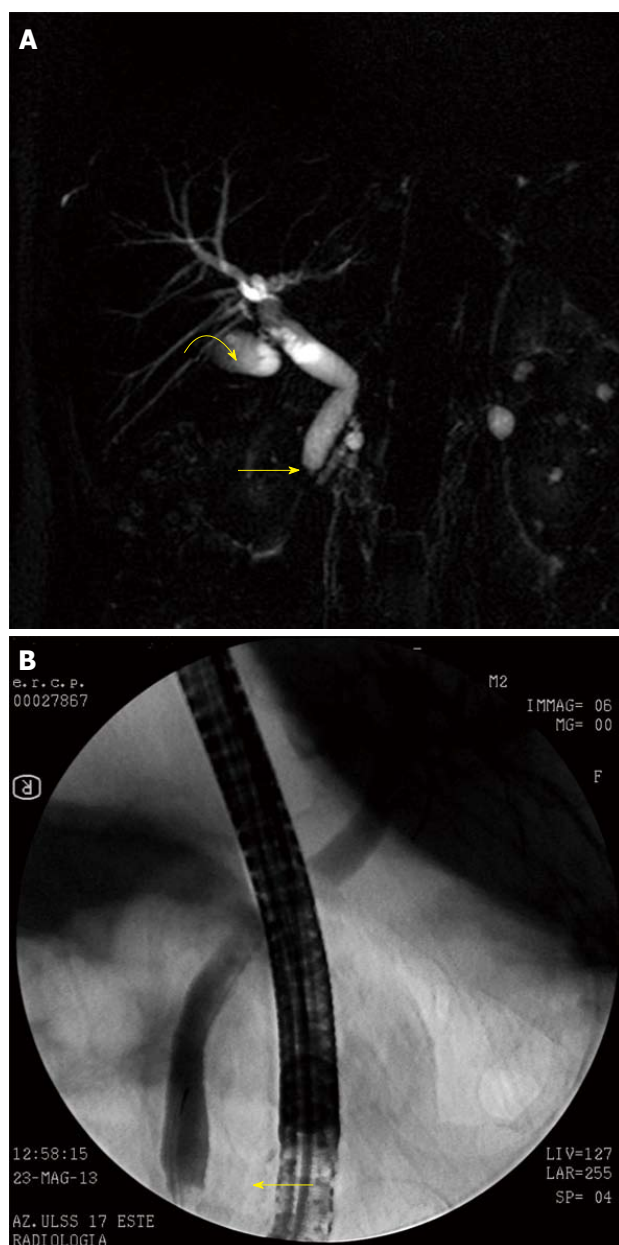


Figure 6 Micro stones in gallbladder (curved arrow), pre-papillary stenosis (arrow) (A) and endoscopic retrograde cholangiopancreatography shows pre-papillary stone (arrow), not the micro stones that were pulled out by balloon-catheter (B).

than 5 mm, and the high incidence of microstones or sludge is a well-recognized factor that negatively influences the overall MRCP performance independently from the use of contrast medium^[11-16,23-25]. The 10 patients diagnosed with microlithiasis of the gallbladder were scheduled for elective surgery; all underwent EUS/ERCP for recurrence of cholestasis or pain. Because some EUS/ERCP was performed with a median interval of 12 d after MRCP, theoretically we cannot exclude that some were true negative at magnetic resonance and developed symptoms of deferred migration of microcalculi. These patients had initially normal blood tests; therefore, the decision not to perform an EUS/

ERCP was correct according to reports from Sakai *et al.*^[24].

The high incidence of microcalculi is responsible for the high incidence of false negatives in our stone disease group. Even in the 10 cases in which we found microcalculi in the gallbladder but not in the choledocus, we can only hypothesize, based on the clinical evolution of the patients, that they could have migrated in the delay time. However, even when these patients showed symptoms, either cholestasis or pain, 4 remained negative on the EUS/ERCP, and choledocholithiasis was diagnosed only at sphincterotomy and balloon extraction. These data have been reported by other series^[25,26].

Our study confirmed that choledocholithiasis continues to be underdiagnosed on MRCP mostly for patients with stones smaller than 5 mm. Nonetheless, MRCP remains the most reliable exam for discriminating which patients to address for more invasive tests (EUS/ERCP) with high sensitivity and specificity. Even if the use of biliary specific contrast is reported to enhance sensitivity, specificity, and NPV^[2,23,27,28], this agent may carry additional morbidity related to the administration of contrast that, in our opinion, is not completely balanced by the increase in performance. Our data show that MRCP without contrast medium is a highly sensitive tool for biliary disease; it even has slightly lower specificity. In our series, most stone misdiagnoses were related to calculi smaller than 5 mm or strictures due to concurrent edema in subclinical cholangitis.

MRCP without intravenous contrast is a highly sensitive tool for diagnosing common bile duct stones larger than 5 mm and biliary strictures. This imaging carries a null morbidity. For stones smaller than 5 mm, sensitivity may decrease, but in our opinion, this potential weakness may be corrected with careful clinical follow-up and avoid many useless ERCPs and related morbidity.

COMMENTS

Background

The present paper presents a single centre experience comparing accuracy, efficacy and safety of magnetic resonance cholangiopancreatography with endoscopic ultrasounds and/or endoscopic retrograde cholangiopancreatography (ERCP). Data on findings are presented with regards to the presence/absence of biliary tree dilation and size of extracted stones.

Research frontiers

Biliary obstruction diagnosis and treatment.

Innovations and breakthroughs

This paper focuses on the small stone disease outlining that even a close follow up may rule diagnosis thus avoiding an excessive use of ERCP.

Applications

May be of some help in clinical decision making.

Terminology

MRCP: Magnetic resonance cholangiopancreatography; EUS: Endoscopic ultrasonography; ERCP: Endoscopic retrograde cholangiopancreatography.

Peer-review

Nicely written article.

REFERENCES

- Rahman R**, Ju J, Shamma's J, Goebel S, Sundaram U. Correlation between MRCP and ERCP findings at a tertiary care hospital. *W J Med J* 2010; **106**: 14-19 [PMID: 21739880]
- Chang JH**, Lee IS, Lim YS, Jung SH, Paik CN, Kim HK, Kim TH, Kim CW, Han SW, Choi MG, Jung IS. Role of magnetic resonance cholangiopancreatography for choledocholithiasis: analysis of patients with negative MRCP. *Scand J Gastroenterol* 2012; **47**: 217-224 [PMID: 22149906 DOI: 10.3109/00365521.2011.638394]
- Sohns JM**, Staab W, Dabir D, Spiro JE, Bergau L, Schwarz A, Sohns C. Current role and future potential of magnetic resonance cholangiopancreatography with an emphasis on incidental findings. *Clin Imaging* 2014; **38**: 35-41 [PMID: 24120879 DOI: 10.1016/j.clinimag.2013.08.015]
- Salminen P**, Laine S, Gullichsen R. Severe and fatal complications after ERCP: analysis of 2555 procedures in a single experienced center. *Surg Endosc* 2008; **22**: 1965-1970 [PMID: 18095023 DOI: 10.1007/s00464-007-9711-0]
- Zuber-Jerger I**, Endlicher E, Kullmann F, Gelbmann CM. A new grading system to evaluate the risk of endoscopic retrograde cholangiopancreatography. *J Gastroenterol* 2009; **44**: 160-165 [PMID: 19214679 DOI: 10.1007/s00535-008-2295-1]
- Navaneethan U**, Konjeti R, Venkatesh PG, Sanaka MR, Parsi MA. Early precut sphincterotomy and the risk of endoscopic retrograde cholangiopancreatography related complications: An updated meta-analysis. *World J Gastrointest Endosc* 2014; **6**: 200-208 [PMID: 24891933 DOI: 10.4253/wjge.v6.i5.200]
- Glomsaker T**, Hoff G, Kvaløy JT, Søreide K, Aabakken L, Søreide JA. Patterns and predictive factors of complications after endoscopic retrograde cholangiopancreatography. *Br J Surg* 2013; **100**: 373-380 [PMID: 23225493 DOI: 10.1002/bjs.8992]
- Wilcox CM**, Kim H, Trevino J, Ramesh J, Monkemuller K, Varadarajulu S. Prevalence of normal liver tests in patients with choledocholithiasis undergoing endoscopic retrograde cholangiopancreatography. *Digestion* 2014; **89**: 232-238 [PMID: 24903214 DOI: 10.1159/000358384]
- Hu KC**, Wang HY, Chang WH, Chu CH, Lin SC, Liu CJ, Wu MS, Shih SC. Clinical presentations of patients from different age cohorts with biliary tract stone diseases. *J Gastroenterol Hepatol* 2014; **29**: 1614-1619 [PMID: 24628028 DOI: 10.1111/jgh.12581]
- Richard F**, Boustany M, Britt LD. Accuracy of magnetic resonance cholangiopancreatography for diagnosing stones in the common bile duct in patients with abnormal intraoperative cholangiograms. *Am J Surg* 2013; **205**: 371-373 [PMID: 23518180 DOI: 10.1016/j.amjsurg.2012.07.033]
- Maccioni F**, Martinelli M, Al Ansari N, Kagarmanova A, De Marco V, Zippi M, Marini M. Magnetic resonance cholangiography: past, present and future: a review. *Eur Rev Med Pharmacol Sci* 2010; **14**: 721-725 [PMID: 20707292]
- Coppens E**, Metens T, Winant C, Matos C. Pineapple juice labeled with gadolinium: a convenient oral contrast for magnetic resonance cholangiopancreatography. *Eur Radiol* 2005; **15**: 2122-2129 [PMID: 15999215 DOI: 10.1007/s00330-005-2835-5]
- Bilgin M**, Toprak H, Burgazli M, Bilgin SS, Chasan R, Erdogan A, Balci C. Diagnostic value of dynamic contrast-enhanced magnetic resonance imaging in the evaluation of the biliary obstruction. *ScientificWorldJournal* 2012; **2012**: 731089 [PMID: 22489200]
- Reiner CS**, Merkle EM, Bashir MR, Walle NL, Nazeer HK, Gupta RT. MRI assessment of biliary ductal obstruction: is there added value of T1-weighted gadolinium-ethoxybenzyl-diethylenetriamine pentaacetic acid-enhanced MR cholangiography? *AJR Am J Roentgenol* 2013; **201**: W49-W56 [PMID: 23789696 DOI: 10.2214/AJR.12.9332]
- Choi IY**, Yeom SK, Cha SH, Lee SH, Chung HH, Hyun JJ, Kim BH. Diagnosis of biliary stone disease: T1-weighted magnetic resonance cholangiography with Gd-EOB-DTPA versus T2-weighted magnetic resonance cholangiography. *Clin Imaging* 2014; **38**: 164-169 [PMID: 24359645 DOI: 10.1016/j.clinimag.2013.11.001]
- Parnaby CN**, Jenkins JT, Ferguson JC, Williamson BW. Prospective validation study of an algorithm for triage to MRCP or ERCP for investigation of suspected pancreatico-biliary disease. *Surg Endosc* 2008; **22**: 1165-1172 [PMID: 18288530 DOI: 10.1007/s00464-008-9775-5]
- De Waele E**, Op de Beeck B, De Waele B, Delvaux G. Magnetic resonance cholangiopancreatography in the preoperative assessment of patients with biliary pancreatitis. *Pancreatology* 2007; **7**: 347-351 [PMID: 17703081 DOI: 10.1159/000107269]
- Shanmugam V**, Beattie GC, Yule SR, Reid W, Loudon MA. Is magnetic resonance cholangiopancreatography the new gold standard in biliary imaging? *Br J Radiol* 2005; **78**: 888-893 [PMID: 16177010 DOI: 10.1259/bjr/51075444]
- Moon JH**, Cho YD, Cha SW, Cheon YK, Ahn HC, Kim YS, Kim YS, Lee JS, Lee MS, Lee HK, Shim CS, Kim BS. The detection of bile duct stones in suspected biliary pancreatitis: comparison of MRCP, ERCP, and intraductal US. *Am J Gastroenterol* 2005; **100**: 1051-1057 [PMID: 15842578 DOI: 10.1111/j.1572-0241.2005.41057.x]
- Kondo S**, Isayama H, Akahane M, Toda N, Sasahira N, Nakai Y, Yamamoto N, Hirano K, Komatsu Y, Tada M, Yoshida H, Kawabe T, Ohtomo K, Omata M. Detection of common bile duct stones: comparison between endoscopic ultrasonography, magnetic resonance cholangiography, and helical-computed-tomographic cholangiography. *Eur J Radiol* 2005; **54**: 271-275 [PMID: 15837409 DOI: 10.1016/j.ejrad.2004.07.007]
- Norero E**, Norero B, Huete A, Pimentel F, Cruz F, Ibáñez L, Martínez J, Jarufe N. [Accuracy of magnetic resonance cholangiopancreatography for the diagnosis of common bile duct stones]. *Rev Med Chil* 2008; **136**: 600-605 [PMID: 18769807 DOI: 10.4067/S0034-98872008000500008]
- Scaffidi MG**, Luigiano C, Consolo P, Pellicano R, Giacobbe G, Gaeta M, Blandino A, Familiari L. Magnetic resonance cholangiopancreatography versus endoscopic retrograde cholangiopancreatography in the diagnosis of common bile duct stones: a prospective comparative study. *Minerva Med* 2009; **100**: 341-348 [PMID: 19910887]
- Li P**, Zhang Z, Li J, Jin L, Han W, Zhang J. Diagnostic value of magnetic resonance cholangiopancreatography for secondary common bile duct stones compared with laparoscopic trans-cystic common bile duct exploration. *Med Sci Monit* 2014; **20**: 920-926 [PMID: 24894946 DOI: 10.12659/MSM.890831]
- Sakai Y**, Tsuyuguchi T, Yukisawa S, Tsuchiya S, Sugiyama H, Miyakawa K, Ohara T, Ebara M, Miyazaki M, Yokosuka O. Diagnostic value of magnetic resonance cholangiopancreatography for clinically suspicious spontaneous passage of bile duct stones. *J Gastroenterol Hepatol* 2008; **23**: 736-740 [PMID: 18070008 DOI: 10.1111/j.1440-1746.2007.05252.x]
- Tofigh AM**, Razmjoe F, Khabbaz A, Ayazi K, Farahmand S, Honar BN, Nikshoar MR. Comparing the efficacy of preoperative magnetic resonance cholangiopancreatography with intraoperative cholangiography in patients suspicious to biliary stones. *Gastroenterol Hepatol Bed Bench* 2013; **6**: 80-85 [PMID: 24834249]
- Kawakubo K**, Kawakami H, Kuwatani M, Haba S, Kudo T, Abe Y, Kawahata S, Onodera M, Ehira N, Yamato H, Eto K, Sakamoto N. Safety and utility of single-session endoscopic ultrasonography and endoscopic retrograde cholangiopancreatography for the evaluation of pancreaticobiliary diseases. *Gut Liver* 2014; **8**: 329-332 [PMID: 24827632 DOI: 10.5009/gnl.2014.8.3.329]
- Fernández-Esparrach G**, Ginès A, Sánchez M, Pagés M, Pellisé M, Fernández-Cruz L, López-Boado MA, Quintó L, Navarro S, Sendino O, Cárdenas A, Ayuso C, Bordas JM, Llach J, Castells A. Comparison of endoscopic ultrasonography and magnetic resonance cholangiopancreatography in the diagnosis of pancreaticobiliary diseases: a prospective study. *Am J Gastroenterol* 2007; **102**: 1632-1639 [PMID: 17521400 DOI: 10.1111/j.1572-0241.2007.01333.x]
- Hossary SH**, Zytoon AA, Eid M, Hamed A, Sharaan M,

Ebrahim AA. MR cholangiopancreatography of the pancreas and biliary system: a review of the current applications. *Curr Probl*

Diagn Radiol 2014; **43**: 1-13 [PMID: 24290199 DOI: 10.1067/j.cpradiol.2013.10.001]

P- Reviewer: Gatselis NK, Losanoff JE, Maroni L **S- Editor:** Ji FF
L- Editor: A **E- Editor:** Jiao XK



Retrospective Study

100 classic papers of interventional radiology: A citation analysis

Matthew T Crockett, Ronan FJ Browne, Peter J MacMahon, Leo Lawler

Matthew T Crockett, Peter J MacMahon, Leo Lawler, Department of Radiology, Mater Misericordiae University Hospital, Dublin 7, Ireland

Ronan FJ Browne, Department of Radiology, Adelaide and Meath Hospital, Dublin 24, Ireland

Author contributions: Crockett MT designed study, acquired data and wrote up the manuscript; Browne RFJ and Lawler L designed study and assisted with write up and editing; MacMahon PJ assisted with write up and editing.

Ethics approval: Due to the nature of this study no ethical approval or institutional board review was required.

Informed consent: Due to the nature of this study no informed consent was required.

Conflict-of-interest: The authors declare no conflict of interest.

Data sharing: Not applicable for this study.

Open-Access: This article is an open-access article which was selected by an in-house editor and fully peer-reviewed by external reviewers. It is distributed in accordance with the Creative Commons Attribution Non Commercial (CC BY-NC 4.0) license, which permits others to distribute, remix, adapt, build upon this work non-commercially, and license their derivative works on different terms, provided the original work is properly cited and the use is non-commercial. See: <http://creativecommons.org/licenses/by-nc/4.0/>

Correspondence to: Dr. Matthew T Crockett, Department of Radiology, Mater Misericordiae University Hospital, Eccles Street, Dublin 7, Ireland. crocketmt@gmail.com

Telephone: +353-8-63669360

Fax: +353-1-8032970

Received: November 10, 2014

Peer-review started: November 11, 2014

First decision: January 8, 2015

Revised: February 18, 2015

Accepted: March 16, 2015

Article in press: March 18, 2015

Published online: April 28, 2015

interventional radiology.

METHODS: Using the database of Journal Citation Reports the 40 highest impact factor radiology journals were chosen. From these journals the 100 most cited interventional radiology papers were chosen and analysed.

RESULTS: The top paper received 2497 citations and the 100th paper 200 citations. The average number of citations was 320. Dates of publication ranged from 1953 - 2005. Most papers originated in the United States ($n = 67$) followed by Italy ($n = 20$) and France ($n = 10$). Harvard University ($n = 18$) and Osped Civile ($n = 11$) were the most prolific institutions. Ten journals produced all of the top 100 papers with "Radiology" and "AJR" making up the majority. SN Goldberg and T Livraghi were the most prolific authors. Nearly two thirds of the papers ($n = 61$) were published after 1990.

CONCLUSION: This analysis identifies many of the landmark interventional radiology papers and provides a fascinating insight into the changing discourse within the field. It also identifies topics, authors and institutions which have impacted greatly on the specialty.

Key words: Interventional radiology; Citation classic; Radiology; Citation; Citation analysis; Classic papers

© **The Author(s) 2015.** Published by Baishideng Publishing Group Inc. All rights reserved.

Core tip: Interventional radiology is a young and rapidly evolving specialty. This study defined and analysed the 100 most cited interventional radiology papers identifying much of the landmark interventional radiology research and providing a fascinating insight into the changing discourse within the field. It also identified the topics, authors and institutions which have impacted greatly on the specialty.

Abstract

AIM: To define the 100 citation classic papers of

Crockett MT, Browne RFJ, MacMahon PJ, Lawler L. 100 classic papers of interventional radiology: A citation analysis. *World J Radiol* 2015; 7(4): 79-86 Available from: URL: <http://www.wjgnet.com/1949-8470/full/v7/i4/79.htm> DOI: <http://dx.doi.org/10.4329/wjr.v7.i4.79>

INTRODUCTION

A citation is the intellectual acknowledgement of a published or unpublished source in order to substantiate fact. Whilst the intellectual acknowledgement that one paper gives to another is known as a reference, the acknowledgement that one paper receives from another is known as a citation^[1]. The field of citation analysis uses the citation rate of a paper as a surrogate marker of a paper's recognition and impact within its biomedical field, the more citations that a paper receives, the greater that paper's impact and recognition^[2]. The most cited papers within a specialty can be defined as that specialty's classic papers, with the 100 most cited papers representing the "best of" of that specialty^[3]. Recent studies have analysed the highly cited papers in other specialties and produced "best of" lists of the top 100 classic papers^[4-6]. From these studies it is clearly evident that highly cited works in a particular field often represent the landmark papers, seminal advances and technical innovations of that specialty. However there are also limitations in using the citation rate of a paper alone to define that paper's scientific quality and impact. Whether a paper is cited by another author can depend upon various factors and biases some of which can lead to citations which are not wholly appropriate^[7]. Despite these limitations, citation analysis remains a well recognised method of objectively identifying classic papers within a specialty.

The purpose of this study is to identify and analyse the 100 most cited papers within the specialty of interventional radiology - the 100 citation classics. This will allow the topics, authors and institutions which have impacted greatly on this rapidly evolving specialty to be reviewed whilst also critically evaluating the strengths and weaknesses of citation analysis as a method of defining a paper's quality and impact within its specialty.

MATERIALS AND METHODS

Using the database of Journal Citation Reports, 40 radiology journals were chosen for analysis from the subcategory of "Radiology, Nuclear Medicine and Medical Imaging" (Table 1). The subcategory of "Radiology, Nuclear Medicine and Medical Imaging" covers a broad range of journals and therefore excluded from our selection were those journals dealing purely with nuclear medicine, those dealing with basic imaging science and physics as well as radiotherapy journals.

These 40 journals were then analysed using the Science Citation Index of the Institute of Scientific

Information and the 100 most cited interventional radiology papers were chosen. Each of the papers was categorised by body system involved, interventional procedure performed, country of origin, institution of origin, author of paper and year of publication.

Statistical analysis

No biostatistics were used in this study.

RESULTS

Table 2 lists the 100 most cited interventional radiology papers in descending order according to the number of citations received.

Table 3 below summarises some of the analysed characteristics of the 100 most cited papers in interventional radiology.

The top paper received 2497 citations whilst the 100th paper in the list was cited 200 times. Seven papers received 500 citations or more with the average number of citations being 320.

The oldest paper is Seldinger's 1953 seminal work on the technique of percutaneous arteriography and this paper also occupies first place in this top 100 list. The most recent paper is published in 2005 by Goldberg *et al*^[8]. This is one of Goldberg's six 1st name papers in this list whilst he is also a named author on another nine papers. Nine persons were named authors on four or more papers.

The papers were published between 1953 and 2005. Two thirds of the papers ($n = 61$) were published after 1990 with just 5 originating before 1970.

The 100 papers originated from just seven countries. The vast majority of the papers ($n = 67$) originated in the United States followed by Italy ($n = 20$) and France ($n = 10$).

Eleven institutions produced more than two publications in the top 100. Harvard University (United States) tops the list with 18 publications followed by Ospedale Civile (Italy) with 11 publications. Several multicentre studies spanned more than one country or institution. For papers published from these studies all countries or institutions involved have been credited.

The most cited papers in interventional radiology were published in 10 specialist radiology journals with nearly two thirds published in *Radiology* ($n = 62$) and a fifth ($n = 20$) published in the *American Journal of Roentgenology*. No papers originated from the high impact factor general medical journals analysed.

The interventional technique of radiofrequency ablation is well represented when the papers are broken down by procedure, with 29 entries in the top 100. This is followed by angiography and embolization with 14 papers a piece and subsequently image guided biopsy with 11 papers. The hepatobiliary system is the most studied body system with 30 papers focusing upon it and this is followed by 20 papers focusing upon the vascular system. Although categorising these papers

Table 1 Radiology journals analysed in order of 5 year impact factor

Rank	Journal	5 yr impact factor
1	Neuroimage	6.817
2	Radiology	6.409
3	JACC Cardiovascular Imaging	5.528
4	Circulation Cardiovascular Imaging	4.757
5	Investigative Radiology	4.328
6	Magnetic Resonance in Medicine	3.885
7	Radiographics	3.602
8	American Journal of Neuroradiology	3.413
9	European Radiology	3.384
10	American Journal of Roentgenology	2.979
11	Journal of Magnetic Resonance Imaging	2.97
12	European Journal of Radiology	2.673
13	Neuroradiology	2.556
14	Journal of Vascular and Interventional Radiology	2.433
15	Radiologic Clinics of North America	2.404
16	British Journal of Radiology	2.354
17	Academic Radiology	2.201
18	Magnetic Resonance Imaging	2.144
19	Neuroimaging Clinics of North America	2.109
20	Korean Journal of Radiology	1.863
21	Cardiovascular and Interventional Radiology	1.792
22	Clinical Radiology	1.754
23	Abdominal Imaging	1.716
24	International Journal of Cardiovascular Imaging	1.682
25	Journal of Thoracic Imaging	1.592
26	Journal of Neuroimaging	1.586
27	Journal of Computer Assisted Tomography	1.551
28	Paediatric Radiology	1.535
29	Radiologica Medica	1.448
30	Skeletal Radiology	1.443
31	Acta Radiologica	1.312
32	Seminars in Musculoskeletal Radiology	1.201
33	Journal of Neuroradiology	1.148
34	Seminars in Ultrasound, CT and MRI	1.005
35	Clinical Imaging	0.869
36	Seminars in Roentgenology	0.823
37	Current Medical Imaging Reviews	0.776
38	Canadian Association of Radiologists Journal	0.665
39	Journal de Radiologie	0.51
40	Der Radiologe	0.454
41	Interventional Neuroradiology	0.173
42	Clinical Neuroradiology	-
43	Diagnostic and Interventional Radiology	-
44	Seminars in Interventional Radiology	-

by body system studied or interventional procedure performed gives a useful overall picture of the studies included in this list, it is obvious that the two categories are interlinked. Closer inspection reveals 10 papers in the top 20, and 26 papers in the top 100 focusing upon liver metastases. Most look specifically at ablation or embolization of these metastases and this goes some way to explaining why the hepatobiliary system and radiofrequency ablation are so highly represented.

DISCUSSION

This list of the 100 citation classic papers of interventional radiology provides a fascinating insight into the history and development of the specialty over the

last 60 years. It identifies many of the topics, authors and institutions which have contributed most heavily to the field and includes many landmark papers.

Many authors featuring prominently here might be considered to be the forerunners in the development of interventional radiology as a specialty. The impact of authors such as Seldinger, Judkins, Gianturco, vanSonnenburg and Mueller cannot be underestimated and techniques and equipment bear their names to this day.

Despite the prominence of these authors, it must be noted that inclusion in this list of the 100 citation classics of interventional radiology does not necessarily mean that the cited authors contributed to the development of a particular technique. Goodwin's paper which is in 89th place in this top 100 list is a good example. This paper dealt with preliminary results of uterine artery embolization, but it was not him who introduced this technique, but Ravina *et al*^[9] 1995. It is also surprising that important developments such as the pioneering work of Serbinenko and Djindjian in the development of intracerebral embolization, Porstman's occlusion technique of the Ductus arteriosus, and Volodos work in the development of the first aortic endograft are not covered by this citation analysis. This is likely due to the fact that their papers were published outside of the specialist radiology journals and therefore are not captured by this study. This flaw is covered later in the discussion section.

It is interesting to see the changing topics covered by papers over the last 60 years which mirror the history of interventional radiology. The very early papers, representing the birth of the specialty, focus almost solely on cardiac and vascular interventional techniques. As time progresses the variety of interventions rises to include neurological and musculoskeletal procedures and there is also increasing focus on techniques dealing with malignant metastatic disease. This represents interventional radiology branching out into oncology where it now plays an important role within the multidisciplinary structure. Some other techniques, such as coronary angiography, began as the role of the interventional radiologist but have now been subsumed by other specialties and consequently recent papers concerning these techniques are now likely to be published outside of radiology journals.

Just under two thirds of the papers were published after 1990 which is surprising as it is natural to assume that older papers will accumulate more citations. However this is only true to a certain degree. It will generally take 1-2 years after publication for a paper to be cited. This is followed by an increase in citation rate up to a maximum point which is usually between 5 and 10 years after publication. After this maximum point the rate of citation gradually starts to decline^[1]. This has two main implications; firstly older papers do not continue to accumulate citations in proportion to their age, this is why the top of this list is not solely made up

Table 2 The 100 most cited interventional radiology papers of all time

Rank	Paper	No. of citations
1	Seldinger SI. "Catheter replacement of the needle in percutaneous arteriography; a new technique," <i>Acta Radiologica</i> 39, no. 5 (May 1953): 368-376	2497
2	Judkins MP. "Selective coronary arteriography. I. A percutaneous transfemoral technic," <i>Radiology</i> 89, no. 5 (November 1967): 815-824	1071
3	Livraghi T, Goldberg SN, Lazzaroni S, Meloni F, Solbiati L, Gazelle GS. "Small hepatocellular carcinoma: treatment with radio-frequency ablation versus ethanol injection". <i>Radiology</i> 210, no. 3 (March 1999): 655-661	735
4	Yamada R, Sato M, Kawabata M, Nakatsuka H, Nakamura K, Takashima S. "Hepatic artery embolization in 120 patients with unresectable hepatoma," <i>Radiology</i> 148, no. 2 (August 1983): 397-401.	625
5	Livraghi T, Giorgio A, Marin G, Salmi A, de Sio I, Bolondi L, Pompili M, Brunello F, Lazzaroni S, Torzilli G. "Hepatocellular carcinoma and cirrhosis in 746 patients: long-term results of percutaneous ethanol injection," <i>Radiology</i> 197, no. 1 (October 1995): 101-108	612
6	Jensen ME, Evans AJ, Mathis JM, Kallmes DF, Cloft HJ, Dion JE. "Percutaneous polymethylmethacrylate vertebroplasty in the treatment of osteoporotic vertebral body compression fractures: technical aspects," <i>AJNR</i> 18, no. 10 (December 1997): 1897-1904	529
7	Livraghi T, Goldberg SN, Lazzaroni S, Meloni F, Ierace T, Solbiati L, Gazelle GS. "Hepatocellular carcinoma: radio-frequency ablation of medium and large lesions," <i>Radiology</i> 214, no. 3 (March 2000): 761-768	516
8	Rossi S, Di Stasi M, Buscarini E, Quaretti P, Garbagnati F, Squassante L, Paties CT, Silverman DE, Buscarini L. "Percutaneous RF interstitial thermal ablation in the treatment of hepatic cancer," <i>AJR</i> 167, no. 3 (September 1996): 759-768	497
9	Parker SH, Burbank F, Jackman RJ, Aucreman CJ, Cardenosa G, Cink TM, Coscia JL Jr, Eklund GW, Evans WP 3rd, Garver PR. "Percutaneous large-core breast biopsy: a multi-institutional study," <i>Radiology</i> 193, no. 2 (November 1994): 359-364	461
10	Hessel SJ, Adams DF, Abrams HL. "Complications of angiography," <i>Radiology</i> 138, no. 2 (February 1981): 273-281	448
11	H Deramond, Depriester C, Galibert P, Le Gars D. "Percutaneous vertebroplasty with polymethylmethacrylate. Technique, indications, and results," <i>Radiologic Clinics of North America</i> 36, no. 3 (May 1998): 533-546	432
12	L Solbiati, Livraghi T, Goldberg SN, Ierace T, Meloni F, Dellanoce M, Cova L, Halpern EF, Gazelle GS. "Percutaneous radio-frequency ablation of hepatic metastases from colorectal cancer: long-term results in 117 patients," <i>Radiology</i> 221, no. 1 (October 2001): 159-166	424
13	Livraghi T, Solbiati L, Meloni MF, Gazelle GS, Halpern EF, Goldberg SN. "Treatment of focal liver tumors with percutaneous radio-frequency ablation: complications encountered in a multicenter study," <i>Radiology</i> 226, no. 2 (February 2003): 441-451	421
14	Cotton A, Dewatre F, Cortet B, Assaker R, Leblond D, Duquesnoy B, Chastanet P, Clarisse J. "Percutaneous vertebroplasty for osteolytic metastases and myeloma: effects of the percentage of lesion filling and the leakage of methyl methacrylate at clinical follow-up," <i>Radiology</i> 200, no. 2 (August 1996): 525-530	417
15	LaBerge JM, Ring EJ, Gordon RL, Lake JR, Doherty MM, Somberg KA, Roberts JP, Ascher NL. "Creation of transjugular intrahepatic portosystemic shunts with the wallstent endoprosthesis: results in 100 patients," <i>Radiology</i> 187, no. 2 (May 1993): 413-420	410
16	Solbiati L, Goldberg SN, Ierace T, Livraghi T, Meloni F, Dellanoce M, Sironi S, Gazelle GS. "Hepatic metastases: percutaneous radio-frequency ablation with cooled-tip electrodes," <i>Radiology</i> 205, no. 2 (November 1997): 367-373	402
17	Riccardo RA, Allgaier HP, Cioni D, Olschewski M, Deibert P, Crocetti L, Frings H, Laubenberger J, Zuber I, Blum HE, Bartolozzi C. "Small hepatocellular carcinoma in cirrhosis: randomized comparison of radio-frequency thermal ablation versus percutaneous ethanol injection," <i>Radiology</i> 228, no. 1 (July 2003): 235-240	396
18	Judkins MP. "Percutaneous transfemoral selective coronary arteriography," <i>Radiologic Clinics of North America</i> 6, no. 3 (December 1968): 467-492	392
19	Rossi S, Buscarini E, Garbagnati F, Di Stasi M, Quaretti P, Rago M, Zangrandi A, Andreola S, Silverman D, Buscarini L. "Percutaneous treatment of small hepatic tumors by an expandable RF needle electrode," <i>AJR</i> 170, no. 4 (April 1998): 1015-1022	387
20	Gianturco C, Anderson JH, Wallace S. "Mechanical devices for arterial occlusion," <i>The American Journal of Roentgenology, Radium Therapy, and Nuclear Medicine</i> 124, no. 3 (July 1975): 428-435	384
21	Solbiati L, Ierace T, Goldberg SN, Sironi S, Livraghi T, Fiocca R, Servadio G, Rizzatto G, Mueller PR, Del Maschio A, Gazelle GS. "Percutaneous US-guided radio-frequency tissue ablation of liver metastases: treatment and follow-up in 16 patients," <i>Radiology</i> 202, no. 1 (January 1997): 195-203	378
22	Weill A, Chiras J, Simon JM, Rose M, Sola-Martinez T, Enkaoua E. "Spinal metastases: indications for and results of percutaneous injection of acrylic surgical cement," <i>Radiology</i> 199, no. 1 (April 1996): 241-247	356
23	Castaneda-Zuniga WR, Formanek A, Tadavarthy M, Vlodever Z, Edwards JE, Zollikofer C, Amplatz K. "The mechanism of balloon angioplasty," <i>Radiology</i> 135, no. 3 (June 1980): 565-571	354
24	Goldberg SN, Gazelle GS, Mueller PR. "Thermal ablation therapy for focal malignancy: a unified approach to underlying principles, techniques, and diagnostic imaging guidance," <i>AJR</i> 174, no. 2 (February 2000): 323-331	349
25	Waugh JR, Sacharias N. "Arteriographic complications in the DSA era," <i>Radiology</i> 182, no. 1 (January 1992): 243-246	332
26	Heiserman JE, Dean BL, Hodak JA, Flom RA, Bird CR, Drayer BP, Fram EK. "Neurologic complications of cerebral angiography," <i>AJNR</i> 15, no. 8 (September 1994): 1401-1407; discussion 1408-1411.	321
27	Gazelle GS, Goldberg SN, Solbiati L, Livraghi T. "Tumor ablation with radio-frequency energy," <i>Radiology</i> 217, no. 3 (December 2000): 633-646	321
28	Livraghi T, Goldberg SN, Monti F, Bizzini A, Lazzaroni S, Meloni F, Pellicano S, Solbiati L, Gazelle GS. "Saline-enhanced radio-frequency tissue ablation in the treatment of liver metastases," <i>Radiology</i> 202, no. 1 (January 1997): 205-210	311
29	Smith EH. "Complications of percutaneous abdominal fine-needle biopsy. Review," <i>Radiology</i> 178, no. 1 (January 1991): 253-258	308
30	Parker SH. "Stereotactic breast biopsy with a biopsy gun," <i>Radiology</i> 176, no. 3 (September 1990): 741-747	306
31	Dodd GD, Soulen MC, Kane RA, Livraghi T, Lees WR, Yamashita Y, Gillams AR, Karahan OI, Rhim H. "Minimally invasive treatment of malignant hepatic tumors: at the threshold of a major breakthrough," <i>Radiographics</i> 20, no. 1 (February 2000): 9-27	304
32	Livraghi T, Festi D, Monti F, Salmi A, Vettori C. "US-guided percutaneous alcohol injection of small hepatic and abdominal tumors," <i>Radiology</i> 161, no. 2 (November 1986): 309-312	295

33	Lang EK. "A survey of the complications of percutaneous retrograde arteriography: Seldinger Technic", <i>Radiology</i> 81 (August 1963): 257-263	292
34	Nakamura H, Hashimoto T, Oi H, Sawada S. "Transcatheter oily chemoembolization of hepatocellular carcinoma," <i>Radiology</i> 170, no. 3 Pt 1 (March 1989): 783-786	290
35	Rösch J, Dotter CT, Brown MJ. "Selective arterial embolization. A new method for control of acute gastrointestinal bleeding," <i>Radiology</i> 102, no. 2 (February 1972): 303-306	285
36	Shiina S, Tagawa K, Niwa Y, Unuma T, Komatsu Y, Yoshiura K, Hamada E, Takahashi M, Shiratori Y, Terano A. "Percutaneous ethanol injection therapy for hepatocellular carcinoma: results in 146 patients," <i>AJR</i> 160, no. 5 (May 1993): 1023-1028	283
37	Theron JG, Payelle GG, Coskun O, Huet HF, Guimaraens L. "Carotid artery stenosis: treatment with protected balloon angioplasty and stent placement," <i>Radiology</i> 201, no. 3 (December 1996): 627-636	283
38	Chilcote WA, Modic MT, Pavlicek WA, Little JR, Furlan AJ, Duchesneau PM, Weinstein MA. "Digital subtraction angiography of the carotid arteries: a comparative study in 100 patients," <i>Radiology</i> 139, no. 2 (May 1981): 287-295	268
39	Parker SH, Jobe WE, Dennis MA, Stavros AT, Johnson KK, Yakes WF, Truell JE, Price JG, Kortz AB, Clark DG. US-guided automated large-core breast biopsy, <i>Radiology</i> 187, no. 2 (May 1993): 507-511	268
40	McNamara TO, Fischer JR. "Thrombolysis of peripheral arterial and graft occlusions: improved results using high-dose urokinase," <i>AJR</i> 144, no. 4 (April 1985): 769-775	266
41	Goodwin SC, McLucas B, Lee M, Chen G, Perrella R, Vedantham S, Muir S, Lai A, Sayre JW, DeLeon M. "Uterine artery embolization for the treatment of uterine leiomyomata midterm results," <i>JVIR</i> 10, no. 9 (October 1999): 1159-1165	260
42	Grüntzig A, Kumpke DA. "Technique of percutaneous transluminal angioplasty with the Grüntzig balloon catheter," <i>AJR</i> 132, no. 4 (April 1979): 547-552	259
43	Rossi S, Garbagnati F, Lencioni R, Allgaier HP, Marchianò A, Fornari F, Quaretti P, Tolla GD, Ambrosi C, Mazzaferro V, Blum HE, Bartolozzi C. "Percutaneous radio-frequency thermal ablation of nonresectable hepatocellular carcinoma after occlusion of tumor blood supply," <i>Radiology</i> 217, no. 1 (October 2000): 119-126	257
44	Goldstein HM, Wallace S, Anderson JH, Bree RL, Gianturco C. "Transcatheter occlusion of abdominal tumors," <i>Radiology</i> 120, no. 3 (September 1976): 539-545	257
45	Cotton A, Boutry N, Cortet B, Assaker R, Demondion X, Leblond D, Chastanet P, Duquesnoy B, Deramond H. "Percutaneous vertebroplasty: state of the art," <i>Radiographics</i> 18, no. 2 (April 1998): 311-320	257
46	vanSonnenberg E, Mueller PR, Ferrucci Jr JT. "Percutaneous drainage of 250 abdominal abscesses and fluid collections. Part I: Results, failures, and complications," <i>Radiology</i> 151, no. 2 (May 1984): 337-341	256
47	Krepel VM, van Andel GJ, van Erp WF, Breslau PJ. "Percutaneous transluminal angioplasty of the femoropopliteal artery: initial and long-term results," <i>Radiology</i> 156, no. 2 (August 1985): 325-328	255
48	Goldberg SN, Gazelle GS, Solbiati L, Rittman WJ, Mueller PR. "Radiofrequency tissue ablation: increased lesion diameter with a perfusion electrode," <i>Academic Radiology</i> 3, no. 8 (August 1996): 636-644	254
49	Mewissen MW, Seabrook GR, Meissner MH, Cynamon J, Labropoulos N, Haughton SH. "Catheter-directed thrombolysis for lower extremity deep venous thrombosis: report of a national multicenter registry," <i>Radiology</i> 211, no. 1 (April 1999): 39-49	254
50	Baum S, Nusbaum M. "The control of gastrointestinal hemorrhage by selective mesenteric arterial infusion of vasopressin," <i>Radiology</i> 98, no. 3 (March 1971): 497-505	253
51	White Jr RL, Lynch-Nyhan A, Terry P, Buescher PC, Farmlett EJ, Charnas L, Shuman K, Kim W, Kinnison M, Mitchell SE. "Pulmonary arteriovenous malformations: techniques and long-term outcome of embolotherapy," <i>Radiology</i> 169, no. 3 (December 1988): 663-669	251
52	Goldberg SN, Solbiati L, Hahn PF, Cosman E, Conrad JE, Fogle R, Gazelle GS. "Large-volume tissue ablation with radio frequency by using a clustered, internally cooled electrode technique: laboratory and clinical experience in liver metastases," <i>Radiology</i> 209, no. 2 (November 1998): 371-379	251
53	Chuang VP, Wallace S. "Hepatic artery embolization in the treatment of hepatic neoplasms," <i>Radiology</i> 140, no. 1 (July 1981): 51-58	249
54	Goldberg SN, Hahn PF, Tanabe KK, Mueller PR, Schima W, Athanasoulis CA, Compton CC, Solbiati L, Gazelle GS. "Percutaneous radiofrequency tissue ablation: does perfusion-mediated tissue cooling limit coagulation necrosis?," <i>JVIR</i> 9, no. 1 Pt 1 (February 1998): 101-111	249
55	McAfee JG. "A survey of complications of abdominal aortography," <i>Radiology</i> 68, no. 6 (June 1957): 825-838	248
56	Johnston KW. "Femoral and popliteal arteries: reanalysis of results of balloon angioplasty," <i>Radiology</i> 183, no. 3 (June 1992): 767-771	248
57	Willinsky RA, Taylor SM, TerBrugge K, Farb RI, Tomlinson G, Montanera W. "Neurologic complications of cerebral angiography: prospective analysis of 2,899 procedures and review of the literature," <i>Radiology</i> 227, no. 2 (May 2003): 522-528	248
58	Dupuy DE, Zagoria RJ, Akerley W, Mayo-Smith WW, Kavanagh PV, Safran H. "Percutaneous radiofrequency ablation of malignancies in the lung," <i>AJR</i> 174, no. 1 (January 2000): 57-59	245
59	Vogl TJ, Müller PK, Hammerstingl R, Weinhold N, Mack MG, Philipp C, Deimling M, Beuthan J, Pegios W, Riess H, et al. "Malignant liver tumors treated with MR imaging-guided laser-induced thermotherapy: technique and prospective results," <i>Radiology</i> 196, no. 1 (July 1995): 257-265	244
60	Becker GJ, Katzen BT, Dake MD. "Noncoronary angioplasty," <i>Radiology</i> 170, no. 3 Pt 2 (March 1989): 921-940	241
61	Ferrucci Jr JT, Wittenberg J, Mueller PR, Simeone JF, Harbin WP, Kirkpatrick RH, Taft PD. "Diagnosis of abdominal malignancy by radiologic fine-needle aspiration biopsy," <i>AJR</i> 134, no. 2 (February 1980): 323-330	239
62	Min RJ, Khilnani N, Zimmet SE. "Endovenous laser treatment of saphenous vein reflux: long-term results," <i>JVIR</i> 14, no. 8 (August 2003): 991-996	238
63	Gerzof SG, Robbins AH, Birkett DH, Johnson WC, Pugatch RD, Vincent ME. "Percutaneous catheter drainage of abdominal abscesses guided by ultrasound and computed tomography," <i>AJR</i> 133, no. 1 (July 1979): 1-8	237
64	Haaga JR, Alfidi RJ. "Precise biopsy localization by computer tomography," <i>Radiology</i> 118, no. 3 (March 1976): 603-607	236
65	Lencioni R, Cioni D, Crocetti L, Franchini C, Pina CD, Lera J, Bartolozzi C. "Early-stage hepatocellular carcinoma in patients with cirrhosis: long-term results of percutaneous image-guided radiofrequency ablation," <i>Radiology</i> 234, no. 3 (March 2005): 961-967	233
66	Mueller PR, van Sonnenberg E, Ferrucci Jr JT. "Percutaneous biliary drainage: technical and catheter-related problems in 200 procedures," <i>AJR</i> 138, no. 1 (January 1982): 17-23	232

67	de Baere T, Elias D, Dromain C, Din MG, Kuoch V, Ducreux M, Boige V, Lassau N, Marteau V, Lasser P, Roche A. "Radiofrequency ablation of 100 hepatic metastases with a mean follow-up of more than 1 year," <i>AJR</i> 175, no. 6 (December 2000): 1619-1625	232
68	Ferrucci Jr JT, Mueller PR, Harbin WP. "Percutaneous transhepatic biliary drainage: technique, results, and applications," <i>Radiology</i> 135, no. 1 (April 1980): 1-13	231
69	Khourri NF, Stitik FP, Erozan YS, Gupta PK, Kim WS, Scott WW Jr, Hamper UM, Mann RB, Eggleston JC, Baker RR. "Transthoracic needle aspiration biopsy of benign and malignant lung lesions," <i>AJR</i> 144, no. 2 (February 1985): 281-288	230
70	Meaney TF, Weinstein MA, Buonocore E, Pavlicek W, Borkowski GP, Gallagher JH, Sufka B, MacIntyre WJ. "Digital subtraction angiography of the human cardiovascular system," <i>AJR</i> 135, no. 6 (December 1980): 1153-1160	229
71	Padovani B, Kasriel O, Brunner P, Peretti-Viton P. "Pulmonary embolism caused by acrylic cement: a rare complication of percutaneous vertebroplasty," <i>AJNR</i> 20, no. 3 (March 1999): 375-377	229
72	Palmaz JC, Laborde JC, Rivera FJ, Encarnacion CE, Lutz JD, Moss JG. "Stenting of the iliac arteries with the Palmaz stent: experience from a multicenter trial" <i>Cardiovascular and Interventional Radiology</i> 15, no. 5 (October 1992): 291-297	228
73	Matsui O, Kadoya M, Yoshikawa J, Gabata T, Arai K, Demachi H, Miyayama S, Takashima T, Unoura M, Kogayashi K. "Small hepatocellular carcinoma: treatment with subsegmental transcatheter arterial embolization," <i>Radiology</i> 188, no. 1 (July 1993): 79-83	228
74	Elvecrog EL, Lechner MC, Nelson MT. "Nonpalpable breast lesions: correlation of stereotaxic large-core needle biopsy and surgical biopsy results," <i>Radiology</i> 188, no. 2 (August 1993): 453-455	228
75	Burbank F. "Stereotactic breast biopsy of atypical ductal hyperplasia and ductal carcinoma in situ lesions: improved accuracy with directional, vacuum-assisted biopsy," <i>Radiology</i> 202, no. 3 (March 1997): 843-847	228
76	Molnar W, Stockum AE. "Relief of obstructive jaundice through percutaneous transhepatic catheter--a new therapeutic method," <i>The American Journal of Roentgenology, Radium Therapy, and Nuclear Medicine</i> 122, no. 2 (October 1974): 356-367	227
77	Rémy J, Arnaud A, Fardou H, Giraud R, Voisin C. "Treatment of hemoptysis by embolization of bronchial arteries," <i>Radiology</i> 122, no. 1 (January 1977): 33-37	226
78	Gangi A, Kastler BA, Dietemann JL. "Percutaneous vertebroplasty guided by a combination of CT and fluoroscopy," <i>AJNR</i> 15, no. 1 (January 1994): 83-86	226
79	Haaga JR, Alfidi RJ, Havrilla TR, Cooperman AM, Seidelmann FE, Reich NE, Weinstein AJ, Meaney TF. "CT detection and aspiration of abdominal abscesses," <i>AJR</i> 128, no. 3 (March 1977): 465-474	225
80	Earnest F 4th, Forbes G, Sandok BA, Piegras DG, Faust RJ, Ilstrup DM, Arndt LJ. "Complications of cerebral angiography: prospective assessment of risk," <i>AJR</i> 142, no. 2 (February 1984): 247-253	225
81	Amin Z, Donald JJ, Masters A, Kant R, Steger AC, Bown SG, Lees WR. "Hepatic metastases: interstitial laser photocoagulation with real-time US monitoring and dynamic CT evaluation of treatment," <i>Radiology</i> 187, no. 2 (May 1993): 339-347	223
82	Mills SR, Jackson DC, Older RA, Heaston DK, Moore AV. "The incidence, etiologies, and avoidance of complications of pulmonary angiography in a large series," <i>Radiology</i> 136, no. 2 (August 1980): 295-299	222
83	vanSonnenberg E, Ferrucci JT Jr, Mueller PR, Wittenberg J, Simeone JF. "Percutaneous drainage of abscesses and fluid collections: technique, results, and applications," <i>Radiology</i> 142, no. 1 (January 1982): 1-10	221
84	Richter GM, Noeldge G, Palmaz JC, Roessle M, Slegersstetter V, Franke M, Gerok W, Wenz W, Farthman E. "Transjugular intrahepatic portacaval stent shunt: preliminary clinical results," <i>Radiology</i> 174, no. 3 Pt 2 (March 1990): 1027-1030	219
85	Zeumer H, Freitag HJ, Zanella F, Thie A, Arning C. "Local intra-arterial fibrinolytic therapy in patients with stroke: urokinase versus recombinant tissue plasminogen activator (r-TPA)," <i>Neuroradiology</i> 35, no. 2 (1993): 159-162	219
86	Westcott JL. "Direct percutaneous needle aspiration of localized pulmonary lesions: result in 422 patients," <i>Radiology</i> 137, no. 1 Pt 1 (October 1980): 31-35	216
87	Cognard C, Weill A, Spelle L, Piotin M, Castaings L, Rey A, Moret J. "Long-term angiographic follow-up of 169 intracranial berry aneurysms occluded with detachable coils," <i>Radiology</i> 212, no. 2 (August 1999): 348-356	216
88	Cammà C, Schepis F, Orlando A, Albanese M, Shahied L, Trevisani F, Andreone P, Craxi A, Cottone M. "Transarterial chemoembolization for unresectable hepatocellular carcinoma: meta-analysis of randomized controlled trials," <i>Radiology</i> 224, no. 1 (July 2002): 47-54	215
89	Goodwin SC, Vedantham S, McLucas B, Forno AE, Perrella R. "Preliminary experience with uterine artery embolization for uterine fibroids," <i>JVIR</i> 8, no. 4 (August 1997): 517-526	211
90	Goldberg SN, Gazelle GS, Dawson SL, Rittman WJ, Mueller PR, Rosenthal DI. "Tissue ablation with radiofrequency: effect of probe size, gauge, duration, and temperature on lesion volume," <i>Academic Radiology</i> 2, no. 5 (May 1995): 399-404	208
91	McGhana JP, Dodd GD, 3rd. "Radiofrequency ablation of the liver: current status," <i>AJR</i> 176, no. 1 (January 2001): 3-16	207
92	Mani RL, Eisenberg RL, McDonald EJ Jr, Pollock JA, Mani JR. "Complications of catheter cerebral arteriography: analysis of 5,000 procedures. I. Criteria and incidence," <i>AJR</i> 131, no. 5 (November 1978): 861-865	206
93	Katzen BT, van Breda A. "Low dose streptokinase in the treatment of arterial occlusions," <i>AJR</i> 136, no. 6 (June 1981): 1171-1178	206
94	Goldberg, Grassi CJ, Cardella JF, Charboneau JW, Dodd GD 3rd, Dupuy DE, Gervais D, Gillams AR, Kane RA, Lee FT Jr, Livraghi T, McGahan J, Phillips DA, Rhim H, Silverman SG. "Image-guided tumor ablation: standardization of terminology and reporting criteria," <i>Radiology</i> 235, no. 3 (June 2005): 728-739	205
95	Gervais DA, McGovern FJ, Arellano RS, McDougal WS, Mueller PR. "Renal cell carcinoma: clinical experience and technical success with radio-frequency ablation of 42 tumors," <i>Radiology</i> 226, no. 2 (February 2003): 417-424	204
96	Bookstein JJ, Goldstein HM. "Successful management of postbiopsy arteriovenous fistula with selective arterial embolization," <i>Radiology</i> 109, no. 3 (December 1973): 535-536	203
97	Jackman RJ, Nowels KW, Rodriguez-Soto J, Marzoni FA Jr, Finkelstein SI, Shepard MJ. "Stereotactic, automated, large-core needle biopsy of nonpalpable breast lesions: false-negative and histologic underestimation rates after long-term follow-up," <i>Radiology</i> 210, no. 3 (March 1999): 799-805	202
98	Dupuy DE, Goldberg SN. "Image-guided radiofrequency tumor ablation: challenges and opportunities--part II," <i>JVIR</i> 12, no. 10 (October 2001): 1135-1148	202
99	Ferris EJ, McCowan TC, Carver DK, McFarland DR. "Percutaneous inferior vena caval filters: follow-up of seven designs in 320 patients," <i>Radiology</i> 188, no. 3 (September 1993): 851-856	200
100	Worthington-Kirsch RL, Popky GL, Hutchins Jr FL. "Uterine arterial embolization for the management of leiomyomas: quality-of-life assessment and clinical response," <i>Radiology</i> 208, no. 3 (September 1998): 625-629	200

Table 3 Summary of characteristics of 100 most cited papers

Year of publication		Country of origin		Institution of origin		Journal of publication		Named author	
Year	No. pubs.	Country	No. pubs.	Institution	No. pubs.	Journal	No. pubs.	Author	No. pubs.
1950's	2	United States	67	Harvard Uni.	18	<i>Radiology</i>	62	Goldberg SN	15
1960's	3	Italy	20	Osped Civile	11	<i>AJR</i>	20	Gazelle GS	13
1970's	12	France	10	Mass.Gen.	9	<i>JVIR</i>	5	Livraghi T	12
1980's	22	Germany	5	Osped Gen.	8	<i>AJNR</i>	4	Mueller PR	11
1990's	43	Japan	5	Beth Israel	8	<i>Academic Radiology</i>	2	Solbiati L	11
2000 -	18	Canada	2	Univ Texas	6	<i>Radiographics</i>	2	Ferrucci FT	5

by the oldest papers; secondly very recently published papers will not be included in this list as, despite their scientific originality and impact, they have not had time to accumulate sufficient citations. Whilst it is reassuring that older doesn't necessarily mean more cited, the fact that recently published papers are inherently excluded from citation analysis demonstrates one of its major flaws. Another limitation of citation analysis is the process of "obliteration by incorporation"^[10]. This describes the phenomenon where information from landmark papers becomes incorporated and absorbed into current knowledge and thus these papers are not explicitly cited. For this reason it has been noted that many true "classic papers" and seminal works in a particular field are not found in the most cited list itself but rather in the reference lists of the most cited papers.

This list is dominated by the United States with 67 papers in the top 100. This correlates with similar studies in other fields such as dermatology^[11] (United States = 75%), general surgery^[12] (United States = 78%) and orthopaedics^[5] (United States = 77%). It reflects the huge influence of the United States on medical research and the massive scientific output of the country. It has also been noted that there is a tendency for American authors to preferentially cite other papers from the United States and this is likely to increase their dominance^[7,13]. In fact interventional radiology appears to be less dominated by the United States than other specialties with significant contributions from the European power houses of Italy ($n = 20$) and France ($n = 10$).

All papers were published in only 10 journals. With 60 publications in the top 100 *Radiology* is by far the most prolific publisher followed by the *American Journal of Roentgenology* (*AJR*) with 20 publications. Most papers are published in general radiology journals with only a handful ($n = 6$) published in the two specific interventional journals in the list – *Cardiovascular and Interventional Radiology* and the *Journal of Vascular and Interventional Radiology*. However this is likely to reflect relatively recent emergence of specialised interventional radiology journals (1977 and 1990 respectively) when compared to the traditional pre eminent radiology journals such as *Radiology* and the *AJR*.

One flaw of this study is that, due to technological

limitations of the database of Journal Citation Reports, the search for papers was limited to specialist radiology journals. This meant that papers published in non-radiology journals would not be included in this "top 100 list". This is particularly relevant when considering older papers which would have been more likely to have been published in non specialist radiology journals.

Citation bias towards authors of the same nationality has already been discussed. Other limitations of this study can be linked to the inherent weakness of using citation rate alone in measuring a paper's strength. Instead of using a citation to give credit to those who have significantly influenced their work, some authors use citations to support their own results or to persuade the reader towards a particular conclusion, a process known as incomplete citing^[14]. Many other biases are recognised which might influence the citation of papers. These include self or in house citation bias, bias towards citing review articles over original research and English language bias.

It is clear from discussion of the flaws and limitations of this study, as well as the biases inherent in the field of citation analysis, that the number of citations that a paper receives should not be used alone as a measure of its scientific quality^[1,15]. However it is also clear that the citation rate of a paper is one of many useful tools in measuring the recognition that a paper has received and therefore the impact that a paper has had on its specialty^[16]. Whilst this list of citation classics in interventional radiology should not be considered the definitive "top 100" of this specialty, it does reveal many landmark papers and identifies many of the topics, authors and institutions which have dominated the specialty over the last sixty years.

This is the first study to use citation analysis in an attempt to identify the research papers which have had the greatest impact on the specialty of interventional radiology. Although citation analysis does have limitations, many of the seminal papers of interventional radiology and pioneers of the field are included in this list of "100 citation classics".

COMMENTS

Background

The value of a scientific paper may be defined by its impact on the biomedical

field in which it is published. Papers which impact greatly on their field may achieve the status of a "classic paper". This may be defined using the concept of a citation classic - the number of times a paper is cited reflects its impact and relevance. The aim of this study was to define the top 100 citation classics of the rapidly evolving specialty of interventional radiology and in the process identify the topics, authors and institutions that have impacted greatly on this rapidly evolving specialty.

Research frontiers

Interventional radiology is a young and rapidly evolving specialty. For the last 40 years interventional radiologists have been at the vanguard of innovation with the development of numerous minimally invasive procedures which have revolutionised patient management in multiple areas. The specialty has rapidly grown and evolved from its origins with Seldinger's refinement of arterial cannulisation and Dodder's development of angioplasty and the catheter delivered stents. Embolization of arterial haemorrhage in trauma, catheter directed thrombolysis and coiling of aneurysms are now the gold standard treatments in their respective areas. Recent advances in the specialty include drug eluting balloons and stents in peripheral vascular disease, microwave tumor ablation for liver, kidney and lung tumors and transarterial catheter directed chemotherapy or radionuclide therapy in primary liver tumors and metastases. This study has used citation analysis to define many of the seminal papers within interventional radiology.

Innovations and breakthroughs

This is the first study which has used citation analysis in an attempt to define the most innovative and significant papers in interventional radiology and those which have had the most significant impact on this field. Although citation analysis does have limitations, many of the seminal papers of interventional radiology are included in this list of "100 citation classics".

Applications

This study has used citation analysis to identify the 100 classic papers of interventional radiology. These papers included many of the seminal works in this field by many of the pioneers of the specialty providing a fascinating discourse on the evolution and development of interventional radiology.

Terminology

IR: Interventional radiology.

Peer-review

Nice paper with good analyses.

REFERENCES

- 1 Marx WSH, Wanitschek M. Citation analysis using online databases: feasibilities and shortcomings. *Scientometrics* 2001; **52**: 59-82 [DOI: 10.1023/A: 1012798911792]
- 2 Seglen PO. Citation frequency and journal impact: valid indicators of scientific quality? *J Intern Med* 1991; **229**: 109-111 [PMID: 1997634]
- 3 Hall GM. BJA citation classics 1945-1992. *Br J Anaesth* 1998; **80**: 4-6 [PMID: 9505768]
- 4 Heldwein FL, Rhoden EL, Morgentaler A. Classics of urology: a half century history of the most frequently cited articles (1955-2009). *Urology* 2010; **75**: 1261-1268 [PMID: 19962736]
- 5 Kelly JC, Glynn RW, O'Briain DE, Felle P, McCabe JP. The 100 classic papers of orthopaedic surgery: a bibliometric analysis. *J Bone Joint Surg Br* 2010; **92**: 1338-1343 [PMID: 20884968]
- 6 Li Z, Wu FX, Yang LQ, Sun YM, Lu ZJ, Yu WF. Citation classics in main pain research journals. *J Anesth* 2012; **26**: 85-93 [PMID: 22008797]
- 7 Seglen PO. Citation rates and journal impact factors are not suitable for evaluation of research. *Acta Orthop Scand* 1998; **69**: 224-229 [PMID: 9703393]
- 8 Goldberg SN, Grassi CJ, Cardella JF, Charboneau JW, Dodd GD, Dupuy DE, Gervais D, Gillams AR, Kane RA, Lee FT, Livraghi T, McGahan J, Phillips DA, Rhim H, Silverman SG. Image-guided tumor ablation: standardization of terminology and reporting criteria. *J Vasc Interv Radiol* 2005; **16**: 765-778 [PMID: 15947040]
- 9 Ravina JH, Merland JJ, Ciraru-Vigneron N, Bouret JM, Herbreteau D, Houdart E, Aymard A. [Arterial embolization: a new treatment of menorrhagia in uterine fibroma]. *Presse Med* 1995; **24**: 1754 [PMID: 8545421]
- 10 Picknett T, Davis K. The 100 most-cited articles from JMB. *J Mol Biol* 1999; **293**: 171-176 [PMID: 10529345]
- 11 Dubin D, Häfner AW, Arndt KA. Citation classics in clinical dermatologic journals. Citation analysis, biomedical journals, and landmark articles, 1945-1990. *Arch Dermatol* 1993; **129**: 1121-1129 [PMID: 8363395]
- 12 Paladugu R, Schein M, Gardezi S, Wise L. One hundred citation classics in general surgical journals. *World J Surg* 2002; **26**: 1099-1105 [PMID: 12209239]
- 13 Paris G, De Leo G, Menozzi P, Gatto M. Region-based citation bias in science. *Nature* 1998; **396**: 210 [PMID: 10744503]
- 14 Cole S. Citations and the evaluation of individual scientists. *Trends Biochem Sci* 1989; **14**: 9-13 [DOI: 10.1016/0968-0004(89)90078-9]
- 15 Braun T. The reliability of total citation rankings. *J Chem Inf Comput Sci* 2003; **43**: 45-46 [PMID: 12546536]
- 16 Dumont JE. The bias of citations. *Trends Biochem Sci* 1989; **14**: 327-328 [PMID: 2799904]

P- Reviewer: Lakhdar F, Pinto A, Sener RN S- Editor: Ji FF
L- Editor: A E- Editor: Jiao XK





Published by **Baishideng Publishing Group Inc**

8226 Regency Drive, Pleasanton, CA 94588, USA

Telephone: +1-925-223-8242

Fax: +1-925-223-8243

E-mail: bpgoffice@wjgnet.com

Help Desk: <http://www.wjgnet.com/esps/helpdesk.aspx>

<http://www.wjgnet.com>



World Journal of *Radiology*

World J Radiol 2015 May 28; 7(5): 87-109





Editorial Board

2014-2017

The *World Journal of Radiology* Editorial Board consists of 365 members, representing a team of worldwide experts in radiology. They are from 36 countries, including Afghanistan (1), Argentina (2), Australia (5), Austria (7), Belgium (2), Brazil (8), Canada (6), Chile (1), China (43), Croatia (1), Denmark (4), Egypt (6), France (5), Germany (22), Greece (10), India (12), Iran (6), Ireland (2), Israel (3), Italy (47), Japan (13), Netherlands (1), New Zealand (1), Pakistan (1), Poland (2), Portugal (1), Serbia (1), Singapore (3), Slovakia (1), South Korea (18), Spain (4), Sweden (2), Switzerland (4), Thailand (1), Turkey (26), United Kingdom (11), and United States (82).

EDITORS-IN-CHIEF

Kai U Juergens, *Bremen*
Edwin JR van Beek, *Edinburgh*
Thomas J Vogl, *Frankfurt*

GUEST EDITORIAL BOARD MEMBERS

Wing P Chan, *Taipei*
Chung-Huei Hsu, *Taipei*
Chin-Chang Huang, *Taipei*
Tsong-Long Hwang, *Taoyuan*
Jung-Lung Hsu, *Taipei*
Chia-Hung Kao, *Taichung*
Yu-Ting Kuo, *Tainan*
Hon-Man Liu, *Taipei*
Hui-Lung Liang, *Kaohsiung*
Chun Chung Lui, *Kaohsiung*
Sen-Wen Teng, *Taipei*
Yung-Liang (William) Wan, *Taoyuan*

MEMBERS OF THE EDITORIAL BOARD



Afghanistan

Takao Hiraki, *Okayama*



Argentina

Patricia Carrascosa, *Vicente Lopez*
Maria C Ziadi, *Rosario*



Australia

Lourens Bester, *Sydney*
Gemma A Figtree, *Sydney*



Austria

Herwig R Cerwenka, *Graz*
Gudrun M Feuchtnner, *Innsbruck*
Benjamin Henninger, *Innsbruck*
Rupert Lanzenberger, *Vienna*
Shu-Ren Li, *Vienna*
Veronika Schopf, *Vienna*
Tobias De Zordo, *Innsbruck*



Belgium

Steve Majerus, *Liege*
Kathelijne Peremans, *Merelbeke*



Brazil

Clerio F Azevedo, *Rio de Janeiro*
Patrícia P Alfredo, *São Paulo*
Eduardo FC Fleury, *São Paulo*
Edward Araujo Júnior, *São Paulo*
Wellington P Martins, *Ribeirão Preto*
Ricardo A Mesquita, *Belo Horizonte*
Vera MC Salemi, *São Paulo*
Claudia Szobot, *Porto Alegre*
Lilian YI Yamaga, *São Paulo*



Canada

Marie Arsalidou, *Toronto*
Otman A Basir, *Waterloo*

Tarik Zine Belhocine, *Toronto*
James Chow, *Toronto*
Tae K Kim, *Toronto*
Anastasia Oikonomou, *Toronto*



China

Hong-Wei Chen, *Wuxi*
Feng Chen, *Hangzhou*
Jian-Ping Chu, *Guangzhou*
Guo-Guang Fan, *Shenyang*
Bu-Lang Gao, *Shijiazhuang*
Qi-Yong Gong, *Chengdu*
Ying Han, *Beijing*
Xian-Li Lv, *Beijing*
Yi-Zhuo Li, *Guangzhou*
Xiang-Xi Meng, *Harbin*
Yun Peng, *Beijing*
Jun Shen, *Guangzhou*
Ze-Zhou Song, *Hangzhou*
Wai Kwong Tang, *Hong Kong*
Gang-Hua Tang, *Guangzhou*
Jie Tian, *Beijing*
Lu-Hua Wang, *Beijing*
Xiao-bing Wang, *Xi'an*
Yi-Gen Wu, *Nanjing*
Kai Wu, *Guangzhou*
Hui-Xiong Xu, *Shanghai*
Zuo-Zhang Yang, *Kunming*
Xiao-Dan Ye, *Shanghai*
David T Yew, *Hong Kong*
Ting-He Yu, *Chongqing*
Zheng Yuan, *Shanghai*
Min-Ming Zhang, *Hangzhou*
Yudong Zhang, *Nanjing*
Dong Zhang, *Chongqing*
Wen-Bin Zeng, *Changsha*

Yue-Qi Zhu, *Shanghai*



Croatia

Goran Kusec, *Osijek*



Denmark

Poul E Andersen, *Odense*

Lars J Petersen, *Aalborg*

Thomas Z Ramsøy, *Frederiksberg*

Morten Ziebell, *Copenhagen*



Egypt

Mohamed F Bazeed, *Mansoura*

Mohamed Abou El-Ghar, *Mansoura*

Reem HA Mohamed, *Cairo*

Mohamed R Nouh, *Alexandria*

Ahmed AKA Razek, *Mansoura*

Ashraf A Zytoon, *Shebin El-Koom*



France

Sabine F Bensamoun, *Compiègne*

Romarc Loffroy, *Dijon*

Stephanie Nougaret, *Montpellier*

Hassane Oudadesse, *Rennes*

Vincent Vinh-Hung, *Fort-de-France*



Germany

Henryk Barthel, *Leipzig*

Peter Bannas, *Hamburg*

Martin Beeres, *Frankfurt*

Ilja F Ciernik, *Dessau*

A Dimitrakopoulou-Strauss, *Heidelberg*

Peter A Fasching, *Erlangen*

Andreas G Schreyer, *Regensburg*

Philipp Heusch, *Duesseldorf*

Sonja M Kirchhoff, *Munich*

Sebastian Ley, *Munich*

Adel Maataoui, *Frankfurt am Main*

Stephan M Meckel, *Freiburg*

Hans W Muller, *Duesseldorf*

Kay Raum, *Berlin*

Dirk Rades, *Luebeck*

Marc-Ulrich Regier, *Hamburg*

Alexey Surov, *Halle*

Martin Walter, *Magdeburg*

Axel Wetter, *Essen*

Christoph Zilkens, *Düsseldorf*



Greece

Panagiotis Antoniou, *Thessaloniki*

Nikos Efthimiou, *Athens*

Dimitris Karnabatidis, *Patras*

George Latsios, *Athens*

Stylianios Megremis, *Iraklion*

Alexander D Rapidis, *Athens*

Kiki Theodorou, *Larissa*

Ioannis A Tsalafoutas, *Athens*

Evanthia E Tripoliti, *Ioannina*

Athina C Tsili, *Ioannina*



India

Ritesh Agarwal, *Chandigarh*

Chandan J Das, *New Delhi*

Prathamesh V Joshi, *Mumbai*

Naveen Kalra, *Chandigarh*

Chandrasekharan Kesavadas, *Trivandrum*

Jyoti Kumar, *New Delhi*

Atin Kumar, *New Delhi*

Kaushala P Mishra, *Allahabad*

Daya N Sharma, *New Delhi*

Binit Sureka, *New Delhi*

Sanjay Sharma, *New Delhi*

Raja R Yadav, *Allahabad*



Iran

Majid Assadi, *Bushehr*

SeyedReza Najafizadeh, *Tehran*

Mohammad Ali Oghabian, *Tehran*

Amir Reza Radmard, *Tehran*

Ramin Sadeghi, *Mashhad*

Hadi Rokni Yazdi, *Tehran*



Ireland

Tadhg Gleeson, *Wexford*

Frederik JAI Vernimmen, *Cork*



Israel

Dafna Ben Bashat, *Tel Aviv*

Amit Gefen, *Tel Aviv*

Tamar Sella, *Jerusalem*



Italy

Adriano Alippi, *Rome*

Dante Amelio, *Trento*

Michele Anzidei, *Rome*

Filippo F Angileri, *Messinas*

Stefano Arcangeli, *Rome*

Roberto Azzoni, *San Donato milanese*

Tommaso V Bartolotta, *Palermo*

Tommaso Bartalena, *Imola*

Livia Bernardin, *San Bonifacio*

Federico Boschi, *Verona*

Sergio Casciaro, *Lecce*

Emanuele Casciani, *Rome*

Musa M Can, *Napoli*

Alberto Cuocolo, *Napoli*

Michele Ferrara, *Coppito*

Mauro Feola, *Fossano*

Giampiero Francica, *Castel Volturno*

Luigi De Gennaro, *Rome*

Giulio Giovannetti, *Pisa*

Francesca Iacobellis, *Napoli*

Formato Invernizzi, *Monza Brianza*

Francesco Lassandro, *Naples*

Lorenzo Livi, *Florence*

Pier P Mainenti, *Napoli*

Laura Marzetti, *Chieti*

Giuseppe Malinverni, *Crescentino*

Enrica Milanese, *Turin*

Giovanni Morana, *Treviso*

Lorenzo Monti, *Milan*

Silvia D Morbelli, *Genoa*

Barbara Palumbo, *Perugia*

Cecilia Parazzini, *Milan*

Stefano Pergolizzi, *Messina*

Antonio Pinto, *Naples*

Camillo Porcaro, *Rome*

Carlo C Quattrocchi, *Rome*

Alberto Rebonato, *Perugia*

Giuseppe Rizzo, *Rome*

Roberto De Rosa, *Naples*

Domenico Rubello, *Rovigo*

Andrea Salvati, *Bari*

Sergio Sartori, *Ferrara*

Luca M Sconfienza, *Milano*

Giovanni Storto, *Rionero*

Nicola Sverzellati, *Parma*

Alberto S Tagliafico, *Genova*

Nicola Troisi, *Florence*



Japan

Yasuhiko Hori, *Chiba*

Hidetoshi Ikeda, *Koriyama*

Masahito Kawabori, *Sapporo*

Tamotsu Kamishima, *Sapporo*

Hiro Kiyosue, *Yufu*

Yasunori Minami, *Osaka-sayama*

Yasuhiro Morimoto, *Kitakyushu*

Satoru Murata, *Tokyo*

Shigeki Nagamachi, *Miyazaki*

Hiroshi Onishi, *Yamanashi*

Morio Sato, *Wakayama Shi*

Yoshito Tsushima, *Maebashi*

Masahiro Yanagawa, *Suita*



Netherlands

Willem Jan van Rooij, *Tilburg*



New Zealand

W Howell Round, *Hamilton*



Pakistan

Wazir Muhammad, *Abbottabad*



Poland

Maciej S Baglaj, *Wroclaw*

Piotr Czauderna, *Gdansk*



Portugal

Joao Manuel RS Tavares, *Porto*



Serbia

Olivera Ciraj-Bjelac, *Belgrade*



Singapore

Gopinathan Anil, *Singapore*

Terence KB Teo, *Singapore*

Cher Heng Tan, *Singapore*



Slovakia

Stefan Sivak, *Martin*



South Korea

Ki Seok Choo, *Busan*

Seung Hong Choi, *Seoul*

Dae-Seob Choi, *Jinju*

Hong-Seok Jang, *Seoul*

Yong Jeong, *Daejeon*

Chan Kyo Kim, *Seoul*

Se Hyung Kim, *Seoul*

Joong-Seok Kim, *Seoul*

Sang Eun Kim, *Seongnam*

Sung Joon Kwon, *Seoul*

Jeong Min Lee, *Seoul*

In Sook Lee, *Busan*

Noh Park, *Goyang*

Chang Min Park, *Seoul*

Sung Bin Park, *Seoul*

Deuk Jae Sung, *Seoul*

Choongsoo Shin, *Seoul*

Kwon-Ha Yoon, *Iksan*



Spain

Miguel A De Gregorio, *Zaragoza*

Antonio Luna, *Jaén*

Enrique Marco de Lucas, *Santander*

Fernando Ruiz Santiago, *Granada*



Sweden

Dmitry Grishenkov, *Stockholm*

Tie-Qiang Li, *Stockholm*



Switzerland

Nicolau Beckmann, *Basel*

Christian Boy, *Bern*

Giorgio Treglia, *Bellinzona*

Stephan Ulmer, *Kiel*



Thailand

Sirianong Namwongprom, *Chiang Mai*



Turkey

Kubilay Aydin, *Istanbul*

Ramazan Akdemir, *Sakarya*

Serhat Avcu, *Ankara*

Ayşe Aralasmak, *Istanbul*

Oktay Algin, *Ankara*

Nevbahar Akcar, *Meselik*

Bilal Battal, *Ankara*

Zulkif Bozgeyik, *Elazig*

Nazan Ciledag, *Aakara*

Fuldem Y Donmez, *Ankara*

Gulgun Engin, *Istanbul*

Ahmet Y Goktay, *Izmir*

Oguzhan G Gumustas, *Bursa*

Kaan Gunduz, *Ankara*

Pelin Ozcan Kara, *Mersin*

Kivanc Kamburoglu, *Ankara*

Ozgur Kilickesmez, *Istanbul*

Furuzan Numan, *Istanbul*

Cem Onal, *Adana*

Ozgur Oztekin, *Izmir*

Seda Ozbek (Boruban), *Konya*

Selda Sarikaya, *Zonguldak*

Figen Taser, *Kutahya*

Baran Tokar, *Eskisehir*

Ender Uysal, *Istanbul*

Ensar Yekeler, *Istanbul*



United Kingdom

Indran Davagnanam, *London*

M DC Valdés Hernández, *Edinburgh*

Alan Jackson, *Manchester*

Suneil Jain, *Belfast*

Long R Jiao, *London*

Miltiadis Krokidis, *Cambridge*

Pradesh Kumar, *Liverpool*

Peter D Kuzmich, *Derby*

Georgios Plataniotis, *Brighton*

Vanessa Sluming, *Liverpool*



United States

Garima Agrawal, *Saint Louis*

James R Brasic, *Baltimore*

Rajendra D Badgaiyan, *Buffalo*

Ulas Bagci, *Bethesda*

Anat Biegon, *Stony Brook*

Ramon Casanova, *Winston Salem*

Wenli Cai, *Boston*

Zheng Chang, *Durham*

Corey J Chakarun, *Long Beach*

Kai Chen, *Los Angeles*

Hyun-Soon Chong, *Chicago*

Marco Cura, *Dallas*

Ravi R Desai, *Bensalem*

Delia DeBuc, *Miami*

Carlo N De Cecco, *Charleston*

Timm-Michael L Dickfeld, *Baltimore*

Subba R Digumarthy, *Boston*

Huy M Do, *Stanford*

Todd A Faasse, *Grand Rapids*

Salomao Faintuch, *Boston*

Girish M Fatterpekar, *New York*

Dhakshinamoorthy Ganesan, *Houston*

Robert J Griffin, *Little Rock*

Andrew J Gunn, *Boston*

Sandeep S Hedgire, *Boston*

Timothy J Hoffman, *Columbia*

Mai-Lan Ho, *San Francisco*

Juebin Huang, *Jackson*

Abid Irshad, *Charleston*

Matilde Inglese, *New York*

El-Sayed H Ibrahim, *Jacksonville*

Paul R Julsrud, *Rochester*

Pamela T Johnson, *Baltimore*

Ming-Hung Kao, *Tempe*

Sunil Krishnan, *Houston*

Richard A Komoroski, *Cincinnati*

Sandi A Kwee, *Honolulu*

King Kim, *Ft. Lauderdale*

Guozheng Liu, *Worcester*

Yiyan Liu, *Newark*

Venkatesh Mani, *New York*

Lian-Sheng Ma, *Pleasanton*

Rachna Madan, *Boston*

Zeyad A Metwalli, *Houston*

Yilong Ma, *Manhasset*

Hui Mao, *Atlanta*

Feroze B Mohamed, *Philadelphia*

Gul Moonis, *Boston*

John L Noshier, *New Brunswick*

Rahmi Oklu, *Boston*

Aytekun Oto, *Chicago*

Bishnuhari Paudyal, *Philadelphia*

Rajul Pandya, *Youngstown*

Chong-Xian Pan, *Sacramento*

Jay J Pillai, *Baltimore*

Neal Prakash, *Duarte*

Reza Rahbar, *Boston*

Ali S Raja, *Boston*

Gustavo J Rodriguez, *El Paso*

David J Sahn, *Portland*

Steven Schild, *Scottsdale*

Ali R Sepahdari, *Los Angeles*

Li Shen, *Indianapolis*

JP Sheehan, *Charlottesville*

Atul B Shinagare, *Boston*

Sarabjeet Singh, *Boston*

Charles J Smith, *Columbia*

Kenji Suzuki, *Chicago*

Monvadi Srichai-Parsia, *Washington*

Sree H Tirumani, *Boston*

Hebert A Vargas, *New York*

Sachit Verma, *Philadelphia*

Yoichi Watanabe, *Minneapolis*

Li Wang, *Chapel Hill*

Carol C Wu, *Boston*

Shoujun Xu, *Houston*

Min Yao, *Cleveland*

Xiaofeng Yang, *Atlanta*

Qingbao Yu, *Albuquerque*

Aifeng Zhang, *Chicago*

Chao Zhou, *Bethlehem*

Hongming Zhuang, *Philadelphia*

**EDITORIAL**

- 87 Dento-maxillofacial radiology as a specialty
Kamburoğlu K

REVIEW

- 89 "To-and-fro" waveform in the diagnosis of arterial pseudoaneurysms
Mahmoud MZ, Al-Saadi M, Abuderman A, Alzimami KS, Alkhorayef M, Almagli B, Sulieman A

CASE REPORT

- 100 Silver nitrate mimicking a foreign body in the pharyngeal mucosal space
Livingstone D, Alghonaim Y, Jowett N, Sela E, Mlynarek A, Forghani R
- 104 Diagnosis of prostatic neuroendocrine carcinoma: Two cases report and literature review
He HQ, Fan SF, Xu Q, Chen ZJ, Li Z

ABOUT COVER

Editorial Board Member of *World Journal of Radiology*, Yi-Zhuo Li, MD, PhD, Associate Professor, Imaging Diagnosis and Minimally Invasive Interventional Center, State Key Laboratory of Oncology in Southern China, Cancer Center, Sun Yat-Sen University, Collaborative Innovation Center for Cancer Medicine, Guangzhou 510060, Guangdong Province, China

AIM AND SCOPE

World Journal of Radiology (*World J Radiol*, *WJR*, online ISSN 1949-8470, DOI: 10.4329) is a peer-reviewed open access academic journal that aims to guide clinical practice and improve diagnostic and therapeutic skills of clinicians.

WJR covers topics concerning diagnostic radiology, radiation oncology, radiologic physics, neuroradiology, nuclear radiology, pediatric radiology, vascular/interventional radiology, medical imaging achieved by various modalities and related methods analysis. The current columns of *WJR* include editorial, frontier, diagnostic advances, therapeutics advances, field of vision, mini-reviews, review, topic highlight, medical ethics, original articles, case report, clinical case conference (clinicopathological conference), and autobiography.

We encourage authors to submit their manuscripts to *WJR*. We will give priority to manuscripts that are supported by major national and international foundations and those that are of great basic and clinical significance.

INDEXING/ABSTRACTING

World Journal of Radiology is now indexed in PubMed Central, PubMed, Digital Object Identifier, and Directory of Open Access Journals.

FLYLEAF

I-III Editorial Board

EDITORS FOR THIS ISSUE

Responsible Assistant Editor: *Xiang Li*
Responsible Electronic Editor: *Su-Qing Liu*
Proofing Editor-in-Chief: *Lian-Sheng Ma*

Responsible Science Editor: *Xue-Mei Gong*
Proofing Editorial Office Director: *Xiu-Xia Song*

NAME OF JOURNAL
World Journal of Radiology

ISSN
ISSN 1949-8470 (online)

LAUNCH DATE
December 31, 2009

FREQUENCY
Monthly

EDITORS-IN-CHIEF
Kai U Juergens, MD, Associate Professor, MRT und PET/CT, Nuklearmedizin Bremen Mitte, ZEMODI - Zentrum für morphologische und molekulare Diagnostik, Bremen 28177, Germany

Edwin JR van Beek, MD, PhD, Professor, Clinical Research Imaging Centre and Department of Medical Radiology, University of Edinburgh, Edinburgh EH16 4TJ, United Kingdom

Thomas J Vogl, MD, Professor, Reader in Health Technology Assessment, Department of Diagnostic and Interventional Radiology, Johann Wolfgang

Goethe University of Frankfurt, Frankfurt 60590, Germany

EDITORIAL OFFICE
Jin-Lei Wang, Director
Xiu-Xia Song, Vice Director
World Journal of Radiology
Room 903, Building D, Ocean International Center, No. 62 Dongsihuan Zhonglu, Chaoyang District, Beijing 100025, China
Telephone: +86-10-59080039
Fax: +86-10-85381893
E-mail: editorialoffice@wjnet.com
Help Desk: <http://www.wjnet.com/esps/helpdesk.aspx>
<http://www.wjnet.com>

PUBLISHER
Baishideng Publishing Group Inc
8226 Regency Drive,
Pleasanton, CA 94588, USA
Telephone: +1-925-223-8242
Fax: +1-925-223-8243
E-mail: bpgoffice@wjnet.com
Help Desk: <http://www.wjnet.com/esps/helpdesk.aspx>
<http://www.wjnet.com>

PUBLICATION DATE
May 28, 2015

COPYRIGHT
© 2015 Baishideng Publishing Group Inc. Articles published by this Open-Access journal are distributed under the terms of the Creative Commons Attribution Non-commercial License, which permits use, distribution, and reproduction in any medium, provided the original work is properly cited, the use is non commercial and is otherwise in compliance with the license.

SPECIAL STATEMENT
All articles published in journals owned by the Baishideng Publishing Group (BPG) represent the views and opinions of their authors, and not the views, opinions or policies of the BPG, except where otherwise explicitly indicated.

INSTRUCTIONS TO AUTHORS
Full instructions are available online at http://www.wjnet.com/1949-8470/g_info_20100316162358.htm.

ONLINE SUBMISSION
<http://www.wjnet.com/esps/>

Dento-maxillofacial radiology as a specialty

Kıvanç Kamburoğlu

Kıvanç Kamburoğlu, Department of Dentomaxillofacial Radiology, Faculty of Dentistry, Ankara University, 06560 Ankara, Turkey

Author contributions: Kamburoğlu K wrote the paper.

Conflict-of-interest: Kamburoğlu K declares no conflict of interest.

Open-Access: This article is an open-access article which was selected by an in-house editor and fully peer-reviewed by external reviewers. It is distributed in accordance with the Creative Commons Attribution Non Commercial (CC BY-NC 4.0) license, which permits others to distribute, remix, adapt, build upon this work non-commercially, and license their derivative works on different terms, provided the original work is properly cited and the use is non-commercial. See: <http://creativecommons.org/licenses/by-nc/4.0/>

Correspondence to: Kıvanç Kamburoğlu, DDS, MSc, PhD, Associate Professor, Department of Dentomaxillofacial Radiology, Faculty of Dentistry, Ankara University, Döğol Caddesi, 06560 Ankara, Turkey. dkivo@yahoo.com

Telephone: +90-312-2965632

Fax: +90-312-2123954

Received: November 7, 2014

Peer-review started: November 8, 2014

First decision: January 8, 2015

Revised: January 12, 2015

Accepted: April 16, 2015

Article in press: April 20, 2015

Published online: May 28, 2015

Key words: Dentistry; Dento-maxillofacial radiology; Specialty

© The Author(s) 2015. Published by Baishideng Publishing Group Inc. All rights reserved.

Core tip: Dento-maxillofacial radiology is one of the dental specialties recognized under different names and divisions by around forty countries in the world. It includes, intra-oral imaging, dental panoramic imaging, cephalometric imaging, sialography, cone beam computed tomography (CT), multislice medical CT, ultrasonography, magnetic resonance imaging, positron emission tomography and nuclear medicine. All over the world, assigned committees work on the development of the training curriculum, determination of scientific and physical standards for institutions offering specialty training and arrangement of dental codes for reimbursement issues.

Kamburoğlu K. Dento-maxillofacial radiology as a specialty. *World J Radiol* 2015; 7(5): 87-88 Available from: URL: <http://www.wjgnet.com/1949-8470/full/v7/i5/87.htm> DOI: <http://dx.doi.org/10.4329/wjr.v7.i5.87>

Abstract

This editorial discusses a relatively new specialty in dental and medical field namely dentomaxillofacial radiology. As a relatively newborn specialty it is obvious that there is a long way to go before dentomaxillofacial radiology is commonly known and respected by the society. All over the world, assigned committees work on the development of the training curriculum, determination of scientific and physical standards for institutions offering specialty training and arrangement of dental codes for reimbursement issues. Furthermore, adjustment of educational, scientific and legal regulations and prospective benefits are expected to boost this specialty's attractiveness to colleagues' worldwide.

DENTO-MAXILLOFACIAL RADIOLOGY AS A SPECIALTY

Dento-maxillofacial radiology is one of the dental specialties recognized under different names and divisions by around forty countries in the world. Diagnostic imaging techniques have always been a tremendous asset in clinical dentistry. Since the early 1900s, dental faculties in developed world have been engaged in teaching Oral Radiology^[1]. It includes, intra-oral imaging, dental panoramic imaging, cephalometric imaging, sialography, cone beam computed tomography (CBCT), multislice medical computed tomography, ultrasonography (US), magnetic resonance imaging (MRI), positron emission tomography and Nuclear Medicine. Also, application of

computer aided and image guided procedures with Haptic and Robotic devices are in progress^[2]. In addition, visible light, optical coherence tomography, and terahertz imaging are other methods in use or under development^[3,4].

Intraoral imaging, continues to provide the best spatial resolution of any imaging method currently available. Also, panoramic radiography is a commonly used two-dimensional technique which gives the broad view of both jaws without the detail offered by the intraoral images. In response to the high demand for a technique that could provide three-dimensional data at a lower cost and with lower radiation doses than the conventional computed tomography used in medical radiology, CBCT was developed specifically for dento-maxillofacial imaging. A spate of revolutionary CBCT applications reached the dental market in the 2000s, marking the beginning of a new era in the field of dento-maxillofacial radiology. New technological specifications and settings include multiple field of views and voxels that can better address a variety of specific tasks. There are also several hybrid machines offering CBCT imaging along with panoramic and cephalometric radiography. CBCT has come into common use for a variety of purposes in the fields of endodontics, dental implantology, dento-maxillofacial surgery and orthodontics^[5].

On the other hand, scientists have also been searching for safer and comparable alternative imaging modalities to X-ray imaging due to increasing concerns regarding radiation dose and economic limitations. In this context, MRI and US were introduced and now widely utilized for a variety of tasks in medicine. MRI is a powerful and versatile imaging modality and most work in the field of dental MRI aimed at imaging soft tissues and imaging of the morphology and function of the temporomandibular joint^[6]. Recent development of the US equipment enables the visualization of fine detail of the surface structure of the oral and maxillofacial tissues without the use of ionizing radiation. In the field of dentistry, US technique can be used in clinical practice for bone and superficial soft tissue examination, major salivary gland or duct stone and salivary gland lesion detection, temporomandibular joint imaging, detection of fractures and vascular lesions, lymph node examination, measurement of the thickness of muscles and visualization of vessels of the neck including the carotid for atherosclerotic plaques. More recently, development of three-dimensional US imaging allowed multiplanar reformatting, volume rendering and color power doppler (CPD). In endodontics, CPD is used in the evaluation of periapical lesions and follow up of periapical bone healing and for differentiation between vital and root filled teeth. US imaging is also used to

guide fine-needle aspiration biopsy in the neck with the advantage of low cost, ease of usage and radiation safety. Ultrasound provides a number of advantages for dento-maxillofacial imaging when compared to other advanced imaging modalities such as; absence of harmful ionizing radiation, portability, possibility of dynamic and repeated examinations and relatively low cost^[7].

Depending on the imaged area, diagnostic images obtained from the dento-maxillofacial region may show part or the entire nasal cavity, paranasal sinuses, airway, cervical vertebrae and temporal bone. Finally, even when scans are taken for primarily unrelated reasons, assessment of the all imaged area, should always be performed in order to rule out any significant pathological changes. Incidental findings require follow-up, and further treatment options may be identified in conjunction with clinical findings, including referral to a specialist not directly linked to the field of dentistry, where appropriate.

As a relatively newborn specialty it is obvious that there is a long way to go before dento-maxillofacial radiology is commonly known and respected by the society. All over the world, assigned committees work on the development of the training curriculum, determination of scientific and physical standards for institutions offering specialty training and arrangement of dental codes for reimbursement issues. Furthermore, adjustment of educational, scientific and legal regulations and prospective benefits are expected to boost this specialty's attractiveness to colleagues' worldwide.

REFERENCES

- 1 **Ruprecht A.** The status of oral and maxillofacial radiology worldwide in 2007. *Dentomaxillofac Radiol* 2009; **38**: 98-103 [PMID: 19176652 DOI: 10.1259/dmfr/30358437]
- 2 **Morimoto Y**, Oda M, Kito S, Tanaka T, Wakasugi-Sato N, Matsumoto-Takeda S, Nishimura S, Koga H. Clinical Applications of Current and Advanced Diagnostic Imaging Modalities for Oral Diseases. *J Radiol Radiat Ther* 2014; **2**: 1027
- 3 **Kamburoğlu K**, Kurt H, Kolsuz E, Öztas B, Tatar I, Çelik HH. Occlusal caries depth measurements obtained by five different imaging modalities. *J Digit Imaging* 2011; **24**: 804-813 [PMID: 21116675 DOI: 10.1007/s10278-010-9355-9]
- 4 **Kamburoğlu K**, Yetimoğlu NÖ, Altan H. Characterization of primary and permanent teeth using terahertz spectroscopy. *Dentomaxillofac Radiol* 2014; **43**: 20130404 [PMID: 24940807 DOI: 10.1259/dmfr.20130404]
- 5 **Acar B**, Kamburoğlu K. Use of cone beam computed tomography in periodontology. *World J Radiol* 2014; **6**: 139-147 [PMID: 24876918 DOI: 10.4329/wjr.v6.i5.139]
- 6 **Yetimoglu NÖ**, Kamburoglu K. Magnetic Resonance Imaging in Dentistry. *OMICS J Radiology* 2014; **3**: e125 [DOI: 10.4172/2167-7964.1000e125]
- 7 **Kamburoğlu K**, Kursun ES. Applications of Ultrasonography in Dentistry. *OMICS J Radiology* 2013; **2**: e114 [DOI: 10.4172/2167-7964.1000e114]

P- Reviewer: Li YZ, Nohu MR, Vinh-Hung V **S- Editor:** Tian YL
L- Editor: A **E- Editor:** Liu SQ



"To-and-fro" waveform in the diagnosis of arterial pseudoaneurysms

Mustafa Z Mahmoud, Mohammed Al-Saadi, Abdulwahab Abuderman, Khalid S Alzimami, Mohammed Alkhorayef, Babikir Almagli, Abdelmoneim Sulieman

Mustafa Z Mahmoud, Mohammed Al-Saadi, Abdelmoneim Sulieman, Radiology and Medical Imaging Department, College of Applied Medical Sciences, Prince Sattam bin Abdulaziz University, Al-Kharj 11942, Saudi Arabia

Mustafa Z Mahmoud, Basic Medical Sciences Department, College of Medical Radiological Sciences, Sudan University of Science and Technology, Khartoum 11111, Sudan

Abdulwahab Abuderman, Basic Medical Sciences Department, College of Medicine, Prince Sattam bin Abdulaziz University, Al-Kharj 11942, Saudi Arabia

Khalid S Alzimami, Mohammed Alkhorayef, Radiological Sciences Department, College of Applied Medical Sciences, King Saud University, Riyadh 11433, Saudi Arabia

Babikir Almagli, Diagnostic Radiology Department, Faculty of Radiology and Nuclear Medicine, the National Ribat University, Khartoum 1111, Sudan

Author contributions: All authors contributed to this paper.

Supported by College of Applied Medical Sciences Research Center and the Deanship of Scientific Research at King Saud University, Riyadh, Saudi Arabia.

Conflict-of-interest: The authors declare that there is no conflict of interest.

Open-Access: This article is an open-access article which was selected by an in-house editor and fully peer-reviewed by external reviewers. It is distributed in accordance with the Creative Commons Attribution Non Commercial (CC BY-NC 4.0) license, which permits others to distribute, remix, adapt, build upon this work non-commercially, and license their derivative works on different terms, provided the original work is properly cited and the use is non-commercial. See: <http://creativecommons.org/licenses/by-nc/4.0/>

Correspondence to: Dr. Mustafa Z Mahmoud, Radiology and Medical Imaging Department, College of Applied Medical Sciences, Prince Sattam bin Abdulaziz University, PO Box 422, Al-Kharj 11942, Saudi Arabia. m.alhassen@sau.edu.sa

Telephone: +966-11-5886331

Fax: +966-11-5453852

Received: October 20, 2014

Peer-review started: October 20, 2014

First decision: December 12, 2014

Revised: March 6, 2015

Accepted: April 1, 2015

Article in press: April 7, 2015

Published online: May 28, 2015

Abstract

Medical ultrasound imaging with Doppler plays an essential role in the diagnosis of vascular disease. This study intended to review the clinical use of "to-and-fro" waveform at duplex Doppler ultrasonography (DDU) in the diagnosis of pseudoaneurysms in the arterial vessels of upper and lower extremities, abdominal aorta, carotid and vertebral arteries as well as to review our personal experiences of "to-and-fro" waveform at DDU also. After receiving institutional review board approval, an inclusive literature review was carried out in order to review the scientific foundation of "to-and-fro" waveform at DDU and its clinical use in the diagnosis of pseudoaneurysms in various arterial vessels. Articles published in the English language between 2000 and 2013 were evaluated in this review study. Pseudoaneurysms in arterial vessels of the upper and lower extremities, abdominal aorta, carotid and vertebral arteries characterized by an extraluminal pattern of blood flow, which shows variable echogenicity, interval complexity, and "to-and-fro" flow pattern on color Doppler ultrasonography. In these arterial vessels, Duplex ultrasonography can demonstrate the degree of clotting, pseudoaneurysm communication, the blood flow patterns and velocities. Spectral Doppler applied to pseudoaneurysms lumen revealed systolic and diastolic turbulent blood flow with traditional "to-and-fro" waveform in the communicating channel. Accurate diagnosis of pseudoaneurysm by spectral Doppler is based on the documentation of the "to-and-fro" waveform. The size of pseudoaneurysm determines the appropriate treatment approach as surgical or conservative.

Key words: Pseudoaneurysm; To-and-fro waveform; Ultrasonography; Percutaneous thrombin injection; Yin-Yang sign

© The Author(s) 2015. Published by Baishideng Publishing Group Inc. All rights reserved.

Core tip: A review of the clinical use of “to-and-fro” waveform at duplex Doppler ultrasonography (DDU) in the diagnosis of pseudoaneurysms in the arterial vessels of upper and lower extremities, abdominal aorta, carotid and vertebral arteries as well as to review our personal experiences of “to-and-fro” waveform at DDU also.

Mahmoud MZ, Al-Saadi M, Abuderman A, Alzimami KS, Alkhorayef M, Almagli B, Sulieman A. "To-and-fro" waveform in the diagnosis of arterial pseudoaneurysms. *World J Radiol* 2015; 7(5): 89-99 Available from: URL: <http://www.wjgnet.com/1949-8470/full/v7/i5/89.htm> DOI: <http://dx.doi.org/10.4329/wjcr.v7.i5.89>

INTRODUCTION

A pseudoaneurysm is defined as an arterial wall deficiency, which leads to accumulation of oxygenated blood in the nearby extra-luminal region. Therefore arterial blood spread out of the vessel, forming a sac surrounding by soft tissue and compressed thrombus^[1]. Consequently, a pseudoaneurysm is formed as a result of fibrin wall formation nearby the swelling^[2]. The basic difference of arterial aneurysm and pseudoaneurysm is that the three-layers of the arterial wall don't bind the later one^[3]. Pseudoaneurysms which are the most common in the femoral and radial arteries, often noticed in the groin and forearm after cardiac catheterization. Furthermore, it may observe also after arterial punctures of blood gas analysis, after the placement of indwelling catheter or after direct arterial trauma^[2-5].

Ultrasonography (US) has been widely utilized as a noninvasive imaging modality for the investigation of vascular diseases^[6-9]. US which is a valuable tool for diagnosis of pseudoaneurysms has been widely utilized as a noninvasive imaging modality for investigation of vascular disease. The main advantage of US imaging is no use of ionizing radiation, cheap, and availability^[10,11]. It has been reported that US has 94% and 97% of sensitivity and specificity, respectively in the diagnosis of postcatheterization pseudoaneurysms, but this sensitivity is not enough to diagnose the pseudoaneurysms of the deep visceral arteries^[12,13]. The major limitation of US it is an operator dependent imaging technique, has low sensitivity in the evaluation of deep visceral artery pseudoaneurysm, and evaluation of vessels in trauma patient accompanied with hematoma or fracture^[14].

In pseudoaneurysms, Analog US images (grayscale) usually illustrate hypoechoic cystic structures nearby a supplying artery^[15,16]. Grayscale can be used to evaluate many pseudoaneurysmal findings such as the size, the number of pseudoaneurysm, and its relation to the artery^[17]. However, grayscale is not a conclusive evidence in diagnosis pseudoaneurysm because its findings are accompanied by other clinical conditions such as hematomas and cystic masses either simple or

complex^[1].

Therefore, Doppler US can be used to confirm the diagnosis. In addition to that, blood flow in a cystic structure distinguished by swirling motion pattern “yin-yang sign”. Also, this type of flow can be detected in saccular aneurysm. Therefore, differential diagnosis is essential for pseudoaneurysm. The cornerstone of pseudoaneurysm diagnosis is dependent upon the appearance of the communicating neck between the arterial vessel and pseudoaneurysmal sac with “to-and-fro” waveform at duplex Doppler ultrasonography (DDU). The “to” represents the arterial blood going into the pseudoaneurysmal sac in systolic cycle, while “fro” illustrate blood exiting the sac in diastolic cycle^[18].

In this article authors review the clinical use of “to-and-fro” waveform at DDU in the diagnosis of pseudoaneurysms in various arterial vessels, as well as our personal experiences of “to-and-fro” waveform at DDU in the Radiology Department of King Fahad Medical City (KFMC) at Riyadh, Saudi Arabia.

LITERATURE SEARCH

After receiving institutional review board approval, an inclusive literature review was carried out in order to review the scientific foundation of “to-and-fro” waveform at DDU and its clinical use in the diagnosis of pseudoaneurysms in various arterial vessels of the upper and lower extremities, abdominal Aorta, carotid arteries and vertebral arteries.

The ScienceDirect, PubMed, MEDLINE, NCBI and SAGE database were searched in April 2014 for publications containing information about “to-and-fro” sign in the diagnosis of pseudoaneurysms in various arterial vessels in the title of the report. Abstracts resulting from this search were reviewed for relevance to the clinical outcomes from the procedure. Full manuscripts were retrieved and reviewed if they contained information regarding the evaluation of the evidence on the role of “to-and-fro” sign in the diagnosis of pseudoaneurysms and the published clinical literature in this field.

Only those papers published between 2000 and 2013 were included in the outcomes analysis, and this was due to the tremendous development in this medical diagnostic specialty at the beginning of the new millennium so far. Regarding place of the study or journal type in order to include all available sources of experience.

GENERAL SONOGRAPHIC FEATURES REGARDING ARTERIAL PSEUDOANEURYSMS

US is a readily available imaging modality, which does not expose the patient to ionizing radiation. Grayscale and color Doppler techniques are utilized, and standardized protocols in an accredited ultrasound

laboratory will increase the likelihood of detection of pseudoaneurysm. Grayscale is often initially performed. Linear (high frequency) US probe has acceptable depth penetration and visualization should be used. After a general overview of the area of concern, attention should be given to any anechoic collections or regions of hematoma^[19].

Color Doppler is placed in any anechoic collection to detect flow. The flow can be characterized if the scale is properly set to avoid aliasing due to under sampling. Spectral Doppler is then performed if flow is detected to help characterize arterial vs venous flow. Spectral waveforms may be diagnostic of the pseudoaneurysm and help to exclude arteriovenous fistula (AVF). A low wall filter may be initially used to detect slow flow, and the waveform should fill at least two-thirds of the spectral window. In grayscale, a patent pseudoaneurysm appears as an anechoic rounded or ovoid structure. Because other fluid collections, including cysts, seromas, or hematomas can have this appearance, color Doppler imaging is used to confirm the presence of blood flow within the pseudoaneurysm. When present, thrombus in the pseudoaneurysm appears mildly echogenic or hypoechoic without flow; it may be mural or centrally fill a portion of the pseudoaneurysm lumen^[1]. Turbulent blood flow is illustrated by interchangeable coloring appearance, either in red or blue color. If large areas of color aliasing are identified in the adjacent tissues, grayscale may help to differentiate pseudoaneurysm from tissue reverberation associated with AVF^[19].

The scientific foundation of "to-and-fro" waveform at DDU and its clinical use in the diagnosis of pseudoaneurysms in various arterial vessels, could be discussed on the basis that, the DDU monitoring will present the conventional "to-and-fro" waveform with blood flow of the bidirectional pattern at the neck of pseudoaneurysm. Occasionally, the neck is the only patent portion of the pseudoaneurysm if partial thrombosis has occurred^[19].

INCIDENCE OF PSEUDOANEURYSM IN THE PERIPHERAL ARTERIES, ABDOMINAL AORTA AND NECK ARTERIES

The incidence of pseudoaneurysms has increased in hospital based practice, due to the large number of invasive procedures performed^[20]. Their incidence varies in the literature due to different definitions, methods of interrogation and presence of certain complications^[21]. According to medical literature, the incidence of pseudoaneurysms ranges from 0.1% to 6% and up to 0.5% to 9%, depending on the diagnostic or therapeutic procedure performed^[22,23].

The frequency of peripheral arteries pseudoaneurysms is much less in the upper extremities than in the lower extremities (less than 2% of all lesions)^[24,25].

Aortic pseudoaneurysms are rare, life-threatening sequelae of cardiac surgery^[26]. The incidence, risk factors, and natural history of aortic pseudoaneurysm are unknown, because so few cases have been reported^[27]. Pseudoaneurysms of the abdominal aorta are rare, especially those found to be mycotic. Abdominal aorta pseudoaneurysms following trauma have been reported fairly often^[28]. Common carotid artery pseudoaneurysms are rare and potentially lethal, and adequate treatment is warranted in order to prevent rupture or neurologic sequelae^[29]. Vertebral arteries pseudoaneurysm formation after central line placement has been well documented in the literature, with an incidence rate of 0.05% to 2%^[30,31].

AETIOLOGY OF PSEUDOANEURYSM IN THE PERIPHERAL ARTERIES, ABDOMINAL AORTA AND NECK ARTERIES

Iatrogenic complication

Unintentional pseudoaneurysm due to surgical intervention for numerous medical procedure (e.g., pseudoaneurysm can be induced in femoral artery during cardiac catheterization). It accounts up to 70%-80% of the incidence of pseudoaneurysms^[32].

Trauma

It had been estimated that 79% of pseudoaneurysms are traumatic in origin of the internal solid organs such as liver, kidneys, pancreas, and gastrointestinal tract of the digestive system^[33].

Injury by tumor

Pseudoaneurysm can be initiated due to blood vessel erosion by an erosive tumor, either benign or malignant. This is most commonly seen in osteochondroma, neurofibromatosis, leukemia, and lymphoma^[34]. Yang *et al*^[35] reported that 25% of pseudoaneurysms are caused by neoplastic aneurysms as choriocarcinoma. Kim *et al*^[36] also reported leukemia and lymphoma as a cause of pseudoaneurysm by damaging the arterial vessel wall.

Infection

Pseudoaneurysm can be initiated by primary (wall infection) or secondary (adjacent focus) infection of blood vessels. It has been reported that pseudoaneurysms are more frequent in incidence than true aneurysms, this is because the infection can disturb blood vessels wall more easily^[37].

Vasculitis and inflammation

Formation of pseudoaneurysm in blood vessels is caused by destroying the elastic fibers of the media, induced by inflammation. The majority of pseudoaneurysms is caused by Behcet's syndrome, while pseudoaneurysms caused by primary vasculitis are not common in incidence^[38].

Atherosclerosis

Aortic pseudoaneurysms are caused by atherosclerotic ulcer due to disturbance of internal elastic lamina, which can lead to aortic rupture or aortic dissection^[39].

Infarction

Another cause of pseudoaneurysm is infarction of the left ventricle. It occurs due to separation of the left ventricle free wall enclosed by superimposing adherent pericardium, generated what has been named "pseudoaneurysm of the left ventricle"^[40].

MANAGEMENT OF PSEUDOANEURYSM IN THE PERIPHERAL ARTERIES, ABDOMINAL AORTA AND NECK ARTERIES

Surgical approach

The gold standard of pseudoaneurysm treatment in general is surgical intervention. The intervention includes arterial ligation, organectomy either partially or totally, and resection using bypass techniques. Surgical treatment is associated with increased morbidity and mortality as compared with minimally invasive treatment options. The complications associated with surgery include bleeding, infection, lymphocele formation, radiculopathy, perioperative myocardial infarction, and death^[41].

Endovascular approaches

Endovascular approaches to therapy offers distinct advantage to conventional surgical repair in patients with visceral pseudoaneurysms^[42]. Several endovascular techniques have been described to treat pseudoaneurysms. These techniques include catheter-guided embolization with use of coils or detachable balloons^[43,44]. Similar management principles are applied to management of aortic pseudoaneurysms^[45]. Compared to other techniques, endovascular procedures have lower morbidity and mortality rate in the management of pseudoaneurysm compared to surgical intervention^[19].

Percutaneous approach

Percutaneous US-guided thrombin injection is an important treatment option for the treatment of pseudoaneurysms. This approach appears to be a safe and expeditious method for treating postcatheterization femoral pseudoaneurysms. It has significant advantages with respect to ultrasound guided compression repair or surgical repair^[19]. Recently, the percutaneous thrombin injection was introduced for the treatment of iatrogenic pseudoaneurysm of femoral artery^[46,47].

In addition to that, this procedure can be used to treat arteries above the inguinal ligament and is considered as an alternative technique to US-guided compression in order to avoid arterial rupture^[48]. Complications of thrombin injection are uncommon, occurring in 0%-4%

of cases^[12]. Most reported complications involve the escape of thrombin into the native circulation, causing distal embolization. This occurs in as many as 2% of all patients treated^[41].

US-guided compression

US-guided compression of pseudoaneurysms is a safe and cost-effective method for achieving pseudoaneurysm thrombosis. However, it has been demonstrated that the success rate is higher and procedure time is much shorter for thrombin injection compared with US compression^[48]. Furthermore, compression of pseudoaneurysm is painful to the patient and time-consuming for the practitioner. US-guided compression is more likely to fail in a patient with anticoagulation, large pseudoaneurysm size, chronic pseudoaneurysm, and longer procedure time. The incidence of complications is small but they occasionally do occur^[19].

TO-AND-FRO WAVEFORM IN PSEUDOANEURYSMS OF UPPER EXTREMITY ARTERIAL VESSELS

The characteristic appearance of pseudoaneurysm in upper extremities arterial vessels is the extraluminal pattern of blood flow, which shows variable echogenicity, interval complexity, and "to-and-fro" flow pattern on color Doppler ultrasonography (CDUS)^[49,50]. It has been estimated that 2% to 3% of pseudoaneurysm in Subclavian artery occur due to blunt trauma, or injuries after clavicle fracture^[51].

Pseudoaneurysm of radial artery could be caused also as a result of bacterial infection at cannulation site^[8]. It has been considered that radial artery pseudoaneurysm is a rare pathological condition accounting and incidence of 0.048%^[52].

Rozen *et al*^[53] reported that pseudoaneurysm of radial artery are a common finding in patients with anticoagulated or patient under antiplatelet treatment. It's crucial to deliberate pseudoaneurysm diagnosis in any swelling that may presents swelling in order to avoid puncture or incision of the vessel because this swelling could be tender and warm^[54].

Several imaging modalities may be used to detect pseudoaneurysms in upper extremity arterial vessels, including conventional arteriography, computed tomography (CT) angiography, radionuclide angiography, and CDUS. US imaging is a diagnostic method of choice required to access pseudoaneurysm before US guided intervention is established for pseudoaneurysm of radial artery^[55,56]. CDUS is accurate, noninvasive imaging technique, and widely available. Therefore, it can be used to diagnose pseudoaneurysm of radial artery without even a side effect^[51,57,58]. US imaging procedure has the ability to differentiate between solid and cystic lesions adjacent to the radial artery in the wrist area^[53]. The sonographic appearance of the

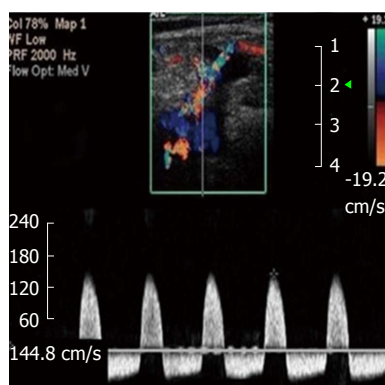


Figure 1 To-and-fro spectral waveform of a pseudoaneurysm; neck wasn't depicted^[65].

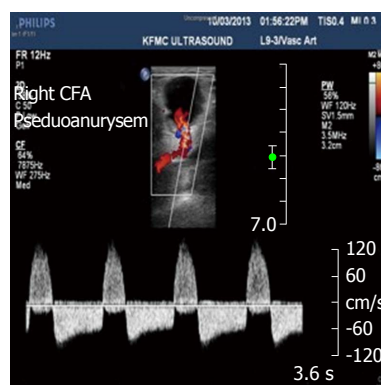


Figure 2 Right common femoral artery pseudoaneurysms associated with the characteristic findings of a pulsatile mass, a palpable thrill, and an audible "to-and-fro" murmur. CFA: Common femoral artery.

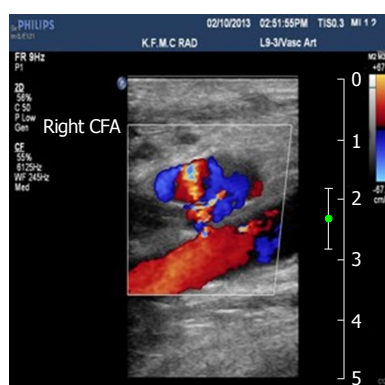


Figure 3 Pseudoaneurysm communicated with the right common femoral artery, and the blood flow patterns and velocities in the affected area. CFA: Common femoral artery.

radial artery characterized by a feature of sonolucent pulsatile tube^[59]. Spectral Doppler of the radial artery pseudoaneurysm is usually shown both "yin-yang" sign and "to-and-fro" waveform^[51,57,60].

A recent report describes the attempted repair of a brachial artery pseudoaneurysm in an infant that resulted in the thrombosis of the underlying brachial artery and an emergent thrombectomy^[61]. The light of the fact that neonates brachial artery injuries are uncommon, but induced by a brachial artery puncture. Therefore, this intervention is not recommended in neonates^[62]. In the literature induction of brachial artery pseudoaneurysm due to venipuncture was documented in two instances^[63]. Arterial injuries can be diagnosed promptly by using Duplex US imaging technique (Figure 1), without any further need for angiography^[64,65]. Also DDU can be up to 95% to 100% sensitive for diagnosing vascular injuries in the hands of highly qualified personnel with a high index of suspicion^[5].

TO-AND-FRO WAVEFORM IN PSEUDOANEURYSMS OF LOWER EXTREMITY ARTERIAL VESSELS

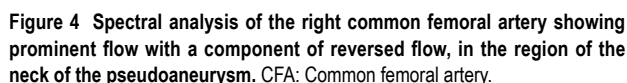
The incidence of pseudoaneurysm in lower extremity

arterial vessels was estimated to be ranged from 3.5%-5.5% and 0.1%-0.2% of the Interventional examination and diagnostic radiography, in that order^[66,67]. Femoral artery pseudoaneurysms are usually accompanied with a certain features of an audible "to-and-fro" pulsatile mass and touchable thrill (Figure 2). Duplex US of femoral artery (Figure 3) is the diagnostic method of choice for the diagnosis of Pseudoaneurysm^[67]. This imaging technique can reveal the blood flow waveform, blood clotting, and the relation with the femoral artery^[67].

The common femoral artery is the most frequent site of pseudoaneurysm in the lower extremities (Figure 4). This can be attributed to the localization of the common femoral artery inside the neurovascular sheet and it's supported by the head of the femur. Also the common femoral artery site is the place of choice to introduce cardiac catheterization. The incidence of pseudoaneurysm in the superficial femoral artery is less frequent in occurrence when compare with the common femoral artery because this artery is usually not selected for cardiac catheterization as a result of insufficient supportive tissue around it^[68,69].

Also popliteal artery is the most frequent region for pseudoaneurysm incidence because this artery is not supported by muscular tissue to shield it from dilatation and bending, compared to superficial and deep femoral arteries^[70]. Enlarging and pulsatile mass located in the popliteal artery are the common features of aneurysmal lesion^[70,71]. There are a similarity in diagnostic findings between popliteal artery mycotic pseudoaneurysm and other pseudoaneurysms on the basis of CDUS finding^[2,72].

Pseudoaneurysms of the anterior tibial artery and tibioperoneal trunk are exceedingly rare^[73,74]. Owen *et al*^[75] reported that pseudoaneurysms of the tibial arteries can be treated using percutaneous injection of thrombin and tissue adhesive. To prevent sudden incidence of a thrombosis in the native vessel, occlusion balloon can be used. An important study reported by Davis *et al*^[76] showed that pseudoaneurysm can be treated with percutaneous injection of thrombin at the posterior tibial and distal superficial femoral arteries. Pseudoaneurysm



can be formed during surgical replacement of the knee joint. This can occur either direct (intra-operative) or indirect (intimal plaque disruption)^[77].

Some studies reported that the incidence of pseudoaneurysms or aneurysms are rare in the dorsalis pedis artery and usually accompanied with trauma^[78-80]. Surgical intervention is preferred to reduce the risk of complication, such as ischemia, arterial rupture, and thrombosis^[80,81].

To differentiate between a hematoma and pseudoaneurysm in lower extremities arterial vessels, DDU can be used to establish the accurate diagnosis by demonstrating the relation between the injured artery and aneurysmal neck^[82]. In addition, triplex Doppler US can be used for diagnosis of pseudoaneurysm, by presenting “yin-yang” pattern. Bearing in mind that this pattern don’t usually differentiate between pseudoaneurysm and pulsating hematoma^[83].

The incidence of abdominal aneurysms has been established by Ertürk *et al*^[84] to be 1% of the overall abdominal aneurysms, concluding that pseudoaneurysms of abdominal aorta has a very low incidence. Pseudoaneurysms of the abdominal aorta are often diagnosed late or after catastrophic complications^[85]. Pseudoaneurysms of abdominal aorta caused by medical interventions, these interventions are abdominal surgery, Interventional guided by X-ray imaging of the abdomen, as a complication of abdominal aortic aneurysm, vasculitis, external abdominal trauma, and mycotic aneurysms. Pseudoaneurysms due to external abdominal trauma showed a high incidence in patients treated with anticoagulant or antiplatelet^[86].

Shanley *et al*^[87] reported that pseudoaneurysms could be developed in the majority of the visceral artery. A different incidence rate was noted in the splenic artery (46%), renal artery (22%), hepatic artery (16.2%),

Pseudoaneurysms also took place as a result of a combination of an artery impeded with the wall of pseudocysts^[91]. Gastroduodenal and splenic artery pseudoaneurysms are silent in the majority of cases, but in some cases, patients may experience upper abdominal pain or anemia due to bleeding in the gastrointestinal tract or peritoneal cavity^[92].

Pseudoaneurysms of splenic artery in different patients are caused by pancreatitis, either chronic or acute pancreatitis. The majority of these patients is characterized by a history of excessive alcohol consumption. The main cause of pseudoaneurysms formation by the aforementioned method is due to the digestion of splenic artery by pancreatic enzymes^[93]. Pseudoaneurysm development in the splenic artery due to blunt abdominal trauma had been reported by Sugg *et al*^[94]. Splenic artery slow blood flow is a predisposing factor of pseudoaneurysm as reported by Norotsky *et al*^[95]. In recent year's noninvasive procedure, therefore the incidence of pseudoaneurysm of splenic artery is increasing in incidence among patients^[96]. It has been reported that pseudoaneurysm may develop rarely due to peptic ulcer or as a result of iatrogenic causes. An a tiny number of patients developed pseudoaneurysm in the splenic artery without specific reasons^[10].

False aneurysms of the gastroduodenal artery can arise from an impairment in the integrity of the arterial wall, by direct injury *via* a biopsy needle, enzymatic digestion, as a result of pancreatitis, surgery, or trauma^[97]. This defect can lead to the formation of an open communication between the lumen of the artery and its surroundings, which can have two fates. If no soft tissues surround the site of injury, hemorrhage into the peritoneal cavity can occur. The presence of surrounding soft tissue, conversely, can result in containment of the hematoma, which can be followed by fibrosis and enlargement^[98]. Pseudoaneurysms have been reported to spontaneous thrombosis, but this is a rare event occurring only under certain conditions^[99]. More often, the hematomas become unstable and rupture, being associated with a mortality rate of around 50%^[100].

Diagnosis of gastroduodenal and splenic pseudoaneurysm can be made with a number of imaging methods. Contrast-enhanced CT and Doppler sonography are widely used as noninvasive techniques in the diagnosis and monitoring of the lesion^[101,102]. On contrast-enhanced CT, a pseudoaneurysm appears as an eccentric mass with a well-defined region of central enhancement in the arterial phase. Doppler sonography shows a mass that generally has a well-defined, solid peripheral component composed of a thrombus and a central anechoic area of varying size. This cavity fills on color Doppler imaging and produces the typical "yin-yang" pattern of pseudoaneurysms anywhere in the body. A "to-and-fro" pattern at the neck of the lesion is confirmatory of a pseudoaneurysm.

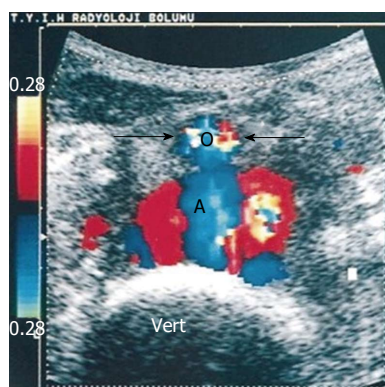


Figure 5 Transverse color Doppler sonogram shows turbulent flow in the pseudoaneurysm. Note the anterior displacement of the normal-sized aorta (arrows and AO) and the drape of the posterior wall of the pseudoaneurysm over the anterior aspect of the spine (vert)^[84].



Figure 6 Color Doppler sonogram showing the blood flow of the right common carotid artery, and the haematoma with the rotatory flow within its cavity (arrows). Note the large neck connecting the carotid to the pseudoaneurysm^[90].

Angiography remains the definitive modality used to diagnose, locate, and evaluate the presence of a gastroduodenal and splenic pseudoaneurysm^[101,102]. The advantage of this method is that it can be used in the treatment of the lesion as well. Angiography is useful in establishing confirmation of the diagnosis and in cases of an acute rupture or major gastrointestinal bleeding requiring immediate care^[93]. The sonographic appearance of abdominal aortic pseudoaneurysm is anechoic blood accumulation in a sac nearby within the artery. This accumulation can be detected by using color Doppler^[84]. Sonographic examination of patient using color duplex Doppler revealed a pattern of turbulent flow within pseudoaneurysm illustrated in (Figure 5). Whirlwind flow and “to-and-fro” waveform are seen in the neck of pseudoaneurysm also by using pulsed Doppler^[103].

The limitations of color duplex Doppler in the diagnosis of pseudoaneurysms are obese patients and the presence of excessive gasses in the bowel. Nevertheless ultrasound should be used to establish preliminary diagnosis, especially for patient with pulsatile abdominal masses^[84,104].

TO-AND-FRO WAVEFORM IN PSEUDOANEURYSMS OF CAROTID AND VERTEBRAL ARTERIES

Carotid and vertebral artery pseudoaneurysms are uncommon lesions that may occur as sequelae of blunt trauma, cancer or radiation necrosis, and mycotic infection^[104]. Although Doppler ultrasound is a noninvasive imaging procedure, more accurate imaging modalities have been developed such as magnetic resonance angiogram or angiography. However US is the imaging method of choice (Figure 6) to study the midcervical portion of the carotid or vertebral arteries^[105-107].

The degree of confidence is high in detection carotid (mid cervical region) and vertebral artery pseudoaneurysms. While the degree of confidence is low in the detection of an intrathoracic segment of the carotid and vertebral arteries^[108].

Duplex ultrasound is used on a routine basis to evaluate atherosclerotic lesions. The main findings include dissection, occlusion, pseudoaneurysms, and intimal flaps. Nemours studies used DDU reported that around 92%-100% sensitivity in detection of arterial lesions due to neck trauma^[109-111]. The contour of pseudoaneurysms affecting carotid arteries showed variable color flow, depending on the presence of thrombosis^[112], while swirling blood flow and “to-and-fro” pattern is shown by spectral Doppler^[113]. In common carotid arteries, ultrasound is an effective means of diagnosing a pseudoaneurysm. It may also be used for serial follow the progression of these occurrences once they are diagnosed, as well as to aid in treatment in certain cases^[114]. When investigated internal carotid artery pseudoaneurysm by color Doppler it shows swirling of blood flow within the pseudoaneurysm with a communicating channel of the parent artery (yin-yang phenomenon), while pulse Doppler shows “to-and-fro” waveforms^[115].

Vertebral artery pseudoaneurysms typically present over the course of several days as a pulsatile mass. Duplex US is used to define the size of the pseudoaneurysms. Adequate visualization of the pseudoaneurysms neck of lesions arising vertebral arteries is limited owing to the overlying clavicle. Angiography is often indicated in order to precisely define the site of injury^[30]. However, US examination of vertebral artery pseudoaneurysms is necessary in uncertain or difficult case from the beginning because it is convenient and sensitive in follow-up evaluation^[116].

CONCLUSION

In conclusion, this review study showed that gray scale and Doppler ultrasound play an essential role in the diagnosis of pseudoaneurysms. The use of spectral Doppler in the diagnosis of pseudoaneurysms depends upon the presence of “to-and-fro” waveform. Incidence

of arterial pseudoaneurysms are varied in the different body vasculature. Also the choice of pseudoaneurysms treatment is size dependent.

ACKNOWLEDGMENTS

The authors extend their appreciation to the College of Applied Medical Sciences Research Center and the Deanship of Scientific Research at King Saud University for funding this research. In addition, the authors would like to thank the staff of the Radiology Department at KFMC at Riyadh, Saudi Arabia for their cooperation and support during data collection for this article.

REFERENCES

- 1 **Saad NE**, Saad WE, Davies MG, Waldman DL, Fultz PJ, Rubens DJ. Pseudoaneurysms and the role of minimally invasive techniques in their management. *Radiographics* 2005; **25** Suppl 1: S173-S189 [PMID: 16227490 DOI: 10.1148/rg.25si055503]
- 2 **Pellerito JS**, Taylor KJ. Doppler color imaging. Peripheral arteries. *Clin Diagn Ultrasound* 1992; **27**: 97-112 [PMID: 1386746]
- 3 **Zierler RE**, Zierler BK. Duplex sonography of lower extremity arteries. *Semin Ultrasound CT MR* 1997; **18**: 39-56 [DOI: 10.1016/S0887-2171(97)90037-8]
- 4 **Pozniak MA**, Mitchell C, Ledwidge M. Radial artery pseudoaneurysm: a maneuver to decrease the risk of thrombin therapy. *J Ultrasound Med* 2005; **24**: 119-122 [PMID: 15615938]
- 5 **Levis JT**, Garmel GM. Radial artery pseudoaneurysm formation after cat bite to the wrist. *Ann Emerg Med* 2008; **51**: 668-670 [PMID: 18325629 DOI: 10.1016/j.annemergmed.2007.11.031]
- 6 **Pellerito JS**. Current approach to peripheral arterial sonography. *Radiol Clin North Am* 2001; **39**: 553-567 [DOI: 10.1016/S0033-8389(05)70297-9]
- 7 **Wang HK**, Chou YH, Chiou HJ, Chio SY, Chang CY. B-flow ultrasonography of peripheral vascular diseases. *J Med Ultrasound* 2005; **13**: 186-195 [DOI: 10.1016/S0929-6441(09)60108-9]
- 8 **Gudena R**, Khetan N. Swelling of volar aspect of the wrist. *Postgrad Med J* 2005; **81**: e9-e11 [DOI: 10.1136/pgmj.2004.028720]
- 9 **Zitsman JL**. Pseudoaneurysm after penetrating trauma in children and adolescents. *J Pediatr Surg* 1998; **33**: 1574-1577 [DOI: 10.1016/S0022-3468(98)90504-8]
- 10 **Tessier DJ**, Stone WM, Fowl RJ, Abbas MA, Andrews JC, Bower TC, Gloviczki P. Clinical features and management of splenic artery pseudoaneurysm: case series and cumulative review of literature. *J Vasc Surg* 2003; **38**: 969-974 [DOI: 10.1016/S0741-5214(03)00710-9]
- 11 **Katz DS**, Hon M. CT angiography of the lower extremities and aortoiliac system with a multi-detector row helical CT scanner: promise of new opportunities fulfilled. *Radiology* 2001; **221**: 7-10 [PMID: 11568315 DOI: 10.1148/radiol.2211011087]
- 12 **Morgan R**, Belli AM. Current treatment methods for post-catheterization pseudoaneurysms. *J Vasc Intervent Radiol* 2003; **14**: 697-710 [DOI: 10.1097/01.RV1.0000071089.76348.6A]
- 13 **Katyal S**, Oliver JH, Buck DG, Federle MP. Detection of vascular complications after liver transplantation: early experience in multislice CT angiography with volume rendering. *AJR Am J Roentgenol* 2000; **175**: 1735-1739 [PMID: 11090412 DOI: 10.2214/ajr.175.6.1751735]
- 14 **Soto JA**, Múnera F, Morales C, Lopera JE, Holguín D, Guarín O, Castrillón G, Sanabria A, García G. Focal arterial injuries of the proximal extremities: helical CT arteriography as the initial method of diagnosis. *Radiology* 2001; **218**: 188-194 [PMID: 11152800 DOI: 10.1148/radiology.218.1.r01ja13188]
- 15 **Crossin JD**, Muradali D, Wilson SR. US of liver transplants: normal and abnormal. *Radiographics* 2003; **23**: 1093-1114 [PMID: 12975502 DOI: 10.1148/rg.235035031]
- 16 **Kwon JH**, Kim GS. Obstetric iatrogenic arterial injuries of the uterus: diagnosis with US and treatment with transcatheter arterial embolization. *Radiographics* 2002; **22**: 35-46 [PMID: 11796896 DOI: 10.1148/radiographics.22.1.g02ja0735]
- 17 **Krüger K**, Zähringer M, Söhngen FD, Gossmann A, Schulte O, Feldmann C, Strohe D, Lackner K. Femoral pseudoaneurysms: management with percutaneous thrombin injections--success rates and effects on systemic coagulation. *Radiology* 2003; **226**: 452-458 [PMID: 12563139 DOI: 10.1148/radiol.2262012107]
- 18 **Polak JF**. The peripheral arteries. In: Rumack CM, Wilson SR, Charboneau JW. Diagnostic ultrasound. St Louis: Mosby, 1998: 921-941
- 19 **Kapoor BS**, Haddad HL, Saddekni S, Lockhart ME. Diagnosis and management of pseudoaneurysms: an update. *Curr Probl Diagn Radiol* 2009; **38**: 170-188 [PMID: 19464587 DOI: 10.1067/j.cpradiol.2008.11.001]
- 20 **Fransson SG**, Nylander E. Vascular injury following cardiac catheterization, coronary angiography, and coronary angioplasty. *Eur Heart J* 1994; **15**: 232-235 [PMID: 8005125]
- 21 **Kacila M**, Vranic H, Hadzimehmedagic A, Sehic S, Granov N. The frequency of complications of pseudoaneurysms after cardiac interventional diagnostic and therapeutic interventions. *Med Arh* 2011; **65**: 78-81 [PMID: 21585178]
- 22 **Görge G**, Kunz T, Kirstein M. [Non-surgical therapy of iatrogenic false aneurysms]. *Dtsch Med Wochenschr* 2003; **128**: 36-40 [PMID: 12510248 DOI: 10.1055/s-2003-36329]
- 23 **Righini M**, Quéré I, Laroche JP. [Treatment of postcatheterization femoral false aneurysms]. *J Mal Vasc* 2004; **29**: 63-72 [PMID: 15229401 DOI: 10.1016/S0398-0499(04)96717-0]
- 24 **Wielenberg A**, Borge MA, Demos TC, Lomasney L, Marra G. Traumatic pseudoaneurysm of the brachial artery. *Orthopedics* 2000; **23**: 1250, 1322-1324 [PMID: 11144492]
- 25 **Szendro G**, Goleman L, Klimov A, Yefim C, Johnatan B, Avrahami E, Yechieli B, Yurfest S. Arterial false aneurysms and their modern management. *Isr Med Assoc J* 2001; **3**: 5-8 [PMID: 11344804]
- 26 **Dhadwal AK**, Abrol S, Zisbrod Z, Cunningham JN. Pseudoaneurysms of the ascending aorta following coronary artery bypass surgery. *J Card Surg* 2006; **21**: 221-224 [PMID: 16684045 DOI: 10.1111/j.1540-8191.2006.00220.x]
- 27 **Garisto JD**, Medina A, Williams DB, Carrillo RG. Surgical management of a giant ascending aortic pseudoaneurysm. *Tex Heart Inst J* 2010; **37**: 710-713 [PMID: 21224953]
- 28 **Potts RG**, Alguire PC. Pseudoaneurysm of the abdominal aorta: a case report and review of the literature. *Am J Med Sci* 1991; **301**: 265-268 [PMID: 2012114 DOI: 10.1097/00000441-199104000-00008]
- 29 **Kim HO**, Ji YB, Lee SH, Jung C, Tae K. Cases of common carotid artery pseudoaneurysm treated by stent graft. *Case Rep Otolaryngol* 2012; **2012**: 674827 [PMID: 22953119 DOI: 10.1155/2012/674827]
- 30 **Bernik TR**, Friedman SG, Scher LA, Safa T. Pseudoaneurysm of the subclavian-vertebral artery junction--case report and review of the literature. *Vasc Endovascular Surg* 2002; **36**: 461-464 [PMID: 12476236 DOI: 10.1177/153857440203600607]
- 31 **Cihangiroglu M**, Rahman A, Yildirim H, Burma O, Uysal H. Iatrogenic vertebral artery pseudoaneurysm: US, CT and MRI findings. *Eur J Radiol* 2002; **43**: 14-18 [PMID: 12065115 DOI: 10.1016/S0720-048X(01)00451-X]
- 32 **Franklin JA**, Brigham D, Bogey WM, Powell CS. Treatment of iatrogenic false aneurysms. *J Am Coll Surg* 2003; **197**: 293-301 [PMID: 12892815 DOI: 10.1016/S1072-7515(03)00375-2]
- 33 **Feliciano DV**, Mattox KL. Traumatic aneurysms. In: Rutherford RB. Vascular surgery. Philadelphia: Saunders, 1989: 996-1003
- 34 **Smith BL**, Munschauer CE, Diamond N, Rivera F. Ruptured internal carotid aneurysm resulting from neurofibromatosis: treatment with intraluminal stent graft. *J Vasc Surg* 2000; **32**: 824-828 [PMID: 11013049 DOI: 10.1067/mva.2000.107769]
- 35 **Yang DM**, Yoon MH, Kim HS, Kim HS, Shin DB. Intrarenal pseudoaneurysms complicating renal choriocarcinoma metastases: treatment with coil embolization. *Clin Imaging* 2000; **24**: 217-220

- [PMID: 11274886 DOI: 10.1016/S0899-7071(00)00220-5]
- 36 **Kim MD**, Kim H, Kang SW, Jeong BG. Nontraumatic hepatic artery pseudoaneurysm associated with acute leukemia: a possible complication of pyogenic liver abscess. *Abdom Imaging* 2002; **27**: 458-460 [PMID: 12066246 DOI: 10.1007/s00261-001-0078-8]
- 37 **Gomes MN**, Choyke PL. Infected aortic aneurysms: CT diagnosis. *J Cardiovasc Surg (Torino)* 1992; **33**: 684-689 [PMID: 1287005]
- 38 **Ko GY**, Byun JY, Choi BG, Cho SH. The vascular manifestations of Behçet's disease: angiographic and CT findings. *Br J Radiol* 2000; **73**: 1270-1274 [PMID: 11205670 DOI: 10.1259/bjr.73.876.11205670]
- 39 **Macura KJ**, Corl FM, Fishman EK, Bluemke DA. Pathogenesis in acute aortic syndromes: aortic dissection, intramural hematoma, and penetrating atherosclerotic aortic ulcer. *AJR Am J Roentgenol* 2003; **181**: 309-316 [PMID: 12876003 DOI: 10.2214/ajr.181.2.1810309]
- 40 **Brown SL**, Gropler RJ, Harris KM. Distinguishing left ventricular aneurysm from pseudoaneurysm. A review of the literature. *Chest* 1997; **111**: 1403-1409 [PMID: 9149600 DOI: 10.1378/chest.111.5.1403]
- 41 **La Perna L**, Olin JW, Goines D, Childs MB, Ouriel K. Ultrasound-guided thrombin injection for the treatment of postcatheterization pseudoaneurysms. *Circulation* 2000; **102**: 2391-2395 [PMID: 11067794 DOI: 10.1161/01.CIR.102.19.2391]
- 42 **Tulsyan N**, Kashyap VS, Greenberg RK, Sarac TP, Clair DG, Pierce G, Ouriel K. The endovascular management of visceral artery aneurysms and pseudoaneurysms. *J Vasc Surg* 2007; **45**: 276-283; discussion 283 [PMID: 17264002 DOI: 10.1016/j.jvs.2006.10.049]
- 43 **Nicholson AA**, Patel J, McPherson S, Shaw DR, Kessel D. Endovascular treatment of visceral aneurysms associated with pancreatitis and a suggested classification with therapeutic implications. *J Vasc Interv Radiol* 2006; **17**: 1279-1285 [PMID: 16923974 DOI: 10.1097/01.RVI.0000231948.08617.04]
- 44 **Sharma RP**, Shetty PC, Burke TH, Shepard AD, Khaja F. Treatment of false aneurysm by using a detachable balloon. *AJR Am J Roentgenol* 1987; **149**: 1279-1280 [PMID: 3500621 DOI: 10.2214/ajr.149.6.1279]
- 45 **Mitchell JH**, Dougherty KG, Strickman NE, Mortazavi A, Krajcer Z. Endovascular repair of paraanastomotic aneurysms after aortic reconstruction. *Tex Heart Inst J* 2007; **34**: 148-153 [PMID: 17622359]
- 46 **Brophy DP**, Sheiman RG, Amatulle P, Akbari CM. Iatrogenic femoral pseudoaneurysms: thrombin injection after failed US-guided compression. *Radiology* 2000; **214**: 278-282 [PMID: 10644137 DOI: 10.1148/radiology.214.1.r00ja10278]
- 47 **Bydewell G**. Percutaneous thrombin injection for pseudoaneurysm treatment. *S Afr J Rad* 2013; **17**: 41-42 [DOI: 10.7196/SAJR.792]
- 48 **Paulson EK**, Sheafor DH, Kliewer MA, Nelson RC, Eisenberg LB, Sebastian MW, Sketch MH. Treatment of iatrogenic femoral arterial pseudoaneurysms: comparison of US-guided thrombin injection with compression repair. *Radiology* 2000; **215**: 403-408 [PMID: 10796916 DOI: 10.1148/radiology.215.2.r00ap35403]
- 49 **Eisenberg L**, Paulson EK, Kliewer MA, Hudson MP, DeLong DM, Carroll BA. Sonographically guided compression repair of pseudoaneurysms: further experience from a single institution. *AJR Am J Roentgenol* 1999; **173**: 1567-1573 [PMID: 10584803]
- 50 **Chiou HJ**, Chou YH, Chiou SY, Wang HK. High-resolution ultrasonography in superficial soft tissue tumors. *J Med Ultrasound* 2007; **15**: 152-174 [DOI: 10.1016/S0929-6441(08)60033-8]
- 51 **Falk PS**, Scuderi PE, Sherertz RJ, Motsinger SM. Infected radial artery pseudoaneurysms occurring after percutaneous cannulation. *Chest* 1992; **101**: 490-495 [PMID: 1735278 DOI: 10.1378/chest.101.2.490]
- 52 **Cozzi DA**, Morini F, Casati A, Pacilli M, Salvini V, Cozzi F. Radial artery pseudoaneurysm successfully treated by compression bandage. *Arch Dis Child* 2003; **88**: 165-166 [PMID: 12538327 DOI: 10.1136/adc.88.2.165]
- 53 **Rozen G**, Samuels DR, Blank A. The to and fro sign: the hallmark of pseudoaneurysm. *Isr Med Assoc J* 2001; **3**: 781-782 [PMID: 11692560]
- 54 **Barker C**, Jefferson P, Ball DR. Portable ultrasound to diagnose true radial artery aneurysm. *Anesth Analg* 2007; **105**: 890-891 [PMID: 17717274 DOI: 10.1213/01.ane.0000269691.81976.67]
- 55 **Gooding GA**. Sonography of the radial artery at the wrist. *AJR Am J Roentgenol* 1988; **150**: 629-631 [PMID: 3277353 DOI: 10.2214/ajr.150.3.629]
- 56 **Carrafiello G**, Laganà D, Mangini M, Recaldini C, Mandas X, Fugazzola C. Post-traumatic pseudoaneurysm of radial artery: percutaneous treatment with thrombin injection. *Injury Extra* 2006; **37**: 78-81 [DOI: 10.1016/j.injury.2005.08.012]
- 57 **Lennox A**, Griffin M, Nicolaides A, Mansfield A. Regarding "Percutaneous ultrasound guided thrombin injection: a new method for treating postcatheterization femoral pseudoaneurysms". *J Vasc Surg* 1998; **28**: 1120-1121 [PMID: 9917209 DOI: 10.1016/S0741-5214(98)70041-2]
- 58 **Davison BD**, Polak JF. Arterial injuries: a sonographic approach. *Radiol Clin North Am* 2004; **42**: 383-396 [PMID: 15136023 DOI: 10.1016/j.rcl.2004.01.007]
- 59 **Truong AT**, Thakar DR. Radial artery pseudoaneurysm: a rare complication with serious risk to life and limb. *Anesthesiology* 2013; **118**: 188 [DOI: 10.1097/ALN.0b013e318279f925]
- 60 **Landau D**, Schreiber R, Szendro G, Golcman L. Brachial artery pseudoaneurysm in a premature infant. *Arch Dis Child Fetal Neonatal Ed* 2003; **88**: F152-F153 [PMID: 12598507 DOI: 10.1136/fn.88.2.F152]
- 61 **Demircin M**, Peker O, Tok M, Ozen H. False aneurysm of the brachial artery in an infant following attempted venipuncture. *Turk J Pediatr* 1996; **38**: 389-391 [PMID: 8827913]
- 62 **Verlato F**, Zanon GF, Gamba PG, Verlato G, Rocco S, Orzali A, Camporese G, Signorini GP. Echo Doppler color flow (EDCF) evaluation of vascular pathology in pediatric age groups. *Int Angiol* 1996; **15**: 321-327 [PMID: 9127773]
- 63 **Dzepina I**, Unusic J, Mijatovic D, Bulic K. Pseudoaneurysms of the brachial artery following venipuncture in infants. *Pediatr Surg Int* 2004; **20**: 594-597 [PMID: 15338170 DOI: 10.1007/s00383-004-1238-z]
- 64 **Gullo J**, Singletary EM, Larese S. Emergency bedside sonographic diagnosis of subclavian artery pseudoaneurysm with brachial plexopathy after clavicle fracture. *Ann Emerg Med* 2013; **61**: 204-206 [PMID: 22762908 DOI: 10.1016/j.annemergmed.2012.05.037]
- 65 **Pero T**, Herrick J. Pseudoaneurysm of the radial artery diagnosed by bedside ultrasound. *West J Emerg Med* 2009; **10**: 89-91 [PMID: 19561825]
- 66 **Goel PK**, Modi N, Baijal SS, Kathuria M, Agrawal SK. Sonographically guided thrombin injection for the treatment of femoral artery pseudoaneurysm. *Indian Heart J* 2003; **55**: 365-367 [PMID: 14686668]
- 67 **Kronzon I**. Diagnosis and treatment of iatrogenic femoral artery pseudoaneurysm: a review. *J Am Soc Echocardiogr* 1997; **10**: 236-245 [DOI: 10.1016/S0894-7317(97)70061-0]
- 68 **Fellmeth BD**, Roberts AC, Bookstein JJ, Freischlag JA, Forsythe JR, Buckner NK, Hye RJ. Postangiographic femoral artery injuries: nonsurgical repair with US-guided compression. *Radiology* 1991; **178**: 671-675 [PMID: 1994400 DOI: 10.1148/radiology.178.3.1994400]
- 69 **Demirbas O**, Batyraliev T, Eksi Z, Pershukov I. Femoral pseudoaneurysm due to diagnostic or interventional angiographic procedures. *Angiology* 2005; **56**: 553-556 [PMID: 16193193 DOI: 10.1177/000331970505600505]
- 70 **Sadler L**, Bolden RO, Lenkey JL. Diagnosis of a ruptured deep femoral artery aneurysm--a case report. *Angiology* 1989; **40**: 678-681 [PMID: 2742211 DOI: 10.1177/000331978904000711]
- 71 **Harman M**, Irmak H, Arslan H, Arslan U, Kayan M. Popliteal artery pseudoaneurysm: a rare complication of brucellosis. *J Clin Ultrasound* 2004; **32**: 33-36 [PMID: 14705176 DOI: 10.1002/jcu.10217]
- 72 **Murashita T**, Yasuda K, Takigami T, Sakuma M, Matsui Y, Sasaki S, Shiiya N. Mycotic aneurysm of the bilateral tibioperoneal trunks associated with bacterial endocarditis: a case report. *Int Angiol* 1997; **16**: 176-179 [PMID: 9405011]
- 73 **Cappendijk VC**, Mouthaan PJ. A true aneurysm of the tibioperoneal trunk. Case report and literature review. *Eur J Vasc Endovasc Surg*

- 1999; **18**: 536-537 [PMID: 10637155 DOI: 10.1053/ejvs.1999.0938]
- 74 **McKee MA**, Ballard JL. Mycotic aneurysms of the tibioperoneal arteries. *Ann Vasc Surg* 1999; **13**: 188-190 [PMID: 10072460 DOI: 10.1007/s100169900240]
- 75 **Owen RJ**, Haslam PJ, Elliott ST, Rose JD, Loose HW. Percutaneous ablation of peripheral pseudoaneurysms using thrombin: a simple and effective solution. *Cardiovasc Intervent Radiol* 2000; **23**: 441-446 [PMID: 11232891 DOI: 10.1007/s002700010101]
- 76 **Davis KA**, Mansour MA, Kang SS, Labropoulos N, Esposito TJ, Silver GM, Reed RL. Pseudoaneurysms of the extremity without fracture: treatment with percutaneous ultrasound-guided thrombin injection. *J Trauma* 2000; **49**: 818-821 [PMID: 11086770 DOI: 10.1097/00005373-200011000-00005]
- 77 **Law KY**, Cheung KW, Chiu KH, Antonio GE. Pseudoaneurysm of the geniculate artery following total knee arthroplasty: a report of two cases. *J Orthop Surg (Hong Kong)* 2007; **15**: 386-389 [PMID: 18162694]
- 78 **McKee TI**, Fisher JB. Dorsalis pedis artery aneurysm: case report and literature review. *J Vasc Surg* 2000; **31**: 589-591 [DOI: 10.1067/mva.2000.102130]
- 79 **Tempest HV**, Wilson YG. Acute forefoot ischaemia: an unreported complication of dorsalis pedis artery aneurysm. *Eur J Vasc Endovasc Surg* 2001; **22**: 472-473 [PMID: 11735189 DOI: 10.1053/ejvs.2001.1486]
- 80 **Taylor DT**, Mansour MA, Bergin JT, Reyes CV, Stuck RM. Aneurysm of the dorsalis pedis artery -- a case report. *Vasc Endovascular Surg* 2002; **36**: 241-245 [PMID: 12075392 DOI: 10.1177/153857440203600314]
- 81 **Ozdemir H**, Mahmutyazicioğlu K, Ozkökeli M, Savranlar A, Ozer T, Demirel F. Pseudoaneurysm of the dorsalis pedis artery: color Doppler sonographic and angiographic findings. *J Clin Ultrasound* 2003; **31**: 283-287 [PMID: 12767024 DOI: 10.1002/jcu.10164]
- 82 **Abu-Yousef MM**, Wiese JA, Shamma AR. The „to-and-fro“ sign: duplex Doppler evidence of femoral artery pseudoaneurysm. *AJR Am J Roentgenol* 1988; **150**: 632-634 [PMID: 3277354 DOI: 10.2214/ajr.150.3.632]
- 83 **Carroll BA**, Graif M, Orron DE. Vascular ultrasound. In: Kim DS, Orron DE. Peripheral vascular imaging and intervention. St. Louis: Mosby, 1992: 211-225.
- 84 **Ertürk H**, Erden A, Yurdakul M, Calikoğlu U, Olçer T, Cumhuri T. Pseudoaneurysm of the abdominal aorta diagnosed by color duplex Doppler sonography. *J Clin Ultrasound* 1999; **27**: 202-205 [DOI: 10.1002/(SICI)1097-0096(199905)27:4<202::AID-JCU7>3.3.CO;2-5]
- 85 **van Herwaarden JA**, Waasdorp EJ, Bendermacher BL, van den Berg JC, Teijink JA, Moll FL. Endovascular repair of paraanastomotic aneurysms after previous open aortic prosthetic reconstruction. *Ann Vasc Surg* 2004; **18**: 280-286 [PMID: 15354628 DOI: 10.1007/s10016-004-0002-0]
- 86 **Siegel CL**, Cohan RH. CT of abdominal aortic aneurysms. *AJR Am J Roentgenol* 1994; **163**: 17-29 [PMID: 8010207 DOI: 10.2214/ajr.163.1.8010207]
- 87 **Shanley CJ**, Shah NL, Messina LM. Uncommon splanchnic artery aneurysms: pancreaticoduodenal, gastroduodenal, superior mesenteric, inferior mesenteric, and colic. *Ann Vasc Surg* 1996; **10**: 506-515 [PMID: 8905073 DOI: 10.1007/BF02000601]
- 88 **Deterling RA Jr**. Aneurysm of the visceral arteries. *J Cardiovasc Surg (Torino)* 1997; **12**: 309-322 [PMID: 5171538]
- 89 **White AF**, Baum S, Buranasiri S. Aneurysms secondary to pancreatitis. *AJR Am J Roentgenol* 1976; **127**: 393-396 [PMID: 183522 DOI: 10.2214/ajr.127.3.393]
- 90 **Walter JF**, Chuang VP, Bookstein JJ, Reuter SR, Cho KJ, Pulmano CM. Angiography of massive hemorrhage secondary to pancreatic diseases. *Radiology* 1977; **124**: 337-342 [PMID: 301642 DOI: 10.1148/124.2.337]
- 91 **Friedman AC**. Radiology of the liver, biliary tract, pancreas and spleen. Baltimore: Williams and Wilkins, 1987: 674
- 92 **Stanley JC**, Zelenock GB. Splanchnic artery aneurysms. In: Rutherford RB. Vascular surgery. Philadelphia: W.B. Saunders Company, 1995: 1124-1128
- 93 **Golzarian J**, Nicaise N, Devière J, Ghysels M, Wery D, Dussaussois L, Van Gansbeke D, Struyven J. Transcatheter embolization of pseudoaneurysms complicating pancreatitis. *Cardiovasc Intervent Radiol* 1997; **20**: 435-440 [PMID: 9354712 DOI: 10.1007/s002709900189]
- 94 **Sugg SL**, Gerndt SJ, Hamilton BJ, Francis IR, Taheri PA, Rodriguez JL. Pseudoaneurysms of the intraparenchymal splenic artery after blunt abdominal trauma: a complication of nonoperative therapy and its management. *J Trauma* 1995; **39**: 593-595 [PMID: 7473932 DOI: 10.1097/00005373-199509000-00034]
- 95 **Norotsky MC**, Rogers FB, Shackford SR. Delayed presentation of splenic artery pseudoaneurysms following blunt abdominal trauma: case reports. *J Trauma* 1995; **38**: 444-447 [PMID: 7897735 DOI: 10.1097/00005373-199503000-00029]
- 96 **Davis KA**, Fabian TC, Croce MA, Gavant ML, Flick PA, Minard G, Kudsk KA, Pritchard FE. Improved success in nonoperative management of blunt splenic injuries: embolization of splenic artery pseudoaneurysms. *J Trauma* 1998; **44**: 1008-1013; discussion 1013-1015 [PMID: 9637156 DOI: 10.1097/00005373-199806000-00013]
- 97 **Parildar M**, Oran I, Memis A. Embolization of visceral pseudoaneurysms with platinum coils and N-butyl cyanoacrylate. *Abdom Imaging* 2003; **28**: 36-40 [PMID: 12483381 DOI: 10.1007/s00261-002-0021-7]
- 98 **Bergan J**, Yao J. Aneurysms: Diagnosis and Treatment. New York: Grune and Stratton, 1982
- 99 **Vanlangenhove P**, Defreyne L, Kunnen M. Spontaneous thrombosis of a pseudoaneurysm complicating pancreatitis. *Abdom Imaging* 1999; **24**: 491-493 [PMID: 10475934 DOI: 10.1007/s002619900546]
- 100 **Stanley JC**, Wakefield TW, Graham LM, Whitehouse WM, Zelenock GB, Lindenaue SM. Clinical importance and management of splanchnic artery aneurysms. *J Vasc Surg* 1986; **3**: 836-840 [PMID: 3701947 DOI: 10.1016/0741-5214(86)90059-5]
- 101 **Gabelmann A**, Görich J, Merkle EM. Endovascular treatment of visceral artery aneurysms. *J Endovasc Ther* 2002; **9**: 38-47 [PMID: 11958324 DOI: 10.1583/1545-1550(2002)009<0038:ETOVA>2.0.CO;2]
- 102 **Pilleul F**, Dugougeat F. Transcatheter embolization of splanchnic aneurysms/pseudoaneurysms: early imaging allows detection of incomplete procedure. *J Comput Assist Tomogr* 2002; **26**: 107-112 [PMID: 11801912 DOI: 10.1097/00004728-200201000-00016]
- 103 **González Llorente J**, Gallego Gallego M, Martínez Arnaiz A. Chronic post-traumatic pseudoaneurysm of the abdominal aorta diagnosed by duplex Doppler ultrasonography. A case report. *Acta Radiol* 1997; **38**: 121-123 [PMID: 9059414 DOI: 10.1080/02841859709171254]
- 104 **Chaikof EL**, Shamberger RC, Brewster DC. Traumatic pseudoaneurysms of the abdominal aorta. *J Trauma* 1985; **25**: 169-173 [PMID: 3882976 DOI: 10.1097/00005373-198502000-00018]
- 105 **Maras D**, Lioupis C, Magoufis G, Tsamopoulos N, Moulakakis K, Andrikopoulos V. Covered stent-graft treatment of traumatic internal carotid artery pseudoaneurysms: a review. *Cardiovasc Intervent Radiol* 2006; **29**: 958-968 [PMID: 16897263 DOI: 10.1007/s00270-005-0367-7]
- 106 **Flor N**, Sardanelli F, Ghilardi G, Tentori A, Franceschelli G, Felisati G, Cornalba GP. Common carotid artery pseudoaneurysm after neck dissection: colour Doppler ultrasound and multidetector computed tomography findings. *J Laryngol Otol* 2007; **121**: 497-500 [PMID: 17140463 DOI: 10.1017/S0022215106005342]
- 107 **Nebelsieck J**, Sengelhoff C, Nassenstein I, Maintz D, Kühlenbäumer G, Nabavi DG, Ringelstein EB, Dittich R. Sensitivity of neurovascular ultrasound for the detection of spontaneous cervical artery dissection. *J Clin Neurosci* 2009; **16**: 79-82 [PMID: 19017557 DOI: 10.1016/j.jocn.2008.04.005]
- 108 **Kochan JP**, Kanamalla US. Imaging in carotid and vertebral artery dissection. Medscape serial online, 2013-07-24, cited 2014-04-10; 1(1): 7 screens. Available from: URL: <http://emedicine.medscape.com/article/417341-overview#showall>
- 109 **Montalvo BM**, LeBlang SD, Nuñez DB, Ginzburg E, Klose KJ,

- Becerra JL, Kochan JP. Color Doppler sonography in penetrating injuries of the neck. *AJNR Am J Neuroradiol* 1996; **17**: 943-951 [PMID: 8733972]
- 110 **Ginzberg E**, Montalvo B, LeBlang S, Nunez D, Martin L. The use of duplex ultrasonography in penetrating neck trauma. *Arch Surg* 1996; **131**: 691-693 [DOI: 10.1001/archsurg.1996.01430190013002]
- 111 **Demetriades D**, Theodorou D, Cornwell E, Berne TV, Asensio J, Belzberg H, Velmahos G, Weaver F, Yellin A. Evaluation of penetrating injuries of the neck: prospective study of 223 patients. *World J Surg* 1997; **21**: 41-47; discussion 47-48 [PMID: 8943176 DOI: 10.1007/s002689900191]
- 112 **LeBlang SD**, Nu-ez DB Jr, Rivas LA, Falcone S, Pogson SE. Helical computed tomographic angiography in penetrating neck trauma. *Emerg Radiol* 1997; **4**: 200-206 [DOI: 10.1007/BF01508171]
- 113 **LeBlang SD**, Nunez DB. Noninvasive imaging of cervical vascular injuries. *AJR Am J Roentgenol* 2000; **174**: 1269-1278 [PMID: 10789775 DOI: 10.2214/ajr.174.5.1741269]
- 114 **Scalf TC**, Drose JA. Ultrasound diagnosis of a common carotid artery pseudoaneurysm. *J Diagn Med Sonogr* 2000; **16**: 202-204 [DOI: 10.1177/875647930001600505]
- 115 **Ramesh A**, Muthukumarassamy R, Karthikeyan VS, Rajaraman G, Mishra S. Pseudoaneurysm of internal carotid artery after carotid body tumor excision. *Indian J Radiol Imaging* 2013; **23**: 208-211 [PMID: 24347849 DOI: 10.4103/0971-3026.120264]
- 116 **Lu CJ**, Sun Y, Jeng JS, Huang KM, Hwang BS, Lin WH, Chen RC, Yip PK. Imaging in the diagnosis and follow-up evaluation of vertebral artery dissection. *J Ultrasound Med* 2000; **19**: 263-270 [PMID: 10759350]

P- Reviewer: Aydogdu O, Seicean A **S- Editor:** Song XX
L- Editor: A **E- Editor:** Liu SQ



Silver nitrate mimicking a foreign body in the pharyngeal mucosal space

Devon Livingstone, Yazeed Alghonaim, Nathan Jowett, Eyal Sela, Alex Mlynarek, Reza Forghani

Devon Livingstone, Department of Otolaryngology–Head and Neck Surgery, University of Calgary, Calgary, Alberta T2N 2T9, Canada

Yazeed Alghonaim, Nathan Jowett, Eyal Sela, Alex Mlynarek, Department of Otolaryngology–Head and Neck Surgery, McGill University, Montreal, Quebec H3A 1A1, Canada
Reza Forghani, Department of Radiology, Sir Mortimer B. Davis Jewish General Hospital and McGill University, Montreal, Quebec H3T 1E2, Canada

Author contributions: All authors contributed to this manuscript.
Ethics approval: The study was reviewed and approved by the Institutional Review Board of the Jewish General Hospital and informed consent was waived.

Informed consent: The study was reviewed and approved by the Institutional Review Board of the Jewish General Hospital and informed consent was waived.

Conflict-of-interest: The authors do not have any conflict of interest to declare pertaining to this manuscript.

Open-Access: This article is an open-access article which was selected by an in-house editor and fully peer-reviewed by external reviewers. It is distributed in accordance with the Creative Commons Attribution Non Commercial (CC BY-NC 4.0) license, which permits others to distribute, remix, adapt, build upon this work non-commercially, and license their derivative works on different terms, provided the original work is properly cited and the use is non-commercial. See: <http://creativecommons.org/licenses/by-nc/4.0/>

Correspondence to: Reza Forghani, MD, PhD, Associate Chief, Assistant Professor of Radiology, Department of Radiology, Sir Mortimer B. Davis Jewish General Hospital and McGill University, Room C-210.2, 3755 Cote Ste-Catherine Road, Montreal, Quebec H3T 1E2, Canada. rforghani@jgh.mcgill.ca
Telephone: +1-514-3408222

Received: December 24, 2014

Peer-review started: December 26, 2014

First decision: January 8, 2015

Revised: February 9, 2015

Accepted: April 1, 2015

Article in press: April 7, 2015

Published online: May 28, 2015

cauterization for control of minor bleeding and management of hypergranulation tissue following bedside head and neck procedures. There are only few reports available on the imaging appearance of silver nitrate and its potential to mimic a foreign body. We report a case of a patient presenting with dysphagia, odynophagia, and fever following dental work who had a peritonsillar incision and drainage for treatment of a deep neck space infection. During the procedure, silver nitrate was applied to halt the bleeding. Patient was subsequently transferred to another institution. Since the patient was not showing significant clinical improvement on antibiotic therapy, a computed tomography (CT) scan was performed demonstrating a hyperdense structure lodged in the pharyngeal mucosal space in the oropharynx and soft palate that was mistaken for a foreign body such as bone. Silver nitrate can have density similar to bone but does not have the normal architecture of bone with cortex and marrow on CT. Familiarity with the appearance of silver nitrate on CT, lack of bone architecture, and proper documentation and communication of the use of silver nitrate to the consultant radiologist and medical personnel could help avoid misdiagnosis and potentially unnecessary surgical exploration.

Key words: Silver nitrate; Computed tomography; Bony foreign body; Soft tissues neck; Deep neck infections; Pharyngeal mucosal space

© **The Author(s) 2015.** Published by Baishideng Publishing Group Inc. All rights reserved.

Core tip: This manuscript describes the imaging features of silver nitrate on computed tomography (CT). Silver nitrate is sometimes used as a means of chemical cauterization during bedside head and neck procedures. Silver nitrate has high attenuation on CT and has the potential to mimic a radio-opaque foreign body such as bone. However, it does not have the normal architecture of bone with cortex and marrow on CT. Familiarity with the appearance of silver nitrate on CT and proper communication of its use to the consultant radiologist

Abstract

Silver nitrate is sometimes used as a means of chemical

could help avoid misinterpretation as a foreign body on imaging.

Livingstone D, Alghonaim Y, Jowett N, Sela E, Mlynarek A, Forghani R. Silver nitrate mimicking a foreign body in the pharyngeal mucosal space. *World J Radiol* 2015; 7(5): 100-103 Available from: URL: <http://www.wjgnet.com/1949-8470/full/v7/i5/100.htm> DOI: <http://dx.doi.org/10.4329/wjr.v7.i5.100>

INTRODUCTION

Silver nitrate is a form of chemical cautery commonly used for control of minor hemorrhage in the head and neck and in the management of hypergranulation tissue. Only few case reports describe the radiographic appearance of silver nitrate and its potential for imitation of a foreign body. We report a case of silver nitrate residue within the pharyngeal mucosal space in the oropharynx and soft palate imitating a foreign body on computed tomography (CT) imaging. Knowledge of the radiographic appearance of silver nitrate as well communication and documentation of its use can help prevent misdiagnosis as a foreign body and unnecessary surgical exploration.

CASE REPORT

A 52-year-old man presented to an outside emergency department with dysphagia, odynophagia, and fever following recent dental work. On examination, the patient was febrile with a temperature of 38.6 °C and swelling and tenderness of the anterior triangle of the neck on the left. A CT scan of the neck was performed, demonstrating phlegmon involving the pharyngeal mucosal space and parapharyngeal space including phlegmon in the peritonsillar region with only minimal areas of liquefaction (Figure 1). Complete blood count demonstrated an elevated white count with left shift. An outside consultant incised the peritonsillar space to rule out a peritonsillar abscess. Intravenous antibiotic therapy was initiated, and the patient was transferred to our service the following day.

Forty eight hours later, the patient showed no significant improvement and therefore a repeat CT scan of the neck was performed. The scan demonstrated a linear hyperdense structure with irregular margins along the pharyngeal mucosal space in the oropharynx and soft palate (Figure 2). The density of the structure was between approximately 380 and 580 Hounsfield units. The possibility of a foreign body, such as a chicken bone, was entertained based on the appearance, even though typical bone architecture with cortex and medulla was not identified. The patient's clinical history was, however, inconsistent with ingested foreign body impaction and its location was somewhat unusual. Furthermore, there was no sign of a foreign body on direct visualization. A thorough review of the management at the outside

hospital was then performed, revealing that silver nitrate had been applied at the time of the peritonsillar incision for control of minor bleeding. A presumptive diagnosis of hyperdensity secondary to silver nitrate application was then made, supported by a literature review and identification of a few case reports describing that silver nitrate can be radiopaque on X-ray^[1-3]. The patient's outside CT scan obtained prior to peritonsillar incision was then obtained and revised at our institution, revealing no evidence of a foreign body. This confirmed that silver nitrate was the source of the hyperdense structure. Conservative management with intravenous antibiotic therapy and observation was continued. The patient's symptoms resolved, and he was discharged 5 d following admission.

DISCUSSION

This report presents a case of a patient with a surgically explored pharyngeal mucosal space and peritonsillar region phlegmon who was not responding to treatment with the radiologic diagnosis confounded by silver nitrate application imitating a foreign body.

Infection of deep neck spaces can result in life threatening complications including airway compromise, sepsis, acute respiratory distress syndrome, jugular vein thrombosis, mediastinitis, disseminated intravascular coagulation, and death^[4]. Foreign body trauma to the pharynx, dental infections, and oral surgical procedures are all known to initiate deep neck infections. CT scan is currently considered the gold standard imaging modality in the setting of a deep space neck infection. CT is widely available, can be obtained rapidly, and is helpful in identifying the etiology, establishing the extent of disease, and guiding the management of these patients.

Silver nitrate is an inorganic compound often used in emergency departments as topical chemical cautery due to its efficacy and ease of use. Silver nitrate is an oxidizing agent, producing free radicals and heat in aqueous solution, resulting in a necrosis and coagulation hemostasis^[5]. Silver nitrate has also been used as an antiseptic for centuries, and has been shown to have antibacterial properties^[6]. It is often used for coagulation of minor head and neck procedural bleeding. Importantly, silver nitrate is also radiopaque on X-ray^[1-3].

There is a general lack of published literature regarding the radiographic appearance of silver nitrate, particularly on cross-sectional imaging and in the head and neck. To the best of our knowledge, there are 3 case reports describing the radiodense appearance of silver nitrate on plain radiographs of the extremities^[1-3]. Madan *et al*^[2] described a case of silver nitrate mimicking a foreign body on plain radiographs of the foot, where manual exploration was done and no foreign body found. Healy *et al*^[1] reported two cases where silver nitrate was mistaken for a foreign body and/or dystrophic calcification on plain radiographs of the fingers^[1]. Finally, Tong *et al*^[3] reported a case of silver nitrate masquerading as an avulsion fracture or foreign body in the finger. The patient

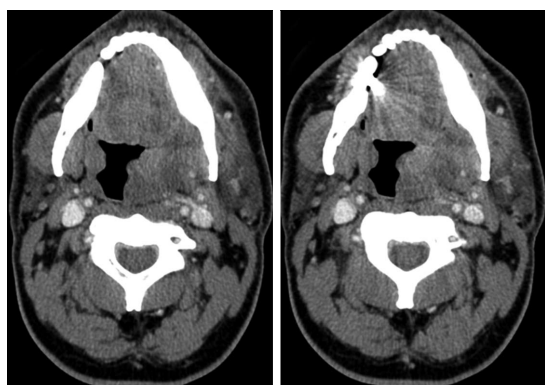


Figure 1 Axial computed tomography images at the level of the oropharynx prior to incision, drainage and silver nitrate application demonstrate swelling and enlargement of the left palatine tonsil and peritonsillar tissues with heterogeneous relatively low attenuation areas.

was managed conservatively and subsequent X-rays performed 2 wk later showed spontaneous resolution of the opacity. Our report appears to be the first case report describing the misleading appearance of silver nitrate both in terms of imaging modality (CT) and location in the soft tissues of the head and neck. In this case, we were able to avoid unnecessary pharyngeal exploration through careful analysis of the clinical context and CT images, supported by the limited medical literature on the topic.

This case highlights many important points. The use of silver nitrate in cauterizing soft tissue must be clearly documented and communicated to medical personnel, particularly in complex cases and those involving transfer of patient care to another institution. Furthermore, it is of special importance to communicate such history to the consultant radiologist. Although the lack of normal bone architecture in the hyperdensity reported raises the possibility of other etiologies as an imaging differential diagnosis, the provision of proper clinical information in such cases enables a much more confident diagnosis and helps avoid a misdiagnosis as a foreign body. This is of paramount importance in the context of pharyngeal mucosal space or parapharyngeal foreign bodies and deep space neck infections, where there is potential for unnecessary surgical exploration and associated morbidity for the patient. Given the widespread use of CT imaging in the evaluation and diagnosis of head and neck infections, it is important for radiologists and otolaryngologists to be familiar with the appearance of silver nitrate on CT and its potential to mimic radiodense foreign bodies and bone. Other imaging clues that may help avoid misdiagnosis include the absence of a typical bone structure such as cortex and medullary cavity.

COMMENTS

Case characteristics

Fifty five years old man transferred from another hospital post incision and drainage for a deep neck space infection who is not improving clinically on antibiotics.

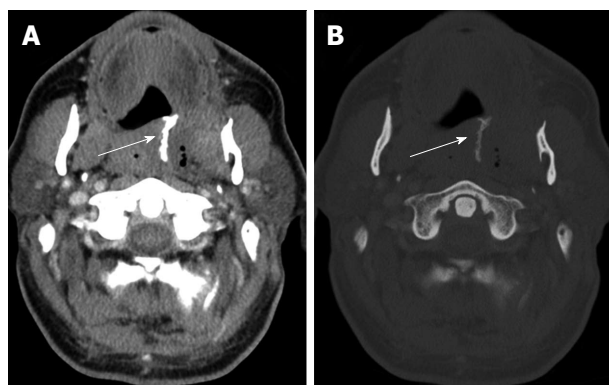


Figure 2 Axial computed tomography images from a scan performed 2 d after surgical exploration are shown, displayed in (A) soft tissue and (B) bone windows. The images demonstrate post-treatment changes with fluid and gas in the left palatine tonsil and peritonsillar region. In addition, there is a radiodense structure (arrow) in the pharyngeal mucosal space of the oropharynx and soft palate with density similar to bone, corresponding to the region of silver nitrate application. Note the absence of normal bone architecture such as cortex and medulla.

Clinical diagnosis

Persistent swelling and pain in the neck without obvious abscess or foreign body on physical exam.

Differential diagnosis

Slowly resolving infection, infection resistant to antibiotic regimen, or infection complicated by abscess or other etiology such as foreign body.

Laboratory diagnosis

White blood cell count $16.1 \times 10^9/L$.

Imaging diagnosis

Computed tomography (CT) scan demonstrated a hyperdense linear structure along the pharyngeal mucosal space in the oropharynx and soft palate with density ranging between approximately 380 and 580 Hounsfield units that was initially interpreted as a potential foreign body such as bone. Re-review of the CT scan revealed no evidence of typical bone architecture, the patient's clinical history was inconsistent with ingested foreign body, and there was no sign of a foreign body on direct visualization. A thorough review of the management at the outside hospital was then performed, revealing that silver nitrate had been applied at the time of the peritonsillar incision. The CT scan at the time of initial presentation was also subsequently obtained and did not demonstrate any evidence of foreign body prior to incision and drainage and application of silver nitrate.

Treatment

Conservative management with intravenous antibiotic therapy was continued and the patient's symptoms resolved and patient discharged 5 d following admission.

Related reports

There are only few reports in the literature on silver nitrate mimicking foreign body on X-rays in the extremities. To the best of our knowledge, there are no descriptions of silver nitrate in the neck or on CT.

Term explanation

Silver nitrate is an inorganic compound often used in emergency departments as topical chemical cautery and also used for coagulation of bleeding associated with minor head and neck procedures.

Experiences and lessons

Awareness of the imaging appearance of silver nitrate and its use can prevent false diagnosis as a foreign body.

Peer-review

It is a well written case report.

REFERENCES

- 1 Healy C, Canney M, Murphy A, Regan P. Silver nitrate mas-

- querading as a radiopaque foreign body. *Emerg Radiol* 2007; **14**: 63-64 [PMID: 17342469 DOI: 10.1007/s10140-006-0542-4]
- 2 **Madan SI**, Heilpern KL. Silver nitrate as a radiopaque foreign body. *J Emerg Med* 1999; **17**: 1045 [PMID: 10595894]
- 3 **Tong SHY**, Chan WL, Lee YL. Silver nitrate stain masquerading as an avulsion fracture of the finger. *Hong Kong J Emerg Med* 2011; **18**: 47-49
- 4 **Vieira F**, Allen SM, Stocks RM, Thompson JW. Deep neck infection. *Otolaryngol Clin North Am* 2008; **41**: 459-483, vii [PMID: 18435993]
- 5 **Barr GD**. Silver nitrate cautery and epistaxis. *Arch Emerg Med* 1989; **6**: 233 [PMID: 2789592]
- 6 **Spacciapoli P**, Buxton D, Rothstein D, Friden P. Antimicrobial activity of silver nitrate against periodontal pathogens. *J Periodontal Res* 2001; **36**: 108-113 [PMID: 11327077]

P- Reviewer: Kamburoglu K, Triantopoulou C **S- Editor:** Ji FF
L- Editor: A **E- Editor:** Liu SQ



Diagnosis of prostatic neuroendocrine carcinoma: Two cases report and literature review

Hai-Qing He, Shu-Feng Fan, Qiong Xu, Zhen-Jing Chen, Zheng Li

Hai-Qing He, Radiology Department, Enze Hospital, Taizhou 318000, Zhejiang Province, China

Hai-Qing He, Shu-Feng Fan, Zhen-Jing Chen, Radiology Department, Taizhou Hospital affiliated to Wenzhou Medical University, Linhai 317000, Zhejiang Province, China

Qiong Xu, Radiology Department, Women's Hospital School of Medicine Zhejiang University, HangZhou 310006, Zhejiang Province, China

Zheng Li, VIP Department, Taizhou Hospital affiliated to Wenzhou Medical University, Linhai 317000, Zhejiang Province, China

Author contributions: Fan SF conceived and designed the study, and made critical revisions related to important intellectual content of the manuscript; He HQ performed acquisition of data, analysis and interpretation of data; Xu Q and Chen ZJ drafted, reviewed and edited the manuscript; Li Z performed the survey, follow-up and summarize; all authors had read and approved the version of the article to be published.

Supported by Zhejiang Medical Science and Technology Program funded projects, No. 08B195.

Ethics approval: The study was reviewed and approved by the Taizhou Hospital (Linhai, Zhejiang Province, China) Institutional Review Board.

Informed consent: All study participants, or their legal guardian, provided informed written consent prior to study enrollment.

Conflict-of-interest: All authors of the paper declare having no conflicting interests (including but not limited to commercial, personal, political, intellectual, or religious interests) in the title page that are related to the work submitted for consideration of publication.

Open-Access: This article is an open-access article which was selected by an in-house editor and fully peer-reviewed by external reviewers. It is distributed in accordance with the Creative Commons Attribution Non Commercial (CC BY-NC 4.0) license, which permits others to distribute, remix, adapt, build upon this work non-commercially, and license their derivative works on different terms, provided the original work is properly cited and the use is non-commercial. See: <http://creativecommons.org/licenses/by-nc/4.0/>

Correspondence to: Shu-Feng Fan, MD, Radiology Department, Taizhou Hospital affiliated to Wenzhou Medical University, #150 Ximen Street, Linhai 317000, Zhejiang Province, China. shufengfan@163.com

Telephone: +86-576-85199360

Fax: +86-576-85199876

Received: January 2, 2015

Peer-review started: January 7, 2015

First decision: March 20, 2015

Revised: April 24, 2015

Accepted: April 28, 2015

Article in press: April 30, 2015

Published online: May 28, 2015

Abstract

Two cases of prostatic neuroendocrine carcinoma (PNEC) imaged by computed tomography (CT) and magnetic resonance imaging (MRI), and literature review are presented. Early enhanced CT, MRI, especially diffusion-weighted image were emphasized, the complementary roles of ultrasound, CT, MRI, clinical and laboratory characteristic's features in achieving accurate diagnosis were valued in the preoperative diagnosis of PNEC.

Key words: Magnetic resonance imaging; Computed tomography; Neuroendocrine carcinoma; Diagnosis; Prostate

© **The Author(s) 2015.** Published by Baishideng Publishing Group Inc. All rights reserved.

Core tip: Prostatic neuroendocrine carcinoma (PNEC) comprised 0.5%-2% of all prostate carcinoma, commonly presents with lymph node, bone, or organ metastases and has a poor prognosis when a definite diagnosis was given in clinic. Our cases and literature suggest it is usually insufficient that the prostate is examined by ultrasound and computed tomography (CT), or prostate specific antigen in serum for the symptomatic and/or with high risk factors crowd. Emphasizing the complementary roles of the malignant signs in diffusion-weighted image, early enhancement in CT or magnetic resonance imaging, self-contradictory clinical appearance and laboratory results can help achieving the accurate diagnosis of PNEC, maybe in early stage.

He HQ, Fan SF, Xu Q, Chen ZJ, Li Z. Diagnosis of prostatic neuroendocrine carcinoma: Two cases report and literature review. *World J Radiol* 2015; 7(5): 104-109 Available from: URL: <http://www.wjgnet.com/1949-8470/full/v7/i5/104.htm> DOI: <http://dx.doi.org/10.4329/wjcr.v7.i5.104>

INTRODUCTION

According to the World Health Organization 2004 lung tumor classification, neuroendocrine carcinoma (NEC) was classified as carcinoid tumors, high-grade neuroendocrine carcinoma, small cell neuroendocrine carcinoma, and mixed tumors. Prostatic NEC (PNEC) comprised 0.5%-2% of all prostate carcinoma, commonly presents with lymph nodes, bone, or organ metastases and has a poor prognosis when a definite diagnosis was given in clinic^[1-4]. Despite some clinical reports in the literature on the management of PNEC, there are limited articles describing its imaging features and diagnosis. To improve the preoperative diagnosis of PNEC, especially in its early stage, we review the related literature, and present two cases of PNEC with imaging, clinical, laboratory and pathologic findings, all showing metastasis at the time of diagnosis.

The study was approved by the Ethics Committee of Taizhou Hospital (Linhai, Zhejiang Province, China). Written informed consent was obtained from the patient's family.

CASE REPORT

Case 1

A 78-year-old male patient presented with pollakisuria and an episode of painless gross hematuria for about six-month duration. The patient had no family history of prostate cancer. Rectal examination outlined an irregularly enlarged prostate with an endured right lobe firmer than normal. In laboratory examination, prostate specific antigen (PSA) in serum at admission was within the normal range (0.2 ng/mL). In urine analysis, hemoglobin of 4.3 g/dL and red blood cells were found, while acid and alkaline phosphatase level was within normal range.

Ultrasonography showed an irregularly enlarged prostate size of 7.1 cm × 7.5 cm × 6.7 cm with inhomogeneous hypoechoic-isoechoic appearance. The diagnosis of ultrasonography was reported as prostatic hyperplasia. Computed tomography (CT) (Figure 1A and B) scans and magnetic resonance imaging (MRI) (Figure 1C and E) of pelvic revealed the prostate was approximately 6.5 cm × 7.5 cm × 7.2 cm in size with an irregular border and multiple enlarged lymph nodes in the pelvic region. CT images demonstrated the mass was slightly low density with small necrosis in the center region. The solid part enhanced obviously in contrast enhanced CT scanning, while the necrosis part did not. In MR examination, the solid part of the lesion appeared

as slightly low signal on T1WI, while higher signal on T2WI and diffusion-weighted image (DWI), its ADC value was $0.860 \pm 0.130 \text{ mm}^2/\text{s}$. Abdominal CT, chest CT and/or lumbar MRI revealed several metastases in two lungs, liver, and multiple lumbar vertebrae (Figure 1F and H).

Based on the findings of laboratory examination, CT, MRI and literature review, a preferred diagnosis was offered that it was PNEC with pulmonary, hepatic, spine and lymph nodes metastasis.

To confirm the diagnosis in pathology, a biopsy of the enlarged prostate was performed. Microscopic finding showed infiltrating nests of small cell in the fibrotic stroma, the tumor cells of which had small hyperchromatic nuclei and scanty cytoplasm, Gleason 3 + 4 (Figure 2). In immunohistochemical staining, the lesion were positive for CgA and CD56, negative for PSA, which was consistent with small cell neuroendocrine carcinoma (Figure 3).

Systemic chemotherapy was offered to the patient but he refused it because of personal reasons. To palliate symptoms of the tumor and metastatic lesions, radiotherapy of 300 cGy/d for 10 d was carried out on the prostate, pelvic region and lumbar vertebrae. He died 7 mo after diagnosis.

Case 2

A 72-year-old male patient presented with one month of dysuria. Sonography showed the prostate enlarged to 4.0 cm × 5.1 cm × 4.2 cm with incomplete envelope, irregular shape and heterogeneous echo texture (Figure 4A). The serum level of PSA was within the normal range (0.73 ng/mL). CT scans of pelvic revealed the boundaries of increased prostate were unclear with bladder, seminal vesicle, and multiple enlarged lymph nodes in the retroperitoneal region (Figure 4B). In contrast enhanced CT scanning, obvious enhancement parts of enlarged prostate and lymph nodes were showed in arterial phase (Figure 4C and D). Chest and abdominal CT were obtained to check the other organs of the body, and found no evidence of lesions. CT signs suggested a diagnosis of prostatic malignant tumor accompanied by lymphatic metastasis. A preferred diagnosis of PNEC with lymph nodes metastasis was offered.

A biopsy of the prostate mass was adopted to confirm the diagnosis in pathology. Pathologic analysis of the fully sampled prostate and adjacent areas identified small cell carcinoma (Figure 5A, Gleason score 4 + 3 = 7), immunohistochemical studies (Figure 5B and D) showed positive staining with Syn(++), CgA(++), CD56(++), CK(+), AR(+++), and negative with CK20(-), PSA(-).

To remit and relieve symptoms of the tumor and metastatic lymph nodes, radiotherapy and systemic chemotherapy were carried out on the prostate and pelvic region. He survived for longer than the first case and died 29 mo after diagnosis.

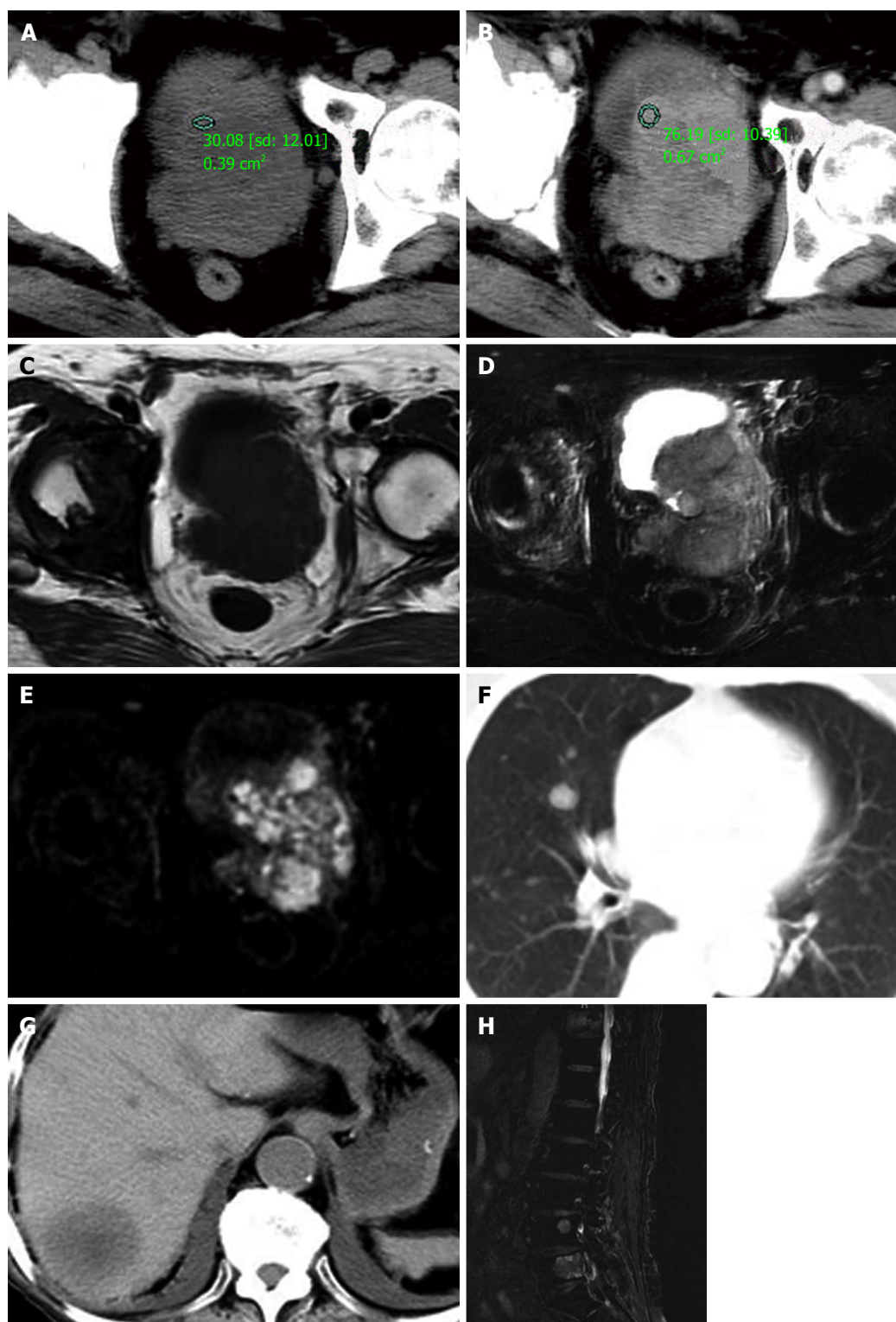


Figure 1 The diagnosis. Precontrast (A) and postcontrast (B) computed tomography (CT) images show the prostate approximately 6.5 cm × 7.5 cm × 7.2 cm in size with an irregular border and small necrosis in the center region, the solid part enhanced obviously in arterial phase of contrast enhancement CT scanning. T1-weighted image (T1WI, C) show the lesion to be slightly heterogeneous low signal intensity, T2WI (D), and diffusion-weighted image (E) show the same region to be heterogeneous hyperintense. Chest (F), abdominal (G) CT and lumbar (H) magnetic resonance imaging revealed multiple metastases to lungs, liver, and lumbar vertebrae.

DISCUSSION

PNEC, most identical to small cell carcinomas in clinic, is rare with different presentations and mostly diagnosed at the advanced stage by biopsy or surgery and generally

believed to have a high metastatic potential and a poor prognosis^[3-5]. Preoperative diagnosis, especially at the early stage of PNCE, may be helpful for surgery, adjuvant therapy and improving prognosis though it is difficult separately dependent on clinical, laboratory or imaging

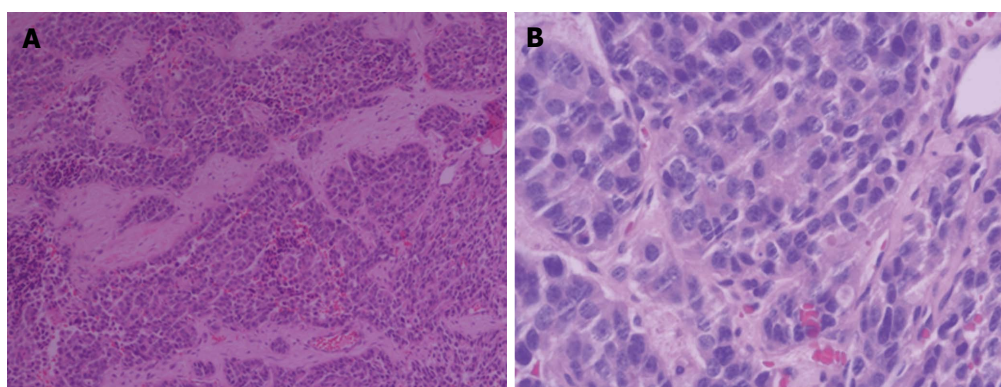


Figure 2 Microscopic finding showed infiltrating nests of small cells in fibrotic stroma. Tumor cells had small hyperchromatic nuclei and scanty cytoplasm. H and E: $\times 100$ (A), and $\times 200$ (B).

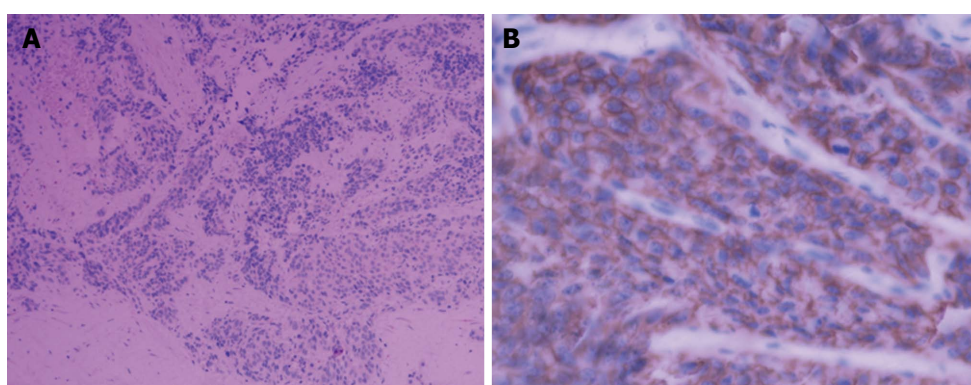


Figure 3 Immunohistochemical stain showed positivity of tumor cells for CgA (A) and a positive staining with CD56, CD56 (+) (B).

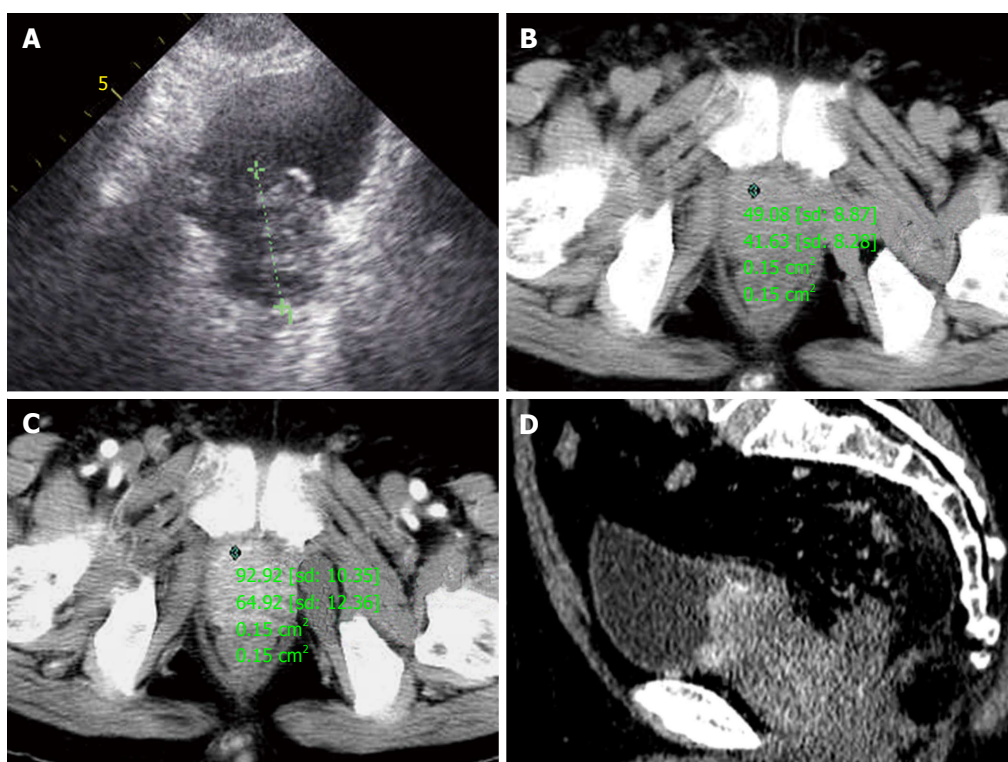


Figure 4 A 72-year-old male patient presented with one month of dysuria. A: Prostate enlarged to 4.0 cm \times 5.1 cm \times 4.2 cm with incomplete envelope, irregular shape and heterogeneous echo texture; B: A pre-enhanced computed tomography (CT) scan image of the pelvis showed a marked enlarged prostatic tumor invading to bladder, seminal vesicle; C: The enlarged prostate was inhomogeneous moderately enhancement in arterial phase; D: Coronal oblique multiplanar reconstruction of enhanced CT scan shows the enhanced inhomogeneous prostate with high attenuation protruding into bladder and unclear with surrounding tissue.

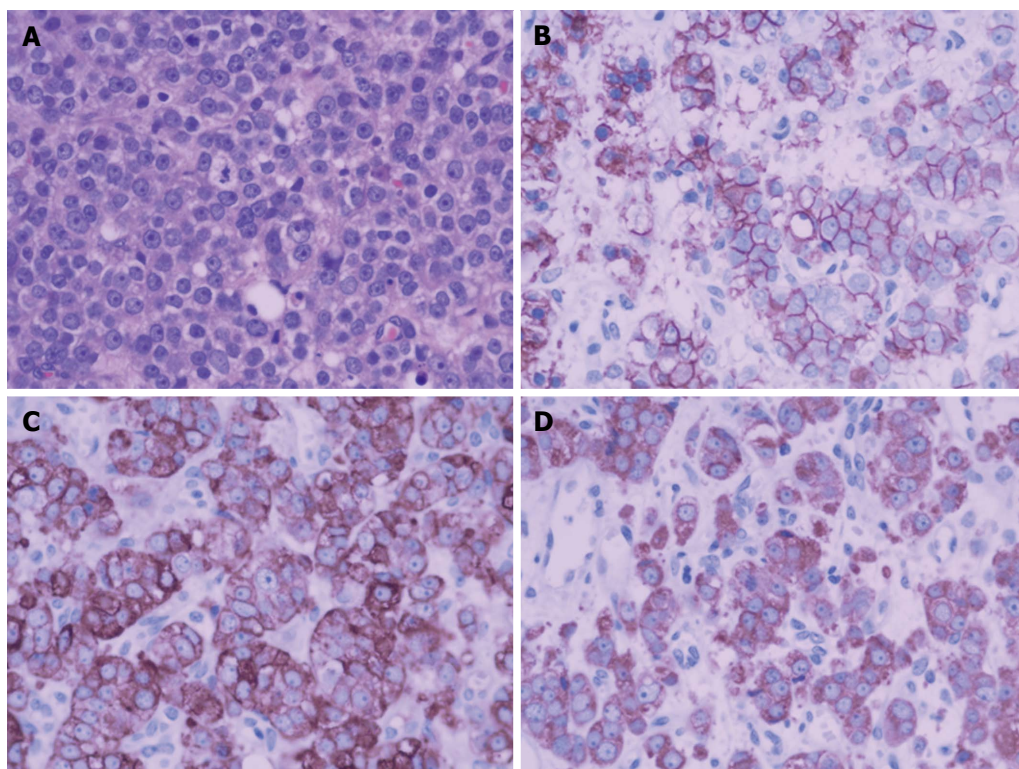


Figure 5 A biopsy of the prostate mass. Microscopic findings (A) showed infiltrating nests of small cells in fibrotic stroma. Tumor cells had small hyperchromatic nuclei and scanty cytoplasm (H and E, $\times 200$). Immunohistochemical stain showed strong positivity of tumor cells for CD56(++) (B), CgA(++) (C), Syn(++) (D).

presentations.

The clinical features of this disease are similar to those of prostate adenocarcinoma. The most frequent symptoms at presentation include lower urinary tract symptoms and acute urinary retention, but pain and paraneoplastic syndromes may be the first manifestations in rare cases^[2,4]. In our cases, the symptoms of the patients mainly include frequent urination, hematuria and dysuria, there were no paraneoplastic syndromes. Neuroendocrine cells of PNEC do not produce PSA, the serum level of PSA of the majority was within the normal range, except a few cases with mixed tumors with PSA slightly increased in serum^[6,7]. In our cases, the serum level of PSA all were normal which is infrequent in prostate cancer.

The morphologic features of NEC of the prostate are similar to those of other sites. As for the prostate, the most widely used imaging examination is the pelvic ultrasonography, CT and MRI scan. To our knowledge, there are only several cases of PNEC which imaging signs have been primitively described in literatures by now^[7,8], which are not sufficient to characterize the imaging findings of the tumor, but which hint MRI and contrast-enhanced CT examination may be sensitive in showing the abnormal signs. The radiologic findings of our cases were similar to the NEC in other sites. The imaging differences of PNEC to the benign diseases of prostate may include its higher signal in T2WI and DWI, more enhanced in arterial phase, irregular form

infiltrated and/or metastasized to other regional, such as lymph nodes, bone or the liver and so on, which all can be seen in other malignant neoplasm of prostate though some signs are infrequency in others.

In summary, there usually isn't enough characteristic evidence for preoperative diagnosis, especially at early stage of PNEC alone in clinical, laboratory, plain ultrasound (US) or CT imaging presentations. If there are paraneoplastic syndromes though it is rare in clinic and malignant imaging signs, the diagnosis of PNEC can be made^[8-10]. If there are malignant imaging signs, but without correspondingly increased PSA in serum and without paraneoplastic syndromes in clinic, PNEC should be considered in the differential diagnosis, which can be confirmed by biopsy, histology and immunohistochemistry^[2,4,10]. Our cases and literature suggest PNEC often locate at the central zone of prostate with obviously contrast enhancement, abnormal signal in MR images, especially in DWI. It usually is insufficient that the prostate is examined by US and CT, or PSA in serum within normal range for the symptomatic and/or with high risk factors crowd. For patients with symptom and/or with high risk factors, DWI, early enhancement in CT, MRI should be emphasized, and the complementary roles of the imaging malignant signs, self-contradictory clinical appearance and laboratory results should be emphasized. Which can help achieving accurate diagnosis, maybe in early stage, in the preoperative diagnosis of PNEC. We believe it will test and enrich the imaging

characteristics of PNEC to check more cases in future.

COMMENTS

Case characteristics

The clinical symptoms of the two cases were also dissimilar, one presented with pollakisuria and an episode of painless gross hematuria, and the other presented with dysuria.

Clinical diagnosis

Two men with prostatic malignant tumor.

Differential diagnosis

Malignant tumors (prostatic carcinoma, sarcoma, carcinoma sarcomatodes and malignant fibrous histiocytoma), benign neoplasms (prostatic hyperplasia, granuloma).

Laboratory diagnosis

The first patient had hemoglobin of 4.3 g/dL and red blood cells in urine analysis, while the second patient had no remarkable findings for the laboratory tests.

Imaging diagnosis

For both cases, computed tomography (CT) scan and ultrasonography showed an irregularly enlarged prostate. The first case also underwent magnetic resonance examination.

Pathological diagnosis

For both cases, histological examination showed small cell carcinoma, immunohistochemical studies showed positive for CgA and CD56, negative for prostate specific antigen.

Treatment

The first case underwent only radiotherapy for 10 d on the prostate, pelvic region and lumbar vertebrae, while radiotherapy and systemic chemotherapy were all carried out on the prostate and pelvic region for the second patient.

Related reports

Very few ultrasound, CT and magnetic resonance imaging (MRI) findings of prostatic neuroendocrine carcinoma (PNEC) have been reported in the literature. The diagnostic value of imaging findings remains unclear and the role of treatment in early stage of PNEC is controversial.

Term explanation

PNCE: Prostatic neuroendocrine carcinoma.

Experiences and lessons

This case report presents the clinical and imaging characteristics of PNEC and also discusses the diagnostic value of imaging findings of PNEC. The authors recommend that more attention should be paid to the complementary roles of the malignant signs in diffusion-weighted image, early enhancement in CT or MRI, self-contradictory clinical appearance and laboratory findings.

Peer-review

Concise review of imaging and pathological findings of neuroendocrine prostate cancer.

REFERENCES

- 1 **Ather MH**, Siddiqui T. The genetics of neuroendocrine prostate cancers: a review of current and emerging candidates. *Appl Clin Genet* 2012; **5**: 105-110 [PMID: 23776386 DOI: 10.2147/TACG.S28881]
- 2 **Wang W**, Epstein JI. Small cell carcinoma of the prostate. A morphologic and immunohistochemical study of 95 cases. *Am J Surg Pathol* 2008; **32**: 65-71 [PMID: 18162772 DOI: 10.1097/PAS.0b013e318058a96b]
- 3 **Walenkamp AM**, Sonke GS, Sleijfer DT. Clinical and therapeutic aspects of extrapulmonary small cell carcinoma. *Cancer Treat Rev* 2009; **35**: 228-236 [PMID: 19068273 DOI: 10.1016/j.ctrv.2008.10.007]
- 4 **Addeo A**, Rinaldi C, Panades M. A case of small cell carcinoma of the prostate and review of the literature. *Tumori* 2012; **98**: 76e-78e [PMID: 22825523 DOI: 10.1700/1125.12415]
- 5 **Ketata S**, Ketata H, Fakhfakh H, Sahnoun A, Bahloul A, Boudawara T, Mhiri MN. Pure primary neuroendocrine tumor of the prostate: a rare entity. *Clin Genitourin Cancer* 2006; **5**: 82-84 [PMID: 16859584 DOI: 10.3816/CGC.2006.n.022]
- 6 **Uemura KI**, Nakagawa G, Chikui K, Moriya F, Nakiri M, Hayashi T, Suekane S, Matsuoka K. A useful treatment for patients with advanced mixed-type small cell neuroendocrine carcinoma of the prostate: A case report. *Oncol Lett* 2013; **5**: 793-796 [PMID: 23426029 DOI: 10.3892/ol.2013.1136]
- 7 **Giordano S**, Tolonen T, Tolonen T, Hirsimäki S, Kataja V. A pure primary low-grade neuroendocrine carcinoma (carcinoid tumor) of the prostate. *Int Urol Nephrol* 2010; **42**: 683-687 [PMID: 19866370 DOI: 10.1007/s11255-009-9660-8]
- 8 **Albisinni S**, De Nunzio C, Tubaro A. Pure small cell carcinoma of the prostate: A rare tumor. *Indian J Urol* 2012; **28**: 89-91 [PMID: 22557725 DOI: 10.4103/0970-1591.94964]
- 9 **Alwani RA**, Neggers SJ, van der Klift M, Baggen MG, van Leenders GJ, van Aken MO, van der Lely AJ, de Herder WW, Feelders RA. Cushing's syndrome due to ectopic ACTH production by (neuroendocrine) prostate carcinoma. *Pituitary* 2009; **12**: 280-283 [PMID: 18322802 DOI: 10.1007/s11102-008-0100-z]
- 10 **Simon RA**, di Sant'Agnese PA, Huang LS, Xu H, Yao JL, Yang Q, Liang S, Liu J, Yu R, Cheng L, Oh WK, Palapattu GS, Wei J, Huang J. CD44 expression is a feature of prostatic small cell carcinoma and distinguishes it from its mimickers. *Hum Pathol* 2009; **40**: 252-258 [PMID: 18835619 DOI: 10.1016/j.humpath.2008.07.014]

P- Reviewer: Chu JP, Jain S **S- Editor:** Ji FF

L- Editor: A **E- Editor:** Liu SQ





Published by **Baishideng Publishing Group Inc**

8226 Regency Drive, Pleasanton, CA 94588, USA

Telephone: +1-925-223-8242

Fax: +1-925-223-8243

E-mail: bpgoffice@wjgnet.com

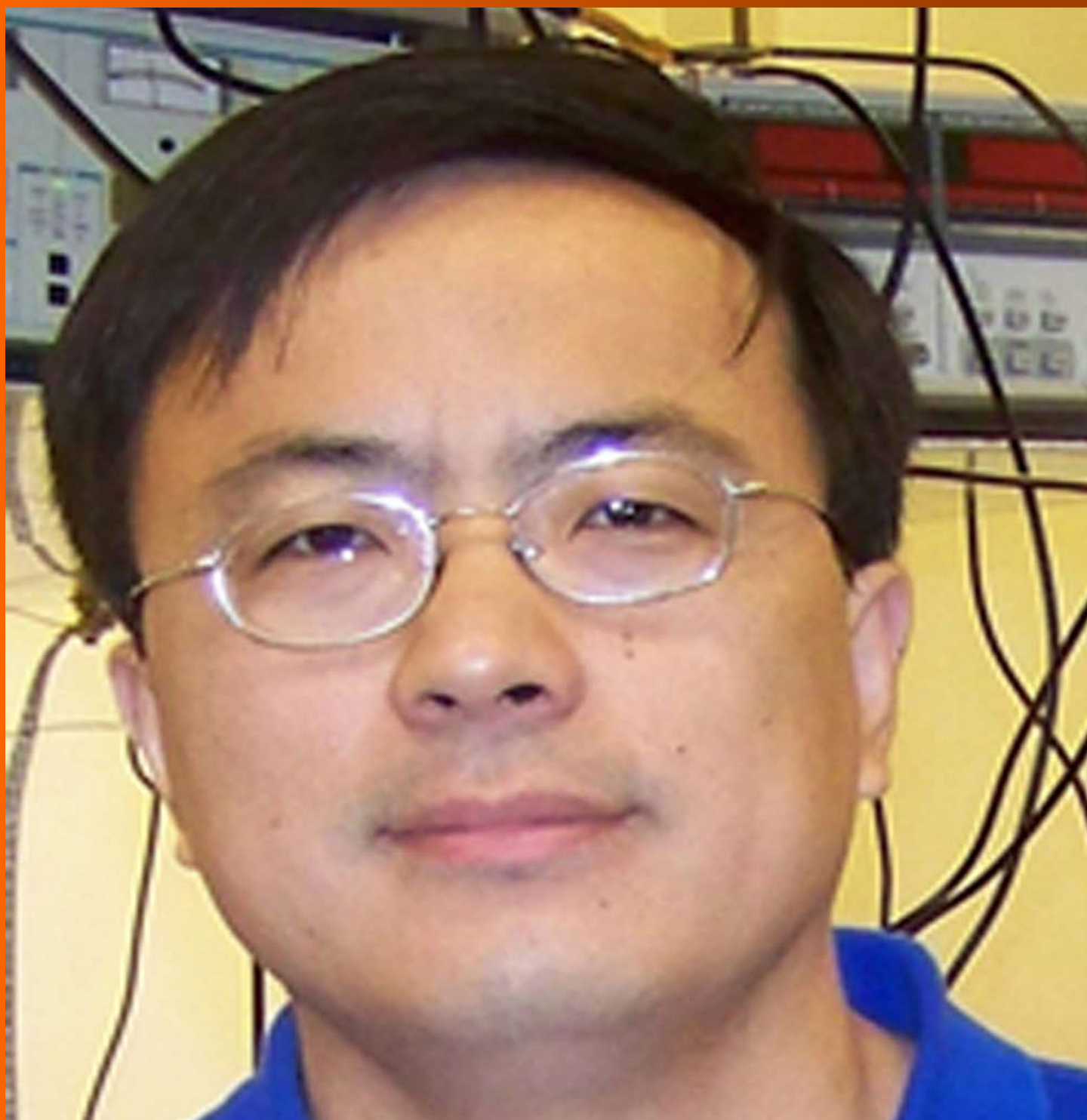
Help Desk: <http://www.wjgnet.com/esps/helpdesk.aspx>

<http://www.wjgnet.com>



World Journal of *Radiology*

World J Radiol 2015 June 28; 7(6): 110-142





Editorial Board

2014-2017

The *World Journal of Radiology* Editorial Board consists of 365 members, representing a team of worldwide experts in radiology. They are from 36 countries, including Afghanistan (1), Argentina (2), Australia (5), Austria (7), Belgium (2), Brazil (8), Canada (6), Chile (1), China (43), Croatia (1), Denmark (4), Egypt (6), France (5), Germany (22), Greece (10), India (12), Iran (6), Ireland (2), Israel (3), Italy (47), Japan (13), Netherlands (1), New Zealand (1), Pakistan (1), Poland (2), Portugal (1), Serbia (1), Singapore (3), Slovakia (1), South Korea (18), Spain (4), Sweden (2), Switzerland (4), Thailand (1), Turkey (26), United Kingdom (11), and United States (82).

EDITORS-IN-CHIEF

Kai U Juergens, *Bremen*
Edwin JR van Beek, *Edinburgh*
Thomas J Vogl, *Frankfurt*

GUEST EDITORIAL BOARD MEMBERS

Wing P Chan, *Taipei*
Chung-Huei Hsu, *Taipei*
Chin-Chang Huang, *Taipei*
Tsong-Long Hwang, *Taoyuan*
Jung-Lung Hsu, *Taipei*
Chia-Hung Kao, *Taichung*
Yu-Ting Kuo, *Tainan*
Hon-Man Liu, *Taipei*
Hui-Lung Liang, *Kaohsiung*
Chun Chung Lui, *Kaohsiung*
Sen-Wen Teng, *Taipei*
Yung-Liang (William) Wan, *Taoyuan*

MEMBERS OF THE EDITORIAL BOARD



Afghanistan

Takao Hiraki, *Okayama*



Argentina

Patricia Carrascosa, *Vicente Lopez*
Maria C Ziadi, *Rosario*



Australia

Lourens Bester, *Sydney*
Gemma A Figtree, *Sydney*

Stuart M Grieve, *Sydney*
Wai-Kit Lee, *Fitzroy*
Prabhakar Ramachandran, *Melbourne*



Austria

Herwig R Cerwenka, *Graz*
Gudrun M Feuchtnner, *Innsbruck*
Benjamin Henninger, *Innsbruck*
Rupert Lanzenberger, *Vienna*
Shu-Ren Li, *Vienna*
Veronika Schopf, *Vienna*
Tobias De Zordo, *Innsbruck*



Belgium

Steve Majerus, *Liege*
Kathelijne Peremans, *Merelbeke*



Brazil

Clerio F Azevedo, *Rio de Janeiro*
Patrícia P Alfredo, *São Paulo*
Eduardo FC Fleury, *São Paulo*
Edward Araujo Júnior, *São Paulo*
Wellington P Martins, *Ribeirao Preto*
Ricardo A Mesquita, *Belo Horizonte*
Vera MC Salemi, *São Paulo*
Claudia Szobot, *Porto Alegre*
Lilian YI Yamaga, *São Paulo*



Canada

Marie Arsalidou, *Toronto*
Otman A Basir, *Waterloo*

Tarik Zine Belhocine, *Toronto*
James Chow, *Toronto*
Tae K Kim, *Toronto*
Anastasia Oikonomou, *Toronto*



China

Hong-Wei Chen, *Wuxi*
Feng Chen, *Hangzhou*
Jian-Ping Chu, *Guangzhou*
Guo-Guang Fan, *Shenyang*
Bu-Lang Gao, *Shijiazhuang*
Qi-Yong Gong, *Chengdu*
Ying Han, *Beijing*
Xian-Li Lv, *Beijing*
Yi-Zhuo Li, *Guangzhou*
Xiang-Xi Meng, *Harbin*
Yun Peng, *Beijing*
Jun Shen, *Guangzhou*
Ze-Zhou Song, *Hangzhou*
Wai Kwong Tang, *Hong Kong*
Gang-Hua Tang, *Guangzhou*
Jie Tian, *Beijing*
Lu-Hua Wang, *Beijing*
Xiao-bing Wang, *Xi'an*
Yi-Gen Wu, *Nanjing*
Kai Wu, *Guangzhou*
Hui-Xiong Xu, *Shanghai*
Zuo-Zhang Yang, *Kunming*
Xiao-Dan Ye, *Shanghai*
David T Yew, *Hong Kong*
Ting-He Yu, *Chongqing*
Zheng Yuan, *Shanghai*
Min-Ming Zhang, *Hangzhou*
Yudong Zhang, *Nanjing*
Dong Zhang, *Chongqing*
Wen-Bin Zeng, *Changsha*

Yue-Qi Zhu, *Shanghai*



Croatia

Goran Kusec, *Osijek*



Denmark

Poul E Andersen, *Odense*

Lars J Petersen, *Aalborg*

Thomas Z Ramsøy, *Frederiksberg*

Morten Ziebell, *Copenhagen*



Egypt

Mohamed F Bazeed, *Mansoura*

Mohamed Abou El-Ghar, *Mansoura*

Reem HA Mohamed, *Cairo*

Mohamed R Nouh, *Alexandria*

Ahmed AKA Razek, *Mansoura*

Ashraf A Zytoon, *Shebin El-Koom*



France

Sabine F Bensamoun, *Compiègne*

Romarc Loffroy, *Dijon*

Stephanie Nougaret, *Montpellier*

Hassane Oudadesse, *Rennes*

Vincent Vinh-Hung, *Fort-de-France*



Germany

Henryk Barthel, *Leipzig*

Peter Bannas, *Hamburg*

Martin Beeres, *Frankfurt*

Ilja F Ciernik, *Dessau*

A Dimitrakopoulou-Strauss, *Heidelberg*

Peter A Fasching, *Erlangen*

Andreas G Schreyer, *Regensburg*

Philipp Heusch, *Duesseldorf*

Sonja M Kirchhoff, *Munich*

Sebastian Ley, *Munich*

Adel Maataoui, *Frankfurt am Main*

Stephan M Meckel, *Freiburg*

Hans W Muller, *Duesseldorf*

Kay Raum, *Berlin*

Dirk Rades, *Luebeck*

Marc-Ulrich Regier, *Hamburg*

Alexey Surov, *Halle*

Martin Walter, *Magdeburg*

Axel Wetter, *Essen*

Christoph Zilkens, *Düsseldorf*



Greece

Panagiotis Antoniou, *Thessaloniki*

Nikos Efthimiou, *Athens*

Dimitris Karnabatidis, *Patras*

George Latsios, *Athens*

Stylianios Megremis, *Iraklion*

Alexander D Rapidis, *Athens*

Kiki Theodorou, *Larissa*

Ioannis A Tsalafoutas, *Athens*

Evanthia E Tripoliti, *Ioannina*

Athina C Tsili, *Ioannina*



India

Ritesh Agarwal, *Chandigarh*

Chandan J Das, *New Delhi*

Prathamesh V Joshi, *Mumbai*

Naveen Kalra, *Chandigarh*

Chandrasekharan Kesavadas, *Trivandrum*

Jyoti Kumar, *New Delhi*

Atin Kumar, *New Delhi*

Kaushala P Mishra, *Allahabad*

Daya N Sharma, *New Delhi*

Binit Sureka, *New Delhi*

Sanjay Sharma, *New Delhi*

Raja R Yadav, *Allahabad*



Iran

Majid Assadi, *Bushehr*

SeyedReza Najafizadeh, *Tehran*

Mohammad Ali Oghabian, *Tehran*

Amir Reza Radmard, *Tehran*

Ramin Sadeghi, *Mashhad*

Hadi Rokni Yazdi, *Tehran*



Ireland

Tadhg Gleeson, *Wexford*

Frederik JAI Vernimmen, *Cork*



Israel

Dafna Ben Bashat, *Tel Aviv*

Amit Gefen, *Tel Aviv*

Tamar Sella, *Jerusalem*



Italy

Adriano Alippi, *Rome*

Dante Amelio, *Trento*

Michele Anzidei, *Rome*

Filippo F Angileri, *Messinas*

Stefano Arcangeli, *Rome*

Roberto Azzoni, *San Donato milanese*

Tommaso V Bartolotta, *Palermo*

Tommaso Bartalena, *Imola*

Livia Bernardin, *San Bonifacio*

Federico Boschi, *Verona*

Sergio Casciaro, *Lecce*

Emanuele Casciani, *Rome*

Musa M Can, *Napoli*

Alberto Cuocolo, *Napoli*

Michele Ferrara, *Coppito*

Mauro Feola, *Fossano*

Giampiero Francica, *Castel Volturno*

Luigi De Gennaro, *Rome*

Giulio Giovannetti, *Pisa*

Francesca Iacobellis, *Napoli*

Formato Invernizzi, *Monza Brianza*

Francesco Lassandro, *Naples*

Lorenzo Livi, *Florence*

Pier P Mainenti, *Napoli*

Laura Marzetti, *Chieti*

Giuseppe Malinverni, *Crescentino*

Enrica Milanese, *Turin*

Giovanni Morana, *Treviso*

Lorenzo Monti, *Milan*

Silvia D Morbelli, *Genoa*

Barbara Palumbo, *Perugia*

Cecilia Parazzini, *Milan*

Stefano Pergolizzi, *Messina*

Antonio Pinto, *Naples*

Camillo Porcaro, *Rome*

Carlo C Quattrocchi, *Rome*

Alberto Rebonato, *Perugia*

Giuseppe Rizzo, *Rome*

Roberto De Rosa, *Naples*

Domenico Rubello, *Rovigo*

Andrea Salvati, *Bari*

Sergio Sartori, *Ferrara*

Luca M Sconfienza, *Milano*

Giovanni Storto, *Rionero*

Nicola Sverzellati, *Parma*

Alberto S Tagliafico, *Genova*

Nicola Troisi, *Florence*



Japan

Yasuhiko Hori, *Chiba*

Hidetoshi Ikeda, *Koriyama*

Masahito Kawabori, *Sapporo*

Tamotsu Kamishima, *Sapporo*

Hiro Kiyosue, *Yufu*

Yasunori Minami, *Osaka-sayama*

Yasuhiro Morimoto, *Kitakyushu*

Satoru Murata, *Tokyo*

Shigeki Nagamachi, *Miyazaki*

Hiroshi Onishi, *Yamanashi*

Morio Sato, *Wakayama Shi*

Yoshito Tsushima, *Maebashi*

Masahiro Yanagawa, *Suita*



Netherlands

Willem Jan van Rooij, *Tilburg*



New Zealand

W Howell Round, *Hamilton*



Pakistan

Wazir Muhammad, *Abbottabad*



Poland

Maciej S Baglaj, *Wroclaw*

Piotr Czauderna, *Gdansk*



Portugal

Joao Manuel RS Tavares, *Porto*



Serbia

Olivera Ciraj-Bjelac, *Belgrade*



Singapore

Gopinathan Anil, *Singapore*

Terence KB Teo, *Singapore*

Cher Heng Tan, *Singapore*



Slovakia

Stefan Sivak, *Martin*



South Korea

Ki Seok Choo, *Busan*

Seung Hong Choi, *Seoul*

Dae-Seob Choi, *Jinju*

Hong-Seok Jang, *Seoul*

Yong Jeong, *Daejeon*

Chan Kyo Kim, *Seoul*

Se Hyung Kim, *Seoul*

Joong-Seok Kim, *Seoul*

Sang Eun Kim, *Seongnam*

Sung Joon Kwon, *Seoul*

Jeong Min Lee, *Seoul*

In Sook Lee, *Busan*

Noh Park, *Goyang*

Chang Min Park, *Seoul*

Sung Bin Park, *Seoul*

Deuk Jae Sung, *Seoul*

Choongsoo Shin, *Seoul*

Kwon-Ha Yoon, *Iksan*



Spain

Miguel A De Gregorio, *Zaragoza*

Antonio Luna, *Jaén*

Enrique Marco de Lucas, *Santander*

Fernando Ruiz Santiago, *Granada*



Sweden

Dmitry Grishenkov, *Stockholm*

Tie-Qiang Li, *Stockholm*



Switzerland

Nicolau Beckmann, *Basel*

Christian Boy, *Bern*

Giorgio Treglia, *Bellinzona*

Stephan Ulmer, *Kiel*



Thailand

Sirianong Namwongprom, *Chiang Mai*



Turkey

Kubilay Aydin, *Istanbul*

Ramazan Akdemir, *Sakarya*

Serhat Avcu, *Ankara*

Ayşe Aralasmak, *Istanbul*

Oktay Algin, *Ankara*

Nevbahar Akcar, *Meselik*

Bilal Battal, *Ankara*

Zulkif Bozgeyik, *Elazig*

Nazan Ciledag, *Aakara*

Fuldem Y Donmez, *Ankara*

Gulgun Engin, *Istanbul*

Ahmet Y Goktay, *Izmir*

Oguzhan G Gumustas, *Bursa*

Kaan Gunduz, *Ankara*

Pelin Ozcan Kara, *Mersin*

Kivanc Kamburoglu, *Ankara*

Ozgur Kilickesmez, *Istanbul*

Furuzan Numan, *Istanbul*

Cem Onal, *Adana*

Ozgur Oztekin, *Izmir*

Seda Ozbek (Boruban), *Konya*

Selda Sarikaya, *Zonguldak*

Figen Taser, *Kutahya*

Baran Tokar, *Eskisehir*

Ender Uysal, *Istanbul*

Ensar Yekeler, *Istanbul*



United Kingdom

Indran Davagnanam, *London*

M DC Valdés Hernández, *Edinburgh*

Alan Jackson, *Manchester*

Suneil Jain, *Belfast*

Long R Jiao, *London*

Miltiadis Krokidis, *Cambridge*

Pradesh Kumar, *Liverpool*

Peter D Kuzmich, *Derby*

Georgios Plataniotis, *Brighton*

Vanessa Sluming, *Liverpool*



United States

Garima Agrawal, *Saint Louis*

James R Brasic, *Baltimore*

Rajendra D Badgaiyan, *Buffalo*

Ulas Bagci, *Bethesda*

Anat Biegon, *Stony Brook*

Ramon Casanova, *Winston Salem*

Wenli Cai, *Boston*

Zheng Chang, *Durham*

Corey J Chakarun, *Long Beach*

Kai Chen, *Los Angeles*

Hyun-Soon Chong, *Chicago*

Marco Cura, *Dallas*

Ravi R Desai, *Bensalem*

Delia DeBuc, *Miami*

Carlo N De Cecco, *Charleston*

Timm-Michael L Dickfeld, *Baltimore*

Subba R Digumarthy, *Boston*

Huy M Do, *Stanford*

Todd A Faasse, *Grand Rapids*

Salomao Faintuch, *Boston*

Girish M Fatterpekar, *New York*

Dhakshinamoorthy Ganesan, *Houston*

Robert J Griffin, *Little Rock*

Andrew J Gunn, *Boston*

Sandeep S Hedgire, *Boston*

Timothy J Hoffman, *Columbia*

Mai-Lan Ho, *San Francisco*

Juebin Huang, *Jackson*

Abid Irshad, *Charleston*

Matilde Inglese, *New York*

El-Sayed H Ibrahim, *Jacksonville*

Paul R Julsrud, *Rochester*

Pamela T Johnson, *Baltimore*

Ming-Hung Kao, *Tempe*

Sunil Krishnan, *Houston*

Richard A Komoroski, *Cincinnati*

Sandi A Kwee, *Honolulu*

King Kim, *Ft. Lauderdale*

Guozheng Liu, *Worcester*

Yiyan Liu, *Newark*

Venkatesh Mani, *New York*

Lian-Sheng Ma, *Pleasanton*

Rachna Madan, *Boston*

Zeyad A Metwalli, *Houston*

Yilong Ma, *Manhasset*

Hui Mao, *Atlanta*

Feroze B Mohamed, *Philadelphia*

Gul Moonis, *Boston*

John L Noshier, *New Brunswick*

Rahmi Oklu, *Boston*

Aytekun Oto, *Chicago*

Bishnuhari Paudyal, *Philadelphia*

Rajul Pandya, *Youngstown*

Chong-Xian Pan, *Sacramento*

Jay J Pillai, *Baltimore*

Neal Prakash, *Duarte*

Reza Rahbar, *Boston*

Ali S Raja, *Boston*

Gustavo J Rodriguez, *El Paso*

David J Sahn, *Portland*

Steven Schild, *Scottsdale*

Ali R Sepahdari, *Los Angeles*

Li Shen, *Indianapolis*

JP Sheehan, *Charlottesville*

Atul B Shinagare, *Boston*

Sarabjeet Singh, *Boston*

Charles J Smith, *Columbia*

Kenji Suzuki, *Chicago*

Monvadi Srichai-Parsia, *Washington*

Sree H Tirumani, *Boston*

Hebert A Vargas, *New York*

Sachit Verma, *Philadelphia*

Yoichi Watanabe, *Minneapolis*

Li Wang, *Chapel Hill*

Carol C Wu, *Boston*

Shoujun Xu, *Houston*

Min Yao, *Cleveland*

Xiaofeng Yang, *Atlanta*

Qingbao Yu, *Albuquerque*

Aifeng Zhang, *Chicago*

Chao Zhou, *Bethlehem*

Hongming Zhuang, *Philadelphia*

**EDITORIAL**

- 110** Advances of multidetector computed tomography in the characterization and staging of renal cell carcinoma
Tsili AC, Argyropoulou MI
- 128** Use of dentomaxillofacial cone beam computed tomography in dentistry
Kamburoğlu K
- 131** Contrast-enhanced ultrasound imaging of the vasa vasorum of carotid artery plaque
Song ZZ, Zhang YM

MINIREVIEWS

- 134** Risk management in radiology departments
Craciun H, Mankad K, Lynch J

CASE REPORT

- 139** Endovascular retrieval of a prematurely deployed covered stent
Miley JT, Rodriguez GJ, Tummala RP

ABOUT COVER

Editorial Board Member of *World Journal of Radiology*, Shoujun Xu, PhD, Associate Professor, Department of Chemistry, University of Houston, Houston, TX 77204, United States

AIM AND SCOPE

World Journal of Radiology (*World J Radiol*, *WJR*, online ISSN 1949-8470, DOI: 10.4329) is a peer-reviewed open access academic journal that aims to guide clinical practice and improve diagnostic and therapeutic skills of clinicians.

WJR covers topics concerning diagnostic radiology, radiation oncology, radiologic physics, neuroradiology, nuclear radiology, pediatric radiology, vascular/interventional radiology, medical imaging achieved by various modalities and related methods analysis. The current columns of *WJR* include editorial, frontier, diagnostic advances, therapeutics advances, field of vision, mini-reviews, review, topic highlight, medical ethics, original articles, case report, clinical case conference (clinicopathological conference), and autobiography.

We encourage authors to submit their manuscripts to *WJR*. We will give priority to manuscripts that are supported by major national and international foundations and those that are of great basic and clinical significance.

INDEXING/ABSTRACTING

World Journal of Radiology is now indexed in PubMed Central, PubMed, Digital Object Identifier, and Directory of Open Access Journals.

FLYLEAF

I-III Editorial Board

EDITORS FOR THIS ISSUE

Responsible Assistant Editor: *Xiang Li*
Responsible Electronic Editor: *Su-Qing Liu*
Proofing Editor-in-Chief: *Lian-Sheng Ma*

Responsible Science Editor: *Yue-Li Tian*
Proofing Editorial Office Director: *Xiu-Xia Song*

NAME OF JOURNAL
World Journal of Radiology

ISSN
ISSN 1949-8470 (online)

LAUNCH DATE
December 31, 2009

FREQUENCY
Monthly

EDITORS-IN-CHIEF
Kai U Juergens, MD, Associate Professor, MRT und PET/CT, Nuklearmedizin Bremen Mitte, ZEMODI - Zentrum für morphologische und molekulare Diagnostik, Bremen 28177, Germany

Edwin JR van Beek, MD, PhD, Professor, Clinical Research Imaging Centre and Department of Medical Radiology, University of Edinburgh, Edinburgh EH16 4TJ, United Kingdom

Thomas J Vogl, MD, Professor, Reader in Health Technology Assessment, Department of Diagnostic and Interventional Radiology, Johann Wolfgang

Goethe University of Frankfurt, Frankfurt 60590, Germany

EDITORIAL OFFICE
Jin-Lei Wang, Director
Xiu-Xia Song, Vice Director
World Journal of Radiology
Room 903, Building D, Ocean International Center, No. 62 Dongsihuan Zhonglu, Chaoyang District, Beijing 100025, China
Telephone: +86-10-59080039
Fax: +86-10-85381893
E-mail: editorialoffice@wjnet.com
Help Desk: <http://www.wjnet.com/esps/helpdesk.aspx>
<http://www.wjnet.com>

PUBLISHER
Baishideng Publishing Group Inc
8226 Regency Drive,
Pleasanton, CA 94588, USA
Telephone: +1-925-223-8242
Fax: +1-925-223-8243
E-mail: bpgoffice@wjnet.com
Help Desk: <http://www.wjnet.com/esps/helpdesk.aspx>
<http://www.wjnet.com>

PUBLICATION DATE
June 28, 2015

COPYRIGHT
© 2015 Baishideng Publishing Group Inc. Articles published by this Open-Access journal are distributed under the terms of the Creative Commons Attribution Non-commercial License, which permits use, distribution, and reproduction in any medium, provided the original work is properly cited, the use is non commercial and is otherwise in compliance with the license.

SPECIAL STATEMENT
All articles published in journals owned by the Baishideng Publishing Group (BPG) represent the views and opinions of their authors, and not the views, opinions or policies of the BPG, except where otherwise explicitly indicated.

INSTRUCTIONS TO AUTHORS
Full instructions are available online at http://www.wjnet.com/1949-8470/g_info_20100316162358.htm.

ONLINE SUBMISSION
<http://www.wjnet.com/esps/>

Advances of multidetector computed tomography in the characterization and staging of renal cell carcinoma

Athina C Tsili, Maria I Argyropoulou

Athina C Tsili, Maria I Argyropoulou, Department of Radiology, Medical School, University of Ioannina, 45110 Ioannina, Greece

Author contributions: Tsili AC and Argyropoulou MI contributed to this paper.

Conflict-of-interest: None.

Open-Access: This article is an open-access article which was selected by an in-house editor and fully peer-reviewed by external reviewers. It is distributed in accordance with the Creative Commons Attribution Non Commercial (CC BY-NC 4.0) license, which permits others to distribute, remix, adapt, build upon this work non-commercially, and license their derivative works on different terms, provided the original work is properly cited and the use is non-commercial. See: <http://creativecommons.org/licenses/by-nc/4.0/>

Correspondence to: Athina C Tsili, MD, Assistant Professor, Department of Radiology, Medical School, University of Ioannina, Leoforos Panepistimiou, 45110 Ioannina, Greece. a_tsili@yahoo.gr
Telephone: +30-697-6510904
Fax: +30-265-1007862

Received: January 30, 2015

Peer-review started: January 31, 2015

First decision: February 7, 2015

Revised: March 18, 2015

Accepted: April 27, 2015

Article in press: April 29, 2015

Published online: June 28, 2015

Abstract

Renal cell carcinoma (RCC) accounts for approximately 90%-95% of kidney tumors. With the widespread use of cross-sectional imaging modalities, more than half of RCCs are detected incidentally, often diagnosed at an early stage. This may allow the planning of more conservative treatment strategies. Computed tomography (CT) is considered the examination of choice for the

detection and staging of RCC. Multidetector CT (MDCT) with the improvement of spatial resolution and the ability to obtain multiphase imaging, multiplanar and three-dimensional reconstructions in any desired plane brought about further improvement in the evaluation of RCC. Differentiation of RCC from benign renal tumors based on MDCT features is improved. Tumor enhancement characteristics on MDCT have been found closely to correlate with the histologic subtype of RCC, the nuclear grade and the cytogenetic characteristics of clear cell RCC. Important information, including tumor size, localization, and organ involvement, presence and extent of venous thrombus, possible invasion of adjacent organs or lymph nodes, and presence of distant metastases are provided by MDCT examination. The preoperative evaluation of patients with RCC was improved by depicting the presence or absence of renal pseudocapsule and by assessing the possible neoplastic infiltration of the perirenal fat tissue and/or renal sinus fat compartment.

Key words: Carcinoma; Kidney; Computed tomography; Renal cell carcinoma; Staging; Multidetector computed tomography

© The Author(s) 2015. Published by Baishideng Publishing Group Inc. All rights reserved.

Core tip: Multidetector computed tomography (MDCT) remains the most widely available and most effective modality for the detection and staging of renal cell carcinoma (RCC), with a staging accuracy up to 91%. MDCT scanners with the improvement of spatial resolution and the ability to obtain multiplanar and 3D-reconstructions greatly improved the diagnostic performance of CT in characterizing RCC and estimating the extent of the disease. Important information for treatment planning is provided by CT examination, including tumor location and size, renal arterial and venous anatomy and relationship to the pelvicaliceal system.

Tsili AC, Argyropoulou MI. Advances of multidetector computed tomography in the characterization and staging of renal cell carcinoma. *World J Radiol* 2015; 7(6): 110-127 Available from: URL: <http://www.wjgnet.com/1949-8470/full/v7/i6/110.htm> DOI: <http://dx.doi.org/10.4329/wjrr.v7.i6.110>

INTRODUCTION

Renal cell carcinoma (RCC) represents the commonest primary malignancy of the kidney, accounting for about 2%-3% of all cancers^[1-3]. In 2012, approximately 84400 new cases of RCC were diagnosed within the European Union and 34700 kidney cancer-related deaths occurred^[2]. The estimated number of new cases of kidney cancer in the United States during 2014 was 63920, the great majority representing RCCs, accounting for the seventh most common malignancy in men and the 12th commonest malignancy in women^[3]. An estimated 13860 deaths from kidney cancer were expected to occur in 2014^[3].

The widespread use of cross-sectional imaging modalities has resulted in incidental detection of more than 50% of RCCs^[1-4]. These tumors are often small, of low stage and grade, and therefore have a better prognosis^[1-4]. Early-stage RCC is usually asymptomatic. The classic clinical triad of flank pain, gross haematuria, and palpable abdominal mass is not common (6%-10% of cases) and usually correlates with aggressive histology and advanced-stage disease^[1,5,6]. There is a 1.5:1 predominance in men over women, with a peak incidence occurring during the 6th and 7th decades of life. The main predisposing factors for renal cancer are smoking, obesity, hypertension, chronic renal failure, chemical exposure and radiation exposure^[1-3]. Heredity also plays a role, with approximately 4% of all RCCs seen in patients with an underlying tumor syndrome^[7,8].

In patients with RCC, tumor stage at diagnosis, nuclear grade according to Fuhrman, and histologic subtype represent the most important prognostic factors^[1]. Tumor stage greatly affects patient's prognosis and survival, and has an important impact on treatment planning. The tumor, node, metastasis (TNM) staging classification system is most commonly used, closely correlating with potential curability of the disease and prognosis^[1,9]. The latest version of the TNM classification was published in 2010^[1,9] and is presented in Table 1.

The grading classification of RCC is based on the microscopic characteristics of the neoplasm with hematoxylin and eosin staining. Fuhrman nuclear grade is the most widely accepted histological grading system for RCC^[10]. Although affected by intra- and inter-observer discrepancies, it represents one of the most significant prognostic variables in patients with all stages of RCC^[10-13]. This system categorizes RCC with grades 1, 2, 3, and 4, varying from tumors with small, round hyperchromatic nuclei, no visible nucleoli

and little detail in the chromatin to those with larger, pleomorphic nuclei, single or multiple macronucleoli and coarsely granular chromatin^[10]. Some researchers have simplified the Fuhrman grading system in order to improve interobserver reproducibility. More specifically, a modified two- or three-tiered Fuhrman grading system could probably have a virtually equal accuracy as the conventional 4-tiered Fuhrman grading system in predicting cancer-specific mortality^[11-13].

The 2004 World Health Organization classification for renal neoplasms recognizes several distinct histologic subtypes of RCC, of which three main types are important: conventional (clear cell) RCC (ccRCC, accounting for approximately 80%-90% of RCCs); papillary RCC (10%-15%); and chromophobe RCC (4%-5%)^[14,15]. In univariate analysis, there is a trend towards a better prognosis for patients with chromophobe vs papillary vs conventional RCC^[16,17].

The 5-year overall survival for all types of RCC is 49%. More than half of cases are diagnosed at early-stage, for which the 5-year relative survival rate is 92%^[1].

Radical nephrectomy with ipsilateral adrenalectomy, as established by Robson, was the treatment of choice since 1969^[1]. During the last decades, there is a growing trend for more limited surgical resection, such as adrenal-sparing radical nephrectomy, laparoscopic nephrectomy, or nephron-sparing partial nephrectomy^[1-4,18-24]. Partial nephrectomy can be performed, either with an open, pure laparoscopic or robot-assisted approach, based on surgeon's expertise and skills. Similar oncological outcomes have been reported for both nephron-sparing surgery (NSS) and radical nephrectomy^[1,22-24]. NSS is primarily recommended in patients with T1a tumors, and when technically feasible in T1b neoplasms^[1]. Non-surgical treatment, including ablative techniques such as cryoablation, and radiofrequency ablation have been proposed for RCCs less than 4 cm in diameter^[1,25]. However, due to the low quality of the available data no published recommendations still exist on these techniques^[1]. Active surveillance may be offered to some patients, especially in elderly and/or comorbid patients with small renal tumors^[26,27].

ROLE OF COMPUTED TOMOGRAPHY

Computed tomography (CT) is widely accepted as the examination of choice for the detection, characterization and staging of RCC, with a staging accuracy up to 91%^[4,28-47]. The wide availability of CT and its relative ease of performance and interpretation compared with magnetic resonance imaging (MRI) render it the main imaging method for staging RCC. In surgical cases, accurate preoperative imaging and exact tumor staging is of paramount importance for planning the optimal surgical approach and strategy, and for providing accurate prognostic information for the patient. Knowledge of the renal and tumor vascular supply and the relationship of the neoplasm to the adjacent renal

Table 1 New tumor, node, metastasis classification system for renal cell carcinoma

T-primary tumor			
Tx	Primary tumour cannot be assessed		
T0	No evidence of primary tumour		
T1	Tumour ≤ 7 cm in greatest dimension, limited to kidney		
T1a	Tumour ≤ 4 cm in greatest dimension, limited to kidney		
T1b	Tumour > 4 cm but ≤ 7 cm in greatest dimension, limited to kidney		
T2	Tumour > 7 cm in greatest dimension, limited to kidney		
T2a	Tumour > 7 cm but ≤ 10 cm in greatest dimension, limited to kidney		
T2b	Tumour > 10 cm in greatest dimension, limited to kidney		
T3	Tumour extends into major veins or perinephric tissues but not into the ipsilateral adrenal gland and not beyond Gerota fascia		
T3a	Tumour grossly extends into the renal vein or its segmental branches, or tumour invades perirenal and/or renal sinus fat but not beyond Gerota fascia		
T3b	Tumour grossly extends into the vena cava below the diaphragm		
T3c	Tumour grossly extends into the vena cava above the diaphragm or invades the wall of the vena cava		
T4	Tumour invades beyond Gerota's fascia (including contiguous extension into the ipsilateral adrenal gland)		
N-regional lymph nodes			
Nx	Regional nodes cannot be assessed		
N0	No regional lymph nodes metastases		
N1	Metastases in a single regional lymph node		
N2	Metastases in more than 1 regional lymph node		
M-distant metastases			
M0	No distant metastases		
M1	Distant metastases		
TNM stage grouping			
Stage I	T1	N0	M0
Stage II	T2	N0	M0
Stage III	T3	N0	M0
	T1,T2,T3	N1	M0
Stage IV	T4	Any N	M0
	Any T	N2	M0
	Any T	Any N	M1

TNM: Tumor, node, metastasis.

parenchyma and the pelvicaliceal system are crucial for operative planning, particularly in patients planned for NSS^[48-51].

According to the recommendations by the American College of Radiology, multidetector, multiphasic CT of the abdomen is considered appropriate for staging of small or incidentally detected renal tumors (equal or smaller than 3 cm in diameter)^[52]. For renal tumors larger than 3 cm in diameter, multidetector CT (MDCT) is the diagnostic modality of choice. MRI of the abdomen is a suitable substitute, when patient cannot undergo contrast-enhanced CT. Ultrasonography may be considered more appropriate for staging small renal tumors, when the intravenous administration of contrast medium is contraindicated. Positron emission tomography (PET) does not yet have an established role in staging RCC. PET with the tracer fluorine-18-2-fluoro-2-deoxy-D-glucose-PET may find difficulties even in the detection of primary carcinoma against the normal background of hyperactivity in the kidneys. PET may be used as a complementary examination for confirming metastatic disease in lesions detected by CT, MRI, or bone scan, and it may be used to detect unsuspected metastases in high-risk patients^[52].

The most recent technical advances introduced

with the use of MDCT scanners brought about further advancements in the preoperative evaluation of RCC^[4,31-51]. The main advantages of MDCT are fast scanning time, increased volume coverage, acquisition of thin slices and improved spatial and temporal resolution. Rapid coverage of the kidneys and scanning during specific organ perfusion phases after the intravenous administration of iodinated contrast material has improved the diagnostic performance of CT in the detection and characterization of renal masses^[34-41]. The use of thin slices and the acquisition of near-isotropic or isotropic data improve the quality of volume data set for workstation analysis and multiplanar reformations (MPRs) and 3D reconstructions in any desired plane with excellent anatomic details are possible^[30-33,49-51].

MDCT protocol

MDCT examination in cases of a known or suspected renal mass should include multiple phases, proper timing of each post-contrast enhanced phase, and use of MPRs and 3D-reconstructions. The CT protocol includes an unenhanced acquisition, combined with two or more post-contrast enhanced series (corticomedullary phase, nephrographic phase, and excretory phase)^[4,28-47].

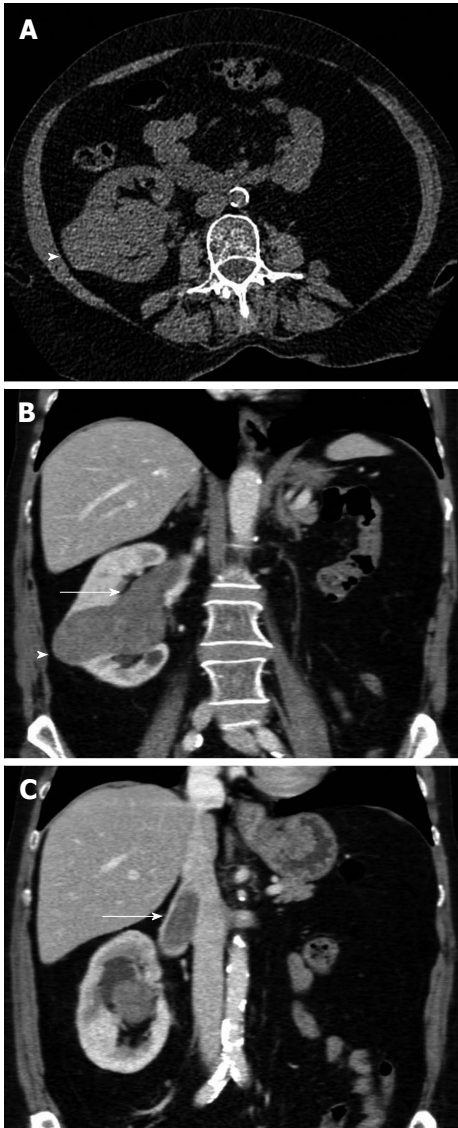


Figure 1 The 65-year-old woman with papillary renal cell carcinoma of the right kidney and tumoral invasion of the ipsilateral renal vein and the inferior vena cava (stage T3b, grade 2). The patient had left radical nephrectomy years ago for renal cell carcinoma. A: Transverse unenhanced computed tomography (CT) image shows a lobular right renal mass (arrowhead), located in the interlobar region. The mass is relatively homogeneous, slightly hyperdense (CT density: 40 HU), when compared to the normal renal parenchyma; B and C: Contrast-enhanced coronal multiplanar reformations during the corticomedullary phase depict right renal tumor, with moderate, homogeneous enhancement (arrowhead, mean CT density: 65 HU). Venous tumour thrombus is diagnosed as a filling defect within right renal vein and the infrahepatic part of the inferior vena cava (arrow). Neoplastic thrombus is seen extending directly from the neoplasm, enhancing with a similar pattern with primary malignancy.

The unenhanced scanning is always necessary to serve as a baseline for measurements of enhancement after contrast material administration. Areas of hemorrhage and/or presence of calcifications are also seen on these images. In the corticomedullary phase, obtained 25-70 s after the start of injection, an intense enhancement of the renal cortex is observed, while the medulla does not enhance and remains hypodense. This phase is essential for staging RCC. An accurate diagnosis of venous

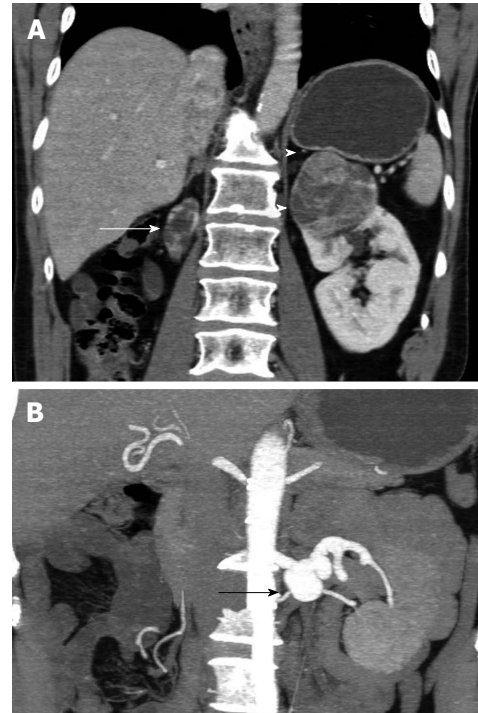


Figure 2 The 70-year-old man with clear cell renal cell carcinoma of the left solitary functioning kidney (stage T1b, grade 2). A: Post-contrast enhanced coronal multiplanar reformation during the corticomedullary phase depicts left upper pole renal mass, strongly and heterogeneously enhancing, after contrast material administration. A thin hyperdense rim (arrowheads) is detected around the tumor, proved to correspond to fibrous pseudocapsule on pathology. Atrophic right kidney (arrow); B: Coronal 3D-reconstruction during the same phase, using maximum intensity projection algorithm shows left renal artery aneurysm (arrow).

extension of tumoral tissue is possible (Figure 1). This phase may be also used as a map for the delineation of the arterial anatomy of the kidneys (Figure 2), especially helpful in selected cases to plan NSS. Hypervascular arterialized metastases from RCC may be more evident on this phase (Figure 3). The nephrographic phase, with a delay of 80-180 s after contrast administration is considered the most important for detecting and characterizing renal tumors. During this phase, normal renal parenchyma enhances homogeneously, allowing the best opportunity for the delineation of renal masses, which are often detected with relatively less contrast enhancement (Figure 4). The excretory phase is acquired after a 4-8 min delay, resulting in excretion of contrast material into the pelvicaliceal system. The relationship of the tumor to the renal collecting system (Figure 5) and possible signs of invasion are evaluated in this acquisition.

In addition to multiphase imaging, multiplanar display techniques, including MPRs and 3D-reconstructions, more often with maximum intensity projection and volume rendering technique are essential and improve the diagnostic performance of CT in detecting, characterizing and staging of RCC^[28-33,48-51]. MPRs and 3D-reconstructions can be viewed in multiple planes and orientations, providing a useful interactive road map when planning treatment, either surgery or conservative. Accurate depiction of the position of the kidney relative to the



Figure 3 The 52-year-old man with advanced-stage clear cell renal cell carcinoma of the right kidney. Contrast-enhanced (A) coronal and (B and C) sagittal reformations during the corticomedullary phase show a large right renal tumor (arrow), strongly and inhomogeneously enhancing. Central hypodense parts within malignancy corresponded to areas of necrosis on histology. There is perinephric stranding and contrast-enhancing nodules in the perinephric fat (long arrow, B), a finding strongly suggestive for perinephric fat invasion. The tumor is seen extending and invading the undersurface of the liver (long arrow, C). Lung metastases are detected (arrowheads, A and C). There is also a small amount of ascites and nodular peritoneal masses (arrowheads, B), with heterogeneous enhancement, identical to that of the primary neoplasm, findings suggestive of peritoneal metastases. Peritoneal metastases from renal cell carcinoma (RCC) are extremely rare. Neoplastic invasion of the peritoneum by RCC may occur either, by contiguous spread of renal tumor through the renal capsule, the anterior renal fascia and the posterior parietal peritoneum, or via tumoral emboli.



Figure 4 The 62-year-old man with clear cell renal cell carcinoma of the left kidney (stage T1a, grade II). A: Transverse plain computed tomography image barely depicts lower pole left kidney mass (arrow), slightly hyperdense. This finding was appreciated after studying the post-contrast enhanced images; B: Coronal reformations during the corticomedullary; C: The nephrographic phase. The tumor (arrow) is seen enhancing strongly and heterogeneously during the corticomedullary phase, a finding strongly suggestive for the diagnosis of renal cell carcinoma (RCC). Hypervascular RCCs as in this case, may enhance to the same degree as the renal cortex and may be mistaken for normal renal parenchyma at the corticomedullary phase. The neoplasm is clearly delineated in the nephrographic phase, detected mainly hypodense, when compared to the contrast-enhancing normal renal parenchyma.

surrounding bones is helpful in guiding the initial surgical incision. Delineation of tumor location and depth of extension into the kidney, ensures maximal preservation of the surrounding normal renal parenchyma after surgery (Figure 6). The arterial and venous anatomy of the kidney is clearly depicted at 3D-CT angiography (Figure 2). Identification of renal vessels, possible anatomic variants and depiction of their relationship with the neoplasm may help minimize ischemic injuries and intraoperative complications. Depiction of the relationship of RCC to the collecting system and assessment of possible neoplastic infiltration represent valuable information in treatment planning, especially in cases of conservative surgery. The pelvicaliceal system is best visualized on coronal MPRs and volume rendering 3D-displays, with images closely resembling those of conventional intravenous urography^[47-51].

CT findings of RCC

Most RCCs are solid tumors with CT density of 20 HU or greater at unenhanced scanning^[4,28-33]. The tumor may not be clearly visible on plain images, because its density is usually similar to that of the surrounding normal renal parenchyma. In these cases, a focal bulging of the renal contour (Figure 7) may raise the suspicion of a space-occupying lesion. Small tumors (smaller than 3 cm in diameter) are usually homogeneous, while larger lesions tend to be more heterogeneous due to the presence of central necrosis and/or hemorrhage (Figures 3 and 5). Calcifications are seen in up to 30% of RCCs (Figure 5A).

RCC typically has a rich vascular supply^[4,28-33]. Therefore, the hallmark diagnosis of RCC is the presence of strong, mainly heterogeneous contrast enhancement (Figures 2-6 and 8). A contrast enhancement value of more than 20 HU with respect to the noncontrast scan is

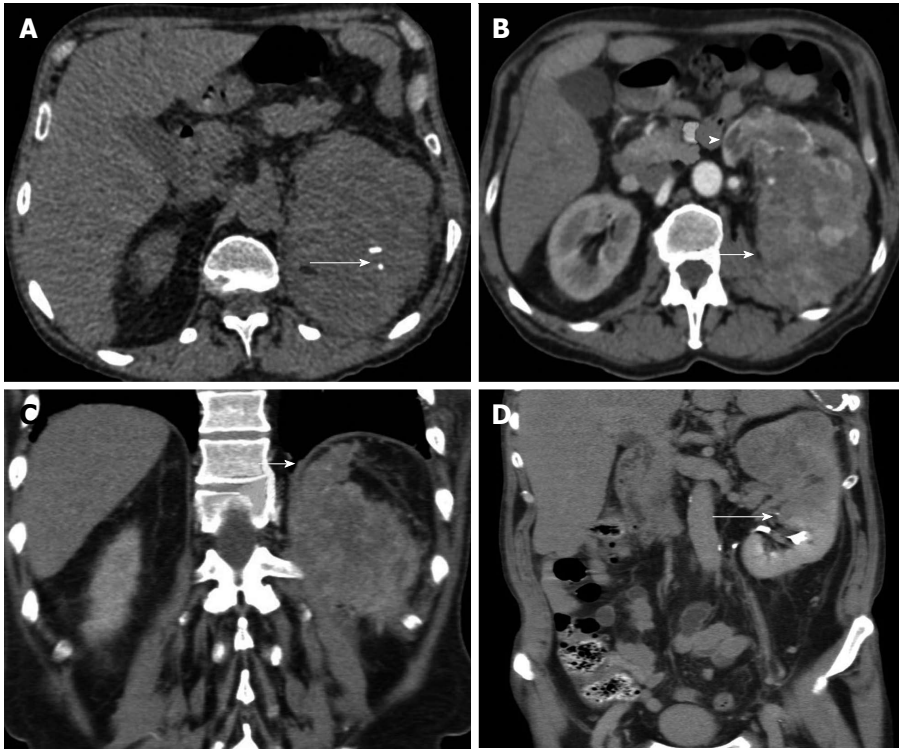


Figure 5 The 62-year-old man with clear cell renal cell carcinoma of the left kidney (stage T3a, grade 3). A: Transverse unenhanced computed tomography (CT) image shows large heterogenous left renal mass, with small areas of calcifications (long arrow); B: Transverse multiplanar reformation (MPR) during the corticomedullary phase demonstrates left renal malignancy (arrow), inhomogeneously enhancing. The left renal vein is dilated and enhances heterogeneously (arrowhead) due to neoplastic invasion. VTT enhances with a same pattern as renal cell carcinoma; C: Coronal reformations during the corticomedullary phase depicts tumor ill-defined margins and extension into the perinephric fat tissue (arrow). Thickening of the diaphragms of the perinephric space is also seen; D: Coronal MPR during the excretory phase shows nonvisualization of the upper calyces and invasion of the middle calyceal group (arrow), a finding strongly suggestive of invasion of renal sinus fat. CT findings were confirmed both surgically and pathologically.

considered suspicious for malignancy. An enhancement value between 10 and 20 HU, is considered indeterminate^[45]. On the nephrographic phase, RCCs typically appear hypodense compared to the normally enhancing renal parenchyma (Figure 4).

DIFFERENTIATION OF RCC FROM BENIGN RENAL TUMORS

The wide use of cross-sectional imaging studies has also led to an increase of incidentally discovered benign renal masses, including angiomyolipoma (AML) and renal oncocytoma. Because radical nephrectomy is not desirable for a benign tumor, the accurate characterization of renal masses is required to avoid unwanted surgery. CT findings may prove helpful in characterizing the nature of renal tumors^[53-62].

AML can be accurately diagnosed on CT, by detecting the intratumoral fat component with negative density on unenhanced scanning. However, in approximately 4.5% of all AMLs intratumoral fat cannot be visualized at CT. Kim *et al.*^[53] in a retrospective study of 19 AMLs with minimal fat and 62 RCCs on two-phase helical CT, reported that homogeneous tumor enhancement and prolonged enhancement pattern were the most valuable CT findings in differentiating these tumors, more often

detected in the first group. Hyperdensity of a renal mass on plain CT images is another CT finding reported for AML with minimal fat^[54]. Zhang *et al.*^[56] in a retrospective study of 44 AMLs with minimal fat and papillary RCCs reported that the unenhanced CT density, the presence of intratumoral vessels, and the CT density of early excretory phase images may be used to differentiate these tumors. Woo *et al.*^[57] reported unenhanced tumor-kidney CT density difference and long-to-short axis ratio as the simplest and more accurate features in differentiating AMLs with minimal fat from non-clear cell RCCs on three-phase MDCT.

Several studies have described CT imaging features of renal oncocytoma, including well-defined margins, homogeneous contrast enhancement, presence of a central stellate scar, spoke-wheel pattern of arterial enhancement and absence of hemorrhage, calcifications and necrosis^[58,59]. More specifically, renal oncocytoma has been described as a sharply-demarcated solid homogeneous mass, with homogeneous contrast enhancement, except for a hypodense stellate, central area. However, these classic findings do not always allow a confident characterization of this tumor, because they are often seen in patients with RCC^[58,59]. MDCT improved the diagnostic performance of CT in differentiating these tumors^[60-62]. The enhancement and washout values

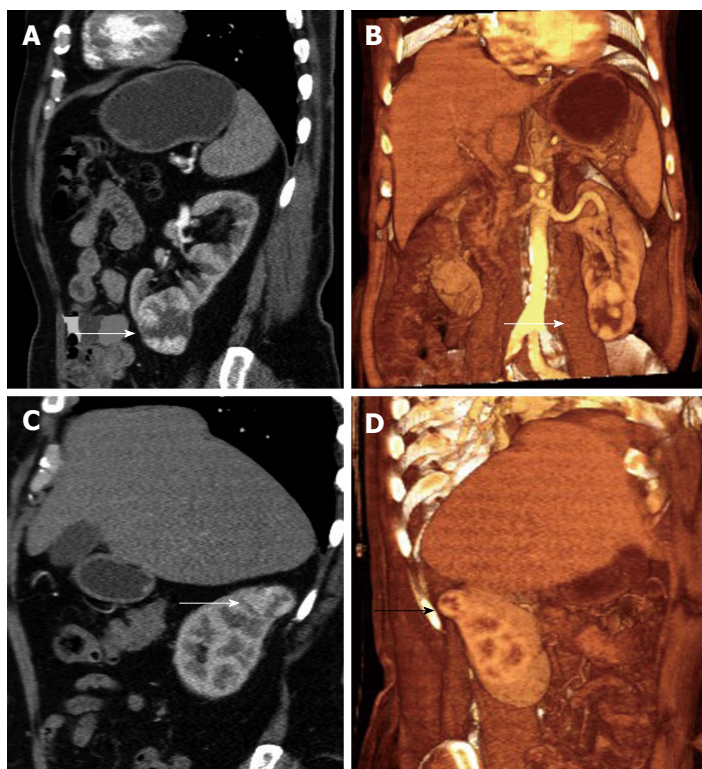


Figure 6 The 74-year-old man with synchronous bilateral renal cell carcinomas of clear cell type (stage T1). Bilateral synchronous renal cell carcinomas (RCCs) are uncommon, reported in less than 2% of patients with RCCs. The patient had left radical nephrectomy and right partial nephrectomy. Sagittal multiplanar reformations (MPR) (A) and coronal 3D reformation with volume rendering technique (B) during the corticomedullary phase depict a sharply-demarcated tumor in the lower pole of the left kidney (arrow, A), strongly and heterogeneously enhancing. Sagittal (C) MPR and (D) 3D reformation with the same algorithm depict a second, smaller tumor in the upper pole of the right kidney, with a similar pattern of contrast enhancement. Preoperative information obtained with computed tomography examination enabled conservative surgery for the right renal malignancy.

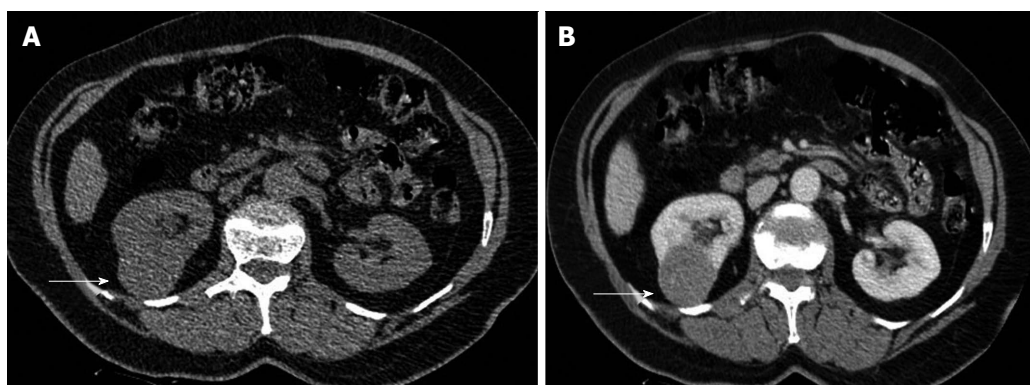


Figure 7 The 60-year-old woman with clear cell renal cell carcinoma of the left kidney (stage T1a, grade II). A: Transverse plain computed tomography (CT) image depicts lower pole right renal mass as a focal bulging of the renal contour (arrow), mainly isodense (CT density: 35 HU) to the renal parenchyma; B: Axial multiplanar reformation during the corticomedullary phase clearly shows renal malignancy (arrow) moderately and heterogeneously enhancing (mean CT density: 60 HU). Heterogeneous contrast enhancement on imaging should always suggest renal malignancy preoperatively.

in MDCT may aid in distinguishing small oncocytomas from RCCs of similar size^[60,61]. Bird *et al*^[60] reported that early phase enhancement greater than 500% and washout values of greater than 50% were mostly seen in renal oncocytomas. Kim *et al*^[62] reported characteristic contrast enhancement patterns for renal oncocytomas smaller than 4 cm in diameter on MDCT. The authors assessed segmental enhancement inversion during the corticomedullary phase and early excretory

phase, defined as follows: in a renal mass showing two parts with different degrees of enhancement during corticomedullary phase, the relatively more enhanced part became less enhanced during early excretory phase, whereas the less-enhanced part during corticomedullary phase became highly enhanced during early excretory phase. Segmental enhancement inversion was found to be characteristic of small renal oncocytomas in this study^[62].

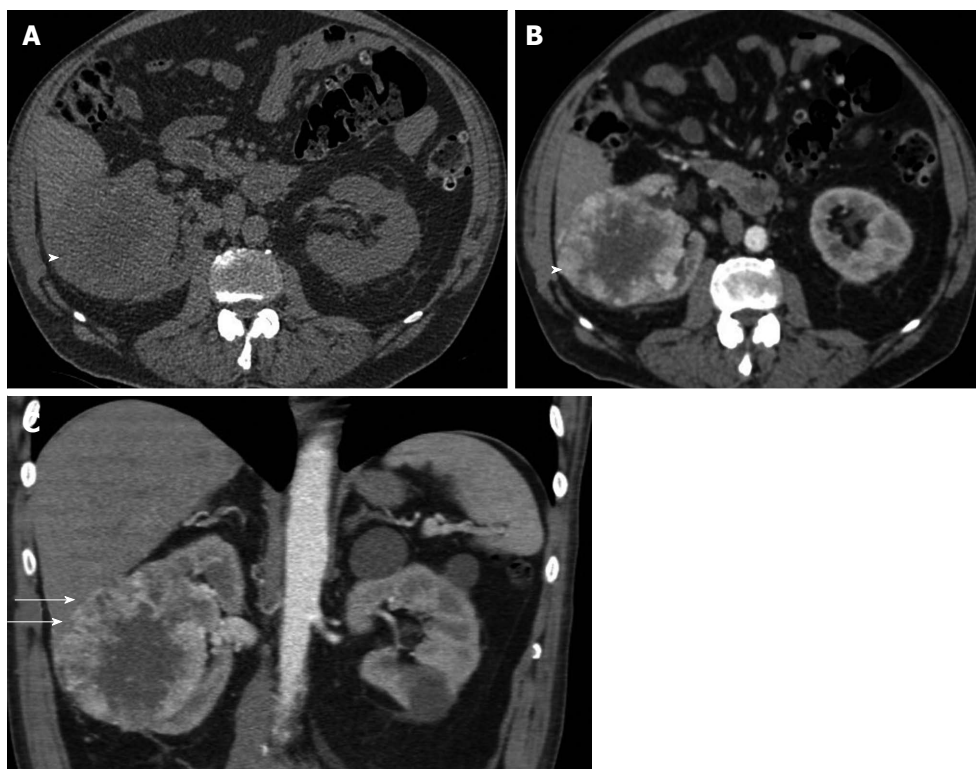


Figure 8 The 75-year-old man with clear cell renal cell carcinoma of the right kidney, invading the liver. A: Axial plain image shows right heterogeneous right renal tumor (arrowhead); B: Transverse reformation during the corticomedullary phase depicts strong, heterogeneous mass enhancement. The tumor (arrowhead) enhances mainly in the periphery, with a mean computed tomography density of 110 HU (compared to that of 40 HU on the unenhanced images), a finding more compatible with the diagnosis of renal cell carcinoma of the clear cell variety. Central non-enhancing areas corresponded to areas of necrosis on pathology; C: Coronal reformation during the same phase shows renal tumor invading the liver (small arrows), a finding confirmed both on surgery and histopathology.

HISTOLOGIC CHARACTERIZATION OF RCC

RCC is considered a clinicopathologically heterogeneous disease and is classified into clear cell (conventional), papillary, chromophobe, collecting duct carcinoma, medullary carcinoma, and unclassified type^[15-17]. The commonest histologic subtypes are clear cell, papillary, and chromophobe, accounting for 70%-80%, 14%-17%, and 4%-8% of RCCs, respectively. Each subtype is associated with a different prognosis. Clear cell RCC has the worst prognosis, with a 5-year survival rate of 44%-69%, when compared to the 5-year survival rate of 82%-92% for papillary RCC and the 5-year survival of 78%-87% for chromophobe RCC^[15-17]. It has been proposed that a preoperative characterization of the histologic type of RCC may lead to improvements in predicting tumor response to treatment, in providing patient counseling, and in individualizing follow-up regimens^[16,17].

CT findings have been reported to correlate closely with the histopathologic characteristics of the more common types of RCC^[63-73]. Among CT criteria, degree of enhancement proved to be the most valuable parameter^[63-69]. More specifically, ccRCCs are more often detected as highly hypervascular tumors (Figures 2-6 and 8), with areas of cystic degeneration and/or

necrosis, whereas papillary (Figure 1) and chromophobe (Figure 9) types are usually more homogeneous and hypovascular^[63-73]. Kim *et al.*^[63] studied the helical CT features of 110 RCCs, including tumor size, degree and patterns of enhancement, presence or absence of calcifications and tumor-spreading patterns. Clear cell RCCs showed stronger enhancement than the other histologic types, with a mean CT density of 106 ± 48 HU in the corticomedullary phase and 62 ± 25 HU in the excretory phase. When using 84 HU as the cutoff value in the corticomedullary phase and 44 HU in the excretory phase, the sensitivity and specificity for differentiating ccRCC from the other subtypes were 74% and 100%, 84% and 91%, respectively^[63].

Jung *et al.*^[67] in a study of 149 small RCCs with MDCT, confirmed the presence of heterogeneous and strong contrast enhancement as more suggestive for the diagnosis of ccRCC, than the papillary and the chromophobe type. Young *et al.*^[68] recently reported their results on the histologic characterization of 277 RCCs with multiphasic MDCT, using up to four phases (unenhanced, corticomedullary, nephrographic, and excretory phase). Clear cell RCCs showed significantly greater enhancement in the corticomedullary phase (mean CT density: 125.0 HU) than do papillary RCCs (53.6 HU), and chromophobe RCCs (73.8 HU), reporting accuracies of 85% and 84%, respectively in their differentiation^[68].

During the last 15 years, advances in the study of

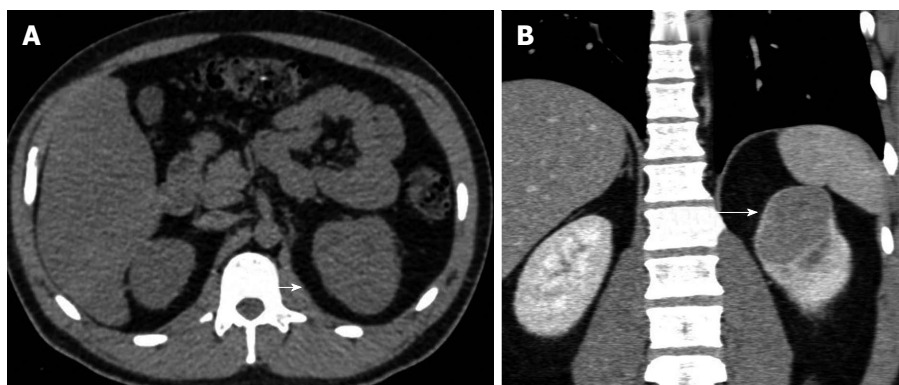


Figure 9 The 31-year-old man with chromophobe renal cell carcinoma of the left kidney (stage T1b, grade II). A: Axial plain image barely depicts upper pole left renal mass mainly isodense, with a slight bulging of the renal contour (arrow); B: Coronal reformation during the nephrographic phase clearly depicts left renal tumor (arrow). The neoplasm enhances moderately and homogeneously [computed tomography (CT) density: 70 HU, when compared to the CT density of 35 HU on unenhanced images]. A thin hyperdense rim surrounds renal malignancy, proved to correspond to fibrous pseudocapsule histologically.

ccRCC genetics have led to an improved understanding of the biological characteristics of this tumor, closely correlating with patient's prognosis and to the development of molecular targeted therapies^[74-78]. More specifically, the gain of the long arm of chromosome 5 (5q), detected in a sub-set of ccRCCs, correlates with an improved 5-year survival rate and the loss of the short-arm of chromosome 9 (9p) correlates with a lower 5-year survival rate^[74-78]. Common chromosomal anomalies in patients with ccRCC also include the loss of the short arm of chromosome 3, the loss of chromosome Y, the gain of the short arm of chromosome 5 and the gain of chromosome 7^[73-77]. Sauk *et al*^[78] in a retrospective study of 58 histologically proved and karyotyped ccRCCs reported a correlation between multiphasic MDCT features and cytogenetic characteristics of ccRCCs. In their study, ccRCCs with a deletion of chromosome 3p had fewer calcifications than those without this deletion. After contrast material administration, the authors reported greater enhancement for ccRCCs with loss of the Y chromosome than those without the anomaly during the corticomedullary phase (mean CT density: 130.0 HU vs 102.5 HU), also for ccRCCs with trisomy 5 than those with disomy 5 during the excretory phase (115.5 HU vs 83.4 HU), and for ccRCCs with disomy 7 than those with trisomy 7 during the corticomedullary phase (139.3 HU vs 105.8 HU)^[78].

GRADING OF RCC

Advances in minimally invasive techniques and active surveillance protocols have allowed treatment of RCC without radical nephrectomy^[1]. In these patients, core biopsy can be used to assess the pathologic characteristics of the tumor. However, core biopsy is not always adequate for the assessment of tumor nuclear grade (NG)^[79,80]. NG is considered an independent predictor of cancer-specific survival^[10-12]. RCCs of high NG are associated with early disease recurrence after therapy and with cancer-related mortality in patients with recurrent disease^[10-12]. Therefore, a non-invasive method that could

help to predict the histologic characteristics, and more specifically NG in patients with RCC would be valuable. An inverse association between CT tumor enhancement and NG has been reported, with neoplasms of higher NG detected with lower enhancement on multiphasic contrast-enhanced CT examination^[81-83]. Villalobos-Gollás *et al*^[81] in a retrospective study of 48 RCCs, 44 of which were of clear cell variety evaluated the enhancement of the entire neoplasm on the image with most prominent areas of enhancement. The authors reported an association between higher NG and more advanced-stage disease with areas of lower enhancement of the tumor^[81]. Zhu *et al*^[80] examined tumor enhancement and relative enhancement values in the corticomedullary and nephrographic phases, by placing a region of interest as large as possible within the solid, more avidly enhancing parts of 255 ccRCCs. Age older than 58 years, irregular tumor margin, and corticomedullary phase relative enhancement value of 0.65 or less were identified as independent predictors of high tumor NG^[80]. One possible explanation for the negative association between CT enhancement and NG is the presence of histologic necrosis within the tumor. Histologic necrosis has been reported to correlate with tumor aggressiveness, including higher NG and stage and larger size at diagnosis^[80].

RCC SIZE

Tumor size is a significant part of the current TNM staging system^[1,9]. It represents a highly important predictor of pathologic stage and survival in RCC^[84,85]. Moreover, the selection of appropriate candidates for NSS, along with ablative therapies and active follow-up has been largely guided by tumor sizes evaluated by imaging modalities.

Although, some reports have shown a certain degree of discrepancy between the preoperative CT size of renal tumors and the pathologic size^[86,87], discrepancies are minimal and clinically insignificant in most cases^[88-90]. Chen *et al*^[88] in a study of 169 renal tumors treated with NSS reported an overestimation of renal tumor

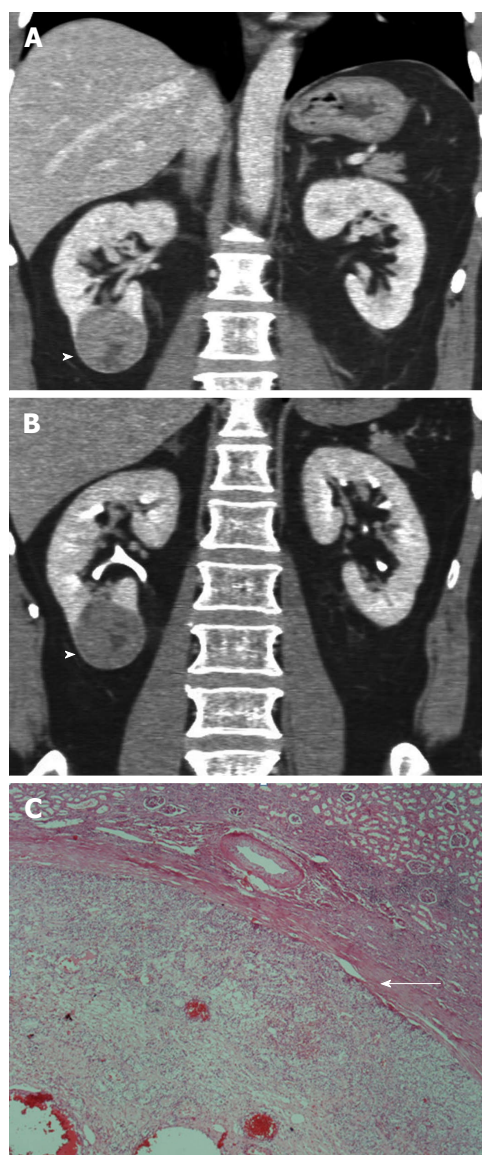


Figure 10 The 50-year-old man with clear cell-chromophobe renal cell carcinoma of right kidney (grade 3, pT1b). A: Coronal reformatted images in corticomedullary; B: Nephrographic phases depict hyperdense rim (arrowhead) surrounding the tumor; C: Histologic section (H and E, $\times 400$) shows fibrous pseudocapsule (arrow) between tumor and adjacent normal renal parenchyma.

size by CT, as compared with the histopathology report. But the discrepancy was only 0.22 cm with little clinical significance, suggesting that CT is an accurate method to measure renal tumor size preoperatively^[88]. Choi *et al.*^[89] in a study of 175 localized RCCs on a 16-row CT scanner, reported a good correlation between the CT and pathologic tumor sizes, although an overestimation of the size was observed for tumors less than 6 cm in diameter. Lee *et al.*^[90] in a retrospective study of 435 RCCs compared the radiographic tumor size, defined as the largest diameter measured on CT images with the pathologic size. Although, the authors found that CT size overestimated pathologic size, the observed differences were minimal, less than 1 mm, even for small-sized RCCs (4-5 cm in diameter, for which the discrepancies

were only about 2 mm), and therefore insignificant^[90].

STAGING OF RCC

RCC confined to renal capsule

RCCs generally do not have a true histologic capsule, but are surrounded by a pseudocapsule^[91]. The presence of a pseudocapsule surrounding RCC is considered as a histologic feature of early-stage disease^[1,91]. These neoplasms are often of small size and of low grade^[1,91]. Pseudocapsule formation is the result of tumor growth, producing compression, ischemia, and necrosis of the adjacent renal parenchyma, and resulting in deposition of fibrous tissue^[91,92].

MRI has been reported as an accurate technique in the detection of renal pseudocapsule, when compared with CT, angiography and gray-scale sonography, with accuracies ranging from 74%-93%^[93-96]. Pseudocapsule appears as a hypointense rim between the neoplasm and the normal renal parenchyma on T2-weighted images^[93-96]. Yamashita *et al.*^[94] in a study of 54 RCCs reported an accuracy of 74% in the detection of renal pseudocapsule with MRI and T2-weighted images. At contrast-enhanced CT, the pseudocapsule was not visible in any tumors in this study, probably due to the similar contrast enhancement by both the pseudocapsule and the surrounding renal parenchyma^[94]. Takahashi *et al.*^[95] assessed the diagnostic performance of multidetector CT, selective angiography and MRI in the detection of renal pseudocapsule in 42 RCCs. A pseudocapsule was detected on 26% of neoplasms on CT, as a hypodense or hyperdense rim surrounding RCC, on 67% of neoplasms on angiography, as a radiolucent rim and on 93% of tumors on T2-weighted sequences on MRI, as a low signal intensity rim^[95]. Contrast-enhanced sonography improved the diagnostic performance of conventional ultrasound in the preoperative detection of renal pseudocapsule^[97]. A sensitivity of 85.7% has been reported by Ascenti *et al.*^[97] with sonographic contrast agents, detecting pseudocapsule, as a contrast-enhancing rim, surrounding the tumor, usually with late enhancement.

Multiphase MDCT improved the diagnostic performance of CT in the detection of this finding^[98]. A retrospective study of 29 RCCs reported an accuracy of 83% in the detection of renal pseudocapsule with MDCT. In this study a four-phase (unenhanced, arterial, portal and nephrographic-excretory phase) CT protocol and multiplanar reformations in the transverse, coronal and sagittal planes of each post-contrast phase were used for CT data interpretation. Portal and nephrographic phase, with coronal and sagittal reformations proved more accurate in the detection of this finding. Renal pseudocapsule was mainly detected as a hyperdense rim surrounding RCC, seen on both phases (Figures 2A, 9B and 10) and this was due to the presence of fibrous tissue. In four cases, a hypodense renal pseudocapsule was revealed (Figure 11) detected only on portal phase



Figure 11 The 44-year-old woman with clear cell renal cell carcinoma of left kidney (grade 2, pT1a). Computed tomography image demonstrates hypodense rim (arrowhead) around neoplasm detected only on coronal reformations during portal phase. The presence of pseudocapsule was confirmed on histology.

reformations^[98].

Spread to perinephric tissues

The TNM classification system characterizes advanced RCC within Gerota's fascia as T3. T3a stage RCCs are characterized by tumor grossly invading the renal vein or its segmental branches, or invading perinephric (PN) fat and/or renal sinus (RS) fat^[1]. RCCs with PN fat invasion have to penetrate the renal capsule, and tumors with RS fat invasion directly invade the RS fat, due to lack of any capsule at this area. The presence of either PN fat invasion or RS fat invasion, and invasion of both renal fat compartments were significantly associated with synchronous nodal or distant metastases, higher tumor grade and greater tumor dimensions, when compared to patients with no PN fat invasion^[99]. Siddiqui *et al.*^[99] in a retrospective study of 163 pT3a RCCs concluded that PN and RS fat infiltration was associated with death from RCC independent of tumor size. Infiltration of the perinephric fat is also a crucial point when planning NSS. Radical nephrectomy is mandatory in these patients^[1].

Perirenal or perinephric space is a cone-shaped retroperitoneal compartment, which is bounded by the anterior (Gerota's fascia) and posterior (Zuckerkandl's fascia) layers of the renal fascia and contains the kidney, adrenal gland, proximal ureter, a prominent amount of fat, a rich network of perirenal vessels and lymphatics, and small-sized lymph nodes^[100,101].

The renal fascia measures 1-3 mm in thickness, and the posterior layer is thicker and more often visualized than the anterior layer^[100,101]. Thickening of the renal fascia is a sensitive but nonspecific sign, indicating either neoplastic or non-neoplastic adjacent diseases^[100,101]. Perinephric space is divided into multiple compartments by thin fibrous lamellae and bridging septa^[102]. Kunin^[102] described three groups of septa. Group I septa arise from the renal capsule and extend to the renal fascia. Group II septa are attached to the renal capsule, paralleling more or less the renal surface. Group III represents the commonest type, connecting the anterior and posterior

leaves of the perinephric space^[102]. Thickening of the bridging septa (perinephric stranding) is not a reliable or specific sign in diagnosing neoplastic infiltration of the PN fat tissue^[100,101]. A variety of neoplastic and nonneoplastic processes, may involve the perirenal space, including RCC, inflammation, edema, vascular engorgement, hematoma, or fat necrosis^[100,101]. Perinephric stranding is also reported in about half of RCCs confined within the kidney.

Detection of PN fat invasion in RCC and differentiation between T1/T2 and T3a stages was the commonest staging error with spiral CT^[5,33]. CT criteria used to diagnose neoplastic invasion of PN fat include the following: thickening of the renal fascia, thickening of the bridging septa (perinephric stranding), presence of fluid, presence of peritumoral vessels, defined as asymmetrically enlarged, often irregular vessels within Gerota's fascia, tumor margins and presence of neoplastic nodules within the PN fat, enhancing after contrast material administration^[33,103-106]. Multiphase MDCT with multiplanar reformations improved the diagnostic performance of CT in detecting PN fat infiltration^[33,103-106]. Catalano *et al.*^[33] by using three-phase MDCT protocol with thin slices reported an overall accuracy of 95% in diagnosing PN fat invasion, using the presence of hyperdense streaks and nodules surrounding RCC as CT signs to suggest neoplastic infiltration. Kim *et al.*^[105,106] reported high accuracies for MDCT in detecting PN fat invasion, using tumor size, irregular tumor margins and nodular appearance of the PN fat, as predictors for PN fat invasion. In a retrospective study of 48 RCCs on a 16-row CT scanner, the most significant predictors in diagnosing PN fat invasion were the presence of contrast-enhancing nodules in the PN fat and tumoral margins, with an overall accuracy of 85.4%, for both CT criteria (Figures 3B and 5C)^[103].

The renal sinus is a central compartment formed by the extension of the PN space into the medial surface of renal parenchyma. The fibrous capsule terminates at the RS region, resulting in the absence of any barrier preventing the extension of neoplastic cells into the rich network of lymphatics vessels and veins within the RS^[107]. RS fat invasion is associated with aggressive tumors at increased risk for dissemination. Thompson *et al.*^[108] showed that ccRCCs invading the RS fat are more aggressive than tumors with PN fat infiltration only. These neoplasms were more likely to have high NG, regional lymph node metastases and sarcomatoid differentiation. CT criteria used to diagnose invasion of RS fat include the following: extension to the renal sinus, proximity to the pelviciceal system, and invasion of the pelviciceal system^[103]. Among them, renal collecting system invasion was proved to be the single most significant predictor of RS fat invasion (Figure 5D)^[103]. None of the other two CT signs proved reliable in the diagnosis of RS fat infiltration. Some RCCs may distort the RS complex and protrude, without signs of invasion. The proximity of a tumor to a neighboring structure, as

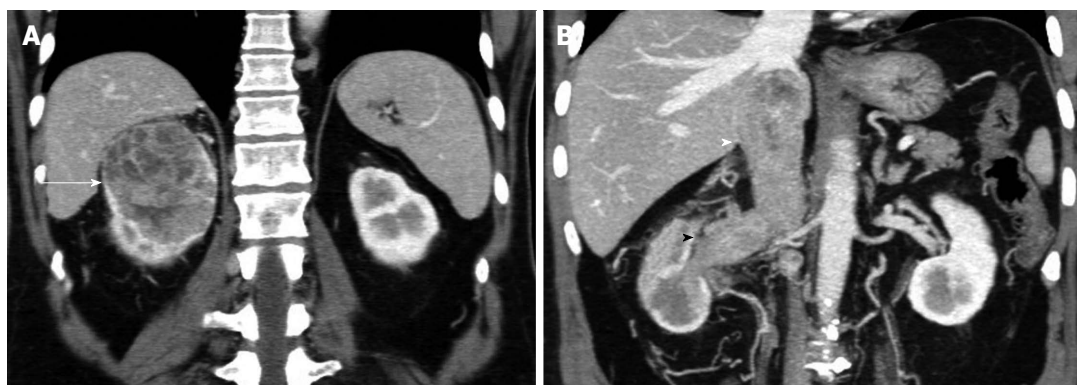


Figure 12 The 64-year-old man with clear cell renal cell carcinoma of the right kidney, invading the renal vein and the inferior vena cava (stage T3b, grade 3). A: Coronal multiplanar reformations during the corticomedullary phase depicts large, inhomogeneously enhancing right renal tumor (arrow); B: Coronal 3D-display with maximum intensity projection technique during the same phase shows neoplastic thrombus invading left renal vein and the inferior vena cava (arrowheads). Coronal reformations clearly show venous invasion extending below the level of the diaphragm. Perinephric stranding and abnormal vessels are detected in the ipsilateral perinephric space, although pathology was negative for perinephric fat invasion.

the pelvicaliceal system, does not always correspond to neoplastic infiltration on histopathology^[103].

Venous extension

Extension of RCC into the renal vein alone (stage T3a) occurs in approximately 23% of patients^[4]. Tumor involvement of the inferior vena cava (T3b, T3c) is seen in approximately 4%-10% of patients and is more common in right-sided tumors^[4]. A venous tumour thrombus (VTT) into the inferior vena cava in patients with RCC is a significant adverse prognostic factor^[1]. Excision of the VTT is recommended in patients with non-metastatic RCC^[1]. Accurate preoperative evaluation for the presence and extent of the VTT in the renal vein and/or the inferior vena cava is important for planning the appropriate surgical approach for thrombectomy, and minimizing the risk of intraoperative tumoral embolism^[4,28-33,109-112]. The level of involvement of the inferior vena cava, whether infrahepatic, retrohepatic or supradiaphragmatic dictates the mode of surgical approach^[113].

MDCT has been reported as highly accurate in the diagnosis of spread of RCC into the renal vein, with a reported negative predictive value of 97% and a positive predictive value of 92%^[4,28-33,109-112]. MDCT is also effective in delineating the superior extent of inferior vena cava thrombus, with staging results similar to that of MRI^[4,28-33,109-112]. Venous extension is optimally detected during the corticomedullary phase, when contrast enhancement of the venous system is maximal. The use of combination of axial images and multiplanar reconstructions is necessary for the assessment of the extension of VTT. The most specific sign of venous invasion is the presence of a low-attenuation filling defect within the vein. The CT characteristics of the thrombus help differentiate neoplastic from bland thrombus. Direct continuity of the thrombus with the primary malignancy suggests metastatic invasion. Heterogeneous enhancement of the thrombus, with a pattern similar to that of RCC also indicates tumoral thrombus (Figures

1B, 1C, 5B and 12)^[4,28-33,109-112]. An abrupt change in the caliber of the vein and/or the presence of a clot within collateral veins are considered as ancillary findings suggesting neoplastic involvement. Enlargement of the renal vein alone is not a reliable sign, since it may be due to increased blood flow within a hypervascular RCC or it may represent a normal variant^[4,28-33,109-112].

Invasion of the inferior vena cava wall (T3c) is considered an adverse prognostic sign, with a 5-year survival rate of 25% and 69% for patients with tumor invading the inferior vena cava wall and those with free-floating neoplastic thrombus into the inferior vena cava, respectively^[45]. Infiltration of the inferior vena cava wall will also complicate surgical resection, because prosthetic reconstruction is usually needed in these patients^[45,114]. Focal enhancement of the vena cava wall, or infiltration of adjacent soft tissues, indicates vena cava wall invasion on CT examination^[45].

Local organ invasion (beyond the Gerota's fascia, including contiguous extension into the ipsilateral adrenal gland)

Assessment of the adrenal gland is important in patients with RCC for surgical planning. Multivariate analysis in a prospective study comparing the outcomes of radical or partial nephrectomy with, or without, ipsilateral adrenalectomy showed that upper pole tumor location was not predictive of adrenal involvement, but tumour size was predictive^[115]. The current trend is to spare the ipsilateral adrenal gland, because ipsilateral adrenalectomy does not provide a survival advantage^[1,115]. Adrenalectomy is justified in cases suspicious for metastatic spread, based on radiographic and/or intra-operative findings^[1].

MDCT with multiplanar and 3D-reconstructions provide satisfactory results in assessing possible invasion of the adrenal gland^[4,8-33,45]. Visualization of a normal adrenal gland at CT has been reported to be associated with a 100% negative predictive value for tumoral invasion, at pathologic analysis. CT signs that strongly suggest

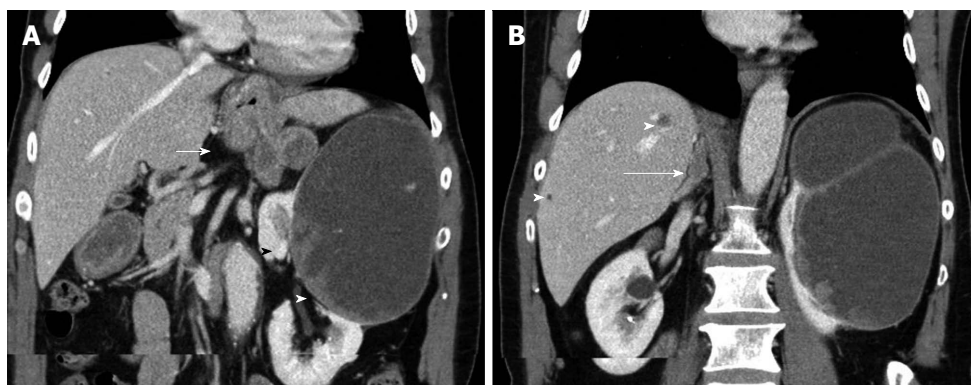


Figure 13 The 70-year-old man with advanced-stage papillary renal cell carcinoma of the left kidney. Coronal multiplanar reformations during the nephrographic phase show large, mainly cystic left renal mass, with solid contrast-enhancing components (arrowheads). Enlarged retroperitoneal LNs, inhomogeneously enhancing (arrow, A) are detected, compatible with metastatic lymphadenopathy. Liver (arrowhead, B) and right adrenal (long arrow, B) metastases are also seen. All metastatic deposits have a similar pattern of enhancement.

invasion of the adrenal gland include the following: adrenal enlargement, displacement, or nonvisualization; adrenalectomy should be performed in these cases^[4,28-33,45].

Direct extension of RCC outside Gerota's fascia and into neighboring organs (stage T4) is not always straightforward to diagnose, unless there is a definite focal change in CT density within the affected organ (Figures 3C and 8). Loss of fat tissue planes and irregular margins between RCC and adjacent organs raise the possibility of neoplastic invasion, although this is not always confirmed on histopathology^[4,28-33,45]. Multiplanar and 3D-reconstructions help in depicting the relationship of RCC to the adjacent organs in multiple planes and orientations, therefore improving the diagnostic performance of MDCT^[4,28-33,45].

Regional lymph node metastases

The presence of regional lymph node (LN) metastases in RCC implies a poor prognosis, with reported 5-year survival rates of 5%-30%^[4]. The role of lymph node dissection in RCC remains controversial^[4,116]. In patients with localized RCC, without clinical evidence of LN metastases, lymph node dissection is not recommended^[1]. In patients with localized disease and clinically enlarged LNs, the survival benefit of LN dissection is unclear. In these cases, LN dissection is suggested mainly for staging purposes or local control^[1]. Clinical assessment of LNs status is based on enlargement of LNs on CT and/or MRI and on intraoperative assessment by direct palpation. However, in patients with clinically enlarged LNs, only less than 20% of clinically positive LNs are confirmed to be metastatic at histologic examination^[1].

The main CT criterion to diagnose metastatic LN involvement is the size^[4,28-33,45]. Retroperitoneal LNs with a short-axis diameter larger than 1 cm are suspicious for neoplastic invasion (Figure 13). A cutoff value of 1 cm as the upper limit for normal LNs has significant limitations. One is the inability to recognize possible micro-metastases, resulting in false-negative findings in approximately 10% of cases. Furthermore, false-positive findings vary between 3%-43%, mostly due

to LN enlargement caused by reactive hyperplasia. The enhancement pattern of the node may also help differentiate reactive from malignant adenopathy; metastatic LNs usually present with heterogeneous enhancement. The presence of a hypodense center after contrast material administration, proved to correspond to necrosis on pathology, is considered a highly specific finding, with a positive predictive value of 100% in diagnosing metastatic lymphadenopathy. LNs enhancement with a pattern similar to that of the primary tumor also signifies metastatic disease (Figure 13).

Distant metastases

Metastatic disease occurs in a significant percentage of patients with RCC. At presentation, 25%-30% of RCCs have distant metastases^[1]. A median survival of 6-9 mo has been reported for metastases left untreated and a 2-year survival rate of 10%-20% after treatment. The sites of distant metastases from RCC, in order of decreasing frequency are: lungs (50%-60%), bones (30%-40%), liver (30%-40%), and adrenal gland, contralateral kidney, retroperitoneum, and brain (5% each)^[117]. Practically any organ may be affected.

Imaging has an important role in assessing the extent of metastatic disease. CT is considered the examination of choice in the detection of intraabdominal metastases (Figures 3, 13 and 14). Like the primary RCC, metastatic lesions are often hypervascular. The optimal phase for their detection is the corticomedullary phase, because they may be obscured on late-phase images.

CONCLUSION

Multidetector multiphase CT with multiplanar and 3D-displays remains the primary imaging modality for the detection of RCC, with high staging accuracies. CT features may prove useful in differentiating RCC from benign renal tumors. CT examination may help in the preoperative characterization of the histologic subtype of RCC. Tumor enhancement patterns of ccRCC

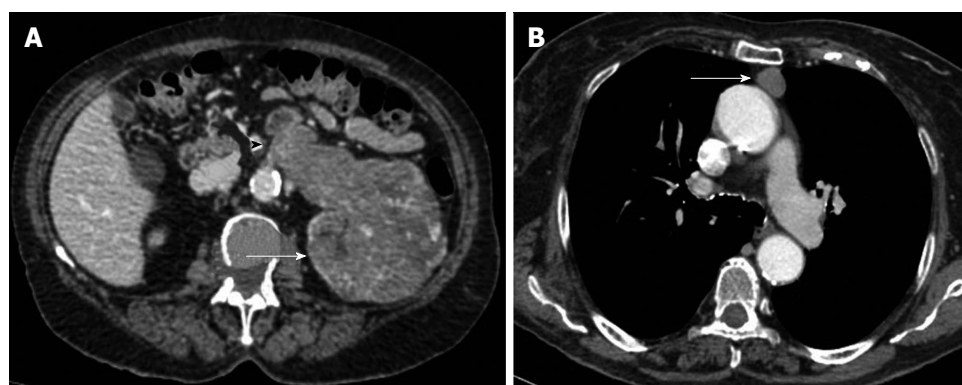


Figure 14 The 81-year-old woman with advanced-stage clear cell renal cell carcinoma of the left kidney. A: Transverse multiplanar reformation during the nephrographic phase shows large, inhomogeneously enhancing left renal malignancy (arrow), invading the ipsilateral renal vein (arrowhead); B: Contrast-enhanced computed tomography image of the thorax demonstrates enlarged mediastinal lymph nodes (arrow), with heterogeneous enhancement, suggestive for metastatic invasion.

are associated with Fuhrman grade and cytogenetic characteristics.

REFERENCES

- 1 **Ljungberg B**, Bensalah K, Bex A, Canfield S, Dabestani S, Hofmann F, Hora M, Kuczyk MA, Lam T, Volpe A; European Association of Urology. Guidelines on renal cell carcinoma. 2014. Available from: URL: <http://uroweb.org/guideline/renal-cell-carcinoma/>
- 2 **Ferlay J**, Steliarova-Foucher E, Lortet-Tieulent J, Rosso S, Coebergh JW, Comber H, Forman D, Bray F. Cancer incidence and mortality patterns in Europe: estimates for 40 countries in 2012. *Eur J Cancer* 2013; **49**: 1374-1403 [PMID: 23485231 DOI: 10.1016/j.ejca.2012.12.027]
- 3 **American Cancer Society**. Cancer facts and figures 2014. Available from: URL: <http://www.cancer.org/acs/groups/content/@research/documents/webcontent/acspsc-042151.pdf>
- 4 **Sheth S**, Scatarige JC, Horton KM, Corl FM, Fishman EK. Current concepts in the diagnosis and management of renal cell carcinoma: role of multidetector ct and three-dimensional CT. *Radiographics* 2001; **21** Spec No: S237-S254 [PMID: 11598260 DOI: 10.1148/radiographics.21.suppl_1.g01oc18s237]
- 5 **Lee CT**, Katz J, Fearn PA, Russo P. Mode of presentation of renal cell carcinoma provides prognostic information. *Urol Oncol* 2002; **7**: 135-140 [PMID: 12474528 DOI: 10.1016/j.purol.2011.02.013]
- 6 **Patard JJ**, Leray E, Rodriguez A, Rioux-Leclercq N, Guillé F, Lobel B. Correlation between symptom graduation, tumor characteristics and survival in renal cell carcinoma. *Eur Urol* 2003; **44**: 226-232 [PMID: 12875943 DOI: 10.1016/j.eururo.2008.07.053]
- 7 **Northrup BE**, Jokerst CE, Grubb RL, Menias CO, Khanna G, Siegel CL. Hereditary renal tumor syndromes: imaging findings and management strategies. *AJR Am J Roentgenol* 2012; **199**: 1294-1304 [PMID: 23169721 DOI: 10.2214/AJR.12.9079]
- 8 **Choyke PL**, Glenn GM, Walther MM, Zbar B, Linehan WM. Hereditary renal cancers. *Radiology* 2003; **226**: 33-46 [PMID: 12511666 DOI: 10.1148/radiol.2261011296]
- 9 **Eggerer S**. TNM staging for renal cell carcinoma: time for a new method. *Eur Urol* 2010; **58**: 517-519; discussion 519-521 [PMID: 20728266 DOI: 10.1016/j.eururo.2010.08.007]
- 10 **Fuhrman SA**, Lasky LC, Limas C. Prognostic significance of morphologic parameters in renal cell carcinoma. *Am J Surg Pathol* 1982; **6**: 655-663 [PMID: 7180965 DOI: 10.1186/2193-1801-2-378]
- 11 **Zisman A**, Pantuck AJ, Dorey F, Said JW, Shvarts O, Quintana D, Gitlitz BJ, deKernion JB, Figlin RA, Belldegrun AS. Improved prognostication of renal cell carcinoma using an integrated staging system. *J Clin Oncol* 2001; **19**: 1649-1657 [PMID: 11250993 DOI: 10.1016/j.purol.2009.07.007]
- 12 **Rioux-Leclercq N**, Karakiewicz PI, Trinh QD, Ficarra V, Cindolo L, de la Taille A, Tostain J, Zigeuner R, Mejean A, Patard JJ. Prognostic ability of simplified nuclear grading of renal cell carcinoma. *Cancer* 2007; **109**: 868-874 [PMID: 17262800]
- 13 **Sun M**, Lughezzani G, Jeldres C, Isbarn H, Shariat SF, Arjane P, Widmer H, Pharand D, Latour M, Perrotte P, Patard JJ, Karakiewicz PI. A proposal for reclassification of the Fuhrman grading system in patients with clear cell renal cell carcinoma. *Eur Urol* 2009; **56**: 775-781 [PMID: 19573980 DOI: 10.1016/j.eururo.2009.06.008]
- 14 **Eble JN**, Sauter G, Epstein JI, Sesterhenn IA. Pathology and genetics of tumours of the urinary system and male genital organs. Lyon, France: IARC Press, 2004
- 15 **Prasad SR**, Humphrey PA, Catena JR, Narra VR, Srigley JR, Cortez AD, Dalrymple NC, Chintapalli KN. Common and uncommon histologic subtypes of renal cell carcinoma: imaging spectrum with pathologic correlation. *Radiographics* 2006; **26**: 1795-1806; discussion 1806-1810 [PMID: 17102051 DOI: 10.1148/rg.266065010]
- 16 **Cheville JC**, Lohse CM, Zincke H, Weaver AL, Blute ML. Comparisons of outcome and prognostic features among histologic subtypes of renal cell carcinoma. *Am J Surg Pathol* 2003; **27**: 612-624 [PMID: 12717246 DOI: 10.1309/AJCPLBK9L9KDYQZP]
- 17 **Patard JJ**, Leray E, Rioux-Leclercq N, Cindolo L, Ficarra V, Zisman A, De La Taille A, Tostain J, Artibani W, Abbou CC, Lobel B, Guillé F, Chopin DK, Mulders PF, Wood CG, Swanson DA, Figlin RA, Belldegrun AS, Pantuck AJ. Prognostic value of histologic subtypes in renal cell carcinoma: a multicenter experience. *J Clin Oncol* 2005; **23**: 2763-2771 [PMID: 15837991 DOI: 10.1200/JCO.2005.07.055]
- 18 **Novick AC**. Renal-sparing surgery for renal cell carcinoma. *Urol Clin North Am* 1993; **20**: 277-282 [PMID: 8493750 DOI: 10.1016/j.juro.2011.02]
- 19 **Van Poppel H**, Bamelis B, Oyen R, Baert L. Partial nephrectomy for renal cell carcinoma can achieve long-term tumor control. *J Urol* 1998; **160**: 674-678 [PMID: 9720519 DOI: 10.1016/S0022-5347(01)62751-4]
- 20 **Krejić KG**, Blute ML, Cheville JC, Sebo TJ, Lohse CM, Zincke H. Nephron-sparing surgery for renal cell carcinoma: clinicopathologic features predictive of patient outcome. *Urology* 2003; **62**: 641-646 [PMID: 14550434 DOI: 10.1016/S0090-4295(03)00489-8]
- 21 **Zincke H**, Ghavamian R. Partial nephrectomy for renal cell cancer is here to stay--more data on this issue. *J Urol* 1998; **159**: 1161-1162 [PMID: 9507822 DOI: 10.1097/00005392-199804000-00013]
- 22 **MacLennan S**, Imamura M, Lapitan MC, Omar MI, Lam TB, Hilvano-Cabungcal AM, Royle P, Stewart F, MacLennan G, MacLennan SJ, Canfield SE, McClinton S, Griffiths TR, Ljungberg B, N'Dow J. Systematic review of oncological outcomes following

- surgical management of localised renal cancer. *Eur Urol* 2012; **61**: 972-993 [PMID: 22405593 DOI: 10.1016/j.eururo.2012.02.039]
- 23 **Gratzke C**, Seitz M, Bayrle F, Schlenker B, Bastian PJ, Haseke N, Bader M, Tilki D, Roosen A, Karl A, Reich O, Khoder WY, Wyler S, Stief CG, Staehler M, Bachmann A. Quality of life and perioperative outcomes after retroperitoneoscopic radical nephrectomy (RN), open RN and nephron-sparing surgery in patients with renal cell carcinoma. *BJU Int* 2009; **104**: 470-475 [PMID: 19239445 DOI: 10.1111/j.1464-410X.2009.08439.x]
 - 24 **Van Poppel H**, Da Pozzo L, Albrecht W, Matveev V, Bono A, Borkowski A, Colombel M, Klotz L, Skinner E, Keane T, Marreud S, Collette S, Sylvester R. A prospective, randomised EORTC intergroup phase 3 study comparing the oncologic outcome of elective nephron-sparing surgery and radical nephrectomy for low-stage renal cell carcinoma. *Eur Urol* 2011; **59**: 543-552 [PMID: 21186077 DOI: 10.1016/j.eururo.2010.12.013]
 - 25 **Whitson JM**, Harris CR, Meng MV. Population-based comparative effectiveness of nephron-sparing surgery vs ablation for small renal masses. *BJU Int* 2012; **110**: 1438-1443; discussion 1443 [PMID: 22639860 DOI: 10.1111/j.1464-410X.2012.11113.x]
 - 26 **Jewett MA**, Mattar K, Basiuk J, Morash CG, Pautler SE, Siemens DR, Tanguay S, Rendon RA, Gleave ME, Drachenberg DE, Chow R, Chung H, Chin JL, Fleshner NE, Evans AJ, Gallie BL, Haider MA, Kachura JR, Kurban G, Fernandes K, Finelli A. Active surveillance of small renal masses: progression patterns of early stage kidney cancer. *Eur Urol* 2011; **60**: 39-44 [PMID: 21477920 DOI: 10.1016/j.eururo.2011.03.030]
 - 27 **Abouassaly R**, Lane BR, Novick AC. Active surveillance of renal masses in elderly patients. *J Urol* 2008; **180**: 505-508; discussion 508-509 [PMID: 18550113 DOI: 10.1016/j.juro.2008.04.033]
 - 28 **Pavlica P**, Derchi L, Martorana G, Bertaccini A, Pavlica P, Martorana G, Barozzi L. Renal Cell Carcinoma Imaging. *Eur Urol Sup* 2006; **5**: 580-592 [DOI: 10.1016/j.eursup.2006.03.010]
 - 29 **Heidenreich A**, Ravary V. Preoperative imaging in renal cell cancer. *World J Urol* 2004; **22**: 307-315 [PMID: 15290202 DOI: 10.1590/S1677-55382007000300002]
 - 30 **Coll DM**, Smith RC. Update on radiological imaging of renal cell carcinoma. *BJU Int* 2007; **99**: 1217-1222 [PMID: 17441914 DOI: 10.1111/j.1464-410X.2007.06824.x]
 - 31 **Gardner TA**, Tirkles T, Mellon M, Koch MO. Imaging techniques for the patient with renal cell carcinoma. *Semin Nephrol* 2011; **31**: 245-253 [PMID: 21784273 DOI: 10.1016/j.semnephrol.2011.05.004]
 - 32 **Kang SK**, Kim D, Chandarana H. Contemporary imaging of the renal mass. *Curr Urol Rep* 2011; **12**: 11-17 [PMID: 20949339 DOI: 10.1007/s11934-010-0148-y]
 - 33 **Catalano C**, Fraioli F, Laghi A, Napoli A, Pediconi F, Danti M, Nardis P, Passariello R. High-resolution multidetector CT in the preoperative evaluation of patients with renal cell carcinoma. *AJR Am J Roentgenol* 2003; **180**: 1271-1277 [PMID: 12704036 DOI: 10.2214/ajr.180.5]
 - 34 **Johnson PT**, Horton KM, Fishman EK. How not to miss or mischaracterize a renal cell carcinoma: protocols, pearls, and pitfalls. *AJR Am J Roentgenol* 2010; **194**: W307-W315 [PMID: 20308475 DOI: 10.2214/AJR.09.3033]
 - 35 **Silverman SG**, Lee BY, Seltzer SE, Bloom DA, Corless CL, Adams DF. Small (< or = 3 cm) renal masses: correlation of spiral CT features and pathologic findings. *AJR Am J Roentgenol* 1994; **163**: 597-605 [PMID: 8079852 DOI: 10.2214/ajr.163.3.8079852]
 - 36 **Zhang J**, Lefkowitz RA, Ishill NM, Wang L, Moskowitz CS, Russo P, Eisenberg H, Hricak H. Solid renal cortical tumors: differentiation with CT. *Radiology* 2007; **244**: 494-504 [PMID: 17641370]
 - 37 **Hsu RM**, Chan DY, Siegelman SS. Small renal cell carcinomas: correlation of size with tumor stage, nuclear grade, and histologic subtype. *AJR Am J Roentgenol* 2004; **182**: 551-557 [PMID: 14975944 DOI: 10.2214/ajr.182.3.1820551]
 - 38 **Kopka L**, Fischer U, Zoeller G, Schmidt C, Ringert RH, Grabbe E. Dual-phase helical CT of the kidney: value of the corticomedullary and nephrographic phase for evaluation of renal lesions and preoperative staging of renal cell carcinoma. *AJR Am J Roentgenol* 1997; **169**: 1573-1578 [PMID: 9393168]
 - 39 **Birnbaum BA**, Jacobs JE, Ramchandani P. Multiphasic renal CT: comparison of renal mass enhancement during the corticomedullary and nephrographic phases. *Radiology* 1996; **200**: 753-758 [PMID: 8756927 DOI: 10.1148/radiology.200.3.8756927]
 - 40 **Yuh BI**, Cohan RH. Different phases of renal enhancement: role in detecting and characterizing renal masses during helical CT. *AJR Am J Roentgenol* 1999; **173**: 747-755 [PMID: 10470916 DOI: 10.2214/ajr.173.3.10470916]
 - 41 **Cohan RH**, Sherman LS, Korobkin M, Bass JC, Francis IR. Renal masses: assessment of corticomedullary-phase and nephrographic-phase CT scans. *Radiology* 1995; **196**: 445-451 [PMID: 7617859 DOI: 10.1148/radiology.196.2.7617859]
 - 42 **Johnson CD**, Dunnick NR, Cohan RH, Illescas FF. Renal adenocarcinoma: CT staging of 100 tumors. *AJR Am J Roentgenol* 1987; **148**: 59-63 [PMID: 3491524 DOI: 10.2214/ajr.148.1.59]
 - 43 **Hallscheidt PJ**, Bock M, Riedasch G, Zuna I, Schoenberg SO, Autschbach F, Soder M, Noeldge G. Diagnostic accuracy of staging renal cell carcinomas using multidetector-row computed tomography and magnetic resonance imaging: a prospective study with histopathologic correlation. *J Comput Assist Tomogr* 2004; **28**: 333-339 [PMID: 15100536 DOI: 10.1097/00004728-200405000-00005]
 - 44 **Hallscheidt P**, Wagener N, Gholipour F, Aghabozorgi N, Dreyhaupt J, Hohenfellner M, Haferkamp A, Pfitzenmaier J. Multislice computed tomography in planning nephron-sparing surgery in a prospective study with 76 patients: comparison of radiological and histopathological findings in the infiltration of renal structures. *J Comput Assist Tomogr* 2006; **30**: 869-874 [PMID: 17082687 DOI: 10.1097/01.rct.0000230009.31715.5b]
 - 45 **Türkvtan A**, Akdur PO, Altinel M, Olçer T, Turhan N, Cumhur T, Akinci S, Ozkul F. Preoperative staging of renal cell carcinoma with multidetector CT. *Diagn Interv Radiol* 2009; **15**: 22-30 [PMID: 19263370]
 - 46 **Ganeshan D**, Morani A, Ladha H, Bathala T, Kang H, Gupta S, Lalwani N, Kundra V. Staging, surveillance, and evaluation of response to therapy in renal cell carcinoma: role of MDCT. *Abdom Imaging* 2014; **39**: 66-85 [PMID: 24077815 DOI: 10.1007/s00261-013-0040-6]
 - 47 **Zagoria RJ**, Bechtold RE, Dyer RB. Staging of renal adenocarcinoma: role of various imaging procedures. *AJR Am J Roentgenol* 1995; **164**: 363-370 [PMID: 7839970 DOI: 10.2214/ajr.164.2.7839970]
 - 48 **Coll DM**, Herts BR, Davros WJ, Uzzo RG, Novick AC. Preoperative use of 3D volume rendering to demonstrate renal tumors and renal anatomy. *Radiographics* 2000; **20**: 431-438 [PMID: 10715341 DOI: 10.1148/radiographics.20.2.g00mc16431]
 - 49 **Coll DM**, Uzzo RG, Herts BR, Davros WJ, Wirth SL, Novick AC. 3-dimensional volume rendered computerized tomography for preoperative evaluation and intraoperative treatment of patients undergoing nephron sparing surgery. *J Urol* 1999; **161**: 1097-1102 [PMID: 10081846 DOI: 10.4103/0974-7796.134256]
 - 50 **Ueda T**, Tobe T, Yamamoto S, Motoori K, Murakami Y, Igarashi T, Ito H. Selective intra-arterial 3-dimensional computed tomography angiography for preoperative evaluation of nephron-sparing surgery. *J Comput Assist Tomogr* 2004; **28**: 496-504 [PMID: 15232381 DOI: 10.1097/00004728-200407000-00010]
 - 51 **Smith PA**, Marshall FF, Corl FM, Fishman EK. Planning nephron-sparing renal surgery using 3D helical CT angiography. *J Comput Assist Tomogr* 1999; **23**: 649-654 [PMID: 10524840]
 - 52 **American College of Radiology**. ACR Appropriateness Criteria: Urologic Imaging. Renal cell carcinoma staging. [Accessed 2011 January 26]. Available from: URL: <http://www.acr.org/>
 - 53 **Kim JK**, Park SY, Shon JH, Cho KS. Angiomyolipoma with minimal fat: differentiation from renal cell carcinoma at biphasic helical CT. *Radiology* 2004; **230**: 677-684 [PMID: 14990834 DOI: 10.1148/radiol.2303030003]
 - 54 **Jinzaki M**, Tanimoto A, Narimatsu Y, Ohkuma K, Kurata T, Shinmoto H, Hiramatsu K, Mukai M, Murai M. Angiomyolipoma: imaging findings in lesions with minimal fat. *Radiology* 1997; **205**:

- 497-502 [PMID: 9356635 DOI: 10.1148/radiology.205.2.9356635]
- 55 **Obuz F**, Karabay N, Seçil M, Igci E, Kovanlikaya A, Yörükoglu K. Various radiological appearances of angiomyolipomas in the same kidney. *Eur Radiol* 2000; **10**: 897-899 [PMID: 10879697 DOI: 10.1007/s003300051031]
 - 56 **Zhang YY**, Luo S, Liu Y, Xu RT. Angiomyolipoma with minimal fat: differentiation from papillary renal cell carcinoma by helical CT. *Clin Radiol* 2013; **68**: 365-370 [PMID: 23321146 DOI: 10.1016/j.crad.2012.08.028]
 - 57 **Woo S**, Cho JY, Kim SH, Kim SY. Angiomyolipoma with minimal fat and non-clear cell renal cell carcinoma: differentiation on MDCT using classification and regression tree analysis-based algorithm. *Acta Radiol* 2014; **55**: 1258-1269 [PMID: 24259298 DOI: 10.1177/0284185113513887]
 - 58 **Jasinski RW**, Amendola MA, Glazer GM, Bree RL, Gikas PW. Computed tomography of renal oncocytomas. *Comput Radiol* 1985; **9**: 307-314 [PMID: 4064635 DOI: 10.1016/0730-4862(85)90057-5]
 - 59 **Davidson AJ**, Hayes WS, Hartman DS, McCarthy WF, Davis CJ. Renal oncocytoma and carcinoma: failure of differentiation with CT. *Radiology* 1993; **186**: 693-696 [PMID: 8430176 DOI: 10.1148/radiology.186.3.8430176]
 - 60 **Bird VG**, Kanagarajah P, Morillo G, Caruso DJ, Ayyathurai R, Leveillee R, Jorda M. Differentiation of oncocytoma and renal cell carcinoma in small renal masses (< 4 cm): the role of 4-phase computerized tomography. *World J Urol* 2011; **29**: 787-792 [PMID: 20717829 DOI: 10.1007/s00345-010-0586-7]
 - 61 **Gakis G**, Kramer U, Schilling D, Kruck S, Stenzl A, Schlemmer HP. Small renal oncocytomas: differentiation with multiphase CT. *Eur J Radiol* 2011; **80**: 274-278 [PMID: 20667676 DOI: 10.1016/j.ejrad.2010.06.049]
 - 62 **Kim JI**, Cho JY, Moon KC, Lee HJ, Kim SH. Segmental enhancement inversion at biphasic multidetector CT: characteristic finding of small renal oncocytoma. *Radiology* 2009; **252**: 441-448 [PMID: 19508984 DOI: 10.2214/AJR.12.8616]
 - 63 **Kim JK**, Kim TK, Ahn HJ, Kim CS, Kim KR, Cho KS. Differentiation of subtypes of renal cell carcinoma on helical CT scans. *AJR Am J Roentgenol* 2002; **178**: 1499-1506 [PMID: 12034628 DOI: 10.2214/ajr.178.6.1781499]
 - 64 **Herts BR**, Coll DM, Novick AC, Obuchowski N, Linnell G, Wirth SL, Baker ME. Enhancement characteristics of papillary renal neoplasms revealed on triphasic helical CT of the kidneys. *AJR Am J Roentgenol* 2002; **178**: 367-372 [PMID: 11804895 DOI: 10.2214/ajr.178.2.1780367]
 - 65 **Sheir KZ**, El-Azab M, Mosbah A, El-Baz M, Shaaban AA. Differentiation of renal cell carcinoma subtypes by multislice computerized tomography. *J Urol* 2005; **174**: 451-455; discussion 455 [PMID: 16006863]
 - 66 **Jinzaki M**, Tanimoto A, Mukai M, Ikeda E, Kobayashi S, Yuasa Y, Narimatsu Y, Murai M. Double-phase helical CT of small renal parenchymal neoplasms: correlation with pathologic findings and tumor angiogenesis. *J Comput Assist Tomogr* 2000; **24**: 835-842 [PMID: 11105696 DOI: 10.4103/0973-1482.137924]
 - 67 **Jung SC**, Cho JY, Kim SH. Subtype differentiation of small renal cell carcinomas on three-phase MDCT: usefulness of the measurement of degree and heterogeneity of enhancement. *Acta Radiol* 2012; **53**: 112-118 [PMID: 22114020 DOI: 10.1258/ar.2011.110221]
 - 68 **Young JR**, Margolis D, Sauk S, Pantuck AJ, Sayre J, Raman SS. Clear cell renal cell carcinoma: discrimination from other renal cell carcinoma subtypes and oncocytoma at multiphase multidetector CT. *Radiology* 2013; **267**: 444-453 [PMID: 23382290]
 - 69 **Bata P**, Gyebnar J, Tarnoki DL, Tarnoki AD, Kekesi D, Szendroi A, Fejer B, Szasz AM, Nyirady P, Karlinger K, Berezi V. Clear cell renal cell carcinoma and papillary renal cell carcinoma: differentiation of distinct histological types with multiphase CT. *Diagn Interv Radiol* 2013; **19**: 387-392 [PMID: 23864331 DOI: 10.5152/dir.2013.13068]
 - 70 **Zokali I**, Marotti M, Kolarić B. Pretreatment differentiation of renal cell carcinoma subtypes by CT: the influence of different tumor enhancement measurement approaches. *Int Urol Nephrol* 2014; **46**: 1089-1100 [PMID: 24381132 DOI: 10.1007/s11255-013-0631-8]
 - 71 **Lee-Felker SA**, Felker ER, Tan N, Margolis DJ, Young JR, Sayre J, Raman SS. Qualitative and quantitative MDCT features for differentiating clear cell renal cell carcinoma from other solid renal cortical masses. *AJR Am J Roentgenol* 2014; **203**: W516-W524 [PMID: 25341166 DOI: 10.2214/AJR.14.12460]
 - 72 **Pierorazio PM**, Hyams ES, Tsai S, Feng Z, Trock BJ, Mullins JK, Johnson PT, Fishman EK, Allaf ME. Multiphasic enhancement patterns of small renal masses (≤ 4 cm) on preoperative computed tomography: utility for distinguishing subtypes of renal cell carcinoma, angiomyolipoma, and oncocytoma. *Urology* 2013; **81**: 1265-1271 [PMID: 23601445 DOI: 10.1016/j.urol.2012.12.049]
 - 73 **Veloso Gomes F**, Matos AP, Palas J, Mascarenhas V, Herédia V, Duarte S, Ramalho M. Renal cell carcinoma subtype differentiation using single-phase corticomedullary contrast-enhanced CT. *Clin Imaging* 2014; **39**: 273-277 [PMID: 25457534 DOI: 10.1016/j.clinimag.2014]
 - 74 **Gunawan B**, Huber W, Holtrup M, von Heydebreck A, Efferth T, Poustka A, Ringert RH, Jakse G, Füzesi L. Prognostic impacts of cytogenetic findings in clear cell renal cell carcinoma: gain of 5q31-qter predicts a distinct clinical phenotype with favorable prognosis. *Cancer Res* 2001; **61**: 7731-7738 [PMID: 11691785]
 - 75 **Presti JC**, Wilhelm M, Reuter V, Russo P, Motzer R, Waldman F. Allelic loss on chromosomes 8 and 9 correlates with clinical outcome in locally advanced clear cell carcinoma of the kidney. *J Urol* 2002; **167**: 1464-1468 [PMID: 11832771 DOI: 10.1002/cncr.25279]
 - 76 **Mitsumori K**, Kittleson JM, Itoh N, Delahunt B, Heathcott RW, Stewart JH, McCredie MR, Reeve AE. Chromosome 14q LOH in localized clear cell renal cell carcinoma. *J Pathol* 2002; **198**: 110-114 [PMID: 12210070 DOI: 10.1002/path.1165]
 - 77 **Brunelli M**, Eccher A, Gobbo S, Ficarra V, Novara G, Cossu-Rocca P, Bonetti F, Menestrina F, Cheng L, Eble JN, Martignoni G. Loss of chromosome 9p is an independent prognostic factor in patients with clear cell renal cell carcinoma. *Mod Pathol* 2008; **21**: 1-6 [PMID: 17906617 DOI: 10.1038/modpathol.3800967]
 - 78 **Sauk SC**, Hsu MS, Margolis DJ, Lu DS, Rao NP, Belldgrun AS, Pantuck AJ, Raman SS. Clear cell renal cell carcinoma: multiphase multidetector CT imaging features help predict genetic karyotypes. *Radiology* 2011; **261**: 854-862 [PMID: 22025734 DOI: 10.1148/radiol.11101508]
 - 79 **Lane BR**, Samplaski MK, Herts BR, Zhou M, Novick AC, Campbell SC. Renal mass biopsy--a renaissance? *J Urol* 2008; **179**: 20-27 [PMID: 17997455 DOI: 10.1016/j.juro.2009.01.061]
 - 80 **Zhu YH**, Wang X, Zhang J, Chen YH, Kong W, Huang YR. Low enhancement on multiphase contrast-enhanced CT images: an independent predictor of the presence of high tumor grade of clear cell renal cell carcinoma. *AJR Am J Roentgenol* 2014; **203**: W295-W300 [PMID: 25148187]
 - 81 **Villalobos-Gollás M**, Aguilar-Davidov B, Culebro-García C, Gómez-Alvarado MO, Rojas-García P, Ibarra-Fombona R, Uribe-Uribe N, Feria-Bernal G, Castillejos-Molina R, Sotomayor M, Gabilondo F, Rodríguez-Covarrubias F. Pathological implications of areas of lower enhancement on contrast-enhanced computed tomography in renal-cell carcinoma: additional information for selecting candidates for surveillance protocols. *Int Urol Nephrol* 2012; **44**: 1369-1374 [PMID: 22648292 DOI: 10.1007/s11255-012-0199-8]
 - 82 **Wang JH**, Min PQ, Wang PJ, Cheng WX, Zhang XH, Wang Y, Zhao XH, Mao XQ. Dynamic CT Evaluation of Tumor Vascularity in Renal Cell Carcinoma. *AJR Am J Roentgenol* 2006; **186**: 1423-1430 [PMID: 16632740 DOI: 10.2214/AJR.04.1408]
 - 83 **Birnbaum BA**, Bosniak MA, Krinsky GA, Cheng D, Waisman J, Ambrosino MM. Renal cell carcinoma: correlation of CT findings with nuclear morphologic grading in 100 tumors. *Abdom Imaging* 1994; **19**: 262-266 [PMID: 8019359 DOI: 10.1007/BF00203523]
 - 84 **Karakiewicz PI**, Lewinshtein DJ, Chun FK, Briganti A, Guille F, Perrotte P, Lobel B, Ficarra V, Artibani W, Cindolo L, Tostain J, Abbou CC, Chopin D, De La Taille A, Patard JJ. Tumor size

- improves the accuracy of TNM predictions in patients with renal cancer. *Eur Urol* 2006; **50**: 521-528; discussion 529 [PMID: 16530322 DOI: 10.1016/j.eururo.2006.02.034]
- 85 **Steiner T**, Knels R, Schubert J. Prognostic significance of tumour size in patients after tumour nephrectomy for localised renal cell carcinoma. *Eur Urol* 2004; **46**: 327-330 [PMID: 15306102 DOI: 10.1016/j.eururo.2004.06]
 - 86 **Schlomer B**, Figenshau RS, Yan Y, Bhayani SB. How does the radiographic size of a renal mass compare with the pathologic size? *Urology* 2006; **68**: 292-295 [PMID: 16904439]
 - 87 **Kurta JM**, Thompson RH, Kundu S, Kaag M, Manion MT, Herr HW, Russo P. Contemporary imaging of patients with a renal mass: does size on computed tomography equal pathological size? *BJU Int* 2009; **103**: 24-27 [PMID: 18710440 DOI: 10.1111/j.1464-410X.2008.07941.x]
 - 88 **Chen W**, Wang L, Yang Q, Liu B, Sun Y. Comparison of radiographic and pathologic sizes of renal tumors. *Int Braz J Urol* 2013; **39**: 189-194 [PMID: 23683665 DOI: 10.1590/S1677-5538.IBJU.2013.02.06]
 - 89 **Choi JY**, Kim BS, Kim TH, Yoo ES, Kwon TG. Correlation between Radiologic and Pathologic Tumor Size in Localized Renal Cell Carcinoma. *Korean J Urol* 2010; **51**: 161-164 [PMID: 20414390 DOI: 10.4111/kju.2010.51.3.161]
 - 90 **Lee SE**, Lee WK, Kim DS, Doo SH, Park HZ, Yoon CY, Hwang SI, Lee HJ, Choe G, Hong SK. Comparison of radiographic and pathologic sizes of renal tumors. *World J Urol* 2010; **28**: 263-267 [PMID: 20119641]
 - 91 **Minervini A**, di Cristofano C, Lapini A, Marchi M, Lanzi F, Giubilei G, Tosi N, Tuccio A, Mancini M, della Rocca C, Serni S, Bevilacqua G, Carini M. Histopathologic analysis of peritumoral pseudocapsule and surgical margin status after tumor enucleation for renal cell carcinoma. *Eur Urol* 2009; **55**: 1410-1418 [PMID: 18692300 DOI: 10.1016/j.eururo.2008.07.038]
 - 92 **Huang SQ**, Zou SS, Huang QL. MR appearance of the pseudocapsule of renal cell carcinoma and its pathologic basis. *Urol Radiol* 1992; **13**: 158-161 [PMID: 1539405 DOI: 10.1007/BF02924611]
 - 93 **Yamashita Y**, Takahashi M, Watanabe O, Yoshimatsu S, Ueno S, Ishimaru S, Kan M, Takano S, Ninomiya N. Small renal cell carcinoma: pathologic and radiologic correlation. *Radiology* 1992; **184**: 493-498 [PMID: 1620854 DOI: 10.1148/radiology.184.2.1620854]
 - 94 **Yamashita Y**, Honda S, Nishiharu T, Urata J, Takahashi M. Detection of pseudocapsule of renal cell carcinoma with MR imaging and CT. *AJR Am J Roentgenol* 1996; **166**: 1151-1155 [PMID: 8615260 DOI: 10.2214/AJR.08.1727]
 - 95 **Takahashi S**, Ueda J, Furukawa T, Higashino K, Tsujihata M, Itatani H, Narumi Y, Nakamura H. Renal cell carcinoma: preoperative assessment for enucleative surgery with angiography, CT, and MRI. *J Comput Assist Tomogr* 1996; **20**: 863-870 [PMID: 8933783 DOI: 10.1007/s11604-009-0347-y]
 - 96 **Roy C**, El Ghali S, Buy X, Lindner V, Lang H, Saussine C, Jacqmin D. Significance of the pseudocapsule on MRI of renal neoplasms and its potential application for local staging: a retrospective study. *AJR Am J Roentgenol* 2005; **184**: 113-120 [PMID: 15615960 DOI: 10.2214/ajr.184.1.01840113]
 - 97 **Ascenti G**, Gaeta M, Magno C, Mazziotti S, Blandino A, Melloni D, Zimbaro G. Contrast-enhanced second-harmonic sonography in the detection of pseudocapsule in renal cell carcinoma. *AJR Am J Roentgenol* 2004; **182**: 1525-1530 [PMID: 15150001 DOI: 10.2214/ajr.182.6.1821525]
 - 98 **Tsili AC**, Argyropoulou MI, Gousia A, Kalef-Ezra J, Sofikitis N, Malamou-Mitsi V, Tsampoulas K. Renal cell carcinoma: value of multiphase MDCT with multiplanar reformations in the detection of pseudocapsule. *AJR Am J Roentgenol* 2012; **199**: 379-386 [PMID: 22826400 DOI: 10.2214/AJR.11.7747]
 - 99 **Siddiqui SA**, Frank I, Leibovich BC, Cheville JC, Lohse CM, Zincke H, Blute ML. Impact of tumor size on the predictive ability of the pT3a primary tumor classification for renal cell carcinoma. *J Urol* 2007; **177**: 59-62 [PMID: 17162000 DOI: 10.1016/j.juro.2006.08.069]
 - 100 **Bechtold RE**, Dyer RB, Zagoria RJ, Chen MY. The perirenal space: relationship of pathologic processes to normal retroperitoneal anatomy. *Radiographics* 1996; **16**: 841-854 [PMID: 8835975 DOI: 10.1148/radiographics.16.4.8835975]
 - 101 **Surabhi VR**, Menias C, Prasad SR, Patel AH, Nagar A, Dalrymple NC. Neoplastic and non-neoplastic proliferative disorders of the perirenal space: cross-sectional imaging findings. *Radiographics* 2008; **28**: 1005-1017 [PMID: 18635626 DOI: 10.1148/rg.284075157]
 - 102 **Kunin M**. Bridging septa of the perinephric space: anatomic, pathologic, and diagnostic considerations. *Radiology* 1986; **158**: 361-365 [PMID: 3941862 DOI: 10.1148/radiology.158.2.3941862]
 - 103 **Tsili AC**, Goussia AC, Baltogiannis D, Astrakas L, Sofikitis N, Malamou-Mitsi V, Argyropoulou MI. Perirenal fat invasion on renal cell carcinoma: evaluation with multidetector computed tomography-multivariate analysis. *J Comput Assist Tomogr* 2013; **37**: 450-457 [PMID: 23674020 DOI: 10.1097/RCT.0b013e318283bc8e]
 - 104 **Hedgire SS**, Elmi A, Nadkarni ND, Cao K, McDermott S, Harisinghani MG. Preoperative evaluation of perinephric fat invasion in patients with renal cell carcinoma: correlation with pathological findings. *Clin Imaging* 2013; **37**: 91-96 [PMID: 23206613 DOI: 10.1016/j.clinimag.2012.03.005]
 - 105 **Kim C**, Choi HJ, Cho KS. Diagnostic performance of multidetector computed tomography in the evaluation of perinephric fat invasion in renal cell carcinoma patients. *J Comput Assist Tomogr* 2014; **38**: 268-273 [PMID: 24448501 DOI: 10.1097/RCT.0b013e3182aa672a]
 - 106 **Kim C**, Choi HJ, Cho KS. Diagnostic value of multidetector computed tomography for renal sinus fat invasion in renal cell carcinoma patients. *Eur J Radiol* 2014; **83**: 914-918 [PMID: 24713489 DOI: 10.1016/j.ejrad.2014.02.025]
 - 107 **Rha SE**, Byun JY, Jung SE, Oh SN, Choi YJ, Lee A, Lee JM. The renal sinus: pathologic spectrum and multimodality imaging approach. *Radiographics* 2004; **24** Suppl 1: S117-S131 [PMID: 15486236 DOI: 10.1148/rg.24si045503]
 - 108 **Thompson RH**, Leibovich BC, Cheville JC, Webster WS, Lohse CM, Kwon ED, Frank I, Zincke H, Blute ML. Is renal sinus fat invasion the same as perinephric fat invasion for pT3a renal cell carcinoma? *J Urol* 2005; **174**: 1218-1221 [PMID: 16145373 DOI: 10.1097/01.ju.0000173942.19990.40]
 - 109 **Hallscheidt PJ**, Fink C, Haferkamp A, Bock M, Luburic A, Zuna I, Noeldge G, Kauffmann G. Preoperative staging of renal cell carcinoma with inferior vena cava thrombus using multidetector CT and MRI: prospective study with histopathological correlation. *J Comput Assist Tomogr* 2005; **29**: 64-68 [PMID: 15665685 DOI: 10.1097/01.rct.0000146113.56194.6d]
 - 110 **Sokhi HK**, Mok WY, Patel U. Stage T3a renal cell carcinoma: staging accuracy of CT for sinus fat, perinephric fat or renal vein invasion. *Br J Radiol* 2015; **88**: 20140504 [PMID: 25410425 DOI: 10.1259/bjr.20140504]
 - 111 **Guzzo TJ**, Pierorazio PM, Schaeffer EM, Fishman EK, Allaf ME. The accuracy of multidetector computerized tomography for evaluating tumor thrombus in patients with renal cell carcinoma. *J Urol* 2009; **181**: 486-490; discussion 491 [PMID: 19100567]
 - 112 **Stern Padovan R**, Perkov D, Smiljanic R, Oberman B, Potocki K. Venous spread of renal cell carcinoma: MDCT. *Abdom Imaging* 2005; **32**: 530-537 [PMID: 16947069 DOI: 10.1007/s00261-006-9088-x]
 - 113 **Staehler G**, Brkovic D. The role of radical surgery for renal cell carcinoma with extension into the vena cava. *J Urol* 2000; **163**: 1671-1675 [PMID: 10799157 DOI: 10.1590/S1677-55382009000600003]
 - 114 **Schimmer C**, Hillig F, Riedmiller H, Elert O. Surgical treatment of renal cell carcinoma with intravascular extension. *Interact Cardiovasc Thorac Surg* 2004; **3**: 395-397 [PMID: 17670271 DOI: 10.1016/j.icvts.2004.02.014]
 - 115 **Lane BR**, Tiong HY, Campbell SC, Fergany AF, Weight CJ, Larson BT, Novick AC, Flechner SM. Management of the adrenal gland during partial nephrectomy. *J Urol* 2009; **181**: 2430-2436; discussion 2436-2437 [PMID: 19371896 DOI: 10.1016/j.juro.2009.02.027]
 - 116 **Bekema HJ**, MacLennan S, Imamura M, Lam TB, Stewart F,

Scott N, MacLennan G, McClinton S, Griffiths TR, Skolarikos A, MacLennan SJ, Sylvester R, Ljungberg B, N'Dow J. Systematic review of adrenalectomy and lymph node dissection in locally advanced renal cell carcinoma. *Eur Urol* 2013; **64**: 799-810 [PMID:

23643550 DOI: 10.1016/j.eururo.2013.04.033]

- 117 **Griffin N**, Gore ME, Sohaib SA. Imaging in metastatic renal cell carcinoma. *AJR Am J Roentgenol* 2007; **189**: 360-370 [PMID: 17646462 DOI: 10.2214/AJR.07.2077]

P- Reviewer: Liu HM, Vinh-Hung V, Yuan Z **S- Editor:** Tian YL
L- Editor: A **E- Editor:** Liu SQ





Published by **Baishideng Publishing Group Inc**

8226 Regency Drive, Pleasanton, CA 94588, USA

Telephone: +1-925-223-8242

Fax: +1-925-223-8243

E-mail: bpgoffice@wjgnet.com

Help Desk: <http://www.wjgnet.com/esps/helpdesk.aspx>

<http://www.wjgnet.com>



Use of dentomaxillofacial cone beam computed tomography in dentistry

Kıvanç Kamburoğlu

Kıvanç Kamburoğlu, Department of Dentomaxillofacial Radiology, Faculty of Dentistry, Ankara University, 06500 Beşevler, Ankara, Turkey

Author contributions: Kamburoğlu K wrote the paper.

Conflict-of-interest: The Author declares no conflict of interest.

Open-Access: This article is an open-access article which was selected by an in-house editor and fully peer-reviewed by external reviewers. It is distributed in accordance with the Creative Commons Attribution Non Commercial (CC BY-NC 4.0) license, which permits others to distribute, remix, adapt, build upon this work non-commercially, and license their derivative works on different terms, provided the original work is properly cited and the use is non-commercial. See: <http://creativecommons.org/licenses/by-nc/4.0/>

Correspondence to: Kıvanç Kamburoğlu, DDS, MSc, PhD, Associate Professor, Department of Dentomaxillofacial Radiology, Faculty of Dentistry, Ankara University, Emniyet Mah. İncitaş Sok., 06500 Beşevler, Ankara, Turkey. dkivo@yahoo.com
 Telephone: +90-312-2965632
 Fax: +90-312-2123954

Received: December 9, 2014
 Peer-review started: December 11, 2014
 First decision: January 8, 2015
 Revised: April 21, 2015
 Accepted: May 5, 2015
 Article in press: May 6, 2015
 Published online: June 28, 2015

Abstract

Cone-beam computed tomography (CBCT) was developed and introduced specifically for dento-maxillofacial imaging. CBCT possesses a number of advantages over medical CT in clinical practice, such as lower effective radiation doses, lower costs, fewer space requirements,

easier image acquisition, and interactive display modes such as multiplanar reconstruction that are applicable to maxillofacial imaging. However, the disadvantages of CBCT include higher doses than two-dimensional imaging; the inability to accurately represent the internal structure of soft tissues and soft-tissue lesions; a limited correlation with Hounsfield Units for standardized quantification of bone density; and the presence of various types of image artifacts, mainly those produced by metal restorations. CBCT is now commonly used for a variety of purposes in oral implantology, dento-maxillofacial surgery, image-guided surgical procedures, endodontics, periodontics and orthodontics. CBCT applications provide obvious benefits in the assessment of dentomaxillofacial region, however; it should be used only in correct indications considering the necessity and the potential hazards of the examination.

Key words: Radiography; Dentistry; Dentomaxillofacial; Radiology; Cone-beam computed tomography

© **The Author(s) 2015.** Published by Baishideng Publishing Group Inc. All rights reserved.

Core tip: Cone-beam computed tomography (CBCT) is now commonly used for a variety of purposes in oral implantology, dento-maxillofacial surgery, image-guided surgical procedures, endodontics, periodontics and orthodontics. CBCT applications provide obvious benefits in the assessment of dentomaxillofacial region, however; it should be used only in correct indications considering the necessity and the potential hazards of the examination.

Kamburoğlu K. Use of dentomaxillofacial cone beam computed tomography in dentistry. *World J Radiol* 2015; 7(6): 128-130 Available from: URL: <http://www.wjgnet.com/1949-8470/full/v7/i6/128.htm> DOI: <http://dx.doi.org/10.4329/wjr.v7.i6.128>

CONE BEAM COMPUTED TOMOGRAPHY

Cone-beam computed tomography (CBCT) was developed and introduced specifically for dento-maxillofacial imaging^[1]. A practical cone-beam algorithm for tomographic reconstruction of 2-D projection data was first illustrated by Feldkamp in 1984, who, used a back-projection formula to directly reconstruct a 3-D density function from a set of two-dimensional projections. CBCT units dedicated to dento-maxillofacial radiology could not be marketed for another 15 years because economic X-ray tubes, high-quality detector systems and sufficiently powerful personal computers were unavailable. Eventually, in 1999, the first dento-maxillofacial CBCT unit, the NewTom DVT 9000, designed by Attilio Tacconi and Piero Mozzo and produced by QR, Inc. of Verona, Italy, was introduced in Europe^[2,3]. Today, new technological specifications and settings include multiple field of views (FOVs) and voxels that can better address a variety of specific tasks. There are also several hybrid machines offering CBCT imaging along with panoramic and cephalometric radiography. CBCT possesses a number of advantages over medical CT in clinical practice, such as lower effective radiation doses, lower costs, fewer space requirements, easier image acquisition, and interactive display modes such as multiplanar reconstruction that are applicable to maxillofacial imaging. However, the disadvantages of CBCT include higher doses than two-dimensional imaging; the inability to accurately represent the internal structure of soft tissues and soft-tissue lesions; a limited correlation with Hounsfield Units for standardized quantification of bone density; and the presence of various types of image artifacts, mainly those produced by metal restorations^[4-6].

CBCT is now commonly used for a variety of purposes in oral implantology, dento-maxillofacial surgery, image-guided surgical procedures, endodontics, periodontics and orthodontics. Whereas early CBCT devices were dedicated to implantology and dental imaging, today, applications extend to the face and skull base as a whole. Depending on the FOV used, CBCT images may show part or all of the nasal cavity, paranasal sinuses, airway, cervical vertebrae and temporal bone. In fact, specific ear, nose and throat imaging programs have been increasingly included in CBCT systems, suggesting that CBCT may at some point entirely replace medical CT imaging in certain otolaryngology-related applications^[3]. CBCT has also been found to provide reliable and accurate 3D analysis of the upper airway that can be of help in assessing the presence and severity of obstructive sleep apnea^[7]. Imaging of the temporal bone represents another promising area for CBCT, whose high-resolution and nearly artifact-free multi-planar reconstruction images make it possible to precisely assess the intra-cochlear position of the electrode, including visualization of each individual contact^[8].

Concerns over liability issues related to CBCT remain unresolved. CBCT machines are increasingly being

marketed specifically to orthodontists and implantologists or dentists who place implants in private practices. Unlike other advanced medical imaging systems, CBCT scanners are generally owned and operated by non-radiologists who lack the training necessary to interpret CBCT images. However, clinicians who order CBCT scans are responsible for interpreting the entire image volume, given the possibility that incidental findings - the likelihood of which increase when a larger head volume is included in the scan - may have significant health consequences for the patient^[6]. There is no informed consent process or signature waiver that would allow the clinician to interpret only a specific area of an image volume. As a result, the clinician may be considered liable for a missed diagnosis, even one that falls outside the area of his/her expertise. In case of any questions regarding image data interpretation, referral to a specialist in oral and maxillofacial or medical radiology is recommended^[6,9].

CBCT applications provide obvious benefits in the assessment of dentomaxillofacial region, however; it should be used only in correct indications considering the necessity and the potential hazards of the examination. Comparative radiation dosages should be weighed against diagnostic benefits in selecting the appropriate imaging modality for specific purposes. Future improvements in CBCT imaging can be expected to result in novel systems with better diagnostic abilities and lower effective doses^[10].

REFERENCES

- 1 **Angelopoulos C**, Scarfe WC, Farman AG. A comparison of maxillofacial CBCT and medical CT. *Atlas Oral Maxillofac Surg Clin North Am* 2012; **20**: 1-17 [PMID: 22365427 DOI: 10.1016/j.cxom.2011.12.008]
- 2 **Miracle AC**, Mukherji SK. Conebeam CT of the head and neck, part 1: physical principles. *AJNR Am J Neuroradiol* 2009; **30**: 1088-1095 [PMID: 19439484 DOI: 10.3174/ajnr.A1653]
- 3 **Miracle AC**, Mukherji SK. Conebeam CT of the head and neck, part 2: clinical applications. *AJNR Am J Neuroradiol* 2009; **30**: 1285-1292 [PMID: 19461061 DOI: 10.3174/ajnr.A1654]
- 4 **Acar B**, Kamburoğlu K. Use of cone beam computed tomography in periodontology. *World J Radiol* 2014; **6**: 139-147 [PMID: 24876918 DOI: 10.4329/wjr.v6.i5.139]
- 5 **Scarfe WC**, Li Z, Abuelmaaty W, Scott SA, Farman AG. Maxillofacial cone beam computed tomography: essence, elements and steps to interpretation. *Aust Dent J* 2012; **57** Suppl 1: 46-60 [PMID: 22376097 DOI: 10.1111/j.1834-7819.2011.01657.x]
- 6 **Benavides E**, Rios HF, Ganz SD, An CH, Resnik R, Reardon GT, Feldman SJ, Mah JK, Hatcher D, Kim MJ, Sohn DS, Palti A, Perel ML, Judy KW, Misch CE, Wang HL. Use of cone beam computed tomography in implant dentistry: the International Congress of Oral Implantologists consensus report. *Implant Dent* 2012; **21**: 78-86 [PMID: 22382748 DOI: 10.1097/ID.0b013e31824885b5]
- 7 **Enciso R**, Nguyen M, Shigeta Y, Ogawa T, Clark GT. Comparison of cone-beam CT parameters and sleep questionnaires in sleep apnea patients and control subjects. *Oral Surg Oral Med Oral Pathol Oral Radiol Endod* 2010; **109**: 285-293 [PMID: 20123412 DOI: 10.1016/j.tripleo.2009.09.033]
- 8 **Ruivo J**, Mermuys K, Bacher K, Kuhweide R, Offeciers E, Casselman JW. Cone beam computed tomography, a low-dose imaging technique in the postoperative assessment of cochlear implantation. *Otol Neurotol* 2009; **30**: 299-303 [PMID: 19174709]

DOI: 10.1097/MAO.0b013e31819679f9]

- 9 **Wright B.** Contemporary medico-legal dental radiology. *Aust Dent J* 2012; **57** Suppl 1: 9-15 [PMID: 22376092 DOI: 10.1111/j.1834-7819.2011.01653.x]

- 10 **Senel B,** Kamburoglu K, Uçok O, Yüksel SP, Ozen T, Avsever H. Diagnostic accuracy of different imaging modalities in detection of proximal caries. *Dentomaxillofac Radiol* 2010; **39**: 501-511 [PMID: 21062944 DOI: 10.1259/dmfr/28628723]

P- Reviewer: Galiatsatos AA, Kanzaki H, Li YZ, Peker I, Rattan V

S- Editor: Ji FF **L- Editor:** A **E- Editor:** Liu SQ



Contrast-enhanced ultrasound imaging of the vasa vasorum of carotid artery plaque

Ze-Zhou Song, Yan-Ming Zhang

Ze-Zhou Song, Yan-Ming Zhang, Department of Ultrasound, Zhejiang Provincial People's Hospital, Hangzhou 310014, Zhejiang Province, China

Author contributions: Both the authors contributed to this work.

Conflict-of-interest: The authors have no conflict of interest related to the manuscript.

Open-Access: This article is an open-access article which was selected by an in-house editor and fully peer-reviewed by external reviewers. It is distributed in accordance with the Creative Commons Attribution Non Commercial (CC BY-NC 4.0) license, which permits others to distribute, remix, adapt, build upon this work non-commercially, and license their derivative works on different terms, provided the original work is properly cited and the use is non-commercial. See: <http://creativecommons.org/licenses/by-nc/4.0/>

Correspondence to: Ze-Zhou Song, MS, Department of Ultrasound, Zhejiang Provincial People's Hospital, #158 Shangtang Road, Hangzhou 310014, Zhejiang Province, China. zezhou_song@126.com
Fax: +86-571-87061007

Received: January 17, 2015
Peer-review started: January 19, 2015
First decision: February 7, 2015
Revised: March 10, 2015
Accepted: April 10, 2015
Article in press: April 14, 2015
Published online: June 28, 2015

Abstract

The vasa vasorum of carotid artery plaque is a novel marker of accurately evaluating the vulnerability of carotid artery plaque, which was associated with symptomatic cerebrovascular and cardiovascular disease. The presence of ultrasound contrast agents in carotid artery plaque represents the presence of the vasa vasorum in carotid artery plaque because the ultrasound

contrast agents are strict intravascular tracers. Therefore, contrast-enhanced ultrasound (CEUS) is a novel and safe imaging modality for evaluating the vasa vasorum in carotid artery plaque. However, there are some issues that needs to be assessed to embody fully the clinical utility of the vasa vasorum in carotid artery plaque with CEUS.

Key words: Vasa vasorum; Carotid artery; Plaque; Vulnerability; Contrast-enhanced ultrasound

© The Author(s) 2015. Published by Baishideng Publishing Group Inc. All rights reserved.

Core tip: Stroke is a major cause of morbidity and mortality all over the world. At-risk patients is so-called vulnerable patients because they possess a higher likelihood of developing symptomatic stroke compared with those low-risk patients. Vulnerable patients usually have carotid artery vulnerable plaques and vulnerable plaques possess a higher likelihood of rupture to lead to acute stroke. The vasa vasorum of carotid artery plaque has been confirmed as same as vulnerable plaques and contrast-enhanced ultrasonography could detect the vasa vasorum of carotid artery plaque.

Song ZZ, Zhang YM. Contrast-enhanced ultrasound imaging of the vasa vasorum of carotid artery plaque. *World J Radiol* 2015; 7(6): 131-133 Available from: URL: <http://www.wjgnet.com/1949-8470/full/v7/i6/131.htm> DOI: <http://dx.doi.org/10.4329/wjr.v7.i6.131>

INTRODUCTION

The plaques with a thin fibrous cap covering a large lipid necrotic core, and active inflammation is so-called vulnerable atherosclerotic plaque, which that make the plaque at increased risk of rupture^[1]. The vasa

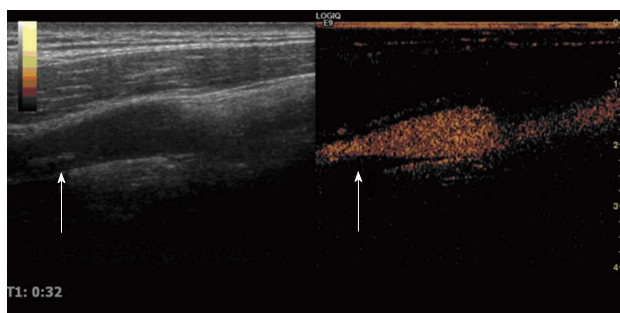


Figure 1 Presence of the vasa vasorum in carotid artery plaque. There are mild ultrasound contrast agents in carotid artery plaque (arrow).

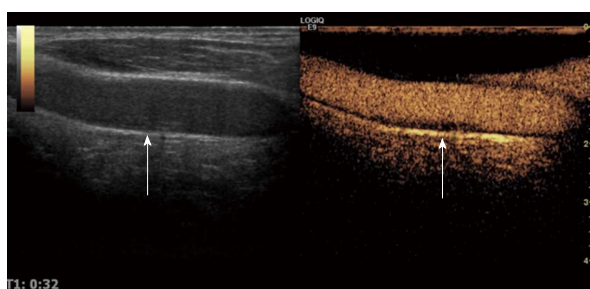


Figure 2 Presence of the vasa vasorum in carotid artery plaque. There are abundant ultrasound contrast agents in carotid artery plaque (arrow).

vasorum of carotid artery plaque is a novel marker of accurately evaluating the vulnerability of carotid artery plaque^[1,2]. The presence of vasa vasorum in carotid artery plaque has been associated with symptomatic cerebrovascular and cardiovascular disease^[3,4] because the vasa vasorum in carotid artery plaque is increased risk for rupture, causing intraplaque hemorrhage and subsequent rapid progression to symptomatic disease.

Recently, contrast-enhanced ultrasound (CEUS) has been introduced for identifying the presence of the vasa vasorum in carotid artery plaque^[5-9], therefore, CEUS is capable of assessing atherosclerotic carotid lesions at risk for rupture^[5,10]. The currently approved and used agents are SonoVue (Bracco SpA, Milan, Italy) in china. Ultrasound contrast agents have been administrated in millions of patients and are safe and side effects are extremely rare^[11]. The presence of ultrasound contrast agents in carotid artery plaque represents the presence of the vasa vasorum in carotid artery plaque (Figures 1 and 2) because the ultrasound contrast agents (SonoVue) are strict intravascular tracers, and the appearance of contrast enhancement of CEUS was shown to correlate with the presence and degree of the vasa vasorum in carotid artery plaque which were assessed by histology^[12,13].

PERFORMANCE OF CEUS

After implemented in the routine carotid ultrasound scan acquisition protocol, CEUS of carotid artery plaque can be relatively straightforward^[8,9]. Firstly, a venous access catheter is placed into median vein of

elbow. Secondly, the contrast presets of the ultrasound system are selected, which are available in nearly all currently used vascular ultrasound systems. Carotid CEUS imaging usually uses a linear array transducer that transmits frequencies are between 5 and 10 MHz and a low-level mechanical index condition is used to avoid destruction of the microbubbles^[8,9]. Thirdly, high quality CEUS dynamical images of the continuous appearance of carotid artery plaque can be obtained after ultrasound contrast agent followed by a 5 mL saline flush are injected into median vein of elbow according to venous access catheter^[8,9]. Usually, the optimal time window for the performance of CEUS after administration of the contrast agent is approximately in 2 min^[8,9]. Lastly, the ultrasound contrast signal intensity becomes weaker because the ultrasound contrast agent is eliminated after a few minutes, and administration of the ultrasound contrast agent can be repeated^[8,9].

FUTURE PERSPECTIVES

Criterion of assessment

There are too many criterions about assessment of the vasa vasorum in carotid artery plaque with CEUS at the present^[4-9,12,13], which includes quantitative criterion, semi-quantitative criterion and qualitative criterion^[4-9], therefore, the criterion of assessment of the vasa vasorum in carotid artery plaque with CEUS is inconsistent among all kinds of clinical studies^[4-9,12,13]. Thus, the clinical value of the vasa vasorum in carotid artery plaque with CEUS yet remain sure accurately, therefore, the criterion about assessment of the vasa vasorum in carotid artery plaque with CEUS should be assessed in the future studies.

Dosage of ultrasound contrast agent

The dosage of ultrasound contrast agent was different among some studies^[4-9]. To our experience^[8,9], 1.2 mL ultrasound contrast agent followed by a 5 mL saline flush acquire high quality CEUS dynamical images of the continuous appearance of carotid artery plaque, although some studies and authors propose 2.4 mL or 2.0 mL ultrasound contrast agent followed by a 5 mL saline flush^[4-6,12,13]. However, the different dosage of ultrasound contrast agent could cause the results according to quantitative criterion, semi-quantitative criterion and qualitative criterion significantly discrepancy, therefore, the dosage of ultrasound contrast agent should be unified according to the quality of CEUS dynamical images and cost-effectiveness.

Consistency and repetition

The clinical studies^[4-9,12,13] about the vasa vasorum in carotid artery plaque with CEUS are exciting because the authors think the method could provide early detection and classification of atherosclerotic disease, however, consistency and repetition of the method is poorly established^[4-9,12,13]. The lowness of consistency and repetition could cause the method not extensive

use, therefore, consistency and repetition of the method needs to be assessed in prospective studies.

Accuracy of diagnosis

It is well known that the vasa vasorum in carotid artery plaque with CEUS were well correlated with histologic specimens obtained after endarterectomy^[5-7], however, the diagnosis accuracy of the histologic degree of the vasa vasorum in carotid artery plaque using CEUS remain unclear. Therefore, this issue should be assessed in the future perspective study.

Perspective study

Most of the studies about the vasa vasorum in carotid artery plaque with CEUS are retrospective studies^[7-9], therefore, too many issues about the clinical utility of the vasa vasorum in carotid artery plaque with CEUS remain unclear. In addition, most of studies about the vasa vasorum in carotid artery plaque with CEUS are small-scale, which causes the results of these studies unimpressive. Therefore, the large-scale perspective studies should be performed to assess the clinical utility of the vasa vasorum in carotid artery plaque with CEUS.

CONCLUSION

CEUS is a novel and safe imaging modality for evaluating the vasa vasorum in carotid artery plaque, which could detect the vulnerable plaque at risk for rupture. However, there are some issues that needs to be assessed to embody fully the clinical utility of the vasa vasorum in carotid artery plaque with CEUS and the perspective studies needs to be performed to resolve the above-mentioned issues and assess the clinical utility of the vasa vasorum in carotid artery plaque with CEUS.

REFERENCES

- 1 **Schaar JA**, Muller JE, Falk E, Virmani R, Fuster V, Serruys PW, Colombo A, Stefanadis C, Ward Casscells S, Moreno PR, Maseri A, van der Steen AF. Terminology for high-risk and vulnerable coronary artery plaques. Report of a meeting on the vulnerable plaque, June 17 and 18, 2003, Santorini, Greece. *Eur Heart J* 2004; **25**: 1077-1082 [PMID: 15191780]
- 2 **Virmani R**, Kolodgie FD, Burke AP, Finn AV, Gold HK, Tulenko TN, Wrenn SP, Narula J. Atherosclerotic plaque progression and vulnerability to rupture: angiogenesis as a source of intraplaque hemorrhage. *Arterioscler Thromb Vasc Biol* 2005; **25**: 2054-2061 [PMID: 16037567]
- 3 **McCarthy MJ**, Loftus IM, Thompson MM, Jones L, London NJ, Bell PR, Naylor AR, Brindle NP. Angiogenesis and the atherosclerotic carotid plaque: an association between symptomatology and plaque morphology. *J Vasc Surg* 1999; **30**: 261-268 [PMID: 10436445]
- 4 **Staub D**, Patel MB, Tibrewala A, Ludden D, Johnson M, Espinosa P, Coll B, Jaeger KA, Feinstein SB. Vasa vasorum and plaque neovascularization on contrast-enhanced carotid ultrasound imaging correlates with cardiovascular disease and past cardiovascular events. *Stroke* 2010; **41**: 41-47 [PMID: 19910551]
- 5 **Feinstein SB**. Contrast ultrasound imaging of the carotid artery vasa vasorum and atherosclerotic plaque neovascularization. *J Am Coll Cardiol* 2006; **48**: 236-243 [PMID: 16843169]
- 6 **Vicenzini E**, Giannoni MF, Puccinelli F, Ricciardi MC, Altieri M, Di Piero V, Gossetti B, Valentini FB, Lenzi GL. Detection of carotid adventitial vasa vasorum and plaque vascularization with ultrasound cadence contrast pulse sequencing technique and echo-contrast agent. *Stroke* 2007; **38**: 2841-2843 [PMID: 17761913]
- 7 **Shah F**, Balan P, Weinberg M, Reddy V, Neems R, Feinstein M, Dainauskas J, Meyer P, Goldin M, Feinstein SB. Contrast-enhanced ultrasound imaging of atherosclerotic carotid plaque neovascularization: a new surrogate marker of atherosclerosis? *Vasc Med* 2007; **12**: 291-297 [PMID: 18048465]
- 8 **Song ZZ**, Zhang YM, Fu YF, Geng Y. The relationship of posterior circulation cerebral infarction to grade of carotid plaque by contrast enhanced ultrasonography. *Zhongguo Chaosheng Yixue Zazhi* 2014; **30**: 1038-1040
- 9 **Song ZZ**, Zhang YM, Fu YF, Geng Y. The relationship of volume of cerebral infarction to grade of carotid plaque by contrast enhanced ultrasonography. *Zhongguo Chaosheng Yixue Zazhi* 2014; **23**: 539-541
- 10 **Feinstein SB**, Coll B, Staub D, Adam D, Schinkel AF, ten Cate FJ, Thomenius K. Contrast enhanced ultrasound imaging. *J Nucl Cardiol* 2010; **17**: 106-115 [PMID: 19921346]
- 11 **Main ML**, Ryan AC, Davis TE, Albano MP, Kusnetzky LL, Hibberd M. Acute mortality in hospitalized patients undergoing echocardiography with and without an ultrasound contrast agent (multicenter registry results in 4,300,966 consecutive patients). *Am J Cardiol* 2008; **102**: 1742-1746 [PMID: 19064035]
- 12 **Coli S**, Magnoni M, Sangiorgi G, Marrocco-Trischitta MM, Melisurgo G, Mauriello A, Spagnoli L, Chiesa R, Cianflone D, Maseri A. Contrast-enhanced ultrasound imaging of intraplaque neovascularization in carotid arteries: correlation with histology and plaque echogenicity. *J Am Coll Cardiol* 2008; **52**: 223-230 [PMID: 18617072]
- 13 **Giannoni MF**, Vicenzini E, Citone M, Ricciardi MC, Irace L, Laurito A, Scucchi LF, Di Piero V, Gossetti B, Mauriello A, Spagnoli LG, Lenzi GL, Valentini FB. Contrast carotid ultrasound for the detection of unstable plaques with neoangiogenesis: a pilot study. *Eur J Vasc Endovasc Surg* 2009; **37**: 722-727 [PMID: 19328729]

P- Reviewer: Akcar N, Hsu WH, Marandola M, Sharma V

S- Editor: Ji FF **L- Editor:** A **E- Editor:** Liu SQ



Risk management in radiology departments

Horea Craciun, Kshitij Mankad, Jeremy Lynch

Horea Craciun, University Hospitals of Morecambe Bay NHS Trust, LA1 4RP Lancaster, United Kingdom
Kshitij Mankad, Great Ormond Street Hospital for Children NHS Trust, WC1N 3JH London, United Kingdom
Jeremy Lynch, Chelsea Westminster Hospital NHS Trust, SW10 9NH London, United Kingdom

Author contributions: Craciun H generated the paper concepts and design, completed the literature review and wrote the manuscript; Mankad K and Lynch J contributed to the writing of the manuscript and to its preparation and editing.

Conflict-of-interest: I wish to confirm that there are no known conflicts of interest associated with this publication and there has been no significant financial support for this work that could have influenced its outcome.

Open-Access: This article is an open-access article which was selected by an in-house editor and fully peer-reviewed by external reviewers. It is distributed in accordance with the Creative Commons Attribution Non Commercial (CC BY-NC 4.0) license, which permits others to distribute, remix, adapt, build upon this work non-commercially, and license their derivative works on different terms, provided the original work is properly cited and the use is non-commercial. See: <http://creativecommons.org/licenses/by-nc/4.0/>

Correspondence to: Dr. Horea Craciun, University Hospitals of Morecambe Bay NHS Trust, 414 Mill View House, Aalborg Place, LA1 4RP Lancaster, United Kingdom. horea_craciun@yahoo.com
Telephone: +44-7463-460219

Received: January 6, 2015
Peer-review started: January 7, 2015
First decision: March 6, 2015
Revised: April 20, 2015
Accepted: May 5, 2015
Article in press: May 6, 2015
Published online: June 28, 2015

Abstract

Medical imaging and interventional radiology sustained prompt changes in the last few years, mainly as a

result of technology breakthroughs, rise in workload, deficit in workforce and globalization. Risk is considered to be the chance or possibility of incurring loss or of a negative event happening that may cause injury to patients or medical practitioners. There are various causes of risks leading to harm and injury in radiology departments, and it is one of the objectives of this paper to scrutinize some of the causes. This will drive to consideration of some of the approaches that are used in managing risks in radiology. This paper aims at investigating risk management in radiology, and this will be achieved through a thorough assessment of the risk control measures that are used in the radiology department. It has been observed that the major focus of risk management in such medical setting is to reduce and eliminate harm and injury to patients through integration of various medical precautions. The field of Radiology is rapidly evolving due to technology advances and the globalization of healthcare. This ongoing development will have a great impact on the level of quality of care and service delivery. Thus, risk management in radiology is essential in protecting the patients, radiologists, and the medical organization in terms of capital and widening of the reputation of the medical organization with the patients.

Key words: Risk management; Radiology; Patient safety

© The Author(s) 2015. Published by Baishideng Publishing Group Inc. All rights reserved.

Core tip: This paper serves as a review of risk management in radiology. It investigates the potential sources of risk within radiology departments and proposes measures that may potentially mitigate these risks. A major focus of risk management is to reduce harm and injury to patients and personnel and it aims to improve the outcomes from radiology departments. Risk management in radiology is essential in protecting the patients, radiologists, and the medical organization.

Craciun H, Mankad K, Lynch J. Risk management in radiology

departments. *World J Radiol* 2015; 7(6): 134-138 Available from: URL: <http://www.wjgnet.com/1949-8470/full/v7/i6/134.htm> DOI: <http://dx.doi.org/10.4329/wjtr.v7.i6.134>

INTRODUCTION

Medical imaging and interventional radiology have sustained dramatic changes in the last few years, mainly as a result of technological breakthroughs, the rise in workload, a deficit in the workforce and globalisation. Consequently there is an expanding concern about standards of care, maintaining patient safety and the management of risk in radiology.

People understand the concepts of risk and risk management in a medical setting in different ways. Risk is considered to be the possibility of incurring loss or of a negative event occurring that may cause injury to patients or medical practitioners^[1]. One cannot predict all risks. That is to say, injury to patients may occur even in the best hospitals where patients receive high-quality services and treatments. Then risk management refers to the various approaches that medical practitioners and professionals integrate to reduce risk^[2]. This is a proactive concept that involves practices such as identification of risk, quantification and evaluation of risk and consideration of measures that can be used to eliminate or control risk in a medical setting. All those involved in providing healthcare services participate in risk management. This includes management of the medical centres obligated to provide adequate facilities, staff, resources, financial support and equipment, thus helping professionals and nursing practitioners reduce the odds of harm's occurring^[3].

This paper aims at investigating risk management in radiology through a thorough assessment of the risk control measures that are used in the radiology department^[4]. The major focus of risk management in such medical settings is to reduce and eliminate harm and injury to patients through the incorporation of various medical precautions^[5]. As depicted in Figure 1 risks leading to harm and injury in radiology departments stem from various causes. One objective of this paper is to scrutinise some of these. This will expand into the consideration of some of the approaches healthcare practitioners implement to manage risk in radiology.

RISK MANAGEMENT

Safeguarding patients and personnel

The rapid expansion of services, the globalization of healthcare and the imbalance between workload and workforce are a few of the factors that may threaten the standards of health services as well as patient safety^[6]. There is a rising demand for radiologists and for 24/7 services. Therefore, international teleradiology is leading the globalisation occurring in the field of radiology^[7].

To meet the expectations of quality services, systems

should be put in place to pave the way for higher standards of care. Quality systems are effective risk control measures, hence the importance of professional organisations to lead, establish, uphold and improve them^[8]. Quality improvement measures range from quality maps, measurable metrics and performance indicators to audits and accreditation programmes. These collective efforts may decrease a department's risk and benefit patients^[9].

Risk management in radiology is primarily developed and fostered to help safeguard patients, working personnel and the entire organisation. Protection of the organisation is largely grasped in terms of finance management and potential drawbacks linked to unreliable results that could damage its reputation^[10].

Managers and clinicians in the radiology department should focus on improving the general quality of care medical staff deliver to patients. Radiology professionals subject themselves to risk every time they perform a procedure because some of the techniques and instruments they use in scanning and imaging are complex^[11]. Thus, players in the healthcare setting must work carefully and diligently to ensure that they minimise health risk to patients and to themselves. In practice, inherent hazards to safety and quality manifest in relation to personnel availability, workload and financial predicaments. They consist of insubstantial funding for new equipment in the workplace, difficulty retaining professionals, the escalating complexity of the work, the increasing workload, difficulty recruiting due to a national shortage of medical staff and the lessening budget that is not keeping up with current of demands.

Radiology professionals must persuade administrators and managers that standards of care relate closely to performance metrics like workload, diagnostic precision and patient safety concerns^[12]. Thus, managers must make sensible decisions about resource allocation and performance expectations to mirror this reality and curtail risks^[10].

All health professionals must identify some of the issues that tend to cause harm to patients in advance and work on them before subjecting the patient to potentially faulty processes^[13]. The concept of ALARP, or "as low as reasonably practicable", essentially refers to the assessment of risk, and the comparison of this risk with the amount of time, money and resources needed to address it. It is used throughout the healthcare system and is particularly important when it comes to radiology. When assessing whether a risk is ALARP, it is essential to compare the measures being proposed with those that would normally be used, also known as "good practice". Good practice is decided upon after detailed discussion with stakeholders. However, good practice is not always enough, and if an issue is particularly complicated, or if no good practice has yet been formulated for the issue, it is often necessary to revert back to the "first principle". In sum, ALARP is about calculating the amount of risk attached to measures, and assessing how difficult, in terms of resources, controlling this risk is. It offers those

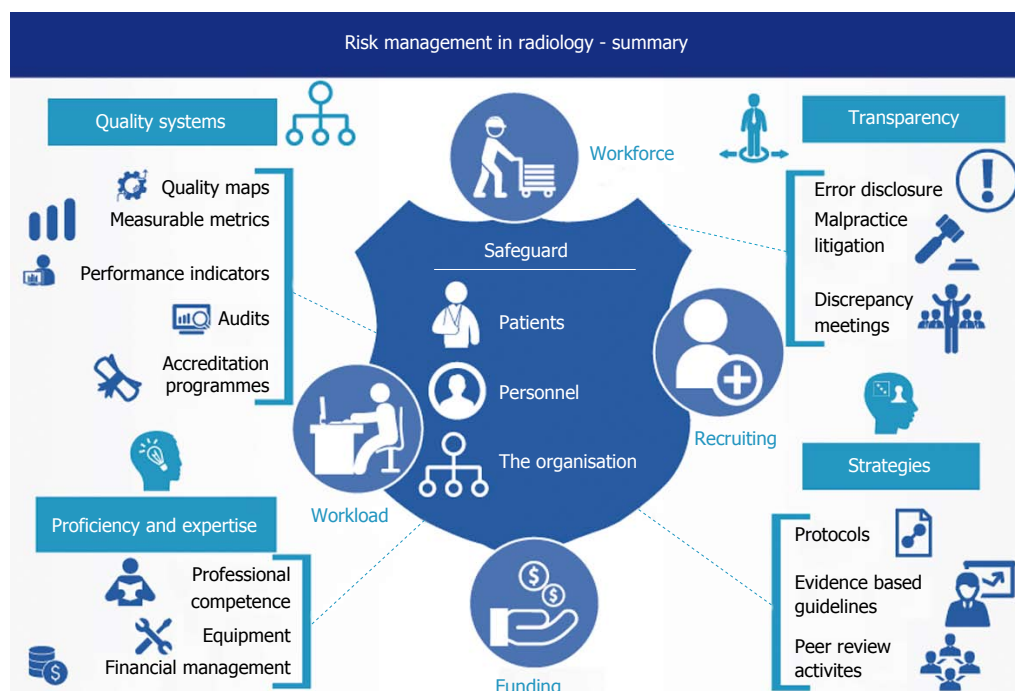


Figure 1 Summary of control measures in risk management in radiology.

who use it a great deal of flexibility, as it involves the setting of goals, thus allowing room to manoeuvre if necessary.

Risk management allows radiologists to focus on measures for reducing potential risk. This ensures that medical staff follow appropriate and relevant protocols and guidelines to reduce risk in radiology departments^[14].

Error disclosure and malpractice litigation

Recent studies on malpractice suits^[15] revealed that amongst the most frequent causes of legal claims against radiology professionals were: diagnostic errors followed by procedural complications, poor communication with the referring doctor and poor physician-patient rapport^[16]. Risk management is a crucial instrument in preventing and limiting adverse events and errors in medical settings^[17].

The most common medical errors encountered in malpractice suits are vascular injuries and complications after needle biopsies in interventional radiology^[18], missed or delayed cancer diagnosis especially in imaging of the breast^[19] and missing diagnosis in skeletal radiology^[17]. A major objective in risk management is the reduction of litigation and the associated costs. The magnitude of these costs should suffice to argue that avoiding the problems that may cause lawsuits positively impacts the patients and radiologists^[20].

The reduction of errors in a radiology department is attainable if all parties in the department are aware of and up to date with all the methods and protocols involved in risk reduction^[21].

One can manage litigation risk in a radiology department through a number of approaches. Healthcare professionals should set up and follow high standards of

care, employ prudence when using devices off label^[22,23], improve communication skills with colleagues and patients^[24] and obtain professional liability insurance.

Stakeholders, including radiologists, must possess competence and significant knowledge and skills in working with all the implements within the radiology department as a way of reducing the number of errors^[25]. Every radiologist should be conscious of error sources, particularly those typically constituting origins of litigation^[26]. Medical staff must unveil and emphasise error pitfalls to prevent the recurrence of inaccuracies^[27].

In the future, various factors will shape radiological malpractice: the emergence of new imaging techniques, innovation in image processing, new protocols scientific societies publish and guidelines professional organisations delineate^[28]. To minimise risk, medical staff should cultivate a safety culture in every radiology department and perceive feedback on a possible error as a learning experience^[29]. The radiologists and other key players in the department need to understand that their practice and performance significantly contribute to the trust patients place in them^[30]. Radiologists need to provide good standards of practice and care and show respect for a patient^[31].

Disclosing radiological errors to patients stands out as the most demanding challenge a radiologist may encounter. With a misguided error disclosure approach, radiologists risk not meeting professional norms in addition to creating erratic and unsafe practice patterns^[32].

Failure to acknowledge responsibility and achieve transparency around errors subverts patient safety. Despite this, risk management concerns about litigation have long precluded the endorsement of standards around error disclosure. More recently, risk managers

have emphasised that clear disclosure after radiological errors is crucial to risk management and can reduce exposure to liability^[33].

Professional competence and equipment

Medical practitioners in the department must ensure that they keep their knowledge and skills updated. To achieve competencies and proficiency in their areas of expertise, radiologists must perform their duties within the limits of their understanding and competence^[34]. This allows them to do what they understand best, thus reducing the probability of causing danger, harm or injury to patients^[8]. The requirement is closely related to the recommendation that the radiologists need to maintain high trust and confidentiality with their clients through the establishment of a professional relationship^[35]. Moreover, workers attain competence in a medical setting if they comprehend and appreciate the benefits of collaborating with other professionals in their field^[36]. This implies that to reduce risk in radiology departments, doctors need to work as a team, combine their knowledge and skills and, more importantly, share their experience as a way of promoting excellence in their field^[37].

Modern radiology is greatly reliant on the application of state-of-the-art diagnostic and therapeutic devices, but such state-of-the-art technology carries risk. To avoid the risk associated with the use of faulty devices in the radiology sector, quality assurance departments must be diligent in ensuring that all the equipment used is in good condition and of high quality^[38].

Risk management relating to the use of therapeutic devices requires all professionals to possess sufficient knowledge, skills and technical ability to operate the devices, recognise when they break down and identify inaccurate results.

Through integration of appropriate skills and operational strategies in radiology, professionals can guarantee the highest accuracy. The attainment of excellent results and a foolproof reporting procedure highlights a department's competence, indicating the department's use of protocols and guidelines focused on reducing operational and decisional risk^[39].

Discrepancy, errors and critical incidents

Integrated teamwork among radiologists would support risk reduction and prevent any issue that may cause harm or injury to patients through inadequate reporting, resulting in unreliable results^[40]. Radiologists must justify their individual decisions and actions. To be able to manage risk in the radiology sector, practitioners need to learn from previous mistakes and, more importantly, scrutinise critical clinical situations and near misses. Physicians are prone to making errors, but integrating certain operational decisions and measures would reduce the rate of errors and near misses^[41].

Risk management is founded on the idea that mistakes happen and processes and procedures sometimes go wrong. Therefore, holding regular meetings where medical staff can report and evaluate discrepancies,

errors and near misses is crucial^[42]. Discrepancy meetings are invaluable in medical practice and offer the opportunity to assess current practice and highlight areas that might need improvement^[11]. The Royal College of Radiologists recommends that all radiologists attend discrepancy meetings and morbidity and mortality meetings. Evidence of attendance may be required to support the revalidation process, so doctors should carry out personal reflections^[43]. Inappropriate conduct, such as unethical handling of a patient's records and intentional carelessness, is a contributing factor to errors. However, medical staff can mitigate this factor through adherence to department and/or organisational procedures and protocols^[39].

CONCLUSION

The field of radiology is rapidly evolving due to technological advances and the globalisation of healthcare. This ongoing development greatly affects the quality of care and service delivery. Doctors and professional organisations should display initiative and oversee and tackle challenging conditions in an effective manner to safeguard patient safety and standards of care. The quality of a radiological report relies on the various important steps outlined above. The essence of risk management is to survey all potential reasons for an inaccurate report in advance so that procedures can be put in place to prevent them. More importantly, the medical organisation offering radiology services needs to allow innovation and responsive measures that can improve radiology. Thus, risk management in radiology is essential in protecting the patients, radiologists and medical organisation (*i.e.*, protecting the organisation's capital and its reputation with patients).

REFERENCES

- 1 **Messano GA**, De Bono V, Di Folco F, Marsella LT. Past and present of risk management in healthcare. *Ig Sanita Pubbl* 2014; **70**: 423-430 [PMID: 25353272]
- 2 **Robinson PJ**, Wilson D, Coral A, Murphy A, Verow P. Variation between experienced observers in the interpretation of accident and emergency radiographs. *Br J Radiol* 1999; **72**: 323-330 [PMID: 10474490 DOI: 10.1259/bjr.72.856.10474490]
- 3 **Nitrosi A**, Bertolini M, Sghedoni R, Notari P, Pattacini P, Corazza A, Iori M. RIS-PACS, patient safety, and clinical risk management. *Radiol Med* 2015; **120**: 498-503 [PMID: 25511184]
- 4 **Orders AB**, Wright D. Expanding the scope of practice for radiology managers: radiation safety duties. *Radiol Manage* 2003; **25**: 40-47 [PMID: 12918277]
- 5 **Paterick TE**. Risk management principles for physicians. *J Med Pract Manage* 2014; **29**: 216-218 [PMID: 24696957]
- 6 **Oliseimeke B**, Chen YF, Hemming K, Girling A. The effectiveness of service delivery initiatives at improving patients' waiting times in clinical radiology departments: a systematic review. *J Digit Imaging* 2014; **27**: 751-778 [PMID: 24888629 DOI: 10.1007/s10278-014-9706-z]
- 7 **Gunderman R**. Teleradiology: The Importance of Communication. *Virtual Mentor* 2014; **16**: 960-963 [PMID: 25493363 DOI: 10.1001/virtualmentor.2014.16.12.ecas1-1412]
- 8 **Mendiratta-Lala M**, Eisenberg RL, Steele JR, Boiselle PM, Kruskal JB. Quality initiatives: measuring and managing the procedural competency of radiologists. *Radiographics* 2011; **31**:

- 1477-1488 [PMID: 21719719 DOI: 10.1148/rg.315105242]
- 9 **Lau L.** Leadership and management in quality radiology. *Biomed Imaging Interv J* 2007; **3**: e21 [PMID: 21614284 DOI: 10.2349/biij.3.3.e21]
- 10 **The European Society of Radiology.** Risk management in Radiology in Europe. Available from: URL: http://www.myesr.org/html/img/pool/ESR_2006_IV_Riskmanagement_Web.pdf
- 11 **Chakraborty S, Wright J.** Adverse events in British hospitals. "Errors meetings" in radiology did not identify errors leading to complaints and litigation. *BMJ* 2001; **322**: 1425-1426; author reply 1427 [PMID: 11417557]
- 12 **Bruno MA, Nagy P.** Fundamentals of quality and safety in diagnostic radiology. *J Am Coll Radiol* 2014; **11**: 1115-1120 [PMID: 25467723 DOI: 10.1016/j.jacr.2014.08.028]
- 13 **Kruskal JB, Eisenberg R, Sosna J, Yam CS, Kruskal JD, Boiselle PM.** Quality initiatives: Quality improvement in radiology: basic principles and tools required to achieve success. *Radiographics* 2011; **31**: 1499-1509 [PMID: 21997978 DOI: 10.1148/rg.316115501]
- 14 **The Royal College of Radiologists.** Good practice guide for clinical radiologists. Available from: URL: [http://www.rcr.ac.uk/docs/radiology/pdf/BFCR\(12\)1_GoodPractice.pdf](http://www.rcr.ac.uk/docs/radiology/pdf/BFCR(12)1_GoodPractice.pdf)
- 15 **Halpin SF.** Medico-legal claims against English radiologists: 1995-2006. *Br J Radiol* 2009; **82**: 982-988 [PMID: 19470570 DOI: 10.1259/bjr/61782960]
- 16 **Wallis A, McCoubrie P.** The radiology report--are we getting the message across? *Clin Radiol* 2011; **66**: 1015-1022 [PMID: 21788016 DOI: 10.1016/j.crad.2011.05.01]
- 17 **Cannavale A, Santoni M, Mancarella P, Passariello R, Arbarello P.** Malpractice in radiology: what should you worry about? *Radiol Res Pract* 2013; **2013**: 219259 [PMID: 23691316 DOI: 10.1155/2013/219259]
- 18 **Mavroforou A, Giannoukas A, Mavrophoros D, Michalodimitrakis E.** Physicians' liability in interventional radiology and endovascular therapy. *Eur J Radiol* 2003; **46**: 240-243 [PMID: 12758118 DOI: 10.1016/S0720-048X(02)00192-4]
- 19 **van Breest Smullenburg V, Setz-Pels W, Groenewoud JH, Voogd AC, Jansen FH, Louwman MW, Tielbeek AV, Duijm LE.** Malpractice claims following screening mammography in The Netherlands. *Int J Cancer* 2012; **131**: 1360-1366 [PMID: 22173962 DOI: 10.1002/ijc.27398]
- 20 **Berlin L.** Radiologic errors and malpractice: a blurry distinction. *AJR Am J Roentgenol* 2007; **189**: 517-522 [PMID: 17715094 DOI: 10.2214/AJR.07.2209]
- 21 **Cannavale A, Santoni M, Passariello R, Arbarello P.** Risk management in radiology. *Radiol Manage* 2013; **35**: 14-19; quiz 20-21 [PMID: 24303642]
- 22 **Zvavanjanja RC, Odetoyinbo TO, Rowlands PC, Healey A, Abdelsalam H, Powell S, Evans JC, Hughes ML, Gould DA, McWilliams RG.** Off label use of devices and drugs in interventional radiology. *Clin Radiol* 2012; **67**: 239-243 [PMID: 21978818 DOI: 10.1016/j.crad.2011.06.017]
- 23 **Society of Interventional Radiology.** SIR Policy on Off-Label Use. Available from: URL: http://www.sirweb.org/clinical/cpg/SIR_Off-label_use_statement11-18-07.pdf
- 24 **Gunderman RB, Brown BP.** Teaching interpersonal and communication skills. *Acad Radiol* 2012; **19**: 1589-1590 [PMID: 23122574 DOI: 10.1016/j.acra.2012.05.014]
- 25 **Whang JS, Baker SR, Patel R, Luk L, Castro A.** The causes of medical malpractice suits against radiologists in the United States. *Radiology* 2013; **266**: 548-554 [PMID: 23204547 DOI: 10.1148/radiol.12111119]
- 26 **Baker SR, Whang JS, Luk L, Clarkin KS, Castro A, Patel R.** The demography of medical malpractice suits against radiologists. *Radiology* 2013; **266**: 539-547 [PMID: 23192777 DOI: 10.1148/radiol.12110971]
- 27 **The Royal College of Radiologists.** Standards for the NPSA and RCR Safety Checklist for Radiological Interventions. London: The Royal College of Radiologists, 2010
- 28 **Sokol DK.** Law, ethics, and the duty of care. *BMJ* 2012; **345**: e6804 [PMID: 23054053 DOI: 10.1136/bmj.e6804]
- 29 **Pinto A, Brunese L.** Spectrum of diagnostic errors in radiology. *World J Radiol* 2010; **2**: 377-383 [PMID: 21161023 DOI: 10.4329/wjr.v2.i10.377]
- 30 **Quinn MA, Wilcox A, Orav EJ, Bates DW, Simon SR.** The relationship between perceived practice quality and quality improvement activities and physician practice dissatisfaction, professional isolation, and work-life stress. *Med Care* 2009; **47**: 924-928 [PMID: 19543122 DOI: 10.1097/MLR.0b013e3181a393e4]
- 31 **Kaldjian LC, Jones EW, Wu BJ, Forman-Hoffman VL, Levi BH, Rosenthal GE.** Disclosing medical errors to patients: attitudes and practices of physicians and trainees. *J Gen Intern Med* 2007; **22**: 988-996 [PMID: 17473944 DOI: 10.1007/s11606-007-0227-z]
- 32 **Hannawa AF.** "Explicitly implicit": examining the importance of physician nonverbal involvement during error disclosures. *Swiss Med Wkly* 2012; **142**: w13576 [PMID: 22573515 DOI: 10.4414/smw.2012.13576]
- 33 **Brown SD, Lehman CD, Truog RD, Browning DM, Gallagher TH.** Stepping out further from the shadows: disclosure of harmful radiologic errors to patients. *Radiology* 2012; **262**: 381-386 [PMID: 22282177 DOI: 10.1148/radiol.11110829]
- 34 **Epstein RM, Hundert EM.** Defining and assessing professional competence. *JAMA* 2002; **287**: 226-235 [PMID: 11779266 DOI: 10.1001/jama.287.2.226]
- 35 **Gunderman RB, Beckman ES.** Confidentiality: an essential element of professionalism. *AJR Am J Roentgenol* 2012; **199**: W683-W685 [PMID: 23169740 DOI: 10.2214/AJR.11.8344]
- 36 **Alkasab TK, Harvey HB, Gowda V, Thrall JH, Rosenthal DI, Gazelle GS.** Consensus-oriented group peer review: a new process to review radiologist work output. *J Am Coll Radiol* 2014; **11**: 131-138 [PMID: 24139321 DOI: 10.1016/j.jacr.2013.04.013]
- 37 **Chandy J, Goodfellow T, Vohrah A.** Clinical governance in action: radiology. *Hosp Med* 2000; **61**: 326-329 [PMID: 10953738 DOI: 10.12968/hosp.2000.61.5.1331]
- 38 **European Society of Radiology (ESR).** Renewal of radiological equipment. *Insights Imaging* 2014; **5**: 543-546 [PMID: 25230589 DOI: 10.1007/s13244-014-0345-1]
- 39 **Association of Healthcare Technology Providers for Imaging, Radiotherapy and Care.** Declining investment in Radiology Equipment stores up problems for the NHS. Available from: URL: http://www.axrem.org.uk/Axrem_Editorial_on_Stats_11th_October_2013_FINAL.pdf
- 40 **The Royal College of Radiologists.** Specialty standards and supporting information for revalidation. London: The Royal College of Radiologists, 2010
- 41 **Driscoll DO, Halpenny D, Guiney M.** Radiological error--an early assessment of departmental radiology discrepancy meetings. *Ir Med J* 2012; **105**: 172-174 [PMID: 22973653]
- 42 **Brady A, Laoide RÓ, McCarthy P, McDermott R.** Discrepancy and error in radiology: concepts, causes and consequences. *Ulster Med J* 2012; **81**: 3-9 [PMID: 23536732]
- 43 **The Royal College of Radiologists.** Personal reflection on discrepancies and adverse events. London: The Royal College of Radiologists, 2010

P- Reviewer: Chen F, Kilickesmez O, Kara PO **S- Editor:** Ji FF
L- Editor: A **E- Editor:** Liu SQ



Endovascular retrieval of a prematurely deployed covered stent

Jefferson T Miley, Gustavo J Rodriguez, Ramachandra P Tummala

Jefferson T Miley, Seton Brain and Spine Institute, Dell Medical School, the University of Texas at Austin, El Paso, TX 79905, United States

Gustavo J Rodriguez, Department of Neurology and Radiology, Texas Tech University Health Sciences Center, El Paso, TX 79905, United States

Ramachandra P Tummala, Department of Neurosurgery, University of Minnesota, Minneapolis, MN 55455, United States

Author contributions: Miley JT manuscript designed this work, collected the data and drafted the main work; Rodriguez GJ contributed to reviewing the literature; Rodriguez GJ and Tummala RP gave the critical review of the manuscript; Tummala RP approved to the final manuscript.

Ethics approval: The procedure was reviewed and approved by the University of Minnesota/Fairview Institutional Review Board.

Informed consent: The patient provided informed written consent prior to the procedure.

Conflict-of-interest: None.

Open-Access: This article is an open-access article which was selected by an in-house editor and fully peer-reviewed by external reviewers. It is distributed in accordance with the Creative Commons Attribution Non Commercial (CC BY-NC 4.0) license, which permits others to distribute, remix, adapt, build upon this work non-commercially, and license their derivative works on different terms, provided the original work is properly cited and the use is non-commercial. See: <http://creativecommons.org/licenses/by-nc/4.0/>

Correspondence to: Gustavo J Rodriguez, MD, Associate Professor, Department of Neurology and Radiology, Texas Tech University Health Sciences Center, 4800 Alberta Avenue, El Paso, TX 79905, United States. gustavo.j.rodriguez@ttuhsc.edu
Telephone: +1-915-2155911
Fax: +1-915-5456705

Received: September 16, 2014
Peer-review started: September 16, 2014
First decision: October 28, 2014
Revised: April 20, 2015
Accepted: May 5, 2015
Article in press: May 6, 2015
Published online: June 28, 2015

Abstract

Several techniques have been reported to address different endovascular device failures. We report the case of a premature deployment of a covered balloon mounted stent during endovascular repair of a post-traumatic carotid-cavernous fistula (CCF). A 50-year-old male suffered a fall resulting in loss of consciousness and multiple facial fractures. Five weeks later, he developed decreased left visual acuity, proptosis, chemosis, limited eye movements and cranial/orbit bruit. Cerebral angiography demonstrated a direct left CCF and endovascular repair with a 5.0 mm × 19 mm covered stent was planned. Once in the lacerum segment, increased resistance was encountered and the stent was withdrawn resulting in premature deployment. A 3 mm × 9 mm balloon was advanced over an exchange length microwire and through the stent lumen. Once distal to the stent, the balloon was inflated and slowly pulled back in contact with the stent. All devices were successfully withdrawn as a unit. The use of a balloon to retrieve a prematurely deployed balloon mounted stent is a potential rescue option if leaving the stent *in situ* carries risks.

Key words: Stent retrieval; Covered stent; Premature stent deployment

© **The Author(s) 2015.** Published by Baishideng Publishing Group Inc. All rights reserved.

Core tip: Increasingly complex neurovascular lesions are now amenable to endovascular therapy due to the development of new devices and techniques. However, malfunction or failure of these devices remains a potential hurdle to a successful treatment. Consequently, a growing body of reports describing rescue and salvage techniques have emerged. In this report, we discuss the endovascular retrieval of a prematurely deployed covered stent during the treatment of a traumatic carotid-cavernous fistula.

Miley JT, Rodriguez GJ, Tummala RP. Endovascular retrieval of a prematurely deployed covered stent. *World J Radiol* 2015; 7(6): 139-142 Available from: URL: <http://www.wjgnet.com/1949-8470/full/v7/i6/139.htm> DOI: <http://dx.doi.org/10.4329/wjr.v7.i6.139>

INTRODUCTION

Increasingly complex neurovascular lesions are now amenable to endovascular therapy due to the development of new devices and techniques. However, malfunction or failure of these devices remains a potential hurdle to a successful treatment. More commonly, endovascular device malfunction has been reported in the setting of intracranial aneurysm coil embolization or stent placement. Consequently, a growing body of reports describing rescue and salvage techniques has emerged^[1-6]. In this report, we discuss the endovascular retrieval of a prematurely deployed covered stent during an attempted treatment of a traumatic carotid-cavernous fistula (CCF).

Clinical presentation

A 50-year-old right-handed man was repairing an elevator when he sustained a 20-foot fall, resulting in loss of consciousness. He was taken to a local hospital where a left wrist, multiple rib and craniofacial fractures were discovered. All fractures were managed conservatively. By the end of his five-week hospital stay, he began to experience a roaring tinnitus that was only mainly audible at night, horizontal diplopia, decreased visual acuity, chemosis and proptosis of the left eye.

One week later, the patient was referred to our institution to address his worsening left ocular symptoms. On initial examination, we noted a cranial and orbital bruit, decreased left visual acuity (20/100), left afferent papillary defect, proptosis, chemosis and limited eye movements in all directions. The remainder of his neurological examination was unremarkable. Computerized tomography of the head demonstrated fractures of the left zygomatic arch, left lateral orbital wall, a prominent left superior orbital vein, and a left parietal hypodensity consistent with a subacute ischemic infarct. A conventional diagnostic cerebral angiogram demonstrated a left CCF in the horizontal cavernous segment of the left intracranial cavernous angiomas (ICA) (barrow type A)^[7] with angiographic steal from the intracranial circulation and flow reversal into the cavernous sinus tributary veins.

CASE REPORT

Intended treatment

Due to the symptoms of the patient and concerns for visual loss conservative management was not considered. Given the lack of established guidelines in the treatment of CCFs and our previous successful

experience in the treatment of CCFs with a covered stent, it was decided to use a covered stent in the left cavernous ICA at the site of the fistula. In our experience previous cases of CCFs treated at our institution were mainly performed with coil embolization of the cavernous sinus but often requiring several procedures, recently we had a success with the use of a covered stent. Prior to the procedure, emergent internal review board consent was obtained for the off label use of a covered stent. Through a 7 French (Fr) introducer sheath (Cordis, Miami, FL) in the right femoral artery, a 7 Fr Brite Tip multipurpose catheter (Cordis, Miami, FL) was advanced into the distal cervical segment of the left ICA. We navigated a microcatheter (Excelsior SL-10, Boston Scientific, Natick, MA) into the proximal left middle cerebral artery and exchanged it over a microwire (Luge Wire, Boston Scientific, Natick, MA) for the covered stent delivery system. With the microwire positioned in the distal M2 division, we advanced intracranially a 5 mm × 19 mm covered stent (Graft-Master JoStent, Abbott Laboratories, Abbott Park, IL) over the microwire.

Once the stent delivery system was in the proximal vertical segment of the left cavernous ICA, we noted increased resistance and difficulty in advancing the system past the posterior genu of the cavernous segment. The guide catheter was pushed back proximally as the resistance increased, therefore we determined that the covered stent could not be delivered through our system and it had to be withdrawn. Upon withdrawal of the devices, we noted the stent was not mounted on the balloon. Fluoroscopy demonstrated that the stent had been prematurely deployed into the lacerum segment of the ICA (Figure 1) and the un-inflated balloon of the stent system was not abating the wall of the vessel.

Covered stent retrieval

Under roadmap guidance, a 3 mm × 9 mm Maverick balloon (Boston Scientific, Natick, MA) was advanced over a 0.014 microwire (Transcend, Boston Scientific, Natick, MA) through the lumen of the stent. The distal end of the microwire was positioned in the left A1. Once the balloon was distal to the stent, the balloon was inflated to a subnominal pressure and pulled back in contact with the distal end of the stent (Figure 2). The stent was dragged back over the wire to the distal end of the guide catheter. Ensuring the stent was trapped between the guide catheter and the balloon all the devices were withdrawn at once (Figure 3).

Clinical outcome

The patient in the same procedure underwent transvenous coil embolization of the cavernous sinus, however it was required to keep the patient intubated and be brought back the next day to achieve complete embolization of the fistula (coil length of 390 cm). At follow up a few weeks later, the proptosis, chemosis and bruit resolved along with improvement in the extraocular movements and visual acuity.

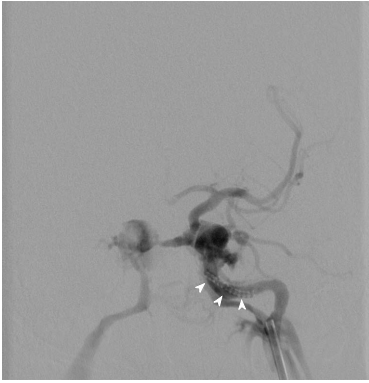


Figure 1 Anteroposterior view of left internal carotid injection (early arterial phase) showing the carotid cavernous fistula and prematurely deployed stent in the petrous segment (arrowheads).

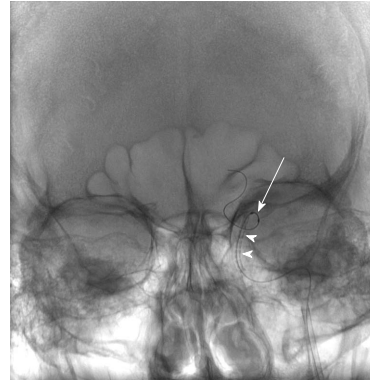


Figure 2 Anteriorposterior fluoroscopic view, that demonstrates the microwire in the left anterior cerebral artery and the balloon markers (arrow) distal to the stent (arrowheads) in preparation for the stent retrieval.

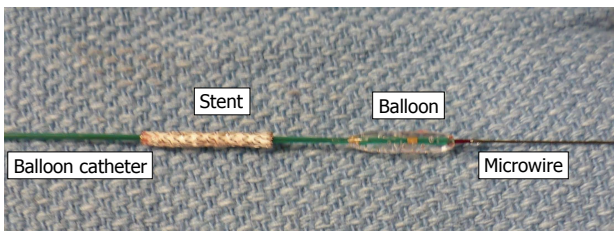


Figure 3 Balloon-catheter, stent, balloon and microwire following retrieval.

DISCUSSION

There is a growing body of literature focused on salvage techniques for neuroendovascular complications, and the operator must be prepared to manage intraprocedural complications including those related to device failure. Effective and successful rescue maneuvers unique to each device should be reported.

The successful use of covered stents in the treatment of CCF has been reported^[8-12], but their poor navigability in the intracranial circulation is also well-described. Factors that contribute to a difficult stent delivery into the intracranial circulation include tortuous vascular anatomy, unstable positioning of the guide catheter, and poor stent navigability. The Graft-Master JoStent (Abbott Laboratories, Abbott Park, IL) is composed of a polytetrafluoroethylene sheet fixed between two stainless steel stents, mounted on a semi-compliant balloon that requires a ≥ 7 Fr guide catheter and ≤ 0.014 inch wire for device delivery. This design results in inherent stiffness and poor navigability of the device. Excessive application of force may not overcome the poor navigability and may lead to proximal herniation of the guide catheter or premature deployment of the stent. Our patient did not appear to have prominent tortuous vessels, consequently, we believed that we could advance the covered stent to the cavernous segment with minimal resistance. Although large series are lacking, failure to deploy a covered stent has been previously reported^[13]. A better proximal support by having a telescoping system with the guide catheter supported by an additional long sheath may have helped

with navigation and prevented premature deployment of the stent. A shorter covered stent (12 mm) could have been easier to advance, however we were not convinced that its length would properly have covered the fistulous point.

The prematurely deployed stent was noted after the removal of the stent delivery microcatheter and its guide wire. In addition, this resulted in loss of access to the lumen of the stent and posed the challenging task to pass a wire back through the stent. Nevertheless, we were concerned that leaving a stent not abating the wall of the vessel could increase the risk of thromboembolic complications with or without stent migration, therefore we chose to attempt the stent retrieval.

The retrieval of misplaced or malfunctioning devices in neuroendovascular procedures have been performed using snares^[1], the Alligator retrieval device (Chestnut Medical, Menlo Park, CA)^[3] or the Merci retriever (Concentric, Mountain View, CA)^[6]. In coronary procedures however, the reported incidence of coronary stent loss or premature stent-balloon separation resulting in embolism is reported to be in the range of 0.27%-3.4%^[14,15]. The retrieval in this setting often involves the use of a small distal balloon, loop snare, two wires around the stent or biopsy forceps^[14-19]. This migration or premature deployment in neuroendovascular procedures is a relatively uncommon complication since most commercially available intracranial stents are self-expandable^[20,21].

The technique of passing a balloon within the lumen of the stent is a well described technique in interventional cardiology for the retrieval of migrated stents^[14-16,22,23]. The balloon is used to drag the stent proximally to the tip of the guide catheter. Once all are in contact (balloon-stent-guide catheter), the entire system is removed in one unit. Although in this case the rescue was successful, we acknowledge that the rescue might have carried additional challenges such as failure of retrieval and arterial dissection.

The retrieval of an early deployed balloon mounted stent is possible. The use of a balloon to drag the stent back into the guide catheter is a potential rescue option

if leaving the stent *in situ* carries risks.

COMMENTS

Case characteristics

Blurred left eye vision, double vision and tinnitus developed after a fall.

Clinical diagnosis

Chemosis, proptosis of the left eye, an orbital bruit was noted.

Differential diagnosis

An arteriovenous fistula was suspected and demonstrated with neuroimaging.

Imaging diagnosis

A conventional angiogram demonstrated a direct carotid-cavernous fistula (CCF).

Treatment

Failure of a stent placement led to the definitive transvenous coil embolization.

Related reports

Unforeseen device failure occurs. Experiences in this regard should be reported.

Term explanation

Covered-stent: No flow is allowed within the struts of the stent, impermeable.

Experiences and lessons

Tortuous vasculature may prevent smooth navigation of rigid devices.

Peer-review

This was described as an interesting manuscript that reviews treatment options of a CCF, and limitations when a covered stent is planned to be used. The authors' experience in the retrieval of a prematurely deployed covered stent may help the reader if facing a similar case.

REFERENCES

- 1 **Dinc H**, Kuzeyli K, Kosucu P, Sari A, Cekirge S. Retrieval of prolapsed coils during endovascular treatment of cerebral aneurysms. *Neuroradiology* 2006; **48**: 269-272 [PMID: 16534608 DOI: 10.1007/s00234-006-0051-x]
- 2 **Fessler RD**, Ringer AJ, Qureshi AI, Guterman LR, Hopkins LN. Intracranial stent placement to trap an extruded coil during endovascular aneurysm treatment: technical note. *Neurosurgery* 2000; **46**: 248-251; discussion 251-253 [PMID: 10626961 DOI: 10.1097/00006123-200001000-00056]
- 3 **Henkes H**, Lowens S, Preiss H, Reinartz J, Miloslavsky E, Kühne D. A new device for endovascular coil retrieval from intracranial vessels: alligator retrieval device. *AJNR Am J Neuroradiol* 2006; **27**: 327-329 [PMID: 16484403]
- 4 **Lavine SD**, Larsen DW, Giannotta SL, Teitelbaum GP. Parent vessel Guglielmi detachable coil herniation during wide-necked aneurysm embolization: treatment with intracranial stent placement: two technical case reports. *Neurosurgery* 2000; **46**: 1013-1017 [PMID: 10764283 DOI: 10.1097/00006123-200004000-00051]
- 5 **Prestigiacomo CJ**, Fidlow K, Pile-Spellman J. Retrieval of a fractured Guglielmi detachable coil with use of the Goose Neck snare "twist" technique. *J Vasc Interv Radiol* 1999; **10**: 1243-1247 [PMID: 10527203 DOI: 10.1016/S1051-0443(99)70226-5]
- 6 **Vora N**, Thomas A, Germanwala A, Jovin T, Horowitz M. Retrieval of a displaced detachable coil and intracranial stent with an L5 Merci Retriever during endovascular embolization of an intracranial aneurysm. *J Neuroimaging* 2008; **18**: 81-84 [PMID: 18190501 DOI: 10.1111/j.1552-6569.2007.00165.x]
- 7 **Barrow DL**, Spector RH, Braun IF, Landman JA, Tindall SC, Tindall GT. Classification and treatment of spontaneous carotid-cavernous sinus fistulas. *J Neurosurg* 1985; **62**: 248-256 [PMID: 3968564 DOI: 10.3171/jns.1985.62.2.0248]
- 8 **Archondakis E**, Pero G, Valvassori L, Boccardi E, Scialfa G. Angiographic follow-up of traumatic carotid cavernous fistulas treated with endovascular stent graft placement. *AJNR Am J Neuroradiol* 2007; **28**: 342-347 [PMID: 17297009]
- 9 **Gomez F**, Escobar W, Gomez AM, Gomez JF, Anaya CA. Treatment of carotid cavernous fistulas using covered stents: midterm results in seven patients. *AJNR Am J Neuroradiol* 2007; **28**: 1762-1768 [PMID: 17885249]
- 10 **Hoit DA**, Schirmer CM, Malek AM. Stent graft treatment of cerebrovascular wall defects: intermediate-term clinical and angiographic results. *Neurosurgery* 2008; **62**: ONS380-ONS388; discussion ONS388-389 [PMID: 18596518 DOI: 10.1227/01.neu.0000326022.08973.b2]
- 11 **Lv XL**, Li YX, Liu AH, Lv M, Jiang P, Zhang JB, Wu ZX. A complex cavernous sinus dural arteriovenous fistula secondary to covered stent placement for a traumatic carotid artery-cavernous sinus fistula: case report. *J Neurosurg* 2008; **108**: 588-590 [PMID: 18312107 DOI: 10.3171/JNS/2008/108/3/0588]
- 12 **Madan A**, Mujic A, Daniels K, Hunn A, Liddell J, Rosenfeld JV. Traumatic carotid artery-cavernous sinus fistula treated with a covered stent. Report of two cases. *J Neurosurg* 2006; **104**: 969-973 [PMID: 16776343 DOI: 10.3171/jns.2006.104.6.969]
- 13 **Wang C**, Xie X, You C, Zhang C, Cheng M, He M, Sun H, Mao B. Placement of covered stents for the treatment of direct carotid cavernous fistulas. *AJNR Am J Neuroradiol* 2009; **30**: 1342-1346 [PMID: 19342540 DOI: 10.3174/ajnr.A1583]
- 14 **Brilakis ES**, Best PJ, Elesber AA, Barsness GW, Lennon RJ, Holmes DR, Rihal CS, Garratt KN. Incidence, retrieval methods, and outcomes of stent loss during percutaneous coronary intervention: a large single-center experience. *Catheter Cardiovasc Interv* 2005; **66**: 333-340 [PMID: 16142808 DOI: 10.1002/ccd.20449]
- 15 **Eggebrecht H**, Haude M, von Birgelen C, Oldenburg O, Baumgart D, Herrmann J, Welge D, Bartel T, Dagnes N, Erbel R. Nonsurgical retrieval of embolized coronary stents. *Catheter Cardiovasc Interv* 2000; **51**: 432-440 [PMID: 11108675 DOI: 10.1002/1522-726X(20012)51:4<432::AID-CCD12>3.3.CO;2-T]
- 16 **Colkesen AY**, Baltali M, Acil T, Tekin G, Tekin A, Erol T, Sezgin AT, Muderrisoglu H. Coronary and systemic stent embolization during percutaneous coronary interventions: a single center experience. *Int Heart J* 2007; **48**: 129-136 [PMID: 17409578]
- 17 **Juszkat R**, Dziarmaga M, Zabicki B, Bychowicz B. Successful coronary stent retrieval from the renal artery. *Cardiol J* 2007; **14**: 87-90 [PMID: 18651440]
- 18 **Steinberg DH**, Satler LF, Pichard AD. Snare extraction of a fractured coronary stent in a saphenous vein graft. *Catheter Cardiovasc Interv* 2007; **70**: 241-243 [PMID: 17377995 DOI: 10.1002/ccd.21113]
- 19 **Ahmar W**, Malaipan Y, Meredith IT. Transradial retrieval of a dislodged stent from the left main coronary artery. *J Invasive Cardiol* 2008; **20**: 545-547 [PMID: 18830000]
- 20 **Kelly ME**, Turner RD, Moskowitz SI, Gonugunta V, Hussain MS, Fiorella D. Delayed migration of a self-expanding intracranial microstent. *AJNR Am J Neuroradiol* 2008; **29**: 1959-1960 [PMID: 18719038 DOI: 10.3174/ajnr.A1224]
- 21 **Lubicz B**, François O, Levivier M, Brothi J, Balériaux D. Preliminary experience with the enterprise stent for endovascular treatment of complex intracranial aneurysms: potential advantages and limiting characteristics. *Neurosurgery* 2008; **62**: 1063-1069; discussion 1069-1070 [PMID: 18580804 DOI: 10.1227/01.neu.0000325868.06764.de]
- 22 **Qiao S**, Gao R, Chen J, Yao M, Yang Y, Qin X, Xu B. Successful retrieval of intracoronary lost balloon-mounted stent using a small balloon. *Chin Med J (Engl)* 2000; **113**: 93-94 [PMID: 11775220]
- 23 **Kammler J**, Leisch F, Kerschner K, Kypta A, Steinwender C, Kratochwill H, Lukas T, Hofmann R. Long-term follow-up in patients with lost coronary stents during interventional procedures. *Am J Cardiol* 2006; **98**: 367-369 [PMID: 16860025]

P-Reviewer: Battal B, Chen F, El-Ghar MA, Vinh-Hung V

S-Editor: Tian YL L-Editor: A E-Editor: Liu SQ





Published by **Baishideng Publishing Group Inc**

8226 Regency Drive, Pleasanton, CA 94588, USA

Telephone: +1-925-223-8242

Fax: +1-925-223-8243

E-mail: bpgoffice@wjgnet.com

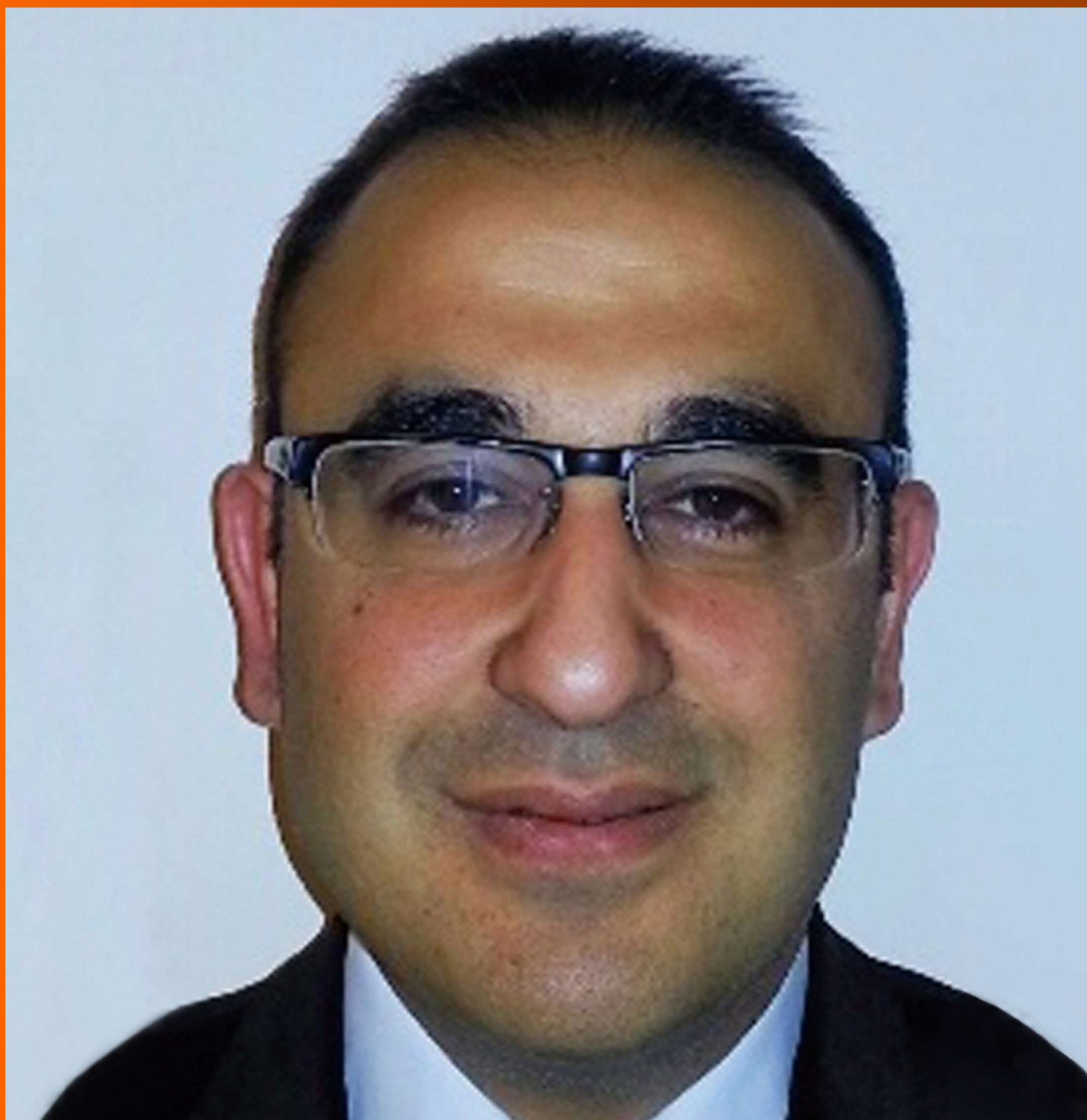
Help Desk: <http://www.wjgnet.com/esps/helpdesk.aspx>

<http://www.wjgnet.com>



World Journal of *Radiology*

World J Radiol 2015 July 28; 7(7): 143-183





Editorial Board

2014-2017

The *World Journal of Radiology* Editorial Board consists of 365 members, representing a team of worldwide experts in radiology. They are from 36 countries, including Afghanistan (1), Argentina (2), Australia (5), Austria (7), Belgium (2), Brazil (8), Canada (6), Chile (1), China (43), Croatia (1), Denmark (4), Egypt (6), France (5), Germany (22), Greece (10), India (12), Iran (6), Ireland (2), Israel (3), Italy (47), Japan (13), Netherlands (1), New Zealand (1), Pakistan (1), Poland (2), Portugal (1), Serbia (1), Singapore (3), Slovakia (1), South Korea (18), Spain (4), Sweden (2), Switzerland (4), Thailand (1), Turkey (26), United Kingdom (11), and United States (82).

EDITORS-IN-CHIEF

Kai U Juergens, *Bremen*
Edwin JR van Beek, *Edinburgh*
Thomas J Vogl, *Frankfurt*

GUEST EDITORIAL BOARD MEMBERS

Wing P Chan, *Taipei*
Chung-Huei Hsu, *Taipei*
Chin-Chang Huang, *Taipei*
Tsong-Long Hwang, *Taoyuan*
Jung-Lung Hsu, *Taipei*
Chia-Hung Kao, *Taichung*
Yu-Ting Kuo, *Tainan*
Hon-Man Liu, *Taipei*
Hui-Lung Liang, *Kaohsiung*
Chun Chung Lui, *Kaohsiung*
Sen-Wen Teng, *Taipei*
Yung-Liang (William) Wan, *Taoyuan*

MEMBERS OF THE EDITORIAL BOARD



Afghanistan

Takao Hiraki, *Okayama*



Argentina

Patricia Carrascosa, *Vicente Lopez*
Maria C Ziadi, *Rosario*



Australia

Lourens Bester, *Sydney*
Gemma A Figtree, *Sydney*



Austria

Herwig R Cerwenka, *Graz*
Gudrun M Feuchtnner, *Innsbruck*
Benjamin Henninger, *Innsbruck*
Rupert Lanzenberger, *Vienna*
Shu-Ren Li, *Vienna*
Veronika Schopf, *Vienna*
Tobias De Zordo, *Innsbruck*



Belgium

Steve Majerus, *Liege*
Kathelijne Peremans, *Merelbeke*



Brazil

Clerio F Azevedo, *Rio de Janeiro*
Patrícia P Alfredo, *São Paulo*
Eduardo FC Fleury, *São Paulo*
Edward Araujo Júnior, *São Paulo*
Wellington P Martins, *Ribeirao Preto*
Ricardo A Mesquita, *Belo Horizonte*
Vera MC Salemi, *São Paulo*
Claudia Szobot, *Porto Alegre*
Lilian YI Yamaga, *São Paulo*



Canada

Marie Arsalidou, *Toronto*
Otman A Basir, *Waterloo*

Tarik Zine Belhocine, *Toronto*
James Chow, *Toronto*
Tae K Kim, *Toronto*
Anastasia Oikonomou, *Toronto*



China

Hong-Wei Chen, *Wuxi*
Feng Chen, *Hangzhou*
Jian-Ping Chu, *Guangzhou*
Guo-Guang Fan, *Shenyang*
Bu-Lang Gao, *Shijiazhuang*
Qi-Yong Gong, *Chengdu*
Ying Han, *Beijing*
Xian-Li Lv, *Beijing*
Yi-Zhuo Li, *Guangzhou*
Xiang-Xi Meng, *Harbin*
Yun Peng, *Beijing*
Jun Shen, *Guangzhou*
Ze-Zhou Song, *Hangzhou*
Wai Kwong Tang, *Hong Kong*
Gang-Hua Tang, *Guangzhou*
Jie Tian, *Beijing*
Lu-Hua Wang, *Beijing*
Xiao-bing Wang, *Xi'an*
Yi-Gen Wu, *Nanjing*
Kai Wu, *Guangzhou*
Hui-Xiong Xu, *Shanghai*
Zuo-Zhang Yang, *Kunming*
Xiao-Dan Ye, *Shanghai*
David T Yew, *Hong Kong*
Ting-He Yu, *Chongqing*
Zheng Yuan, *Shanghai*
Min-Ming Zhang, *Hangzhou*
Yudong Zhang, *Nanjing*
Dong Zhang, *Chongqing*
Wen-Bin Zeng, *Changsha*

Yue-Qi Zhu, *Shanghai*



Croatia

Goran Kusec, *Osijek*



Denmark

Poul E Andersen, *Odense*

Lars J Petersen, *Aalborg*

Thomas Z Ramsøy, *Frederiksberg*

Morten Ziebell, *Copenhagen*



Egypt

Mohamed F Bazeed, *Mansoura*

Mohamed Abou El-Ghar, *Mansoura*

Reem HA Mohamed, *Cairo*

Mohamed R Nouh, *Alexandria*

Ahmed AKA Razek, *Mansoura*

Ashraf A Zytoon, *Shebin El-Koom*



France

Sabine F Bensamoun, *Compiègne*

Romarc Loffroy, *Dijon*

Stephanie Nougaret, *Montpellier*

Hassane Oudadesse, *Rennes*

Vincent Vinh-Hung, *Fort-de-France*



Germany

Henryk Barthel, *Leipzig*

Peter Bannas, *Hamburg*

Martin Beeres, *Frankfurt*

Ilja F Ciernik, *Dessau*

A Dimitrakopoulou-Strauss, *Heidelberg*

Peter A Fasching, *Erlangen*

Andreas G Schreyer, *Regensburg*

Philipp Heusch, *Duesseldorf*

Sonja M Kirchhoff, *Munich*

Sebastian Ley, *Munich*

Adel Maataoui, *Frankfurt am Main*

Stephan M Meckel, *Freiburg*

Hans W Muller, *Duesseldorf*

Kay Raum, *Berlin*

Dirk Rades, *Luebeck*

Marc-Ulrich Regier, *Hamburg*

Alexey Surov, *Halle*

Martin Walter, *Magdeburg*

Axel Wetter, *Essen*

Christoph Zilkens, *Düsseldorf*



Greece

Panagiotis Antoniou, *Thessaloniki*

Nikos Efthimiou, *Athens*

Dimitris Karnabatidis, *Patras*

George Latsios, *Athens*

Stylianios Megremis, *Iraklion*

Alexander D Rapidis, *Athens*

Kiki Theodorou, *Larissa*

Ioannis A Tsalafoutas, *Athens*

Evanthia E Tripoliti, *Ioannina*

Athina C Tsili, *Ioannina*



India

Ritesh Agarwal, *Chandigarh*

Chandan J Das, *New Delhi*

Prathamesh V Joshi, *Mumbai*

Naveen Kalra, *Chandigarh*

Chandrasekharan Kesavadas, *Trivandrum*

Jyoti Kumar, *New Delhi*

Atin Kumar, *New Delhi*

Kaushala P Mishra, *Allahabad*

Daya N Sharma, *New Delhi*

Binit Sureka, *New Delhi*

Sanjay Sharma, *New Delhi*

Raja R Yadav, *Allahabad*



Iran

Majid Assadi, *Bushehr*

SeyedReza Najafizadeh, *Tehran*

Mohammad Ali Oghabian, *Tehran*

Amir Reza Radmard, *Tehran*

Ramin Sadeghi, *Mashhad*

Hadi Rokni Yazdi, *Tehran*



Ireland

Tadhg Gleeson, *Wexford*

Frederik JAI Vernimmen, *Cork*



Israel

Dafna Ben Bashat, *Tel Aviv*

Amit Gefen, *Tel Aviv*

Tamar Sella, *Jerusalem*



Italy

Adriano Alippi, *Rome*

Dante Amelio, *Trento*

Michele Anzidei, *Rome*

Filippo F Angileri, *Messinas*

Stefano Arcangeli, *Rome*

Roberto Azzoni, *San Donato milanese*

Tommaso V Bartolotta, *Palermo*

Tommaso Bartalena, *Imola*

Livia Bernardin, *San Bonifacio*

Federico Boschi, *Verona*

Sergio Casciaro, *Lecce*

Emanuele Casciani, *Rome*

Musa M Can, *Napoli*

Alberto Cuocolo, *Napoli*

Michele Ferrara, *Coppito*

Mauro Feola, *Fossano*

Giampiero Francica, *Castel Volturno*

Luigi De Gennaro, *Rome*

Giulio Giovannetti, *Pisa*

Francesca Iacobellis, *Napoli*

Formato Invernizzi, *Monza Brianza*

Francesco Lassandro, *Naples*

Lorenzo Livi, *Florence*

Pier P Mainenti, *Napoli*

Laura Marzetti, *Chieti*

Giuseppe Malinverni, *Crescentino*

Enrica Milanese, *Turin*

Giovanni Morana, *Treviso*

Lorenzo Monti, *Milan*

Silvia D Morbelli, *Genoa*

Barbara Palumbo, *Perugia*

Cecilia Parazzini, *Milan*

Stefano Pergolizzi, *Messina*

Antonio Pinto, *Naples*

Camillo Porcaro, *Rome*

Carlo C Quattrocchi, *Rome*

Alberto Rebonato, *Perugia*

Giuseppe Rizzo, *Rome*

Roberto De Rosa, *Naples*

Domenico Rubello, *Rovigo*

Andrea Salvati, *Bari*

Sergio Sartori, *Ferrara*

Luca M Sconfienza, *Milano*

Giovanni Storto, *Rionero*

Nicola Sverzellati, *Parma*

Alberto S Tagliafico, *Genova*

Nicola Troisi, *Florence*



Japan

Yasuhiko Hori, *Chiba*

Hidetoshi Ikeda, *Koriyama*

Masahito Kawabori, *Sapporo*

Tamotsu Kamishima, *Sapporo*

Hiro Kiyosue, *Yufu*

Yasunori Minami, *Osaka-sayama*

Yasuhiro Morimoto, *Kitakyushu*

Satoru Murata, *Tokyo*

Shigeki Nagamachi, *Miyazaki*

Hiroshi Onishi, *Yamanashi*

Morio Sato, *Wakayama Shi*

Yoshito Tsushima, *Maebashi*

Masahiro Yanagawa, *Suita*



Netherlands

Willem Jan van Rooij, *Tilburg*



New Zealand

W Howell Round, *Hamilton*



Pakistan

Wazir Muhammad, *Abbottabad*



Poland

Maciej S Baglaj, *Wroclaw*

Piotr Czauderna, *Gdansk*



Portugal

Joao Manuel RS Tavares, *Porto*



Serbia

Olivera Ciraj-Bjelac, *Belgrade*



Singapore

Gopinathan Anil, *Singapore*

Terence KB Teo, *Singapore*

Cher Heng Tan, *Singapore*



Slovakia

Stefan Sivak, *Martin*



South Korea

Ki Seok Choo, *Busan*

Seung Hong Choi, *Seoul*

Dae-Seob Choi, *Jinju*

Hong-Seok Jang, *Seoul*

Yong Jeong, *Daejeon*

Chan Kyo Kim, *Seoul*

Se Hyung Kim, *Seoul*

Joong-Seok Kim, *Seoul*

Sang Eun Kim, *Seongnam*

Sung Joon Kwon, *Seoul*

Jeong Min Lee, *Seoul*

In Sook Lee, *Busan*

Noh Park, *Goyang*

Chang Min Park, *Seoul*

Sung Bin Park, *Seoul*

Deuk Jae Sung, *Seoul*

Choongsoo Shin, *Seoul*

Kwon-Ha Yoon, *Iksan*



Spain

Miguel A De Gregorio, *Zaragoza*

Antonio Luna, *Jaén*

Enrique Marco de Lucas, *Santander*

Fernando Ruiz Santiago, *Granada*



Sweden

Dmitry Grishenkov, *Stockholm*

Tie-Qiang Li, *Stockholm*



Switzerland

Nicolau Beckmann, *Basel*

Christian Boy, *Bern*

Giorgio Treglia, *Bellinzona*

Stephan Ulmer, *Kiel*



Thailand

Sirianong Namwongprom, *Chiang Mai*



Turkey

Kubilay Aydin, *Istanbul*

Ramazan Akdemir, *Sakarya*

Serhat Avcu, *Ankara*

Ayşe Aralasmak, *Istanbul*

Oktay Algin, *Ankara*

Nevbahar Akcar, *Meselik*

Bilal Battal, *Ankara*

Zulkif Bozgeyik, *Elazig*

Nazan Ciledag, *Aakara*

Fuldem Y Donmez, *Ankara*

Gulgun Engin, *Istanbul*

Ahmet Y Goktay, *Izmir*

Oguzhan G Gumustas, *Bursa*

Kaan Gunduz, *Ankara*

Pelin Ozcan Kara, *Mersin*

Kivanc Kamburoglu, *Ankara*

Ozgur Kilickesmez, *Istanbul*

Furuzan Numan, *Istanbul*

Cem Onal, *Adana*

Ozgur Oztekin, *Izmir*

Seda Ozbek (Boruban), *Konya*

Selda Sarikaya, *Zonguldak*

Figen Taser, *Kutahya*

Baran Tokar, *Eskisehir*

Ender Uysal, *Istanbul*

Ensar Yekeler, *Istanbul*



United Kingdom

Indran Davagnanam, *London*

M DC Valdés Hernández, *Edinburgh*

Alan Jackson, *Manchester*

Suneil Jain, *Belfast*

Long R Jiao, *London*

Miltiadis Krokidis, *Cambridge*

Pradesh Kumar, *Liverpool*

Peter D Kuzmich, *Derby*

Georgios Plataniotis, *Brighton*

Vanessa Sluming, *Liverpool*



United States

Garima Agrawal, *Saint Louis*

James R Brasic, *Baltimore*

Rajendra D Badgaiyan, *Buffalo*

Ulas Bagci, *Bethesda*

Anat Biegon, *Stony Brook*

Ramon Casanova, *Winston Salem*

Wenli Cai, *Boston*

Zheng Chang, *Durham*

Corey J Chakarun, *Long Beach*

Kai Chen, *Los Angeles*

Hyun-Soon Chong, *Chicago*

Marco Cura, *Dallas*

Ravi R Desai, *Bensalem*

Delia DeBuc, *Miami*

Carlo N De Cecco, *Charleston*

Timm-Michael L Dickfeld, *Baltimore*

Subba R Digumarthy, *Boston*

Huy M Do, *Stanford*

Todd A Faasse, *Grand Rapids*

Salomao Faintuch, *Boston*

Girish M Fatterpekar, *New York*

Dhakshinamoorthy Ganesan, *Houston*

Robert J Griffin, *Little Rock*

Andrew J Gunn, *Boston*

Sandeep S Hedgire, *Boston*

Timothy J Hoffman, *Columbia*

Mai-Lan Ho, *San Francisco*

Juebin Huang, *Jackson*

Abid Irshad, *Charleston*

Matilde Inglese, *New York*

El-Sayed H Ibrahim, *Jacksonville*

Paul R Julsrud, *Rochester*

Pamela T Johnson, *Baltimore*

Ming-Hung Kao, *Tempe*

Sunil Krishnan, *Houston*

Richard A Komoroski, *Cincinnati*

Sandi A Kwee, *Honolulu*

King Kim, *Ft. Lauderdale*

Guozheng Liu, *Worcester*

Yiyan Liu, *Newark*

Venkatesh Mani, *New York*

Lian-Sheng Ma, *Pleasanton*

Rachna Madan, *Boston*

Zeyad A Metwalli, *Houston*

Yilong Ma, *Manhasset*

Hui Mao, *Atlanta*

Feroze B Mohamed, *Philadelphia*

Gul Moonis, *Boston*

John L Noshier, *New Brunswick*

Rahmi Oklu, *Boston*

Aytekun Oto, *Chicago*

Bishnuhari Paudyal, *Philadelphia*

Rajul Pandya, *Youngstown*

Chong-Xian Pan, *Sacramento*

Jay J Pillai, *Baltimore*

Neal Prakash, *Duarte*

Reza Rahbar, *Boston*

Ali S Raja, *Boston*

Gustavo J Rodriguez, *El Paso*

David J Sahn, *Portland*

Steven Schild, *Scottsdale*

Ali R Sepahdari, *Los Angeles*

Li Shen, *Indianapolis*

JP Sheehan, *Charlottesville*

Atul B Shinagare, *Boston*

Sarabjeet Singh, *Boston*

Charles J Smith, *Columbia*

Kenji Suzuki, *Chicago*

Monvadi Srichai-Parsia, *Washington*

Sree H Tirumani, *Boston*

Hebert A Vargas, *New York*

Sachit Verma, *Philadelphia*

Yoichi Watanabe, *Minneapolis*

Li Wang, *Chapel Hill*

Carol C Wu, *Boston*

Shoujun Xu, *Houston*

Min Yao, *Cleveland*

Xiaofeng Yang, *Atlanta*

Qingbao Yu, *Albuquerque*

Aifeng Zhang, *Chicago*

Chao Zhou, *Bethlehem*

Hongming Zhuang, *Philadelphia*

**EDITORIAL**

- 143 Endovascular management of visceral artery aneurysms: When to watch, when to intervene?

Loffroy R, Favelier S, Pottecher P, Genson PY, Estivalet L, Gehin S, Cercueil JP, Krausé D

- 149 Diffusion-weighted and diffusion-tensor imaging of normal and diseased uterus

Kara Bozkurt D, Bozkurt M, Nazli MA, Mutlu IN, Kilickesmez O

REVIEW

- 157 Non-invasive diagnostic imaging of colorectal liver metastases

Mainenti PP, Romano F, Pizzuti L, Segreto S, Storto G, Mannelli L, Imbriaco M, Camera L, Maurea S

MINIREVIEWS

- 170 Perfusion computed tomography in renal cell carcinoma

Das CJ, Thingujam U, Panda A, Sharma S, Gupta AK

CASE REPORT

- 180 Isolated renal hydatid presenting as a complex renal lesion followed by spontaneous hydatiduria

Bhaya A, Shinde AP

ABOUT COVER

Editorial Board Member of *World Journal of Radiology*, Ozgur Kilickesmez, MD, Associate Professor, Department of Diagnostic and Interventional Radiology, Istanbul Education and Research Hospital, Istanbul 34098, Turkey

AIM AND SCOPE

World Journal of Radiology (*World J Radiol*, *WJR*, online ISSN 1949-8470, DOI: 10.4329) is a peer-reviewed open access academic journal that aims to guide clinical practice and improve diagnostic and therapeutic skills of clinicians.

WJR covers topics concerning diagnostic radiology, radiation oncology, radiologic physics, neuroradiology, nuclear radiology, pediatric radiology, vascular/interventional radiology, medical imaging achieved by various modalities and related methods analysis. The current columns of *WJR* include editorial, frontier, diagnostic advances, therapeutics advances, field of vision, mini-reviews, review, topic highlight, medical ethics, original articles, case report, clinical case conference (clinicopathological conference), and autobiography.

We encourage authors to submit their manuscripts to *WJR*. We will give priority to manuscripts that are supported by major national and international foundations and those that are of great basic and clinical significance.

INDEXING/ABSTRACTING

World Journal of Radiology is now indexed in PubMed Central, PubMed, Digital Object Identifier, and Directory of Open Access Journals.

FLYLEAF

I-III Editorial Board

EDITORS FOR THIS ISSUE

Responsible Assistant Editor: *Xiang Li*
Responsible Electronic Editor: *Su-Qing Liu*
Proofing Editor-in-Chief: *Lian-Sheng Ma*

Responsible Science Editor: *Fang-Fang Ji*
Proofing Editorial Office Director: *Xiu-Xia Song*

NAME OF JOURNAL
World Journal of Radiology

ISSN
ISSN 1949-8470 (online)

LAUNCH DATE
December 31, 2009

FREQUENCY
Monthly

EDITORS-IN-CHIEF
Kai U Juergens, MD, Associate Professor, MRT und PET/CT, Nuklearmedizin Bremen Mitte, ZEMODI - Zentrum für morphologische und molekulare Diagnostik, Bremen 28177, Germany

Edwin JR van Beek, MD, PhD, Professor, Clinical Research Imaging Centre and Department of Medical Radiology, University of Edinburgh, Edinburgh EH16 4TJ, United Kingdom

Thomas J Vogl, MD, Professor, Reader in Health Technology Assessment, Department of Diagnostic and Interventional Radiology, Johann Wolfgang

Goethe University of Frankfurt, Frankfurt 60590, Germany

EDITORIAL OFFICE
Jin-Lei Wang, Director
Xiu-Xia Song, Vice Director
World Journal of Radiology
Room 903, Building D, Ocean International Center, No. 62 Dongsihuan Zhonglu, Chaoyang District, Beijing 100025, China
Telephone: +86-10-59080039
Fax: +86-10-85381893
E-mail: editorialoffice@wjnet.com
Help Desk: <http://www.wjnet.com/esps/helpdesk.aspx>
<http://www.wjnet.com>

PUBLISHER
Baishideng Publishing Group Inc
8226 Regency Drive,
Pleasanton, CA 94588, USA
Telephone: +1-925-223-8242
Fax: +1-925-223-8243
E-mail: bpgoffice@wjnet.com
Help Desk: <http://www.wjnet.com/esps/helpdesk.aspx>
<http://www.wjnet.com>

PUBLICATION DATE
July 28, 2015

COPYRIGHT
© 2015 Baishideng Publishing Group Inc. Articles published by this Open-Access journal are distributed under the terms of the Creative Commons Attribution Non-commercial License, which permits use, distribution, and reproduction in any medium, provided the original work is properly cited, the use is non commercial and is otherwise in compliance with the license.

SPECIAL STATEMENT
All articles published in journals owned by the Baishideng Publishing Group (BPG) represent the views and opinions of their authors, and not the views, opinions or policies of the BPG, except where otherwise explicitly indicated.

INSTRUCTIONS TO AUTHORS
Full instructions are available online at http://www.wjnet.com/1949-8470/g_info_20100316162358.htm.

ONLINE SUBMISSION
<http://www.wjnet.com/esps/>

Endovascular management of visceral artery aneurysms: When to watch, when to intervene?

Romarc Loffroy, Sylvain Favelier, Pierre Pottecher, Pierre-Yves Genson, Louis Estivalet, Sophie Gehin, Jean-Pierre Cercueil, Denis Krausé

Romarc Loffroy, Sylvain Favelier, Pierre Pottecher, Pierre-Yves Genson, Louis Estivalet, Sophie Gehin, Jean-Pierre Cercueil, Denis Krausé, Department of Vascular, Oncologic and Interventional Radiology, University of Dijon School of Medicine, Bocage Teaching Hospital, 21079 Dijon Cedex, France

Author contributions: Loffroy R, Favelier S and Pottecher P wrote the paper; Genson PY, Estivalet L, Gehin S, Cercueil JP and Krausé D revised the article for important intellectual content; all authors read and approved the final manuscript.

Conflict-of-interest statement: The authors have no conflict of interest to declare.

Open-Access: This article is an open-access article which was selected by an in-house editor and fully peer-reviewed by external reviewers. It is distributed in accordance with the Creative Commons Attribution Non Commercial (CC BY-NC 4.0) license, which permits others to distribute, remix, adapt, build upon this work non-commercially, and license their derivative works on different terms, provided the original work is properly cited and the use is non-commercial. See: <http://creativecommons.org/licenses/by-nc/4.0/>

Correspondence to: Romarc Loffroy, MD, PhD, Professor, Department of Vascular, Oncologic and Interventional Radiology, Le2i UMR CNRS 6306, University of Dijon School of Medicine, Bocage Teaching Hospital, 14 Rue Paul Gaffarel, BP 77908, 21079 Dijon Cedex, France. romarc.loffroy@chu-dijon.fr
 Telephone: +33-380-293677
 Fax: +33-380-295455

Received: January 12, 2015
 Peer-review started: January 15, 2015
 First decision: April 10, 2015
 Revised: April 17, 2015
 Accepted: May 5, 2015
 Article in press: May 6, 2015
 Published online: July 28, 2015

Abstract

Visceral artery aneurysms (VAA) include splanchnic and

renal artery aneurysms. They represent a rare clinical entity, although their detection is rising due to an increased use of cross-sectional imaging. Rupture is the most devastating complication, and is associated with a high morbidity and mortality. In addition, increased percutaneous endovascular interventions have raised the incidence of iatrogenic visceral artery pseudoaneurysms (VAPAs). For this reason, elective repair is preferable in the appropriately chosen patient. Controversy still exists regarding their treatment. Over the past decade, there has been steady increase in the utilization of minimally invasive, non-operative interventions, for vascular aneurysmal disease. All VAAs and VAPAs can technically be fixed by endovascular techniques but that does not mean they should. These catheter-based techniques constitute an excellent approach in the elective setting. However, in the emergent setting it may carry a higher morbidity and mortality. The decision for intervention has to take into account the size and the natural history of the lesion, the risk of rupture, which is high during pregnancy, and the relative risk of surgical or radiological intervention. For splanchnic artery aneurysms, we should recognize that we are not, in reality, well informed about their natural history. For most asymptomatic aneurysms, expectant treatment is acceptable. For large, symptomatic or aneurysms with a high risk of rupture, endovascular treatment has become the first-line therapy. Treatment of VAPAs is always mandatory because of the high risk of rupture. We present our point of view on interventional radiology in the splanchnic arteries, focusing on what has been achieved and the remaining challenges.

Key words: Visceral artery; Aneurysm; False aneurysm; Angiography; Embolization; Stent-graft

© **The Author(s) 2015.** Published by Baishideng Publishing Group Inc. All rights reserved.

Core tip: This editorial deals with interventional radiological techniques in the splanchnic arteries, focusing on

what has been achieved and the remaining challenges. For splanchnic artery aneurysms, we should recognize that we are not, in reality, well informed about their natural history. The indications for the embolization of aneurysms are limited depending on the morphology of the aneurysm and surrounding vessels. Rotational angiography and other recently developed imaging techniques can help analyze the vascular anatomy of every lesion in decision making on the appropriate treatment for each patient when choosing between embolization, surgery and surveillance.

Loffroy R, Favelier S, Pottecher P, Genson PY, Estivalet L, Gehin S, Cercueil JP, Krausé D. Endovascular management of visceral artery aneurysms: When to watch, when to intervene? *World J Radiol* 2015; 7(7): 143-148 Available from: URL: <http://www.wjgnet.com/1949-8470/full/v7/i7/143.htm> DOI: <http://dx.doi.org/10.4329/wjr.v7.i7.143>

INTRODUCTION

Visceral aneurysms represent a rare clinical entity; however, 10%-20% will rupture and this is accompanied by a significant mortality rate of 20%-70%, depending on the location of the aneurysm. Their incidence is increasing and controversy still exists regarding their treatment^[1]. The decision for intervention has to take into account the size and the natural history of the lesion, the risk of rupture, which is high during pregnancy, and the relative risk of surgical or radiological intervention. For most asymptomatic aneurysms, expectant treatment is acceptable. For large, symptomatic or aneurysms with a high risk of rupture, endovascular treatment has become the first-line therapy^[2]. Treatment of visceral artery pseudoaneurysms (VAPAs) is always mandatory because of the high risk of rupture. The purpose of this article is to answer some questions about the current use of interventional techniques in the treatment of visceral artery aneurysms (VAAs) and VAPAs.

WHAT ARE THE CURRENT THRESHOLDS FOR INTERVENTION IN VISCERAL ANEURYSMS?

We can divide the discussion between true VAAs and VAPAs because the thresholds are completely different. For VAPAs due to inflammation or pancreatitis [e.g., splenic, gastroduodenal (GDA), superior mesenteric artery (SMA), hepatic, or even renal aneurysms], trauma, or those occurring after surgery, the thresholds for treatment are very low. Even small aneurysms (2-5 mm) should be treated regardless of diameter because the risk of rupture for VAPAs is not related to their size. The type of aneurysm may (rarely) spontaneously heal, but in most cases, VAPAs will increase over time and eventually rupture. We should treat all of these aneurysms immediately after diagnosis, irrespective of

their location or origin^[1-3].

For true aneurysms, the treatment threshold is different and depends mainly on anatomic location. The threshold for most true splenic artery aneurysms is 2 cm in diameter at the largest axis. Even if peripheral thrombus is present, these aneurysms should be treated in cases of an overall diameter larger than 2 cm. Women of childbearing age should be treated regardless of the diameter because the risk increase significantly during pregnancy^[3].

One of the vascular complications of portal hypertension, which could occur in cirrhotic patients, is the development of intrasplenic or extrasplenic aneurysms. These lesions should not be treated systematically except in cases of aneurysms > 4 cm in diameter and in extrasplenic locations. In most cases, multiple, diffuse, small aneurysms related to portal hypertension should be left untreated and followed by repeat computed tomography (CT) or magnetic resonance imaging (MRI) examinations. Once the portal hypertension and underlying cirrhotic disease is treated (e.g., via liver transplantation), the aneurysm may spontaneously decrease and completely disappear over time.

Other types of true aneurysms such as GDAs or those in the pancreaticoduodenal arcades, which can be caused by chronic hyperkinetic flow, should be treated as soon as they are diagnosed because they are at high risk of rupture, even when small in size. In such aneurysms associated with celiac trunk stenosis, inversion of the flow in the pancreaticoduodenal arcades to revascularize the liver or spleen needs to be preserved during the embolization procedure, which is sometimes a technical challenge^[4].

For true hepatic or SMA aneurysms, the threshold for treatment is slightly lower than for splenic aneurysms. In most cases, we treat hepatic or SMA aneurysms when the large axis is > 1 to 1.5 cm.

The treatment of renal aneurysms is intended to prevent rupture either in the urinary tract or in the unclosed retroperitoneal space, as well as the development of systemic hypertension or renal failure in cases of intrarenal arteriovenous fistula development. Even small aneurysms could be the cause of changes to intrarenal hemodynamics and systemic hypertension and should, in this case, be treated endovascularly or surgically, depending on the type (saccular or fusiform) and location. In the case of isolated, non-symptomatic aneurysms in the renal arteries, the treatment threshold is around 1 to 1.5 cm^[1-4].

For both visceral and renal arteries, extraparenchymal aneurysms take priority over intraparenchymal aneurysms because the risks and severity of major rupture and hemorrhage seem significantly higher for proximal extraparenchymal lesions.

HOW HAVE THRESHOLDS EVOLVED OVER THE LAST TWO DECADES?

The threshold for aneurysm treatment due to pancreaticoduodenal arcade has evolved and is now very

low. This was different 15 to 20 years ago. Considering this type of true aneurysm, the relationship between the celiac trunk or SMA stenosis and the development of hyperkinetic aneurysms was not well known. Only in the last 8 to 10 years has the relationship between these two conditions been established^[4].

The threshold for treatment of renal, hepatic, SMA, or splenic aneurysm has been established for 10 or 15 years, and it has not significantly changed. However, we actually can treat all of these types of aneurysms by endovascular approaches instead of a more aggressive, invasive surgical approach. It's easier to treat these aneurysms now due to the evolution of endovascular techniques through a better understanding of peripheral conditions, as well as employment of neurovascular techniques. For the last 10 years, we have been performing peripheral interventions, applying neuro techniques for peripheral purposes with success. We know that the risks of rupture are very low in SMA or hepatic aneurysms < 1 cm, but we can treat these small aneurysms efficiently and safely with the endovascular approach. Most clinicians and patients prefer that these aneurysms are treated, because after treatment, the problem is solved. These patients, if left untreated, should have follow-up with CT scan, MRI, or ultrasonography each year or even every 6 mo.

ARE THERE DIFFERENT THRESHOLDS FOR PATIENTS WITH OTHER UNDERLYING CONDITIONS?

Patients with vasculitis such as Ehlers-Danlos disease type IV who develop even very small, true aneurysms should be treated regardless of the size because the risk of rupture is very high due to intrinsic defects in the vascular wall. Aneurysms in patients with Ehlers-Danlos syndrome will invariably increase over time and should be treated as soon as the diagnosis has been established, preferentially by endovascular reconstruction or segmental vascular exclusion instead of simple aneurysm coiling^[1,2].

IS THERE A RELATIONSHIP BETWEEN THE TREATMENT THRESHOLD AND THE TYPE OF MATERIAL USED?

The threshold to decide if we treat is never directly related to the material we use. For example, a proximal 3-cm-diameter splenic aneurysm can be treated with coiling, stent graft placement, segmental vascular exclusion, or even potentially a flow diverter.

Ten years ago, we only used coils or glue, because we didn't have very smooth and flexible microcoils. We also didn't have flexible stent grafts or flow diverters, and we couldn't use an imaging-guided direct percutaneous approach in cases of inaccessible lesions due to vascular sinuosity or proximal obstruction. With

the tools and techniques we have today, by preserving vessel patency, we can conservatively treat even large-neck and fusiform aneurysms that could have only been treated by segmental vascular exclusion before. Now, we can exclude the entire aneurysm and preserve the afferent arteries in more than 90% to 95% of cases. It is particularly important for splenic and renal function that we can treat extraparenchymal or hilar aneurysms while preserving the parent arteries and distal flow^[1-3].

WHAT ARE SOME ADVANCEMENTS IN ACCESS TECHNOLOGIES AND TECHNIQUES FOR THE TREATMENT OF VISCERAL ANEURYSMS?

We have now the opportunity to use neuroendovascular tools for peripheral aneurysm exclusion. Over the last 10 years, many neurological techniques have been developed into dedicated peripheral applications. For instance, the use of a balloon remodeling technique was created initially for neurointerventions by Moret *et al*^[5] 15 years ago. Ten years ago, one main limiting factor in treating visceral aneurysms with large necks was the risk of coils protruding outside the aneurysm or occluding the parent arteries. The first use of a balloon remodeling technique to increase coil density and avoid protrusion of coils in the parent artery was performed by Moret *et al*^[5] in 1997. This technique is routinely used in some centers to overcome limitations due to broad neck, unstable microcatheter, or to treat complex renal/splenic/SMA aneurysms. The combination of Onyx (Covidien) as an embolic agent with Onyx-compatible remodeling balloon has been used by several physicians to treat hilar renal and SMA aneurysms^[6]. To preserve the parent artery, we can use bare stents and coiling through the mesh of the stent with a microcatheter and microcoils^[7-11]. Alternatively, we can use kissing stents in cases of aneurysms located at bifurcations, which is often the case with renal arteries. To preserve vascularization of the kidney, we use a double-kissing stent or kissing-balloon remodeling technique and detachable coils. Another great technical advancement is the use of detachable coils instead of pushable coils. For neurointerventions, 20 years ago, radiologists started using exclusively detachable coils for cerebral aneurysm embolization, and now there are many types of detachable coils for peripheral applications provided by various companies (e.g., Terumo Interventional Systems, Boston Scientific Corporation, Cook Medical, and Covidien).

This is a significant advancement because it has increased the safety of treatment of even large-necked aneurysms by reducing the risk of periprocedural distal embolization of coils, especially for splenic and renal locations.

Hepatic artery aneurysms are probably the easiest to treat, as there is dual flow to the liver (arterial and portal), and we can we can completely exclude seg-

mentally the parent artery that is responsible for the aneurysm without any risk of ischemia to the liver. Hepatic aneurysms can be treated by different methods including coil packing of the aneurysm sac, segmental coil trapping of the parent artery ("sandwich technique"), placement of a covered stent in cases of proximal or relatively straight distal artery, or a combination of bare stent and microcoils through the mesh^[8-10].

The main challenge is with the SMA and renal arteries because we must preserve distal flow and therefore maintain parent vessel patency by using remodeling coils/Onyx techniques, stent grafts, or a combination of bare stent and microcoils. Conversely, in cases of extraparenchymal splenic aneurysm, we use a different approach. The splenic artery is sometimes difficult to navigate, even with small and soft microcatheters. However, in most cases of splenic aneurysm, we can perform segmental splenic artery exclusion by deploying coils distally and proximally. Coil placement on both sides of the aneurysm is safe because there is enough collateralization through the gastric and pancreatic arteries, and this collateralization will revascularize the spleen at the ileum and help to preserve the intrasplenic blood flow.

We believe that the medial or proximal part of the splenic artery can be completely excluded without risk. It is probably the best treatment for splenic aneurysms, especially for pancreatitis-related pseudoaneurysm.

As mentioned previously, pseudoaneurysm due to inflammation, pancreatitis, trauma, and mycotic aneurysm should normally not be treated by packing the aneurysm alone, even if good results have been reported with this technique^[12]. These pseudoaneurysms should preferentially be treated by segmental artery exclusion because the aneurysm is secondary to progressive regional arterial wall deterioration. If we only treat the aneurysm, the patient is at risk of aneurysm recurrence on both sides of the occluded neck because the wall is destroyed by the inflammatory process. In this case, the best and only efficient and safe treatment is to completely exclude the parent artery, distally and proximally, to be sure you've completely solved the regional problem. Placement of a covered stent with extensive proximal and distal landing zones could be an acceptable alternative.

Stent grafts may be useful to preserve the distal vascularization. We have used coronary stent grafts because of their high flexibility; they can be navigated through tortuous arteries^[9-11]. These balloon-expandable stent grafts are mounted on very thin microcatheters and can reach distal aneurysms. Coronary stent grafts are limited by the length and diameters available, which range between 9 and 22 mm and 2 and 4.5 mm, respectively. Small dedicated stents are now available on the market for visceral aneurysms (V12, Maquet).

Inaccessible small aneurysms or pseudoaneurysms in the GDA or pancreaticoduodenal arcades may also be treated with liquid embolics, such as N-butyl cyanoacrylate glue (Glubran2, GEM) or Onyx instead of

coils^[6,13]. If we cannot reach a distal aneurysm due to a tortuous access, we place a small catheter as close as possible to the aneurysm and inject a mixture of glue diluted by Lipiodol (Guerbet) in variable ratios depending on the flow and distance between the point of injection and the target. We can inject the glue slowly, moving distally to exclude both the aneurysm and the arterial segments beyond and behind the aneurysm. This is the so-called front-and-back-door occlusion.

In the same way, for inaccessible aneurysms, we can use liquid embolics injected through collaterals when the main artery has been occluded for another reason and the aneurysm still grows or after previous artery occlusion, or if coils have been placed but were not sufficiently packed. The aneurysm remains open because collaterals revascularize the aneurysm, requiring navigation of very thin neuro microcatheters through tortuous collaterals to occlude the aneurysm using Onyx or glue^[6,13].

In cases when the aneurysms cannot be accessed by an endovascular approach or if proximal injection of liquid embolic agents is considered too dangerous, we can use a direct percutaneous ultrasound/CT-guided approach. This method could be used not only for intraparenchymal aneurysms in the spleen, liver, kidney, and pancreas, but also for extraparenchymal aneurysms, especially for SMA, GDA, or pancreaticoduodenal aneurysms that we cannot access safely.

Using cone-beam CT imaging guidance or conventional spiral CT, an 18-G guiding needle is first placed from the abdominal or back entry site to the target to stiffen the tract, and a microcatheter is navigated through the external needle into the aneurysm. Thrombin or even glue is slowly injected to get an immediate occlusion. Sometimes, we can fill the aneurysm with microcoils. If the lesion is clearly visible by ultrasonography, it's easy to place the needle through the splenic/renal or hepatic parenchyma into the aneurysm. The needle tip is clearly visible in the aneurysm by using color duplex ultrasonography. This is a major improvement in the treatment of visceral aneurysms inaccessible by an endovascular approach.

ARE THERE ANY OTHER DEVICES OR TECHNIQUES THAT ARE AVAILABLE?

In cases of small aneurysms, there is a risk of perforation when you place the first coils. If this occurs, the coils should be completely placed and detached as quickly as possible to stop the bleeding. When using the balloon technique, inflation of the balloon stops the flow or the bleeding if it occurs and helps solve the problem. During placement of the first coil in a small aneurysm, the remodeling balloon technique is very useful to avoid or address bleeding complications.

Another interesting technical approach to treat pseudoaneurysms with liquids while avoiding distal untargeted embolization is to inject liquid embolic or glue

through the microcatheter just in front of the aneurysm. The exact volume of contrast media necessary to fill the aneurysmal cavity and segmental arteries in front and back is estimated. Before injecting the glue, epinephrine, a vasoconstrictor, is injected to induce occlusive spasm of the artery distal to the aneurysm^[13]. Using this technique, there is no risk of glue migration far into the distal arteries and parenchyma.

ARE THERE ANY CLINICAL SCENARIOS IN WHICH A SURGICAL APPROACH IS PREFERRED?

The remaining indications for a surgical approach for visceral aneurysms are few, even for the less common types of fusiform aneurysms. These aneurysms are normally not treated if the dilatation is less than two times the normal diameter of the artery. These may be treated with a combination of stents and coils, stent grafts (often too rigid), as well as by new devices used for neurointervention, such as flow diverters or multilayer uncovered metallic stents. Due to vascular intima remodeling combined with modification of the hemodynamic flow leading to progressive thrombotic phenomena inside the aneurysm, the placement of such a new device leads to complete aneurysm occlusion in most cases while the arterial lumen is kept patent. Flow diverter stents are more and more often used to treat aneurysms with very large necks or that cannot be managed by a remodeling technique or covered stent placement because of insufficient safe landing zone^[14]. When using a covered stent, especially for renal aneurysms, we often do not have sufficient landing zones on both sides of the aneurysm. This angiographic condition seems to be a good indication to use a flow diverter stent because there is no need for a landing zone with flow diverter implantation. Flow diverters keep the side branches patent, which is the main advantage of these devices compared to stent grafts.

Some European physicians have used multilayer stents to treat fusiform renal artery aneurysms or visceral aneurysms that cannot be coiled for technical reasons^[14]. Preliminary results of the use of multilayer intra-arterial stents for peripheral applications are very promising. However, flow diverter placement requires dual-antiplatelet therapy for a minimum of 4 to 6 mo because of the risk of platelet aggregation on the dense metallic surface.

For splenic aneurysms, or aneurysms that can be treated by parent artery occlusion, we can also place Amplatzer plugs (St. Jude Medical). Plugs deployed distally and proximally to the aneurysm will lead quickly to complete occlusion of the parent artery^[1-4]. This technique, mainly used for splenic aneurysms as well as hepatic aneurysms, seems very promising because it is quick, highly efficient, and probably less expensive compared to other treatment options. Furthermore, Amplatzer vascular plugs are safe in high-flow or

short-segmental lesion cases, because the device can be retrieved and repositioned if the initial location is unsatisfactory. The main limiting factor is the rigidity of the device. The AVP IV family from St. Jude Medical is the most flexible, but we are still limited because the device requires a 4-F, 0.0038-inch inner lumen catheter. A new, more flexible microplug from Reverse Medical, the MVP microvascular plug, is available in two sizes for peripheral vascular use. Comparative trials with conventional microcoils are needed.

WHAT TRIALS ARE NEEDED IN THIS FIELD?

The thresholds for indication to treat are well known, but understanding which type of treatment is best to use remains questionable. It will be interesting to see if we can get better results by using new devices such as flow diverters compared with more conventional coiling or balloon remodeling^[5,14]. When we coil an aneurysm, we completely exclude the aneurysm, but the neck remains unclosed even if there is some endothelialization over time. When using flow diverter stents, we do not treat the aneurysm itself, but we treat the arterial wall defect by closing the neck and reinforcing the adjacent side wall.

For standard coiling of simple aneurysms, it will be interesting to know if better results can be obtained in terms of completion and stability of aneurysm occlusion if we use hydrogel-coated coils instead of conventional uncoated coils.

Studies could also compare the mid- and long-term results of coiling with hydrogel-coated coils to flow diverting stents. For cerebral aneurysms, interventional neuro are using more and more flow diverters instead of coiling so why not the same trends in visceral aneurysms?

REFERENCES

- 1 **Belli AM**, Markose G, Morgan R. The role of interventional radiology in the management of abdominal visceral artery aneurysms. *Cardiovasc Intervent Radiol* 2012; **35**: 234-243 [PMID: 21674280 DOI: 10.1007/s00270-011-0201-3]
- 2 **Jana M**, Gamanagatti S, Mukund A, Paul S, Gupta P, Garg P, Chattopadhyay TK, Sahni P. Endovascular management in abdominal visceral arterial aneurysms: A pictorial essay. *World J Radiol* 2011; **3**: 182-187 [PMID: 21860714 DOI: 10.4329/wjr.v3.i7.182]
- 3 **Loffroy R**, Guiu B, Cercueil JP, Lepage C, Cheynel N, Steinmetz E, Ricolfi F, Krausé D. Transcatheter arterial embolization of splenic artery aneurysms and pseudoaneurysms: short- and long-term results. *Ann Vasc Surg* 2008; **22**: 618-626 [PMID: 18504106 DOI: 10.1016/j.avsg.2008.02.018]
- 4 **Flood K**, Nicholson AA. Inferior pancreaticoduodenal artery aneurysms associated with occlusive lesions of the celiac axis: diagnosis, treatment options, outcomes, and review of the literature. *Cardiovasc Intervent Radiol* 2013; **36**: 578-587 [PMID: 23152034 DOI: 10.1007/s00270-012-0473-2]
- 5 **Moret J**, Cognard C, Weill A, Castaings L, Rey A. The "Remodelling Technique" in the Treatment of Wide Neck Intracranial Aneurysms. Angiographic Results and Clinical Follow-up in 56 Cases. *Interv Neuroradiol* 1997; **3**: 21-35 [PMID: 20678369]

- 6 **Bratby MJ**, Lehmann ED, Bottomley J, Kessel DO, Nicholson AA, McPherson SJ, Morgan RA, Belli AM. Endovascular embolization of visceral artery aneurysms with ethylene-vinyl alcohol (Onyx): a case series. *Cardiovasc Intervent Radiol* 2006; **29**: 1125-1128 [PMID: 16625409 DOI: 10.1007/s00270-005-0148-3]
- 7 **Ikeda O**, Nakasone Y, Tamura Y, Yamashita Y. Endovascular management of visceral artery pseudoaneurysms: transcatheter coil embolization using the isolation technique. *Cardiovasc Intervent Radiol* 2010; **33**: 1128-1134 [PMID: 20857110 DOI: 10.1007/s00270-010-9973-0]
- 8 **Yasumoto T**, Osuga K, Yamamoto H, Ono Y, Masada M, Mikami K, Kanamori D, Nakamura M, Tanaka K, Nakazawa T, Higashihara H, Maeda N, Tomiyama N. Long-term outcomes of coil packing for visceral aneurysms: correlation between packing density and incidence of coil compaction or recanalization. *J Vasc Interv Radiol* 2013; **24**: 1798-1807 [PMID: 23810652 DOI: 10.1016/j.jvir.2013.04.030]
- 9 **Künzle S**, Glenck M, Puipe G, Schadde E, Mayer D, Pfammatter T. Stent-graft repairs of visceral and renal artery aneurysms are effective and result in long-term patency. *J Vasc Interv Radiol* 2013; **24**: 989-996 [PMID: 23727420 DOI: 10.1016/j.jvir.2013.03.025]
- 10 **Manninen HI**, Berg M, Vanninen RL. Stent-assisted coil embolization of wide-necked renal artery bifurcation aneurysms. *J Vasc Interv Radiol* 2008; **19**: 487-492 [PMID: 18375290 DOI: 10.1016/j.jvir.2007.10.026]
- 11 **Favelier S**, Kretz B, Tanter Y, Loffroy R. Stent-assisted detachable coil embolization of a late-onset wide-necked anastomotic renal allograft artery pseudoaneurysm. *J Vasc Surg* 2012; **56**: 1131 [PMID: 23026424 DOI: 10.1016/j.jvs.2011.09.097]
- 12 **Loffroy R**, Rao P, Ota S, De Lin M, Kwak BK, Krause D, Geschwind JF. Packing technique for endovascular coil embolisation of peripheral arterial pseudo-aneurysms with preservation of the parent artery: safety, efficacy and outcomes. *Eur J Vasc Endovasc Surg* 2010; **40**: 209-215 [PMID: 20399122 DOI: 10.1016/j.ejvs.2010.03.009]
- 13 **Morishita H**, Yamagami T, Takeuchi Y, Matsumoto T, Asai S, Masui K, Sato H, Taniguchi F, Sato O, Nishimura T. A new flow control technique using diluted epinephrine in the N-butyl-2-cyanoacrylate embolization of visceral artery pseudoaneurysms secondary to chronic pancreatitis. *Cardiovasc Intervent Radiol* 2012; **35**: 932-937 [PMID: 22037708 DOI: 10.1007/s00270-011-0294-8]
- 14 **Sfyroeras GS**, Dalainas I, Giannakopoulos TG, Antonopoulos K, Kakisis JD, Liapis CD. Flow-diverting stents for the treatment of arterial aneurysms. *J Vasc Surg* 2012; **56**: 839-846 [PMID: 22840737 DOI: 10.1016/j.jvs.2012.04.020]

P- Reviewer: Murata S, Setacci C, Schoenhagen P
S- Editor: Ji FF **L- Editor:** A **E- Editor:** Liu SQ



Diffusion-weighted and diffusion-tensor imaging of normal and diseased uterus

Duygu Kara Bozkurt, Murat Bozkurt, Mehmet Ali Nazli, Ilhan Nahit Mutlu, Ozgur Kilickesmez

Duygu Kara Bozkurt, Department of Radiology, School of Medicine, Kafkas University, 36000 Kars, Turkey

Murat Bozkurt, Department of Obstetrics and Gynecology, School of Medicine, Kafkas University, 36000 Kars, Turkey

Mehmet Ali Nazli, Ilhan Nahit Mutlu, Ozgur Kilickesmez, Department of Diagnostic and Interventional Radiology, Istanbul Training and Research Hospital, 34098 Samatya, Istanbul, Turkey

Author contributions: Kara Bozkurt D and Kilickesmez O had equally contributed to this paper; Kara Bozkurt D and Bozkurt M wrote the paper; Nazli MA and Mutlu IN collected the figures and the literatures; Kilickesmez O approved the final version.

Conflict-of-interest statement: There's no conflict of interest.

Open-Access: This article is an open-access article which was selected by an in-house editor and fully peer-reviewed by external reviewers. It is distributed in accordance with the Creative Commons Attribution Non Commercial (CC BY-NC 4.0) license, which permits others to distribute, remix, adapt, build upon this work non-commercially, and license their derivative works on different terms, provided the original work is properly cited and the use is non-commercial. See: <http://creativecommons.org/licenses/by-nc/4.0/>

Correspondence to: Ozgur Kilickesmez, MD, Associate Professor of Radiology, Department of Diagnostic and Interventional Radiology, Istanbul Training and Research Hospital, Org. Nafiz Gurman St, 34098 Samatya, Istanbul, Turkey. okilickesmez@yahoo.com
 Telephone: +90-532-7346196
 Fax: +90-216-4693796

Received: February 9, 2015

Peer-review started: February 9, 2015

First decision: March 20, 2015

Revised: April 25, 2015

Accepted: May 7, 2015

Article in press: May 8, 2015

Published online: July 28, 2015

Abstract

Owing to technical advances and improvement of the software, diffusion weighted imaging and diffusion tensor imaging (DWI and DTI) greatly improved the diagnostic value of magnetic resonance imaging (MRI) of the pelvic region. These imaging sequences can exhibit important tissue contrast on the basis of random diffusion (Brownian motion) of water molecules in tissues. Quantitative measurements can be done with DWI and DTI by apparent diffusion coefficient (ADC) and fractional anisotropy (FA) values respectively. ADC and FA values may be changed by various physiological and pathological conditions providing additional information to conventional MRI. The quantitative DWI assists significantly in the differentiation of benign and malignant lesions. It can demonstrate the microstructural architecture and cellular density of the normal and diseased uterine zones. On the other hand, DWI and DTI are useful for monitoring the treatment outcome of the uterine lesions. In this review, we discussed advantages of DWI and DTI of the normal and diseased uterus.

Key words: Magnetic resonance imaging; Diffusion weighted imaging; Diffusion tensor imaging; Uterus

© **The Author(s) 2015.** Published by Baishideng Publishing Group Inc. All rights reserved.

Core tip: Diffusion weighted imaging (DWI) and diffusion tensor imaging (DTI) sequences greatly improved the diagnostic value of magnetic resonance imaging of the uterus with the additional benefits of functional information. They reflect the microstructural architecture and cellular density of the uterine zones and enable quantitative evaluation. Depending on this review, DWI and DTI appear to be applicable and reliable methods for demonstrating physiological changes of the uterus, benign and malignant characteristics of uterine zones

and monitoring the treatment outcome of the uterine diseases.

Kara Bozkurt D, Bozkurt M, Nazli MA, Mutlu IN, Kilickesmez O. Diffusion-weighted and diffusion-tensor imaging of normal and diseased uterus. *World J Radiol* 2015; 7(7): 149-156 Available from: URL: <http://www.wjgnet.com/1949-8470/full/v7/i7/149.htm> DOI: <http://dx.doi.org/10.4329/wjr.v7.i7.149>

INTRODUCTION

Diffusion weighted imaging (DWI) is a magnetic resonance imaging (MRI) sequence structured on the basis of diffusion (Brownian motion) of water molecules in the extracellular space and is being increasingly used to evaluate the female pelvis. The quantitative parameter acquired from DWI sequence is the apparent diffusion coefficient (ADC) value. The basic factors affecting the ADC values are tissue structures, interactions between the molecules and cellular density. Thus, ADC is altered by many physiological and pathological conditions of the body^[1].

Uterus is a fibromuscular solid organ under the effect of the hormones and is composed of three layers: the endometrial, the junctional and the myometrial zones. Physiological (menstrual cycle, menopausal period) fluctuations of these zones change the ADC values used in the evaluation of uterine abnormalities^[1].

Diffusion is a multi-dimensional process, which occurs in different values in different directions depending on the microstructure of the tissues. Since uterine myometrium is composed of smooth muscle bundles and connective tissue diffusion reflects anisotropic features. Though DWI gives information about the direction of diffusion and cellularity of the tissue, anisotropic characteristics of tissues can be assessed appropriately by diffusion tensor imaging (DTI). It can be used to detect water diffusion directionality which in turn shows the microstructural architecture of normal and diseased tissue. Fractional anisotropy (FA) is the main quantitative parameter obtained from DTI data. Initially DTI has been used to show and evaluate the integrity of white matter tracts in neuroradiology. With the improvement of the MRI hardware and softwares, fast imaging techniques, after the use of DWI also DTI was implemented to abdominal imaging for some of the abdominal organs like uterus. The initial researches have been published regarding DTI of the uterus specimens of the patients to whom hysterectomy was performed for medical reasons^[2-4] and then *in vivo* on the uterus of the patients^[5].

Non-functional (conventional) MRI provides excellent anatomical information of the uterus, however, the morphological appearance still may not differentiate some of the benign and malignant uterine lesions^[6]. DWI and DTI which provide functional information and when combined with conventional MRI become a

complementary diagnostic tool for the uterus and giving more information for the differentiation and extension of benign and malignant lesions, and for the follow up of treatment outcome after uterine arterial embolization (UAE), oncological therapies^[7].

In this paper, we aimed to focus on and review their diagnostic importance of the DWI and DTI techniques of the normal and diseased uterus.

DWI AND DTI TECHNIQUE

Optimal MRI of the female pelvis should be performed on a high field strength MRI system (1.5 or 3 T) using local phased-array coils. High field strength MRI and phased-array coils increase the signal-to-noise ratio, provide high resolution images for the DWI and DTI sequences. Besides development of ultra-fast pulse sequences such as echo-planar imaging and parallel imaging technique, enabled to prevent motion artefacts and consequently functional MRI of the female pelvis^[8].

For conventional MRI T1, T2 and fat saturated T2-weighted fast spin echo sequences followed with pre and post contrast three dimensional gradient-recalled echo volumetric interpolated breath-hold sequences and three plane imaging is necessary which give morphological information about the uterine zones. The addition of DWI and DTI sequences to the conventional MRI gives functional data about the uterus.

DWI is acquired by the measurement of signal loss after a series of two motion-providing gradient (MPG) pulses with the addition of a 180° refocusing radio frequency pulse to both sides for enhancing the variations of molecular diffusion between tissues. The density of MPG pulses is shown by the *b*-value, an paramount criterion affecting the signal intensity of the DWI^[7]. An appropriate *b* value is necessary for the female pelvic MRI.

In several studies, DTI has been used to demonstrate fiber structures of the *ex vivo* uterus, because of problematic conditions leading to artefacts such as body motions, heartbeat, intestinal and respiratory movements, and uterine peristalses^[2-4]. Focchi *et al*^[5], examined the DTI of *in vivo* uterus with a 3 T MRI using a 3D tractography algorithm and revealed that DTI is useful for imaging fibre architecture of *in vivo* human uterus.

DWI AND DTI OF NORMAL UTERUS

In reproductive age groups, T1 and T2 signal intensity characteristics of the uterine zones (endometrial, junctional and myometrial) demonstrate variations during ongoing phases of the menstrual cycle and with menapausal status. Physiological fluctuations affect the normal ADC values used in the evaluation of uterine pathologies^[6].

On conventional MRI, the endometrial zone reflects high signal on T2-weighted sequences, however not so high like urinary bladder and low signal intensity on

T1-weighted sequences^[9]. The junctional zone is the inner band of the myometrium and shows a low signal intensity in comparison to myometrial zone on T2-weighted sequences, probably because of multifactorial reasons^[10]. Existence of compact smooth muscles, low water content of the cells, and increased large nuclei are the contributing factors^[10,11]. The outer band of myometrial zone shows high signal intensity on T2-weighted sequences than the junctional zone, with high cellular water content and low cell density^[9].

The cervix is composed of three different cervical zones that may be identified on high-resolution T2-weighted sequences. There is a hyperintense central layer, named endocervical canal including mucosa, secretions, and plica. Outside of this, there is a middle zone, that's characterized by hypointense signal on T2-weighted sequences because of fibrous stroma and smooth muscle. The peripheral exterior zone includes fibromuscular stroma reflecting low-intermediate signal on T2-weighted sequences^[12].

The menstrual cycle includes of three different phases. The initial four days of the menstrual phase is named as menstruation. On the fifth day the proliferative (follicular) phase begins and continues until the ovulation which is estimated to occur on the 14th day of the menstrual cycle. The secretory (luteal) phase begins with ovulation and lasts on the first day of the next menstrual period^[13].

Tsili *et al.*^[13], reported that the ADC values of the endometrial and myometrial zones were different in the three phases of the cycle (menstrual phase: 1.25 ± 0.27 , 1.91 ± 0.35 ; proliferative phase: 1.39 ± 0.20 , 1.72 ± 0.27 ; secretory phase: 1.50 ± 0.18 , 1.87 ± 0.28 , respectively). A wide variation of ADC values of normal endometrial and myometrial zones is detected during different periods of the menstrual cycle. These variations probably depend on the physiologic-histologic fluctuations^[14]. In the menstrual period, periodic contractions of the spiral artery walls in the normal endometrial zone, cause interruption of the epithelium and rupture of the vessels. Endometrial discharge caused by the torn ends of venous structures, arteries and glands result in restricted diffusion in the endometrial zone during the menstrual phase. In the secretory phase, expanded uterine glands, prominent arteries in the normal endometrial zone, accompanied by less amount of cells in stratum basalis and higher interstitial fluid can be among the probable explanations for the higher ADC values^[13].

Kido *et al.*^[11], examined both intraindividual and interindividual differences of the ADC values of the normal uterine zones during the phases of the menstrual cycle in young age group. In this report, the ADC values for myometrial and endometrial zones were lower in the menstrual phase in comparison to the periovulatory and the secretory phase, although significant variability among individuals was reported. These preliminary results must be kept in mind, that the menstrual cycle and individual differences in reproductive women should be taken into account during the interpretation of the

ADC values of uterine zones^[11].

Kuang *et al.*^[6], studied the ADCs of the normal uterine zones during different periods of the menstrual cycle between reproductive women with different ages. The ADC values of the uterine zones were statistically different from each other. Endometrial ADC values of the females in their 30 s were higher than the ones in their 20 s and in their 30 s in the midproliferative and midsecretory periods. Also the ADC values of endometrial zone for all age groups were lower in the midproliferative phase in comparison to midsecretory phase, however the ADC values of the myometrial and junctional zones were not statistically different between the phases and age groups. According to this study patient age, menstrual period and the zone evaluated should be taken into consideration during quantitative evaluation^[6].

The relationship of the uterine zonal ADC values were investigated by Fornasa *et al.*^[15], between the different periods of the cycle. The ADC values of the endometrium calculated on the fifth day of the cycle were lower when compared with periovulatory ADC values at the fundus (mean $0.923 \text{ mm}^2/\text{s}$ vs $1.256 \times 10^{-3} \text{ mm}^2/\text{s}$) and at the isthmus (mean $1.297 \text{ mm}^2/\text{s}$ vs $1.529 \times 10^{-3} \text{ mm}^2/\text{s}$). Isthmic endometrial ADC values were higher than the fundal ADC values (mean $1.420 \times 10^{-3} \text{ mm}^2/\text{s}$ vs $1.132 \text{ mm}^2/\text{s}$). These findings were statistically significant. Physiological fluctuations occurring in the ADC values of the endometrium of normal females should be kept in mind during the interpretation of the DW images of the patients^[15].

DTI revealed two basic systems of fibers: circular and longitudinally oriented fibers as shown *ex-vivo*. Examination of the non cesarean scarred uteri showed anisotropy and fiber directions could be depicted^[5]. Knowledge of the architectural data can help to understand the details of functionality during gestation and birth. The connective tissue architecture in the uterus of reproductive age is composed of three different layers. The first inner layer is a non-organized cluster-like interweaving of the fiber complex, secondly circular fibers in the middle layer and finally longitudinal fibers in the exterior layer^[16]. In the postmenopausal uterus, the cervical region primarily includes well oriented longitudinal fibers^[4].

Fiocchi *et al.*^[5], argued that two third of the caesarean scarred uteri had altered fiber structure in comparison to normal uteri in sutural zone. Numeric data of 13 volunteers (8 nulliparous- I group, 5 with caesarean delivery- II group) revealed lowest regional fiber number and density in the anterior isthmic portion (respectively 105, 77 and 9.3, 6.7), suture localization, especially in two patients with a big scar caused placental complication at subsequent delivery. The mean FA and ADC of the whole uterus were 0.4 ± 0.0 and $3.4 \pm 0.4 \times 10^{-3} \text{ mm}^2/\text{s}$ respectively. The ADC of group I was higher than group II, but not statistically significant. In this study they concluded that 3 T DTI may show *in-vivo* human uterine fiber structures and may detect significant caesarean scars which may lead to subsequent placental

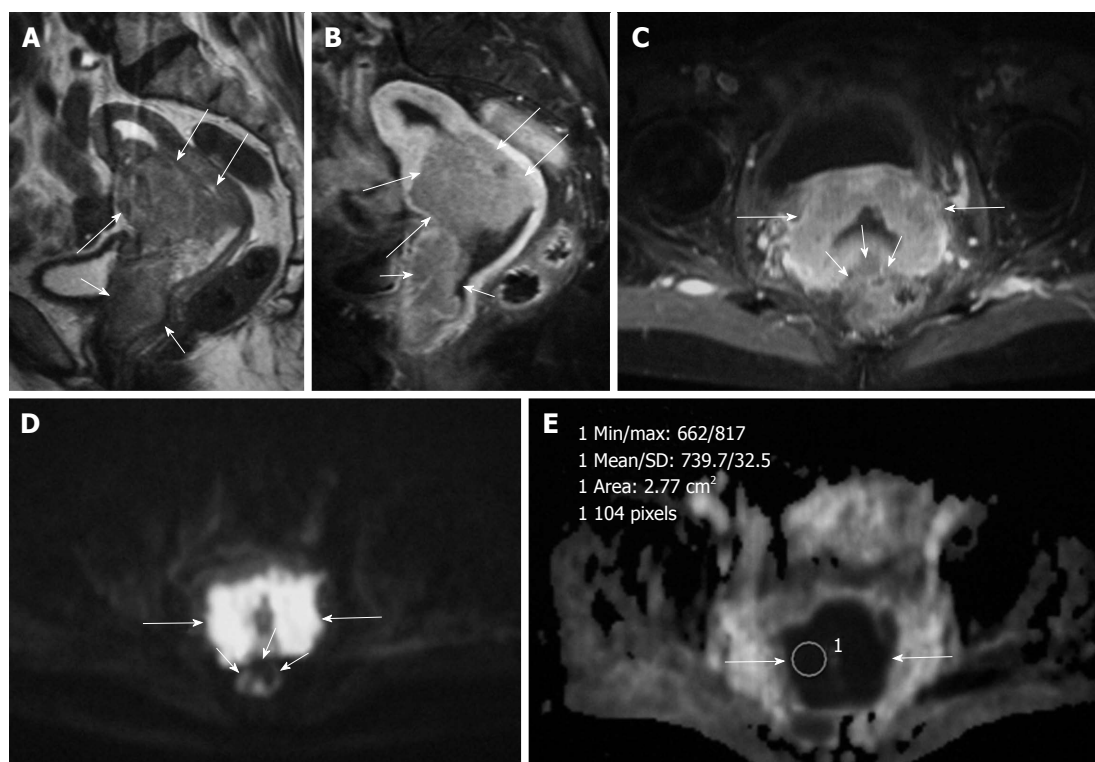


Figure 1 Forty-three years old woman with stage III squamous cell carcinoma of the uterine cervix invading vagina. A: Sagittal T2-weighted image of the uterus shows cervical cancer (long arrows) extending both to the corpus uteri and vagina (short arrows); B: Sagittal contrast-enhanced T1-weighted image with fat suppression shows enhancing cervical cancer (arrows). The tumor invades anterior vaginal wall (short arrows); C: Axial contrast-enhanced T1-weighted image with fat suppression shows enhancing cervical cancer (long arrows). There is suspicious invasion of the mass to the rectum (short arrows); D: Diffusion-weighted imaging with $b = 1000 \text{ s/mm}^2$ clearly shows a well-defined hyperintensity mass in the cervical area with no invasion to rectum (short arrows); E: On the apparent diffusion coefficient (ADC) map the tumor is hypointense (arrows). The ADC value within the mass is $0.73 \times 10^{-3} \text{ mm}^2/\text{s}$.

complications.

DWI AND DTI OF DISEASED UTERUS

The addition of DWI, and DTI sequences which serve as functional imaging in the MRI protocol for the evaluation of uterine pathologies have been offered by several papers^[2,3,7,8]. Besides quantitative evaluation with values has been found out to be effective in the discrimination of malignancy from benign lesions^[17-20].

Owing to the amount of water and cellular density uterine zones exhibit different signal intensities on the DWI. The endometrial zone and cervix display high signal, however the myometrial zone reflects a lower signal and the junctional zone shows a very low signal. Kilickesmez *et al*^[8] reported that the mean ADC values of the volunteers for myometrial zone $1.76 \times 10^{-3} \text{ mm}^2/\text{s}$, junctional zone $0.99 \times 10^{-3} \text{ mm}^2/\text{s}$, endometrial zone $1.65 \times 10^{-3} \text{ mm}^2/\text{s}$, and cervix as $1.71 \times 10^{-3} \text{ mm}^2/\text{s}$. Malignant lesions mostly display markedly high signal intensity on the DWI, due to water diffusion restriction in high cellular tissues of the malignant lesions^[17,21].

Both DWI and DTI of the uterus is generally acquired in the axial slices, since the basic sequences of abdomen is in the axial plane, to decrease the acquisition time for covering whole pelvis along with the uterus.

DWI clearly detects the malignant tumors and

metastatic lymph nodes with high signal against suppressed background signal of normal tissues, and this sequence may be used like a positron emission tomography image for fast and accurate cancer detection^[8] (Figure 1).

Myometrial lesions

The most frequent lesions encountered in the myometrial zone are fibroids. These are benign overgrowths of uterine muscle, reported to be probably to be found in up to 70% of females of reproductive age^[22].

Myometrial malignant lesions are leiomyosarcomas and stromal sarcomas^[23]. Some of the benign fibroids, in association with different types of degeneration or cellular types may lead to high signal intensity on T2-weighted sequences. Thus, the discrimination of benign and malignant myometrial lesions are challenging on conventional MRI.

Tamai *et al*^[24] reported that DWI may be an useful for discriminating uterine sarcomas from benign fibroids. The ADC values of normal myometrial zone and degenerated fibroids were higher than uterine sarcomas and there was no overlap; however, there was an overlap with non-degenerated and cellular fibroids^[24]. Pathological examination of the large fibroids with central necrosis revealed fibrosis. This finding was consistent with isotropic diffusion in DTI of the associated lesion. Fibrotic leiomyomas include non-parallel collagen fibrils, whereas

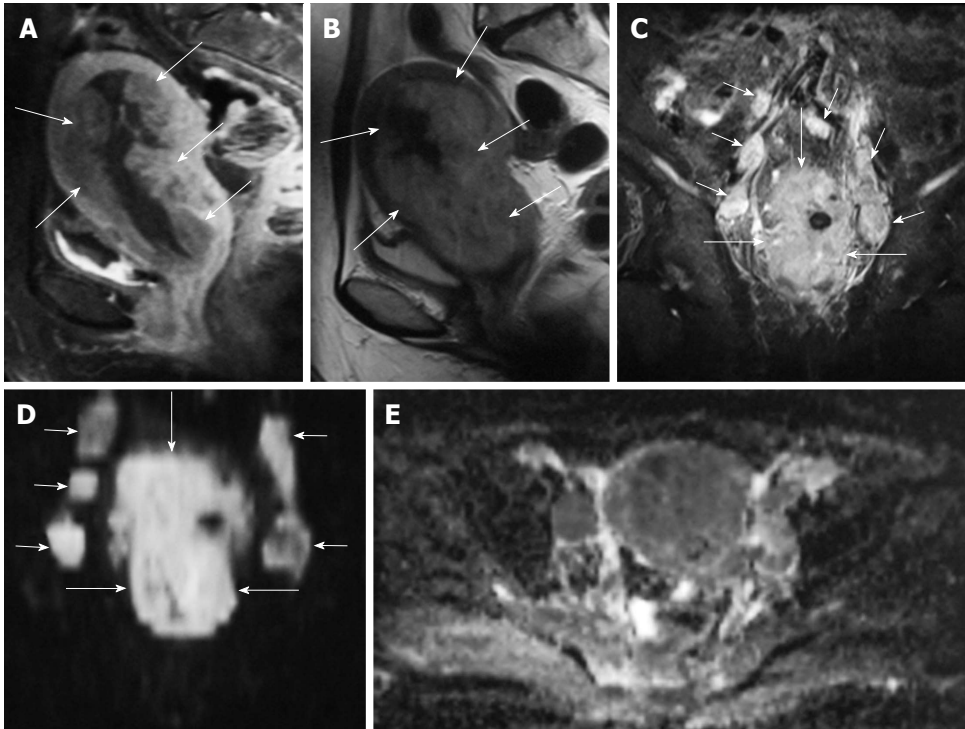


Figure 2 A 57-year-old woman with endometrial carcinoma. A: Sagittal contrast-enhanced T1-weighted image with fat suppression shows enhancing endometrial cancer with infiltration of myometrium (arrows); B: Sagittal T2-weighted image demonstrating hyperintense endometrial cancer with infiltration of myometrium (arrows); C: Coronal fat suppressed T2-weighted image reveals a tumor in the corpus uteri (long arrows), and bilateral metastatic lymphadenopathies along the iliac chains (short arrows); D: Coronal DWI ($b = 1000 \text{ s/mm}^2$) shows a marked hyperintense tumor in the corpus uteri (long arrows), and bilateral metastatic lymphadenopathies along the iliac chains (short arrows); E: Axial apparent diffusion coefficient map reveals the right sided metastatic lymph node and endometrium with restricted diffusion.

there were well-structured collagen bundles neighbouring to smooth muscle cells in the normal myometrial zone^[25,26]. Irregularity of these collagen bundles could be the reason for the lower degree of anisotropy in the fibroids when compared with the neighbouring myometrium.

The ADC values may also be beneficial for determining the therapeutic outcome after UAE, radiotherapy and/or chemotherapy^[7]. The effect of UAE or focused ultrasound may be evaluated by the detection of ablated tissue with DWI. The ADC values of fibroids after treatment are lower when compared with initial ADC values^[27,28].

Endometrial lesions

The most frequent gynecologic malignancy is endometrial cancer. It should be discriminated from benign hyperplasia of the endometrium along with polyps.

The ADC value of polyps ($1.27\text{--}1.58 \times 10^{-3} \text{ mm}^2/\text{s}$) and of normal endometrial zone ($1.53 \times 10^{-3} \text{ mm}^2/\text{s}$) is significantly higher than endometrial cancer ($0.88\text{--}0.98 \times 10^{-3} \text{ mm}^2/\text{s}$)^[24,29] (Figures 2 and 3).

Histologic grade, stage, level of myometrium invasion, existence of nodal metastases, invasion of lymphoid and vascular structures all effect the prognosis of endometrial cancer. However the most important factor effecting prognosis is the depth of myometrium invasion^[30]. The success of DWI has been improved in the assessment of accurate myometrium invasion detection and in

differentiating tumor recurrence from post-therapeutic findings^[31]. The first surgical staging of endometrium cancer was proposed in 1988, and then the update of the International Federation of Gynecology and Obstetrics (FIGO) staging was done in 2009^[32]. In this revised FIGO staging system, stage I A tumors include the tumors invading solely the inner half of the myometrial zone and the tumors confined to endometrium^[32,33]. Tumors infiltrating the exterior half of the myometrial zone are defined as stage I B tumors. These revisions include simplification of stage I disease and determination of cervical infiltration as a distinct stage to increase the diagnostic value of MRI^[30].

According to Fujii *et al.*^[29], the ADC value was 84.6% successful in detecting endometrial cancer. Toba *et al.*^[2] investigated the feasibility of DTI for evaluating the myometrial invasion of endometrial cancer. The degree of myometrium invasion was subgrouped as stage E (confined to endometrial zone), more than 50%. The ADC values of the cancer, inner or exterior myometrial zones were not statistically different. Tumoral FA values (0.21 ± 0.05) were lower than the inner layer of the myometrial zone (0.44 ± 0.01) and exterior myometrium (0.32 ± 0.08) ($P < 0.01$). The inner or exterior myometrial FA values, (0.45 ± 0.05 vs 0.43 ± 0.04) were not statistically different in stage E cancers. However, in stage S and D tumors the FA values of the inner or exterior myometrial FA zones were significantly different (0.5 ± 0.05 vs 0.3 ± 0.04 , $P < 0.01$; 0.39 ± 0.03

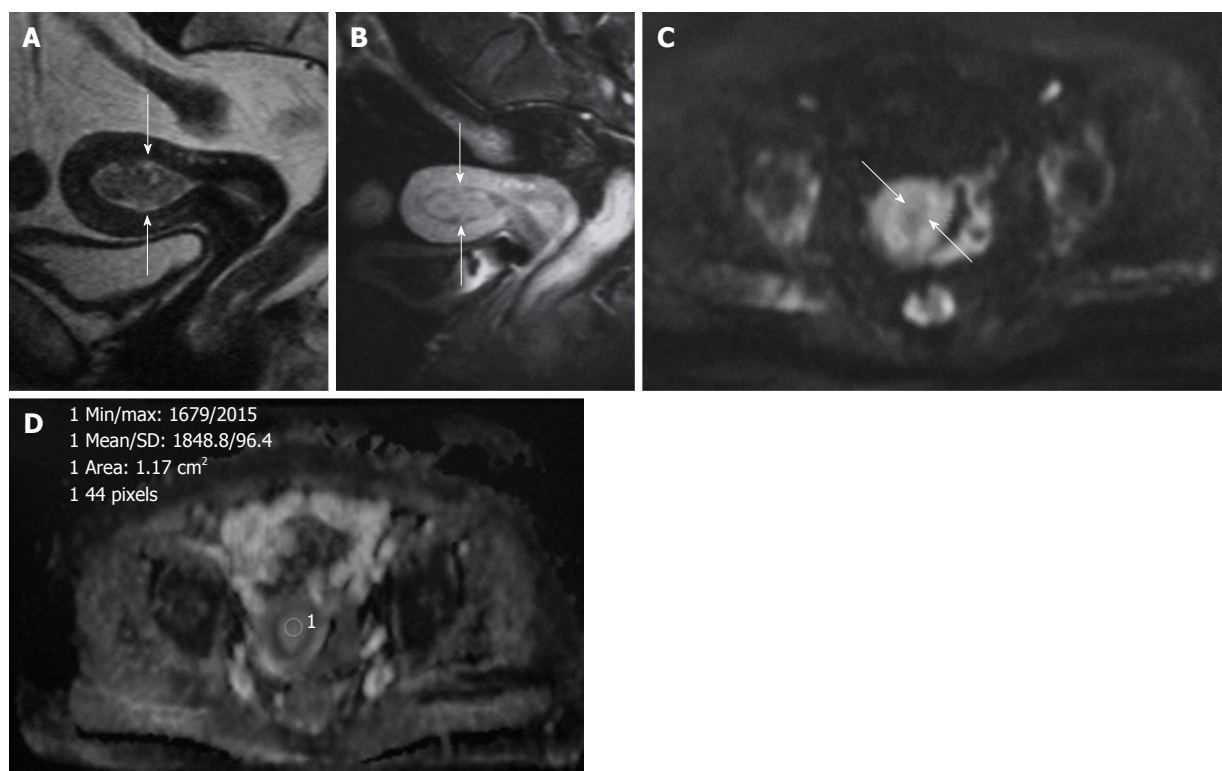


Figure 3 A 42-year-old woman with endometrial polyp. A: Hypointense polyp in the endometrial cavity on sagittal T2-weighted image mimicking low grade endometrial carcinoma (arrows); B: Sagittal contrast-enhanced T1-weighted image with fat suppression shows enhancing endometrial polyp (arrows); C: On the axial DWI ($b = 1000 \text{ s/mm}^2$) image, the mass is hypointense clearly excluding malignancy (arrows); D: Corresponding axial apparent diffusion coefficient (ADC) map. The ADC value within the mass is $1.85 \times 10^{-3} \text{ mm}^2/\text{s}$.

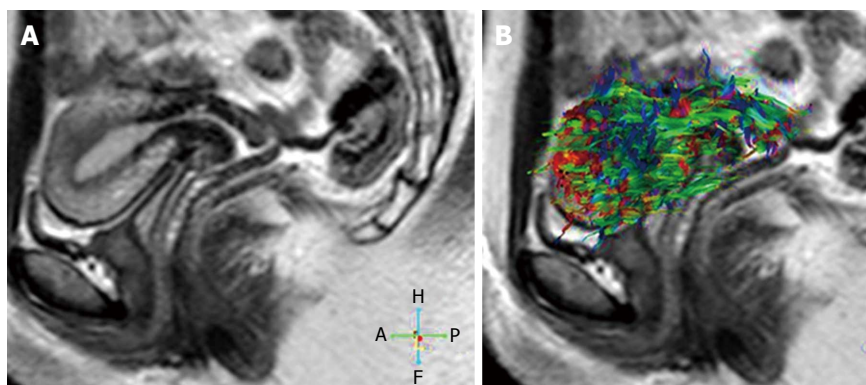


Figure 4 Thirty two years old volunteer. A: Sagittal T2-weighted image of a normal uterus; B: 3D whole tractography image of the normal uterus. Red colors represent a right-left orientation, blue represents a cranio-caudal orientation and green represents an antero-posterior orientation of diffusion. Changes in the intensity of the color represent different strengths of anisotropy.

vs 0.22 ± 0.01 , $P < 0.01$; respectively). Myometrial infiltration of endometrial tumor may be detected with the disruption of the anisotropic layer.

DWI and DTI have a potential role for the discrimination of benign and malignant endometrial masses. It may also give additional information for preoperative assessment and should be performed as a part of routine MRI for endometrial tumors. Besides, DWI is a useful technique increasing the accuracy of staging^[30].

Cervical lesions

Cervical cancer is a common gynaecological tumor.

However, its incidence has decreased in developed countries as a result of screening with the Papanicolaou test (Pap smear), cervical cancer is still an important cause of tumor-related death in developing countries^[34].

ADC measurements made significant supplement for the discrimination of normal cervical zone and cancers preoperatively. Besides there was correlation between tumor type, stage and ADC values^[35].

According to McVeigh *et al.*^[36] the average median ADC of normal cervix was statistically higher than cervical cancers ($2.09 \times 10^{-3} \text{ mm}^2/\text{s}$ vs $1.09 \times 10^{-3} \text{ mm}^2/\text{s}$), and returned to the normal level following

chemotherapy and/or radiotherapy.

Kilickesmez *et al*^[8] found out a statistically significant difference between the ADC values of malignant (0.88 ± 0.11) and benign (1.55 ± 0.33 ; $P < 0.01$) uterine lesions. In this study they reported a cut-off ADC level for malignant lesions at $1.05 \times 10^{-3} \text{ mm}^2/\text{s}$ with a sensitivity, specificity, and accuracy of 95.83%, 94.55%, and 94.94%, respectively. This study demonstrated that quantitative DWI has the potential to discriminate normal and malignant lesions of the uterus.

However, correlation of DWI and DTI with reference sequences is essential for the reason that resolution is relatively low and normal structures such as lymph nodes, bowel loops, and hemorrhage, endometromas, may show high signal like cancers on DWI^[8] (Figure 4). This phenomenon may lead to false-positive visual assessment. However, quantitative evaluation with ADC and FA values or correlation of DWI, DTI with reference sequences may overcome this^[37].

Although not clearly proved like DWI (low ADC in malignant tumors), quantitative DTI also reveals difference in the FA value of benign vs malignant tissue, however statistical significance can be much more less detected. Besides there is confusion regarding FA value alterations which should be evaluated with further studies^[2,38,39].

CONCLUSION

According to this review, DWI and DTI emerge to be applicable and reliable sequences for the determination of physiological fluctuations of the uterus, detection of malignant lesions of the uterus and monitoring the therapeutic outcome. When combined with conventional MRI sequences, DWI and DTI provide further data about physiological and pathological conditions of the uterus. DWI and DTI are noninvasive, do not cause radiation exposure or need for contrast injection.

REFERENCES

- 1 **Kido A**, Kataoka M, Koyama T, Yamamoto A, Saga T, Togashi K. Changes in apparent diffusion coefficients in the normal uterus during different phases of the menstrual cycle. *Br J Radiol* 2010; **83**: 524-528 [PMID: 20505034 DOI: 10.1259/bjr/11056533]
- 2 **Toba M**, Miyasaka N, Sakurai U, Yamada I, Eishi Y, Kubota T. Diagnostic possibility of diffusion tensor imaging for the evaluation of myometrial invasion in endometrial cancer: an ex vivo study. *J Magn Reson Imaging* 2011; **34**: 616-622 [PMID: 21751283 DOI: 10.1002/jmri.22693]
- 3 **Thrippleton MJ**, Bastin ME, Munro KI, Williams AR, Oniscu A, Jansen MA, Merrifield GD, McKillop G, Newby DE, Semple SI, Marshall I, Critchley HO. Ex vivo water diffusion tensor properties of the fibroid uterus at 7 T and their relation to tissue morphology. *J Magn Reson Imaging* 2011; **34**: 1445-1451 [PMID: 21953730 DOI: 10.1002/jmri.22793]
- 4 **Weiss S**, Jaermann T, Schmid P, Staempfli P, Boesiger P, Niederer P, Caduff R, Bajka M. Three-dimensional fiber architecture of the nonpregnant human uterus determined ex vivo using magnetic resonance diffusion tensor imaging. *Anat Rec A Discov Mol Cell Evol Biol* 2006; **288**: 84-90 [PMID: 16345078]
- 5 **Fiocchi F**, Nocetti L, Siopis E, Currà S, Costi T, Ligabue G, Torricelli P. In vivo 3 T MR diffusion tensor imaging for detection of the fibre architecture of the human uterus: a feasibility and quantitative study. *Br J Radiol* 2012; **85**: e1009-e1017 [PMID: 22744322 DOI: 10.1259/bjr/76693739]
- 6 **Kuang F**, Ren J, Huan Y, Chen Z, Zhong Q. Apparent diffusion coefficients of normal uterus in premenopausal women with 3.0-T magnetic resonance imaging. *J Comput Assist Tomogr* 2012; **36**: 54-59 [PMID: 22261770 DOI: 10.1097/RCT.0b013e3182418885]
- 7 **Namimoto T**, Awai K, Nakaura T, Yanaga Y, Hirai T, Yamashita Y. Role of diffusion-weighted imaging in the diagnosis of gynecological diseases. *Eur Radiol* 2009; **19**: 745-760 [PMID: 18839179 DOI: 10.1007/s00330-008-1185-5]
- 8 **Kilickesmez O**, Bayramoglu S, Inci E, Cimilli T, Kayhan A. Quantitative diffusion-weighted magnetic resonance imaging of normal and diseased uterine zones. *Acta Radiol* 2009; **50**: 340-347 [PMID: 19235579 DOI: 10.1080/02841850902735858]
- 9 **Wasnik AP**, Mazza MB, Liu PS. Normal and variant pelvic anatomy on MRI. *Magn Reson Imaging Clin N Am* 2011; **19**: 547-566; viii [PMID: 21816330]
- 10 **Brown HK**, Stoll BS, Nicosia SV, Fiorica JV, Hambley PS, Clarke LP, Silbiger ML. Uterine junctional zone: correlation between histologic findings and MR imaging. *Radiology* 1991; **179**: 409-413 [PMID: 1707545]
- 11 **Scoutt LM**, Flynn SD, Luthringer DJ, McCauley TR, McCarthy SM. Junctional zone of the uterus: correlation of MR imaging and histologic examination of hysterectomy specimens. *Radiology* 1991; **179**: 403-407 [PMID: 2014282]
- 12 **Brown MA**, Kubik-huch RA, Reinhold C. Uterus and cervix. In: Semelka RC, editor. 2nd edition, Abdominal pelvic MRI, vol. 1. New Jersey: John Wiley & Sons, Inc, 2006: 1251-1332
- 13 **Tsili AC**, Argyropoulou MI, Tzarouchi L, Dalkalitsis N, Koliopoulos G, Paraskevaidis E, Tsampoulas K. Apparent diffusion coefficient values of the normal uterus: Interindividual variations during menstrual cycle. *Eur J Radiol* 2012; **81**: 1951-1956 [PMID: 21621360 DOI: 10.1016/j.ejrad.2011.04.057]
- 14 **Longacre TA**, Bartow SA. A correlative morphologic study of human breast and endometrium in the menstrual cycle. *Am J Surg Pathol* 1986; **10**: 382-393 [PMID: 3717495]
- 15 **Fornasa F**, Montemezzi S. Diffusion-weighted magnetic resonance imaging of the normal endometrium: temporal and spatial variations of the apparent diffusion coefficient. *Acta Radiol* 2012; **53**: 586-590 [PMID: 22619357 DOI: 10.1258/ar.2012.110717]
- 16 **Dubrauszy V**, Schwalm H, Fleischer M. [The fibre system of connective tissue in the childbearing age, menopause, and pregnancy]. *Arch Gynakol* 1971; **210**: 276-292 [PMID: 5109671]
- 17 **Koyama T**, Togashi K. Functional MR imaging of the female pelvis. *J Magn Reson Imaging* 2007; **25**: 1101-1112 [PMID: 17520731]
- 18 **Ichikawa T**, Erturk SM, Motosugi U, Sou H, Iino H, Araki T, Fujii H. High-B-value diffusion-weighted MRI in colorectal cancer. *AJR Am J Roentgenol* 2006; **187**: 181-184 [PMID: 16794174]
- 19 **Nasu K**, Kuroki Y, Nawano S, Kuroki S, Tsukamoto T, Yamamoto S, Motoori K, Ueda T. Hepatic metastases: diffusion-weighted sensitivity-encoding versus SPIO-enhanced MR imaging. *Radiology* 2006; **239**: 122-130 [PMID: 16493012]
- 20 **Takahara T**, Imai Y, Yamashita T, Yasuda S, Nasu S, Van Cauteren M. Diffusion weighted whole body imaging with background body signal suppression (DWIBS): technical improvement using free breathing, STIR and high resolution 3D display. *Radiat Med* 2004; **22**: 275-282 [PMID: 15468951]
- 21 **Koh DM**, Collins DJ. Diffusion-weighted MRI in the body: applications and challenges in oncology. *AJR Am J Roentgenol* 2007; **188**: 1622-1635 [PMID: 17515386]
- 22 **Tropeano G**, Amoroso S, Scambia G. Non-surgical management of uterine fibroids. *Hum Reprod Update* 2008; **14**: 259-274 [PMID: 18344356 DOI: 10.1093/humupd/dmn006]
- 23 **Goto A**, Takeuchi S, Sugimura K, Maruo T. Usefulness of Gd-DTPA contrast-enhanced dynamic MRI and serum determination of LDH and its isozymes in the differential diagnosis of leiomyosarcoma from degenerated leiomyoma of the uterus. *Int J*

- Gynecol Cancer* 2002; **12**: 354-361 [PMID: 12144683]
- 24 **Tamai K**, Koyama T, Saga T, Morisawa N, Fujimoto K, Mikami Y, Togashi K. The utility of diffusion-weighted MR imaging for differentiating uterine sarcomas from benign leiomyomas. *Eur Radiol* 2008; **18**: 723-730 [PMID: 17929022]
- 25 **Catherino WH**, Leppert PC, Stenmark MH, Payson M, Potlog-Nahari C, Nieman LK, Segars JH. Reduced dermatopontin expression is a molecular link between uterine leiomyomas and keloids. *Genes Chromosomes Cancer* 2004; **40**: 204-217 [PMID: 15139000]
- 26 **Leppert PC**, Baginski T, Prupas C, Catherino WH, Pletcher S, Segars JH. Comparative ultrastructure of collagen fibrils in uterine leiomyomas and normal myometrium. *Fertil Steril* 2004; **82** Suppl 3: 1182-1187 [PMID: 15474093]
- 27 **Jacobs MA**, Herskovits EH, Kim HS. Uterine fibroids: diffusion-weighted MR imaging for monitoring therapy with focused ultrasound surgery--preliminary study. *Radiology* 2005; **236**: 196-203 [PMID: 15987974]
- 28 **Liapi E**, Kamel IR, Bluemke DA, Jacobs MA, Kim HS. Assessment of response of uterine fibroids and myometrium to embolization using diffusion-weighted echoplanar MR imaging. *J Comput Assist Tomogr* 2005; **29**: 83-86 [PMID: 15665689]
- 29 **Fujii S**, Matsusue E, Kigawa J, Sato S, Kanasaki Y, Nakanishi J, Sugihara S, Kaminou T, Terakawa N, Ogawa T. Diagnostic accuracy of the apparent diffusion coefficient in differentiating benign from malignant uterine endometrial cavity lesions: initial results. *Eur Radiol* 2008; **18**: 384-389 [PMID: 17917730]
- 30 **Beddy P**, O'Neill AC, Yamamoto AK, Addley HC, Reinhold C, Sala E. FIGO staging system for endometrial cancer: added benefits of MR imaging. *Radiographics* 2012; **32**: 241-254 [PMID: 22236905]
- 31 **Sala E**, Rockall A, Rangarajan D, Kubik-Huch RA. The role of dynamic contrast-enhanced and diffusion weighted magnetic resonance imaging in the female pelvis. *Eur J Radiol* 2010; **76**: 367-385 [PMID: 20810230]
- 32 **Creasman W**. Revised FIGO staging for carcinoma of the endometrium. *Int J Gynaecol Obstet* 2009; **105**: 109 [PMID: 19345353]
- 33 **Odicino F**, Pecorelli S, Zigliani L, Creasman WT. History of the FIGO cancer staging system. *Int J Gynaecol Obstet* 2008; **101**: 205-210 [PMID: 18199437]
- 34 **Solomon D**, Breen N, McNeel T. Cervical cancer screening rates in the United States and the potential impact of implementation of screening guidelines. *CA Cancer J Clin* 2007; **57**: 105-111 [PMID: 17392387]
- 35 **Demirbaş T**, Cimilli T, Bayramoğlu S, Güner NT, Hocaoglu E, Inci E. Contribution of diffusion-weighted imaging to diagnosis and staging of cervical cancer. *Balkan Med J* 2014; **31**: 154-157 [PMID: 25207188]
- 36 **McVeigh PZ**, Syed AM, Milosevic M, Fyles A, Haider MA. Diffusion-weighted MRI in cervical cancer. *Eur Radiol* 2008; **18**: 1058-1064 [PMID: 18193428 DOI: 10.1007/s00330-007-0843-3]
- 37 **Shen SH**, Chiou YY, Wang JH, Yen MS, Lee RC, Lai CR, Chang CY. Diffusion-weighted single-shot echo-planar imaging with parallel technique in assessment of endometrial cancer. *AJR Am J Roentgenol* 2008; **190**: 481-488 [PMID: 18212236 DOI: 10.2214/AJR.07.2155]
- 38 **Li C**, Chen M, Li S, Zhao X, Zhang C, Liu M, Zhou C. Diffusion tensor imaging of prostate at 3.0 Tesla. *Acta Radiol* 2011; **52**: 813-817 [PMID: 21586608 DOI: 10.1258/ar.2011.100487]
- 39 **Kinoshita M**, Hashimoto N, Goto T, Kagawa N, Kishima H, Izumoto S, Tanaka H, Fujita N, Yoshimine T. Fractional anisotropy and tumor cell density of the tumor core show positive correlation in diffusion tensor magnetic resonance imaging of malignant brain tumors. *Neuroimage* 2008; **43**: 29-35 [PMID: 18672074 DOI: 10.1016/j.neuroimage.2008.06.041]

P- Reviewer: Chu JP, Gao BL, Gumustas OG, Nouh MR

S- Editor: Ji FF **L- Editor:** A **E- Editor:** Liu SQ



Non-invasive diagnostic imaging of colorectal liver metastases

Pier Paolo Mainenti, Federica Romano, Laura Pizzuti, Sabrina Segreto, Giovanni Storto, Lorenzo Mannelli, Massimo Imbriaco, Luigi Camera, Simone Maurea

Pier Paolo Mainenti, Laura Pizzuti, IBB CNR, 80145 Naples, Italy

Federica Romano, Sabrina Segreto, Massimo Imbriaco, Luigi Camera, Simone Maurea, Advanced Biomedical Science Department, Radiology Section, University of Naples "Federico II", 80145 Naples, Italy

Giovanni Storto, IRCCS, CROB, 85028 Rionero in Vulture, Italy

Lorenzo Mannelli, Radiology Department, Memorial Sloan-Kettering Cancer Center, New York, NY 10022, United States

Author contributions: All authors contributed to this paper.

Conflict-of-interest statement: The review has not been published before, is not under consideration for publication elsewhere and its publication has been approved by all co-authors. All the authors do not have any conflicting interests (including but not limited to commercial, personal, political, intellectual, or religious interests) related to the manuscript.

Open-Access: This article is an open-access article which was selected by an in-house editor and fully peer-reviewed by external reviewers. It is distributed in accordance with the Creative Commons Attribution Non Commercial (CC BY-NC 4.0) license, which permits others to distribute, remix, adapt, build upon this work non-commercially, and license their derivative works on different terms, provided the original work is properly cited and the use is non-commercial. See: <http://creativecommons.org/licenses/by-nc/4.0/>

Correspondence to: Pier Paolo Mainenti, MD, IBB CNR, Via De Amicis, 95, 80145 Naples, Italy. pierpamainenti@hotmail.com
 Telephone: +39-081-7613060
 Fax: +39-081-7616013

Received: January 28, 2015
 Peer-review started: January 29, 2015
 First decision: April 27, 2015
 Revised: May 10, 2015
 Accepted: June 1, 2015

Article in press: June 2, 2015
 Published online: July 28, 2015

Abstract

Colorectal cancer is one of the few malignant tumors in which synchronous or metachronous liver metastases [colorectal liver metastases (CRLMs)] may be treated with surgery. It has been demonstrated that resection of CRLMs improves the long-term prognosis. On the other hand, patients with un-resectable CRLMs may benefit from chemotherapy alone or in addition to liver-directed therapies. The choice of the most appropriate therapeutic management of CRLMs depends mostly on the diagnostic imaging. Nowadays, multiple non-invasive imaging modalities are available and those have a pivotal role in the workup of patients with CRLMs. Although extensive research has been performed with regards to the diagnostic performance of ultrasonography, computed tomography, positron emission tomography and magnetic resonance for the detection of CRLMs, the optimal imaging strategies for staging and follow up are still to be established. This largely due to the progressive technological and pharmacological advances which are constantly improving the accuracy of each imaging modality. This review describes the non-invasive imaging approaches of CRLMs reporting the technical features, the clinical indications, the advantages and the potential limitations of each modality, as well as including some information on the development of new imaging modalities, the role of new contrast media and the feasibility of using parametric image analysis as diagnostic marker of presence of CRLMs.

Key words: Advances in imaging; Colorectal cancer; Liver metastases

© The Author(s) 2015. Published by Baishideng Publishing Group Inc. All rights reserved.

Core tip: The present review describes the non invasive imaging approaches of colorectal liver metastases (CRLMs) reporting the technical features, the clinical indications, the advantages and the potential limitations of each modality [ultrasonography, computed tomography (CT); magnetic resonance imaging (MRI), positron emission tomography (PET)/CT, PET/MRI] as well as including some information on the development of new imaging modalities, the role of new contrast media and the feasibility of using parametric image analysis as diagnostic marker of presence of CRLMs.

Mainenti PP, Romano F, Pizzuti L, Segreto S, Storto G, Mannelli L, Imbriaco M, Camera L, Maurea S. Non-invasive diagnostic imaging of colorectal liver metastases. *World J Radiol* 2015; 7(7): 157-169 Available from: URL: <http://www.wjgnet.com/1949-8470/full/v7/i7/157.htm> DOI: <http://dx.doi.org/10.4329/wjcr.v7.i7.157>

INTRODUCTION

Annually over 130000 new cases of colorectal cancer (CRC) are diagnosed in the United States, representing the third most common cancer in both men and women, with more than 50000 deaths each year^[1].

Liver metastases are detected approximately in up to 20%-25% of patients with CRC at the time of diagnosis^[2]. The 5-year cumulative rate of metachronous colorectal liver metastases [colorectal liver metastases (CRLMs)] is reported to be 15%^[2]. Overall, approximately 50% of patients with CRC will develop liver metastases^[3].

CRC is one of the few malignant tumors in which synchronous or metachronous liver metastases may be treated with surgery. CRLMs are resectable in about 20%-30% of the cases^[4] with a 5-year survival of about 50%-60% in comparison to a survival of less than 5% of patients with CRLMs not amenable to liver surgery^[5].

In patients who are not suitable candidates for surgery, chemotherapy alone or in addition to local hepatic treatments, such as intrahepatic arterial infusion chemotherapy or radiofrequency ablation or laser therapy or cryotherapy, may be performed. These treatments options have been shown to increase survival, too^[6-11].

Common to any therapy is the need for pretreatment anatomic planning to assess feasibility and avoid injury to adjacent structures such as vasculature, biliary ducts and surrounding organs.

The surgical criteria, which permit to select the candidates for liver resection, are represented by the size of the lesion, number and location with respect to anatomic landmarks of the CRLMs, as well as the number of segments involved, the volume of the remaining liver and the general clinical parameters^[6,7]. Metastases can be completely resected if at least 2 adjacent liver segments can be spared and if the future liver remnant is at least 20% of total pre-resection liver volume^[8] in patients with normal liver function and more than 40% in patients with

reduced liver function^[12,13].

Moreover anatomic variants of hepatic arteries, biliary tree and portal venous system need to be excluded because the surgical resection may be problematic, and thus additional surgery steps may be required^[14].

Obviously, diagnostic imaging plays a crucial role in selecting the more appropriate therapy for patients with CRLMs, by detecting the lesions, determining the resectability and assessing the response to treatments.

Even though many non invasive imaging modalities are now available and effective in detection and follow up of CRLMs, such as ultrasonography (US), computed tomography (CT), positron emission tomography (PET) and magnetic resonance imaging (MRI), each offering some advantages as disadvantages over the others, the optimal imaging strategy in patients with CRLMs have still to be designed.

The lack of a worldwide well defined CRLMs imaging protocol is in part due to continuous and rapid technological and pharmacological developments which are progressively improving the performance of each imaging modality.

This review describes the non-invasive imaging approaches of CRLMs reporting the technical features, the clinical indications, the advantages and the potential limitations of each modality, as well as including some information on the development of new imaging modalities, the role of new contrast media and the feasibility of using parametric image analysis as diagnostic marker of presence of CRLMs.

US

Because of its non-invasive character, low cost, no radiation exposure, good patient acceptance and widespread availability, US is often the first choice for screening patients with malignancy and/or suspected liver lesions, and it is widely used in the evaluation of liver metastases^[15-19].

In particular, the sensitivity of US for CRLMs detection is variable ranging from 50% to 76%^[17,20]; however US sensitivity depends mostly on the size of the lesion and it can be as low as 20% if liver lesions are less than 10 mm^[15,16]. Despite of this limitation, in daily practice, US plays still a clinical role in distinguishing two different groups of patients with liver metastases: (1) patients with diffuse metastases who are no longer eligible for curative treatment; and (2) patients without metastases or a very limited number of them. Further diagnostic investigation with tomographic imaging is mandatory for the patients of the group 2 to define the correct therapeutic management.

During the last few years, the contrast-enhanced ultrasound (CEUS) has progressively gained a huge role in the evaluation of liver lesions, improving detection and characterization of both primary or secondary liver lesions^[21-28]. The added role of CEUS compared to the baseline US (b-US) has been observed for CRLMs detection, too^[29]. A few studies have shown a

significantly better sensitivity of CEUS vs b-US in the identification of CRLMs measuring less than 10 mm; moreover CEUS should replace b-US for the detection of CRLMs in patients being treated with neoadjuvant systemic chemotherapy^[30-33].

Westwood *et al.*^[29] in their recent meta-analysis of 19 studies on liver CEUS with Sonovue stated that CEUS shows a similar performance to liver CT and MRI in the characterization of incidentally detected focal liver lesions with lower costs respect to MRI and it may be adequate to rule out CRLMs; in particular, similarly to CT and MRI even with CEUS the CRLMs are better detected in post-contrast portal and late phases^[31].

Nevertheless some limitations of CEUS need to be considered. CEUS presents still low sensitivity for very small focal liver lesions (< 5 mm), due to the low spatial resolution, and thus very small CRLMs might be missed^[29]. In addition, CEUS does not go beyond certain limitations of the US examinations, like the difficulty in the evaluation of the sub-diaphragmatic liver or the interposition of the intestine, and above all the notable weakness of being operator dependent. Moreover liver steatosis and fibrosis are an important limitation that can increase the possibility of missing deep seated metastases^[34]. Finally, another aspect to consider is that CEUS does not offer comprehensive information for surgical planning as both CT and MRI do. Bolondi *et al.*^[35] report that even if the use of CEUS is largely accepted in clinical practice its role in the diagnostic algorithm of liver lesions has not yet been established.

Beyond the scope of the present review because of the invasive approach, the following US technique merit to be mentioned: the US-guided percutaneous biopsy which allow characterizing indeterminate hepatic lesions and the intra-operative ultra-sonography which offer the highest accuracy rates in CRLMs detection^[36,37].

MULTIDETECTOR CT

Multidetector CT MDCT is considered the imaging modality of choice for CRC staging and follow up, because it provides excellent coverage of the entire chest/abdomen/pelvis offering a global one session staging. Nevertheless up to 25% of CRLMs may be missed^[38]. The current MDCT devices enable high spatial resolution studies of the entire liver generating slice thickness ≤ 1 mm and isotropic pixel sizes and, thus, allowing high quality reformatted multiplanar (MPR) and volumetric three-dimensional rendering (3D VR) reconstructions. The resulting high definition images define accurately the main features of each lesion, as the sizes, the margins, the segmental spatial distribution, the relation with the vascular and biliary structure, and the volume of the remaining liver.

The additional diagnostic value of using thin collimation in the detection of hepatic lesions is debated. Some authors have demonstrated that the use of a thinner section thickness (*i.e.*, 2.5 mm vs ≥ 5 mm slice thickness) at CT improves the detection of hepatic

lesions^[39], as well as, the accuracy of 16-MDCT using a 1.5 mm collimation might be superior to previous CT techniques in differentiating between hepatic metastases and hepatic cysts^[40]. On the contrary, other authors reported that image reconstruction with MDCT at collimations less than 5 mm did not improve sensitivity in the detection of hepatic metastases 1.5 cm or smaller^[41], as well as, a slice thickness ≤ 1 mm does not improve hepatic lesion detection and it provides a significant increase of image noise^[42]. As a result of the above information, a CRLMs protocol scanning of 2-4 mm of collimation may be recommended.

The value of unenhanced scans lies mainly in the characterization of small lesions as being solid or cystic or in the identification of calcified CRLMs. About the contrast-enhanced (ce) scanning protocol, the venous phase is well recognized as the optimal timing to detect CRLMs. Arterial and equilibrium phase CT have no incremental value compared to hepatic venous phase MDCT in the detection of CRLMs, as a result a multiphasic scanning protocol implies an unjustified additional radiation exposure^[43,44]. Moreover the single portal venous phase contrast enhanced MDCT (ce-MDCT) scanning protocol enables accurate preoperative assessment of the local CRC staging (T and N), too^[45].

The performance of MDCT in the CRLMs detection is variable showing unsatisfactory sensitivity and specificity values for lesions < 10 mm^[46] or in presence of fatty liver which is often a consequence of chemotherapy^[47]. Furthermore, incidental findings such as small hemangiomas and cysts measuring less than 10 mm in size can be difficult to differentiate from metastases because of volume averaging^[48,49].

Contrast medium allergies as well as renal impairment may limit the use of the ce-CT; however they do not represent absolute contraindications because of the possibility of a supporting therapy.

MRI

Currently, MRI represents the most accurate modality for evaluating CRLMs; it provides anatomic details and has a high detection rate, even for lesions smaller than 10 mm^[38,48-51].

The recent technological advances (high magnetic field strength > 1 T, high gradients, parallel imaging techniques, fast dynamic sequences, breath-hold sequences) have improved the liver application of MRI increasing the signal-to-noise ratio, the contrast-to-noise ratio (CNR), the spatial resolution and the image quality as well as reducing the scan times.

The unenhanced standard MRI protocol for detecting and characterizing focal liver lesions includes both T1- and T2-weighted images. For T1-weighted imaging, the in-phase and opposed-phase gradient-recalled echo (GRE) sequences are acquired to assess the presence of parenchymal fatty infiltration or focal sparing of diffuse fatty infiltration. For T2-weighted imaging, the turbo-spin echo (TSE) or the fast spin echo without and with

fat suppression are preferred over the single-shot TSE pulse sequences, because the latter do not offer an optimal soft tissue contrast. For detection of focal lesions a TE of approximately 80-100 ms is adopted, however a heavily T2-weighted sequences with a time of echo of approximately 160-180 ms may help in differentiation between solid and non-solid lesions (e.g., metastasis/HCC vs haemangioma/cyst)^[52-54].

Recent clinically important advances in MRI include the addition of diffusion-weighted imaging (DWI). DWI is a functional technique that looks at the Brownian motion of water in tissues. In biological tissues, the Brownian motion is restricted by interactions with cell membranes and macromolecules on a microscopic level as well as it is modified by any architectural tissue changes^[55]. Increased tissue cellularity observed in tumors restricts Brownian motion, which can be quantified by calculation of the apparent diffusion coefficient (ADC) on derived ADC parametric maps. Of note, ADC has been shown to be inversely correlated with tumor cellularity and it can be considered a quantitative biomarker parameter of pathology. Metastases tend to restrict diffusion and the addition of DWI to the standard liver MRI protocol improves sensitivity and specificity for lesion detection and characterization^[56-58]. The added value of DWI is even more evident in the detection of CRLMs ≤ 1 cm with sensitivity of 92% compared to 71% of late phase hepato-biliary contrast agent MRI^[59]. Hence, these sequences are now routinely included in a liver MRI protocols.

Successively, the contrast-enhanced sequences are performed. Three different groups of MRI contrast agents for hepatic imaging are available: the non-specific extracellular gadolinium chelates, the organs-specific (reticulo-endothelial) and the liver-specific intracellular (hepato-biliary) contrast agents.

Non-specific gadolinium chelates

Extracellular gadolinium chelates are the contrast agent more frequently used for MRI. Several agents with similar properties are on the market, including gadopentetate dimeglumine (Magnevist, Schering, Berlin, Germany), Gd-DTPA-BMA (Omniscan[®], GE Healthcare, Chalfont St. Giles, United Kingdom) and Gd-DOTA (Dotarem, Guerbet, Aulnay-sous-Bois, France).

Non-specific extracellular gadolinium chelates have pharmacokinetics similar to those of iodinated contrast agents and are excreted almost exclusively by passive glomerular filtration through the kidneys. Because of their small size, gadolinium chelates are rapidly cleared from the intravascular space into the extracellular interstitial space according to the concentration difference of the contrast agent between the two compartments. The transfer of the molecules occurs in the opposite direction, when the concentration gradient inverts^[60].

About the contrast-enhanced scanning protocol, the T1-weighted 3D-GRE breath hold (BH) sequences are obtained during the arterial, portal venous phase and the equilibrium phase. The following considerations

have to be reported about the differences between MRI and CT contrast-enhanced scanning protocol: the exposure to ionizing radiation suggests to use single phase CT protocol and to reserve multiphasic studies only when really necessary; although the MRI of the liver is the most accurate modality for detecting CRLMs, in the clinical practice it is frequently used after a staging whole-body ce-MDCT to solve problems of differential diagnosis; that is why a multiphasic MRI liver protocol may be necessary to characterize correctly a liver lesion defined as undetermined at ce-MDCT.

Gadolinium-based contrast agents may cause collateral effects, such as acute non-renal adverse reactions (e.g., anaphylactoid reactions), acute renal adverse reactions (e.g., contrast induced nephropathy), delayed adverse reactions [nephrogenic systemic fibrosis (NSF)] and problems at the site of injection (e.g., local necrosis)^[60]. NSF is a rare potentially fatal disease that has been observed in patients with severe renal insufficiency exposed to gadolinium contrast agent. To prevent the risk of NSF it is suggested to avoid the intravenous (iv) administration of gadolinium contrast agents in patients who have a glomerular filtration rate lower than 30 mL/min per 1.73 m² as well as in those who are on dialysis or have acutely renal impairment. This point represents a recommendation rather than an absolute contraindication.

Reticulo-endothelial contrast agents

All reticuloendothelial system (RES) agents are super-paramagnetic iron oxide-based contrast agents (SPIO). SPIO particles are taken up by RES cells of the normal liver parenchyma, the spleen and the lymph nodes. They shorten T2 and T2* relaxation times resulting in a loss of signal intensity in normal liver parenchyma. On the opposite, malignant liver lesions do not have a substantial number of RES cells and appear as hyperintense lesions with distinct borders in contrast to the hypointense liver parenchyma after application of SPIO on T2-weighted MRI.

Although SPIO agents have showed high accuracy in the detection of liver lesions^[40,61-64], hepatocyte-specific contrast agents are preferred to these molecules in clinical practice^[65].

Hepato-biliary contrast agents

Hepatobiliary agents represent a heterogeneous group of paramagnetic molecules of which a fraction is taken up by hepatocytes and excreted into the bile. On T1 weighted images, lesions not containing hepatocytes are hypointense to the surrounding enhanced parenchyma during the hepato-biliary phase (HBP). Presently, the hepatobiliary agents actually available are mangafodipir trisodium (MT, Teslascan[®], GE Healthcare), gadobenate dimeglumine (Gd-BOPTA, Multihance[®], Bracco) and gadoxetic acid (Gd-EOB-DTPA, Primovist[®], Schering).

MT has limited assessment of vascular structures due to its inability to be administered as a bolus. Gd-BOPTA and Gd-EOB-DTPA show biphasic liver enhancement

with an early vascular and extracellular phase allowing arterial, portal venous and equilibrium phase and a delayed HBP with a peak to 20-40 min for Gd-EOB-DTPA and 60-90 min for Gd-BOPTA. The advantages of the Gd-EOB-DTPA over Gd-BOPTA are the higher biliary excretion approximately close to the 50% of the delivered dose respect to 3%-5%, the high relaxivity, the earlier onset and the longer duration of contrast, which facilitates imaging and image quality^[65,66].

HBP improves the sensitivity of MRI in the detection of CRLMs^[59]. In addition hepatocyte-specific contrast agents allow detection of the "disappearing liver metastases"^[13], which mimic a complete response to neoadjuvant chemotherapy leading to a mismatch between imaging response and true pathological complete response. A false complete imaging response is more often observed with CT and PET-CT^[67], while the current data suggest that MRI with hepato-biliary contrast agents represent the most appropriate imaging modality for assessment of patients with CRLMs treated with neoadjuvant chemotherapy^[68].

Despite of the great ability of MRI in detection of CRLMs, above all with the introduction of DWI and HBP, this modality still presents some limitations in patients who have difficulty holding their breath. Motion artefacts can heavily degrade images especially in dynamic acquisitions. Different sequences can be performed to study dynamic and HBP such as volumetric interpolated BH examination (Siemens Healthcare, Erlangen, Germany), liver acquisition with acceleration volume acquisition (GE Healthcare, Waukesha, Wis), or enhanced high-resolution isotropic volume excitation (Philips Healthcare, Best, the Netherlands) or respiratory-triggered T1-WI, this latter independent from patient's collaboration^[69]. Recently Yoon *et al*^[70] have evaluated in a large number of patients the image quality and diagnostic performance in evaluation of focal liver lesions of the respiratory-triggered 3D T1W-GRE sequence compared to standard BH T1W-GRE in HBP. Their results demonstrate that in no-collaborative patients respiratory-triggered 3D T1W-GRE images showed clearer liver margins and intrahepatic vascular structures as well as better image quality, so providing a better diagnostic performance. Overall image quality of respiratory-triggered 3D T1W-GRE was also better than that of BH T1W-GRE in patients with sufficient breath-holding capacity ($n = 309$, 3.96 ± 0.88 , 3.81 ± 0.6 , respectively, $P < 0.001$).

¹⁸F-FDG-PET AND ¹⁸F-FDG-PET/CT

¹⁸F-FDG-PET is the most sensitive non-invasive imaging modality for the detection of CRLMs on a per patient basis^[15,38,49,50]; however PET is limited by the low spatial resolution, the lack of clear anatomic landmarks, and the physiological uptake of the parenchyma which can mask small hepatic lesions. As a result, the detection of CRLMs by ¹⁸F-FDG-PET is directly related to the size of the liver metastases: 14% of hepatic lesions ≤ 15

mm^[71] and 5%-36% of hepatic lesion ≤ 10 mm^[72-74] were identified by ¹⁸F-FDG-PET.

Therefore, to overcome the above limitations, PET has been combined with CT to realize the hybrid modality PET/CT. This combination provides simultaneous functional and anatomic diagnostic information. The combination of PET with CT improves the distinction of physiological ¹⁸F-FDG uptake from pathology and also aids the localization of metastases within the segmental anatomy of the liver, but does not overcome the intrinsic limits of PET modality such as the poor spatial resolution or the inaccurate identification of small non-hyper-metabolic lesions. That is why performing the CT of the PET/CT examination with the administration of *iv* iodinated contrast medium improves the performance of the PET/CT modality. ¹⁸F-FDG-PET/ce-CT increases significantly the detection of CRLMs compared with ¹⁸F-FDG-PET/CT^[75].

¹⁸F-FDG-PET does not require breath holding during acquisition, thus respiratory movements may reduce conspicuity of small liver lesions with potential errors in the detection of focal sub-diaphragmatic ¹⁸F-FDG uptakes and respiratory phase mismatch between the PET and CT data. Revheim *et al*^[76] have recently investigated the added role of two tailored ¹⁸F-FDG-PET liver protocols [prolonged liver acquisition time (PL-PET) and repeated breath-hold respiratory gated liver acquisition (RGL-PET)] to a standard whole body (SWB) ¹⁸F-FDG-PET/CT protocol to improve detection of CRLMs. The PL-PET protocol lasted 8 min and covered the liver with two bed positions, while patients of the RGL-PET protocol were asked to alternate breaths and BHs for 10 min. The addition of tailored liver-specific ¹⁸F-FDG PET protocols to SWB-PET scan improved the detection of CRLMs compared to SWB-PET alone; more lesions were detected and a higher CRLMs SUV max was measured, with a substantial reduction of the background noise related to physiologic liver uptake.

The role of PET/CT in CRLMs is yet evolving. Due to the high cost and an additional radiation exposure, ¹⁸F-FDG-PET/CT is reserved for the detection of occult extra-hepatic disease in patients with CRLMs amenable of surgical resection to avoid the morbidity of a futile invasive therapy^[77].

Moreover further clinical roles of ¹⁸F-FDG-PET/CT may be the following: (1) identification of the primary colorectal neoplasm and evaluation of its local extent^[78,79]; (2) after a curative resection, the detection of local or distant recurrence of the disease^[80] as well as solving ambiguous cases of unexplained CEA rise without conventional radiological explanation and in their prognostic stratification^[81]; and (3) metabolic monitoring of the tumor response to the therapy^[82].

¹⁸F-FDG-PET/MRI

As stated above, both PET and CT show a few limitations in the evaluation of liver lesions; recently PET/MRI has been proposed as an alternative hybrid imaging modality.

Because of the great sensitivity of MRI in recognizing small liver metastases, its combination with the metabolic data obtained by PET may lead to an improved diagnostic accuracy.

Nowadays, the role of PET-MRI in evaluating CRLMs is becoming a topic of major interest, however at present insufficient data is available because hybrid devices are present in few highly specialized centers.

Recent studies have enrolled patients with CRLMs to evaluate the performance of PET-MRI^[83-85]. Drzezga *et al.*^[85] compared PET/CT and PET-MRI in 32 oncologic patients, four of those had CRC and with seven liver lesions. Overall conclusion of this study was that PET/MRI was comparable to PET/CT. Quick *et al.*^[86] studied 80 patients who underwent a double-scanning protocol with PET/MRI and PET/CT with 195 tracer-avid lesions and rated image quality. Their results show that integrated PET/MR hybrid imaging is feasible in clinical setting with similar detection rates as those of PET/CT. Partovi *et al.*^[87] and Kershah *et al.*^[88] investigated the role of PET/MRI in 120 patients with various primary neoplasms (13 CRCs) who underwent double-scanning protocol with PET/MR and PET/CT in a sequential design following a single-tracer injection of FDG. They observed that hybrid PET-MRI imaging led to a better diagnostic confidence in the characterization of focal liver lesions, taking advantage from the synergic evaluation of ADC and SUVmax. Nielsen *et al.*^[89] investigated the possible role of PET/MRI in evaluation of therapeutic response in twenty patients with CRLMs treated with radiofrequency or microwave ablation. The sensitivity of MRI in detecting small intrahepatic lesions combined with the ability of ¹⁸F-FDG-PET to visualize enhanced metabolism at the ablation site suggests that ¹⁸F-FDG-PET/MRI could potentially improve the accuracy of early detection of progressive disease, and thus allow swifter and more effective decision-making regarding appropriate treatment.

NON-CONVENTIONAL PARAMETRIC IMAGING OF CRLMs

This section is dedicated to morphological and functional liver parametric imaging proposed for detecting occult CRLMs and predicting which patients are at risk to develop metachronous liver disease. At present, the real role of parametric images has to be further investigated, as a result they are not routinely performed in the diagnostic clinical management of patients with CRC.

Different studies^[90,91] have focused on methods targeting liver perfusion to individuate occult CRLMs before they become overt on morphological imaging. Changes of liver hemodynamics may indeed be related to the presence of occult liver metastases and may also predict the development of metachronous ones. It is well known that the liver receives a dual blood supply from the portal and systemic circulation. Normally in healthy subjects approximately two thirds of this blood supply is carried by the portal vein and one third by the common

hepatic artery. During the onset of liver metastases this relation changes because of the increase of arterial blood flow (arterialization) and decrease of portal venous inflow^[92].

Imaging can allow recognizing and quantifying these perfusional changes occurring in the liver microvasculature even before any visible morphological signs. For this purpose, doppler perfusion index (DPI) is an US measure of the ratio of arterial hepatic blood flow to total hepatic blood flow^[93,94]. Kopljari *et al.*^[95] compared two different groups with and without liver metastases and observed that patients with liver metastases showed greater DPI determined by increased arterial hepatic blood flow associated to a smaller portal cross-sectional area portal blood flow. The strong operator dependence of the technique represents the major limit of this method.

Perfusion CT allows evaluation hepatic hemodynamic changes and provides quantitative perfusional data useful for the precocious detection of liver metastases^[96]. However, to produce reliable enhancement curves the perfusion CT necessitates of multiple high temporal resolution acquisitions after administration of *iv* contrast medium, this leads to radiation overexposure; moreover the breathing cycle can cause severe motion and distortion artifacts^[97].

Thanks to the lack of ionizing exposure, perfusion MRI seems to be more promising as a reliable tool for the evaluation of focal and global perfusion indexes^[98]. The perfusion parameters evaluated with dynamic contrast-enhanced MRI are essentially represented by Ktrans (volume transfer constant) and Kep (rate constant). Ktrans is the rate constant of contrast agent transfer from the plasma compartment into the extracellular extravascular space, whereas Kep is the rate constant of contrast agent that escape from the extracellular extravascular space back into the plasma compartment. De Bruyne *et al.*^[99] found that a decrease in Ktrans of more than 40% after bevacizumab-containing chemotherapy was associated with better progression-free survival. Further investigations are needed to understand the real role of perfusion MRI in CRLMs.

Different authors^[100-103] have investigated the role of CT texture analysis (TA) to identify the early changes in liver texture heralding the possible presence of occult liver micro-metastases. Texture analysis does not require any additional phase and it can be easily obtained from routinely acquired clinical CT data. This technique is based on the assumption that presence of liver occult lesions can be suspected by the amount of spatial heterogeneity on CT which can be assessed quantifying the texture parameters. These parameters go beyond human visual evaluation and include as main explored values the brightness (quantitative measurement of the mean grey level intensity), entropy (grade of inhomogeneity) and uniformity (distribution of grey levels). As different studies are investigating the potential role of TA, it is debated which is the more appropriate CT phase to analyze. Ganeshan *et al.*^[100] applied TA to non-

contrast enhanced CT scan of patients with CRC showing significant changes of TA parameters in the non diseased part of the liver of patients with CRLMs compared to those without. Similar results are reached even using TA on routinely acquired portal phase images^[101-103]. The exact reasons to explain the relationship between an altered texture in apparently disease-free liver areas and the presence of occult micro-metastases or the development of metachronous live metastases are not quite clear. Probably the alterations of texture features are related to subtle tumor-induced structural and/or hemodynamic changes.

As it has been well demonstrated that the presence of micro-metastasis is related to subtle changes in liver hemodynamics, some authors are investigating the role of blood oxygenation level dependent MRI in early detection of CRLMs. Barash *et al.*^[104,105] evaluated in mice the pathological changes in liver perfusion assessing the hemodynamic response imaging (HRI), a method that involves hypercapnic challenge with brief inhalation of 5% CO₂ followed by hyperoxic challenge with brief inhalation of carbogen. They demonstrated that during CO₂ enrichment there is an increase in portal flow compared to arterial hepatic flow, and that the higher deoxyhemoglobin levels produced a decrease in fMRI signal intensity. Conversely hyperoxia signifies vascular density and tissue perfusion. Edrei *et al.*^[106,107] more recently applied this method to demonstrate in a mouse model the early hemodynamic changes that occur in CRLMs, and their modification with advance of liver involvement. The HRI method showed enhanced sensitivity for small CRLM (1-2 mm) detection compared with ce-MRI (82% vs 38%, respectively) as well as it demonstrated hemodynamic changes occurring during CRLMs antiangiogenic treatment.

DETECTION OF CRLMs: WHICH IS THE MOST ACCURATE MODALITY?

A huge literature is available about the performances of each imaging modality in the evaluation of CRLMs; as a consequence, we will describe mostly the data of meta-analysis reports in this section.

Kinkel *et al.*^[15] performed a meta-analysis including papers published between 1985 and 2000 and concluded that, at equivalent specificity ($\geq 85\%$), ¹⁸F-FDG-PET (90%; CI: 80, 97) is the most sensitive non invasive imaging modality compared to US (55%; CI: 41, 68), CT (72%; CI: 63, 80) and MR (76%; CI: 57, 91) for the detection of hepatic metastases from colorectal, gastric and esophageal cancers on a patient basis.

Bipat *et al.*^[49] performed a meta-analysis including papers published between 1990 and 2003 and concluded that ¹⁸F-FDG-PET is the most sensitive diagnostic tool for the detection of hepatic metastases from CRC on a per patient basis, but not on a per lesion basis. On a per patient basis, the sensitivity of CT, MR, ¹⁸F-FDG-PET were 64% (CI: 55, 72), 65% (CI: 58, 70) and 76% (CI:

61, 86), respectively. For lesion of 1 cm or larger SPIO-enhanced MRI was the most accurate modality.

Nielke *et al.*^[38] performed a meta-analysis including papers published between 1990 and 2010 and concluded that, MRI is the preferred first-line modality for evaluating CRLMs in patients who have not previously undergone therapy; it provides anatomic details and has a high detection rate for lesions smaller than 10 mm. ¹⁸F-FDG-PET can be used as the second line-modality because it is valuable in the evaluation of extra-hepatic disease. The role of ¹⁸F-FDG-PET/CT was not clear owing the small number of studies. At equivalent specificity, the sensitivity of CT, MR and ¹⁸F-FDG-PET was 75% (CI: 69, 79), 80% (CI: 75, 82) and 81% (CI: 66, 91), respectively, on a per lesion basis, and 84% (CI: 67, 93), 88% (CI: 65, 97) and 94% (CI: 92, 96), respectively, on a per patient basis.

van Kessel *et al.*^[68] performed a meta-analysis including papers published between 2005 and 2011 and concluded that, MRI is the most appropriate imaging modality for preoperative assessment of patients with CRLMs treated with neoadjuvant chemotherapy. The sensitivity of CT, MRI, ¹⁸F-FDG-PET and ¹⁸F-FDG-PET/CT were 70% (CI: 47, 82), 86% (CI: 70, 94), 54% (CI: 47, 62) and 52% (CI: 38, 65), respectively, on a per patient basis.

Seo *et al.*^[108] reported the comparison of Gd-EOB-DTPA-MRI and ¹⁸F-FDG-PET/ce-CT in 68 patients with 103 CRLMs and concluded that Gd-EOB-DTPA-MRI is more accurate than ¹⁸F-FDG-PET/ce-CT, especially for detection of small (≤ 1 cm) lesions. The sensitivity, the specificity, the positive and negative predictive values on a patients basis were 100%, 71%, 97% and 100% respectively for Gd-EOB-DTPA-MRI, and 93%, 71%, 97% and 57% respectively for ¹⁸F-FDG-PET/ce-CT.

Muhi *et al.*^[109] reported the comparison of ce-CT, ce-US, SPIO-MRI and Gd-EOB-DTPA-MRI in 111 patients with CRC, 46 of whom presented 112 hepatic metastases. The sensitivity of ce-US, ce-CT, SPIO-MRI and Gd-EOB-DTPA-MRI, was 73%, 63%, 80% and 95%, respectively, considering all the lesions, and 41%, 26%, 63% and 92%, respectively, considering the lesions ≤ 10 mm. The sensitivity of MRI was significantly better than the other modalities. Although the sensitivity of Gd-EOB-DTPA-MRI was superior to that of SPIO-MRI especially for lesions ≤ 10 mm, the difference was not statistically significant. No significant differences in positive predictive value were disclosed between any of the images sets for all the lesions, lesions > 1 cm and lesions ≤ 1 cm.

Berger-Kulemann *et al.*^[47] evaluated the performance of ce-MDCT and gadoteric acid enhanced MRI in the detection of CRLMs in patients with diffuse fatty infiltration of the liver. MDCT identified 49 (72%) and MRI 66 (97%) of 68 lesions confirmed by histopathology. Statistical analysis showed that the MRI was superior to MDCT with a significant difference considering all the lesions ($P < 0.001$) and small lesions (≤ 1 cm; $P < 0.001$), while there was no-significant difference between

the two modalities in the detection of lesions > 1 cm.

Zech *et al*^[110] reported that Gd-EOB-DTPA-MRI can lead to cost savings respect to extracellular-contrast-medium-MRI by improving pre-operative planning, reducing additional imaging and decreasing intra-operative changes.

Chen *et al*^[111] performed a meta-analysis including 13 papers published between 2011 and 2012 (6/13 papers dealt with CRLMs) and concluded that, Gd-EOB-DTPA-MRI presents high sensitivity (93%; CI: 90, 95) and specificity (95%; CI: 91, 97) for detection of CRLMs.

Maffione *et al*^[112] have evaluated the diagnostic performance of ¹⁸F-FDG PET and PET/CT for staging liver metastases in patients with CRC including in their meta-analysis studies published from 2004 to 2014. They conclude that ¹⁸F-FDG-PET/CT is highly accurate for the detection of CRLMs on a per-patient basis (pooled sensitivity and specificity of 93%) while on a per-lesion basis results were lower (pooled sensitivity and specificity of 60% and 79%). Comparing PET with different imaging modalities their results show that PET had a lower sensitivity than MRI and CT on a per-patient basis (93%, 100% and 98%) and a per-lesion basis (66%, 89% and 79%). In contrast, PET appeared more specific than MRI and CT (86%, 81% and 67%).

Maas *et al*^[80] published a meta-analysis comparing PET, PET-CT and CT for whole body staging in patients with suspected recurrence of CRC. The Authors found PET and PET-CT to have the highest diagnostic performance with an area under the curve of 0.94 for both PET and PET-CT compared to 0.83 for CT scan. PET/CT appears as the whole body technique of choice because of its greater ability respect to CT to identify extra-hepatic and additional sites of disease and also for the detection of local recurrence.

MANAGEMENT OF CRLMS: WHICH IMAGING PROTOCOL?

The main clinical scenarios to be managed in patients with CRLMs are the following: (1) detection of liver metastases as part of global staging of newly diagnosed CRC; and (2) pre-surgical planning of CRLMs resection; c) surveillance/monitoring of treatment response of the CRLMs.

Although the optimal imaging strategy is not well established, yet, we will suggest a diagnostic algorithm for each clinical scenario underscoring in part information just reported above.

Detection of CRLMs of newly diagnosed CRC

ce-CT is currently regarded as the standard for one session whole-body staging, including the liver, for initially diagnosed CRC patients. However, as stated above, ce-CT may miss up to 25% of CRLMs also using a multiphasic acquisition protocol and its performance worsens in presence of hepatic steatosis^[47]. Furthermore,

ce-CT shows limitations in characterizing small (< 1 cm) hypoattenuating lesions, which may be defined as indeterminate or "too-small-to-characterize" (TSCT)^[46].

Currently, liver MRI is increasingly used to evaluate CRLMs. The higher accuracy of MRI in comparison with CT and PET/CT for detection of CRLMs, especially for lesions < 1 cm, has been just largely mentioned in the previous section. However, it is unclear which CRC patients should receive liver MRI in addition to standard staging CT. Recently, Han *et al*^[113] have investigated the clinical impact of liver MRI in staging evaluation of newly diagnosed CRC patients in three ce-CT groups of patients: (1) patients who demonstrate diminutive indeterminate hypoattenuating TSCT lesions; (2) patients with metastasis-negative hepatic findings; and (3) suspicious or non-TSCT indeterminate lesions. The Authors concluded that liver MRI provides little benefit for detecting synchronous CRLMs in the groups 1 and 2, while it has a significant impact in the group 3. Moreover in the setting of hepatic steatosis, MRI with hepato-biliary contrast agents is superior to ce-MDCT in detecting CRLMs^[47].

Both US and PET/CT play a marginal role. As stated above, US may be used to identify patients with diffuse liver metastases who may not need further hepatic diagnostic investigation, whereas PET/CT show a high performance in identifying patients with liver metastases.

Pre-surgical planning of CRLMs resection

The current National Comprehensive Cancer Network (NCCN) guidelines state that liver MRI can be consider to further evaluate patients diagnosed with potentially resectable CRLMs on CT^[114]. This recommendation takes into account the fact that liver MRI is most reliable in defining the number, the size and the location of CRLMs, may detect additional CRLMs that are undiagnosed on CT and therefore may change the treatment plan. Moreover it provides information about the volume of the future liver remnant, of the biliary ductal system and of the hepatic parenchyma, such as steatosis, iron deposition, fibrosis, that may impair liver function.

ce-MDCT and ce-MRI angiography have shown similar performance for preoperative hepatic vascular anatomic evaluation^[115], however CT may have some advantages over MRI as rapid acquisition, less susceptibility to motion, thin collimation, which assure excellent MPR and 3D images. ce-MDCT may be preferred to ce-MRI angiography in situations where detailed vascular information is necessary prior to complex hepatic resection.

¹⁸F-FDG-PET/CT may be recommended for the detection of occult extra-hepatic disease prior of CRLMs surgical resection to avoid not useful invasive treatment.

Surveillance/monitoring of the treatment response of the CRLMs

As diagnostic imaging can help identify the best therapeutic strategy for treatment of CRLMs, equally it plays a key role in assessing response to treatment.

The criteria for monitoring CRLMs response to chemotherapy are the response evaluation criteria in solid tumors, which consist of a simple single dimension measurement of tumor size with efficacy determined by tumor shrinkage^[116]. In the evaluation of patients with CRLMs treated with chemotherapy, ce-MRI should be preferred to both ce-MDCT and ¹⁸F-FDG-PET/CT for the following reasons: (1) the steatosis induced by chemotherapy decreases the liver-to-lesion contrast, hindering the detection and delineation of the lesions on ce-MDCT; and (2) the necrosis, the reduction of the size of the lesions and the decrease in metabolic activity of cancer cells hamper the diagnostic performance of ¹⁸F-FDG-PET/CT; it is still not clear if the disappearance of metabolic activity of a lesion can be considered a complete response^[117,118]. Today, MRI with DWI and liver specific contrast agents provide the most sensitive tool for detecting CRLMs in patients who have undergone neoadjuvant chemotherapy.

After systemic or local therapy, the change in size of the CRLMs may not be representative of a response, because the initial post-treatment examinations often fail to demonstrate shrinkage of the tumor. In such cases radiologists can misinterpret a slight increase in size of a recently treated lesion as tumor progression, whereas it is often sign of early response to anti-angiogenic treatment. The CT "pseudo-progression" is defined as the increase in size of a lesion after treatment associated with a reduction of attenuation, due to intra-lesional edema, together with a decrease in the tumor markers^[119]. In these instances, the evaluation of changes in size and enhancement of the lesion as well as following the lesion up over time, preferably using the same modality, helps determine the efficacy of the treatment^[120].

After a local hepatic treatment, the current NCCN guidelines^[114] suggest surveillance imaging with CT or MRI every 3-6 mo for 2 years, then every 6 mo for 3-5 years. The NCCN guidelines do not recommend PET/CT for assessing treatment response, because of false-negative (necrotic lesions) and false-positive (inflammation and surgery) results may occur.

CONCLUSION

Several imaging techniques are available in management of CRLMs.

US plays a marginal role due to the operator-dependence, the lack of panoramic view and the low sensitivity for lesions < 10 mm. US may select patients with diffuse secondary liver involvement who do not benefit of further hepatic imaging.

Actually, ce-MDCT is the preferred imaging modality for initial global staging, allowing also an optimal pre-treatment planning for curative CRLMs resection.

MRI provides additional information respect to ce-MDCT when suspicious or non-TSCT indeterminate hepatic lesions are present on ce-MDCT, in presence of hepatic steatosis or in the post-chemotherapy liver

evaluation.

¹⁸F-FDG-PET/CT may be proposed to detect occult extra-hepatic disease prior of CRLMs resection to avoid inappropriate surgical treatment.

¹⁸F-PET-MRI may represent the future elective diagnostic tool because it combines the high accuracy for CRLMs detection of MRI with the high performance of extra-hepatic metastases evaluation of PET.

Non-conventional parametric imaging may play a future role for detecting occult CRLMs and predicting which patients are at risk to develop metachronous liver disease, but these techniques have to be further investigated.

REFERENCES

- 1 **American Cancer Society.** Cancer Facts & Figures 2014. Atlanta: American Cancer Society, 2014. [Accessed 2014 Jan 21]. Available from: URL: <http://www.cancer.org/research/cancerfactsstatistics/index>
- 2 **Manfredi S,** Lepage C, Hatem C, Coatmeur O, Faivre J, Bouvier AM. Epidemiology and management of liver metastases from colorectal cancer. *Ann Surg* 2006; **244**: 254-259 [PMID: 16858188 DOI: 10.1097/01.sla.0000217629.94941.cf]
- 3 **Kanas GP,** Taylor A, Primrose JN, Langeberg WJ, Kelsh MA, Mowat FS, Alexander DD, Choti MA, Poston G. Survival after liver resection in metastatic colorectal cancer: review and meta-analysis of prognostic factors. *Clin Epidemiol* 2012; **4**: 283-301 [PMID: 23152705 DOI: 10.2147/CLEP.S34285]
- 4 **Simmonds PC,** Primrose JN, Colquitt JL, Garden OJ, Poston GJ, Rees M. Surgical resection of hepatic metastases from colorectal cancer: a systematic review of published studies. *Br J Cancer* 2006; **94**: 982-999 [PMID: 16538219 DOI: 10.1038/sj.bjc.6603033]
- 5 **Tzeng CW,** Aloia TA. Colorectal liver metastases. *J Gastrointest Surg* 2013; **17**: 195-201; quiz p.201-202 [PMID: 23054896 DOI: 10.1007/s11605-012-2022-3]
- 6 **Fong Y,** Cohen AM, Fortner JG, Enker WE, Turnbull AD, Coit DG, Marrero AM, Prasad M, Blumgart LH, Brennan MF. Liver resection for colorectal metastases. *J Clin Oncol* 1997; **15**: 938-946 [PMID: 9060531]
- 7 **Nakamura S,** Suzuki S, Baba S. Resection of liver metastases of colorectal carcinoma. *World J Surg* 1997; **21**: 741-747 [PMID: 9276706 DOI: 10.1007/s002689900300]
- 8 **Alberts SR,** Poston GJ. Treatment advances in liver-limited metastatic colorectal cancer. *Clin Colorectal Cancer* 2011; **10**: 258-265 [PMID: 21820974 DOI: 10.1016/j.clcc.2011.06.008]
- 9 **Tanada M,** Saeki T, Takashima S, Mogami H, Hyoudou I, Jinno K. [Intrahepatic arterial infusion chemotherapy for the colon cancer patients with liver metastases--a comparison of arterial embolization chemotherapy versus continuous arterial infusion chemotherapy]. *Gan To Kagaku Ryoho* 1996; **23**: 1440-1442 [PMID: 8854774]
- 10 **Dodd GD,** Soulen MC, Kane RA, Livraghi T, Lees WR, Yamashita Y, Gillams AR, Karahan OI, Rhim H. Minimally invasive treatment of malignant hepatic tumors: at the threshold of a major breakthrough. *Radiographics* 2000; **20**: 9-27 [PMID: 10682768 DOI: 10.1148/radiographics.20.1.g00ja019]
- 11 **Ruers T,** Bleichrodt RP. Treatment of liver metastases, an update on the possibilities and results. *Eur J Cancer* 2002; **38**: 1023-1033 [PMID: 11978527]
- 12 **Clavien PA,** Petrowsky H, DeOliveira ML, Graf R. Strategies for safer liver surgery and partial liver transplantation. *N Engl J Med* 2007; **356**: 1545-1559 [PMID: 17429086]
- 13 **Shah KN,** Clary BM. Selection of Patients with Colorectal/Liver Metastases for Surgical Intervention: Current Issues and Challenges. *Curr Surg Rep* 2014; **2**: 1-7 [DOI: 10.1007/s40137-014-0065-y]
- 14 **Catalano OA,** Singh AH, Uppot RN, Hahn PF, Ferrone CR, Sahani

- DV. Vascular and biliary variants in the liver: implications for liver surgery. *Radiographics* 2008; **28**: 359-378 [PMID: 18349445 DOI: 10.1148/rg.282075099]
- 15 **Kinkel K**, Lu Y, Both M, Warren RS, Thoeni RF. Detection of hepatic metastases from cancers of the gastrointestinal tract by using noninvasive imaging methods (US, CT, MR imaging, PET): a meta-analysis. *Radiology* 2002; **224**: 748-756 [PMID: 12202709 DOI: 10.1148/radiol.2243011362]
 - 16 **Wernecke K**, Rummeny E, Bongartz G, Vassallo P, Kivelitz D, Wiesmann W, Peters PE, Reers B, Reiser M, Pircher W. Detection of hepatic masses in patients with carcinoma: comparative sensitivities of sonography, CT, and MR imaging. *AJR Am J Roentgenol* 1991; **157**: 731-739 [PMID: 1892027 DOI: 10.2214/ajr.157.4.1892027]
 - 17 **Glover C**, Douse P, Kane P, Karani J, Meire H, Mohammadtaghi S, Allen-Mersh TG. Accuracy of investigations for asymptomatic colorectal liver metastases. *Dis Colon Rectum* 2002; **45**: 476-484 [PMID: 12006929]
 - 18 **Clarke MP**, Kane RA, Steele G, Hamilton ES, Ravikumar TS, Onik G, Clouse ME. Prospective comparison of preoperative imaging and intraoperative ultrasonography in the detection of liver tumors. *Surgery* 1989; **106**: 849-855 [PMID: 2554519]
 - 19 **Ohlsson B**, Tranberg KG, Lundstedt C, Ekberg H, Hederström E. Detection of hepatic metastases in colorectal cancer: a prospective study of laboratory and imaging methods. *Eur J Surg* 1993; **159**: 275-281 [PMID: 8103361]
 - 20 **Ong KO**, Leen E. Radiological staging of colorectal liver metastases. *Surg Oncol* 2007; **16**: 7-14 [PMID: 17499498]
 - 21 **Albrecht T**, Hohmann J, Oldenburg A, Skrok J, Wolf KJ. Detection and characterisation of liver metastases. *Eur Radiol* 2004; **14** Suppl 8: P25-P33 [PMID: 15700330]
 - 22 **Albrecht T**, Hoffmann CW, Schmitz SA, Schettler S, Overberg A, Germer CT, Wolf KJ. Phase-inversion sonography during the liver-specific late phase of contrast enhancement: improved detection of liver metastases. *AJR Am J Roentgenol* 2001; **176**: 1191-1198 [PMID: 11312180 DOI: 10.2214/ajr.176.5.1761191]
 - 23 **Albrecht T**, Blomley MJ, Burns PN, Wilson S, Harvey CJ, Leen E, Claudon M, Calliada F, Correia JM, LaFortune M, Campani R, Hoffmann CW, Cosgrove DO, LeFevre F. Improved detection of hepatic metastases with pulse-inversion US during the liver-specific phase of SHU 508A: multicenter study. *Radiology* 2003; **227**: 361-370 [PMID: 12649417 DOI: 10.1148/radiol.2272011833]
 - 24 **Esteban JM**, Mollá MA, Tomás C, Maldonado L. Improved detection of liver metastases with contrast-enhanced wideband harmonic imaging: comparison with CT findings. *Eur J Ultrasound* 2002; **15**: 119-126 [PMID: 12423737 DOI: 10.1016/S0929-8266(02)00032-0]
 - 25 **Quaia E**, D'Onofrio M, Palumbo A, Rossi S, Bruni S, Cova M. Comparison of contrast-enhanced ultrasonography versus baseline ultrasound and contrast-enhanced computed tomography in metastatic disease of the liver: diagnostic performance and confidence. *Eur Radiol* 2006; **16**: 1599-1609 [PMID: 16552507 DOI: 10.1007/s00330-006-0192-7]
 - 26 **Dalla Palma L**, Bertolotto M, Quaia E, Locatelli M. Detection of liver metastases with pulse inversion harmonic imaging: preliminary results. *Eur Radiol* 1999; **9** Suppl 3: S382-S387 [PMID: 10602934 DOI: 10.1007/PL00014079]
 - 27 **Celli N**, Gaiani S, Piscaglia F, Zironi G, Camaggi V, Leoni S, Righini R, Bolondi L. Characterization of liver lesions by real-time contrast-enhanced ultrasonography. *Eur J Gastroenterol Hepatol* 2007; **19**: 3-14 [PMID: 17206071 DOI: 10.1097/01.meg.0000250585.53608.3c]
 - 28 **Larsen LP**, Rosenkilde M, Christensen H, Bang N, Bolvig L, Christiansen T, Laurberg S. The value of contrast enhanced ultrasonography in detection of liver metastases from colorectal cancer: a prospective double-blinded study. *Eur J Radiol* 2007; **62**: 302-307 [PMID: 17194561 DOI: 10.1016/j.ejrad.2006.11.033]
 - 29 **Westwood M**, Joore M, Grutters J, Redekop K, Armstrong N, Lee K, Gloy V, Raatz H, Misso K, Severens J, Kleijnen J. Contrast-enhanced ultrasound using SonoVue® (sulphur hexafluoride microbubbles) compared with contrast-enhanced computed tomography and contrast-enhanced magnetic resonance imaging for the characterisation of focal liver lesions and detection of liver metastases: a systematic review and cost-effectiveness analysis. *Health Technol Assess* 2013; **17**: 1-243 [PMID: 23611316 DOI: 10.3310/hta17160]
 - 30 **Rafaelson SR**, Jakobsen A. Contrast-enhanced ultrasound vs multidetector-computed tomography for detecting liver metastases in colorectal cancer: a prospective, blinded, patient-by-patient analysis. *Colorectal Dis* 2011; **13**: 420-425 [PMID: 20412096 DOI: 10.1111/j.1463-1318.2010.02288.x]
 - 31 **Cantisani V**, Ricci P, Erturk M, Pagliara E, Drudi F, Calliada F, Mortelet K, D'Ambrosio U, Marigliano C, Catalano C, Marin D, Di Seri M, Longo F, Passariello R. Detection of hepatic metastases from colorectal cancer: prospective evaluation of gray scale US versus SonoVue® low mechanical index real time-enhanced US as compared with multidetector-CT or Gd-BOPTA-MRI. *Ultraschall Med* 2010; **31**: 500-505 [PMID: 20408122 DOI: 10.1055/s-0028-1109751]
 - 32 **Larsen LP**, Rosenkilde M, Christensen H, Bang N, Bolvig L, Christiansen T, Laurberg S. Can contrast-enhanced ultrasonography replace multidetector-computed tomography in the detection of liver metastases from colorectal cancer? *Eur J Radiol* 2009; **69**: 308-313 [PMID: 18068925 DOI: 10.1016/j.ejrad.2007.10.023]
 - 33 **Konopke R**, Bunk A, Kersting S. Contrast-enhanced ultrasonography in patients with colorectal liver metastases after chemotherapy. *Ultraschall Med* 2008; **29** Suppl 4: S203-S209 [PMID: 18833498 DOI: 10.1055/s-2008-1027795]
 - 34 **Cantisani V**, Grazhdani H, Fioravanti C, Rosignuolo M, Calliada F, Messineo D, Bernieri MG, Redler A, Catalano C, D'Ambrosio F. Liver metastases: Contrast-enhanced ultrasound compared with computed tomography and magnetic resonance. *World J Gastroenterol* 2014; **20**: 9998-10007 [PMID: 25110428 DOI: 10.3748/wjg.v20.i29.9998]
 - 35 **Bolondi L**. The appropriate allocation of CEUS in the diagnostic algorithm of liver lesions: a debated issue. *Ultrasound Med Biol* 2013; **39**: 183-185 [PMID: 23140590]
 - 36 **Choti MA**, Sitzmann JV, Tiburi MF, Sumetthotimetha W, Rangsin R, Schulick RD, Lillemo KD, Yeo CJ, Cameron JL. Trends in long-term survival following liver resection for hepatic colorectal metastases. *Ann Surg* 2002; **235**: 759-766 [PMID: 12035031]
 - 37 **Rojas Llimpe FL**, Di Fabio F, Ercolani G, Giampalma E, Cappelli A, Serra C, Castellucci P, D'Errico A, Golfieri R, Pinna AD, Pinto C. Imaging in resectable colorectal liver metastasis patients with or without preoperative chemotherapy: results of the PROMETEO-01 study. *Br J Cancer* 2014; **111**: 667-673 [PMID: 24983362 DOI: 10.1038/bjc.2014.351]
 - 38 **Niekel MC**, Bipat S, Stoker J. Diagnostic imaging of colorectal liver metastases with CT, MR imaging, FDG PET, and/or FDG PET/CT: a meta-analysis of prospective studies including patients who have not previously undergone treatment. *Radiology* 2010; **257**: 674-684 [PMID: 20829538 DOI: 10.1148/radiol.10100729]
 - 39 **Weg N**, Scheer MR, Gabor MP. Liver lesions: improved detection with dual-detector-array CT and routine 2.5-mm thin collimation. *Radiology* 1998; **209**: 417-426 [PMID: 9807568]
 - 40 **Kim YK**, Ko SW, Hwang SB, Kim CS, Yu HC. Detection and characterization of liver metastases: 16-slice multidetector computed tomography versus superparamagnetic iron oxide-enhanced magnetic resonance imaging. *Eur Radiol* 2006; **16**: 1337-1345 [PMID: 16453115 DOI: 10.1007/s00330-005-0140-y]
 - 41 **Haider MA**, Amitai MM, Rappaport DC, O'Malley ME, Hanbidge AE, Redston M, Lockwood GA, Gallinger S. Multi-detector row helical CT in preoperative assessment of small (< or = 1.5 cm) liver metastases: is thinner collimation better? *Radiology* 2002; **225**: 137-142 [PMID: 12354997 DOI: 10.1148/radiol.2251011225]
 - 42 **Kulinna C**, Helmberger T, Kessler M, Reiser M. [Improvement in diagnosis of liver metastases with the multi-detector CT]. *Radiologie* 2001; **41**: 16-23 [PMID: 11220094 DOI: 10.1007/s001170050923]
 - 43 **Ch'en IY**, Katz DS, Jeffrey RB, Daniel BL, Li KC, Beaulieu CF, Mindelzun RE, Yao D, Olcott EW. Do arterial phase helical CT images improve detection or characterization of colorectal liver

- metastases? *J Comput Assist Tomogr* 2011; **21**: 391-397 [PMID: 9135646 DOI: 10.1097/00004728-199705000-00010]
- 44 **Wicherts DA**, de Haas RJ, van Kessel CS, Bisschops RH, Takahara T, van Hillegersberg R, Bipat S, Rinkes IH, van Leeuwen MS. Incremental value of arterial and equilibrium phase compared to hepatic venous phase CT in the preoperative staging of colorectal liver metastases: an evaluation with different reference standards. *Eur J Radiol* 2011; **77**: 305-311 [PMID: 19695807 DOI: 10.1016/j.ejrad.2009.07.026]
 - 45 **Mainenti PP**, Cirillo LC, Camera L, Persico F, Cantalupo T, Pace L, De Palma GD, Persico G, Salvatore M. Accuracy of single phase contrast enhanced multidetector CT colonography in the preoperative staging of colo-rectal cancer. *Eur J Radiol* 2006; **60**: 453-459 [PMID: 16965883 DOI: 10.1016/j.ejrad.2006.08.001]
 - 46 **Bajpai SK**, Sahani D. Recent progress in imaging of colorectal cancer liver metastases. *Curr Colorectal Cancer Rep* 2009; **5**: 99-107 [DOI: 10.1007/s11888-009-0015-8]
 - 47 **Berger-Kulemann V**, Schima W, Baroud S, Koelblinger C, Kaczirek K, Gruenberger T, Schindl M, Maresch J, Weber M, Ba-Ssalamah A. Gadoxetic acid-enhanced 3.0 T MR imaging versus multidetector-row CT in the detection of colorectal metastases in fatty liver using intraoperative ultrasound and histopathology as a standard of reference. *Eur J Surg Oncol* 2012; **38**: 670-676 [PMID: 22652037 DOI: 10.1016/j.ejso.2012.05.004]
 - 48 **Bipat S**, Niekel MC, Comans EF, Nio CY, Bemelman WA, Verhoef C, Stoker J. Imaging modalities for the staging of patients with colorectal cancer. *Neth J Med* 2012; **70**: 26-34 [PMID: 22271811]
 - 49 **Bipat S**, van Leeuwen MS, Comans EF, Pijl ME, Bossuyt PM, Zwinderman AH, Stoker J. Colorectal liver metastases: CT, MR imaging, and PET for diagnosis--meta-analysis. *Radiology* 2005; **237**: 123-131 [PMID: 16100087 DOI: 10.1148/radiol.2371042060]
 - 50 **Mainenti PP**, Mancini M, Mainolfi C, Camera L, Maurea S, Manchia A, Tanga M, Persico F, Addeo P, D'Antonio D, Speranza A, Bucci L, Persico G, Pace L, Salvatore M. Detection of colorectal liver metastases: prospective comparison of contrast enhanced US, multidetector CT, PET/CT, and 1.5 Tesla MR with extracellular and reticulo-endothelial cell specific contrast agents. *Abdom Imaging* 2010; **35**: 511-521 [PMID: 19562412 DOI: 10.1007/s00261-009-9555-2]
 - 51 **Blyth S**, Blakeborough A, Peterson M, Cameron IC, Majeed AW. Sensitivity of magnetic resonance imaging in the detection of colorectal liver metastases. *Ann R Coll Surg Engl* 2008; **90**: 25-28 [PMID: 18201494 DOI: 10.1308/003588408X242303]
 - 52 **Schima W**, Saini S, Echeverri JA, Hahn PF, Harisinghani M, Mueller PR. Focal liver lesions: characterization with conventional spin-echo versus fast spin-echo T2-weighted MR imaging. *Radiology* 1997; **202**: 389-393 [PMID: 9015063]
 - 53 **Bennett GL**, Petersein A, Mayo-Smith WW, Hahn PF, Schima W, Saini S. Addition of gadolinium chelates to heavily T2-weighted MR imaging: limited role in differentiating hepatic hemangiomas from metastases. *AJR Am J Roentgenol* 2000; **174**: 477-485 [PMID: 10658728 DOI: 10.2214/ajr.174.2.1740477]
 - 54 **Cittadini G**, Santacroce E, Giasotto V, Rescinito G. [Focal liver lesions: characterization with quantitative analysis of T2 relaxation time in TSE sequence with double echo time]. *Radiol Med* 2004; **107**: 166-173 [PMID: 15031682]
 - 55 **Patterson DM**, Padhani AR, Collins DJ. Technology insight: water diffusion MRI--a potential new biomarker of response to cancer therapy. *Nat Clin Pract Oncol* 2008; **5**: 220-233 [PMID: 18301415 DOI: 10.1038/npcnol1073]
 - 56 **Bruegel M**, Holzapfel K, Gaa J, Woertler K, Waldt S, Kiefer B, Stemmer A, Ganter C, Rummeny EJ. Characterization of focal liver lesions by ADC measurements using a respiratory triggered diffusion-weighted single-shot echo-planar MR imaging technique. *Eur Radiol* 2008; **18**: 477-485 [PMID: 17960390 DOI: 10.1007/s00330-007-0785-9]
 - 57 **Parikh T**, Drew SJ, Lee VS, Wong S, Hecht EM, Babb JS, Taouli B. Focal liver lesion detection and characterization with diffusion-weighted MR imaging: comparison with standard breath-hold T2-weighted imaging. *Radiology* 2008; **246**: 812-822 [PMID: 18223123 DOI: 10.1148/radiol.2463070432]
 - 58 **Kenis C**, Deckers F, De Foer B, Van Mieghem F, Van Laere S, Pouillon M. Diagnosis of liver metastases: can diffusion-weighted imaging (DWI) be used as a stand alone sequence? *Eur J Radiol* 2012; **81**: 1016-1023 [PMID: 21377305 DOI: 10.1016/j.ejrad.2011.02.019]
 - 59 **Löwenthal D**, Zeile M, Lim WY, Wybranski C, Fischbach F, Wieners G, Pech M, Kropf S, Rieke J, Dudeck O. Detection and characterisation of focal liver lesions in colorectal carcinoma patients: comparison of diffusion-weighted and Gd-EOB-DTPA enhanced MR imaging. *Eur Radiol* 2011; **21**: 832-840 [PMID: 20886339 DOI: 10.1007/s00330-010-1977-2]
 - 60 **Bellin MF**, Van Der Molen AJ. Extracellular gadolinium-based contrast media: an overview. *Eur J Radiol* 2008; **66**: 160-167 [PMID: 18358659 DOI: 10.1016/j.ejrad.2008.01.023]
 - 61 **del Frate C**, Bazzocchi M, Mortelet KJ, Zuiani C, Londero V, Como G, Zanardi R, Ros PR. Detection of liver metastases: comparison of gadobenate dimeglumine-enhanced and ferumoxides-enhanced MR imaging examinations. *Radiology* 2002; **225**: 766-772 [PMID: 12461259 DOI: 10.1148/radiol.2253011854]
 - 62 **Ward J**, Robinson PJ, Guthrie JA, Downing S, Wilson D, Lodge JP, Prasad KR, Toogood GJ, Wyatt JI. Liver metastases in candidates for hepatic resection: comparison of helical CT and gadolinium- and SPIO-enhanced MR imaging. *Radiology* 2005; **237**: 170-180 [PMID: 16126930 DOI: 10.1148/radiol.2371041444]
 - 63 **Kim YK**, Lee JM, Kim CS, Chung GH, Kim CY, Kim IH. Detection of liver metastases: gadobenate dimeglumine-enhanced three-dimensional dynamic phases and one-hour delayed phase MR imaging versus superparamagnetic iron oxide-enhanced MR imaging. *Eur Radiol* 2005; **15**: 220-228 [PMID: 15624108 DOI: 10.1007/s00330-004-2570-3]
 - 64 **Maurea S**, Mainenti PP, Tambasco A, Imbriaco M, Mollica C, Laccetti E, Camera L, Liuzzi R, Salvatore M. Diagnostic accuracy of MR imaging to identify and characterize focal liver lesions: comparison between gadolinium and superparamagnetic iron oxide contrast media. *Quant Imaging Med Surg* 2014; **4**: 181-189 [PMID: 24914419 DOI: 10.3978/j.issn.2223-4292.2014.01.02]
 - 65 **Hamm B**, Staks T, Mühler A, Bollow M, Taupitz M, Frenzel T, Wolf KJ, Weinmann HJ, Lange L. Phase I clinical evaluation of Gd-EOB-DTPA as a hepatobiliary MR contrast agent: safety, pharmacokinetics, and MR imaging. *Radiology* 1995; **195**: 785-792 [PMID: 7754011]
 - 66 **Dahlström N**, Persson A, Albiin N, Smedby O, Brismar TB. Contrast-enhanced magnetic resonance cholangiography with Gd-BOPTA and Gd-EOB-DTPA in healthy subjects. *Acta Radiol* 2007; **48**: 362-368 [PMID: 17453513 DOI: 10.1080/02841850701196922]
 - 67 **Auer RC**, White RR, Kemeny NE, Schwartz LH, Shia J, Blumgart LH, Dematteo RP, Fong Y, Jarnagin WR, D'Angelica MI. Predictors of a true complete response among disappearing liver metastases from colorectal cancer after chemotherapy. *Cancer* 2010; **116**: 1502-1509 [PMID: 20120032 DOI: 10.1002/cncr.24912]
 - 68 **van Kessel CS**, Buckens CF, van den Bosch MA, van Leeuwen MS, van Hillegersberg R, Verkooijen HM. Preoperative imaging of colorectal liver metastases after neoadjuvant chemotherapy: a meta-analysis. *Ann Surg Oncol* 2012; **19**: 2805-2813 [PMID: 22396005 DOI: 10.1245/s10434-012-2300-z]
 - 69 **Tran PV**, Jhaveri KS. Comparison of high spatial resolution respiratory triggered inversion recovery-prepared spoiled gradient echo sequence with standard breathhold T1 sequence MRI of the liver using gadoxetic acid. *J Magn Reson Imaging* 2013; **37**: 700-706 [PMID: 23335396 DOI: 10.1002/jmri.23864]
 - 70 **Yoon JH**, Lee JM, Lee ES, Baek J, Lee S, Iwade Y, Han JK, Choi BI. Navigated three-dimensional T1-weighted gradient-echo sequence for gadoxetic acid liver magnetic resonance imaging in patients with limited breath-holding capacity. *Abdom Imaging* 2015; **40**: 278-288 [PMID: 25112454]
 - 71 **Ruers TJ**, Langenhoff BS, Neeleman N, Jager GJ, Strijk S, Wobbes T, Corstens FH, Oyen WJ. Value of positron emission tomography with [¹⁸F]fluorodeoxyglucose in patients with

- colorectal liver metastases: a prospective study. *J Clin Oncol* 2002; **20**: 388-395 [PMID: 11786565 DOI: 10.1200/JCO.20.2.388]
- 72 **Rappeport ED**, Loft A, Berthelsen AK, von der Recke P, Larsen PN, Mogensen AM, Wettergren A, Rasmussen A, Hillingsøe J, Kirkegaard P, Thomsen C. Contrast-enhanced FDG-PET/CT vs. SPIO-enhanced MRI vs. FDG-PET vs. CT in patients with liver metastases from colorectal cancer: a prospective study with intraoperative confirmation. *Acta Radiol* 2007; **48**: 369-378 [PMID: 17453514 DOI: 10.1080/02841850701294560]
 - 73 **Fong Y**, Saldinger PF, Akhurst T, Macapinlac H, Yeung H, Finn RD, Cohen A, Kemeny N, Blumgart LH, Larson SM. Utility of 18F-FDG positron emission tomography scanning on selection of patients for resection of hepatic colorectal metastases. *Am J Surg* 1999; **178**: 282-287 [PMID: 10587184 DOI: 10.1016/S0002-9610(99)00187-7]
 - 74 **Sahani DV**, Kalva SP, Fischman AJ, Kadavigere R, Blake M, Hahn PF, Saini S. Detection of liver metastases from adenocarcinoma of the colon and pancreas: comparison of mangafodipir trisodium-enhanced liver MRI and whole-body FDG PET. *AJR Am J Roentgenol* 2005; **185**: 239-246 [PMID: 15972430 DOI: 10.2214/ajr.185.1.01850239]
 - 75 **Badiee S**, Franc BL, Webb EM, Chu B, Hawkins RA, Coakley F, Singer L. Role of IV iodinated contrast material in 18F-FDG PET/CT of liver metastases. *AJR Am J Roentgenol* 2008; **191**: 1436-1439 [PMID: 18941082 DOI: 10.2214/AJR.07.3750]
 - 76 **Revheim ME**, Haugvik SP, Johnsrud K, Mathisen Ø, Fjeld JG, Skretting A. Respiratory gated and prolonged acquisition 18F-FDG PET improve preoperative assessment of colorectal liver metastases. *Acta Radiol* 2015; **56**: 397-403 [PMID: 24682406 DOI: 10.1177/0284185114529563]
 - 77 **Ruers TJ**, Wiering B, van der Sijp JR, Roumen RM, de Jong KP, Comans EF, Pruijm J, Dekker HM, Krabbe PF, Oyen WJ. Improved selection of patients for hepatic surgery of colorectal liver metastases with (18)F-FDG PET: a randomized study. *J Nucl Med* 2009; **50**: 1036-1041 [PMID: 19525451 DOI: 10.2967/jnumed.109.063040]
 - 78 **Mainenti PP**, Salvatore B, D'Antonio D, De Falco T, De Palma GD, D'Armiento FP, Bucci L, Pace L, Salvatore M. PET/CT colonography in patients with colorectal polyps: a feasibility study. *Eur J Nucl Med Mol Imaging* 2007; **34**: 1594-1603 [PMID: 17492447 DOI: 10.1007/s00259-007-0422-5]
 - 79 **Mainenti PP**, Iodice D, Segreto S, Storto G, Magliulo M, De Palma GD, Salvatore M, Pace L. Colorectal cancer and 18FDG-PET/CT: what about adding the T to the N parameter in loco-regional staging? *World J Gastroenterol* 2011; **17**: 1427-1433 [PMID: 21472100 DOI: 10.3748/wjg.v17.i11.1427]
 - 80 **Maas M**, Rutten IJ, Nelemans PJ, Lambregts DM, Cappendijk VC, Beets GL, Beets-Tan RG. What is the most accurate whole-body imaging modality for assessment of local and distant recurrent disease in colorectal cancer? A meta-analysis: imaging for recurrent colorectal cancer. *Eur J Nucl Med Mol Imaging* 2011; **38**: 1560-1571 [PMID: 21468765 DOI: 10.1007/s00259-011-1785-1]
 - 81 **Giacomobono S**, Gallicchio R, Capacchione D, Nardelli A, Gattozzi D, Lettini G, Molinari L, Mainenti P, Cammarota A, Storto G. F-18 FDG PET/CT in the assessment of patients with unexplained CEA rise after surgical curative resection for colorectal cancer. *Int J Colorectal Dis* 2013; **28**: 1699-1705 [PMID: 23846517 DOI: 10.1007/s00384-013-1747-0]
 - 82 **Storto G**, Nicolai E, Salvatore M. [18F]FDG-PET-CT for early monitoring of tumor response: when and why. *Q J Nucl Med Mol Imaging* 2009; **53**: 167-180 [PMID: 19293765]
 - 83 **Partovi S**, Kohan A, Gaeta C, Rubbert C, Vercher-Conejero JL, Jones RS, O'Donnell JK, Wojtylak P, Faulhaber P. Image quality assessment of automatic three-segment MR attenuation correction vs. CT attenuation correction. *Am J Nucl Med Mol Imaging* 2013; **3**: 291-299 [PMID: 23638340]
 - 84 **Schwenzer NF**, Schmidt H, Claussen CD. Whole-body MR/PET: applications in abdominal imaging. *Abdom Imaging* 2012; **37**: 20-28 [PMID: 22002195 DOI: 10.1007/s00261-011-9809-7]
 - 85 **Drzezga A**, Souvatzoglou M, Eiber M, Beer AJ, Fürst S, Martinez-Möller A, Nekolla SG, Ziegler S, Ganter C, Rummeny EJ, Schwaiger M. First clinical experience with integrated whole-body PET/MR: comparison to PET/CT in patients with oncologic diagnoses. *J Nucl Med* 2012; **53**: 845-855 [PMID: 22534830 DOI: 10.2967/jnumed.111.098608]
 - 86 **Quick HH**, von Gall C, Zeilinger M, Wiesmüller M, Braun H, Ziegler S, Kuwert T, Uder M, Dörfler A, Kalender WA, Lell M. Integrated whole-body PET/MR hybrid imaging: clinical experience. *Invest Radiol* 2013; **48**: 280-289 [PMID: 23442775 DOI: 10.1097/RLI.0b013e3182845a08]
 - 87 **Partovi S**, Kohan A, Paspulati RM, Ros PR, Herrmann KA. PET/MRI in Colorectal cancer. In: Carrio I, Ros P. PET/MRI Methodology and Clinical Applications. *Springer* 2014; **7**: 95-108
 - 88 **Kershah S**, Partovi S, Traugber BJ, Muzic RF, Schluchter MD, O'Donnell JK, Faulhaber P. Comparison of standardized uptake values in normal structures between PET/CT and PET/MRI in an oncology patient population. *Mol Imaging Biol* 2013; **15**: 776-785 [PMID: 23632951 DOI: 10.1007/s11307-013-0629-8]
 - 89 **Nielsen K**, Scheffler HJ, Pieters IC, van Tilborg AA, van Waesberghe JH, Oprea-Lager DE, Meijerink MR, Kazemier G, Hoekstra OS, Schreurs HW, Sietses C, Meijer S, Comans EF, van den Tol PM. The use of PET-MRI in the follow-up after radiofrequency- and microwave ablation of colorectal liver metastases. *BMC Med Imaging* 2014; **14**: 27 [PMID: 25103913 DOI: 10.1186/1471-2342-14-27]
 - 90 **Sheafor DH**, Killius JS, Paulson EK, DeLong DM, Foti AM, Nelson RC. Hepatic parenchymal enhancement during triple-phase helical CT: can it be used to predict which patients with breast cancer will develop hepatic metastases? *Radiology* 2000; **214**: 875-880 [PMID: 10715061]
 - 91 **Miles KA**, Colyvas K, Griffiths MR, Bunce IH. Colon cancer: risk stratification using hepatic perfusion CT. *Eur Radiol* 2004; **14** (Suppl 2): 129
 - 92 **Ridge JA**, Bading JR, Gelbard AS, Benua RS, Daly JM. Perfusion of colorectal hepatic metastases. Relative distribution of flow from the hepatic artery and portal vein. *Cancer* 1987; **59**: 1547-1553 [PMID: 3828954]
 - 93 **Leen E**, Goldberg JA, Robertson J, Sutherland GR, McArdle CS. The use of duplex sonography in the detection of colorectal hepatic metastases. *Br J Cancer* 1991; **63**: 323-325 [PMID: 1997115]
 - 94 **Leen E**, Goldberg JA, Robertson J, Sutherland GR, Hemingway DM, Cooke TG, McArdle CS. Detection of hepatic metastases using duplex/color Doppler sonography. *Ann Surg* 1991; **214**: 599-604 [PMID: 1953113]
 - 95 **Kopljär M**, Brkljacic B, Doko M, Horzic M. Nature of Doppler perfusion index changes in patients with colorectal cancer liver metastases. *J Ultrasound Med* 2004; **23**: 1295-1300 [PMID: 15448318]
 - 96 **Anzidei M**, Napoli A, Zaccagna F, Cartocci G, Saba L, Menichini G, Cavallo Marincola B, Marotta E, Di Mare L, Catalano C, Passariello R. Liver metastases from colorectal cancer treated with conventional and antiangiogenetic chemotherapy: evaluation with liver computed tomography perfusion and magnetic resonance diffusion-weighted imaging. *J Comput Assist Tomogr* 2011; **35**: 690-696 [PMID: 22082538 DOI: 10.1097/RCT.0b013e318230d905]
 - 97 **Meijerink MR**, van Waesberghe JH, van der Weide L, van den Tol P, Meijer S, van Kuijk C. Total-liver-volume perfusion CT using 3-D image fusion to improve detection and characterization of liver metastases. *Eur Radiol* 2008; **18**: 2345-2354 [PMID: 18491094 DOI: 10.1007/s00330-008-0996-8]
 - 98 **Kanematsu M**, Goshima S, Watanabe H, Kondo H, Kawada H, Noda Y, Moriyama N. Diffusion/perfusion MR imaging of the liver: practice, challenges, and future. *Magn Reson Med Sci* 2012; **11**: 151-161 [PMID: 23037559]
 - 99 **De Bruyne S**, Van Damme N, Smeets P, Ferdinande L, Ceelen W, Mertens J, Van de Wiele C, Troisi R, Libbrecht L, Laurent S, Geboes K, Peeters M. Value of DCE-MRI and FDG-PET/CT in the prediction of response to preoperative chemotherapy with bevacizumab for colorectal liver metastases. *Br J Cancer* 2012; **106**: 1926-1933 [PMID: 22596235 DOI: 10.1038/bjc.2012.184]
 - 100 **Ganeshan B**, Miles KA, Young RC, Chatwin CR. Texture analysis

- in non-contrast enhanced CT: impact of malignancy on texture in apparently disease-free areas of the liver. *Eur J Radiol* 2009; **70**: 101-110 [PMID: 18242909 DOI: 10.1016/j.ejrad.2007.12.005]
- 101 **Miles KA**, Ganeshan B, Griffiths MR, Young RC, Chatwin CR. Colorectal cancer: texture analysis of portal phase hepatic CT images as a potential marker of survival. *Radiology* 2009; **250**: 444-452 [PMID: 19164695 DOI: 10.1148/radiol.2502071879]
 - 102 **Rao SX**, Lambregts DM, Schnerr RS, van Ommen W, van Nijnatten TJ, Martens MH, Heijnen LA, Backes WH, Verhoef C, Zeng MS, Beets GL, Beets-Tan RG. Whole-liver CT texture analysis in colorectal cancer: Does the presence of liver metastases affect the texture of the remaining liver? *United European Gastroenterol J* 2014; **2**: 530-538 [PMID: 25452849 DOI: 10.1177/2050640614552463]
 - 103 **Ganeshan B**, Miles KA. Quantifying tumour heterogeneity with CT. *Cancer Imaging* 2013; **13**: 140-149 [PMID: 23545171 DOI: 10.1102/1470-7330.2013.0015]
 - 104 **Barash H**, Gross E, Edrei Y, Pappo O, Spira G, Vlodavsky I, Galun E, Matot I, Abramovitch R. Functional magnetic resonance imaging monitoring of pathological changes in rodent livers during hyperoxia and hypercapnia. *Hepatology* 2008; **48**: 1232-1241 [PMID: 18629804 DOI: 10.1002/hep.22394]
 - 105 **Barash H**, Gross E, Matot I, Edrei Y, Tsarfaty G, Spira G, Vlodavsky I, Galun E, Abramovitch R. Functional MR imaging during hypercapnia and hyperoxia: noninvasive tool for monitoring changes in liver perfusion and hemodynamics in a rat model. *Radiology* 2007; **243**: 727-735 [PMID: 17463135]
 - 106 **Edrei Y**, Gross E, Corchia N, Tsarfaty G, Galun E, Pappo O, Abramovitch R. Vascular profile characterization of liver tumors by magnetic resonance imaging using hemodynamic response imaging in mice. *Neoplasia* 2011; **13**: 244-253 [PMID: 21390187]
 - 107 **Edrei Y**, Freiman M, Sklair-Levy M, Tsarfaty G, Gross E, Jaskowicz L, Abramovitch R. Quantitative functional MRI biomarkers improved early detection of colorectal liver metastases. *J Magn Reson Imaging* 2014; **39**: 1246-1253 [PMID: 24006217 DOI: 10.1002/jmri.24270]
 - 108 **Seo HJ**, Kim MJ, Lee JD, Chung WS, Kim YE. Gadoxetate disodium-enhanced magnetic resonance imaging versus contrast-enhanced 18F-fluorodeoxyglucose positron emission tomography/computed tomography for the detection of colorectal liver metastases. *Invest Radiol* 2011; **46**: 548-555 [PMID: 21577131 DOI: 10.1097/RLI.0b013e31821a2163]
 - 109 **Muhi A**, Ichikawa T, Motosugi U, Sou H, Nakajima H, Sano K, Sano M, Kato S, Kitamura T, Fatima Z, Fukushima K, Iino H, Mori Y, Fujii H, Araki T. Diagnosis of colorectal hepatic metastases: comparison of contrast-enhanced CT, contrast-enhanced US, superparamagnetic iron oxide-enhanced MRI, and gadoxetic acid-enhanced MRI. *J Magn Reson Imaging* 2011; **34**: 326-335 [PMID: 21780227 DOI: 10.1002/jmri.22613]
 - 110 **Zech CJ**, Grazioli L, Jonas E, Ekman M, Niebecker R, Gschwend S, Breuer J, Jönsson L, Kienbaum S. Health-economic evaluation of three imaging strategies in patients with suspected colorectal liver metastases: Gd-EOB-DTPA-enhanced MRI vs. extracellular contrast media-enhanced MRI and 3-phase MDCT in Germany, Italy and Sweden. *Eur Radiol* 2009; **19** Suppl 3: S753-S763 [PMID: 19484243 DOI: 10.1007/s00330-009-1432-4]
 - 111 **Chen L**, Zhang J, Zhang L, Bao J, Liu C, Xia Y, Huang X, Wang J. Meta-analysis of gadoxetic acid disodium (Gd-EOB-DTPA)-enhanced magnetic resonance imaging for the detection of liver metastases. *PLoS One* 2012; **7**: e48681 [PMID: 23144927 DOI: 10.1371/journal.pone.0048681]
 - 112 **Maffione AM**, Lopci E, Bluemel C, Giammarile F, Herrmann K, Rubello D. Diagnostic accuracy and impact on management of (18)F-FDG PET and PET/CT in colorectal liver metastasis: a meta-analysis and systematic review. *Eur J Nucl Med Mol Imaging* 2015; **42**: 152-163 [PMID: 25319712 DOI: 10.1007/s00259-014-2930-4]
 - 113 **Han K**, Park SH, Kim KW, Kim HJ, Lee SS, Kim JC, Yu CS, Lim SB, Joo YS, Kim AY, Ha HK. Use of liver magnetic resonance imaging after standard staging abdominopelvic computed tomography to evaluate newly diagnosed colorectal cancer patients. *Ann Surg* 2015; **261**: 480-486 [PMID: 24866542]
 - 114 National Comprehensive Cancer Network Oncologic Guidelines. Colon cancer. Version 2. 2012. Available from: URL: <http://nccn.org>
 - 115 **Sahani D**, Mehta A, Blake M, Prasad S, Harris G, Saini S. Preoperative hepatic vascular evaluation with CT and MR angiography: implications for surgery. *Radiographics* 2004; **24**: 1367-1380 [PMID: 15371614 DOI: 10.1148/rg.245035224]
 - 116 **Therasse P**, Arbuck SG, Eisenhauer EA, Wanders J, Kaplan RS, Rubinstein L, Verweij J, Van Glabbeke M, van Oosterom AT, Christian MC, Gwyther SG. New guidelines to evaluate the response to treatment in solid tumors. European Organization for Research and Treatment of Cancer, National Cancer Institute of the United States, National Cancer Institute of Canada. *J Natl Cancer Inst* 2000; **92**: 205-216 [PMID: 10655437 DOI: 10.1093/jnci/92.3.205]
 - 117 **Catenacci DV**, Kozloff M, Kindler HL, Polite B. Personalized colon cancer care in 2010. *Semin Oncol* 2011; **38**: 284-308 [PMID: 21421118]
 - 118 **Chibaudel B**, Maindrault-Goebel F, Lledo G, Mineur L, André T, Bennamoun M, Mabro M, Artru P, Carola E, Flesch M, Dupuis O, Colin P, Larsen AK, Afchain P, Tournigand C, Louvet C, de Gramont A. Can chemotherapy be discontinued in unresectable metastatic colorectal cancer? The GERCOR OPTIMO2 Study. *J Clin Oncol* 2009; **27**: 5727-5733 [PMID: 19786657 DOI: 10.1200/JCO.2009.23.4344]
 - 119 **Chung WS**, Park MS, Shin SJ, Baek SE, Kim YE, Choi JY, Kim MJ. Response evaluation in patients with colorectal liver metastases: RECIST version 1.1 versus modified CT criteria. *AJR Am J Roentgenol* 2012; **199**: 809-815 [PMID: 22997372]
 - 120 **Schima W**, Ba-Ssalamah A, Kurtaran A, Schindl M, Gruenberger T. Post-treatment imaging of liver tumours. *Cancer Imaging* 2007; **7** Spec No A: S28-S36 [PMID: 17921098 DOI: 10.1102/1470-7330.2007.9047]

P- Reviewer: Kita K S- Editor: Ji FF
L- Editor: A E- Editor: Liu SQ



Perfusion computed tomography in renal cell carcinoma

Chandan J Das, Usha Thingujam, Ananya Panda, Sanjay Sharma, Arun Kumar Gupta

Chandan J Das, Usha Thingujam, Ananya Panda, Sanjay Sharma, Arun Kumar Gupta, Department of Radiology, All India Institute of Medical Sciences, Ansari Nagar, New Delhi 110029, India

Author contributions: Das CJ, Thingujam U and Panda A contributed equally to conception, article design, literature search, article drafting, critical revision and image preparation; Das CJ and Sharma S helped with the article concept and revision; Das CJ and Gupta AK helped in article preparation and final approval of version of article to be published.

Conflict-of-interest statement: None.

Open-Access: This article is an open-access article which was selected by an in-house editor and fully peer-reviewed by external reviewers. It is distributed in accordance with the Creative Commons Attribution Non Commercial (CC BY-NC 4.0) license, which permits others to distribute, remix, adapt, build upon this work non-commercially, and license their derivative works on different terms, provided the original work is properly cited and the use is non-commercial. See: <http://creativecommons.org/licenses/by-nc/4.0/>

Correspondence to: Dr. Chandan J Das, MD, DNB, MNAMS, Assistant Professor, Department of Radiology, All India Institute of Medical Sciences, Room No. 63, Ansari Nagar, New Delhi 110029, India. docchandan17@gmail.com
 Telephone: +91-11-26594889
 Fax: +91-11-26588663

Received: December 1, 2014
 Peer-review started: December 2, 2014
 First decision: February 7, 2015
 Revised: March 30, 2015
 Accepted: June 4, 2015
 Article in press: June 8, 2015
 Published online: July 28, 2015

Abstract

Various imaging modalities are available for the diagnosis, staging and response evaluation of patients with renal cell carcinoma (RCC). While contrast enhanced computed tomography (CT) is used as the standard of

imaging for size, morphological evaluation and response assessment in RCC, a new functional imaging technique like perfusion CT (pCT), goes down to the molecular level and provides new perspectives in imaging of RCC. pCT depicts regional tumor perfusion and vascular permeability which are indirect parameters of tumor angiogenesis and thereby provides vital information regarding tumor microenvironment. Also response evaluation using pCT may predate the size criteria used in Response Evaluation Criteria in Solid Tumors, as changes in the perfusion occurs earlier following tissue kinase inhibitors before any actual change in size. This may potentially help in predicting prognosis, better selection of therapy and more accurate and better response evaluation in patients with RCC. This article describes the techniques and role of pCT in staging and response assessment in patients with RCCs.

Key words: Angiogenesis; Anti-angiogenic therapy; Perfusion computed tomography; Renal cell carcinoma

© The Author(s) 2015. Published by Baishideng Publishing Group Inc. All rights reserved.

Core tip: Perfusion computed tomography is a functional imaging technique. It can be used to predict the histologic grade and early as well as more accurate response evaluation in renal cell carcinoma (RCC). This has the potential to help in better selection of therapy and improve prognosis in RCC.

Das CJ, Thingujam U, Panda A, Sharma S, Gupta AK. Perfusion computed tomography in renal cell carcinoma. *World J Radiol* 2015; 7(7): 170-179 Available from: URL: <http://www.wjgnet.com/1949-8470/full/v7/i7/170.htm> DOI: <http://dx.doi.org/10.4329/wjr.v7.i7.170>

INTRODUCTION

Renal cell carcinoma (RCC) is the most common primary tumor of the kidney. Hypervascularity is

an important feature of primary RCC as well as its metastases. Angiogenesis plays an important role in the growth of the primary tumor and the spread of distant metastases.

Depending on the histologic type and the stage of tumors, the treatment options vary from surgery to chemotherapy. With the advent of new anti-angiogenic agents acting at a molecular level, the treatment of RCC has undergone a paradigm shift. These drugs include sorafenib, sunitinib, pazopanib, and axitinib that target key growth factors like the vascular endothelial growth factor and tyrosine kinase, monoclonal antibody (*e.g.*, bevacizumab), and mammalian target of rapamycin inhibitors (*e.g.*, temsirolimus and everolimus).

The evaluation of the treatment response in patients on these drugs is a challenge. Because of their cytostatic nature, most of these agents produce no significant change in the size of tumor as compared to earlier agents which were cytotoxic. Thus traditional response evaluation based only on size will not be accurate in predicting actual response.

Hence there is a need for tumor evaluation with new functional imaging techniques like perfusion computed tomography (pCT) and dynamic contrast enhanced magnetic resonance imaging. These make feasible grading of the tumor, prognosticating and targeted therapy. These are predicted based on certain perfusion parameters, namely blood flow (BF), blood volume (BV), mean transit time (MTT) and permeability (PMB) which shall be dealt in detail in the subsequent paragraphs. Also different histologic types of tumors have been shown to have different perfusion parameters which will have an impact on the prognosis^[1].

PCT: PRINCIPLE

pCT is based on the temporal changes in tissue attenuation after intravenous administration of iodinated contrast media. Tissue iodine concentration determines enhancement and is an indirect reflection of tissue vascularity and vascular physiology^[2,3]. Two phases are seen in tissue enhancement based on the contrast dynamics and contrast distribution in the intravascular and extravascular compartment^[2]. Initial phase contrast enhancement is due to intravascular space distribution and lasts for approximately 40 to 60 s^[2-4]. Contrast extravasation from the intravascular to the extravascular compartment across the capillary basement membrane marks the onset of the second phase.

BF and BV determine the first phase, whereas vascular PMB to the contrast media is the main determining factor during the second phase^[2]. In pCT, images are taken in quick succession in the region of interest during these two phases. A tissue attenuation curve is plotted after recording the temporal changes in tissue attenuation. Quantification of tissue perfusion is done by applying proper mathematical modeling^[2].

Table 1 Protocol for dynamic perfusion computed tomography acquisition

No. of scans	Cycle time (s)	Accumulated time since start of scan (s)
3	3	9
9	1.5	22.5
5	3	37.5
5	6	68.0
22 (in total)		Examination time: 68

PCT: TECHNIQUE

pCT protocol consists of a baseline image acquisition without contrast enhancement. Dynamic acquisition performed sequentially after intravenous injection of contrast media follows subsequently^[2].

Unenhanced CT acquisition

An unenhanced CT scan of the upper abdomen covering the kidneys is initially performed to locate the renal lesion. It also acts as a localizer to further select the region of interest in the contrast-enhanced dynamic imaging phase. Larger coverage (8-16 cm) is currently obtained with the use of newer scanners having increased rows of detectors^[2].

Dynamic CT acquisition

Images are acquired every 3 to 5 s (Table 1) in the initial cine phase for a total of approximately 40 to 60 s during the first-pass study^[2-4]. For obtaining PMB measurements, a second phase lasting from 2 to 10 min is supplemented after the first-pass study^[2,3]. The second phase images are acquired every 10 to 20 s^[2].

In the pCT study, a predefined scan volume (80 mm for shuttle axial technique and 40 mm for cine technique) in the Z-axis is selected to cover the lesion^[5]. For lesions smaller than 20 mm, cine technique is useful. One hundred milliliters of non-ionic iodinated contrast is administered intravenously for the pCT study maintaining a flow rate of 5 mL/s followed by 40 mL of normal saline flush at the same flow rate^[5].

In cine mode acquisition, 8 contiguous sections, collimated to 5 mm, with temporal resolution of 1 s by are obtained without table movement using the following parameters: 100 Kv, 80 mAs, rotation time 0.5 s, and scan field of view of 50 cm^[5]. Whereas in shuttle-mode acquisition, 8 contiguous sections, collimated to 5 mm, with temporal resolution of 2.8 s are obtained with table movement (21 passes) and using following parameters: 100 Kv, 80 mAs, rotation time 0.4 s, and scan field of view of 50 cm^[5]. In order to include both first-pass enhancement and delayed phase, the total duration of scan is approximately 60 s. After pCT scans, a conventional contrast enhanced CT of the abdomen and thorax is performed immediately. Excretory phase CT urography may be obtained after 5 to 10 min after the contrast media injection whenever required^[5].

Table 2 Computed tomography perfusion parameters^[2-4]

Perfusion parameters	Definition	Unit	Biomarker
Regional blood flow	Blood flow per unit volume or mass of tissue	mL/100 mL per minute	Tumour vascularization
Regional tumour blood volume	Ratio of blood volume to tumour volume	mL/100 mL	Tumour vascularization
Permeability/blood flow extraction (PMB/PS/k-trans)	Rate of transfer of contrast agent from the intravascular to the extravascular compartment	mL/100 gm per minute	Vascular immaturity
Mean transit time	Average time taken to travel from artery to vein	s	Perfusion pressure
Time to peak	Time from arrival of the contrast in major arterial vessels to the peak enhancement	s	Perfusion pressure
Maximum peak intensity	Maximum increase in tissue density after contrast injection	HU	Tissue blood volume

Table 3 Perfusion computed tomography parameter values for kidney (renal cell carcinoma *vs* normal renal cortex)^[7]

	Normal renal cortex (mean \pm SD)	Renal cell carcinoma (mean \pm SD)	<i>t</i> value	<i>P</i> value
Blood flow (mL/min per 100 g)	454.32 \pm 110.90	261.96 \pm 175.86	-7.620	0.000
Blood volume (mL/100 g)	23.53 \pm 5.71	17.17 \pm 8.34	-5.193	0.000
Mean transit time (s)	3.62 \pm 1.38	7.08 \pm 3.42	7.670	0.000
Permeability (mL/min per 100 g)	63.95 \pm 18.85	25.07 \pm 13.20	-14.193	0.000

PCT: IMAGE INTERPRETATION

Post processing is done to correct for the motion artifacts and the data are analyzed at a work station. The slice showing the maximal transverse tumor diameter is chosen for further analysis. An arterial input is defined by putting a circular region-of-interest (ROI) over the abdominal aorta at the level of the renal vessels. Similarly, ROIs are also placed manually (covering 1 cm²) over the renal tumor and the normal renal cortex of the affected kidney or the contralateral kidney. Tumor ROI is placed in solid enhancing area avoiding necrosis, calcification, hemorrhage and cysts.

A tissue time attenuation curve is generated using in-built software. Perfusion parameters (BV, BF, MTT, PMB, MIP) are also calculated. The perfusion parameters are obtained and their definitions have been enumerated in Table 2.

Histogram analysis in pCT

Differentiation between the different tumor types on the basis of qualitative interpretation of contrast enhancement patterns may be possible but quantitative methods of measuring enhancement provides a higher degree of accuracy^[6]. Quantitative method is associated with less subjective variability. ROI-based method of assessing enhancement has demonstrated high accuracy in differentiating clear cell RCC (ccRCC) from papillary RCC (pRCC)^[6]. Limitations of ROI-based methods include invariability in ROI placement amongst different observers, difficulty in selecting the exact location of ROI and technical problems such as misregistration between pre- and post-contrast acquisitions^[6].

Therefore, to overcome the limitations of ROI placement, a tool that can perform automatic registration, lesion segmentation, and whole-lesion (WL) enhancement analysis is needed. Furthermore, histogram distribution has been used to discriminate ccRCC from pRCC using analysis of the WL enhancement pattern^[6].

Whole lesion parameter of third quartile enhancement has been found to have the highest accuracy (area under curve 0.98), with sensitivity of 96% and specificity of 90%^[6]. Special software is used to obtain a histogram of the voxel-based enhancement values and computation of the mean, median, and third quartile enhancement of the sorted values done. Histogram distribution parameters like kurtosis and skewness off-line are subsequently obtained from the values computed^[6].

pCT parameters in normal kidneys

Chen *et al*^[7] have reported CT perfusion values for normal renal cortex; the average BF was reported to be 454.32 mL/100 mL per minute (Figure 1). Difference between BF, BV, MTT, and PMB of normal renal cortex and RCC are shown in Table 3. Perfusion parameters in two representative cases are shown in Table 4.

pCT in renal tumours

Predicting the histologic grade: Pre-operative tumor histotyping using perfusion parameters can be used to prognosticate patients and is important in patients with small renal tumors. Chen *et al*^[7] found that mean values of BF, BV were significantly higher and mean MTT was significantly lower in ccRCC than in pRCC ($P < 0.05$ (Figures 1 and 2).

Similarly Gigli *et al*^[1] have shown a correlation between tumor histological subtype and perfusion index. Significant differences in perfusion values were found in ccRCC of different Fuhrman grades. High perfusion index corresponded with high microvessel density (MVD) while those with lower MVD showed lower perfusion indices.

Previous studies have shown that there was a significant difference in PS and MTT values of malignant lesions (ccRCCs, pRCCs, and chromophobe RCCs) and the normal renal cortex ($P < 0.001$ and $P = 0.029$, respectively) but BF and BV values did not differ

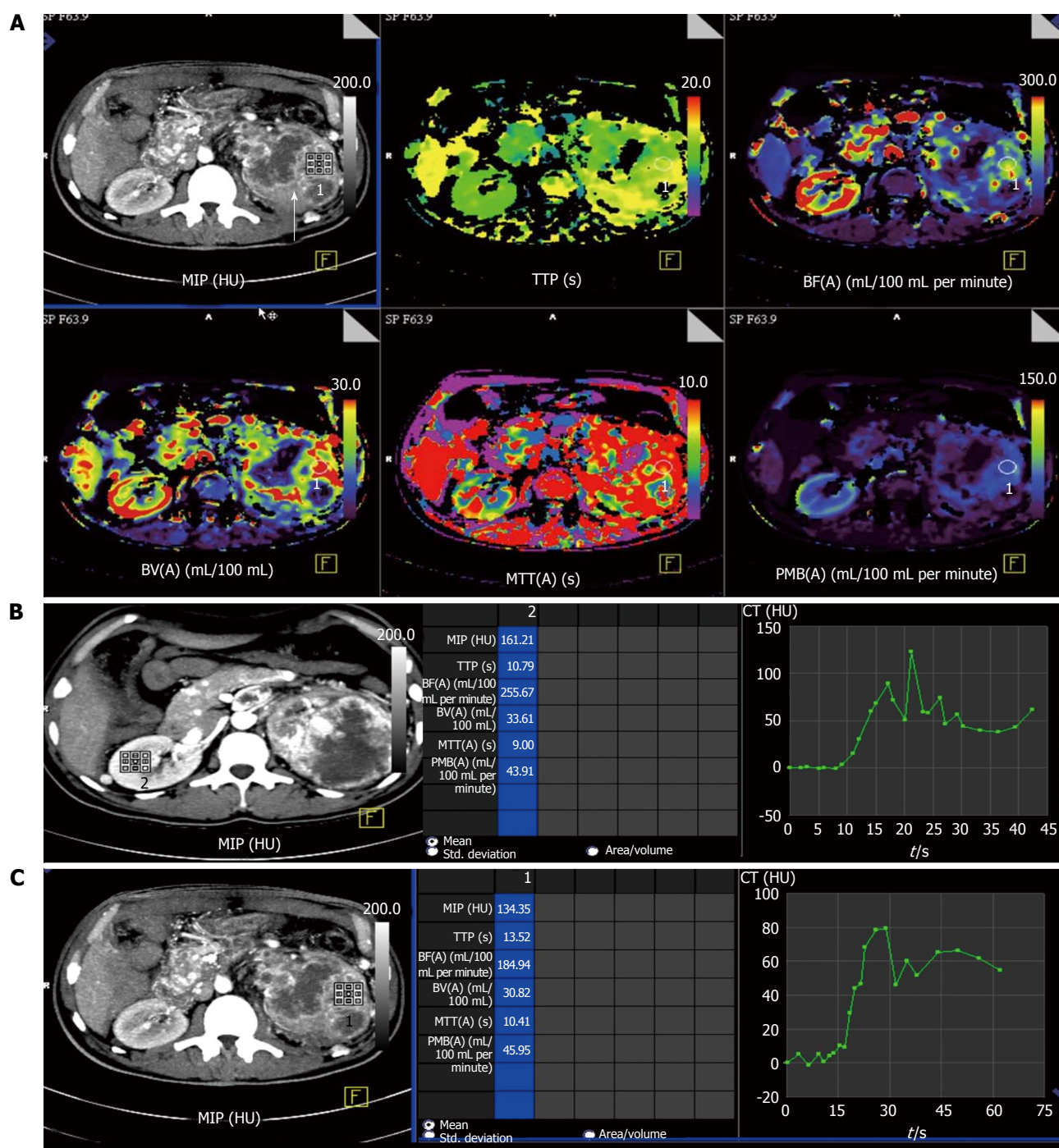


Figure 1 Perfusion computed tomography in normal renal parenchyma vs renal cell carcinoma in a 50-year-old man with left renal cell carcinoma (clear cell type). A: Contrast computed tomography (CT) images showed a large, hyperenhancing mass in left kidney with central necrosis (arrow). Colour-coded perfusion maps show various perfusion parameters in normal right kidney and diseased left kidney. Red being the region with highest perfusion parameter with purple being the least; B: Time attenuation curve and the perfusion parameters in normal right kidney. Normal renal parenchyma is seen to have high perfusion in the range of 255 mL/100 mL per minute; C: Time attenuation curve and perfusion parameters in the left renal cell carcinoma. There is delayed wash-out of contrast in the region of the tumour as depicted in the graph. MIP: Maximum peak intensity; TTP: Time to peak; BF: Blood flow; BV: Blood volume; MTT: Mean transit time; PMB: Permeability.

significantly^[8,9]. Also the permeability surface area product, MTT, and BF values were reported to be significantly lower in malignant lesions as compared with oncocytomas^[8].

BF and BV are two perfusion parameters which have been found to have significant histological correlation ($P < 0.01$) with MVD as a prognostic marker for RCCs

and the neoangiogenesis associated with RCCs^[8]. The difference in normal cortex and tumoral PS values has been found to best predict RCCs with a cutoff greater than 2.5 mL/100 g per minute having sensitivity, specificity, and accuracy of 100%, 66.67%, and 95.92%^[5]. Hence, evaluation of the different perfusion parameters can depict histologic grade of RCCs.

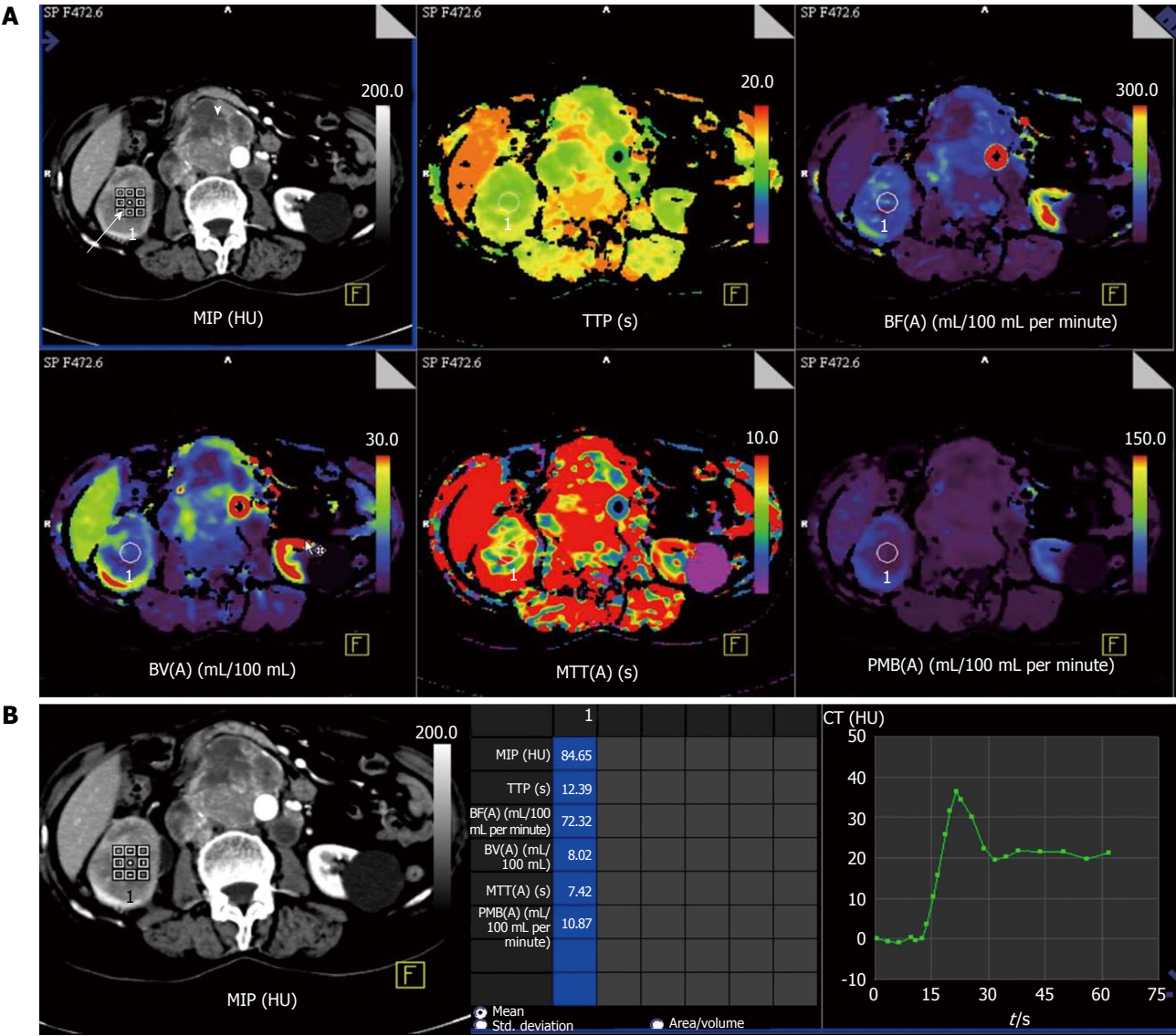


Figure 2 Perfusion computed tomography in a 63-year-old lady with right renal cell carcinoma (chromophobe type). A: Contrast computed tomography (CT) images show tumor in right kidney (white arrow) with retroperitoneal nodal metastases (arrowhead). Colour-coded perfusion maps show the perfusion parameters; B: Time attenuation curve and perfusion parameters with region-of-interest in the right renal cell carcinoma depict delayed wash-out of contrast. MIP: Maximum peak intensity; TTP: Time to peak; BF: Blood flow; BV: Blood volume; MTT: Mean transit time; PMB: Permeability.

Table 4 Response evaluation using changes in computed tomography perfusion parameters in two representative cases								
Date of study			MIP (HU)	TTP (s)	BF (mL/100 mL per minute)	BV (mL/100 mL)	MTT (s)	PMB (mL/100 mL per minute)
Case 1	2013-4-2	Normal cortex	120	11.1	202.9	31.6	8.7	47.1
		Renal tumour	134	13.5	184.9	30.8	10.4	45.95
	2013-9-11	Normal cortex	121	13.2	209	30.2	9.2	50.2
		Renal tumour	79	11.5	174	13.2	5	18.1
	2013-11-20	Normal cortex	130	10.8	229	32	9.6	45.3
		Renal tumour	42	12.3	5.7	1.2	12.4	8.2
Case 2	2013-10-23	Normal cortex	157	11.9	236	27.8	8.9	43.7
		Renal tumour	88	12.3	64.4	9.3	8.9	18.7
	2013-12-26	Normal cortex	140	15.2	170.9	29.5	10.5	42.1
		Renal tumour	82.7	14.8	60.9	7.9	8.4	13.8
	2013-8-3	Normal cortex	216	12.5	315	38	72	55.2
		Renal tumour	84.6	12.3	72.3	8	7.4	10.8

BF: Blood flow; BV: Blood volume; MTT: Mean transit time; PMB: Permeability; MIP: Maximum peak intensity; TTP: Time to peak.

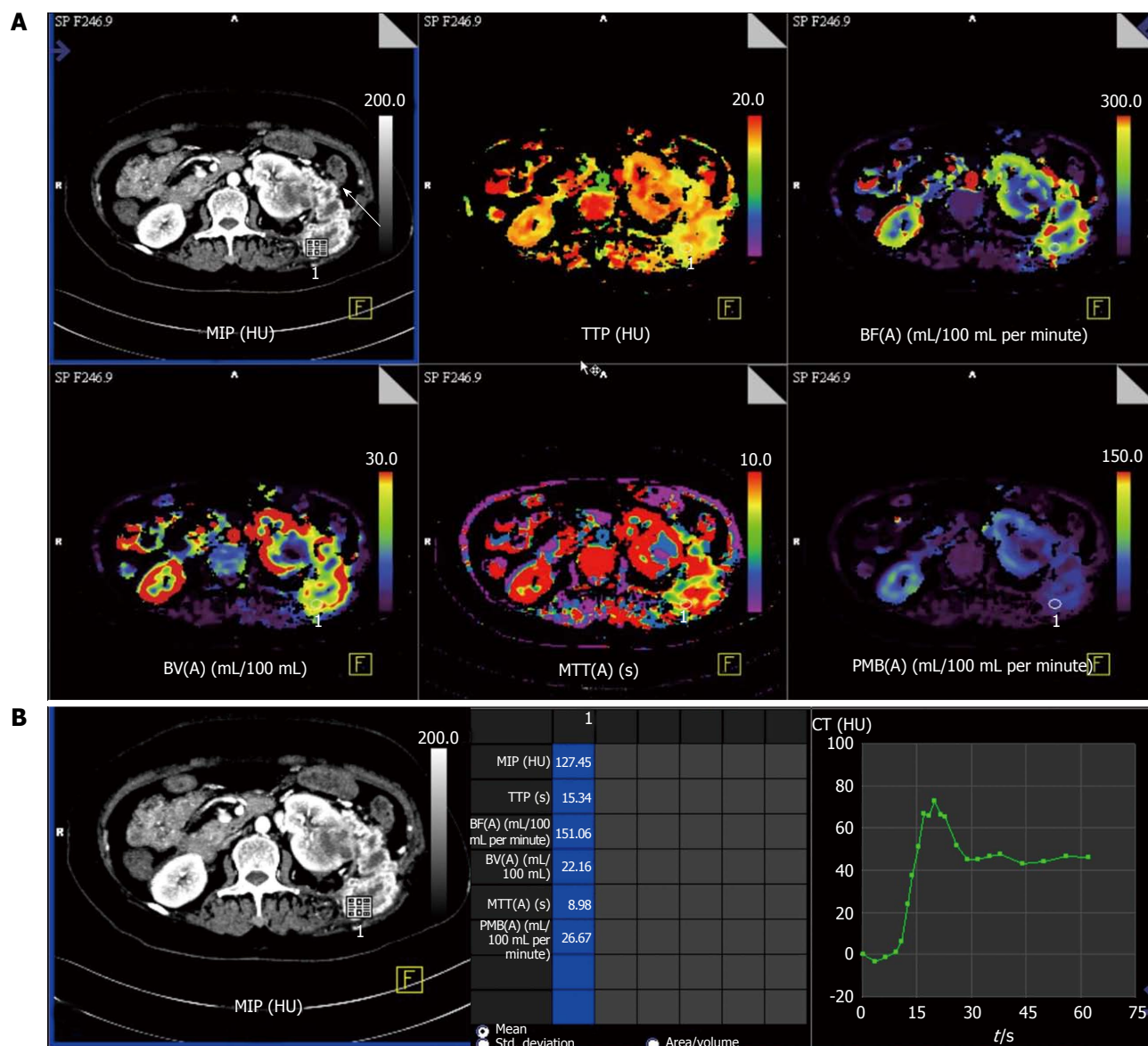


Figure 3 Perfusion computed tomography in a 55-year-old lady with metastatic left renal cell carcinoma. A: Contrast computed tomography (CT) images show heterogeneous necrotic mass in left kidney with abdominal wall metastatic deposit in left lumbar region (arrow) and colour-coded perfusion maps show the perfusion parameters; B: Time attenuation curve and perfusion parameters with region-of-interest placed in the metastatic left lumbar lesion depict delayed wash-out of contrast from the tumour deposit. MIP: Maximum peak intensity; TTP: Time to peak; BF: Blood flow; BV: Blood volume; MTT: Mean transit time; PMB: Permeability.

Response evaluation with anti-angiogenic therapy:

Predicting response assessment with anti-angiogenic therapy can be done with pCT (e.g., colorectal)^[10]. It is known that growth of primary tumor as well as seeding of distant metastasis in patients with renal tumors requires angiogenesis. By inhibiting angiogenesis, it is possible to target both the primary tumor as well as metastases.

The role of several antiangiogenic therapies in RCC are currently being evaluated in clinical trials^[11-14]. However, these anti-angiogenic therapies are predominantly cytostatic in action rather than cytotoxic and induce disease stabilization rather than tumor regression (Figures 3-5). Thereby, traditional response assessment based on size criteria by using the Response Evaluation Criteria in Solid Tumors (RECIST) is rendered

inadequate for follow-up and prognostication of patients on anti-angiogenic therapy. In such instances, functional evaluation with pCT can play a major role. There are few studies highlighting the role of pCT for assessing effect of antiangiogenesis^[15-17].

Significant differences in pCT parameters have been described between treated tumors and control tumors in a rat model by Kan *et al.*^[16]. There was significant difference in these parameters after interventional therapy as compared with the pre-therapy in an investigation in a rabbit model^[17].

Maksimovic *et al.*^[18] in their study using tyrosine kinase inhibitor sorafenib found that perfusion parameters changes appear much earlier before changes in size during therapy. Also early disease progression identification seen as new areas of tumour perfusion

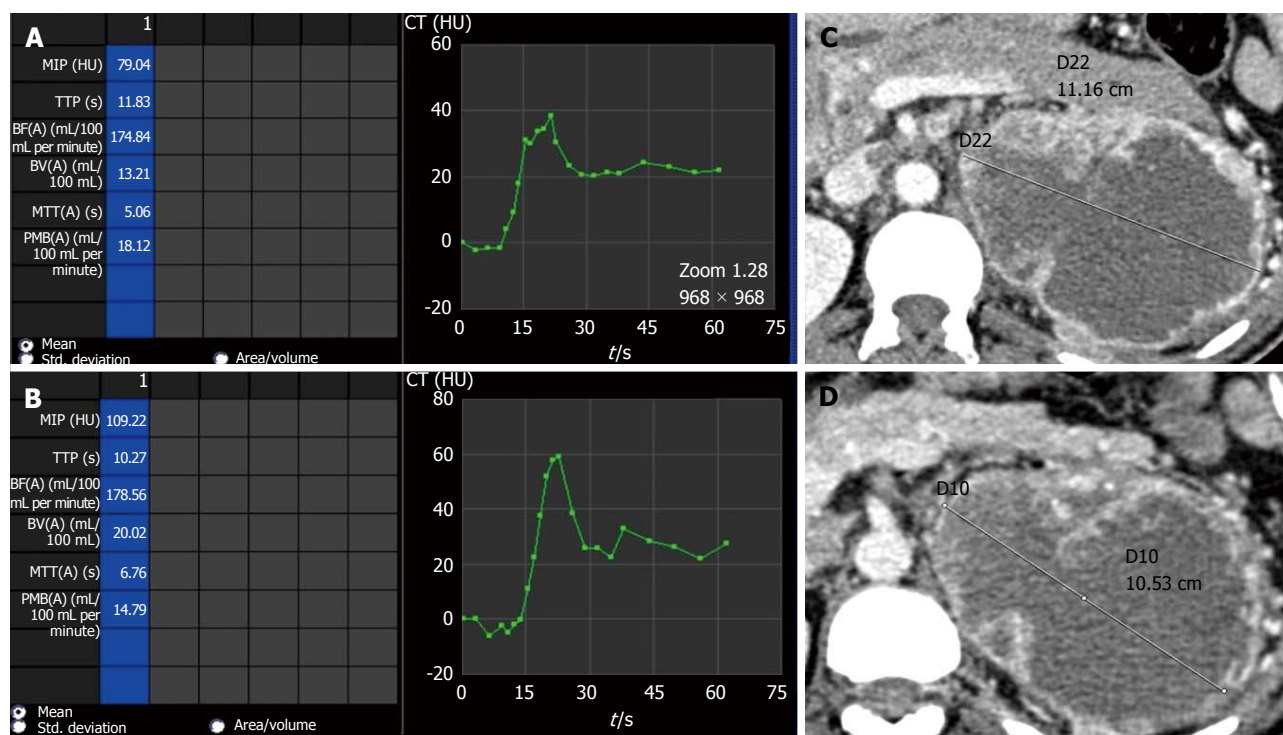


Figure 4 Perfusion parameters vs size evaluation in depicting partial response. Comparison of perfusion parameters in a case of left side clear cell renal cell carcinoma after start of anti-angiogenic therapy. Follow-up scan at 6 mo interval (B) showed at 6 mo interval shows decrease in permeability as compared to baseline scan (A) suggestive of partial response. However, no change in size of lesion noted between baseline (C) and follow-up (D) scans which would have been labelled as stable disease. MIP: Maximum peak intensity; TTP: Time to peak; BF: Blood flow; BV: Blood volume; MTT: Mean transit time; PMB: Permeability; CT: Computed tomography.

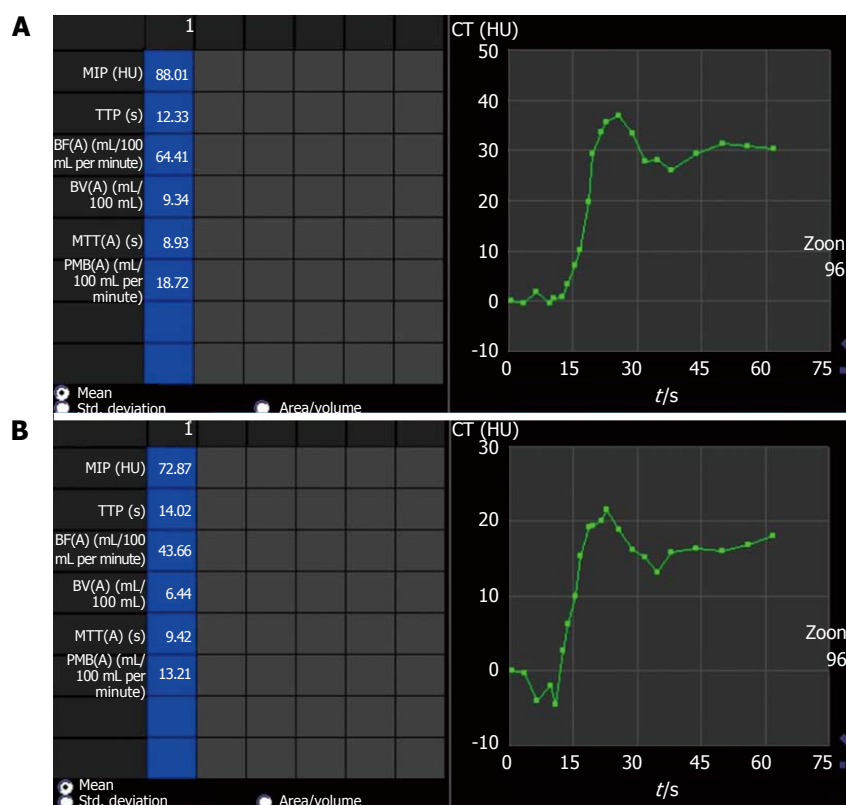


Figure 5 Perfusion parameters showing partial response with anti-angiogenic therapy. Comparison of perfusion parameters in right side chromophobe renal cell carcinoma (same patient as shown in Figure 2) after start of anti-angiogenic therapy shows partial response as permeability (PMB) in follow-up scan (B) at 6 mo interval decreased compared to baseline scan (A). The PMB measured 18.72 mL/100 mL per minute at baseline (A) while in follow-up scan (B), PMB was 13.2 mL/100 mL per minute. There was no interval change in lesion size and would have been labeled as stable disease in absence of perfusion parameters. MIP: Maximum peak intensity; TTP: Time to peak; BF: Blood flow; BV: Blood volume; MTT: Mean transit time; CT: Computed tomography.

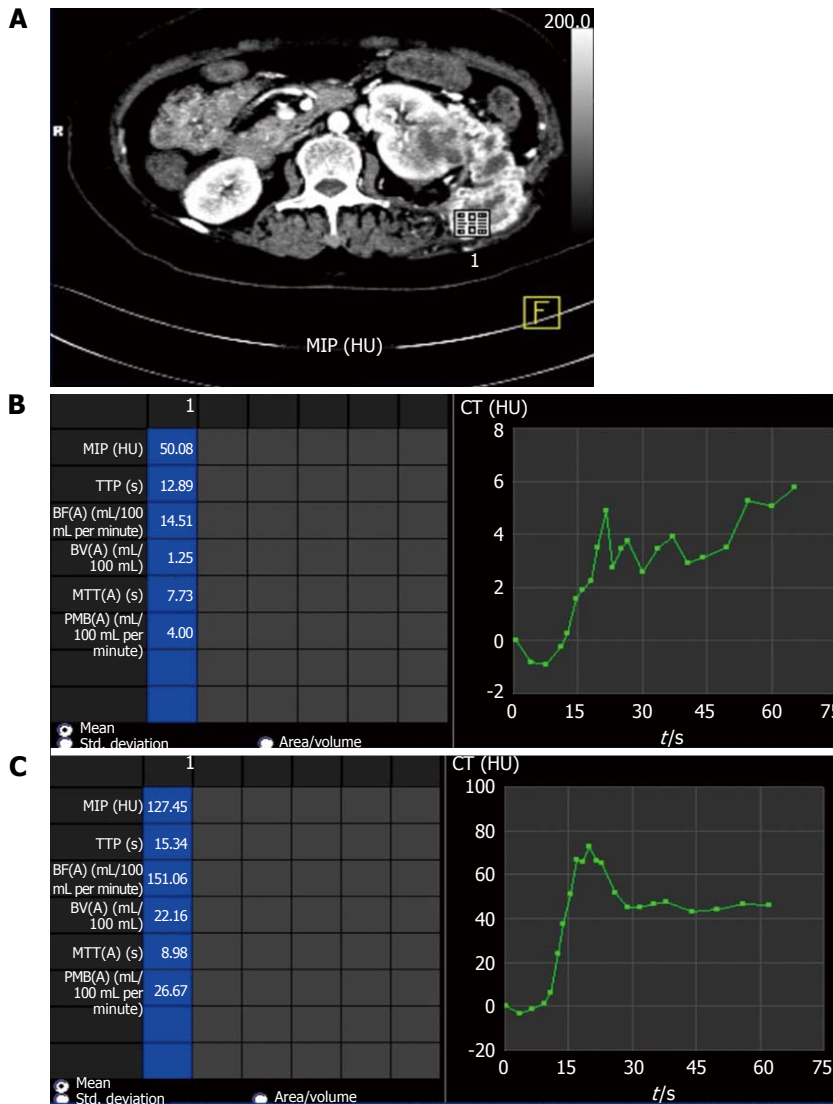


Figure 6 Perfusion parameters showing progressive disease with anti-angiogenic therapy. Comparison of perfusion parameters in left metastatic renal cell carcinoma (A) after start of anti-angiogenic therapy at 6 mo interval shows progressive disease as permeability (PMB) at baseline scan (B) was 4.00 mL/10 mL per minute which increased to 26.67 mL/100 mL per minute in follow-up scan (C). There was also increase in size and extent of lesions during this interval (not shown). MIP: Maximum peak intensity; TTP: Time to peak; BF: Blood flow; BV: Blood volume; MTT: Mean transit time; CT: Computed tomography.

would enable clinicians to change therapy. A targeted biopsy and therapy by identification of the specific area at an early stage can be performed^[19].

Perfusion parameters can also be utilized to prognosticate response to therapy. Patients responding to antiangiogenic therapy had higher baseline values of BF and BV than in those patients whose perfusion parameters remained stable throughout follow-up^[20].

Significant decrease in BF, BV and PMB can be seen in those patients responding to antiangiogenic therapy (case 1 in Table 4) (Figures 3 and 4) while those showing progression showed increase in these perfusion parameters over serial follow-up (case 2 in Table 4) (Figure 5).

Evaluation of metastases: Metastases are commonly seen in RCCs. Most are hematogenous and are highly vascular. Amongst the different histologic subtypes,

ccRCCs have the highest risk of developing metastatic disease and is seen in more than 90% of cases^[21]. Since maximum anatomic coverage during pCT is limited, hence evaluation of distant metastasis is challenging considering the increasing radiation burden with increase in the region covered. However, evaluation of RCC metastases is made possible in most cases because of the characteristic distribution of these metastases in lung bases, liver, adrenal glands, pancreas, retroperitoneal lymph nodes (Figure 2) and lumbar fossa (Figure 6)^[22]. The renal metastases show similar contrast enhancement as the parent tumor and may be evaluated for treatment response by using pCT.

Pitfalls of pCT

As true for any imaging technique, pCT also has certain technical limitations. These include high radiation burden as shown in Table 5 because of the repetitive scans

Table 5 Comparison of the acquisition parameters and dose in dynamic acquisition of perfusion computed tomography and normal contrast enhanced computed tomography chest and abdomen in our institute

	Dynamic acquisition	Chest and abdomen scan (routine)
Exposure time (s)	33	14.24
Scan length (mm)	155	655
Collimation (mm)	1.2	0.6
KVp	100	100
Ma	523	211
CTDI vol (mGy)	180.1	7.2
DLP (mGycm)	2789.69	458.68

CTDI vol: Computed tomography dose index volumetric; DLP: Dose length product.

acquired over a period of time and limited anatomic coverage. As the scan has to be repeated within a short span of time, the actual anatomic length that can be covered is limited (maximum up to about 20 cm). This imposes a limitation on the evaluation of distant metastases which may be present in such patients.

CONCLUSION

pCT is an evolving imaging modality which provides deeper insights into the molecular behavior of tumor angiogenesis and thereby facilitating targeted therapy. It has revolutionized oncologic imaging by prognosticating and evaluating therapy response at an earlier stage. Other potential benefits include identifying tumor histological subtype and predicting potentially aggressive tumors which can help clinicians to better plan the therapy of patients. As an emerging technique, pCT is currently used in evaluation of malignancies of different body parts such as kidneys, brain, lung, liver, pancreas and colon. In the future, pCT is likely to become the *in vivo* biomarker for tumor behavior and response evaluation in malignant lesions of different body parts.

REFERENCES

- Gigli F, Zattoni F, Zamboni G, Valotto C, Bernardin L, Mucelli RP, Zattoni F. [Correlation between pathologic features and perfusion CT of renal cancer: a feasibility study]. *Urologia* 2010; **77**: 223-231 [PMID: 21234864]
- Miles KA. Tumour angiogenesis and its relation to contrast enhancement on computed tomography: a review. *Eur J Radiol* 1999; **30**: 198-205 [PMID: 10452718 DOI: 10.1016/S0720-048X(99)00012-1]
- Miles KA, Griffiths MR. Perfusion CT: a worthwhile enhancement? *Br J Radiol* 2003; **76**: 220-231 [PMID: 12711641 DOI: 10.1259/bjr/13564625]
- Miles KA. Functional CT imaging in oncology. *Eur Radiol* 2003; **13** Suppl 5: M134-M138 [PMID: 14989624 DOI: 10.1016/S0959-8049(02)00386-6]
- Mazzei FG, Mazzei MA, Cioffi Squitieri N, Pozzessere C, Righi L, Cirigliano A, Guerrini S, D'Elia D, Ambrosio MR, Barone A, del Vecchio MT, Volterrani L. CT perfusion in the characterisation of renal lesions: an added value to multiphasic CT. *Biomed Res Int* 2014; **2014**: 135013 [PMID: 25184133 DOI: 10.1155/2014/135013]
- Chandarana H, Rosenkrantz AB, Mussi TC, Kim S, Ahmad AA, Raj SD, McMenamy J, Melamed J, Babb JS, Kiefer B, Kiraly AP. Histogram analysis of whole-lesion enhancement in differentiating clear cell from papillary subtype of renal cell cancer. *Radiology* 2012; **265**: 790-798 [PMID: 23175544 DOI: 10.1148/radiol.12111281]
- Chen Y, Zhang J, Dai J, Feng X, Lu H, Zhou C. Angiogenesis of renal cell carcinoma: perfusion CT findings. *Abdom Imaging* 2010; **35**: 622-628 [PMID: 19763683 DOI: 10.1007/s00261-009-9565-0]
- Chen C, Liu Q, Hao Q, Xu B, Ma C, Zhang H, Shen Q, Lu J. Study of 320-slice dynamic volume CT perfusion in different pathologic types of kidney tumor: preliminary results. *PLoS One* 2014; **9**: e85522 [PMID: 24465588 DOI: 10.1371/journal.pone.0085522]
- Reiner CS, Roessle M, Thiesler T, Eberli D, Klotz E, Frauenfelder T, Sulser T, Moch H, Alkadhi H. Computed tomography perfusion imaging of renal cell carcinoma: systematic comparison with histopathological angiogenic and prognostic markers. *Invest Radiol* 2013; **48**: 183-191 [PMID: 23328912 DOI: 10.1097/RLI.0b013e31827c63a3]
- Sahani DV, Kalva SP, Hamberg LM, Hahn PF, Willett CG, Saini S, Mueller PR, Lee TY. Assessing tumor perfusion and treatment response in rectal cancer with multisection CT: initial observations. *Radiology* 2005; **234**: 785-792 [PMID: 15734934 DOI: 10.1148/radiol.2343040286]
- Dhanabal M, Ramchandran R, Volk R, Stillman IE, Lombardo M, Iruela-Arispe ML, Simons M, Sukhatme VP. Endostatin: yeast production, mutants, and antitumor effect in renal cell carcinoma. *Cancer Res* 1999; **59**: 189-197 [PMID: 9892206]
- Morita T, Shinohara N, Tokue A. Antitumour effect of a synthetic analogue of fumagillin on murine renal carcinoma. *Br J Urol* 1994; **74**: 416-421 [PMID: 7529632 DOI: 10.1111/j.1464-410X.1994.tb00415.x]
- Fujioka T, Hasegawa M, Ogiu K, Matsushita Y, Sato M, Kubo T. Antitumor effects of angiogenesis inhibitor 0-(chloroacetyl-carbamoyl) fumagillol (TNP-470) against murine renal cell carcinoma. *J Urol* 1996; **155**: 1775-1778 [PMID: 8627882 DOI: 10.1016/S0022-5347(01)66196-2]
- Stadler WM, Kuzel T, Shapiro C, Sosman J, Clark J, Vogelzang NJ. Multi-institutional study of the angiogenesis inhibitor TNP-470 in metastatic renal carcinoma. *J Clin Oncol* 1999; **17**: 2541-2545 [PMID: 10561320]
- Koukourakis MI, Mavanis I, Kouklakis G, Pitiakoudis M, Minopoulos G, Manolas C, Simopoulos C. Early antivascular effects of bevacizumab anti-VEGF monoclonal antibody on colorectal carcinomas assessed with functional CT imaging. *Am J Clin Oncol* 2007; **30**: 315-318 [PMID: 17551312 DOI: 10.1097/01.coc.0000258119.90805.ca]
- Kan Z, Phongkitkarun S, Kobayashi S, Tang Y, Ellis LM, Lee TY, Charnsangavej C. Functional CT for quantifying tumor perfusion in antiangiogenic therapy in a rat model. *Radiology* 2005; **237**: 151-158 [PMID: 16183931 DOI: 10.1148/radiol.2363041293]
- Zhang J, Wang R, Lou H, Zou Y, Zhang M. Functional computed tomographic quantification of angiogenesis in rabbit VX2 soft-tissue tumor before and after interventional therapy. *J Comput Assist Tomogr* 2008; **32**: 697-705 [PMID: 18830097 DOI: 10.1097/RCT.0b013e31815b7dcf]
- Maksimovic O, Schraml C, Hartmann JT, Bitzer M, Claussen CD, Pintoff J, Horger M. Evaluation of response in malignant tumors treated with the multitargeted tyrosine kinase inhibitor sorafenib: a multitechnique imaging assessment. *AJR Am J Roentgenol* 2010; **194**: 5-14 [PMID: 20028898 DOI: 10.2214/AJR.09.2744]
- Sabir A, Schor-Bardach R, Wilcox CJ, Rahmanuddin S, Atkins MB, Kruskal JB, Signoretti S, Raptopoulos VD, Goldberg SN. Perfusion MDCT enables early detection of therapeutic response to antiangiogenic therapy. *AJR Am J Roentgenol* 2008; **191**: 133-139 [PMID: 18562736 DOI: 10.2214/AJR.07.2848]
- Fournier LS, Oudard S, Thiam R, Trinquart L, Banu E, Medioni J, Balvay D, Chatellier G, Fria G, Cuenod CA. Metastatic renal

- carcinoma: evaluation of antiangiogenic therapy with dynamic contrast-enhanced CT. *Radiology* 2010; **256**: 511-518 [PMID: 20551183 DOI: 10.1148/radiol.10091362]
- 21 **Motzer RJ**, Bacik J, Mariani T, Russo P, Mazumdar M, Reuter V. Treatment outcome and survival associated with metastatic renal cell carcinoma of non-clear-cell histology. *J Clin Oncol* 2002; **20**: 2376-2381 [PMID: 11981011 DOI: 10.1200/JCO.2002.11.123]
- 22 **Bianchi M**, Sun M, Jeldres C, Shariat SF, Trinh QD, Briganti A, Tian Z, Schmitges J, Graefen M, Perrotte P, Menon M, Montorsi F, Karakiewicz PI. Distribution of metastatic sites in renal cell carcinoma: a population-based analysis. *Ann Oncol* 2012; **23**: 973-980 [PMID: 21890909 DOI: 10.1093/annonc/mdr362]

P- Reviewer: Cerwenka HR, Chen F, Nouh MR

S- Editor: Tian YL **L- Editor:** A **E- Editor:** Liu SQ



Isolated renal hydatid presenting as a complex renal lesion followed by spontaneous hydatiduria

Anil Bhaya, Archana P Shinde

Anil Bhaya, Department of Radio Diagnosis, Apple Hospitals and Research Institute Ltd., Kolhapur 416001, India

Archana P Shinde, Department of Pathology, Apple Hospitals and Research Institute Ltd., Kolhapur 416001, India

Author contributions: Bhaya A contributed to concept, design, preparation of manuscript, literature search and final review; Shinde AP contributed to patient diagnosis, provided diagnostic inputs.

Institutional review board statement: As this was an outpatient and study observational case report on only one patient hence IRB approval was not obtained.

Informed consent statement: All involved subjects have provided their written/verbal consent for performance of all diagnostic studies and inclusion in this case report. The subject has been made aware that all identifying data has been removed and kept confidential.

Conflict-of-interest statement: The authors declare no financial, professional or personal conflict of interest.

Open-Access: This article is an open-access article which was selected by an in-house editor and fully peer-reviewed by external reviewers. It is distributed in accordance with the Creative Commons Attribution Non Commercial (CC BY-NC 4.0) license, which permits others to distribute, remix, adapt, build upon this work non-commercially, and license their derivative works on different terms, provided the original work is properly cited and the use is non-commercial. See: <http://creativecommons.org/licenses/by-nc/4.0/>

Correspondence to: Dr. Anil Bhaya, MD, DNB, CCST, Senior Consultant and HOD Advanced Imaging, Department of Radio Diagnosis, Apple Hospitals and Research Institute Ltd., 525/E, Vyapari Peth, Shahupuri, Kolhapur 416001, Maharashtra, India. anilbhaya@hotmail.com
 Telephone: +91-231-2651207
 Fax: +91-231-2654850

Received: February 26, 2015
 Peer-review started: February 27, 2015
 First decision: March 20, 2015

Revised: April 14, 2015

Accepted: May 7, 2015

Article in press: May 8, 2015

Published online: July 28, 2015

Abstract

Echinococcosis is a zoonotic disease. Liver is the most common site of involvement. Renal involvement is seen in 2% to 3% of patients. Computed tomography findings in renal hydatid typically include: a cyst with thick or calcified wall, unilocular cyst with detached membrane, a multiloculated cyst with mixed internal density and daughter cysts with lower density than maternal matrix. Rarely type IV hydatid cysts may mimic hypovascular renal cell carcinoma. We report a case of previously asymptomatic middle aged female who presented with mild intermittent pain and a complex renal lesion on imaging which was considered to be a hypovascular renal carcinoma or urothelial neoplasm. However, by serendipity, the patient had spontaneous hydatiduria and later was definitively diagnosed and stented. Hydatid disease should always be considered amongst the top differential diagnosis of an isolated "complex" renal lesion which remains indeterminate on imaging.

Key words: Hydatidoses; Echinococcosis; Hydatiduria; Kidney diseases; Cystic; Hydatid; Renal

© **The Author(s) 2015.** Published by Baishideng Publishing Group Inc. All rights reserved.

Core tip: Renal hydatid is generally secondary to disseminated hydatidoses or associated with hepatic involvement. Isolated renal involvement is far less common and reported in less than 5% of all hydatid cases. Without appropriate history a subset of renal hydatid, especially type 4 cyst may simulate cystic renal/urothelial neoplasm or other complex cystic lesions

such as abscess. Radiologists must harbour a high index of suspicion and look for subtle imaging signs such as calcification and non enhancing "solid" component to include this diagnosis in the differential of complex renal lesion. Absence of relevant history or hepatic involvement should not prevent diagnosticians from entertaining this rare diagnosis.

Bhaya A, Shinde AP. Isolated renal hydatid presenting as a complex renal lesion followed by spontaneous hydatiduria. *World J Radiol* 2015; 7(7): 180-183 Available from: URL: <http://www.wjgnet.com/1949-8470/full/v7/i7/180.htm> DOI: <http://dx.doi.org/10.4329/wjr.v7.i7.180>

INTRODUCTION

Hydatid disease is mainly caused by *Echinococcus granulosus*^[1]. It often manifests as a slow growing cystic lesion. We report a case of renal hydatid disease suspicious for complex cyst/urothelial neoplasm on computed tomography (CT) scan. The patient was extensively investigated and later presented with spontaneous hydatiduria.

CASE REPORT

A 42-year-old female patient, resident of central India presented with mild right lumbar pain over one month. There was no dysuria, vomiting or fever. Routine laboratory investigations were within normal range except for urinary pus cells (10-12/hpf). Ultrasonography (USG) revealed a complex hetero-echoic lesion in the right kidney (Figure 1).

CT scan revealed a poorly demarcated lobulated, isodense lesion on plain images becoming better delineated on contrast study and measuring 2.2 (craniocaudal) cm × 2.8 (anteroposterior) cm × 3.5 (transverse) cm within interpolar region. The lesion exhibited few small irregular calcific foci and mild contrast enhancement. In addition, a hypo-attenuating, non-enhancing cystic area was noted adjacent to the lesion (Figure 2).

The right kidney revealed delayed contrast excretion. The previously noted cystic component did not opacify on the delayed scan. The left kidney was normal. The ureters and bladder were normal (Figure 3).

This was provisionally diagnosed as renal abscess possibly tubercular. The differential diagnosis of urothelial neoplasm was communicated to the referring general physician and urological consultation was strongly recommended.

A few days later she reported passage of fleshy/mucoid matter per urethra which she collected in a container. These were submitted for histopathological analysis. In view of high index of suspicion of a neoplastic lesion, the patient underwent ureteroscopy following which a double J stent was placed. Urine did not reveal

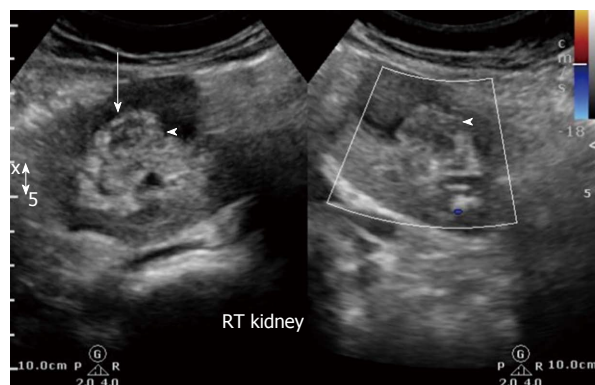


Figure 1 Initial ultrasound image reveals heteroechoic indeterminate renal sinus/renal pelvic lesion (white arrow). Doppler revealed negligible vascularity.

any malignant cells. The patient improved clinically and was discharged on a course of antibiotics.

Histopathology

Gross examination: Multiple flat membranous pieces, the largest measuring 2 cm × 1 cm × 0.3 cm. These were greyish white, translucent and soft with smooth surfaces (Figure 4).

Microscopic examination: Lamellated layer with focal calcification and occasional brood capsules consistent with hydatid cyst (Figure 5).

Follow up

Serological test for *Echinococcus* antibody was done and reported as positive. The patient remained asymptomatic. Follow up USG a month later revealed resolution of the lesion. The right kidney appeared normal without hydronephrosis (Figure 6). The left kidney and bladder were normal. No lesions were detected in the liver or spleen. The chest radiograph was unremarkable.

DISCUSSION

Echinococcosis is a zoonotic disease and is endemic in Mediterranean and other sheep rearing countries. However, due to increasing travel and tourism it may be found even in developed countries. In India, annual incidence of Hydatid disease per 100000 persons vary from 1 to 200^[1]. The liver is most common site of involvement^[2]. Renal involvement is seen in 2% to 3%^[2,3].

Gharbi *et al*^[4], classified hydatid cysts based upon sonographic morphology into five types (Table 1)^[5].

Type 4 hydatid cysts have heterogeneous appearance similar to pseudotumor. CT scan is reportedly a problem solving modality in these cases especially as it is sensitive to calcifications and enhancement of the cyst wall^[6].

Imaging spectrum of CT Renal hydatid varies and depends on stage of cyst. Typical CT findings for renal hydatidosis include a cyst with thick or calcified wall, a unilocular cyst with detached membrane, a multiloculated cyst with mixed internal density and daughter cysts with lower density than maternal matrix^[4,6].

Despite multimodality imaging, in a subset of



Figure 2 Composite of non contrast axial MDCT-post contrast corticomedullary and post contrast nephrographic phases reveals poorly enhancing isodense lesion within the renal pelvis exhibiting calcific specks (white arrow) and hypo-attenuating lesion along its lateral aspect (red arrows). Subtle thickening of the urothelial walls is present.



Figure 3 Delayed oblique coronal multiplanar reformat MDCT image shows the lesion as a filling defect within the collecting system. The lesion and laterally placed cortical cyst are inseparable. Additionally, persistent nephrogram is noted.

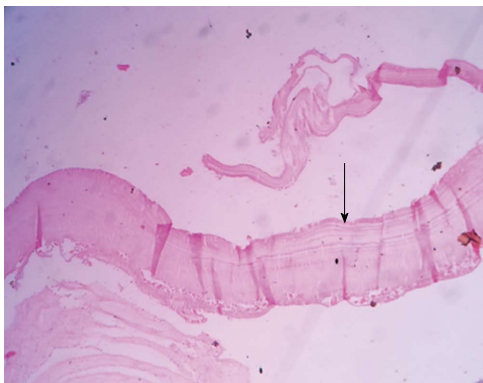


Figure 5 Microscopy (magnification 100 ×) revealed characteristic hydatid lamellated layer (arrow) with occasional brood capsules.

patients, no definitive diagnosis can be made and the differential diagnosis often includes infected renal cysts, abscess, pyonephrosis and neoplasms^[7,8]. Rarely Type IV hydatid cysts may mimic hypo vascular renal cell carcinoma^[9].

On the other hand, in endemic countries, unusual neoplasms such as mucinous cystadenoma/carcinoma may be misdiagnosed as renal hydatid^[10].

Hydatiduria accompanies 10%-20% of cases of renal hydatidoses and is basically microscopic. Gross



Figure 4 Photograph of the fleshy membranes passed spontaneously by the patient few days after ureteroscopy.

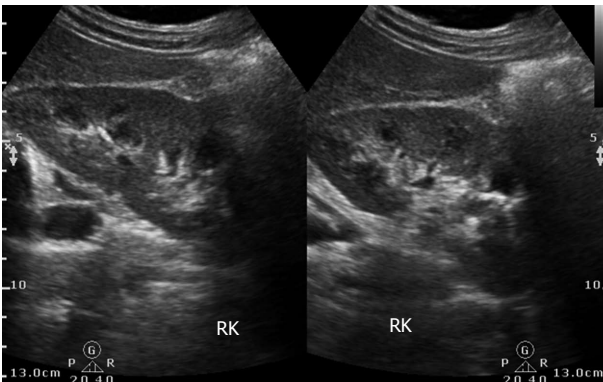


Figure 6 Follow up ultrasound revealed normal right kidney.

Table 1 Sonographic appearance of hydatid cysts in Gharbi classification^[5]

Type I	Well-defined, purely anechoic lesions that may be indistinguishable from simple renal cysts. Multiple echogenic foci due to hydatid sands may be seen in the cyst (22%)
Type II	Focal or diffuse detachment of the inner germinal layer results in a floating membrane inside the cyst (4%)
Type III	Multiseptated cysts with multiple daughter cysts (54%)
Type IV	Heterogeneous, solid appearance with infolded membranes, and internal echoes (12%)
Type V	Solid appearance, calcifications in the cyst wall, and germinative membranes (8%)

passage of hydatid cysts in urine though near diagnostic is rather uncommon and infrequently reported. We came across only two reports of gross hydatiduria in the Indian scenario - one with extensive liver and renal hydatid while the other revealed cystic renal lesion following investigation for hydatiduria. Both did not report any dilemma on imaging unlike our case^[11,12].

Histologically, Hydatid cyst comprises of pericyst or fibrous layer, middle lamellated membrane and inner germinal layer which produces scolices. In patients with ruptured cysts and hydatiduria the membranes do not reveal pericyst^[12].

Isolated renal hydatid involvement presents a further diagnostic challenge (as occurred in our patient). In our opinion, hydatid cyst should always be considered in the differential diagnosis of isolated complex cystic renal lesion. Absence of relevant history or hepatic involvement should not prevent diagnosticians from entertaining this rare diagnosis.

Renal hydatid may present with unusual imaging characteristics, resembling complex cyst or hypovascular solid-cystic neoplasm. This is particularly relevant in non-endemic countries wherein the Radiologists may not be aware of these unusual imaging features resulting in delayed and/or misdiagnosis.

COMMENTS

Case characteristics

Middle aged lady with non colicky right lumbar pain.

Clinical diagnosis

Neither tenderness nor any mass felt.

Differential diagnosis

Chronic renal infection, renal stone disease or occult neoplasm.

Laboratory diagnosis

Urine analysis revealed mild pyuria suggestive of urinary tract infection.

Imaging diagnosis

Ultrasound and computed tomography scan suspicious for urothelial cystic neoplasm.

Pathological diagnosis

Histopathology and microscopy suggestive of ruptured hydatid cyst.

Treatment

Albendazole 15 mg/kg per day for 28 d followed by 2 wk interval and repeated total three cycles.

Related reports

Enzyme-linked immunosorbent assay ELISA for detection of anti-Echinococcus antibodies (immunoglobulin G) was positive.

Peer-review

This is an interesting case.

REFERENCES

- 1 **Eckert J**, Deplazes P. Biological, epidemiological, and clinical aspects of echinococcosis, a zoonosis of increasing concern. *Clin Microbiol Rev* 2004; **17**: 107-135 [PMID: 14726458 DOI: 10.1128/CMR.17.1.107-135.2004]
- 2 **Silber SJ**, Moyad RA. Renal echinococcus. *J Urol* 1972; **108**: 669-672 [PMID: 5081694]
- 3 **Buckley RJ**, Smith S, Herschorn S, Comisarow RH, Barkin M. Echinococcal disease of the kidney presenting as a renal filling defect. *J Urol* 1985; **133**: 660-661 [PMID: 3981719]
- 4 **Gharbi HA**, Hassine W, Brauner MW, Dupuch K. Ultrasound examination of the hydatid liver. *Radiology* 1981; **139**: 459-463 [PMID: 7220891 DOI: 10.1148/radiology]
- 5 **Zmerli S**, Ayed M, Horchani A, Chami I, El Ouakdi M, Ben Slama MR. Hydatid cyst of the kidney: diagnosis and treatment. *World J Surg* 2001; **25**: 68-74 [PMID: 11213158]
- 6 **Pedrosa I**, Saiz A, Arrazola J, Ferreirós J, Pedrosa CS. Hydatid disease: radiologic and pathologic features and complications. *Radiographics* 2000; **20**: 795-817 [PMID: 10835129 DOI: 10.1148/radiographics.20.3.g00ma06795]
- 7 **Turgut AT**, Altin L, Topçu S, Kılıçoğlu B, Aliinok T, Kaptanoğlu E, Karademir A, Koşar U. Unusual imaging characteristics of complicated hydatid disease. *Eur J Radiol* 2007; **63**: 84-93 [PMID: 17275238 DOI: 10.1016/j.ejrad.2007.01.001]
- 8 **Horchani A**, Noura Y, Kbaier I, Attiaoui F, Zribi AS. Hydatid cyst of the kidney. A report of 147 controlled cases. *Eur Urol* 2000; **38**: 461-467 [PMID: 11025387]
- 9 **Nouira K**, Nouira Y, Belhiba H, Mekni A, Menif E, Horchani A. A misleading renal tumour. *Tunis Med* 2007; **85**: 535-536 [PMID: 17644913]
- 10 **Sonmez FC**, Esen HH, Tavlı L, Kılınç M. Well-Differentiated Mucinous cystadenocarcinoma of the renal pelvis. *Eur J Gen Med* 2014; Suppl 1: 63-65 [DOI: 10.15197/sabad.1.11.36]
- 11 **Saxena S**, Gupta R, Nigam DK, Tahiliani ND, Saxena KN. Hydatid cyst of kidney presenting as hydatiduria. *J Assoc Physicians India* 1990; **38**: 359-356 [PMID: 2201677]
- 12 **Mongha R**, Narayan S, Kundu AK. Primary hydatid cyst of kidney and ureter with gross hydatiduria: A case report and evaluation of radiological features. *Indian J Urol* 2008; **24**: 116-117 [PMID: 19468374 DOI: 10.4103/0970-1591.38617]

P- Reviewer: Nishio K, Schoenhagen P S- Editor: Ji FF

L- Editor: A E- Editor: Liu SQ





Published by **Baishideng Publishing Group Inc**

8226 Regency Drive, Pleasanton, CA 94588, USA

Telephone: +1-925-223-8242

Fax: +1-925-223-8243

E-mail: bpgoffice@wjgnet.com

Help Desk: <http://www.wjgnet.com/esps/helpdesk.aspx>

<http://www.wjgnet.com>



World Journal of *Radiology*

World J Radiol 2015 August 28; 7(8): 184-219





Editorial Board

2014-2017

The *World Journal of Radiology* Editorial Board consists of 365 members, representing a team of worldwide experts in radiology. They are from 36 countries, including Afghanistan (1), Argentina (2), Australia (5), Austria (7), Belgium (2), Brazil (8), Canada (6), Chile (1), China (43), Croatia (1), Denmark (4), Egypt (6), France (5), Germany (22), Greece (10), India (12), Iran (6), Ireland (2), Israel (3), Italy (47), Japan (13), Netherlands (1), New Zealand (1), Pakistan (1), Poland (2), Portugal (1), Serbia (1), Singapore (3), Slovakia (1), South Korea (18), Spain (4), Sweden (2), Switzerland (4), Thailand (1), Turkey (26), United Kingdom (11), and United States (82).

EDITORS-IN-CHIEF

Kai U Juergens, *Bremen*
Edwin JR van Beek, *Edinburgh*
Thomas J Vogl, *Frankfurt*

GUEST EDITORIAL BOARD MEMBERS

Wing P Chan, *Taipei*
Chung-Huei Hsu, *Taipei*
Chin-Chang Huang, *Taipei*
Tsong-Long Hwang, *Taoyuan*
Jung-Lung Hsu, *Taipei*
Chia-Hung Kao, *Taichung*
Yu-Ting Kuo, *Tainan*
Hon-Man Liu, *Taipei*
Hui-Lung Liang, *Kaohsiung*
Chun Chung Lui, *Kaohsiung*
Sen-Wen Teng, *Taipei*
Yung-Liang (William) Wan, *Taoyuan*

MEMBERS OF THE EDITORIAL BOARD



Afghanistan

Takao Hiraki, *Okayama*



Argentina

Patricia Carrascosa, *Vicente Lopez*
Maria C Ziadi, *Rosario*



Australia

Lourens Bester, *Sydney*
Gemma A Figtree, *Sydney*

Stuart M Grieve, *Sydney*
Wai-Kit Lee, *Fitzroy*
Prabhakar Ramachandran, *Melbourne*



Austria

Herwig R Cerwenka, *Graz*
Gudrun M Feuchtnner, *Innsbruck*
Benjamin Henninger, *Innsbruck*
Rupert Lanzenberger, *Vienna*
Shu-Ren Li, *Vienna*
Veronika Schopf, *Vienna*
Tobias De Zordo, *Innsbruck*



Belgium

Steve Majerus, *Liege*
Kathelijne Peremans, *Merelbeke*



Brazil

Clerio F Azevedo, *Rio de Janeiro*
Patrícia P Alfredo, *São Paulo*
Eduardo FC Fleury, *São Paulo*
Edward Araujo Júnior, *São Paulo*
Wellington P Martins, *Ribeirao Preto*
Ricardo A Mesquita, *Belo Horizonte*
Vera MC Salemi, *São Paulo*
Claudia Szobot, *Porto Alegre*
Lilian YI Yamaga, *São Paulo*



Canada

Marie Arsalidou, *Toronto*
Otman A Basir, *Waterloo*

Tarik Zine Belhocine, *Toronto*
James Chow, *Toronto*
Tae K Kim, *Toronto*
Anastasia Oikonomou, *Toronto*



China

Hong-Wei Chen, *Wuxi*
Feng Chen, *Hangzhou*
Jian-Ping Chu, *Guangzhou*
Guo-Guang Fan, *Shenyang*
Bu-Lang Gao, *Shijiazhuang*
Qi-Yong Gong, *Chengdu*
Ying Han, *Beijing*
Xian-Li Lv, *Beijing*
Yi-Zhuo Li, *Guangzhou*
Xiang-Xi Meng, *Harbin*
Yun Peng, *Beijing*
Jun Shen, *Guangzhou*
Ze-Zhou Song, *Hangzhou*
Wai Kwong Tang, *Hong Kong*
Gang-Hua Tang, *Guangzhou*
Jie Tian, *Beijing*
Lu-Hua Wang, *Beijing*
Xiao-bing Wang, *Xi'an*
Yi-Gen Wu, *Nanjing*
Kai Wu, *Guangzhou*
Hui-Xiong Xu, *Shanghai*
Zuo-Zhang Yang, *Kunming*
Xiao-Dan Ye, *Shanghai*
David T Yew, *Hong Kong*
Ting-He Yu, *Chongqing*
Zheng Yuan, *Shanghai*
Min-Ming Zhang, *Hangzhou*
Yudong Zhang, *Nanjing*
Dong Zhang, *Chongqing*
Wen-Bin Zeng, *Changsha*

Yue-Qi Zhu, *Shanghai*



Croatia

Goran Kusec, *Osijek*



Denmark

Poul E Andersen, *Odense*

Lars J Petersen, *Aalborg*

Thomas Z Ramsøy, *Frederiksberg*

Morten Ziebell, *Copenhagen*



Egypt

Mohamed F Bazeed, *Mansoura*

Mohamed Abou El-Ghar, *Mansoura*

Reem HA Mohamed, *Cairo*

Mohamed R Nouh, *Alexandria*

Ahmed AKA Razek, *Mansoura*

Ashraf A Zytoon, *Shebin El-Koom*



France

Sabine F Bensamoun, *Compiègne*

Romarc Loffroy, *Dijon*

Stephanie Nougaret, *Montpellier*

Hassane Oudadesse, *Rennes*

Vincent Vinh-Hung, *Fort-de-France*



Germany

Henryk Barthel, *Leipzig*

Peter Bannas, *Hamburg*

Martin Beeres, *Frankfurt*

Ilja F Ciernik, *Dessau*

A Dimitrakopoulou-Strauss, *Heidelberg*

Peter A Fasching, *Erlangen*

Andreas G Schreyer, *Regensburg*

Philipp Heusch, *Duesseldorf*

Sonja M Kirchhoff, *Munich*

Sebastian Ley, *Munich*

Adel Maataoui, *Frankfurt am Main*

Stephan M Meckel, *Freiburg*

Hans W Muller, *Duesseldorf*

Kay Raum, *Berlin*

Dirk Rades, *Luebeck*

Marc-Ulrich Regier, *Hamburg*

Alexey Surov, *Halle*

Martin Walter, *Magdeburg*

Axel Wetter, *Essen*

Christoph Zilkens, *Düsseldorf*



Greece

Panagiotis Antoniou, *Thessaloniki*

Nikos Efthimiou, *Athens*

Dimitris Karnabatidis, *Patras*

George Latsios, *Athens*

Stylianios Megremis, *Iraklion*

Alexander D Rapidis, *Athens*

Kiki Theodorou, *Larissa*

Ioannis A Tsalafoutas, *Athens*

Evanthia E Tripoliti, *Ioannina*

Athina C Tsili, *Ioannina*



India

Ritesh Agarwal, *Chandigarh*

Chandan J Das, *New Delhi*

Prathamesh V Joshi, *Mumbai*

Naveen Kalra, *Chandigarh*

Chandrasekharan Kesavadas, *Trivandrum*

Jyoti Kumar, *New Delhi*

Atin Kumar, *New Delhi*

Kaushala P Mishra, *Allahabad*

Daya N Sharma, *New Delhi*

Binit Sureka, *New Delhi*

Sanjay Sharma, *New Delhi*

Raja R Yadav, *Allahabad*



Iran

Majid Assadi, *Bushehr*

SeyedReza Najafizadeh, *Tehran*

Mohammad Ali Oghabian, *Tehran*

Amir Reza Radmard, *Tehran*

Ramin Sadeghi, *Mashhad*

Hadi Rokni Yazdi, *Tehran*



Ireland

Tadhg Gleeson, *Wexford*

Frederik JAI Vernimmen, *Cork*



Israel

Dafna Ben Bashat, *Tel Aviv*

Amit Gefen, *Tel Aviv*

Tamar Sella, *Jerusalem*



Italy

Adriano Alippi, *Rome*

Dante Amelio, *Trento*

Michele Anzidei, *Rome*

Filippo F Angileri, *Messinas*

Stefano Arcangeli, *Rome*

Roberto Azzoni, *San Donato milanese*

Tommaso V Bartolotta, *Palermo*

Tommaso Bartalena, *Imola*

Livia Bernardin, *San Bonifacio*

Federico Boschi, *Verona*

Sergio Casciaro, *Lecce*

Emanuele Casciani, *Rome*

Musa M Can, *Napoli*

Alberto Cuocolo, *Napoli*

Michele Ferrara, *Coppito*

Mauro Feola, *Fossano*

Giampiero Francica, *Castel Volturno*

Luigi De Gennaro, *Rome*

Giulio Giovannetti, *Pisa*

Francesca Iacobellis, *Napoli*

Formato Invernizzi, *Monza Brianza*

Francesco Lassandro, *Naples*

Lorenzo Livi, *Florence*

Pier P Mainenti, *Napoli*

Laura Marzetti, *Chieti*

Giuseppe Malinverni, *Crescentino*

Enrica Milanese, *Turin*

Giovanni Morana, *Treviso*

Lorenzo Monti, *Milan*

Silvia D Morbelli, *Genoa*

Barbara Palumbo, *Perugia*

Cecilia Parazzini, *Milan*

Stefano Pergolizzi, *Messina*

Antonio Pinto, *Naples*

Camillo Porcaro, *Rome*

Carlo C Quattrocchi, *Rome*

Alberto Rebonato, *Perugia*

Giuseppe Rizzo, *Rome*

Roberto De Rosa, *Naples*

Domenico Rubello, *Rovigo*

Andrea Salvati, *Bari*

Sergio Sartori, *Ferrara*

Luca M Sconfienza, *Milano*

Giovanni Storto, *Rionero*

Nicola Sverzellati, *Parma*

Alberto S Tagliafico, *Genova*

Nicola Troisi, *Florence*



Japan

Yasuhiko Hori, *Chiba*

Hidetoshi Ikeda, *Koriyama*

Masahito Kawabori, *Sapporo*

Tamotsu Kamishima, *Sapporo*

Hiro Kiyosue, *Yufu*

Yasunori Minami, *Osaka-sayama*

Yasuhiro Morimoto, *Kitakyushu*

Satoru Murata, *Tokyo*

Shigeki Nagamachi, *Miyazaki*

Hiroshi Onishi, *Yamanashi*

Morio Sato, *Wakayama Shi*

Yoshito Tsushima, *Maebashi*

Masahiro Yanagawa, *Suita*



Netherlands

Willem Jan van Rooij, *Tilburg*



New Zealand

W Howell Round, *Hamilton*



Pakistan

Wazir Muhammad, *Abbottabad*



Poland

Maciej S Baglaj, *Wroclaw*

Piotr Czauderna, *Gdansk*



Portugal

Joao Manuel RS Tavares, *Porto*



Serbia

Olivera Ciraj-Bjelac, *Belgrade*



Singapore

Gopinathan Anil, *Singapore*

Terence KB Teo, *Singapore*

Cher Heng Tan, *Singapore*



Slovakia

Stefan Sivak, *Martin*



South Korea

Ki Seok Choo, *Busan*

Seung Hong Choi, *Seoul*

Dae-Seob Choi, *Jinju*

Hong-Seok Jang, *Seoul*

Yong Jeong, *Daejeon*

Chan Kyo Kim, *Seoul*

Se Hyung Kim, *Seoul*

Joong-Seok Kim, *Seoul*

Sang Eun Kim, *Seongnam*

Sung Joon Kwon, *Seoul*

Jeong Min Lee, *Seoul*

In Sook Lee, *Busan*

Noh Park, *Goyang*

Chang Min Park, *Seoul*

Sung Bin Park, *Seoul*

Deuk Jae Sung, *Seoul*

Choongsoo Shin, *Seoul*

Kwon-Ha Yoon, *Iksan*



Spain

Miguel A De Gregorio, *Zaragoza*

Antonio Luna, *Jaén*

Enrique Marco de Lucas, *Santander*

Fernando Ruiz Santiago, *Granada*



Sweden

Dmitry Grishenkov, *Stockholm*

Tie-Qiang Li, *Stockholm*



Switzerland

Nicolau Beckmann, *Basel*

Christian Boy, *Bern*

Giorgio Treglia, *Bellinzona*

Stephan Ulmer, *Kiel*



Thailand

Sirianong Namwongprom, *Chiang Mai*



Turkey

Kubilay Aydin, *Istanbul*

Ramazan Akdemir, *Sakarya*

Serhat Avcu, *Ankara*

Ayşe Aralasmak, *Istanbul*

Oktay Algin, *Ankara*

Nevbahar Akcar, *Meselik*

Bilal Battal, *Ankara*

Zulkif Bozgeyik, *Elazig*

Nazan Ciledag, *Aakara*

Fuldem Y Donmez, *Ankara*

Gulgun Engin, *Istanbul*

Ahmet Y Goktay, *Izmir*

Oguzhan G Gumustas, *Bursa*

Kaan Gunduz, *Ankara*

Pelin Ozcan Kara, *Mersin*

Kivanc Kamburoglu, *Ankara*

Ozgur Kilickesmez, *Istanbul*

Furuzan Numan, *Istanbul*

Cem Onal, *Adana*

Ozgur Oztekin, *Izmir*

Seda Ozbek (Boruban), *Konya*

Selda Sarikaya, *Zonguldak*

Figen Taser, *Kutahya*

Baran Tokar, *Eskisehir*

Ender Uysal, *Istanbul*

Ensar Yekeler, *Istanbul*



United Kingdom

Indran Davagnanam, *London*

M DC Valdés Hernández, *Edinburgh*

Alan Jackson, *Manchester*

Suneil Jain, *Belfast*

Long R Jiao, *London*

Miltiadis Krokidis, *Cambridge*

Pradesh Kumar, *Liverpool*

Peter D Kuzmich, *Derby*

Georgios Plataniotis, *Brighton*

Vanessa Sluming, *Liverpool*



United States

Garima Agrawal, *Saint Louis*

James R Brasic, *Baltimore*

Rajendra D Badgaiyan, *Buffalo*

Ulas Bagci, *Bethesda*

Anat Biegon, *Stony Brook*

Ramon Casanova, *Winston Salem*

Wenli Cai, *Boston*

Zheng Chang, *Durham*

Corey J Chakarun, *Long Beach*

Kai Chen, *Los Angeles*

Hyun-Soon Chong, *Chicago*

Marco Cura, *Dallas*

Ravi R Desai, *Bensalem*

Delia DeBuc, *Miami*

Carlo N De Cecco, *Charleston*

Timm-Michael L Dickfeld, *Baltimore*

Subba R Digumarthy, *Boston*

Huy M Do, *Stanford*

Todd A Faasse, *Grand Rapids*

Salomao Faintuch, *Boston*

Girish M Fatterpekar, *New York*

Dhakshinamoorthy Ganesan, *Houston*

Robert J Griffin, *Little Rock*

Andrew J Gunn, *Boston*

Sandeep S Hedgire, *Boston*

Timothy J Hoffman, *Columbia*

Mai-Lan Ho, *San Francisco*

Juebin Huang, *Jackson*

Abid Irshad, *Charleston*

Matilde Inglese, *New York*

El-Sayed H Ibrahim, *Jacksonville*

Paul R Julsrud, *Rochester*

Pamela T Johnson, *Baltimore*

Ming-Hung Kao, *Tempe*

Sunil Krishnan, *Houston*

Richard A Komoroski, *Cincinnati*

Sandi A Kwee, *Honolulu*

King Kim, *Ft. Lauderdale*

Guozheng Liu, *Worcester*

Yiyan Liu, *Newark*

Venkatesh Mani, *New York*

Lian-Sheng Ma, *Pleasanton*

Rachna Madan, *Boston*

Zeyad A Metwalli, *Houston*

Yilong Ma, *Manhasset*

Hui Mao, *Atlanta*

Feroze B Mohamed, *Philadelphia*

Gul Moonis, *Boston*

John L Noshier, *New Brunswick*

Rahmi Oklu, *Boston*

Aytekun Oto, *Chicago*

Bishnuhari Paudyal, *Philadelphia*

Rajul Pandya, *Youngstown*

Chong-Xian Pan, *Sacramento*

Jay J Pillai, *Baltimore*

Neal Prakash, *Duarte*

Reza Rahbar, *Boston*

Ali S Raja, *Boston*

Gustavo J Rodriguez, *El Paso*

David J Sahn, *Portland*

Steven Schild, *Scottsdale*

Ali R Sepahdari, *Los Angeles*

Li Shen, *Indianapolis*

JP Sheehan, *Charlottesville*

Atul B Shinagare, *Boston*

Sarabjeet Singh, *Boston*

Charles J Smith, *Columbia*

Kenji Suzuki, *Chicago*

Monvadi Srichai-Parsia, *Washington*

Sree H Tirumani, *Boston*

Hebert A Vargas, *New York*

Sachit Verma, *Philadelphia*

Yoichi Watanabe, *Minneapolis*

Li Wang, *Chapel Hill*

Carol C Wu, *Boston*

Shoujun Xu, *Houston*

Min Yao, *Cleveland*

Xiaofeng Yang, *Atlanta*

Qingbao Yu, *Albuquerque*

Aifeng Zhang, *Chicago*

Chao Zhou, *Bethlehem*

Hongming Zhuang, *Philadelphia*



EDITORIAL

- 184 Updates in advanced diffusion-weighted magnetic resonance imaging techniques in the evaluation of prostate cancer
Vargas HA, Lawrence EM, Mazaheri Y, Sala E
- 189 Lung cancer screening: Computed tomography or chest radiographs?
van Beek EJR, Mirsadraee S, Murchison JT
- 194 Magnetic resonance imaging-based interpretation of degenerative changes in the lower lumbar segments and therapeutic consequences
Maataoui A, Vogl TJ, Khan MF
- 198 Small bowel imaging of inflammatory bowel disease
Casciani E, De Vincentiis C, Gualdi GF

MINIREVIEWS

- 202 Imaging of bone metastasis: An update
O'Sullivan GJ, Carty FL, Cronin CG

ORIGINAL ARTICLE

Basic study

- 212 Development of biodegradable radiopaque microsphere for arterial embolization-a pig study
Liu YS, Lin XZ, Tsai HM, Tsai HW, Chen GC, Chen SF, Kang JW, Chou CM, Chen CY

ABOUT COVER

Editorial Board Member of *World Journal of Radiology*, Kenji Suzuki, PhD, Assistant Professor, Department of Radiology, Division of the Biological Sciences, the University of Chicago, Chicago, IL 60637, United States

AIM AND SCOPE

World Journal of Radiology (*World J Radiol*, *WJR*, online ISSN 1949-8470, DOI: 10.4329) is a peer-reviewed open access academic journal that aims to guide clinical practice and improve diagnostic and therapeutic skills of clinicians.

WJR covers topics concerning diagnostic radiology, radiation oncology, radiologic physics, neuroradiology, nuclear radiology, pediatric radiology, vascular/interventional radiology, medical imaging achieved by various modalities and related methods analysis. The current columns of *WJR* include editorial, frontier, diagnostic advances, therapeutics advances, field of vision, mini-reviews, review, topic highlight, medical ethics, original articles, case report, clinical case conference (clinicopathological conference), and autobiography.

We encourage authors to submit their manuscripts to *WJR*. We will give priority to manuscripts that are supported by major national and international foundations and those that are of great basic and clinical significance.

INDEXING/ABSTRACTING

World Journal of Radiology is now indexed in PubMed Central, PubMed, Digital Object Identifier, and Directory of Open Access Journals.

FLYLEAF

I-III Editorial Board

EDITORS FOR THIS ISSUE

Responsible Assistant Editor: *Xiang Li*
Responsible Electronic Editor: *Xiao-Kang Jiao*
Proofing Editor-in-Chief: *Lian-Sheng Ma*

Responsible Science Editor: *Fang-Fang Ji*
Proofing Editorial Office Director: *Xiu-Xia Song*

NAME OF JOURNAL
World Journal of Radiology

ISSN
ISSN 1949-8470 (online)

LAUNCH DATE
December 31, 2009

FREQUENCY
Monthly

EDITORS-IN-CHIEF
Kai U Juergens, MD, Associate Professor, MRT und PET/CT, Nuklearmedizin Bremen Mitte, ZEMODI - Zentrum für morphologische und molekulare Diagnostik, Bremen 28177, Germany

Edwin JR van Beek, MD, PhD, Professor, Clinical Research Imaging Centre and Department of Medical Radiology, University of Edinburgh, Edinburgh EH16 4TJ, United Kingdom

Thomas J Vogl, MD, Professor, Reader in Health Technology Assessment, Department of Diagnostic and Interventional Radiology, Johann Wolfgang

Goethe University of Frankfurt, Frankfurt 60590, Germany

EDITORIAL OFFICE
Jin-Lei Wang, Director
Xiu-Xia Song, Vice Director
World Journal of Radiology
Room 903, Building D, Ocean International Center, No. 62 Dongsihuan Zhonglu, Chaoyang District, Beijing 100025, China
Telephone: +86-10-59080039
Fax: +86-10-85381893
E-mail: editorialoffice@wjnet.com
Help Desk: <http://www.wjnet.com/esps/helpdesk.aspx>
<http://www.wjnet.com>

PUBLISHER
Baishideng Publishing Group Inc
8226 Regency Drive,
Pleasanton, CA 94588, USA
Telephone: +1-925-223-8242
Fax: +1-925-223-8243
E-mail: bpgoffice@wjnet.com
Help Desk: <http://www.wjnet.com/esps/helpdesk.aspx>
<http://www.wjnet.com>

PUBLICATION DATE
August 28, 2015

COPYRIGHT
© 2015 Baishideng Publishing Group Inc. Articles published by this Open-Access journal are distributed under the terms of the Creative Commons Attribution Non-commercial License, which permits use, distribution, and reproduction in any medium, provided the original work is properly cited, the use is non commercial and is otherwise in compliance with the license.

SPECIAL STATEMENT
All articles published in journals owned by the Baishideng Publishing Group (BPG) represent the views and opinions of their authors, and not the views, opinions or policies of the BPG, except where otherwise explicitly indicated.

INSTRUCTIONS TO AUTHORS
Full instructions are available online at http://www.wjnet.com/1949-8470/g_info_20100316162358.htm.

ONLINE SUBMISSION
<http://www.wjnet.com/esps/>

Updates in advanced diffusion-weighted magnetic resonance imaging techniques in the evaluation of prostate cancer

Hebert Alberto Vargas, Edward Malnor Lawrence, Yousef Mazaheri, Evis Sala

Hebert Alberto Vargas, Edward Malnor Lawrence, Yousef Mazaheri, Evis Sala, Department of Radiology, Memorial Sloan Kettering Cancer Center, New York, NY 10065, United States

Author contributions: Vargas HA drafted the manuscript; all authors participated in the literature search, summary and interpretation; all authors edited and approved the final manuscript.

Conflict-of-interest statement: The authors have no conflicts of interest to disclose.

Open-Access: This article is an open-access article which was selected by an in-house editor and fully peer-reviewed by external reviewers. It is distributed in accordance with the Creative Commons Attribution Non Commercial (CC BY-NC 4.0) license, which permits others to distribute, remix, adapt, build upon this work non-commercially, and license their derivative works on different terms, provided the original work is properly cited and the use is non-commercial. See: <http://creativecommons.org/licenses/by-nc/4.0/>

Correspondence to: Hebert Alberto Vargas, MD, Department of Radiology, Memorial Sloan Kettering Cancer Center, 1275 York Av., New York, NY 10065, United States. vargasah@mskcc.org
Telephone: +1-212-6392000

Received: February 28, 2015

Peer-review started: March 2, 2015

First decision: March 20, 2015

Revised: June 2, 2015

Accepted: June 18, 2015

Article in press: June 19, 2015

Published online: August 28, 2015

Abstract

Diffusion-weighted magnetic resonance imaging (DW-MRI) is considered part of the standard imaging protocol for the evaluation of patients with prostate cancer.

It has been proven valuable as a functional tool for qualitative and quantitative analysis of prostate cancer beyond anatomical MRI sequences such as T2-weighted imaging. This review discusses ongoing controversies in DW-MRI acquisition, including the optimal number of b-values to be used for prostate DWI, and summarizes the current literature on the use of advanced DW-MRI techniques. These include intravoxel incoherent motion imaging, which better accounts for the non-mono-exponential behavior of the apparent diffusion coefficient as a function of b-value and the influence of perfusion at low b-values. Another technique is diffusion kurtosis imaging (DKI). Metrics from DKI reflect excess kurtosis of tissues, representing its deviation from Gaussian diffusion behavior. Preliminary results suggest that DKI findings may have more value than findings from conventional DW-MRI for the assessment of prostate cancer.

Key words: Prostate cancer; Diffusion-weighted imaging; Diffusion kurtosis imaging; Magnetic resonance imaging; Include intravoxel incoherent motion

© The Author(s) 2015. Published by Baishideng Publishing Group Inc. All rights reserved.

Core tip: Diffusion-weighted magnetic resonance imaging (DW-MRI) is considered part of the standard imaging protocol for the evaluation of patients with prostate cancer. In this review we discuss the ongoing controversies in DW-MRI acquisition, including the optimal number of b-values to be used for prostate DWI, and summarize the current literature on the use of advanced DW-MRI techniques such as intravoxel incoherent motion imaging and diffusion kurtosis imaging.

Vargas HA, Lawrence EM, Mazaheri Y, Sala E. Updates in advanced diffusion-weighted magnetic resonance imaging

techniques in the evaluation of prostate cancer. *World J Radiol* 2015; 7(8): 184-188 Available from: URL: <http://www.wjgnet.com/1949-8470/full/v7/i8/184.htm> DOI: <http://dx.doi.org/10.4329/wjr.v7.i8.184>

INTRODUCTION

Diffusion-weighted (DW) techniques have been applied extensively for the evaluation of patients with prostate cancer and are now part of most standard prostate magnetic resonance imaging (MRI) clinical protocols. Multiple studies have demonstrated that DW-MRI contributes incremental value to T2-weighted MRI in the detection and localization of prostate cancer^[1]. Straightforward, quantitative metrics from DW-MRI – most commonly apparent diffusion coefficient (ADC) values – have been used to distinguish between benign and malignant prostate tissue and also to evaluate prostate cancer aggressiveness^[2]. ADC values have been found to correlate inversely with prostate cancer Gleason score as well as tumor proliferation markers such as Ki-67^[2-4]. Nevertheless, ADC values of prostate cancer overlap substantially with those of normal prostate and benign conditions, such as prostatitis and post-biopsy inflammation. Therefore, advanced methods for DW-MRI acquisition, processing and interpretation are now being investigated with the goal of further strengthening the value of DW-MRI for prostate cancer assessment.

SELECTION OF *b*-VALUES FOR PROSTATE DW-MRI

The *b*-value is one of the main factors reflecting the strength of the diffusion effects in DW-MRI, with higher *b*-values representing stronger diffusion effects. There is as yet no consensus regarding the optimal choice of *b*-values for acquiring prostate DW-MRI. Absolute ADC values are highly dependent on the *b*-values selected and must therefore be applied cautiously, especially when attempting to define “cut-offs” for distinguishing particular conditions or disease states^[5]. Higher *b*-values offer greater tumor-to-normal-tissue contrast but also decrease the signal-to-noise ratio. Tamada *et al*^[6] evaluated 50 patients with prostate cancer undergoing 3T prostate DW-MRI acquired with *b*-values of 0, 1000 and 2000 s/mm²; they found that lesion conspicuity and tumor-to-normal signal intensity ratio were higher when using *b*-values of 0 and 2000 s/mm² compared to those using *b*-values of 0 and 1000 s/mm²^[6]. There was a significant correlation between ADC values of tumor regions and Gleason scores at both *b*-values of 0 and 1000 s/mm² ($\rho = -0.602$; $P < 0.001$) and 0 and 2000 s/mm² ($\rho = -0.645$; $P < 0.001$)^[6]. As an alternative to the acquisition of high-*b*-value images, some investigators have proposed “computing” them through voxelwise fitting from a set of images acquired

at lower *b*-values. Using numerical simulations, Tamada *et al*^[6] found that noise and the contrast-to-noise ratio were comparable between DW-MRI images that were “calculated” and those that were “acquired” at a *b*-value of 1400 s/mm² ($P = 0.395$). In one study, diagnostic performance of DW-MRI in prostate tumor detection was compared for four different combinations of measured and acquired *b*-values^[7]. The AUCs for protocol A (T2-weighted images alone), B (T2-weighted images in combination with measured DW images with *b* 1000), C (T2-weighted images in combination with measured DW images with *b* 2000) and D (T2-weighted images in combination with computed DW images with *b* 2000) were 0.67, 0.80, 0.86 and 0.84, respectively^[7]. Protocols C and D had significantly higher AUCs when compared to protocol B ($P < 0.05$)^[7].

INTRAVOXEL INCOHERENT MOTION IMAGING

The optimal number of *b*-values for prostate DW-MRI also continues to be debated. A minimum of two *b*-values is required for monoexponential calculation of ADC. However, to better account for the non-monoexponential behavior of the diffusion signal intensity at different *b*-values and the influence of perfusion at low *b*-values, intravoxel incoherent motion (IVIM), a model based on the use of three or more *b*-values, can be applied. The use of multiple *b*-values also reduces the influence of *b*-value selection on ADC measurements^[8]. One study evaluated prostate DW-MRI acquired with four *b*-values (0, 50, 500, and 800 s/mm²) in 13 biopsy-proven prostate cancer patients and found that ADC ($\mu\text{m}^2/\text{ms}$), molecular diffusion coefficient (*D*, $\mu\text{m}^2/\text{ms}$) and perfusion fraction (*f*, %) were significantly lower ($P < 0.005$) in cancer (1.01 ± 0.22 , 0.84 ± 0.19 and $14.27 \pm 7.10\%$ for ADC, *D* and *f*) than in benign tissue (1.49 ± 0.17 , 1.21 ± 0.22 and $21.25\% \pm 8.32\%$, for ADC, *D* and *f*)^[9]. Another study applied monoexponential and biexponential fits to diffusion decay curves obtained from 26 patients with prostate cancer using 10 *b*-values ranging from 10 to 1000 s/mm²^[10]. In 81% of cases, biexponential functions were found to provide statistically better fits than monoexponential functions^[10]. Biexponential IVIM was used to calculate the parameters *D*, *f*, and *D**. Significantly lower values of ADC, *D*, and *f* were found in prostate cancer compared to the values in the normal prostatic peripheral zone (PZ), but similar values for *f* were reported in both benign hyperplastic changes and prostate cancer^[10]. There were no significant differences between the *D** values found in prostate cancer, benign hyperplasia, and PZ^[10].

Some investigators have questioned whether IVIM truly contributes incremental value as compared to simple monoexponential ADC measurements in prostate cancer^[11]. One study compared two different algorithms for generating IVIM metrics in 50 patients (27 known prostate cancer patients and 23 without

Table 1 Clinical studies of intravoxel incoherent motion imaging in prostate cancer

Ref.	No. of patients	Pathologic reference	<i>b</i> -values (s/mm ²)	MR parameters	PCa values ¹	Normal prostate values ¹	Significance
Döpfert <i>et al</i> ^[9]	13	TRUS biopsy	0, 50, 500, 800	3.0 T; TR/TE: 2600/66 ms; FOV: 204 mm × 204 mm; Matrix: 136 × 136; slice thickness: 3 mm; 8 averages	ADC: 1.01 ± 0.22 D: 0.84 ± 0.19 D*: 7.52 ± 4.77 f: 14.27 ± 7.10	ADC: 1.49 ± 0.17 D: 1.21 ± 0.22 D*: 6.82 ± 2.78 f: 21.25 ± 8.32	ADC, D, f significantly lower in PCa <i>vs</i> healthy prostate tissue Higher variation in maps of D and f compared to ADC
Shinmoto <i>et al</i> ^[10]	26	TRUS biopsy or RP	0, 10, 20, 30, 50, 80, 100, 200, 400, 1000	3.0 T; TR/TE: 5132/40 ms; Matrix: 80 × 80; slice thickness/gap: 3.5/0.1 mm; iPAT factor, 2; NEX = 2	ADC: 0.90 ± 0.16 D: 0.50 ± 0.15 D*: 5.35 ± 6.27 f: 35 ± 13	ADC: 1.76 ± 0.22 D: 0.89 ± 0.24 D*: 3.02 ± 0.86 f: 58 ± 11	ADC, D, f significantly lower in PCa <i>vs</i> noncancerous PZ Improved fit in 81% of study subjects for biexponential curve
Kuru <i>et al</i> ^[11]	27	MR-TRUS fusion biopsy	0, 50, 100, 150, 200, 250, 800	3.0 T; TR/TE: 3100/52 ms; FOV: 280 mm × 210 mm; Matrix: 128 × 96; slice thickness: 3 mm; iPAT factor, 2; 5 averages	ADC: 0.88 ± 0.29 D: 1.04 ± 0.23 D*: 31.1 ± 45.0 f: 9.5 ± 5.5	ADC: 1.56 ± 0.23 D: 1.44 ± 0.19 D*: 10.9 ± 4.0 f: 11.1 ± 5.0	Only D and ADC showed high AUC (≥ 0.90) for PCa <i>vs</i> normal Limited differentiation of PCa grade using f or D*
Pang <i>et al</i> ^[12]	33	MR-TRUS fusion biopsy	0, 188, 375, 563	3.0 T; TR/TE: 4584/59 ms; FOV: 160 × 180 mm; slice thickness: 3.0 mm; iPAT factor, 2; 4+ averages	D: 0.99 ± 0.29 f: 7.2 ± 2.6 K ^{trans} : 0.39 ± 0.22 V _p : 8.4 ± 6.6	D: 1.76 ± 0.35 f: 3.7 ± 1.9 K ^{trans} : 0.18 ± 0.10 V _p : 3.4 ± 2.6	Significant increase in f for PCa <i>vs</i> normal prostate Pearson's correlation coefficient (r) for f and K ^{trans} of 0.51

¹Values are mean ± SD [ADC: Apparent diffusion coefficient (μm²/ms); D: molecular diffusion coefficient (μm²/ms); D*: Perfusion-related diffusion coefficient (μm²/ms); f: Perfusion fraction (%); K^{trans}: Volume transfer constant (min⁻¹); V_p: Plasma fractional volume (%)]. AUC: Area under curve; FOV: Field of view; GS: Gleason score; iPAT: Integrated parallel acquisition techniques; IVIM: Intravoxel incoherent motion; MR: Magnetic resonance; NEX: Number of excitations; PCa: Prostate cancer; PZ: Peripheral zone; RP: Radical prostatectomy; T: Tesla; TE: Time of echo; TR: Time of repetition; TRUS: Transrectal ultrasound.

known cancer) who underwent prostate DWI acquired with 7 *b*-values (0, 50, 100, 150, 200, 250, and 800 s/mm²)^[11]. D was similar with the two algorithms (*P* = 0.22), but *f* was significantly different between the 2 (higher with algorithm 1) (*P* < 0.05). The AUCs for differentiating tumor and normal tissues were ≥ 0.90 for D (from the 2 algorithms) and ADC (but not *f* or D*). IVIM-derived parameters are also influenced by the range of *b*-values used. Pang *et al*^[12] analyzed prostate DW-MRI acquired with five *b*-values ranging between 188 and 750 s/mm² and assessed the influence of the choice of *b*-values on the measured D and *f*. Both parameters were markedly influenced by the choice of *b*-values. The best correlation with DCE-MRI was achieved when the IVIM parameters were calculated without the highest *b*-value (750 s/mm²). Using this approach, significantly higher *f* from IVIM and *k*_{trans} and plasma fractional volume from DCE-MRI were found for prostate cancers (7.2%, 0.39/min and 8.4% respectively) compared to normal prostate tissue (3.7%, 0.18/min and 3.4% respectively)^[12]. In summary, further research into prostate IVIM is needed, with a focus on selecting the most appropriate patient population and on standardizing image acquisition techniques and approaches to fit the IVIM parameters from the DW-MRI data. A summary of clinical studies of IVIM imaging in prostate cancer is presented in Table 1.

DIFFUSION KURTOSIS IMAGING IN PROSTATE CANCER

Diffusion kurtosis imaging (DKI) is another technique

that has been used in attempts to more accurately characterize the multi-exponential behavior of diffusion decay in prostate cancer^[13-18]. Metrics from DKI reflect excess kurtosis of the tissue, representing its deviation from Gaussian diffusion behavior^[15]. Preliminary results suggest that DKI findings may have more value than findings from conventional DW-MRI for prostate cancer assessment.

In a study of 31 subjects (including healthy volunteers and patients undergoing evaluation for raised PSA levels), Quentin *et al*^[14] performed DKI with 4 *b*-values ranging between 0 and 1000 s/mm² and with diffusion gradients applied in 20 different spatial directions; they found that there was a better fit to the diffusion weighted signal when using DKI compared to when using the monoexponential ADC^[14]. Significantly higher mean (*K*_{mean}) and axial (*K*_{ax}) kurtosis were reported in prostate tumors (*K*_{mean} 1.84 ± 0.43; *K*_{ax} 1.78 ± 0.39,) compared to the normal PZ (*K*_{mean} 1.16 ± 0.13; *K*_{ax} 1.09 ± 0.12, *P* < 0.001) or the transition/central zone (*K*_{ax} 1.40 ± 0.12, *K*_{mean} 1.44 ± 0.17; *P* = 0.01, respectively)^[14].

Another study of 47 patients with prostate cancer who underwent 3T DW-MRI using *b*-values up to 2000 s/mm² found that the DKI metric *K*, which represents non-Gaussian diffusion behavior, was significantly higher in prostate sextants involved by tumor compared to sextants containing non-cancerous prostate tissue (0.96 ± 0.24 *vs* 0.57 ± 0.07, *P* < 0.001) and was also significantly greater in Gleason score > 6 tumors (1.05 ± 0.26) compared to tumors with Gleason scores ≤ 6 (0.89 ± 0.20; *P* < 0.001)^[16]. For differentiating prostate sextants involved by cancer from non-cancerous prostate sextants, *K* showed significantly greater

Table 2 Clinical studies of diffusion kurtosis imaging in prostate cancer

Ref.	No. of patients	Pathologic reference	b-values (s/mm ²)	MR parameters	Quantitative parameters ¹	Significance
Quentin <i>et al</i> ^[14]	31	Biopsy	0, 300, 600, 1000	3.0 T; TR/TE: 1700/101 ms; FOV: 204 × 204 mm; Matrix: 136 × 136; slice thickness: 6 mm; iPAT factor, 2; 4 averages	K _{axial} , PCa: 1.78 ± 0.39 K _{axial} , TZ: 1.40 ± 0.12 K _{axial} , PZ: 1.09 ± 0.12	DKI better fit than monoexponential; Difference for K between PCa and normal TZ/PZ is significant
Rosenkrantz <i>et al</i> ^[16]	47	Biopsy	0, 500, 1000, 1500, 2000	3.0 T; TR/TE: 3500/81 ms; FOV: 280 mm × 218 mm; Matrix: 100 × 100; slice thickness: 4 mm; iPAT factor, 2; 6 averages	K, high GS: 1.05 ± 0.26 K, low GS: 0.89 ± 0.20 K, PZ: 0.57 ± 0.07	Significant difference between K in high GS vs low GS sextants; K found to have better sensitivity, AUC than ADC or D for PCa
Suo <i>et al</i> ^[17]	19	RP	0, 500, 800, 1200, 1500, 2000	3.0 T; TR/TE: 3940/106 ms; FOV: 280 mm × 280 mm; Matrix: 128 × 128; slice thickness/gap: 3/1 mm; 4 averages	K, PCa: 0.96 ± 0.20 K, PZ: 0.59 ± 0.08	Significant difference for K between PCa and normal PZ; GS correlates significantly with K
Tamura <i>et al</i> ^[18]	20	RP	0, 10, 20, 30, 50, 80, 100, 200, 400, 1000, 1500	3.0 T; TR/TE: 5000/49 ms; FOV: 240 × 240 mm; Matrix: 80 × 80; slice thickness/gap: 3.5/0.1 mm; iPAT factor, 2; NEX = 2	K, PCa: 1.19 ± 0.24 K, BPH: 0.99 ± 0.28 K, PZ: 0.63 ± 0.23	Significant difference for K between PCa and normal PZ but marked overlap for K between PCa and BPH

¹Values are mean ± SD [K: Kurtosis parameter (unitless); K_{axial}: Axial kurtosis (unitless)]. AUC: Area under curve; BPH: Benign prostatic hyperplasia; DKI: Diffusional kurtosis imaging; FOV: Field of view; GS: Gleason score; iPAT: Integrated parallel acquisition techniques; MR: Magnetic resonance; NEX: Number of excitations; PCa: Prostate cancer; PZ: Peripheral zone; RP: Radical prostatectomy; T: Tesla; TE: Time of echo; TR: Time of repetition; TZ: Transitional zone.

sensitivity (0.93) than ADC (0.79) or the DKI parameter D (0.84; $P < 0.001$), which represents diffusion corrected for non-Gaussianity. There was no significant difference in specificity; $P > 0.99$ ^[16]. The sensitivity of K (0.69) was significantly greater than that of ADC (0.51) or D (0.49) for differentiating between low- and high-grade cancer sextants but the specificity was lower (0.70, 0.81 and 0.83 for K, ADC and D; $P \leq 0.023$)^[16]. The AUC for differentiating prostate sextants with Gleason Score ≤ 6 tumors from those with Gleason Score > 6 tumors was greater for K (0.70) than ADC (0.62) ($P = 0.010$)^[16]. Similar findings were reported in a study that evaluated 19 prostate patients undergoing DW-MRI^[17]. ADC and D values were significantly lower and K values were significantly higher in cancerous compared to non-cancerous PZ (ADC = $0.79 \text{ } \mu\text{m}^2/\text{ms} \pm 0.14$ vs $1.23 \pm 0.19 \text{ } \mu\text{m}^2/\text{ms}$; D = $1.56 \text{ } \mu\text{m}^2/\text{ms} \pm 0.23$ vs $2.54 \pm 0.24 \text{ } \mu\text{m}^2/\text{ms}$; K 0.96 ± 0.20 vs 0.59 ± 0.08 ; $P < 0.001$ for all)^[17]. In benign PZ and prostate cancer, D and K values overlapped less often than did ADC values^[17]. A significant inverse correlation was observed between prostate cancer D and K values (Pearson correlation coefficient $r = -0.729$; $P < 0.001$)^[17]. ADC and K values differed significantly in tumors with different Gleason scores ($P \leq 0.001$), however D values were similar across tumors with different Gleason scores ($P = 0.325$)^[17]. Gleason score correlated significantly with both the ADC value ($r = -0.828$; $P < 0.001$) and the K ($r = 0.729$; $P < 0.001$).

Li *et al*^[13] evaluated the utility of diffusion tensor imaging (DTI) and DCE-MRI for detecting prostate cancer of the PZ in 33 patients undergoing 3T MRI of the prostate before biopsy. DTI does not require the introduction of a diffusional kurtosis tensor in addition to the diffusion tensor used in DTI, and can be obtained

with 2 b values. They found significant differences in the ADC, fractional anisotropy (FA), volume transfer constant (K_{trans}), and rate constant (k_{ep}) values between prostate sextants containing prostate cancer vs prostate sextants containing benign PZ tissue ($P < 0.0001$ for all)^[13]. For tumor detection, a significantly greater AUC was found for the combined DTI and DCE-MRI findings (0.93) compared to DTI (0.86,) or DCE-MRI (0.84) alone ($P = 0.0017$ -0.0034)^[13].

Despite the encouraging results obtained in the evaluation of prostate cancer with DKI and DTI, both alone and in combination with other MRI techniques, differentiating benign conditions such as prostatic hyperplasia from prostate cancer remains problematic. Tamura *et al*^[18] performed DKI using 11 b-values (0-1500 s/mm²) before radical prostatectomy in 20 patients and found DKI parameter K showed a trend toward higher levels in prostate cancer than in stromal benign prostatic hypertrophy, but there was marked overlap between the values in the 2 conditions (1.19 ± 0.24 vs 0.99 ± 0.28 , $P = 0.051$)^[13]. Further efforts to aid discrimination between benign (e.g., inflammatory or hyperplastic) and malignant prostatic tissue are warranted.

DTI has also been applied in an effort to delineate the location and distribution of the periprostatic nerve fibers prior to prostatectomy, with the aim of improving nerve-sparing approaches. Panebianco *et al*^[19] compared 2D and 3D T2-weighted images to DTI obtained with 16 gradient directions and $b = 0$ and 1000 s/mm^2 in 36 prostate cancer patients; reporting a partial ability to depict periprostatic nerve fibers using 2D and 3D T2 morphological sequences; with 3D-DTI allowing visualization in all directions of the entire plexus of the periprostatic nerve fibers^[19]. A summary of the clinical studies of DKI in prostate cancer is presented in Table 2.

CONCLUSION

Preliminary results suggest that IVIM, DKI and DTI may contribute incremental value to conventional DW-MRI for the detection of prostate cancer, the assessment of tumor aggressiveness, and the prediction of adverse final pathologic outcomes. However, IVIM DKI and DTI metrics have been found to overlap substantially between different prostate cancer grades as well as between cancer and benign conditions. While combining these techniques with other multiparametric MR sequences may further increase their usefulness, they are still in the early stages of development, and further research is needed to establish their roles in the evaluation of prostate cancer.

ACKNOWLEDGMENTS

We thank Mrs Ada Muellner, MS for editing this manuscript.

REFERENCES

- 1 **Tan CH**, Wei W, Johnson V, Kundra V. Diffusion-weighted MRI in the detection of prostate cancer: meta-analysis. *AJR Am J Roentgenol* 2012; **199**: 822-829 [PMID: 22997374 DOI: 10.2214/ajr.11.7805]
- 2 **Vargas HA**, Akin O, Franiel T, Mazaheri Y, Zheng J, Moskowitz C, Udo K, Eastham J, Hricak H. Diffusion-weighted endorectal MR imaging at 3 T for prostate cancer: tumor detection and assessment of aggressiveness. *Radiology* 2011; **259**: 775-784 [PMID: 21436085 DOI: 10.1148/radiol.11102066]
- 3 **Turkbey B**, Shah VP, Pang Y, Bernardo M, Xu S, Kruecker J, Locklin J, Baccala AA, Rastinehad AR, Merino MJ, Shih JH, Wood BJ, Pinto PA, Choyke PL. Is apparent diffusion coefficient associated with clinical risk scores for prostate cancers that are visible on 3-T MR images? *Radiology* 2011; **258**: 488-495 [PMID: 21177390 DOI: 10.1148/radiol.10100667]
- 4 **Zhang J**, Jing H, Han X, Huang Z, Cao Z, Liu Q. Diffusion-weighted imaging of prostate cancer on 3T MR: Relationship between apparent diffusion coefficient values and Ki-67 expression. *Acad Radiol* 2013; **20**: 1535-1541 [PMID: 24200480 DOI: 10.1016/j.acra.2013.09.007]
- 5 **Thörmer G**, Otto J, Reiss-Zimmermann M, Seiwerts M, Moche M, Garnov N, Franz T, Do M, Stolzenburg JU, Horn LC, Kahn T, Busse H. Diagnostic value of ADC in patients with prostate cancer: influence of the choice of b-values. *Eur Radiol* 2012; **22**: 1820-1828 [PMID: 22527373 DOI: 10.1007/s00330-012-2432-3]
- 6 **Tamada T**, Kanomata N, Sone T, Jo Y, Miyaji Y, Higashi H, Yamamoto A, Ito K. High b-value (2,000 s/mm²) diffusion-weighted magnetic resonance imaging in prostate cancer at 3 Tesla: comparison with 1,000 s/mm² for tumor conspicuity and discrimination of aggressiveness. *PLoS One* 2014; **9**: e96619 [PMID: 24802652 DOI: 10.1371/journal.pone.0096619]
- 7 **Ueno Y**, Takahashi S, Kitajima K, Kimura T, Aoki I, Kawakami F, Miyake H, Ohno Y, Sugimura K. Computed diffusion-weighted imaging using 3-T magnetic resonance imaging for prostate cancer diagnosis. *Eur Radiol* 2013; **23**: 3509-3516 [PMID: 23881300 DOI: 10.1007/s00330-013-2958-z]
- 8 **Mazaheri Y**, Vargas HA, Akin O, Goldman DA, Hricak H. Reducing the influence of b-value selection on diffusion-weighted imaging of the prostate: evaluation of a revised monoexponential model within a clinical setting. *J Magn Reson Imaging* 2012; **35**: 660-668 [PMID: 22069141 DOI: 10.1002/jmri.22888]
- 9 **Döpfert J**, Lemke A, Weidner A, Schad LR. Investigation of prostate cancer using diffusion-weighted intravoxel incoherent motion imaging. *Magn Reson Imaging* 2011; **29**: 1053-1058 [PMID: 21855241 DOI: 10.1016/j.mri.2011.06.001]
- 10 **Shinmoto H**, Tamura C, Soga S, Shiomi E, Yoshihara N, Kaji T, Mulkern RV. An intravoxel incoherent motion diffusion-weighted imaging study of prostate cancer. *AJR Am J Roentgenol* 2012; **199**: W496-W500 [PMID: 22997399 DOI: 10.2214/ajr.11.8347]
- 11 **Kuru TH**, Roethke MC, Stieltjes B, Maier-Hein K, Schlemmer HP, Hadaschik BA, Fenchel M. Intravoxel incoherent motion (IVIM) diffusion imaging in prostate cancer - what does it add? *J Comput Assist Tomogr* 2014; **38**: 558-564 [PMID: 24733005 DOI: 10.1097/rct.0000000000000088]
- 12 **Pang Y**, Turkbey B, Bernardo M, Kruecker J, Kadoury S, Merino MJ, Wood BJ, Pinto PA, Choyke PL. Intravoxel incoherent motion MR imaging for prostate cancer: an evaluation of perfusion fraction and diffusion coefficient derived from different b-value combinations. *Magn Reson Med* 2013; **69**: 553-562 [PMID: 22488794 DOI: 10.1002/mrm.24277]
- 13 **Li C**, Chen M, Li S, Zhao X, Zhang C, Luo X, Zhou C. Detection of prostate cancer in peripheral zone: comparison of MR diffusion tensor imaging, quantitative dynamic contrast-enhanced MRI, and the two techniques combined at 3.0 T. *Acta Radiol* 2014; **55**: 239-247 [PMID: 23892233 DOI: 10.1177/0284185113494978]
- 14 **Quentin M**, Pentang G, Schimmöller L, Kott O, Müller-Lutz A, Blondin D, Arsov C, Hiester A, Rabenalt R, Wittsack HJ. Feasibility of diffusional kurtosis tensor imaging in prostate MRI for the assessment of prostate cancer: preliminary results. *Magn Reson Imaging* 2014; **32**: 880-885 [PMID: 24848289 DOI: 10.1016/j.mri.2014.04.005]
- 15 **Rosenkrantz AB**, Prabhu V, Sigmund EE, Babb JS, Deng FM, Taneja SS. Utility of diffusional kurtosis imaging as a marker of adverse pathologic outcomes among prostate cancer active surveillance candidates undergoing radical prostatectomy. *AJR Am J Roentgenol* 2013; **201**: 840-846 [PMID: 24059373 DOI: 10.2214/ajr.12.10397]
- 16 **Rosenkrantz AB**, Sigmund EE, Johnson G, Babb JS, Mussi TC, Melamed J, Taneja SS, Lee VS, Jensen JH. Prostate cancer: feasibility and preliminary experience of a diffusional kurtosis model for detection and assessment of aggressiveness of peripheral zone cancer. *Radiology* 2012; **264**: 126-135 [PMID: 22550312 DOI: 10.1148/radiol.12112290]
- 17 **Suo S**, Chen X, Wu L, Zhang X, Yao Q, Fan Y, Wang H, Xu J. Non-Gaussian water diffusion kurtosis imaging of prostate cancer. *Magn Reson Imaging* 2014; **32**: 421-427 [PMID: 24602826 DOI: 10.1016/j.mri.2014.01.015]
- 18 **Tamura C**, Shinmoto H, Soga S, Okamura T, Sato H, Okuaki T, Pang Y, Kosuda S, Kaji T. Diffusion kurtosis imaging study of prostate cancer: preliminary findings. *J Magn Reson Imaging* 2014; **40**: 723-729 [PMID: 24924835 DOI: 10.1002/jmri.24379]
- 19 **Panebianco V**, Barchetti F, Sciarra A, Marcantonio A, Zini C, Salciccia S, Colletini F, Gentile V, Hamm B, Catalano C. In vivo 3D neuroanatomical evaluation of periprostatic nerve plexus with 3T-MR Diffusion Tensor Imaging. *Eur J Radiol* 2013; **82**: 1677-1682 [PMID: 23773553 DOI: 10.1016/j.ejrad.2013.05.013]

P- Reviewer: Cai T, Ghatak S

S- Editor: Ji FF L- Editor: A E- Editor: Jiao XK



Lung cancer screening: Computed tomography or chest radiographs?

Edwin JR van Beek, Saeed Mirsadraee, John T Murchison

Edwin JR van Beek, Saeed Mirsadraee, Clinical Research Imaging Centre, Queen's Medical Research Institute, University of Edinburgh, Edinburgh EH16 4TJ, United Kingdom

Edwin JR van Beek, Saeed Mirsadraee, John T Murchison, Department of Radiology, Royal Infirmary of Edinburgh, Edinburgh EH16 4TJ, United Kingdom

Author contributions: The authors equally contributed to the literature research and editing of the manuscript; van Beek EJ was the guarantor for this work.

Conflict-of-interest statement: The authors have no conflicts of interest to declare.

Open-Access: This article is an open-access article which was selected by an in-house editor and fully peer-reviewed by external reviewers. It is distributed in accordance with the Creative Commons Attribution Non Commercial (CC BY-NC 4.0) license, which permits others to distribute, remix, adapt, build upon this work non-commercially, and license their derivative works on different terms, provided the original work is properly cited and the use is non-commercial. See: <http://creativecommons.org/licenses/by-nc/4.0/>

Correspondence to: Edwin JR van Beek, MD, PhD, FRCR, FRCPE, Professor, Clinical Research Imaging Centre, Queen's Medical Research Institute, University of Edinburgh, CO.19, CRIC, QMRI, 47 Little France Crescent, Edinburgh EH16 4TJ, United Kingdom. edwin-vanbeek@ed.ac.uk
 Telephone: +44-131-2427760
 Fax: +44-131-2427773

Received: March 30, 2015
 Peer-review started: April 4, 2015
 First decision: April 27, 2015
 Revised: April 29, 2015
 Accepted: May 27, 2015
 Article in press: May 28, 2015
 Published online: August 28, 2015

due to malignancy. The vast majority of cases of lung cancer are smoking related and the most effective way of reducing lung cancer incidence and mortality is by smoking cessation. In the Western world, smoking cessation policies have met with limited success. The other major means of reducing lung cancer deaths is to diagnose cases at an earlier more treatable stage employing screening programmes using chest radiographs or low dose computed tomography. In many countries smoking is still on the increase, and the sheer scale of the problem limits the affordability of such screening programmes. This short review article will evaluate the current evidence and potential areas of research which may benefit policy making across the world.

Key words: Lung cancer; Chest radiograph; Computed tomography; Screening; Health economics

© **The Author(s) 2015.** Published by Baishideng Publishing Group Inc. All rights reserved.

Core tip: The use of low dose computed tomography (CT) for lung cancer screening is superior to the use of standard chest radiograph (CXR), and therefore standard CXR should not be used for this purpose. However, the application of novel computer assisted diagnosis software may influence the utility of CXR and may ultimately be a cost-efficient method in those countries where delivery of low-dose CT is not feasible due to infrastructure or costs constraints.

van Beek EJ, Mirsadraee S, Murchison JT. Lung cancer screening: Computed tomography or chest radiographs? *World J Radiol* 2015; 7(8): 189-193 Available from: URL: <http://www.wjgnet.com/1949-8470/full/v7/i8/189.htm> DOI: <http://dx.doi.org/10.4329/wjr.v7.i8.189>

Abstract

Worldwide, lung cancer is the leading cause of mortality

INTRODUCTION

Lung cancer is the most common cause of cancer

death in the United Kingdom accounting for 6% of overall national mortality and around 35000 deaths a year. In 2008 lung cancer was estimated to account for 18% of deaths world wide. Both one year and 5 years survival are inversely proportional to disease stage^[1]. Current statistics in Scotland, which has a population of approximately 5.2 million, show an incidence of approximately 1 in 1000 with 8 in 10000 people dying due to lung cancer^[2]. Similar incidence rates exist in other countries, and in the United States approximately 160000 deaths are due to lung cancer each year^[3].

Most lung cancers are smoking related and smoking cessation is the most effective way of preventing this frequently fatal illness. The disease can be cured, especially if caught early. Stage 1, screening detected lung cancer has a 5-year survival rate in excess of 85%, whereas more advanced lung cancer invariably leads to death in less than 2 years^[4]. As the lung cancer epidemic has grown and spread, ways of detecting the disease earlier, to improve the cure rate, have been explored. These have mainly been based around imaging using the chest radiograph (CXR) and computed tomography (CT).

CXR

In the early 1980s, a lung screening programme using 4-monthly CXRs in high risk patients was developed at the Mayo Clinic^[5]. Subjects selected were over 45 years old male heavy smokers defined as one pack/day. They were randomly assigned to a control group (4593 patients) or repeated CXR follow up at 4 mo interval (4618 patients) after they had undergone an initial CXR and sputum cytology examination that were both normal. The follow up success was 75% at 4 mo, and 92 lung cancers were detected by CXR (of which 7 also had sputum cytology positive findings), while 15 patients had normal CXR with abnormal sputum cytology for an overall incidence of 109 (2.4%). A significant number of these lung cancers were visible in retrospect. Furthermore, 52 of the lung cancer were classified as stage I (early disease; 35 of these were peripheral lesions), 4 were stage 2 disease (3 perihilar and 1 with hilar enlargement) while the 35 had stage 3 disease (15 peripheral lesions, 4 perihilar and 13 with hilar enlargement).

Another study in New York randomised a similar population of 10040 subjects to annual CXR only vs additional 4-monthly sputum cytology^[6]. This study showed similar outcome between the two groups, with 288 detected lung cancers equally distributed between the two groups.

It was concluded from this study that the 4-monthly screening for lung cancer using chest radiography and sputum cytology, although capable of detecting up to 20% of lung cancers, was unable to improve mortality advantage over patients who were offered annual testing^[7].

A more recent attempt at using CXR screening

was carried out in the Prostate, Lung, Colorectal and Ovarian cancer screening trial^[8]. This study randomised 154901 men and women aged 55-74 years to either standard care (77456) or annual screening (77445) for four years during the period 1993-2001. The number of lung cancer deaths was equal in both groups (1213 vs 1230) with similar stage and histology of lung cancers. Therefore, it was concluded that annual CXR screening does not benefit outcome of lung cancer mortality.

From these large scale studies, as well as from the National Lung Screening Trial (NLST) (see below), it is concluded that the application of routine annual chest radiography for screening of high-risk patients for lung cancer, although detecting a significant number of lung cancer cases, is not beneficial in terms of improvement of mortality.

CT

The NLST compared CXRs with computed tomography for the screening of patients at high risk for developing lung cancer^[9]. Men and women were selected in the age group 55-74 years with a history of cigarette smoking of at least 30 pack years or had these exposure rates but had quit smoking within 15 years. The subjects were randomised to either three annual screening posterior-anterior CXRs (26732) or low-dose CT (26722). Almost 4-fold higher positive screening tests were obtained with CT (24.2% vs 6.9%), with the false positive rate slightly lower in the CXRs group (94.5% vs 96.4%). The incidence of proven lung cancer was higher in the CT group compared to the CXR group (relative risk 1.13; 95%CI: 1.03-1.23). More importantly, mortality due to lung cancer decreased from 309 deaths per 100000 person-years in the radiography group to 247 deaths from lung cancer per 100000 person-years in the low-dose CT group, a decrease of 20%. In addition, the CT group benefitted from other diagnoses that positively affected mortality rates, with 6.7% fewer patients dying in the low-dose CT group.

In Europe, several studies were started to evaluate the potential role of low-dose chest CT for lung cancer screening. Three studies did not demonstrate a benefit of lung cancer screening with CT in terms of mortality, but these were insufficiently powered to reliably draw such conclusion^[10-12]. There are a further five ongoing studies that are yet to report on the final results, but some will be able to give answers to the question whether CT screening improves outcome of lung cancer patients^[13-17].

The Netherlands-Leuven Longkanker Screening Onderzoek (NELSON) study is a Dutch/Belgian project, which recruited 20000 high-risk subjects and randomised half of them for low-dose CT and the other half for CXR screening^[13]. It is the largest European study and has sufficient power to enable a statement whether low-dose CT screening has benefit over chest radiography screening.

Another study from Canada has reported the first

screening round results and is focused on inclusion of cytology using autofluorescence bronchoscopy as well as modelling approaches towards optimisation of predictive value for lung nodules^[18].

A potential risk associated with screening is the false positive results that can lead to further investigations and additional costs. A randomized, controlled trial of low-dose CT vs chest radiography ($n = 3318$ in both arms) as part of the NLST demonstrated a false-positive rate of 21% and 9% for single low-dose CT and chest radiography screening, respectively^[19]. A total of 7% of participants with a false-positive low-dose CT examination and 4% with a false-positive chest radiography subsequently underwent an invasive procedure.

Another potential risk associate with lung cancer screening is the potential increased risk of lifetime cancers as a result of ionising radiation. The estimated risk of cancer from exposure to CT ionising radiation is reported to be more when the screening is started earlier in life, or on annual basis, and in females. A study reported an estimated 5.5% increase in lung cancer risk attributable to annual CT-related radiation exposure and concluded that a mortality benefit of considerably more than 5% may be necessary to outweigh the potential radiation risks^[20].

Screening programs are associated with additional costs, both from the screening procedure and the follow up interventions. Previous studies reported that screening for lung cancer appeared to be cost-effective in high risk, more elderly populations^[21,22]. Other studies questioned the potential cost effectiveness of lung cancer screening. However, their results were based on lower estimated effectiveness of screening than what was demonstrated by the NLST^[23,24].

A more recent cost-utility analysis of lung cancer screening by low dose CT reported that repeat annual lung cancer screening in high risk adults aged 50-64 was highly cost-effective^[25]. The study also indicated that offering smoking cessation interventions with the screening program improved the cost-effectiveness of lung cancer screening between 20%-45%.

A contrary report was published as part of a health technology assessment, which suggested that lung cancer screening would not be cost-effective^[26]. However, it should be considered that this report was issued prior to the results of most of the recent large lung cancer screening trials.

The largest and most recent study, the NLST, also had an economic analysis and cost-effectiveness analysis performed^[27]. This study demonstrated that the additional healthcare costs of performing low-dose CT screening would cost \$1631 per person, with the incremental costs per life-year gained and the costs per quality adjusted life year gained coming in at \$52000 and \$81000, respectively. Importantly, there was quite a wide range of life year gains depending on age (optimal age range 60-69 years), risk for developing lung cancer (highest risk groups benefitting most) and gender (with

women benefitting least). This caused a range of costs for quality adjusted life year gained anywhere between \$32000-\$615000. The study did not show a cost-effective benefit for chest radiography screening.

DISCUSSION

Clearly, based on the above studies, CT is superior to CXRs for screening in lung cancer. Although the NLST appears to have answered the question conclusively, there are still ongoing studies that may influence the manner in which screening will be approached in the future. Significant debate is still ongoing as to how often we should be screening, the optimal population that could benefit, interpretation of nodules, avoidance of false positive results and approaches including positron emission tomography-computed tomography, magnetic resonance imaging and autofluorescence bronchoscopy for instance^[28-34]. Many of these points are still undergoing evaluation, and future study results are eagerly awaited.

There are some additional points to be taken into consideration, which may still give CXRs a potential role for screening of lung cancer.

First, CXRs have matured from a technical perspective, and the wide introduction of digital CXRs offers a new approach to application of computer assisted diagnosis (CAD). Thus, several studies have shown greater sensitivity for lung nodule detection using CAD methodologies, and this may be of benefit when using the test as a screening test^[35,36]. However, a conclusive study showing the benefit of screening with chest radiography and added CAD has not been performed and could be important in this respect.

Second, CXRs are by far the cheaper of the two imaging modalities and more commonly available. This is an important issue, particularly in countries that are less well developed and where smoking continues to be on the increase and the lung cancer epidemic is on the rise. There is a high false negative rate using the CXR. CXR screening programmes should be backed up with cross-sectional imaging with a low threshold in place for investigating even small abnormalities detected on the CXR with CT scan. It may not be feasible to arrange for large-scale screening using CT and in these circumstances, one could consider using the CXR.

Whilst NLST demonstrated that benefits from early detection of lung cancer outweighs the risk of ionizing radiation, the potential risk is substantial. In NLST, participants received an average exposure of 8 mSv over 3 years of screening/diagnostic examinations which can potentially cause 1 cancer in every 2500 screened^[37]. Recently, multiple studies have been investigating the feasibility of radiation dose reduction to sub-mSv level whilst the diagnostic accuracy is maintained^[38,39]. Since there is a high contrast resolution between air and lung nodules, significant radiation dose reduction can be achieved while maintaining good diagnostic quality. Various strategies such as reduced

tube voltage, tube current, or both is being used. The application of iterative reconstruction would maintain spatial resolution in low dose studies whilst maintain diagnostic accuracy^[40].

Overall, it is highly likely that low-dose CT screening for patients at high risk for developing lung cancer is a cost-effective approach which will lead to improved outcome due to earlier detection and treatment of this highly lethal malignancy. In countries that have the resources available, it makes sense therefore to use low-dose CT as a screening methodology. For countries where finances or logistics render low-dose CT screening impossible to deliver, CXRs on an annual basis should be considered and additional use of CAD may improve sensitivity for earlier lesions.

REFERENCES

- Cancer Research UK.** Lung cancer mortality statistics. [accessed 2013 May 11]. Available from: URL: <http://www.cancerresearchuk.org/cancer-info/cancerstats/types/lung/mortality/uk-lung-cancer-mortality-statistics>
- ISD Scotland.** Information and Statistics. Lung cancer and mesothelioma. [accessed 2013 August 7]. Available from: URL: <http://www.isdscotland.org/Health-Topics/Cancer/Cancer-Statistics/Lung-Cancer-and-Mesothelioma/>
- Siegel R, Naishadham D, Jemal A.** Cancer statistics, 2013. *CA Cancer J Clin* 2013; **63**: 11-30 [PMID: 23335087 DOI: 10.3322/caac.21166]
- Henschke CI, Yankelevitz DF, Libby DM, Pasmantier MW, Smith JP, Miettinen OS.** Survival of patients with stage I lung cancer detected on CT screening. *N Engl J Med* 2006; **355**: 1763-1771 [PMID: 17065637 DOI: 10.1056/NEJMoa060476]
- Muhm JR, Miller WE, Fontana RS, Sanderson DR, Uhlenhopp MA.** Lung cancer detected during a screening program using four-month chest radiographs. *Radiology* 1983; **148**: 609-615 [PMID: 6308709 DOI: 10.1148/radiology.148.3.6308709]
- Melamed MR, Flehinger BJ, Zaman MB, Heelan RT, Perchick WA, Martini N.** Screening for early lung cancer. Results of the Memorial Sloan-Kettering study in New York. *Chest* 1984; **86**: 44-53 [PMID: 6734291 DOI: 10.1378/chest.86.1.44]
- Fontana RS, Sanderson DR, Woolner LB, Taylor WF, Miller WE, Muhm JR.** Lung cancer screening: the Mayo program. *J Occup Med* 1986; **28**: 746-750 [PMID: 3528436]
- Oken MM, Hocking WG, Kvale PA, Andriole GL, Buys SS, Church TR, Crawford ED, Fouad MN, Isaacs C, Reding DJ, Weissfeld JL, Yokochi LA, O'Brien B, Ragard LR, Rathmell JM, Riley TL, Wright P, Caparaso N, Hu P, Izmirlian G, Pinsky PF, Prorok PC, Kramer BS, Miller AB, Gohagan JK, Berg CD.** Screening by chest radiograph and lung cancer mortality: the Prostate, Lung, Colorectal, and Ovarian (PLCO) randomized trial. *JAMA* 2011; **306**: 1865-1873 [PMID: 22031728 DOI: 10.1001/jama.2011.1591]
- Aberle DR, Adams AM, Berg CD, Black WC, Clapp JD, Fagerstrom RM, Gareen IF, Gatsonis C, Marcus PM, Sicks JD.** Reduced lung-cancer mortality with low-dose computed tomographic screening. *N Engl J Med* 2011; **365**: 395-409 [PMID: 21714641 DOI: 10.1056/NEJMoa1102873]
- Pedersen JH, Ashraf H, Dirksen A, Bach K, Hansen H, Toennesen P, Thorsen H, Brodersen J, Skov BG, Døssing M, Mortensen J, Richter K, Clementsen P, Seersholm N.** The Danish randomized lung cancer CT screening trial--overall design and results of the prevalence round. *J Thorac Oncol* 2009; **4**: 608-614 [PMID: 19357536 DOI: 10.1097/JTO.0b013e3181a0d98f]
- Infante M, Cavuto S, Lutman FR, Brambilla G, Chiesa G, Ceresoli G, Passera E, Angeli E, Chiarenza M, Aranzulla G, Cariboni U, Errico V, Inzirillo F, Bottoni E, Voulaz E, Alloisio M, Destro A, Roncalli M, Santoro A, Ravasi G.** A randomized study of lung cancer screening with spiral computed tomography: three-year results from the DANTE trial. *Am J Respir Crit Care Med* 2009; **180**: 445-453 [PMID: 19520905 DOI: 10.1164/rccm.200901-0076OC]
- Pastorino U, Rossi M, Rosato V, Marchianò A, Sverzellati N, Morosi C, Fabbri A, Galeone C, Negri E, Sozzi G, Pelosi G, La Vecchia C.** Annual or biennial CT screening versus observation in heavy smokers: 5-year results of the MILD trial. *Eur J Cancer Prev* 2012; **21**: 308-315 [PMID: 22465911 DOI: 10.1097/CEJ.0b013e328351e1b6]
- van Iersel CA, de Koning HJ, Draisma G, Mali WP, Scholten ET, Nackaerts K, Prokop M, Habbema JD, Oudkerk M, van Klaveren RJ.** Risk-based selection from the general population in a screening trial: selection criteria, recruitment and power for the Dutch-Belgian randomised lung cancer multi-slice CT screening trial (NELSON). *Int J Cancer* 2007; **120**: 868-874 [PMID: 17131307 DOI: 10.1002/ijc.22134]
- Blanchon T, Bréchet JM, Grenier PA, Ferretti GR, Lemarié E, Milleron B, Chagué D, Laurent F, Martinet Y, Beigelman-Aubry C, Blanchon F, Revel MP, Friard S, Rémy-Jardin M, Vasile M, Santelmo N, Lecalier A, Lefebvre P, Moro-Sibilot D, Breton JL, Carrette MF, Brambilla C, Fournel F, Kieffer A, Fria G, Flahault A.** Baseline results of the Depiscan study: a French randomized pilot trial of lung cancer screening comparing low dose CT scan (LDCT) and chest X-ray (CXR). *Lung Cancer* 2007; **58**: 50-58 [PMID: 17624475]
- Lopes Pegna A, Picozzi G, Mascalchi M, Maria Carozzi F, Carozzi L, Comin C, Spinelli C, Falaschi F, Grazzini M, Innocenti F, Ronchi C, Paci E.** Design, recruitment and baseline results of the ITALUNG trial for lung cancer screening with low-dose CT. *Lung Cancer* 2009; **64**: 34-40 [PMID: 18723240 DOI: 10.1016/j.lungcan.2008.07.003]
- Becker N, Motsch E, Gross ML, Eigentopf A, Heussel CP, Dienemann H, Schnabel PA, Pilz L, Eichinger M, Optazait DE, Puderbach M, Tremper J, Delorme S.** Randomized study on early detection of lung cancer with MSCT in Germany: study design and results of the first screening round. *J Cancer Res Clin Oncol* 2012; **138**: 1475-1486 [PMID: 22526165 DOI: 10.1007/s00432-012-1228-9]
- Baldwin DR, Duffy SW, Wald NJ, Page R, Hansell DM, Field JK.** UK Lung Screen (UKLS) nodule management protocol: modelling of a single screen randomised controlled trial of low-dose CT screening for lung cancer. *Thorax* 2011; **66**: 308-313 [PMID: 21317179]
- McWilliams A, Tammemagi MC, Mayo JR, Roberts H, Liu G, Soghrati K, Yasufuku K, Martel S, Laberge F, Gingras M, Atkar-Khattra S, Berg CD, Evans K, Finley R, Yee J, English J, Nasute P, Goffin J, Puksa S, Stewart L, Tsai S, Johnston MR, Manos D, Nicholas G, Goss GD, Seely JM, Amjadi K, Tremblay A, Burrows P, MacEachern P, Bhatia R, Tsao MS, Lam S.** Probability of cancer in pulmonary nodules detected on first screening CT. *N Engl J Med* 2013; **369**: 910-919 [PMID: 24004118 DOI: 10.1056/NEJMoa1214726]
- Croswell JM, Baker SG, Marcus PM, Clapp JD, Kramer BS.** Cumulative incidence of false-positive test results in lung cancer screening: a randomized trial. *Ann Intern Med* 2010; **152**: 505-12, W176-80 [PMID: 20404381 DOI: 10.7326/0003-4819-152-8-2010-04200-00007]
- Brenner DJ.** Radiation risks potentially associated with low-dose CT screening of adult smokers for lung cancer. *Radiology* 2004; **231**: 440-445 [PMID: 15128988 DOI: 10.1148/radiol.2312030880]
- Henschke CI, McCauley DI, Yankelevitz DF, Naidich DP, McGuinness G, Miettinen OS, Libby DM, Pasmantier MW, Koizumi J, Altorki NK, Smith JP.** Early Lung Cancer Action Project: overall design and findings from baseline screening. *Lancet* 1999; **354**: 99-105 [PMID: 10408484 DOI: 10.1016/S0140-6736(99)06093-6]
- Marshall D, Simpson KN, Earle CC, Chu CW.** Economic decision analysis model of screening for lung cancer. *Eur J Cancer* 2001; **37**: 1759-1767 [PMID: 11549429 DOI: 10.1016/S0959-8049(01)0

- 0205-2]
- 23 **Mahadevia PJ**, Fleisher LA, Frick KD, Eng J, Goodman SN, Powe NR. Lung cancer screening with helical computed tomography in older adult smokers: a decision and cost-effectiveness analysis. *JAMA* 2003; **289**: 313-322 [PMID: 12525232 DOI: 10.1001/jama.289.3.313]
 - 24 **Manser R**, Dalton A, Carter R, Byrnes G, Elwood M, Campbell DA. Cost-effectiveness analysis of screening for lung cancer with low dose spiral CT (computed tomography) in the Australian setting. *Lung Cancer* 2005; **48**: 171-185 [PMID: 15829317 DOI: 10.1016/j.lungcan.2004.11.001]
 - 25 **Villanti AC**, Jiang Y, Abrams DB, Pyenson BS. A cost-utility analysis of lung cancer screening and the additional benefits of incorporating smoking cessation interventions. *PLoS One* 2013; **8**: e71379 [PMID: 23940744]
 - 26 **Black C**, Bagust A, Boland A, Walker S, McLeod C, De Verteuil R, Ayres J, Bain L, Thomas S, Godden D, Waugh N. The clinical effectiveness and cost-effectiveness of computed tomography screening for lung cancer: systematic reviews. *Health Technol Assess* 2006; **10**: iii-iv, ix-x, 1-90 [PMID: 16409881]
 - 27 **Black WC**, Gareen IF, Soneji SS, Sicks JD, Keeler EB, Aberle DR, Naeim A, Church TR, Silvestri GA, Gorelick J, Gatsonis C. Cost-effectiveness of CT screening in the National Lung Screening Trial. *N Engl J Med* 2014; **371**: 1793-1802 [PMID: 25372087 DOI: 10.1056/NEJMoa1312547]
 - 28 **Field JK**, Oudkerk M, Pedersen JH, Duffy SW. Prospects for population screening and diagnosis of lung cancer. *Lancet* 2013; **382**: 732-741 [PMID: 23972816 DOI: 10.1016/S0140-6736(13)61614-1]
 - 29 **Wood DE**. Maximizing the benefit and minimizing the risks of lung cancer screening. *J Thorac Imaging* 2012; **27**: 211-212 [PMID: 22695062 DOI: 10.1097/RTI.0b013e318256c22f]
 - 30 **van Klaveren RJ**, Oudkerk M, Prokop M, Scholten ET, Nackaerts K, Vernhout R, van Iersel CA, van den Bergh KA, van 't Westeinde S, van der Aalst C, Thunnissen E, Xu DM, Wang Y, Zhao Y, Gietema HA, de Hoop BJ, Groen HJ, de Bock GH, van Ooijen P, Weenink C, Verschakelen J, Lammers JW, Timens W, Willebrand D, Vink A, Mali W, de Koning HJ. Management of lung nodules detected by volume CT scanning. *N Engl J Med* 2009; **361**: 2221-2229 [PMID: 19955524 DOI: 10.1056/NEJMoa0906085]
 - 31 **Heuvelmans MA**, Oudkerk M, de Bock GH, de Koning HJ, Xie X, van Ooijen PM, Greuter MJ, de Jong PA, Groen HJ, Vliegenthart R. Optimisation of volume-doubling time cutoff for fast-growing lung nodules in CT lung cancer screening reduces false-positive referrals. *Eur Radiol* 2013; **23**: 1836-1845 [PMID: 23508275 DOI: 10.1007/s00330-013-2799-9]
 - 32 **Pastorino U**, Bellomi M, Landoni C, De Fiori E, Arnaldi P, Picchio M, Pelosi G, Boyle P, Fazio F. Early lung-cancer detection with spiral CT and positron emission tomography in heavy smokers: 2-year results. *Lancet* 2003; **362**: 593-597 [PMID: 12944057 DOI: 10.1016/S0140-6736(03)14188-8]
 - 33 **McWilliams AM**, Mayo JR, Ahn MI, MacDonald SL, Lam SC. Lung cancer screening using multi-slice thin-section computed tomography and autofluorescence bronchoscopy. *J Thorac Oncol* 2006; **1**: 61-68 [PMID: 17409828]
 - 34 **Sommer G**, Tremper J, Koenigkam-Santos M, Delorme S, Becker N, Biederer J, Kauczor HU, Heussel CP, Schlemmer HP, Puderbach M. Lung nodule detection in a high-risk population: comparison of magnetic resonance imaging and low-dose computed tomography. *Eur J Radiol* 2014; **83**: 600-605 [PMID: 24364923 DOI: 10.1016/j.ejrad.2013.11.012]
 - 35 **van Beek EJ**, Mullan B, Thompson B. Evaluation of a real-time interactive pulmonary nodule analysis system on chest digital radiographic images: a prospective study. *Acad Radiol* 2008; **15**: 571-575 [PMID: 18423313 DOI: 10.1016/j.acra.2008.01.018]
 - 36 **White CS**, Flukinger T, Jeudy J, Chen JJ. Use of a computer-aided detection system to detect missed lung cancer at chest radiography. *Radiology* 2009; **252**: 273-281 [PMID: 19561261 DOI: 10.1148/radiol.2522081319]
 - 37 **Bach PB**, Mirkin JN, Oliver TK, Azzoli CG, Berry DA, Brawley OW, Byers T, Colditz GA, Gould MK, Jett JR, Sabichi AL, Smith-Bindman R, Wood DE, Qaseem A, Detterbeck FC. Benefits and harms of CT screening for lung cancer: a systematic review. *JAMA* 2012; **307**: 2418-2429 [PMID: 22610500 DOI: 10.1001/jama.2012.5521]
 - 38 **Mathieu KB**, Ai H, Fox PS, Godoy MC, Munden RF, de Groot PM, Pan T. Radiation dose reduction for CT lung cancer screening using ASIR and MBIR: a phantom study. *J Appl Clin Med Phys* 2014; **15**: 4515 [PMID: 24710436 DOI: 10.1120/jacmp.v15i2.4515]
 - 39 **Tekath M**, Dutheil F, Bellini R, Roche A, Pereira B, Naughton G, Chamoux A, Michel JL. Comparison of the ultra-low-dose Veo algorithm with the gold standard filtered back projection for detecting pulmonary asbestos-related conditions: a clinical observational study. *BMJ Open* 2014; **4**: e004980 [PMID: 24879827 DOI: 10.1136/bmjopen-2014-004980]
 - 40 **Rampinelli C**, Origgi D, Bellomi M. Low-dose CT: technique, reading methods and image interpretation. *Cancer Imaging* 2013; **12**: 548-556 [PMID: 23400217 DOI: 10.1102/1470-7330.2012.0049]

P- Reviewer: Hida T, Lassandro F, Pereira-Vega A, Yamaguchi K

S- Editor: Ji FF **L- Editor:** A **E- Editor:** Jiao XK



Magnetic resonance imaging-based interpretation of degenerative changes in the lower lumbar segments and therapeutic consequences

Adel Maataoui, Thomas J Vogl, M Fawad Khan

Adel Maataoui, Thomas J Vogl, M Fawad Khan, Institute for Diagnostic and Interventional Radiology, Goethe University, 60590 Frankfurt am Main, Germany

Author contributions: Maataoui A, Vogl TJ and Khan MF wrote the editorial and approved the version to be published.

Conflict-of-interest statement: The corresponding authors confirm that there are no conflicts of interest.

Open-Access: This article is an open-access article which was selected by an in-house editor and fully peer-reviewed by external reviewers. It is distributed in accordance with the Creative Commons Attribution Non Commercial (CC BY-NC 4.0) license, which permits others to distribute, remix, adapt, build upon this work non-commercially, and license their derivative works on different terms, provided the original work is properly cited and the use is non-commercial. See: <http://creativecommons.org/licenses/by-nc/4.0/>

Correspondence to: Adel Maataoui, MD, Institute for Diagnostic and Interventional Radiology, Goethe University, Frankfurt, Theodor-Stern-Kai 7, 60590 Frankfurt am Main, Germany. adel.maataoui@gmx.de
Telephone: +49-69-63015534
Fax: +49-69-63014222

Received: January 29, 2015
Peer-review started: January 29, 2015
First decision: March 6, 2015
Revised: April 17, 2015
Accepted: May 16, 2015
Article in press: July 8, 2015
Published online: August 28, 2015

Abstract

Intervertebral disc degeneration and facet joint osteoarthritis of the lumbar spine are, among others, well

known as a cause of low back and lower extremity pain. Together with their secondary disorders they set a big burden on health care systems and economics worldwide. Despite modern imaging modalities, such as magnetic resonance imaging, for a large proportion of patients with low back pain (LBP) it remains difficult to provide a specific diagnosis. The fact that nearly all the lumbar structures are possible sources of LBP, may serve as a possible explanation. Furthermore, our clinical experience confirms, that imaging alone is not a sufficient approach explaining LBP. Here, the Oswestry Disability Index, as the most commonly used measure to quantify disability for LBP, may serve as an easy-to-apply questionnaire to evaluate the patient's ability to cope with everyday life. For therapeutic purposes, among the different options, the lumbar facet joint intra-articular injection of corticosteroids in combination with an anaesthetic solution is one of the most frequently performed interventional procedures. Although widely used the clinical benefit of intra-articular steroid injections remains controversial. Therefore, prior to therapy, standardized diagnostic algorithms for an accurate assessment, classification and correlation of degenerative changes of the lumbar spine are needed.

Key words: Low back pain; Spine; Intervertebral disc disease; Facet joint osteoarthritis; Magnetic resonance imaging; Oswestry Disability Index

© **The Author(s) 2015.** Published by Baishideng Publishing Group Inc. All rights reserved.

Core tip: Low back pain, caused by intervertebral disc degeneration (IDD) and facet joint osteoarthritis (FJOA), is a widely spread musculoskeletal disorder in all ages worldwide. Although IDD and FJOA are common findings on lumbar magnetic resonance-imaging, the relationship between imaging findings and clinical pain-presentation

as well as the benefit of different therapeutic options often remains unclear. This article briefly reviews the correlation of IDD and FJOA with clinical pain scores and discusses possible treatment options of FJOA with focus on the intra-articular injection of corticosteroids.

Maataoui A, Vogl TJ, Khan MF. Magnetic resonance imaging-based interpretation of degenerative changes in the lower lumbar segments and therapeutic consequences. *World J Radiol* 2015; 7(8): 194-197 Available from: URL: <http://www.wjgnet.com/1949-8470/full/v7/i8/194.htm> DOI: <http://dx.doi.org/10.4329/wjr.v7.i8.194>

INTRODUCTION

Among others, intervertebral disc degeneration (IDD) and facet joint osteoarthritis (FJOA) have been identified as causes for low back pain (LBP). Magnetic resonance imaging (MRI) is the imaging method of choice for the evaluation of IDD and FJOA of the lumbar spine^[1,2]. For the grading of IDD of the lumbar spine Pfirrmann *et al*^[3] proposed a MRI-based 5-point scale which is based on MRI signal intensity, disc structure, distinction between nucleus and annulus and disc height on T2-weighted, midsagittal images. Due to its more precise demonstration of bony details computed tomography (CT) often is the preferred modality in the evaluation of FJOA. Weishaupt *et al*^[4] evaluated the significance of MRI in comparison to CT using an established 4-point scale. In summary, the authors conclude that an additional CT scan is not required in the presence of a MRI examination. Due to the fact that nearly all lumbar structures are possible sources of LBP, for a large proportion of patients it remains difficult to provide a specific diagnosis. The Oswestry Disability Index (ODI) is the most commonly used measure to quantify disability for LBP^[5] and could reflect the relationship between pain and increasing grades of IDD and FJOA. If FJOA is identified as source of pain, multiple therapeutic options have been described and established^[6]. Among the different options, the lumbar facet joint (LFJ) intra-articular injection of corticosteroids in combination with an anaesthetic solution is one of the most frequently performed interventional procedures^[7]. The theory of this particular therapeutic approach is based on the idea that there is inflammation of the synovial structures of the degenerated facet joints. Thus intra-articular steroid injection is performed to generate an anti-inflammatory effect in order to achieve pain relief. Although widely used the clinical benefit of intra-articular steroid injections remains controversial^[8]. The aim of the presented article is to highlight the relationship of increasing grades of IDD/FJOA and clinical pain scores and to discuss therapeutic success of minimally invasive therapeutic procedures, such as intra-articular steroid injections in degenerated facet joints.

SOURCES OF BACK PAIN

FJOA and pain correlation

Since the facet joints are the only synovial joints in the spine with hyaline cartilage overlying subchondral bone, a synovial membrane and a joint capsule, they develop degenerative changes that are equivalent to other peripheral joints. Different studies reported contradicting results about the prevalence of FJOA at lumbar levels. Kalichman *et al*^[9] reported that FJOA is more prevalent at L4/5 (45.1%) followed by L5/S1 (38.2%) and L3/4 (30.6%) whereas Abbas *et al*^[10] describe a different descending order: L5/S1 (55%), L4/5 (27%) and L3/4 (16%). Additionally, Abbas *et al*^[10] describe that FJOA is an age dependant phenomenon, which increases cephalocaudally, whereas they found no correlation of FJOA with sex or the Body mass index. For the assessment of FJOA our group applied the 4-point scale as proposed by Weishaupt *et al*^[4] on approximately 2400 facet joints of the lumbar segments L4/5 and L5/S1. Assuming that grade I changes already represent mild degenerative changes, nearly all patients in our study group showed degenerative alterations of the facet joints (97% L4/5; 98% L5/S1). In 150 patients Ashraf *et al*^[11] classified degenerative changes of the lumbar spine on lateral radiographs according to the criteria of Kellgren and Lawrence. Additionally, functional disability was measured using the ODI. They found no significant correlation between the morphological severity of osteoarthritis and ODI scores. Peterson *et al*^[12] evaluated 172 consecutive patients with LBP. Lumbar radiographs were judged with regard to the severity of disc and facet joint degeneration. Results were correlated with the data of the ODI. The authors describe a weak correlation between the values of LBP and radiologically assessed lumbar spine degeneration. A major limitation of the mentioned studies is the fact that degenerative changes of the cervical and lumbar spine were graded on plain film radiographs, which are because of superposition of limited diagnostic value. Additionally, severity of degeneration of intervertebral discs as well as of facet joints was taken into account for scoring. As already mentioned nearly all-lumbar structures are possible sources of LBP, so that an isolated contemplation of anatomic structures (facet joint, intervertebral disc) and their degenerative changes with regard to clinical importance is necessary. Therefore we correlated degenerative changes of facet joints at lumbar levels L4/5 and L5/S1 with the ODI. Our results demonstrate that there is only a weak correlation between signs of degeneration and clinical disability scores as evaluated by ODI. Taking into account that a huge majority of patients of all ages show degenerative changes of facet joints in the lower motion segments of the lumbar spine, these results should be considered in the future evaluation of lumbar MRIs. In the presence of other degenerative changes like IDD, osteochondrosis or Morbus Bastrup the finding of FJOA shouldn't be



Figure 1 Computed tomography-guided puncture of the facet joints at lumbar levels L4/5 showing the needle trajectory.

considered evidentiary as the cause of LBP. In fact, the presented results seem to prove that chronic LBP is a multifactorial disorder, which cannot be explained with a constricted view on one lumbar compartment.

IDD and pain correlation

It is widely accepted that IDD of the lumbar spine is one of the main cause of lower back pain^[13,14]. The etiology of IDD is not fully explained - heavy physical loading^[15], overweight^[16,17], vibrations during vehicle driving^[18] and smoking^[19] have been suggested to be associated with IDD. Since radiological features of IDD are almost universal in adults, it often remains unclear to what extent these changes are responsible for the clinical symptoms of the patient. From the radiological point of view, in the first place a standardized nomenclature in the evaluation of intervertebral disc alterations is needed. Pfirrmann *et al*^[3] proposed a morphologic grading system which is based on MRI T2-weighted sagittal imaging and showed a good intra- and interobserver reliability. The grading system reflects the loss of proteoglycan concentration^[20] in the nucleus pulposus of the lumbar disc, which goes along with a decreasing signal intensity in T2-weighted imaging. The experience of our group confirms the fact that IDD is a general finding in MRI of the lower (L4/5 and L5/S1) lumbar segments even in young-aged patients. The vast majority of examined patients presents with Pfirrmann grade II - grade IV changes, whereas a relatively low percentage of lumbar discs present with grade V changes. Only a small number of lumbar discs show no degenerative changes. These experiences impressively illustrate the dilemma to rate the clinical symptoms of the patient correctly, based on a pervasive imaging finding. In consensus to the above mentioned results regarding the correlation of FJOA and ODI scores, also the presence of IDD in lumbar MRI can't be considered evidentiary as a reason for LBP.

LFJ intra-articular steroid injections

LFJ intra-articular injections of corticosteroids in combination with an anaesthetic solution is one of the most frequently performed interventional procedures worldwide^[7]. The theory of this particular therapeutic approach is based on the idea that there is inflammation

of the synovial structures of the degenerated facet joints. Thus intra-articular steroid injection is performed to generate an anti-inflammatory effect in order to achieve pain relief. Although widely used the clinical benefit of intra-articular steroid injections remains controversial^[8]. Lakemeier *et al*^[21] compared the effectiveness of intra-articular steroid injections and radiofrequency denervation in relief of LBP associated with L3/L4 - L5/S1 FJOA^[21]. They investigated the therapeutic effect of aforementioned interventional procedures in a cohort of 56 patients randomized in two therapeutic groups. In their double-blinded study the authors found no significant differences in the therapeutic success between the two procedures over a follow-up period of 6 mo. Ribeiro *et al*^[22] compared the therapeutic success of intra-articular steroid injection vs intramuscular steroid application in patients with facet joint- related CLP. The experimental group received bilateral intra-articular steroid injection of segments L3/4 - L5/S1 (in total 6 injections), while the control group received 6 intramuscular injections on bilateral surface points of the paravertebral lumbar musculature. Both treatments were effective over the follow-up period of 6 mo compared to the baseline. Regarding pain - relief no significant difference between the procedures was observed. It is well known that besides technical modifications many additional factors are involved in therapeutic outcome. Gryll *et al*^[23] reported about situational factors contributing to placebo effect during oral surgery (status of communicator of drug effects, attitude of dentist, attitude of dental technician and message of drug effects). Among the four variables only the attitude of the dentist and the dental technician led to a statistically significantly reduced fear of injection and lower ratings of pain experience from mandibular-block injection. Initial results of our group show, that the therapist's attitude and empathy may increase the therapeutic effect of LFJ intra-articular steroid injections in patients suffering from chronic LBP. Therefore, we performed a CT-guided puncture (Figure 1) of the facet joints at lumbar levels L4/5 or L5/S1, followed by an injection of a mixture of 4 mL of 0.5% bupivacaine and 1 mL of triamcinolone acetate (20 mg). After the therapeutic procedure we encouraged the patients of an experimental group to ask questions about the procedure and showed them representative CT-images. Patients of the control group left the interventional unit without further contact with the interventional radiologist. The initial results show a significant effect on pain relief during the early post-interventional phase in the experimental group as compared to the control group. It seems that in patients who better understand therapies applied on them, an increase in therapeutic efficacy can be observed. Explanatory behind the higher efficacy might be the phenomenon of hetero-suggestion, which occurs during the post-interventional patient-radiologist dialog during image presentation and might be conveying a message into the subconscious^[24]. This shows how the open and transparent handling can lead to a strong therapeutic alliance between patients and physicians for the benefit of patients.

CONCLUSION

Age-dependent IDD and FJOA of the lumbar spine is reliably detected by MRI. The lack of significant correlation of IDD and FJOA with clinical pain scores such as the ODI confirms our experience that imaging alone is an insufficient approach explaining LBP. Clinical correlation is not an adjunct only but imperative for an adequate clinical approach in patients with LBP and lower extremity pain. Thus further studies are needed to correlate imaging data and clinical scores such as the Oswestry disability index. Among the different options for the treatment of LFJ-associated LBP, the intra-articular injection of corticosteroids and anaesthetic solutions is one of the most frequently performed procedures. Beside technical modifications it seems that patients who better understand therapies applied on them experience an increased therapeutic efficacy. This could be helpful in the daily clinical routine, where psychological phenomena such as hetero-suggestion can be used as a powerful and easy-to-apply tool, to support therapeutic procedures such as intra-articular injections.

REFERENCES

1. **Emch TM**, Modic MT. Imaging of lumbar degenerative disk disease: history and current state. *Skeletal Radiol* 2011; **40**: 1175-1189 [PMID: 21847748 DOI: 10.1007/s00256-011-1163-x]
2. **Sasiadek MJ**, Bladowska J. Imaging of degenerative spine disease--the state of the art. *Adv Clin Exp Med* 2012; **21**: 133-142 [PMID: 23214277]
3. **Pfirschnig CW**, Metzendorf A, Zanetti M, Hodler J, Boos N. Magnetic resonance classification of lumbar intervertebral disc degeneration. *Spine (Phila Pa 1976)* 2001; **26**: 1873-1878 [PMID: 11568697 DOI: 10.1097/00007632-200109010-00011]
4. **Weishaupt D**, Zanetti M, Boos N, Hodler J. MR imaging and CT in osteoarthritis of the lumbar facet joints. *Skeletal Radiol* 1999; **28**: 215-219 [PMID: 10384992 DOI: 10.1007/s002560050503]
5. **Fairbank JC**, Couper J, Davies JB, O'Brien JP. The Oswestry low back pain disability questionnaire. *Physiotherapy* 1980; **66**: 271-273 [PMID: 6450426]
6. **Cohen SP**, Huang JH, Brummett C. Facet joint pain--advances in patient selection and treatment. *Nat Rev Rheumatol* 2013; **9**: 101-116 [PMID: 23165358 DOI: 10.1038/nrrheum.2012.198]
7. **Manchikanti L**, Pampati V, Singh V, Falco FJ. Assessment of the escalating growth of facet joint interventions in the medicare population in the United States from 2000 to 2011. *Pain Physician* 2013; **16**: E365-E378 [PMID: 23877460]
8. **Manchikanti L**, Datta S, Gupta S, Munglani R, Bryce DA, Ward SP, Benyamin RM, Sharma ML, Helm S, Fellows B, Hirsch JA. A critical review of the American Pain Society clinical practice guidelines for interventional techniques: part 2. Therapeutic interventions. *Pain Physician* 2010; **13**: E215-E264 [PMID: 20648212]
9. **Kalichman L**, Li L, Kim DH, Guermazi A, Berkin V, O'Donnell CJ, Hoffmann U, Cole R, Hunter DJ. Facet joint osteoarthritis and low back pain in the community-based population. *Spine (Phila Pa 1976)* 2008; **33**: 2560-2565 [PMID: 18923337 DOI: 10.1097/BRS.0b013e318184ef95]
10. **Abbas J**, Hamoud K, Peleg S, May H, Masharawi Y, Cohen H, Peled N, Hershkovitz I. Facet joints arthrosis in normal and stenotic lumbar spines. *Spine (Phila Pa 1976)* 2011; **36**: E1541-E1546 [PMID: 21270684 DOI: 10.1097/BRS.0b013e318210c889]
11. **Ashraf A**, Farahangiz S, Pakniat Jahromi B, Setayeshpour N, Naseri M, Nasser A. Correlation between Radiologic Sign of Lumbar Lordosis and Functional Status in Patients with Chronic Mechanical Low Back Pain. *Asian Spine J* 2014; **8**: 565-570 [PMID: 25346808 DOI: 10.4184/asj.2014.8.5.565]
12. **Peterson CK**, Bolton JE, Wood AR. A cross-sectional study correlating lumbar spine degeneration with disability and pain. *Spine (Phila Pa 1976)* 2000; **25**: 218-223 [PMID: 10685487 DOI: 10.1097/00007632-200001150-00013]
13. **Cheung KM**, Samartzis D, Karppinen J, Luk KD. Are "patterns" of lumbar disc degeneration associated with low back pain?: new insights based on skipped level disc pathology. *Spine (Phila Pa 1976)* 2012; **37**: E430-E438 [PMID: 22466575 DOI: 10.1097/BRS.0b013e3182304dfc]
14. **Takatalo J**, Karppinen J, Niinimäki J, Taimela S, Näyhä S, Mutanen P, Sequeiros RB, Kyllönen E, Tervonen O. Does lumbar disc degeneration on magnetic resonance imaging associate with low back symptom severity in young Finnish adults? *Spine (Phila Pa 1976)* 2011; **36**: 2180-2189 [PMID: 21358475 DOI: 10.1097/BRS.0b013e3182077122]
15. **Hangai M**, Kaneoka K, Kuno S, Hinotsu S, Sakane M, Mamizuka N, Sakai S, Ochiai N. Factors associated with lumbar intervertebral disc degeneration in the elderly. *Spine J* 2008; **8**: 732-740 [PMID: 18037353 DOI: 10.1016/j.spinee.2007.07.392]
16. **Samartzis D**, Karppinen J, Chan D, Luk KD, Cheung KM. The association of lumbar intervertebral disc degeneration on magnetic resonance imaging with body mass index in overweight and obese adults: a population-based study. *Arthritis Rheum* 2012; **64**: 1488-1496 [PMID: 22287295 DOI: 10.1002/art.33462]
17. **Takatalo J**, Karppinen J, Taimela S, Niinimäki J, Laitinen J, Sequeiros RB, Samartzis D, Korpelainen R, Näyhä S, Remes J, Tervonen O. Association of abdominal obesity with lumbar disc degeneration--a magnetic resonance imaging study. *PLoS One* 2013; **8**: e56244 [PMID: 23418543 DOI: 10.1371/journal.pone.0056244]
18. **Luoma K**, Riihimäki H, Raininko R, Luukkainen R, Lamminen A, Viikari-Juntura E. Lumbar disc degeneration in relation to occupation. *Scand J Work Environ Health* 1998; **24**: 358-366 [PMID: 9869307 DOI: 10.5271/sjweh.356]
19. **Wahlström J**, Burström L, Nilsson T, Järvholm B. Risk factors for hospitalization due to lumbar disc disease. *Spine (Phila Pa 1976)* 2012; **37**: 1334-1339 [PMID: 22281487 DOI: 10.1097/BRS.0b013e31824b5464]
20. **Pearce RH**, Thompson JP, Beauld GM, Flak B. Magnetic resonance imaging reflects the chemical changes of aging degeneration in the human intervertebral disk. *J Rheumatol Suppl* 1991; **27**: 42-43 [PMID: 2027127]
21. **Lakemeier S**, Lind M, Schultz W, Fuchs-Winkelmann S, Timmesfeld N, Foelsch C, Peterlein CD. A comparison of intraarticular lumbar facet joint steroid injections and lumbar facet joint radiofrequency denervation in the treatment of low back pain: a randomized, controlled, double-blind trial. *Anesth Analg* 2013; **117**: 228-235 [PMID: 23632051 DOI: 10.1016/j.spinee.2013.10.007]
22. **Ribeiro LH**, Furtado RN, Konai MS, Andreo AB, Rosenfeld A, Natour J. Effect of facet joint injection versus systemic steroids in low back pain: a randomized controlled trial. *Spine (Phila Pa 1976)* 2013; **38**: 1995-2002 [PMID: 23921331 DOI: 10.1097/BRS.0b013e3182a76df1]
23. **Gryll SL**, Katahn M. Situational factors contributing to the placebo effect. *Psychopharmacology (Berl)* 1978; **57**: 253-261 [PMID: 97705 DOI: 10.1007/bf00426747]
24. **Mommaerts JL**, Devroey D. The placebo effect: how the subconscious fits in. *Perspect Biol Med* 2012; **55**: 43-58 [PMID: 22643715 DOI: 10.1353/pbm.2012.0005]

P- Reviewer: Kara PO, Kilickesmez O

S- Editor: Tian YL L- Editor: A E- Editor: Jiao XK



Small bowel imaging of inflammatory bowel disease

Emanuele Casciani, Chiara De Vincentiis, Gianfranco Gualdi

Emanuele Casciani, Gianfranco Gualdi, Department of Emergency Radiology, "La Sapienza" University-Hospital Umberto I, 00166 Rome, Italy

Chiara De Vincentiis, Department of Radiology, "La Sapienza" University-Sant'Andrea's Hospital, 00189 Rome, Italy

Author contributions: Casciani E designed the study and wrote the manuscript; De Vincentiis C acquired the material, analysed data and helped to write the manuscript; Gualdi GF provided the collection of part of the material.

Conflict-of-interest statement: We have read and understood BPG's revision policy on declaration of interests and declare that we have no competing interests.

Open-Access: This article is an open-access article which was selected by an in-house editor and fully peer-reviewed by external reviewers. It is distributed in accordance with the Creative Commons Attribution Non Commercial (CC BY-NC 4.0) license, which permits others to distribute, remix, adapt, build upon this work non-commercially, and license their derivative works on different terms, provided the original work is properly cited and the use is non-commercial. See: <http://creativecommons.org/licenses/by-nc/4.0/>

Correspondence to: Dr. Emanuele Casciani, Department of Emergency Radiology, "La Sapienza" University-Hospital Umberto I, Viale del Policlinico 155, 00166 Rome, Italy. emanuelecasciani@gmail.com
 Telephone: +39-6-49979465
 Fax: +39-6-6630218

Received: January 28, 2015
 Peer-review started: February 1, 2015
 First decision: March 6, 2015
 Revised: March 26, 2015
 Accepted: May 26, 2015
 Article in press: May 27, 2015
 Published online: August 28, 2015

Abstract

The study of the small bowel (SB) has always been

challenging both for clinicians and radiologist. It is a long and tortuous tube that can be affected by various pathologies whose signs and symptoms are usually non specific and can mimic other acute abdominal disorders. For these reasons, imaging plays a central role in the diagnosis of the different pathological conditions that can occur. They are important also in the management and follow up of chronic diseases. We expose and evaluate all the radiological methods that are now available for the study of the SB with particular emphasis on the technological improvement of cross-sectional imaging, such as computed tomography (CT) and magnetic resonance imaging (MRI). These techniques have, infact, highly improved in terms of execution times (fast acquisitions images), patients discomfort and radiation dose, for CT, with consequent reduced biological risks. Moreover, the new post-processing options with multiplanar reconstruction and isotropic images have made significant changes in the evaluation of the exams. Especially MRI scans have been improved by the advent of new sequences, such as diffusion weighted imaging and cine-MRI, parallel imaging and breath-hold sequences and can provide excellent soft-tissue contrast without the use of ionizing radiations.

Key words: Small bowel imaging; Magnetic resonance; Cross-sectional imaging; Computed tomography; Positron emission tomography-computed tomography

© **The Author(s) 2015.** Published by Baishideng Publishing Group Inc. All rights reserved.

Core tip: The small bowel (SB) has always been a challenging organ for clinical and radiologic evaluation. The purpose of our article is to evaluate all the imaging methods now available for the study of the SB with particular emphasis on the technological improvement of cross-sectional imaging.

Casciani E, De Vincentiis C, Gualdi GF. Small bowel imaging of inflammatory bowel disease. *World J Radiol* 2015; 7(8): 198-201

Available from: URL: <http://www.wjgnet.com/1949-8470/full/v7/i8/198.htm> DOI: <http://dx.doi.org/10.4329/wjv.v7.i8.198>

INTRODUCTION

Radiological studies of the small bowel were firstly performed at the beginning of this century by Morse and Cole^[1] in 1927 and Pesquera^[2] in 1929. From then until the early 2000s, barium contrast studies have been the only imaging methods to study the small bowel. In the last decade, a tremendous technological improvement of cross-sectional imaging [Ultrasound (US), computed tomography (CT), and magnetic resonance imaging (MRI)] have occurred. US scanners have significantly improved, now allowing a good visualization of the small bowel loops. Both CT and MRI scanners have become very fast (short execution times and less discomfort for the patients) and can create multiplanar reconstruction and isotropic images, the former with less radiation dose and the latter in the lack of ionizing radiations, particularly important in young patients who need periodic imaging examinations. Especially MRI scans have been improved by the advent of new sequences, such as diffusion weighted (DWI) and cine-MRI, parallel imaging and breath-hold sequences and can provide excellent soft-tissue contrast.

A complete exam requires the use of both intravenous and endoluminal contrast. The latter is necessary to obtain a good distension of the bowel loops and can be administered orally (MRI-Enterography) or through a nasojejunal tube (MRI-Enteroclysis). The MRI-Enterography is more comfortable for the patient but the MRI-Enteroclysis provides a better bowel distension, especially of the proximal loops, and, for this reason, is always the method of choice in patients with suspected jejunal lesions or recurrent intestinal subocclusion. Finally, since 2001, wireless capsule endoscopy has been introduced as another non-invasive technique for the evaluation of the entire small bowel, in which traditional endoscopy had severe limits^[3]. Despite the important diagnostic innovation, the impossibility to perform therapeutic interventions is a high limit and, for this reason new endoscopic method were proposed in the subsequent years, such as Double-balloon endoscopy, in 2003, Single-balloon enteroscopy in 2007 and spiral enteroscopy in 2008^[3].

Alternatively, also scintigraphy and positron emission tomography/computed tomography (PET/CT) has been reported, in several studies^[4-6], as valid and non-invasive method to diagnose and assess disease activity in IBD. Regarding Scintigraphy, various biomarkers of inflammation, used to label white blood cells, such as technetium-99m hexamethylpropylene amine oxime (Tc-99m HMPAO WBC), pentavalent Tc-99m dimercaptosuccinic acid [Tc-99m (V) DMSA] and fluorine-18 fluorodeoxyglucose (18F-FDG), are widely accepted as accurate for the diagnosis of IBD^[4]. Studies

on ¹⁸F-FDG PET/CT showed a significant correlation between the ¹⁸F-FDG uptake PET-CT and the Crohn's disease endoscopy index of severity especially in segments with moderate to severe lesions. Moreover, ¹⁸F-FDG PET may potentially provide information on the dynamic inflammatory changes occurring in inflammatory bowel disease (IBD), particularly Crohn's disease, being useful not only in the diagnosis but also in the follow up of the disease^[5,6].

Thanks to these technical improvements in imaging, the cross-sectional techniques are replacing barium exams in the study of the small intestine, especially in IBD, both in adult and pediatric patients.

The "Porto criteria" recommend small-bowel follow-through (SBFT) as the imaging modality of choice in children^[7]. However, SBFT requires high radiation dose with associated risks and, when possible, should be replaced by alternative techniques, such as low-dose CT or MRI^[8-10], whose high accuracy is stated in the European Crohn's and Colitis Organization (ECCO) guidelines^[10]. Particularly, ECCO guidelines, in the pediatric section^[11,12], report dynamic contrast-enhanced MRI as the best imaging method to study CD's lesions. Also the Appropriateness Criteria of the American College of Radiology^[13] confirm the high sensitivity and specificity of MRI (enterography or enteroclysis) in pediatric patients, similar to that of CT enterography but without the use of ionizing radiation.

However, many questions remain unsolved. First of all, it is important to determine whether these non-invasive imaging techniques can replace endoscopy in the evaluation of the mucosal healing. In a recent study, MRE has shown an accuracy of 90% and 84% in determining ulcer healing and endoscopic remission, respectively^[14], but these data need to be confirmed.

In the last years, the eradication of bowel inflammation at the level of all wall layers has been suggested as a goal of treatment more appropriate than the mucosal healing alone that seems to be too superficial.

Compared to endoscopy, cross sectional imaging, especially MRI, can provide information on the entire bowel wall. However, transmural healing has not yet been studied as the primary therapeutic endpoint in CD patients, unlike the mucosal healing that is becoming more and more a therapeutic goal^[15].

Preliminary studies have reported encouraging results on the diagnostic accuracy of DWI sequence in patients with IBD so that it can be considered, in the future, as an alternative to contrast-enhanced sequences^[16,17].

Future studies should also consider the interobserver variability due to the different experience of radiologists in evaluating DWI images and standard MRI images.

Another concrete future possibility for the diagnosis and management of IBD is represented by the new hybrid imaging modalities, such as PET/CT and PET/MRI, which combine the morphological CT or MRI images with the functional PET information in a single diagnostic investigation. CT enterography combined

with the ^{18}F -FDG PET exam seems to be particularly promising^[18].

Groshar *et al.*^[19] reported a good accuracy of PET/CT in the differential diagnosis between acute and chronic inflammation. Infact, they found an important relation between the maximum standardized uptake value [SUV(max)] and the mural CT patterns, such as submucosal edema or fat, expression of active and chronic inflammation, respectively. However, a high number of false positive results have been registered due to the physiologic ^{18}F -FDG uptake by the bowel wall^[20,21]. Another important limitation is the high cumulative radiation dose required for the PET/CT exam, particularly because the IBD patients require numerous and repeated examinations^[18].

Finally, no articles have been published on the use of PET/MRI in the diagnosis and follow up of IBD, even though this combined use of nuclear medicine and MRI, providing information on molecular and morphological events without the use of ionizing radiations, could change the future diagnostic approach. Infact, they seem to have high potential and can count on the advent of new MRI techniques, such as DWI and Spectroscopy, and new radiopharmaceuticals to label cells, such as radionuclides, fluorescent or bioluminescent markers (optical imaging) and MRI contrast agents (molecular MRI)^[22]. A great hope is placed in this imaging investigation which could effectively help in the diagnosis and follow up of IBD providing information on involved inflammatory cells and cytokines.

REFERENCES

- Morse RW, Cole LG. The anatomy of the normal small intestine as observed roentgenographically. *Radiology* 1927; **8**: 149-53 [DOI: 10.1148/8.2.149]
- Pesquera GS. A method for the direct visualisation of lesions in the small intestine. *AJR* 1929; **22**: 254-7
- Moeschler O, Mueller MK. Deep enteroscopy - indications, diagnostic yield and complications. *World J Gastroenterol* 2015; **21**: 1385-1393 [PMID: 25663758 DOI: 10.3748/wjg.v21.i5.1385]
- Stathaki MI, Koukouraki SI, Karkavitsas NS, Koutroubakis IE. Role of scintigraphy in inflammatory bowel disease. *World J Gastroenterol* 2009; **15**: 2693-2700 [PMID: 19522018 DOI: 10.3748/wjg.15.2693]
- Louis E, Ancion G, Colard A, Spote V, Belaiche J, Hustinx R. Noninvasive assessment of Crohn's disease intestinal lesions with (18)F-FDG PET/CT. *J Nucl Med* 2007; **48**: 1053-1059 [PMID: 17574978 DOI: 10.2967/jnumed.107.040436]
- Saboury B, Salavati A, Brothers A, Basu S, Kwee TC, Lam MG, Hustinx R, Louis E, Torigian DA, Alavi A. FDG PET/CT in Crohn's disease: correlation of quantitative FDG PET/CT parameters with clinical and endoscopic surrogate markers of disease activity. *Eur J Nucl Med Mol Imaging* 2014; **41**: 605-614 [PMID: 24253895 DOI: 10.1007/s00259-013-2625-2]
- IBD Working Group of the European Society for Paediatric Gastroenterology, Hepatology and Nutrition. Inflammatory bowel disease in children and adolescents: recommendations for diagnosis--the Porto criteria. *J Pediatr Gastroenterol Nutr* 2005; **41**: 1-7 [DOI: 10.1097/01.MPG.0000163736.30261.82]
- Desmond AN, O'Regan K, Curran C, McWilliams S, Fitzgerald T, Maher MM, Shanahan F. Crohn's disease: factors associated with exposure to high levels of diagnostic radiation. *Gut* 2008; **57**: 1524-1529 [PMID: 18443021 DOI: 10.1136/gut.2008.151415]
- Gaca AM, Jaffe TA, Delaney S, Yoshizumi T, Toncheva G, Nguyen G, Frush DP. Radiation doses from small-bowel follow-through and abdomen/pelvis MDCT in pediatric Crohn disease. *Pediatr Radiol* 2008; **38**: 285-291 [PMID: 18183380 DOI: 10.1007/s00247-007-0702-z]
- Panes J, Bouhnik Y, Reinisch W, Stoker J, Taylor SA, Baumgart DC, Danese S, Halligan S, Marincek B, Matos C, Peyrin-Biroulet L, Rimola J, Rogler G, van Assche G, Ardizzone S, Ba-Salamah A, Bali MA, Bellini D, Biancone L, Castiglione F, Ehehalt R, Grassi R, Kucharzik T, Maccioni F, Maconi G, Magro F, Martín-Comín J, Morana G, Pendsé D, Sebastian S, Signore A, Tolan D, Tielbeek JA, Weishaupt D, Wiarda B, Laghi A. Imaging techniques for assessment of inflammatory bowel disease: joint ECCO and ESGAR evidence-based consensus guidelines. *J Crohns Colitis* 2013; **7**: 556-585 [PMID: 23583097 DOI: 10.1016/j.crohns.2013.02.020]
- Van Assche G, Dignass A, Panes J, Beaugerie L, Karagiannis J, Allez M, Ochsenkühn T, Orchard T, Rogler G, Louis E, Kupcinskis L, Mantzaris G, Travis S, Stange E. The second European evidence-based Consensus on the diagnosis and management of Crohn's disease: Definitions and diagnosis. *J Crohns Colitis* 2010; **4**: 7-27 [PMID: 21122488 DOI: 10.1016/j.crohns.2009.12.003]
- Van Assche G, Dignass A, Reinisch W, van der Woude CJ, Sturm A, De Vos M, Guslandi M, Oldenburg B, Dotan I, Marteau P, Ardizzone A, Baumgart DC, D'Haens G, Gionchetti P, Portela F, Vucelic B, Söderholm J, Escher J, Koletzko S, Kolho KL, Lukas M, Mottet C, Tilg H, Vermeire S, Carbonnel F, Cole A, Novacek G, Reinshagen M, Tsianos E, Herrlinger K, Oldenburg B, Bouhnik Y, Kiesslich R, Stange E, Travis S, Lindsay J. The second European evidence-based Consensus on the diagnosis and management of Crohn's disease: Special situations. *J Crohns Colitis* 2010; **4**: 63-101 [PMID: 21122490 DOI: 10.1016/j.crohns.2009.09.009]
- Huprich JE, Rosen MP, Fidler JL, Gay SB, Grant TH, Greene FL, Lalani T, Miller FH, Rockey DC, Sudakoff GS, Gunderman R, Coley BD. ACR Appropriateness Criteria on Crohn's disease. *J Am Coll Radiol* 2010; **7**: 94-102 [PMID: 20142082 DOI: 10.1016/j.jacr.2009.10.009]
- Ordás I, Rimola J, Rodríguez S, Paredes JM, Martínez-Pérez MJ, Blanc E, Arévalo JA, Aduna M, Andreu M, Radosevic A, Ramírez-Morros AM, Pinó S, Gallego M, Jauregui-Amezaga A, Ricart E, Panés J. Accuracy of magnetic resonance enterography in assessing response to therapy and mucosal healing in patients with Crohn's disease. *Gastroenterology* 2014; **146**: 374-82.e1 [PMID: 24177375 DOI: 10.1053/j.gastro.2013.10.055]
- Daperno M, Castiglione F, de Ridder L, Dotan I, Färkkilä M, Florholmen J, Fraser G, Fries W, Hebuterne X, Lakatos PL, Panés J, Rimola J, Louis E. Results of the 2nd part Scientific Workshop of the ECCO. II: Measures and markers of prediction to achieve, detect, and monitor intestinal healing in inflammatory bowel disease. *J Crohns Colitis* 2011; **5**: 484-498 [PMID: 21939926 DOI: 10.1016/j.crohns.2011.07.003]
- Oussalah A, Laurent V, Bruot O, Bressenot A, Bigard MA, Régent D, Peyrin-Biroulet L. Diffusion-weighted magnetic resonance without bowel preparation for detecting colonic inflammation in inflammatory bowel disease. *Gut* 2010; **59**: 1056-1065 [PMID: 20525970 DOI: 10.1136/gut.2009.197665]
- Neubauer H, Pabst T, Dick A, Machann W, Evangelista L, Wirth C, Köstler H, Hahn D, Beer M. Small-bowel MRI in children and young adults with Crohn disease: retrospective head-to-head comparison of contrast-enhanced and diffusion-weighted MRI. *Pediatr Radiol* 2013; **43**: 103-114 [PMID: 23212595 DOI: 10.1007/s00247-012-2492-1]
- Shyn PB, Morteale KJ, Britz-Cunningham SH, Friedman S, Odze RD, Burakoff R, Goldberg JE, Erturk M, Silverman SG. Low-dose 18F-FDG PET/CT enterography: improving on CT enterography assessment of patients with Crohn disease. *J Nucl Med* 2010; **51**: 1841-1848 [PMID: 21078803 DOI: 10.2967/jnumed.110.080796]
- Groshar D, Bernstine H, Stern D, Sosna J, Eligalashvili M, Gurbuz EG, Niv Y, Fraser G. PET/CT enterography in Crohn disease: correlation of disease activity on CT enterography with 18F-FDG

- uptake. *J Nucl Med* 2010; **51**: 1009-1014 [PMID: 20554741 DOI: 10.2967/jnumed.109.073130]
- 20 **Spier BJ**, Perlman SB, Jaskowiak CJ, Reichelderfer M. PET/CT in the evaluation of inflammatory bowel disease: studies in patients before and after treatment. *Mol Imaging Biol* 2010; **12**: 85-88 [PMID: 19430844 DOI: 10.1007/s11307-009-0232-1]
 - 21 **Lemberg DA**, Issenman RM, Cawdron R, Green T, Mernagh J, Skehan SJ, Nahmias C, Jacobson K. Positron emission tomography in the investigation of pediatric inflammatory bowel disease. *Inflamm Bowel Dis* 2005; **11**: 733-738 [PMID: 16043988 DOI: 10.1097/01.MIB.0000172810.49619.cb]
 - 22 **Cassidy PJ**, Radda GK. Molecular imaging perspectives. *J R Soc Interface* 2005; **2**: 133-144 [PMID: 16849174 DOI: 10.1098/rsif.2005.0040]

P- Reviewer: Djodjevic I, Suzuki H

S- Editor: Song XX **L- Editor:** A **E- Editor:** Jiao XK



Imaging of bone metastasis: An update

Gerard J O'Sullivan, Fiona L Carty, Carmel G Cronin

Gerard J O'Sullivan, Fiona L Carty, Carmel G Cronin, Department of Radiology, Mater Misericordiae University Hospital, Dublin 7, Ireland

Author contributions: O'Sullivan GJ, Carty FL and Cronin CG contributed equally to this work; O'Sullivan GJ wrote the paper.

Conflict-of-interest statement: None.

Open-Access: This article is an open-access article which was selected by an in-house editor and fully peer-reviewed by external reviewers. It is distributed in accordance with the Creative Commons Attribution Non Commercial (CC BY-NC 4.0) license, which permits others to distribute, remix, adapt, build upon this work non-commercially, and license their derivative works on different terms, provided the original work is properly cited and the use is non-commercial. See: <http://creativecommons.org/licenses/by-nc/4.0/>

Correspondence to: Carmel G Cronin, MB, BCh, BAO, Consultant Radiologist, Department of Radiology, Mater Misericordiae University Hospital, Eccles Street, Dublin 7, Ireland. ccronin@mater.ie
Telephone: +353-1-8032274
Fax: +353-1-8032970

Received: July 17, 2014
Peer-review started: July 19, 2014
First decision: November 27, 2014
Revised: February 13, 2015
Accepted: June 18, 2015
Article in press: June 19, 2015
Published online: August 28, 2015

Abstract

Early detection of skeletal metastasis is critical for accurate staging and optimal treatment. This paper briefly reviews our current understanding of the biological mechanisms through which tumours metastasise to bone and describes the available imaging methods to diagnose bone metastasis and monitor response to treatment. Among the various imaging modalities currently available for imaging skeletal metastasis, hybrid techniques which

fuse morphological and functional data are the most sensitive and specific, and positron emission tomography (PET)/computed tomography and PET/magnetic resonance imaging will almost certainly continue to evolve and become increasingly important in this regard.

Key words: Neoplasm metastasis; Radionuclide imaging; Magnetic resonance imaging; Computed tomography; Bone and bones

© **The Author(s) 2015.** Published by Baishideng Publishing Group Inc. All rights reserved.

Core tip: Early detection of skeletal metastasis is critical for accurate staging and optimal treatment. This paper briefly reviews our current understanding of the biological mechanisms through which tumours metastasise to bone and describes the available imaging methods to diagnose bone metastasis and monitor response to treatment.

O'Sullivan GJ, Carty FL, Cronin CG. Imaging of bone metastasis: An update. *World J Radiol* 2015; 7(8): 202-211 Available from: URL: <http://www.wjgnet.com/1949-8470/full/v7/i8/202.htm> DOI: <http://dx.doi.org/10.4329/wjr.v7.i8.202>

INTRODUCTION

Metastasis of malignant neoplasms to bone is common with metastases being far more prevalent than primary bone malignancies^[1,2]. Indeed, bone is the third most common organ affected by metastasis, surpassed only by the lungs and liver^[2-4], and is the most common site of distant metastasis from primary breast carcinoma^[5].

Over the past twenty years, advances in our understanding of tumour biology have led to the development of improved treatment strategies for many cancers. As a result, many patients are living longer with metastatic disease and the incidence of skeletal metastasis is continuing to rise. Based on post-mortem findings, approximately 70% of patients with breast or prostate

cancer have bone metastases^[1,4]. Commensurate with the increased prevalence of bone metastasis, there is potential for significant comorbidities such as pain, limited mobility, hypercalcaemia, spinal cord or nerve root compression, myelosuppression and pathologic fracture^[2,6]. Therefore, early detection of skeletal metastasis is critical for (1) accurate staging and optimal treatment; and (2) to allow the implementation of treatment strategies such as surgical fixation, radiotherapy, or bisphosphonate therapy to reduce the risk of complications and improve quality of life^[7,8].

This paper briefly reviews our current understanding of the biological mechanisms through which tumours metastasise to bone and describes the available imaging methods to diagnose bone metastasis and monitor response to treatment.

PATHOPHYSIOLOGY OF BONE METASTASIS

Certain primary malignant neoplasms such as breast carcinoma and prostate adenocarcinoma have a propensity for metastasising to bone and are, therefore, termed osteotropic. Conversely, patients with cervical, endometrial, bladder and gastrointestinal tract tumours rarely develop skeletal metastases^[9]. The selective deposition and proliferation of discrete circulating malignant cells within the skeleton relates to the "seed and soil" hypothesis of tumour biology originally conceptualised by Stephen Paget in the late 19th century. In accordance with this hypothesis, the bone environment represents a "fertile soil" in which some, but not all, cancer cell types (seeds) can flourish.

Metastasis to bone can occur *via* direct extension, arterial or venous spread with the latter representing the most common form. Once in the circulation, entry of the cancer cells into the venous circulation of the bone marrow is facilitated by the slow blood flow and the fact that hematopoietically active bone marrow is well vascularised^[1]. Adhesion molecules produced by tumour cells bind to marrow stromal cells and bone matrix^[8]. The normal remodelling process of bone provides chemotactic and growth factors which support these cancer cells once in place^[1]. After skeletal colonisation, the malignant cells interrupt normal bone cell turnover by releasing local cytokines and growth factors. Certain tumours release factors which upregulate osteoclast activity such as parathyroid hormone-related protein, tumour necrosis factor α or β , and other cytokines such as interleukin-1 and interleukin-6 which results in net osteolysis. Other cancer cell types release factors such as epidermal growth factor, transforming growth factor α and β , and insulin-like growth factors which upregulate osteoblasts resulting in net osteosclerosis^[8,10]. Thus, osseous metastases can be osteoblastic (bone forming) or osteolytic (bone destructive), however, a combination of both processes occurs in most cancers^[4]. Osseous

metastases from kidney, thyroid and lung malignancies are predominantly osteolytic, while osteoblastic lesions are usually seen in prostate cancer and breast cancer^[7]. Furthermore, osteolytic metastases tend to be aggressive, whereas sclerotic metastases typically demonstrate slower progression. An important point to realise is that tumour cell proliferation within the bone marrow invariably predates bone destruction which is, consequently, a relatively delayed manifestation in bone metastasis which has important implications in terms of diagnosis^[6].

DISTRIBUTION OF BONE METASTASIS

Considering benign osseous lesions and bone metastases oftentimes have similar imaging features, the location of a lesion in the skeleton can sometimes be used to help distinguish between the two in equivocal cases. The vertebrae, pelvis, ribs and the ends of long bones are preferred destinations of metastases because of their high red marrow content^[1,9,11]. Within the spine, most metastases are located in the lumbar spine, less frequently in the thoracic spine, and rarely in the cervical spine (52%, 36% and 12% respectively)^[12]. Less frequent metastatic sites include the mandible, patella, and distal extremities. In the majority of instances, metastases in the appendicular skeleton are secondary to lung cancer and are typically located in the scaphoid, lunate or phalanges^[7] (Figure 1).

PLAIN FILM

Plain radiographs are recommended to assess abnormal radionuclide uptake or the risk of pathological fracture and as initial imaging studies in patients with bone pain^[5]. However, radiography is considered insensitive to screen for asymptomatic metastases^[9]. Limited contrast in trabecular bone *vis a vis* cortical bone renders radiographic detection of lesions in the former more difficult and studies have shown that more than 50% to 70% of bone must be destroyed to be reliably detected by plain radiographs^[2,7]. Osteolytic lesions typically demonstrate thinning of trabeculae and ill-defined margins with the latter representing abnormal trabeculae between the centre of the lesion and the radiologically normal bone. Conversely, sclerotic metastases classically appear as nodular, rounded and fairly well circumscribed lesions secondary to thickened coarse trabeculae^[8].

Skeletal metastases may respond to treatment with reactive new bone formation, or sclerosis. Sclerosis tends to be initiated at the margins of the lesion and progress over time towards the centre. Sclerotic change in an osteolytic metastasis usually indicates a healing response to therapy, whereas worsening or developing osteolysis within sclerotic or mixed lesions, or progressive enlargement of an existing lesion, are indicators of disease progression^[7]. Disadvantages of plain film for monitoring

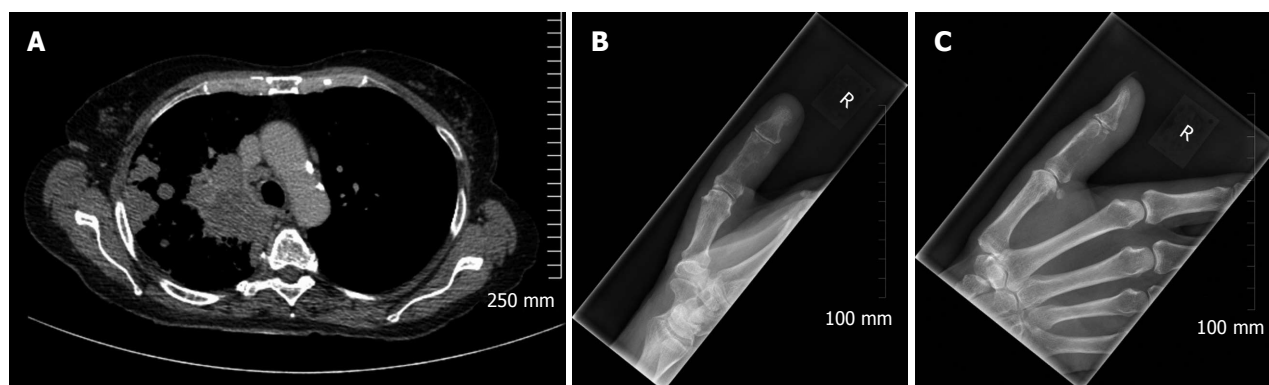


Figure 1 Bone metastasis in the appendicular skeleton is most commonly due to primary lung malignancy. A: Axial computed tomography image of the upper thorax (soft tissue window) demonstrating a large right upper lobe mass with ipsilateral pulmonary and lymph node metastasis; B and C: PA and lateral views of the right thumb demonstrating a lytic metastatic deposit in the middle phalanx.

Table 1 Sensitivity and specificity of imaging modalities in bone metastasis

Imaging modality	Sensitivity (%) ^[12]	Specificity (%) ^[12]
18F NaF-PET/CT	100	97
MRI	95	90
SPECT	87	91
18F FDG-PET	98	56
CT	74	56
Bone Scintigraphy	78	48

PET: Positron emission tomography; CT: Computed tomography; MRI: Magnetic resonance imaging; SPECT: Single photon emission tomography; 18F FDG: Fluorine 18 labelled fluorodeoxyglucose; 18F NaF: Fluorine 18 labelled sodium fluoride.

treatment response are that (1) typically 3-6 mo are required before any changes manifest radiographically; and (2) plain films only reveal structural bone alterations, and do not provide information on the malignant cells within the metastatic soft tissue deposit. Furthermore, differentiating new sclerotic metastases secondary to disease progression from sclerotic lesions caused by healing and re-ossification is often challenging^[3,6].

COMPUTED TOMOGRAPHY

Computed tomography (CT) provides excellent resolution of cortical and trabecular bone and is the imaging modality of choice for evaluating the ribs which have a high cortex to marrow ratio. The ability to apply dedicated bone algorithms to acquired images, adjust the window width and level, and view the skeleton in multiple planes using multiplanar reformatted images all serve to maximise the conspicuity of bone lesions and results in a higher sensitivity of CT compared to plain radiography in detecting both osteolytic and osteosclerotic metastases. The sensitivity and specificity of CT for detection of bone metastasis is 74% and 56%, respectively (Table 1). A major advantage of CT is that investigation for skeletal metastasis or evaluating treatment response can be performed at the time

of staging or restaging other organs which reduces the burden of imaging for the patient. Despite the limited soft tissue resolution of CT vis a vis magnetic resonance imaging (MRI), in many instances, CT can demonstrate bone marrow metastases before bone destruction occurs which results in earlier diagnosis and can improve prognosis and prevent complications^[6]. A further advantage of CT is that it can be used to guide percutaneous biopsy when a tissue diagnosis is required^[7].

Clinical trials have demonstrated a role for CT in evaluating for sclerotic change within a metastatic deposit which can occur in response to treatment of skeletal metastases with chemo/radiotherapy. Specifically, reactive sclerosis may be quantified by calculating the change in Hounsfield units within metastatic deposits following bisphosphonate therapy, thereby providing a valid objective measure of treatment response^[3].

MRI

Due to its excellent soft tissue resolution, MRI is the imaging modality of choice for assessing metastatic spread in the marrow cavity, extension of tumour from the marrow cavity and involvement of surrounding structures^[5]. Furthermore, MRI is highly sensitive for detecting skeletal metastasis as it has the capability to demonstrate an intramedullary metastatic deposit in advance of cortical destruction occurs and before a pathologic osteoblastic process manifests as focal accumulation of radiotracer on a bone scan (Figure 2)^[6,8]. The sensitivity and specificity of MRI for detection of bone metastasis is 95% and 90%, respectively (Table 1). In addition, MRI is the technique of choice in suspected cases of cord compression from pathologic vertebral body fracture where a compromised oedematous spinal cord will demonstrate abnormal focal high T2 and turbo-short tau inversion recovery (STIR) signal. Given that MRI does not involve ionising radiation, it is especially suited for the investigation of suspected bony metastasis in pregnant women.

Normal bone marrow contains a high percentage

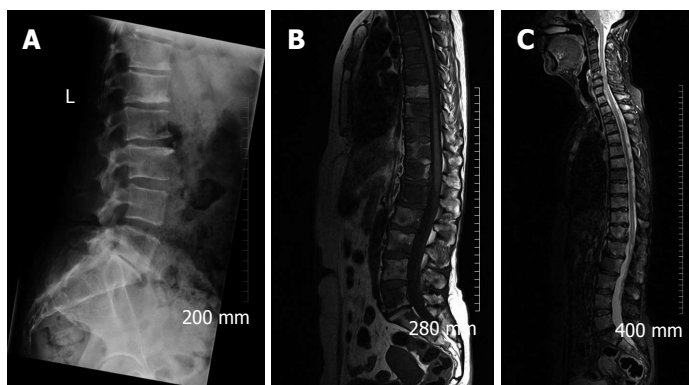


Figure 2 Magnetic resonance imaging is superior to plain radiography for detection of bone metastasis. A: Lateral lumbar spine radiograph demonstrates subtle sclerotic metastatic deposits at the inferior endplate of T12 and L1 from a primary breast malignancy; Sagittal T1 (B) and short tau inversion recovery (STIR) (C) images of the spine acquired one day later demonstrate diffuse bone metastasis (abnormal low T1 and high STIR signal in the bone marrow) which is not evident on the radiograph.

of fat and demonstrates high signal intensity on T1-weighted sequences. Osseous metastases usually manifest as discrete foci of low T1 signal, corresponding to the replacement of normal fatty marrow by malignant cells. On a T2-weighted sequence, bone metastases usually demonstrate T2 hyperintensity due to their elevated water content and gadolinium enhancement due to increased vascularity^[4,7].

The development of whole-body MRI in recent years, which uses fast pulse sequences over multiple anatomic stations to achieve a survey of the entire body, has resulted in the ability to use unenhanced T1-weighted spin echo and STIR sequences to screen the whole body for marrow abnormalities with a sensitivity and specificity superior to skeletal scintigraphy^[5-7]. One limitation of MRI is that cortical bone, with its very short T2 relaxation time, is very poorly interrogated. Therefore, bones with a low marrow volume such as the ribs are better evaluated with CT as described above^[6].

An advantage of MRI is that it can sometimes be used to distinguish osteoporotic from malignant vertebral compression fractures. Oedema from osteoporotic compression fractures should subside within 3 mo. If marrow oedema persists on a follow-up MRI study performed at least 12 wk after the initial scan, a pathologic fracture is likely^[5], however, this correlation can be inconsistent and determining if marrow signal changes are due to fracture or tumour remains a diagnostic challenge using MRI alone^[4].

MRI can be used to assess treatment response by evaluating the size and number of osseous metastases over time. It is important to note, however, that alteration in signal intensity alone on a T1-weighted sequence does not constitute a response to therapy. Recent studies suggest that quantitative diffusion weighted imaging (DWI) can be used to evaluate treatment response before a change in the tumour burden can be seen using non quantitative assessment. More specifically, early reduction in tumour cell volume following cell death with a corresponding increase in the extracellular space

is manifested on DWI as an increase in the apparent diffusion coefficient (ADC) value of the metastatic deposit^[6]. However, further studies are needed to define the precise imaging criteria, for example T1 and DWI signal characteristics and/or percentage signal change pre and post contrast, which should be used to evaluate the treatment response^[3].

NUCLEAR MEDICINE

Morphological imaging techniques such as plain film, CT and MRI described above interrogate the structure of a lesion within bone. Conversely, nuclear medicine techniques quantitatively assess the function of bone or tumour cells^[6]. Prior to describing the role of the nuclear medicine imaging modalities most commonly used for imaging skeletal metastases, it is pertinent to briefly review the various radioisotopes that are employed in these studies. For more comprehensive coverage of this topic the reader is referred to the recent review by Cuccurullo *et al*^[2].

Osteotropic radioisotopes are bone seeking agents that accumulate at the site of active bone production regardless of whether the aetiology is benign or malignant. The predominant osteotropic agents used in skeletal scintigraphy are metastable technetium 99 labelled diphosphonates, among which methylene diphosphonate (99mTc-MDP) is used most commonly based on its effectiveness, low cost, widespread availability and favourable dosimetry. 18F labelled sodium fluoride (NaF) is an osteotropic compound used in positron emission tomography (PET) which has a higher first pass extraction rate than 99mTc-MDP. Indeed, studies indicate that the regional extraction of 18F NaF from plasma to bone is on average approximately three times higher in metastatic lesions than in adjacent normal bone tissue. Consequently, 18F NaF has very high selectivity for bone metastases, however its relatively low specificity when not used in conjunction with morphological imaging techniques (see hybrid

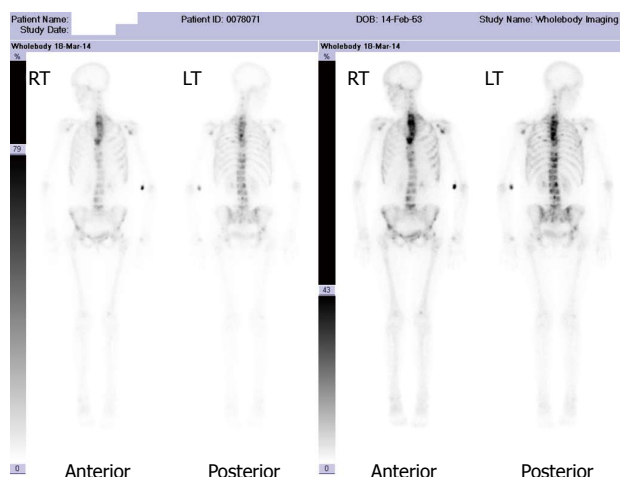


Figure 3 Diffuse bone metastasis on bone scintigraphy. Abnormal accumulation of radiotracer throughout the spine, most pronounced in the upper thoracic spine with additional pelvic and bilateral rib metastases in a patient with primary breast malignancy. Focal accumulation of radiotracer in the left antecubital fossa represents artefact at the radiotracer injection site.

imaging below) and the requirement of a cyclotron for production are limiting factors in its use^[2].

In contrast to osteotropic agents, which have a high affinity for calcium, oncotropic radioisotopes demonstrate uptake into malignant cells and are classified as either specific or non-specific. Specific oncotropic agents are available to investigate for bone metastases from neuroendocrine tumours. For example, metaiodobenzylguanidine is a noradrenaline analogue, taken up specifically by the sympathetic nervous system and related tumours. When labelled with Iodine 123 or Iodine 131 it may detect bone metastases from pheochromocytomas and paragangliomas. In addition, somatostatin receptor scintigraphy with Indium 111 pentetreotide (octreoscan) and PET-CT using Gallium 68 labelled somatostatin analogues can be used to diagnose both organ confined and metastatic neuroendocrine malignancies. Further information regarding available specific oncotropic tracers can be found on the Molecular Imaging and Contrast Agent Database <http://www.ncbi.nlm.nih.gov> details. The most commonly used non-specific oncotropic radioisotope is the glucose analogue 18F labelled fluorodeoxyglucose (18F FDG). Uptake of 18F FDG occurs in cells with increased glucose metabolism such as neurons and mitotic neoplastic cells. Therefore, similar to osteotropic compounds, and as their name suggests, non-specific oncotropic radioisotopes are sensitive but not specific for skeletal metastasis.

SKELTAL SCINTIGRAPHY

Bone scintigraphy continues to be the most widely used radionuclide technique for investigation of skeletal metastasis primarily due to its widespread availability^[2]. Radiotracer uptake depends on local blood flow, osteoblastic activity and extraction efficiency. Once

accumulated in bone diphosphonates are absorbed by hydroxyapatite crystals on mineralizing bone surfaces^[13].

A major advantage of radionuclide bone scanning is that imaging of the whole skeleton can be performed (Figure 3). This is important given that metastatic lesions can occur in regions of the appendicular skeleton that are not routinely included in a skeletal survey^[9]. A further advantage relates the high sensitivity of scintigraphy which enables earlier detection of osseous metastases. The sensitivity and specificity of bone scintigraphy for detection of bone metastasis is 78% and 48%, respectively (Table 1). In particular, studies indicate that only a 5%-10% alteration in the ratio of lesion to normal bone is necessary to manifest abnormal tracer accumulation on a bone scan. As a result, osteosclerotic bone metastases can be detected on bone scintigraphy up to 18 mo earlier than on plain radiographs^[7].

Skeletal scintigraphy has some notable limitations. For example, bone scintigraphy is non-specific and multiple benign osseous lesions, such as eosinophilic granuloma fibrous dysplasia and enchondroma, can lead to a false positive diagnosis of bone metastasis^[14]. Interpreting focal accumulation of radiotracer in the spine can be particularly problematic as degenerative disease may be indistinguishable from bone metastases. Consequently, other imaging modalities such as plain radiography, CT or MRI are often required for correlation to exclude benign causes^[8]. Secondly, the spatial resolution of scintigraphy is poor measuring approximately 1 cm and can result in difficulty determining the precise location of a lesion within a bone which can be of diagnostic significance^[2]. Thirdly, bone scintigraphy assesses osteoblastic processes rather than tumour proliferation and, consequently, false negative results can occur^[8]. Furthermore, primarily osteolytic lesions with limited reactive osteoblastic reaction, such as renal cell carcinoma metastases, typically demonstrate low or absent tracer accumulation leading to a false negative result (Figure 4)^[6]. Finally, when bone metastases are extensive and diffuse, a bone scan on first inspection may appear normal due to the confluent nature of the lesions (referred to as a super scan because of the apparent good quality of the scan) and can be misinterpreted as a negative study^[9,13]. It is therefore import to carefully assess for uptake in the kidneys on skeletal scintigraphy indicative of renal excretion of radiotracer which is characteristically absent on a super scan.

Certain clues and techniques can help to determine if focal uptake of radiotracer is secondary to a benign osseous lesion or metastasis. For example, vertebral body fractures have a characteristic appearance on bone scintigraphy, showing a horizontal linear pattern of increased tracer accumulation. Multiple linear abnormalities of varying intensity favour a benign aetiology with presumed osteoporotic fracture occurring at different time points. In addition, a short interval follow-up scan that shows reducing activity at a vertebral fracture site

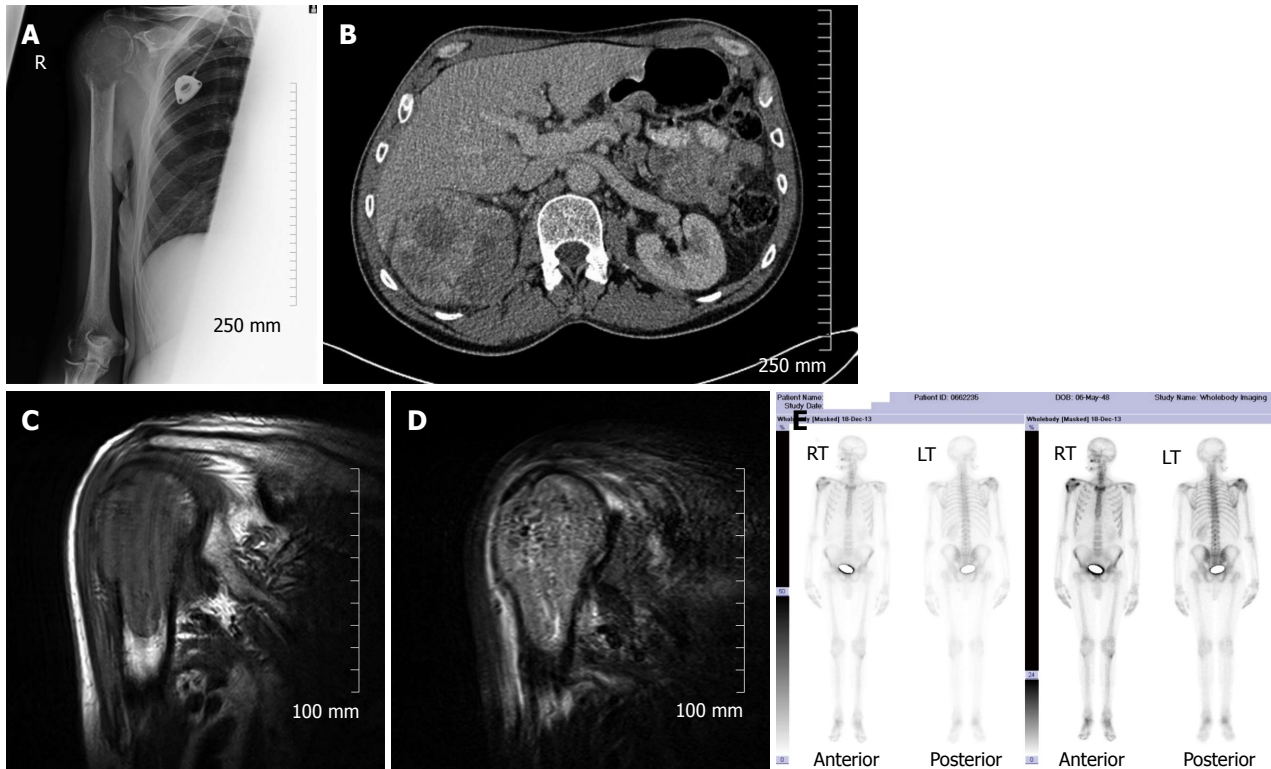


Figure 4 Lytic bone metastases are poorly demonstrated on bone scintigraphy. Plain radiograph (A) demonstrating a lytic metastatic deposit in the right proximal humerus in a patient with a large right renal cell carcinoma (B); Corresponding abnormal low T1 and high short tau inversion recovery signal on magnetic resonance imaging (C and D); Only the small osteoblastic component of the metastatic deposit demonstrates abnormal accumulation of radiotracer on bone scintigraphy (E).

suggests a benign aetiology and a healing fracture. Secondly, lesions that extend from the vertebral body into the posterior vertebral elements or involve the pedicle are more likely to represent metastases^[13]. Finally, linear uptake of radiotracer in contiguous ribs is highly suggestive of trauma and not metastasis.

Bone metastases responding to treatment will demonstrate reduced or absent radiotracer uptake when compared with the pretreatment scan^[6]. It is important to recognise, however, that early in the course of treatment a flare response can occur, which is characterized by a transient elevation in radiotracer accumulation secondary to the stimulation of osteoblasts during the repair process which can be misinterpreted as treatment failure, as it can have an imaging appearance indistinguishable from disease progression^[7]. The flare response is most commonly associated with hormone based therapies and may last for up to 6 mo after therapy^[13]. Progression of disease is suggested when new deposits develop or there is an interval increase in the activity or size of existing deposits^[3].

SINGLE PHOTON EMISSION CT

Single photon emission CT (SPECT) imaging of the skeleton uses ^{99m}Tc-MDP, the same radionuclide used in conventional skeletal scintigraphy, however images are acquired in a cross-sectional rather than a planar fashion. Whereas planar imaging is limited by

superimposition of structures, SPECT can show axial slices through the body, providing better localisation of abnormal radionuclide uptake^[5,7]. The sensitivity and specificity of SPECT for detection of bone metastasis is 87% and 91%, respectively (Table 1). A limitation of SPECT when compared with other available nuclear medicine technique is an inability to generate absolute quantification values^[6].

PET

PET is a nuclear medicine technique that produces high-resolution tomographic images through the detection of high-energy photon pairs emitted during positron decay of a radioisotope. PET is superior to conventional bone scanning in terms of spatial resolution. For skeletal metastases, ¹⁸F NaF or ¹⁸F FDG are the radiopharmaceuticals most frequently employed^[7].

The uptake mechanism of ¹⁸F NaF is similar to that of ^{99m}Tc-MDP. Specifically, following diffusion through the capillary wall into the extracellular fluid, fluoride ions undergo gradual exchange with the hydroxyl groups of hydroxy-apatite crystal within bone to form fluoro-apatite and subsequently deposited primarily on the surface of bone where re-modelling is maximal. Therefore, ¹⁸F NaF-PET demonstrates radiotracer accumulation at foci of osteoblastic activity^[6,7]. The available literature indicates that ¹⁸F NaF-PET is substantially more sensitive and specific than skeletal

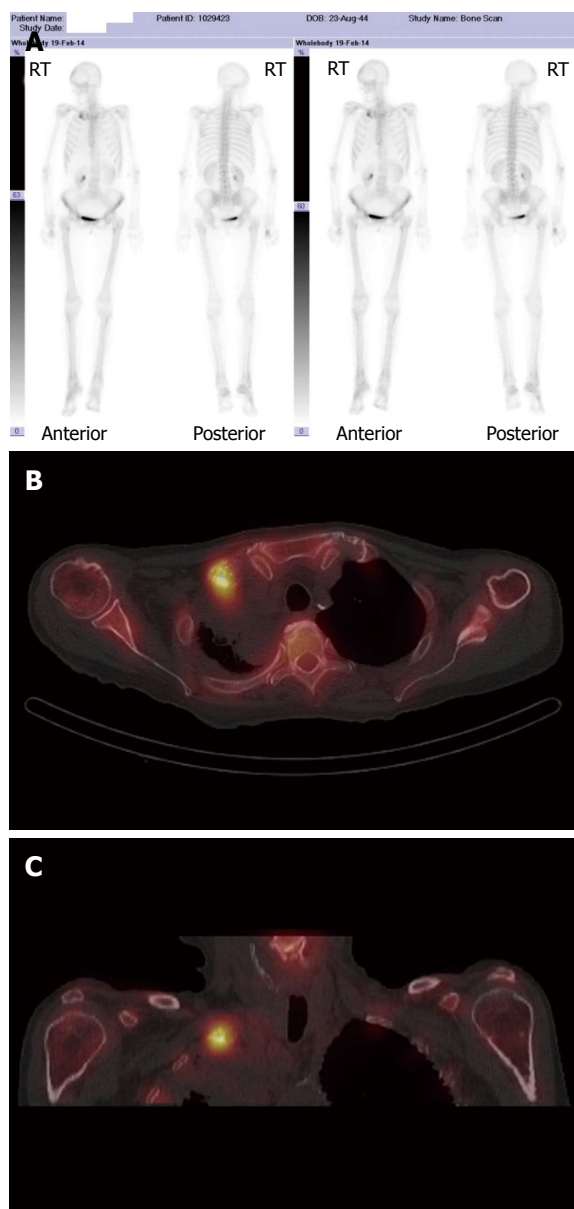


Figure 5 Single photon emission computed tomography has higher sensitivity and specificity for detection of bone metastasis when compared with bone scintigraphy. A: Abnormal accumulation of radiotracer in the right clavicle on bone scintigraphy in a patient with primary lung malignancy; Axial (B) and coronal (C) single photon emission CT/CT images demonstrate the superior spatial and contrast resolution of this hybrid technique which enables improved detection and characterisation on bone metastases.

scintigraphy and SPECT for detection of metastases, particularly for osteolytic lesions^[4,15]. In addition, comparative studies have demonstrated that 18F NaF-PET demonstrates higher sensitivity for detection of bone lesions when compared with 18F FDG-PET^[6].

18F FDG-PET is a functional rather than anatomic imaging method that detects cellular metabolism of a glucose analogue. Many radiopharmaceuticals are available that can be imaged with PET, but 18F FDG is commonly used in oncology because of the high glucose uptake by many tumours^[5]. Accumulation of 18F FDG is predominantly related to the amount of viable

tumour cells. However, the sensitivity of 18F FDG-PET may vary among different histologies^[4]. For example, it has been established that certain well-differentiated and indolent tumours, such as neuroendocrine and bronchial tumours, go undetected by 18F FDG because of the poor 18F FDG accumulation. Furthermore, in patients with primarily osteosclerotic metastases from prostate cancer, 18F FDG-PET has reduced sensitivity for the detection of skeletal metastases compared with 99mTc-MDP scintigraphy^[6]. This is due to the reduced metabolic activity in sclerotic bone metastases. The sensitivity and specificity of 18F FDG-PET for detection of bone metastasis is 98% and 56%, respectively (Table 1).

A major advantage of 18F FDG-PET is the ability to compare the maximum standardised uptake value of a metastatic skeletal deposit between studies which provides an objective measure of the response to treatment. However, similar to skeletal scintigraphy, a potential limitation of 18F FDG-PET in assessing the treatment response of metastatic bone disease is the flare phenomenon (described above) which may be seen after hormone therapy, which can be challenging to distinguish from bone marrow replacement by malignant cells, and result in false positive findings^[3,6].

HYBRID IMAGING TECHNIQUES

It is clear from the preceding sections that the various imaging modalities traditionally used to investigate skeletal metastasis have idiosyncratic strengths and weaknesses. For example, an alteration in the structure of bone in response to treatment may be well demonstrated on CT, whereas tumour cell response is usually best evaluated using PET^[6]. It is intuitive, therefore, that combining imaging modalities can increase sensitivity and specificity to improve diagnostic accuracy. The sensitivity and specificity of 18F NaF-PET/CT for detection of bone metastasis is 100% and 97%, respectively (Table 1). Indeed, technological advances have enabled the development of hybrid imaging techniques including SPECT/CT, PET/CT (Figures 5 and 6) and, more recently, PET/MRI. These techniques are (semi-) quantitative providing a standardized uptake value and allow the fusion of anatomic data from cross sectional imaging with functional information from nuclear medicine studies. As a result, the radiologist can determine if focal radiotracer uptake on a nuclear medicine study corresponds to a discrete skeletal lesion. Similarly, diagnostic confidence increases when an osseous lesion suspicious for metastasis on cross sectional imaging avidly accumulates radiotracer. A recent meta-analysis by Liu *et al.*^[16] found that 18F FDG-PET was the best modality to detect bone metastasis in patients with lung cancer, both on a per-patient and per-lesion basis while MRI had the highest specificity on a per-lesion basis. Furthermore, PET/CT was shown to be better than PET alone.

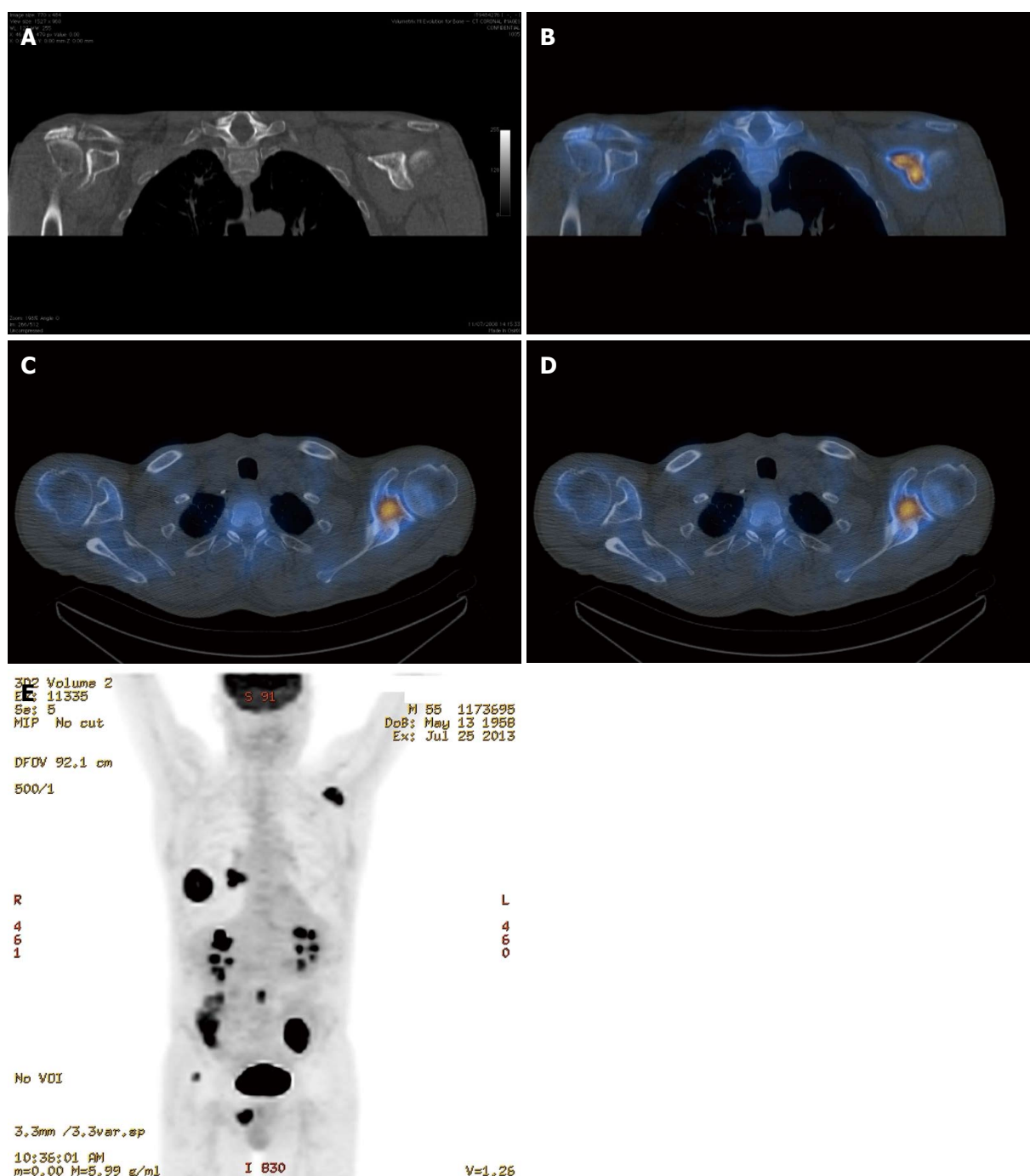


Figure 6 Single photon emission emission computed tomography-computed tomography is more sensitive for detection of bone metastasis than computed tomography alone. A: Coronal CT image of the left scapula (bone window) in a patient with primary lung malignancy does not demonstrate an aggressive bone lesion; Coronal and axial single photon emission CT/CT (B, C) and axial 18F fluorodeoxyglucose-positron emission tomography (FDG-PET)/CT (D) demonstrate abnormal radiotracer accumulation in the left clavicle consistent with bone metastasis; E: Coronal PET maximum intensity projection image demonstrating 18F FDG avid primary lung malignancy and right hilar lymph node metastasis in addition to the metastatic deposit in the left scapula.

The highest potential for early diagnosis of skeletal metastasis should, therefore, involve a combination of MRI and PET. To our knowledge, there is currently no published article comparing the accuracy of PET/CT and PET/MRI in diagnosing skeletal metastases and work in this area is warranted. One disadvantage of the hybrid imaging techniques involving CT is the radiation dose incurred by the patient, with a typical effective dose of

approximately 22 mSv^[5]. A low dose CT protocol can be used without significantly affecting the improved spatial localisation afforded by PET/CT vs PET alone, however, much of the precise anatomic detail is lost. Recent improvements in iterative reconstruction techniques are enabling low dose image acquisition while maintaining excellent contrast resolution and continued progress in this regard is likely.

EXPERIMENTAL IMAGING OF BONE METASTASIS

In this overview of imaging skeletal metastasis, it seems appropriate to briefly highlight experimental imaging strategies currently being explored that may influence the future of oncologic imaging.

Optical imaging techniques which involve transgenic expression of bioluminescent or fluorescent proteins in cancer cell lines are yielding novel information on how tumour cells invade, spread, proliferate and respond to treatment in small animal models of bone metastasis^[17,18]. While such advances are critical to advancing our understanding of tumour biology, it will likely take many years before the results of this research manifest clinically.

Imaging research focused on tumour stimulated angiogenesis may well lead to improvements in imaging skeletal metastasis in the near future. Vascularity of osseous metastases can be visualised by cross sectional imaging and quantitative data obtained. Specifically, dynamic contrast-enhanced (DCE) MRI or CT can be employed to quantify variables in tissue vascularity, such as blood volume and perfusion. DCE imaging can be achieved by sequentially imaging the distribution of a systemically administered contrast agent producing imaging biomarkers that which can then be used to evaluate the response of a tumour to therapies designed to inhibit angiogenesis. Using this approach, potential treatment responses can be detected at an early stage using MRI and CT, before a change in the tumour volume can be reliably detected^[6]. Therefore, DCE will likely continue to develop as a sensitive method to evaluate early tumour response.

CONCLUSION

The availability of improved chemotherapy regimens for many cancers together with a more aggressive approach by surgical oncologists means that many patients are now living longer with metastatic disease. Prolonged survival of patients with cancer results in a greater likelihood of developing distant metastasis which has, in turn, led to a higher prevalence of skeletal metastasis^[19]. In line with these changes, considerable advances in imaging technology have enabled more reliable evaluation of bone metastases and treatment response. Among the various imaging modalities currently available for imaging skeletal metastasis, hybrid techniques which fuse morphological and functional data are the most sensitive and specific, and PET/CT and PET/MRI will almost certainly continue to evolve and become increasingly important in this regard. At present, however, no single imaging strategy is consistently superior for the assessment of metastatic bone disease across all tumour types and clinical scenarios^[9]. The future of imaging bone metastasis will likely involve the development of an array of new radiotracers which will be tumour specific

and greatly increase diagnostic accuracy.

REFERENCES

- 1 **Bussard KM**, Gay CV, Mastro AM. The bone microenvironment in metastasis; what is special about bone? *Cancer Metastasis Rev* 2008; **27**: 41-55 [PMID: 18071636 DOI: 10.1007/s10555-007-9109-4]
- 2 **Cuccurullo V**, Cascini GL, Tamburrini O, Rotondo A, Mansi L. Bone metastases radiopharmaceuticals: an overview. *Curr Radiopharm* 2013; **6**: 41-47 [PMID: 23470032 DOI: 10.2174/1874471011306010007]
- 3 **Vassiliou V**, Andreopoulos D, Frangos S, Tselis N, Giannopoulou E, Lutz S. Bone metastases: assessment of therapeutic response through radiological and nuclear medicine imaging modalities. *Clin Oncol (R Coll Radiol)* 2011; **23**: 632-645 [PMID: 21530193 DOI: 10.1016/j.clon.2011.03.010]
- 4 **Yu HH**, Tsai YY, Hoffer SE. Overview of diagnosis and management of metastatic disease to bone. *Cancer Control* 2012; **19**: 84-91 [PMID: 22487970]
- 5 **Costelloe CM**, Rohren EM, Madewell JE, Hamaoka T, Theriault RL, Yu TK, Lewis VO, Ma J, Stafford RJ, Tari AM, Hortobagyi GN, Ueno NT. Imaging bone metastases in breast cancer: techniques and recommendations for diagnosis. *Lancet Oncol* 2009; **10**: 606-614 [PMID: 19482249 DOI: 10.1016/S1470-2045(09)70088-9]
- 6 **Bäuerle T**, Semmler W. Imaging response to systemic therapy for bone metastases. *Eur Radiol* 2009; **19**: 2495-2507 [PMID: 19468736 DOI: 10.1007/s00330-009-1443-1]
- 7 **Choi J**, Raghavan M. Diagnostic imaging and image-guided therapy of skeletal metastases. *Cancer Control* 2012; **19**: 102-112 [PMID: 22487972]
- 8 **Rajarubendra N**, Bolton D, Lawrentschuk N. Diagnosis of bone metastases in urological malignancies--an update. *Urology* 2010; **76**: 782-790 [PMID: 20346492 DOI: 10.1016/j.urol.2009.12.050]
- 9 **Roberts CC**, Daffner RH, Weissman BN, Bancroft L, Bennett DL, Blebea JS, Bruno MA, Fries IB, Germano IM, Holly L, Jacobson JA, Luchs JS, Morrison WB, Olson JJ, Payne WK, Resnik CS, Schweitzer ME, Seeger LL, Taljanovic M, Wise JN, Lutz ST. ACR appropriateness criteria on metastatic bone disease. *J Am Coll Radiol* 2010; **7**: 400-409 [PMID: 20522392 DOI: 10.1016/j.jacr.2010.02.015]
- 10 **Longo V**, Brunetti O, D'Oronzo S, Ostuni C, Gatti P, Silvestris F. Bone metastases in hepatocellular carcinoma: an emerging issue. *Cancer Metastasis Rev* 2014; **33**: 333-342 [PMID: 24357055 DOI: 10.1007/s10555-013-9454-4]
- 11 **Saha S**, Burke C, Desai A, Vijayanathan S, Gnanasegaran G. SPECT-CT: applications in musculoskeletal radiology. *Br J Radiol* 2013; **86**: 20120519 [PMID: 24096590 DOI: 10.1259/bjr.20120519]
- 12 **Talbot JN**, Paycha F, Balogova S. Diagnosis of bone metastasis: recent comparative studies of imaging modalities. *Q J Nucl Med Mol Imaging* 2011; **55**: 374-410 [PMID: 21738113]
- 13 **Gnanasegaran G**, Cook G, Adamson K, Fogelman I. Patterns, variants, artifacts, and pitfalls in conventional radionuclide bone imaging and SPECT/CT. *Semin Nucl Med* 2009; **39**: 380-395 [PMID: 19801218 DOI: 10.1053/j.semnuclmed.2009.07.003]
- 14 **Zhang Y**, Zhao C, Liu H, Hou H, Zhang H. Multiple metastasis-like bone lesions in scintigraphic imaging. *J Biomed Biotechnol* 2012; **2012**: 957364 [PMID: 22505821 DOI: 10.1155/2012/957364]
- 15 **Yang HL**, Liu T, Wang XM, Xu Y, Deng SM. Diagnosis of bone metastases: a meta-analysis comparing ¹⁸F-FDG PET, CT, MRI and bone scintigraphy. *Eur Radiol* 2011; **21**: 2604-2617 [PMID: 21887484 DOI: 10.1007/s00330-011-2221-4]
- 16 **Liu T**, Xu JY, Xu W, Bai YR, Yan WL, Yang HL. Fluorine-18 deoxyglucose positron emission tomography, magnetic resonance imaging and bone scintigraphy for the diagnosis of bone metastases in patients with lung cancer: which one is the best?--a meta-analysis. *Clin Oncol (R Coll Radiol)* 2011; **23**: 350-358 [PMID: 21094027 DOI: 10.1016/j.clon.2010.10.002]
- 17 **Kaijzel EL**, Snoeks TJ, Buijs JT, van der Pluijm G, Löwik CW.

- Multimodal imaging and treatment of bone metastasis. *Clin Exp Metastasis* 2009; **26**: 371-379 [PMID: 18941911 DOI: 10.1007/s10585-008-9217-8]
- 18 **Snoeks TJ**, Khmelinskii A, Lelieveldt BP, Kaijzel EL, Löwik CW. Optical advances in skeletal imaging applied to bone metastases. *Bone* 2011; **48**: 106-114 [PMID: 20688203 DOI: 10.1016/j.bone.2010.07.027]
- 19 **Gralow JR**, Biermann JS, Farooki A, Fornier MN, Gagel RF, Kumar R, Litsas G, McKay R, Podoloff DA, Srinivas S, Van Poznak CH. NCCN Task Force Report: Bone Health In Cancer Care. *J Natl Compr Canc Netw* 2013; **11** Suppl 3: S1-S50; quiz S51 [PMID: 23997241]

P- Reviewer: Boy C, Kara PO, Sakamoto A
S- Editor: Tian YL **L- Editor:** A **E- Editor:** Jiao XK



Basic study

Development of biodegradable radiopaque microsphere for arterial embolization-a pig study

Yi-Sheng Liu, Xi-Zhang Lin, Hong-Ming Tsai, Hung-Wen Tsai, Guan-Cheng Chen, Syuan-Fong Chen, Jui-Wen Kang, Chen-Miao Chou, Chiung-Yu Chen

Yi-Sheng Liu, Hong-Ming Tsai, Chen-Miao Chou, Department of Radiology, College of Medicine, National Cheng Kung University, Tainan 704, Taiwan

Xi-Zhang Lin, Guan-Cheng Chen, Syuan-Fong Chen, Jui-Wen Kang, Chiung-Yu Chen, Department of Internal Medicine, College of Medicine, National Cheng Kung University, Tainan 704, Taiwan

Hung-Wen Tsai, Department of Pathology, College of Medicine, National Cheng Kung University, Tainan 704, Taiwan

Author contributions: Lin XZ, Chen CY and Liu YS designed research; Liu YS, Chen GC, Chen SF and Kang JW performed research; Tsai HW contributed pathology reading; Lin XZ and Chen CY analyzed data; Chen CY and Liu YS wrote paper; all authors contributed to this paper.

Supported by The National Cheng-Kung University Hospital, No. NCKUH-102-01003.

Institutional review board statement: The experiment was approved by the ethical committee of the animal center of National Cheng Kung University (IACUC approval No. 102046).

Institutional animal care and use committee statement: The experiment was approved by the ethical committee of the animal center of National Cheng Kung University (IACUC approval No. 102046).

Conflict-of-interest statement: No potential conflicts of interest relevant to this article were reported.

Data sharing statement: No additional data are available.

Open-Access: This article is an open-access article which was selected by an in-house editor and fully peer-reviewed by external reviewers. It is distributed in accordance with the Creative Commons Attribution Non Commercial (CC BY-NC 4.0) license, which permits others to distribute, remix, adapt, build upon this work non-commercially, and license their derivative works on different terms, provided the original work is properly cited and the use is non-commercial. See: <http://creativecommons.org/licenses/by-nc/4.0/>

Correspondence to: Chiung-Yu Chen, Medicinae Doctor, Department of Internal Medicine, College of Medicine, National Cheng Kung University, #138 Sheng-Li Road, Tainan 704, Taiwan. chiungyu@mail.ncku.edu.tw
 Telephone: +886-6-2353535-2689
 Fax: +886-6-2347270

Received: May 3, 2015

Peer-review started: May 3, 2015

First decision: June 18, 2015

Revised: July 7, 2015

Accepted: July 29, 2015

Article in press: August 3, 2015

Published online: August 28, 2015

Abstract

AIM: To develop a new type of calibrated, biodegradable, and imaging detectable microsphere and evaluated its embolization safety and efficacy on pig's liver and spleen.

METHODS: Six kinds of pharmaceutical excipient were combined and atomized to form our microsphere. Twenty-four male Lanyu pigs weighing 25-30 kg were used. The arteries of spleen and liver were embolized with Gelfoam, Embosphere, or our microsphere. The serum biochemical tests, computed tomography (CT), liver perfusion scan, and tissue microscopy examination were done to evaluate the safety and efficacy of embolization.

RESULTS: Radiopaque microspheres with a size ranging from 300 to 400 μ m were produced. Embolization of hepatic and splenic artery of pigs with our microsphere significantly reduced the blood flow of liver and resulted in splenic infarction. The follow-up CT imaging and the microscopic examination showed intraarterial degradation of Gelfoam and microsphere. The blood tests

demonstrated insignificant changes with regards to liver and renal functions.

CONCLUSION: Our microspheres, with the unique characteristics, can be used for transcatheter arterial embolization with effects equivalent to or better than Gelfoam and Embosphere in pigs.

Key words: Atomization; Pharmaceutical excipient; Microsphere; Arterial embolization

© **The Author(s) 2015.** Published by Baishideng Publishing Group Inc. All rights reserved.

Core tip: Transcatheter arterial embolization (TAE) is the treatment of choice for intermediate stage hepatocellular carcinoma. Various embolization materials have been designed for this purpose. By using atomization technique and a mixture of pharmaceutical excipient, we developed a new type of calibrated, biodegradable, and imaging detectable microsphere. We proved that our microspheres, with the unique characteristics, can be used for TAE with effects equivalent to or better than Gelfoam and Embosphere in pigs.

Liu YS, Lin XZ, Tsai HM, Tsai HW, Chen GC, Chen SF, Kang JW, Chou CM, Chen CY. Development of biodegradable radiopaque microsphere for arterial embolization-a pig study. *World J Radiol* 2015; 7(8): 212-219 Available from: URL: <http://www.wjgnet.com/1949-8470/full/v7/i8/212.htm> DOI: <http://dx.doi.org/10.4329/wjr.v7.i8.212>

INTRODUCTION

Hepatocellular carcinoma (HCC), the most common primary liver cancer, is the sixth most commonly diagnosed malignancy worldwide^[1]. It is also the third leading cause of cancer-related mortality^[1]. Conventional transcatheter arterial chemoembolization (cTACE) stands for the treatment of choice for Barcelona Clinic Liver Cancer stage B HCC^[2,3]. By introducing embolic agents through an angio-catheter into the blood vessel, transcatheter arterial embolization (TAE) occludes tumor feeding vessels and thereby results in tumor shrinkage^[4,5]. By adding chemotoxic agent(s) to the embolic materials, the cTACE evolved into more a controlled delivery of chemotherapy in the form of drug-eluting bead transcatheter arterial chemoembolization (DEB-TACE)^[6].

Commercially available embolic materials include metallic coils, oils (lipiodol), non-spherical particles (Gelfoam) and microspheres (Embosphere, DC Bead and Hepasphere)^[7]. As a tumor may recanalize the occluded vessels or form new vessels, repeated TAE is required in order to control tumor growth and a biodegradable embolic material allowing for the re-catheterization of previously embolized vessels is therefore, ideally preferred. Gelfoam is the only commercially available

biodegradable embolic material at this time; however, it is non-spherical which makes it unable to precisely control the level of embolization^[8].

Calibrated microspheres allow the radiologist to choose the size of microspheres according to the size of the targeting vessels. The DEB-TACE using drug-loaded microspheres showed less systemic toxicity and drug-related side-effects as compared to the cTACE^[9]. However, both the Hepasphere and the DC Bead are not biodegradable, and it is reported that the long-term presence of DC Bead microspheres containing a potentially harmful drug in the body elicits chronic inflammation and thus causes more tissue injury^[10]. Furthermore, these microspheres including the Embosphere are not radiopaque and interventional radiologists can only estimate the devascularization through an angiography, but do not know the precise site of occlusion of the injected microspheres^[11].

To develop a new type of spherical, biodegradable, imaging detectable, and drug-loadable embolic material is therefore crucial in order to improve the efficacy of tumor embolization treatment. A biodegradable excipient able to be formulated with chemotoxic agent(s) and radiopaque contrast with suitable consistency will be a candidate of material to construct a microsphere for drug delivery and vascular embolization. Atomizing technique which breaks up bulk liquids into droplets can be applied to produce particles of desired shape, size, and density. In this study, we constructed a biodegradable radiopaque microsphere by atomizing a mixture of pharmaceutical excipient and conducted arterial embolization study in pigs in an attempt to explore a new microsphere that fulfills the above requirements for arterial embolization of HCC.

MATERIALS AND METHODS

Design of animal study

The experiment was conducted after the approval of the ethical committee of the animal center of our university and in accordance with the guidelines set forth by the Agriculture Council of Taiwan on animal care. The animal protocol was designed to minimize pain or discomfort to the animals. The animals were acclimatized to laboratory conditions (23 °C, 12 h/12 h light/dark, 50% humidity, ad libitum access to food and water) during experimentation. Twenty-four male Lanyu pigs weighing 25-30 kg were included in the study. Arterial embolization of the liver with concomitant partial embolization of the spleen was used to test our newly developed embolic microsphere. Two other commonly used embolic materials for cTACE-Gelfoam and Embosphere were used for comparison. To better understand the acute and midterm effect of the embolic materials on pigs while avoid the potential anesthesia effects on pigs, blood tests were only checked on the day before embolization, 1 and 25 d after the embolization. To observe the evolutionary change of our microsphere, non-enhanced CT scans were performed

on Day 4, 12, and 25 after the embolization. To estimate the blockade extent of liver blood flow by embolization materials, CT perfusion scans were performed on the pigs without embolization and immediately after embolization. All the animals were sacrificed 28 d after the embolization to examine the pathological changes in liver and/or spleen relating to embolization.

Manufacture of new microsphere

We combined several kinds of excipient from the handbook of pharmaceutical excipient to construct an excipient possessing suitable consistency for embolization. The excipient that we used included Lipiodol, Cetyl alcohol, Glycol monostearate, Stearyl acid, Polycaprolactone, and Cholesterol. All these materials are biodegradable and water insoluble. All these excipients were solid at room and body temperature, and become self-emulsifying oils at 65 °C. Such a characteristic allowed us to melt and atomize it to make it into microsphere. In brief, the atomization procedure included a pressure type atomization technique for mass production of microspheres and a high frequency resonated technique to produce microspheres with a specific range of size. The size of microspheres was further examined by using a scanning electron microscope. With an aim to embolize intrahepatic arteries, microspheres with sizes of 300 to 450 μm were selected for the following embolization experiment.

Procedures of arterial embolization

The animals were fasted overnight and given free access to water. They were premedicated with intramuscular injection of Atropine (Sintong, Taoyuan, Taiwan) 0.02 mg/kg, Xylazine (Bayer, Leverkusen, Germany) 0.1 mL/kg, and Zoletil 50 (Virbac, Carros, France) 10 mg/kg. Following endotracheal intubation, the animals were anesthetized by using Propofol 12-20 mg/kg per hour (Tongchou, Taipei, Taiwan) intravenous injection or Isoflurane (Baxter, Guayama, United States) 1%-3% 200 mL/kg per minute inhalation throughout the operation. All animals were subjected to celiac artery angiography before the embolization. The procedure was performed with a femoral approach by using the Seldinger technique. After placing a 4-F introducer sheath (Cordis, Roden, the Netherlands), a 2.7-F microcatheter catheter (Progreat, Terumo, Tokyo, Japan) was used to catheterize the hepatic proper artery for liver embolization and one of the branches of splenic artery for splenic embolization because complete embolization of spleen caused a significant morbidity and mortality. As many embolization materials were introduced as possible and the end point of the procedure was to obtain blood flow stasis of the selected hepatic and splenic arteries.

Blood tests

By using intramuscular injection of Xylazine (Bayer, Leverkusen, Germany) 0.1 mL/kg and Zoletil 50 (Virbac,

Carros, France) 10 mg/kg to anesthetize pig, serum samples were obtained on the day before embolization and 1 and 25 d after the embolization. Serum levels of blood urea nitrogen (BUN), creatinine, aspartate aminotransferase (AST), alanine aminotransferase (ALT), and total bilirubin were analyzed by using D and P modular analyzer (Roche, Mannheim, Germany).

Computed tomography

Each pig was anesthetized when undergoing computed tomography (CT) scanning and liver perfusion study. CT scanning and perfusion study was performed by a 128-section multidetector CT scanner (Definition Flash, Siemens Medical Systems; Erlangen, Germany). A dynamic study of the selected area was performed in a single breath hold at the end of expiration at a static table position. A total of 50 mL of nonionic iodinated contrast medium was injected at a rate of 5 mL/s, through an 18-gauge intravenous cannula. The liver blood volume (mL/100 mL) and the time that the liver started to be enhanced by contrast (time to start, second) were used to estimate the immediate embolization effects on liver perfusion.

Histological examinations

All animals were euthanized by barbiturate overdose (intravenous injection, 150 mg/kg pentobarbital sodium) for tissue collection. The transected liver and spleen harvested on the day of sacrifice were immediately fixed in a 10% formalin, sectioned, and stained with hematoxylin-eosin to investigate the changes of embolized arteries and peripheral tissues of both the spleen and liver.

Statistical analysis

The blood test results and the CT perfusion index between each group of pigs undergoing different treatments were analyzed by using one way ANOVA with LSD post-hoc test. A *P* value of < 0.05 was considered to be statistically significant.

RESULTS

New microsphere

As shown in Figure 1, microspheres with a size ranging from 300 to 400 μm were successfully produced. The size and shape were comparable to the current commercially used microsphere-Embosphere. Furthermore, due to radiopaque lipiodol being contained in our excipient mixture, our microsphere was different from the Embosphere in that it was radiopaque under fluoroscopy (Figure 2).

Transcatheter arterial embolization of liver and spleen

Figure 3A presents the angiography of the liver of pig. As there were no liver tumors, embolization materials were injected into the hepatic proper artery to embolize bilateral intrahepatic arteries. Besides the liver, we also

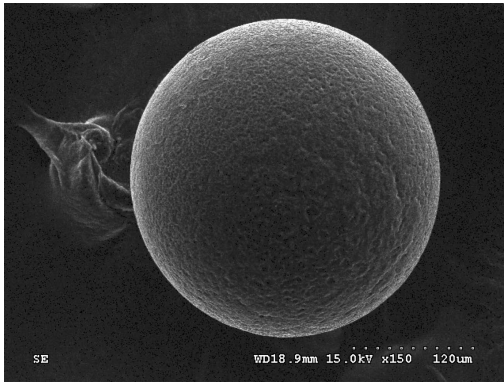


Figure 1 The microspheres in scanning electron microscope with a magnification of 150 ×.



Figure 2 The gross appearance and fluoroscopy picture of DC bead (left), Hepasphere (middle), and our microsphere (right).

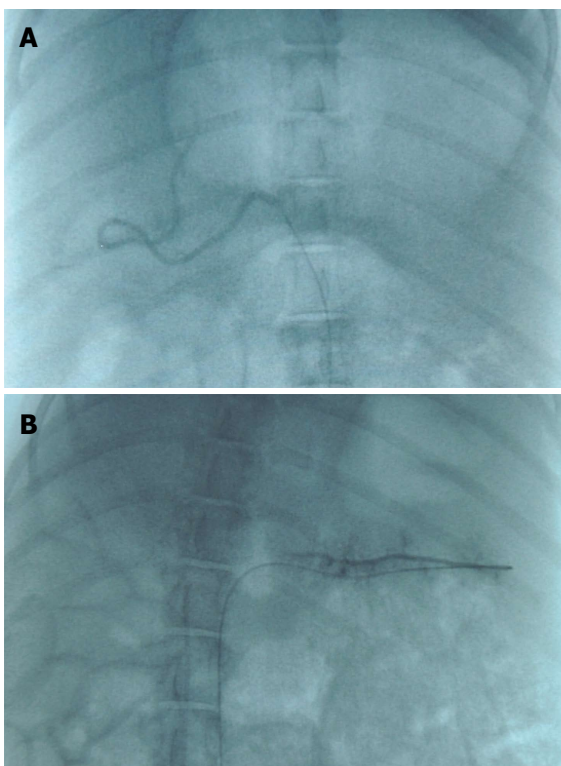


Figure 3 The angiography of hepatic artery (A) and splenic artery (B).

embolized one of the branches of splenic artery to test the embolization effect on spleen (Figure 3B).

Serum biochemical test

The blood tests confirmed the safety of the new microsphere based on our pig embolization experiment (Table 1). Similar to pigs embolized by Embosphere or Gelfoam, our microsphere embolization only caused mild increases in the serum levels of BUN, AST and ALT on the day after embolization and all returned to baseline at the end of experiment. Although the serum creatinine levels were higher in pigs receiving Gelfoam embolization on Day 25, the embolization did not cause any biochemical abnormality with regards to pig liver and the kidneys among groups embolized by different materials.

CT perfusion imaging and study

As shown in Table 2, the embolization effect of our microsphere was comparable to that of Embosphere and Gelfoam, in that all showed a significant reduction of perfused liver blood volume and a delayed contrast enhancement of the liver. The liver perfusion scan further demonstrated areas in the liver with a reduced blood flow after embolization (Figure 4).

CT imaging

As shown in Figure 5, the CT imaging showed retention of lipiodol in the liver after embolization by using our microsphere which faded away gradually in the subsequent follow up imaging. In contrast, both Embosphere and Gelfoam are radiolucent and there was no hyper-intensity area found in the liver of pigs embolized with either one of them.

Pathology examination

Although the ingredients we used for our microsphere were all pharmaceutical excipient, the possible liver toxicity caused by such mixture can be a concern and was checked at first. Microscopically, the liver lobules did not have a significant pathology change after embolization with any of the three embolization materials (Figure 6). Infarction with shrinkage of the embolized part of spleen was noted in the pigs that underwent Embosphere and our microsphere embolization (Figure 7A and B) but grossly normal, in pigs embolized with Gelfoam (Figure 7C). Upon microscopic examination, partial degradation of our microsphere and Gelfoam with peripheral leukocyte infiltration within and around the embolized splenic vessels was observed which was in contrast to the presence of intact Embosphere within the embolized vessels (Figure 8). The different severity of splenic infarction among gelfoam, embosphere, and our microsphere may be therefore, caused by the selection of arterial branch on TAE rather than the character of embolization materials *per se*.

DISCUSSION

In this study, we successfully manufactured a micros-

Table 1 Sequential changes of biochemical tests before and after embolization

	Day 0			Day 1			Day 25		
	Gelfoam (<i>n</i> = 8)	Embosphere (<i>n</i> = 8)	Microsphere (<i>n</i> = 8)	Gelfoam (<i>n</i> = 8)	Embosphere (<i>n</i> = 8)	Microsphere (<i>n</i> = 8)	Gelfoam (<i>n</i> = 7)	Embosphere (<i>n</i> = 8)	Microsphere (<i>n</i> = 8)
AST	27.8 ± 15.3	24.4 ± 9.9	29.5 ± 12.3	56.4 ± 30.8 ^{a,c}	34.9 ± 16.7 ^a	103.0 ± 80.4 ^b	23.1 ± 10.5	30.1 ± 20.6	35.4 ± 10.8
ALT	48.3 ± 23.9	34.8 ± 12.1	44.4 ± 20.6	58.9 ± 20.1	46.4 ± 17.3	51.5 ± 26.7	34.3 ± 19.6 ^{a,c}	22.8 ± 12.6 ^c	40.8 ± 17.0 ^c
T-BIL	0.38 ± 0.15	0.40 ± 0.23	0.39 ± 0.15	0.29 ± 0.20	0.73 ± 1.00	0.68 ± 0.58	0.40 ± 0.14	0.39 ± 0.22	0.56 ± 0.34
BUN	12.1 ± 11.6	8.7 ± 6.4	8.5 ± 3.5	19.4 ± 9.4	18.3 ± 8.5	16.4 ± 9.2	8.7 ± 7.2	7.2 ± 4.1	10.5 ± 4.6
Cr	0.85 ± 0.19	0.75 ± 0.27	0.81 ± 0.21	0.84 ± 0.17	0.73 ± 0.28	0.86 ± 0.25	1.03 ± 0.26	0.86 ± 0.33	0.91 ± 0.18

^{a,c}*P* < 0.05 by one way ANOVA test with LSD post-hoc test. AST: Aspartate aminotransferase; ALT: Alanine aminotransferase; T-BIL: Total bilirubin; BUN: Blood urea nitrogen; Cr: Creatinine.

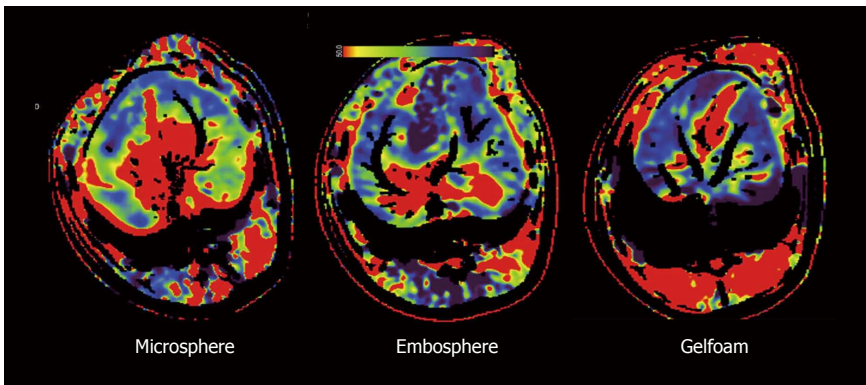


Figure 4 The liver perfusion scan after our microsphere, Embosphere, or Gelfoam embolization showing blood flow reduced areas (green to blue areas) over the periphery of liver.

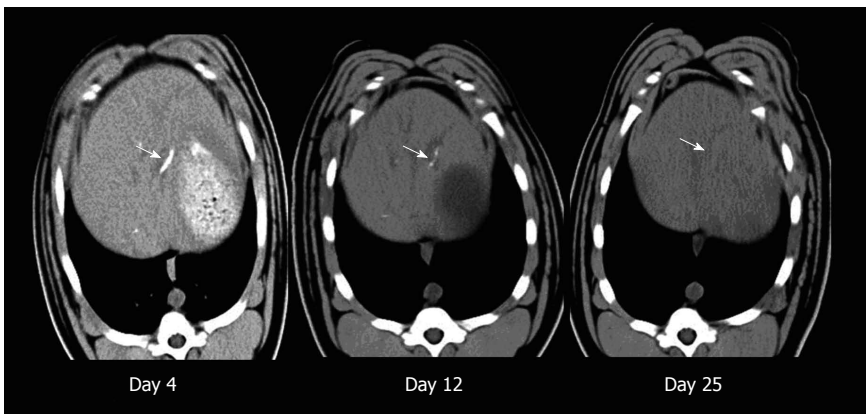


Figure 5 Serial non-enhanced computed tomography scans of pig's liver taken on 4, 12, and 25 d after the microsphere embolization showing its radiopaque characteristic and the gradual fade along with time (white arrow).

phere by atomizing mixture of pharmaceutical excipient. By using pig model, our microsphere was proven to be as safe and effective as currently used embolization materials-Embosphere and Gelfoam. Our microsphere was similar to Gelfoam in that it was biodegradable and Embosphere in that it was calibrated. Besides, our microsphere was radiopaque which can help radiologists to observe and monitor the entire embolization process.

Because the liver has dual blood supply coming from both portal vein and hepatic artery, arterial embolization by using commercial embolization materials or our

microsphere did not cause any significant pathological or serum biochemical changes. The efficacy of embolization can only be investigated from the reduced blood flow of liver on CT perfusion imaging and the extent of splenic infarction after embolization of splenic artery. Based on these two findings, our microsphere was proven to be as effective as Embosphere and Gelfoam.

The size and the accurate caliber range of embolization microspheres is important to correctly deliver it to tumoral or peritumoral vessels. Drug-eluting or simple particles of 100-500 μm size are delivered into

Table 2 Hemodynamic changes of liver before and after embolization

Treatment	Non-embolized (<i>n</i> = 3)	Embosphere (<i>n</i> = 3)	Microsphere (<i>n</i> = 2)	Gelfoam (<i>n</i> = 2)
Blood volume ¹	12.75 ± 0.69	9.60 ± 1.48	9.42 ± 0.24	10.22 ± 1.24
Mean decrease		3.16 ± 0.82	3.33 ± 0.73	2.54 ± 0.82
<i>P</i> value		0.008	0.004	0.021
Time to Start ²	11.40 ± 1.57	15.44 ± 2.10	15.91 ± 0.39	15.44 ± 1.74
Mean delay		4.04 ± 1.33	4.51 ± 1.19	4.04 ± 1.33
<i>P</i> value		0.023	0.009	0.023

¹Blood volume estimated by arterial enhancement; ²Time elapsed from contrast injection to the beginning of arterial enhancement; Data was expressed as mean ± SD; *P* value: Embolized group *vs* non-embolized group by one way ANOVA test with LSD post-hoc test.

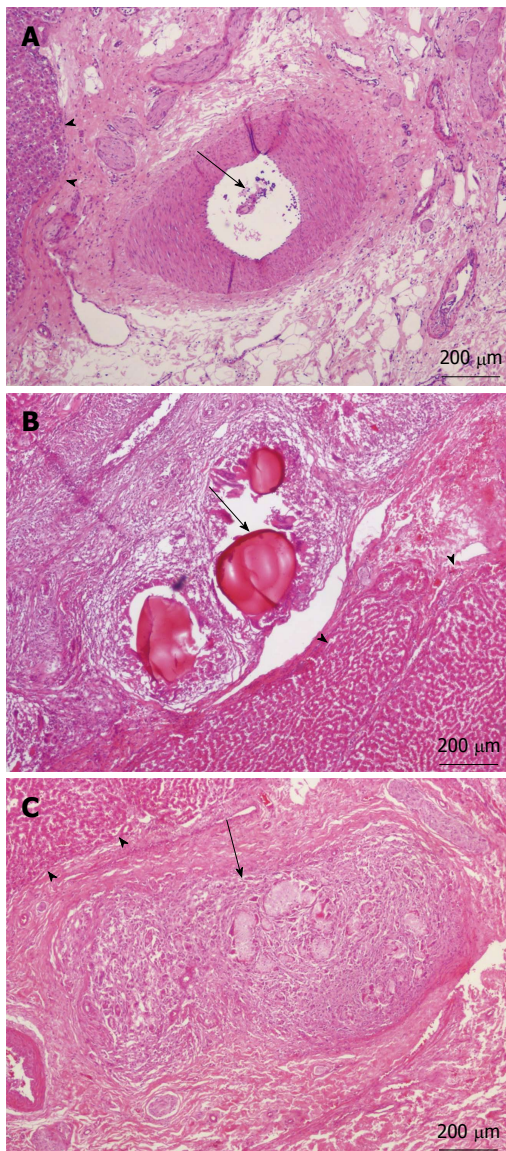


Figure 6 Microscopic findings of liver showing intraarterial embolization materials (black arrow) and intact peripheral liver lobules (black arrow heads) after Gelfoam (A), Embosphere (B), or our microsphere (C) embolization (H-E stain, original magnification × 40).

medium-sized vessels that irrigate tumor nodules with the aim of producing ischemia and finally exposing tumor cells to high concentrations of cytotoxic agents. Particles

more than 500 μm occlude tumor feeding vessels and cause ischemia of both tumor and peritumoral liver^[12]. By applying the atomizing technique, we were able to manufacture microspheres with a narrow size distribution as other calibrated materials such as DC-bead does using a microfluidics technique.

Drug eluting beads significantly reduced the peak plasma concentration of chemotoxic drug when compared with cTACE^[13] and therefore, DEB-TACE has a lower frequency of adverse events than cTACE^[14]. The mechanism of drug elution is attributed to an ionic exchange process between the hydrogel sulfonate or carboxyl counter ions of bead and anionic drug moieties^[15,16]. Such a characteristic has limited the selection of chemotoxic drug to only drugs with anionic moieties. Excipient is a pharmacologically inactive substance and it can be formulated with the active gradient of a medication to give it a suitable consistency or form to a drug. Our microsphere was constructed by a mixture of excipient and thus has a greater potential to combine with various chemotoxic agents for cTACE.

Visualization of the microspheres during embolization would allow radiologists to investigate microsphere distribution within the tumor and liver and to evaluate as to whether distribution is homogeneous in the vasculature and whether the entire target tissue is embolized. All of this information regarding the distribution of the microsphere can be further correlated with the outcome of patients and would be extremely valuable to support the optimization of embolization protocols for a given type and size of tumor. Owing to the fact that lipiodol was included in our formulation of excipient, our microsphere therefore has an additional advantage over the currently used microsphere (*i.e.*, Embosphere and DC-bead) in that it was visible under fluoroscopy.

Gelfoam is the only commercially available biodegradable embolic material at this time; however, it is not spherical and thus unable to accurately control the level of embolization. For temporary embolization such as repeated TAE designated for controlling tumor growth, a biodegradable embolic material clearly preferred. Our microsphere was manufactured by biodegradable excipient. As evidenced by the histology examination and serial follow up CT scan, our microsphere was proven to be biodegradable and was therefore, a more

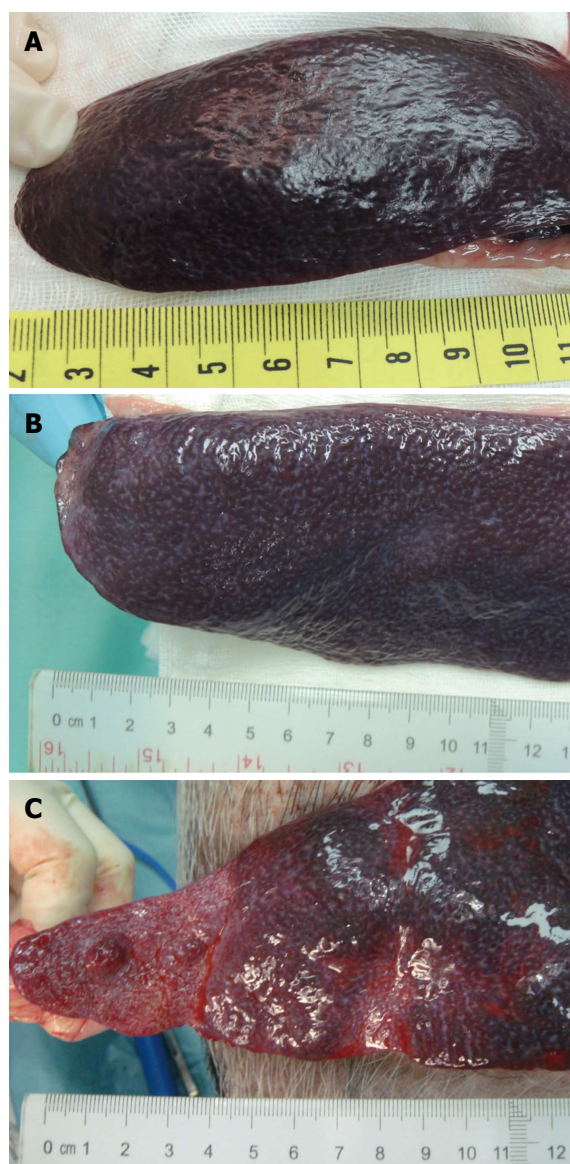


Figure 7 Gross appearance of spleen after Gelfoam (A), Embosphere (B), or our microsphere (C) embolization showing various degree of infarction over the distal end of spleen.

advantageous embolization material than Embosphere.

Although our microsphere has been proven to be useful for transcatheter arterial embolization in a pig model, the detailed physical properties such as rigidity to compression and *in vivo* deformation have not been studied. Deformation of microsphere in arteries and micro-catheters may lead to a more distal occlusion, and thus it is crucial when choosing a optimal sized microsphere to embolized targeted arteries^[11]. In addition, we have not added chemotoxic agent to microsphere to evaluate the rate of drug eluting as it may complicate the evaluation of adverse effect of our microsphere if its safety has not been proved in advance. Studies regarding to these properties of our new microsphere are now ongoing.

In summary, our microspheres possess the characteristics of calibrated, radiopaque, and biodegradable and we proved their efficacy for TAE is equal to or better

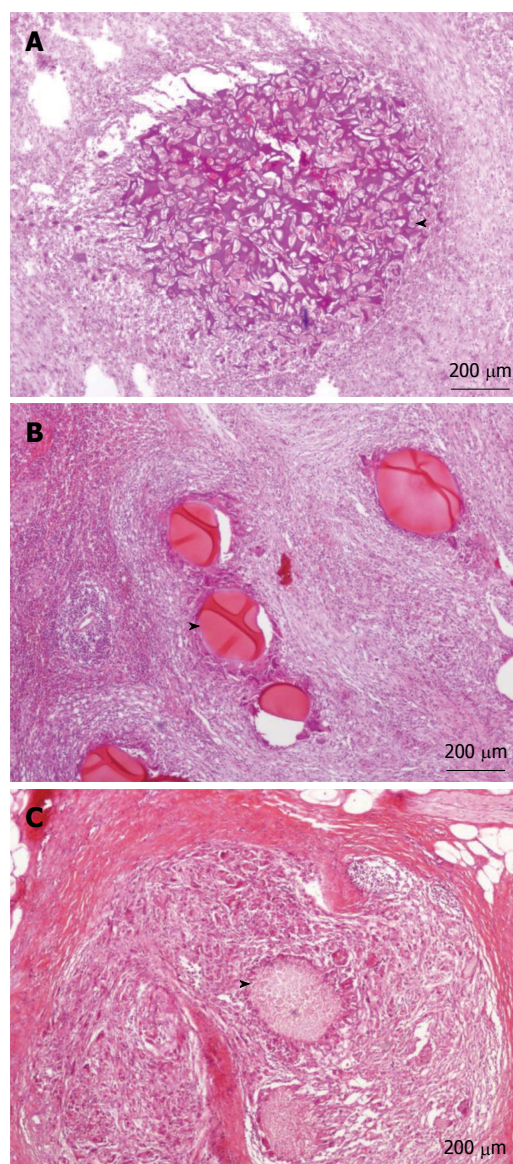


Figure 8 Microscopic findings of spleen showing intraarterial embolization materials (arrow heads) and periarterial reactions after Gelfoam (A), Embosphere (B), or our microsphere (C) embolization (H-E stain, original magnification × 40). Note the degrading Gelfoam and our microsphere and the intact Embosphere at 28 d after the embolization.

than Gelfoam and Embosphere.

COMMENTS

Background

Conventional transcatheter arterial chemoembolization (TACE) stands for the treatment of choice for Barcelona Clinic Liver Cancer stage B hepatocellular carcinoma (HCC). Drug-eluting bead transcatheter arterial chemoembolization controls the delivery of chemotoxic agent and reduces the side effects of chemotherapy. Biodegradable embolic material allows for the re-catheterization of embolized vessels and therefore, repetitive TACE. Calibrated microspheres allow the radiologist to choose the size of microspheres according to the size of the targeting vessels. Currently, there is no commercial microsphere that fulfills the above characteristics of an ideal embolization material.

Research frontiers

The authors constructed a biodegradable radiopaque microsphere by atomizing a mixture of pharmaceutical excipient. The conducted arterial embolization

study in pigs in an attempt to explore a new microsphere that fulfills the above requirements for arterial embolization of HCC.

Innovations and breakthroughs

Unlike DC-bead using a microfluidics technique to produce calibrated microsphere, the authors applied atomizing technique to manufacture microspheres with a narrow size distribution. The authors' microsphere was constructed by a mixture of excipient and thus has a greater potential to combine with various chemotoxic agents than the currently developed drug-eluting beads which uses ionic exchange process between the bead and anionic drug moieties. As evidenced by the histology examination and serial follow up CT scan, the authors' microsphere was proven to be biodegradable and was therefore, a more advantageous embolization material than Embosphere. By using pig model, their microsphere was proven to be as safe and effective as currently used embolization materials-Embosphere and Gelfoam.

Applications

Before applying the microsphere to patients with HCC, studies for the detailed physical properties such as rigidity to compression and *in vivo* deformation of microsphere and the rate of drug eluting from microsphere would be required. However, the study has demonstrated a brand new way and idea to produce embolization material for future arterial embolization.

Terminology

Atomization is a technique which breaks up bulk liquids into droplets and has been applied to produce particles of desired shape, size, and density. Excipient is a pharmacologically inactive substance and it can be formulated with the active gradient of a medication to give it a suitable consistency or form to a drug.

Peer-review

This is a very well designed animal study. This biodegradable radiopaque microsphere has a high potential to develop into a commercial product used for transcatheter arterial embolization of HCC.

REFERENCES

- 1 Jemal A, Bray F, Center MM, Ferlay J, Ward E, Forman D. Global cancer statistics. *CA Cancer J Clin* 2011; **61**: 69-90 [PMID: 21296855 DOI: 10.3322/caac.20107]
- 2 Bruix J, Sherman M. Management of hepatocellular carcinoma. *Hepatology* 2005; **42**: 1208-1236 [PMID: 16250051 DOI: 10.1002/hep.20933]
- 3 Bruix J, Sherman M, Llovet JM, Beaugrand M, Lencioni R, Burroughs AK, Christensen E, Pagliaro L, Colombo M, Rodés J. Clinical management of hepatocellular carcinoma. Conclusions of the Barcelona-2000 EASL conference. European Association for the Study of the Liver. *J Hepatol* 2001; **35**: 421-430 [PMID: 11592607]
- 4 Oerlemans C, Seevinck PR, van de Maat GH, Boukhlef H, Bakker CJ, Hennink WE, Nijssen JF. Alginate-lanthanide microspheres for MRI-guided embolotherapy. *Acta Biomater* 2013; **9**: 4681-4687 [PMID: 22947326 DOI: 10.1016/j.actbio.2012.08.038]
- 5 Kang MJ, Park JM, Choi WS, Lee J, Kwak BK, Lee J. Highly spherical and deformable chitosan microspheres for arterial embolization. *Chem Pharm Bull (Tokyo)* 2010; **58**: 288-292 [PMID: 20190430]
- 6 Salem R, Lewandowski RJ. Chemoembolization and radioembolization for hepatocellular carcinoma. *Clin Gastroenterol Hepatol* 2013; **11**: 604-611; quiz e43- e44 [PMID: 23357493 DOI: 10.1016/j.cgh.2012.12.039]
- 7 Weng L, Rostamzadeh P, Nooryshokry N, Le HC, Golzarian J. In vitro and in vivo evaluation of biodegradable embolic microspheres with tunable anticancer drug release. *Acta Biomater* 2013; **9**: 6823-6833 [PMID: 23419554 DOI: 10.1016/j.actbio.2013.02.017]
- 8 Laurent A, Wassef M, Chapot R, Houdart E, Merland JJ. Location of vessel occlusion of calibrated tris-acryl gelatin microspheres for tumor and arteriovenous malformation embolization. *J Vasc Interv Radiol* 2004; **15**: 491-496 [PMID: 15126660]
- 9 Namur J, Citron SJ, Sellers MT, Dupuis MH, Wassef M, Manfait M, Laurent A. Embolization of hepatocellular carcinoma with drug-eluting beads: doxorubicin tissue concentration and distribution in patient liver explants. *J Hepatol* 2011; **55**: 1332-1338 [PMID: 21703190 DOI: 10.1016/j.jhep.2011.03.024]
- 10 Lammer J, Malagari K, Vogl T, Pilleul F, Denys A, Watkinson A, Pitton M, Sergeant G, Pfammatter T, Terraz S, Benhamou Y, Avajon Y, Gruenberger T, Pomoni M, Langenberger H, Schuchmann M, Dumortier J, Mueller C, Chevallier P, Lencioni R. Prospective randomized study of doxorubicin-eluting-bead embolization in the treatment of hepatocellular carcinoma: results of the PRECISION V study. *Cardiovasc Intervent Radiol* 2010; **33**: 41-52 [PMID: 19908093 DOI: 10.1007/s00270-009-9711-7]
- 11 Laurent A. Microspheres and nonspherical particles for embolization. *Tech Vasc Interv Radiol* 2007; **10**: 248-256 [PMID: 18572137 DOI: 10.1053/j.tvir.2008.03.010]
- 12 Sangro B, Iñarrairaegui M, Bilbao JJ. Radioembolization for hepatocellular carcinoma. *J Hepatol* 2012; **56**: 464-473 [PMID: 21816126 DOI: 10.1016/j.jhep.2011.07.012]
- 13 Gonzalez MV, Tang Y, Phillips GJ, Lloyd AW, Hall B, Stratford PW, Lewis AL. Doxorubicin eluting beads-2: methods for evaluating drug elution and in-vitro/in-vivo correlation. *J Mater Sci Mater Med* 2008; **19**: 767-775 [PMID: 17653626 DOI: 10.1007/s10856-006-0040-y]
- 14 Vogl TJ, Lammer J, Lencioni R, Malagari K, Watkinson A, Pilleul F, Denys A, Lee C. Liver, gastrointestinal, and cardiac toxicity in intermediate hepatocellular carcinoma treated with PRECISION TACE with drug-eluting beads: results from the PRECISION V randomized trial. *AJR Am J Roentgenol* 2011; **197**: W562- W570 [PMID: 21940527 DOI: 10.2214/AJR.10.4379]
- 15 Lencioni R, Crocetti L, Petruzzi P, Vignali C, Bozzi E, Della Pina C, Bargellini I, Cioni D, Oliveri F, De Simone P, Bartolozzi C, Brunetto M, Filippini F. Doxorubicin-eluting bead-enhanced radiofrequency ablation of hepatocellular carcinoma: a pilot clinical study. *J Hepatol* 2008; **49**: 217-222 [PMID: 18486261 DOI: 10.1016/j.jhep.2008.03.021]
- 16 Liu DM, Kos S, Buczkowski A, Kee S, Munk PL, Klass D, Wasan E. Optimization of doxorubicin loading for superabsorbent polymer microspheres: in vitro analysis. *Cardiovasc Intervent Radiol* 2012; **35**: 391-398 [PMID: 21567274 DOI: 10.1007/s00270-011-0168-0]

P- Reviewer: Kim HC, Lau WY, Morris DL
S- Editor: Ji FF L- Editor: A E- Editor: Jiao XK





Published by **Baishideng Publishing Group Inc**

8226 Regency Drive, Pleasanton, CA 94588, USA

Telephone: +1-925-223-8242

Fax: +1-925-223-8243

E-mail: bpgoffice@wjgnet.com

Help Desk: <http://www.wjgnet.com/esps/helpdesk.aspx>

<http://www.wjgnet.com>



World Journal of *Radiology*

World J Radiol 2015 September 28; 7(9): 220-305





Editorial Board

2014-2017

The *World Journal of Radiology* Editorial Board consists of 365 members, representing a team of worldwide experts in radiology. They are from 36 countries, including Afghanistan (1), Argentina (2), Australia (5), Austria (7), Belgium (2), Brazil (8), Canada (6), Chile (1), China (43), Croatia (1), Denmark (4), Egypt (6), France (5), Germany (22), Greece (10), India (12), Iran (6), Ireland (2), Israel (3), Italy (47), Japan (13), Netherlands (1), New Zealand (1), Pakistan (1), Poland (2), Portugal (1), Serbia (1), Singapore (3), Slovakia (1), South Korea (18), Spain (4), Sweden (2), Switzerland (4), Thailand (1), Turkey (26), United Kingdom (11), and United States (82).

EDITORS-IN-CHIEF

Kai U Juergens, *Bremen*
Edwin JR van Beek, *Edinburgh*
Thomas J Vogl, *Frankfurt*

GUEST EDITORIAL BOARD MEMBERS

Wing P Chan, *Taipei*
Chung-Huei Hsu, *Taipei*
Chin-Chang Huang, *Taipei*
Tsong-Long Hwang, *Taoyuan*
Jung-Lung Hsu, *Taipei*
Chia-Hung Kao, *Taichung*
Yu-Ting Kuo, *Tainan*
Hon-Man Liu, *Taipei*
Hui-Lung Liang, *Kaohsiung*
Chun Chung Lui, *Kaohsiung*
Sen-Wen Teng, *Taipei*
Yung-Liang (William) Wan, *Taoyuan*

MEMBERS OF THE EDITORIAL BOARD



Afghanistan

Takao Hiraki, *Okayama*



Argentina

Patricia Carrascosa, *Vicente Lopez*
Maria C Ziadi, *Rosario*



Australia

Lourens Bester, *Sydney*
Gemma A Figtree, *Sydney*



Austria

Herwig R Cerwenka, *Graz*
Gudrun M Feuchtnner, *Innsbruck*
Benjamin Henninger, *Innsbruck*
Rupert Lanzenberger, *Vienna*
Shu-Ren Li, *Vienna*
Veronika Schopf, *Vienna*
Tobias De Zordo, *Innsbruck*



Belgium

Steve Majerus, *Liege*
Kathelijne Peremans, *Merelbeke*



Brazil

Clerio F Azevedo, *Rio de Janeiro*
Patrícia P Alfredo, *São Paulo*
Eduardo FC Fleury, *São Paulo*
Edward Araujo Júnior, *São Paulo*
Wellington P Martins, *Ribeirao Preto*
Ricardo A Mesquita, *Belo Horizonte*
Vera MC Salemi, *São Paulo*
Claudia Szobot, *Porto Alegre*
Lilian YI Yamaga, *São Paulo*



Canada

Marie Arsalidou, *Toronto*
Otman A Basir, *Waterloo*

Tarik Zine Belhocine, *Toronto*
James Chow, *Toronto*
Tae K Kim, *Toronto*
Anastasia Oikonomou, *Toronto*



China

Hong-Wei Chen, *Wuxi*
Feng Chen, *Hangzhou*
Jian-Ping Chu, *Guangzhou*
Guo-Guang Fan, *Shenyang*
Bu-Lang Gao, *Shijiazhuang*
Qi-Yong Gong, *Chengdu*
Ying Han, *Beijing*
Xian-Li Lv, *Beijing*
Yi-Zhuo Li, *Guangzhou*
Xiang-Xi Meng, *Harbin*
Yun Peng, *Beijing*
Jun Shen, *Guangzhou*
Ze-Zhou Song, *Hangzhou*
Wai Kwong Tang, *Hong Kong*
Gang-Hua Tang, *Guangzhou*
Jie Tian, *Beijing*
Lu-Hua Wang, *Beijing*
Xiao-bing Wang, *Xi'an*
Yi-Gen Wu, *Nanjing*
Kai Wu, *Guangzhou*
Hui-Xiong Xu, *Shanghai*
Zuo-Zhang Yang, *Kunming*
Xiao-Dan Ye, *Shanghai*
David T Yew, *Hong Kong*
Ting-He Yu, *Chongqing*
Zheng Yuan, *Shanghai*
Min-Ming Zhang, *Hangzhou*
Yudong Zhang, *Nanjing*
Dong Zhang, *Chongqing*
Wen-Bin Zeng, *Changsha*

Yue-Qi Zhu, *Shanghai*



Croatia

Goran Kusec, *Osijek*



Denmark

Poul E Andersen, *Odense*

Lars J Petersen, *Aalborg*

Thomas Z Ramsøy, *Frederiksberg*

Morten Ziebell, *Copenhagen*



Egypt

Mohamed F Bazeed, *Mansoura*

Mohamed Abou El-Ghar, *Mansoura*

Reem HA Mohamed, *Cairo*

Mohamed R Nouh, *Alexandria*

Ahmed AKA Razek, *Mansoura*

Ashraf A Zytoon, *Shebin El-Koom*



France

Sabine F Bensamoun, *Compiègne*

Romarc Loffroy, *Dijon*

Stephanie Nougaret, *Montpellier*

Hassane Oudadesse, *Rennes*

Vincent Vinh-Hung, *Fort-de-France*



Germany

Henryk Barthel, *Leipzig*

Peter Bannas, *Hamburg*

Martin Beeres, *Frankfurt*

Ilja F Ciernik, *Dessau*

A Dimitrakopoulou-Strauss, *Heidelberg*

Peter A Fasching, *Erlangen*

Andreas G Schreyer, *Regensburg*

Philipp Heusch, *Duesseldorf*

Sonja M Kirchhoff, *Munich*

Sebastian Ley, *Munich*

Adel Maataoui, *Frankfurt am Main*

Stephan M Meckel, *Freiburg*

Hans W Muller, *Duesseldorf*

Kay Raum, *Berlin*

Dirk Rades, *Luebeck*

Marc-Ulrich Regier, *Hamburg*

Alexey Surov, *Halle*

Martin Walter, *Magdeburg*

Axel Wetter, *Essen*

Christoph Zilkens, *Düsseldorf*



Greece

Panagiotis Antoniou, *Thessaloniki*

Nikos Efthimiou, *Athens*

Dimitris Karnabatidis, *Patras*

George Latsios, *Athens*

Stylianios Megremis, *Iraklion*

Alexander D Rapidis, *Athens*

Kiki Theodorou, *Larissa*

Ioannis A Tsalafoutas, *Athens*

Evanthia E Tripoliti, *Ioannina*

Athina C Tsili, *Ioannina*



India

Ritesh Agarwal, *Chandigarh*

Chandan J Das, *New Delhi*

Prathamesh V Joshi, *Mumbai*

Naveen Kalra, *Chandigarh*

Chandrasekharan Kesavadas, *Trivandrum*

Jyoti Kumar, *New Delhi*

Atin Kumar, *New Delhi*

Kaushala P Mishra, *Allahabad*

Daya N Sharma, *New Delhi*

Binit Sureka, *New Delhi*

Sanjay Sharma, *New Delhi*

Raja R Yadav, *Allahabad*



Iran

Majid Assadi, *Bushehr*

SeyedReza Najafizadeh, *Tehran*

Mohammad Ali Oghabian, *Tehran*

Amir Reza Radmard, *Tehran*

Ramin Sadeghi, *Mashhad*

Hadi Rokni Yazdi, *Tehran*



Ireland

Tadhg Gleeson, *Wexford*

Frederik JAI Vernimmen, *Cork*



Israel

Dafna Ben Bashat, *Tel Aviv*

Amit Gefen, *Tel Aviv*

Tamar Sella, *Jerusalem*



Italy

Adriano Alippi, *Rome*

Dante Amelio, *Trento*

Michele Anzidei, *Rome*

Filippo F Angileri, *Messinas*

Stefano Arcangeli, *Rome*

Roberto Azzoni, *San Donato milanese*

Tommaso V Bartolotta, *Palermo*

Tommaso Bartalena, *Imola*

Livia Bernardin, *San Bonifacio*

Federico Boschi, *Verona*

Sergio Casciaro, *Lecce*

Emanuele Casciani, *Rome*

Musa M Can, *Napoli*

Alberto Cuocolo, *Napoli*

Michele Ferrara, *Coppito*

Mauro Feola, *Fossano*

Giampiero Francica, *Castel Volturno*

Luigi De Gennaro, *Rome*

Giulio Giovannetti, *Pisa*

Francesca Iacobellis, *Napoli*

Formato Invernizzi, *Monza Brianza*

Francesco Lassandro, *Naples*

Lorenzo Livi, *Florence*

Pier P Mainenti, *Napoli*

Laura Marzetti, *Chieti*

Giuseppe Malinverni, *Crescentino*

Enrica Milanese, *Turin*

Giovanni Morana, *Treviso*

Lorenzo Monti, *Milan*

Silvia D Morbelli, *Genoa*

Barbara Palumbo, *Perugia*

Cecilia Parazzini, *Milan*

Stefano Pergolizzi, *Messina*

Antonio Pinto, *Naples*

Camillo Porcaro, *Rome*

Carlo C Quattrocchi, *Rome*

Alberto Rebonato, *Perugia*

Giuseppe Rizzo, *Rome*

Roberto De Rosa, *Naples*

Domenico Rubello, *Rovigo*

Andrea Salvati, *Bari*

Sergio Sartori, *Ferrara*

Luca M Sconfienza, *Milano*

Giovanni Storto, *Rionero*

Nicola Sverzellati, *Parma*

Alberto S Tagliafico, *Genova*

Nicola Troisi, *Florence*



Japan

Yasuhiko Hori, *Chiba*

Hidetoshi Ikeda, *Koriyama*

Masahito Kawabori, *Sapporo*

Tamotsu Kamishima, *Sapporo*

Hiro Kiyosue, *Yufu*

Yasunori Minami, *Osaka-sayama*

Yasuhiro Morimoto, *Kitakyushu*

Satoru Murata, *Tokyo*

Shigeki Nagamachi, *Miyazaki*

Hiroshi Onishi, *Yamanashi*

Morio Sato, *Wakayama Shi*

Yoshito Tsushima, *Maebashi*

Masahiro Yanagawa, *Suita*



Netherlands

Willem Jan van Rooij, *Tilburg*



New Zealand

W Howell Round, *Hamilton*



Pakistan

Wazir Muhammad, *Abbottabad*



Poland

Maciej S Baglaj, *Wroclaw*

Piotr Czauderna, *Gdansk*



Portugal

Joao Manuel RS Tavares, *Porto*



Serbia

Olivera Ciraj-Bjelac, *Belgrade*



Singapore

Gopinathan Anil, *Singapore*

Terence KB Teo, *Singapore*

Cher Heng Tan, *Singapore*



Slovakia

Stefan Sivak, *Martin*



South Korea

Ki Seok Choo, *Busan*

Seung Hong Choi, *Seoul*

Dae-Seob Choi, *Jinju*

Hong-Seok Jang, *Seoul*

Yong Jeong, *Daejeon*

Chan Kyo Kim, *Seoul*

Se Hyung Kim, *Seoul*

Joong-Seok Kim, *Seoul*

Sang Eun Kim, *Seongnam*

Sung Joon Kwon, *Seoul*

Jeong Min Lee, *Seoul*

In Sook Lee, *Busan*

Noh Park, *Goyang*

Chang Min Park, *Seoul*

Sung Bin Park, *Seoul*

Deuk Jae Sung, *Seoul*

Choongsoo Shin, *Seoul*

Kwon-Ha Yoon, *Iksan*



Spain

Miguel A De Gregorio, *Zaragoza*

Antonio Luna, *Jaén*

Enrique Marco de Lucas, *Santander*

Fernando Ruiz Santiago, *Granada*



Sweden

Dmitry Grishenkov, *Stockholm*

Tie-Qiang Li, *Stockholm*



Switzerland

Nicolau Beckmann, *Basel*

Christian Boy, *Bern*

Giorgio Treglia, *Bellinzona*

Stephan Ulmer, *Kiel*



Thailand

Sirianong Namwongprom, *Chiang Mai*



Turkey

Kubilay Aydin, *Istanbul*

Ramazan Akdemir, *Sakarya*

Serhat Avcu, *Ankara*

Ayşe Aralasmak, *Istanbul*

Oktay Algin, *Ankara*

Nevbahar Akcar, *Meselik*

Bilal Battal, *Ankara*

Zulkif Bozgeyik, *Elazig*

Nazan Ciledag, *Aakara*

Fuldem Y Donmez, *Ankara*

Gulgun Engin, *Istanbul*

Ahmet Y Goktay, *Izmir*

Oguzhan G Gumustas, *Bursa*

Kaan Gunduz, *Ankara*

Pelin Ozcan Kara, *Mersin*

Kivanc Kamburoglu, *Ankara*

Ozgur Kilickesmez, *Istanbul*

Furuzan Numan, *Istanbul*

Cem Onal, *Adana*

Ozgur Oztekin, *Izmir*

Seda Ozbek (Boruban), *Konya*

Selda Sarikaya, *Zonguldak*

Figen Taser, *Kutahya*

Baran Tokar, *Eskisehir*

Ender Uysal, *Istanbul*

Ensar Yekeler, *Istanbul*



United Kingdom

Indran Davagnanam, *London*

M DC Valdés Hernández, *Edinburgh*

Alan Jackson, *Manchester*

Suneil Jain, *Belfast*

Long R Jiao, *London*

Miltiadis Krokidis, *Cambridge*

Pradesh Kumar, *Liverpool*

Peter D Kuzmich, *Derby*

Georgios Plataniotis, *Brighton*

Vanessa Sluming, *Liverpool*



United States

Garima Agrawal, *Saint Louis*

James R Brasic, *Baltimore*

Rajendra D Badgaiyan, *Buffalo*

Ulas Bagci, *Bethesda*

Anat Biegon, *Stony Brook*

Ramon Casanova, *Winston Salem*

Wenli Cai, *Boston*

Zheng Chang, *Durham*

Corey J Chakarun, *Long Beach*

Kai Chen, *Los Angeles*

Hyun-Soon Chong, *Chicago*

Marco Cura, *Dallas*

Ravi R Desai, *Bensalem*

Delia DeBuc, *Miami*

Carlo N De Cecco, *Charleston*

Timm-Michael L Dickfeld, *Baltimore*

Subba R Digumarthy, *Boston*

Huy M Do, *Stanford*

Todd A Faasse, *Grand Rapids*

Salomao Faintuch, *Boston*

Girish M Fatterpekar, *New York*

Dhakshinamoorthy Ganesan, *Houston*

Robert J Griffin, *Little Rock*

Andrew J Gunn, *Boston*

Sandeep S Hedgire, *Boston*

Timothy J Hoffman, *Columbia*

Mai-Lan Ho, *San Francisco*

Juebin Huang, *Jackson*

Abid Irshad, *Charleston*

Matilde Inglese, *New York*

El-Sayed H Ibrahim, *Jacksonville*

Paul R Julsrud, *Rochester*

Pamela T Johnson, *Baltimore*

Ming-Hung Kao, *Tempe*

Sunil Krishnan, *Houston*

Richard A Komoroski, *Cincinnati*

Sandi A Kwee, *Honolulu*

King Kim, *Ft. Lauderdale*

Guozheng Liu, *Worcester*

Yiyan Liu, *Newark*

Venkatesh Mani, *New York*

Lian-Sheng Ma, *Pleasanton*

Rachna Madan, *Boston*

Zeyad A Metwalli, *Houston*

Yilong Ma, *Manhasset*

Hui Mao, *Atlanta*

Feroze B Mohamed, *Philadelphia*

Gul Moonis, *Boston*

John L Noshier, *New Brunswick*

Rahmi Oklu, *Boston*

Aytekun Oto, *Chicago*

Bishnuhari Paudyal, *Philadelphia*

Rajul Pandya, *Youngstown*

Chong-Xian Pan, *Sacramento*

Jay J Pillai, *Baltimore*

Neal Prakash, *Duarte*

Reza Rahbar, *Boston*

Ali S Raja, *Boston*

Gustavo J Rodriguez, *El Paso*

David J Sahn, *Portland*

Steven Schild, *Scottsdale*

Ali R Sepahdari, *Los Angeles*

Li Shen, *Indianapolis*

JP Sheehan, *Charlottesville*

Atul B Shinagare, *Boston*

Sarabjeet Singh, *Boston*

Charles J Smith, *Columbia*

Kenji Suzuki, *Chicago*

Monvadi Srichai-Parsia, *Washington*

Sree H Tirumani, *Boston*

Hebert A Vargas, *New York*

Sachit Verma, *Philadelphia*

Yoichi Watanabe, *Minneapolis*

Li Wang, *Chapel Hill*

Carol C Wu, *Boston*

Shoujun Xu, *Houston*

Min Yao, *Cleveland*

Xiaofeng Yang, *Atlanta*

Qingbao Yu, *Albuquerque*

Aifeng Zhang, *Chicago*

Chao Zhou, *Bethlehem*

Hongming Zhuang, *Philadelphia*

**DIAGNOSTIC ADVANCES**

- 220 Role of computed tomography angiography in detection and staging of small bowel carcinoid tumors
Bonekamp D, Raman SP, Horton KM, Fishman EK

REVIEW

- 236 Ankylosing spondylitis: A state of the art factual backbone
Ghasemi-rad M, Attaya H, Lesha E, Vegh A, Maleki-Miandoab T, Nosair E, Sepehrvand N, Davarian A, Rajebi H, Pakniat A, Fazeli SA, Mohammadi A

MINIREVIEWS

- 253 Imaging evaluation of traumatic thoracolumbar spine injuries: Radiological review
Gamanagatti S, Rathinam D, Rangarajan K, Kumar A, Farooque K, Sharma V
- 266 Radiation signature on exposed cells: Relevance in dose estimation
Perumal V, Gnana Sekaran TS, Raavi V, Basheerudeen SAS, Kanagaraj K, Chowdhury AR, Paul SFD

ORIGINAL ARTICLES**Retrospective Cohort Study**

- 279 Inter- and intra-rater reliability of diffusion tensor imaging parameters in the normal pediatric spinal cord
Barakat B, Shah P, Faro SH, Gaughan JP, Middleton D, Mulcahey MJ, Mohamed FB

Retrospective Study

- 286 Intraperitoneal tuberculous abscess: Computed tomography features
Dong P, Chen JJ, Wang XZ, Wang YQ

Observational Study

- 294 Pulmonary fibrosis and emphysema: Is the emphysema type associated with the pattern of fibrosis?
Oikonomou A, Mintzopoulou P, Tzouveleakis A, Zazos P, Zacharis G, Koutsopoulos A, Bouros D, Prassopoulos P

ABOUT COVER

Editorial Board Member of *World Journal of Radiology*, Vincent Vinh-Hung, MD, MSc, PhD, Senior Lecturer, Department of Radiation Oncology, Centre Hospitalier Universitaire de Martinique, Fort-de-France 97200, Martinique

AIM AND SCOPE

World Journal of Radiology (*World J Radiol*, *WJR*, online ISSN 1949-8470, DOI: 10.4329) is a peer-reviewed open access academic journal that aims to guide clinical practice and improve diagnostic and therapeutic skills of clinicians.

WJR covers topics concerning diagnostic radiology, radiation oncology, radiologic physics, neuroradiology, nuclear radiology, pediatric radiology, vascular/interventional radiology, medical imaging achieved by various modalities and related methods analysis. The current columns of *WJR* include editorial, frontier, diagnostic advances, therapeutics advances, field of vision, mini-reviews, review, topic highlight, medical ethics, original articles, case report, clinical case conference (clinicopathological conference), and autobiography.

We encourage authors to submit their manuscripts to *WJR*. We will give priority to manuscripts that are supported by major national and international foundations and those that are of great basic and clinical significance.

INDEXING/ABSTRACTING

World Journal of Radiology is now indexed in PubMed Central, PubMed, Digital Object Identifier, and Directory of Open Access Journals.

FLYLEAF

I-III Editorial Board

EDITORS FOR THIS ISSUE

Responsible Assistant Editor: *Xiang Li*
Responsible Electronic Editor: *Huan-Liang Wu*
Proofing Editor-in-Chief: *Lian-Sheng Ma*

Responsible Science Editor: *Shui Qiu*
Proofing Editorial Office Director: *Xiu-Xia Song*

NAME OF JOURNAL
World Journal of Radiology

ISSN
ISSN 1949-8470 (online)

LAUNCH DATE
December 31, 2009

FREQUENCY
Monthly

EDITORS-IN-CHIEF
Kai U Juergens, MD, Associate Professor, MRT und PET/CT, Nuklearmedizin Bremen Mitte, ZEMODI - Zentrum für morphologische und molekulare Diagnostik, Bremen 28177, Germany

Edwin JR van Beek, MD, PhD, Professor, Clinical Research Imaging Centre and Department of Medical Radiology, University of Edinburgh, Edinburgh EH16 4TJ, United Kingdom

Thomas J Vogl, MD, Professor, Reader in Health Technology Assessment, Department of Diagnostic and Interventional Radiology, Johann Wolfgang

Goethe University of Frankfurt, Frankfurt 60590, Germany

EDITORIAL OFFICE
Jin-Lei Wang, Director
Xiu-Xia Song, Vice Director
World Journal of Radiology
Room 903, Building D, Ocean International Center, No. 62 Dongsihuan Zhonglu, Chaoyang District, Beijing 100025, China
Telephone: +86-10-59080039
Fax: +86-10-85381893
E-mail: editorialoffice@wjnet.com
Help Desk: <http://www.wjnet.com/esps/helpdesk.aspx>
<http://www.wjnet.com>

PUBLISHER
Baishideng Publishing Group Inc
8226 Regency Drive,
Pleasanton, CA 94588, USA
Telephone: +1-925-223-8242
Fax: +1-925-223-8243
E-mail: bpgoffice@wjnet.com
Help Desk: <http://www.wjnet.com/esps/helpdesk.aspx>
<http://www.wjnet.com>

PUBLICATION DATE
September 28, 2015

COPYRIGHT
© 2015 Baishideng Publishing Group Inc. Articles published by this Open-Access journal are distributed under the terms of the Creative Commons Attribution Non-commercial License, which permits use, distribution, and reproduction in any medium, provided the original work is properly cited, the use is non commercial and is otherwise in compliance with the license.

SPECIAL STATEMENT
All articles published in journals owned by the Baishideng Publishing Group (BPG) represent the views and opinions of their authors, and not the views, opinions or policies of the BPG, except where otherwise explicitly indicated.

INSTRUCTIONS TO AUTHORS
Full instructions are available online at http://www.wjnet.com/1949-8470/g_info_20100316162358.htm.

ONLINE SUBMISSION
<http://www.wjnet.com/esps/>

Role of computed tomography angiography in detection and staging of small bowel carcinoid tumors

David Bonekamp, Siva P Raman, Karen M Horton, Elliot K Fishman

David Bonekamp, Siva P Raman, Karen M Horton, Elliot K Fishman, the Russell H. Morgan Department of Radiology and Radiological Science, the Johns Hopkins Medical Institutions, Baltimore, MD 21287, United States

Author contributions: Bonekamp D and Fishman EK made the conception of study; Fishman EK acquired the data; Bonekamp D drafted up the manuscript; all the authors analyzed the imaging studies, revised the paper and made the final approval.

Conflict-of-interest statement: All the author have no conflict of interest.

Open-Access: This article is an open-access article which was selected by an in-house editor and fully peer-reviewed by external reviewers. It is distributed in accordance with the Creative Commons Attribution Non Commercial (CC BY-NC 4.0) license, which permits others to distribute, remix, adapt, build upon this work non-commercially, and license their derivative works on different terms, provided the original work is properly cited and the use is non-commercial. See: <http://creativecommons.org/licenses/by-nc/4.0/>

Correspondence to: Elliot K Fishman, MD, Professor, the Russell H. Morgan Department of Radiology and Radiological Science, the Johns Hopkins Medical Institutions, 601 N. Caroline Street, JHOC 3140C, Baltimore, MD 21287, United States. efishman@jhmi.edu
 Telephone: +1-410-9555173
 Fax: +1-410-6140341

Received: May 4, 2015
 Peer-review started: May 5, 2015
 First decision: June 3, 2015
 Revised: June 18, 2015
 Accepted: August 4, 2015
 Article in press: August 7, 2015
 Published online: September 28, 2015

Abstract

Small-bowel carcinoid tumors are the most common form (42%) of gastrointestinal carcinoids, which by

themselves comprise 70% of neuroendocrine tumors. Although primary small bowel neoplasms are overall rare (3%-6% of all gastrointestinal neoplasms), carcinoids still represent the second most common (20%-30%) primary small-bowel malignancy after small bowel adenocarcinoma. Their imaging evaluation is often challenging. State-of-the-art high-resolution multiphasic computed tomography together with advanced postprocessing methods provides an excellent tool for their depiction. The manifold interactive parameter choices however require knowledge of when to use which technique. Here, we discuss the imaging appearance and evaluation of duodenal, jejunal and ileal carcinoid tumors, including the imaging features of the primary tumor, locoregional mesenteric nodal metastases, and distant metastatic disease. A protocol for optimal lesion detection is presented, including the use of computed tomography enterography, volume acquisition, computed tomography angiography and three-dimensional mapping. Imaging findings are illustrated with a series of challenging cases which illustrate the spectrum of possible disease in the small bowel and mesentery, the range of possible appearances in the bowel itself on multiphase data and extraluminal findings such as the desmoplastic reaction in mesentery and hypervascular liver metastases. Typical imaging pitfalls and pearls are illustrated.

Key words: Small bowel carcinoid; Multidetector computed tomography; Multiplanar analysis; Volume rendered technique; Maximum intensity projection; Surface shading technique

© **The Author(s) 2015.** Published by Baishideng Publishing Group Inc. All rights reserved.

Core tip: Small-bowel carcinoid tumors are neuroendocrine tumors and represent most common form of gastrointestinal carcinoids. Although primary small bowel neoplasms are overall rare, carcinoids still represent the second most common primary small-bowel malignancy. State-of-the-art high-resolution multiphasic computed

tomography with advanced postprocessing methods provides an excellent tool to overcome the challenges of their depiction. Here, we discuss their imaging appearance, focusing on the primary tumor, locoregional mesenteric nodal metastases, and distant metastatic disease. Guidance for imaging protocol selection is given. Imaging findings are illustrated with a series of challenging cases which illustrate the spectrum of disease. Typical imaging pitfalls and pearls are illustrated.

Bonekamp D, Raman SP, Horton KM, Fishman EK. Role of computed tomography angiography in detection and staging of small bowel carcinoid tumors. *World J Radiol* 2015; 7(9): 220-235 Available from: URL: <http://www.wjgnet.com/1949-8470/full/v7/i9/220.htm> DOI: <http://dx.doi.org/10.4329/wjv7.i9.220>

INTRODUCTION

Small-bowel carcinoid tumors are classically defined as histologically well-defined neuroendocrine tumors (NET). NET arise from cells of the diffuse neuroendocrine system and occur primarily in the form of gastrointestinal carcinoid (GI-carcinoid) (70%)^[1,2], tracheobronchial carcinoid (25%)^[2,3] and pancreatic neuroendocrine tumors. GI-carcinoid and pancreatic neuroendocrine tumors are occasionally classified together into a group of gastroenteropancreatic tumors^[4]. Many other organs can be site of origin for NET, such as the kidney, gonads and gallbladder^[5,6]. Gastrointestinal carcinoids occur most commonly in the small bowel (42%), while 27% occur in the rectum and 9% in the stomach^[2]. Gastrointestinal carcinoids are multiple in up to 40% and associated with second primary malignancies in up to 50%. Gastrointestinal carcinoids are relatively uncommon and represent only about 2% of all gastrointestinal tumors^[7], with an incidence of 2 per 100000 worldwide annually^[8]. As primary small bowel neoplasms are overall rare (3%-6% of all gastrointestinal neoplasms), carcinoids still represent the second most common (20%-30%) primary small-bowel malignancy^[7,9,10] after small bowel adenocarcinoma^[9].

In this article, we discuss the imaging appearance and evaluation of duodenal, jejunal and ileal carcinoid tumors, including the imaging features of the primary tumor, locoregional mesenteric nodal metastases, and distant metastatic disease are discussed. In addition, a protocol for optimal lesion detection is presented, including the use of CT enterography, volume acquisition, CT angiography (CTA) and three-dimensional (3D) mapping. Imaging findings are illustrated with a series of challenging cases which nicely illustrate the spectrum of possible disease in the small bowel and mesentery, the range of possible appearances in the bowel itself on multiphase data and extraluminal findings such as the desmoplastic reaction in mesentery and hypervascular liver metastases. Typical imaging pitfalls and pearls are

illustrated.

SMALL BOWEL CARCINOID TUMORS, PATHOLOGY, CLINICAL PRESENTATION AND EPIDEMIOLOGY

Small bowel carcinoid tumors arise from as many as 14 different specialized endocrine cell types (*e.g.*, EC-cells, G-cells, D-cells, *etc.*) of the diffuse endocrine system that lines the gastrointestinal mucosa and submucosa^[11-14], and belong to the group of apudomas (amine precursor uptake and decarboxylation tumors). Most small bowel carcinoids arise from enterochromaffine (argentaffine) Kulchitsky's cells in the Lieberkuhn crypts which are most prevalent in the distal ileum and which produce serotonin^[15]. Forty percent of small bowel carcinoids are located within 60 cm of the ileocecal valve^[16]. These classic serotonin-producing small intestinal carcinoids are the most common form, and represent about 42% of gastrointestinal carcinoids^[3]. Once hormone production overwhelms the metabolic capacity of the liver, commonly after the development of liver metastases, the carcinoid syndrome ensues (observed in up to 20% of patients), which consists of diarrhea, bronchospasm, flushing, abdominal cramps and carcinoid heart disease^[17]. In some instances, small bowel carcinoid tumors may be found as an unusual cause of gastrointestinal bleeding^[18] or incidentally after resection of a Meckel's diverticulum^[19]. In rare instances a midgut carcinoid tumor may invade the retroperitoneal venous circulation and lead to the earlier development of carcinoid syndrome before liver metastases occur^[20]. Conversely, nonfunctioning carcinoids have a propensity to present with extensive liver metastases^[12]. The average age at diagnosis is 61-64 years^[2,12,21], and GI carcinoids are more common in males and African Americans, except for appendiceal and bronchopulmonary carcinoid tumors^[2,8]. The diagnosis is suggested by elevated plasma serotonin or chromogranin A levels and elevated urinary 5-hydroxyindoleacetic acid levels^[12]. Synchronous and metachronous malignancies occur in 30%^[2], most commonly gastrointestinal adenocarcinoma^[22], however the increased rates of other primary malignancies may reflect the relatively good prognosis of patients with this diagnosis compared to other GI cancers^[14]. Focal nodular, polypoid and infiltrative growth patterns of small bowel carcinoid tumors occur. An infiltrative growth pattern with associated desmoplastic reaction is typical, in which tumor cells insinuate between the muscularis propria. There, tumor cells locally release serotonin and other (including vasoactive) substances, which incite a dense fibrosis and desmoplasia. Vasoactive substances may cause strictures and caliber irregularities of local mesenteric vessels, which result in elastic vascular sclerosis. While overall less aggressive and slower growing than small-bowel adenocarcinoma, small bowel carcinoid tumors are not uncommonly

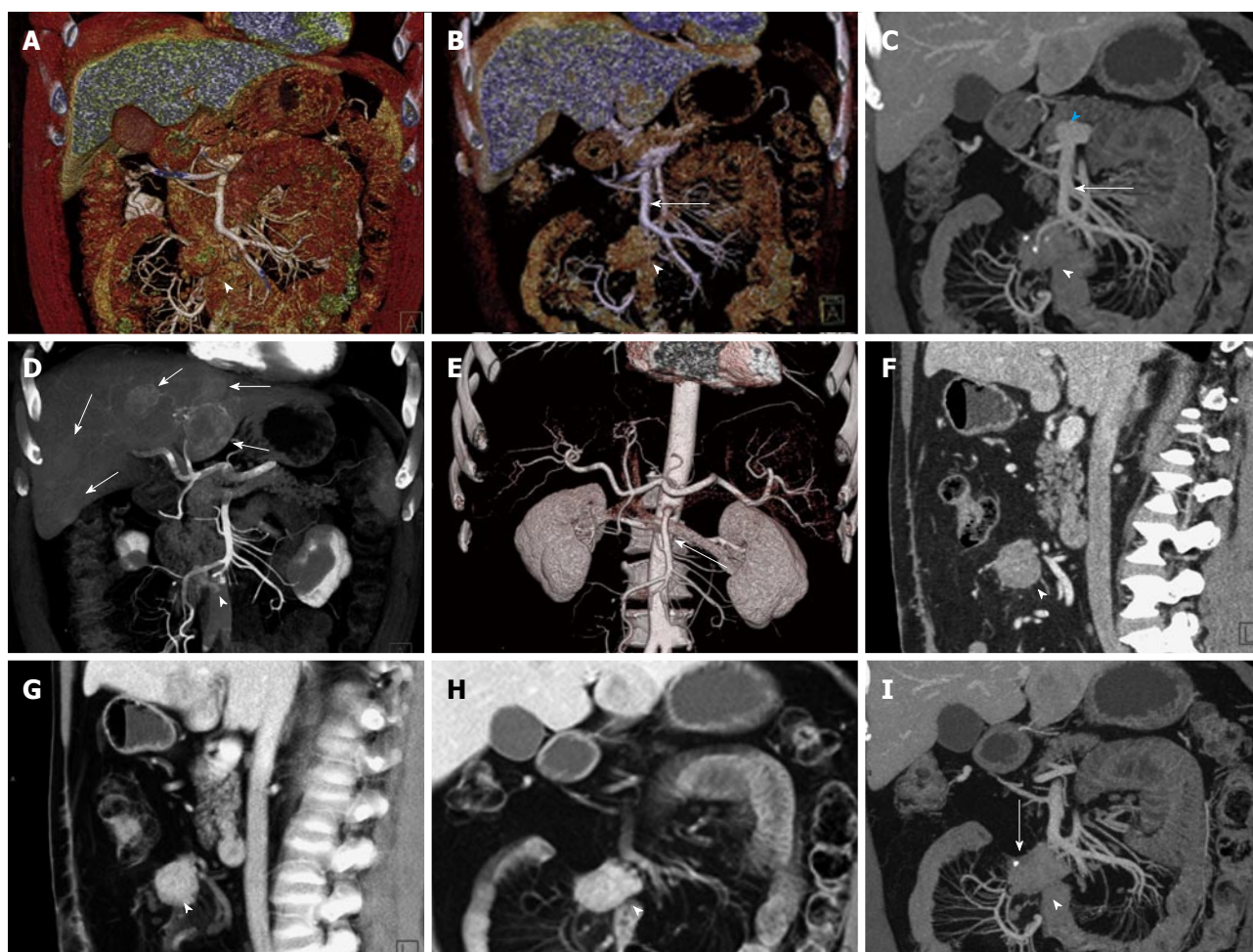


Figure 1 General use of maximum intensity projections, multiplanar reconstructions, volume rendered technique and surface shading. A, B: Coronal surface rendering technique with two different window settings allows to obtain a 3D understanding of a mesenteric mass (arrowhead) and its relationship to the SMV (arrow). The lower window setting (A) includes more soft tissue detail, and better depicts the mesenteric structures and adjacent bowel loops, while the higher window setting (B) excludes structures with lower attenuation and focuses the view on vascular morphology; C: Coronal venous phase VRT image showing the mesenteric mass with calcifications (arrowhead), and the relationship to the SMV (arrow), which can be visualized in its entire course to the portosplenic confluence (blue arrowhead); D: Volume rendering of arterial phase CTA data simultaneously depicts hypervascular liver metastases (arrows) and the relationship of the mesenteric mass to the SMA with vascular encasement and rarefaction of SMA branches (arrowhead); E: 3D surface shading has its major advantage in the depiction the vascular anatomy (SMA, arrow), while the chosen windowing reduces the conspicuity of the mesenteric mass (arrowhead) and removes the voxels pertaining to the liver metastases and the hepatic parenchyma for depiction of the hepatic arteries; F, G: Comparison of sagittal venous phase slice (F) and VRT postprocessed image (G). The mesenteric mass (arrowheads) and its relationship to the adjacent vessels is better defined with VRT (G); H, I: Comparison of coronal VRT (H) to coronal thick slab MPR (I). While VRT makes the spatial relationships more apparent, MPR better demonstrates vascular anatomical detail and the relationship of vessels to the mesenteric mass (arrowheads). Also, a small calcification in the mesenteric mass (arrow) is only visualized with MPR, while the VRT algorithm hides this important detail. VRT: Volume rendered technique; MPR: Multiplanar reconstructions; MIP: Maximum intensity projections; SMV: Superior mesenteric vein; CTA: Computed tomography angiography; SMA: Superior mesenteric artery; 3D: Three-dimensional.

diagnosed in advanced stages (metastatic disease is present in 43% and distant metastases in 13%-24% of patients at the time of diagnosis), such that the rate of metastatic disease approaches that of other GI cancers^[2,14]. The rate of metastatic disease depends on the size of the primary tumor: Nodal metastatic disease occurs in 20%-30% of tumors less than 1 cm in size and increases to more than 80% in tumors more than 2 cm in size. Liver metastases are observed in up to 20% if the primary tumor is less than 2 cm in size, and more than 40% if it is larger than 2 cm^[23-25]. Compared to all GI cancers, GI carcinoid has an overall favorable prognosis, with a relative survival rate of 87% (compared to 53% for GI cancers). GI carcinoid 5-year survival rates are 89% for regional and 59%

for distant stage disease, compared to 56% and 9% for all GI cancers^[14]. The main potentially curative therapy is surgical resection, as carcinoid tumors are often resistant to chemotherapy, although somatostatin analogs (*e.g.*, octreotide) can significantly prolong the time to disease progression in patients with functioning carcinoids^[26]. If tumor control by the use of surgery, chemotherapy or somatostatin therapy cannot be achieved, median patient survival is 30 mo, whereas patients with distant metastatic disease have a reduced median survival of 23 mo. In patients who died of the disease after a mean follow-up of 70 mo in a study of more than 25000 patients, the 5 year survival rate was 29%, underlining the aggressive potential of the disease in some patients^[14]. The median survival of treatment

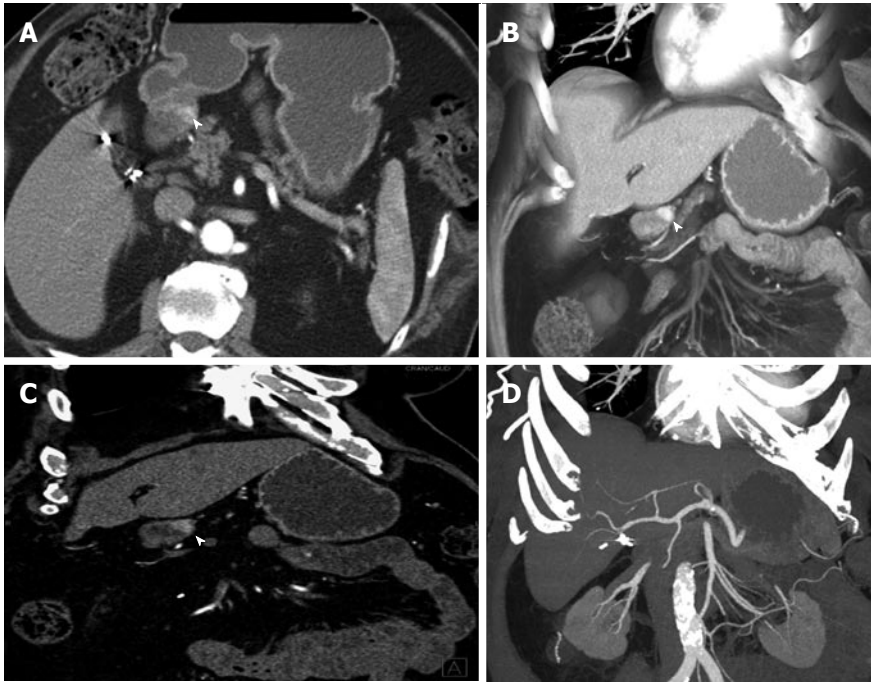


Figure 2 Duodenal carcinoid. A 80-year-old male with duodenal carcinoid. Upper endoscopy for screening showed 1.5 cm mass in the 1st portion of the duodenum. An attempt at endoscopic resection failed, as the mass was too deeply located and invaded the muscularis propria. This case well demonstrates the imaging appearance of the intramural primary tumor as hypervascular mass and the choice of 3D postprocessing methods for optimal evaluation. A: On axial arterial phase imaging, the mass in the wall of the 1st portion of the duodenum is quite subtle (arrowhead). The mass is much better depicted on a coronal VRT image (B) or a thin slab coronal MPR (C), improving diagnostic confidence, while coronal MIP (D) does not provide good contrast in this case. VRT: Volume rendered technique; MPR: Multiplanar reconstructions; 3D: Three-dimensional; MIP: Maximum intensity projections.

resistant GI carcinoids has not improved over time, and the overall mortality has increased, suggesting that the overall improved prognosis, which may be due to increased incidence (higher rates of incidental and early diagnosis), is not counterbalanced by improved therapeutic success in advanced stage or treatment resistant disease^[14].

A traditional belief has been that appendiceal carcinoids are the most common form of GI carcinoid^[27], with a distinctly higher 5 year survival rate approximating 99% for all stages compared to other gastrointestinal carcinoid tumors^[27]. Earlier studies were based on data from large epidemiological programs, where data recorded between 1950 and 1969 from the End Results Group (ERG) yielded a partition of appendiceal carcinoids of 44%, and data recorded between 1969 and 1971 from the Third National Cancer Survey (TNCS) of the National Cancer Institute (NCI) of 36%^[2,27]. More recent data extracted from the Surveillance, Epidemiology and End Results (SEER) program of the NCI between 1973 and 1999 showed a drastically different result, with appendiceal carcinoids representing only 2.4% of gastrointestinal carcinoids, with a pan-SEER incidence of 4.8%^[2]. A recent updated analysis of the SEER database between 1973 and 2009 showed an annual percent decrease of appendiceal carcinoid of 3.6%, suggesting a noticeable decrease over time. Advances in immunohistochemistry and histological analysis as well as differences in data reporting may be responsible for the observed discrepancies of the

reported numbers of appendiceal carcinoid tumors in the pre-SEER period. Further contributing factors may be the decreasing number of appendectomies performed, and better ability to differentiate carcinoid from inflammatory appendicitis on pathology^[2,14,28,29]. A large study by Modlin *et al.*^[2] reported data accumulated over 30 years, and suggested an overall increase of the incidence of carcinoid tumors over the past decades, and this finding has been supported by other studies^[8,14,30,31], including a recent update^[32]. Gastric and rectal carcinoids demonstrated a marked increase (up to approximately 4-fold). The increase of gastric carcinoids has been associated with the increased use of proton pump inhibitors^[33]. Rectal carcinoid, appendiceal carcinoid and gastric carcinoid are more commonly discovered incidentally, as these tumors are less often hormonally active and exhibit a more indolent clinical course, with the exception of the sporadic Type 3 gastric carcinoids.

Duodenal carcinoid

Although the duodenum can be considered the most proximal part of the small bowel, it is anatomically formed at the junction between foregut and midgut, while the jejunum and ileum are exclusively midgut derivatives. As a result, the cellular composition of duodenal carcinoid tumors and their syndromic association varies from other small bowel carcinoids. Duodenal carcinoid is rare, and accounts for only 2%-3% of all gastrointestinal neuroendocrine tumors^[2]. The majority

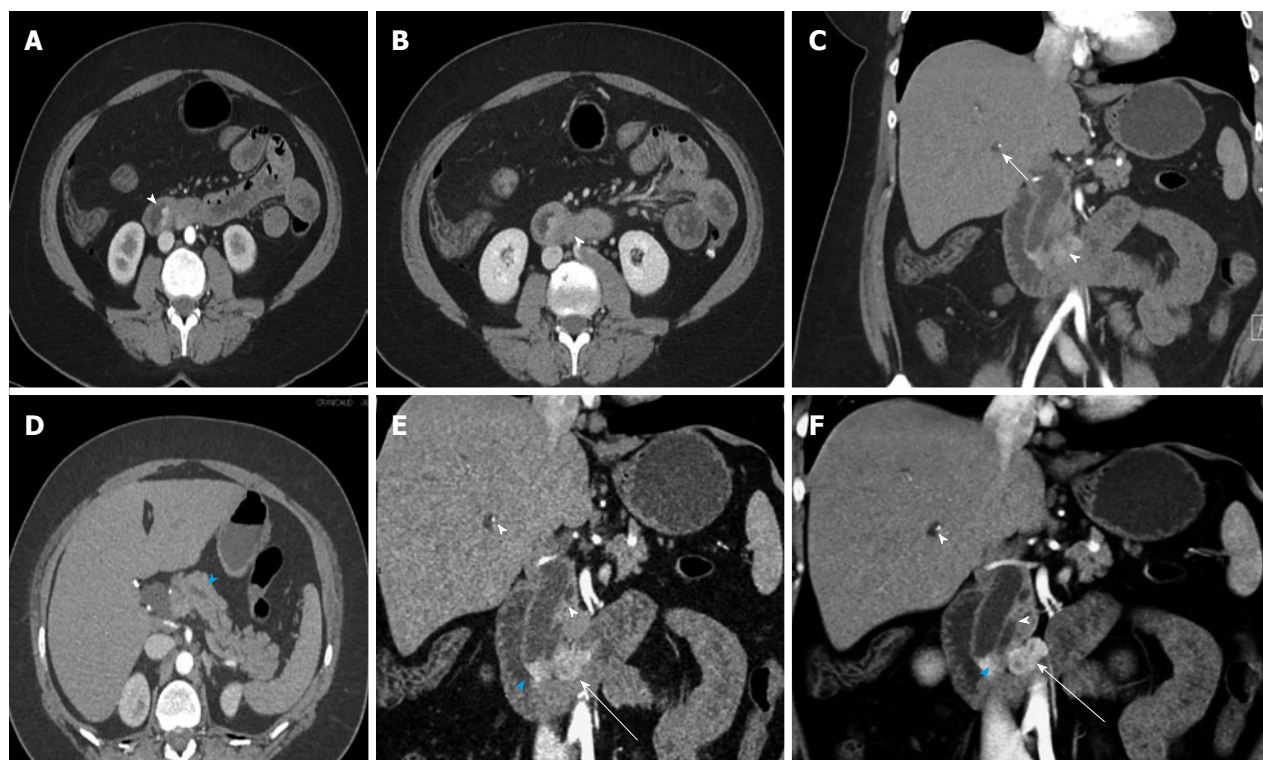


Figure 3 Ampullary neuroendocrine tumor. A 49-year-old female with 1.2 cm neuroendocrine neoplasm of the ampulla, metastatic to the liver. The tumor was incidentally found due to dilated biliary and pancreatic ducts on a renal protocol computed tomography (CT). The patient underwent classic pancreaticoduodenectomy and liver wedge resection, confirming a low grade (G1) 1.2 cm neuroendocrine neoplasm of the ampulla with invasion of the pancreas and peripancreatic tissues. 1 of 19 lymph nodes was involved and lymphovascular invasion was present. This case demonstrates the typical imaging appearance of a hypervascular intramural primary carcinoid, with additional specific imaging features of a periampullary mass. The case also illustrates important aspects of 3D postprocessing. Axial arterial phase (A) and venous phase (B) CT angiography (CTA) images of the 2nd portion of the duodenum show a hypervascular mass in the ampulla (arrowheads). C: Coronal arterial phase image shows the hypervascular mass extending outside the duodenal wall, with adjacent hypervascular peripancreatic lymph nodes (arrowhead). Intrahepatic biliary ductal dilation is noted (arrow); D: Pancreatic ductal dilation results from the obstructing ampullary mass (arrowhead); E, F: Thick slab MPR (E) and VRT (F) images better depict the spatial relationships: The ampullary mass (blue arrowheads) causes moderate extrahepatic and intrahepatic biliary ductal dilation (arrowheads). Peripancreatic hypervascular lymph node metastases (arrows) are present. Note the advantage of MPR and VRT over axial slices in making the mass much more apparent. VRT: Volume rendered technique; MPR: Multiplanar reconstructions; 3D: Three-dimensional.

of duodenal carcinoids are G-cell tumors (62%). A more rare form, D-cell carcinoids, produce somatostatin, and account for 21% of duodenal carcinoids. They occur exclusively around the ampulla of Vater and are strongly associated with neurofibromatosis type 1, with up to 50% of patients with D-cell duodenal carcinoid carrying a diagnosis of neurofibromatosis type 1. The periampullary location is associated with symptoms of ampullary obstruction, including obstructive pancreatitis and biliary obstruction with jaundice. On histology, psammoma bodies are typically found. Classic EC-cell serotonin producing carcinoids, which are most common in the midgut, are rare in the duodenum. Of all duodenal carcinoids, one third are functioning (hormonally active) carcinoids, typically G-cell tumors producing gastrin, resulting in the clinical manifestation of Zollinger-Ellison syndrome (ZES). G-cell tumors with elevated serum gastrin are termed gastrinomas. Duodenal carcinoids are associated with multiple endocrine neoplasia type 1 (MEN-1), and 90% of duodenal carcinoids occurring in MEN-1 are G-cell carcinoids. These MEN-1 duodenal carcinoids are typically multiple, with individual tumors measuring less 5 mm and showing a predilection for

the proximal duodenum. The mean age at diagnosis is 53 years, however the observed age range is wide, and tumors have been diagnosed in patients ranging from 19-90 years old. 85% of sporadic gastrinomas occur anatomically in the gastrinoma triangle, which is formed by the cystic duct/CBD junction superiorly, the inferior genu of the duodenum inferiorly and the junction of the neck and body of the pancreas medially. Not all of these tumors are technically small bowel carcinoids in the narrow sense if they primarily arise from the biliary ductal system or the pancreas, although there may not be a clear distinction as to the origin if the lesion is large. Duodenal carcinoids demonstrate an intraluminal polypoid growth in 50%, while an intramural growth pattern is found in 40%.

Jejunal and ileal carcinoids

Jejunal and ileal carcinoids form the group of midgut carcinoids that include the classical serotonin producing carcinoids, which represent the most common form of small bowel carcinoids. The majority of jejunal and ileal carcinoids are classic serotonin-producing EC cell carcinoids, and they occur more frequently in the distal

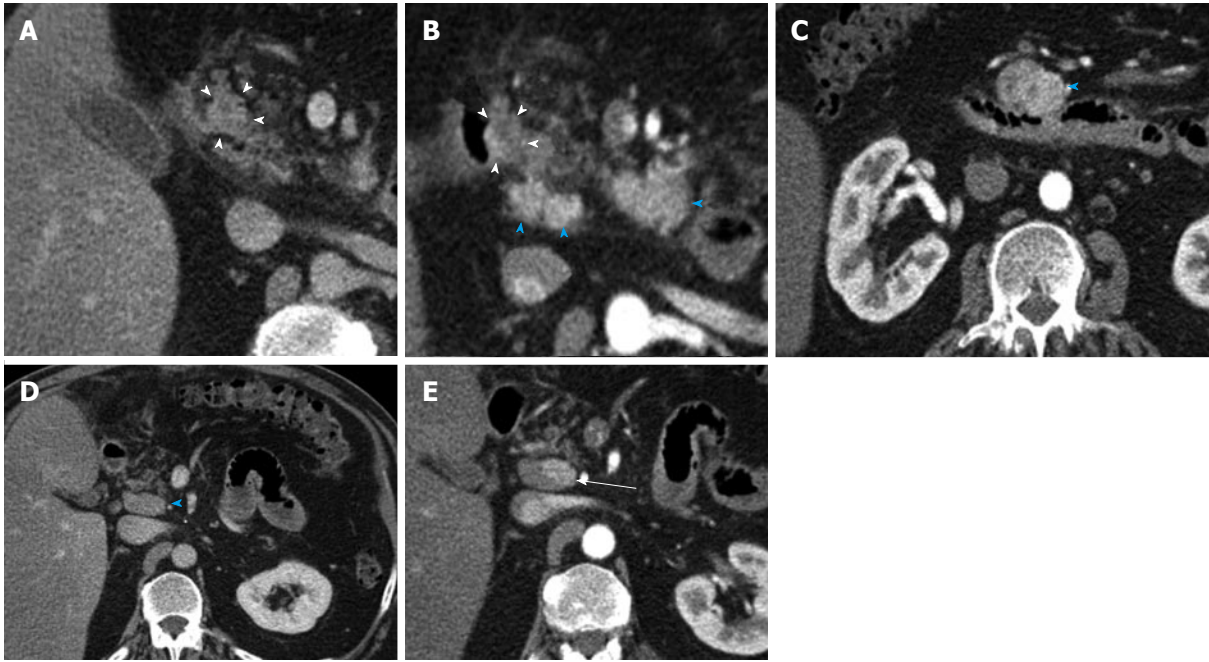


Figure 4 Duodenal Carcinoid. A 61-year-old male with duodenal carcinoid, status-post exploratory laparotomy for a mesenteric mass at an outside institution. Subsequent Whipple procedure demonstrated a 1.8 cm unifocal duodenal carcinoid (pT3, invading pancreas), with 6 of 15 regional lymph node metastases (pN1). This case illustrates the distinction of the primary mass from adjacent nodal metastatic disease and poses an example for nodal metastatic disease having a much larger volume than the primary tumor. A: Venous phase axial computed tomography image shows a 1.8 cm mass in the medial wall of the duodenum, extending into the moderately fatty replaced pancreas, compatible with the primary tumor (arrowheads); B: Arterial phase axial image (magnified, similar slice position) demonstrates heterogeneous hypervascularity in the primary tumor (arrowheads). Multiple metastatic hypervascular peripancreatic lymph nodes are present (blue arrowheads); C: Arterial phase axial image shows a large hypervascular nodal metastasis in the inferior pancreatic groove (blue arrowhead); D: Axial venous phase image shows an enlarged portocaval lymph node (arrowhead); E: Note that in the same node on arterial phase axial image a left-sided hypervascular metastasis can be identified, which was not discernible on the venous phase (D) (arrow).

ileum, reflecting the natural abundance of serotonin-producing EC-cells^[10]. These carcinoids are most commonly malignant, and commonly present with lymph node and liver metastases. There is no significant gender predilection. The mean age at diagnosis is 65 years. The tumors are often asymptomatic during their early stages, during which the liver metabolizes the hormonally active substances until local spread or liver metastases occur. Unless detected incidentally, tumors present either with complications of the primary tumor spread or of metastatic disease. Primary tumor complications are most frequently small intestinal obstruction, bowel ischemia or gastrointestinal bleeding. However, typically the primary tumor is small, commonly below 3.5 cm, and metastatic lesions are found to be significantly larger. Small intramural lesions may occur. Polypoid intraluminal lesions may form lead points for intussusceptions. Characteristically, tumors tend to infiltrate through the bowel wall into the subserosa and the adjacent mesentery, leading to a desmoplastic reaction with kinking, retraction and angulation of the adjacent bowel. Typical metastatic sites of jejunal and ileal carcinoids are locoregional lymph nodes, the mesentery and the liver, and these types of metastases are present in 65% of patients at diagnosis. Thirty percent of jejunal and ileal carcinoids are multiple at diagnosis.

IMAGING OF SMALL BOWEL CARCINOID TUMORS

Scan protocols, data acquisition and image interpretation

Volume acquisition with thin collimation (0.5-1 mm) is preferred for all phases, and provided at our institution by a 64-slice CT scanner (Somatom Sensation 64, Siemens Healthcare).

Typical scan parameters include a tube voltage of 120 kVp, with an effective tube current of 120-160 effective mAs [adjusted in real time by automatic tube current modulation (Care dose, Siemens Healthcare)], gantry rotation time of 0.5 s, beam pitch of 1.2 and table speed of 46 mm per gantry rotation. The resulting submillimeter isotropic dataset is suitable for high quality multiplanar reformations and 3D analysis. CT enterography requires optimal patient preparation with neutral endoluminal contrast. We use a total of 1350 mL of a barium sulfate suspension (VoLumen, Bracco Diagnostics, Monroe Township, NJ, United States) split into three doses of 450 mL each to be administered slowly orally in 10 min intervals before the start of the scan.

For confident detection of the disease manifestations of small bowel carcinoids, we typically perform a dual-phase CT examination, which includes arterial and venous phase imaging. A good early arterial CT

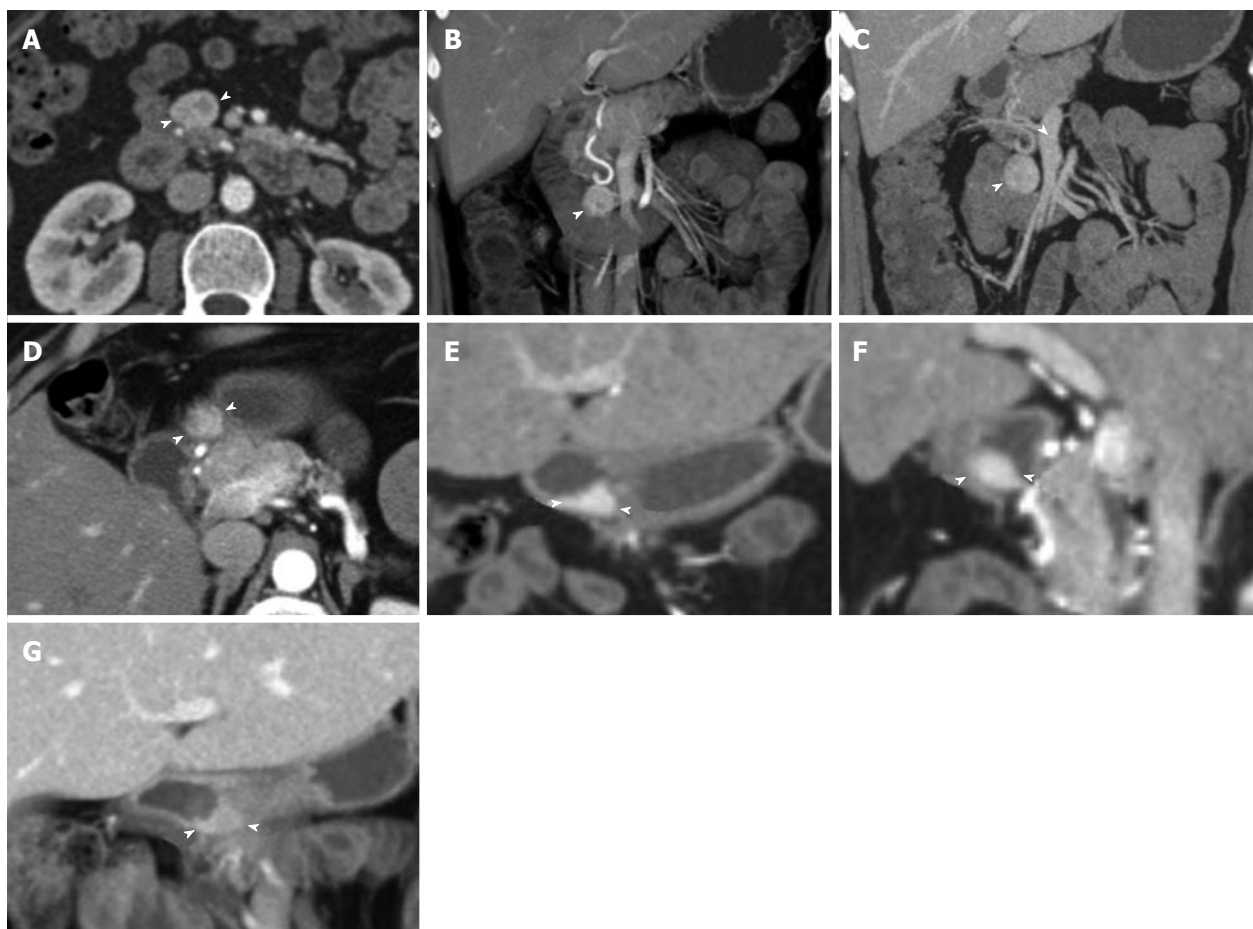


Figure 5 Duodenal carcinoid. Duodenal carcinoid tumor illustrated at two distinct time points. 46-year-old female status-post surgery for removal of an omental carcinoid metastasis, at the first time point presenting with a peripancreatic hypervascular nodal metastasis, which was subsequently surgically removed. A: Axial arterial phase computed tomography (CT) image shows a hypervascular peripancreatic nodal carcinoid metastasis (arrowheads); B: Coronal arterial phase VRT image well demonstrates the location of the hypervascular nodal mass (arrowhead) in the pancreatic groove, abutting the second portion of the duodenum; C: Coronal thick slab MIP image delineates the hypervascular nodal metastasis (arrowhead) in relationship to the SMV (arrow). One year later, at the second time point, a follow-up CT showed appearance of the primary tumor in the duodenal bulb, which was subsequently treated with pancreaticoduodenectomy (Whipple procedure); D, E: Axial (D) and coronal (E) arterial phase CT images show a hyperenhancing mural mass (arrowheads) in the duodenal bulb, just distal to the pylorus, compatible with the patient's primary carcinoid tumor; F: Sagittal arterial phase CT image shows the hyperenhancing mural mass (arrowheads) in the duodenal bulb; G: Coronal arterial phase VRT image demonstrates the intramural hyperenhancing mass (arrowheads). This case illustrates that while the primary tumor may not be initially apparent, it may demarcate itself in the course of the disease, and it also shows the typical imaging appearance of the primary tumor in the form of a hypervascular intramural mass. SMV: Superior mesenteric vein; VRT: Volume rendered technique; MIP: Maximum intensity projections.

angiographic (CTA) imaging acquisition is essential, for which we use a fixed delay of 30 s after start of the intravenous injection. A typical power injection consists of 100-120 mL of nonionic iodinated contrast agent at a rate of 4-5 mL/s.

During image interpretation, axial arterial phase (CTA) images are carefully reviewed for small enhancing bowel lesions. Primary tumors are often small and not well differentiated from bowel wall on the venous phase. Small hyperenhancing masses can still be very inconspicuous on axial images and may be missed if not correlated to multiplanar and 3D analysis.

Multiplanar and 3D analysis consists of volume rendered technique (VRT), multiplanar reconstructions (MPR), maximum intensity projections (MIP) and 3D mapping with surface shading techniques. Figure 1 illustrates how these techniques can supplement the imaging review. Thick slab multiplanar MIP images

support the interactive review by providing a sliding window approach to data review, where small findings are more conspicuous as they appear in a larger number of thick slabs as compared to the review of the individual thin slices. Especially small high contrast structures such as vessels and calcifications are easier to detect and can be shown in contiguity rather than thin interrupted cross-sections. Surface shading is especially useful for the depiction of vessels, specifically of the CTA dataset (Figure 1E). However, interactive choice of the window settings allows the inclusion of variable degrees of soft tissue detail (compare Figure 1A and B). VRT provides depth-encoded shading and is in our experience the best technique to review high contrast vascular, bone and calcified structures together with parenchymal morphology. The relationship between masses and vessels may be easier to discern on VRT (comparison of Figure 1F and G).

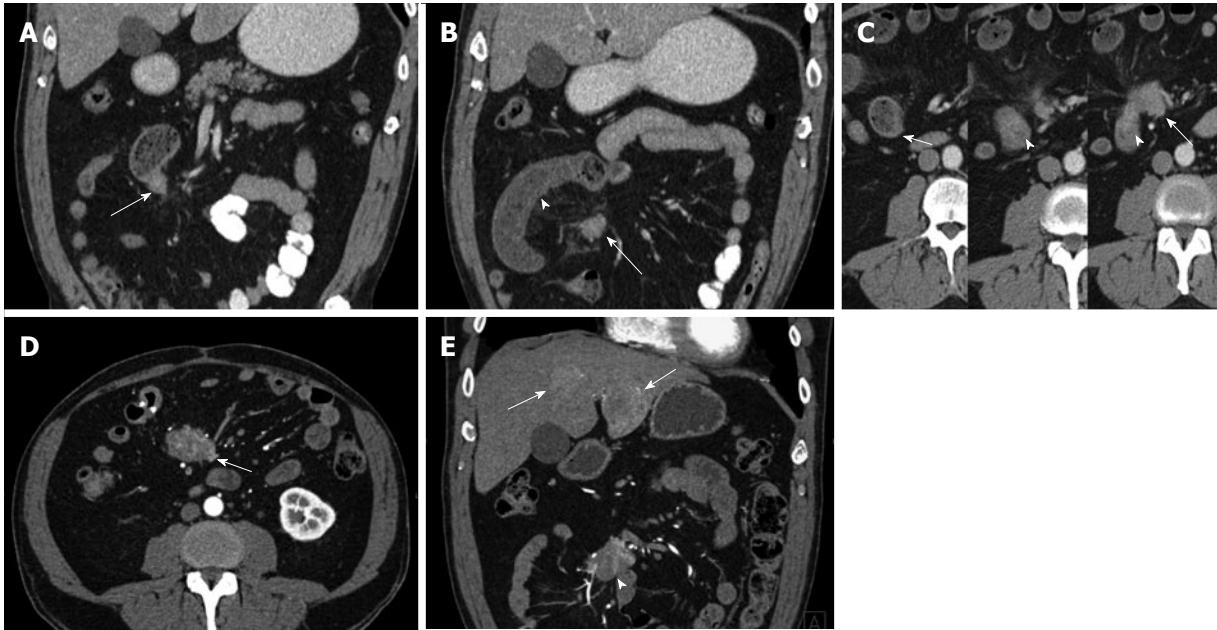


Figure 6 Ileal Carcinoid. A 53-year-old male with stage IV ileal carcinoid tumor, who presented acutely with small bowel obstruction and a history of several months of weight loss, crampy abdominal pain and distention. The patient underwent exploratory laparotomy with surgical resection of an ileal mass (biopsy-proven carcinoid) with primary anastomosis. A large mesenteric mass involving the main superior mesenteric vein and bilateral liver metastases were not resectable. A: Coronal venous phase computed tomography (CT) image shows a hypervascular mass in the wall of a distal ileal loop (arrow) representing the primary carcinoid tumor; B: Coronal venous phase CT image slightly more anterior shows dilated small bowel (arrowhead) with mural thickening and hypoenhancement, compatible with small bowel obstruction and suggestive of hypoperfusion. A portion of a mesenteric nodal mass (arrow) representing regional metastatic disease is shown (arrow); C: Serial axial CT images from the venous phase acquisition; Left: a dilated small bowel loop proximal to the obstruction demonstrates normal bowel wall enhancement and thickness; Middle: Compare the wall thickness and enhancement of the bowel wall at the site of the primary tumor (circumferential mass, invading the mesentery on the left side, arrowhead); Right: The next slice shows the hyperenhancing bowel wall mass (arrowhead) directly abutting the mesenteric lymph nodal metastatic conglomerate mass (arrow); D: Axial arterial phase computed tomography angiography (CTA) image shows the hypervascular mesenteric mass (arrow) reflecting regional lymph node metastatic disease; E: Coronal arterial phase CTA image shows the hypervascular mesenteric mass (arrowhead) reflecting regional lymph node metastatic disease. Hypervascular liver metastases (arrows) are depicted.

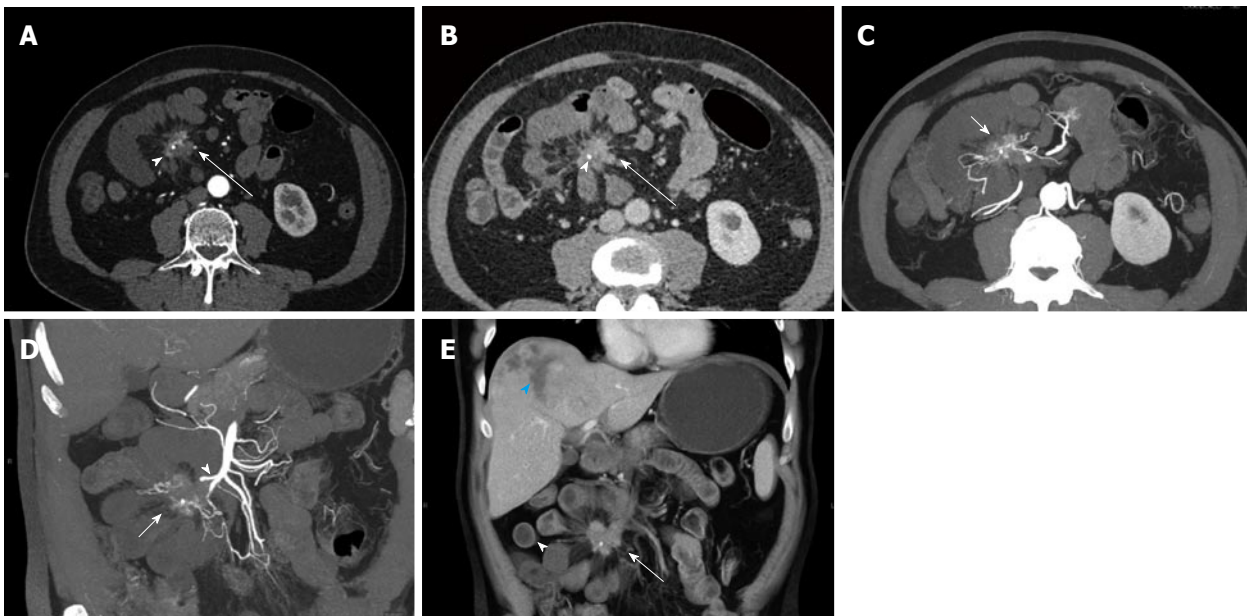


Figure 7 Small bowel carcinoid. A 74-year-old male with small bowel carcinoid (Stage IV), incidentally detected during computed tomography (CT) for presumed kidney stones. He subsequently described a history of flushing and diarrhea, and his urine 5-HIAA level was found elevated. In this case the primary tumor could not be detected on CT. Surgery and pathology demonstrated a polypoid 2 cm mass in the small bowel, likely not detected on CT due to bowel ischemia of the bowel segment involving the tumor. Local nodal metastatic and liver metastatic disease were present. A, B: Axial arterial phase (A) and venous phase (B) images show a hyperenhancing mesenteric mass surrounded by spiculations (arrows) with a small focal calcification (arrowheads), compatible with local nodal metastatic disease with desmoplastic reaction. Multiple dilated small bowel loops with hypoenhancing walls surround the mesenteric mass compatible with the surgical finding of bowel ischemia; C, D: Axial (C) and coronal (D) thick slab MPR images allow the depiction of the relationship of the mesenteric mass (arrows) to the SMA (arrowhead) and the adjacent bowel. The SMA appears irregular and is partially encased by the mass; E: Coronal VRT image allows good visualization of spatial relationships of mesenteric mass (arrow) with calcification, ischemic dilated small bowel loops (arrowhead) and a necrotic liver metastasis in the liver dome (blue arrowhead). VRT: Volume rendered technique; MPR: Multiplanar reconstructions; SMA: Superior mesenteric artery.

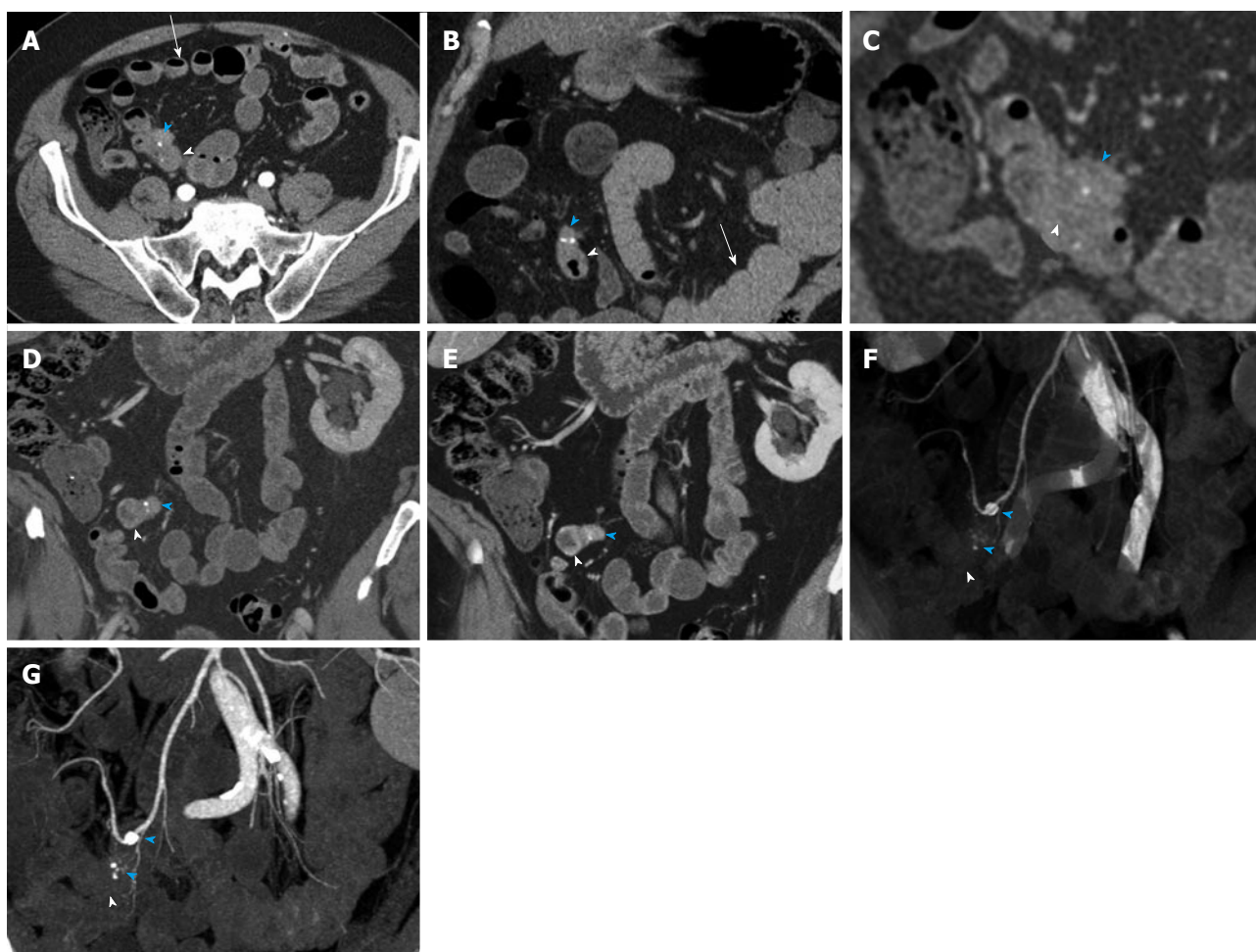


Figure 8 Small bowel carcinoid. A 71-year-old male with small bowel carcinoid, who presented with intermittent abdominal pain and small bowel obstruction. He underwent a 40 cm distal ileal resection, demonstrating a 1.5 cm carcinoid tumor (pT3, invading into subserosal tissue), with regional nodal metastases (2 of 21). After 6 mo of available follow up, there is currently no evidence of metastatic or residual disease. This case illustrates the evaluation of a primary tumor in an underdistended small bowel segment in the setting of small bowel obstruction caused by the mass. Depiction of locoregional metastatic disease. A: Axial arterial phase CTA image shows a small focal area of asymmetric wall thickening in an underdistended small bowel loop (arrowhead), representative of the primary tumor. There is directly adjacent metastatic adenopathy with small calcifications (blue arrowhead). Note that these findings are rather subtle on the axial images. Multiple proximal small bowel loops with fluid levels are compatible with partial small bowel obstruction (arrow). The presence of SBO limits the ability of oral contrast to aid in adequate distention of the pathological small bowel segment; B: Coronal arterial phase image better demonstrates asymmetric wall thickening (arrowhead) and extramural mesenteric extension of tumor with calcifications (blue arrowhead). Multiple dilated proximal small bowel loops are compatible with partial small bowel obstruction (arrow); C: Thin slice reconstructions (0.75 mm) of the venous phase data allow better evaluation of the small bowel mass (arrowhead) and the adjacent calcified mesenteric mass (blue arrowhead); D, E: Coronal thin (D) and thick (E) slab MIP images of the venous phase data demonstrate the small bowel mass (arrowheads) and the adjacent metastatic calcified adenopathy (blue arrowheads) to better advantage; F, G: Coronal VRT (F) and MIP (G) of the CTA data demonstrate the mass (arrowheads) and associated calcified nodal masses (blue arrowheads) in relation to the mesenteric vessels. VRT: Volume rendered technique; MIP: Maximum intensity projections; CTA: Computed tomography angiography. SBO: Small bowel obstruction.

Challenging cases highlighting opportunities and pitfalls in imaging small bowel carcinoid tumors

Characteristic imaging findings of small bowel carcinoid tumors are shown in 14 challenging cases. Cases are ordered in four groups, beginning with duodenal carcinoid and periampullary carcinoid (Figures 2-5), followed by ileal and jejunal carcinoid (Figures 6-10). An example of metastatic carcinoid of unknown primary is shown in Figure 11. Finally, the imaging appearance of recurrent and previously treated small bowel carcinoid tumors is shown (Figures 12-14). Primary tumors may be solitary or multifocal, occur predominantly in the distal ileum and may show evidence of ulceration, in the latter case associated with the classic target sign

on fluoroscopic enteroclysis. If a solitary small bowel mass is found on imaging, the classical differential diagnosis includes small-bowel carcinoid, primary bowel adenocarcinoma, lymphoma, gastrointestinal stromal tumor and mesenchymal neoplasm (*e.g.*, small bowel sarcoma), and non-neoplastic inflammatory bowel disease such as Crohn's disease, which has a propensity to involve the small bowel in the form of skip lesions. Primary carcinoid tumors are classically not well identified on standard venous phase thick section CT and their confident detection is aided by state of the art imaging with volumetric CTA with CT enterography or enteroclysis. Mural thickening is often the earliest, however also an unspecific manifestation

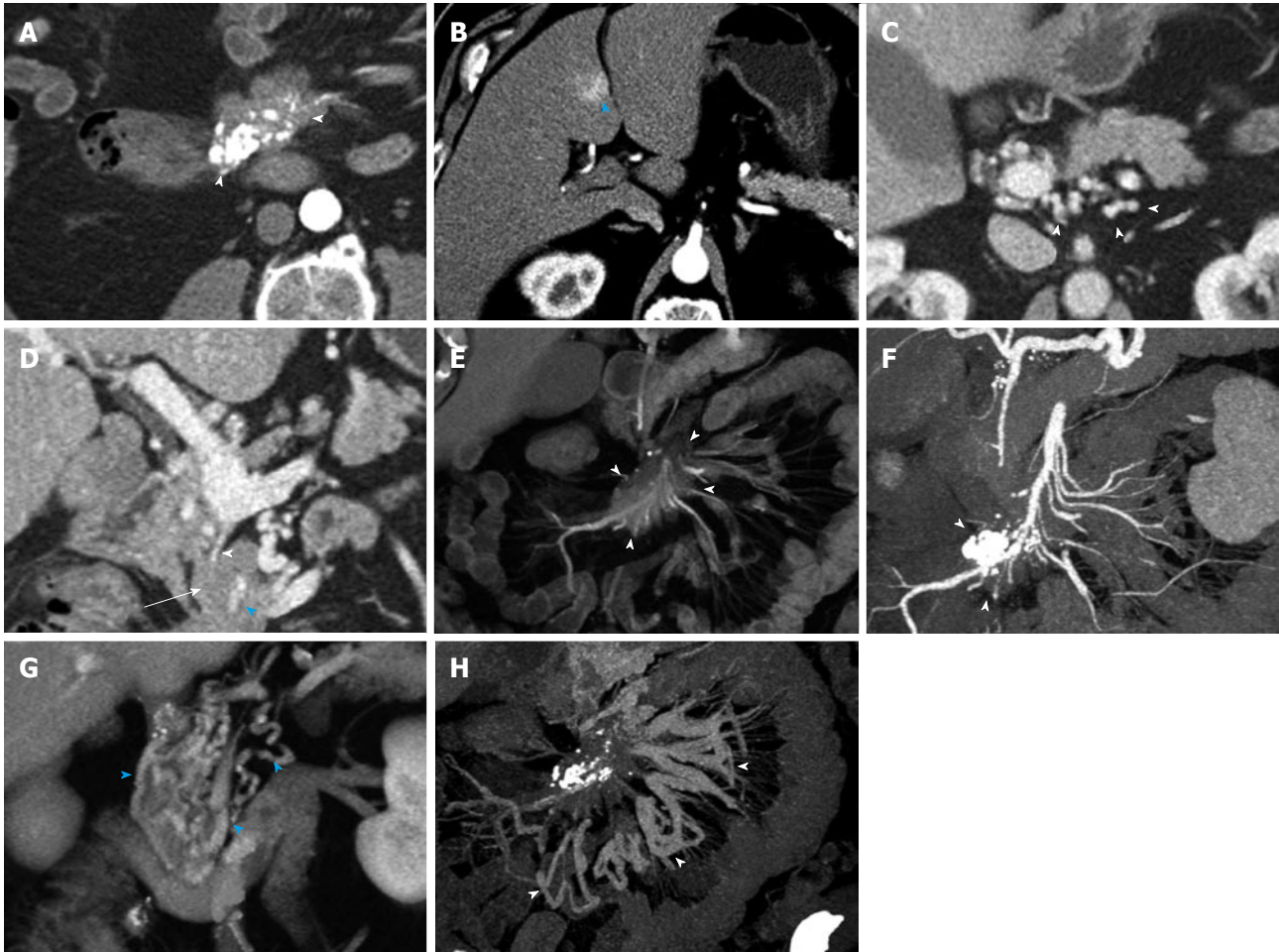


Figure 9 Metastatic small bowel carcinoid. A 66-year-old male with metastatic small bowel carcinoid. The tumor was found unresectable with large mesenteric nodal metastatic disease encasing SMA and SMV, and with liver metastases. In this case the primary tumor location is unknown (and possibly very small), in the presence of bulky regional metastatic disease and liver metastatic disease. It also demonstrates the evaluation of vascular complications (SMV occlusion, encasement of SMV and SMA) using 3D imaging. It is not unusual that the primary tumor is much smaller than the nodal metastatic disease. A: Arterial phase axial image demonstrates a large mesenteric mass with surrounding desmoplastic reaction (arrowheads), compatible with regional nodal metastatic disease from carcinoid tumor. The primary tumor was not identified on the exam; B: Arterial phase axial image demonstrates a hypervascular metastasis in segment IV B of the liver; C: Axial venous phase image shows extensive peripancreatic collateral vessels (arrowheads) as a result of SMV occlusion by tumor encasement; D: Encasement of the SMV (arrowhead) and SMA (blue arrowhead) by the tumor. The distal SMV is severely narrowed (arrowhead), while the more proximal SMV is completely occluded by the tumor (arrow); E: Coronal VRT arterial phase image demonstrates the large mesenteric mass (arrowheads), which encases the SMA and its branches; F: Coronal thick slab MIP arterial phase image demonstrates the calcified mesenteric mass (arrowheads), encasing SMA branches; G: Coronal VRT venous phase image shows multiple peripancreatic collateral vessels (blue arrowheads) to better advantage than axial or multiplanar imaging; H: Coronal thick slab venous phase MIP image shows moderately dilated mesenteric veins (arrowheads) resulting from SMV occlusion. VRT: Volume rendered technique; MIP: Maximum intensity projections; SMA: Superior mesenteric artery; SMV: Superior mesenteric vein.

of small bowel carcinoid tumors^[10,20,34]. Primary tumors are not uncommonly small, often less than 2 cm. Characteristically, the primary tumor may be notably smaller than the mesenteric and nodal disease (Figure 4B). Especially if the primary tumor is not notably hypervascular, it can be very inconspicuous in underdistended bowel segments^[34,35]. While good bowel distention can be achieved by proper bowel preparation in otherwise healthy patients with small non-obstructing tumors, if small bowel obstruction is present, an evaluation for the location and size of the primary tumor in the presence of underdistended small bowel can often not be avoided (Figure 8). Focal bowel wall thickening can provide a clue that leads to further evaluation of a specific area. A characteristic appearance of a submucosal mass with extramural extension

and mesenteric disease in underdistended bowel in the setting of bowel obstruction is shown in Figure 6. Not uncommonly, the primary tumor site is located in proximity to the lead point of the bowel obstruction. Even with high resolution submillimeter isotropic CT enterography or enteroclysis, primary tumors less than 10 mm in size can be missed in 14% of patients even with excellent technique and patient preparation^[20]. While initial reports using CT protocols without specific bowel preparation were able to detect less than half of the primary tumors seen at surgery^[34], CT enteroclysis has recently shown a high sensitivity (up to 93%) in the detection of small bowel tumors^[35-38]. Small primary tumors may present as a well-defined polypoid mass in mucosal or submucosal location, often with associated hyperenhancement (Figures 2, 3A, 5 and

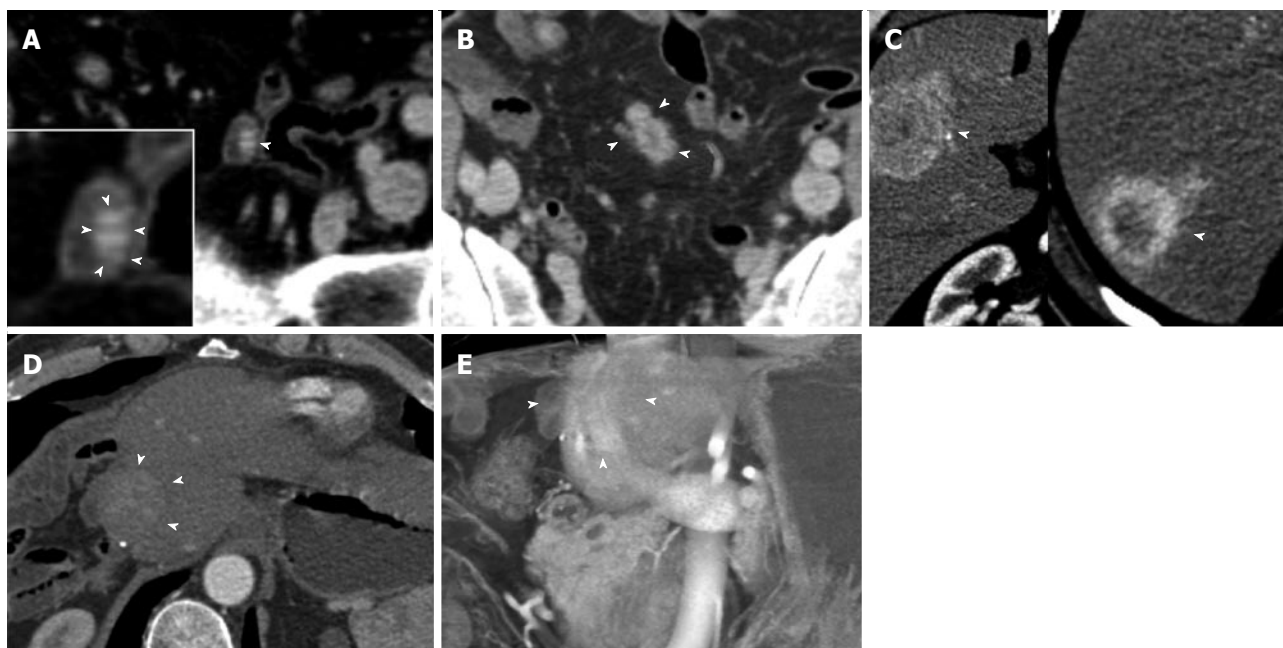


Figure 10 Metastatic terminal ileal carcinoid. Terminal ileal small bowel carcinoid tumor with liver metastases. A 57-year-old male with longstanding history of flushing, diarrhea and sweating. Three hypervascular hepatic metastases were found during a computed tomography (CT) evaluation performed after he presented with a diverticular perforation to an outside institution. A Hartmann procedure was performed. After diagnosis, he underwent an extended right hemihepatectomy. An ileal resection proved a terminal ileal 1.5 cm primary carcinoid tumor. Four years later, he presented with a recurrence at the liver resection margin. This case illustrates the imaging appearance of the primary tumor as a hypervascular mural mass and extensive locoregional nodal metastatic and liver metastatic disease despite a small (1.5 cm) primary tumor. A: Axial venous phase CECT demonstrates a small bowel loop (terminal ileum) with a small hyperenhancing mural mass (arrowhead). A detail view better demonstrates the mass (inset, arrowheads), which represents the primary tumor and was confirmed at surgery. The primary tumor is subtle and easily missed on the axial CT slices; B: Axial venous phases CECT image slightly superiorly demonstrates matted hypervascular mesenteric lymph node metastases with minimal surrounding desmoplastic reaction (arrowheads), typical for carcinoid tumor local metastases; C: Axial arterial phase images demonstrate segment VIII/V (left) and segment VII (right) hypervascular, centrally necrotic liver metastases (arrowheads). Note that this advanced disease is associated with the small (1.5 cm) primary tumor. It is not uncommon that metastatic disease is significantly larger than the primary carcinoid tumor; D, E: Follow-up exam 4 years after extended right hepatectomy shows recurrence at the resection margin (arrowheads), shown on the axial venous phase image (D) and a coronal volume rendered technique image (E). CETC: Contrast enhanced computed tomography.

10A). A duodenal carcinoid tumor may be imaged as a periampullary mass with biliary and pancreatic ductal obstruction (Figure 3). Not always is the primary tumor found on initial imaging or initial surgery. In these cases the patient may undergo resection of limited metastatic disease. On imaging follow-up, evaluation should focus not only on the detection of recurrent or progressive metastatic disease, but also observe the first imaging manifestation of a previously occult primary small bowel carcinoid tumor (Figure 5).

Once extramural extension occurs, the segmental morphology of the bowel may be altered. A hairpin turn morphology (a fixed narrow turn or kink of the bowel) or angulation reflects underlying bowel infiltration and fibrosis, which may itself be subtle on imaging. Transmural tumor extension may manifest itself as concentric wall thickening, or as a focal soft-tissue mass transgressing the bowel wall (Figure 6C)^[39]. Small bowel carcinoids may also exhibit primarily a diffuse infiltrative growth pattern, in which case only bowel wall thickening and desmoplastic reaction may be observable. The tumor itself typically shows associated contrast enhancement, while the surrounding desmoplastic reaction will appear as a slowly enhancing spiculated mass (Figures 7A and 11). Carcinoid tumors have a propensity to encase and occlude large, medium

and small vessels, related to fibrosis and their secretion of vasoactive substances, with the possible result of an interruption of blood supply to the bowel and subsequent bowel ischemia^[40]. The typical imaging appearance of arterial encasement, arterial narrowing and arterial caliber irregularities is shown in Figures 9 and 12. An example of venous encasement leading to occlusion of the superior mesenteric vein with the formation of peripancreatic collateral vessels and engorgement of the mesenteric vein arcades is depicted in Figure 9. The surrounding bowel is not uncommonly thickened (with preserved wall enhancement) as a result of chronic venous and lymphatic obstruction secondary to the mesenteric mass. In addition to small bowel obstruction which often accompanies small bowel ischemia, the additional lack of contrast enhancement of the affected bowel segments combined with edematous bowel wall thickening will make detection of the primary tumor more difficult (Figure 7). Frank acute bowel ischemia is relatively uncommon due to the relatively slow involvement by the tumor of the adjacent vasculature, but ischemia should be suspected if bowel wall thickening is found in combination with lack of enhancement or hypoenhancement of the bowel wall.

As the primary tumor may be difficult to detect and may remain occult even on repeat imaging, the



Figure 11 Carcinoid of unknown primary. Functional carcinoid tumor of unknown primary, metastatic to liver and mesenteric root. A 43-year-old female with history of postprandial nausea. Ultrasound exam detected bilobar liver metastases. Subsequent computed tomography (CT) demonstrated hypervascularity of the liver metastases. Liver biopsy confirmed carcinoid metastases. She underwent systemic chemotherapy with VP-16 and carboplatin and locoregional therapy to the liver metastases (Yttrium-90 microsphere embolization). This case illustrates the evaluation of and appearance of locoregional nodal metastatic and liver metastatic disease. A: Axial arterial phase CT shows multiple hypervascular liver metastases with treatment changes after chemoembolization (arrowheads) and diffuse perfusion change in the left liver lobe related to prior locoregional therapy; B: Axial arterial phase CT image shows a hypervascular mesenteric mass (arrowhead) compatible with metastatic nodal disease; C: Coronal thick slab MIP image demonstrates the hypervascular mesenteric mass (arrow) and its relationship to the SMA and portal vein (arrowhead); D: Coronal VRT image demonstrates hypervascular liver metastasis (arrowhead) and mesenteric mass (arrow). The extensive desmoplastic reaction surrounding the mesenteric mass is well shown. VRT: Volume rendered technique; MIP: Maximum intensity projections; SMA: Superior mesenteric artery.

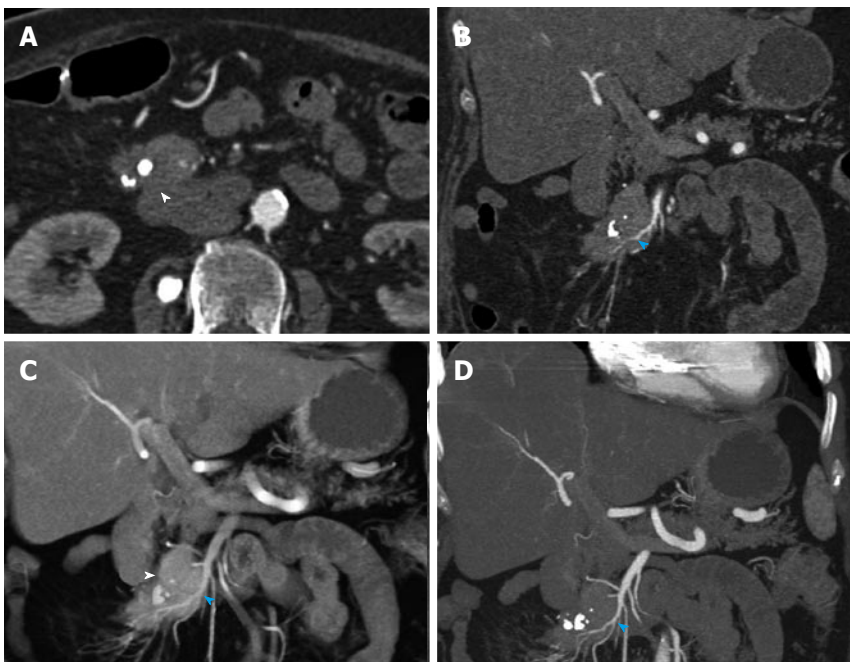


Figure 12 Recurrent metastatic small bowel carcinoid. A 72-year-old female with metastatic small bowel carcinoid. She underwent right hemicolectomy and partial small bowel resection 10 years ago, and is currently on long-acting octreotide. This case illustrates the imaging appearance and evaluation of mesenteric locoregional nodal metastatic disease recurrence with 3D imaging. A: Axial arterial phase imaging shows a calcified mass in the mesentery (arrowhead) compatible with recurrent metastatic carcinoid tumor; B: Coronal CTA image shows encasement of branches of superior mesenteric artery (blue arrowhead), with associated luminal irregularities and narrowing of the artery; C: Coronal VRT image depicts the calcified mass (arrowhead) and allows analysis of the morphology of the SMA branches within and distal to the tumor. Encased SMA branches demonstrate luminal narrowing and irregularity (blue arrowhead); D: Thick slab coronal MIP is of high diagnostic value in this case, as it benefits from the excellent contrast between vascular lumen and tumor tissue, probably providing the best assessment of the morphology of the encased SMA branches (blue arrowhead). VRT: Volume rendered technique; MIP: Maximum intensity projections; SMA: Superior mesenteric artery.



Figure 13 Recurrent metastatic small bowel carcinoid. 52-year-old male with metastatic small bowel carcinoid. He presented for follow-up one year after small bowel resection for carcinoid tumor. This case illustrates the imaging appearance of recurrent locoregional nodal metastatic disease. Axial arterial phase axial images show a small mass in the small bowel mesentery (arrowhead) with surrounding mild desmoplastic reaction, compatible with recurrence of metastatic carcinoid tumor. A surgical small bowel anastomosis is noted (blue arrowhead).

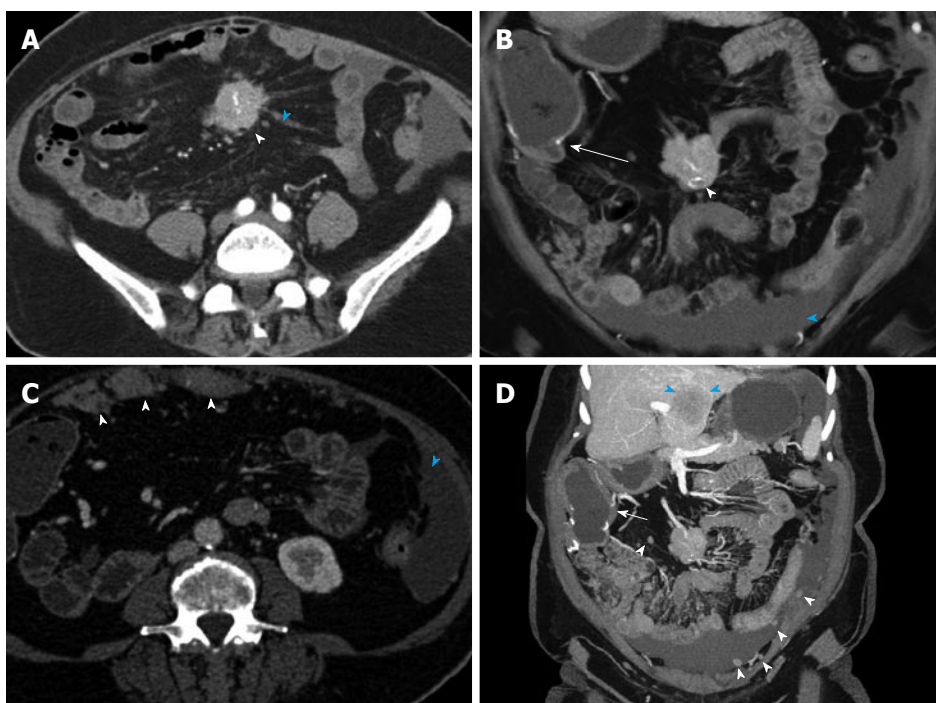


Figure 14 Recurrent metastatic small bowel carcinoid. 71-year-old female with metastatic small bowel carcinoid. Twelve years ago she had undergone a segmental distal ileal resection and liver segmental resection for metastatic carcinoid. This case illustrates advanced recurrent metastatic carcinoid with extensive abdominal and pelvic peritoneal implants and hepatic metastatic disease. A: Axial arterial phase axial image shows a calcified mass in the small bowel mesentery (arrowhead) with surrounding linear desmoplastic reaction (blue arrowhead), compatible with carcinoid tumor metastasis; B: Coronal arterial phase VRT image shows the calcified mesenteric mass (arrowhead). The patient is status post terminal ileal and proximal colonic resection with ileocolic anastomosis (arrow). Moderate ascites is present (blue arrowhead); C: Axial arterial phase axial image shows multiple metastatic omental implants (arrowheads). Ascites is present (open arrowhead); D: Many additional omental implants are noted (arrowheads) on this coronal thick slab MIP image. Ileocolic anastomosis and colonic thickening (arrow) in the setting of ascites are noted. Large segment IVB liver metastasis (blue arrowheads). VRT: Volume rendered technique; MIP: Maximum intensity projections.

diagnosis of small bowel carcinoids is not uncommonly made on the basis of secondary tumor manifestations. The main secondary manifestations of locoregional tumor spread include locoregional and mesenteric disease, and distant metastases. Duodenal carcinoid tumor metastases may cause peripancreatic (Figure 5) or portocaval metastatic adenopathy (Figure 4). Mesenteric disease characteristically leads to desmoplastic reaction surrounding the metastatic lesions, appearing as mesenteric retraction, spiculation

and tethering of adjacent bowel loops (Figures 9 and 12). The desmoplastic reaction in itself reflects fibrosis, but may also contain diffuse infiltration by tumor cells. Usually centrally embedded in the desmoplastic reaction lies matted carcinoid-related mesenteric nodal metastatic disease, which can be calcified in up to 70% of cases, and not uncommonly demonstrates avid contrast enhancement^[41-44]. The identification of a stellate configuration of radiating strands of fibrosis in the mesentery surrounding an enhancing calcified

mesenteric mass that itself is detached from the bowel wall is nearly pathognomonic for locoregionally metastatic carcinoid tumor (Figure 7)^[41,45]. The main alternative differential considerations of treated lymphoma and retractile or sclerosing mesenteritis can usually be differentiated by clinical history, additional imaging findings and laboratory testing. The location can also be very helpful in such cases, as mesenteric carcinoid in most cases is located in the right lower quadrant ileal mesentery, while calcified retractile mesenteritis is most often located in the jejunal mesentery in the left upper quadrant. Rarely, carcinoid metastases may cause diffuse mesenteric and peritoneal disease with miliary peritoneal implants, omental or mesenteric caking, or large mesenteric masses (Figure 14). Distant metastatic disease occurs most frequently to the liver, where liver metastases characteristically appear hypervascular (Figures 9 and 11), and are well depicted in the arterial phase, although larger liver metastases may exhibit central hypoenhancement due to necrosis (Figure 10C).

After surgical resection, common sites of disease recurrence include locoregional and nodal disease recurrence, *e.g.*, in the form of a mesenteric mass (Figure 13), demarcation of a previously occult primary carcinoid (Figure 5), recurrence at the hepatic resection margin after surgical partial hepatectomy for distant metastatic disease (Figure 10D and E), and omental and peritoneal dissemination (Figure 14).

CONCLUSION

3D CT and CTA of small bowel carcinoid tumors with CT enterography provides many opportunities in the early detection of small bowel carcinoids. The most important factors for the optimal detection of the often small hypervascular primary tumor are the use of a negative endoluminal contrast agent with good distention of the small bowel, and the utilization of an optimal multi-detector computed tomography (MDCT) scan protocol at submillimeter resolution with the acquisition of good CTA and venous phase data^[35,42]. Optimal bowel distention is necessary to detect submucosal masses and determine the endoluminal morphology of the small bowel, while a good CTA acquisition and high-resolution data allow the detection of hyperenhancement even of very small lesions. Extraluminal disease, such as the extent of bowel wall invasion, desmoplastic reaction and local and distal metastatic disease, together with their effects on the arterial and venous supply can be evaluated with a high degree of confidence by reviewing the high resolution multiphase MDCT data with the utilization of MIP, MPR, VRT and surface shading techniques. Spatial resolution is the main determinant of small lesion detection, accompanied by scan speed which helps to reduce motion artifacts that may otherwise blur small lesions. Faster scanners and higher spatial resolution are therefore expected to detect smaller lesions in the

future, helped by a further increase in the quality of the resulting 3D techniques. The higher speed of acquisition and higher isotropic spatial coverage of modern MDCT are also advantages over current magnetic resonance imaging techniques such as MR enterography and diffusion-weighted imaging^[46]. The arterial phase highlights the typical hypervascularity of the primary tumor, nodal metastatic disease and liver and peritoneal metastases. The patients discussed above were examined with a CT enterography technique that does not require the placement of a duodenal catheter as typically used for CT enteroclysis. CT enterography has the advantage of higher patient comfort during the study and during the fluoroscopically guided catheter placement, while the enterographic technique provides high quality imaging of the small bowel mucosal surface compared to standard abdominal CT protocols. While overall better bowel distention may be achieved by enterodysis^[15,47], in our experience, the CT enterography protocol achieves good bowel distention in most patients. As shown in the cases, patients may present emergently with bowel obstruction or ischemia, leading to an unavoidably limited luminal evaluation. While small tumors can remain a diagnostic challenge, if all the above criteria are met, CT can have high accuracy in the diagnosis of carcinoid tumors.

REFERENCES

- 1 **Bader TR**, Semelka RC, Chiu VC, Armao DM, Woosley JT. MRI of carcinoid tumors: spectrum of appearances in the gastrointestinal tract and liver. *J Magn Reson Imaging* 2001; **14**: 261-269 [PMID: 11536403 DOI: 10.1002/jmri.1182]
- 2 **Modlin IM**, Lye KD, Kidd M. A 5-decade analysis of 13,715 carcinoid tumors. *Cancer* 2003; **97**: 934-959 [PMID: 12569593 DOI: 10.1002/cncr.11105]
- 3 **Levy AD**, Sobin LH. From the archives of the AFIP: Gastrointestinal carcinoids: imaging features with clinicopathologic comparison. *Radiographics* 2007; **27**: 237-257 [PMID: 17235010 DOI: 10.1148/rg.271065169]
- 4 **Modlin IM**, Oberg K, Chung DC, Jensen RT, de Herder WW, Thakker RV, Caplin M, Delle Fave G, Kaltsas GA, Krenning EP, Moss SF, Nilsson O, Rindi G, Salazar R, Ruzsiewicz P, Sundin A. Gastroenteropancreatic neuroendocrine tumours. *Lancet Oncol* 2008; **9**: 61-72 [PMID: 18177818 DOI: 10.1016/S1470-2045(07)70410-2]
- 5 **Pinchot SN**, Holen K, Sippel RS, Chen H. Carcinoid tumors. *Oncologist* 2008; **13**: 1255-1269 [PMID: 19091780 DOI: 10.1634/theoncologist.2008-0207]
- 6 **Moran CA**, Suster S. Neuroendocrine carcinomas (carcinoid, atypical carcinoid, small cell carcinoma, and large cell neuroendocrine carcinoma): current concepts. *Hematol Oncol Clin North Am* 2007; **21**: 395-407; vii [PMID: 17548031 DOI: 10.1016/j.hoc.2007.04.011]
- 7 **Wallace S**, Ajani JA, Charnsangavej C, DuBrow R, Yang DJ, Chuang VP, Carrasco CH, Dodd GD. Carcinoid tumors: imaging procedures and interventional radiology. *World J Surg* 1996; **20**: 147-156 [PMID: 8661810 DOI: 10.1007/s002689900023]
- 8 **Crocetti E**, Paci E. Malignant carcinoids in the USA, SEER 1992-1999. An epidemiological study with 6830 cases. *Eur J Cancer Prev* 2003; **12**: 191-194 [PMID: 12771556 DOI: 10.1097/01.cej.0000072851.07402.96]
- 9 **Gore RM**, Mehta UK, Berlin JW, Rao V, Newmark GM. Diagnosis and staging of small bowel tumours. *Cancer Imaging* 2006; **6**: 209-212 [PMID: 17208678 DOI: 10.1102/1470-7330.2006.0031]

- 10 **Buck JL**, Sobin LH. Carcinoids of the gastrointestinal tract. *Radiographics* 1990; **10**: 1081-1095 [PMID: 2259762 DOI: 10.1148/radiographics.10.6.2259762]
- 11 **Frilling A**, Akerström G, Falconi M, Pavel M, Ramos J, Kidd M, Modlin IM. Neuroendocrine tumor disease: an evolving landscape. *Endocr Relat Cancer* 2012; **19**: R163-R185 [PMID: 22645227 DOI: 10.1530/ERC-12-0024]
- 12 **Modlin IM**, Kidd M, Latich I, Zikusoka MN, Shapiro MD. Current status of gastrointestinal carcinoids. *Gastroenterology* 2005; **128**: 1717-1751 [PMID: 15887161 DOI: 10.1053/j.gastro.2005.03.038]
- 13 **Klöppel G**, Anlauf M. Epidemiology, tumour biology and histopathological classification of neuroendocrine tumours of the gastrointestinal tract. *Best Pract Res Clin Gastroenterol* 2005; **19**: 507-517 [PMID: 16183524 DOI: 10.1016/j.bpg.2005.02.010]
- 14 **Mocellin S**, Nitti D. Gastrointestinal carcinoid: epidemiological and survival evidence from a large population-based study (n = 25 531). *Ann Oncol* 2013; **24**: 3040-3044 [PMID: 24050954 DOI: 10.1093/annonc/mdt377]
- 15 **Kamaoui I**, De-Luca V, Ficarelli S, Mennesson N, Lombard-Bohas C, Pilleul F. Value of CT enteroclysis in suspected small-bowel carcinoid tumors. *AJR Am J Roentgenol* 2010; **194**: 629-633 [PMID: 20173138 DOI: 10.2214/AJR.09.2760]
- 16 **Verma D**, Strohlein JR. Adenocarcinoma of the small bowel: a 60-yr perspective derived from M. D. Anderson Cancer Center Tumor Registry. *Am J Gastroenterol* 2006; **101**: 1647-1654 [PMID: 16863573 DOI: 10.1111/j.1572-0241.2006.00625.x]
- 17 **Dierdorf SF**. Carcinoid tumor and carcinoid syndrome. *Curr Opin Anaesthesiol* 2003; **16**: 343-347 [PMID: 17021482 DOI: 10.1097/0001503-200306000-00017]
- 18 **Thomas AM**, Beumer JD, Suppiah A, Devitt PG.. Unusual cause of gastrointestinal bleeding: multiple small bowel carcinoid tumours. *ANZ J Surg* 2014; Epub ahead of print [PMID: 25251986 DOI: 10.1111/ans.12853]
- 19 **Caracappa D**, Gullà N, Lombardo F, Burini G, Castellani E, Boselli C, Gemini A, Burattini MF, Covarelli P, Noya G. Incidental finding of carcinoid tumor on Meckel's diverticulum: case report and literature review, should prophylactic resection be recommended? *World J Surg Oncol* 2014; **12**: 144 [PMID: 24884768 DOI: 10.1186/1477-7819-12-144]
- 20 **Datta S**, Williams N, Suortamo S, Mahmood A, Oliver C, Hedley N, Ray P. Carcinoid syndrome from small bowel endocrine carcinoma in the absence of hepatic metastasis. *Age Ageing* 2011; **40**: 760-762 [PMID: 21903639 DOI: 10.1093/ageing/afr122]
- 21 **Klöppel G**, Perren A, Heitz PU. The gastroenteropancreatic neuroendocrine cell system and its tumors: the WHO classification. *Ann N Y Acad Sci* 2004; **1014**: 13-27 [PMID: 15153416 DOI: 10.1196/annals.1294.002]
- 22 **Burke AP**, Thomas RM, Elsayed AM, Sobin LH. Carcinoids of the jejunum and ileum: an immunohistochemical and clinicopathologic study of 167 cases. *Cancer* 1997; **79**: 1086-1093 [PMID: 9070484 DOI: 10.1002/(SICI)1097-0142(19970315)79]
- 23 **Eller R**, Frazee R, Roberts J. Gastrointestinal carcinoid tumors. *Am Surg* 1991; **57**: 434-437 [PMID: 2058850]
- 24 **Strodel WE**, Talpos G, Eckhauser F, Thompson N. Surgical therapy for small-bowel carcinoid tumors. *Arch Surg* 1983; **118**: 391-397 [PMID: 6830429 DOI: 10.1001/archsurg.1983.01390040003001]
- 25 **Thompson GB**, van Heerden JA, Martin JK, Schutt AJ, Ilstrup DM, Carney JA. Carcinoid tumors of the gastrointestinal tract: presentation, management, and prognosis. *Surgery* 1985; **98**: 1054-1063 [PMID: 4071383]
- 26 **Toumpanakis C**, Caplin ME. Update on the role of somatostatin analogs for the treatment of patients with gastroenteropancreatic neuroendocrine tumors. *Semin Oncol* 2013; **40**: 56-68 [PMID: 23391113 DOI: 10.1053/j.seminoncol.2012.11.006]
- 27 **Godwin JD**. Carcinoid tumors. An analysis of 2,837 cases. *Cancer* 1975; **36**: 560-569 [PMID: 1157019 DOI: 10.1002/1097-0142(197508)36]
- 28 **Addiss DG**, Shaffer N, Fowler BS, Tauxe RV. The epidemiology of appendicitis and appendectomy in the United States. *Am J Epidemiol* 1990; **132**: 910-925 [PMID: 2239906]
- 29 **Hemminki K**, Li X. Incidence trends and risk factors of carcinoid tumors: a nationwide epidemiologic study from Sweden. *Cancer* 2001; **92**: 2204-2210 [PMID: 11596039]
- 30 **Ellis L**, Shale MJ, Coleman MP. Carcinoid tumors of the gastrointestinal tract: trends in incidence in England since 1971. *Am J Gastroenterol* 2010; **105**: 2563-2569 [PMID: 20823835 DOI: 10.1038/ajg.2010.341]
- 31 **Yao JC**, Hassan M, Phan A, Dagohoy C, Leary C, Mares JE, Abdalla EK, Fleming JB, Vauthey JN, Rashid A, Evans DB. One hundred years after "carcinoid": epidemiology of and prognostic factors for neuroendocrine tumors in 35,825 cases in the United States. *J Clin Oncol* 2008; **26**: 3063-3072 [PMID: 18565894 DOI: 10.1200/JCO.2007.15.4377]
- 32 **Fitzgerald TL**, Dennis SO, Kachare SD, Vohra NA, Zervos EE. Increasing incidence of duodenal neuroendocrine tumors: Incidental discovery of indolent disease? *Surgery* 2015; **158**: 466-471 [PMID: 26013986 DOI: 10.1016/j.surg.2015.03.042]
- 33 **Hodgson N**, Koniaris LG, Livingstone AS, Franceschi D. Gastric carcinoids: a temporal increase with proton pump introduction. *Surg Endosc* 2005; **19**: 1610-1612 [PMID: 16211437 DOI: 10.1007/s00464-005-0232-4]
- 34 **Picus D**, Glazer HS, Levitt RG, Husband JE. Computed tomography of abdominal carcinoid tumors. *AJR Am J Roentgenol* 1984; **143**: 581-584 [PMID: 6331739 DOI: 10.2214/ajr.143.3.581]
- 35 **Soyer P**, Boudiaf M, Fishman EK, Hoeffel C, Dray X, Manfredi R, Marteau P. Imaging of malignant neoplasms of the mesenteric small bowel: new trends and perspectives. *Crit Rev Oncol Hematol* 2011; **80**: 10-30 [PMID: 21035353 DOI: 10.1016/j.critrevonc.2010.09.010]
- 36 **Soyer P**, Aout M, Hoeffel C, Vicaute E, Placé V, Boudiaf M. Helical CT-enteroclysis in the detection of small-bowel tumours: a meta-analysis. *Eur Radiol* 2013; **23**: 388-399 [PMID: 22865269 DOI: 10.1007/s00330-012-2595-y]
- 37 **Maglente DD**, Sandrasegaran K, Lappas JC, Chiorean M. CT Enteroclysis. *Radiology* 2007; **245**: 661-671 [PMID: 18024448 DOI: 10.1148/radiol.2453060798]
- 38 **Soyer P**. Obscure gastrointestinal bleeding: difficulties in comparing CT enterography and video capsule endoscopy. *Eur Radiol* 2012; **22**: 1167-1171 [PMID: 22447355 DOI: 10.1007/s00330-012-2398-1]
- 39 **Scarsbrook AF**, Ganeshan A, Statham J, Thakker RV, Weaver A, Talbot D, Boardman P, Bradley KM, Gleeson FV, Phillips RR. Anatomic and functional imaging of metastatic carcinoid tumors. *Radiographics* 2007; **27**: 455-477 [PMID: 17374863 DOI: 10.1148/rg.272065058]
- 40 **Martínez-Sapiña Llanas MJ**, Ríos Reboredo A, Romay Cousido G, Romero González JA. Severe intestinal ischemia as a presenting feature of metastatic ileal carcinoid tumor: role of MDCT with coronal reformation in the early diagnosis. *Abdom Imaging* 2012; **37**: 558-560 [PMID: 22052449 DOI: 10.1007/s00261-011-9815-9]
- 41 **Pantongrag-Brown L**, Buetow PC, Carr NJ, Lichtenstein JE, Buck JL. Calcification and fibrosis in mesenteric carcinoid tumor: CT findings and pathologic correlation. *AJR Am J Roentgenol* 1995; **164**: 387-391 [PMID: 7839976 DOI: 10.2214/ajr.164.2.7839976]
- 42 **Hristova L**, Placé V, Nemeth J, Boudiaf M, Laurent V, Soyer P. Small bowel tumors: spectrum of findings on 64-section CT enteroclysis with pathologic correlation. *Clin Imaging* 2012; **36**: 104-112 [PMID: 22370131 DOI: 10.1016/j.clinimag.2011.08.011]
- 43 **Pelage JP**, Soyer P, Boudiaf M, Brocheriou-Spelle I, Dufresne AC, Coumbaras J, Rymer R. Carcinoid tumors of the abdomen: CT features. *Abdom Imaging* 1999; **24**: 240-245 [PMID: 10227886]
- 44 **Hoeffel C**, Crema MD, Belkacem A, Azizi L, Lewin M, Arrivé L, Tubiana JM. Multi-detector row CT: spectrum of diseases involving the ileocecal area. *Radiographics* ; **26**: 1373-1390 [PMID: 16973770 DOI: 10.1148/rg.265045191]
- 45 **Sheth S**, Horton KM, Garland MR, Fishman EK. Mesenteric neoplasms: CT appearances of primary and secondary tumors and differential diagnosis. *Radiographics* 2006; **23**: 457-473; quiz 535-536 [PMID: 12640160 DOI: 10.1148/rg.232025081]
- 46 **Horton KM**, Kamel I, Hofmann L, Fishman EK. Carcinoid tumors of the small bowel: a multitechnique imaging approach. *AJR Am J*

Roentgenol 2004; **182**: 559-567 [PMID: 14975946 DOI: 10.2214/ajr.182.3.1820559]

47 **Soyer P**, Dohan A, Eveno C, Dray X, Hamzi L, Hoeffel C, Kaci R,

Boudiaf M. Carcinoid tumors of the small-bowel: evaluation with 64-section CT-enteroclysis. *Eur J Radiol* 2013; **82**: 943-950 [PMID: 23480964 DOI: 10.1016/j.ejrad.2013.02.013]

P- Reviewer: Faintuch S, Juergens KU, Srivastava M

S- Editor: Tian YL **L- Editor:** A **E- Editor:** Wu HL



Ankylosing spondylitis: A state of the art factual backbone

Mohammad Ghasemi-rad, Hosam Attaya, Emal Lesha, Andrea Vegh, Tooraj Maleki-Miandoab, Emad Nosair, Nariman Sepehrvand, Ali Davarian, Hamid Rajebi, Abdolghader Pakniat, Seyed Amirhossein Fazeli, Afshin Mohammadi

Mohammad Ghasemi-rad, Hosam Attaya, Division of Interventional Radiology, Massachusetts General Hospital, Harvard Medical School, Boston, MA 02114, United States

Mohammad Ghasemi-rad, Emal Lesha, Andrea Vegh, Harvard-MIT Division of Health Sciences and Technology, Massachusetts Institute of Technology, Cambridge, MA 02139, United States

Emal Lesha, College of Science and Mathematics, University of Massachusetts Boston, Boston, MA 02138, United States

Andrea Vegh, Department of Materials Science and Engineering, Faculty of Applied Science and Engineering, University of Toronto, Toronto, Ontario M5S1A4, Canada

Tooraj Maleki-Miandoab, Department of Radiology, Urmia University of Medical Sciences, Urmia 5716763111, Iran

Emad Nosair, Anatomical Sciences, Basic Medical Sciences Department, College of Medicine, Sharjah University, Sharjah 27272, The United Arab Emirates

Nariman Sepehrvand, Department of Medicine, University of Alberta, Edmonton T6G 2R3, Canada

Ali Davarian, Ischemic Disorders Research Center, Golestan University of Medical Sciences, Gorgan 49177-53715, Iran

Hamid Rajebi, Radiology Department, SUNY Upstate Medical University, Syracuse, NY 13210, United States

Abdolghader Pakniat, Department of Emergency Medicine, Arak University of Medical Science, Arak 3815934798, Iran

Seyed Amirhossein Fazeli, Department of Medicine, Zahedan University of Medical Sciences, Zahedan 981691339, Iran

Afshin Mohammadi, Solid Tumor Research Center, Imam Khomani Hospital, University of Medical Sciences, Urmia, West Azarbaijan 5716763111, Iran

Author contributions: All authors contributed to this manuscript.

Conflict-of-interest statement: All authors declare that there is no conflict of interest.

Open-Access: This article is an open-access article which was selected by an in-house editor and fully peer-reviewed by external reviewers. It is distributed in accordance with the Creative Commons Attribution Non Commercial (CC BY-NC 4.0) license, which permits others to distribute, remix, adapt, build upon this work non-commercially, and license their derivative works on different terms, provided the original work is properly cited and the use is non-commercial. See: <http://creativecommons.org/licenses/by-nc/4.0/>

Correspondence to: Afshin Mohammadi, Professor of Radiology, Solid Tumor Research Center, Imam Khomani Hospital, University of Medical Sciences, Ershad Street, Urmia, West Azarbaijan 5716763111, Iran. afshin.mohdi@gmail.com
Telephone: +98-914-3480425

Received: November 22, 2014

Peer-review started: November 22, 2014

First decision: December 26, 2014

Revised: May 12, 2015

Accepted: June 15, 2015

Article in press: June 16, 2015

Published online: September 28, 2015

Abstract

Ankylosing spondylitis (AS) is a chronic inflammatory disease that affects 1% of the general population. As one of the most severe types of spondyloarthropathy, AS affects the spinal vertebrae and sacroiliac joints, causing debilitating pain and loss of mobility. The goal of this review is to provide an overview of AS, from the pathophysiological changes that occur as the disease progresses, to genetic factors that are involved with its onset. Considering the high prevalence in the population, and the debilitating life changes that occur as a result of the disease, a strong emphasis is placed

on the diagnostic imaging methods that are used to detect this condition, as well as several treatment methods that could improve the health of individuals diagnosed with AS.

Key words: Ankylosing spondylitis; Magnetic resonance imaging; Ultrasound; Computed tomography; Treatment; Diagnosis

© **The Author(s) 2015.** Published by Baishideng Publishing Group Inc. All rights reserved.

Core tip: Considering the high prevalence of ankylosing spondylitis (AS) in the population, and the debilitating life changes that occur as a result of the disease, this article places a strong emphasis on the diagnostic imaging methods that are used to detect this condition, as well as several treatment methods that could improve the health of individuals diagnosed with AS. However, we have also tried to provide a summary of current knowledge on AS in this manuscript, which can be used as a handbook for physicians handling patients with this condition.

Ghasemi-rad M, Attaya H, Lesha E, Vegh A, Maleki-Miandoab T, Nosair E, Sepehrvand N, Davarian A, Rajebi H, Pakniat A, Fazeli SA, Mohammadi A. Ankylosing spondylitis: A state of the art factual backbone. *World J Radiol* 2015; 7(9): 236-252 Available from: URL: <http://www.wjgnet.com/1949-8470/full/v7/i9/236.htm> DOI: <http://dx.doi.org/10.4329/wjrr.v7.i9.236>

INTRODUCTION

Ankylosing spondylitis (AS) is a chronic and systemic seronegative inflammatory spondyloarthropathy, which causes destruction and fusion of the spinal vertebrae and sacroiliac joints. It has been proposed that the sites of attachment of the ligaments or tendons to the bone, called entheses, are the major target of the inflammatory, traumatic and degenerative pathological changes occurring in AS. Enthesitis is believed to play a primary role in the ligament calcification process, which results in pain. It can lead to reduced flexibility of the spine, and eventually complete loss of spinal mobility, destruction as well as ankylosis (fusion) of the spine and sacroiliac joints.

Accordingly, comprehension of the microanatomy and mechanical function of spinal ligaments and entheses is necessary in order to provide a better understanding of the operating mechanisms of AS, and propose treatment options.

The goal of this review is to provide an overview of AS, from the anatomy and pathophysiological changes that occur as the disease progresses, to genetic factors that are involved with its onset. Considering the high prevalence of AS in the population, and the debilitating life changes that occur as a result of the disease, a

strong emphasis is placed on the diagnostic imaging methods that are used to detect this condition, as well as several treatment methods that could improve the health of individuals diagnosed with AS.

ANATOMY OF THE SPINAL LIGAMENTS

The articulation mechanisms between any two vertebrae and the connecting soft tissues form what is called the motion segment. The anterior and posterior longitudinal ligaments connect the vertebral bodies. The intervertebral disc consists of an external fibrous ring, the annulus fibrosus, and a gelatinous core, the nucleus pulposus. On each side of the vertebral arch, the laminae of the upper and lower vertebrae are joined by a ligamentum flavum. There is a spinous process at the junction of the two laminae. The interspinous ligament joins the spinous processes of the upper and lower vertebrae, and the supraspinous ligament connects their tips. The zygapophyseal joints (facet joints) form between the superior articular process of the lower vertebra and the inferior articular process of the upper vertebrae^[1].

Anatomy of sacroiliac joints

The sacroiliac (SI) joint is a strong diarthrodial weight-bearing compound joint. It consists of an anterior synovial joint (between the articular surfaces of the sacrum and ilium), whose irregular interlocking surfaces are covered with articular cartilage as well as a posterior syndesmosis located between the tuberosities of these bones. The SI joint has unique characteristics not typically found in other diarthrodial joints. These characteristics include the presence of fibrocartilage in addition to hyaline cartilage, discontinuity of the posterior capsule, many ridges and depressions in the articular surfaces, and limited range of mobility compared to other synovial joints. Three main ligaments stabilize the SI joint: The thin anterior SI ligament, the thick interosseous ligament lying deep between the tuberosities of the sacrum and ilium, which is critically involved in transmitting weight from the sacrum to the iliac bones, and the posterior SI ligament, which is the external continuation of the same mass of fibrous tissue^[2,3]. Histological examination reveals rich innervation of the SI joint as well as the presence of free nerve fibers within the joint capsule and the adjoining ligaments^[4].

Structure of the entheses

There are two different types of entheses. *Fibrous entheses*, characterized by pure, dense fibrous tissue; and *fibrocartilaginous entheses*, which have a transition zone of fibrocartilage at the bony interface. Typically, four zones of tissue are present in the latter type: Pure, dense fibrous tissue, un-calcified fibrocartilage, calcified fibrocartilage and bone. The two-fibrocartilage zones are separated by a basophilic (calcification) line known as

the *tidemark*. Type I-collagen is the dominant collagen in the tendons/ligaments and bone, whereas type II-collagen is a special feature of fibrocartilage tissue, both calcified and un-calcified, as it accounts for its compression-tolerance properties^[5]. Most tendons and ligaments have fibrocartilaginous entheses. Typically in AS, enthesitis is the primary trigger of the disease, while all other joint manifestations are secondary.

Diffusion of the pathological changes in the tissues surrounding entheses, *e.g.*, fibrocartilages, bursa, fat pads and the entheses collectively constitute the concept of *entheses organ*, which helps to explain synovitis and osteitis in AS^[6,7]. Entheses are metabolically active and are nourished by blood supplies from the perichondrium and periosteum. However, normal entheses organs are avascular in their fibrocartilaginous regions, and are completely devoid of immune cells. Microdamage of the entheses appears to be associated with tissue repair responses and vessel ingrowth^[6,8].

Pathophysiology

Enthesopathy occurs in the subchondral bone area, with an erosive inflammatory infiltrate composed of lymphoplasmacytes and sometimes polymorphonuclear cells, followed by fibrous tissue proliferation leading to cartilage and then bone formation. Spinal and SI enthesitis limit the ability of the spine to move and the ability of the thoracolumbar fascia to influence the alignment of the lumbar vertebrae, thereby it increases their risk of destructive injury^[9]. This phenomenon decreases the length of the visco-elastic portion of the spinal ligaments, and affects the myxoid subchondral bone marrow. As the disease progresses, it destroys the nearby articular tissues or joint tissues. The calcification of the entheses organ is the final step before the appearance of the "bamboo spine" where original and new cartilages are replaced by bone causing fusion of the joint bones, leading to stiffness and immobility. Enthesitis is also associated with underlying osteitis. Whether mechanically induced or inflammatory-related, the extent of osteitis is determined by human leukocyte antigen-B27 gene^[10].

BONE DENSITY LOSS IN AS

Bone mineral density (BMD) loss occurs in the course of AS with high prevalence. The severity of BMD loss depends on the disease duration and the presence of syndesmophytes in the spine. A decrease in BMD can be found both in the hip as well as in the spine in both early and late stages of the disease. Dual-energy X-ray Absorption (DEXA) is the most reliable method for the measurement of BMD. Normal bone density is defined as T score ≥ -1.0 , osteopenia as $-2.5 < \text{T score} < -1.0$, and osteoporosis as T score ≤ -2.5 ^[11]. The T score corresponds to the number of standard deviations (SD) from any result of the peak bone mass. Osteoporosis of the spine (L1-L4) is much more common than that

of the hip in AS, and BMD of the spine still remains the most important site to define osteoporosis in patients with AS^[12]. Low BMD becomes clinically pertinent as it increases the risk of fracture, since these fractures are a considerable cause of morbidity and reduced quality of life^[13].

Significant local and systemic inflammatory responses may play an important role in the development of osteoporosis (defined as T scores less than -2.5 in one region in the lumbar spine or proximal femur) in clinically established AS patients. Genetic susceptibility, immobility and impaired calcium and vitamin D absorption are other possible mechanisms that facilitate the bone loss process in AS. DEXA measurements of the hip can detect continuing bone loss represented by a low BMD with better sensitivity than in the spine. Although the deleterious effects of AS are considered to be more distinguished in the spine, the Bath Ankylosing Spondylitis Disease Activity Index, an accepted indicator of disease activity, demonstrates pronounced activity in the hips rather than the spine^[14].

Increased bony sclerosis that is seen in the expected disease evolution of AS can artificially cause an augmentation of BMD in routine DEXA of the spine, despite the ongoing bone loss that is depicted in hip measurements of DEXA. Enthesitis of the vertebral margins, sclerosis of vertebral end-plates, syndesmophyte formation, interapophyseal joint and interpedicular joint ankylosis can all justify this paradoxical increased BMD of spinal involvement in AS. Studies where BMD has not increased may reflect the heterogeneity of the selected sample, since they have included AS patients in all stages of the disease, probably some of them without syndesmophytes. It has been shown that BMD measured by lateral DEXA or on Quantitative Computerized Tomography is less affected by syndesmophytes than anteroposterior lumbar DEXA in late stage AS patients^[12].

Genetics in AS

AS is a systemic disease with a strong genetic predisposition. Previous studies have indicated that several genetic factors implicate the susceptibility to AS^[15-17]. Brown *et al*^[15] in 1997 reported a disease concordance of about 12.5% and 75% in di- and monozygotic twins, respectively (18). In addition to the role of genetics in susceptibility to AS, some studies have focused on the impact of genetic predisposition on important clinical parameters, including the age of disease onset and disease activity in AS patients. Brophy *et al*^[13] found a correlation between disease severity among siblings and a parent-child concordance for ophthalmic involvement at the onset of disease in early adulthood^[18].

The major histocompatibility complex (MHC) locus on chromosome 6p and other non-MHC loci have been shown to be associated with the genetic basis of AS^[19]. In 1973, Brewerton *et al*^[20] revealed the amazingly strong association between HLA-B27 and AS. Human

leukocyte antigen (HLA) B27 is a surface antigen class-I that presents antigenic peptides to T-cells. It is encoded in the MHC^[20,21]. HLA-B27 consists of a family of more than 40 subtypes named HLA-B*2701 to HLA-B*2728. HLA-B*2702, B*2704, and B*2705 have the strongest association with AS^[22]. The overall prevalence of HLA-B27 in the general population is 8%, however, there are regional differences in prevalence. For instance, the prevalence of HLA-B27 among the general population in the United States is 6.1%, however, in New Zealand the prevalence is 9.2%^[23-25]. HLA-B27 seems to be rare in the African population, which is consistent with a low disease incidence^[26].

The prevalence of polymorphisms of the HLA-B27 gene is different around the world. B*2705 is the most prevalent variant among HLA-B27 carriers in the white British population^[27]. However, a combination of B*2704 and B*2705 is the prevalent variant in Chinese populations^[28].

To explain the association of HLA-B27 with the pathogenesis of AS two essential theories have been proposed, namely the canonical and non-canonical theories. The "arthritogenic peptide" theory is a canonical theory that suggests HLA-B27 mediated antigen presentation as the center of pathogenesis. The theory suggests that the T-cell mediated cytotoxic response to self-antigens can result in autoimmunity and inflammation^[29-33]. "Misfolded protein" and "HLA-B27 surface homodimer" hypotheses are two non-canonical theories explaining the pathogenesis through the accumulation of inappropriate HLA-B27 proteins and abnormal intracellular signaling, respectively^[34-40].

Although the association of HLA-B27 with AS is very significant, some *non-B-27 MHC* genes and *non-MHC* genes may be associated with this disease. The *HLA-B60* gene, an MHC class I gene, is associated with AS in British and Chinese populations^[41,42]. In addition, Brown *et al.*^[43] (1998) and Sims *et al.*^[19] (2007) showed that the *HLA-DRB1* gene, MHC class II, can be associated with AS. In the case of *non-MHC* genes, the *IL-1* gene complex is associated with AS^[44-47]. The *CYP2D6* gene encoding cytochrome P450 debrisoquine 4-hydroxylase may be implicated in AS pathogenesis^[48,49]. Other identified candidate non-MHC genes associating with AS are *ERAP1*, *IL23R*, *ANTXR2*, *RUNX3*, and *LTBR-TNFRSF1 A*^[50-52].

In AS, the association of radiographic severity with HLA-B27 seems to be different to those with spondyloarthritis (SpA). *Non-B27* genes such as SNP rs8092336 and SNP rs1236913 were found to be associated with HLA-B27 radiographic severity rather than HLA-B2^[53].

Diagnosis of AS

AS is the most severe subtype of spondyloarthritis, affecting up to 1% of the general population^[54,55]. Its main clinical manifestations are inflammatory back pain (IBP), inflammation in other parts of the body or the

axial skeleton, anterior uveitis, enthesitis, as well as peripheral arthritis^[54] (Figures 1 and 2).

Genetic factors play a large role in the diagnosis of AS. Although the effect of the gene is unclear, more than 90% of patients with AS carry HLA-B27^[54,55]. However, only 1 in 15 people who carry this gene are likely to develop AS; this fact brings speculations of environmental factors and stress having the ability to influence the progress of the disease^[55]. The average age of onset for patients who were HLA-B27 positive (in a study involving 1080 patients) was 24.8 years, whereas those who were HLA-B27 negative had an average onset age of 27.7 years^[56,57].

One of the main problems in diagnosing AS is the fact that there are no diagnostic criteria, making early diagnosis difficult. Due to this issue, there is a delay in diagnosis between five to ten years, leading to unnecessary diagnostic and therapeutic procedures as well as increased morbidity^[54,55]. Early diagnosis of the disease is important in order to allow for effective therapy and to improve patient outcome^[58-60].

The first standardized classification criteria were brought forth by the European Spondyloarthritis Study Group in 1991^[61]. The classification criteria for SpA were seen as the presence of inflammatory back pain (IBP) or asymmetric synovitis, along with one of the following: Positive family history of SpA or related disease, inflammatory bowel disease (IBD), psoriasis, enthesopathy, alternating pain in the buttocks, preceding infection in the urogenital or enteral tract^[54,61]. More recently, this work has been continued by the Assessment of Spondyloarthritis International Society (ASAS), who have published recommendations for clinical trials and management of AS. In 2009, the ASAS also published a statement on the classification of axial SpA, which was written with the objective of validating and refining the classification/diagnostic criteria of axial SpA^[55,56,62]. The brief criteria from this publication, which can be seen in Table 1, have a sensitivity of 82.9% and a specificity of 84.4%^[55,62].

Earlier criteria include the Rome criteria (published in 1963 and revised in 1968)^[63], and modifications made to this in New York (1984)^[64], which have been scrutinized for some shortcomings, including inability to establish early diagnosis of AS^[55,65]. The newer ASAS criteria allow for a broader spectrum of diagnostic features^[54,61].

There is some confusion between diagnostic and classification criteria for SpA. As of now, all criteria that have been developed are classification criteria, although they are sometimes used as diagnostic criteria^[54]. This can be problematic as using classification criteria to diagnose patients with possible AS leads to overshooting the probability of the diagnosis, as the pretest probability of the disease is not considered^[54]. The classification criteria are also more suited to detect later stages of the disease, rather than helping make an early diagnosis^[56].

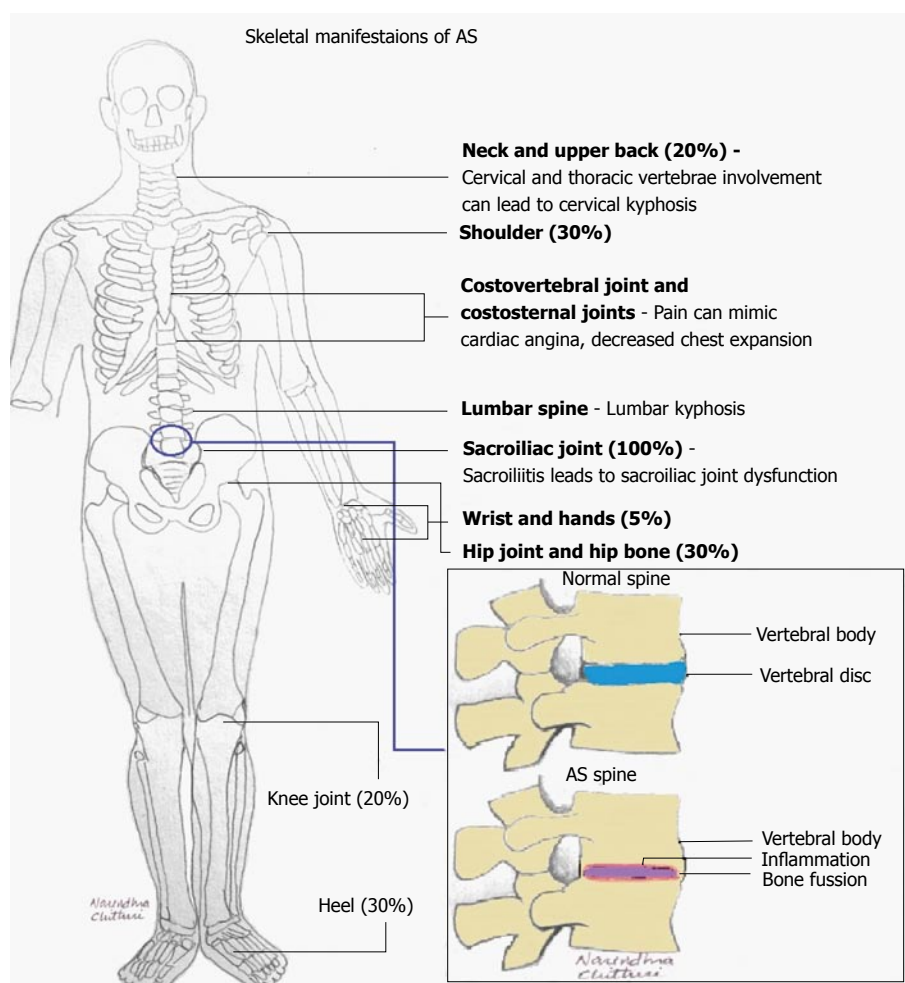


Figure 1 Schematic of skeletal manifestations of ankylosing spondylitis. AS: Ankylosing spondylitis.

Table 1 Classification criteria for axial spondyloarthritis defined by the Assessment of SpondyloArthritis International Society, to be used for patients with back pain for more than 3 mo and an onset of less than 45 years

Sacroiliitis on imaging plus one or more axial spondyloarthritis feature or
Positive test for <i>HLA-B27</i> gene plus 2 or more other axial spondyloarthritis features
Sacroiliitis on imaging
Active (acute) inflammation on magnetic resonance imaging highly suggestive of sacroiliitis associated with axial spondyloarthritis
Definite radiographic sacroiliitis according to the modified New York criteria
Axial spondyloarthritis features
Inflammatory back pain
Arthritis
Enthesitis (heel)
Uveitis
Dactylitis
Psoriasis
Crohn's disease or diagnosis of colitis
Good response to non-steroidal anti-inflammatory drugs
Family history of axial spondyloarthritis
Positive test for <i>HLA-B27</i> gene
Elevated C-reactive protein levels

"diagnostic algorithm" has been developed by Rudwaleit *et al*^[66] (2004). With this algorithm, patients experiencing chronic back pain can be diagnosed with axial SpA if they experience IBP along with three or more of the outlined SpA features^[65,66]. Additionally, HLA-B27 genotyping may be recommended for patients experiencing IBP and one or two SpA features. If HLA-B27 typing is positive, patients can then be diagnosed with axial SpA. Finally, patients who have IBP, but no other SpA features, should undergo HLA-B27 testing as well as MRI imaging, from which they will be diagnosed as having axial SpA if HLA-B27 is positive and MRI demonstrates inflammation of the sacroiliac joints^[65,66].

To come closer to diagnosing AS in its earlier stages, the distinction must be made between a patient's back pain that is caused by AS (characterized as IBP) vs pain caused by mechanical lower back pain (MLBP). Four parameters have been proposed to distinguish AS from MLBP. The parameters defining IBP include: Improvement of back pain with exercise, but not with rest, waking up during the second half of the night or early morning due to back pain, experiencing morning stiffness of at least 30 min, and alternating buttock pain^[54,65,67]. The criteria can be used on adults

As a solution to the lack of diagnostic criteria, a

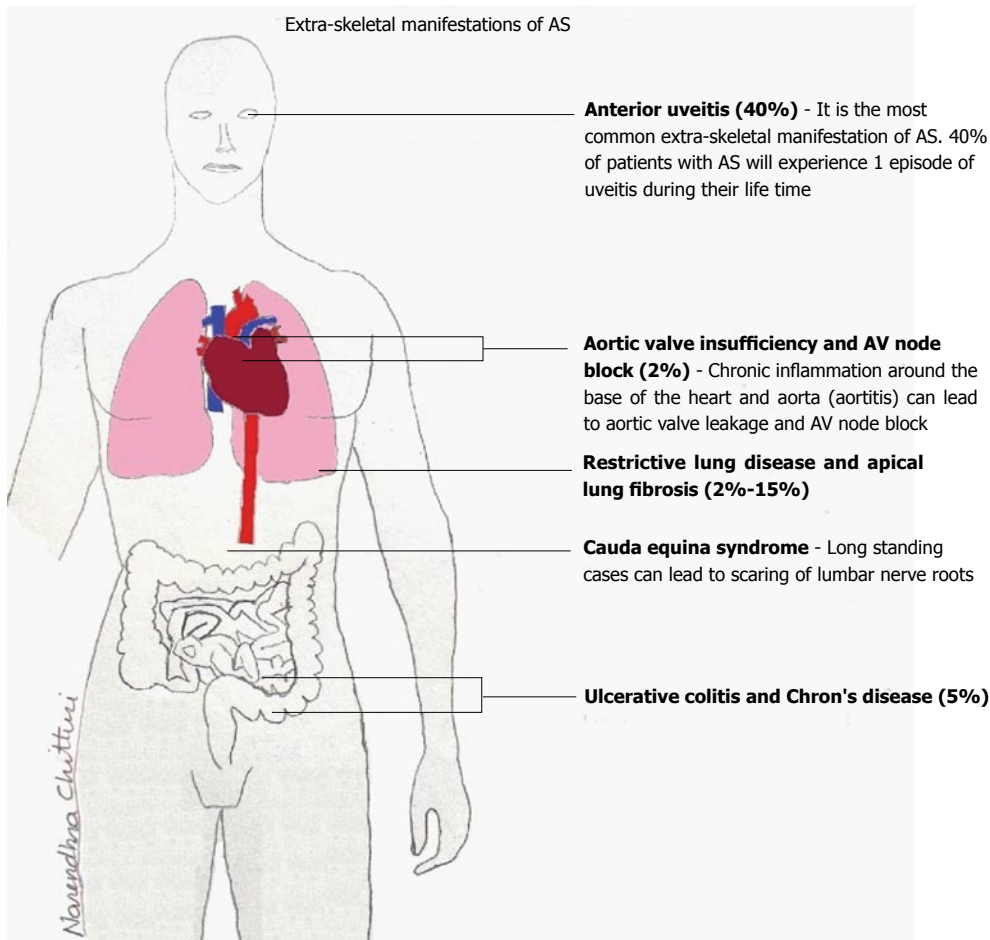


Figure 2 Schematic of extra-skeletal manifestations of ankylosing spondylitis. AS: Ankylosing spondylitis.

aged less than 50 years with chronic back pain, and are considered positive if two or more of the four parameters are experienced (sensitivity = 70.3% and specificity = 81.2%)^[54].

To attain this information, clinical symptoms, history, examination, laboratory parameters and imaging must be obtained from the patient^[54]. Clinical symptoms that may indicate the presence of SpA include IBP, arthritis (seen by swelling, joint effusion or by imaging), enthesitis (seen as swelling where tendons and ligaments attach to the bone - commonly near the heel if there is pain during walking, specifically in the morning^[55]) and any accompanying features such as psoriasis, Crohn-like colitis and anterior uveitis^[54]. Other symptoms can include stiffness that can take anywhere from a few minutes to two hours to relieve, particularly in the morning, and can be seen to reappear after long periods of sitting or rest^[55]. Symptoms can also include fatigue that does not subside with sleep, pain in the spine that is worse during rest and that improves with exercise^[68,69]; shortness of breath once AS is in the later stages, as fusion of thoracic vertebrae can restrict expansion of the chest^[55]; feverishness or night sweats, however, these can also be associated with other types of inflammatory and autoimmune diseases^[70]; as well as flare-ups of AS, where it has been seen that 70% of

patients with AS will have flares in any one week^[55,71].

It is important to determine if the patient has a family history of SpA or diseases like psoriasis or IBD. A history of rheumatic symptoms or other suspicious skin or gut findings must also be noted^[54].

Clinical examination for early AS is limited, as major deformities of the spine have probably not yet occurred, and sacroiliitis and spondylitis cannot be diagnosed through clinical means alone. The earliest signs to look for include reduced lateral spinal flexion of the lumbar spine (10 cm), decreased chest expansion (4 cm) and limited cervical rotation (70°)^[54]. If only pain is present, further imaging is recommended. The two main laboratory parameters useful for diagnosis include HLA-B27 genotype and C-reactive protein levels^[54]. HLA-B27 remains of high importance, especially early on in the disease, whereas only one half of patients with AS also have high serum levels of C-reactive protein^[54,72].

X-RAY

Imaging in AS has been synonymous for decades with conventional radiography (CR). However, developments in computed tomography (CT), ultrasonography (US) and magnetic resonance imaging (MRI) have increased



Figure 3 Anteroposterior pelvic X-ray shows pseudodilatation of the sacroiliac joint due to subchondral erosion and subchondral bone sclerosis.



Figure 4 Anteroposterior vertebral X-ray shows bilateral thickening of the syndesmophytes resulting in the appearance of the "bamboo sign" in radiographs.

the amount of information that can be obtained by imaging. Imaging is necessary in AS to establish diagnoses, determine the extent of disease in axial or peripheral joints and/or entheses, and monitor the change in disease^[73,74].

Radiographs are the most important imaging technique for the detection, diagnosis, and follow-up monitoring of patients with AS^[75]. Typical findings of AS are sacroiliitis and bridging syndesmophyte of the spine, which usually take many years to develop. Sacroiliitis is the hallmark of AS and is found in the early stages^[73]. Subchondral bone erosion on the iliac side of the SI joint is seen first, followed by subchondral sclerosis and bony proliferation^[76], as seen in Figure 3.

In the spine, first visualized are small erosions at the corner of the vertebral bodies that are caused by periosteal bone formation^[77,78]. After these erosions, ossification of outer fibers results in syndesmophytes, which leads to bridging between the vertebrae. Thickening of the syndesmophytes results in the appearance of the "bamboo sign" in radiographs^[78], as in Figure 4.

The "dagger sign" is another finding that results from ossification of the posterior interspinous ligament^[78].



Figure 5 Anteroposterior pelvic X-ray shows ill-defined erosions with sclerosis at the side of ligaments, and tendonitis is seen as enthesopathy at certain sites around the pelvis, at the ischial tuberosity.

Pseudoarthrosis manifested by disco-vertebral destruction and sclerosis presents as a hypodense and linear shape in the sclerotic border. Pseudoarthrosis appears in radiographs similar to vertebral disks infected by diseases such as tuberculosis, although it is caused by undetected vertebral fractures or unfused segments^[74]. Ill-defined erosions with sclerosis at the side of ligaments and tendonitis are seen as enthesopathy. These lesions are typically bilateral and symmetrical in distribution. Enthesopathic changes are particularly prominent at certain sites around the pelvis, such as the ischial tuberosity^[79] (Figure 5).

Knee changes consist of uniform joint space narrowing and surrounding bony proliferation. The glenohumeral joint space may be narrow and a large erosion may be present in the upper greater tuberosity. The hips are typically involved symmetrically demonstrated as joint space narrowing, femoral head axial migration, and osteophyte formation at the femoral head-neck junction. In the hands, the joints are usually involved asymmetrically. Erosions are smaller and shallower. Marginal periostitis is seen, and bone density is usually preserved. Lung manifestations of AS are seen as progressive fibrosis and bullous changes in the upper lobes. Lung changes are usually seen several years after the joint disease develops^[74]. Conventional radiography is relatively inexpensive and widely available, however, it is not sensitive in the early stages of AS. The amount of data documenting a prognostic value of CR findings is limited in low-grade (grade 1) sacroiliitis, and it has a predictive value for the progression of AS^[80].

CT

CT scanning may be useful in patients with suspected AS where radiography results are normal or equivocal. CT is rapid, reliable and produces high-resolution images.

CT demonstrates pathological findings similar to CR such as erosion, osteoporosis, sclerosis as well as new bone formation, with better visualization and localization^[81] (Figure 6).

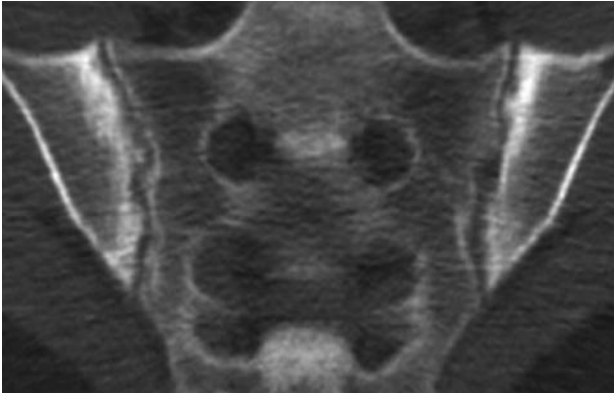


Figure 6 Computed tomography of sacroiliac joint shows bilateral subchondral sclerosis and dentate joint contour due to bone erosion.

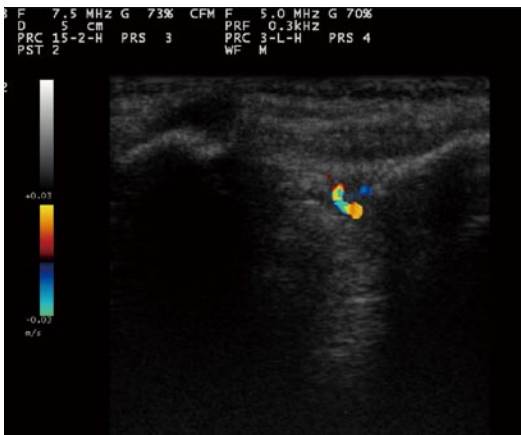


Figure 7 Color Doppler sonogram of sacroiliac joint in a patient with active sacroiliitis reveals vascularization within the posterior portion of the right sacroiliac joint.

CT provides better visualization for the measurement of syndesmophyte growth^[82]. Other useful applications of CT scanning are the detection of atlantoaxial instability, manubriosternal disease, paraspinal muscle atrophy and costovertebral disease. In patients with advanced AS, CT is the imaging of choice for the assessment of fractures of the cervical spine and soft-tissue injuries^[81]. CT is also effective as a navigation tool in screw fixation of spinal and lumbar fractures^[83,84].

APPLICATION OF US IN THE MANAGEMENT OF PATIENTS WITH AS

Although MRI has become a reference modality in the lack of any gold standard method for definite diagnosis of AS, US still maintains a major role in the diagnosis of AS because it is simple, inexpensive and pervasively available. Also, recent studies and the efforts of the ultrasound taskforce (OMERACT-EULAR) have validated US as a diagnostic tool, proving it to be a highly sensitive, non-invasive and a practical tool in the assessment of joint pathology^[85].

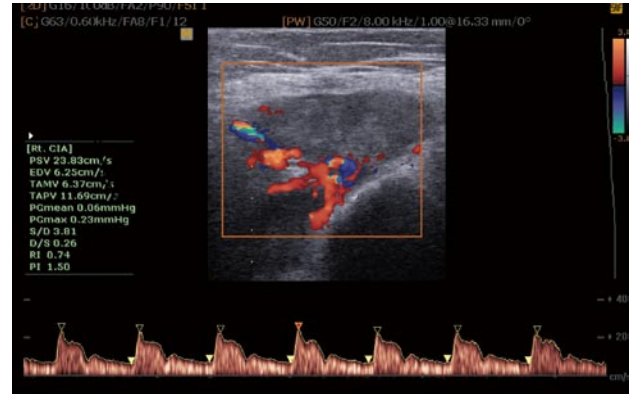


Figure 8 Color and spectral waveform Doppler ultrasonogram of the ischial tuberosity in a patient with severe enthesopathy with a mean resistive index of 0.74 before treatment.

US of the sacroiliac joint

The presence or absence of sacroiliitis continues to be the mainstay of early diagnosis of AS^[86]. Several recent studies have provided data on the usefulness of color Doppler ultrasound (CDUS) in the assessment of the sacroiliac joints and spine^[87-89] (Figure 7).

Klauser *et al.*^[90] showed sensitivity, specificity, positive and negative predictive values of 100% for contrast-enhanced US in the detection of clinically active sacroiliitis (Figure 8). Although contrast-enhanced CDUS has been reported to have a high negative predictive value for the detection of sacroiliitis^[63], the role of US in the assessment of sacroiliitis and spine involvements in AS is still minimal.

US in the assessment of enthesitis

US is superior in the evaluation of rheumatologic diseases with peripheral involvement. Active enthesitis is an ultrasonographic finding highly suggestive of AS^[91-95]. Enthesitis is the inflammation of the insertion of tendons, ligaments and capsules into the bone. Calcaneal entheses (plantar fascia and Achilles tendon), knee entheses (quadricipital tendon and proximal and distal attachments of patellar tendon), hip entheses (gluteus medius tendon) and elbow entheses (medial and lateral epicondyle tendon) are common sites of enthesitis in patients with AS. A national consortium of Rheumatology experts in 2006 recommended the use of Doppler US (or MRI) to evaluate the enthesal involvement in patients with AS (level of evidence 2b/3; grade of recommendation D)^[96].

Gandjbakhch *et al.*^[97] have systematically reviewed the studies regarding the use of US in the evaluation of entheses; they found a heterogeneity in the US technique and definitions in different studies, and thus suggested the determination of specific US definitions for enthesitis to be used universally in both research and clinical settings^[97]. The ultrasound taskforce (OMERACT-EULAR) has made an enormous effort to provide definitions and to validate US techniques in the diagnosis of rheumatologic diseases.

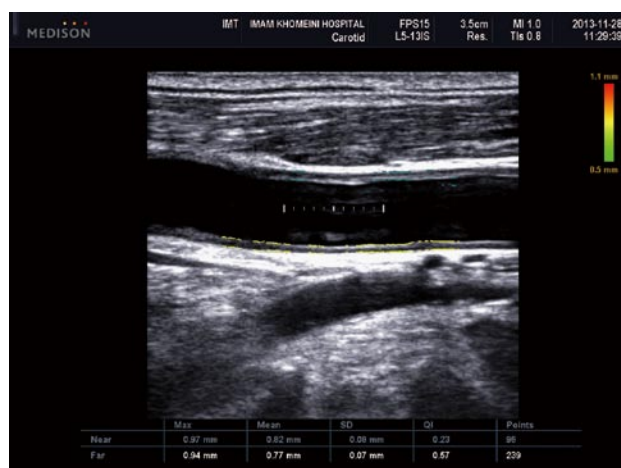


Figure 9 Ultrasonogram shows increased intima-media thickness of both near (0.82 mm) and far wall (0.77 mm) of common carotid artery in patients with ankylosing spondylitis.

US in the evaluation of atherosclerosis and cardiovascular complications

Accelerated atherosclerosis is a major problem in rheumatic inflammatory disorders^[98,99], therefore US has a substantial role in the evaluation of patients with AS. Two US techniques have been widely accepted as non-invasive methods for evaluating atherosclerosis. One is brachial artery flow-mediated dilation, which was demonstrated to be lower in AS patients compared to healthy controls^[98], and is an indicator of endothelial dysfunction, which itself is an initiator of atherosclerotic processes. The second method is the measurement of intima-media thickness (IMT) for the early detection of atherosclerotic lesions. In the study by Sari *et al.*^[98], there was no significant difference between the carotid IMT of AS patients and controls, but it was positively correlated with age and the severity of AS disease, suggesting that patients with severe AS suffer from more advanced intimal thickening or atherosclerotic changes^[98] (Figure 9).

A recent meta-analysis demonstrated a higher weighted IMT in AS patients ($n = 1214$) compared to controls ($n = 1000$) using 15 case-control studies and 9 abstracts^[100].

Cardiac abnormalities are well recognized in AS. It has been shown that in many cases, cardiac change could even be prior to the onset of clinical AS disease^[101,102]. Trans-thoracic echocardiography and Doppler US are useful techniques in the assessment of cardiac disease in AS, and may detect aortic valve disease at an early pre-clinical stage^[103].

Aortic root and valve disease is a frequent complication in AS patients. It includes aortic root thickening and dilation, aortic cusp thickening and retraction, subaortic bump as well as aortic and mitral regurgitation^[103-106]. The prevalence ranges between 24% and 100% according to autopsy reports, and 8%-31% according to trans-thoracic echocardiography^[103,107-110]. The prevalence rate was higher when using trans-esophageal

echocardiography as the diagnostic modality (82% in AS compared to 24% in healthy controls)^[106]. Except for the duration of AS, these anatomical changes are reported to be unrelated to disease features (activity, severity or therapy), but they are associated with clinically important cardiovascular morbidity^[106]. Conduction disturbances, yet another cardiovascular complication in AS, result from the progression of fibrosis through the interventricular septum to the atrioventricular node, thus they occur after aortic and valvular changes, and could be predicted in advance by early diagnosis of valvular changes^[111,112].

Early detection of AS-related valvular abnormalities may provide the potential to prevent their progression to irreversible phases. Townsend *et al.*^[113] reported that immunosuppressive therapy could prevent or delay valvular replacement in rheumatic patients with aortic regurgitation.

Cardiomyopathy and pericarditis, two other comorbidities in patients with AS, can be assessed by echocardiography^[103,114-116]. The myocardial dysfunction seen in AS patients, which was demonstrated to be a diastolic variant (lower E wave velocity, higher A wave velocity and overall low E/A ratio) rather than a systolic variant, could be evaluated by echocardiography as well^[102,117]. Caliskan *et al.*^[101] used trans-thoracic Doppler echocardiography to measure the coronary flow reserve (CFR), which is an indicator of coronary microvascular circulation, and they reported a decline in CFR in AS patients.

US in treatment monitoring

Doppler US was demonstrated to be useful in monitoring the patients' response to enthesitis treatment^[89,94,118-120]. Some studies have suggested the use of the resistive index (RI) of CDUS for following up the patients' response to treatment^[88].

Limitations of the ultrasound study

Since the bone cortex blocks ultrasound beams, US cannot visualize the foci of the bone marrow inflammation in the process of AS disease^[121]. Operator dependency and its inter-observer variability is always a challenge for the clinical application of US.

Considerations regarding the physician performing the Ultrasound study

Another issue that should be addressed here is whether US for diagnosing AS should be performed by rheumatologists during the patient's clinic visit or by radiologists.

There are no data to support the superiority of one over the other in the setting of AS. A study related to the assessment of rotator cuff tears, compared arthrography performed by radiologists to sonography performed by rheumatologists, and showed equivalency between their sensitivity and specificity rates^[122]. So far, no one has studied the competency

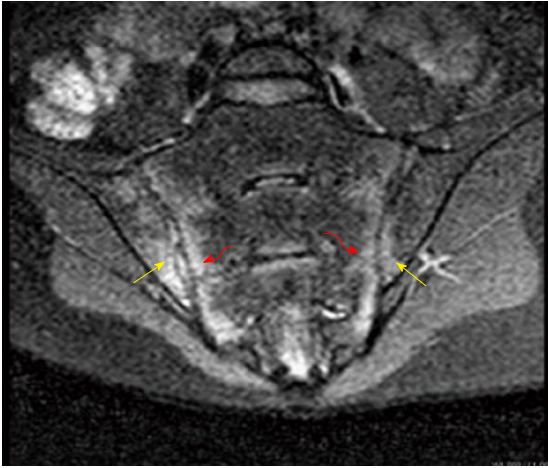


Figure 10 Oblique coronal magnetic resonance imaging (short tau inversion recovery sequence) of a patient with active ankylosing spondylitis revealed bilateral high signal intensity in both the sacral and iliac components of the sacroiliac joint.

of the ultrasonographer, whether a radiologist or a rheumatologist, in the assessment of musculoskeletal disease^[123].

Regardless of who performs the US assessment, it is important for the ultrasonographer to be competent in order to minimize the risk of misdiagnosis or unnecessary examination^[123,124].

Nearly one-quarter of rheumatologists in US are using this technique, but it is still far from being incorporated into routine clinical practice^[125]. In many European countries such as Germany, Italy and Spain, rheumatologists routinely perform US; and in some countries, musculoskeletal US training is a compulsory part of rheumatology training^[126,127].

There is no doubt that it is unreasonable to expect every rheumatologist to be competent in all US procedures indicated for rheumatology^[123], and that would remain within the remit of radiologists^[128], however, training rheumatologists for a more selective list of procedures such as identifying synovitis in a joint, *etc.*, which could improve clinical practice in rheumatology and enhance the care provided for patients, would be beneficial.

The best case scenario is a close cooperation between rheumatologists and radiologists. The cooperation and task division between these two specialties would facilitate a cost-effective, more convenient and the least risky care for patients, whilst providing the required information for diagnosis and treatment of patients for the physician^[128].

MRI

Spinal inflammation can be demonstrated by MRI using the fat-saturating short tau inversion recovery (STIR) technique, especially in early and active disease, by showing inflammation, bone marrow edema, and pre-radiographic erosions at the sacroiliac joint Figure 10.

The ability to diagnose AS before any bony deformities occur can significantly improve patient outcome and

allow for effective therapies to be used before the later and more detrimental phases of the disease occur^[58-60]. MRI is the most sensitive tool for imaging early AS and it can show both active inflammation as well as chronic structural changes near the sacroiliac joints and near the spine, both typical places for AS^[58]. More recently, diffusion-weighted MRI (DWI) has been shown to be helpful in the early diagnosis of AS^[58]. In comparison, CT is limited by its lower sensitivity to characterize lesions in soft tissue and bone marrow, and is associated with considerable radiation exposure^[58]. For these reasons, MRI has been recommended in recent classification criteria of AS^[60,129].

In a study by Ai *et al.*^[58], 34 patients aged 15-38 years experiencing lower back pain for 3 mo to 2 years were studied using MRI examination. By comparing the apparent diffusion coefficient (ADC) values in subchondral bone marrow and sacroiliac joints, patients with typical uncomplicated musculoskeletal low back pain were able to be differentiated from those patients with AS^[58]. In the study, the mean ADC values in early AS patients were significantly higher than the ADC values in LBP patients and healthy patient controls^[58]. Early AS patients had mean ADC values of subchondral bone marrow along the bilateral sacroiliac joints that increased because of ongoing pathologically inflammatory penetration^[58].

In addition, as shown by Ai *et al.*^[58], WB-MRI can detect many abnormalities in the sacroiliac joints, peripheral joints, attachment points of ligaments and tendons as well as in the spine, with one single scan. This is ideal because AS can manifest in parts of the body other than the sacroiliac joints^[130], which it is well known for. MRI combined with a number of novel techniques, such as spectral pre-saturation inversion recovery echo planar imaging (SPIR-EPI) or short TI inversion recovery echo planar imaging (STIR-EPI), can create high-quality images, allowing for a better early diagnosis of AS^[58]. For example, an efficient evaluation of AS patients can be done with WB-DWI combined with the background signal suppression technique (DWIBS) to create better lesion contrast and higher spatial resolution^[58]. These novel techniques can create better imaging of lesion sites, with decreased interfering signal from other tissues, which leads to earlier diagnosis of patients with AS^[58].

TREATMENT OF AS

Treatment of AS consists of a broad range of methods, which target different pathways involved with the progression of the disease. The most common treatment methods involve reduction of the inflammatory response, which is the primary complication resulting from AS, physical therapy, as well as surgical treatment to address deformities of the spine.

Anti-inflammatory treatment

The focus of the anti-inflammatory therapy in AS

patients with high disease activity is the inhibition of the tumor necrosis factor α (TNF- α). Several studies have shown TNF- α inhibitors to be successful in reducing the inflammatory response caused by AS^[131,132]. The use of TNF- α inhibitors as effective treatment methods for AS is considered a relatively new method, with its effects being recognized only in the last two decades. This treatment method is mostly effective in the early stages of the disease, where reduction of inflammation can prevent deformities of the skeleton. The two categories of TNF- α inhibitor drugs are anti-TNF antibodies and TNF receptors. Infliximab and adalimumab are monoclonal antibodies, while etanercept is a TNF receptor drug; both of these drugs are approved for use in AS treatment^[133]. A study that analyzed the results of the effect of 5 inhibitor drugs through 13 controlled trials (adalimumab, etanercept, golimumab, infliximab and infliximab-biosimilar), showed that all of these drugs were significantly better than placebo in treating the symptoms of AS^[134]. Nonsteroidal anti-inflammatory drugs (NSAIDs) are another line of therapy used in AS. NSAIDs are more commonly used to alleviate back pain and increase mobility in patients with AS, however, several studies have shown that NSAIDs are also effective in reducing progression of the disease^[135,136]. A recent study showed that patients not exposed to NSAIDs had a higher risk of developing morbidities and cardiovascular diseases, when compared to NSAIDs such as etoricoxib, celecoxib, as well as non-selective NSAIDs^[137].

Physical therapy

Physical therapy is employed to increase muscle strength and mobility and reduce pain in patients with AS. Different exercise therapy methods have been used in the rehabilitation of AS patients, including weight training, cardiovascular training, and aquatic exercises. In general, these exercise methods provide similar treatment outcomes, which result in an increase in mobility, decrease in back stiffness, as well as a decrease in pain and fatigue^[138]. However, compared to the more common exercise therapies, cardiovascular training has been shown to increase fitness in AS patients^[139], while aquatic exercise has been more effective in reducing pain^[140]. Spa therapy is another method recently introduced, which provides a more passive treatment^[141]. Despite some significant indication of the effectiveness of these therapies, several studies have shown that improvement in patients is much higher when physical therapies are combined with anti-inflammatory drug treatments^[142,143]. Considering the importance of exercise in the quality of life and mobility in AS patients, home exercise programs have been developed for patients to perform on their own after hospitalization. However, several studies have discussed the possibility that many patients do not perform these exercises at home on a regular basis, likely due to pain. Pain associated with AS not only induces fatigue in patients^[144], but can also be a factor in the lack of

exercise. A combination of anti-inflammatory drugs with physical therapy can be beneficial in this aspect, as pain reduction due to anti-inflammatory drugs can ultimately increase motivation for exercise^[145].

Surgical intervention

Progression of AS may lead to deformities in the axial skeleton. One of the most common deformities in AS patients is the fixed thoracolumbar kyphotic deformity (TLKD) of the spine. The sole treatment method of this deformity is surgical. There are currently three surgical techniques used in spine surgery to fix TLKD, namely the opening wedge osteotomy (OWO), closing wedge osteotomy (CWO) and polysegmental wedge osteotomy (PWO). The OWO technique involves performing osteotomies of vertebrae L1, L2 and L3, followed by a manual extension of the lumbar spine to open a wedge of the anterior column, by closing the posterior osteotomies^[146]. Unfortunately, disruption of the anterior longitudinal ligament from the manual extension of the spine is entailed in the procedure and major risks from this method include vascular and neurological complications^[147,148]. The CWO technique involves resecting the posterior elements of a vertebra, followed by an extension of the spine, which closes the posterior osteotomy by creating an opening on the anterior part of the column^[149]. The PWO technique involves performing several closing wedges of posterior lumbar osteotomies, which results in smaller closing angles of the osteotomies, and leads to a more gradual extension of the spine^[147]. In general, there is no preference in choosing between the three techniques. However, studies have shown that the CWO and PWO have resulted in better outcomes in patients, compared to the OWO^[150].

Spinal fractures in the thoracolumbar region are another complication that can result from AS. Surgical intervention is the ideal treatment method as it prevents further fractures of the spine, and improves the neurological status of patients^[151]. Surgery has also been used for the treatment of other complications that arise from AS, such as deformities in the cervical region of the spine and in the sacroiliac joint.

CONCLUSION

This review provides a detailed summary of AS, one of the most common spondyloarthropathies. AS affects quality of life by causing debilitating pain and a significant decrease in mobility, but also occurs in high prevalence with a loss of bone mineral density and atherosclerosis. The discovery of several genetic factors that increase susceptibility to AS, as well as the use of CT, MRI and US in the diagnosis of the disease, could result in the early diagnosis of AS, which is very important in improving treatment outcome. Physical therapy, NSAIDs and inhibitor drugs have proven successful in alleviating disease symptoms, and in preventing further disease progression. Surgical

intervention is necessary when the disease causes deformities to the spine in the later stages.

ACKNOWLEDGMENTS

Many thanks to Narendra Chetori for drawing the first two figures.

REFERENCES

- Hukins DWL, Meakin JR. Relationship between structure and mechanical function of the tissues of the intervertebral joint. *American Zoology* 2000; **40**: 42-52
- Vleeming A, Schuenke MD, Masi AT, Carreiro JE, Danneels L, Willard FH. The sacroiliac joint: an overview of its anatomy, function and potential clinical implications. *J Anat* 2012; **221**: 537-567 [PMID: 22994881 DOI: 10.1111/j.1469-7580.2012.01564.x]
- Moore KL, Dalley AF, Agur AMR. Clinically Oriented Anatomy, 7th ed. PA: Lippincott Williams & Wilkins, 2014
- Forst SL, Wheeler MT, Fortin JD, Vilensky JA. The sacroiliac joint: anatomy, physiology and clinical significance. *Pain Physician* 2006; **9**: 61-67 [PMID: 16700283]
- Benjamin M, Ralphs JR. Enteses--the bony attachments of tendons and ligaments. *Ital J Anat Embryol* 2001; **106**: 151-157 [PMID: 11729950]
- Benjamin M, McGonagle D. The enthesis organ concept and its relevance to the spondyloarthropathies. *Adv Exp Med Biol* 2009; **649**: 57-70 [PMID: 19731620]
- Benjamin M, Toumi H, Ralphs JR, Bydder G, Best TM, Milz S. Where tendons and ligaments meet bone: attachment sites ('entheses') in relation to exercise and/or mechanical load. *J Anat* 2006; **208**: 471-490 [PMID: 16637873]
- McGonagle D, Aydin SZ, Tan AL. The synovio-entheseal complex and its role in tendon and capsular associated inflammation. *J Rheumatol Suppl* 2012; **89**: 11-14 [PMID: 22751582 DOI: 10.3899/jrheum.120233]
- Willard FH. The muscular, ligamentous, and neural structure of the lumbosacrum and its relationship to low back pain. Movement, stability and lumbopelvic pain Intergration of Research and Therapy, 2007: 5-45
- McGonagle D, Benjamin M, Marzo-Ortega H, Emery P. Advances in the understanding of enthesal inflammation. *Curr Rheumatol Rep* 2002; **4**: 500-506 [PMID: 12427365]
- Singh HJ, Nimarpreet K, Ashima S, Kumar A, Prakash S. Study of bone mineral density in patients with ankylosing spondylitis. *J Clin Diagn Res* 2013; **7**: 2832-2835 [PMID: 24551650 DOI: 10.7860/JCDR/2013/6779.3770]
- van der Weijden MA, Claushuis TA, Nazari T, Lems WF, Dijkman BA, van der Horst-Bruinsma IE. High prevalence of low bone mineral density in patients within 10 years of onset of ankylosing spondylitis: a systematic review. *Clin Rheumatol* 2012; **31**: 1529-1535 [PMID: 22706444 DOI: 10.1007/s10067-012-2018-0]
- Brophy S, Hickey S, Menon A, Taylor G, Bradbury L, Hamersma J, Calin A. Concordance of disease severity among family members with ankylosing spondylitis? *J Rheumatol* 2004; **31**: 1775-1778 [PMID: 15338499]
- Kaya A, Ozgocmen S, Kamanli A, Ardicoglu O. Bone loss in ankylosing spondylitis: does syndesmophyte formation have an influence on bone density changes? *Med Princ Pract* 2009; **18**: 470-476 [PMID: 19797924]
- Brown MA, Kennedy LG, MacGregor AJ, Darke C, Duncan E, Shatford JL, Taylor A, Calin A, Wordsworth P. Susceptibility to ankylosing spondylitis in twins: the role of genes, HLA, and the environment. *Arthritis Rheum* 1997; **40**: 1823-1828 [PMID: 9336417 DOI: 10.1002/1529-0131(199710)40]
- Jacobs JH, Rose FC. The familial occurrence of ankylosing spondylitis. *Br Med J* 1954; **2**: 1139-1140 [PMID: 13209064]
- Järvinen P. Occurrence of ankylosing spondylitis in a nationwide series of twins. *Arthritis Rheum* 1995; **38**: 381-383 [PMID: 7880193]
- Brown MA, Brophy S, Bradbury L, Hamersma J, Timms A, Laval S, Cardon L, Calin A, Wordsworth BP. Identification of major loci controlling clinical manifestations of ankylosing spondylitis. *Arthritis Rheum* 2003; **48**: 2234-2239 [PMID: 12905477 DOI: 10.1002/art.11106]
- Sims AM, Barnardo M, Herzberg I, Bradbury L, Calin A, Wordsworth BP, Darke C, Brown MA. Non-B27 MHC associations of ankylosing spondylitis. *Genes Immun* 2007; **8**: 115-123 [PMID: 17167495 DOI: 10.1038/sj.gene.6364362]
- Brewerton DA, Hart FD, Nicholls A, Caffrey M, James DC, Sturrock RD. Ankylosing spondylitis and HL-A 27. *Lancet* 1973; **1**: 904-907 [PMID: 4123836]
- Khan MA, Ball EJ. Genetic aspects of ankylosing spondylitis. *Best Pract Res Clin Rheumatol* 2002; **16**: 675-690 [PMID: 12406434]
- Khan MA, Mathieu A, Sorrentino R, Akkoc N. The pathogenetic role of HLA-B27 and its subtypes. *Autoimmun Rev* 2007; **6**: 183-189 [PMID: 17289555 DOI: 10.1016/j.autrev.2006.11.003]
- Reveille JD, Hirsch R, Dillon CF, Carroll MD, Weisman MH. The prevalence of HLA-B27 in the US: data from the US National Health and Nutrition Examination Survey, 2009. *Arthritis Rheum* 2012; **64**: 1407-1411 [PMID: 22139851 DOI: 10.1002/art.33503]
- Roberts RL, Wallace MC, Jones GT, van Rij AM, Merriman TR, Harrison A, White D, Stamp LK, Ching D, Highton J, Stebbings SM. Prevalence of HLA-B27 in the New Zealand population: effect of age and ethnicity. *Arthritis Res Ther* 2013; **15**: R158 [PMID: 24286455 DOI: 10.1186/ar4341]
- Firestein GS, Kelley WN. Kelley's Textbook of Rheumatology. 9th ed. Philadelphia, PA: Elsevier/Saunders, 2013
- Hill AV, Aillsopp CE, Kwiatkowski D, Anstey NM, Twumasi P, Rowe PA, Bennett S, Brewster D, McMichael AJ, Greenwood BM. Common west African HLA antigens are associated with protection from severe malaria. *Nature* 1991; **352**: 595-600 [PMID: 1865923 DOI: 10.1038/352595a0]
- Brown MA. Human leucocyte antigen-B27 and ankylosing spondylitis. *Intern Med J* 2007; **37**: 739-740 [PMID: 17908085 DOI: 10.1111/j.1445-5994.2007.01491.x]
- Liu Y, Jiang L, Cai Q, Danoy P, Barnardo MC, Brown MA, Xu H. Predominant association of HLA-B*2704 with ankylosing spondylitis in Chinese Han patients. *Tissue Antigens* 2010; **75**: 61-64 [PMID: 19804562 DOI: 10.1111/j.1399-0039.2009.01379.x]
- Benjamin R, Parham P. Guilt by association: HLA-B27 and ankylosing spondylitis. *Immunol Today* 1990; **11**: 137-142 [PMID: 2187471]
- Hermann E, Yu DT, Meyer zum Büschenfelde KH, Fleischer B. HLA-B27-restricted CD8 T cells derived from synovial fluids of patients with reactive arthritis and ankylosing spondylitis. *Lancet* 1993; **342**: 646-650 [PMID: 8103147]
- Scofield RH, Kurien B, Gross T, Warren WL, Harley JB. HLA-B27 binding of peptide from its own sequence and similar peptides from bacteria: implications for spondyloarthropathies. *Lancet* 1995; **345**: 1542-1544 [PMID: 7791441]
- Fraundorf E, von Goessel H, May E, Märker-Hermann E. HLA-B27-restricted T cells from patients with ankylosing spondylitis recognize peptides from B*2705 that are similar to bacteria-derived peptides. *Clin Exp Immunol* 2003; **134**: 351-359 [PMID: 14616798]
- Ramos M, Alvarez I, Sesma L, Logean A, Rognan D, López de Castro JA. Molecular mimicry of an HLA-B27-derived ligand of arthritis-linked subtypes with chlamydial proteins. *J Biol Chem* 2002; **277**: 37573-37581 [PMID: 12122005 DOI: 10.1074/jbc.M205470200]
- Mear JP, Schreiber KL, Münz C, Zhu X, Stevanović S, Rammensee HG, Rowland-Jones SL, Colbert RA. Misfolding of HLA-B27 as a result of its B pocket suggests a novel mechanism for its role in susceptibility to spondyloarthropathies. *J Immunol* 1999; **163**: 6665-6670 [PMID: 10586062]
- Dangoria NS, DeLay ML, Kingsbury DJ, Mear JP, Uchanska-Ziegler B, Ziegler A, Colbert RA. HLA-B27 misfolding is associated with

- aberrant intermolecular disulfide bond formation (dimerization) in the endoplasmic reticulum. *J Biol Chem* 2002; **277**: 23459-23468 [PMID: 11978783 DOI: 10.1074/jbc.M110336200]
- 36 **Pahl HL**, Baeuerle PA. The ER-overload response: activation of NF-kappa B. *Trends Biochem Sci* 1997; **22**: 63-67 [PMID: 9048485]
 - 37 **Bowness P**. HLA B27 in health and disease: a double-edged sword? *Rheumatology* (Oxford) 2002; **41**: 857-868 [PMID: 12154202]
 - 38 **Allen RL**, O'Callaghan CA, McMichael AJ, Bowness P. Cutting edge: HLA-B27 can form a novel beta 2-microglobulin-free heavy chain homodimer structure. *J Immunol* 1999; **162**: 5045-5048 [PMID: 10227970]
 - 39 **Kollnberger S**, Bird L, Sun MY, Retiere C, Braud VM, McMichael A, Bowness P. Cell-surface expression and immune receptor recognition of HLA-B27 homodimers. *Arthritis Rheum* 2002; **46**: 2972-2982 [PMID: 12428240 DOI: 10.1002/art.10605]
 - 40 **Bird LA**, Peh CA, Kollnberger S, Elliott T, McMichael AJ, Bowness P. Lymphoblastoid cells express HLA-B27 homodimers both intracellularly and at the cell surface following endosomal recycling. *Eur J Immunol* 2003; **33**: 748-759 [PMID: 12616495 DOI: 10.1002/eji.200323678]
 - 41 **Brown M**, Bunce M, Calin A, Darke C, Wordsworth P. HLA-B associations of HLA-B27 negative ankylosing spondylitis: comment on the article by Yamaguchi et al. *Arthritis Rheum* 1996; **39**: 1768-1769 [PMID: 8843876]
 - 42 **Wei JC**, Tsai WC, Lin HS, Tsai CY, Chou CT. HLA-B60 and B61 are strongly associated with ankylosing spondylitis in HLA-B27-negative Taiwan Chinese patients. *Rheumatology* (Oxford) 2004; **43**: 839-842 [PMID: 15113995 DOI: 10.1093/rheumatology/keh193]
 - 43 **Brown MA**, Kennedy LG, Darke C, Gibson K, Pile KD, Shatford JL, Taylor A, Calin A, Wordsworth BP. The effect of HLA-DR genes on susceptibility to and severity of ankylosing spondylitis. *Arthritis Rheum* 1998; **41**: 460-465 [PMID: 9506574 DOI: 10.1002/1529-0131(199803)41]
 - 44 **Timms AE**, Crane AM, Sims AM, Cordell HJ, Bradbury LA, Abbott A, Coyne MR, Beynon O, Herzberg I, Duff GW, Calin A, Cardon LR, Wordsworth BP, Brown MA. The interleukin 1 gene cluster contains a major susceptibility locus for ankylosing spondylitis. *Am J Hum Genet* 2004; **75**: 587-595 [PMID: 15309690 DOI: 10.1086/424695]
 - 45 **van der Paardt M**, Crusius JB, García-González MA, Baudoin P, Kostense PJ, Alizadeh BZ, Dijkman BA, Peña AS, van der Horst-Bruinsma IE. Interleukin-1beta and interleukin-1 receptor antagonist gene polymorphisms in ankylosing spondylitis. *Rheumatology* (Oxford) 2002; **41**: 1419-1423 [PMID: 12468823]
 - 46 **McGarry F**, Neilly J, Anderson N, Sturrock R, Field M. A polymorphism within the interleukin 1 receptor antagonist (IL-1Ra) gene is associated with ankylosing spondylitis. *Rheumatology* (Oxford) 2001; **40**: 1359-1364 [PMID: 11752505]
 - 47 **Chou CT**, Timms AE, Wei JC, Tsai WC, Wordsworth BP, Brown MA. Replication of association of IL1 gene complex members with ankylosing spondylitis in Taiwanese Chinese. *Ann Rheum Dis* 2006; **65**: 1106-1109 [PMID: 16361275 DOI: 10.1136/ard.2005.046847]
 - 48 **Brown MA**, Laval SH, Brophy S, Calin A. Recurrence risk modelling of the genetic susceptibility to ankylosing spondylitis. *Ann Rheum Dis* 2000; **59**: 883-886 [PMID: 11053066]
 - 49 **Beyeler C**, Armstrong M, Bird HA, Idle JR, Daly AK. Relationship between genotype for the cytochrome P450 CYP2D6 and susceptibility to ankylosing spondylitis and rheumatoid arthritis. *Ann Rheum Dis* 1996; **55**: 66-68 [PMID: 8572738]
 - 50 **Burton PR**, Clayton DG, Cardon LR, Craddock N, Deloukas P, Duncanson A, Kwiatkowski DP, McCarthy MI, Ouwehand WH, Samani NJ, Todd JA, Donnelly P, Barrett JC, Davison D, Easton D, Evans DM, Leung HT, Marchini JL, Morris AP, Spencer CC, Tobin MD, Attwood AP, Boorman JP, Cant B, Everson U, Hussey JM, Jolley JD, Knight AS, Koch K, Meech E, Nutland S, Prowse CV, Stevens HE, Taylor NC, Walters GR, Walker NM, Watkins NA, Winzer T, Jones RW, McArdle WL, Ring SM, Strachan DP, Pembrey M, Breen G, St Clair D, Caesar S, Gordon-Smith K, Jones L, Fraser C, Green EK, Grozeva D, Hamshire ML, Holmans PA, Jones IR, Kirov G, Moskvina V, Nikolov I, O'Donovan MC, Owen MJ, Collier DA, Elkin A, Farmer A, Williamson R, McGuffin P, Young AH, Ferrier IN, Ball SG, Balmforth AJ, Barrett JH, Bishop TD, Iles MM, Maqbool A, Yuldasheva N, Hall AS, Braund PS, Dixon RJ, Mangino M, Stevens S, Thompson JR, Bredin F, Tremelling M, Parkes M, Drummond H, Lees CW, Nimmo ER, Satsangi J, Fisher SA, Forbes A, Lewis CM, Onnie CM, Prescott NJ, Sanderson J, Matthew CG, Barbour J, Mohiuddin MK, Todhunter CE, Mansfield JC, Ahmad T, Cummings FR, Jewell DP, Webster J, Brown MJ, Lathrop MG, Connell J, Dominiczak A, Marcano CA, Burke B, Dobson R, Gungadoo J, Lee KL, Munroe PB, Newhouse SJ, Onipinla A, Wallace C, Xue M, Caulfield M, Farrall M, Barton A, Bruce IN, Donovan H, Eyre S, Gilbert PD, Hilder SL, Hinks AM, John SL, Potter C, Silman AJ, Symmons DP, Thomson W, Worthington J, Dunger DB, Widmer B, Frayling TM, Freathy RM, Lango H, Perry JR, Shields BM, Weedon MN, Hattersley AT, Hitman GA, Walker M, Elliott KS, Groves CJ, Lindgren CM, Rayner NW, Timpson NJ, Zeggini E, Newport M, Sirugo G, Lyons E, Vannberg F, Hill AV, Bradbury LA, Farrar C, Pointon JJ, Wordsworth P, Brown MA, Franklyn JA, Heward JM, Simmonds MJ, Gough SC, Seal S, Stratton MR, Rahman N, Ban M, Goris A, Sawcer SJ, Compston A, Conway D, Jallow M, Newport M, Sirugo G, Rockett KA, Bumpstead SJ, Chaney A, Downes K, Ghorri MJ, Gwilliam R, Hunt SE, Inouye M, Keniry A, King E, McGinnis R, Potter S, Ravindrarajah R, Whittaker P, Widdens C, Withers D, Cardin NJ, Davison D, Ferreira T, Pereira-Gale J, Hallgrimsdóttir IB, Howie BN, Su Z, Teo YY, Vukcevic D, Bentley D, Brown MA, Compston A, Farrall M, Hall AS, Hattersley AT, Hill AV, Parkes M, Pembrey M, Stratton MR, Mitchell SL, Newby PR, Brand OJ, Carr-Smith J, Pearce SH, McGinnis R, Keniry A, Deloukas P, Reveille JD, Zhou X, Sims AM, Dowling A, Taylor J, Doan T, Davis JC, Savage L, Ward MM, Learch TL, Weisman MH, Brown M. Association scan of 14,500 nonsynonymous SNPs in four diseases identifies autoimmunity variants. *Nat Genet* 2007; **39**: 1329-1337 [PMID: 17952073 DOI: 10.1038/ng.2007.17]
 - 51 **Reveille JD**, Sims AM, Danoy P, Evans DM, Leo P, Pointon JJ, Jin R, Zhou X, Bradbury LA, Appleton LH, Davis JC, Diekmann L, Doan T, Dowling A, Duan R, Duncan EL, Farrar C, Hadler J, Harvey D, Karaderi T, Mogg R, Pomeroy E, Pryce K, Taylor J, Savage L, Deloukas P, Kumanduri V, Peltonen L, Ring SM, Whittaker P, Glazov E, Thomas GP, Maksymowych WP, Inman RD, Ward MM, Stone MA, Weisman MH, Wordsworth BP, Brown MA. Genome-wide association study of ankylosing spondylitis identifies non-MHC susceptibility loci. *Nat Genet* 2010; **42**: 123-127 [PMID: 20062062 DOI: 10.1038/ng.513]
 - 52 **Evans DM**, Spencer CC, Pointon JJ, Su Z, Harvey D, Kochan G, Oppermann U, Dilthey A, Pirinen M, Stone MA, Appleton L, Moutsianas L, Leslie S, Wordsworth T, Kenna TJ, Karaderi T, Thomas GP, Ward MM, Weisman MH, Farrar C, Bradbury LA, Danoy P, Inman RD, Maksymowych W, Gladman D, Rahman P, Morgan A, Marzo-Ortega H, Bowness P, Gaffney K, Gaston JS, Smith M, Bruges-Armas J, Couto AR, Sorrentino R, Paladini F, Ferreira MA, Xu H, Liu Y, Jiang L, Lopez-Larrea C, Díaz-Peña R, López-Vázquez A, Zayats T, Band G, Bellenguez C, Blackburn H, Blackwell JM, Bramon E, Bumpstead SJ, Casas JP, Corvin A, Craddock N, Deloukas P, Dronov S, Duncanson A, Edkins S, Freeman C, Gillman M, Gray E, Gwilliam R, Hammond N, Hunt SE, Jankowski J, Jayakumar A, Langford C, Liddle J, Markus HS, Mathew CG, McCann OT, McCarthy MI, Palmer CN, Peltonen L, Plomin R, Potter SC, Rautanen A, Ravindrarajah R, Ricketts M, Samani N, Sawcer SJ, Strange A, Trembath RC, Viswanathan AC, Waller M, Weston P, Whittaker P, Widaa S, Wood NW, McVean G, Reveille JD, Wordsworth BP, Brown MA, Donnelly P. Interaction between ERAP1 and HLA-B27 in ankylosing spondylitis implicates peptide handling in the mechanism for HLA-B27 in disease susceptibility. *Nat Genet* 2011; **43**: 761-767 [PMID: 21743469 DOI: 10.1038/ng.873]

- 53 **Cortes A**, Maksymowych WP, Wordsworth BP, Inman RD, Danoy P, Rahman P, Stone MA, Corr M, Gensler LS, Gladman D, Morgan A, Marzo-Ortega H, Ward MM, Learch TJ, Reveille JD, Brown MA, Weisman MH. Association study of genes related to bone formation and resorption and the extent of radiographic change in ankylosing spondylitis. *Ann Rheum Dis* 2015; **74**: 1387-1393 [PMID: 24651623 DOI: 10.1136/annrheumdis-2013-204835]
- 54 **Braun J**, Sieper J. Early diagnosis of spondyloarthritis. *Nat Clin Pract Rheumatol* 2006; **2**: 536-545 [PMID: 17016479 DOI: 10.1038/ncprheum0296]
- 55 **Bond D**. Ankylosing spondylitis: diagnosis and management. *Nurs Stand* 2013; **28**: 52-9; quiz 60 [PMID: 24345154 DOI: 10.7748/ns2013.12.28.16.52.e7807]
- 56 **Shaikh SA**. Ankylosing spondylitis: recent breakthroughs in diagnosis and treatment. *J Can Chiropr Assoc* 2007; **51**: 249-260 [PMID: 18060011]
- 57 **Feldtkeller E**, Khan MA, van der Heijde D, van der Linden S, Braun J. Age at disease onset and diagnosis delay in HLA-B27 negative vs. positive patients with ankylosing spondylitis. *Rheumatol Int* 2003; **23**: 61-66 [PMID: 12634937 DOI: 10.1007/s00296-002-0237-4]
- 58 **Ai F**, Ai T, Li X, Hu D, Zhang W, Morelli JN. Value of diffusion-weighted magnetic resonance imaging in early diagnosis of ankylosing spondylitis. *Rheumatol Int* 2012; **32**: 4005-4013 [PMID: 22212412 DOI: 10.1007/s00296-011-2333-9]
- 59 **Boonen A**, van der Linden SM. The burden of ankylosing spondylitis. *J Rheumatol Suppl* 2006; **78**: 4-11 [PMID: 17042055]
- 60 **Weber U**, Maksymowych WP. Sensitivity and specificity of magnetic resonance imaging for axial spondyloarthritis. *Am J Med Sci* 2011; **341**: 272-277 [PMID: 21358308 DOI: 10.1097/MAJ.0b013e31820f8c59]
- 61 **Dougados M**, van der Linden S, Juhlin R, Huitfeldt B, Amor B, Calin A, Cats A, Dijkman B, Olivieri I, Pasero G. The European Spondylarthropathy Study Group preliminary criteria for the classification of spondylarthropathy. *Arthritis Rheum* 1991; **34**: 1218-1227 [PMID: 1930310]
- 62 **Rudwaleit M**, van der Heijde D, Landewé R, Listing J, Akkoc N, Brandt J, Braun J, Chou CT, Collantes-Estevez E, Dougados M, Huang F, Gu J, Khan MA, Kirazli Y, Maksymowych WP, Mielants H, Sørensen JH, Ozgocmen S, Roussou E, Valle-Oñate R, Weber U, Wei J, Sieper J. The development of Assessment of SpondyloArthritis international Society classification criteria for axial spondyloarthritis (part II): validation and final selection. *Ann Rheum Dis* 2009; **68**: 777-783 [PMID: 19297344 DOI: 10.1136/ard.2009.108233]
- 63 **Moll JM**, Wright V. New York clinical criteria for ankylosing spondylitis. A statistical evaluation. *Ann Rheum Dis* 1973; **32**: 354-363 [PMID: 4269429]
- 64 **Goie The HS**, Steven MM, van der Linden SM, Cats A. Evaluation of diagnostic criteria for ankylosing spondylitis: a comparison of the Rome, New York and modified New York criteria in patients with a positive clinical history screening test for ankylosing spondylitis. *Br J Rheumatol* 1985; **24**: 242-249 [PMID: 3160423]
- 65 **Song IH**, Sieper J, Rudwaleit M. Diagnosing early ankylosing spondylitis. *Curr Rheumatol Rep* 2007; **9**: 367-374 [PMID: 17915092]
- 66 **Rudwaleit M**, van der Heijde D, Khan MA, Braun J, Sieper J. How to diagnose axial spondyloarthritis early. *Ann Rheum Dis* 2004; **63**: 535-543 [PMID: 15082484 DOI: 10.1136/ard.2003.011247]
- 67 **Rudwaleit M**, Metter A, Listing J, Sieper J, Braun J. Inflammatory back pain in ankylosing spondylitis: a reassessment of the clinical history for application as classification and diagnostic criteria. *Arthritis Rheum* 2006; **54**: 569-578 [PMID: 16447233 DOI: 10.1002/art.21619]
- 68 **Mengshoel AM**. Life strain-related tiredness and illness-related fatigue in individuals with ankylosing spondylitis. *Arthritis Care Res (Hoboken)* 2010; **62**: 1272-1277 [PMID: 20506402 DOI: 10.1002/acr.20216]
- 69 **Sieper J**, van der Heijde D, Landewé R, Brandt J, Burgos-Vagas R, Collantes-Estevez E, Dijkman B, Dougados M, Khan MA, Leirisalo-Repo M, van der Linden S, Maksymowych WP, Mielants H, Olivieri I, Rudwaleit M. New criteria for inflammatory back pain in patients with chronic back pain: a real patient exercise by experts from the Assessment of SpondyloArthritis international Society (ASAS). *Ann Rheum Dis* 2009; **68**: 784-788 [PMID: 19147614 DOI: 10.1136/ard.2008.101501]
- 70 **Mold JW**, Holtzclaw BJ, McCarthy L. Night sweats: a systematic review of the literature. *J Am Board Fam Med* 2012; **25**: 878-893 [PMID: 23136329 DOI: 10.3122/jabfm.2012.06.120033]
- 71 **Cooksey R**, Brophy S, Gravenor MB, Brooks CJ, Burrows CL, Siebert S. Frequency and characteristics of disease flares in ankylosing spondylitis. *Rheumatology (Oxford)* 2010; **49**: 929-932 [PMID: 20123954 DOI: 10.1093/rheumatology/kep435]
- 72 **Spoorenberg A**, van der Heijde D, de Klerk E, Dougados M, de Vlam K, Mielants H, van der Tempel H, van der Linden S. Relative value of erythrocyte sedimentation rate and C-reactive protein in assessment of disease activity in ankylosing spondylitis. *J Rheumatol* 1999; **26**: 980-984 [PMID: 10229432]
- 73 **Braun J**, Sieper J, Bollow M. Imaging of sacroiliitis. *Clin Rheumatol* 2000; **19**: 51-57 [PMID: 10752500]
- 74 **Karasick D**, Schweitzer ME, Abidi NA, Cotler JM. Fractures of the vertebrae with spinal cord injuries in patients with ankylosing spondylitis: imaging findings. *AJR Am J Roentgenol* 1995; **165**: 1205-1208 [PMID: 7572504 DOI: 10.2214/ajr.165.5.7572504]
- 75 **Resnick D**. Diagnosis of Bone and Joint Disorders. Philadelphia, PA: WB Saunders, 2002
- 76 **Resnick D**, Niwayama G, Goergen TG. Comparison of radiographic abnormalities of the sacroiliac joint in degenerative disease and ankylosing spondylitis. *AJR Am J Roentgenol* 1977; **128**: 189-196 [PMID: 401599 DOI: 10.2214/ajr.128.2.189]
- 77 **Berens DL**. Roentgen features of ankylosing spondylitis. *Clin Orthop Relat Res* 1971; **74**: 20-33 [PMID: 5540400]
- 78 **Jacobson JA**, Girish G, Jiang Y, Resnick D. Radiographic evaluation of arthritis: inflammatory conditions. *Radiology* 2008; **248**: 378-389 [PMID: 18641245 DOI: 10.1148/radiol.2482062110]
- 79 **Vinson EN**, Major NM. MR imaging of ankylosing spondylitis. *Semin Musculoskelet Radiol* 2003; **7**: 103-113 [PMID: 12920648 DOI: 10.1055/s-2003-41344]
- 80 **Huerta-Sil G**, Casasola-Vargas JC, Londoño JD, Rivas-Ruiz R, Chávez J, Pacheco-Tena C, Cardiel MH, Vargas-Alarcón G, Burgos-Vargas R. Low grade radiographic sacroiliitis as prognostic factor in patients with undifferentiated spondyloarthritis fulfilling diagnostic criteria for ankylosing spondylitis throughout follow up. *Ann Rheum Dis* 2006; **65**: 642-646 [PMID: 16219705 DOI: 10.1136/ard.2005.043471]
- 81 **Geijer M**, Sihlbom H, Göthlin JH, Nordborg E. The role of CT in the diagnosis of sacro-iliitis. *Acta Radiol* 1998; **39**: 265-268 [PMID: 9571940]
- 82 **Tan S**, Yao J, Flynn JA, Yao L, Ward MM. Quantitative syndesmophyte measurement in ankylosing spondylitis using CT: longitudinal validity and sensitivity to change over 2 years. *Ann Rheum Dis* 2015; **74**: 437-443 [PMID: 24297375 DOI: 10.1136/annrheumdis-2013-203946]
- 83 **Huwart L**, Amoretti N. CT- and fluoroscopy-guided percutaneous screw fixation of a "carrot-stick" spinal fracture in an elderly man with ankylosing spondylitis. *Skeletal Radiol* 2013; **42**: 1767-1773 [PMID: 23842576 DOI: 10.1007/s00256-013-1684-6]
- 84 **Fan Chiang CY**, Tsai TT, Chen LH, Lai PL, Fu TS, Niu CC, Chen WJ. Computed tomography-based navigation-assisted pedicle screw insertion for thoracic and lumbar spine fractures. *Chang Gung Med J* 2012; **35**: 332-338 [PMID: 22913860]
- 85 **Roemer FW**, van Holsbeeck M, Genant HK. Musculoskeletal ultrasound in rheumatology: a radiologic perspective. *Arthritis Rheum* 2005; **53**: 491-493 [PMID: 16082632 DOI: 10.1002/art.21318]
- 86 **O'Shea F**, Salonen D, Inman R. The challenge of early diagnosis in ankylosing spondylitis. *J Rheumatol* 2007; **34**: 5-7 [PMID: 17216671]
- 87 **Klauser A**, Halpern EJ, Frauscher F, Gvozdic D, Duftner C,

- Springer P, Schirmer M. Inflammatory low back pain: high negative predictive value of contrast-enhanced color Doppler ultrasound in the detection of inflamed sacroiliac joints. *Arthritis Rheum* 2005; **53**: 440-444 [PMID: 15934066 DOI: 10.1002/art.21161]
- 88 **Mohammadi A**, Ghasemi-rad M, Aghdashi M, Mladkova N, Baradaransafa P. Evaluation of disease activity in ankylosing spondylitis; diagnostic value of color Doppler ultrasonography. *Skeletal Radiol* 2013; **42**: 219-224 [PMID: 22552315 DOI: 10.1007/s00256-012-1412-7]
- 89 **Unlü E**, Pamuk ON, Kahir N. Color and duplex Doppler sonography to detect sacroiliitis and spinal inflammation in ankylosing spondylitis. Can this method reveal response to anti-tumor necrosis factor therapy? *J Rheumatol* 2007; **34**: 110-116 [PMID: 17216679]
- 90 **Klauser AS**, De Zordo T, Bellmann-Weiler R, Feuchtnr GM, Sailer-Höck M, Sögner P, Gruber J. Feasibility of second-generation ultrasound contrast media in the detection of active sacroiliitis. *Arthritis Rheum* 2009; **61**: 909-916 [PMID: 19565547 DOI: 10.1002/art.24648]
- 91 **Balint PV**, Kane D, Wilson H, McInnes IB, Sturrock RD. Ultrasonography of enthesal insertions in the lower limb in spondyloarthropathy. *Ann Rheum Dis* 2002; **61**: 905-910 [PMID: 12228161]
- 92 **D'Agostino MA**, Said-Nahal R, Hacquard-Bouder C, Brasseur JL, Dougados M, Breban M. Assessment of peripheral enthesitis in the spondylarthropathies by ultrasonography combined with power Doppler: a cross-sectional study. *Arthritis Rheum* 2003; **48**: 523-533 [PMID: 12571863 DOI: 10.1002/art.10812]
- 93 **Fournié B**, Margarit-Coll N, Champetier de Ribes TL, Zabraniecki L, Jouan A, Vincent V, Chiavassa H, Sans N, Railhac JJ. Extrasynovial ultrasound abnormalities in the psoriatic finger. Prospective comparative power-doppler study versus rheumatoid arthritis. *Joint Bone Spine* 2006; **73**: 527-531 [PMID: 16942893 DOI: 10.1016/j.jbspin.2006.01.019]
- 94 **Kiris A**, Kaya A, Ozgocmen S, Kocakoc E. Assessment of enthesitis in ankylosing spondylitis by power Doppler ultrasonography. *Skeletal Radiol* 2006; **35**: 522-528 [PMID: 16470394 DOI: 10.1007/s00256-005-0071-3]
- 95 **Spadaro A**, Iagnocco A, Perrotta FM, Modesti M, Scarno A, Valesini G. Clinical and ultrasonography assessment of peripheral enthesitis in ankylosing spondylitis. *Rheumatology (Oxford)* 2011; **50**: 2080-2086 [PMID: 21875877 DOI: 10.1093/rheumatology/ker284]
- 96 **Pavy S**, Dermis E, Lavie F, Maillefert JF, Mariette X, Schaevebeke T, Cantagrel A, Claudepierre P, Flipo RM, Goupille P, Le Loet X, Saraux A, Tebib J, Wendling D, Combe B. Imaging for the diagnosis and follow-up of ankylosing spondylitis: development of recommendations for clinical practice based on published evidence and expert opinion. *Joint Bone Spine* 2007; **74**: 338-345 [PMID: 17591453 DOI: 10.1016/j.jbspin.2007.04.001]
- 97 **Gandjbakhch F**, Terslev L, Joshua F, Wakefield RJ, Naredo E, D'Agostino MA. Ultrasound in the evaluation of enthesitis: status and perspectives. *Arthritis Res Ther* 2011; **13**: R188 [PMID: 22093457 DOI: 10.1186/ar3516]
- 98 **Sari I**, Okan T, Akar S, Cece H, Altay C, Secil M, Birlik M, Onen F, Akkoc N. Impaired endothelial function in patients with ankylosing spondylitis. *Rheumatology (Oxford)* 2006; **45**: 283-286 [PMID: 16204374 DOI: 10.1093/rheumatology/kei145]
- 99 **Skare TL**, Verceze GC, Oliveira AA, Perreto S. Carotid intima-media thickness in spondyloarthritis patients. *Sao Paulo Med J* 2013; **131**: 100-105 [PMID: 23657512]
- 100 **Mathieu S**, Gossec L, Dougados M, Soubrier M. Cardiovascular profile in ankylosing spondylitis: a systematic review and meta-analysis. *Arthritis Care Res (Hoboken)* 2011; **63**: 557-563 [PMID: 20890982 DOI: 10.1002/acr.20364]
- 101 **Caliskan M**, Erdogan D, Gullu H, Yilmaz S, Gursay Y, Yildirim A, Yucel E, Muderrisoglu H. Impaired coronary microvascular and left ventricular diastolic functions in patients with ankylosing spondylitis. *Atherosclerosis* 2008; **196**: 306-312 [PMID: 17169363 DOI: 10.1016/j.atherosclerosis.2006.11.003]
- 102 **Yildirim A**, Aksoyok S, Calguneri M, Oto A, Kes S. Echocardiographic evidence of cardiac involvement in ankylosing spondylitis. *Clin Rheumatol* 2002; **21**: 129-134 [PMID: 12086163]
- 103 **O'Neill TW**, King G, Graham IM, Molony J, Bresnihan B. Echocardiographic abnormalities in ankylosing spondylitis. *Ann Rheum Dis* 1992; **51**: 652-654 [PMID: 1616332]
- 104 **Bulkley BH**, Roberts WC. Ankylosing spondylitis and aortic regurgitation. Description of the characteristic cardiovascular lesion from study of eight necropsy patients. *Circulation* 1973; **48**: 1014-1027 [PMID: 4751946]
- 105 **Davidson P**, Baggenstoss AH, Slocumb CH, Daugherty GW. Cardiac and aortic lesions in rheumatoid spondylitis. *Proc Staff Meet Mayo Clin* 1963; **38**: 427-435 [PMID: 14054646]
- 106 **Roldan CA**, Chavez J, Wiest PW, Qualls CR, Crawford MH. Aortic root disease and valve disease associated with ankylosing spondylitis. *J Am Coll Cardiol* 1998; **32**: 1397-1404 [PMID: 9809954]
- 107 **Alves MG**, Espirito-Santo J, Queiroz MV, Madeira H, Macieira-Coelho E. Cardiac alterations in ankylosing spondylitis. *Angiology* 1988; **39**: 567-571 [PMID: 3408021]
- 108 **Brunner F**, Kunz A, Weber U, Kissling R. Ankylosing spondylitis and heart abnormalities: do cardiac conduction disorders, valve regurgitation and diastolic dysfunction occur more often in male patients with diagnosed ankylosing spondylitis for over 15 years than in the normal population? *Clin Rheumatol* 2006; **25**: 24-29 [PMID: 16247583 DOI: 10.1007/s10067-005-1117-6]
- 109 **Thomas D**, Hill W, Geddes R, Sheppard M, Arnold J, Fritzsche J, Brooks PM. Early detection of aortic dilatation in ankylosing spondylitis using echocardiography. *Aust N Z J Med* 1982; **12**: 10-13 [PMID: 6952832]
- 110 **Tucker CR**, Fowles RE, Calin A, Popp RL. Aortitis in ankylosing spondylitis: early detection of aortic root abnormalities with two dimensional echocardiography. *Am J Cardiol* 1982; **49**: 680-686 [PMID: 7064818]
- 111 **Dik VK**, Peters MJ, Dijkman PA, Van der Weijden MA, De Vries MK, Dijkman BA, Van der Horst-Bruinsma IE, Nurmohamed MT. The relationship between disease-related characteristics and conduction disturbances in ankylosing spondylitis. *Scand J Rheumatol* 2010; **39**: 38-41 [PMID: 20132069 DOI: 10.3109/03009740903096101]
- 112 **Yildirim A**, Aksoyok S, Calguneri M, Aytemir K, Kabakci G, Ovunc K, Nazli N, Ozmen F, Oto A, Kes S. QT dispersion as a predictor of arrhythmic events in patients with ankylosing spondylitis. *Rheumatology (Oxford)* 2000; **39**: 875-879 [PMID: 10952742]
- 113 **Townend JN**, Emery P, Davies MK, Littler WA. Acute aortitis and aortic incompetence due to systemic rheumatological disorders. *Int J Cardiol* 1991; **33**: 253-258 [PMID: 1743786]
- 114 **Momeni M**, Taylor N, Tehrani M. Cardiopulmonary manifestations of ankylosing spondylitis. *Int J Rheumatol* 2011; **2011**: 728471 [PMID: 21547038 DOI: 10.1155/2011/728471]
- 115 **Moyssakis I**, Gialafos E, Vassiliou VA, Boki K, Votteas V, Sfakakis PP, Tzelepis GE. Myocardial performance and aortic elasticity are impaired in patients with ankylosing spondylitis. *Scand J Rheumatol* 2009; **38**: 216-221 [PMID: 19229673 DOI: 10.1080/0309740802474672]
- 116 **Peters MJ**, van der Horst-Bruinsma IE, Dijkman BA, Nurmohamed MT. Cardiovascular risk profile of patients with spondylarthropathies, particularly ankylosing spondylitis and psoriatic arthritis. *Semin Arthritis Rheum* 2004; **34**: 585-592 [PMID: 15609262]
- 117 **Han C**, Robinson DW, Hackett MV, Paramore LC, Fraeman KH, Bala MV. Cardiovascular disease and risk factors in patients with rheumatoid arthritis, psoriatic arthritis, and ankylosing spondylitis. *J Rheumatol* 2006; **33**: 2167-2172 [PMID: 16981296]
- 118 **Aydin SZ**, Karadag O, Filippucci E, Atagunduz P, Akdogan A, Kalyoncu U, Grassi W, Direskeneli H. Monitoring Achilles enthesitis in ankylosing spondylitis during TNF-alpha antagonist therapy: an ultrasound study. *Rheumatology (Oxford)* 2010; **49**: 578-582 [PMID: 20040527 DOI: 10.1093/rheumatology/kep410]
- 119 **Ozgocmen S**, Kiris A, Ardicoglu O, Kocakoc E, Kaya A.

- Glucocorticoid iontophoresis for Achilles tendon enthesitis in ankylosing spondylitis: significant response documented by power Doppler ultrasound. *Rheumatol Int* 2005; **25**: 158-160 [PMID: 15290088 DOI: 10.1007/s00296-004-0488-3]
- 120 **Stone M**, Salonen D, Lax M, Payne U, Lapp V, Inman R. Clinical and imaging correlates of response to treatment with infliximab in patients with ankylosing spondylitis. *J Rheumatol* 2001; **28**: 1605-1614 [PMID: 11469469]
 - 121 **Chary-Valckenaere I**, d'Agostino MA, Loeuille D. Role for imaging studies in ankylosing spondylitis. *Joint Bone Spine* 2011; **78**: 138-143 [PMID: 20851029 DOI: 10.1016/j.jbspin.2010.07.008]
 - 122 **Swen WA**, Jacobs JW, Neve WC, Bal D, Bijlsma JW. Is sonography performed by the rheumatologist as useful as arthrography executed by the radiologist for the assessment of full thickness rotator cuff tears? *J Rheumatol* 1998; **25**: 1800-1806 [PMID: 9733463]
 - 123 **Wakefield RJ**, Brown AK, O'Connor PJ, Karim Z, Grainger A, Emery P. Musculoskeletal ultrasonography: what is it and should training be compulsory for rheumatologists? *Rheumatology* (Oxford) 2004; **43**: 821-822 [PMID: 15173601 DOI: 10.1093/rheumatology/keh227]
 - 124 **Larché MJ**, McDonald-Blumer H, Bruns A, Roth J, Khy V, de Brum-Fernandes AJ, Wakefield RJ, Brown AK, Bykerk V. Utility and feasibility of musculoskeletal ultrasonography (MSK US) in rheumatology practice in Canada: needs assessment. *Clin Rheumatol* 2011; **30**: 1277-1283 [PMID: 21484225 DOI: 10.1007/s10067-011-1743-0]
 - 125 **Samuels J**, Abramson SB, Kaeley GS. The use of musculoskeletal ultrasound by rheumatologists in the United States. *Bull NYU Hosp Jt Dis* 2010; **68**: 292-298 [PMID: 21162707]
 - 126 **Kane D**, Grassi W, Sturrock R, Balint PV. Musculoskeletal ultrasound-a state of the art review in rheumatology. Part 2: Clinical indications for musculoskeletal ultrasound in rheumatology. *Rheumatology* (Oxford) 2004; **43**: 829-838 [PMID: 15161981 DOI: 10.1093/rheumatology/keh215]
 - 127 **Wakefield RJ**, Goh E, Conaghan PG, Karim Z, Emery P. Musculoskeletal ultrasonography in Europe: results of a rheumatologist-based survey at a EULAR meeting. *Rheumatology* (Oxford) 2003; **42**: 1251-1253 [PMID: 12810933 DOI: 10.1093/rheumatology/keh367]
 - 128 **Tins BJ**, Butler R. Imaging in rheumatology: reconciling radiology and rheumatology. *Insights Imaging* 2013; **4**: 799-810 [PMID: 24127271 DOI: 10.1007/s13244-013-0293-1]
 - 129 **Ostergaard M**, Poggenborg RP, Axelsen MB, Pedersen SJ. Magnetic resonance imaging in spondyloarthritis-how to quantify findings and measure response. *Best Pract Res Clin Rheumatol* 2010; **24**: 637-657 [PMID: 21035085 DOI: 10.1016/j.berh.2010.06.001]
 - 130 **Konca S**, Keskin D, Cılız D, Bodur H, Sakman B. Spinal inflammation by magnetic resonance imaging in patients with ankylosing spondylitis: association with disease activity and outcome parameters. *Rheumatol Int* 2012; **32**: 3765-3770 [PMID: 22159818 DOI: 10.1007/s00296-011-2248-5]
 - 131 **De Keyser F**, Van den Bosch F, Mielants H. Anti-TNF-alpha therapy in ankylosing spondylitis. *Cytokine* 2006; **33**: 294-298 [PMID: 16516484 DOI: 10.1016/j.cyto.2006.01.004]
 - 132 **Sengupta R**, Stone MA. The assessment of ankylosing spondylitis in clinical practice. *Nat Clin Pract Rheumatol* 2007; **3**: 496-503 [PMID: 17762848 DOI: 10.1038/ncprheum0591]
 - 133 **Sfikakis PP**. The first decade of biologic TNF antagonists in clinical practice: lessons learned, unresolved issues and future directions. *Curr Dir Autoimmun* 2010; **11**: 180-210 [PMID: 20173395 DOI: 10.1159/000289205]
 - 134 **Baji P**, Péntek M, Szántó S, Géher P, Gulácsi L, Balogh O, Brodsky V. Comparative efficacy and safety of biosimilar infliximab and other biological treatments in ankylosing spondylitis: systematic literature review and meta-analysis. *Eur J Health Econ* 2014; **15** Suppl 1: S45-S52 [PMID: 24832835 DOI: 10.1007/s10198-014-0593-5]
 - 135 **Wanders A**, Heijde DV, Landewé R, Béhier JM, Calin A, Olivieri I, Zeidler H, Dougados M. Nonsteroidal antiinflammatory drugs reduce radiographic progression in patients with ankylosing spondylitis: a randomized clinical trial. *Arthritis Rheum* 2005; **52**: 1756-1765 [PMID: 15934081 DOI: 10.1002/art.21054]
 - 136 **Dougados M**, Béhier JM, Jolchine I, Calin A, van der Heijde D, Olivieri I, Zeidler H, Herman H. Efficacy of celecoxib, a cyclooxygenase 2-specific inhibitor, in the treatment of ankylosing spondylitis: a six-week controlled study with comparison against placebo and against a conventional nonsteroidal antiinflammatory drug. *Arthritis Rheum* 2001; **44**: 180-185 [PMID: 11212158]
 - 137 **Kristensen LE**, Jakobsen AK, Askling J, Nilsson F, Jacobsson LT. Safety of Etoricoxib, Celecoxib, and Nonselective Nonsteroidal Antiinflammatory Drugs in Ankylosing Spondylitis and Other Spondyloarthritis Patients: A Swedish National Population-Based Cohort Study. *Arthritis Care Res* (Hoboken) 2015; **67**: 1137-1149 [PMID: 25623277 DOI: 10.1002/acr.22555]
 - 138 **Giannotti E**, Trainito S, Arioli G, Rucco V, Masiero S. Effects of physical therapy for the management of patients with ankylosing spondylitis in the biological era. *Clin Rheumatol* 2014; **33**: 1217-1230 [PMID: 24797772 DOI: 10.1007/s10067-014-2647-6]
 - 139 **Niedermann K**, Sidelnikov E, Muggli C, Dagfinrud H, Hermann M, Tamborini G, Ciurea A, Bischoff-Ferrari H. Effect of cardiovascular training on fitness and perceived disease activity in people with ankylosing spondylitis. *Arthritis Care Res* (Hoboken) 2013; **65**: 1844-1852 [PMID: 23836515 DOI: 10.1002/acr.22062]
 - 140 **Dundar U**, Solak O, Toktas H, Demirdal US, Subasi V, Kavuncu V, Evcik D. Effect of aquatic exercise on ankylosing spondylitis: a randomized controlled trial. *Rheumatol Int* 2014; **34**: 1505-1511 [PMID: 24626605 DOI: 10.1007/s00296-014-2980-8]
 - 141 **Aydemir K**, Tok F, Peker F, Safaz I, Taskayatan MA, Ozgul A. The effects of balneotherapy on disease activity, functional status, pulmonary function and quality of life in patients with ankylosing spondylitis. *Acta Reumatol Port* 2010; **35**: 441-446 [PMID: 21245812]
 - 142 **Masiero S**, Bonaldo L, Pigatto M, Lo Nigro A, Ramonda R, Punzi L. Rehabilitation treatment in patients with ankylosing spondylitis stabilized with tumor necrosis factor inhibitor therapy: a randomized controlled trial. *J Rheumatol* 2011; **38**: 1335-1342 [PMID: 21459942 DOI: 10.3899/jrheum.100987]
 - 143 **Gyurcsik Z**, Bodnár N, Szekanez Z, Szántó S. Treatment of ankylosing spondylitis with biologics and targeted physical therapy: positive effect on chest pain, diminished chest mobility, and respiratory function. *Z Rheumatol* 2013; **72**: 997-1004 [PMID: 23929243 DOI: 10.1007/s00393-013-1240-8]
 - 144 **Brophy S**, Davies H, Dennis MS, Cooksey R, Husain MJ, Irvine E, Siebert S. Fatigue in ankylosing spondylitis: treatment should focus on pain management. *Semin Arthritis Rheum* 2013; **42**: 361-367 [PMID: 22901458 DOI: 10.1016/j.semarthrit.2012.06.002]
 - 145 **Stockdale J**, Selfe J, Roddam H. An exploration of the impact of anti-TNF α medication on exercise behaviour in patients with ankylosing spondylitis. *Musculoskeletal Care* 2014; **12**: 150-159 [PMID: 24554566 DOI: 10.1002/msc.1068]
 - 146 **Smith-Petersen MN**, Larson CB, Aufranc OE. Osteotomy of the spine for correction of flexion deformity in rheumatoid arthritis. *Clin Orthop Relat Res* 1969; **66**: 6-9 [PMID: 5357786]
 - 147 **Van Royen BJ**, De Gast A. Lumbar osteotomy for correction of thoracolumbar kyphotic deformity in ankylosing spondylitis. A structured review of three methods of treatment. *Ann Rheum Dis* 1999; **58**: 399-406 [PMID: 10381482]
 - 148 **Simmons E**. Relation of vascular complication to the level of lumbar extension osteotomy in ankylosing spondylitis. 61st Annual Meeting of the American Academy of Orthopedic Surgeons. New Orleans, 1994
 - 149 **Scudese VA**, Calabro JJ. Vertebral wedge osteotomy. correction of rheumatoid (ankylosing) spondylitis. *JAMA* 1963; **186**: 627-631 [PMID: 14053367]
 - 150 **Arun R**, Dabke HV, Mehdian H. Comparison of three types of lumbar osteotomy for ankylosing spondylitis: a case series and evolution of a safe technique for instrumented reduction. *Eur Spine J* 2011; **20**: 2252-2260 [PMID: 21800034 DOI: 10.1007/

s00586-011-1894-3]

- 151 **Lu ML**, Tsai TT, Lai PL, Fu TS, Niu CC, Chen LH, Chen WJ. A retrospective study of treating thoracolumbar spine fractures in

ankylosing spondylitis. *Eur J Orthop Surg Traumatol* 2014; **24** Suppl 1: S117-S123 [PMID: 24306166 DOI: 10.1007/s00590-013-1375-y]

P-Reviewer: Essex MN, Sakkas L, Storto G **S-Editor:** Ji FF
L-Editor: A **E-Editor:** Wu HL



Imaging evaluation of traumatic thoracolumbar spine injuries: Radiological review

Shivanand Gamanagatti, Deepak Rathinam, Krithika Rangarajan, Atin Kumar, Kamran Farooque, Vijay Sharma

Shivanand Gamanagatti, Deepak Rathinam, Krithika Rangarajan, Atin Kumar, Department of Radiology, JPNA Trauma Center, All India Institute of Medical Sciences, Ansari Nagar, New Delhi 110029, India

Kamran Farooque, Vijay Sharma, Department of Orthopedics, JPNA Trauma Center, All India Institute of Medical Sciences, Ansari Nagar, New Delhi 110029, India

Author contributions: Gamanagatti S contributed to the conception, critical revision and image preparation; Rangarajan K helped with the article concept, revision literature search and image preparation; Rathinam D contributed towards article design, literature search, article drafting; Kumar A helped in images procurement, preparation and final approval of version of article to be published; Farooque K and Sharma V contributed in clinical perspective, revision of article and final approval.

Conflict-of-interest statement: The authors have nothing to disclose.

Open-Access: This article is an open-access article which was selected by an in-house editor and fully peer-reviewed by external reviewers. It is distributed in accordance with the Creative Commons Attribution Non Commercial (CC BY-NC 4.0) license, which permits others to distribute, remix, adapt, build upon this work non-commercially, and license their derivative works on different terms, provided the original work is properly cited and the use is non-commercial. See: <http://creativecommons.org/licenses/by-nc/4.0/>

Correspondence to: Dr. Shivanand Gamanagatti, Additional Professor, Department of Radiology, JPNA Trauma Center, All India Institute of Medical Sciences, Ansari Nagar, New Delhi 110029, India. shiv223@gmail.com
 Telephone: +91-11-26594889

Received: March 30, 2015
 Peer-review started: March 31, 2015
 First decision: April 27, 2015
 Revised: May 14, 2015
 Accepted: July 21, 2015
 Article in press: July 23, 2015
 Published online: September 28, 2015

Abstract

Spine fractures account for a large portion of musculoskeletal injuries worldwide. A classification of spine fractures is necessary in order to develop a common language for treatment indications and outcomes. Several classification systems have been developed based on injury anatomy or mechanisms of action, but they have demonstrated poor reliability, have yielded little prognostic information, and have not been widely used. For this reason, the Arbeitsgemeinschaft für Osteosynthesefragen (AO) committee has classified thoracolumbar spine injuries based on the pathomorphological criteria into 3 types (A: Compression; B: Distraction; C: Axial torque and rotational deformity). Each of these types is further divided into 3 groups and 3 subgroups reflecting progressive scale of morphological damage and the degree of instability. Because of its highly detailed sub classifications, the AO system has shown limited interobserver variability. It is similar to its predecessors in that it does not incorporate the patient's neurologic status. The need for a reliable, reproducible, clinically relevant, prognostic classification system with an optimal balance of ease of use and detail of injury description contributed to the development of a new classification system, the thoracolumbar injury classification and severity score (TLICS). The TLICS defines injury based on three clinical characteristics: injury morphology, integrity of the posterior ligamentous complex, and neurologic status of the patient. The severity score offers prognostic information and is helpful in decision making about surgical vs nonsurgical management.

Key words: Trauma; Spine; Thoracolumbar; Classification; Management

© The Author(s) 2015. Published by Baishideng Publishing Group Inc. All rights reserved.

Core tip: The thoracolumbar injury classification and

severity score (TLICS) is the recent thoracolumbar injury grading scale to combine injury morphology, evaluation of mechanical strength pertinent to the posterior ligamentous complex, and neurologic condition into a method efficient of directing injury management. The TLICS provides the best available predictor of surgical vs nonsurgical management. Radiologists should use the key components of the TLICS to analyze, evaluate, and report spine injuries.

Gamanagatti S, Rathinam D, Rangarajan K, Kumar A, Farooque K, Sharma V. Imaging evaluation of traumatic thoracolumbar spine injuries: Radiological review. *World J Radiol* 2015; 7(9): 253-265 Available from: URL: <http://www.wjgnet.com/1949-8470/full/v7/i9/253.htm> DOI: <http://dx.doi.org/10.4329/wjcr.v7.i9.253>

INTRODUCTION

Spinal injuries constitute a significant proportion of musculoskeletal injuries across the world. Nearly 75% to 90% of spinal fractures occur in the thoracic and lumbar regions, most commonly involving at the thoracolumbar junction (T10-L2)^[1-3]. Despite the high frequency of thoracolumbar fractures, there is no single definite consensus on classification and management of such injuries. An ideal classification system is one that is explanatory and analytical, is informal to learn and apply in medical practice, based on a naive algorithm with constant radiologic and clinical features. Furthermore, the classification must give information on severity and expected description of an injury configuration. Lastly, for injury prediction, the classification must help decision-making. Such a classification system would be instrumental clinical research. Numerous thoracolumbar spine injury classification methods have been established to direct clinical and surgical management^[4-6].

Historical perspective

Watson-Jones^[7] defined three patterns of spinal injury: Simple wedge fracture, comminuted fracture, and fracture-dislocation. This classification system was the first of its kind which served as a guide for treatment. This system proposed different reduction methods for the management of different spinal fractures. Chance^[8] described a special type of injury caused by forceful forward flexion. The flexion anteriorly was coupled with distraction injury at the level of posterior elements, and was also known as a seat-belt injury. This distraction injury is characterized by a compression fracture of the anterior part of the vertebral body, a transverse fracture line through the posterior part of the vertebral body which extends into the posterior elements of the spine. Nicoll^[9] reported a series of 166 thoracolumbar injuries in coal miners and categorized these fractures into following categories: (1) anterior wedge fractures;

(2) lateral wedge fractures; (3) fracture dislocations; and (4) isolated neural arch fractures. Nicoll, for the first time, defined stable vs unstable fractures based on the integrity of the interspinous ligament is a major determinant of stability. This served as a basis for subsequent classifications. Holdsworth^[10], described two-column theory. The anterior column comprises of anterior longitudinal ligament (ALL), body of the vertebra and the adjacent intervertebral disc and the posterior longitudinal ligament (PLL). The posterior column includes pedicles, facet joints, transverse processes, Ligamentum flavum, spinous processes and the interspinous and supraspinous ligaments. He also suggested that the posterior column is the major determinant of spinal stability. Kelly and Whiteside^[11] further added to a two-column theory of Holdsworth, described the anterior vertebral bodies as solid column and the neural arches as a hollow posterior column. They highlighted the significance of the posterior elements in the stability the spine, and also described that greater instability reflects more serious type of injury. Denis^[12] later described a three column theory and devised a sagittal profile of the spine into 3 columns: He added the middle column to the anterior and posterior columns described earlier. In this theory, the middle column, constituted by the posterior half of the vertebral body, the PLL, the posterior half of disc and the posterior annulus, is in the neutral axis of the spine.

The middle column is believed to contribute the maximum to mechanical stability and tolerate the maximum axial load during flexion and extension movement. The concept of middle column has introduced 2 distinct fracture types compression and burst fractures. Compression fractures involve only the anterior column whereas burst fractures involve both the anterior and the middle columns. A chance fracture is subsequently re-defined as a transverse injury that involving all anterior, middle and posterior columns^[13].

The AO classification^[14] was the next major development in spinal injury classification and uses the three column concept proposed by Denis^[12].

It categorizes thoracolumbar spinal injuries into three categories based on the patho-morphological criteria: compression injury (Group A), distraction injury (Group B), and translation or rotation injury (Group C), with up to nine subtypes in each category based on morphology, fracture site, osseous or ligamentous disruption, and direction of displacement. One of its principle rationales is that groups A through C represent a continuum of progressively increasing injury severity and instability, with a concomitant increasing likelihood of the need for surgical stabilization. The AO system emphasizes the importance of injuries to soft-tissue structures such as the posterior ligamentous complex, intervertebral discs, and anterior longitudinal ligament with respect to spine instability.

The most recent classification TLICS was developed by the Spine Trauma Study Group^[15]. According to this

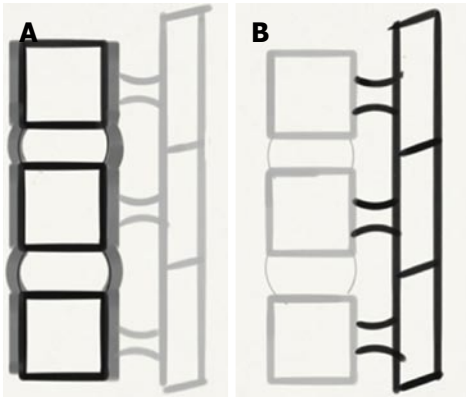


Figure 1 Functional anatomy of the spine (A) and schematic diagrams of the spine (B) depicting the 2 columns in the spine. Anterior portion of the functional unit (A) consist of two aligned vertebral bodies, the intervertebral disc, the anterior and posterior longitudinal ligaments. Posterior portion (B) consists of the vertebral arches, facet joints, posterior elements and posterior ligamentous complex.

system an injury severity score is calculated based on three components: Injury morphology, posterior ligamentous complex integrity, and neurologic status of the patient. In each category, a score is calculated with a smaller score assigned to an injury of lesser severity and a higher score is assigned to an injury of more severity requiring urgent management.

The total score serves as a guide to deciding surgical vs nonsurgical management. The TLICS emphasizes the role of magnetic resonance imaging in assessing PLC injury.

This article reviews the functional anatomy of the thoracolumbar spine, the AO and TLICS classification of spine injuries, highlights the CT and MR imaging appearances of spine injuries and a pattern-based approach for imaging interpretation and communication with spine surgeons.

FUNCTIONAL ANATOMY AND BIOMECHANICS OF SPINE

The two vertebrae and the interlinking soft tissues forms the functional component of the spine^[16]. The anterior portion of the functional unit contains two aligned vertebral bodies, the intervertebral disc, and the anterior and posterior longitudinal ligaments. The posterior portion consists of the vertebral arches, facet joints and posterior elements (Figure 1). The posterior ligamentous complex (PLC) is comprised of the supraspinous ligament, interspinous ligaments, articular facet capsules and ligamentum flavum (Figure 2), serves as posterior tension band of the spinal column. The supraspinous ligament extends from C7 to the sacrum, connecting the tips of the spinous processes. The interspinous ligaments are membranous structures, which are fragile and thin, that connect the adjacent spinous processes. Both the supraspinous and interspinous ligaments have a high collagen content, and their high tensile strength

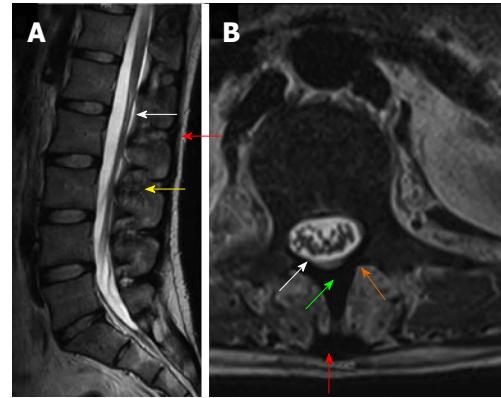


Figure 2 Magnetic resonance anatomy of the spine. T2 weighted sagittal magnetic resonance (MR) image (A) and T2 weighted axial MR image (B) show posterior ligamentous complex with ligamentum flavum (white arrow), interspinous ligament (yellow arrow) supraspinous ligament (red arrow), spinous process (green arrow) and lamina (orange arrow).

limits flexion of the spine^[16]. The ligamentum flavum is a thick broad structure that connects the laminae of the adjacent vertebrae. It has high elastin content and exerts a contractile force on the vertebral arches when it is elongated during flexion. The contractile force of the ligamentum flavum presses the vertebrae together and keeps them aligned^[17]. The facet joints are continuations of the laminae and are covered with hyaline cartilage on their articulating surfaces. They are the primary elements that act against rotational or torsional forces. In active extension, the facets function as a fulcrum, thereby reducing the load on the anterior column^[17,18]. Axial loading is supported primarily by the vertebral bodies and intervertebral discs^[16]. Because the axis of rotation is immediately anterior to or just within the anterior half of the vertebral body in the erect posture, there is a constant counterbalancing of the posterior ligament and erector spinae muscle forces at rest and at motion to resist compressive forces on the vertebral bodies^[19].

AO CLASSIFICATION

AO classifies thoracolumbar spine injuries into three categories based on the mechanical forces causing these injuries (Figures 3 and 4): (1) type A: Compressive force results in compression and burst injuries; (2) type B: Distraction (tensile) force results in transverse disruption injuries; and (3) type C: Axial torque forces results in translation or rotation injuries.

These three types (A, B, C) are further classified into 3 divisions and 3 subdivisions arranged in an increasing scale of morphological damage and instability (Tables 1-3).

Type A injuries involve the vertebral body. No or insignificant injury to posterior column is noted

Type B injuries indicate transverse disruptions with increase of the distance between adjacent vertebrae. In B1 and B2 the distance between posterior elements increases and in B3 distance between anterior vertebral

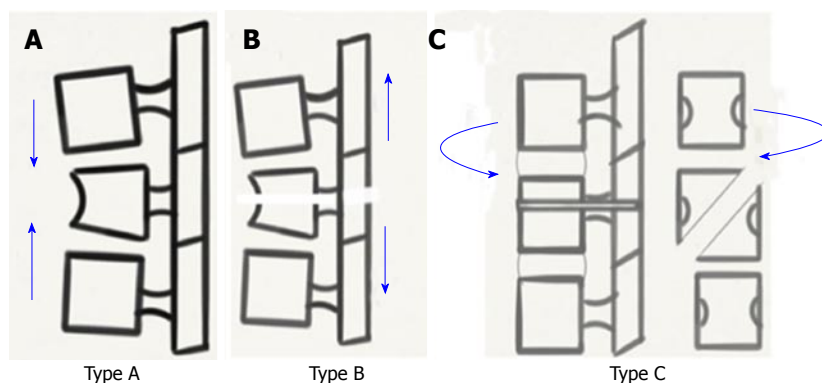


Figure 3 Biomechanics of spinal injury - AO classification. A-C: Schematic diagrams depicting compression (type A), distraction (type B) and Rotation (type C) injuries.

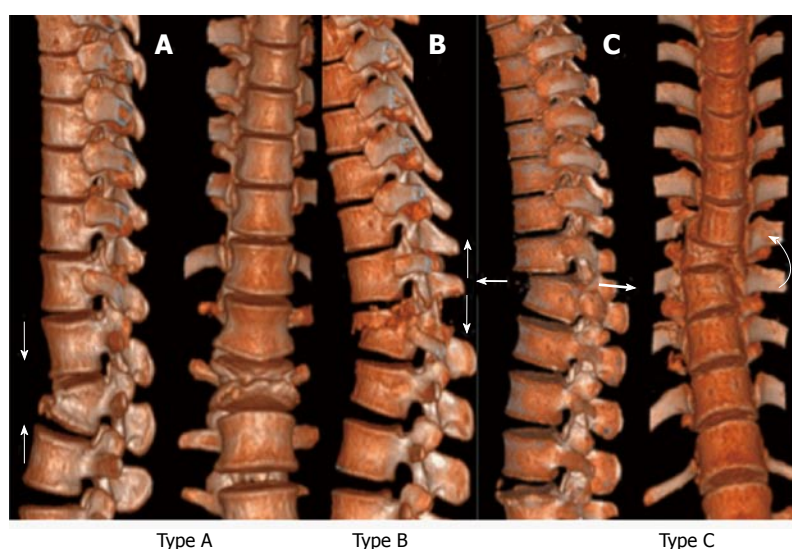


Figure 4 Biomechanics of spinal injury - AO classification. A-C: Computed tomography Volume rendered images depict compression (type A), Distraction (type B) and Rotation (type C) type injuries.

elements increases. The B1 and B2 injuries are further sub grouped depending on the type of injury to the vertebral body.

Type C injury that results from axial torque, and is most frequently combined with either type A or B fractures. Therefore further subdivision of type C injuries depends on the associated type A/B subtype. While shear refers to force which is parallel to the surface in question, torsion refers to twisting force. Such shearing forces in association with twisting forces are also classified under type C category.

In general, type A fractures only affect a single column (anterior), where as type B and C fractures involve either two or all three columns.

Type A: Vertebral body compression

The axial compression with or without flexion injury affects practically solely the vertebral body. Common imaging findings comprise: (1) loss of height of anterior part of vertebral body; (2) at times decrease in height of the posterior wall of the vertebral body, if it is fractured; (3) increased horizontal distance between

pedicles due to a vertical split of the lamina; and (4) increased distance between spinous processes even if posterior wall is intact.

However, if the interspinous distance is considerably increased, it usually indicates that a posterior distraction injury is present. Additionally, although fracture fragments of the posterior wall may be displaced posteriorly into the spinal canal, no cranio-caudal migration or rotation of these fragments is seen. On a computed tomography (CT) scan, displaced fragment have sharp, dense, smooth posterior margin and indistinct anterior margin. Translational dislocation in the horizontal plane does not occur in type A injuries.

The type A1 (Figure 5) injuries are impaction fractures which results in deformity of the vertebral body due to compression of the cancellous bone. There is no fragmentation of bone. These fractures are associated with intact posterior column, and there is no narrowing of spinal canal, therefore neurological deficit is very rare. These are stable injuries.

The subgroup A.1.1 comprises impaction of endplates; A.1.2 is a wedge impaction fracture and A.1.3 is

Table 1 Subcategories of AO type A injury

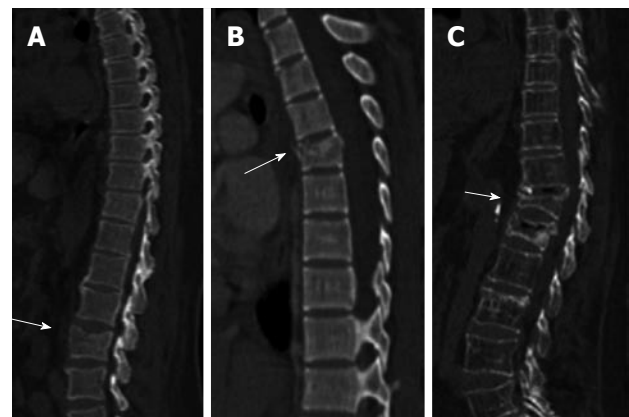
Type A: Vertebral body compression
A1. Impaction fractures
A1.1. Endplate impaction
A1.2. Wedge impaction fractures
A1.2.1. Superior wedge impaction fracture
A1.2.2. Lateral wedge impaction fracture
A1.2.3. Inferior wedge impaction fracture
A1.3. Vertebral body collapse
A2. Split fractures
A2.1. Sagittal split fracture
A2.2. Coronal split fracture
A2.3. Pincer fracture
A3. Burst fractures
A3.1. Incomplete burst fracture
A3.1.1. Superior incomplete burst fracture
A3.1.2. Lateral incomplete burst fracture
A3.1.3. Inferior incomplete burst fracture
A3.2. Burst-split fracture
A3.2.1. Superior burst-split fracture
A3.2.2. Lateral burst-split fracture
A3.2.3. Inferior burst-split fracture
A3.3. Complete burst fracture
A3.3.1. Pincer burst fracture
A3.3.2. Complete flexion burst fracture
A3.3.3. Complete axial burst fracture

Table 2 Subcategories of AO type B injury

Type B: Anterior and posterior element injury with distraction
B1. Posterior disruption predominantly ligamentous (flexion-distraction injury)
B1.1. With transverse disruption of the disc
B1.1.1. Flexion-subluxation
B1.1.2. Anterior dislocation
B1.1.3. Flexion-subluxation/ anterior dislocation with fracture of the articular processes
B1.2. With type A fracture of the vertebral body
B1.2.1. Flexion-subluxation + type A fracture
B1.2.2. Anterior dislocation + type A fracture
B1.2.3. Flexion-subluxation/ anterior dislocation with fracture of the articular processes + type A fracture
B2. Posterior disruption predominantly osseous (flexion-distraction injury)
B2.1. Transverse bicolonn fracture
B2.2. With transverse disruption of the disc
B2.2.1. Disruption through the pedicle and disc
B2.2.2. Disruption through the parsinterarticularis and disc (flexion-spondylolysis)
B2.3. With type A fracture of the vertebral body
B2.3.1. Fracture through the pedicle + type A fracture
B2.3.2. Fracture through the parsinterarticularis (flexion-spondylolysis) + type A fracture
B3. Anterior disruption through the disc (hyperextension-shear injury)
B3.1. Hyperextension-subluxations
B3.1.1. Without injury of the posterior column
B3.1.2. With injury of the posterior column
B3.2. Hyperextension-spondylolysis
B3.3. Posterior dislocation

Table 3 Subcategories of AO type C injury

Type C: Anterior and posterior element injury with rotation
C1. Type A injuries with rotation (compression injuries with rotation)
C1.1. Rotational wedge fracture
C1.2. Rotational split fractures
C1.2.1. Rotational sagittal split fracture
C1.2.2. Rotational coronal split fracture
C1.2.3. Rotational pincer fracture
C1.2.4. Vertebral body separation
C1.3. Rotational burst fractures
C1.3.1. Incomplete rotational burst fractures
C1.3.2. Rotational burst-split fracture
C1.3.3. Complete rotational burst fracture
C2. Type B injuries with rotation (flexion-distraction injuries with rotation)
C2.1. B1 injuries with rotation (flexion-distraction injuries with rotation)
C2.1.1. Rotational flexion subluxation
C2.1.2. Rotational flexion subluxation with unilateral articular process fracture
C2.1.3. Unilateral dislocation
C2.1.4. Rotational anterior dislocation without/with fracture of articular processes
C2.1.5. Rotational flexion subluxation without/with unilateral articular process + type A fracture
C2.1.6. Unilateral dislocation + type A fracture
C2.1.7. Rotational anterior dislocation without/with fracture of articular processes + type A fracture
C2.2. B2 injuries with rotation (flexion distraction injuries with rotation)
C2.2.1. Rotational transverse bicolonn fracture
C2.2.2. Unilateral flexion spondylolysis with disruption of the disc
C2.2.3. Unilateral flexion spondylolysis + type A fracture
C2.3. B3 injuries with rotation (hyperextension-shear injuries with rotation)
C2.3.1. Rotational hyperextension-subluxation without/with fracture of posterior vertebral elements
C2.3.2. Unilateral hyperextension-spondylolysis
C2.3.3. Posterior dislocation with rotation
C3. Rotational-shear injuries
C3.1. Slice fracture
C3.2. Oblique fracture

**Figure 5 Type A1 compression injuries.** Sagittal computed tomography images show (A) end plate impaction (A1.1), (B) wedge impaction (A1.2), and (C) corpus collapse (A1.3).

a vertebral body collapse in osteoporotic spines.

The type A2 (Figure 6) injuries result from splitting of the vertebral body having either a sagittal split (A 2.1), a coronal split fracture (A 2.2) or may have disc material entrapped within (pincer) (A2.3). Neurological deficit is

uncommon and posterior column is intact.

The highest frequency and severity among type A fractures is that of burst sub-type of fractures, *i.e.*, A3-lesion (Figure 7) with the subgroups of A 3.1 (incomplete), A 3.2 (burst split) and A 3.3 (complete) burst

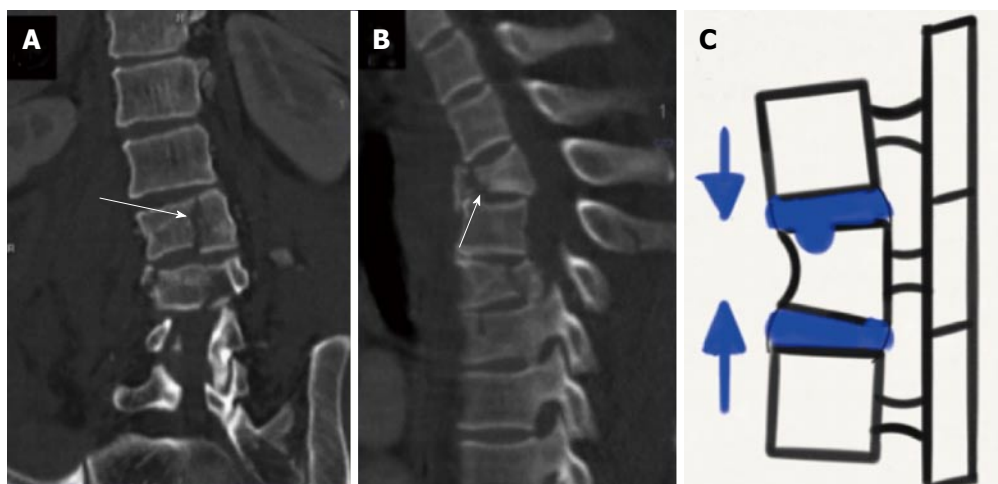


Figure 6 Type A2 compression injuries. Coronal computed tomography (CT) image (A), sagittal CT image (B) and schematic diagram (C) show (A) sagittal split (A2.1), (B) coronal split (A2.2) and (C) pincer type injury (A2.3).

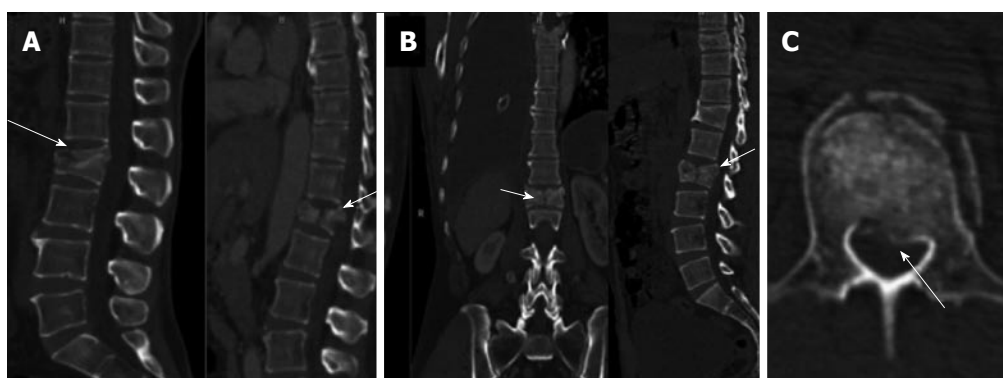


Figure 7 Type A3 compression injuries-burst fractures. Sagittal computed tomography (CT) image (A), sagittal and coronal CT images (B), sagittal and axial CT images (C) show (A) incomplete burst (A3.1) (B) burst-split (A3.2) and (C) retropulsion of fracture fragments suggesting a complete burst injury (A3.3).

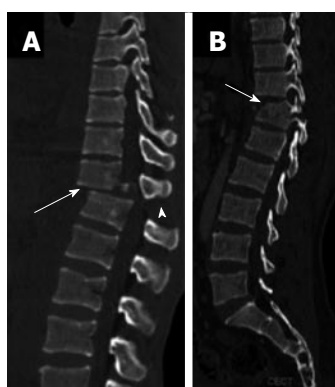


Figure 8 Type B1 flexion distraction injury. Sagittal computed tomography images show disruption through the posterior ligamentous complex (arrowhead) with either anterior disruption through the disc (arrow) constituting B1.1 injury (A) or a type A fracture anteriorly (arrow) constituting type B1.2 injury (B).

fractures. In burst fractures, vertebral body is partly or completely fragmented resulting in centrifugal spread and retropulsion of fragments into the spinal canal. However, PLC is intact. A vertical split through the lamina or spinous process is usually the only injury to

the arch, if present.

Type B: Injury to anterior and posterior elements with distraction

As mentioned earlier, type B injury is one in which there is transverse disruption with increase of the inter-vertebral distance either posteriorly (B1, B2) or anteriorly (B3). Type B1 and B2 indicate Flexion-distraction injuries where as type B3 is a hyperextension injury.

In B1 injuries, there is PLC disruption with subluxation/dislocation/fracture involving facet joints. B1 injuries are further subdivided into B1.1 where the anterior lesion is through soft tissues (through the disc) and B1.2 where the anterior lesion is bony (type A fracture) (Figure 8).

In B2 injuries (Figure 9), there is osseous posterior disruption, *i.e.*, fracture line traversing through the laminae and pedicles or the isthmi. B2 injuries are further subdivided (as in B1 lesions) into B2.2 where the anterior lesion is through soft tissues (disc) and B2.3 where the anterior lesion is bony (type A fracture). The severity of instability and neurological deficit are slightly higher than in B1 injuries except for the transverse



Figure 9 Type B2 flexion distraction injury. Sagittal computed tomography (CT) image (A), sagittal and coronal CT images (B) and sagittal and axial CT images (C) show transverse bicolumn fracture (B 2.1) [arrow in (A)], flexion-spondylolysis (B 2.2) [arrow in (B)] and (C) flexion-distraction with type A fracture (B 2.3) (arrow).

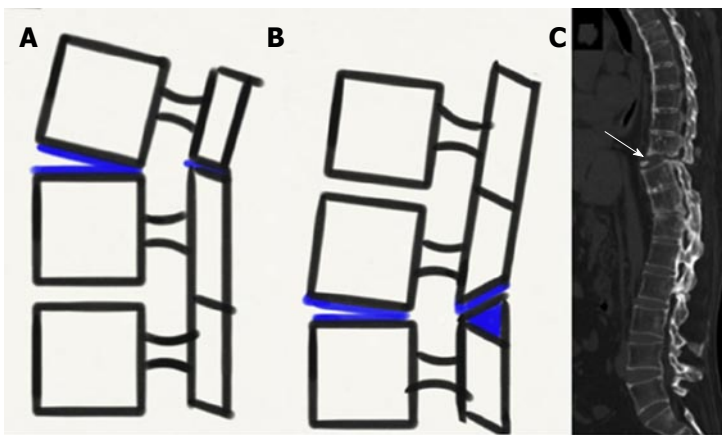


Figure 10 Types of hyperextension injuries (type B3). Schematic diagrams (A, B) and sagittal CT image (C) showing hyperextension with anterior subluxation (B3.1) (A), hyperextension with spondylolysis and anterior displacement (B3.2) (B) and hyperextension with posterior dislocation (B3.3) [arrow in (C)].

bicolumn fracture (B2.1).

Posterior disruption may involve the erector spinae muscles, fascia and even subcutaneous tissue in severe cases of B1 and B2 injuries.

The extent of instability varies from partial to complete, and there is a significantly higher incidence of neurological damage in comparison to type A injuries. Typical radiographic signs of B1 and B2 injuries include, kyphotic deformity with considerably increased interspinous distance; anterolisthesis; bilateral subluxation/dislocation/fracture involving facet joints or other posterior vertebral elements, avulsion fracture of the supraspinous ligament, anterior end plate shear chip fracture; avulsion of the posterior edge of the vertebral body.

When B1 and B2 injuries are seen in association with burst fractures, the fracture fragment is displaced posteriorly as well as cranially unlike in type A burst fractures. In contrast to type A burst fractures, posterior border is indistinct, and irregular than smooth, dense anterior border on CT scan. This sign is described as "inverse cortical sign".

In B3 injuries (Hyperextension type injury) (Figure 10), the disruption in the transverse plane begins anteriorly and may proceed posteriorly depending on the severity of injury. Anterior displacement may be seen in B3.1 and B3.2 injuries, and posterior

displacement is characteristic of B3.3 type injury.

Type C: Anterior and posterior element injuries with rotation

Type C injuries (Figures 11-13) are the most severe thoracolumbar injuries and are accompanied with the maximum degree of neurological deficit. Spinal injury is caused by compression of the spinal cord either by the fragments dislodged into the spinal canal with or without infringement of the spinal canal subsequent to translational displacement. Characteristic features include rotation of two vertebrae against each other, ALL and PLL disruption, disc disruption, articular process fracture (usually unilateral), fracture of transverse processes, rib fractures in proximity to their vertebral end, asymmetrical fractures of the neural arch, and irregular vertebral body fractures. Transverse process fractures are the major indicators of a rotational component of lumbar spine fractures. In presence of transverse process fractures, even if they appear isolated, one should always make a concentrated effort for identifying a concealed type injury. These typical findings of axial rotation are usually seen in association with either type A or type B lesions. The C1 lesion is a rotational injury combined with type A-lesion. The C2-lesion is axial rotation in combination with a type B injury whereas the C3-lesion is characterized by

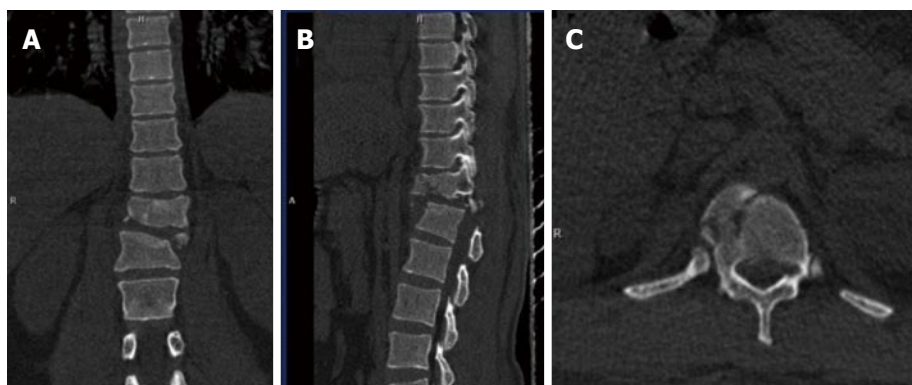


Figure 11 Type C1 rotational injuries. Coronal computed tomography (CT) reformat (A), sagittal CT reformat (B) and axial CT images (C) show C1 injury where rotation is superimposed on a type A injury.

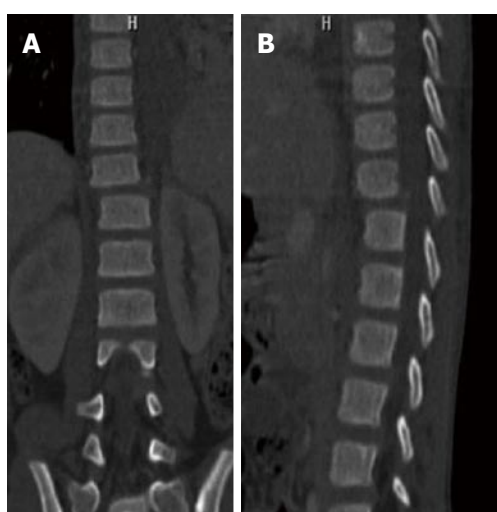


Figure 12 Type C2 rotational injuries. Coronal computed tomography (CT) image (A) and sagittal CT images (B) show C2 injury where rotation is superimposed on type B injury.

multilevel and shear injuries.

TLICS

The TLICS, developed by the Spine Trauma Study Group, is both a scoring and a classification system (Figure 14). The system is based on three injury categories: (1) injury morphology; (2) PLC integrity; and (3) involvement of the neuraxis^[15]. Within each category, subgroups are arranged from least to most significant, with a numeric value assigned to each injury pattern. Point values from these injury categories are totaled and a comprehensive severity score is calculated (Table 4). The TLICS helps in predicting biomechanical and neurologic spinal stability, thereby facilitating appropriate treatment recommendations. Joaquim *et al.*^[20], found correlation between the TLICS and the AO classification in a retrospective study.

INJURY MORPHOLOGY

The TLICS uses straightforward morphologic descrip-

tions based on findings at radiography, CT, or MR imaging. Compression injuries are described at imaging as a loss of vertebral body height or disruption of the endplate^[21]. Milder forms of compression injuries implicate only the anterior part of the vertebral body and increasing severity results in burst fractures. In TLICS injury morphology scoring, compression injury receives 1 point and burst fracture receives 2 points. Compression injuries with a coronal plane distortion of over 15° are allocated a score of 2 points. Translation injuries (3 points) are defined at imaging as a horizontal displacement or rotation of one vertebral body with respect to another. These injuries result from torsional and shear forces and are characterized by rotation of the spinous processes, unilateral or bilateral facet fracture-dislocation, and vertebral subluxation^[15]. Anteroposterior or sagittal translational instability is best seen on lateral radiographs or sagittal CT or MR images, while instability in the mediolateral or coronal plane is best seen on anteroposterior radiographs and coronal CT images. Distraction injuries (4 points) are identified at imaging as anatomic dissociation along the vertical axis. The disruption may involve anterior and posterior supporting ligaments, osseous elements, or a combination of both. When more than one single injury morphology is seen in combination, the single injury with the largest score is used. If the injury involves multiple levels of injury, each injury is scored independently^[15].

PLC INTEGRITY

The PLC serves as the tension band of the spinal column and protects the spine from excessive flexion, rotation, translation, and distraction. Once disrupted, the injured segment of the PLC usually requires surgical intervention because of its poor healing potential. Without surgery, an injured PLC can result in kyphotic progression and subsequent vertebral collapse^[22]. PLC integrity is categorized in the TLICS as intact, indeterminate, or disrupted. Disruption of the PLC is inferred on radiographs or CT images that show widening of the space between adjacent spinous processes, avulsion fracture of the superior or inferior aspects of contiguous

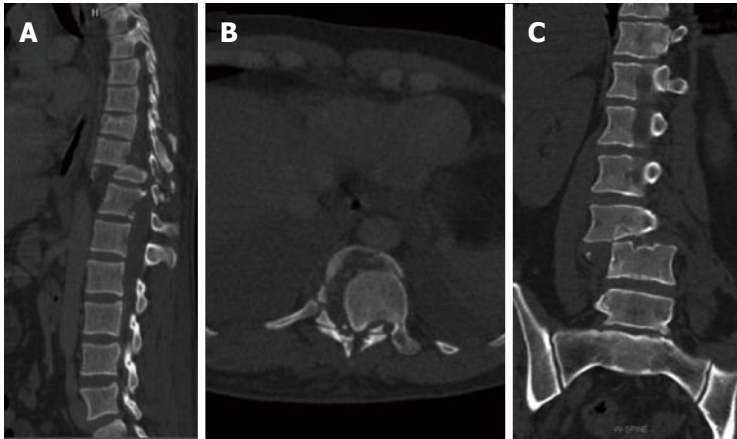


Figure 13 Type C3 rotational injury. Sagittal CT image (A), axial computed tomography (CT) image (B) and Coronal CT image (C) show shear slice fracture [C3.1 in (A) and (B)] and shear oblique fracture [C3.2 in (C)].

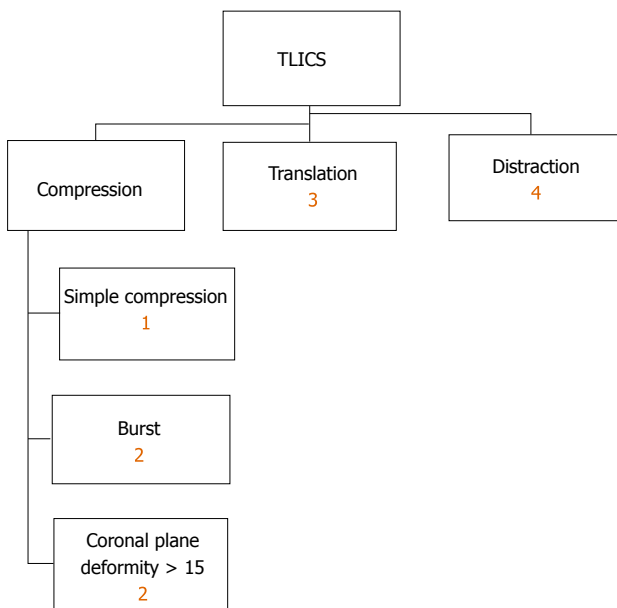


Figure 14 Thoracolumbar injury classification and severity score classification showing points allotted to each injury morphology. TLICS: Thoracolumbar injury classification and severity score.

spinous processes, widening of the facet joints, “naked” facet joints where the joint is uncovered, perched or dislocated facet joints, or vertebral body translation or rotation (Figure 15)^[15,23]. Unlike CT, MR imaging allows direct visualization of the PLC and thus is considered the imaging standard of reference for detecting PLC injury. The ligamentum flavum and supraspinous ligament are best seen on sagittal T1- or T2-weighted MR images as low-signal-intensity continuous black stripes (Figure 2). The interspinous ligaments are best evaluated with sagittal short inversion time inversion-recovery (STIR) or fat-saturated T2-weighted sequences^[24,25]. Axial fat-saturated T2-weighted MR images should be evaluated for facet capsular edema or fluid. The most reliable signs of PLC injury are disruption of the low-signal-intensity black stripe on sagittal T1- or T2-weighted MR images, a finding that indicates a supraspinous ligament or ligamentum flavum tear, and fluid in the facet capsules or edema in the interspinous region on fluid-sensitive MR images, findings that reflect a capsular or

interspinous ligament injury, respectively^[26]. An intact PLC is assigned a score of 0 points on the TLICS, and definite ligamentous injury is allocated 3 points. Isolated edema without clear ligament disruption is considered an indeterminate finding and is given a score of 2. A recent prospective analysis of MR imaging accuracy in diagnosis of traumatic PLC injuries has reported overall sensitivity and specificity of 91% and 100% respectively, with 100% accuracy in diagnosis of surgical fractures^[27]. MR imaging accuracy has been reported to be higher for detecting supraspinous ligament and ligamentum flavum injuries, where the grading is typically either “intact” or “disrupted”, and slightly lower for interspinous ligament and facet capsular injuries, which fall into the “indeterminate” category because they may include a finding of edema without clear disruption^[28].

NEUROLOGIC STATUS

The patient’s neurologic status is a critical indicator of the degree of spinal column injury. The TLICS defines five categories of neurologic status based on deficit severity and the patient’s recovery potential. Intact neurologic status at clinical examination is assigned a score of 0 points, 2 points are assigned to nerve injury or complete injury to the spinal cord. Contrary to expectation, a higher score (3 points) is allocated to incomplete spinal cord injury and cauda equina syndrome because patients with this type of injury may receive greater potential benefit from surgical decompression than patients with complete spinal cord injury or no initial neurologic injury^[4]. Although clinical neurologic status cannot be directly determined at imaging, a cord or nerve root injury should be evaluated on MR images.

TREATMENT APPROACH

The TLICS total score helps surgeons evaluate injury severity and decide between surgical and nonsurgical management (Table 5). A TLICS total score of 3 or lower generally indicates nonsurgical management with immobilization with brace and active patient mobilization. A score of 5 or higher warrants surgical intervention

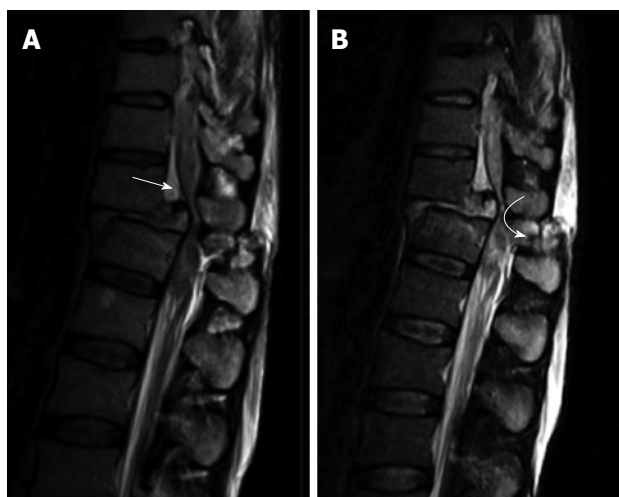


Figure 15 Magnetic resonance imaging in thoraco-lumbar injuries. T2 weighted sagittal magnetic resonance images showing cord compression (arrow in (A)) and disruption of Posterior Ligamentous Complex [curved arrow in (B)].

with correction of deformity, neurologic decompression if necessary, and stabilization. A score of 4 indicates an intermediate zone where surgical or nonsurgical treatment depends on the surgeon's clinical judgment and discretion^[22]. In addition to helping determine the need for surgical intervention, the TLICS can help guide the surgical approach. The surgical approach should be based primarily on the patient's neurologic status and the integrity of the PLC (Table 6). Patients with incomplete spinal cord injury with anterior compression will usually require an anterior surgical approach, while patients with an injured PLC will require posterior surgical stabilization. An anterior surgical approach allows more predictable and complete decompression of the neural elements, avoids damage to the posterior stabilizing structures, and reduces the risk of iatrogenic injury from posterior-approach manipulation of the dural sac^[29]. Patients with both a neurologic deficit and an injured PLC often require a combined anterior and posterior surgical approach.

IMAGING TECHNIQUES

Multidetector CT

Multidetector CT (MDCT), currently, is the imaging modality of choice, when there is a high or moderate index of suspicion of spine injury in a trauma setting. Radiographs are not usually obligatory prior to CT for acute spinal trauma, since a negative radiograph does not exclude getting a spine CT, if the clinical index is high. Recent literature has shown MDCT to be more accurate at identification of thoracolumbar injuries than plain X-ray^[30,31]. In many level I trauma centers, including our center as well, CT has replaced plain radiographs as the initial modality for evaluation of spinal trauma^[32]. CT images are acquired using thinnest collimation of 0.6 mm and images are reconstructed using both bone and soft tissue algorithms. Reformation

is done in sagittal and coronal planes. Images are viewed in all three planes and in both soft tissue and bone window on CT workstation for final analysis and reporting. Intravenous contrast administration is indicated if the CT is done for suspected injuries in other body parts like chest, abdomen and pelvis. In such conditions the coverage of those scans should be modified to include the spine, eliminating twofold irradiation. If patients had undergone CT scan for other body parts, and with raw data still available, then every effort should be made to reconstruct images from the raw data and create reformatted images of the spine. The most critical drawback of CT modality is the failure to recognize ligamentous and spinal cord injuries.

Magnetic resonance imaging

Magnetic resonance imaging (MRI) is the modality of choice for identification of injuries to soft tissue structures like posterior ligamentous complex, spinal cord, intervertebral disks and adjacent muscles. The MR protocol for spine trauma includes sagittal T1W, sagittal T2W, and sagittal STIR images, as well as localized axial imaging (T1W and Gradient Echo). STIR sequence helps in detection of soft tissue injuries where as gradient echo sequence helps in identifying hemorrhagic contusion of the cord, which has prognostic implication. Any patient believed to have spinal cord injury deserves MR imaging examination at earliest possible opportunity. MR imaging has the ability to identify the location, extent, severity of the cord lesion and also cause of cord compression. These information are very useful from management point view where in surgical intervention may prevent further worsening^[33]. Various types of spinal cord injuries seen include hemorrhagic contusion, non-hemorrhagic contusion, compression by epidural hematoma, a bone fragment or herniated disk material, and complete transection of the cord^[34]. Of the spinal hematomas, those in epidural locations are most common. Preoperative diagnostic localization of the hematoma informs the surgeon of the need to open the dura or arachnoid, particularly in cases complicated by the coexistence of epidural and subdural hematomas. MR imaging also helps in prognostication. Neurological recovery is generally poor in patients with hemorrhagic contusion or cord transection than in patients with simple cord edema or non-hemorrhagic contusion^[35,36].

Spinal trauma in children

Spine injuries are relatively uncommon with the frequency of 2% to 5% of all spine injuries^[37]. The flexibility of spine, the growth potential and other biological variations between children and adults manifest in distinctive fracture patterns. The notion of spinal cord injury without radiological abnormality in children is known by the abbreviation SCIWORA. New MR sequences such as diffusion-weighted MR imaging (DWI) and diffusion tensor imaging may help in predicting the severity of spinal cord injury and prognosticate the

Table 4 Thoracolumbar injury classification and severity score injury classification system

Injury category	Point value
Injury morphology	
Compression	1
Burst	2
Translation or rotation	3
Distraction	4
PLC Status	
Intact	0
Injury suspected or indeterminate	2
Injured	3
Neurologic status	
Intact	0
Nerve root involvement	2
Spinal cord or conus medullaris injury	
Incomplete	2
Complete	3
Cauda equina syndrome	3

TLICS: Thoracolumbar injury classification and severity score; PLC: Posterior ligamentous complex.

Table 5 Surgical vs non-surgical decision system according to thoracolumbar injury classification and severity score classification

TLICS score	Treatment recommendation
0-3	Nonsurgical
4	Nonsurgical or surgical
≥ 5	Surgical

TLICS: Thoracolumbar injury classification and severity score.

recovery from SCIWORA^[35].

REPORTING THORACOLUMBAR INJURIES

CT

A basic description of injury and extent includes the degree of comminution, percentage of vertebral height loss, retropulsion distance, percentage of canal compromise, and other contiguous or noncontiguous vertebral injuries. The anterior vertebral body compression percentage is the percentage of anterior vertebral body compression with respect to the average height of the anterior vertebral bodies immediately cephalad and caudal to the injury level^[38,39]. Osseous retropulsion or canal effacement should be reported with the percentage of spinal canal narrowing. Retropulsion is the distance of a line drawn between the posterior margins of the adjacent vertebral bodies and the most posterior margin of the bone fragment. The distance between the posterior canal border and the anterior canal border represents the sagittal canal diameter. The posterior canal border is the point of convergence of the left and right laminae at the midline of the spinous process. The anterior canal border is the posterior extent of the retropulsed midvertebral body. The proportion of

Table 6 Surgical approach based on posterior ligamentous complex integrity

Neurologic status	Surgical approach	
	Intact PLC	Disrupted PLC
Intact or nerve root injury	Posterior	Posterior
Incomplete cord injury	Anterior	Combined
Complete cord injury	Anterior or posterior	Combined or posterior

PLC: Posterior ligamentous complex.

Table 7 Check-list of findings to be reported on computed tomography^[32]

Injury morphology
Primary injury pattern (compression, burst, translation, flexion-distraction)
Basic morphologic description of lesion
Vertebral height loss (approximate percentage)
Retropulsion with central spinal canal narrowing (approximate percentage)
Other contiguous or noncontiguous injuries
Degree of kyphosis
PLC injury predictors
Facet joint widening
Interspinous distance widening
Spinous process avulsion fracture
Vertebral body subluxation or dislocation

PLC: Posterior ligamentous complex; CT: Computed tomography.

spinal canal compromise is estimated using the formula: $a = (1 - x/y) \times 100$, where a = percentage of spinal canal compromise, x = midsagittal diameter of the spinal canal at the level of injury, and y = mean of the midsagittal diameter of the spinal canal one segment above and one segment below the level of injury^[40]. PLC integrity is predicted based on CT findings of facet joint widening, interspinous distance widening, spinous process avulsion fracture, and vertebral body or facet subluxation or dislocation but it should be directly assessed with MRI if there is clinical concern^[41,42]. Table 7 represents the checklist of findings to be evaluated in CT.

MRI

The patient's PLC status should be reported as injured, intact, or indeterminate. Findings of potential spinal cord injury, epidural hematoma, and other ligamentous or disk injuries are also recorded. Although the radiology report may include the TLICS total score if there is clear imaging evidence of neurologic injury, generally the report will not include the total score if the patient's clinical neurologic status is unknown (Table 8).

CONCLUSION

The AO classification is the broadest and the most rational classification system devised till date, which represents a gradual progression of morphological injury using which the extent of instability is determined. A higher category within this system thus indicates more

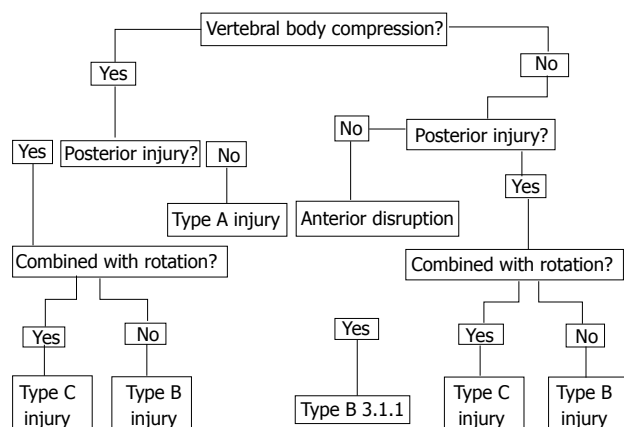


Figure 16 Simplified algorithms showing morphological classification of spinal fractures.

Table 8 Checklist of findings to be evaluated on magnetic resonance imaging

Osseous (similar to injury morphology noted at CT) and soft tissue injuries
PLC status (intact, indeterminate, or disrupted)
Supraspinous ligament
Ligamentum flavum
Interspinous ligaments
Facet capsule
Disks
Anterior and posterior longitudinal ligaments
Neurologic injuries
Spinal cord and conus medullaris
Cauda equina
Nerve root injury
Epidural hematoma

PLC: Posterior ligamentous complex; CT: Computed tomography.

severity, thus greater instability and therefore also gives an indication of the type of treatment and prognosis of the injury. This classification system can also be made concise without much loss of information, making it handy and easy to use in clinical practice. In short by facilitating recognition of a broad injury pattern, it provides an algorithm which serves as a useful guide in for radiologists/ clinicians in training (Figure 16).

The TLICS is the recent thoracolumbar injury grading scale to combine injury morphology, assessment of mechanical stability, and neurologic status into a single system which can guide injury management. The TLICS provides the best available predictor of surgical vs nonsurgical management. Radiologists should use the key components of the TLICS to analyze, evaluate, and report spine injuries and to help guide decisions about surgical management.

REFERENCES

- 1 **Hu R**, Mustard CA, Burns C. Epidemiology of incident spinal fracture in a complete population. *Spine* (Phila Pa 1976) 1996; **21**: 492-499 [PMID: 8658254 DOI: 10.1097/00007632-199602150-00016]
- 2 **Wood KB**, Buttermann GR, Phukan R, Harrod CC, Mehbod A, Shannon B, Bono CM, Harris MB. Operative compared with

nonoperative treatment of a thoracolumbar burst fracture without neurological deficit: a prospective randomized study with follow-up at sixteen to twenty-two years. *J Bone Joint Surg Am* 2015; **97**: 3-9 [PMID: 25568388 DOI: 10.2106/jbjs.n.00226]

- 3 **Gertzbein SD**. Scoliosis Research Society. Multicenter spine fracture study. *Spine* (Phila Pa 1976) 1992; **17**: 528-540 [PMID: 1621152 DOI: 10.1097/00007632-199205000-00010]
- 4 **Sethi MK**, Schoenfeld AJ, Bono CM, Harris MB. The evolution of thoracolumbar injury classification systems. *Spine J* 2009; **9**: 780-788 [PMID: 19482518 DOI: 10.1016/j.spinee.2009.04.003]
- 5 **Ferguson RL**, Allen BL. A mechanistic classification of thoracolumbar spine fractures. *Clin Orthop Relat Res* 1984; **(189)**: 77-88 [PMID: 6478706 DOI: 10.1097/00003086-198410000-00009]
- 6 **McAfee PC**, Yuan HA, Fredrickson BE, Lubicky JP. The value of computed tomography in thoracolumbar fractures. An analysis of one hundred consecutive cases and a new classification. *J Bone Joint Surg Am* 1983; **65**: 461-473 [PMID: 6833320]
- 7 **Watson-Jones R**. The Results of Postural Reduction of Fractures of the Spine. *J Bone Jt Surg* 1938; **20**: 567-586
- 8 **Chance GQ**. Note on a type of flexion fracture of the spine. *Br J Radiol* 1948; **21**: 452 [PMID: 18878306 DOI: 10.1259/0007-1285-21-249-452]
- 9 **Nicoll EA**. Fractures of the dorso-lumbar spine. *J Bone Joint Surg Br* 1949; **31B**: 376-394 [PMID: 18148776]
- 10 **Holdsworth F**. Fractures, dislocations, and fracture-dislocations of the spine. *J Bone Joint Surg Am* 1970; **52**: 1534-1551 [PMID: 5483077]
- 11 **Kelly RP**, Whitesides TE. Treatment of lumbodorsal fracture-dislocations. *Ann Surg* 1968; **167**: 705-717 [PMID: 5646292 DOI: 10.1097/0000658-196805000-00009]
- 12 **Denis F**. The three column spine and its significance in the classification of acute thoracolumbar spinal injuries. *Spine* (Phila Pa 1976) 1983; **8**: 817-831 [PMID: 6670016 DOI: 10.1097/00007632-198311000-00003]
- 13 **White AA**, Panjabi MM. The basic kinematics of the human spine. A review of past and current knowledge. *Spine* (Phila Pa 1976) 1978; **3**: 12-20 [PMID: 347598 DOI: 10.1097/00007632-19780300-0-00003]
- 14 **Magerl F**, Aebi M, Gertzbein SD, Harms J, Nazarian S. A comprehensive classification of thoracic and lumbar injuries. *Eur Spine J* 1994; **3**: 184-201 [PMID: 7866834 DOI: 10.1007/bf02221591]
- 15 **Vaccaro AR**, Lehman RA, Hurlbert RJ, Anderson PA, Harris M, Hedlund R, Harrop J, Dvorak M, Wood K, Fehlings MG, Fisher C, Zeiller SC, Anderson DG, Bono CM, Stock GH, Brown AK, Kuklo T, Oner FC. A new classification of thoracolumbar injuries: the importance of injury morphology, the integrity of the posterior ligamentous complex, and neurologic status. *Spine* (Phila Pa 1976) 2005; **30**: 2325-2333 [PMID: 16227897 DOI: 10.1097/01.brs.0000182986.43345.cb]
- 16 **DirSci MN**, Frankel VH. Basic Biomechanics of the Musculoskeletal System. 3 Sub ed. Philadelphia: Lippincott Williams and Wilkins, 2001: 496
- 17 **Audigé L**, Bhandari M, Hanson B, Kellam J. A concept for the validation of fracture classifications. *J Orthop Trauma* 2005; **19**: 401-406 [PMID: 16003200 DOI: 10.1097/01.bot.0000155310.04886.37]
- 18 **Leone A**, Guglielmi G, Cassar-Pullicino VN, Bonomo L. Lumbar intervertebral instability: a review. *Radiology* 2007; **245**: 62-77 [PMID: 17885181 DOI: 10.1148/radiol.2451051359]
- 19 **Asmussen E**, Klausen K. Form and function of the erect human spine. *Clin Orthop* 1962; **25**: 55-63 [PMID: 13965250 DOI: 10.1111/j.1748-1716.1965.tb04261.x]
- 20 **Joaquim AF**, Fernandes YB, Cavalcante RA, Frago RM, Honorato DC, Patel AA. Evaluation of the thoracolumbar injury classification system in thoracic and lumbar spinal trauma. *Spine* (Phila Pa 1976) 2011; **36**: 33-36 [PMID: 20479700 DOI: 10.1097/brs.0b013e3181c95047]
- 21 **Patel AA**, Dailey A, Brodke DS, Daubs M, Harrop J, Whang PG, Vaccaro AR. Thoracolumbar spine trauma classification: the Thoracolumbar Injury Classification and Severity Score system and case examples. *J Neurosurg Spine* 2009; **10**: 201-206 [PMID: 19482518 DOI: 10.1016/j.spinee.2009.04.003]

- 19320578 DOI: 10.3171/2008.12.spine08388]
- 22 **Rihn JA**, Anderson DT, Harris E, Lawrence J, Jonsson H, Wilsey J, Hurlbert RJ, Vaccaro AR. A review of the TLICS system: a novel, user-friendly thoracolumbar trauma classification system. *Acta Orthop* 2008; **79**: 461-466 [PMID: 18766477 DOI: 10.1080/17453670710015436]
 - 23 **Harris MB**, Stelly MV, Villarraga ML, Schroeder AC, Thomas KA. Modeling of the naked facet sign in the thoracolumbar spine. *J Spinal Disord* 2001; **14**: 252-258 [PMID: 11389377 DOI: 10.1097/00002517-200106000-00011]
 - 24 **Haba H**, Taneichi H, Kotani Y, Terae S, Abe S, Yoshikawa H, Abumi K, Minami A, Kaneda K. Diagnostic accuracy of magnetic resonance imaging for detecting posterior ligamentous complex injury associated with thoracic and lumbar fractures. *J Neurosurg* 2003; **99**: 20-26 [PMID: 12859054 DOI: 10.3171/spi.2003.99.1.0020]
 - 25 **Lee JY**, Vaccaro AR, Schweitzer KM, Lim MR, Baron EM, Rampersaud R, Oner FC, Hurlbert RJ, Hedlund R, Fehlings MG, Arnold P, Harrop J, Bono CM, Anderson PA, Patel A, Anderson DG, Harris MB. Assessment of injury to the thoracolumbar posterior ligamentous complex in the setting of normal-appearing plain radiography. *Spine J* 2007; **7**: 422-427 [PMID: 17630140 DOI: 10.1016/j.spinee.2006.07.014]
 - 26 **Pizones J**, Zúñiga L, Sánchez-Mariscal F, Alvarez P, Gómez-Rice A, Izquierdo E. MRI study of post-traumatic incompetence of posterior ligamentous complex: importance of the supraspinous ligament. Prospective study of 74 traumatic fractures. *Eur Spine J* 2012; **21**: 2222-2231 [PMID: 22722921 DOI: 10.1007/s00586-012-2403-z]
 - 27 **Pizones J**, Izquierdo E, Alvarez P, Sánchez-Mariscal F, Zúñiga L, Chimeno P, Benza E, Castillo E. Impact of magnetic resonance imaging on decision making for thoracolumbar traumatic fracture diagnosis and treatment. *Eur Spine J* 2011; **20** Suppl 3: 390-396 [PMID: 21779855 DOI: 10.1007/s00586-011-1913-4]
 - 28 **Pizones J**, Sánchez-Mariscal F, Zúñiga L, Álvarez P, Izquierdo E. Prospective analysis of magnetic resonance imaging accuracy in diagnosing traumatic injuries of the posterior ligamentous complex of the thoracolumbar spine. *Spine (Phila Pa 1976)* 2013; **38**: 745-751 [PMID: 23089929 DOI: 10.1097/BRS.0b013e31827934e4]
 - 29 **Wood KB**, Khanna G, Vaccaro AR, Arnold PM, Harris MB, Mehbod AA. Assessment of two thoracolumbar fracture classification systems as used by multiple surgeons. *J Bone Joint Surg Am* 2005; **87**: 1423-1429 [PMID: 15995107 DOI: 10.2106/jbjs.c.01530]
 - 30 **Hauser CJ**, Visvikis G, Hinrichs C, Eber CD, Cho K, Lavery RF, Livingston DH. Prospective validation of computed tomographic screening of the thoracolumbar spine in trauma. *J Trauma* 2003; **55**: 228-234; discussion 234-235 [PMID: 12913630 DOI: 10.1097/01.ta.0000076622.19246.cf]
 - 31 **Wintermark M**, Mouhsine E, Theumann N, Mordasini P, van Melle G, Leyvraz PF, Schnyder P. Thoracolumbar spine fractures in patients who have sustained severe trauma: depiction with multi-detector row CT. *Radiology* 2003; **227**: 681-689 [PMID: 12702827 DOI: 10.1148/radiol.2273020592]
 - 32 **Looby S**, Flanders A. Spine trauma. *Radiol Clin North Am* 2011; **49**: 129-163 [PMID: 21111133 DOI: 10.1016/j.rcl.2010.07.019]
 - 33 **Forster BB**, Koopmans RA. Magnetic resonance imaging of acute trauma of the cervical spine: spectrum of findings. *Can Assoc Radiol J* 1995; **46**: 168-173 [PMID: 7538874 DOI: 10.1016/0899-7071(96)80453-0]
 - 34 **Van Goethem JW**, Ozsarlak O, Parizel PM. Cervical spine fractures and soft tissue injuries. *JBR-BTR* 2003; **86**: 230-234 [PMID: 14527066]
 - 35 **Shen H**, Tang Y, Huang L, Yang R, Wu Y, Wang P, Shi Y, He X, Liu H, Ye J. Applications of diffusion-weighted MRI in thoracic spinal cord injury without radiographic abnormality. *Int Orthop* 2007; **31**: 375-383 [PMID: 16835743 DOI: 10.1007/s00264-006-0175-y]
 - 36 **Rajasekaran S**, Kanna RM, Shetty AP. Diffusion tensor imaging of the spinal cord and its clinical applications. *J Bone Joint Surg Br* 2012; **94**: 1024-1031 [PMID: 22844041 DOI: 10.1302/0301-620x.94b8.29618]
 - 37 **Reynolds R**. Pediatric spinal injury. *Curr Opin Pediatr* 2000; **12**: 67-71 [PMID: 10676777 DOI: 10.1097/00008480-200002000-00013]
 - 38 **Keynan O**, Fisher CG, Vaccaro A, Fehlings MG, Oner FC, Dietz J, Kwon B, Rampersaud R, Bono C, France J, Dvorak M. Radiographic measurement parameters in thoracolumbar fractures: a systematic review and consensus statement of the spine trauma study group. *Spine (Phila Pa 1976)* 2006; **31**: E156-E165 [PMID: 16508540 DOI: 10.1097/01.brs.0000201261.94907.0d]
 - 39 **Vaccaro AR**, Nachwalter RS, Klein GR, Sowards JM, Albert TJ, Garfin SR. The significance of thoracolumbar spinal canal size in spinal cord injury patients. *Spine (Phila Pa 1976)* 2001; **26**: 371-376 [PMID: 11224884 DOI: 10.1097/00007632-200102150-00013]
 - 40 **Mohanty SP**, Bhat NS, Abraham R, Ishwara Keerthi C. Neurological deficit and canal compromise in thoracolumbar and lumbar burst fractures. *J Orthop Surg (Hong Kong)* 2008; **16**: 20-23 [PMID: 18453652]
 - 41 **Khurana B**, Sheehan SE, Sodickson A, Bono CM, Harris MB. Traumatic thoracolumbar spine injuries: what the spine surgeon wants to know. *Radiographics* 2013; **33**: 2031-2046 [PMID: 24224597 DOI: 10.1148/rg.337135018]
 - 42 **Radcliff K**, Su BW, Kepler CK, Rubin T, Shimer AL, Rihn JA, Harrop JA, Albert TJ, Vaccaro AR. Correlation of posterior ligamentous complex injury and neurological injury to loss of vertebral body height, kyphosis, and canal compromise. *Spine (Phila Pa 1976)* 2012; **37**: 1142-1150 [PMID: 22146278 DOI: 10.1097/BRS.0b013e318240fed3]

P- Reviewer: Chen F, Razek AAKA, Tsushima Y **S- Editor:** Tian YL
L- Editor: A **E- Editor:** Wu HL



Radiation signature on exposed cells: Relevance in dose estimation

Venkatachalam Perumal, Tamizh Selvan Gnana Sekaran, Venkateswarlu Raavi, Safa Abdul Syed Basheerudeen, Karthik Kanagaraj, Amith Roy Chowdhury, Solomon FD Paul

Venkatachalam Perumal, Tamizh Selvan Gnana Sekaran, Venkateswarlu Raavi, Safa Abdul Syed Basheerudeen, Karthik Kanagaraj, Amith Roy Chowdhury, Solomon FD Paul, Department of Human Genetics, College of Biomedical Sciences, Technology and Research, Sri Ramachandra University, Porur, Chennai 600 116, India

Author contributions: Perumal V made the concept and manuscript preparation; Gnana Sekaran TS, Raavi V, Basheerudeen SAS, Kanagaraj K and Chowdhury AR contributed for review of literature on dicentric assay, micronucleus assay; FISH assay and γ -H2AX assay; Paul SFD provided the expert opinion and made the final editing.

Supported by Department of Science and Technology, Government of India, No. SR-SO/HS-127/2012; Defence Research and Development Organisation, Government of India, No. DLS/81/48222/LSRB-261; and Atomic Energy Regulatory Board, Government of India (AERB/CSRP/Proj. No.58/04/2014).

Conflict-of-interest statement: The authors declare no conflict of interest.

Open-Access: This article is an open-access article which was selected by an in-house editor and fully peer-reviewed by external reviewers. It is distributed in accordance with the Creative Commons Attribution Non Commercial (CC BY-NC 4.0) license, which permits others to distribute, remix, adapt, build upon this work non-commercially, and license their derivative works on different terms, provided the original work is properly cited and the use is non-commercial. See: <http://creativecommons.org/licenses/by-nc/4.0/>

Correspondence to: Venkatachalam Perumal, PhD, Professor, Department of Human Genetics, College of Biomedical Sciences, Technology and Research, Sri Ramachandra University, No.1, Ramachandra Nagar Porur, Chennai 600 116, India. venkip@yahoo.com
 Telephone: +91-44-24768027
 Fax: +91-44-24767008

Received: May 25, 2015
 Peer-review started: May 27, 2015

First decision: June 18, 2015
 Revised: July 3, 2015
 Accepted: July 29, 2015
 Article in press: August 3, 2015
 Published online: September 28, 2015

Abstract

The radiation is considered as a double edged sword, as its beneficial and detrimental effects have been demonstrated. The potential benefits are being exploited to its maximum by adopting safe handling of radionuclide stipulated by the regulatory agencies. While the occupational workers are monitored by personnel monitoring devices, for general publics, it is not a regular practice. However, it can be achieved by using biomarkers with a potential for the radiation triage and medical management. An ideal biomarker to adopt in those situations should be rapid, specific, sensitive, reproducible, and able to categorize the nature of exposure and could provide a reliable dose estimation irrespective of the time of the exposures. Since cytogenetic markers shown to have many advantages relatively than other markers, the origins of various chromosomal abnormalities induced by ionizing radiations along with dose-response curves generated in the laboratory are presented. Current status of the gold standard dicentric chromosome assay, micronucleus assay, translocation measurement by fluorescence *in-situ* hybridization and an emerging protein marker the γ -H2AX assay are discussed with our laboratory data. With the wide choice of methods, an appropriate assay can be employed based on the net.

Key words: Biomarker; Dicentric chromosomes; Micronucleus; Fluorescence *in-situ* hybridization

© The Author(s) 2015. Published by Baishideng Publishing Group Inc. All rights reserved.

Core tip: Of the well-established biomarker, the dicentric chromosome assay remains a gold standard, with sensitivity and specificity to radiation. In contrast, micronucleus is simple, rapid and potential for triage, though the sensitivity is less and not able to differentiate the partial body exposure from that of whole body exposure. The expensive fluorescence *in-situ* hybridization has the advantage that it can be employed in chronic and retrospective dose estimation. The γ -H2AX assay has a potential for triage despite the fact of limited stability. To conclude none of the assay could fulfil all the criteria of an ideal biomarker.

Perumal V, Gnana Sekaran TS, Raavi V, Basheerudeen SAS, Kanagaraj K, Chowdhury AR, Paul SFD. Radiation signature on exposed cells: Relevance in dose estimation. *World J Radiol* 2015; 7(9): 266-278. Available from: URL: <http://www.wjgnet.com/1949-8470/full/v7/i9/266.htm> DOI: <http://dx.doi.org/10.4329/wjr.v7.i9.266>

INTRODUCTION

Ever since the discovery of X-rays and radionuclide, their contribution towards the betterment of humankind is being augmented; thus nuclear technologies, which are finding increasing appliance in almost all walks of human endeavor, be it agriculture, medicine, power generation, research, *etc.* Similar to any other newer technologies, the nuclear technology is not entirely risk free. An increase in the concern of the accidental hazards linked to the use of ionizing radiation is currently being observed due to: (1) increased demand of radiation sources in several industrial applications, may leads to an higher probability of mishandling; (2) major contribution to the man-made sources of radiation, due to multiple procedures involving more time to treat complex and major disorder; and (3) growing nuclear threat, warfare and natural disaster like a recent events in Fukushima (Japan). At last, recently reported non-DNA targeted effects of ionizing radiations like bystander effects, genomic instability further complicates the risk for stochastic effects, have increased more concerns and fear among the public^[1]. The risk associated with a technology can be reduced to satisfactory levels (in terms of cost benefit ratios) by scrupulous observation of practices proven to be safe. Practices of safe handling of radionuclides incurring least radiation exposure have been well established. Regulatory agency, the International Commission on Radiological Protection has laid down the permissible limits of radiation exposure to radiation workers (20 mSv/year) and to the general public (1 mSv/year). The amount of radiation received by a radiation worker is monitored generally by physical dosimeters like thermoluminescence dosimeter and film badge. In contrast, another potential source of exposures to

the publics and radiation workers is due to unplanned activities and natural disaster; it is not a routine practice to wear the personnel monitoring devices by the exposed. Estimating the doses received during accidental conditions and management of exposed individuals, in the absence of personnel monitoring devices is an important issue towards medical management; biomarkers are proven to be a reliable tool for the above purpose.

SOURCES OF RADIATION EXPOSURE

Radioactive materials and radiation there from are a part of nature. Each one of us generally tends to associate radiation and radioactive materials not only with nuclear weapons and nuclear reactors alone. Several of the naturally occurring elements are radioactive, *e.g.*, uranium, thorium, radium, and potassium, which are widely distributed as constituents of the earth's crust. The content of radioactive material in the earth's crust varies from place to place and on average, radiation exposure due to this natural source of radiation is about 41% of the total^[2]. There are certain places in the world where the natural background radiation levels are 5 to 10 times higher than the average levels. In addition to radiation emitted by radioactive materials in the environment, man has also always been exposed to radiation of natural origin from outer space in the form of cosmic rays. Consistent with natural radiation, levels of exposure from both these sources differ from place to place. Cosmic rays are a form of extremely penetrating radiation coming from regions very far away in space. It was estimated that due to cosmic rays alone, the entire population on this earth receives about 16% of the total exposure from natural sources of radiation in a year. Cosmic ray contribution varies with altitude and latitude. While flying in aircraft, the passengers and crew receive about many fold greater exposure than on the ground. In recent times, the use of artificial sources of radiation has grown extensively. Such usage has contributed to human welfare in agriculture, medicine, industry and research. Of which the largest source of human-made radiation exposure are from medical procedures, which is around 0.4 mSv^[3]. Among the medical procedures, amount of exposures depends upon procedures and it is as low 0.2 mSv in chest X-ray examination to as high as 450 mSv among interventional procedures like heart catheterization before by-pass surgery. Recently, it has been shown that the annual per capita effective dose from diagnostic medical uses of radiation increased from 0.54 mSv to about 3.0 mSv to US population; the largest contribution and increases have come primarily from CT scanning and nuclear medicine^[4]. This has also resulted in a small addition to the already present radiation exposure from natural sources. The estimated worldwide annual per capita effective dose from natural background is 2.4 mSv (Table 1). Radiation exposure in principle has a potential for causing harm to the

Table 1 World wide annual per capita effective doses in year 2000 (UNESCAR 2000)

Source	Worldwide annual per capita effective dose (mSv)
Natural background	2.4
Diagnostic and medical examinations	0.4
Atmospheric testing	0.005
Chernobyl	0.002
Nuclear power production	0.0002

Table 2 A few characteristic features of established biomarkers

S. No	Parameter	Technique			
		DC	MN	FISH	γ -H2AX
1	Culture time (h)	48	72	48	Not applicable
2	Scoring speed (cells/d)	About 150	About 750	About 750	About 100/h
3	Type of aberrations detectable	Unstable	Unstable	Stable/unstable	Unstable
4	Period of detection after exposure (yr)	2-3	2-3	> 30	2-3 d
5	Cell type/quality	Metaphases/ good	BN cells/ good	Metaphases/ good	Interphase cells/ good
6	Baseline frequency	0.001	0.015	0.001	0.042
7	Sensitivity (Gy)	0.1	0.25	0.1	0.05

FISH: Fluorescence *in situ* hybridization; MN: Micronucleus; DC: Dicentric chromosome.

life. Therefore, excessive and unnecessary exposures to radiation must be avoided. Exposure to radiation of natural origin cannot be kept in line; even so, the exposure due to radiation of artificial origin can be promptly checked. The level and methods of control are matters of scientific and expert judging.

BIOMARKERS OF RADIATION EXPOSURE

Exposure to radiation induces certain changes on the proteins, carbohydrates, lipids, nucleic acids and gene expression in the exposed cell, which are collectively known as biomarkers. In particular, traversal of ionizing radiation in a cellular system can bring about a variety of changes such as base damages, alkylation, intercalation adduct formation, nucleotide modifications, single strand and double strand breaks in the deoxyribonucleic acid (DNA)^[5]. Those changes can result either due to direct deposition of energy on the nucleic acids (direct action) or can be mediated by the actions of free radicals released at some point in the interaction with water (indirect action) and membrane (lipid peroxidation) covers the cells^[6]. Any measurement

reflecting an interaction between a radiation exposures and biological system is defined as biomarkers^[7]. The biomarkers are classified based on the changes being looked into like chromosomal aberrations, alterations in cell number, change in an enzyme level and or activity, proteins, or expression of genes, etc^[8]. Of late based on the temporal parameters, it has been classified into markers of exposure, marker of susceptibility, markers of late effects and markers of persistent effects^[9]. Thus, the manifestations of any of those changes are resulted due to the traversal of ionization track and deposition of energy in exposed cells/tissues. A summary of biomarkers of radiation exposures listed in the literatures is given in Figure 1.

TECHNIQUES USED IN RADIATION BIODOSIMETRY

Radiation biodosimetry means, the quantification of the absorbed dose with the help of biological material obtained from an exposed individual. Of the various biomarkers, the extent of which can get expresses varied upon the quantum of exposure, absorbed dose, dose rate, energy of incident photons and radio-sensitivity of the exposed system. Similarly, time needed to express the changes and its stability in the exposed system depends upon those physical factors and the division kinetics of the cells^[1]. A large number of protein biomarkers are tested for radiation dosimetry; despite the fact those changes are generally accurate, but cannot be effectively used to quantify the dose, as the level of these changes comes back to normal within short duration after exposure. Alternate to the protein biomarkers, cytogenetic indicators remain stable for a long time and provided a reliable estimate of the dose (Table 2). Dose estimation using the cytogenetic analysis is based on the relationship between chromosome aberration frequency and the amount of absorbed dose. The preferred choice of sample to analyze aberration frequency is the blood lymphocytes as they are easy to collect, culture and processing for biodosimetric studies. Exposed lymphocytes show different types of chromosome aberrations like dicentric chromosome (DC), centric ring, acentrics and translocation, all of which can be related to dose. Low background frequency, specificity to ionizing radiation, a clear dose-effect relationship for high and low linear energy transfer (LET) radiation with different dose and dose rates, reproducibility and comparability of *in vitro* to *in vivo* results^[10] are several important biological parameters for reliable dose estimation. To keep above views in mind, we have established a laboratory to employ the DC, micronucleus (MN), Translocations and γ -H2AX assay for biodosimetry applications. Two decades experience of those methodology development, improvements and implementation of the assay for regular biodosimetry application is discussed in the present review along with current international status.

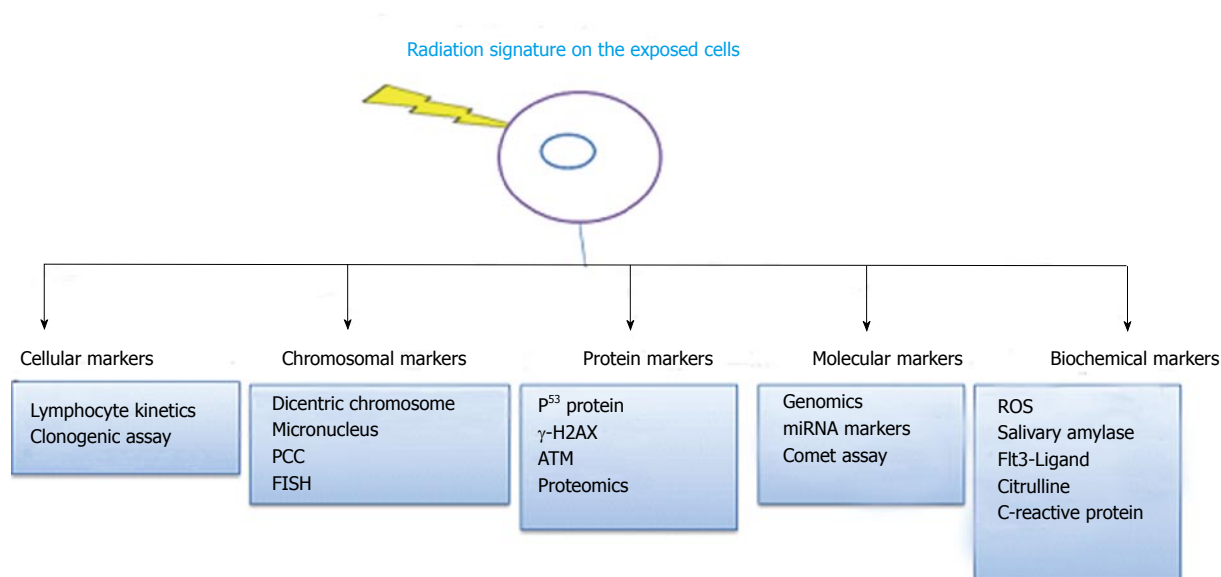


Figure 1 Various biomarkers of ionizing radiation exposure. FISH: Fluorescence *in situ* hybridization; PCC: Premature chromosome condensation; ROS: Reactive oxygen species; ATM: Ataxia telangiectasia mutated.

ORIGIN OF CHROMOSOMAL ABERRATIONS

In general, the chromosomes present in a cell are highly vibrant and undergoes extreme morphological changes at different phases within the cell cycle. When an ionization track travels along the cell nucleus, it can induce ionization on the DNA. Alternate, more than one track can pass through in different directions and induce much ionization within the same cell nucleus. Upon the energy deposition, it can induce many changes in the exposed cells and in turn the cells respond to those changes explicitly activation player molecules involved in check points activation, DNA repair and apoptosis^[11]. The end result and fate of the cells depends on the many physical parameters of the incident photon as well as the cellular biological machinery. The chromosome aberrations are formed predominantly due to the repair activation that results in perfect rejoining or mis-rejoin to form chromosome aberrations. Thus, the aberration produced depends on the number of breaks, chromatids and chromosomes as well as its proximity of induced breaks involved^[12]. The type, complexity and frequency of aberrations induced by radiations are diverse which are traditionally being in use to quantify and relate to the absorbed dose (Figure 2). Among chromosomal changes, they are named based on the methodology employed, or stain used (giemsa or fluorescence) to observe those changes or the end product (micronucleus, translocations)^[13].

CHROMOSOME ABERRATION ASSAY

Studies on chromosomal aberration in *Tradescantia* microspore with X-rays in the 1930s marked the birth of radiation Cytogenetics^[14]. In later years Sax^[14] constructed the dose-response curves for both X-ray and neutron and defined chromosome and chromatid

type of aberrations. In 1955, Revell^[15] proposed the concept of intra and inter chromosomal exchanges and indicated that two lesions are necessary to initiate the exchange followed by forming an exchange type aberration, and failure to complete the exchange will give rise to deletions. The discovery of the clastogenic effect of radiation, gave rise to developmental studies of the dose - effect relationship. In 1962, Lea *et al.*^[16] formulated an equation for the dose-response curve obtained with X-ray. He proposed that the pattern of chromosome aberrations follows a Poisson distribution. The pioneering work on cytogenetics, has evolved and come a long way and made possible determination of dose by monitoring the effect and brought into the study of cytogenetic indicators, to estimate radiation absorbed dose. The various biological indicators, which have been reviewed by several authors^[7,9,13].

Among the various indicators, DC aberration in the blood lymphocytes of exposed individual is the one which is mainly used for dose measurement^[3]. They are chromosomes with two centromeres, which differ from its normal structure with one centromere; complex exchanges even a chromosome with more than two centromeres also is possible. It means, formation of DC is a complex event, because it needs double strand breaks (DSB) in at least two different chromosomes, which should in close proximity to each other so that the probability is high to form abnormal structure^[17]. This technique, is well standardized as it is specific, and comparatively sensitive. However, each laboratory should generate its own dose-response curves, this includes the DC of the control population living in that area. It is because the baseline frequency greatly influences the co-efficient in a reference dose response curve^[18]. The background DC frequency obtained is 0.002 (0.001, from 8000 metaphases scored), which are comparable to the published values obtained within India^[19] and others^[3]. In order to estimate the dose

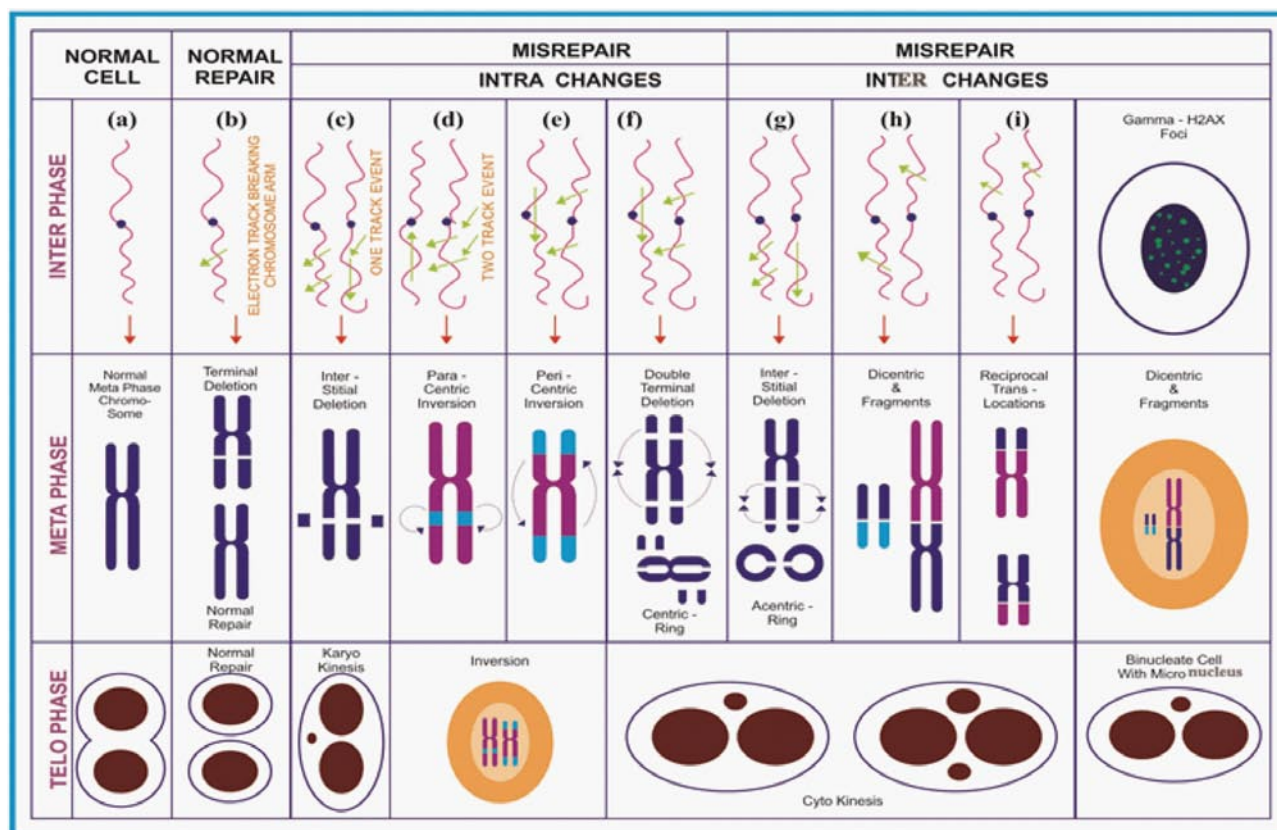


Figure 2 Diagrammatic illustration on the formation of ionizing radiation induced chromosome aberrations.

during accidental exposures the dose-response should be constructed from the result obtained with blood samples irradiated in less than 15 min with sufficient dose points. Then the exposed lymphocytes are cultured for 48 h under aseptic conditions to prepare a good quality metaphase chromosome and high mitotic index. Later stained slides are used to measure the number of DC at each dose and their frequency is used to construct a reference dose-response curve. Accurate identification of DC from that of twist or artefacts in poorly prepared metaphases are the challenges involved in this assay. The uncertainties can be reduced in combining centromere FISH technique^[20]. It has been shown that the number of DC obtained with a given amount of dose is the same when irradiated either *in vitro* or *in vivo* condition^[21]. Thus the dose-response curve constructed under *in vitro* condition is applicable for estimating the accidental radiation exposure to plant personnel. The dose response curve follows the equation $Y = C + \alpha D$ or $Y = C + \alpha D + \beta D^2$ depending upon the nature of radiation (Figure 3). The linear component (αD) often interpreted as the number of aberrations formed due to the traversal of single particle track and is expected to be independent of dose-rate. In alternate the dose squared (βD^2) term is formed due to the interaction between two independent particle tracks and its degree determined by the time interval between the two tracks. Thus a delay of time permits repair of damage thereby decreasing the yield of aberration involving interchanges between two chromosomes. In

the case of high LET radiation the dose-response curve mostly follows the equation $Y = C + \alpha D$. Representative images of normal metaphase and a metaphase with DC obtained from a human blood lymphocytes exposed to ^{60}Co - γ -irradiation and the co-efficient for the obtained dose response is given in Figure 4.

MN ASSAY

The chromosome fragments or whole chromosomes, which are failing to incorporate in the nuclei of daughter cells are known as micronuclei. Generally they are regular in shape with a similar staining intensity to that of daughter nuclei and within the cytoplasm of the daughter cells are called as micronuclei (Figure 5)^[22]. MN reflects chromosomal damage and is a useful index for monitoring environmental effects on genetic material in human cells^[23]. Due to the simplicity and the rapidity of scoring, this assay has shown promising potential in the triage medical management. However, due to background frequency of spontaneous MN frequency (0.002 to 0.036/cells) the sensitivity is 0.25 Gy^[3]. Matter *et al*^[24] coined the term MN based on its size and appearance. Fenech *et al*^[22] developed a simple, most effective and reliable methodology to select cells between first and second mitosis division using cytochalasin-B; it inhibits cell division at cytokinesis in a cycling cell and, results in the binucleated cells and named as cytokinesis blocked micronucleus (CBMN) assay. The CBMN assay in addition to measuring the

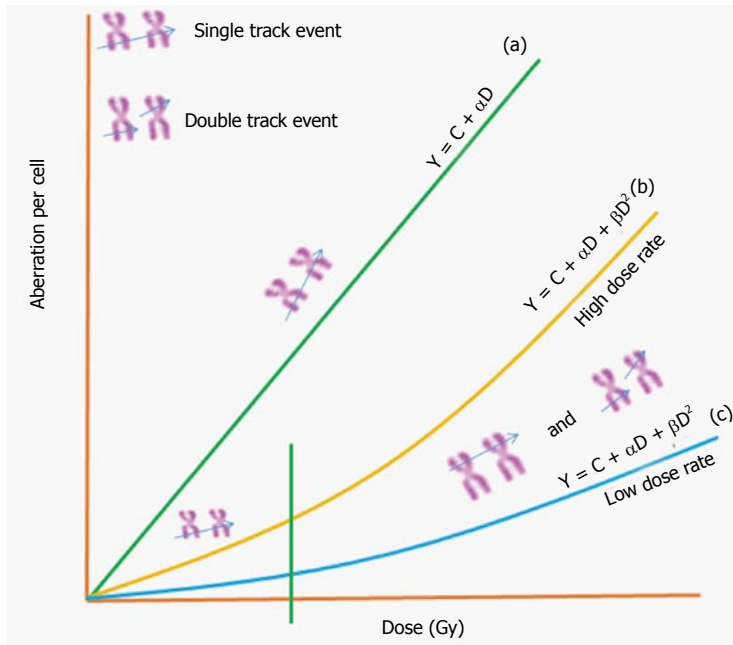


Figure 3 General dose response relationship for chromosome aberrations induced by different types of ionizing radiations.

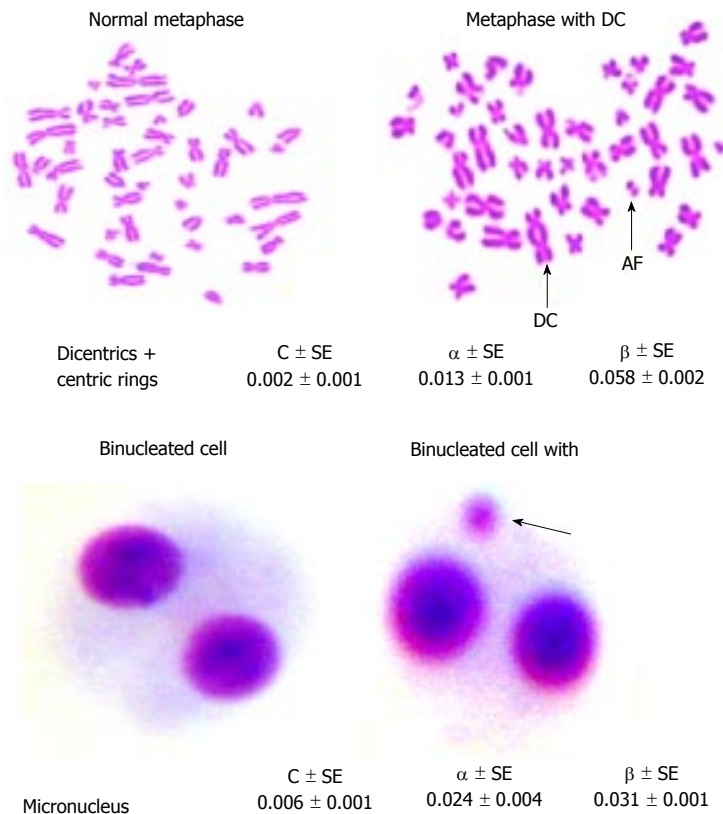


Figure 4 Metaphase chromosomes with (or) without dicentric chromosomes and dose response curve coefficients obtained from peripheral blood lymphocytes. AF: Acentric fragment; DC: Dicentric chromosome.

Figure 5 Binucleated cell with (or) without micronucleus and dose response curve coefficients obtained from peripheral blood lymphocytes.

MN, it can also be used to measure nuclear-plasmic bridges, nuclear buds, necrotic cells, apoptotic cell and nuclear division rate collectively known as cytome assay^[25]. Several studies have been carried out using the MN analysis *in vitro* and *in vivo*, for the purposes of biological dosimetry. A good correlation between the doses estimated from the MN frequency was observed in radiation workers^[26] and in thyroid cancer patients undergoing radioiodine treatment^[27]. A large volume of published reports for *in vitro* dose response curves is available^[19,28-30]. An important caution is that many

factors like age, genetic makeup and storage of blood samples could influence the dose estimation using the MN assay^[31]. Similar to DC many laboratories has established dose response curve to estimate the dose; it follows linear-quadratic pattern despite the fact that there are differences in the obtained co-efficients among the established laboratories.

FISH ASSAY

Despite the fact that scoring DC and MN is cost effective

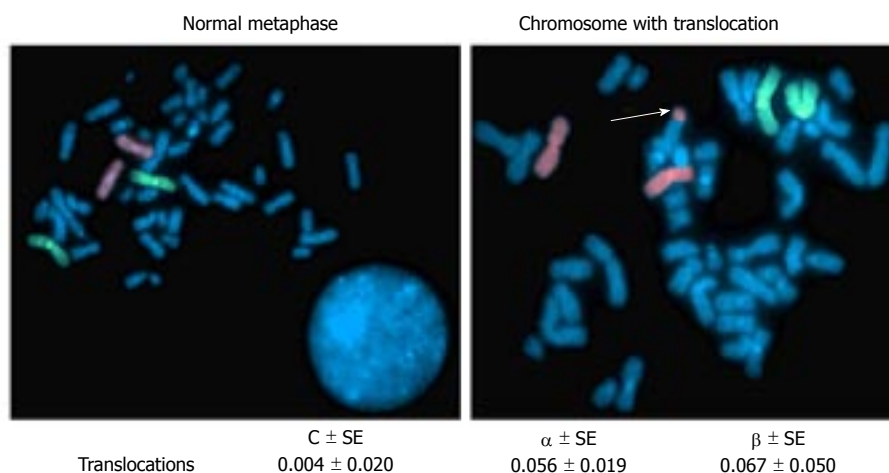


Figure 6 Metaphase chromosomes with (or) without translocation and dose response curve coefficients after whole chromosome painting.

and well established assays for biodosimetry, both DC and MN are of unstable type aberrations and can get eliminated in a cycling cell over a period of time. Whereas, stable aberrations like reciprocal translocation (RT), induced by radiation has been shown to remain in circulation for longer periods. Provided if the progenitor cells are also exposed^[3]. As it has been suggested that measurement of such RT may provide cumulative radiation exposure, we standardized FISH technique to score translocations (TL). This technique is based on the higher affinity among nucleotide bases in homologous sequences compared to non-homologous sequences. By using fluorescent labelled DNA probes, one could selectively paint a chromosome/set of chromosomes, which can be seen easily under fluorescence microscope. During hybridization the fluorescent labelled DNA probes bind to its complementary strand which helps in the detection of rearrangement, if any, which has taken place in these labelled chromosomes. The chromosomes which are not painted with fluorescent material are stained with different colors. The fluorescent labelled chromosome if undergone translocations will exhibit a bicolour and one can easily identify. Since the introduction of assays to measure RT, FISH have been pre-dominantly used in various laboratories^[32-39] because of its simplicity in scoring and rapidity. Generally, the dose was estimated by measuring the RT in painting few chromosomes and extrapolating to the whole genome translocation frequency; else if any exchanges between non-painted chromosomes go undetected. However, it was extrapolated to whole genome with assumptions that radiation induced break points and translocation formation are randomly distributed throughout the genome, frequency of translocation is directly proportional to the DNA content and size of chromosomes without any hotspots on selective chromosomes. However, literature evidenced that radiation induced break points are distributed randomly in A-bomb survivors^[40]. *In vitro* exposure as well as non-randomly^[41-43]. Many laboratories have established dose-response curves by a selective painting

of few chromosomes (Figure 6). Rapid developments in the probe labelling methodology, optics and imaging modalities, the assay has evolved in different directions like m-FISH, SKY-FISH, and m-band^[44] where exchanges involved in any chromosomes or regions within chromosomes can be identified easily similar to that, GTG-banding technique have been in use for the identification of aberrations in individual chromosomes^[45] as well as in entire genomes. It was an attractive option for many years back; however, RT measurements with latest FISH technology, and G-banding, in dosimetry is limited because of either time factor and/or cost factor. However, it can provide a true estimation of translocation frequency by analyzing the individual chromosomes for chronic dose estimation.

γ -H2AX ASSAY

Markers based on the chromosome abnormalities and/or gene mutations are suitable to quantify the residual damage and not the actual amount of damages induced due to exposure. This is for the reason that, to score the aberrations, the exposed cells have to be cultured, arrested in to suitable stage and then to score sufficient number of cells does extrapolate into the dose. Exposures of living organisms to radiation can induce assortment of DNA damages including DSB. Many molecules of histone H2AX at the broken site are rapidly phosphorylated on serine 139 in the C-terminus among the living organisms. In turn multiple factors involved in DNA repair and chromatin remodelling are assembled at the broken site and forms the γ -H2AX foci^[46]. The γ -H2AX are simply visualized with antibodies to γ -H2AX with each DSB yielding one focus. Currently, γ -H2AX foci frequency is measured by immunocytochemistry, Western blot analysis and single-well flow cytometry (Figure 7). Measurement of γ -H2AX foci from peripheral blood lymphocytes (PBL) is used as a prospective biomarker to assess the radiation dose^[47]. A dose-dependent increase and time-dependent reduction of γ -H2AX foci has been reported in cancer cells after

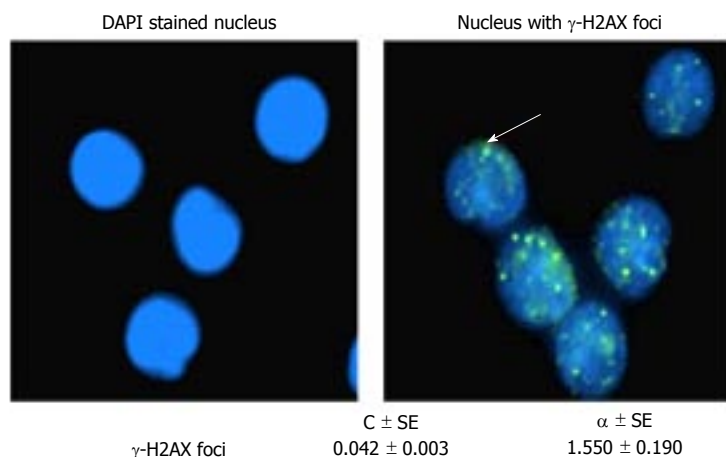


Figure 7 4',6-diamidino-2-phenylindole, dihydrochloride stained nucleus with (or) without γ -H2AX foci and their coefficients obtained from peripheral blood lymphocytes.

exposure to ionizing radiation, patients who underwent radiation therapy, and in personnel after computer tomography (CT) imaging^[48]. The assay was reported to distinguish partial and total body irradiation^[49]. Flow cytometry measurement of γ -H2AX fluorescence intensity suggests that more samples can be analyzed in a short duration with lower sensitivity when compared to foci counting using microscopy^[50].

In spite of rapid progress in technical development and advantages, variables like age^[51], smoking^[52], oxidative stress, inflammation^[53], heat^[54], genetic factors, etc., have been reported to influence the γ -H2AX foci levels. Inter-individual variability of γ -H2AX fluorescence intensity was observed in human PBL of healthy individuals^[55]. Consistent with cytogenetic abnormalities, baseline γ -H2AX foci has been reported have been shown wide inter-individual variation^[56,57]. Amusingly, though speed is an added advantage, a difference in γ -H2AX foci yields obtained from the same samples by different laboratories and methodical underestimation of doses was a major concern when using flow cytometry; variations in foci loss during shipment of blood samples, or variations in immunofluorescence staining quality were listed and should be minimized to reduce the uncertainties^[58]. It was also emphasized that one should not look upon any calibration curves for this assay as set in standard like that of DC and MN assays; as an alternative, the γ -H2AX foci assay should be frequently recalibrated to take into account any drift in foci yields, and protocols should be optimized to reduce variability and ensure consistency. The mean γ -H2AX foci frequency obtained from our laboratory by scoring 26400 cells from healthy subjects ($n = 130$) is 0.042 ± 0.001 (unpublished data) which is comparable to that of reported values; thus the mean yield of γ -H2AX \pm SD reported was 0.09 ± 0.05 with a range of 0.01 to 0.17 foci per lymphocyte^[59].

RECENT DEVELOPMENTS TOWARDS TRIAGE

Inter-laboratory comparisons

The preliminary dose estimation and segregation of

exposed and non-exposed individuals are the main step in the management of triage. Moreover the first responders also need to be monitored periodically, to ensure the dose levels they exposed during evacuation. In such scenario, to meet the demand alternative strategies is being developed as classical cytogenetic methods (DC and MN) by manual scoring is time consuming; sharing of the workload among the expert groups, automation of analytical methods, and early markers to ionizing radiation are the recent advancements in biodosimetry. Available literature has demonstrated ample evidences that many laboratories are well equipped and use more than one methodology to estimate the dose in an exposed individual. The scoring of DC from the PBL of individuals exposed to radiation remains the "gold standard" in biological dosimetry^[3]. However, it has its limitation in potential scenarios of radiation exposure resulting in mass casualties owing the time needed for analysis. Of late to handle mass radiation casualties, countries have developed competencies in biological dosimetry^[60]. In parallel to handle radiation triage, an inter-laboratory comparison exercise has been carried out among the established facility with a good sensitivity and minimize uncertainties in dose estimation^[61]. The International Atomic Energy Agency and International Organization for Standardization played a vital role and provided guidelines to achieve the above goal^[60]. As per the directions WHO a revised regulation in the field of radio nuclear incidents has been well established among the "BioDoseNet", connected laboratories^[62,63]. Such a networking and quality assurance in biodosimetry, is well established in the United States^[64], Canada^[65], Japan^[66], Europe^[67], Portuguese^[68] and India^[20,69].

Inter-laboratory comparisons and automation of MN scoring

Significant efforts were made to harmonize protocol to utilize simple and rapid scoring of MN as an alternative to manage large scale radiation accidents^[3]. To minimize the individual discrepancies in the scoring of MN, an intra and inter-laboratory exercise was carried out among 34 laboratories; however, it was emphasized

that it is paramount important to rectify scorers variation in analyzing the micro nucleated cells^[70] and this can be reduced minimally by an automation in scoring of MN as it reduces labor and individuals scoring variations in addition to enhancing throughput.

There are two different kinds of automated methods that are presently being used to analyze the MN are (1) flow cytometry^[71]; and (2) MN counting by image analysis^[72]. While, the common advantage of both the methods is fast acquisition and analysis of the data in less time, it was cautioned that sensitivity is a limitation in case of flow cytometry based scoring of MN due to unspecified debris^[73]. In spite of the potential for rapid scoring of MN with flow-cytometry, difficulty in discriminating MN from artifacts leading to a false-positive interpretation^[74] and compromise in the sensitivity; furthermore, sample preservation and re-analysis are added limitations^[75]. Therefore the automated image cytometry is preferred, as improved computer algorithms and allow rapid image analysis on cell-by-cell basis with a higher sensitivity. Moreover, with automated imaging system one can score the same slides repeatedly provided steps are taken to reduce background signals of the slides, which can be accounted as the MN in binucleate (BN) cells^[76]. Though the speed was increased using automated scoring, it is able to detect fifty percent of the BN cells and seventy five percent of the MN in those cells. It was attributed that relative high inaccuracy in the classification of the BN cells^[77,78]. Of late, systems like Meta Systems Metafer MN Score^[79], IMSTAR Pathfinder™ Screentox Auto-MN^[80] and Compucyte iCyte® Laser Scanning cytometer^[81], which are commercially available to increase the scoring speed of MN with a better accuracy in identifying the MN and BN cells. The RABiT system developed by the Columbia University can be used to estimate absorbed dose based in MN and γ -H2AX scoring in a large number of populations with less time and small quantity of sample^[82,83]. But, however, all labs cannot have this fully automated facility and it is not feasible to use at all places due to its cost.

Considering the importance of the time, rapid analysis in case of large population exposures, methods is being developed for automated scoring of MN^[78]. Nonetheless, it is significant to observe that there exists a variation in the yield of MN scored in BN cells stained with giemsa depend on the adopted scoring method; it was suggested that the difference in the MN yield due to scoring methods can be reduced when they were scored the cells stained with fluorescence dyes like propidium iodide (PI) and 4', 6-diamidino-2-phenylindole^[76]. In considering the potential of the methodology, we carried out a systemic analysis of MN frequencies induced for different doses of γ -radiation in giemsa and PI stained BN cells, obtained from PBL by manual and automated scoring methods in-lieu of biological dosimetry for triage medical management. Immediate triage and high throughput dosimetry are more important in the medical management of radiation accidents. At the

same time, it is equally important that the accuracy of the assay and reliable dose estimation at a later time for important cases identified by triage. The obtained results suggest that automated MN scoring in PI stained slides analysed with Meta Systems would be a better choice for the segregation and dose estimation than scoring in the BN cells stained with giemsa^[30].

Inter-laboratory comparison and automation of γ -H2AX scoring

In explicit during triage owing to its time factor as one need not culture the sample for a few days to enumerate the damage, the γ -H2AX foci assay is an emerging technology. The γ -H2AX changes after irradiation are quantified mainly using either microscopy or flow cytometry^[84,85]. Of which, the microscope counting of γ -H2AX foci (manual and automated) is the most preferred method than the flow cytometry as, it permits in detecting very low doses of radiation, differentiate the partial body exposures from that of whole body uniform exposure, higher specificity and its capability to estimate the doses even after 24 h of irradiation^[49]. However, scoring the foci frequency manually with a microscope is somewhat time consuming than that of automated scoring. Whereas, automatic scoring of γ -H2AX foci could decrease the time of analysis, albeit its associated complication, like a higher standard error linked with fitted coefficient, loss on the sensitivity, and inability to categorize the nature of exposure due to over dispersed foci in automated scoring^[86]. Moreover, the γ -H2AX foci method is sensitive and accurate after exposure to low doses, at higher doses overlapping of foci leads to underestimation of doses. Relative fluorescence intensity measurement using flow cytometry looks as a better option in case of radiological emergency at higher doses^[55]. Nevertheless, speed is an added advantage of this assay, the difference in foci yields obtained from the same samples by different laboratories and systematic underestimation of doses were reported^[87]. Thus, improvements have been made to reduce processing time^[88], analysis speed^[89], and time required to access dose in case of radiological emergencies using the γ -H2AX assay^[90].

Realizing the prospective, many researchers have established the assay with modifications for a variety of applications in addition to biodosimetry and radiation triage. Similar to the well-established radiation specific DC assay, while many laboratories established their own dose-response curve^[56], an inter-laboratory exercise has been carried out among the five European laboratories. Even though, there is no significant difference between the manual and automated scoring, the sensitivity of the assay is compromised and was unable to distinguish the partial exposures^[86], NATO biodosimetry inter-comparison on γ -H2AX assay as tool for triage, revealed an increased time delay was inversely proportional to the foci frequency, in blood samples measured at 2 and 24 h post irradiation; variations in foci loss

during shipment of blood samples or by differences in the immuno-fluorescence staining quality were listed as variables and should be minimized to reduce the uncertainties. Lately, technological advancement permitted of tele scoring of γ -H2AX foci among RENEB (Realizing European Network of Biodosimetry) laboratories; while the participant laboratories were able to distinguish critically high (> 2 Gy) and low dose and triage segregation of samples at 4 h, triage segregation of the 24 h samples shows high unpredictability. Apart from the variation in the shipment, variability in the staining quality under microscope (spectral and brightness differences in the light sources and fluorophores, wavelength ranges between different filters) and antibody could influence the foci analysis^[58]. While, the manual scoring with the microscopy has the higher sensitivity of dose estimation, automated scoring with image analyser is a faster method for triage. However, flow cytometry can be employed for larger population. Despite the fact, those methods provides early dose estimation and radiation triage, it should be employed within 48 h post exposure, because the kinetic study demonstrated a reduction and reaches base line level of γ -H2AX foci.

CRITERIA FOR AN IDEAL BIOMARKER

There are many biomarkers reported for radiation exposure. An ideal biomarker should be specific, sensitive, and reproducible. Moreover, able to discriminate the nature of exposure (whole body from that of partial body) and could provide a reliable dose estimation irrespective of the time of exposures. Analysis of the marker and quantification of the dose should be rapid in particular at the time of triage. An, additional desirable characteristic is the possibility of using non-invasive and easy procedures for collection of biological samples^[91]. Finally, validity of the assay measuring the biomarker and known variables influences the assay methods should be clearly established.

CONCLUSION

While all the techniques discussed in this review demonstrate the hallmark characteristic features the sensitivity and reproducibility, other features differ among the techniques. The DC is specific, sensitive (0.1 Gy), able to differentiate the nature of exposure partial body exposure from that of whole body exposure. Moreover being the unstable type of aberration, quantification of chronic exposure is difficult and it require more expertise and time despite the automated scoring as it need manual intervention even to score limited number of cells (about 50) in triage application. In alternate the MN is simple, rapid to score and easy to automate with a less sensitivity (0.25 Gy). Similarly, being an unstable type of aberration gets eliminated over a period of time and not suitable for chronic exposure as well as unable to discriminate the nature of

exposure. Alternatively, the translocation measurement with fluorescence *in situ* hybridization is an expensive or labour intensive in case of G bands by trypsin using giemsa (GTG); nonetheless it provides an estimate of chronic and retrospective dose estimation with an equal sensitivity to DC, an essential criterion for occupational workers though it is not specific to radiation. However, the time needed to culture to look for all those aberrations is not needed, in γ -H2AX assay; thus the inter-phase cells could provide a reliable dose estimate with a sensitivity of 1 mGy using microscopy or triage with flow cytometry within 24-48 h beyond which is of limited use. To conclude none of the assay could fulfil all the criteria of ideal biomarkers. However with the wider choice an appropriate assay can be employed based on the need.

REFERENCES

- 1 **Little JB.** Radiation carcinogenesis. *Carcinogenesis* 2000; **21**: 397-404 [PMID: 10688860 DOI: 10.1093/carcin/21.3.397]
- 2 **Meenakshisundaram V,** Rajagopal V, Mathiyarasu R. Lecture notes on radiation protection (Nucleonic well logging training programme). India: Institute of petroleum safety and environmental management, ONGC, DAE, GOI, 2005: 14-24
- 3 **World Health Organization.** Cytogenetic dosimetry: applications in preparedness for and response to radiation emergencies. Vienna, Austria: International Atomic Energy Agency, Department of Nuclear Safety and Security, Incident and Emergency Centre, 2011
- 4 **Mettler FA,** Bhargavan M, Thomadsen BR, Gilley DB, Lipoti JA, Mahesh M, McCrohan J, Yoshizumi TT. Nuclear medicine exposure in the United States, 2005-2007: preliminary results. *Semin Nucl Med* 2008; **38**: 384-391 [PMID: 18662559 DOI: 10.1053/j.semnulmed.2008.05.004]
- 5 **Bedford JS,** Dewey WC. Radiation Research Society. 1952-2002. Historical and current highlights in radiation biology: has anything important been learned by irradiating cells? *Radiat Res* 2002; **158**: 251-291 [PMID: 12175305]
- 6 **Hall EJ,** Giaccia AJ. Radiobiology for the Radiologist. Lippincott Williams and Wilkins, 2006
- 7 **Amundson SA,** Fornace AJ. Gene expression profiles for monitoring radiation exposure. *Radiat Prot Dosimetry* 2001; **97**: 11-16 [PMID: 11763352 DOI: 10.1093/oxfordjournals.rpd.a006632]
- 8 **Guipaud O,** Benderitter M. Protein biomarkers for radiation exposure: towards a proteomic approach as a new investigation tool. *Ann Ist Super Sanita* 2009; **45**: 278-286 [PMID: 19861733]
- 9 **Pernot E,** Hall J, Baatout S, Benotmane MA, Blanchardon E, Bouffler S, El Saghiere H, Gomolka M, Guertler A, Harms-Ringdahl M, Jeggo P, Kreuzer K, Laurier D, Lindholm C, Mkacher R, Quintens R, Rothkamm K, Sabatier L, Tapio S, de Vathaire F, Cardis E. Ionizing radiation biomarkers for potential use in epidemiological studies. *Mutat Res* 2012; **751**: 258-286 [PMID: 22677531 DOI: 10.1016/j.mrrev.2012.05.003]
- 10 **Romm H,** Oestreicher U, Kulka U. Cytogenetic damage analysed by the dicentric assay. *Ann Ist Super Sanita* 2009; **45**: 251-259 [PMID: 19861729]
- 11 **Sancar A,** Lindsey-Boltz LA, Unsal-Kaçmaz K, Linn S. Molecular mechanisms of mammalian DNA repair and the DNA damage checkpoints. *Annu Rev Biochem* 2004; **73**: 39-85 [PMID: 15189136 DOI: 10.1146/annurev.biochem.73.011303.073723]
- 12 **Sasaki MS.** Advances in the biophysical and molecular bases of radiation cytogenetics. *Int J Radiat Biol* 2009; **85**: 26-47 [PMID: 19205983 DOI: 10.1080/09553000802641185]
- 13 **Manning G,** Rothkamm K. Deoxyribonucleic acid damage-associated biomarkers of ionising radiation: current status and future relevance for radiology and radiotherapy. *Br J Radiol* 2013; **86**: 20130173 [PMID: 23659923 DOI: 10.1259/bjr.20130173]
- 14 **Sax K.** Chromosome Aberrations Induced by X-Rays. *Genetics*

- 1938; **23**: 494-516 [PMID: 17246897]
- 15 **Revell SH**. A new hypothesis for chromatid exchanges. *Radiobiolog* (Proc. Symp. Liège, 1954), London: Butterworths, 1955: 243-253 [DOI: 10.1111/j.1749-6632.1958.tb42641.x]
- 16 **Lea D**, Catcheside D. The mechanism of the induction by radiation on chromosome aberrations in tradesoantia. *Journal of Genetics* 1942; **44**: 216-245 [DOI: 10.1007/BF02982830]
- 17 **Durante M**, Bedford JS, Chen DJ, Conrad S, Cornforth MN, Natarajan AT, van Gent DC, Obe G. From DNA damage to chromosome aberrations: joining the break. *Mutat Res* 2013; **756**: 5-13 [PMID: 23707699 DOI: 10.1016/j.mrgentox.2013.05.014]
- 18 **Lloyd DC**. Chromosomal analysis to assess radiation dose. *Stem Cells* 1997; **15** Suppl 2: 195-201 [PMID: 9368304 DOI: 10.1002/stem.5530150727]
- 19 **Paul SF**, Venkatachalam P, Jeevanram RK. A comparative study of synchronised and conventional culture methods on the micronucleus dose-response curve. *Mutat Res* 1997; **391**: 91-98 [PMID: 9219553 DOI: 10.1016/S0165-1218(97)00038-4]
- 20 **Bhavani M**, Tamizh Selvan G, Kaur H, Adhikari JS, Vijayalakshmi J, Venkatachalam P, Chaudhury NK. Dicentric chromosome aberration analysis using giemsa and centromere specific fluorescence in-situ hybridization for biological dosimetry: An inter- and intra-laboratory comparison in Indian laboratories. *Appl Radiat Isot* 2014; **92**: 85-90 [PMID: 25014548 DOI: 10.1016/j.apradiso.2014.06.004]
- 21 **Bender MA**, Awa AA, Brooks AL, Evans HJ, Groer PG, Littlefield LG, Pereira C, Preston RJ, Wachholz BW. Current status of cytogenetic procedures to detect and quantify previous exposures to radiation. *Mutat Res* 1988; **196**: 103-159 [PMID: 3047567 DOI: 10.1016/0165-1110(88)90017-6]
- 22 **Fenech M**, Morley A. Solutions to the kinetic problem in the micronucleus assay. *Cytobios* 1985; **43**: 233-246 [PMID: 4075848]
- 23 **Odagiri Y**, Uchida H, Shibasaki S. Interindividual variation in cytogenetic response to X-ray and colchicine measured with the cytokinesis-block micronucleus assay. *Mutat Res* 1997; **381**: 1-13 [PMID: 9403025 DOI: 10.1016/S0027-5107(97)00138-3]
- 24 **Matter B**, Schmid W. Trenimon-induced chromosomal damage in bone-marrow cells of six mammalian species, evaluated by the micronucleus test. *Mutat Res* 1971; **12**: 417-425 [PMID: 4999599 DOI: 10.1016/0027-5107(71)90092-3]
- 25 **Fenech M**. Cytokinesis-block micronucleus assay evolves into a "cytome" assay of chromosomal instability, mitotic dysfunction and cell death. *Mutat Res* 2006; **600**: 58-66 [PMID: 16822529 DOI: 10.1016/j.mrfmm.2006.05.028]
- 26 **Lee TK**, O'Brien KF, Naves JL, Christie KI, Arastu HH, Eaves GS, Wiley AL, Karlsson UL, Salehpour MR. Micronuclei in lymphocytes of prostate cancer patients undergoing radiation therapy. *Mutat Res* 2000; **469**: 63-70 [PMID: 10946243 DOI: 10.1016/S1383-5718(00)00072-3]
- 27 **Monsieurs MA**, Bacher K, Brans B, Vral A, De Ridder L, Dierckx RA, Thierens HM. Patient dosimetry for 131I-lipiodol therapy. *Eur J Nucl Med Mol Imaging* 2003; **30**: 554-561 [PMID: 12690415 DOI: 10.1007/s00259-002-1108-7]
- 28 **Sridevi K**, Rao KP. Modification of genetic damage by dihomogamma-linolenic acid. *Bull Environ Contam Toxicol* 1994; **52**: 457-464 [PMID: 8142720 DOI: 10.1007/BF00197837]
- 29 **Paillole N**, Voisin P. Is micronuclei yield variability a problem for overexposure dose assessment to ionizing radiation? *Mutat Res* 1998; **413**: 47-56 [PMID: 9602858 DOI: 10.1016/S1383-5718(98)00015-1]
- 30 **Selvan GT**, Bhavani M, Vijayalakshmi J, Paul Solomon FD, Chaudhury NK, Venkatachalam P. Delayed mitogenic stimulation decreases DNA damage assessed by micronucleus assay in human peripheral blood lymphocytes after (60)co irradiation. *Dose Response* 2014; **12**: 498-508 [PMID: 25249838 DOI: 10.2203/dose-response.13-060]
- 31 **Fenech M**. Important variables that influence base-line micronucleus frequency in cytokinesis-blocked lymphocytes-a biomarker for DNA damage in human populations. *Mutat Res* 1998; **404**: 155-165 [PMID: 9729354 DOI: 10.1016/S0027-5107(98)00109-2]
- 32 **Pinkel D**, Gray JW, Trask B, van den Engh G, Fuscoe J, van Dekken H. Cytogenetic analysis by in situ hybridization with fluorescently labeled nucleic acid probes. *Cold Spring Harb Symp Quant Biol* 1986; **51** Pt 1: 151-157 [PMID: 3472711 DOI: 10.1101/SQB.1986.051.01.018]
- 33 **Natarajan AT**, Vyas RC, Darroudi F, Vermeulen S. Frequencies of X-ray-induced chromosome translocations in human peripheral lymphocytes as detected by in situ hybridization using chromosome-specific DNA libraries. *Int J Radiat Biol* 1992; **61**: 199-203 [PMID: 1351907 DOI: 10.1080/09553009214550821]
- 34 **Straume T**, Lucas JN, Tucker JD, Bigbee WL, Langlois RG. Biodosimetry for a radiation worker using multiple assays. *Health Phys* 1992; **62**: 122-130 [PMID: 1730553 DOI: 10.1097/00004032-199202000-00001]
- 35 **Schmid E**, Zitzelsberger H, Braselmann H, Gray JW, Bauchinger M. Radiation-induced chromosome aberrations analysed by fluorescence in situ hybridization with a triple combination of composite whole chromosome-specific DNA probes. *Int J Radiat Biol* 1992; **62**: 673-678 [PMID: 1362760 DOI: 10.1080/0955300921455262]
- 36 **Bauchinger M**, Schmid E, Zitzelsberger H, Braselmann H, Nahrstedt U. Radiation-induced chromosome aberrations analysed by two-colour fluorescence in situ hybridization with composite whole chromosome-specific DNA probes and a pancentromeric DNA probe. *Int J Radiat Biol* 1993; **64**: 179-184 [PMID: 8103541 DOI: 10.1080/09553009314551271]
- 37 **Nakano M**, Nakashima E, Pawel DJ, Kodama Y, Awa A. Frequency of reciprocal translocations and dicentrics induced in human blood lymphocytes by X-irradiation as determined by fluorescence in situ hybridization. *Int J Radiat Biol* 1993; **64**: 565-569 [PMID: 7902396 DOI: 10.1080/09553009314551781]
- 38 **Finnon P**, Lloyd DC, Edwards AA. Fluorescence in situ hybridization detection of chromosomal aberrations in human lymphocytes: applicability to biological dosimetry. *Int J Radiat Biol* 1995; **68**: 429-435 [PMID: 7594969 DOI: 10.1080/09553009514551391]
- 39 **Lucas JN**, Hill F, Burk C, Fester T, Straume T. Dose-response curve for chromosome translocations measured in human lymphocytes exposed to 60Co gamma rays. *Health Phys* 1995; **68**: 761-765 [PMID: 7759253 DOI: 10.1097/00004032-199506000-00001]
- 40 **Tanaka K**, Popp S, Fischer C, Van Kaick G, Kamada N, Cremer T, Cremer C. Chromosome aberration analysis in atomic bomb survivors and Thorotrast patients using two- and three-colour chromosome painting of chromosomal subsets. *Int J Radiat Biol* 1996; **70**: 95-108 [PMID: 8691041 DOI: 10.1080/095530096145373]
- 41 **Garcia-Canton C**, Anadón A, Meredith C. γ H2AX as a novel endpoint to detect DNA damage: applications for the assessment of the in vitro genotoxicity of cigarette smoke. *Toxicol In Vitro* 2012; **26**: 1075-1086 [PMID: 22735693 DOI: 10.1016/j.tiv.2012.06.006]
- 42 **Rave-Fränk M**, Virsik-Peuckert P, Schmidberger H, Rodemann HP. Reciprocal translocation frequency in irradiated sensitive and resistant human tumor cells in correlation with clonogenic in vitro cell survival: a possibility of tumor radiosensitivity prediction? *Radiother Oncol* 1996; **38**: 163-170 [PMID: 8966229 DOI: 10.1016/0167-8140(95)01654-6]
- 43 **Boei JJ**, Vermeulen S, Natarajan AT. Differential involvement of chromosomes 1 and 4 in the formation of chromosomal aberrations in human lymphocytes after X-irradiation. *Int J Radiat Biol* 1997; **72**: 139-145 [PMID: 9269306 DOI: 10.1080/095530097143356]
- 44 **Trask BJ**. Human cytogenetics: 46 chromosomes, 46 years and counting. *Nat Rev Genet* 2002; **3**: 769-778 [PMID: 12360235 DOI: 10.1038/nrg905]
- 45 **Kumagai E**, Tanaka R, Kumagai T, Onomichi M, Sawada S. Effects of long-term radiation exposure on chromosomal aberrations in radiological technologists. *J Radiat Res* 1990; **31**: 270-279 [PMID: 2246752 DOI: 10.1269/jrr.31.270]
- 46 **Rogakou EP**, Boon C, Redon C, Bonner WM. Megabase chromatin domains involved in DNA double-strand breaks in vivo. *J Cell Biol* 1999; **146**: 905-916 [PMID: 10477747 DOI: 10.1083/jcb.146.5.905]
- 47 **Redon CE**, Dickey JS, Bonner WM, Sedelnikova OA. γ -H2AX as a biomarker of DNA damage induced by ionizing radiation in human peripheral blood lymphocytes and artificial skin. *Adv*

- Space Res* 2009; **43**: 1171-1178 [PMID: 20046946 DOI: 10.1016/j.asr.2008.10.011]
- 48 **Löbrich M**, Rief N, Kühne M, Heckmann M, Fleckenstein J, Rube C, Uder M. In vivo formation and repair of DNA double-strand breaks after computed tomography examinations. *Proc Natl Acad Sci USA* 2005; **102**: 8984-8989 [PMID: 15956203 DOI: 10.1073/pnas.0501895102]
 - 49 **Horn S**, Barnard S, Rothkamm K. Gamma-H2AX-based dose estimation for whole and partial body radiation exposure. *PLoS One* 2011; **6**: e25113 [PMID: 21966430 DOI: 10.1371/journal.pone.0025113]
 - 50 **Tanaka T**, Halicka D, Traganos F, Darzynkiewicz Z. Cytometric analysis of DNA damage: phosphorylation of histone H2AX as a marker of DNA double-strand breaks (DSBs). *Methods Mol Biol* 2009; **523**: 161-168 [PMID: 19381940 DOI: 10.1007/978-1-59745-190-1_11]
 - 51 **Mah LJ**, El-Osta A, Karagiannis TC. GammaH2AX as a molecular marker of aging and disease. *Epigenetics* 2010; **5**: 129-136 [PMID: 20150765 DOI: 10.4161/epi.5.2.11080]
 - 52 **Ishida M**, Ishida T, Tashiro S, Uchida H, Sakai C, Hironobe N, Miura K, Hashimoto Y, Arihiro K, Chayama K, Kihara Y, Yoshizumi M. Smoking cessation reverses DNA double-strand breaks in human mononuclear cells. *PLoS One* 2014; **9**: e103993 [PMID: 25093845 DOI: 10.1371/journal.pone.0103993]
 - 53 **Li Z**, Yang J, Huang H. Oxidative stress induces H2AX phosphorylation in human spermatozoa. *FEBS Lett* 2006; **580**: 6161-6168 [PMID: 17064697 DOI: 10.1016/j.febslet.2006.10.016]
 - 54 **Kaneko H**, Igarashi K, Kataoka K, Miura M. Heat shock induces phosphorylation of histone H2AX in mammalian cells. *Biochem Biophys Res Commun* 2005; **328**: 1101-1106 [PMID: 15707990 DOI: 10.1016/j.bbrc.2005.01.073]
 - 55 **Ismail IH**, Wadhwa TI, Hammarsten O. An optimized method for detecting gamma-H2AX in blood cells reveals a significant interindividual variation in the gamma-H2AX response among humans. *Nucleic Acids Res* 2007; **35**: e36 [PMID: 17284459 DOI: 10.1093/nar/gkl1169]
 - 56 **Sharma PM**, Ponnaiya B, Taveras M, Shuryak I, Turner H, Brenner DJ. High throughput measurement of γ H2AX DSB repair kinetics in a healthy human population. *PLoS One* 2015; **10**: e0121083 [PMID: 25794041 DOI: 10.1371/journal.pone.0121083]
 - 57 **Sedelnikova OA**, Horikawa I, Redon C, Nakamura A, Zimonjic DB, Popescu NC, Bonner WM. Delayed kinetics of DNA double-strand break processing in normal and pathological aging. *Aging Cell* 2008; **7**: 89-100 [PMID: 18005250 DOI: 10.1111/j.1474-9726.2007.00354.x]
 - 58 **Barnard S**, Ainsbury EA, Al-hafidh J, Hadjidekova V, Hristova R, Lindholm C, Monteiro Gil O, Moquet J, Moreno M, Rößler U, Thierens H, Vandevoorde C, Vral A, Wojewódzka M, Rothkamm K. The first gamma-H2AX biodosimetry intercomparison exercise of the developing European biodosimetry network RENEB. *Radiat Prot Dosimetry* 2015; **164**: 265-270 [PMID: 25118318 DOI: 10.1093/rpd/ncu259]
 - 59 **Roch-Lefèvre S**, Mandina T, Voisin P, Gaëtan G, Mesa JE, Valente M, Bonnesœur P, García O, Voisin P, Roy L. Quantification of gamma-H2AX foci in human lymphocytes: a method for biological dosimetry after ionizing radiation exposure. *Radiat Res* 2010; **174**: 185-194 [PMID: 20681785 DOI: 10.1667/RR1775.1]
 - 60 **Roy L**, Buard V, Delbos M, Durand V, Paillole N, Grégoire E, Voisin P. International intercomparison for criticality dosimetry: the case of biological dosimetry. *Radiat Prot Dosimetry* 2004; **110**: 471-476 [PMID: 15353693 DOI: 10.1093/rpd/nch349]
 - 61 **Garcia OF**, Ramalho AT, Di Giorgio M, Mir SS, Espinoza ME, Manzano J, Nasazzi N, López I. Intercomparison in cytogenetic dosimetry among five laboratories from Latin America. *Mutat Res* 1995; **327**: 33-39 [PMID: 7870095 DOI: 10.1016/0027-5107(94)00066-E]
 - 62 **Di Giorgio M**, Barquinero JF, Vallerga MB, Radl A, Taja MR, Seoane A, De Luca J, Oliveira MS, Valdivia P, Lima OG, Lamadrid A, Mesa JG, Aguilera IR, Cardoso TM, Carvajal YC, Maldonado CA, Espinoza ME, Martínez-López W, Méndez-Acuña L, Di Tomaso MV, Roy L, Lindholm C, Romm H, Güçlü I, Lloyd DC. Biological dosimetry intercomparison exercise: an evaluation of triage and routine mode results by robust methods. *Radiat Res* 2011; **175**: 638-649 [PMID: 21306200 DOI: 10.1667/RR2425.1]
 - 63 **Christie DH**, Chu MC, Carr Z. Global networking for biodosimetry laboratory capacity surge in radiation emergencies. *Health Phys* 2010; **98**: 168-171 [PMID: 20065679 DOI: 10.1097/HP.0b013e3181abaad4]
 - 64 **Wilkins RC**, Romm H, Oestreicher U, Marro L, Yoshida MA, Suto Y, Prasanna PG. Biological Dosimetry by the Triage Dicentric Chromosome Assay - Further validation of International Networking. *Radiat Meas* 2011; **46**: 923-928 [PMID: 21949482 DOI: 10.1016/j.radmeas.2011.03.012]
 - 65 **Miller SM**, Ferrarotto CL, Vlahovich S, Wilkins RC, Boreham DR, Dolling JA. Canadian Cytogenetic Emergency network (CEN) for biological dosimetry following radiological/nuclear accidents. *Int J Radiat Biol* 2007; **83**: 471-477 [PMID: 17538797 DOI: 10.1080/09553000701370860]
 - 66 **Yoshida MA**, Hayata I, Tateno H, Tanaka K, Sonta S. The chromosome network for biodosimetry in Japan. *Radiat Mes* 2007; **42**: 1125-1127 [DOI: 10.1016/j.radmeas.2007.05.047]
 - 67 **Wojcik A**, Lloyd D, Romm H, Roy L. Biological dosimetry for triage of casualties in a large-scale radiological emergency: capacity of the EU member states. *Radiat Prot Dosimetry* 2010; **138**: 397-401 [PMID: 19951985 DOI: 10.1093/rpd/ncp279]
 - 68 **Martins V**, Antunes AC, Monteiro Gil O. Implementation of a dose-response curve for γ -radiation in the Portuguese population by use of the chromosomal aberration assay. *Mutat Res* 2013; **750**: 50-54 [PMID: 23043763 DOI: 10.1016/j.mrgentox.2012.09.009]
 - 69 **Bakkiam D**, Bhavani M, Anantha Kumar AA, Sonwani S, Venkatachalam P, Sivasubramanian K, Venkatraman B. Dicentric assay: inter-laboratory comparison in Indian laboratories for routine and triage applications. *Appl Radiat Isot* 2015; **99**: 77-85 [PMID: 25728004 DOI: 10.1016/j.apradiso.2015.02.015]
 - 70 **Fenech M**, Chang WP, Kirsch-Volders M, Holland N, Bonassi S, Zeiger E. HUMN project: detailed description of the scoring criteria for the cytokinesis-block micronucleus assay using isolated human lymphocyte cultures. *Mutat Res* 2003; **534**: 65-75 [PMID: 12504755 DOI: 10.1016/S1383-5718(02)00249-8]
 - 71 **Bryce SM**, Avlasevich SL, Bemis JC, Lukamowicz M, Elhajouji A, Van Goethem F, De Boeck M, Beerens D, Aerts H, Van Gompel J, Collins JE, Ellis PC, White AT, Lynch AM, Dertinger SD. Interlaboratory evaluation of a flow cytometric, high content in vitro micronucleus assay. *Mutat Res* 2008; **650**: 181-195 [PMID: 18182318 DOI: 10.1016/j.mrgentox.2007.11.006]
 - 72 **Böcker W**, Streffer C, Müller WU, Yu C. Automated scoring of micronuclei in binucleated human lymphocytes. *Int J Radiat Biol* 1996; **70**: 529-537 [PMID: 8947534 DOI: 10.1080/095530096144734]
 - 73 **Schreiber GA**, Beisker W, Braselmann H, Bauchinger M, Bögl KW, Nüsse M. An automated flow cytometric micronucleus assay for human lymphocytes. *Int J Radiat Biol* 1992; **62**: 695-709 [PMID: 1362763 DOI: 10.1080/09553009214552651]
 - 74 **Laingam S**, Frosio SM, Humpage AR. Flow-cytometric analysis of in vitro micronucleus formation: comparative studies with WIL2-NS human lymphoblastoid and L5178Y mouse lymphoma cell lines. *Mutat Res* 2008; **656**: 19-26 [PMID: 18718554 DOI: 10.1016/j.mrgentox.2008.06.015]
 - 75 **Fenech M**, Kirsch-Volders M, Rossnerova A, Sram R, Romm H, Bolognesi C, Ramakumar A, Soussaline F, Schunck C, Elhajouji A, Anwar W, Bonassi S. HUMN project initiative and review of validation, quality control and prospects for further development of automated micronucleus assays using image cytometry systems. *Int J Hyg Environ Health* 2013; **216**: 541-552 [PMID: 23507632 DOI: 10.1016/j.ijheh.2013.01.008]
 - 76 **Varga D**, Johannes T, Jainta S, Schuster S, Schwarz-Boeger U, Kiechle M, Patino Garcia B, Vogel W. An automated scoring procedure for the micronucleus test by image analysis. *Mutagenesis* 2004; **19**: 391-397 [PMID: 15388812 DOI: 10.1093/mutage/geh047]
 - 77 **Tates AD**, van Welie MT, Ploem JS. The present state of the automated micronucleus test for lymphocytes. *Int J Radiat Biol* 1990;

- 58: 813-825 [PMID: 1977825 DOI: 10.1080/09553009014552191]
- 78 **Castelain P**, Van Hummelen P, Deleener A, Kirsch-Volders M. Automated detection of cytochalasin-B blocked binucleated lymphocytes for scoring micronuclei. *Mutagenesis* 1993; **8**: 285-293 [PMID: 7690875 DOI: 10.1093/mutage/8.4.285]
- 79 **Schunck C**, Johannes T, Varga D, Lörch T, Plesch A. New developments in automated cytogenetic imaging: unattended scoring of dicentric chromosomes, micronuclei, single cell gel electrophoresis, and fluorescence signals. *Cytogenet Genome Res* 2004; **104**: 383-389 [PMID: 15162069 DOI: 10.1159/000077520]
- 80 **Decordier I**, Papine A, Plas G, Roesems S, Vande Loock K, Moreno-Palomo J, Cemeli E, Anderson D, Fucic A, Marcos R, Soussaline F, Kirsch-Volders M. Automated image analysis of cytokinesis-blocked micronuclei: an adapted protocol and a validated scoring procedure for biomonitoring. *Mutagenesis* 2009; **24**: 85-93 [PMID: 18854579 DOI: 10.1093/mutage/gen057]
- 81 **Darzynkiewicz Z**, Smolewski P, Holden E, Luther E, Henriksen M, François M, Leifert W, Fenech M. Laser scanning cytometry for automation of the micronucleus assay. *Mutagenesis* 2011; **26**: 153-161 [PMID: 21164197 DOI: 10.1093/mutage/geq069]
- 82 **Thierens H**, Vral A. The micronucleus assay in radiation accidents. *Ann Ist Super Sanita* 2009; **45**: 260-264 [PMID: 19861730]
- 83 **Nakamura A**, Sedelnikova OA, Redon C, Pilch DR, Sinogeeva NI, Shroff R, Lichten M, Bonner WM. Techniques for gamma-H2AX detection. *Methods Enzymol* 2006; **409**: 236-250 [PMID: 16793405 DOI: 10.1016/S0076-6879(05)09014-2]
- 84 **Redon CE**, Nakamura AJ, Sordet O, Dickey JS, Gouliaeva K, Tabb B, Lawrence S, Kinders RJ, Bonner WM, Sedelnikova OA. γ -H2AX detection in peripheral blood lymphocytes, splenocytes, bone marrow, xenografts, and skin. *Methods Mol Biol* 2011; **682**: 249-270 [PMID: 21057933 DOI: 10.1007/978-1-60327-409-8_18]
- 85 **Muslimovic A**, Ismail IH, Gao Y, Hammarsten O. An optimized method for measurement of gamma-H2AX in blood mononuclear and cultured cells. *Nat Protoc* 2008; **3**: 1187-1193 [PMID: 18600224 DOI: 10.1038/nprot.2008.93]
- 86 **Rothkamm K**, Barnard S, Ainsbury EA, Al-Hafidh J, Barquinero JF, Lindholm C, Moquet J, Perälä M, Roch-Lefèvre S, Scherthan H, Thierens H, Vral A, Vandersickel V. Manual versus automated γ -H2AX foci analysis across five European laboratories: can this assay be used for rapid biodosimetry in a large scale radiation accident? *Mutat Res* 2013; **756**: 170-173 [PMID: 23648320 DOI: 10.1016/j.mrgentox.2013.04.012]
- 87 **Rothkamm K**, Horn S, Scherthan H, Rössler U, De Amicis A, Barnard S, Kulka U, Lista F, Meineke V, Braselmann H, Beinke C, Abend M. Laboratory intercomparison on the γ -H2AX foci assay. *Radiat Res* 2013; **180**: 149-155 [PMID: 23883318 DOI: 10.1667/RR3238.1]
- 88 **Moquet J**, Barnard S, Rothkamm K. Gamma-H2AX biodosimetry for use in large scale radiation incidents: comparison of a rapid '96 well lyse/fix' protocol with a routine method. *PeerJ* 2014; **2**: e282 [PMID: 24688860 DOI: 10.7717/peerj.282]
- 89 **Barber P**, Locke R, Pierce G, Rothkamm K, Vojnovic B. γ -H2AX foci counting: image processing and control software for high-content screening. *Proceedings of SPIE* 2007; **6441**: 64411M-1 [DOI: 10.1117/12.705217]
- 90 **Turner HC**, Sharma P, Perrier JR, Bertucci A, Smilenov L, Johnson G, Taveras M, Brenner DJ, Garty G. The RABiT: high-throughput technology for assessing global DSB repair. *Radiat Environ Biophys* 2014; **53**: 265-272 [PMID: 24477408 DOI: 10.1007/s00411-014-0514-0]
- 91 **Ohtaki K**, Shimba H, Awa AA, Sofuni T. Comparison of type and frequency of chromosome aberrations by conventional and G-staining methods in Hiroshima atomic bomb survivors. *J Radiat Res* 1982; **23**: 441-449 [PMID: 7182494 DOI: 10.1269/jrr.23.441]

P- Reviewer: Storto G, Vinh-Hung V **S- Editor:** Tian YL
L- Editor: A **E- Editor:** Wu HL



Retrospective Cohort Study

Inter- and intra-rater reliability of diffusion tensor imaging parameters in the normal pediatric spinal cord

Nadia Barakat, Pallav Shah, Scott H Faro, John P Gaughan, Devon Middleton, MJ Mulcahey, Feroze B Mohamed

Nadia Barakat, Pallav Shah, Scott H Faro, Devon Middleton, Feroze B Mohamed, Department of Radiology, Temple University, Philadelphia, PA 19140, United States

Nadia Barakat, John P Gaughan, Biostatistics Consulting Center, Temple University School of Medicine, Philadelphia, PA 19140, United States

MJ Mulcahey, Thomas Jefferson University School of Health Professions, Philadelphia, PA 19107, United States

Author contributions: All the authors solely contributed to this paper.

Supported by The Shriners Hospitals for Children, No. #8956.

Institutional review board statement: Subjects and their parents provided written informed assent and consent of the IRB-approved protocol.

Informed consent statement: Subjects and their parents provided written informed assent and consent of the IRB-approved protocol.

Conflict-of-interest statement: All the authors participated in this work do not have any conflict of interest.

Data sharing statement: All the authors participated in this work do not have any data sharing.

Open-Access: This article is an open-access article which was selected by an in-house editor and fully peer-reviewed by external reviewers. It is distributed in accordance with the Creative Commons Attribution Non Commercial (CC BY-NC 4.0) license, which permits others to distribute, remix, adapt, build upon this work non-commercially, and license their derivative works on different terms, provided the original work is properly cited and the use is non-commercial. See: <http://creativecommons.org/licenses/by-nc/4.0/>

Correspondence to: Nadia Barakat, PhD, Department of Radiology, Temple University, 3401 N. Broad St., Philadelphia, PA 19140, United States. nadia.barakat@temple.edu

Telephone: +1-215-7079047

Received: February 11, 2015

Peer-review started: February 11, 2015

First decision: March 6, 2015

Revised: June 24, 2015

Accepted: July 29, 2015

Article in press: August 3, 2015

Published online: September 28, 2015

Abstract

AIM: To assess inter- and intra-rater reliability (agreement) between two region of interest (ROI) methods in pediatric spinal cord diffusion tensor imaging (DTI).

METHODS: Inner-Field-of-View DTI data previously acquired from ten pediatric healthy subjects (mean age = 12.10 years) was used to assess for reliability. ROIs were drawn by two neuroradiologists on each subject data twice within a 3-mo interval. ROIs were placed on axial B_0 maps along the cervical spine using free-hand and fixed-size ROIs. Agreement analyses for fractional anisotropy (FA), axial diffusivity, radial diffusivity and mean diffusivity were performed using intra-class-correlation (ICC) and Cronbach's alpha statistical methods.

RESULTS: Inter- and intra-rater agreement between the two ROI methods showed moderate (ICC = 0.5) to strong (ICC = 0.84). There were significant differences between raters in the number of pixels selected using free-hand ROIs ($P < 0.05$). However, no significant differences were observed in DTI parameter values. FA showed highest variability in ICC values (0.10-0.87). Cronbach's alpha showed moderate-high values for raters and ROI methods.

CONCLUSION: The study showed that high reproducibility in spinal cord DTI can be achieved, and demon-

strated the importance of setting detailed methodology for post-processing DTI data, specifically the placement of ROIs.

Key words: Diffusion tensor imaging; Reproducibility; Reliability; Spinal cord; Inter-rater; Intra-rater

© **The Author(s)** 2015. Published by Baishideng Publishing Group Inc. All rights reserved.

Core tip: We tested the reliability of spinal cord diffusion tensor imaging (DTI) by assessing inter- and intra-rater agreement between two region of interest (ROI) selection methods. Results showed moderate to strong agreement between repeated measurements. There was a variation in DTI parameters at lower and upper spinal cord levels and significant differences between raters in the number of pixels they chose to outline ROIs. There were no significant differences in DTI parameter values derived from these ROIs. The study showed that strong reproducibility in spinal cord DTI can be achieved, and highlighted the importance of setting detailed methodology to standardize ROI drawing techniques.

Barakat B, Shah P, Faro SH, Gaughan JP, Middleton D, Mulcahey MJ, Mohamed FB. Inter- and intra-rater reliability of diffusion tensor imaging parameters in the normal pediatric spinal cord. *World J Radiol* 2015; 7(9): 279-285 Available from: URL: <http://www.wjgnet.com/1949-8470/full/v7/i9/279.htm> DOI: <http://dx.doi.org/10.4329/wjr.v7.i9.279>

INTRODUCTION

Diffusion tensor imaging (DTI) has become an important technique for evaluating the central nervous system noninvasively. The application of DTI in the spinal cord is technically limited by the small cross-sectional size of the spinal cord, cerebral spinal fluid pulsation (CSF), the presence of nearby vascular and osseous structures, respiratory and cardiac motion.

Despite these challenges, studies have successfully reported diffusion measures in the intact human spinal cord^[1-9]. Several studies have investigated the clinical utility of DTI in assessing spinal cord pathology and have shown correlations between DTI and clinical scores^[10-18]. While these studies used different data acquisition methods and post-processing software, they all shared one common technique to delineate the spinal cord: Manual drawing of regions of interests (ROIs) to calculate DTI parameters. Additionally, they all reported that ROI locations were confirmed using the conventional structural MR imaging sequences, and that care was taken to avoid inclusion of CSF. Interestingly, most of these studies reported that the variability seen in DTI parameters could be due to the user-dependent manual selection of ROIs.

Parameters derived from DTI can provide information about tissue properties which may have clinical signifi-

cance. To be proven clinically reliable, the quantitative properties of spinal cord DTI need to be assessed by multiple reviewers. While extensive data is available on the reliability and reproducibility of brain DTI^[19-24], to the best of our knowledge there is lack of research on the reliability of ROI placement to quantify spinal cord DTI measures. The goal of this study was to assess inter-rater (between) and intra-rater (within) agreement in pediatric spinal cord DTI, as well as agreement between two methods of drawing regions of interest.

MATERIALS AND METHODS

Subjects

This is a retrospective study. Ten pediatric subjects with a mean age of 12.10 years (age range 9 to 15) underwent cervical spinal cord DTI^[25]. The subjects had no clinical or imaging evidence of spinal cord injury or pathology. Subjects and their parents provided written informed assent and consent of the IRB-approved protocol.

Imaging

The scans were performed using a 3T Siemens Verio MR scanner with a four-channel neck matrix and an eight-channel spine matrix coils. The protocol consisted of conventional sagittal Turbo Spin Echo T1- and T2-weighted scans, axial TSE T2 weighted scans as well as axial DTI acquisition with an inner Field-of-View single-shot EPI sequence with spatially 2D-selective RF excitations^[26,27]. Anesthesia was not administered to the subjects. Neither cardiac nor respiratory gating was performed. The axial DTI images were acquired in the same anatomical location prescribed for the T2-weighted images to cover the cervical spinal cord (C1 to T1 levels). DTI scanning parameters included: 20 diffusion directions, $b = 1000 \text{ s/mm}^2$, voxel size = $1.2 \text{ mm}^3 \times 1.2 \text{ mm}^3 \times 3 \text{ mm}^3$, axial slices = 35-45 (depending on the subject's height), TR = 6100-8000 ms, TE = 115 ms, number of averages = 3 and acquisition time = 7 min.

Image processing

Initially, the diffusion data sets were corrected for motion-induced artifacts using the Automated-Image-Registration where the target images (20 directional images) were aligned with the reference image (B_0) using a rigid registration algorithm and scaled-least-squares cost function^[28]. Tensor estimation and placement of ROIs were performed on MedINRIA. Fractional anisotropy (FA), axial diffusivity (AD), radial diffusivity (RD) and mean diffusivity (MD) measures were calculated.

Placement of regions of interest

The methodology for ROI placement was devised by two board-certified neuroradiologists. ROIs were manually drawn on axial b_0 maps along the cervical spinal cord at each cervical intervertebral disk and mid vertebral body level. Two methods of selecting ROIs were examined in this study: (1) free-hand: Where the raters

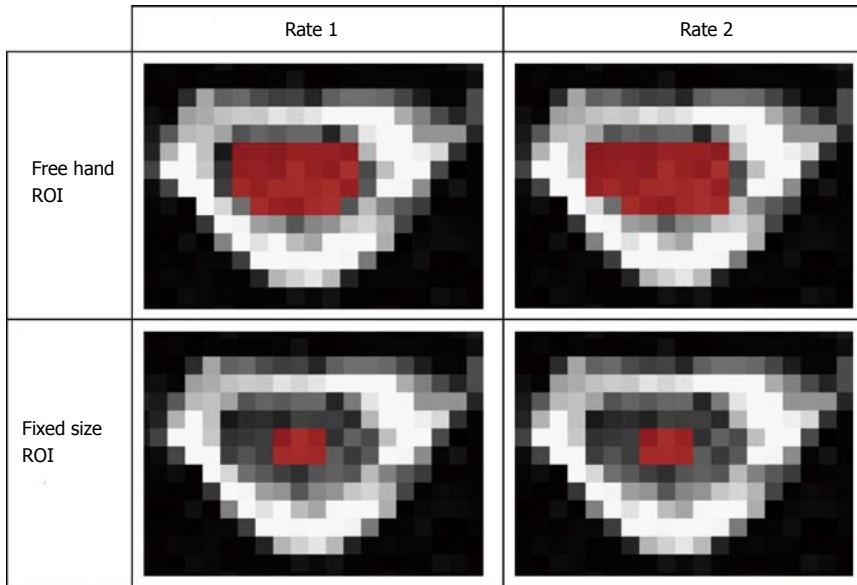


Figure 1 B₀ images show how each rater outlined manual and fixed size regions of interest.

manually outlined the periphery of spinal cord tissue with consistent sparing of the outer margin of the spinal cord that represented approximately one voxel width to minimize volume averaging with the CSF, and (3) pre-set: where raters placed a rectangular 3 by 2 pixels region of interest in the center of the spinal cord (Figure 1).

To assess for inter-rater variability, ROIs were drawn by two board-certified neuroradiologists (rater 1 and rater 2) who received training on using MedINRIA. To assess intra-rater variability, each rater performed ROI analysis on each subject data twice. The two raters worked independently and were blinded to each other's results and were proficient in DTI post-processing. Data generated from the first set of ROIs was not available during the second assessment. Both neuroradiologists were asked to repeat the measurements after 3 mo.

Data analysis

For each ROI, DTI values were extracted from each voxel. The values of each DTI parameter (FA, AD, RD and MD) were averaged per cord level across all subjects. ROI selection was guided by axial TSE T2 and reconstructed sagittal and coronal b₀ maps.

Statistical analysis

Statistical analysis was performed using SAS, version 9.1, to test the inter- and intra-rater agreement between DTI data from the two methods of ROI drawing. This was assessed by (1) calculating the intra-class-correlation (ICC) coefficients^[29,30] with 95%CI for each DTI parameter per spinal cord level and (2) calculating Cronbach's alpha as a measure of test re-test for each rater. Descriptive statistics were calculated for FA, AD, RD, MD, and test re-test differences were compared using paired *t* tests, with *P* value ≤ 0.05 considered statistically significant.

RESULTS

Using B₀ images, ROIs were drawn manually and by placing a pre-set outline (Figure 1). Descriptive data for ROI drawing methods, raters and trials of spinal cord FA, AD, RD and MD are shown in Table 1. Overall, there were significant differences between raters in the number of pixels they chose to outline free-hand ROIs (*P* < 0.05). However, there were no significant differences in average inter- or intra-rater DTI parameter values. When two ROI drawing methods were compared to each other, significant differences were found in DTI parameters. Paired *t* tests were run for spinal cord levels C1 to T1. Data in Table 1 shows mean inter-observer and intra-observer DTI parameter values.

Overall agreement

The ICC coefficients for each DTI parameter as a function of spinal cord level are shown in Figure 2. The agreement was moderate to high among raters and ROI drawing methods. The ROI methods showed moderate (ICC = 0.5) to strong (ICC = 0.84) inter-rater and intra-rater agreement. Of the DTI parameters, FA showed the highest variability of ICC values (0.10-0.87). Low agreement was found in upper spinal cord levels C1 to mid-C3. RD showed slightly higher agreement values than FA (0.26-0.83). The agreement was lower in the pre-set ROIs for FA and RD. Figure 3 shows the Cronbach's Alpha values evaluating test-retest agreement for each rater. There was a decrease in agreement at upper and lower spinal cord levels, especially in FA values. There was low and fluctuating agreement values in RD for rater 2 when placing pre-fixed size ROIs.

DISCUSSION

This study sought to evaluate within and between rater

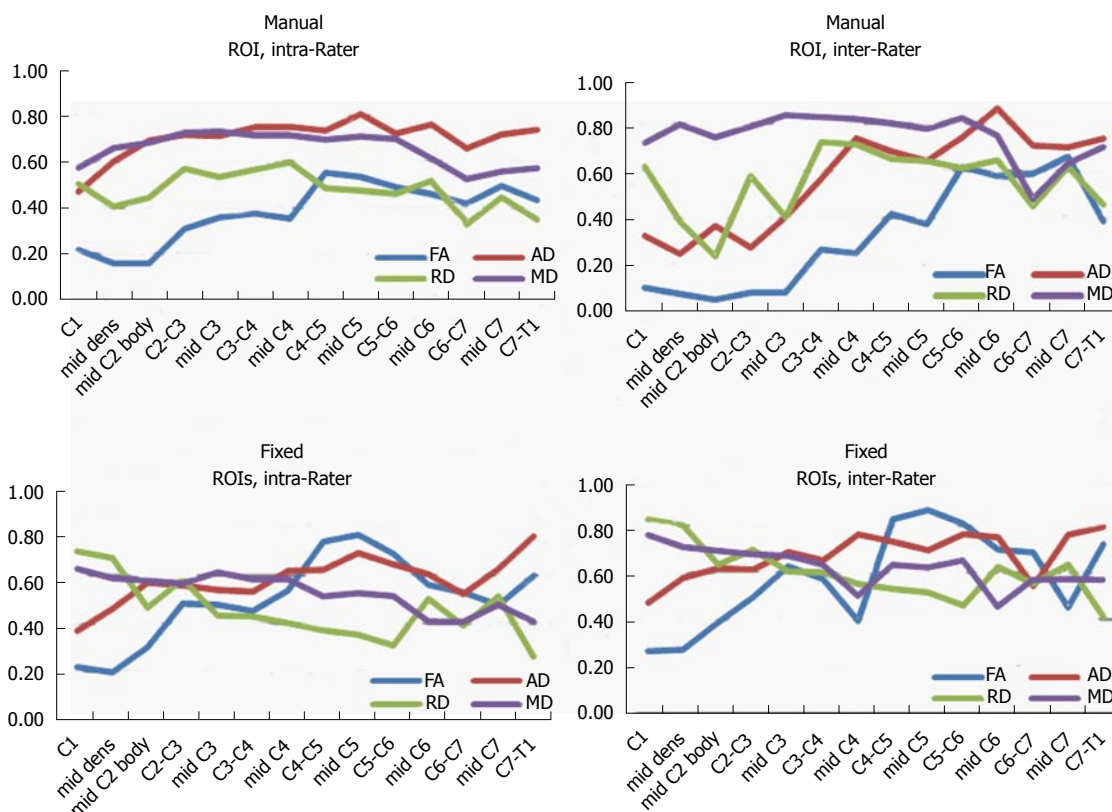


Figure 2 Intra-class-correlation values as a function of spinal cord level for fractional anisotropy, axial diffusivity, radial diffusivity and mean diffusivity. ROI: Region of interest; FA: Fractional anisotropy; AD: Axial diffusivity; RD: Radial diffusivity; MD: Mean diffusivity.

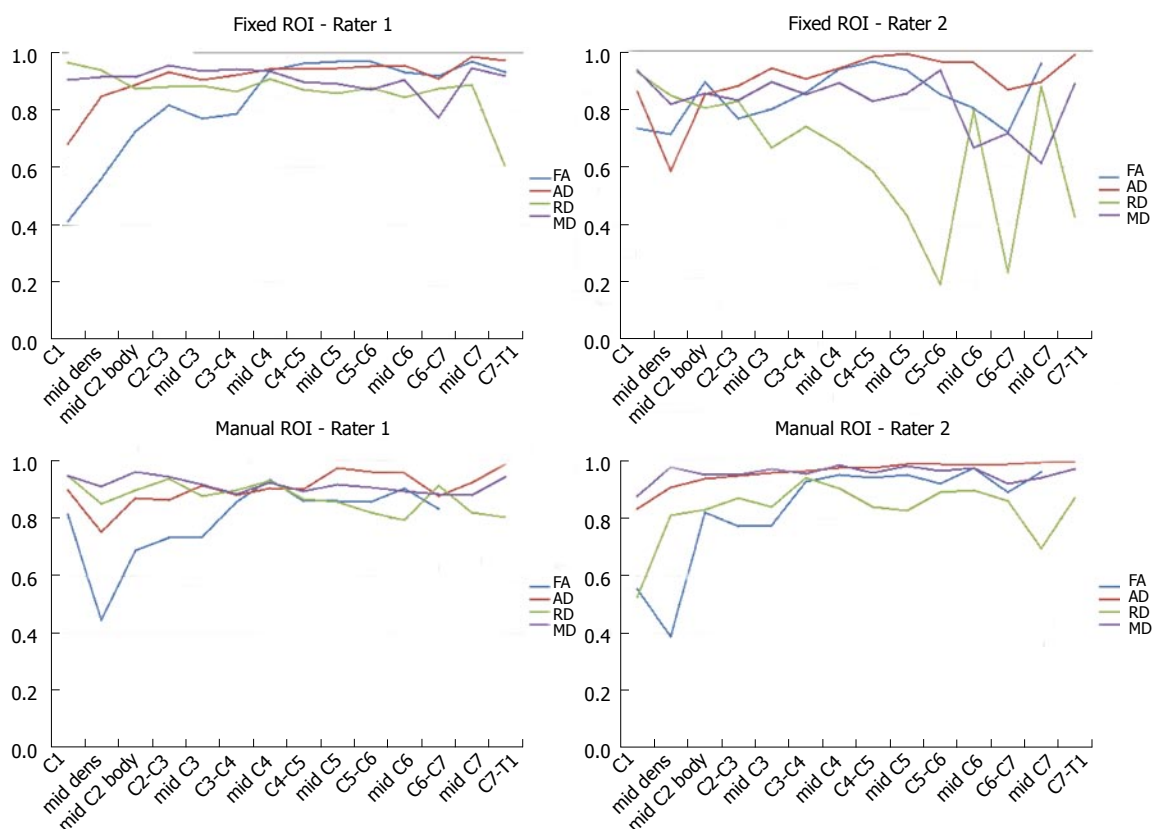


Figure 3 Cronbach's alpha values as a function of spinal cord level for fractional anisotropy, axial diffusivity, radial diffusivity and mean diffusivity. ROI: Region of interest; FA: Fractional anisotropy; AD: Axial diffusivity; RD: Radial diffusivity; MD: Mean diffusivity.

Table 1 Mean SD inter-rater and intra-rater values for fractional anisotropy, axial diffusivity ($\times 10^{-3}$ mm²/s), radial diffusivity ($\times 10^{-3}$ mm²/s), and mean diffusivity ($\times 10^{-3}$ mm²/s), for manually drawn regions of interest and fixed size regions of interest

			Pixels	FA	AD	RD	MD
Freehand ROI	Rater 1	Trial 1	24	0.50 \pm 0.13	1.35 \pm 0.52	0.70 \pm 0.54	0.92 \pm 0.53
		Trial 2	24	0.47 \pm 0.13	1.16 \pm 0.18	0.52 \pm 0.17	0.73 \pm 0.18
	Rater 2	Trial 1	17	0.48 \pm 0.12	1.53 \pm 0.65	0.88 \pm 0.64	1.10 \pm 0.65
		Trial 2	14	0.52 \pm 0.10	1.20 \pm 0.16	0.48 \pm 0.13	0.72 \pm 0.14
Fixed ROI	Rater 1	Trial 1	6	0.54 \pm 0.10	1.18 \pm 0.19	0.46 \pm 0.14	0.70 \pm 0.16
		Trial 2	6	0.54 \pm 0.10	1.18 \pm 0.16	0.47 \pm 0.13	0.71 \pm 0.14
	Rater 2	Trial 1	6	0.53 \pm 0.10	1.64 \pm 0.58	0.91 \pm 0.56	1.16 \pm 0.56
		Trial 2	6	0.54 \pm 0.10	1.19 \pm 0.15	0.45 \pm 0.11	0.70 \pm 0.12

ROI: Region of interest; FA: Fractional anisotropy; AD: Axial diffusivity; RD: Radial diffusivity; MD: Mean diffusivity.

agreements in DTI parameter values of the normal pediatric cervical spinal cord. Inter-rater reliability refers to the variability between raters and intra-rater reliability measures the agreement within raters across multiple trials.

There were significant differences between raters in the number of pixels they chose to outline using free-hand ROIs. There were no significant differences in DTI parameter values derived from these ROIs. Although one rater was more conservative in selecting the area of spinal cord tissue (16 pixels vs 24 pixels), the difference in the number of pixels may not have been large enough to detect difference in DTI parameter values.

When the free-hand and fixed-size ROI drawing methods were compared to each other, significant differences were found in DTI parameters. The large difference between the numbers of pixels selected to outline the spinal cord may reflect the differences found in DTI values. For example, rater 1 outlined 24 pixels using free-hand compared to 6 pixels when placing the pre-fixed ROI. A conservative outline may not be sensitive enough to detect physiological changes whereas a large ROI may include CSF. Thus consensus is needed to standardize ROI drawing techniques.

Overall agreement between and within raters was evaluated using the ICC coefficient and showed moderate to strong agreement between the repeated measurements (0.50-0.84). There was a variation in all DTI parameters at lower and upper spinal cord levels. Contributing factors to these differences could be signal drop-off at the edge of the neck coil. The lower cervical and upper thoracic levels were positioned at the extremities of the neck coil where signal-to-noise decreases, and accidental inclusion of CSF where image artifacts were prominent. Additionally, the lowest cervical levels (C4-C7) are the most sensitive to cardiac motion. Therefore some cardiac-related artifacts may have biased the selection or placement of ROIs. When examining DTI parameters individually, FA and RD showed the highest variability of ICC values. The agreement was lower in the pre-set ROIs, primarily in the upper and lower spinal cord levels (C1, C2, C6 and C7). The variations in these DTI parameters could be due to their relatively high sensitivity to CSF volume averaging. Furthermore, due to the decrease in cord

volume between C1 and T1, consistent ROIs were difficult to maintain. This may have led to the lower agreement in the fixed size ROIs. At levels where the spinal cord cross section is small, the rectangular 3 \times 2 ROI may have been too large and included artifact from surrounding CSF, while with larger cross sectional areas, the 3 \times 2 pixel-ROIs were too small and did not include enough spinal cord tissue. It is important to note that the 3 \times 2 pixel size ROI was chosen to be large enough to obtain sufficient data points but small enough to be potentially suitable for the atrophic spinal cord.

To examine if the raters showed any variability in their repeated measurements Cronbach's alpha was used. The results showed that although one rater was more conservative in outlining spinal cord area and selected less pixels, strong test re-test agreement was seen for all DTI parameters. There were few data points with lower Cronbach's alpha values in the lower and upper spinal cord levels, similar to the ICC analysis.

This study has some limitations. Only normally developed subjects were evaluated. A similar study in subjects with spinal cord injuries could provide different insights about the methodology of segmenting and measuring spinal cord tissue. Additionally, although both raters had extensive experience in DTI post-processing and agreed on the methodology used in this study, they may not have discussed all possible components in ROI drawing methods. There was a consensus of ROI size and shape taking into consideration the anatomical changes in cross sectional area at different levels of the spinal cord.

In conclusion, the usefulness of a non-invasive quantitative measurement depends on the validity, intra-rater and inter-rater reliability of the derived data for different conditions. This study demonstrates the importance of developing a robust method of DTI post-processing analysis, specifically ROI placement, to reduce operator variability and thereby develop accurate imaging biomarkers to examine spinal cord injury.

COMMENTS

Background

Diffusion tensor imaging (DTI) is a relatively new technique to examine the spinal cord *in vivo*. DTI offers a general understanding on structural connectivity

of axonal white matter, and is believed to be a more sensitive measure in assessing damage to tracts in the spinal cord. It quantifies diffusion of water molecules in each voxel of an image in directions parallel and transverse to the plane of neuronal axons. The unique anisotropic characteristics of the spinal cord may allow DTI to localize white matter, separate white from gray matter and assess structural damage of the cord. To be proven clinically reliable, the quantitative properties of spinal cord DTI need to be assessed by multiple reviewers. The purpose of this study was to assess inter- and intra-rater reliability between two ROI methods in pediatric spinal cord DTI.

Research frontiers

Information extracted from DTI might allow analysis of the association between anatomical measures and degree of disability. This can be applied to various spinal cord diseases to assess viable tissue after injury and even guide surgical planning. Poor reproducibility limits the potential clinical application of any imaging technique. This study highlights the importance of assessing inter- and intra-rater agreement in the analysis of DTI data.

Innovations and breakthroughs

While extensive data is available on the reliability and reproducibility of brain DTI, to the best of our knowledge there is lack of research on the reliability of ROI placement to quantify spinal cord DTI measures. The goal of this study was to assess inter-rater (between) and intra-rater (within) agreement in pediatric spinal cord DTI, as well as agreement between two methods of drawing regions of interest.

Applications

DTI provides a means to measure tissue integrity following SCI and can allow an association between physical disability and spinal cord volume loss. Given the sensitivity of DTI to white matter integrity, it could and has been used in demyelinating conditions, traumatic spinal cord injury, Wallerian degeneration, and other conditions where white matter integrity in affected or lost.

Terminology

DTI is a MRI-based technique for non-invasively examining diffusion of water molecules in each voxel of an image in directions parallel and transverse to the plane of neuronal axons. The quantitative characteristics of DTI allows for the characterization of physical and biophysical properties of tissue. Fractional anisotropy is a unit-less index used to characterize the directionality of the fibers. Axial diffusivity is parameter derived from DTI calculations that reflects diffusivity of water molecules parallel to the spinal cord tracts. Radial diffusivity represents diffusivity perpendicular to the spinal cord tracts.

Peer-review

This study evaluated within and between rater agreements in DTI parameter values of the normal pediatric cervical spinal cord. Inter-rater reliability refers to the variability between raters and intra-rater reliability measures the agreement within raters across multiple trials. The data showed that high reproducibility in spinal cord DTI can be achieved, and demonstrated the importance of setting detailed methodology for post-processing DTI data, specifically the placement of ROIs.

REFERENCES

- 1 **van Hecke W**, Nagels G, Emonds G, Leemans A, Sijbers J, van Goethem J, Parizel PM. A diffusion tensor imaging group study of the spinal cord in multiple sclerosis patients with and without T2 spinal cord lesions. *J Magn Reson Imaging* 2009; **30**: 25-34 [PMID: 19557843 DOI: 10.1002/jmri.21817]
- 2 **Vedantam A**, Jirjis MB, Schmit BD, Wang MC, Ulmer JL, Kurpad SN. Characterization and limitations of diffusion tensor imaging metrics in the cervical spinal cord in neurologically intact subjects. *J Magn Reson Imaging* 2013; **38**: 861-867 [PMID: 23389869 DOI: 10.1002/jmri.24039]
- 3 **Ellingson B**, Schmit B, Ulmer J, Kurpad S. Diffusion tensor magnetic resonance imaging in spinal cord injury. *Concepts in Magnetic Resonance Part A* 2008; **32A**: 219-237
- 4 **Ellingson BM**, Ulmer JL, Kurpad SN, Schmit BD. Diffusion tensor MR imaging of the neurologically intact human spinal cord. *AJNR Am J Neuroradiol* 2008; **29**: 1279-1284 [PMID: 18417607 DOI: 10.3174/ajnr.A1064]
- 5 **Fujiyoshi K**, Konomi T, Yamada M, Hikishima K, Tsuji O, Komaki Y, Momoshima S, Toyama Y, Nakamura M, Okano H. Diffusion tensor imaging and tractography of the spinal cord: from experimental studies to clinical application. *Exp Neurol* 2013; **242**: 74-82 [PMID: 22868199 DOI: 10.1016/j.expneurol.2012.07.015]
- 6 **Clark CA**, Werring DJ, Miller DH. Diffusion imaging of the spinal cord in vivo: estimation of the principal diffusivities and application to multiple sclerosis. *Magn Reson Med* 2000; **43**: 133-138 [PMID: 10642740]
- 7 **Andre JB**, Zaharchuk G, Saritas E, Komakula S, Shankaranarayan A, Banerjee S, Rosenberg J, Nishimura DG, Fischbein NJ. Clinical evaluation of reduced field-of-view diffusion-weighted imaging of the cervical and thoracic spine and spinal cord. *AJNR Am J Neuroradiol* 2012; **33**: 1860-1866 [PMID: 22555576 DOI: 10.3174/ajnr.A3134]
- 8 **Akter M**, Hirai T, Minoda R, Murakami R, Saiki S, Okuaki T, Kitajima M, Fukuoka H, Sasao A, Nishimura S, Yumoto E, Awai K, Yamashita Y. Diffusion tensor tractography in the head-and-neck region using a clinical 3-T MR scanner. *Acad Radiol* 2009; **16**: 858-865 [PMID: 19375950]
- 9 **Andre JB**, Bammer R. Advanced diffusion-weighted magnetic resonance imaging techniques of the human spinal cord. *Top Magn Reson Imaging* 2010; **21**: 367-378 [PMID: 22158130]
- 10 **Onu M**, Roceanu A, Sboto-Frankenstien U, Bendic R, Tarta E, Preoteasa F, Bajenaru O. Diffusion abnormality maps in demyelinating disease: correlations with clinical scores. *Eur J Radiol* 2012; **81**: e386-e391 [PMID: 22257426 DOI: 10.1016/j.ejrad.2011.12.014]
- 11 **Cheran S**, Shanmuganathan K, Zhuo J, Mirvis SE, Aarabi B, Alexander MT, Gullapalli RP. Correlation of MR diffusion tensor imaging parameters with ASIA motor scores in hemorrhagic and nonhemorrhagic acute spinal cord injury. *J Neurotrauma* 2011; **28**: 1881-1892 [PMID: 21875333 DOI: 10.1089/neu.2010.1741]
- 12 **Mulcahey MJ**, Samdani AF, Gaughan JP, Barakat N, Faro S, Shah P, Betz RR, Mohamed FB. Diagnostic accuracy of diffusion tensor imaging for pediatric cervical spinal cord injury. *Spinal Cord* 2013; **51**: 532-537 [PMID: 23608812 DOI: 10.1038/sc.2013.36]
- 13 **Oh J**, Saidha S, Chen M, Smith SA, Prince J, Jones C, Diener-West M, van Zijl PC, Reich DS, Calabresi PA. Spinal cord quantitative MRI discriminates between disability levels in multiple sclerosis. *Neurology* 2013; **80**: 540-547 [PMID: 23325903 DOI: 10.1212/WNL.0b013e31828154c5]
- 14 **Tanenbaum LN**. Clinical applications of diffusion imaging in the spine. *Magn Reson Imaging Clin N Am* 2013; **21**: 299-320 [PMID: 23642555 DOI: 10.1016/j.mric.2012.12.002]
- 15 **Shanmuganathan K**, Gullapalli RP, Zhuo J, Mirvis SE. Diffusion tensor MR imaging in cervical spine trauma. *AJNR Am J Neuroradiol* 2008; **29**: 655-659 [PMID: 18238846 DOI: 10.3174/ajnr.A0916]
- 16 **Koskinen E**, Brander A, Hakulinen U, Luoto T, Helminen M, Ylinen A, Ohman J. Assessing the state of chronic spinal cord injury using diffusion tensor imaging. *J Neurotrauma* 2013; **30**: 1587-1595 [PMID: 23758292 DOI: 10.1089/neu.2013.2943]
- 17 **Barakat N**, Mulcahey MJ, Shah P, Samdani A, Krisa L, Faro S, Mohamed FB. Diffusion tensor imaging in pediatric transverse myelitis: a case study. *J Pediatr Rehabil Med* 2012; **5**: 281-286 [PMID: 23411769]
- 18 **Lee JW**, Park KS, Kim JH, Choi JY, Hong SH, Park SH, Kang HS. Diffusion tensor imaging in idiopathic acute transverse myelitis. *AJR Am J Roentgenol* 2008; **191**: W52-W57 [PMID: 18647886 DOI: 10.2214/AJR.07.2800]
- 19 **Bisdas S**, Bohning DE, Besenski N, Nicholas JS, Rumboldt Z. Reproducibility, interrater agreement, and age-related changes of fractional anisotropy measures at 3T in healthy subjects: effect of the applied b-value. *AJNR Am J Neuroradiol* 2008; **29**: 1128-1133 [PMID: 18372415 DOI: 10.3174/ajnr.A1044]

- 20 **Hakulinen U**, Brander A, Ryymin P, Öhman J, Soimakallio S, Helminen M, Dastidar P, Eskola H. Repeatability and variation of region-of-interest methods using quantitative diffusion tensor MR imaging of the brain. *BMC Med Imaging* 2012; **12**: 30 [PMID: 23057584 DOI: 10.1186/1471-2342-12-30]
- 21 **Ozturk A**, Sasson AD, Farrell JA, Landman BA, da Motta AC, Aralasmak A, Yousem DM. Regional differences in diffusion tensor imaging measurements: assessment of intrarater and interrater variability. *AJNR Am J Neuroradiol* 2008; **29**: 1124-1127 [PMID: 18356471 DOI: 10.3174/ajnr.A0998]
- 22 **Brander A**, Kataja A, Saastamoinen A, Ryymin P, Huhtala H, Ohman J, Soimakallio S, Dastidar P. Diffusion tensor imaging of the brain in a healthy adult population: Normative values and measurement reproducibility at 3 T and 1.5 T. *Acta Radiol* 2010; **51**: 800-807 [PMID: 20707664 DOI: 10.3109/02841851.2010.495351]
- 23 **Veenith TV**, Carter E, Grossac J, Newcombe VF, Outtrim JG, Lupson V, Williams GB, Menon DK, Coles JP. Inter subject variability and reproducibility of diffusion tensor imaging within and between different imaging sessions. *PLoS One* 2013; **8**: e65941 [PMID: 23840380 DOI: 10.1371/journal.pone.0065941]
- 24 **Cercignani M**, Bammer R, Sormani MP, Fazekas F, Filippi M. Inter-sequence and inter-imaging unit variability of diffusion tensor MR imaging histogram-derived metrics of the brain in healthy volunteers. *AJNR Am J Neuroradiol* 2003; **24**: 638-643 [PMID: 12695195]
- 25 **Barakat N**, Mohamed FB, Hunter LN, Shah P, Faro SH, Samdani AF, Finsterbusch J, Betz R, Gaughan J, Mulcahey MJ. Diffusion tensor imaging of the normal pediatric spinal cord using an inner field of view echo-planar imaging sequence. *AJNR Am J Neuroradiol* 2012; **33**: 1127-1133 [PMID: 22300927 DOI: 10.3174/ajnr.A2924]
- 26 **Finsterbusch J**. High-resolution diffusion tensor imaging with inner field-of-view EPI. *J Magn Reson Imaging* 2009; **29**: 987-993 [PMID: 19306448]
- 27 **Barakat N**, Hunter L, Finsterbusch J, Shah P, Faro SH, Samdani AF, Betz R, Gaughan J, Mulcahey MJ, Mohamed FB. Diffusion tensor imaging of the pediatric spinal cord using an inner-FoV EPI pulse sequence in normals and patients with SCI. *Proc Intl Soc Mag Reson Med* 2011
- 28 **Barakat N**, Middleton D, Hunter L, Finsterbusch J, Shah P, Faro SH, Samdani AF, Betz R, Gaughan J, Mulcahey MJ, Mohamed FB. An investigation of motion correction algorithms for pediatric spinal cord DTI in normals and patients with SCI. *Proc Intl Soc Mag Reson Med* 2011
- 29 **Haas M**. Statistical methodology for reliability studies. *J Manipulative Physiol Ther* 1991; **14**: 119-132 [PMID: 2019821]
- 30 **Shrout PE**, Fleiss JL. Intraclass correlations: uses in assessing rater reliability. *Psychol Bull* 1979; **86**: 420-428 [PMID: 18839484]

P- Reviewer: Li YZ, Prakash N **S- Editor:** Song XX **L- Editor:** A
E- Editor: Wu HL



Retrospective Study

Intraperitoneal tuberculous abscess: Computed tomography features

Peng Dong, Jing-Jing Chen, Xi-Zhen Wang, Ya-Qin Wang

Peng Dong, Xi-Zhen Wang, Ya-Qin Wang, Medical Imaging Center, the Affiliated Hospital of Weifang Medical University, Weifang 261031, Shandong Province, China

Jing-Jing Chen, Department of Radiology, the Affiliated Hospital of Medical College, Qing Dao University, Qingdao 266000, Shandong Province, China

Author contributions: Dong P and Chen JJ designed the research; Dong P, Chen JJ, Wang XZ and Wang YQ performed the research; Dong P, Chen JJ, Wang XZ and Wang YQ analyzed the data; Dong P, Chen JJ, Wang XZ and Wang YQ wrote the paper.

Supported by Project of Medicine and Health Development Plan of Shandong Province, No. 2011HZ112, China; and Shandong Provincial Natural Science Foundation of China, No. ZR2014HL083.

Institutional review board statement: The study was reviewed and approved by the Institutional Review Board of the Affiliated Hospital of Weifang Medical University.

Informed consent statement: All study participants provided informed written consent prior to study enrollment.

Conflict-of-interest statement: The authors declare that they have no conflicts of interest in this study.

Data sharing statement: No additional data are available.

Open-Access: This article is an open-access article which was selected by an in-house editor and fully peer-reviewed by external reviewers. It is distributed in accordance with the Creative Commons Attribution Non Commercial (CC BY-NC 4.0) license, which permits others to distribute, remix, adapt, build upon this work non-commercially, and license their derivative works on different terms, provided the original work is properly cited and the use is non-commercial. See: <http://creativecommons.org/licenses/by-nc/4.0/>

Correspondence to: Peng Dong, MD, Professor, Medical Imaging Center, the Affiliated Hospital of Weifang Medical University, Shenglidong Street, Weifang 261031, Shandong Province, China. dongpeng98021@sina.com
 Telephone: +86-536-8462397

Fax: +86-536-8462397

Received: March 2, 2015
 Peer-review started: March 4, 2015
 First decision: April 24, 2015
 Revised: May 12, 2015
 Accepted: July 18, 2015
 Article in press: July 27, 2015
 Published online: September 28, 2015

Abstract

AIM: To evaluate the computed tomography (CT) features of intraperitoneal tuberculous abscess (IPTA).

METHODS: Eight patients with IPTA confirmed by pathology were analyzed retrospectively. The clinical symptoms, medical images, and surgical findings were evaluated. Involvement of the intestine, peritoneum, viscera, and lymph nodes was also assessed.

RESULTS: All 8 patients had a history of abdominal discomfort for 1 to 6 mo. Physical examination revealed a palpable abdominal mass in 6 patients. Three patients had no evidence of pulmonary tuberculosis (TB). All IPTAs (11 abscesses) were seen as a multiseptated, peripherally enhanced, hypodense mass with enlarged, rim-enhanced lymph nodes. The largest abscess diameter ranged from 4.5 cm to 12.2 cm. CT showed 2 types of IPTA: Lymph node fusion and encapsulation. Of the 8 patients, one had liver tuberculosis and one had splenic and ovarian tuberculosis. Two cases showed involvement of the terminal ileum and ileocecal junction. Ascites were found in 4 cases. Three patients had peritonitis and mesenteritis. Three patients showed involvement of the omentum. Three patients had histological evidence of caseating granuloma, and 5 had histological evidence of acid-fast bacilli.

CONCLUSION: CT is crucial in the detection and chara-

cterization of IPTA. Certain CT findings are necessary for correct diagnosis.

Key words: Tuberculosis; Abdomen; Abscess; Diagnosis; Computed tomography; X-ray

© **The Author(s) 2015.** Published by Baishideng Publishing Group Inc. All rights reserved.

Core tip: Intra-peritoneal tuberculous abscess (IPTA) is a rare and serious form of extra-pulmonary tuberculosis. Early and accurate diagnosis of tuberculous abscess is important for treatment. This retrospective study was to evaluate the computed tomography (CT) features in 8 patients with pathologically confirmed IPTA. CT is crucial in the detection and characterization of IPTA. Although the qualitative diagnosis of IPTA requires positive pathologic findings, certain CT features (such as a multiseptated, peripherally enhanced, hypodense mass with rim-enhanced lymph nodes, peritoneum/mesentery/omentum changes) are necessary for correct diagnosis.

Dong P, Chen JJ, Wang XZ, Wang YQ. Intraperitoneal tuberculous abscess: Computed tomography features. *World J Radiol* 2015; 7(9): 286-293 Available from: URL: <http://www.wjgnet.com/1949-8470/full/v7/i9/286.htm> DOI: <http://dx.doi.org/10.4329/wjrr.v7.i9.286>

INTRODUCTION

Infection with *Mycobacterium tuberculosis* (TB) is more common in developing countries than in developed countries^[1]. In developed countries, TB remains a health care challenge due to human immunodeficiency virus (HIV) infection and immigration from endemic areas^[2-5].

Although the most commonly involved organ in TB is the lung, approximately 12.5% of cases are extra-pulmonary, and the abdomen is involved in 11%-16% of patients with extra-pulmonary TB^[6]. The more commonly involved sites of abdominal TB are the intestine, peritoneum and lymph nodes^[6-8].

Accurate diagnosis of tuberculous peritonitis is crucial because delayed treatment may lead to high risk of death^[9]. An intra-peritoneal tuberculous abscess (IPTA) is a rare and serious form of extra-pulmonary TB^[6,8,10,11]. Early and accurate diagnosis of tuberculous abscess is important for treatment^[12,13]. Only a few non-HIV patients with IPTA have been reported previously^[6,14]. IPTA in non-HIV patients is a diagnostic challenge as the clinical symptoms and imaging findings can be mistaken for other peritoneal diseases. If computed tomography (CT) findings were helpful in the differentiation between IPTA and other peritoneal diseases, this would reduce or avoid unnecessary invasive diagnostic procedures such as laparoscopy.

The aim of this retrospective study was to evaluate the CT features in 8 patients with pathologically con-

firmed IPTA.

MATERIALS AND METHODS

The clinical symptoms, CT findings and pathological findings of 8 patients with IPTA identified by pathology, including 6 females and 2 males (age range: 22-58 years) were collected from 2001 to 2013. None of the 8 patients had evidence of HIV infection.

Five patients were examined using a 16-detector CT scanner (Siemens Sensation, Germany). Three patients were examined using a 64-slice CT scanner (Brilliance 64, Philips Medical Systems, the Netherlands). CT parameters were as follows: 140 KV, 220-600 mAs, slice thickness 5 mm, and multi-planar reconstruction (MPR) slice width 1 mm. The CT scan was performed following intravenous administration of contrast material (80-100 mL, Ultravist 300 mgI/mL, Bayer Schering Pharma AG, Berlin, Germany) at an injection rate of 2.0-3.0 mL/s in all patients. Oral contrast material (1.2% Angiografin) was administered to all patients.

The CT images were retrospectively reviewed by 2 experienced radiologists with consensus. The CT signs included the abscess itself and its relationship with the adjacent structures. The involvement of lymph nodes, peritoneum, mesentery and other organs were also evaluated.

Laparotomy was performed with abscess removal in 2 cases. Laparoscopy was performed in 2 cases and aspiration biopsy was performed in 4 cases. The pathological diagnosis was established on the basis of the following criteria: Histological evidence of caseating granuloma or histological evidence of acid-fast bacilli.

RESULTS

Clinical symptoms

The clinical symptoms of all patients are shown in Table 1. Eight patients reported a history of abdominal discomfort for 1 to 6 mo. One patient had persistent right upper abdominal pain for 10 d. Physical examination revealed a palpable abdominal mass in 6 patients. Three patients had no history of lung TB.

CT findings

All IPTAs in this study were seen as a multiseptated, peripherally enhanced, hypodense mass with a regular or irregular shape. The location, size, shape, and margin of the abscesses are shown in Table 2. The maximum abscess diameter ranged from 4.5 to 12.2 cm (Figures 1-4).

The enlarged lymph nodes had homogeneous enhancement or rim enhancement. The CT findings of the lymph nodes are shown in Table 2. The CT findings of the peritoneal and visceral lesions are shown in Table 3.

In these 8 patients, a total of 11 abscesses were detected. One patient had 3 abscesses, and the margin of all 3 abscesses was poorly defined. The other 7 patients had 8 abscesses, and their margins were well

Table 1 Clinical findings of 8 patients with intraperitoneal tuberculous abscess

Case	Age (yr)	Sex	Clinical symptoms	Pulmonary TB	Surgery
1	58	Female	Weight loss, low grade fever and night sweats for 5 mo Persistent right upper quadrant pain for 10 d, accompanied by loss of appetite. Right lower quadrant pain and fullness for 1 mo with a clinically palpable abdominal mass	Hematogenous pulmonary TB	Laparoscopy
2	35	Male	Weight loss, low grade fever, night sweats and obscure abdominal pain for 5 mo with a clinically palpable abdominal mass	-	Laparotomy
3	24	Male	Obscure abdominal pain and low grade fever for 2 mo	-	Laparotomy
4	40	Female	Weight loss, low grade fever, night sweats and obscure abdominal pain for 4 mo, with a clinically palpable abdominal mass	Obsolete pulmonary TB	Laparoscopy
5	27	Female	Obscure abdominal pain and low grade fever for 2 mo with a clinically palpable abdominal mass	-	Biopsy
6	22	Female	Obscure abdominal pain and low grade fever for 2 mo with a clinically palpable abdominal mass	Obsolete pulmonary TB	Biopsy
7	37	Female	Weight loss, low grade fever, night sweats, and obscure abdominal pain for 5 mo with a clinically palpable abdominal mass	Obsolete pulmonary TB	Biopsy
8	34	Female	Weight loss, low grade fever, night sweats, and obscure abdominal pain for 5 mo	Obsolete pulmonary TB	Biopsy

TB: Tuberculosis.

Table 2 Computed tomography findings of intraperitoneal tuberculous abscess in 8 patients

Case	Location, size (cm), shape and margin of the abscess	Location of the enlarged lymph node and its size (cm)	Number of rim-enhanced lymph nodes
1	(1) Subphrenic space, 3 × 3.5 × 7.2, irregular shape, the margin was poorly defined (2) Perihepatic space, 5 × 8.9 × 12.2, irregular shape, the margin was poorly defined with adhesion to the gastric wall and gallbladder (3) Lower abdominal cavity, 4.5 × 5.8 × 7.1, irregular shape, the margin was well defined	Pericardial region and para-aortic region; the largest lymph node was < 1	Small number
2	Middle-lower abdominal cavity, 6.5 × 6.8 × 7.6, irregular shape, the margin was well defined encasing the mesenteric vessels	Mesenteric root and beside the abscess; the largest lymph node was < 1	Small number
3	Peripancreatic region, 3.7 × 4.1 × 4.5, regular shape, the regional margin of the abscess was poorly defined	Peripancreatic and portacaval space; the largest lymph node was 2.7 × 1.8	Multiple
4	(1) Lower abdominal cavity, 5.1 × 6.0 × 6.2, irregular shape, the regional margin was poorly defined (2) Lower abdominal cavity, 2.1 × 3.8 × 5.5, irregular shape, the margin was well defined	Lymph nodes clustered in the mesenteric root; the largest lymph node was < 1	Small number
5	Peripancreatic region, 3.1 × 3.8 × 5.1, regular shape, the regional margin was poorly defined	Peripancreatic region and the hepatogastric ligament; the largest lymph node was 2.5 × 1.7	Multiple
6	Beside the jejunum, 2.5 × 4.2 × 5.0, regular shape, the regional margin was poorly defined encasing the mesenteric vessels	Peripancreatic region and the hepatogastric ligament; the largest lymph node was 2.3 × 1.5	Multiple
7	Beside the ileum, 3.2 × 4.0 × 5.1, regular shape; the regional margin was poorly defined encasing the mesenteric vessels	Para-aortic region and mesentery; the largest lymph node was 0.8 × 1.3	Small number
8	Peripancreatic region, 3.2 × 3.9 × 5.2, regular shape, the regional margin was poorly defined	Hepatoduodenal ligament, peripancreatic region and mesentery; the largest lymph node was 1.7 × 1.9	Multiple

CT: Computed tomography; IPTA: Intraperitoneal tuberculous abscess.

defined or the regional margin was poorly defined.

Three cases with abscesses located in the peripancreatic area and one case with an abscess located in the small bowel mesentery had multiple enlarged lymph nodes with rim enhancement and homogeneous enhancement (Figures 1-4).

Four cases with abscesses located in the peritoneal cavity had multiple enlarged lymph nodes, most of which showed homogeneous enhancement and a small number of lymph nodes showed rim enhancement (Figures 1-4).

Of the 8 cases, one was confirmed to have liver TB, and one had splenic and ovarian TB. Two cases showed

involvement of the terminal ileum and ileocecal junction. Two of the 8 cases had a small amount of ascites and another 2 cases had a large number of ascites.

Three cases with tuberculous peritonitis showed a smooth uniform thickened peritoneum (one case) or nodular/irregular thickened peritoneum (2 cases). Five cases showed increasing density of the adjacent mesentery and mesenteric thickening, 2 of which had crowded mesenteric vascular bundles and thickened fiber strands. Two cases showed abscess adhesion to the hepatoduodenal ligament. One case showed a caked appearance of the omentum, and 2 cases showed a nodular omentum (Figure 5).

Table 3 Computed tomography findings of other tuberculous lesions

Case	Peritoneum	Ascites	Other TB sites
1	Irregular or nodular thickening of the diaphragmatic and perihepatic peritoneum with homogeneous enhancement; nodular omentum	Small amount	Liver TB; adjacent cecal wall is thickened
2	Mesenteric thickening with increasing density of the adjacent mesentery; crowded mesenteric vascular bundles and thickened fiber strands in the mesentery	-	-
3	Increasing density in the hepatoduodenal ligament	-	-
4	Mesenteric thickening with increasing density of the adjacent mesentery. Crowded mesenteric vascular bundles and thickened fiber strands in the mesentery	Small amount	Wall of the terminal ileum and ileocecal junction was thickened
5	Increasing density in the hepatoduodenal ligament	-	-
6	Mesenteric thickening with increasing density of the adjacent mesentery	-	Splenic and ovarian involvement
7	Mesenteric thickening with increasing density of the adjacent mesentery and caked omentum. Smooth uniform thickened peritoneum with homogeneous enhancement	Large number	-
8	Mesenteric thickening with increasing density of the adjacent mesentery; multiple nodular shadows in the mesentery; nodular omentum; irregular or nodular thickening of the peritoneum with homogeneous enhancement	Large number	Wall of the terminal ileum was thickened

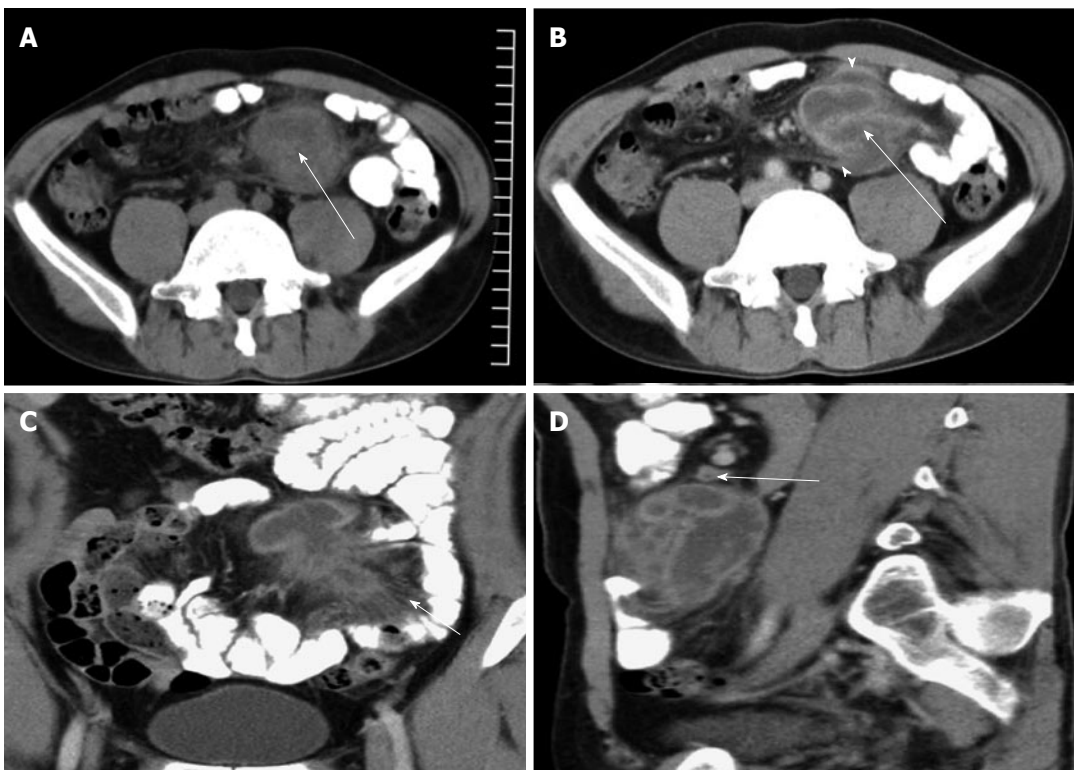


Figure 1 Tuberculous abscess in the mesentery. A: Axial CT image showed a low density abscess measuring 4.5 cm × 6.2 cm in the small bowel mesentery (arrow); B: Axial CT image (venous phase) showing a low density abscess with enhancement of the wall and septa (arrow). Adjacent parietal peritoneum was thickened with heterogeneous enhancement (arrowhead); C: Coronal CT image showed that the abscess was irregular. The density of the mesentery was increasing. Crowded mesenteric vascular bundles and thickened fiber strands were seen (arrow); D: Sagittal CT image showed a low density abscess with rim enhancement and slightly enlarged lymph nodes (arrow). CT: Computed tomography.

Pathological findings

Of the 8 cases, 3 had histological evidence of caseating granuloma, and 5 had histological evidence of acid-fast bacilli.

DISCUSSION

Accurate diagnosis of tuberculous peritonitis is important for clinical treatment^[9]. IPTA (a rare and serious form of tuberculous peritonitis) is a diagnostic challenge for the radiologist as its clinical symptoms and imaging findings may easily be mistaken for other lesions^[6,8,10,11].

Abdominal TB is more common in patients aged 25-45 years, and has a slight female predominance^[15]. In this study, the IPTA patients were aged 22 to 58 years with a female predominance.

Possible routes of abdominal TB include reactivation of a silent tuberculous lesion, infection spreading *via* swallowed sputum, hematogenous dissemination, and contiguity from adjacent tuberculous lesions^[1]. Choi *et al*^[16] reported that the absence of fever or laboratory data and negative cultures for TB cannot reliably rule out involvement of the peritoneum in TB. In the present study, all 8 patients had a history of abdominal

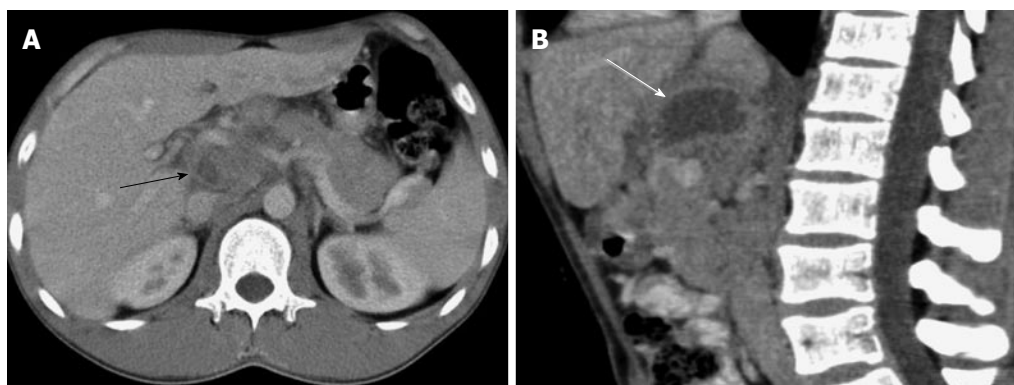


Figure 2 Tuberculous abscess located in the peripancreatic area. A: Axial CT image showed enlarged lymph nodes in the portacaval space and peripancreatic area with rim enhancement (arrow); B: Sagittal CT image showed a peripherally enhancing, hypodense mass in the peripancreatic area (arrow), measuring approximately 3.7 cm × 4.1 cm × 4.5 cm. CT: Computed tomography.

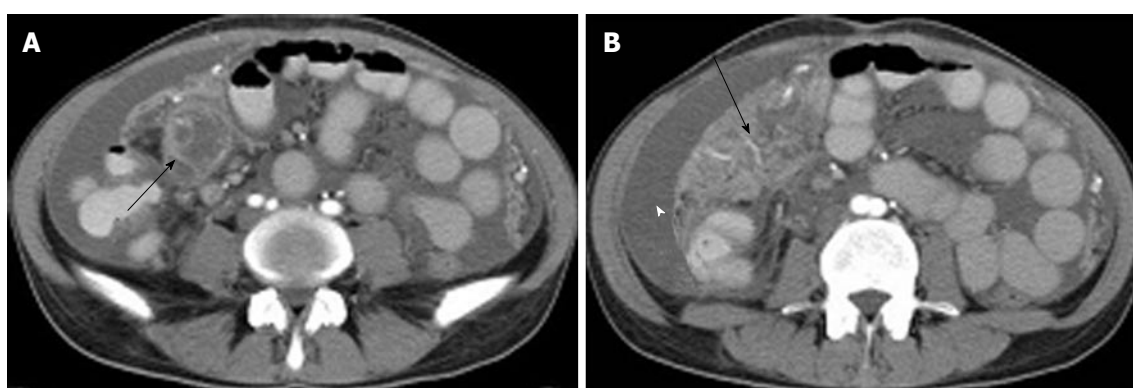


Figure 3 Tuberculous abscess located beside the jejunum. A: Axial CT image showed a multiseptated, peripherally enhancing, hypodense mass beside the jejunum (arrow), measuring approximately 3.2 cm × 4.0 cm × 5.1 cm; B: Axial CT image showed a caked appearance of the omentum (arrow). Irregular thickened peritoneum with homogeneous enhancement and ascites were also seen (arrow head). CT: Computed tomography.

discomfort and fever which supported the diagnosis of TB infection.

In cases with abdominal TB, the chest X-ray films of 10%-68.5% of cases showed evidence of healed or active pulmonary TB^[15]. For patients with isolated pancreatic TB, the chest X-ray film may be negative or show evidence of obsolete TB in areas where TB infection is endemic^[13]. In our study, the chest X-ray films of 37.5% of cases were negative, the chest X-ray films of 50.0% of cases showed evidence of obsolete pulmonary TB, and only 12.5% of patients showed evidence of active pulmonary TB on chest X-ray films. Thus, the lack of evidence of active pulmonary TB on chest X-ray film does not rule out the diagnosis of IPTA.

Nos *et al.*^[11] described an isolated mesenteric tuberculous abscess in a patient with HIV infection as a huge hypodense mass with a thick capsule and multiple septations. There was no associated abdominal lymph node enlargement. In our study, IPTA in non-HIV patients was seen as a multiseptated, peripherally enhanced, hypodense mass, with multiple enlarged lymph nodes. Combining the CT findings of IPTA, the location of the abscesses, and the CT findings of the lymph nodes, the IPTAs in this study were of 2 types: (1) lymph node fusion; and (2) encapsulation.

Lymph node fusion type IPTA: The more common sites of abdominal TB were the intestine, peritoneum, and lymph nodes^[6-8]. Lymphadenopathy resulting from abdominal TB is usually associated with gastrointestinal TB and is less common in peritoneal or solid organ lesions. In some patients with abdominal TB, lymphadenopathy is the only positive imaging finding, especially in the periportal region^[17]. Lymphadenopathy induced by abdominal TB commonly involves the mesenteric root, and celiac and peripancreatic lymph nodes. This is due to drainage of the ingested TB by the lymphatics in the small bowel, right hemicolon and ileocecal region^[17].

In this study, 3 cases showed an isolated abscess located in the peripancreatic area, with multiple enlarged lymph nodes (the diameter of the largest lymph node was > 1.9 cm). The maximum abscess diameter ranged from 4.5 cm to 5.2 cm. The regional margin of the abscesses was poorly defined. Multiple enlarged lymph nodes showed rim enhancement. The abscess and enlarged lymph nodes were the only signs of the disease in 2 cases. One of the 3 cases also showed involvement of the omentum, parietal peritoneum, mesentery, and terminal ileum. Another case showed an isolated abscess located in the jejunal mesentery with multiple, rim-enhanced, enlarged lymph nodes (the diameter of the

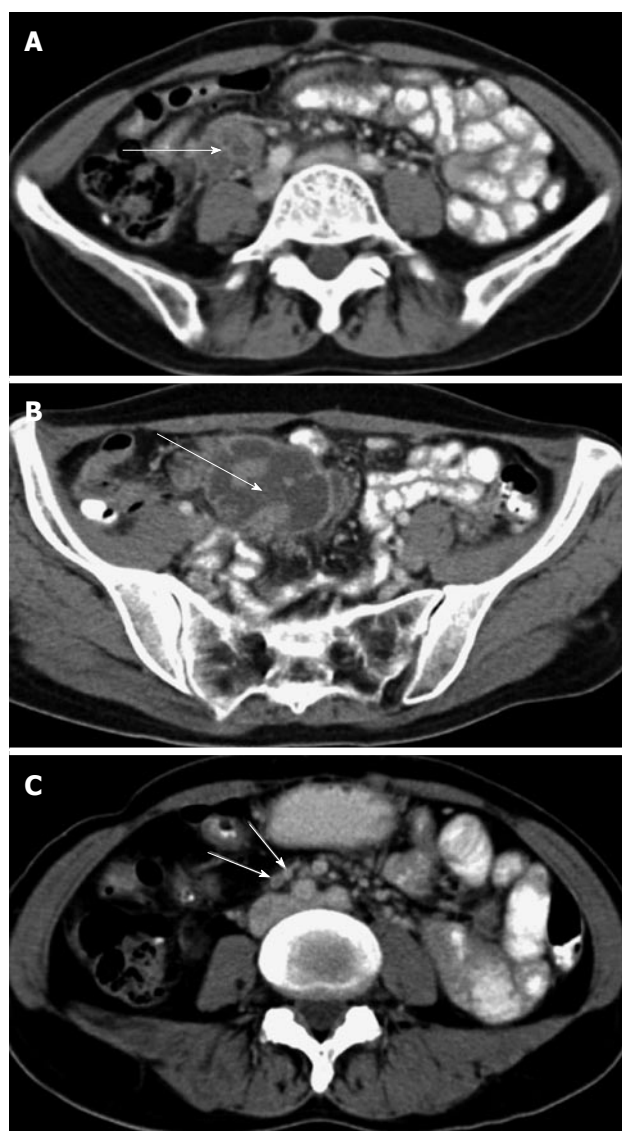


Figure 4 Two tuberculous abscesses located in the lower abdominal cavity. A, B: Axial CT images showed 2 multiseptated, peripherally enhanced, hypodense masses located in the lower abdominal cavity (arrow), measuring approximately 2.1 cm × 3.8 cm × 5.5 cm and 5.1 cm × 6.0 cm × 6.2 cm, respectively; C: Axial CT image showed slightly enlarged lymph nodes with rim enhancement and homogeneous enhancement (arrow). CT: Computed tomography.

largest lymph node was 2.5 cm). The abscess measured 2.5 cm × 4.2 cm × 5.0 cm in size, and the regional margin of the mass was poorly defined. Of these 4 cases, 2 showed obsolete pulmonary tuberculosis and 2 had no evidence of pulmonary TB.

Pereira *et al.*^[17] reported that the caseation and liquefaction substances in the center of the enlarged lymph node with TB infection result in the rim enhancement on contrast-enhanced CT images. It was reported that the enlarged lymph nodes with TB infection measured less than 4.0 cm in diameter because of pathologic self-limiting growth^[18]. In these 4 cases, the abscesses located in the mesenteric root, celiac, porta hepatis, and peripancreatic region with multiple, rim-enhanced, enlarged lymph nodes had unclear

boundaries, and the abscess measured less than 5.2 cm in diameter. Thus, a tuberculous abscess may be the result of the fusion of rim-enhanced, enlarged lymph nodes.

A multiseptated, peripherally enhanced, hypodense mass with a regular shape and multiple, rim-enhanced, enlarged lymph nodes beside the mass were typical features of the lymph node fusion type IPTA.

Encapsulation type IPTA: Tuberculous peritonitis includes the “wet” type, “dry” or “plastic” type, and “fibrotic-fixed” type^[19]. The “dry” or “plastic” type is rare and characterized by caseous nodules, a fibrous peritoneal reaction and dense adhesions^[17].

In this study, 3 cases with abscesses located in the peritoneal cavity and one case with an abscess located in the small bowel mesentery showed multiple enlarged lymph nodes, most of which showed homogeneous enhancement, while a small number showed rim enhancement.

Of these 4 cases, one had active pulmonary tuberculosis, 2 had obsolete pulmonary tuberculosis, and one had no past history of pulmonary tuberculosis. In addition, 2 of these 4 cases had an isolated abscess and 2 had multiple abscesses with or without an irregular shape. The maximum abscess diameter was 5.1 cm to 12.2 cm. A few rim-enhanced, enlarged lymph nodes (the diameter of the largest lymph node was < 1.5 cm) were detected.

Because of the small number of rim-enhanced lymph nodes in these 4 patients and the location of the abscesses (not located in the lymph node gathering area), formation of the IPTA was not caused by rim-enhanced lymph node fusion.

Intraoperative findings in 2 cases showed that the sigmoid colon and jejunum constituted the side walls of the abscess; the front wall was the small bowel mesentery, and the posterior wall was the parietal peritoneum. Based on these findings, this type of IPTA was formed by the bowel loops, peritoneum, mesentery, or organs encapsulating the intraperitoneal caseous substances.

A multiseptated, peripherally enhanced, hypodense mass with a small number of rim-enhanced, enlarged lymph nodes were typical features of the encapsulation type. The appearance of the rim-enhanced lymph nodes was the key feature in the diagnosis.

In our study, involvement of the omentum was shown as a nodular/caked appearance, and peritoneal TB was seen as a uniform or irregular thickening of the peritoneum, which was similar to reports in the literature^[9,20]. Involvement of the mesentery in this study was seen as an increased density of the mesentery and mesenteric thickening, a nodular mesentery appearance, mesenteric vascular bundles, and thickened fiber strands. These findings were consistent with reports in the literature^[9,20].

Heterogeneously enhanced, homogeneously enhanced, and poorly enhanced lymph nodes may occur in patients with TB infection^[21]. Lymph nodes with central low

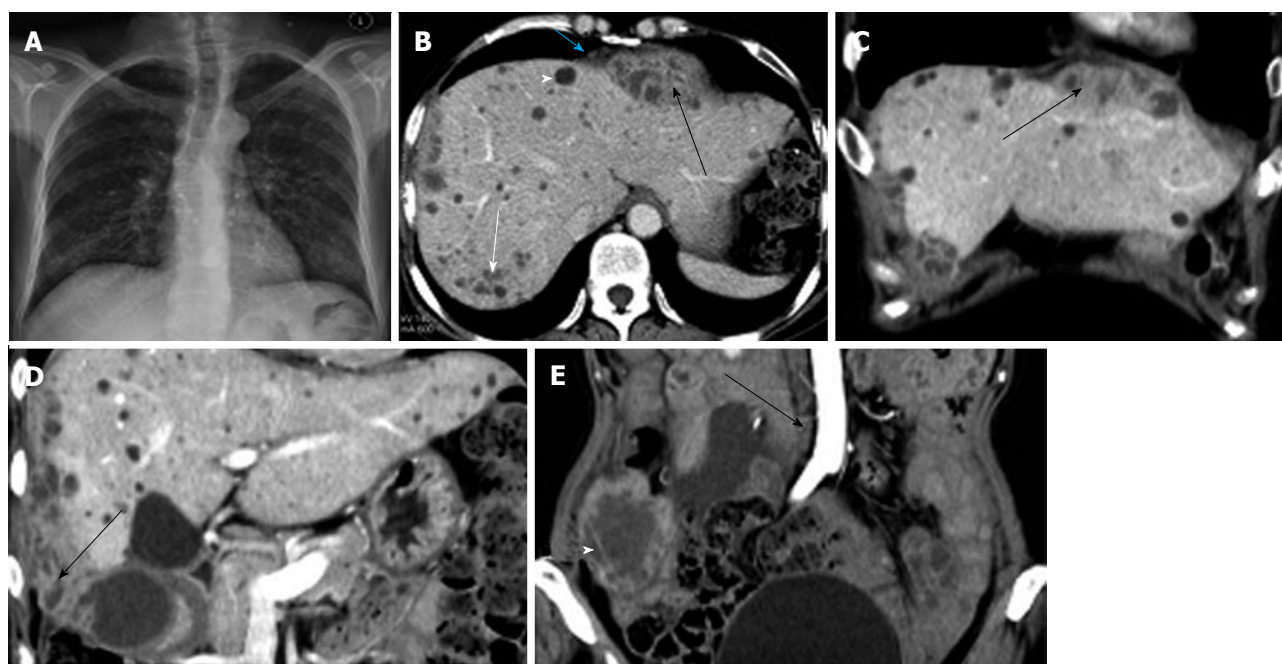


Figure 5 Three tuberculous abscesses located in the abdominal cavity. A: Chest X-ray film showed active pulmonary tuberculosis; B, C: Axial and coronal CT images showed a multisepated, peripherally enhanced, hypodense mass located in the subphrenic space measuring 3.0 cm × 3.5 cm × 7.2 cm (black arrow). A liver tuberculous lesion (white arrow) and liver cyst (arrowhead) were also detected. Nodular thickening of the diaphragmatic peritoneum showed homogeneous enhancement (blue arrow); D: Coronal CT image showed a multisepated, peripherally enhanced, hypodense mass with irregular shape located in the perihepatic space measuring approximately 5.0 cm × 8.9 cm × 12.2 cm (arrow); E: Coronal CT image showed a multisepated, peripherally enhanced, hypodense mass located in the lower abdominal cavity measuring approximately 4.5 cm × 5.8 cm × 7.0 cm (arrow head). Enlarged lymph nodes with rim enhancement located in the para-aortic region were detected (arrow). CT: Computed tomography.

attenuation and rim enhancement in patients with TB infection can be confused with necrotic metastatic lymphadenopathy^[22,23]. In patients with a known primary malignancy, enlarged abdominal lymph nodes are more likely to be nodal metastases^[2]. Patients with non-Hodgkin's lymphoma who have undergone therapy may show rim-enhanced lymph nodes in the mesentery on CT images, simulating tuberculous lymphadenopathy involving the mesentery and other diseases^[24-26]. In patients with a known clinical history of non-Hodgkin's lymphoma, a differential diagnosis is likely to be obtained.

CT findings indicating intra-peritoneal abscess caused by Crohn's disease show involvement of the left colon and homogenously enhanced lymph nodes^[14,27,28]. Intra-abdominal lymphadenopathy of more than 1 cm was observed more frequently in intestinal TB and abdominal TB lymphadenopathy^[29,30].

There are some potential limitations in our study. First, this was a retrospective study and some cases did not have 3-dimensional reconstruction images. Second, the patient sample was not large enough, which limited evaluation of statistical significance.

In conclusion, CT plays an important role in the detection and characterization of IPTA. Understanding the wide spectrum of CT appearances in IPTA should alert the radiologist to consider its diagnosis, especially among high-risk patients. Although the qualitative diagnosis of IPTA requires positive pathologic findings, certain CT features (such as a multisepated, peripherally

enhanced, hypodense mass with rim-enhanced lymph nodes, peritoneum/mesentery/omentum changes) are necessary for diagnosis.

COMMENTS

Background

Intra-peritoneal tuberculous abscess (IPTA) is a rare and serious form of extra-pulmonary tuberculosis. Early and accurate diagnosis of the tuberculous abscess is important for treatment. IPTA in non-human immunodeficiency virus patients is a diagnostic challenge as the clinical symptoms and imaging findings are easily mistaken for other peritoneal diseases. If computed tomography (CT) findings were helpful for the differentiation between IPTA and other peritoneal diseases, this would reduce or avoid unnecessary invasive diagnostic procedures.

Research frontiers

CT plays an important role in the diagnosis of abdominal abscesses. This study reports on the CT features in 8 patients with IPTA.

Innovations and breakthroughs

IPTA represents a diagnostic dilemma. The authors reviewed 8 patients with this condition and reviewed the related literature to identify CT features for diagnosis.

Applications

The identification of relatively specific CT findings of IPTA may help to reduce or avoid unnecessary invasive diagnostic procedures.

Peer-review

The aim pursued by the authors in this work is quite interesting. The computed tomography findings could be very helpful for the differentiation between the intra-peritoneal tuberculous abscess and other peritoneal diseases, because

with this technique it would reduce or avoid unnecessary invasive diagnostic procedures. This would need a good reference for the different lesion forms that can be observed. In this sense, the authors do an excellent description of the 8 cases studied (especially those with three-dimensional reconstruction images).

REFERENCES

- 1 **Flemming GM**, Oberschmid B, Siebolts U, Hirsch W, Schuster V. Abdominal tuberculosis in children and adolescents: to this day a diagnostic challenge. *Klin Padiatr* 2013; **225**: 47-49 [PMID: 22821291 DOI: 10.1055/s-0032-1321729]
- 2 **Lee WK**, Van Tonder F, Tartaglia CJ, Dagia C, Cazzato RL, Duddalwar VA, Chang SD. CT appearances of abdominal tuberculosis. *Clin Radiol* 2012; **67**: 596-604 [PMID: 22212637 DOI: 10.1016/j.crad.2011.11.003]
- 3 **Kapoor VK**. Abdominal tuberculosis. *Postgrad Med J* 1998; **74**: 459-467 [PMID: 9926119 DOI: 10.1136/pgmj.74.874.459]
- 4 **Horvath KD**, Whelan RL. Intestinal tuberculosis: return of an old disease. *Am J Gastroenterol* 1998; **93**: 692-696 [PMID: 9625110 DOI: 10.1111/j.1572-0241.1998.207_a.x]
- 5 **LoBue PA**, Enarson DA, Thoen TC. Tuberculosis in humans and its epidemiology, diagnosis and treatment in the United States. *Int J Tuberc Lung Dis* 2010; **14**: 1226-1232 [PMID: 20843412]
- 6 **Khan R**, Abid S, Jafri W, Abbas Z, Hameed K, Ahmad Z. Diagnostic dilemma of abdominal tuberculosis in non-HIV patients: an ongoing challenge for physicians. *World J Gastroenterol* 2006; **12**: 6371-6375 [PMID: 17072964 DOI: 10.3748/wjg.v12.i39.6371]
- 7 **Maniar JK**, Kamath RR, Mandalia S, Shah K, Maniar A. HIV and tuberculosis: partners in crime. *Indian J Dermatol Venereol Leprol* 2006; **72**: 276-282 [PMID: 16880573 DOI: 10.4103/0378-6323.26723]
- 8 **Lazarus AA**, Thilagar B. Abdominal tuberculosis. *Dis Mon* 2007; **53**: 32-38 [PMID: 17224321 DOI: 10.1016/j.disamonth.2006.10.004]
- 9 **Charoensak A**, Nantavithya P, Apisarnthanarak P. Abdominal CT findings to distinguish between tuberculous peritonitis and peritoneal carcinomatosis. *J Med Assoc Thai* 2012; **95**: 1449-1456 [PMID: 23252212]
- 10 **Lupatkin H**, Bräu N, Flomenberg P, Simberkoff MS. Tuberculous abscesses in patients with AIDS. *Clin Infect Dis* 1992; **14**: 1040-1044 [PMID: 1296588 DOI: 10.1093/clinids/14.5.1040]
- 11 **Nos P**, Ricart C, García E, Moles JR, Lacruz J, Berenguer J. Isolated mesenteric tuberculosis as the first manifestation of AIDS. *Rev Esp Enferm Dig* 1992; **82**: 59-60 [PMID: 1520554]
- 12 **Meesiri S**. Pancreatic tuberculosis with acquired immunodeficiency syndrome: a case report and systematic review. *World J Gastroenterol* 2012; **18**: 720-726 [PMID: 22363146 DOI: 10.3748/wjg.v18.i7.720]
- 13 **Asim S**, Manjari L, Kenneth MS, Alexander CR, Christopher K, Khok-Yu H. Pancreatic tuberculous abscess diagnosed by endoscopic ultrasound-guided fine needle aspiration. *J Pak Med Assoc* 2010; **60**: 499-501 [PMID: 20527655]
- 14 **Zhao XS**, Wang ZT, Wu ZY, Yin QH, Zhong J, Miao F, Yan FH. Differentiation of Crohn's disease from intestinal tuberculosis by clinical and CT enterographic models. *Inflamm Bowel Dis* 2014; **20**: 916-925 [PMID: 24694791 DOI: 10.1097/MIB.0000000000000025]
- 15 **Akgun Y**. Intestinal and peritoneal tuberculosis: changing trends over 10 years and a review of 80 patients. *Can J Surg* 2005; **48**: 131-136 [PMID: 15887793]
- 16 **Choi CH**, Kim CJ, Lee YY, Kim JS, Song T, Park HS, Kim MK, Kim TJ, Lee JW, Lee JH, Bae DS, Kim BG. Peritoneal tuberculosis: a retrospective review of 20 cases and comparison with primary peritoneal carcinoma. *Int J Gynecol Cancer* 2010; **20**: 798-803 [PMID: 20973271 DOI: 10.1111/IGC.0b013e3181e23c8f]
- 17 **Pereira JM**, Madureira AJ, Vieira A, Ramos I. Abdominal tuberculosis: imaging features. *Eur J Radiol* 2005; **55**: 173-180 [PMID: 15908155 DOI: 10.1016/j.ejrad.2005.04.015]
- 18 **Yang ZG**, Min PQ, Sone S, He ZY, Liao ZY, Zhou XP, Yang GQ, Silverman PM. Tuberculosis versus lymphomas in the abdominal lymph nodes: evaluation with contrast-enhanced CT. *AJR Am J Roentgenol* 1999; **172**: 619-623 [PMID: 10063847 DOI: 10.2214/ajr.172.3.10063847]
- 19 **Thoeni RF**, Margulis AR. Gastrointestinal tuberculosis. *Semin Roentgenol* 1979; **14**: 283-294 [PMID: 386522 DOI: 10.1016/0037-198X(79)90025-7]
- 20 **Na-ChiangMai W**, Pojchamarnwiputh S, Lertprasertsuke N, Chitapanarux T. CT findings of tuberculous peritonitis. *Singapore Med J* 2008; **49**: 488-491 [PMID: 18581024]
- 21 **Pombo F**, Rodríguez E, Mato J, Pérez-Fontán J, Rivera E, Valvueda L. Patterns of contrast enhancement of tuberculous lymph nodes demonstrated by computed tomography. *Clin Radiol* 1992; **46**: 13-17 [PMID: 1643775 DOI: 10.1016/S0009-9260(05)80026-1]
- 22 **Puri R**, Vilmann P, Sud R, Kumar M, Taneja S, Verma K, Kaushik N. Endoscopic ultrasound-guided fine-needle aspiration cytology in the evaluation of suspected tuberculosis in patients with isolated mediastinal lymphadenopathy. *Endoscopy* 2010; **42**: 462-467 [PMID: 20432206 DOI: 10.1055/s-0029-1244133]
- 23 **Puri R**, Mangla R, Eloubeidi M, Vilmann P, Thandassery R, Sud R. Diagnostic yield of EUS-guided FNA and cytology in suspected tubercular intra-abdominal lymphadenopathy. *Gastrointest Endosc* 2012; **75**: 1005-1010 [PMID: 22421494 DOI: 10.1016/j.gie.2011.12.032]
- 24 **Dong P**, Wang B, Sun QY, Cui H. Tuberculosis versus non-Hodgkin's lymphomas involving small bowel mesentery: evaluation with contrast-enhanced computed tomography. *World J Gastroenterol* 2008; **14**: 3914-3918 [PMID: 18609719 DOI: 10.3748/wjg.14.3914]
- 25 **Taffel MT**, Khati NJ, Hai N, Yaghmai V, Nikolaidis P. De-mystifying the mesentery: an algorithmic approach to neoplastic and non-neoplastic mesenteric abnormalities. *Abdom Imaging* 2014; **39**: 892-907 [PMID: 24633598 DOI: 10.1007/s00261-014-0113-1]
- 26 **Corwin MT**, Smith AJ, Karam AR, Sheiman RG. Incidentally detected misty mesentery on CT: risk of malignancy correlates with mesenteric lymph node size. *J Comput Assist Tomogr* 2012; **36**: 26-29 [PMID: 22261767 DOI: 10.1097/RCT.0b013e3182436c4d]
- 27 **Sinan T**, Sheikh M, Ramadan S, Sahwney S, Behbehani A. CT features in abdominal tuberculosis: 20 years experience. *BMC Med Imaging* 2002; **2**: 3 [PMID: 12427257 DOI: 10.1186/1471-2342-2-3]
- 28 **Boudiaf M**, Zidi SH, Soyer P, Lavergne-Slove A, Kardache M, Logeay O, Rymer R. Tuberculous colitis mimicking Crohn's disease: utility of computed tomography in the differentiation. *Eur Radiol* 1998; **8**: 1221-1223 [PMID: 9724443 DOI: 10.1007/s003300050539]
- 29 **Kim SH**, Kim JW, Jeong JB, Lee KL, Kim BG, Choi YH. Differential diagnosis of Crohn's disease and intestinal tuberculosis in patients with spontaneous small-bowel perforation. *Dig Surg* 2014; **31**: 151-156 [PMID: 24970687 DOI: 10.1159/000363066]
- 30 **Zhang M**, Li M, Xu GP, Liu HJ. Neoplasm-like abdominal nonhematogenous disseminated tuberculous lymphadenopathy: CT evaluation of 12 cases and literature review. *World J Gastroenterol* 2011; **17**: 4038-4043 [PMID: 22046094 DOI: 10.3748/wjg.v17.i35.4038]

P- Reviewer: Garcia-Jimenez WL S- Editor: Ma YJ L- Editor: A
E- Editor: Wu HL



Observational Study

Pulmonary fibrosis and emphysema: Is the emphysema type associated with the pattern of fibrosis?

Anastasia Oikonomou, Paraskevi Mintzopoulou, Argyris Tzouvelekis, Petros Zazos, George Zacharis, Anastasios Koutsopoulos, Demosthenes Bouros, Panos Prassopoulos

Anastasia Oikonomou, Paraskevi Mintzopoulou, Panos Prassopoulos, Department of Radiology, Democritus University of Thrace, Dragana, 68100 Alexandroupolis, Greece

Anastasia Oikonomou, Department of Medical Imaging, Sunnybrook Health Sciences Centre, Toronto M4N 3M5, Canada

Argyris Tzouvelekis, George Zacharis, Demosthenes Bouros, Department of Pneumology, Democritus University of Thrace, Dragana, 68100 Alexandroupolis, Greece

Argyris Tzouvelekis, Yale School of Medicine, Department of Internal Medicine, Section of Pulmonary, Critical Care and Sleep Medicine, New Haven, CT 06511, United States

Petros Zazos, Department of Endoscopic Unit, Democritus University of Thrace, Dragana, 68100 Alexandroupolis, Greece

Petros Zazos, Department of Internal Medicine, Division of Gastroenterology, Sunnybrook Health Sciences Centre, Toronto M4N 3M5, Canada

Anastasios Koutsopoulos, Department of Pathology, Democritus University of Thrace, Dragana, 68100 Alexandroupolis, Greece

Anastasios Koutsopoulos, Department of Pathology, University of Heraklion, Voutes, 71003 Heraklion, Greece

Author contributions: Oikonomou A designed the research; Oikonomou A, Mintzopoulou P evaluated the CT studies; Mintzopoulou P, Tzouvelekis A performed the literature research; Tzouvelekis A and Zacharis G performed the functional evaluation of the patients and gathered the clinical information from the patients' records; Oikonomou A, Mintzopoulou P, Tzouvelekis A, Zazos P and Zacharis G analyzed the data; Zazos P performed the statistical analysis; Koutsopoulos A evaluated the histologic specimens and analyzed the histologic results; Oikonomou A wrote the paper; Mintzopoulou P, Tzouvelekis A, Zazos P, Zacharis G and Koutsopoulos A edited the paper; Bouros D and Prassopoulos P critically evaluated the final version of the manuscript.

Institutional review board statement: The study was reviewed

and approved by the Institutional Review Board of the University Hospital of Alexandroupolis, Greece.

Informed consent statement: According to our country's legislation, informed consent is not needed for retrospective analysis of data corresponding to current practice.

Conflict-of-interest statement: No conflict of interest related to this manuscript was declared by any of the authors.

Data sharing statement: No additional data are available.

Open-Access: This article is an open-access article which was selected by an in-house editor and fully peer-reviewed by external reviewers. It is distributed in accordance with the Creative Commons Attribution Non Commercial (CC BY-NC 4.0) license, which permits others to distribute, remix, adapt, build upon this work non-commercially, and license their derivative works on different terms, provided the original work is properly cited and the use is non-commercial. See: <http://creativecommons.org/licenses/by-nc/4.0/>

Correspondence to: Anastasia Oikonomou, MD, PhD, Department of Medical Imaging, Sunnybrook Health Sciences Centre, AG 271b - 2075 Bayview Avenue, Toronto M4N 3M5, Canada. anastasia.oikonomou@sunnybrook.ca
 Telephone: +1-416-4806100
 Fax: +1-416-4805855

Received: January 22, 2015

Peer-review started: January 23, 2015

First decision: March 6, 2015

Revised: June 30, 2015

Accepted: August 16, 2015

Article in press: August 17, 2015

Published online: September 28, 2015

Abstract

AIM: To investigate whether the predominant emphysema type is associated with the high resolution

computed tomography (HRCT) pattern of fibrosis in combined pulmonary fibrosis and emphysema (CPFE).

METHODS: Fifty-three smokers with upper lobe emphysema and lower lobe pulmonary fibrosis on - HRCT - were retrospectively evaluated. Patients were stratified into 3 groups according to the predominant type of emphysema: Centrilobular (CLE), paraseptal (PSE), CLE = PSE. Patients were also stratified into 3 other groups according to the predominant type of fibrosis on HRCT: Typical usual interstitial pneumonia (UIP), probable UIP and nonspecific interstitial pneumonia (NSIP). HRCTs were scored at 5 predetermined levels for the coarseness of fibrosis (Coarseness), extent of emphysema (emphysema), extent of interstitial lung disease (TotExtILD), extent of reticular pattern not otherwise specified (RetNOS), extent of ground glass opacity with traction bronchiectasis (extGGOBx), extent of pure ground glass opacity and extent of honeycombing. HRCT mean scores, pulmonary function tests, diffusion capacity (DLCO) and systolic pulmonary arterial pressure were compared among the groups.

RESULTS: The predominant type of emphysema was strongly correlated with the predominant type of fibrosis. The centrilobular emphysema group exhibited a significantly higher extent of emphysema ($P < 0.001$) and a lower extent of interstitial lung disease ($P < 0.002$), reticular pattern not otherwise specified ($P < 0.023$), extent of ground glass opacity with traction bronchiectasis ($P < 0.002$), extent of honeycombing ($P < 0.001$) and coarseness of fibrosis ($P < 0.001$) than the paraseptal group. The NSIP group exhibited a significantly higher extent of emphysema ($P < 0.05$), total lung capacity ($P < 0.01$) and diffusion capacity (DLCO) ($P < 0.05$) than the typical UIP group. The typical UIP group exhibited a significantly higher extent of interstitial lung disease, extent of reticular pattern not otherwise specified, extent of ground glass opacity with traction bronchiectasis, extent of honeycombing and coarseness of fibrosis ($0.039 > P > 0.000$). Although the pulmonary arterial pressure was higher in typical UIP group relative to the NSIP group, the difference was not statistically significant.

CONCLUSION: In CPFE patients, paraseptal emphysema is associated more with UIP-HRCT pattern and higher extent of fibrosis than centrilobular emphysema.

Key words: Emphysema; Pulmonary fibrosis; High resolution computed tomography; Centrilobular; Paraseptal; Nonspecific interstitial pneumonia pattern; Usual interstitial pneumonia pattern

© The Author(s) 2015. Published by Baishideng Publishing Group Inc. All rights reserved.

Core tip: This study aimed to investigate whether the predominant type of emphysema is associated with the pattern of fibrosis in combined pulmonary fibrosis and emphysema (CPFE). Patients were stratified into 3

groups according to predominant type of emphysema and fibrosis. High resolution computed tomography (HRCT) was retrospectively scored at 5 levels for various morphologic parameters characterizing emphysema and fibrosis. The predominant type of emphysema was strongly correlated with the predominant type of fibrosis. The centrilobular emphysema group exhibited a higher extent of emphysema and a lower extent of fibrosis. In CPFE, paraseptal emphysema was more associated with a UIP-HRCT pattern and a higher extent of fibrosis than was centrilobular emphysema.

Oikonomou A, Mintzopoulou P, Tzouveleakis A, Zazos P, Zacharis G, Koutsopoulos A, Bouros D, Prassopoulos P. Pulmonary fibrosis and emphysema: Is the emphysema type associated with the pattern of fibrosis? *World J Radiol* 2015; 7(9): 294-305 Available from: URL: <http://www.wjgnet.com/1949-8470/full/v7/i9/294.htm> DOI: <http://dx.doi.org/10.4329/wjr.v7.i9.294>

INTRODUCTION

Wiggins *et al*^[1] first described the coexistence of emphysema in the upper lobes and pulmonary fibrosis in the lower lobes on high-resolution computed tomography (HRCT), thus enhancing the clinical recognition of the simultaneous occurrence of these two separate entities. In 2005 with the publication of Cottin *et al*^[2], a new syndrome based on clinical and radiological findings emerged under the name "combined pulmonary fibrosis and emphysema" (CPFE). This syndrome is characterized by the coexistence of distinct features, including tobacco smoking, severe dyspnea, pseudonormalization of the pulmonary function tests (PFTs) contrasting with significant impairment of diffusion capacity (DLCO) and hypoxemia during exercise^[3]. CPFE is also associated with pulmonary hypertension, which predicts a dismal prognosis^[4]. The syndrome of CPFE has been recently considered part of the spectrum of smoking-related interstitial lung diseases^[5]. Imaging features are characteristic but various, with centrilobular emphysema (CLE) and/or paraseptal emphysema in the upper lobes and diffuse infiltrative opacities suggestive of pulmonary fibrosis predominating in the lower lobes^[6]. In one study, although CLE was almost always present in the CPFE group, the coexistence of paraseptal emphysema was surprisingly high^[2]; in another study, paraseptal emphysema was more common in the CPFE population compared with the COPD group^[7]. CPFE was previously considered to be characterized more commonly by a usual interstitial pneumonia (UIP) pattern of fibrosis on HRCT, but more recently, CPFE is considered a heterogeneous disease on HRCT that may present with a UIP, a nonspecific interstitial pneumonia (NSIP) pattern or a complex pattern with predominantly reticular opacities^[2,3]. Moreover, the ground glass opacity (GGO) pattern may occasionally be the only HRCT pattern of fibrosis^[8].

Furthermore, the presence of concurrent emphysema and fibrosis may influence the distinction of UIP from nonspecific interstitial pneumonia, and emphysematous cysts surrounded by ground glass opacity may erroneously be mistaken for honeycombing^[9,10].

The purpose of this study was to investigate whether a specific predominant type of emphysema is associated with a specific HRCT pattern of fibrosis in CPFE.

MATERIALS AND METHODS

Study design

This retrospective study recruited patients from the outpatient clinic of the Pulmonology Department of our university hospital. HRCT and functional data were retrospectively collected and analyzed for the cases included in the study between January 2003 and March 2013. Data collection ended on March 31, 2013. According to our country's legislation, informed consent is waived for retrospective analyses of data. Approval was obtained by the Research Ethics Board of our university hospital (530:2/15-2-2011).

Inclusion and exclusion criteria

Cases were included in the study according to the following criteria: (1) presence of emphysema on HRCT scan defined as well-demarcated areas of decreased attenuation relative to contiguous normal lung and marginated by a very thin (< 1 mm) or no wall and/or multiple bullae (> 1 cm) with upper zone predominance; and (2) presence of a diffuse parenchymal lung disease with pulmonary fibrosis on HRCT scan, characterized by reticular opacities with peripheral, subpleural and basal predominance, architectural distortion and/or traction bronchiectasis and bronchiolectasis that might be associated with ground-glass opacity, with or without honeycombing^[2,11]. Only cases that had undergone HRCT and were available for reading were included in the study.

Patients with a known history of connective tissue disease or other known diagnoses of interstitial lung disease, such as sarcoidosis, histiocytosis, lymphangioleiomyomatosis, pneumoconiosis, drug-induced pneumonitis, hypersensitivity pneumonitis or eosinophilic pneumonia were excluded from the study.

HRCT protocol

All patients underwent HRCT of the thorax to determine the diagnosis of pulmonary fibrosis and emphysema. The thin-section CT studies were performed with 120 kVp, 160 mAs, and 1 mm collimation at 10-mm intervals from the apex of the lung to the diaphragm with a helical CT scanner (ProSpeed, SX Power, General Electric, Germany). The images were obtained with the patient in the supine position at full inspiration and were reconstructed using a high-spatial-frequency algorithm.

HRCT evaluation

HRCT images were assessed independently by 2

observers, a senior chest radiologist with 13 years of experience in chest imaging (AO) and a junior radiologist with two years of training in chest imaging (PM), who were blinded to the clinical and functional information but who were aware that the patients had CPFE syndrome. HRCT studies were assessed using a modification of a previously described semiquantitative HRCT scoring system^[12] at five predetermined levels: (1) origin of great vessels; (2) main carina; (3) pulmonary venous confluence; (4) halfway between the third and fifth section; and (5) immediately above the right hemidiaphragm. HRCT scans were assessed for the presence and extent of emphysema, the total extent of interstitial lung disease (including the presence of reticular pattern, ground glass pattern and honeycombing), the extent of reticular pattern not otherwise specified, the extent of ground glass opacity associated with bronchiectasis, the extent of pure ground glass opacity, the extent of honeycombing and the coarseness of fibrosis. The HRCT findings were assessed and analyzed according to the Fleischner glossary of terms^[13]. The variables of the HRCT scoring system are described in detail.

Extent of emphysema (emphysema): Emphysema was defined as areas of decreased attenuation with no walls or discrete walls and was classified as centrilobular or paraseptal. Large air cysts with fibrotic thick walls with a diameter > 2 cm in areas of reticulation, which contained a centrilobular artery in their center, were considered to represent emphysema that was either evaluated as "centrilobular" (CLE) if they were in a non-subpleural location or "paraseptal" (PSE) if they were in a subpleural location. Similarly, emphysematous bullae were classified as "centrilobular" or "paraseptal" if they were located in a non-subpleural or subpleural location, respectively.

The total extent of emphysema was calculated to the nearest five percent in each of the five slices. The total extent of emphysema on HRCT was estimated as the mean of the scores. To establish the diagnosis of CPFE on HRCT, a total extent of emphysema higher than 5% was set as the threshold.

Total extent of interstitial lung disease: The total extent of interstitial lung disease was calculated to the nearest five percent in each of the five slices. The total extent of disease on HRCT was estimated as the mean of the scores.

Extent of reticular pattern not otherwise specified: The extent of reticular pattern non-otherwise specified was calculated to the nearest five percent in each of the five slices, with the total extent of the reticular pattern on HRCT estimated as the mean of the scores. From this total score, the contribution made by reticular pattern NOS to total extent of interstitial lung disease was calculated as the ratio of the reticular pattern to the total extent of interstitial lung disease

(proportion of reticular pattern NOS - RetNOS prop).

Extent of ground-glass opacity with traction bronchiectasis: The extent of ground glass opacity with traction bronchiectasis (ExtGGOBx) was calculated to the nearest five percent in each of the five slices. The total extent was estimated as the mean of the scores. From this total score, the contribution made by GGO with traction bronchiectasis to the total extent of interstitial lung disease was calculated as the ratio of the extent of GGO with traction bronchiectasis to the total extent of interstitial lung disease (proportion of GGO with traction bronchiectasis - ExtGGOBx prop).

Extent of pure ground-glass opacity: The extent of pure GGO was calculated to the nearest five percent in each of the five slices. The total extent was estimated as the mean of the scores. From this total score, the contribution made by the extent of pure GGO to the total extent of interstitial lung disease was calculated as the ratio of the extent of pure GGO to the total extent of interstitial lung disease (proportion of pure GGO - GGO prop).

Extent of honeycombing: The extent of honeycombing (HC) was calculated to the nearest five percent in each of the five slices. The total extent was estimated as the mean of the scores. From this total score, the contribution made by the extent of HC to the total extent of interstitial lung disease was calculated as the ratio of the extent of HC to the total extent of interstitial lung disease (proportion of HC - HC prop).

Coarseness of fibrosis (Coarseness): The most severe disease in each section was quantified as follows: grade 0 = ground-glass attenuation alone; grade 1 = fine intralobular fibrosis; grade 2 = microcystic honeycombing (air spaces less than or equal to 4 mm in diameter); and grade 3 = macrocystic honeycombing (air spaces greater than 4 mm in diameter). The total coarseness score was the summed score for all five levels (range: 0-15).

After the initial assessment of HRCT images for the evaluation of HRCT scoring, each reader made a first-choice diagnosis for the predominant type of emphysema (paraseptal, centrilobular or equal extent of paraseptal and centrilobular). Accordingly, for each patient, the HRCT patterns of fibrosis were classified as typical for UIP, possible UIP and consistent with NSIP^[14]. The HRCT pattern was considered typical for UIP if the following imaging findings were noted: Reticulation in all lobes with basal and peripheral predominance, high extent of honeycombing with or without traction bronchiectasis, and the absence or minimal ground-glass opacity. HRCT pattern consistent with possible diagnosis of UIP included bilateral reticular opacities with basal and peripheral predominance, minimal honeycombing and minimal to moderate ground glass opacity. The HRCT pattern consistent with NSIP included

extensive or moderate ground-glass opacity, associated with mild reticulation and traction bronchiectasis or bronchiolectasis, no honeycombing, basal predominance and relative subpleural sparing^[9].

Functional evaluation

All patients underwent functional assessment within 1 wk maximum from HRCT. Pulmonary function tests, which were all performed according to the current European Respiratory Society (ERS) guidelines, included forced vital capacity (FVC), diffusing capacity of the lung for carbon monoxide (DL_{CO}), maximum midexpiratory flow (MMEF), forced expiratory volume at first second (FEV₁), and the residual volume (RV)/total lung capacity (TLC) ratio^[15]. The reversibility of airflow obstruction was not assessed. Airflow obstruction was defined as a post bronchodilator fixed ratio of FEV₁/FVC < 0.70^[16]. DL_{CO} measurements were performed according to the American Thoracic Society/European Respiratory Society Task Force^[15]. All patients underwent 6-min walking test and arterial blood gases measurements for alveolar-arterial gradient. Pulmonary artery pressure with transthoracic cardiac Doppler ultrasound was reviewed when available. The estimated systolic pulmonary artery pressure (eSPAP) was calculated as previously described^[17].

Statistical analysis

Statistical analysis was performed with statistical software (SPSS software, version 18.0, Chicago, III). A *P* value of less than 0.05 was considered statistically significant.

The two observers stratified the patients into 3 groups according to the predominant type of emphysema on HRCT: group E1: Paraseptal predominant, group E2: Centrilobular predominant and group E3: Paraseptal = centrilobular. Subsequently, the patients were stratified in 3 other groups according to the predominant type of fibrosis on HRCT: group F1: Consistent with "typical UIP pattern", group F2: "Possible UIP pattern" and group F3: "NSIP pattern".

Interobserver agreement for the predominant type of emphysema and the predominant type of fibrosis, as well as for the extent and severity of the HRCT variables (as defined by the HRCT scoring system) were estimated using the Kappa statistic^[18]. Crosstabs analysis was used to demonstrate the association of the predominant type of emphysema with the predominant type of fibrosis for both observers.

Subsequently, the readings (expressed in percentages) of the two observers concerning the extent and presence of the various HRCT findings were combined by calculating the average percentage, which was then used in further analyses for the comparison of the HRCT variables between the groups of emphysema and fibrosis.

Continuous data are presented as the means (95%CI). Categorical data are presented as numbers or proportions (%). Data from each HRCT variable in the

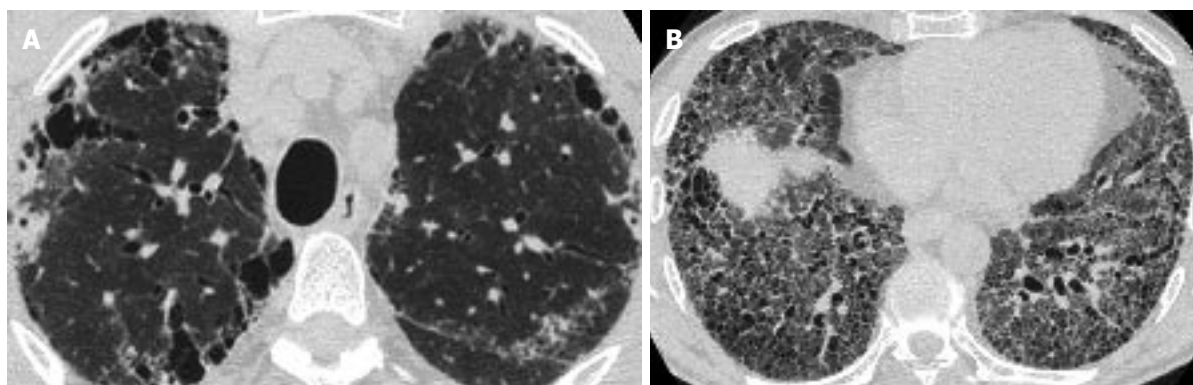


Figure 1 Paraseptal emphysema and usual interstitial pneumonia-pattern of pulmonary fibrosis. A: High resolution computed tomography (HRCT) at the level of the upper lobes shows paraseptal emphysema associated with subpleural reticular pattern and minimal ground glass opacity; B: HRCT of the same patient as in A, at the level of the lower lobes reveals extensive coarse reticular pattern characterized by traction bronchiectasis associated with ground glass opacity and subpleural honeycombing. The HRCT pattern is consistent more with usual interstitial pneumonia.

different groups are presented as the mean percentages (95%CI).

Group comparisons for HRCT variables and functional parameters were performed using the following: (1) Independent samples *t* test for group E1 (paraseptal) and group E2 (centrilobular) (group E3 included only 2 patients and therefore was excluded from the comparisons); and (2) one-way ANOVA for group F1 (typical UIP pattern), group F2 (possible UIP pattern) and group F3 (NSIP pattern).

CT features predictive of a predominant type of emphysema and of fibrosis were identified by means of multinomial logistic regression (OR, 95%CI).

RESULTS

Patient population

Fifty-three patients with emphysema in the upper lobes and pulmonary fibrosis in the lower lobes on HRCT scans were included in the study. All patients were men with a mean age of 62 years (range 37-84 years). All patients were smokers, including 38 current smokers with 68 mean pack-years (range 30-110 years) and 15 ex-smokers with 47 mean pack-years (range 10-135) and mean period of cessation of smoking 19 years (range 3-30).

HRCT results

The interobserver agreement of the severity of the different parameters of the HRCT scoring system was moderate to excellent, with the *K* values ranging between 0.45 and 0.97 (data not shown).

Predominant type of emphysema: The incidence of CLE compared with the incidence of PSE was similar. Observer 1 identified 28 (52.8%) cases as CLE and 23 (45%) cases as PSE (Table 1). Observer 2 identified 26 (49%) cases as CLE and 25 (45%) cases as PSE (Table 1). Both observers evaluated 2 cases with equal extents of CLE and PSE.

The interrater reliability for the 2 observers was

kappa = 0.929 ($P < 0.001$), 95%CI: 0.757-1.000.

Predominant type of pulmonary fibrosis: The incidence of typical - possible UIP compared with the incidence of NSIP type of fibrosis on HRCT was similar. As shown in Table 1, observer 1 evaluated 19 (35.8%) cases as predominant typical UIP pattern plus 10 (18.8%) cases as possible UIP pattern and 24 (45.3%) cases with NSIP pattern on HRCT, whereas observer 2 evaluated 24 (45.3%) cases as predominant typical UIP pattern plus 5 (9.4%) cases as possible UIP pattern and 24 (45.3%) cases as NSIP pattern on HRCT.

The interrater reliability for the observers was kappa = 0.785 ($P < 0.001$), 95%CI (0.646, 0.924).

Correlation comparison of the pattern of fibrosis with the type of emphysema:

According to both observers' readings, there was a strong correlation between the predominant type of emphysema and the predominant type of fibrosis (observer 1: Spearman $r = 0.862$ and observer 2: Spearman $r = 0.827$). More specifically, PSE was more frequently associated with a UIP pattern of pulmonary fibrosis (Figure 1A and 1B), while CLE was associated with an NSIP pattern of fibrosis (Figure 2).

Observer 1 evaluated 19 patients with a predominant type of PSE to have an HRCT pattern of fibrosis consistent with typical UIP and 24 patients with a predominant type of CLE to have an HRCT pattern of fibrosis consistent with NSIP (Table 2).

Similarly, observer 2 evaluated 21 patients with a predominant type of PSE to have an HRCT pattern of fibrosis consistent with typical UIP and 22 patients with a predominant type of CLE to have an HRCT pattern of fibrosis consistent with NSIP (Table 2).

Comparison of HRCT parameters and PFTs between patient groups according to the predominant type of emphysema (Table 3):

(1) HRCT parameters. Only the groups E1 and E2 were included in the analyses of data. Group E3 included only 2 patients

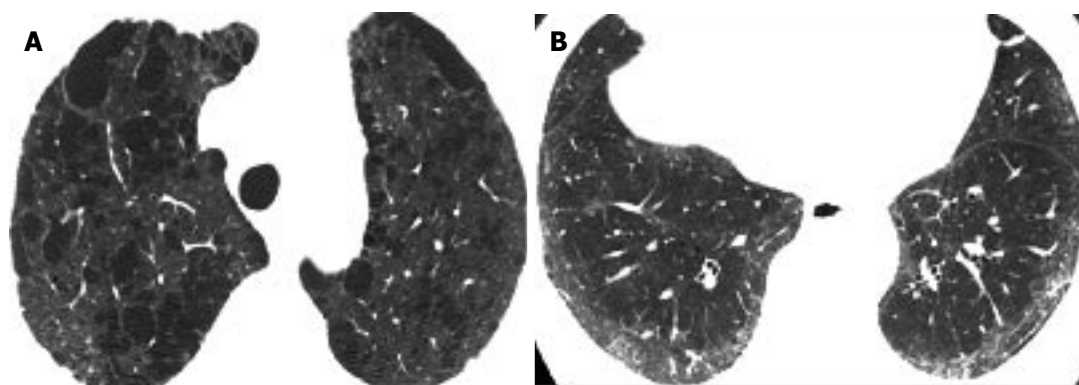


Figure 2 Centrilobular emphysema and nonspecific interstitial pneumonia-pattern of pulmonary fibrosis. A: High resolution computed tomography (HRCT) at the level of the upper lobes shows extensive predominantly centrilobular emphysema; B: HRCT of the same patient as in A, at the level of the lower lobes shows subpleural fine fibrosis characterized mainly by ground glass opacity, reticular pattern non-otherwise specified and absence of honeycombing. The HRCT pattern is consistent more with nonspecific interstitial pneumonia.

Table 1 Predominant type of emphysema and pulmonary fibrosis according to the ratings on high resolution computed tomography of the two observers

		Observer 2			
		Type of emphysema			
Observer 1		CLE = PSE	Paraseptal	Centri-lobular	
Type of emphysema ¹	CLE = PSE	2	0	0	2
	Paraseptal	0	23	0	23
	Centrilobular	0	2	26	28
		2	25	26	
		Type of pulmonary fibrosis			
		Typical UIP	Possible UIP	NSIP	
Type of pulmonary fibrosis ²	Typical UIP	19	0	0	19
	Possible UIP	5	4	1	10
	NSIP	0	1	23	24
		24	5	24	

¹The interrater reliability for the 2 observers was found to be Kappa = 0.929 ($P < 0.001$), 95%CI (0.757-1.000); ²The interrater reliability for the observers was found to be Kappa = 0.785 ($P < 0.001$), 95%CI (0.646-0.924). CLE: Centrilobular emphysema; PSE: Paraseptal emphysema; UIP: Usual interstitial pneumonia; NSIP: Nonspecific interstitial pneumonia.

and therefore was excluded from the comparisons.

The mean HRCT score for the extent of emphysema (Emphysema) in patients with PSE (group E1) was significantly lower than that in patients with CLE (group E2) (6.3 vs 21.89, $P < 0.001$). However, the mean HRCT score for the total extent of interstitial lung disease (TotExtILD) was significantly higher in group E1 relative to group E2 (53.34 vs 29.82, $P = 0.002$). Similarly, the HRCT variables that represented coarser fibrosis, such as extent of reticular disease not otherwise specified (RetNOS), GGO with bronchiectasis (ExtGGOBx), extent of HC and coarseness of fibrosis (coarseness), were significantly higher in group E1 relative to group E2 ($0.039 > P > 0.001$). Similarly, the proportions of the HRCT variables (to the total extent of interstitial lung disease) that represented coarser fibrosis, such as proportion of GGO with bronchiectasis (ExtGGOBx prop) and proportion of HC (HC prop), were

Table 2 Association of predominant type of emphysema with predominant type of fibrosis according to observer 1 and observer 2

		Predominant type ILD			
		Typical UIP	Possible UIP	NSIP	
Observer 1					
Predominant emphysema type	CLE = PSE	0	2	0	2
	Paraseptal	19	4	0	23
	Centrilobular	0	4	24	28
		19	10	24	
Observer 2					
Predominant emphysema type	CLE = PSE	2	0	0	2
	Paraseptal	21	2	2	25
	Centrilobular	1	3	22	26
		24	5	24	

CLE: Centrilobular emphysema; PSE: Paraseptal emphysema; UIP: Usual interstitial pneumonia; NSIP: Nonspecific interstitial pneumonia.

significantly higher in group E1 compared with group E2 ($P < 0.003$ and $P < 0.001$, respectively). However, the proportion of pure GGO (GGO prop) (reflecting less coarse fibrosis) was significantly lower in group E1 relative to group E2 ($P < 0.001$).

(2) Pulmonary function tests. There were no statistically significant differences between the E1 (PSE) and E2 groups (CLE) with respect to pulmonary function parameters.

Comparison of HRCT parameters and PFTs amongst patient groups according to pulmonary fibrosis (Table 4): (1) HRCT parameters. With respect to the 3 different groups of pulmonary fibrosis (groups F1, F2 and F3), group F1 (typical UIP) exhibited a significantly lower extent of emphysema (emphysema) relative to group F3 (NSIP) ($P < 0.002$).

However, group F1 (typical UIP) exhibited a significantly higher extent of interstitial lung disease (TotExtILD), extent of reticular NOS (Ret NOS), extent of GGO with bronchiectasis (ExtGGOBx), extent of HC (HC) and coarseness of fibrosis (Coarseness) ($0.039 > P > 0.000$), thus reflecting coarser fibrosis.

Table 3 Parameters of high resolution computed tomography scoring system and functional pulmonary parameters in the groups according to the predominant type of emphysema

Parameters	Group E1 Paraseptal emphysema <i>n</i> = 23 Mean (95%CI)	Group E2 Centrilobular emphysema <i>n</i> = 28 Mean (95%CI)	Independent samples <i>t</i> test <i>P</i> value
Emphysema	6.3 (2.9-9.7)	21.82 (14.93-28.85)	< 0.001
TotExtILD	53.34 (41.05-65.63)	29.82 (22.09-37.55)	0.002
RetNOS	17.56 (12.45-22.67)	10.75 (7.67-13.82)	0.023
ExtGGOBx	16.73 (11.52-21.89)	6.14 (1.65-10.62)	0.002
GGO	7.86 (3.49-12.23)	12.5 (8.06-16.93)	0.136
HC	11.21 (6.76-15.67)	0.42 (-0.31-1.17)	< 0.001
Coarseness	10.34 (9.36-11.32)	5.42 (4.61-6.24)	< 0.001
RetNOS prop	32.62 (28.57-36.67)	40.51 (34.03-46.99)	0.039
ExtGGOBx prop	30.83 (23.71-37.95)	15.62 (8.76-22.48)	0.003
GGO prop	12.97 (6.64-19.31)	41.70 (32.72-50.67)	< 0.001
HC prop	23.87 (14.80-32.94)	2.14 (-1.56-5.82)	< 0.001
FEV1	72.05	83.81	0.382
FEV1/FVC	81.82	75.79	0.109
PEF	89.47	76.17	0.436
MMEF	78.87	62.07	0.184
75%-25%			
FVC	72.64	82.21	0.256
TLC	58.54	80.98	0.002
RV	53.3	88.54	0.022
RVTLC	89.92	108.3	0.276
DLCOb	32.75	47.64	0.067
DLCOVA	55.22	71.51	0.293
eSPAP	48.12	35.25	0.324
(<i>n</i> = 12)			

TotExtILD: Total extent of interstitial lung disease; RetNOS: Extent of reticular pattern not otherwise specified; ExtGGOBx: Extent of ground glass opacity with traction bronchiectasis; GGO: Extent of pure ground glass opacity; HC: Extent of honeycombing; Coarseness: Coarseness of fibrosis; FEV1: Forced expiratory volume in 1 s; FEV1/FVC: Ratio of forced expiratory volume in 1 s/forced vital capacity; PEF: Peak expiratory flow; MMEF: Maximum midexpiratory flow; FVC: Forced vital capacity; TLC: Total lung capacity; RV: Residual volume; DLCOb: Single-breath diffusing capacity of the lungs for carbon monoxide; DLCOVA: Diffusing capacity of the lungs for carbon monoxide corrected for alveolar volume.

Similarly, group F1 exhibited a significantly higher proportion of GGO with bronchiectasis (ExtGGOBx prop) ($P < 0.001$) and honeycombing (HC prop) ($P < 0.000$) compared with Group F3 (NSIP).

The proportion of pure GGO (GGO prop), reflecting less coarse fibrosis, was significantly lower in group F1 relative to group F3 ($P < 0.000$).

(2) Pulmonary function tests. As expected, TLC ($P < 0.001$) and DL_{CO} ($P < 0.031$) were significantly lower in group F1 ("typical UIP" pattern) compared with group F3 (NSIP pattern) (Table 4). DL_{CO} was also significantly lower in group F1 compared with group F2 ("possible UIP" pattern) ($P < 0.037$) (Table 5).

(3) Pulmonary hypertension results. Systolic pulmonary arterial pressure was measured in only 12 patients by ultrasound, and the average was 44.16 mm/Hg (range: 22-80). Pulmonary arterial pressure was higher in group F1 (typical UIP) (48.12 mm/Hg) than in group F3 (NSIP) (27.33 mm/Hg) (Table 4), although the difference was not statistically significant due to the small number of

Table 4 Comparison of parameters of high resolution computed tomography scoring system and functional parameters within the 3 groups according to the predominant type of fibrosis

Parameters	Group F1 Typical UIP <i>n</i> = 19 Mean (95%CI)	Group F2 Possible UIP <i>n</i> = 10 Mean (95%CI)	Group F3 NSIP <i>n</i> = 24 Mean (95%CI)
Emphysema	7.05 (2.96-11.14) ^c	9.6 (3.33-15.86) ^e	23.08 (15.1-31.06)
TotExtILD	56.84 (43.18-70.49) ^d	39.6 (19.83-59.36)	28.16 (20.94-35.38)
RetNOS	18.68 (12.78-24.58) ^c	9.9 (5.51-14.28)	11.04 (7.48-14.6)
ExtGGOBx	18.05 (12.02-24.08) ^c	17.9 (2.84-32.95) ^e	3.66 (1.84-5.48)
GGO	7.36 (2.34-12.39)	8 (2.98-13.01)	13.45 (8.45-18.45)
HC	12.78 (7.65-17.92) ^{d, a}	3.8 (1.25-6.34)	-
Coarseness	10.73 (9.67-11.80) ^{d, a}	8.5 (7.22-9.77) ^f	4.87 (4.24-5.50)
RetNOS prop	32.44 (27.51-37.36)	30.08 (21.35-38.80)	42.63 (35.51- 49.76)
ExtGGOBx prop	30.86 (22.36-39.35) ^d	36.98 (21.53-52.42) ^f	11.24 (5.63-16.85)
ExtGGO prop	10.44 (4.07-16.81) ^d	19.97 (10.11-29.82) ^f	46.10 (36.95- 55.25)
HC prop	26.63 (16.13-37.13) ^d	12.95 (2.16-23.74)	-
FEV1	66.51 (41.27-91.75)	76.82 (27.32-126.32)	87.39 (70.19-104.58)
FEV1/FVC	81.04 (75.47-86.61)	84.83 (74.00-95.66)	74.98 (68.95-81.00)
PEF	82.80 (44.11-121.50)	85.86 (-55.76-227.49)	80.53 (61.05-100.01)
MMEF	73.90 (47.97-99.84)	75.76 (43.89-107.64)	65.02 (47.55- 82.50)
75%-25%	69.16 (55.02- 83.30)	74.38 (51.03-97.73)	85.66 (73.70-97.62)
TLC	54.77 (41.67-67.87) ^d	67.3 (52.53-82.06)	84.09 (75.99-92.18)
RV	54.69 (17.24-92.13)	71.3 (36.58-106.01)	87.80 (68.45-107.15)
RVTLC	89.92 (47.00-132.84)	97.89 (-64.43- 260.21)	101.06 (88.98-113.14)
DLCOb	27.35 (19.85-34.85) ^{c, a}	54.44 (27.51- 81.36)	47.73 (34.24-61.22)
SPAP (<i>n</i> = 12)	48.12 (32.49-63.75)	-	27.33 (10.42-44.24)

One - way ANOVA: Typical UIP *vs* possible UIP; ^a $P \leq 0.05$, ^b $P \leq 0.001$; Typical UIP *vs* NSIP; ^c $P \leq 0.05$, ^d $P \leq 0.001$; possible UIP *vs* NSIP; ^e $P \leq 0.05$, ^f $P \leq 0.001$. TotExtILD: Total extent of interstitial lung disease; RetNOS: Extent of reticular pattern not otherwise specified; ExtGGOBx: Extent of ground glass opacity with traction bronchiectasis; GGO: Extent of pure ground glass opacity; HC: Extent of honeycombing; Coarseness: Coarseness of fibrosis; FEV1: Forced expiratory volume in 1 s; FEV1/FVC: Ratio of forced expiratory volume in 1 s/forced vital capacity; PEF: Peak expiratory flow; MMEF: Maximum midexpiratory flow; FVC: Forced vital capacity; TLC: Total lung capacity; RV: Residual volume; DLCOb: Single-breath diffusing capacity of the lungs for carbon monoxide; DLCOVA: Diffusing capacity of the lungs for carbon monoxide corrected for alveolar volume.

patients who underwent eSPAP evaluation ($P < 0.063$) (Table 4). No significant difference was observed between group F1 and group F2 (Table 4).

(4) Histopathology. Histological analysis of open

Table 5 High resolution computed tomography - pathology correlation according to the pattern of fibrosis

Patient (no)	Histology	HRCT - observer 1	HRCT - observer 2
1	7	Possible UIP	NSIP
2	10	Possible UIP	Possible UIP
3	11	NSIP	NSIP
4	14	Possible UIP	Typical UIP
5	15	Definite UIP	Typical UIP
6	17	Possible UIP	Typical UIP
7	19	NSIP	NSIP
8	23	Definite UIP	Typical UIP
9	25	Definite UIP	Typical UIP
10	26	Definite UIP	Possible UIP
11	31	Definite UIP	Typical UIP
12	33	Definite UIP	Typical UIP
13	34	Definite UIP	Typical UIP
14	35	Possible UIP	NSIP
15	41	Definite UIP	Possible UIP
16	45	Definite UIP	Typical UIP
17	46	Definite UIP	Possible UIP
18	51	Definite UIP	Typical UIP
19	53	Definite UIP	Typical UIP

HRCT: High resolution computed tomography; UIP: Usual interstitial pneumonia; NSIP: Nonspecific interstitial pneumonia.

lung or thoracoscopic lung biopsy was available for review in nineteen cases and confirmed the presence of emphysema in the upper lobes. Interstitial pneumonia was classified as definite UIP in twelve cases, possible UIP in 5 cases and NSIP in two cases. The pathology correlation of the HRCT readings of the 2 observers is presented in Table 5. The 2 cases of NSIP on pathology were evaluated as NSIP by both observers. Nine of the 12 cases of definite UIP on pathology were evaluated as typical UIP by both observers.

The correlation of histology and HRCT was Kappa = 0.338, $P < 0.042$ (95%CI: 0.692, -0.016) for observer 1 and kappa = 0.289, $P < 0.069$ (95%CI: 0.632, -0.054) for observer 2. When definite UIP and possible UIP were coupled as one diagnosis (UIP) for HRCT and for histologic diagnosis, the correlation between histology and HRCT for both observers improved: kappa = 0.612, $P < 0.004$ (95%CI: 0.14356-1.08044).

(5) Regression analysis. According to multinomial regression analysis, coarseness of fibrosis was the only HRCT feature that could differentiate typical UIP from NSIP (OR = 6.912; 95%CI: 2.493-19.167), possible UIP from NSIP (OR = 3.939; 95%CI: 1.595-9.726) and PSE from CLE (OR = 0.398; 95%CI: 0.248-0.638).

DISCUSSION

Patients with simultaneous emphysema and fibrosis present with dyspnea, pulmonary hypertension, hypoxemia, preserved lung volumes and normal spirometry in the setting of severely impaired diffusion lung capacity, a condition known as CPFE^[3]. The coexistence of emphysema and pulmonary fibrosis may have been underappreciated clinically because the two entities

present dissimilar/opposite physiologic effects; therefore, one entity may partially mask the other. HRCT has significantly contributed to the clinical recognition of the simultaneous occurrence of emphysema and pulmonary fibrosis^[1,6,19].

In the present study, we analyzed the HRCT findings of 53 patients with coexistent emphysema and pulmonary fibrosis and found that PSE is associated with a UIP-HRCT pattern, whereas CLE is associated with an NSIP-HRCT pattern.

All patients were exclusively male (53/53), and all were current or ex-smokers. The sex predominance, the mean age (62 years) and the history of smoking were consistent with those reported in the literature for CPFE patients^[2,3,6], where a male preponderance and a strong association with smoking history has been reported. The relationship between CPFE and smoking is not surprising given the association of both emphysema/COPD^[20] and fibrosis with smoking^[21,22]. Similarly, both emphysema and pulmonary fibrosis are associated with male sex; however, these associations alone are not sufficient to explain the significant male preponderance in CPFE patients^[23,24]. It has been proposed that this preponderance may be explained by the greater vulnerability of men to lung aging^[3].

There was good agreement between the 2 observers with respect to the severity of the different parameters of the HRCT scoring system. Interobserver agreement for the predominant type of emphysema and pulmonary fibrosis on HRCT was also satisfactory.

According to the results of the present study, the incidence of CLE (as the predominant type of emphysema) is similar to the incidence of PSE (CLE/PSE = observer 1: 28/23, observer 2: 26/25). A previous study reported that although CLE was almost always present in the CPFE group, the coexistence of PSE was surprisingly high^[2]; in another study, PSE was more common in the CPFE population compared with the COPD group^[7]. According to the results of our study, in CPFE patients, certain patterns of emphysema are more commonly associated with certain patterns of fibrosis, rather than certain patterns of emphysema being more prevalent than others. Bullous emphysema has also been reported to be common in CPFE patients, as was the case in our study^[3,6,7]. However, we did not evaluate bullous emphysema as a separate category, as bullous emphysema may be the progression of CLE or PSE depending on the intraparenchymal or subpleural location of the bullae. Moreover, in the advanced stages of CLE, the centrilobular distribution of abnormalities is no longer recognizable on HRCT or on pathology, and this appearance can closely mimic the appearance of panlobular emphysema, rendering the distinction between these two entities very difficult on HRCT and of little clinical significance^[25].

Similarly, there was no significant difference between the incidence of the UIP pattern and NSIP pattern on HRCT (as the predominant pattern of fibrosis on HRCT) in CPFE patients (typical UIP + possible UIP/NSIP =

observer 1: 19 + 10/24, observer 2: 24 + 5/24). Cottin *et al.*^[2] reported that 51% of patients presented with HRCT findings consistent with typical IPF, whereas 34% of patients presented with a CT pattern consistent with probable IPF or fibrosing NSIP, and 15% of cases exhibited a complex pattern with predominant reticular opacities. Jankowich *et al.*^[8] reported that 8 of the 10 patients in their study exhibited honeycombing on CT, whereas in Kitaguchi *et al.*^[7]'s paper, 75.6% of patients presented with honeycombing. However, in all three previous studies, GGO was present in 66%, 20% and 62.2% accordingly. The discrepancy in the incidence (lower incidence) of the NSIP pattern in previous studies relative to ours may be explained by the fact that presence of GGO and fibrosis around emphysematous spaces and cysts may erroneously mimic and therefore lead to the overestimation of honeycombing^[9,10]. In accordance with this finding, Akira *et al.*^[9] reported in their study that the coexistence of emphysema renders the distinction between UIP and NSIP more difficult; therefore, NSIP may mimic UIP when it coexists with emphysema. Similarly, Watadani *et al.*^[10] reported that the diagnosis of honeycombing is very variable even amongst experienced readers and may be misdiagnosed, especially when emphysema or traction bronchiolectasis coexist. In our study, we evaluated the subpleural thin-walled cysts (< 1 mm wall thickness) of varying sizes with a centrilobular artery within their center as PSE. On the other hand, the subpleural cluster of cysts with relatively thick walls (1-3 mm) and cysts of the same size that lacked a centrilobular artery at their center were evaluated as honeycombing.

Another interesting finding in our study was that CPFE patients with a predominant type of CLE exhibited a significantly higher extent of emphysema than patients with PSE. On the other hand, CPFE patients with a predominant type of PSE exhibited a higher extent of interstitial lung disease (fibrosis). This finding may be explained by the fact that by definition, in order for the "paraseptal" type to be the predominant type of emphysema, it must be located subpleurally around the periphery of the lungs or along the fissures, which is overall a smaller area than the "non-subpleural" part of the lungs (where CLE is located). Therefore, when PSE predominates, the non-subpleural part of the lungs is not affected by emphysema, and the fibrotic process has "free area" to expand. On the contrary, when CLE predominates, comparatively greater area is affected, and there is limited "free space" for fibrosis to develop. If this sequence of phenomena is correct, then we could speculate that emphysema chronologically precedes the development of fibrosis in CPFE patients. Another intriguing finding in our study was that in CPFE patients, a predominant type of "CLE" was associated with more GGO and less coarse fibrosis and honeycombing (resembling an NSIP pattern), whereas a predominant type of PSE was associated with coarser fibrosis, reticulation and honeycombing, resembling a UIP pattern. These findings were confirmed by the

regression analysis results, which demonstrate that among HRCT features, the "coarseness of fibrosis" most strongly differentiated typical and probable UIP from NSIP and PSE from CLE. There have been no previous studies in the literature exploring the possible relationship between the predominant type of emphysema with the predominant type of fibrosis on HRCT. However, Marten *et al.*^[26] reported that the coexistence of CLE with NSIP patients provided evidence for smoking as a pathogenetic factor in a subset of NSIP patients. Longitudinal studies both in the development of CLE and NSIP have demonstrated that CLE replaces macrophage-related respiratory bronchiolitis^[27,28] and that macrophage accumulation of DIP may recede leaving residual fibrotic NSIP^[26,29]. In a more recent study, Antoniou *et al.*^[30] reported coarser fibrosis and notable honeycombing in smokers with IPF and rheumatoid lung relative to non-smoking counterparts. The latter finding suggests a pathogenetic link between smoking-related damage and lung fibrosis, although differentiation between CLE and PSE was not attempted. Tobacco smoking has been suggested to be a causative agent in both emphysema and lung fibrosis^[11] because cigarette smoke may directly trigger pathways common to pulmonary fibrosis and emphysema, including excessive oxidative stress, induction of inflammation, protease-antiprotease imbalance^[31], promotion of apoptosis, recruitment of macrophages or dysregulation of connective tissue matrix^[30]. In addition to epigenetic modifications, genetic variants, including mutations of the surfactant protein C^[32] and overexpression of platelet-derived growth factor and tumor necrosis factor α and β in animal models^[33], have also been associated with the development of both emphysema and fibrosis. Recently it has been reported that specific genes of the protease-antiprotease balance pathway may be associated with specific emphysema types, particularly MMP9 and TGFB1 to CLE and TIMP2 and TNF to PSE^[31]. Autoimmunity has also been implicated in the pathogenesis of CPFE^[34]. Based on these findings, one could speculate that there may be a possible pathogenetic linkage in CPFE patients leading to combinations of specific patterns of lung fibrosis and emphysema. The above findings could have significant prognostic and therapeutic implications because a predominant type of CLE would be associated with a more reversible type of pulmonary fibrosis that would be more likely to respond to smoking cessation and immunosuppressive therapy^[8], whereas a predominant PSE would be associated with a more irreversible type of pulmonary fibrosis with a worse prognosis^[35]. In support of our results, a recent study by Todd *et al.*^[36] has reported that there is improved prognosis in CPFE patients presenting with advanced CLE compared with PSE. The authors hypothesized that this may be attributed to the more severe pulmonary inflammation present in CLE vs PSE that could be partially protective against the adverse effects of pulmonary fibrosis.

DLC_o and TLC were significantly lower in the "typical

UIP" group compared with the "NSIP group". Systolic pulmonary arterial pressure was found to be higher in the "typical UIP" group (48.12 mm/Hg) compared with the "NSIP" group (27.33 mm/Hg), although the last finding did not exhibit statistical significance due to the small number of patients having undergone eSPAP evaluation. These findings were in accordance with previous studies in which DLCo was found to be a significant predictor of mortality in IPF patients^[37,38] and in which the presence of pulmonary arterial hypertension was found to be associated with poor survival both in IPF^[38] and CPFE patients^[4,39].

There was fair HRCT-pathologic correlation in the 19 out of 53 cases where histology was available. Only 2 out of the 19 cases were consistent with non-UIP histologic diagnosis (2 NSIP). There may have been a bias towards the histologic diagnosis of UIP (definite UIP or possible UIP) because these cases were more likely to have undergone biopsy due to worse clinical symptoms that would require more aggressive treatment. On the other hand, patients with an NSIP pattern on HRCT were more likely to exhibit extensive emphysema (as shown in our study), therefore avoiding a lung biopsy^[40].

There are several limitations in our study that are mainly caused by its observational and uncontrolled design, with retrospective collection of the data from a single center. Our results are also subject to selection bias, as only patients who had undertaken HRCT and patients with evidence of both emphysema and fibrosis on HRCT were included, creating bias towards patients with less typical findings. Another limitation may be the fact that the presence of only 3 considerations in the differential diagnosis of HRCT findings may have resulted in an artificial high interobserver agreement. A potentially important limitation in study design was that the 2 HRCT readers were aware of the fact that patients had coexistence of emphysema and fibrosis on HRCT and that the main goal was to identify any relationship between the predominant type of emphysema and the predominant type of fibrosis on HRCT, although the readers were unaware of the clinical findings and the histology of the cases at the time of evaluation. To overcome this problem, the HRCT readers evaluated the HRCT studies blindly in three different steps with a one month interval between each step: first, they evaluated the predominant type of emphysema for each study; second, they evaluated the predominant type of fibrosis; and last, they scored the different HRCT parameters of the HRCT scoring system. Another limitation of the study was the small number of patients who had undergone eSPAP measurements using cardiac ultrasound due to the poor echo window, which was mainly attributed to the presence of emphysema.

In conclusion, we have found that in CPFE patients, a predominance of PSE may be associated with a higher extent of fibrosis and with a UIP-HRCT pattern, whereas a predominance of CLE may be associated with a higher extent of emphysema and an NSIP-HRCT pattern of

fibrosis that could be more reversible and responsive to smoking cessation and immunosuppression. Thus, although viewed with caution, our observations justify future studies to explore possible common pathogenetic mechanisms that may lead to the simultaneous development of specific types of emphysema and fibrosis affecting the prognosis of CPFE patients.

COMMENTS

Background

"Combined pulmonary fibrosis and emphysema" (CPFE) is a relatively newly reported syndrome in the literature based on clinical and computed tomography (CT) findings. Clinical findings include history of smoking, severe dyspnea, pseudonormalization of the pulmonary function tests contrasting with severe decrease on diffusion capacity and hypoxemia during exercise. Association with pulmonary hypertension significantly impairs prognosis. Imaging findings include presence of emphysema in the upper lobes and pulmonary fibrosis in the lower lobes. The predominant type of emphysema and pulmonary fibrosis when these two entities coexist and their possible association and possible relevant clinical implications has not been fully elucidated in the literature.

Research frontiers

The predominant type of emphysema varies in the few studies about CPFE reported in the literature, with some of them reporting centrilobular type to be more common, while others reporting paraseptal type to be the predominant one. As far as the fibrotic component is concerned, in the earlier days CPFE was considered to be characterized more commonly by a usual interstitial pneumonia (UIP) pattern of fibrosis on High resolution computed tomography (HRCT), however there is a more recent concept according to which CPFE is a heterogeneous disease on HRCT that may present with a UIP, a nonspecific interstitial pneumonia (NSIP) pattern or a complex pattern with predominantly reticular opacities. Moreover ground glass opacity pattern may occasionally be the only HRCT pattern of fibrosis.

Innovations and breakthroughs

In the present study the authors found that in patients with coexistent emphysema and pulmonary fibrosis paraseptal emphysema is associated more with a usual interstitial pneumonia-HRCT pattern, whereas centrilobular emphysema is associated more with a nonspecific interstitial pneumonia-HRCT pattern. The incidence of centrilobular emphysema is similar to the incidence of paraseptal emphysema and similarly there was no significant difference between the incidence of UIP pattern and NSIP pattern on HRCT. According to the results of this study it seems that in CPFE patients a certain pattern of emphysema is associated more often with a certain pattern of fibrosis, rather than a certain pattern of emphysema being more prevalent than the other one. Moreover CPFE patients with a predominant type of centrilobular emphysema demonstrated significantly higher extent of emphysema than patients with paraseptal emphysema. On the other hand, CPFE patients with a predominant type of paraseptal emphysema demonstrated higher extent of pulmonary fibrosis.

Applications

In CPFE patients predominant type of paraseptal emphysema may be associated with higher extent of fibrosis and with a UIP-HRCT pattern, while predominant type of centrilobular emphysema may be associated with higher extent of emphysema and an NSIP-HRCT pattern of fibrosis that could be more reversible and responsive to smoking cessation and immunosuppression. The observations justify future studies in order to explore possible common pathogenetic mechanisms that may lead to the simultaneous development of specific types of emphysema and fibrosis affecting the prognosis in CPFE patients.

Terminology

Centrilobular emphysema is the commonest form of emphysema in cigarette smokers characterized by destroyed centrilobular alveolar walls and enlargement of respiratory bronchioles and associated alveoli. On CT it

presents as centrilobular areas of decreased attenuation, usually without visible walls, of nonuniform distribution and predominantly located in upper lung zones. Paraseptal emphysema is characterized by predominant involvement of the distal alveoli and their ducts and sacs. It borders any pleural surface and the interlobular septa. On CT it presents as subpleural and peribronchovascular regions of low attenuation separated by intact interlobular septa, sometimes associated with bullae. UIP is a histologic pattern of pulmonary fibrosis characterized by temporal and spatial heterogeneity, with established fibrosis and honeycombing interspersed among normal lung. Key findings include fibroblastic foci with fibrotic destruction of lung architecture, often with honeycombing. Honeycombing with a basal and subpleural distribution is regarded as pathognomonic, but not all cases of biopsy-proved UIP have this distinctive CT pattern. NSIP is characterized by a histologic pattern of uniform interstitial involvement by varying degrees of chronic inflammation or fibrosis. NSIP has variable thin-section CT appearances: the most frequent is ground-glass opacities with reticulation, traction bronchiectasis or bronchiolectasis, and little or no honeycombing with a predominantly basal and subpleural distribution.

Peer-review

This study investigated the relationship between specific predominant type of emphysema and the specific HRCT pattern of fibrosis in CPFE. The manuscript is well structured and provides strong data.

REFERENCES

- 1 **Wiggins J**, Strickland B, Turner-Warwick M. Combined cryptogenic fibrosing alveolitis and emphysema: the value of high resolution computed tomography in assessment. *Respir Med* 1990; **84**: 365-369 [PMID: 2247666 DOI: 10.1016/S0954-6111(08)80070-4]
- 2 **Cottin V**, Nunes H, Brillet PY, Delaval P, Devouassoux G, Tillie-Leblond I, Israel-Biet D, Court-Fortune I, Valeyre D, Cordier JF. Combined pulmonary fibrosis and emphysema: a distinct underrecognised entity. *Eur Respir J* 2005; **26**: 586-593 [PMID: 16204587 DOI: 10.1183/09031936.05.00021005]
- 3 **Jankowich MD**, Rounds SI. Combined pulmonary fibrosis and emphysema syndrome: a review. *Chest* 2012; **141**: 222-231 [PMID: 22215830 DOI: 10.1378/chest.11-1062]
- 4 **Mejía M**, Carrillo G, Rojas-Serrano J, Estrada A, Suárez T, Alonso D, Barrientos E, Gaxiola M, Navarro C, Selman M. Idiopathic pulmonary fibrosis and emphysema: decreased survival associated with severe pulmonary arterial hypertension. *Chest* 2009; **136**: 10-15 [PMID: 19225068 DOI: 10.1378/chest.08-2306]
- 5 **Balbi B**, Cottin V, Singh S, De Wever W, Herth FJ, Robalo Cordeiro C. Smoking-related lung diseases: a clinical perspective. *Eur Respir J* 2010; **35**: 231-233 [PMID: 20123840 DOI: 10.1183/09031936.00189309]
- 6 **Brillet PY**, Cottin V, Letoumelin P, Landino F, Brauner MW, Valeyre D, Cordier JF, Nunes H. Combined apical emphysema and basal fibrosis syndrome (emphysema/fibrosis syndrome): CT imaging features and pulmonary function tests. *J Radiol* 2009; **90**: 43-51 [PMID: 19182713]
- 7 **Kitaguchi Y**, Fujimoto K, Hanaoka M, Kawakami S, Honda T, Kubo K. Clinical characteristics of combined pulmonary fibrosis and emphysema. *Respirology* 2010; **15**: 265-271 [PMID: 20051048 DOI: 10.1111/j.1440-1843.2009.01676.x]
- 8 **Jankowich MD**, Polsky M, Klein M, Rounds S. Heterogeneity in combined pulmonary fibrosis and emphysema. *Respiration* 2008; **75**: 411-417 [PMID: 17684315]
- 9 **Akira M**, Inoue Y, Kitaichi M, Yamamoto S, Arai T, Toyokawa K. Usual interstitial pneumonia and nonspecific interstitial pneumonia with and without concurrent emphysema: thin-section CT findings. *Radiology* 2009; **251**: 271-279 [PMID: 19221055 DOI: 10.1148/radiol.2511080917]
- 10 **Wataadani T**, Sakai F, Johkoh T, Noma S, Akira M, Fujimoto K, Bankier AA, Lee KS, Müller NL, Song JW, Park JS, Lynch DA, Hansell DM, Remy-Jardin M, Franquet T, Sugiyama Y. Interobserver variability in the CT assessment of honeycombing in the lungs. *Radiology* 2013; **266**: 936-944 [PMID: 23220902 DOI: 10.1148/radiol.12112516]
- 11 **Cottin V**, Nunes H, Mouthon L, Gamondes D, Lazor R, Hachulla E, Revel D, Valeyre D, Cordier JF, Groupe d'Etudes et de Recherche sur les Maladies "Orphelines" Pulmonaires. Combined pulmonary fibrosis and emphysema syndrome in connective tissue disease. *Arthritis Rheum* 2011; **63**: 295-304 [PMID: 20936629 DOI: 10.1002/art.30077]
- 12 **Goh NS**, Desai SR, Veeraraghavan S, Hansell DM, Copley SJ, Maher TM, Corte TJ, Sander CR, Ratoff J, Devaraj A, Bozovic G, Denton CP, Black CM, du Bois RM, Wells AU. Interstitial lung disease in systemic sclerosis: a simple staging system. *Am J Respir Crit Care Med* 2008; **177**: 1248-1254 [PMID: 18369202 DOI: 10.1164/rccm.200706-877OC]
- 13 **Hansell DM**, Bankier AA, MacMahon H, McLoud TC, Müller NL, Remy J. Fleischner Society: glossary of terms for thoracic imaging. *Radiology* 2008; **246**: 697-722 [PMID: 18195376 DOI: 10.1148/radiol.2462070712]
- 14 **Travis WD**, Costabel U, Hansell DM, King TE, Lynch DA, Nicholson AG, Ryerson CJ, Ryu JH, Selman M, Wells AU, Behr J, Bouros D, Brown KK, Colby TV, Collard HR, Cordeiro CR, Cottin V, Crestani B, Drent M, Dudden RF, Egan J, Flaherty K, Hogaboam C, Inoue Y, Johkoh T, Kim DS, Kitaichi M, Loyd J, Martinez FJ, Myers J, Protzko S, Raghu G, Richeldi L, Sverzellati N, Swigris J, Valeyre D. An official American Thoracic Society/European Respiratory Society statement: Update of the international multidisciplinary classification of the idiopathic interstitial pneumonias. *Am J Respir Crit Care Med* 2013; **188**: 733-748 [PMID: 24032382 DOI: 10.1164/rccm.201308-1483ST]
- 15 **Macintyre N**, Crapo RO, Viegi G, Johnson DC, van der Grinten CP, Brusasco V, Burgos F, Casaburi R, Coates A, Enright P, Gustafsson P, Hankinson J, Jensen R, McKay R, Miller MR, Navajas D, Pedersen OF, Pellegrino R, Wanger J. Standardisation of the single-breath determination of carbon monoxide uptake in the lung. *Eur Respir J* 2005; **26**: 720-735 [PMID: 16204605 DOI: 10.1183/09031936.05.00034905]
- 16 **Global Initiative for Chronic Obstructive Lung Disease**. Global strategy for the diagnosis, management, and prevention of COPD (updated 2013). Available from: URL: http://www.goldcopd.org/uploads/users/files/GOLD_Report_2013_Feb20.pdf
- 17 **Yock PG**, Popp RL. Noninvasive estimation of right ventricular systolic pressure by Doppler ultrasound in patients with tricuspid regurgitation. *Circulation* 1984; **70**: 657-662 [PMID: 6478568 DOI: 10.1161/01.CIR.70.4.657]
- 18 **Brennan P**, Silman A. Statistical methods for assessing observer variability in clinical measures. *BMJ* 1992; **304**: 1491-1494 [PMID: 1611375 DOI: 10.1136/bmj.304.6840.1491]
- 19 **Sakai F**, Tominaga J, Kaga A, Usui Y, Kanazawa M, Ogura T, Yanagawa N, Takemura T. Imaging diagnosis of interstitial pneumonia with emphysema (combined pulmonary fibrosis and emphysema). *Pulm Med* 2012; **2012**: 816541 [PMID: 22448329 DOI: 10.1155/2012/816541]
- 20 **Bauer CM**, Morissette MC, Stämpfli MR. The influence of cigarette smoking on viral infections: translating bench science to impact COPD pathogenesis and acute exacerbations of COPD clinically. *Chest* 2013; **143**: 196-206 [PMID: 23276842 DOI: 10.1378/chest.12-0930]
- 21 **Baumgartner KB**, Samet JM, Stidley CA, Colby TV, Waldron JA. Cigarette smoking: a risk factor for idiopathic pulmonary fibrosis. *Am J Respir Crit Care Med* 1997; **155**: 242-248 [PMID: 9001319 DOI: 10.1164/ajrccm.155.1.9001319]
- 22 **Flaherty KR**, Martinez FJ. Cigarette smoking in interstitial lung disease: concepts for the internist. *Med Clin North Am* 2004; **88**: 1643-1653, xiii [PMID: 15464118 DOI: 10.1016/j.mcna.2004.08.001]
- 23 **Dransfield MT**, Washko GR, Foreman MG, Estepar RS, Reilly J, Bailey WC. Gender differences in the severity of CT emphysema in COPD. *Chest* 2007; **132**: 464-470 [PMID: 17573503 DOI: 10.1378/chest.07-0863]
- 24 **Raghu G**, Weycker D, Edelsberg J, Bradford WZ, Oster G. Incidence and prevalence of idiopathic pulmonary fibrosis. *Am J Respir Crit Care Med* 2006; **174**: 810-816 [PMID: 16809633 DOI: 10.1164/rccm.200602-163OC]

- 25 **Webb WR**, Muller NL, Naidich DP. High-Resolution CT of the lung. 2nd ed. Philadelphia: Lippincott Williams & Wilkins, 1996
- 26 **Marten K**, Milne D, Antoniou KM, Nicholson AG, Tennant RC, Hansel TT, Wells AU, Hansell DM. Non-specific interstitial pneumonia in cigarette smokers: a CT study. *Eur Radiol* 2009; **19**: 1679-1685 [PMID: 19214521 DOI: 10.1007/s00330-009-1308-7]
- 27 **Marten K**, Hansell DM. Imaging of macrophage-related lung diseases. *Eur Radiol* 2005; **15**: 727-741 [PMID: 15633061 DOI: 10.1007/s00330-004-2554-3]
- 28 **Remy-Jardin M**, Edme JL, Boulenguez C, Remy J, Mastora I, Sobaszek A. Longitudinal follow-up study of smoker's lung with thin-section CT in correlation with pulmonary function tests. *Radiology* 2002; **222**: 261-270 [PMID: 11756735 DOI: 10.1148/radiol.2221001154]
- 29 **Craig PJ**, Wells AU, Doffman S, Rassl D, Colby TV, Hansell DM, Du Bois RM, Nicholson AG. Desquamative interstitial pneumonia, respiratory bronchiolitis and their relationship to smoking. *Histopathology* 2004; **45**: 275-282 [PMID: 15330806 DOI: 10.1111/j.1365-2559.2004.01921.x]
- 30 **Antoniou KM**, Walsh SL, Hansell DM, Rubens MR, Marten K, Tennant R, Hansel T, Desai SR, Siafakas NM, du Bois RM, Wells AU. Smoking-related emphysema is associated with idiopathic pulmonary fibrosis and rheumatoid lung. *Respirology* 2013; **18**: 1191-1196 [PMID: 23819865 DOI: 10.1111/resp.12154]
- 31 **Kukkonen MK**, Tiili E, Vehmas T, Oksa P, Piirilä P, Hirvonen A. Association of genes of protease-antiprotease balance pathway to lung function and emphysema subtypes. *BMC Pulm Med* 2013; **13**: 36 [PMID: 23734748 DOI: 10.1186/1471-2466-13-36]
- 32 **Cottin V**, Reix P, Khouatra C, Thivolet-Béjui F, Feldmann D, Cordier JF. Combined pulmonary fibrosis and emphysema syndrome associated with familial SFTPC mutation. *Thorax* 2011; **66**: 918-919 [PMID: 21248320 DOI: 10.1136/thx.2010.151407]
- 33 **Lundblad LK**, Thompson-Figueroa J, Leclair T, Sullivan MJ, Poynter ME, Irvin CG, Bates JH. Tumor necrosis factor-alpha overexpression in lung disease: a single cause behind a complex phenotype. *Am J Respir Crit Care Med* 2005; **171**: 1363-1370 [PMID: 15805183]
- 34 **Tzouvelekis A**, Zacharis G, Oikonomou A, Mikroulis D, Margaritopoulos G, Koutsopoulos A, Antoniadis A, Koulelidis A, Steiropoulos P, Boglou P, Bakali M, Froudarakis M, Bouras D. Increased incidence of autoimmune markers in patients with combined pulmonary fibrosis and emphysema. *BMC Pulm Med* 2013; **13**: 31 [PMID: 23697753 DOI: 10.1186/1471-2466-13-31]
- 35 **Wells AU**. The revised ATS/ERS/JRS/ALAT diagnostic criteria for idiopathic pulmonary fibrosis (IPF)—practical implications. *Respir Res* 2013; **14** Suppl 1: S2 [PMID: 23734820 DOI: 10.1186/1465-9921-14-S1-S2]
- 36 **Todd NW**, Jeudy J, Lavania S, Franks TJ, Galvin JR, Deepak J, Britt EJ, Atamas SP. Centrilobular emphysema combined with pulmonary fibrosis results in improved survival. *Fibrogenesis Tissue Repair* 2011; **4**: 6 [PMID: 21324139 DOI: 10.1186/1755-1536-4-6]
- 37 **Schmidt SL**, Nambiar AM, Tayob N, Sundaram B, Han MK, Gross BH, Kazerooni EA, Chughtai AR, Lagstein A, Myers JL, Murray S, Toews GB, Martinez FJ, Flaherty KR. Pulmonary function measures predict mortality differently in IPF versus combined pulmonary fibrosis and emphysema. *Eur Respir J* 2011; **38**: 176-183 [PMID: 21148225 DOI: 10.1183/09031936.00114010]
- 38 **Hamada K**, Nagai S, Tanaka S, Handa T, Shigematsu M, Nagao T, Mishima M, Kitaichi M, Izumi T. Significance of pulmonary arterial pressure and diffusion capacity of the lung as prognosticator in patients with idiopathic pulmonary fibrosis. *Chest* 2007; **131**: 650-656 [PMID: 17317730 DOI: 10.1378/chest.06-1466]
- 39 **Cottin V**, Le Pavec J, Prévot G, Mal H, Humbert M, Simonneau G, Cordier JF, GERM"O" P. Pulmonary hypertension in patients with combined pulmonary fibrosis and emphysema syndrome. *Eur Respir J* 2010; **35**: 105-111 [PMID: 19643948 DOI: 10.1183/09031936.00038709]
- 40 **Cottin V**, Cordier JF. Combined pulmonary fibrosis and emphysema in connective tissue disease. *Curr Opin Pulm Med* 2012; **18**: 418-427 [PMID: 22781207 DOI: 10.1097/MCP.0b013e328356803b]

P- Reviewer: Bernardin L, Li YZ **S- Editor:** Gong XM

L- Editor: A **E- Editor:** Wu HL





Published by **Baishideng Publishing Group Inc**

8226 Regency Drive, Pleasanton, CA 94588, USA

Telephone: +1-925-223-8242

Fax: +1-925-223-8243

E-mail: bpgoffice@wjgnet.com

Help Desk: <http://www.wjgnet.com/esps/helpdesk.aspx>

<http://www.wjgnet.com>



World Journal of *Radiology*

World J Radiol 2015 October 28; 7(10): 306-360





Editorial Board

2014-2017

The *World Journal of Radiology* Editorial Board consists of 365 members, representing a team of worldwide experts in radiology. They are from 36 countries, including Afghanistan (1), Argentina (2), Australia (5), Austria (7), Belgium (2), Brazil (8), Canada (6), Chile (1), China (43), Croatia (1), Denmark (4), Egypt (6), France (5), Germany (22), Greece (10), India (12), Iran (6), Ireland (2), Israel (3), Italy (47), Japan (13), Netherlands (1), New Zealand (1), Pakistan (1), Poland (2), Portugal (1), Serbia (1), Singapore (3), Slovakia (1), South Korea (18), Spain (4), Sweden (2), Switzerland (4), Thailand (1), Turkey (26), United Kingdom (11), and United States (82).

EDITORS-IN-CHIEF

Kai U Juergens, *Bremen*
Edwin JR van Beek, *Edinburgh*
Thomas J Vogl, *Frankfurt*

GUEST EDITORIAL BOARD MEMBERS

Wing P Chan, *Taipei*
Chung-Huei Hsu, *Taipei*
Chin-Chang Huang, *Taipei*
Tsong-Long Hwang, *Taoyuan*
Jung-Lung Hsu, *Taipei*
Chia-Hung Kao, *Taichung*
Yu-Ting Kuo, *Tainan*
Hon-Man Liu, *Taipei*
Hui-Lung Liang, *Kaohsiung*
Chun Chung Lui, *Kaohsiung*
Sen-Wen Teng, *Taipei*
Yung-Liang (William) Wan, *Taoyuan*

MEMBERS OF THE EDITORIAL BOARD



Afghanistan

Takao Hiraki, *Okayama*



Argentina

Patricia Carrascosa, *Vicente Lopez*
Maria C Ziadi, *Rosario*



Australia

Lourens Bester, *Sydney*
Gemma A Figtree, *Sydney*



Austria

Herwig R Cerwenka, *Graz*
Gudrun M Feuchtnner, *Innsbruck*
Benjamin Henninger, *Innsbruck*
Rupert Lanzenberger, *Vienna*
Shu-Ren Li, *Vienna*
Veronika Schopf, *Vienna*
Tobias De Zordo, *Innsbruck*



Belgium

Steve Majerus, *Liege*
Kathelijne Peremans, *Merelbeke*



Brazil

Clerio F Azevedo, *Rio de Janeiro*
Patrícia P Alfredo, *São Paulo*
Eduardo FC Fleury, *São Paulo*
Edward Araujo Júnior, *São Paulo*
Wellington P Martins, *Ribeirao Preto*
Ricardo A Mesquita, *Belo Horizonte*
Vera MC Salemi, *São Paulo*
Claudia Szobot, *Porto Alegre*
Lilian YI Yamaga, *São Paulo*



Canada

Marie Arsalidou, *Toronto*
Otman A Basir, *Waterloo*

Tarik Zine Belhocine, *Toronto*
James Chow, *Toronto*
Tae K Kim, *Toronto*
Anastasia Oikonomou, *Toronto*



China

Hong-Wei Chen, *Wuxi*
Feng Chen, *Hangzhou*
Jian-Ping Chu, *Guangzhou*
Guo-Guang Fan, *Shenyang*
Bu-Lang Gao, *Shijiazhuang*
Qi-Yong Gong, *Chengdu*
Ying Han, *Beijing*
Xian-Li Lv, *Beijing*
Yi-Zhuo Li, *Guangzhou*
Xiang-Xi Meng, *Harbin*
Yun Peng, *Beijing*
Jun Shen, *Guangzhou*
Ze-Zhou Song, *Hangzhou*
Wai Kwong Tang, *Hong Kong*
Gang-Hua Tang, *Guangzhou*
Jie Tian, *Beijing*
Lu-Hua Wang, *Beijing*
Xiao-bing Wang, *Xi'an*
Yi-Gen Wu, *Nanjing*
Kai Wu, *Guangzhou*
Hui-Xiong Xu, *Shanghai*
Zuo-Zhang Yang, *Kunming*
Xiao-Dan Ye, *Shanghai*
David T Yew, *Hong Kong*
Ting-He Yu, *Chongqing*
Zheng Yuan, *Shanghai*
Min-Ming Zhang, *Hangzhou*
Yudong Zhang, *Nanjing*
Dong Zhang, *Chongqing*
Wen-Bin Zeng, *Changsha*

Yue-Qi Zhu, *Shanghai*



Croatia

Goran Kusec, *Osijek*



Denmark

Poul E Andersen, *Odense*

Lars J Petersen, *Aalborg*

Thomas Z Ramsøy, *Frederiksberg*

Morten Ziebell, *Copenhagen*



Egypt

Mohamed F Bazeed, *Mansoura*

Mohamed Abou El-Ghar, *Mansoura*

Reem HA Mohamed, *Cairo*

Mohamed R Nouh, *Alexandria*

Ahmed AKA Razek, *Mansoura*

Ashraf A Zytoon, *Shebin El-Koom*



France

Sabine F Bensamoun, *Compiègne*

Romarc Loffroy, *Dijon*

Stephanie Nougaret, *Montpellier*

Hassane Oudadesse, *Rennes*

Vincent Vinh-Hung, *Fort-de-France*



Germany

Henryk Barthel, *Leipzig*

Peter Bannas, *Hamburg*

Martin Beeres, *Frankfurt*

Ilja F Ciernik, *Dessau*

A Dimitrakopoulou-Strauss, *Heidelberg*

Peter A Fasching, *Erlangen*

Andreas G Schreyer, *Regensburg*

Philipp Heusch, *Duesseldorf*

Sonja M Kirchhoff, *Munich*

Sebastian Ley, *Munich*

Adel Maataoui, *Frankfurt am Main*

Stephan M Meckel, *Freiburg*

Hans W Muller, *Duesseldorf*

Kay Raum, *Berlin*

Dirk Rades, *Luebeck*

Marc-Ulrich Regier, *Hamburg*

Alexey Surov, *Halle*

Martin Walter, *Magdeburg*

Axel Wetter, *Essen*

Christoph Zilkens, *Düsseldorf*



Greece

Panagiotis Antoniou, *Thessaloniki*

Nikos Efthimiou, *Athens*

Dimitris Karnabatidis, *Patras*

George Latsios, *Athens*

Stylianios Megremis, *Iraklion*

Alexander D Rapidis, *Athens*

Kiki Theodorou, *Larissa*

Ioannis A Tsalafoutas, *Athens*

Evanthia E Tripoliti, *Ioannina*

Athina C Tsili, *Ioannina*



India

Ritesh Agarwal, *Chandigarh*

Chandan J Das, *New Delhi*

Prathamesh V Joshi, *Mumbai*

Naveen Kalra, *Chandigarh*

Chandrasekharan Kesavadas, *Trivandrum*

Jyoti Kumar, *New Delhi*

Atin Kumar, *New Delhi*

Kaushala P Mishra, *Allahabad*

Daya N Sharma, *New Delhi*

Binit Sureka, *New Delhi*

Sanjay Sharma, *New Delhi*

Raja R Yadav, *Allahabad*



Iran

Majid Assadi, *Bushehr*

SeyedReza Najafizadeh, *Tehran*

Mohammad Ali Oghabian, *Tehran*

Amir Reza Radmard, *Tehran*

Ramin Sadeghi, *Mashhad*

Hadi Rokni Yazdi, *Tehran*



Ireland

Tadhg Gleeson, *Wexford*

Frederik JAI Vernimmen, *Cork*



Israel

Dafna Ben Bashat, *Tel Aviv*

Amit Gefen, *Tel Aviv*

Tamar Sella, *Jerusalem*



Italy

Adriano Alippi, *Rome*

Dante Amelio, *Trento*

Michele Anzidei, *Rome*

Filippo F Angileri, *Messinas*

Stefano Arcangeli, *Rome*

Roberto Azzoni, *San Donato milanese*

Tommaso V Bartolotta, *Palermo*

Tommaso Bartalena, *Imola*

Livia Bernardin, *San Bonifacio*

Federico Boschi, *Verona*

Sergio Casciaro, *Lecce*

Emanuele Casciani, *Rome*

Musa M Can, *Napoli*

Alberto Cuocolo, *Napoli*

Michele Ferrara, *Coppito*

Mauro Feola, *Fossano*

Giampiero Francica, *Castel Volturno*

Luigi De Gennaro, *Rome*

Giulio Giovannetti, *Pisa*

Francesca Iacobellis, *Napoli*

Formato Invernizzi, *Monza Brianza*

Francesco Lassandro, *Naples*

Lorenzo Livi, *Florence*

Pier P Mainenti, *Napoli*

Laura Marzetti, *Chieti*

Giuseppe Malinverni, *Crescentino*

Enrica Milanese, *Turin*

Giovanni Morana, *Treviso*

Lorenzo Monti, *Milan*

Silvia D Morbelli, *Genoa*

Barbara Palumbo, *Perugia*

Cecilia Parazzini, *Milan*

Stefano Pergolizzi, *Messina*

Antonio Pinto, *Naples*

Camillo Porcaro, *Rome*

Carlo C Quattrocchi, *Rome*

Alberto Rebonato, *Perugia*

Giuseppe Rizzo, *Rome*

Roberto De Rosa, *Naples*

Domenico Rubello, *Rovigo*

Andrea Salvati, *Bari*

Sergio Sartori, *Ferrara*

Luca M Sconfienza, *Milano*

Giovanni Storto, *Rionero*

Nicola Sverzellati, *Parma*

Alberto S Tagliafico, *Genova*

Nicola Troisi, *Florence*



Japan

Yasuhiko Hori, *Chiba*

Hidetoshi Ikeda, *Koriyama*

Masahito Kawabori, *Sapporo*

Tamotsu Kamishima, *Sapporo*

Hiro Kiyosue, *Yufu*

Yasunori Minami, *Osaka-sayama*

Yasuhiro Morimoto, *Kitakyushu*

Satoru Murata, *Tokyo*

Shigeki Nagamachi, *Miyazaki*

Hiroshi Onishi, *Yamanashi*

Morio Sato, *Wakayama Shi*

Yoshito Tsushima, *Maebashi*

Masahiro Yanagawa, *Suita*



Netherlands

Willem Jan van Rooij, *Tilburg*



New Zealand

W Howell Round, *Hamilton*



Pakistan

Wazir Muhammad, *Abbottabad*



Poland

Maciej S Baglaj, *Wroclaw*

Piotr Czauderna, *Gdansk*



Portugal

Joao Manuel RS Tavares, *Porto*



Serbia

Olivera Ciraj-Bjelac, *Belgrade*



Singapore

Gopinathan Anil, *Singapore*

Terence KB Teo, *Singapore*

Cher Heng Tan, *Singapore*



Slovakia

Stefan Sivak, *Martin*



South Korea

Ki Seok Choo, *Busan*

Seung Hong Choi, *Seoul*

Dae-Seob Choi, *Jinju*

Hong-Seok Jang, *Seoul*

Yong Jeong, *Daejeon*

Chan Kyo Kim, *Seoul*

Se Hyung Kim, *Seoul*

Joong-Seok Kim, *Seoul*

Sang Eun Kim, *Seongnam*

Sung Joon Kwon, *Seoul*

Jeong Min Lee, *Seoul*

In Sook Lee, *Busan*

Noh Park, *Goyang*

Chang Min Park, *Seoul*

Sung Bin Park, *Seoul*

Deuk Jae Sung, *Seoul*

Choongsoo Shin, *Seoul*

Kwon-Ha Yoon, *Iksan*



Spain

Miguel A De Gregorio, *Zaragoza*

Antonio Luna, *Jaén*

Enrique Marco de Lucas, *Santander*

Fernando Ruiz Santiago, *Granada*



Sweden

Dmitry Grishenkov, *Stockholm*

Tie-Qiang Li, *Stockholm*



Switzerland

Nicolau Beckmann, *Basel*

Christian Boy, *Bern*

Giorgio Treglia, *Bellinzona*

Stephan Ulmer, *Kiel*



Thailand

Sirianong Namwongprom, *Chiang Mai*



Turkey

Kubilay Aydin, *Istanbul*

Ramazan Akdemir, *Sakarya*

Serhat Avcu, *Ankara*

Ayşe Aralasmak, *Istanbul*

Oktay Algin, *Ankara*

Nevbahar Akcar, *Meselik*

Bilal Battal, *Ankara*

Zulkif Bozgeyik, *Elazig*

Nazan Ciledag, *Aakara*

Fuldem Y Donmez, *Ankara*

Gulgun Engin, *Istanbul*

Ahmet Y Goktay, *Izmir*

Oguzhan G Gumustas, *Bursa*

Kaan Gunduz, *Ankara*

Pelin Ozcan Kara, *Mersin*

Kivanc Kamburoglu, *Ankara*

Ozgur Kilickesmez, *Istanbul*

Furuzan Numan, *Istanbul*

Cem Onal, *Adana*

Ozgur Oztekin, *Izmir*

Seda Ozbek (Boruban), *Konya*

Selda Sarikaya, *Zonguldak*

Figen Taser, *Kutahya*

Baran Tokar, *Eskisehir*

Ender Uysal, *Istanbul*

Ensar Yekeler, *Istanbul*



United Kingdom

Indran Davagnanam, *London*

M DC Valdés Hernández, *Edinburgh*

Alan Jackson, *Manchester*

Suneil Jain, *Belfast*

Long R Jiao, *London*

Miltiadis Krokidis, *Cambridge*

Pradesh Kumar, *Liverpool*

Peter D Kuzmich, *Derby*

Georgios Plataniotis, *Brighton*

Vanessa Sluming, *Liverpool*



United States

Garima Agrawal, *Saint Louis*

James R Brasic, *Baltimore*

Rajendra D Badgaiyan, *Buffalo*

Ulas Bagci, *Bethesda*

Anat Biegon, *Stony Brook*

Ramon Casanova, *Winston Salem*

Wenli Cai, *Boston*

Zheng Chang, *Durham*

Corey J Chakarun, *Long Beach*

Kai Chen, *Los Angeles*

Hyun-Soon Chong, *Chicago*

Marco Cura, *Dallas*

Ravi R Desai, *Bensalem*

Delia DeBuc, *Miami*

Carlo N De Cecco, *Charleston*

Timm-Michael L Dickfeld, *Baltimore*

Subba R Digumarthy, *Boston*

Huy M Do, *Stanford*

Todd A Faasse, *Grand Rapids*

Salomao Faintuch, *Boston*

Girish M Fatterpekar, *New York*

Dhakshinamoorthy Ganesan, *Houston*

Robert J Griffin, *Little Rock*

Andrew J Gunn, *Boston*

Sandeep S Hedgire, *Boston*

Timothy J Hoffman, *Columbia*

Mai-Lan Ho, *San Francisco*

Juebin Huang, *Jackson*

Abid Irshad, *Charleston*

Matilde Inglese, *New York*

El-Sayed H Ibrahim, *Jacksonville*

Paul R Julsrud, *Rochester*

Pamela T Johnson, *Baltimore*

Ming-Hung Kao, *Tempe*

Sunil Krishnan, *Houston*

Richard A Komoroski, *Cincinnati*

Sandi A Kwee, *Honolulu*

King Kim, *Ft. Lauderdale*

Guozheng Liu, *Worcester*

Yiyan Liu, *Newark*

Venkatesh Mani, *New York*

Lian-Sheng Ma, *Pleasanton*

Rachna Madan, *Boston*

Zeyad A Metwalli, *Houston*

Yilong Ma, *Manhasset*

Hui Mao, *Atlanta*

Feroze B Mohamed, *Philadelphia*

Gul Moonis, *Boston*

John L Noshier, *New Brunswick*

Rahmi Oklu, *Boston*

Aytekun Oto, *Chicago*

Bishnuhari Paudyal, *Philadelphia*

Rajul Pandya, *Youngstown*

Chong-Xian Pan, *Sacramento*

Jay J Pillai, *Baltimore*

Neal Prakash, *Duarte*

Reza Rahbar, *Boston*

Ali S Raja, *Boston*

Gustavo J Rodriguez, *El Paso*

David J Sahn, *Portland*

Steven Schild, *Scottsdale*

Ali R Sepahdari, *Los Angeles*

Li Shen, *Indianapolis*

JP Sheehan, *Charlottesville*

Atul B Shinagare, *Boston*

Sarabjeet Singh, *Boston*

Charles J Smith, *Columbia*

Kenji Suzuki, *Chicago*

Monvadi Srichai-Parsia, *Washington*

Sree H Tirumani, *Boston*

Hebert A Vargas, *New York*

Sachit Verma, *Philadelphia*

Yoichi Watanabe, *Minneapolis*

Li Wang, *Chapel Hill*

Carol C Wu, *Boston*

Shoujun Xu, *Houston*

Min Yao, *Cleveland*

Xiaofeng Yang, *Atlanta*

Qingbao Yu, *Albuquerque*

Aifeng Zhang, *Chicago*

Chao Zhou, *Bethlehem*

Hongming Zhuang, *Philadelphia*

**EDITORIAL**

- 306 Locoregional treatment for hepatocellular carcinoma: The best is yet to come

Kalra N, Gupta P, Chawla Y, Khandelwal N

REVIEW

- 319 Diffusion-weighted imaging of pancreatic cancer

De Robertis R, Tinazzi Martini P, Demozzi E, Dal Corso F, Bassi C, Pederzoli P, D'Onofrio M

MINIREVIEWS

- 329 Malformations of cortical development: 3T magnetic resonance imaging features

Battal B, Ince S, Akgun V, Kocaoglu M, Ozcan E, Tasar M

- 336 Evaluation of primary adrenal insufficiency secondary to tuberculous adrenalitis with computed tomography and magnetic resonance imaging: Current status

Huang YC, Tang YL, Zhang XM, Zeng NL, Li R, Chen TW

- 343 Functional assessment of transplanted kidneys with magnetic resonance imaging

Wang YT, Li YC, Yin LL, Pu H, Chen JY

ORIGINAL ARTICLE**Retrospective Cohort Study**

- 350 Relevant incidental findings at abdominal multi-detector contrast-enhanced computed tomography: A collateral screening?

Sconfienza LM, Mauri G, Muzzupappa C, Poloni A, Bandirali M, Esseridou A, Tritella S, Secchi F, Di Leo G, Sardanelli F

CASE REPORT

- 357 Delayed diagnosis of isolated alar ligament rupture: A case report

Kaufmann RA, Marzi I, Vogl TJ

ABOUT COVER

Editorial Board Member of *World Journal of Radiology*, Giulio Giovannetti, PhD, Research Scientist, Institute of Clinical Physiology, National Research Council, 56124 Pisa, Italy

AIM AND SCOPE

World Journal of Radiology (*World J Radiol*, *WJR*, online ISSN 1949-8470, DOI: 10.4329) is a peer-reviewed open access academic journal that aims to guide clinical practice and improve diagnostic and therapeutic skills of clinicians.

WJR covers topics concerning diagnostic radiology, radiation oncology, radiologic physics, neuroradiology, nuclear radiology, pediatric radiology, vascular/interventional radiology, medical imaging achieved by various modalities and related methods analysis. The current columns of *WJR* include editorial, frontier, diagnostic advances, therapeutics advances, field of vision, mini-reviews, review, topic highlight, medical ethics, original articles, case report, clinical case conference (clinicopathological conference), and autobiography.

We encourage authors to submit their manuscripts to *WJR*. We will give priority to manuscripts that are supported by major national and international foundations and those that are of great basic and clinical significance.

INDEXING/ABSTRACTING

World Journal of Radiology is now indexed in PubMed Central, PubMed, Digital Object Identifier, and Directory of Open Access Journals.

FLYLEAF

I-III Editorial Board

EDITORS FOR THIS ISSUE

Responsible Assistant Editor: *Xiang Li*
Responsible Electronic Editor: *Xiao-Kang Jiao*
Proofing Editor-in-Chief: *Lian-Sheng Ma*

Responsible Science Editor: *Shui Qiu*
Proofing Editorial Office Director: *Jin-Lei Wang*

NAME OF JOURNAL
World Journal of Radiology

ISSN
ISSN 1949-8470 (online)

LAUNCH DATE
December 31, 2009

FREQUENCY
Monthly

EDITORS-IN-CHIEF
Kai U Juergens, MD, Associate Professor, MRT und PET/CT, Nuklearmedizin Bremen Mitte, ZEMODI - Zentrum für morphologische und molekulare Diagnostik, Bremen 28177, Germany

Edwin JR van Beek, MD, PhD, Professor, Clinical Research Imaging Centre and Department of Medical Radiology, University of Edinburgh, Edinburgh EH16 4TJ, United Kingdom

Thomas J Vogl, MD, Professor, Reader in Health Technology Assessment, Department of Diagnostic and Interventional Radiology, Johann Wolfgang

Goethe University of Frankfurt, Frankfurt 60590, Germany

EDITORIAL OFFICE
Jin-Lei Wang, Director
Xiu-Xia Song, Vice Director
World Journal of Radiology
Room 903, Building D, Ocean International Center, No. 62 Dongsihuan Zhonglu, Chaoyang District, Beijing 100025, China
Telephone: +86-10-59080039
Fax: +86-10-85381893
E-mail: editorialoffice@wjnet.com
Help Desk: <http://www.wjnet.com/esps/helpdesk.aspx>
<http://www.wjnet.com>

PUBLISHER
Baishideng Publishing Group Inc
8226 Regency Drive,
Pleasanton, CA 94588, USA
Telephone: +1-925-223-8242
Fax: +1-925-223-8243
E-mail: bpgoffice@wjnet.com
Help Desk: <http://www.wjnet.com/esps/helpdesk.aspx>
<http://www.wjnet.com>

PUBLICATION DATE
October 28, 2015

COPYRIGHT
© 2015 Baishideng Publishing Group Inc. Articles published by this Open-Access journal are distributed under the terms of the Creative Commons Attribution Non-commercial License, which permits use, distribution, and reproduction in any medium, provided the original work is properly cited, the use is non commercial and is otherwise in compliance with the license.

SPECIAL STATEMENT
All articles published in journals owned by the Baishideng Publishing Group (BPG) represent the views and opinions of their authors, and not the views, opinions or policies of the BPG, except where otherwise explicitly indicated.

INSTRUCTIONS TO AUTHORS
Full instructions are available online at http://www.wjnet.com/1949-8470/g_info_20100316162358.htm.

ONLINE SUBMISSION
<http://www.wjnet.com/esps/>

Locoregional treatment for hepatocellular carcinoma: The best is yet to come

Naveen Kalra, Pankaj Gupta, Yogesh Chawla, Niranjana Khandelwal

Naveen Kalra, Pankaj Gupta, Niranjana Khandelwal, Department of Radiodiagnosis and Imaging, PGIMER, Chandigarh 160012, India

Yogesh Chawla, Department of Hepatology, PGIMER, Chandigarh 160012, India

Author contributions: Kalra N conceived the issues which formed the content of the manuscript; Gupta P wrote the manuscript; Kalra N, Gupta P, Chawla Y and Khandelwal N revised the manuscript.

Conflict-of-interest statement: The authors have no conflict of interests.

Open-Access: This article is an open-access article which was selected by an in-house editor and fully peer-reviewed by external reviewers. It is distributed in accordance with the Creative Commons Attribution Non Commercial (CC BY-NC 4.0) license, which permits others to distribute, remix, adapt, build upon this work non-commercially, and license their derivative works on different terms, provided the original work is properly cited and the use is non-commercial. See: <http://creativecommons.org/licenses/by-nc/4.0/>

Correspondence to: Naveen Kalra, MBBS, MD, Professor, Department of Radiodiagnosis and Imaging, PGIMER, Sector 12, Chandigarh 160012, India. navkal2004@yahoo.com
Telephone: +91-172-2756380

Received: April 10, 2015

Peer-review started: April 11, 2015

First decision: June 24, 2015

Revised: September 6, 2015

Accepted: October 1, 2015

Article in press: October 8, 2015

Published online: October 28, 2015

Abstract

Hepatocellular carcinoma (HCC) is the sixth-most common type of cancer worldwide. The only definitive

treatment modalities capable of achieving a cure are hepatic resection and hepatic transplantation. However, most patients are not candidates for these therapies. Overall, treatment options are driven by the stage of HCC. Early-stage disease is treated with ablative therapies, with radiofrequency ablation the ablative therapy of choice. Microwave ablation and irreversible electroporation are the other upcoming alternatives. Intermediate-stage disease is managed with transarterial chemoembolization (TACE), while advanced-stage disease is managed by sorafenib, with TACE and radioembolization as other alternatives.

Key words: Hepatocellular carcinoma; High intensity focussed ultrasound; Irreversible electroporation; Microwave ablation; Radiofrequency ablation

© The Author(s) 2015. Published by Baishideng Publishing Group Inc. All rights reserved.

Core tip: Treatment of hepatocellular carcinoma is dependent on the stage of disease. Early-stage disease is managed by resection. Radiofrequency ablation (RFA), is becoming an attractive alternative for very early-stage disease. Early-stage disease is treated with ablative therapies. RFA is the ablative therapy of choice. RFA, however, is not effective in all cases. Microwave ablation and irreversible electroporation are upcoming alternatives. Transarterial chemoembolization (TACE) is the modality of choice for intermediate-stage disease. TACE-based multimodal treatment is becoming acceptable. Advanced-stage disease is managed by sorafenib. However, TACE and radioembolization are other alternatives.

Kalra N, Gupta P, Chawla Y, Khandelwal N. Locoregional treatment for hepatocellular carcinoma: The best is yet to come. *World J Radiol* 2015; 7(10): 306-318 Available from: URL: <http://www.wjgnet.com/1949-8470/full/v7/i10/306.htm> DOI: <http://dx.doi.org/10.4329/wjr.v7.i10.306>

INTRODUCTION

Hepatocellular carcinoma (HCC) is the sixth-most common type of cancer worldwide and the third-leading cause of cancer-related death^[1]. The Barcelona Clinic Liver Cancer (BCLC) classification not only stages but also guides the clinical management of patients with HCC (Table 1 and Figure 1)^[2]. An integral component of the BCLC staging is the Child-Pugh classification (Table 2)^[3].

The only definitive treatment modalities capable of achieving a cure are hepatic resection and hepatic transplantation. However, a limited number of patients (10% to 20%) are considered fit for these treatments. A large percentage of the remaining patients are managed by so-called liver-directed regional therapies. Among these, methods of tumor ablation (TA) have shown the most clinical promise. In addition to down-staging patients, TA may have a potential curative role, especially in very-early- and early-stage HCCs^[4]. The various options for ablative therapies are listed in Table 3.

There has been a significant evolution of TA therapies as an alternative option for patients with unresectable tumors. This has been rendered feasible by significant technical advancements and evidence from well-conducted studies that have suggested improved outcomes in patients treated with TA^[5-7].

We will discuss the various treatment options for HCC based on the BCLC staging.

VERY-EARLY-STAGE HCC

The standard treatment in this group is surgical resection. Such patients are unlikely to decompensate after resection and have an excellent 5-year survival rate (> 75%)^[8]. The most commonly used surgical technique for this group is anatomic resection, which involves en-bloc removal of a liver segment (supplied by a major portal vein branch and the hepatic artery). This technique is preferred because it theoretically allows the eradication of intrahepatic metastases of HCC. However, a major consideration is treatment-related mortality, which is in the range of 1%-3%^[9]. TA methods provide an alternative treatment option for nodules smaller than 2 cm in diameter. Percutaneous radiofrequency ablation (RFA) is the standard TA technique at most centers worldwide. Lesions that are not sub-capsular, perivascular, or peribiliary are ideal targets for percutaneous RF ablation. In centrally located tumors, RFA perhaps presents a challenge to the dominant position of surgical resection for treatment. A very high complete response rate (97%) and a 5-year survival rate of 68% has been reported with RFA in very-early-stage HCC^[10]. Cho *et al.*^[11], in their recent decision-analysis study, concluded that RFA and hepatic resection should be considered equally effective for the treatment of very-early HCC. Takayama *et al.*^[12] performed a retrospective analysis of 2550 patients (RFA/resection = 1315/1235) with very early HCC, finding no statistically

significant difference in overall survival (OS) rates in the RFA versus resection groups (95% vs 94%). In a recent meta-analysis, there was no significant difference in the overall 1- and 3-year survival and disease-free survival rates between the resection and RFA groups for tumors < 2 cm in diameter^[13].

Based on these published data, it is recommended that RFA be considered a first-line treatment option for very-early-stage HCC, with surgical resection reserved for patients for whom individual variables preclude RFA. In certain patients who are not candidates for RFA (e.g., sub-optimal location) or surgery (e.g., increased bilirubin level or signs of portal hypertension), percutaneous ethanol injection (PEI) may be considered^[14]. In a randomized trial by Giorgio *et al.*^[15], patients with a single HCC \leq 3 cm were randomly assigned to receive PEI or RFA, and comparable 3-year (74% and 78%, respectively, for each treatment) and 5-year (68% for both treatments) survival rates were found.

EARLY-STAGE HCC

Resection, liver transplantation, and percutaneous TA are the various treatment options for this large, heterogeneous group. Besides the percutaneous approach for ablation, other approaches for ablation have been described, including a laparoscopic route and an open surgical route. Advanced techniques are also described for lesions abutting the diaphragm and gastrointestinal tract. The surgical routes for ablation allow treatment of larger lesions, avoiding the hindrances posed by the tissues overlying the liver.

Among the different TA techniques, RFA is currently the favored treatment option for patients with early-stage HCC (Figure 2)^[16]. Percutaneous chemical ablation is cost-effective, easy-to-perform, and has found worldwide acceptance for small lesions. Between PEI and percutaneous acetic-acid injection (PAI), multiple studies have failed to show any superiority of one over the other^[17]. PEI and PAI are limited by the need for multiple sessions to achieve the clinically desired results. With the introduction of RFA, chemical ablation has decreased in popularity.

There are four types of RF electrodes commercially available: Two models of retractable-needle electrodes (model 70 and model 90 Star-burst XL needles, RITA Medical Systems, Mountain View, CA; LeVeen needle electrode, Boston Scientific, Boston, MA), an internally cooled electrode (Cool-Tip RF electrode; Radionics, Burlington, MA), and a separable clustered electrode (Octopus®; STARmed, Goyang, Korea)^[6].

The RITA RF electrode consists of a 14-gauge, insulated outer needle that has nine retractable, curved electrodes of various lengths. When deployed, the device assumes the approximate configuration of a Christmas tree. The LeVeen RF electrode has retractable, curved electrodes and an insulated, 17-gauge outer needle that contains 10 solid, retractable, curved electrodes. It assumes the configuration of an umbrella upon

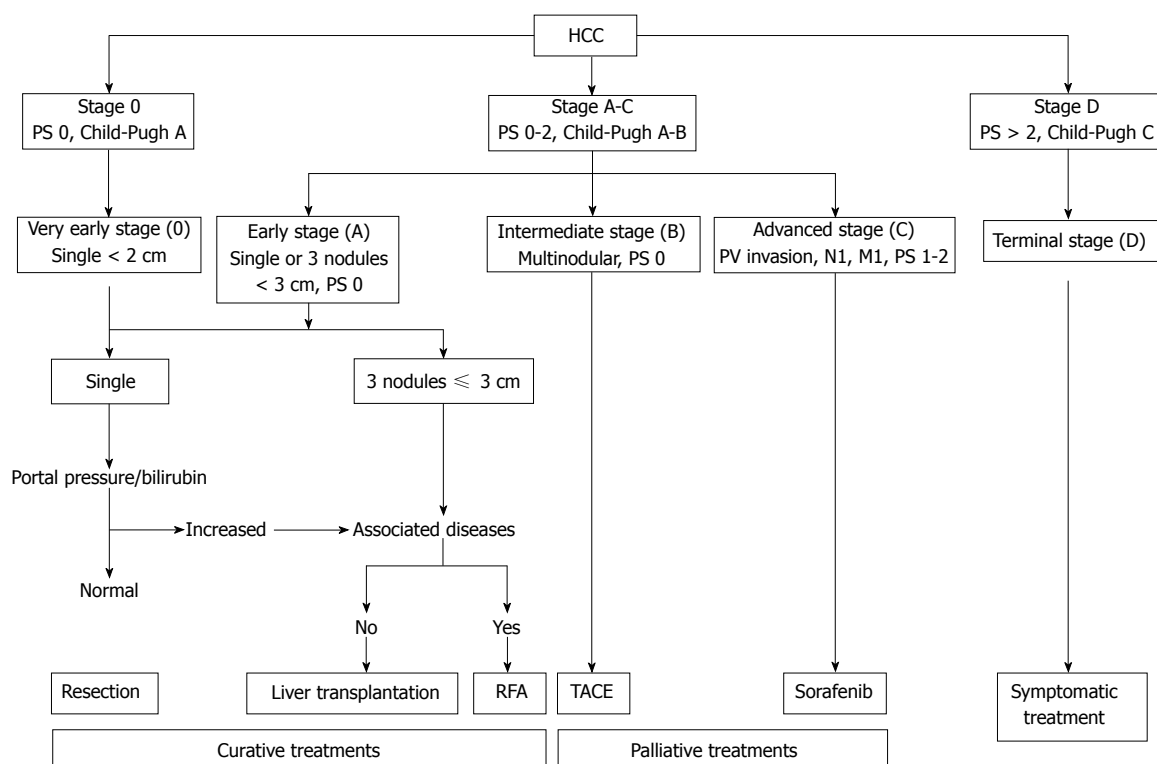


Figure 1 Flow chart of Barcelona Clinic Liver Cancer based management guidelines for hepatocellular carcinoma^[2]. HCC: Hepatocellular carcinoma; RFA: Radiofrequency ablation; TACE: Transarterial chemoembolization.

Table 1 Barcelona Clinic Liver Cancer classification^[2]

BCLC classification	
Stage	Description
Very early	PS 0, Child-Pugh A, single HCC, 2 cm
Early	PS 0, Child-Pugh A-B, single HCC or 3 nodules, 3 cm
Intermediate	PS 0, Child-Pugh A-B, multinodular HCC
Advanced	PS 1-2, Child-Pugh A-B, portal neoplastic invasion, nodal metastases, distant metastases
Terminal	PS 2, Child-Pugh C

HCC: Hepatocellular carcinoma; BCLC: Barcelona clinic liver cancer.

Table 2 Child-Pugh classification^[3]

Child-pugh classification			
Finding	1 point	2 points	3 points
Encephalopathy grade	None	Mild	Severe
Ascites	Absent	Mild to moderate	Severe, refractory
Serum bilirubin (mg/dL)	2	2-3	> 3
Serum albumin (g/dL)	> 3.5	2.8-3.5	< 2.8
INR	< 1.7	1.7-2.2	> 2.2

A: 5-6 points; B: 7-9 points; C: 10-15 points. INR: International normalized ratio.

deployment. The Cool-Tip RF device has an insulated, hollow, 17-gauge needle with an exposed needle tip of variable length. The needle shaft has two internal channels for perfusion with chilled water. In an attempt to increase the size of the possible ablation area, the

Table 3 Various ablative methods for hepatocellular carcinoma

Chemical ablation	PAI PEI
Cryoablation	Nitrous oxide Liquid nitrogen
Thermal ablation	Argon RFA LITT HIFU MWA
Electroporation	IRE

PAI: Percutaneous acetic acid injection; PEI: Percutaneous ethanol injection; RFA: Radiofrequency ablation; LITT: Laser-induced thermotherapy; HIFU: High-intensity focused ultrasound; MWA: Microwave ablation; IRE: Irreversible electroporation.

manufacturer has placed three of the cooled needles in a parallel, triangular cluster with a common hub (a multi-tined electrode). In the Octopus[®], RF energy is applied to two electrodes, while, simultaneously, RF energy is switched between a pair of electrodes. This can create a large ablative zone with a spherical shape that has better efficiency of RF energy delivery over a given treatment time.

In order to achieve therapeutic results similar to those achieved with traditional surgery, surgical margins of approximately 1 cm are required for successful resection by RFA. However, current RFA technology, with internally cooled or expandable electrodes, achieve

Table 4 Comparison of radiofrequency ablation and percutaneous ethanol injection

Study and treatment	Initial complete response rate (%)	Treatment failure rate (%)	Overall survival rate (%)		<i>P</i> value
			1-yr	3-yr	
Lin <i>et al</i> ^[18]					
RFA (<i>n</i> = 52)	96	17	82	74	0.014
PEI (<i>n</i> = 52)	88	45	61	50	
Shiina <i>et al</i> ^[19]					
RFA (<i>n</i> = 18)	100	2	90	80	0.02
PEI (<i>n</i> = 114)	100	11	82	63	
Lin <i>et al</i> ^[20]					
RFA (<i>n</i> = 62)	97	16	88	74	0.031
PEI (<i>n</i> = 62)	89	42	96	51	

PEI: Percutaneous ethanol injection; RFA: Radiofrequency ablation.

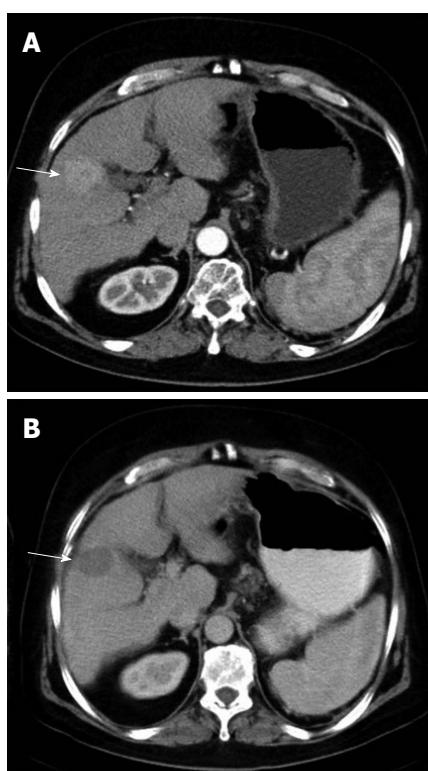


Figure 2 Axial computed tomography images before and after radiofrequency ablation shows an arterial enhancing lesion (arrow, A). That is replaced by a hypodense area without any enhancement following radiofrequency ablation (arrow, B).

a limited volume of coagulation necrosis, resulting in marginal recurrence rates up to 41%, especially with tumors greater than 3 cm in diameter. Several types of electrodes have been developed to overcome this limitation and achieve larger ablation zones, including perfused, clustered, saline-infused expandable, and multipolar electrodes. In addition, a multiple electrode-switching system can achieve substantially larger ablation volumes than techniques using conventional RF ablation with single electrodes having overlapping ablations^[6].

Five randomized, controlled trials (RCTs) have compared RFA and PEI for the treatment of early-stage HCC. The results of three RCTs (Table 4) showed that

RFA is more effective than PEI in terms of better local disease control^[14,18-21]. However, in trials by Lencioni *et al*^[14] and Brunello *et al*^[21], the differences in overall 1- and 3-year survival rates between RFA and PEI were not statistically significant. Further, independent meta-analyses of early-stage HCC cases have confirmed the survival benefit conferred by RFA over PEI^[22-25].

Recent studies regarding the long-term outcomes of RFA-treated patients have shown consistently high 5-year survival rates in early-stage HCC^[26-29]. In studies by Lencioni *et al*^[26] (*n* = 144), Tateishi *et al*^[27] (*n* = 221), Choi *et al*^[28] (*n* = 359), and N'Kontchou *et al*^[29] (*n* = 67), 3- and 5-year survival rates were reported, respectively, as 76% and 51%, 83% and 63%, 78% and 64%, and 82% and 76% for Child A or BCLC resectable disease^[26-29]. In a study by Kalra *et al*^[30], 31 patients with 41 unresectable HCCs were treated with RFA. Over a follow-up period ranging from 3 mo to 6 years, ablation was successful at a rate of 80.5%. Eight patients had tumor recurrences. The survival rate at 1 year in patients who had completed at least 1 year of follow-up was 63.3%^[20].

Thus, a question arises: Can RFA replace surgical resection as a first-line treatment for early-stage HCC? Several retrospective studies and a single RCT found no statistically significant difference in survival rates between surgical resection and RFA^[31-37].

Chen *et al*^[38] conducted an RCT on 180 patients with a solitary HCC ≤ 5 cm who received either percutaneous RFA or surgical resection. No significant difference was noted in the overall and disease-free survival rates between the RFA and resection groups in terms of their respective 1-year (95.8% and 93.3%) and 4-year (67.9% and 64.0%) OS rates. However, in the RCT by Huang *et al*^[39], the 1-, 3-, and 5-year OS and recurrence-free survival rates in the surgical resection group were significantly higher than in the RFA group ($P = 0.001$, $P = 0.017$).

An important factor limiting the success of RFA is tumor size, as RFA may fail to ablate the entire tumor volume for tumors larger than 3 cm along the longest axis, particularly at their periphery. The results of RFA are also greatly affected by tumor location. The presence of a large vessel (3 mm or more) in the

vicinity of the lesion reduces heat deposition by a “heat sink” effect^[40]. Furthermore, lesions in the vicinity of vital structures like the gallbladder, bile ducts, or colon are difficult to treat due to the inherent risk of thermal damage.

Therefore, when RFA is not precluded by tumor location, it is proposed that solitary HCCs larger than 3 cm and smaller than 5 cm in size should be considered for combination therapy with RFA^[41-45]. One of the forms of combination therapy is TACE-preceded RFA. The rationale behind lipiodol TACE-preceded RFA is as follows: a state of transient liver infarction is induced by the lipiodol, which regurgitates into the portal branches *via* the peribiliary venous plexus, thereby decreasing the heat sink effect, expanding the ablative area, and promoting the ablation of satellite lesions^[46]. Several studies have reported significantly better survival rates with TACE-preceded RFA compared to RFA alone for intermediate-sized lesions^[45,47-48]. In another administration method, TACE may follow RFA, with TACE expected to handle the peripheral part of a tumor where RFA achieves sub-optimal temperatures^[45]. A phase III randomized, double-blinded, placebo-controlled study investigating the efficacy and safety of thermally sensitive liposomal doxorubicin in combination with RFA compared to RFA alone in the treatment of unresectable HCC is ongoing^[49].

When RFA cannot be performed, largely in view of tumor location, TACE combined with drug eluting beads (DEB) is an alternative. Complete necrosis was reported in 77% patients undergoing DEB-TACE prior to transplantation^[50].

HCCs larger than 5 cm comprise another critical group in early-stage HCC. These patients are precluded from transplantation, according to the Milan guidelines, yet surgical resection should be considered for these patients as ablative therapies are unlikely to be effective with lesions of this size^[51]. Combination therapies are also expected to be inferior to surgical resection.

Other thermal ablative therapies-including laser-induced thermotherapy (LITT), high-intensity focused ultrasound (HIFU), and microwave ablation (MWA) and irreversible electroporation (IRE) are other alternative modes of therapy; however, these are still evolving technologies and there is too little data at present to put forth concrete recommendations. Of the above-mentioned alternatives, MWA and IRE appear promising and may even supplant RFA in the future.

LITT is based on the use of an Nd-YAG (neodymium: yttrium aluminum garnet) diode laser that allows the delivery of a precise amount of energy to a pre-defined region. Maximal tissue penetration and the desired therapeutic results are achieved by producing slow heating within its therapeutic window. Most studies with LITT have been reported in patients with liver metastases, with favorable survival rates and an acceptable complication profile^[52,53]. A single trial of LITT for HCC evaluated the efficacy of a combination of TACE and LITT compared to TACE alone. TACE and LITT

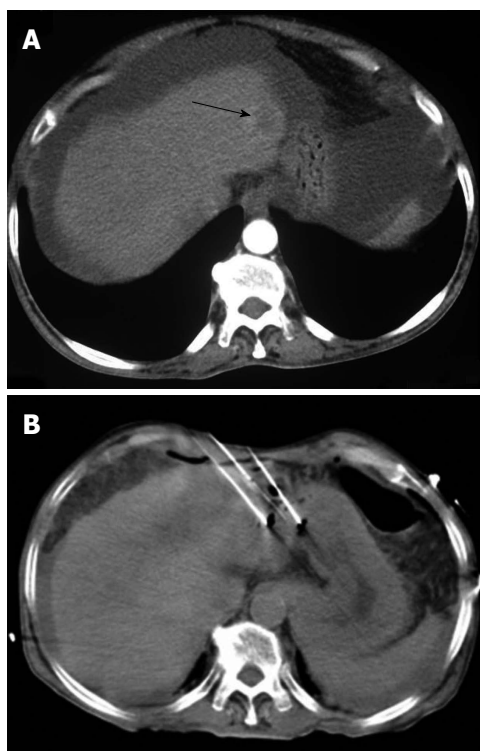
were performed in 54 patients, while TACE alone was administered to 51 patients. After a follow-up of 24 mo, survival rates were significantly better in the TACE and LITT (79.6%) than in the TACE alone (60.8%) group^[54]. A multicenter study (involving 432 cirrhotic patients with a single tumor ≤ 4 cm or three or fewer nodules ≤ 3 cm each, comprising together 548 lesions), reported that the ideal candidates for laser ablation are younger (< 73 years) with normal serum albumin levels. Child-Pugh class A patients with tumor size ≤ 3 cm and a well-differentiated histologic pattern who achieved an initially complete ablation had median survival of 65 mo. Median time to recurrence was 24 mo, and median disease-free survival was 26 mo^[55]. However, this form of treatment is not preferred, largely due to the availability of better alternative ablative therapies.

In HIFU, high-intensity ultrasound in the range of 100-10000 W/cm² is delivered to a focal region. The absorption and subsequent intense acoustic energy generates temperatures above 60 °C in a short span of time, producing coagulative necrosis. Successful ablation of HCC has been reported by several studies^[56-58]. In a recent study, Ng *et al.*^[59] presented data on 49 patients treated with HIFU for unresectable HCC. Complete clinical response in this series was 79.5%, and 1- and 3-year survival rates were 87.7% and 62.4%, respectively. In another series by Xu *et al.*^[55], 145 patients with HCC were treated with HIFU. Symptom improvement and pain relief was achieved in 84.8% of patients^[56]. A two-year survival rate of 80% was reported for early-stage disease. Chan *et al.*^[57] compared HIFU to RFA in 103 patients with HCC. HIFU was associated with higher complication rates (skin burns and pleural effusion) than was RFA. There was no significant difference in the 3-year OS rate between HIFU and RFA^[57]. A completely extracorporeal HIFU device for treatment of HCC, though clinically feasible, is capable of ablating only small-volume lesions unless a partial rib resection is performed. Moreover, this procedure is associated with attenuation and various complications, including skin burns and gastric lesions. For these reasons, an open procedure seems appropriate despite being more invasive. Besides allowing a better staging of malignancies, large areas of liver can be rapidly ablated in an open procedure. In a feasibility study by Dupré *et al.*^[60], this approach was found to be effective in patients with colorectal liver metastases. In 30 ablations performed in 15 patients, intra-operative HIFU was found to be safe, feasible, and without damage to neighboring tissues^[60]. Recently, Gandini evaluated in an animal model the use of HIFU for assisting liver resection in an open procedure^[61]. They found that HIFU-assisted liver resection is associated with reduced bleeding risk.

The basic principle of ablation in MWA is heat generation using dielectric hysteresis. High-frequency microwaves (typically 900 to 2500 MHz) lead to polarization and rapid oscillation of the intracellular water molecules. The resulting kinetic energy transfer

Table 5 Advantages of microwave ablation over radiofrequency ablation

Achieves higher temperatures and relatively larger ablative zones in a shorter time
Ablative zones are more consistent and uniform in character
Better safety profile
Less post procedural pain
Not affected by the heat sink effect
Multiple applicators can be used simultaneously

**Figure 3** Irreversible electroporation for an early stage hepatocellular carcinoma in left lobe (arrow) (A and B).

produces heat, coagulation necrosis, and TA. The advantages of MWA over RFA are tabulated in Table 5. Shibata *et al.*^[62] compared the effectiveness of MWA with that of RFA. There was no statistically significant difference in the effectiveness of the two procedures. However, a trend favoring RFA was recognized in that study with respect to local recurrence and complication rates^[62]. In another study by Yin *et al.*^[63] comparing the therapeutic efficacy of RFA and MWA in treating HCCs > 3 cm, both RFA and MWA were found to be effective and safe. Several studies have evaluated the efficacy of MWA when used alone in treating HCCs^[63]. Sato *et al.*^[64], in one of the earliest studies, demonstrated the safety and efficacy of MWA in 19 patients with unresectable HCCs. MWA was potentially curative in 73.7% of patients^[64]. The authors concluded that MWA is a safe and potentially curative treatment option in patients with HCCs having advanced liver cirrhosis and multifocal or central tumors. In another case series, 60 patients with initial HCC ($n = 15$) and recurrent HCC (n

**Figure 4** Computed tomography 1 mo after irreversible electroporation in the same patient as Figure 4. No residual enhancement is seen (arrow).

= 45) were treated with MWA. Three-year recurrence free survival rates for initial HCC and recurrent HCC were 36.7% and 8.8%, respectively; 5-year OS for all patients was 43.1%^[65]. Several other case series also reported a favorable outcome with MWA^[66-68]. A recent study evaluated the efficacy and safety of percutaneous MWA versus TACE for large HCC (5-7 cm). Sixty-four patients were divided into two groups and treated with either MWA or TACE. A higher rate of complete ablation (75%) was achieved with fewer sessions of MWA than of TACE, and MWA displayed a lower incidence of tumor recurrence, de novo lesions, or post-treatment ascites^[69].

Though several initial studies have shown favorable results with cryoablation, many recent studies have raised concerns regarding serious side effects and complications associated with this technology, including cryoshock, hypothermia, cracking of the ice ball, hemorrhage, biloma, abscess, pleural effusion, and death^[70,71].

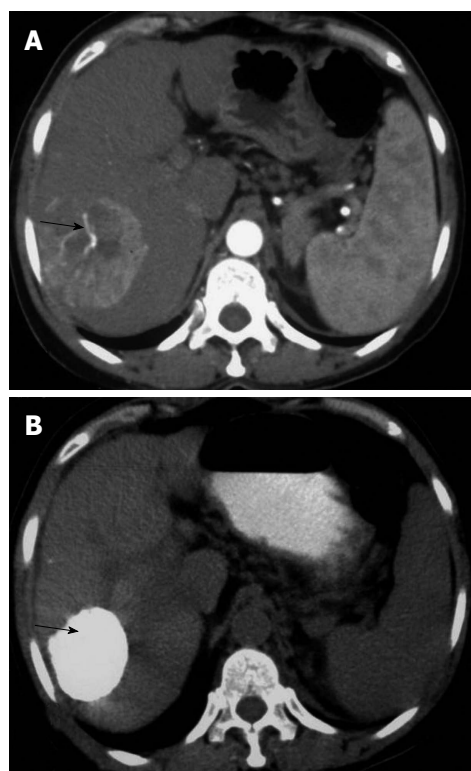
IRE is a non-thermal ablative technique that achieves cell death by creating pores in the lipid bilayer of cell membranes using an electric current. This is accomplished by micro- to millisecond electrical pulses (at 1000–3000 V) delivered *via* needle electrodes, causing loss of cellular homeostasis and eventually cell death (Figures 3 and 4). In contrast to thermal ablative methods that cause coagulative necrosis by gross heat damage to a cell, IRE acts at the level of cellular membranes and produces cell death by apoptosis^[72]. As a result, it spares important structures like blood vessels, bile ducts, and tissue stroma^[73]. The NanoKnife (AngioDynamics, New York) is the most commonly used commercial device. It utilizes a 2500 V generator system. Advantages of IRE over other ablative techniques are listed in Table 6. A comparison of various ablative techniques in terms of ease of ablation titration, cost, and tissue specificity is given in Table 7.

Early clinical experience with IRE regarding safety and efficacy during ablation of HCC is encouraging. However, most of the available data are short-term. In one of the initial reviews, by Charpentier, IRE was not only found to be safe but also potentially superior to other techniques for lesions abutting major vascular

Table 6 Advantages of irreversible electroporation over other thermal ablative techniques

Selective cellular target
Cell death via apoptosis
Sparing effect on important structures
Not affected by heat sink (compared to RFA)
Sharp boundary between the treated and untreated areas

RFA: Radiofrequency ablation.

**Figure 5** Trans-arterial chemoembolisation of a large hepatocellular carcinoma in right lobe of liver (arrow, A). Following transarterial chemoembolization, there is uniform distribution of lipiodol the lesion (arrow, B).

structures^[73]. In another retrospective review, IRE-specific treatment outcomes, rates of recurrence, and complications were evaluated in 28 patients with tumor locations precluding other forms of ablation. IRE was found to be safe, with only 3% of patients suffering complications. At 6-mo follow-up, recurrence was reported in 3 patients (5.7%)^[74]. Several prospective studies have also established the safety and efficacy of IRE. Cannon *et al.*^[75] reported a 100% initial success rate with IRE in 44 patients with HCC. Adverse events were noted in 11% of patients; however, all complications resolved within 30 d. Local recurrence-free survival rates of 97.4% and 59.5% were recorded at 3 and 12 mo, respectively. A multi-institutional study evaluated the learning curve associated with IRE. Over 2 years, 150 consecutive patients participated at seven institutions^[76]. The authors found that treatments of larger lesions and lesions with a greater degree of vascular involvement could be performed safely and

Table 7 Comparison of energy based therapies

	RFA	MWA	IRE
Principle	Thermal	Thermal	Non-thermal
Collateral damage	+	+	-
Ease of ablation titration	+	+	++
Cost	+	+	++
Duration of therapy	+	+	++
Tissue effect			
Tumor	+	+	+
Nerve	+	+	-
Vessels	+	+	-
Hepatic architecture	+	+	-

RFA: Radiofrequency ablation; MWA: Microwave ablation; IRE: Irreversible electroporation.

effectively with increased experience over a period of time. In a recent study, Narayanan *et al.*^[77] compared post-procedural pain and tolerance in patients treated with IRE to that related to RFA. A total of 43 patients (RFA 22, IRE 21) were included, and post-procedural pain was comparable in both groups^[77]. In another recent trial, Niessen *et al.*^[78] evaluated the risk factors associated with short-term local recurrence after IRE. Twenty-five patients with 48 malignant liver lesions (HCC = 22; cholangiocarcinoma = 6; metastases = 20) underwent IRE. Fourteen of the 48 treated lesions (29.2%) showed early local recurrence after 6 mo. Factors predicting short-term local recurrence were tumor volume ($> 5 \text{ cm}^3$) and underlying disease type (HCC had a significantly favorable outcome compared to metastases and cholangiocarcinoma). However, distances to the surrounding vessels and bile ducts were not significantly associated with local recurrence.

Due to limited data regarding long-term safety and efficacy, the use of IRE on a widespread scale is not recommended at present. The best use of this technology, in the meantime, is for selected patients in whom other currently available ablative treatments are not feasible.

INTERMEDIATE STAGE HCC

TACE is recommended as the standard of care for intermediate-stage HCC (Figure 5), based on improved survival demonstrated in a meta-analysis that compared TACE to the best available supportive care or to other, suboptimal therapies^[79]. A limitation of this study was the considerable heterogeneity between the individual study designs as well as the study results. Only 2^[80,81] of the 6 included RCTs reported a 2-year survival benefit over conservative management^[80-85]. Additionally, a recently concluded Cochrane trial concluded that there is no firm evidence to support or refute either TACE or bland transarterial embolization (TAE) for patients with unresectable HCC. The group suggested that more adequately powered and bias-protected trials are needed^[86].

Greater standardization of TACE protocols is needed.

The basic principle guiding an ideal TACE protocol is to achieve a maximum and sustained concentration of the chemotherapeutic agent in the tumor bed. Systemic exposure, if necessary at all, should be minimized. In an attempt to achieve these goals, embolic microspheres (drug-eluting beads, or DEB) were introduced that are capable of sequestering doxorubicin hydro-chloride from solution through controlled release following selective administration. Compared with lipiodol-based regimens, these increase local drug concentration and, in turn, the efficacy^[87]. The PRECISION V trial provides evidence for the efficacy and safety of TACE with DEB compared to conventional TACE^[88]. The results from this trial demonstrated greater tolerance, with significant reductions in doxorubicin-related side effects and serious hepatotoxicity compared to conventional TACE. The objective response rate in the TACE with DEB group was significantly better than in the conventional TACE group^[88]. An important observation from the trial was that high-dose doxorubicin treatment was successfully achieved in the whole DEB group.

A recent study compared the treatment of HCC with TACE using gelatin sponges or microspheres plus lipiodol-doxorubicin versus doxorubicin-loaded DEB^[89]. A total of 158 patients were enrolled in this study. TACE with lipiodol-doxorubicin and gelatin sponges (group A), TACE with lipiodol-doxorubicin and microspheres (group B), and TACE with doxorubicin-loaded DEB (group C) were performed in 64, 41, and 53 patients, respectively. In group C, a significantly higher doxorubicin dosage was achieved and complete response rates were significantly higher^[85].

Studies have investigated the ideal size of the microspheres for drug delivery in DEB-TACE. A recent study compared the safety and efficacy of 70-150 μm DEB to 100-300 μm DEBs^[90]. A cohort of HCC patients who underwent TACE with two vials of 100-300 μm DEBs was compared to those treated with one vial of 70-150 μm DEBs followed by one vial of 100-300 μm DEBs. Though the short-term efficacy did not differ, TACE with smaller DEBs (70-150 μm) followed by larger DEBs (100-300 μm) was found to be more likely to cause hepatobiliary adverse events.

It remains to be thoroughly evaluated whether the addition of the chemotherapeutic agent to embolic microspheres improves treatment effectiveness. This issue has been addressed in a few studies. In one RCT, bland embolization was compared to embolization with beads loaded with doxorubicin^[91]. The results demonstrated a significantly lower tumor-progression rate at 12 mo in the DEB group than in the bland embolization group^[91]. Another study established the superiority of DEB-TACE compared to bland embolization^[50]. The authors studied the degree of necrosis in explanted livers following TACE with epirubicin-loaded DEB and after bland embolization in patients on a transplant waiting list. Complete necrosis was achieved in 77% of tumors in the DEB group and only 27% of tumors in the bland embolization group, a statistically significant difference

between the two groups^[50].

A recent trend has been towards combination therapy in an attempt to achieve better tumor-free survival rates. Published research supports the advantage of various forms of combination therapies with TACE (with lipiodol or DEB). Ginsburg *et al.*^[92] compared retrospectively the outcomes and complications of transcatheter arterial chemoembolization using drug-eluting embolic agents combined with RFA or microwave MWA in the treatment of HCCs^[92]. A total of 89 patients with HCCs were recruited for combination therapy, with TACE plus RFA (group A) administered to 38 patients and TACE plus MWA (group B) administered to 51 patients. Complete local-tumor response rates were 80.4% and 76.6% for groups A and B, respectively, with no statistically significant difference between the two groups. The median tumor PFS and overall PFS were also comparable between the two groups. The authors concluded that both combination therapies are effective treatments for HCC. Iezzi *et al.*^[93], in a recent prospective trial, evaluated the efficacy of single-step RFA and DEB-TACE in patients with single HCCs > 3 cm. The group treated with combined therapy showed significantly lower 2-year recurrence and significantly higher survival rates than did the group treated with chemoembolization alone. In the on-going SPACE trial (Sorafenib or placebo in combination with TACE for intermediate-stage HCC), the potential synergy between TACE (with DEB) and sorafenib is being investigated^[94]. The basis for this trial is that hypoxia can lead to neoangiogenesis (a potential situation with TACE monotherapy). An anti-angiogenic agent might inhibit the post-TACE surge in VEGF-mediated signaling, preventing tumor growth. Moreover, systemic administration may suppress tumor foci distant from the TACE site. In phase II of the SPACE trial, 307 patients undergoing TACE were randomized to sorafenib ($n = 154$) or placebo ($n = 153$) groups. The results from phase II reported a hazard ratio (HR) for time-to-tumor progression (TTP) of 0.797 (95%CI: 0.588-1.080; $P = 0.072$), with median TTP (50th percentile) of 169 and 166 d in the sorafenib and placebo groups, respectively. The primary goal of improving TTP by using sorafenib-TACE with DEB was achieved in the SPACE study. The data from on-going phase III trials are awaited to confirm these favorable results.

Studies have also compared the survival of patients following TACE with the survival of patients following the resection of large HCCs. A recent meta-analysis (comprising 12 studies) reported a survival benefit of resection compared to TACE in patients with BCLC stage A and B HCC.

Radioembolization is another therapeutic option for intermediate-stage HCC. The most commonly employed radioembolization technique at present employs microspheres coated with a β -emitting isotope, yttrium 90 (90Y). Similar to TACE, intra-arterially injected microspheres are preferentially delivered to the HCC, with selective emission of high-energy, low-

penetration radiation to the tumor. Several phase I and II clinical trials have documented the safety of radioembolisation^[95-98]. The efficacy of radioembolization for the treatment of HCC has also been reported by a number of cohort studies and retrospective analyses. Retrospective studies report that patients with intermediate-stage HCCs may have similar survival following treatment with either conventional TACE or radioembolization. However, longer time-to-progression and decreased toxicity have been reported in patients receiving radioembolization^[99].

ADVANCED-STAGE HCC

According to the BCLC guidelines, systemic therapy with the multikinase inhibitor sorafenib is considered the standard choice for patients with advanced HCC^[100].

Conventionally, TACE is contraindicated in advanced HCC patients who have portal-vein invasion, owing to the risk of hepatic insufficiency^[100]. However, recent studies suggest that TACE can be safely performed even in this group^[101-103]. Survival benefits in patients with advanced HCC have been suggested by various studies. Song *et al.*^[104] reported on the efficacy and safety of TACE-based multimodal treatment in patients with large HCCs (> 10 cm). Of the 146 consecutive patients recruited in the study, 119 patients with portal-vein thrombosis received TACE-based multi-modal treatments (including systemic chemotherapy = 46, radiotherapy = 25, RFA or PEI = 21, surgical resection = 13, and liver transplantation = 4). The remaining 27 received conservative management, comprising the control group. Objective tumor response and OS were significantly better in the TACE-based multimodal treatment groups. Kim *et al.*^[105] compared the efficacy of TACE with and without radiotherapy (RT) vs sorafenib for advanced HCC with portal vein tumor thrombosis (PVTT). Of the 557 patients with HCC with PVTT, 295 received TACE, 196 received TACE with RT, and 66 received sorafenib. The TACE plus RT group showed significantly better OS than did either the TACE-alone or the sorafenib groups.

Studies suggest that radioembolization might be an effective treatment option for patients with advanced HCCs. In a recent study by Salem *et al.*^[106], a cohort of 291 patients with HCC was treated with 90Y. Of all patients, 52% were BCLC class C. TTP for the entire cohort was 7.9 mo. Sub-group analyses revealed that TTP in the absence of portal vein thrombosis was 15.5 mo while TTP in the presence of portal vein thrombosis was 5.6 mo, suggesting that treatment with 90Y glass microspheres could represent an effective option, especially in patients with portal vein thrombosis for whom TACE is conventionally not thought suitable. Several other studies have also reported favorable results in advanced HCC^[107-109]. However, major bodies worldwide have recommended further RCTs to evaluate the safety and efficacy of 90Y^[110].

Though there are several emerging techniques for

managing HCCs in different stages of disease, clarity regarding the application and safety of one method over another and about the use of combinations of different methods remains contentious. Well-planned RCTs covering all stages of HCCs are required before a standard of care can be adopted.

REFERENCES

- 1 **Parkin DM**, Bray F, Ferlay J, Pisani P. Global cancer statistics, 2002. *CA Cancer J Clin* 2005; **55**: 74-108 [PMID: 15761078]
- 2 **Llovet JM**, Brú C, Bruix J. Prognosis of hepatocellular carcinoma: the BCLC staging classification. *Semin Liver Dis* 1999; **19**: 329-338 [PMID: 10518312]
- 3 **Pugh RN**, Murray-Lyon IM, Dawson JL, Pietroni MC, Williams R. Transection of the oesophagus for bleeding oesophageal varices. *Br J Surg* 1973; **60**: 646-649 [PMID: 4541913]
- 4 **Toso C**, Mentha G, Kneteman NM, Majno P. The place of downstaging for hepatocellular carcinoma. *J Hepatol* 2010; **52**: 930-936 [PMID: 20385428 DOI: 10.1016/j.jhep.2009.12.032]
- 5 **Forner A**, Llovet JM, Bruix J. Hepatocellular carcinoma. *Lancet* 2012; **379**: 1245-1255 [PMID: 22353262 DOI: 10.1016/S0140-6736(11)61347-0]
- 6 **Ahmed M**, Brace CL, Lee FT, Goldberg SN. Principles of and advances in percutaneous ablation. *Radiology* 2011; **258**: 351-369 [PMID: 21273519 DOI: 10.1148/radiol.10081634]
- 7 **Karanicolas PJ**, Jarnagin WR, Gonen M, Tuorto S, Allen PJ, DeMatteo RP, D'Angelica MI, Fong Y. Long-term outcomes following tumor ablation for treatment of bilateral colorectal liver metastases. *JAMA Surg* 2013; **148**: 597-601 [PMID: 23699996 DOI: 10.1001/jamasurg.2013.1431]
- 8 **Llovet JM**, Fuster J, Bruix J. Intention-to-treat analysis of surgical treatment for early hepatocellular carcinoma: resection versus transplantation. *Hepatology* 1999; **30**: 1434-1440 [PMID: 10573522]
- 9 **Chen J**, Huang K, Wu J, Zhu H, Shi Y, Wang Y, Zhao G. Survival after anatomic resection versus nonanatomic resection for hepatocellular carcinoma: a meta-analysis. *Dig Dis Sci* 2011; **56**: 1626-1633 [PMID: 21082347 DOI: 10.1007/s10620-010-1482-0]
- 10 **Livraghi T**, Meloni F, Di Stasi M, Rolle E, Solbiati L, Tinelli C, Rossi S. Sustained complete response and complications rates after radiofrequency ablation of very early hepatocellular carcinoma in cirrhosis: Is resection still the treatment of choice? *Hepatology* 2008; **47**: 82-89 [PMID: 18008357]
- 11 **Cho YK**, Kim JK, Kim WT, Chung JW. Hepatic resection versus radiofrequency ablation for very early stage hepatocellular carcinoma: a Markov model analysis. *Hepatology* 2010; **51**: 1284-1290 [PMID: 20099299 DOI: 10.1002/hep.23466]
- 12 **Takayama T**, Makuuchi M, Hasegawa K. Single HCC smaller than 2 cm: surgery or ablation?: surgeon's perspective. *J Hepatobiliary Pancreat Sci* 2010; **17**: 422-424 [PMID: 19936598 DOI: 10.1007/s00534-009-0239-7]
- 13 **Xu Q**, Kobayashi S, Ye X, Meng X. Comparison of hepatic resection and radiofrequency ablation for small hepatocellular carcinoma: a meta-analysis of 16,103 patients. *Sci Rep* 2014; **4**: 7252 [PMID: 25429732 DOI: 10.1038/srep07252]
- 14 **Lencioni RA**, Allgaier HP, Cioni D, Olschewski M, Deibert P, Crocetti L, Frings H, Laubenberger J, Zuber I, Blum HE, Bartolozzi C. Small hepatocellular carcinoma in cirrhosis: randomized comparison of radio-frequency thermal ablation versus percutaneous ethanol injection. *Radiology* 2003; **228**: 235-240 [PMID: 12759473]
- 15 **Giorgio A**, Di Sarno A, De Stefano G, Scognamiglio U, Farella N, Mariniello A, Esposito V, Coppola C, Giorgio V. Percutaneous radiofrequency ablation of hepatocellular carcinoma compared to percutaneous ethanol injection in treatment of cirrhotic patients: an Italian randomized controlled trial. *Anticancer Res* 2011; **31**: 2291-2295 [PMID: 21737654]
- 16 **Bruix J**, Sherman M. Management of hepatocellular carcinoma.

- Hepatology* 2005; **42**: 1208-1236 [PMID: 16250051]
- 17 **Schoppmeyer K**, Weis S, Mössner J, Fleig WE. Percutaneous ethanol injection or percutaneous acetic acid injection for early hepatocellular carcinoma. *Cochrane Database Syst Rev* 2009; **3**: CD006745 [PMID: 19588401 DOI: 10.1002/14651858.CD006745.pub2]
- 18 **Lin SM**, Lin CJ, Lin CC, Hsu CW, Chen YC. Radiofrequency ablation improves prognosis compared with ethanol injection for hepatocellular carcinoma < or =4 cm. *Gastroenterology* 2004; **127**: 1714-1723 [PMID: 15578509]
- 19 **Shiina S**, Teratani T, Obi S, Sato S, Tateishi R, Fujishima T, Ishikawa T, Koike Y, Yoshida H, Kawabe T, Omata M. A randomized controlled trial of radiofrequency ablation with ethanol injection for small hepatocellular carcinoma. *Gastroenterology* 2005; **129**: 122-130 [PMID: 16012942]
- 20 **Lin SM**, Lin CJ, Lin CC, Hsu CW, Chen YC. Randomised controlled trial comparing percutaneous radiofrequency thermal ablation, percutaneous ethanol injection, and percutaneous acetic acid injection to treat hepatocellular carcinoma of 3 cm or less. *Gut* 2005; **54**: 1151-1156 [PMID: 16009687]
- 21 **Brunello F**, Veltri A, Carucci P, Pagano E, Ciccone G, Moretto P, Sacchetto P, Gandini G, Rizzetto M. Radiofrequency ablation versus ethanol injection for early hepatocellular carcinoma: A randomized controlled trial. *Scand J Gastroenterol* 2008; **43**: 727-735 [PMID: 18569991 DOI: 10.1080/00365520701885481]
- 22 **Orlando A**, Leandro G, Olivo M, Andriulli A, Cottone M. Radiofrequency thermal ablation vs. percutaneous ethanol injection for small hepatocellular carcinoma in cirrhosis: meta-analysis of randomized controlled trials. *Am J Gastroenterol* 2009; **104**: 514-524 [PMID: 19174803 DOI: 10.1038/ajg.2008.80]
- 23 **Cho YK**, Kim JK, Kim MY, Rhim H, Han JK. Systematic review of randomized trials for hepatocellular carcinoma treated with percutaneous ablation therapies. *Hepatology* 2009; **49**: 453-459 [PMID: 19065676 DOI: 10.1002/hep.22648]
- 24 **Germani G**, Pleguezuelo M, Gurusamy K, Meyer T, Isgrò G, Burroughs AK. Clinical outcomes of radiofrequency ablation, percutaneous alcohol and acetic acid injection for hepatocellular carcinoma: a meta-analysis. *J Hepatol* 2010; **52**: 380-388 [PMID: 20149473 DOI: 10.1016/j.jhep.2009.12.004]
- 25 **Weis S**, Franke A, Mössner J, Jakobsen JC, Schoppmeyer K. Radiofrequency (thermal) ablation versus no intervention or other interventions for hepatocellular carcinoma. *Cochrane Database Syst Rev* 2013; **12**: CD003046 [PMID: 24357457 DOI: 10.1002/14651858.CD003046]
- 26 **Lencioni R**, Cioni D, Crocetti L, Franchini C, Pina CD, Lera J, Bartolozzi C. Early-stage hepatocellular carcinoma in patients with cirrhosis: long-term results of percutaneous image-guided radiofrequency ablation. *Radiology* 2005; **234**: 961-967 [PMID: 15665226]
- 27 **Tateishi R**, Shiina S, Teratani T, Obi S, Sato S, Koike Y, Fujishima T, Yoshida H, Kawabe T, Omata M. Percutaneous radiofrequency ablation for hepatocellular carcinoma. An analysis of 1000 cases. *Cancer* 2005; **103**: 1201-1209 [PMID: 15690326]
- 28 **Choi D**, Lim HK, Rhim H, Kim YS, Lee WJ, Paik SW, Koh KC, Lee JH, Choi MS, Yoo BC. Percutaneous radiofrequency ablation for early-stage hepatocellular carcinoma as a first-line treatment: long-term results and prognostic factors in a large single-institution series. *Eur Radiol* 2007; **17**: 684-692 [PMID: 17093964]
- 29 **N'Kontchou G**, Mahamoudi A, Aout M, Ganne-Carrié N, Grando V, Coderc E, Vicaud E, Trinchet JC, Sellier N, Beaugrand M, Seror O. Radiofrequency ablation of hepatocellular carcinoma: long-term results and prognostic factors in 235 Western patients with cirrhosis. *Hepatology* 2009; **50**: 1475-1483 [PMID: 19731239 DOI: 10.1002/hep.23181]
- 30 **Kalra N**, Kang M, Bhatia A, Duseja AK, Dhiman RK, Arya VK, Rajwanshi A, Chawla YK, Khandelwal N. Role of radiofrequency ablation in unresectable hepatocellular carcinoma: An Indian experience. *Indian J Radiol Imaging* 2013; **23**: 139-144 [PMID: 24082478 DOI: 10.4103/0971-3026.116569]
- 31 **Vivarelli M**, Guglielmi A, Ruzzenente A, Cucchetti A, Bellusci R, Cordiano C, Cavallari A. Surgical resection versus percutaneous radiofrequency ablation in the treatment of hepatocellular carcinoma on cirrhotic liver. *Ann Surg* 2004; **240**: 102-107 [PMID: 15213625]
- 32 **Ogihara M**, Wong LL, Machi J. Radiofrequency ablation versus surgical resection for single nodule hepatocellular carcinoma: long-term outcomes. *HPB (Oxford)* 2005; **7**: 214-221 [PMID: 18333193 DOI: 10.1080/13651820510028846]
- 33 **Wakai T**, Shirai Y, Suda T, Yokoyama N, Sakata J, Cruz PV, Kawai H, Matsuda Y, Watanabe M, Aoyagi Y, Hatakeyama K. Long-term outcomes of hepatectomy vs percutaneous ablation for treatment of hepatocellular carcinoma < or =4 cm. *World J Gastroenterol* 2006; **12**: 546-552 [PMID: 16489666]
- 34 **Guglielmi A**, Ruzzenente A, Valdegamberi A, Pachera S, Campagnaro T, D'Onofrio M, Martone E, Nicoli P, Iacono C. Radiofrequency ablation versus surgical resection for the treatment of hepatocellular carcinoma in cirrhosis. *J Gastrointest Surg* 2008; **12**: 192-198 [PMID: 17999123]
- 35 **Abu-Hilal M**, Primrose JN, Casaril A, McPhail MJ, Pearce NW, Nicoli N. Surgical resection versus radiofrequency ablation in the treatment of small unifocal hepatocellular carcinoma. *J Gastrointest Surg* 2008; **12**: 1521-1526 [PMID: 18592325 DOI: 10.1007/s11605-008-0553-4]
- 36 **Hiraoka A**, Horiike N, Yamashita Y, Koizumi Y, Doi K, Yamamoto Y, Hasebe A, Ichikawa S, Yano M, Miyamoto Y, Ninomiya T, Otomi Y, Kokame M, Iwamura T, Ishimaru Y, Sogabe I, Kashiwara K, Nishiura S, Ootani H, Takamura K, Kawasaki H. Efficacy of radiofrequency ablation therapy compared to surgical resection in 164 patients in Japan with single hepatocellular carcinoma smaller than 3 cm, along with report of complications. *Hepatogastroenterology* 2008; **55**: 2171-2174 [PMID: 19260499]
- 37 **Peng ZW**, Chen MS, Liang HH, Gao HJ, Zhang YJ, Li JQ, Zhang YQ, Lau WY. A case-control study comparing percutaneous radiofrequency ablation alone or combined with transcatheter arterial chemoembolization for hepatocellular carcinoma. *Eur J Surg Oncol* 2010; **36**: 257-263 [PMID: 19643561 DOI: 10.1016/j.ejso.2009.07.007]
- 38 **Chen MS**, Li JQ, Zheng Y, Guo RP, Liang HH, Zhang YQ, Lin XJ, Lau WY. A prospective randomized trial comparing percutaneous local ablative therapy and partial hepatectomy for small hepatocellular carcinoma. *Ann Surg* 2006; **243**: 321-328 [PMID: 16495695]
- 39 **Huang J**, Yan L, Cheng Z, Wu H, Du L, Wang J, Xu Y, Zeng Y. A randomized trial comparing radiofrequency ablation and surgical resection for HCC conforming to the Milan criteria. *Ann Surg* 2010; **252**: 903-912 [PMID: 21107100 DOI: 10.1097/SLA.0b013e3181efc656]
- 40 **Lu DS**, Yu NC, Raman SS, Limanond P, Lassman C, Murray K, Tong MJ, Amado RG, Busuttil RW. Radiofrequency ablation of hepatocellular carcinoma: treatment success as defined by histologic examination of the explanted liver. *Radiology* 2005; **234**: 954-960 [PMID: 15681691]
- 41 **Rossi S**, Garbagnati F, Lencioni R, Allgaier HP, Marchianò A, Fornari F, Quaretti P, Tolla GD, Ambrosi C, Mazzaferro V, Blum HE, Bartolozzi C. Percutaneous radio-frequency thermal ablation of nonresectable hepatocellular carcinoma after occlusion of tumor blood supply. *Radiology* 2000; **217**: 119-126 [PMID: 11012432]
- 42 **Yamasaki T**, Kurokawa F, Shirahashi H, Kusano N, Hironaka K, Okita K. Percutaneous radiofrequency ablation therapy for patients with hepatocellular carcinoma during occlusion of hepatic blood flow. Comparison with standard percutaneous radiofrequency ablation therapy. *Cancer* 2002; **95**: 2353-2360 [PMID: 12436442]
- 43 **Veltri A**, Moretto P, Doriguzzi A, Pagano E, Carrara G, Gandini G. Radiofrequency thermal ablation (RFA) after transarterial chemoembolization (TACE) as a combined therapy for unresectable non-early hepatocellular carcinoma (HCC). *Eur Radiol* 2006; **16**: 661-669 [PMID: 16228211]
- 44 **Helmberger T**, Dogan S, Straub G, Schrader A, Jüngst C, Reiser M, Waggerhauser T, Jakobs T, Hoffmann RT, Löhe F, Graeb C, Rau HG, Schauer R, Jauch KW, Caselmann WH, Göke B, Jüngst D. Liver resection or combined chemoembolization and radiofrequency

- ablation improve survival in patients with hepatocellular carcinoma. *Digestion* 2007; **75**: 104-112 [PMID: 17598962]
- 45 **Lencioni R**, Crocetti L, Petruzzi P, Vignali C, Bozzi E, Della Pina C, Bargellini I, Cioni D, Oliveri F, De Simone P, Bartolozzi C, Brunetto M, Filipponi F. Doxorubicin-eluting bead-enhanced radiofrequency ablation of hepatocellular carcinoma: a pilot clinical study. *J Hepatol* 2008; **49**: 217-222 [PMID: 18486261 DOI: 10.1016/j.jhep.2008.03.021]
- 46 **Kudo M**. Local ablation therapy for hepatocellular carcinoma: current status and future perspectives. *J Gastroenterol* 2004; **39**: 205-214 [PMID: 15064996]
- 47 **Wang YB**, Chen MH, Yan K, Yang W, Dai Y, Yin SS. Quality of life after radiofrequency ablation combined with transcatheter arterial chemoembolization for hepatocellular carcinoma: comparison with transcatheter arterial chemoembolization alone. *Qual Life Res* 2007; **16**: 389-397 [PMID: 17111232]
- 48 **Morimoto M**, Numata K, Kondou M, Nozaki A, Morita S, Tanaka K. Midterm outcomes in patients with intermediate-sized hepatocellular carcinoma: a randomized controlled trial for determining the efficacy of radiofrequency ablation combined with transcatheter arterial chemoembolization. *Cancer* 2010; **116**: 5452-5460 [PMID: 20672352 DOI: 10.1002/cncr.25314]
- 49 **Celsion**. Phase 3 study of ThermoDox with radiofrequency ablation (RFA) in treatment of hepatocellular carcinoma (HCC). In: ClinicalTrials.gov [Internet]. Bethesda (MD): National Library of Medicine (US). Available from: URL: <http://www.clinicaltrial.gov/ct2/show/NCT00617981> NLM Identifier: NCT00617981
- 50 **Nicolini A**, Martinetti L, Crespi S, Maggioni M, Sangiovanni A. Transarterial chemoembolization with epirubicin-eluting beads versus transarterial embolization before liver transplantation for hepatocellular carcinoma. *J Vasc Interv Radiol* 2010; **21**: 327-332 [PMID: 20097098 DOI: 10.1016/j.jvir.2009.10.038]
- 51 **Majno PE**, Mentha G, Mazzaferro V. Partial hepatectomy versus radiofrequency ablation for hepatocellular carcinoma: confirming the trial that will never be, and some comments on the indications for liver resection. *Hepatology* 2010; **51**: 1116-1118 [PMID: 20373366 DOI: 10.1002/hep.23648]
- 52 **Mack MG**, Straub R, Eichler K, Engelmann K, Zangos S, Roggan A, Woitaschek D, Böttger M, Vogl TJ. Percutaneous MR imaging-guided laser-induced thermotherapy of hepatic metastases. *Abdom Imaging* 2001; **26**: 369-374 [PMID: 11441548]
- 53 **Eickmeyer F**, Schwarzmaier HJ, Müller FP, Nakic Z, Yang Q, Fiedler V. [Survival after laser-induced interstitial thermotherapy of colorectal liver metastases--a comparison of first clinical experiences with current therapy results]. *Rofo* 2008; **180**: 35-41 [PMID: 18008194]
- 54 **Zhou ZJ**, Xu RD, Li WK, Zhuang WX, Lu LG, Shao PJ, Chen XM, Luo PF. [Transarterial oily chemoembolization combined with interstitial laser thermotherapy for treatment of hepatocellular carcinoma]. *Nan Fang Yi Ke Da Xue Xue Bao* 2007; **27**: 1866-1868 [PMID: 18159005]
- 55 **Xu G**, Luo G, He L, Li J, Shan H, Zhang R, Li Y, Gao X, Lin S, Wang G. Follow-up of high-intensity focused ultrasound treatment for patients with hepatocellular carcinoma. *Ultrasound Med Biol* 2011; **37**: 1993-1999 [PMID: 22036638 DOI: 10.1016/j.ultrasmedb.2011.08.011]
- 56 **Pacella CM**, Francica G, Di Lascio FM, Arienti V, Antico E, Caspani B, Magnolfi F, Megna AS, Pretolani S, Regine R, Sponza M, Stasi R. Long-term outcome of cirrhotic patients with early hepatocellular carcinoma treated with ultrasound-guided percutaneous laser ablation: a retrospective analysis. *J Clin Oncol* 2009; **27**: 2615-2621 [PMID: 19332729 DOI: 10.1200/JCO.2008.19.0082]
- 57 **Chan AC**, Cheung TT, Fan ST, Chok KS, Chan SC, Poon RT, Lo CM. Survival analysis of high-intensity focused ultrasound therapy versus radiofrequency ablation in the treatment of recurrent hepatocellular carcinoma. *Ann Surg* 2013; **257**: 686-692 [PMID: 23426335 DOI: 10.1097/SLA.0b013e3182822c02]
- 58 **Cheung TT**, Fan ST, Chan SC, Chok KS, Chu FS, Jenkins CR, Lo RC, Fung JY, Chan AC, Sharr WW, Tsang SH, Dai WC, Poon RT, Lo CM. High-intensity focused ultrasound ablation: an effective bridging therapy for hepatocellular carcinoma patients. *World J Gastroenterol* 2013; **19**: 3083-3089 [PMID: 23716988 DOI: 10.3748/wjg.v19.i20.3083]
- 59 **Ng KK**, Poon RT, Chan SC, Chok KS, Cheung TT, Tung H, Chu F, Tso WK, Yu WC, Lo CM, Fan ST. High-intensity focused ultrasound for hepatocellular carcinoma: a single-center experience. *Ann Surg* 2011; **253**: 981-987 [PMID: 21394012 DOI: 10.1097/SLA.0b013e3182128a8b]
- 60 **Dupré A**, Melodelima D, Pérol D, Chen Y, Vincenot J, Chapelon JY, Rivoire M. First clinical experience of intra-operative high intensity focused ultrasound in patients with colorectal liver metastases: a phase I-IIa study. *PLoS One* 2015; **10**: e0118212 [PMID: 25719540 DOI: 10.1371/journal.pone.0118212]
- 61 **Gandini A**, Melodelima D, Schenone F, N'Djin AW, Chapelon JY, Rivoire M. High-intensity focused ultrasound (HIFU)-assisted hepatic resection in an animal model. *Ann Surg Oncol* 2012; **19** Suppl 3: S447-S454 [PMID: 21796492 DOI: 10.1245/s10434-011-1875-0]
- 62 **Shibata T**, Iimuro Y, Yamamoto Y, Maetani Y, Ametani F, Itoh K, Konishi J. Small hepatocellular carcinoma: comparison of radiofrequency ablation and percutaneous microwave coagulation therapy. *Radiology* 2002; **223**: 331-337 [PMID: 11997534]
- 63 **Yin XY**, Xie XY, Lu MD, Xu HX, Xu ZF, Kuang M, Liu GJ, Liang JY, Lau WY. Percutaneous thermal ablation of medium and large hepatocellular carcinoma: long-term outcome and prognostic factors. *Cancer* 2009; **115**: 1914-1923 [PMID: 19241423 DOI: 10.1002/cncr.24196]
- 64 **Sato M**, Watanabe Y, Ueda S, Iseki S, Abe Y, Sato N, Kimura S, Okubo K, Onji M. Microwave coagulation therapy for hepatocellular carcinoma. *Gastroenterology* 1996; **110**: 1507-1514 [PMID: 8613057]
- 65 **Itoh S**, Ikeda Y, Kawanaka H, Okuyama T, Kawasaki K, Eguchi D, Korenaga D, Takenaka K. Efficacy of surgical microwave therapy in patients with unresectable hepatocellular carcinoma. *Ann Surg Oncol* 2011; **18**: 3650-3656 [PMID: 21674268 DOI: 10.1245/s10434-011-1831-z]
- 66 **Dong B**, Liang P, Yu X, Su L, Yu D, Cheng Z, Zhang J. Percutaneous sonographically guided microwave coagulation therapy for hepatocellular carcinoma: results in 234 patients. *AJR Am J Roentgenol* 2003; **180**: 1547-1555 [PMID: 12760916]
- 67 **Liang P**, Dong B, Yu X, Yu D, Wang Y, Feng L, Xiao Q. Prognostic factors for survival in patients with hepatocellular carcinoma after percutaneous microwave ablation. *Radiology* 2005; **235**: 299-307 [PMID: 15731369]
- 68 **Seki S**, Sakaguchi H, Iwai S, Kadoya H, Kabayashi S, Kitada T, Fujii H, Tanaka T. Five-year survival of patients with hepatocellular carcinoma treated with laparoscopic microwave coagulation therapy. *Endoscopy* 2005; **37**: 1220-1225 [PMID: 16329021]
- 69 **Abdelaziz AO**, Nabeel MM, Elbaz TM, Shousha HI, Hassan EM, Mahmoud SH, Rashed NA, Ibrahim MM, Abdelmaksoud AH. Microwave ablation versus transarterial chemoembolization in large hepatocellular carcinoma: prospective analysis. *Scand J Gastroenterol* 2015; **50**: 479-484 [PMID: 25592058 DOI: 10.3109/00365521.2014.1003397]
- 70 **Seifert JK**, Morris DL. World survey on the complications of hepatic and prostate cryotherapy. *World J Surg* 1999; **23**: 109-113; discussion 113-114 [PMID: 9880417]
- 71 **Jungraithmayr W**, Burger D, Olschewski M, Eggstein S. Cryoablation of malignant liver tumors: results of a single center study. *Hepatobiliary Pancreat Dis Int* 2005; **4**: 554-560 [PMID: 16286261]
- 72 **Davalos RV**, Mir IL, Rubinsky B. Tissue ablation with irreversible electroporation. *Ann Biomed Eng* 2005; **33**: 223-231 [PMID: 15771276]
- 73 **Charpentier KP**. Irreversible electroporation for the ablation of liver tumors: are we there yet? *Arch Surg* 2012; **147**: 1053-1061 [PMID: 23165618 DOI: 10.1001/2013.jamasurg.100]
- 74 **Kingham TP**, Karkar AM, D'Angelica MI, Allen PJ, Dematteo RP, Getrajdman GI, Sofocleous CT, Solomon SB, Jarnagin WR, Fong Y.

- Ablation of perivascular hepatic malignant tumors with irreversible electroporation. *J Am Coll Surg* 2012; **215**: 379-387 [PMID: 22704820 DOI: 10.1016/j.jamcollsurg.2012.04.029]
- 75 **Cannon R**, Ellis S, Hayes D, Narayanan G, Martin RC. Safety and early efficacy of irreversible electroporation for hepatic tumors in proximity to vital structures. *J Surg Oncol* 2013; **107**: 544-549 [PMID: 23090720 DOI: 10.1002/jso.23280]
- 76 **Philips P**, Hays D, Martin RC. Irreversible electroporation ablation (IRE) of unresectable soft tissue tumors: learning curve evaluation in the first 150 patients treated. *PLoS One* 2013; **8**: e76260 [PMID: 24223700 DOI: 10.1371/journal.pone.0076260]
- 77 **Narayanan G**, Froud T, Lo K, Barbbery KJ, Perez-Rojas E, Yrizarry J. Pain analysis in patients with hepatocellular carcinoma: irreversible electroporation versus radiofrequency ablation-initial observations. *Cardiovasc Intervent Radiol* 2013; **36**: 176-182 [PMID: 22752100 DOI: 10.1007/s00270-012-0426-9]
- 78 **Niessen C**, Igl J, Pregler B, Beyer L, Noeva E, Dollinger M, Schreyer AG, Jung EM, Stroszczyński C, Wiggemann P. Factors associated with short-term local recurrence of liver cancer after percutaneous ablation using irreversible electroporation: a prospective single-center study. *J Vasc Interv Radiol* 2015; **26**: 694-702 [PMID: 25812712 DOI: 10.1016/j.jvir.2015.02.001]
- 79 **Llovet JM**, Bruix J. Systematic review of randomized trials for unresectable hepatocellular carcinoma: Chemoembolization improves survival. *Hepatology* 2003; **37**: 429-442 [PMID: 12540794]
- 80 **Llovet JM**, Real MI, Montaña X, Planas R, Coll S, Aponte J, Ayuso C, Sala M, Muchart J, Solà R, Rodés J, Bruix J. Arterial embolisation or chemoembolisation versus symptomatic treatment in patients with unresectable hepatocellular carcinoma: a randomised controlled trial. *Lancet* 2002; **359**: 1734-1739 [PMID: 12049862]
- 81 **Lo CM**, Ngan H, Tso WK, Liu CL, Lam CM, Poon RT, Fan ST, Wong J. Randomized controlled trial of transarterial lipiodol chemoembolization for unresectable hepatocellular carcinoma. *Hepatology* 2002; **35**: 1164-1171 [PMID: 11981766]
- 82 A comparison of lipiodol chemoembolization and conservative treatment for unresectable hepatocellular carcinoma. Groupe d'Etude et de Traitement du Carcinome Hépatocellulaire. *N Engl J Med* 1995; **332**: 1256-1261 [PMID: 7708069]
- 83 **Bruix J**, Llovet JM, Castells A, Montaña X, Brú C, Ayuso MC, Vilana R, Rodés J. Transarterial embolization versus symptomatic treatment in patients with advanced hepatocellular carcinoma: results of a randomized, controlled trial in a single institution. *Hepatology* 1998; **27**: 1578-1583 [PMID: 9620330]
- 84 **Lin DY**, Liaw YF, Lee TY, Lai CM. Hepatic arterial embolization in patients with unresectable hepatocellular carcinoma--a randomized controlled trial. *Gastroenterology* 1988; **94**: 453-456 [PMID: 2826285]
- 85 **Pelletier G**, Ducreux M, Gay F, Lubinski M, Hagège H, Dao T, Van Steenberghe W, Buffet C, Rougier P, Adler M, Pignon JP, Roche A. Treatment of unresectable hepatocellular carcinoma with lipiodol chemoembolization: a multicenter randomized trial. Groupe CHC. *J Hepatol* 1998; **29**: 129-134 [PMID: 9696501]
- 86 **Oliveri RS**, Wetterslev J, Gluud C. Transarterial (chemo) embolisation for unresectable hepatocellular carcinoma. *Cochrane Database Syst Rev* 2011; **3**: CD004787 [PMID: 21412886 DOI: 10.1002/14651858.CD004787.pub2]
- 87 **Varela M**, Real MI, Burrell M, Forner A, Sala M, Brunet M, Ayuso C, Castells L, Montaña X, Llovet JM, Bruix J. Chemoembolization of hepatocellular carcinoma with drug eluting beads: efficacy and doxorubicin pharmacokinetics. *J Hepatol* 2007; **46**: 474-481 [PMID: 17239480]
- 88 **Lammer J**, Malagari K, Vogl T, Pilleul F, Denys A, Watkinson A, Pitton M, Sergeant G, Pfammatter T, Terraz S, Benhamou Y, Avajon Y, Gruenberger T, Pomoni M, Langenberger H, Schuchmann M, Dumortier J, Mueller C, Chevallier P, Lencioni R. Prospective randomized study of doxorubicin-eluting-bead embolization in the treatment of hepatocellular carcinoma: results of the PRECISION V study. *Cardiovasc Intervent Radiol* 2010; **33**: 41-52 [PMID: 19908093 DOI: 10.1007/s00270-009-9711-7]
- 89 **Liu YS**, Ou MC, Tsai YS, Lin XZ, Wang CK, Tsai HM, Chuang MT. Transarterial chemoembolization using gelatin sponges or microspheres plus lipiodol-doxorubicin versus doxorubicin-loaded beads for the treatment of hepatocellular carcinoma. *Korean J Radiol* 2015; **16**: 125-132 [PMID: 25598680 DOI: 10.3348/kjr.2015.16.1.125]
- 90 **Deipolyi AR**, Oklu R, Al-Ansari S, Zhu AX, Goyal L, Ganguli S. Safety and efficacy of 70-150 µm and 100-300 µm drug-eluting bead transarterial chemoembolization for hepatocellular carcinoma. *J Vasc Interv Radiol* 2015; **26**: 516-522 [PMID: 25704226 DOI: 10.1016/j.jvir.2014.12.020]
- 91 **Malagari K**, Pomoni M, Kelekis A, Pomoni A, Dourakis S, Spyridopoulos T, Moschouris H, Emmanouil E, Rizos S, Kelekis D. Prospective randomized comparison of chemoembolization with doxorubicin-eluting beads and bland embolization with BeadBlock for hepatocellular carcinoma. *Cardiovasc Intervent Radiol* 2010; **33**: 541-551 [PMID: 19937027 DOI: 10.1007/s00270-009-9750-0]
- 92 **Ginsburg M**, Zivin SP, Wroblewski K, Doshi T, Vasnani RJ, Van Ha TG. Comparison of combination therapies in the management of hepatocellular carcinoma: transarterial chemoembolization with radiofrequency ablation versus microwave ablation. *J Vasc Interv Radiol* 2015; **26**: 330-341 [PMID: 25534635 DOI: 10.1016/j.jvir.2014.10.047]
- 93 **Iezzi R**, Pompili M, La Torre MF, Campanale MC, Montagna M, Saviano A, Cesario V, Siciliano M, Annicchiarico E, Agnes S, Giuliani F, Grieco A, Rapaccini GL, De Gaetano AM, Gasbarrini A, Bonomo L. Radiofrequency ablation plus drug-eluting beads transcatheter arterial chemoembolization for the treatment of single large hepatocellular carcinoma. *Dig Liver Dis* 2015; **47**: 242-248 [PMID: 25577299 DOI: 10.1016/j.dld.2014.12.007]
- 94 **Lencioni R**, Llovet JM, Han G, Tak WY, Yang J, Leberre MA, Niu W, Nicholson K, Meinhardt G, Bruix J. Sorafenib or placebo in combination with transarterial chemoembolization (TACE) with doxorubicin-eluting beads (DEBDOX) for intermediate-stage hepatocellular carcinoma (HCC): phase II, randomized, double-blind SPACE trial. *J Clin Oncol* 2012; **30** Suppl 4: Abs LBA154
- 95 **Geschild JF**, Salem R, Carr BI, Soulen MC, Thurston KG, Goin KA, Van Buskirk M, Roberts CA, Goin JE. Yttrium-90 microspheres for the treatment of hepatocellular carcinoma. *Gastroenterology* 2004; **127**: S194-S205 [PMID: 15508085]
- 96 **Salem R**, Lewandowski RJ, Atassi B, Gordon SC, Gates VL, Barakat O, Sergie Z, Wong CY, Thurston KG. Treatment of unresectable hepatocellular carcinoma with use of 90Y microspheres (TheraSphere): safety, tumor response, and survival. *J Vasc Interv Radiol* 2005; **16**: 1627-1639 [PMID: 16371529]
- 97 **Sangro B**, Bilbao JI, Boan J, Martinez-Cuesta A, Benito A, Rodriguez J, Panizo A, Gil B, Inarrairaegui M, Herrero I, Quiroga J, Prieto J. Radioembolization using 90Y-resin microspheres for patients with advanced hepatocellular carcinoma. *Int J Radiat Oncol Biol Phys* 2006; **66**: 792-800 [PMID: 16904840]
- 98 **Salem R**, Lewandowski RJ, Kulik L, Wang E, Riaz A, Ryu RK, Sato KT, Gupta R, Nikolaidis P, Miller FH, Yaghamai V, Ibrahim SM, Senthilnathan S, Baker T, Gates VL, Atassi B, Newman S, Memon K, Chen R, Vogelzang RL, Nemcek AA, Resnick SA, Chrisman HB, Carr J, Omary RA, Abecassis M, Benson AB, Mulcahy MF. Radioembolization results in longer time-to-progression and reduced toxicity compared with chemoembolization in patients with hepatocellular carcinoma. *Gastroenterology* 2011; **140**: 497-507.e2 [PMID: 21044630 DOI: 10.1053/j.gastro.2010.10.049]
- 99 **Llovet JM**, Di Bisceglie AM, Bruix J, Kramer BS, Lencioni R, Zhu AX, Sherman M, Schwartz M, Lotze M, Talwalkar J, Gores GJ. Design and endpoints of clinical trials in hepatocellular carcinoma. *J Natl Cancer Inst* 2008; **100**: 698-711 [PMID: 18477802 DOI: 10.1093/jnci/djn134]
- 100 **Lee HS**, Kim JS, Choi JJ, Chung JW, Park JH, Kim CY. The safety and efficacy of transcatheter arterial chemoembolization in the treatment of patients with hepatocellular carcinoma and main portal vein obstruction. A prospective controlled study. *Cancer* 1997; **79**: 2087-2094 [PMID: 9179054]

- 101 **Kim KM**, Kim JH, Park IS, Ko GY, Yoon HK, Sung KB, Lim YS, Lee HC, Chung YH, Lee YS, Suh DJ. Reappraisal of repeated transarterial chemoembolization in the treatment of hepatocellular carcinoma with portal vein invasion. *J Gastroenterol Hepatol* 2009; **24**: 806-814 [PMID: 19207681 DOI: 10.1111/j.1440-1746.2008.05728.x]
- 102 **Jang JW**, Bae SH, Choi JY, Oh HJ, Kim MS, Lee SY, Kim CW, Chang UI, Nam SW, Cha SB, Lee YJ, Chun HJ, Choi BG, Byun JY, Yoon SK. A combination therapy with transarterial chemo-lipiodolization and systemic chemo-infusion for large extensive hepatocellular carcinoma invading portal vein in comparison with conservative management. *Cancer Chemother Pharmacol* 2007; **59**: 9-15 [PMID: 16614848]
- 103 **Yen FS**, Wu JC, Kuo BI, Chiang JH, Chen TZ, Lee SD. Transcatheter arterial embolization for hepatocellular carcinoma with portal vein thrombosis. *J Gastroenterol Hepatol* 1995; **10**: 237-240 [PMID: 7548796]
- 104 **Song do S**, Nam SW, Bae SH, Kim JD, Jang JW, Song MJ, Lee SW, Kim HY, Lee YJ, Chun HJ, You YK, Choi JY, Yoon SK. Outcome of transarterial chemoembolization-based multi-modal treatment in patients with unresectable hepatocellular carcinoma. *World J Gastroenterol* 2015; **21**: 2395-2404 [PMID: 25741147 DOI: 10.3748/wjg.v21.i8.2395]
- 105 **Kim GA**, Shim JH, Yoon SM, Jung J, Kim JH, Ryu MH, Ryoo BY, Kang YK, Lee D, Kim KM, Lim YS, Lee HC, Chung YH, Lee YS. Comparison of chemoembolization with and without radiation therapy and sorafenib for advanced hepatocellular carcinoma with portal vein tumor thrombosis: a propensity score analysis. *J Vasc Interv Radiol* 2015; **26**: 320-329.e6 [PMID: 25612807 DOI: 10.1016/j.jvir.2014.10.019]
- 106 **Salem R**, Lewandowski RJ, Mulcahy MF, Riaz A, Ryu RK, Ibrahim S, Atassi B, Baker T, Gates V, Miller FH, Sato KT, Wang E, Gupta R, Benson AB, Newman SB, Omary RA, Abecassis M, Kulik L. Radioembolization for hepatocellular carcinoma using Yttrium-90 microspheres: a comprehensive report of long-term outcomes. *Gastroenterology* 2010; **138**: 52-64 [PMID: 19766639 DOI: 10.1053/j.gastro.2009.09.006]
- 107 **Iñarrairaegui M**, Martínez-Cuesta A, Rodríguez M, Bilbao JI, Arbizu J, Benito A, Alegre F, D'Avola D, Herrero JI, Quiroga J, Prieto J, Sangro B. Analysis of prognostic factors after yttrium-90 radioembolization of advanced hepatocellular carcinoma. *Int J Radiat Oncol Biol Phys* 2010; **77**: 1441-1448 [PMID: 20056355 DOI: 10.1016/j.ijrobp.2009.07.006]
- 108 **Iñarrairaegui M**, Thurston KG, Bilbao JI, D'Avola D, Rodriguez M, Arbizu J, Martínez-Cuesta A, Sangro B. Radioembolization with use of yttrium-90 resin microspheres in patients with hepatocellular carcinoma and portal vein thrombosis. *J Vasc Interv Radiol* 2010; **21**: 1205-1212 [PMID: 20598574 DOI: 10.1016/j.jvir.2010.04.012]
- 109 **Hilgard P**, Hamami M, Fouly AE, Scherag A, Müller S, Ertle J, Heusner T, Cicinnati VR, Paul A, Bockisch A, Gerken G, Antoch G. Radioembolization with yttrium-90 glass microspheres in hepatocellular carcinoma: European experience on safety and long-term survival. *Hepatology* 2010; **52**: 1741-1749 [PMID: 21038413 DOI: 10.1002/hep.23944]
- 110 **National Comprehensive Cancer Network**. NCCN Clinical Practice Guidelines in Oncology. Hepatobiliary Cancers V. 2. 2010. [Accessed March15, 2015] Available from: URL: http://www.nccn.org/professionals/physician_gls/f_guidelines.asp

P- Reviewer: Asirvatham SJ, Baiocchi GL, Francica G

S- Editor: Ji FF **L- Editor:** A **E- Editor:** Jiao XK



Diffusion-weighted imaging of pancreatic cancer

Riccardo De Robertis, Paolo Tinazzi Martini, Emanuele Demozzi, Flavia Dal Corso, Claudio Bassi,
 Paolo Pederzoli, Mirko D'Onofrio

Riccardo De Robertis, Paolo Tinazzi Martini, Department of Radiology, Casa di Cura Pederzoli, 37019 Peschiera del Garda, Italy

Emanuele Demozzi, Flavia Dal Corso, Mirko D'Onofrio, Verona Comprehensive Cancer Network, Department of Radiology, G.B. Rossi Hospital - University of Verona, 37134 Verona, Italy

Claudio Bassi, Verona Comprehensive Cancer Network - Department of Pancreatic Surgery, G.B. Rossi Hospital - University of Verona, 37134 Verona, Italy

Paolo Pederzoli, Department of Pancreatic Surgery, Casa di Cura Pederzoli, 37019 Peschiera del Garda, Italy

Author contributions: All authors contributed equally to this work; Tinazzi Martini P, Bassi C, Pederzoli P and D'Onofrio M designed the research; Demozzi E and Dal Corso F performed the research and analyzed the data; De Robertis R, Demozzi E and Dal Corso F wrote the paper.

Informed consent statement: The authors declare no potential conflicts of interest for this paper.

Open-Access: This article is an open-access article which was selected by an in-house editor and fully peer-reviewed by external reviewers. It is distributed in accordance with the Creative Commons Attribution Non Commercial (CC BY-NC 4.0) license, which permits others to distribute, remix, adapt, build upon this work non-commercially, and license their derivative works on different terms, provided the original work is properly cited and the use is non-commercial. See: <http://creativecommons.org/licenses/by-nc/4.0/>

Correspondence to: Riccardo De Robertis, MD, Department of Radiology, Casa di Cura Pederzoli, via Monte Baldo 24, 37019 Peschiera del Garda, Italy. riccardo.derobertis@hotmail.it
 Telephone: +39-45-8124301
 Fax: +39-45-8027490

Received: January 28, 2015
 Peer-review started: January 28, 2015
 First decision: April 14, 2015
 Revised: April 27, 2015
 Accepted: August 25, 2015

Article in press: August 28, 2015
 Published online: October 28, 2015

Abstract

Magnetic resonance imaging (MRI) is a reliable and accurate imaging method for the evaluation of patients with pancreatic ductal adenocarcinoma (PDAC). Diffusion-weighted imaging (DWI) is a relatively recent technological improvement that expanded MRI capabilities, having brought functional aspects into conventional morphologic MRI evaluation. DWI can depict the random diffusion of water molecules within tissues (the so-called Brownian motions). Modifications of water diffusion induced by different factors acting on the extracellular and intracellular spaces, as increased cell density, edema, fibrosis, or altered functionality of cell membranes, can be detected using this MR sequence. The intravoxel incoherent motion (IVIM) model is an advanced DWI technique that consent a separate quantitative evaluation of all the microscopic random motions that contribute to DWI, which are essentially represented by molecular diffusion and blood microcirculation (perfusion). Technological improvements have made possible the routine use of DWI during abdominal MRI study. Several authors have reported that the addition of DWI sequence can be of value for the evaluation of patients with PDAC, especially improving the staging; nevertheless, it is still unclear whether and how DWI could be helpful for identification, characterization, prognostic stratification and follow-up during treatment. The aim of this paper is to review up-to-date literature data regarding the applications of DWI and IVIM to PDACs.

Key words: Pancreas; Pancreatic neoplasms; Pancreatic ductal carcinoma; Magnetic resonance imaging; Diffusion magnetic resonance imaging

© The Author(s) 2015. Published by Baishideng Publishing

Group Inc. All rights reserved.

Core tip: Diffusion-weighted imaging (DWI) plays an important role for the identification of pancreatic adenocarcinoma, even if small in size, thus allowing early diagnosis. The intravoxel incoherent motion model is a promising DWI technique for the characterization of this tumor, with potential usefulness for the differentiation from mass-forming pancreatitis. Thanks to its high negative prognostic value, DWI should be used to assess the presence of liver metastases in patients with pancreatic adenocarcinoma.

De Robertis R, Tinazzi Martini P, Demozzi E, Dal Corso F, Bassi C, Pederzoli P, D'Onofrio M. Diffusion-weighted imaging of pancreatic cancer. *World J Radiol* 2015; 7(10): 319-328 Available from: URL: <http://www.wjgnet.com/1949-8470/full/v7/i10/319.htm> DOI: <http://dx.doi.org/10.4329/wjv7.i10.319>

INTRODUCTION

Magnetic resonance imaging (MRI) has a well-established role in the evaluation of patients with pancreatic ductal adenocarcinoma (PDAC). MR diffusion-weighted imaging (DWI) is a relatively recent technological improvement of MRI. DW sequence can evaluate the diffusion of water molecules (Brownian motions) within biological tissues: All factors that tends to narrow the extracellular compartment or modify water exchanges through cell membranes lead to an impairment of the diffusion of water molecules. Tissues with restriction of water diffusion present high signal intensity on DW images and low signal intensity on the apparent diffusion coefficient (ADC) map; diffusion restriction can be also quantified through the calculation of the ADC value within specific regions of interest (ROIs).

Thanks to technological improvements that have shortened the acquisition time and improved the signal-to-noise ratio, DWI sequence has been widely adopted as a part of abdominal MRI examination protocols. Several authors have assessed the usefulness of this technique for the evaluation of PDAC and have reported that the addition of DWI sequence might represent an adjunct value, especially improving the staging. Nevertheless, it is still unclear whether and how DWI could be of value for identification, characterization, prognostic stratification and post-treatment follow-up of these patients.

The aim of this paper is to describe the applications of DWI to the evaluation of patients with PDAC, in particular regarding lesion identification, characterization, prognostication and assessment of response to therapy, through a review of up-to-date literature data.

DWI: TECHNICAL BASES

In 1965, Stejskal and Tanner^[1] developed a modified

T2-weighted MRI sequence that included motion-probing gradients for the detection of the diffusion of water molecules. DWI enables the visualization of Brownian random molecular motions in the extracellular and intracellular spaces^[2]. This technique can provide information on the cellular density and the integrity of cell membranes, since the degree of restriction to water diffusion in biologic tissues is inversely correlated to these features^[3-6]. Nevertheless, any factor that modifies the extracellular space (fibrosis, edema, size of the cells, size and density of intratumoral vessels) may also contribute to diffusion restriction.

The first clinical application of DWI has been the evaluation of the hyperacute phase of brain ischemia. Cytotoxic edema induced by ischemia and neuronal death narrows the extracellular space and therefore decreases the diffusion of water molecules. Thereafter, DWI has been proven to be useful for the assessment of a variety of intra-cranial pathologic conditions, as tumors. High cellular density, which is typical of tumors, narrows the extracellular space and determines a high density of hydrophobic cellular membranes^[7], leading to impaired diffusion of water molecules.

Technical advances, as the use of parallel imaging techniques, have shortened the acquisition time and have improved the contrast- and signal-to-noise ratio of this sequence, thus leading to an increased use of DWI in the MR evaluation of the abdomen^[8].

The acquisition technique and parameters may vary from institution to institution. The choice of acquisition using free-breathing, respiratory-triggering, navigator-tracking, or breath-hold is optional; nevertheless, this selection may influence image quality and acquisition time: Free-breathing acquisition provides lower image quality, but the acquisition time is invariably shorter as compared to respiratory-gated acquisitions. Free-breathing DWI acquisition is therefore more widely used for "work horse" MRI abdominal protocols.

The *b*-value is a technical parameter that regulates the strength, duration and interval of bipolar motion-probing gradients and affects the degree of phase dispersion and the diffusion weighting of the images. DW images are acquired using at least two different *b*-values, both low (for example, 0 or 50 s/mm²) and high (for example, 800 or 1000 s/mm²). Changing the *b*-value leads to a variation of the sensitivity of the DW sequence to water motion^[2]. At low *b*-values, lesions with high diffusion (e.g., cysts) appear hyperintense compared to the surrounding tissues, since the T2-weighted contrast is still dominant. Increasing the *b*-value leads to a signal loss of tissues with "free diffusion" (i.e., cysts, cerebro-spinal fluid, necrosis), whereas tissues with restricted diffusion, as solid neoplastic areas, will appear hyperintense.

Low *b*-value images have generally higher spatial resolution and better image quality, being comparable to T2-weighted fat-suppressed images, while high *b*-value images have higher contrast resolution, but

lower spatial resolution.

The ADC quantifies the diffusion of water molecules and can be represented with the ADC map. The evaluation of the ADC map is mandatory: Hyperintense areas on both high *b*-value DW image and the ADC map are typical of tissues with "T2-shine through" effect, that occurs because of long T2 decay time in some cases, as for example subacute infarction with vasogenic edema or epidermoid cysts. In contrast, areas with restricted water diffusion will appear hyperintense on high *b*-value DW image and hypointense on ADC map. Beyond the visual assessment there is also the possibility of a quantitative analysis by the calculation of the ADC value, which can be measured drawing ROIs within the target tissue; ADC measurement can be expressed as a mean value or as a histogram representing the distribution of different ADC values within the ROI.

The ADC is a combined measurement of all molecular random movements of water molecules (diffusion) and blood microcirculation in the capillaries (perfusion)^[9]. The intravoxel incoherent motion (IVIM) model takes these two sources of signal decay into account, thus providing a separate quantification of diffusion (provided by the diffusion coefficient - *D* and the pseudodiffusion coefficient - *D*^{*}) and perfusion (represented by the perfusion fraction - *f*) parameters^[10]. IVIM can therefore quantify the relative contribution of these parameters to the total diffusion restriction and can evaluate perfusional features without the need of contrast medium injection. IVIM acquisition needs in most cases respiratory compensation, and therefore this sequence has a long acquisition time. For this reason, the IVIM model is not completely integrated into clinical practice.

IDENTIFICATION

The sensitivity of computed tomography (CT) in revealing PDAC is high, ranging between 89% and 97%^[11]. MRI offers better soft tissue contrast compared with CT; PDACs are usually well recognized on T1-weighted and DW images, owing to differences between the histological components of the tumor and the circumstant parenchyma. There is however no significant diagnostic advantage of MRI over contrast-enhanced CT for the identification of PDAC^[12].

Studies on DWI revealed that this sequence might have an important role in the identification of PDAC. Both visual analysis^[13-15] and ADC measurement^[14,16-21] can reliably distinguish PDAC from the background pancreatic parenchyma. Pancreatic tumors, even if small in size, almost invariably show diffusion restriction, as revealed by studies conducted on neuroendocrine tumors^[22], presenting as a focal hyperintense area on high *b*-value DW images with hypointensity on ADC map^[13].

Identification of PDAC can be therefore improved by the use of DW images, as tumors are brighter than the circumstant pancreatic parenchyma: The high contrast

resolution of high *b*-value DW images usually leads to a clear identification of these tumors.

PDACs present lower ADC values than the circumstant parenchyma. Nevertheless, it is still unclear which is the histological component that mainly contributes to diffusion restriction in PDACs. Lemke^[23] reported that the IVIM-derived *f* value (perfusion fraction), which reflects blood microcirculation, was significantly lower in PDACs than in the healthy pancreas (mean, 8.59% ± 4.6% vs 25.0% ± 6.2%, respectively): This may be related to the histological composition of PDAC, which is mainly composed by fibrotic stroma with very few vessels.

The best way to reduce mortality in patients with PDAC is through early diagnosis, that necessary derives from an improvement of the identification of this tumor. This is of particular importance in high-risk patients (*i.e.*, those with familiarity). At this regard, Del Chiaro *et al.*^[24] reported the efficacy of a MRI-based screening program in individuals at risk. Unfortunately, this study did not report the accuracy of DWI in PDAC detection; nevertheless, it could be argued that the high contrast resolution of DW images may help in the early identification of PDACs in high-risk patients.

Some authors reported that small or well-differentiated PDACs may lack typical CT features, as ill-defined margins and hypovascularity, and could therefore be missed or misdiagnosed^[25]. Prokesch *et al.*^[26] emphasized that indirect signs such as mass effect, atrophic distal parenchyma, and interrupted duct sign were important indicators of the presence of tumors with no visible tumor-pancreas contrast. MRI could be helpful in these cases. Some old studies have suggested that T1-weighted spin-echo images with fat suppression and dynamic gradient-echo MR images enhanced with gadolinium could be superior to CT for detecting small pancreatic carcinomas^[27,28]. At present, no single study evaluated the efficacy of DW images in the identification of small PDACs; nevertheless, as high *b*-value DW images provide high contrast resolution, this sequence is probably of value in this regard.

Chronic pancreatitis may represent a confusing factor for PDAC identification, as both T1-weighted and DW images may fail to discriminate between fibrotic parenchyma and the tumor, which typically contains large amount of fibrotic tissue. At this regard, Fukukura^[29] reported that visual assessment of DW images might be misleading in these patients, as chronic inflammation frequently appears hyperintense on high *b*-value images. Despite this, the mean ADC value of PDACs ($1.160 \pm 0.22 \times 10^{-3} \text{ mm}^2/\text{s}$) was significantly lower than that of the pancreatic parenchyma affected by chronic pancreatitis ($1.24 \pm 0.23 \times 10^{-3} \text{ mm}^2/\text{s}$, *P* = 0.004). ADC quantification can be therefore helpful when the visual assessment is doubtful but clinical setting (presence of painless jaundice, newly onset diabetes or high CA 19.9 serum levels) or MRI features are highly suspicious for a PDAC associated with chronic

Table 1 Comparison of apparent diffusion coefficient values between different solid pancreatic neoplasms

Ref.	No. of patients	Field strength (T)	<i>b</i> -values (s/mm ²)	Mean ± SD ADC values (× 10 ⁻³ mm ² /s)	<i>P</i> value
Yao <i>et al</i> ^[18]	30 PDACs	3	0, 600	1.57 ± 0.26	< 0.001
	12 SPTs			1.05 ± 0.35	
	15 PanNETs			1.62 ± 0.41	
Barral <i>et al</i> ^[19]	18 malignant ¹	1.5	0, 400, 800	1.150 ²	< 0.05
	10 benign			2.493 ²	
Lee <i>et al</i> ^[33]	47 PDACs	1.5	0, 500, 1000	1.23 ± 0.18	NS
	6 SPTs			1.16 ± 0.36	
	5 PanNETs			1.30 ± 0.41	

¹Including 13 PDACs; ²Median. T: Tesla; ADC: Apparent diffusion coefficient; PDAC: Pancreatic ductal adenocarcinoma; SPT: Solid pseudopapillary tumor; PanNET: Pancreatic neuroendocrine tumor; NS: Not statistically significant.

pancreatitis.

Some technical aspects should be considered regarding PDAC identification using DWI. Respiratory-triggered acquisitions provide higher spatial resolution and signal-to-noise ratio compared to free breathing and breath-hold acquisitions, as reported by Kartalis *et al*^[30]. As previously stated, respiratory-gated acquisition of DW images is time-consuming and is not frequently performed during clinical practice. Contrast medium administration does not induce modifications of DWI features: Liu *et al*^[31] reported no significant differences in ADC measurements when comparing precontrast to postcontrast DWI acquired 6–7 min after contrast medium administration.

Summarizing, it seems that CT and conventional MRI sequences have a similar accuracy for PDAC identification in most cases; further studies should be performed to assess the efficacy of DW images in identification of small/well differentiated PDACs.

CHARACTERIZATION

Pancreatic adenocarcinoma is usually hypointense to the normal pancreas on T1-weighted fat-suppressed sequences, shows hypoenhancement during arterial phase, and shows progressive enhancement on delayed sequences. These features, and particularly the hypointense appearance on pancreatic phase images, are distinctive of this tumor^[32]. Very few studies have focused on the role of DWI for the differential diagnosis of solid pancreatic tumors. Literature data reveal that quantitative analysis of DW images can distinguish between benign and malignant pancreatic lesions^[19]. Nevertheless, ADC quantification could fail in the differentiation of solid pancreatic lesions, due to a wide overlap in ADC values^[18–20,33]. Details regarding ADC quantification of pancreatic solid neoplasms are reported in Table 1. Yao *et al*^[18] reported that ADC measurement using respiratory-triggered DWI at 3. T may aid to disclose the histopathological pattern of normal pancreas and solid pancreatic masses, which may be helpful in characterizing solid pancreatic lesions: statistical difference was noticed in ADC values among

PDAC, solid pseudopapillary tumors and neuroendocrine tumors (PanNETs). Barral *et al*^[19] and Lee *et al*^[33], instead, did not reported significant differences in ADC values between PDACs and other solid pancreatic tumors.

IVIM-derived parameters may be helpful for characterization. Kang *et al*^[34] found that perfusion-related parameters as *f* (perfusion fraction) were significantly lower in PDACs as compared to normal pancreas, chronic pancreatitis, and PanNETs. Concia *et al*^[35] reported that PDACs are characterized by very low ADC_{0,50} and *f* values, significantly different from PanNETs and chronic pancreatitis. These findings are consistently related to the histologic nature of PDACs, which are fibrous tumors with very few internal vessels, as compared to the healthy parenchyma and to PanNETs.

The possibility to differentiate mass-forming inflammatory diseases from PDAC by means of DWI is a topic of particular interest. These entities frequently present overlapping features at conventional MRI evaluation. Overall, mass-forming pancreatitis (MFP) and autoimmune pancreatitis (AIP) tend to present lower ADC values than PDACs; nevertheless, literature data are inhomogeneous and controversial^[18,36–43]. Details regarding the main published studies dealing with this issue are reported in Table 2. A meta-analysis by Niu *et al*^[43], which included 9 studies, reported a pooled sensitivity and specificity of 86% and 82%, with an AUC of 0.91, for the differentiation between PDAC and MFP using DWI alone.

IVIM-derived parameters may be helpful for this differentiation. Lee *et al*^[33] reported that ADC₅₀₀, ADC₁₀₀₀, and *D* of MFP were all significantly lower than those of pancreatic cancer. Klauss *et al*^[41] found that *F* (perfusion fraction) values were significantly higher in focal pancreatitis (16.3%) compared with PDACs (8.2%): This was explained by the increasing perfusion effects at lower *b*-values, which were correlated with a relatively higher vascularity in pancreatitis.

The comparison of ADC values of focal pancreatitis and pancreatic carcinoma to the remaining pancreas may be helpful for the differentiation of these diseases: Fattahi *et al*^[42] reported that ADC values of focal panc-

Table 2 Comparison of apparent diffusion coefficient values between pancreatic ductal adenocarcinomas and mass-forming pancreatitis/autoimmune pancreatitis

Ref.	No. of patients	Field strength (T)	b-values (s/mm ²)	Mean \pm SD ADC values ($\times 10^{-3}$ mm ² /s)	P value
Yao <i>et al</i> ^[118]	30 PDACs	3	0, 600	1.57 \pm 0.26	< 0.001
	15 MFPs			1.19 \pm 0.15	
Barral <i>et al</i> ^[119]	13 PDACs	1.5	0, 400, 800	1.150	NS
	8 MFPs			1.160	
Lee <i>et al</i> ^[33]	47 PDACs	1.5	0, 500, 1000	1.46 \pm 0.20/1.23 \pm 0.18 ¹	< 0.05
	13 MFP			1.23 \pm 0.22 / 1.04 \pm 0.18 ¹	
Hur <i>et al</i> ^[36]	28 PDACs	1.5 or 3	0, 500	1.512	< 0.05
	9 AIPs			1.086	
Ma <i>et al</i> ^[37]	25 PDACs	3	0, 800	1.39 \pm 0.22	< 0.05
	14 MFPs			1.21 \pm 0.23	
Huang <i>et al</i> ^[38]	37 PDACs	3	0, 1000	1.06 \pm 0.15	< 0.05
	14 MFPs			1.35 \pm 0.14	
Kamisawa <i>et al</i> ^[39]	40 PDACs	1.5	800	1.249 \pm 0.113	< 0.001
	13 AIPs			1.012 \pm 0.112	
Wiggermann <i>et al</i> ^[40]	24 PDACs	1.5	50, 500	0.78 \pm 0.11	NS
	20 MFPs			0.69 \pm 0.18	
Klauss <i>et al</i> ^[41]	20 PDACs	1.5	Multiple ²	2.55 \pm 1.09/1.46 \pm 0.31 ¹	< 0.05
	9 MFPs			3.17 \pm 0.67/1.76 \pm 0.19 ¹	
Fattahi <i>et al</i> ^[42]	10 PDACs	1.5	0, 600	1.46 \pm 0.18	NE
	14 MFPs			2.09 \pm 0.18	

¹Two readers; ²0, 25, 50, 75, 100, 150, 200, 300, 400, 600, 800 s/mm². PDAC: Pancreatic ductal adenocarcinoma; MFP: Mass-forming pancreatitis; AIP: Autoimmune pancreatitis; NE: Not evaluated; NS: Not statistically significant.

Table 3 Data derived from studies that have evaluated apparent diffusion coefficient quantification of pancreatic ductal adenocarcinomas with different degree of differentiation

Ref.	No. of patients	Field strength (T)	b-values (s/mm ²)	Mean \pm SD ADC ($\times 10^{-3}$ mm ² /s)	P value
Wang <i>et al</i> ^[20]	21	1.5	0, 500	2.10 \pm 0.42 (MD-WD)	< 0.05
				1.46 \pm 0.17 (PD)	
Legrand <i>et al</i> ^[21]	22	1.5 or 3	Multiple ¹	1.43 \pm 0.12 (WD)	0.05
				1.94 \pm 0.62 (MD-PD)	
Muraoka <i>et al</i> ^[44]	10	1.5	0, 500	1.88 \pm 0.39 (loose fibrosis)	< 0.05
				1.01 \pm 0.29 (dense fibrosis)	
Rosenkrantz <i>et al</i> ^[45]	30	1.5	0, 500	1.78 \pm 0.33/1.75 \pm 0.49 (MD-WD) ²	NS
				1.69 \pm 0.36/1.62 \pm 0.33 (PD) ²	
Fukukura <i>et al</i> ^[46]	92	3	0, 1000	1.10 \pm 0.09 (high cellularity)	< 0.05
				1.25 \pm 0.18 (low cellularity)	

¹0, 50, 200, 400, 600, 800 s/mm²; ²Two readers. T: Tesla; WD: Well differentiated PDAC; MD: Moderately differentiated PDAC; PD: Poorly differentiated PDAC; ADC: Apparent diffusion coefficient; PDAC: Pancreatic ductal adenocarcinoma; NS: Not statistically significant.

reatitis (2.09×10^{-3} mm²/s) were indistinguishable compared with those of the remaining pancreas (2.03×10^{-3} mm²/s), which suggests that the same inflammatory process may be present both in focal pancreatitis and the remaining pancreas; instead, ADC values of pancreatic carcinoma (1.46×10^{-3} mm²/s) were invariably lower than those of the remaining pancreas (2.11×10^{-3} mm²/s).

Summarizing, it seems that DWI can distinguish between benign and malignant solid pancreatic lesions. Despite this, quantitative analysis of DWI features can fail in the differentiation between solid pancreatic tumors due to a wide overlap of ADC values. DWI may be potentially feasible for differentiating PDAC from MFP, especially using the IVIM technique. However, large-

scale randomized control trials are necessary to assess its real clinical value.

PROGNOSTIC STRATIFICATION

Prognosis in patients with PDAC is influenced by the histopathologic grade. Nevertheless, it plays a less important role in clinical management of PDACs as compared to the stage of the disease.

Some studies tried to correlate DWI findings with the histopathologic features of PDACs^[20,21,44-48]; literature data dealing with this specific topic are reported in Table 3. Ideally, well-differentiated PDACs should present higher ADC values as compared to low-grade tumors, but some authors reported opposite findings

as well as non-significant results. It is reasonable to believe that the main contribution to the restriction of water diffusion in PDACs is provided by fibrosis, which is the predominant part of this tumor, while the contribution of the cells - even if less differentiated - and the perfusion effect provided by blood vessels should be minimal. Wang *et al.*^[20] reported that PDACs characterized by dense fibrosis have significantly lower ADC values compared to those characterized by abundant neoplastic tubular structures; moreover, well/moderately differentiated PDACs with dense fibrosis showed also significantly lower ADC values than those with loose fibrosis. Muraoka *et al.*^[44] reported similar findings: In their study, the mean ADC value was significantly higher in PDACs with loose fibrosis ($1.88 \pm 0.39 \times 10^{-3} \text{ mm}^2/\text{s}$) than in those with dense fibrosis ($1.01 \pm 0.29 \times 10^{-3} \text{ mm}^2/\text{s}$, $P < 0.05$). Moreover, Rosenkrantz *et al.*^[45] did not report significant difference in mean ADC between poorly and well/moderately differentiated tumors. Unfortunately, these findings have not been confirmed by other studies. Legrand *et al.*^[21], for example, reported that mean ADC values did not differ significantly between tumors having < 50% of fibrotic stroma and those having > 50% of fibrotic stroma ($P = 0.94$), or between tumors containing dense fibrosis and those containing loose fibrosis ($P = 0.81$). Regarding IVIM, Klauss *et al.*^[47] reported that the difference between the IVIM-derived D value between PDACs with moderate and severe fibrosis was significant, with a respective mean value of $1.02 \pm 0.48 \times 10^{-3} \text{ mm}^2/\text{s}$ and $1.22 \pm 0.76 \times 10^{-3} \text{ mm}^2/\text{s}$, but the cellular complexes surrounded by fibrosis provided more structural limitations than did fibrosis alone.

Some authors have proposed a more practical role for DWI, testing correlations with clinical features or outcomes (e.g., tumor stage, aggressiveness, or survival) rather than the histopathologic grade. Hayano *et al.*^[48] reported a significant negative correlation between ADC and tumor size ($r = -0.59$, $P = 0.004$) and the number of metastatic lymph nodes ($r = -0.56$, $P = 0.007$). Tumors with low ADC values had a significant higher tendency to show portal system and extra-pancreatic nerve plexus invasion ($P = 0.04$ and 0.01 , respectively) than those with high ADC. On the contrary, Rosenkrantz *et al.*^[45] did not report significant difference in mean ADC between tumors with stage T3 vs stage T1/T2, or between tumors with and without metastatic peri-pancreatic lymph nodes. Fukukura *et al.*^[46] reported that the median ADC value of PDACs was not associated with significant differences in survival ($P < 0.001$ for all phases).

It is therefore still unclear whether DWI could be helpful in PDAC prognostication; overall, ADC values tend to be low in less differentiated lesions. Moreover, it seems that PDACs with low ADC values tend to have a worse clinical course and prognosis than PDACs with high ADC values. Larger studies, particularly regarding IVIM-DWI, are needed to further evaluate these findings.

STAGING

About 80% of PDACs are unresectable at diagnosis, due to a locally advanced disease or to the presence of liver metastases: M+ stage precludes most treatments beyond chemotherapy. The detection of liver metastases is related to their size. The lower size threshold of conventional imaging techniques for the detection of metastases lays around 1 cm^[49]; unfortunately, postmortem studies has shown that the ratio between metastases larger than 1 cm and those smaller than 1 cm is approximately 1:4^[50]. These findings clearly indicate that imaging should have a capacity to detect and characterize metastases smaller than 1 cm. A meta-analysis by Niekel *et al.*^[51] reported sensitivity estimates of CT, MR, and FDG-PET on a per-lesion basis of 74.4%, 80.3%, and 81.4%, respectively, whereas on a per-patient basis, the sensitivities of CT, MR, and FDG-PET were 83.6%, 88.2%, and 94.1%, respectively. For lesions smaller than 10 mm, the sensitivity estimates for MR were higher than those for CT.

DWI is a reliable method to detect liver metastases, with a sensitivity and specificity higher than both CT and conventional MR sequences^[51], even though most published studies comprised a small amount of patients with metastatic PDAC. DWI sensitivity and specificity in detecting liver metastases can reach respectively 90.8% and 97.5%^[51-55]. Moreover, DW sequences are able to detect focal liver lesions even down to 3 mm, as reported in a study by Coenegrachts *et al.*^[56]. Some authors have pointed out that DWI alone should not be used for the diagnosis of liver metastases because of possible false positives; the overlap in ADC values among benign and malignant hepatic lesions strengthen this consideration. Whenever possible, MR findings obtained during the hepatobiliary phase after hepatocyte-specific contrast media administration, should be used in association with DW images to obtain a definite diagnosis^[55-60].

Preoperative assessment of the N stage can be very difficult using MRI. The presence of diffusion restriction in multiple peri-pancreatic lymph nodes is not uncommon in patients with PDAC. Moreover, microscopic nodal metastases are frequently found in small peri-pancreatic lymph nodes at histopathological analysis^[61,62]. A study by Imai *et al.*^[63] reported that, despite a low sensitivity, the specificity and accuracy for the detection of para-aortic lymph node metastases from PDAC were relatively high for MRI (96.8% and 88.4%, respectively); unfortunately, their protocol did not include DWI sequence. Literature data suggest that DWI is a good method for the detection of nodal metastases, at least when applied to pelvic, breast, and head/neck tumors^[64-66]; these favorable results may be assumed to be applicable also to PDACs. Unfortunately, studies on diagnostic accuracy of DWI are difficult to perform, mainly because extended lymphadenectomy is not routinely performed during pancreatic resection^[61,62]. Data regarding ADC measurement for the distinction

between inflammatory and metastatic lymphnodes are controversial^[67-71]. Further studies should be therefore performed to assess the usefulness of DWI for the detection of nodal involvement by PDAC.

Several authors have reported the usefulness of DWI to diagnose peritoneal implants, but these studies included a small amount of patients with PDAC. Bozkurt^[72] reported that the association of DW images and conventional MRI images had 83% sensitivity, 94% specificity, and 86% accuracy for the diagnosis of peritoneal implants. Low *et al*^[73] reported high sensitivity and accuracy values when DWI was added to conventional MRI sequences for the detection of peritoneal implants.

DWI should be therefore ideally evaluated for first during the staging of patients with PDAC. In most cases, if no focal liver lesions are detected using DWI, then the presence of liver metastases is extremely unlikely, thanks to its high negative predictive value. Nevertheless, conventional sequences should be always taken into consideration, due to possible false positive results of DWI.

POST-TREATMENT FOLLOW-UP

DWI can depict microstructural changes during therapy. Niwa *et al*^[74] reported differences in ADC values among patients with advanced pancreatic cancer treated with gemcitabine: ADC values were significantly different between the progressive and stable groups at 3 mo' and 6 mo' follow-up ($P = 0.03$ and $P = 0.04$, respectively). The rate of tumor progression was significantly higher in those with a low b -value (400 s/mm^2) ADC than in those with a high b -value ADC (median progression time, 140 d vs 182 d, $P = 0.01$).

Cuneo *et al*^[75] reported a significant correlation between pre treatment mean ADC values of resectable PDACs and the amount of tumor cell destruction after chemoradiation evaluated on surgical specimens, with a Pearson correlation coefficient of 0.94 ($P = 0.001$). Mean pre-treatment ADC was $1.61 \times 10^{-3} \text{ mm}^2/\text{s}$ in responding patients ($> 90\%$ tumor cell destruction) compared to $1.25 \times 10^{-3} \text{ mm}^2/\text{s}$ in non-responding patients.

Overall, a very limited number of studies focused on the post-treatment DWI assessment of PDACs. This topic deserves further studies in order to establish the real usefulness of DWI for early assessment of chemotherapy outcome.

CONCLUSION

DWI is a robust imaging technique that should be performed during MRI evaluation of PDACs. The high contrast resolution of PDACs on DW images is useful for the identification of even very small lesions, thus allowing earlier diagnosis. IVIM, although not fully integrated into clinical practice, represent a promising DWI technique for characterization of PDACs, with particular interest on

the differentiation between PDACs and MFPs. Considered its high negative prognostic values, DWI findings should be considered for the staging of patients with PDAC. Further studies are needed to evaluate the usefulness of DWI for treatment monitoring.

REFERENCES

- 1 Stejskal EO, Tanner JE. Spin diffusion measurements: spin echoes in the presence of a time dependent field gradient. *J Chem Phys* 1965; **42**: 288 [DOI: 10.1063/1.1695690]
- 2 Koh DM, Collins DJ. Diffusion-weighted MRI in the body: applications and challenges in oncology. *AJR Am J Roentgenol* 2007; **188**: 1622-1635 [PMID: 17515386]
- 3 Guo Y, Cai YQ, Cai ZL, Gao YG, An NY, Ma L, Mahankali S, Gao JH. Differentiation of clinically benign and malignant breast lesions using diffusion-weighted imaging. *J Magn Reson Imaging* 2002; **16**: 172-178 [PMID: 12203765]
- 4 Gauvain KM, McKinstry RC, Mukherjee P, Perry A, Neil JJ, Kaufman BA, Hayashi RJ. Evaluating pediatric brain tumor cellularity with diffusion-tensor imaging. *AJR Am J Roentgenol* 2001; **177**: 449-454 [PMID: 11461881]
- 5 Sugahara T, Korogi Y, Kochi M, Ikushima I, Shigematu Y, Hirai T, Okuda T, Liang L, Ge Y, Komohara Y, Ushio Y, Takahashi M. Usefulness of diffusion-weighted MRI with echo-planar technique in the evaluation of cellularity in gliomas. *J Magn Reson Imaging* 1999; **9**: 53-60 [PMID: 10030650]
- 6 Lang P, Wendland MF, Saeed M, Gindele A, Rosenau W, Mathur A, Gooding CA, Genant HK. Osteogenic sarcoma: noninvasive in vivo assessment of tumor necrosis with diffusion-weighted MR imaging. *Radiology* 1998; **206**: 227-235 [PMID: 9423677]
- 7 Taouli B, Koh DM. Diffusion-weighted MR imaging of the liver. *Radiology* 2010; **254**: 47-66 [PMID: 20032142 DOI: 10.1148/radiol.09090021]
- 8 Dietrich O, Biffar A, Baur-Melnyk A, Reiser MF. Technical aspects of MR diffusion imaging of the body. *Eur J Radiol* 2010; **76**: 314-322 [PMID: 20299172 DOI: 10.1016/j.ejrad.2010.02.018]
- 9 Le Bihan D, Breton E, Lallemand D, Grenier P, Cabanis E, Laval-Jeantet M. MR imaging of intravoxel incoherent motions: application to diffusion and perfusion in neurologic disorders. *Radiology* 1986; **161**: 401-407 [PMID: 3763909]
- 10 Le Bihan D, Breton E, Lallemand D, Aubin ML, Vignaud J, Laval-Jeantet M. Separation of diffusion and perfusion in intravoxel incoherent motion MR imaging. *Radiology* 1988; **168**: 497-505 [PMID: 3393671]
- 11 Valls C, Andia E, Sanchez A, Fabregat J, Pozuelo O, Quintero JC, Serrano T, Garcia-Borobia F, Jorba R. Dual-phase helical CT of pancreatic adenocarcinoma: assessment of resectability before surgery. *AJR Am J Roentgenol* 2002; **178**: 821-826 [PMID: 11906855]
- 12 Takakura K, Sumiyama K, Munakata K, Ashida H, Arihiro S, Kakutani H, Tajiri H. Clinical usefulness of diffusion-weighted MR imaging for detection of pancreatic cancer: comparison with enhanced multidetector-row CT. *Abdom Imaging* 2011; **36**: 457-462 [PMID: 21643939 DOI: 10.1007/s00261-011-9728-7]
- 13 Shinya S, Sasaki T, Nakagawa Y, Guiquing Z, Yamamoto F, Yamashita Y. Usefulness of diffusion-weighted imaging (DWI) for the detection of pancreatic cancer: 4 case reports. *Hepatogastroenterology* 2008; **55**: 282-285 [PMID: 18507125]
- 14 Matsuki M, Inada Y, Nakai G, Tatsugami F, Tanikake M, Narabayashi I, Masuda D, Arisaka Y, Takaori K, Tanigawa N. Diffusion-weighted MR imaging of pancreatic carcinoma. *Abdom Imaging* 2007; **32**: 481-483 [PMID: 17431713]
- 15 Ichikawa T, Erturk SM, Motosugi U, Sou H, Iino H, Araki T, Fujii H. High-b value diffusion-weighted MRI for detecting pancreatic adenocarcinoma: preliminary results. *AJR Am J Roentgenol* 2007; **188**: 409-414 [PMID: 17242249]
- 16 Hao JG, Wang JP, Gu YL, Lu ML. Importance of b value in diffusion weighted imaging for the diagnosis of pancreatic cancer.

- World J Gastroenterol* 2013; **19**: 6651-6655 [PMID: 24151395 DOI: 10.3748/wjg.v19.i39.6651]
- 17 **Kim H**, Arnoletti PJ, Christein J, Heslin MJ, Posey JA, Pednekar A, Mark Beasley T, Morgan DE. Pancreatic adenocarcinoma: a pilot study of quantitative perfusion and diffusion-weighted breath-hold magnetic resonance imaging. *Abdom Imaging* 2014; **39**: 744-752 [PMID: 24549880 DOI: 10.1007/s00261-014-0107-z]
 - 18 **Yao XZ**, Yun H, Zeng MS, Wang H, Sun F, Rao SX, Ji Y. Evaluation of ADC measurements among solid pancreatic masses by respiratory-triggered diffusion-weighted MR imaging with inversion-recovery fat-suppression technique at 3.0T. *Magn Reson Imaging* 2013; **31**: 524-528 [PMID: 23200681 DOI: 10.1016/j.mri.2012.09.006]
 - 19 **Barral M**, Sebbag-Sfez D, Hoeffel C, Chaput U, Dohan A, Eveno C, Boudiaf M, Soyer P. Characterization of focal pancreatic lesions using normalized apparent diffusion coefficient at 1.5-Tesla: preliminary experience. *Diagn Interv Imaging* 2013; **94**: 619-627 [PMID: 23545001 DOI: 10.1016/j.diii.2013.02.011]
 - 20 **Wang Y**, Chen ZE, Nikolaidis P, McCarthy RJ, Merrick L, Sternick LA, Horowitz JM, Yaghmai V, Miller FH. Diffusion-weighted magnetic resonance imaging of pancreatic adenocarcinomas: association with histopathology and tumor grade. *J Magn Reson Imaging* 2011; **33**: 136-142 [PMID: 21182131 DOI: 10.1002/jmri.22414]
 - 21 **Legrand L**, Duchatelle V, Molinié V, Boulay-Coletta I, Sibileau E, Zins M. Pancreatic adenocarcinoma: MRI conspicuity and pathologic correlations. *Abdom Imaging* 2015; **40**: 85-94 [PMID: 25030776 DOI: 10.1007/s00261-014-0196-8]
 - 22 **Brenner R**, Metens T, Bali M, Demetter P, Matos C. Pancreatic neuroendocrine tumor: added value of fusion of T2-weighted imaging and high b-value diffusion-weighted imaging for tumor detection. *Eur J Radiol* 2012; **81**: e746-e749 [PMID: 22386133 DOI: 10.1016/j.ejrad.2012.01.032]
 - 23 **Lemke A**, Laun FB, Klauss M, Re TJ, Simon D, Delorme S, Schad LR, Stieltjes B. Differentiation of pancreas carcinoma from healthy pancreatic tissue using multiple b-values: comparison of apparent diffusion coefficient and intravoxel incoherent motion derived parameters. *Invest Radiol* 2009; **44**: 769-775 [PMID: 19838121 DOI: 10.1097/RLI.0b013e3181b62271]
 - 24 **Del Chiaro M**, Verbeke CS, Kartalis N, Pozzi Mucelli R, Gustafsson P, Hansson J, Haas SL, Segersvärd R, Andren-Sandberg Å, Löhr JM. Short-term Results of a Magnetic Resonance Imaging-Based Swedish Screening Program for Individuals at Risk for Pancreatic Cancer. *JAMA Surg* 2015; **150**: 512-518 [PMID: 25853369 DOI: 10.1001/jamasurg.2014.3852]
 - 25 **Yoon SH**, Lee JM, Cho JY, Lee KB, Kim JE, Moon SK, Kim SJ, Baek JH, Kim SH, Kim SH, Lee JY, Han JK, Choi BI. Small (≤ 20 mm) pancreatic adenocarcinomas: analysis of enhancement patterns and secondary signs with multiphasic enhanced detector CT. *Radiology* 2011; **259**: 442-452 [PMID: 21406627 DOI: 10.1148/radiol.11101133]
 - 26 **Prokesch RW**, Chow LC, Beaulieu CF, Bammer R, Jeffrey RB. Isoattenuating pancreatic adenocarcinoma at multi-detector row CT: secondary signs. *Radiology* 2002; **224**: 764-768 [PMID: 12202711]
 - 27 **Gabata T**, Matsui O, Kadoya M, Yoshikawa J, Miyayama S, Takashima T, Nagakawa T, Kayahara M, Nonomura A. Small pancreatic adenocarcinomas: efficacy of MR imaging with fat suppression and gadolinium enhancement. *Radiology* 1994; **193**: 683-688 [PMID: 7972808]
 - 28 **Vellet AD**, Romano W, Bach DB, Passi RB, Taves DH, Munk PL. Adenocarcinoma of the pancreatic ducts: comparative evaluation with CT and MR imaging at 1.5 T. *Radiology* 1992; **183**: 87-95 [PMID: 1312736]
 - 29 **Fukukura Y**, Takumi K, Kamimura K, Shindo T, Kumagai Y, Tateyama A, Nakajo M. Pancreatic adenocarcinoma: variability of diffusion-weighted MR imaging findings. *Radiology* 2012; **263**: 732-740 [PMID: 22623694 DOI: 10.1148/radiol.12011222]
 - 30 **Kartalis N**, Loizou L, Edsberg N, Segersvärd R, Albiin N. Optimising diffusion-weighted MR imaging for demonstrating pancreatic cancer: a comparison of respiratory-triggered, free-breathing and breath-hold techniques. *Eur Radiol* 2012; **22**: 2186-2192 [PMID: 22549106 DOI: 10.1007/s00330-012-2469-3]
 - 31 **Liu K**, Peng W, Zhou Z. The effect of gadolinium chelate contrast agent on diffusion-weighted imaging of pancreatic ductal adenocarcinoma. *Acta Radiol* 2013; **54**: 364-368 [PMID: 23386737 DOI: 10.1177/0284185112471795]
 - 32 **Miller FH**, Rini NJ, Kepke AL. MRI of adenocarcinoma of the pancreas. *AJR Am J Roentgenol* 2006; **187**: W365-W374 [PMID: 16985107]
 - 33 **Lee SS**, Byun JH, Park BJ, Park SH, Kim N, Park B, Kim JK, Lee MG. Quantitative analysis of diffusion-weighted magnetic resonance imaging of the pancreas: usefulness in characterizing solid pancreatic masses. *J Magn Reson Imaging* 2008; **28**: 928-936 [PMID: 18821618 DOI: 10.1002/jmri.21508]
 - 34 **Kang KM**, Lee JM, Yoon JH, Kiefer B, Han JK, Choi BI. Intravoxel incoherent motion diffusion-weighted MR imaging for characterization of focal pancreatic lesions. *Radiology* 2014; **270**: 444-453 [PMID: 24126370 DOI: 10.1148/radiol.13122712]
 - 35 **Concia M**, Sprinkart AM, Penner AH, Brossart P, Gieseke J, Schild HH, Willinek WA, Mürtz P. Diffusion-weighted magnetic resonance imaging of the pancreas: diagnostic benefit from an intravoxel incoherent motion model-based 3 b-value analysis. *Invest Radiol* 2014; **49**: 93-100 [PMID: 24089021 DOI: 10.1097/RLI.0b013e3182a71cc3]
 - 36 **Hur BY**, Lee JM, Lee JE, Park JY, Kim SJ, Joo I, Shin CI, Baek JH, Kim JH, Han JK, Choi BI. Magnetic resonance imaging findings of the mass-forming type of autoimmune pancreatitis: comparison with pancreatic adenocarcinoma. *J Magn Reson Imaging* 2012; **36**: 188-197 [PMID: 22371378 DOI: 10.1002/jmri.23609]
 - 37 **Ma X**, Zhao X, Ouyang H, Sun F, Zhang H, Zhou C. Quantified ADC histogram analysis: a new method for differentiating mass-forming focal pancreatitis from pancreatic cancer. *Acta Radiol* 2014; **55**: 785-792 [PMID: 24167322 DOI: 10.1177/0284185113509264]
 - 38 **Huang WC**, Sheng J, Chen SY, Lu JP. Differentiation between pancreatic carcinoma and mass-forming chronic pancreatitis: usefulness of high b value diffusion-weighted imaging. *J Dig Dis* 2011; **12**: 401-408 [PMID: 21955434 DOI: 10.1111/j.1751-2980.2011.00517.x]
 - 39 **Kamisawa T**, Takuma K, Anjiki H, Egawa N, Hata T, Kurata M, Honda G, Tsuruta K, Suzuki M, Kamata N, Sasaki T. Differentiation of autoimmune pancreatitis from pancreatic cancer by diffusion-weighted MRI. *Am J Gastroenterol* 2010; **105**: 1870-1875 [PMID: 20216538 DOI: 10.1038/ajg.2010.87]
 - 40 **Wiggermann P**, Grützmänn R, Weissenböck A, Kamusella P, Dittert DD, Stroszczynski C. Apparent diffusion coefficient measurements of the pancreas, pancreas carcinoma, and mass-forming focal pancreatitis. *Acta Radiol* 2012; **53**: 135-139 [PMID: 22262868 DOI: 10.1258/ar.2011.100252]
 - 41 **Klauss M**, Lemke A, Grünberg K, Simon D, Re TJ, Wente MN, Laun FB, Kauczor HU, Delorme S, Grenacher L, Stieltjes B. Intravoxel incoherent motion MRI for the differentiation between mass forming chronic pancreatitis and pancreatic carcinoma. *Invest Radiol* 2011; **46**: 57-63 [PMID: 21139505 DOI: 10.1097/RLI.0b013e3181fb3bf2]
 - 42 **Fattahi R**, Balci NC, Perman WH, Hsueh EC, Alkaade S, Havlioglu N, Burton FR. Pancreatic diffusion-weighted imaging (DWI): comparison between mass-forming focal pancreatitis (FP), pancreatic cancer (PC), and normal pancreas. *J Magn Reson Imaging* 2009; **29**: 350-356 [PMID: 19161187 DOI: 10.1002/jmri.21651]
 - 43 **Niu X**, Das SK, Bhetuwal A, Xiao Y, Sun F, Zeng L, Wang W, Yang H, Yang H. Value of diffusion-weighted imaging in distinguishing pancreatic carcinoma from mass-forming chronic pancreatitis: a meta-analysis. *Chin Med J (Engl)* 2014; **127**: 3477-3482 [PMID: 25269917]
 - 44 **Muraoka N**, Uematsu H, Kimura H, Imamura Y, Fujiwara Y, Murakami M, Yamaguchi A, Itoh H. Apparent diffusion coefficient in pancreatic cancer: characterization and histopathological correlations. *J Magn Reson Imaging* 2008; **27**: 1302-1308 [PMID: 18504750 DOI: 10.1002/jmri.21340]

- 45 **Rosenkrantz AB**, Matza BW, Sabach A, Hajdu CH, Hindman N. Pancreatic cancer: lack of association between apparent diffusion coefficient values and adverse pathological features. *Clin Radiol* 2013; **68**: e191-e197 [PMID: 23312674 DOI: 10.1016/j.crad.2012.11.006]
- 46 **Fukukura Y**, Takumi K, Higashi M, Shinchi H, Kamimura K, Yoneyama T, Tateyama A. Contrast-enhanced CT and diffusion-weighted MR imaging: performance as a prognostic factor in patients with pancreatic ductal adenocarcinoma. *Eur J Radiol* 2014; **83**: 612-619 [PMID: 24418286 DOI: 10.1016/j.ejrad.2013.12.016]
- 47 **Klauss M**, Gaida MM, Lemke A, Grünberg K, Simon D, Wente MN, Delorme S, Kauczor HU, Grenacher L, Stieltjes B. Fibrosis and pancreatic lesions: counterintuitive behavior of the diffusion imaging-derived structural diffusion coefficient d. *Invest Radiol* 2013; **48**: 129-133 [PMID: 23296083 DOI: 10.1097/RLI.0b013e31827ac0f1]
- 48 **Hayano K**, Miura F, Amano H, Toyota N, Wada K, Kato K, Sano K, Takeshita K, Aoyagi T, Shuto K, Matsubara H, Asano T, Takada T. Correlation of apparent diffusion coefficient measured by diffusion-weighted MRI and clinicopathologic features in pancreatic cancer patients. *J Hepatobiliary Pancreat Sci* 2013; **20**: 243-248 [PMID: 22311389 DOI: 10.1007/s00534-011-0491-5]
- 49 **Wernecke K**, Rummeny E, Bongartz G, Vassallo P, Kivelitz D, Wiesmann W, Peters PE, Reers B, Reiser M, Pircher W. Detection of hepatic masses in patients with carcinoma: comparative sensitivities of sonography, CT, and MR imaging. *AJR Am J Roentgenol* 1991; **157**: 731-739 [PMID: 1892027]
- 50 **Schulz W**, Borchard F. [The size of the liver metastases in a low metastatic count. A quantitative study of postmortem livers]. *Rofa* 1992; **156**: 320-324 [PMID: 1571511]
- 51 **Nickel MC**, Bipat S, Stoker J. Diagnostic imaging of colorectal liver metastases with CT, MR imaging, FDG PET, and/or FDG PET/CT: a meta-analysis of prospective studies including patients who have not previously undergone treatment. *Radiology* 2010; **257**: 674-684 [PMID: 20829538 DOI: 10.1148/radiol.10100729]
- 52 **Albiin N**. MRI of Focal Liver Lesions. *Curr Med Imaging Rev* 2012; **8**: 107-116 [PMID: 23049491]
- 53 **Holzappel K**, Reiser-Erkan C, Fingerle AA, Erkan M, Eiber MJ, Rummeny EJ, Friess H, Kleeff J, Gaa J. Comparison of diffusion-weighted MR imaging and multidetector-row CT in the detection of liver metastases in patients operated for pancreatic cancer. *Abdom Imaging* 2011; **36**: 179-184 [PMID: 20563868 DOI: 10.1007/s00261-010-9633-5]
- 54 **Holzappel K**, Bruegel M, Eiber M, Ganter C, Schuster T, Heinrich P, Rummeny EJ, Gaa J. Characterization of small (≤ 10 mm) focal liver lesions: value of respiratory-triggered echo-planar diffusion-weighted MR imaging. *Eur J Radiol* 2010; **76**: 89-95 [PMID: 19501995 DOI: 10.1016/j.ejrad.2009.05.014]
- 55 **Kim YK**, Lee MW, Lee WJ, Kim SH, Rhim H, Lim JH, Choi D, Kim YS, Jang KM, Lee SJ, Lim HK. Diagnostic accuracy and sensitivity of diffusion-weighted and of gadoxetic acid-enhanced 3-T MR imaging alone or in combination in the detection of small liver metastasis (≤ 1.5 cm in diameter). *Invest Radiol* 2012; **47**: 159-166 [PMID: 22330426 DOI: 10.1097/RLI.0b013e31823a1495]
- 56 **Coenegrachts K**, Orlent H, ter Beek L, Haspelslagh M, Bipat S, Stoker J, Rigauts H. Improved focal liver lesion detection: comparison of single-shot spin-echo echo-planar and superparamagnetic iron oxide (SPIO)-enhanced MRI. *J Magn Reson Imaging* 2008; **27**: 117-124 [PMID: 18050350]
- 57 **Kenis C**, Deckers F, De Foer B, Van Mieghem F, Van Laere S, Pouillon M. Diagnosis of liver metastases: can diffusion-weighted imaging (DWI) be used as a stand alone sequence? *Eur J Radiol* 2012; **81**: 1016-1023 [PMID: 21377305 DOI: 10.1016/j.ejrad.2011.02.019]
- 58 **Kim YK**, Kim CS, Han YM, Lee YH. Detection of liver malignancy with gadoxetic acid-enhanced MRI: is addition of diffusion-weighted MRI beneficial? *Clin Radiol* 2011; **66**: 489-496 [PMID: 21367403 DOI: 10.1016/j.crad.2010.09.007]
- 59 **Miller FH**, Hammond N, Siddiqi AJ, Shroff S, Khatri G, Wang Y, Merrick LB, Nikolaidis P. Utility of diffusion-weighted MRI in distinguishing benign and malignant hepatic lesions. *J Magn Reson Imaging* 2010; **32**: 138-147 [PMID: 20578020 DOI: 10.1002/jmri.22235]
- 60 **Shimada K**, Isoda H, Hirokawa Y, Arizono S, Shibata T, Togashi K. Comparison of gadolinium-EOB-DTPA-enhanced and diffusion-weighted liver MRI for detection of small hepatic metastases. *Eur Radiol* 2010; **20**: 2690-2698 [PMID: 20563726 DOI: 10.1007/s00330-010-1842-3]
- 61 **Matsuno S**, Egawa S, Fukuyama S, Motoi F, Sunamura M, Isaji S, Imaizumi T, Okada S, Kato H, Suda K, Nakao A, Hiraoka T, Hosotani R, Takeda K. Pancreatic Cancer Registry in Japan: 20 years of experience. *Pancreas* 2004; **28**: 219-230 [PMID: 15084961]
- 62 **Riall TS**, Cameron JL, Lillemoe KD, Campbell KA, Sauter PK, Coleman J, Abrams RA, Laheru D, Hruban RH, Yeo CJ. Pancreaticoduodenectomy with or without distal gastrectomy and extended retroperitoneal lymphadenectomy for periampullary adenocarcinoma--part 3: update on 5-year survival. *J Gastrointest Surg* 2005; **9**: 1191-204; discussion 1204-6 [PMID: 16332474]
- 63 **Imai H**, Doi R, Kanazawa H, Kamo N, Koizumi M, Masui T, Iwanaga Y, Kawaguchi Y, Takada Y, Isoda H, Uemoto S. Preoperative assessment of para-aortic lymph node metastasis in patients with pancreatic cancer. *Int J Clin Oncol* 2010; **15**: 294-300 [PMID: 20232101 DOI: 10.1007/s10147-010-0066-5]
- 64 **Mizukami Y**, Ueda S, Mizumoto A, Sasada T, Okumura R, Kohno S, Takabayashi A. Diffusion-weighted magnetic resonance imaging for detecting lymph node metastasis of rectal cancer. *World J Surg* 2011; **35**: 895-899 [PMID: 21327602 DOI: 10.1007/s00268-011-0986-x]
- 65 **Heijnen LA**, Lambregts DM, Mondal D, Martens MH, Riedl RG, Beets GL, Beets-Tan RG. Diffusion-weighted MR imaging in primary rectal cancer staging demonstrates but does not characterise lymph nodes. *Eur Radiol* 2013; **23**: 3354-3360 [PMID: 23821022 DOI: 10.1007/s00330-013-2952-5]
- 66 **Kamitani T**, Hatakenaka M, Yabuuchi H, Matsuo Y, Fujita N, Jinnouchi M, Nagao M, Shirahane K, Tokunaga E, Honda H. Detection of axillary node metastasis using diffusion-weighted MRI in breast cancer. *Clin Imaging* 2013; **37**: 56-61 [PMID: 23206608 DOI: 10.1016/j.clinimag.2012.02.014]
- 67 **Cho EY**, Kim SH, Yoon JH, Lee Y, Lim YJ, Kim SJ, Baek HJ, Eun CK. Apparent diffusion coefficient for discriminating metastatic from non-metastatic lymph nodes in primary rectal cancer. *Eur J Radiol* 2013; **82**: e662-e668 [PMID: 24016824 DOI: 10.1016/j.ejrad.2013.08.007]
- 68 **Cheng J**, Wang Y, Deng J, McCarthy RJ, Wang G, Wang H, Ye Y. Discrimination of metastatic lymph nodes in patients with gastric carcinoma using diffusion-weighted imaging. *J Magn Reson Imaging* 2013; **37**: 1436-1444 [PMID: 23172760 DOI: 10.1002/jmri.23925]
- 69 **Chen YB**, Liao J, Xie R, Chen GL, Chen G. Discrimination of metastatic from hyperplastic pelvic lymph nodes in patients with cervical cancer by diffusion-weighted magnetic resonance imaging. *Abdom Imaging* 2011; **36**: 102-109 [PMID: 19953246 DOI: 10.1007/s00261-009-9590-z]
- 70 **Roy C**, Bierry G, Matau A, Bazille G, Pasquali R. Value of diffusion-weighted imaging to detect small malignant pelvic lymph nodes at 3 T. *Eur Radiol* 2010; **20**: 1803-1811 [PMID: 20182732 DOI: 10.1007/s00330-010-1736-4]
- 71 **Wu LM**, Xu JR, Hua J, Gu HY, Zhu J, Hu J. Value of diffusion-weighted MR imaging performed with quantitative apparent diffusion coefficient values for cervical lymphadenopathy. *J Magn Reson Imaging* 2013; **38**: 663-670 [PMID: 23737291 DOI: 10.1002/jmri.24014]
- 72 **Bozkurt M**, Doganay S, Kantarci M, Yalcin A, Eren S, Atamanalp SS, Yuce I, Yildiran MI. Comparison of peritoneal tumor imaging using conventional MR imaging and diffusion-weighted MR imaging with different b values. *Eur J Radiol* 2011; **80**: 224-228 [PMID: 20598823 DOI: 10.1016/j.ejrad.2010.06.004]
- 73 **Low RN**, Sebrechts CP, Barone RM, Muller W. Diffusion-weighted MRI of peritoneal tumors: comparison with conventional MRI and

- surgical and histopathologic findings--a feasibility study. *AJR Am J Roentgenol* 2009; **193**: 461-470 [PMID: 19620444 DOI: 10.2214/AJR.08.1753]
- 74 **Niwa T**, Ueno M, Ohkawa S, Yoshida T, Doiuchi T, Ito K, Inoue T. Advanced pancreatic cancer: the use of the apparent diffusion coefficient to predict response to chemotherapy. *Br J Radiol* 2009; **82**: 28-34 [PMID: 19095814 DOI: 10.1259/bjr/43911400]
- 75 **Cuneo KC**, Chenevert TL, Ben-Josef E, Feng MU, Greenson JK, Hussain HK, Simeone DM, Schipper MJ, Anderson MA, Zalupski MM, Al-Hawary M, Galban CJ, Rehemtulla A, Feng FY, Lawrence TS, Ross BD. A pilot study of diffusion-weighted MRI in patients undergoing neoadjuvant chemoradiation for pancreatic cancer. *Transl Oncol* 2014; **7**: 644-649 [PMID: 25389460 DOI: 10.1016/j.tranon.2014.07.005]

P- Reviewer: Gonzalez-Reimers E, Guan YS, Ranieri G
S- Editor: Ji FF **L- Editor:** A **E- Editor:** Jiao XK



Malformations of cortical development: 3T magnetic resonance imaging features

Bilal Battal, Selami Ince, Veysel Akgun, Murat Kocaoglu, Emrah Ozcan, Mustafa Tasar

Bilal Battal, Selami Ince, Veysel Akgun, Murat Kocaoglu, Emrah Ozcan, Mustafa Tasar, Department of Radiology, Gulhane Military Medical School, 06018 Etlik, Ankara, Turkey

Murat Kocaoglu, Department of Radiology, Near East University, Faculty of Medicine, Nicosia, North Cyprus, Turkey

Author contributions: Battal B, Ince S, Akgun V, Ozcan E and Kocaoglu M designed and collected data; Battal B, Ince S and Akgun V written of the article; Battal B, Kocaoglu M and Tasar M reviewed and supervised the manuscript.

Conflict-of-interest statement: The authors declare no conflict of interests.

Open-Access: This article is an open-access article which was selected by an in-house editor and fully peer-reviewed by external reviewers. It is distributed in accordance with the Creative Commons Attribution Non Commercial (CC BY-NC 4.0) license, which permits others to distribute, remix, adapt, build upon this work non-commercially, and license their derivative works on different terms, provided the original work is properly cited and the use is non-commercial. See: <http://creativecommons.org/licenses/by-nc/4.0/>

Correspondence to: Bilal Battal, MD, Department of Radiology, Gulhane Military Medical School, General Doktor Tevfik Saglam Caddesi, 06018 Etlik, Ankara, Turkey. bilbat_23@yahoo.com
Telephone: +90-533-4330667
Fax: +90-312-3260551

Received: April 26, 2015
Peer-review started: May 11, 2015
First decision: June 24, 2015
Revised: July 31, 2015
Accepted: August 20, 2015
Article in press: August 21, 2015
Published online: October 28, 2015

Abstract

Malformation of cortical development (MCD) is a term representing an inhomogeneous group of central

nervous system abnormalities, referring particularly to embryological aspect as a consequence of any of the three developmental stages, *i.e.*, cell proliferation, cell migration and cortical organization. These include cortical dysgenesis, microcephaly, polymicrogyria, schizencephaly, lissencephaly, hemimegalencephaly, heterotopia and focal cortical dysplasia. Since magnetic resonance imaging is the modality of choice that best identifies the structural anomalies of the brain cortex, we aimed to provide a mini review of MCD by using 3T magnetic resonance scanner images.

Key words: Cortical development; Cortical dysplasia; Lissencephaly; Malformation; Polymicrogyria; Magnetic resonance imaging

© The Author(s) 2015. Published by Baishideng Publishing Group Inc. All rights reserved.

Core tip: Malformations of cortical development reflect embryological disruptions in neuronal proliferation, neuronal migration, cortical organization or multiple steps of the cortical development. Malformation of cortical development (MCDs) are important causes of refractory epilepsy. Magnetic resonance imaging including the advanced MRI techniques has a pivotal role in diagnosis of MCDs and prediction of feasibility of surgical management in cases that are refractory to medication.

Battal B, Ince S, Akgun V, Kocaoglu M, Ozcan E, Tasar M. Malformations of cortical development: 3T magnetic resonance imaging features. *World J Radiol* 2015; 7(10): 329-335 Available from: URL: <http://www.wjgnet.com/1949-8470/full/v7/i10/329.htm> DOI: <http://dx.doi.org/10.4329/wjr.v7.i10.329>

INTRODUCTION

Malformations of cortical development (MCDs) are a

complex group of abnormalities that may occur due to interruption the stages of proliferation, migration or postmigrational development of cortex. MCDs are common and important cause of seizures particularly in children. MCDs may result from lack of migration, over migration or ectopic migration of immature neurons^[1]. Magnetic resonance imaging (MRI) is the modality of choice that allows diagnosis of MCDs and correlation between radiologic and clinicopathologic findings related to MCDs^[2]. New techniques such as functional MRI (fMRI), MR spectroscopy and diffusion tensor imaging (DTI) are useful particularly for the detection of small sized or subtle MCDs^[2]. Barkovich *et al.*^[3] described the latest updated version of classification scheme for MCDs in 2012.

In this mini-review article, we discuss different types of cortical malformations in terms of their MRI characteristics. We illustrate their imaging features with emphasis on lesion location and direction of extension.

ADVANCED MRI IN MCD

MRI is the preferred imaging technique for determination and detailed assessment of MCD, with detailed information available from ultimate MR sequences and modalities. Advanced MRI sequences and techniques including volumetric three-dimensional (3D) gradient recalled echo (GRE) T1-weighted sequences, volumetric fluid attenuated inversion recovery (FLAIR), susceptibility weighted imaging (SWI), MR spectroscopy, fMRI and DTI have improved image quality and have been helpful in detection and characterization of MCDs and detailed evaluation of its extent and relationship with the surrounding white and gray matter areas.

Volumetric 3D GRE T1-weighted sequences allow high resolution multiplanar reformatted images, and support accurate diagnosis and detailed evaluation. For this purpose, slices of 1 mm thickness are gained with isotropic voxels. This allows high spatial resolution, more detailed evaluation of cortical thickness and morphology, and gray-white matter differentiation in three orthogonal planes in a reasonable time frame for clinical use. Volumetric FLAIR sequence may be useful in the determination of small signal changes and correct delineation of the borders of MCD and related signal changes, especially in 3T. SWI is a new, full-velocity-compensated high-resolution 3D GE sequence, useful for the evaluation of various pathologies characterized with punctate hemorrhages and calcification in brain parenchyma^[4,5].

Metabolic components of the brain tissue can be determined by proton MR spectroscopy *in vivo*. Simister *et al.*^[6] reported that large cortical malformations had abnormal levels of both glutamate + glutamine and gamma-aminobutyric acid. Low N-acetylaspartate (NAA) and high choline (Cho) levels were also observed. They concluded that MCD showed spectroscopic features of primitive tissue and abnormal metabolisms of both

inhibitory and excitatory neurotransmitters. MR spectroscopy technique demonstrated that MCD extends beyond the borders determined by the conventional MR imaging, even with sophisticated volumetric techniques^[7,8]. In a phosphorus MR spectroscopic study, Andrade *et al.*^[9] demonstrated widespread acidosis in the normal appearing parenchyma, and they concluded that visible lesions of the MCD are only the tip of the iceberg. MR spectroscopy examination can also be useful in differentiating low-grade tumor from focal cortical dysplasia (FCD) based on imaging can be challenging but important for treatment planning. The main difference was low level of NAA in gliomas compared to nearly normal levels of NAA in FCD and dysembryoplastic neuroectodermal tumor (DNET). In contrast, there were increased Cho levels in low-grade glioma compared to FCD.

fMRI can localize brain functions based on changes in blood flow and its data can be used in pre-surgical mapping. For the functional evaluation of the MCD, simple (sensomotor, visual) or complex (language, memory) fMRI paradigms can be used. fMRI technique can visualize the functions of the MCDs and their relationship to the eloquent cortex, and can provide important information to surgeons prior to epilepsy surgery^[10].

DTI gives microstructural data about tissues and provides further information on brain tissue that cannot be obtained by using conventional MR sequences. Microstructure of the tissue may change due to increase or decrease of neuronal cell volume, enlarged or reduced extracellular space and tissue damage, thus altered diffusion and fractional anisotropy may occur^[11]. MCD have features of loss of tissue organization and abnormalities of neuronal structure, but preserved normal cellular density. Therefore, reduced anisotropy but normal diffusivity values similar to the normal tissue are characteristic DTI findings of the MCD^[12,13].

MALFORMATIONS OF CORTICAL DEVELOPMENT

Disorders of proliferation

Cortical dysgenesis: Hemimegalencephaly is determined as a cortical dysgenesis in this new classification^[3]. Hemimegalencephaly is a hamartomatous malformation characterized by overgrowth of all or part of one cerebral hemisphere. Three different types are described. First type is isolated hemimegalencephaly, which is no hemispherical hypertrophy and not associated with cutaneous or systemic involvement (Figure 1). Second type is hemimegalencephaly associated with various neurocutaneous syndromes such as neurofibromatosis type 1, epidermal nevus syndrome, proteus syndrome, and tuberous sclerosis and also typically including hemispherical hypertrophy of the ipsilateral part of the body. The last and the rarest one is total hemimegalencephaly associated with hypertrophy of the ipsilateral cerebellar

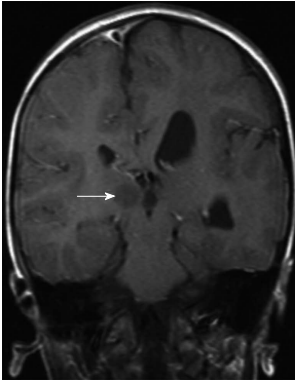


Figure 1 A 10-year-old boy with hemimegalencephaly. Coronal T1-weighted magnetic resonance image shows hypertrophy of the left cerebral hemisphere, mild enlargement of the left lateral ventricle, hamartoma (white arrow) in postero-medial area of the right thalamus.

hemisphere and brainstem. The cerebral cortical structures may be normal or dysplastic^[14,15].

Unlike other types of FCDs, FCD type II (FCD-II) is accepted in-group of cortical dysgenesis in the new classification of Barkovich *et al.*^[3] FCD-II has divided into two subgroups as type a and b^[16]. FCD-II is characterized by focal area of cortical thickening, marked blurring of gray and white matter junction, and in some cases signal change in adjacent white matter on T2-weighted and FLAIR images^[17]. On the other hand, it is harder to identify FCD-IIa than FCD-II b, and FCD-IIa cannot be always detected on MRI^[16].

FCDs can mimic gliomas. FCD-II often occurs in extra-temporal location especially frontal region, whereas a temporal location suggests gliomas^[18]. Since the cortical dysplasia primarily affect the gray matter and generally not associated with edema and gliosis, the increased signal on T2-weighted images is less distinct in FCDs when compared with the tumors (Figure 2). Gliomas may cause mass effect and frequently show intravenous contrast enhancement^[1].

Microcephaly: Congenital microcephaly refers to a head circumference of patient < 3 standard deviation below normal for that age without history of intrauterine damage^[1]. There is also another microcephaly entity, which is classified in abnormal postmigrational development group. This type patients born with normal or small head size, and severe microcephaly progresses within 1-2 years after the birth^[3].

Microcephaly with a simplified gyral pattern is a mild form of microlissencephaly, and characterized with profound microcephaly, significantly decreased number of sulci, sulcation abnormality, but normal cortical thickness (Figure 3). This malformation is generally not associated with other congenital structural anomalies^[1].

Disorders of migration

Periventricular heterotopia (subependymal nodular): Heterotopia is an abnormal location of neu-

rons anyplace between the subependymal region of the lateral ventricles and cerebral cortex secondary to arrest of radial migration^[1].

Periventricular (subependymal nodular) heterotopias are often bilateral and placed adjacent to the walls of the lateral ventricles, frequently in the peritrigonal regions, the temporal and occipital horns^[1]. The characteristic appearances of nodular heterotopia are small, round or oval shaped nodules isointense with gray matter on all MR sequences, located in subependymal layer, and do not show contrast enhancement (Figure 4). Periventricular heterotopia may project into the ventricular lumen (Figure 5)^[1].

Subcortical heterotopia (Band heterotopia): Subcortical band heterotopias (SCH) are located within the subcortical or deep white matter between the ventricular ependymal surface and the cerebral cortex. SCH may be in various forms including nodular, curvilinear or mixed. Thin overlying cortex and shallow sulci are characteristic findings for SCH (Figure 6)^[1,19].

SCH is a rare developmental malformation seen primarily in female and may be familial with X-linked dominant inheritance. On MRI, it shows a characteristic two parallel layers of gray matter separated by a thin white matter layer (3-layer cake: A thin outer ribbon, a very thin layer of white matter and a thick inner band (Figure 7)^[1,19].

Lissencephaly: Lissencephaly is defined as smooth brain and characterized with the absent normal gyral and sulcal pattern of the brain. The neocortex of lissencephalic patients lacks the normal cortical lamination and contains four layers instead of the six^[19]. Classic or type 1 lissencephaly appears as a complete or incomplete agyria. The complete form is characterized with smooth surface of entire brain. In the incomplete form, which is more commonly seen type, temporal lobes and inferior regions of frontal lobes have some gyral formation (Figure 8). The important MRI findings of classical lissencephaly are hourglass configuration, thick cortex and thin subcortical white matter, pachygyria-agyria areas, lack of gray-white matter interdigitation, and shallow Sylvian fissure^[1,19].

Cobblestone malformation: Cobblestone lissencephaly or formerly called type 2 lissencephaly is characterized by a nodular cortical surface accompanied by ocular anomalies and congenital muscular disorders^[1]. Cobblestone lissencephaly has been divided into three different groups based on severity: (1) Cobblestone lissencephaly occurs in various genetic conditions, with Walker-Warburg syndrome being the most severe form; (2) Fukuyama congenital muscular dystrophy, the mildest form; and (3) muscle-eye brain disease, the moderate form. Congenital muscular dystrophy is a key feature (Figure 9)^[19].

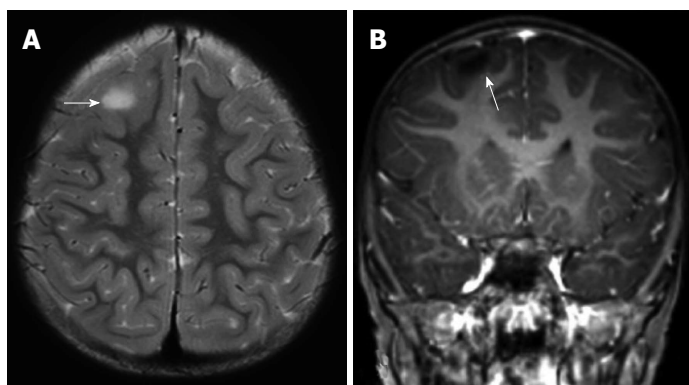


Figure 2 Focal cortical dysplasia type IIb of the left frontal cortex in a 3-year-old girl. Axial T2-weighted (A) and coronal T1-weighted (B) magnetic resonance images reveal a slight increase of white matter signal on T2-weighted image, significant blurring on T1-weighted image in gray matter-white matter junction (arrow).

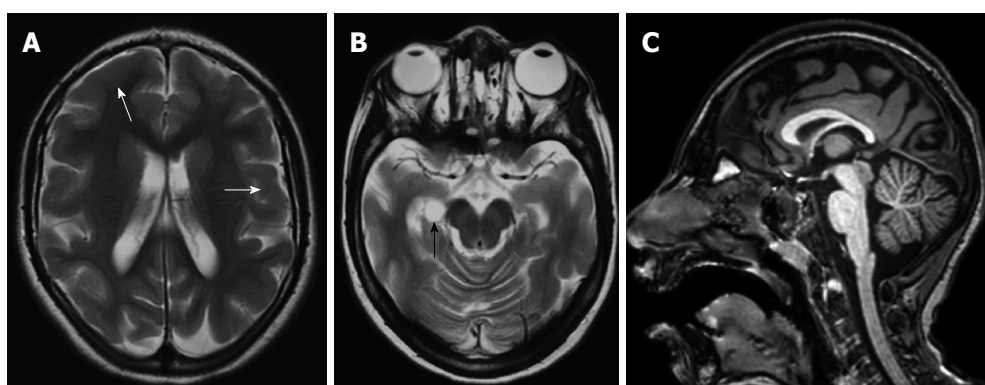


Figure 3 An 8-year-old girl with microlissencephaly. Axial T2-weighted images (A, B) show reduction in the number and depth of the sulcus, thickened cortex (white arrows) with choroidal fissure cyst (black arrow). Thinning of posterior parts of the corpus callosum is also seen on sagittal three-dimensional (3D) T1-weighted image (C).

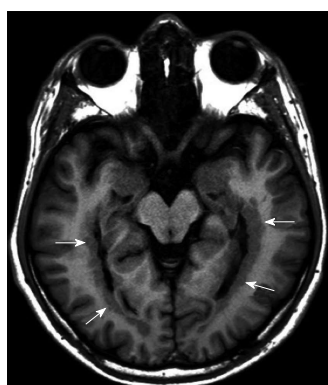


Figure 4 An 18-year-old boy with subependymal heterotopia. Axial inversion recovery T1-weighted image shows gray matter nodules located adjacent to bilateral periventricular temporal horn region (arrows).



Figure 5 A 7-mo girl with subependymal heterotopia. Sagittal T1-weighted image shows gray matter nodule located in the periventricular region that protrudes into the ventricular wall (arrow).

Disorders of postmigrational development

Polymicrogyria: Polymicrogyria (PMG) is caused by an interruption in normal cerebral cortical development in the late neuronal migration or early postmigrational development periods^[20]. The cortical surface appears thick and irregular or can have multiple small gyri separated by shallow sulci.

In the cases of PMG, the cerebral cortex may be

affected various degrees: Unilateral or bilateral; asymmetrical or symmetrical; single focal focus, multifocal, or diffuse. Around the Sylvian fissure, mostly posterior perisylvian area is the most common location (Figure 10)^[21].

For identifying PMG the combination of three characteristics on MR images has been used: (1) abnormal gyral pattern; (2) increased cortical thickness; and (3)

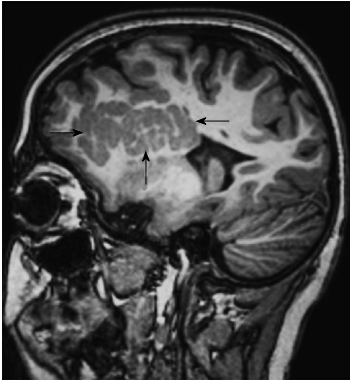


Figure 6 A 12-year-old boy with subcortical heterotopia. Sagittal 3D T1-weighted image shows large nodular form subcortical heterotopia (arrows) extends from the ventricle into the white matter in frontotemporal region.

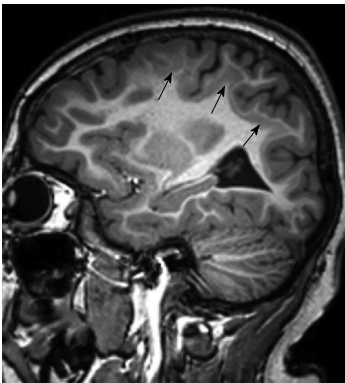


Figure 7 An 8-year-old girl with subcortical heterotopia. Sagittal 3D T1-weighted image shows band heterotopia (double cortex) located between the ventricular wall and the cerebral cortex (arrows).

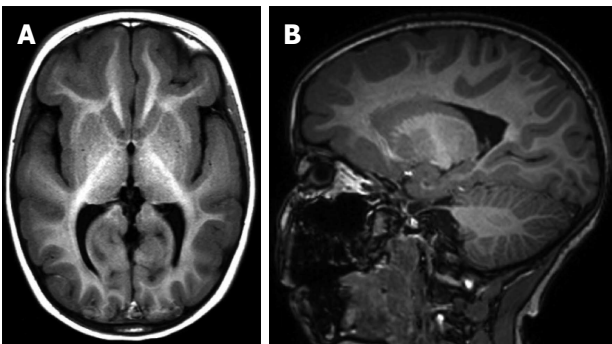


Figure 8 A 5-year-old girl with incomplete lissencephaly. Axial T1-weighted (A) and sagittal 3D T1-weighted (B) magnetic resonance images show pachygyria in frontotemporal region.

irregularity of the cortical–white matter junction due to packing of microgyri^[22]. These can be readily detected when thin sliced volumetric images are obtained^[21].

Schizencephaly: Schizencephaly is characterized by unilateral or bilateral full thickness cleft that is extending from the subarachnoid spaces to the ventricular system, and lined with gray matter^[23]. The cleft is often found in

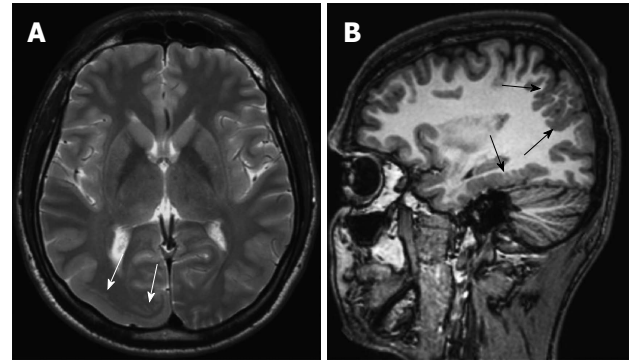


Figure 9 An 18-year-old boy with cobblestone lissencephaly. Axial T2-weighted image (A) shows incomplete lissencephaly in right occipital region (white arrows). Sagittal 3D T1-weighted image (B) reveals multiple areas of shallow microgyri (black arrows) in the parietal and temporal lobes.

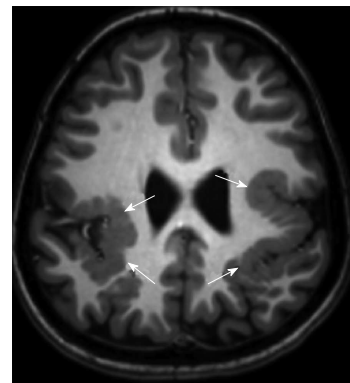


Figure 10 A 7-year-old boy with polymicrogyria. Axial 3D T1-weighted image shows bilateral perisylvian polymicrogyria (arrows).

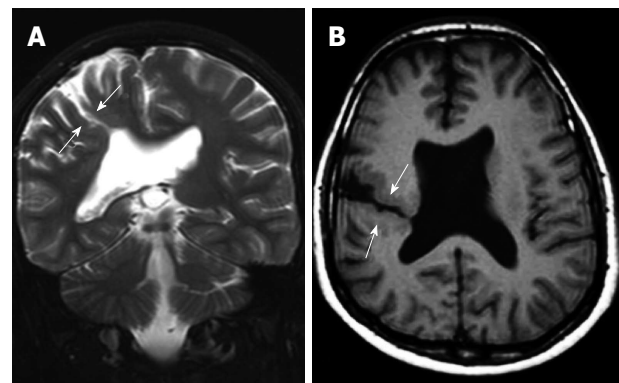


Figure 11 A 12-year-old boy with schizencephaly. T2-weighted coronal (A) and T1-weighted axial (B) images show oblique gray matter lined holohemispheric cleft (arrows) extending into the lateral ventricle that suggest open lip type schizencephaly with agenesis of septum pellucidum.

perisylvian areas, and may be small (closed lip type) or large (open lip type)^[24]. It may be associated with other malformations such as agenesis or dysgenesis of optic nerves, septum pellucidum (Figure 11), corpus callosum or hippocampus^[25].

FCD: FCD type I (FCD-I) and type III (FCD-III) are

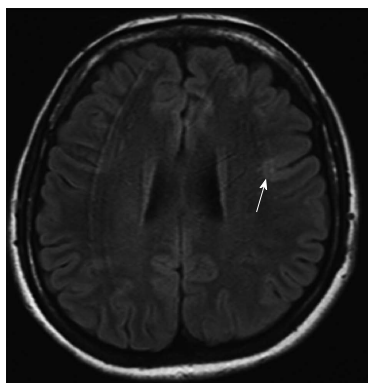


Figure 12 An 18-year-old girl with focal cortical dysplasia type I. Axial fluid attenuated inversion recovery image shows blurring at gray-white matter junction with normal gray matter signal in the posterior of the left frontal lobe (arrows).

in this group according to Barkovich *et al.*^[3] new MCD classification.

FCD- I is a malformation presenting with abnormal cortical layering, either settle with radial cortical lamination and maturation of neurons (FCD- I a) or the six-layered tangential cortical lamination of the neocortex (FCD- I b). The combination of these two subgroups is categorized as FCD- I c^[16].

MRI examination of FCD- I cases is usually normal^[15]. Hippocampal atrophy is frequently coexistent with FCD- I^[17]. In some cases, prominent segmental or lobar hypoplastic/atrophic changes and decrease the volume of subcortical white matter (Figure 12), sulcal and gyral pattern abnormalities may be seen. The most common location of FCD- I is the temporal lobe^[1,17].

FCD-III is divided into four subgroups; FCD-III a is in combination with hippocampal sclerosis. FCD-III b is associated with adjacent glial or glioneuronal tumors (*i.e.*, DNET, ganglioglioma). FCD-III c is characterized with cortical lamination abnormalities adjacent to vascular malformations, whereas FCD-III d is associated with any other acquired lesions in early life period (*i.e.*, post-traumatic lesions, ischemic injury, encephalitis)^[3,16,17].

CONCLUSION

MCD are an inhomogeneous group of central nervous system abnormalities and their diagnosis during the routine clinical and radiologic practice may be challenging. The suspicion of this kind of lesions arises when a sign is observed in clinical history, radiologic imaging or EEG findings. In some cases routine MRI scanning permit detection and definitive diagnosis of these pathologies. However, in most of the cases, careful evaluation of the MR imaging that contains some special sequences and special orientations are needed for definitive diagnosis and to determine the distribution and extent of MCD.

REFERENCES

- 1 Abdel Razek AA, Kandell AY, Elsorogy LG, Elmongy A, Basett

- AA. Disorders of cortical formation: MR imaging features. *AJNR Am J Neuroradiol* 2009; **30**: 4-11 [PMID: 18687750 DOI: 10.3174/ajnr.A2135]
- 2 Aronica E, Becker AJ, Spreafico R. Malformations of cortical development. *Brain Pathol* 2012; **22**: 380-401 [PMID: 22497611 DOI: 10.1111/j.1750-3639.2012.00581.x]
- 3 Barkovich AJ, Guerrini R, Kuzniecky RI, Jackson GD, Dobyns WB. A developmental and genetic classification for malformations of cortical development: update 2012. *Brain* 2012; **135**: 1348-1369 [PMID: 22427329 DOI: 10.1093/brain/aws019]
- 4 Andrade CS, Leite Cda C. Malformations of cortical development: current concepts and advanced neuroimaging review. *Arg Neuropsiquiatr* 2011; **69**: 130-138 [PMID: 21359436 DOI: 10.1590/S0004-282X2009000300041]
- 5 Battal B, Sari S, Hamcan S, Akgun V. Susceptibility-weighted imaging in the diagnosis of isolated cortical vein thrombosis. *Eur Neurol* 2014; **71**: 57-58 [PMID: 24334915 DOI: 10.1159/000355942]
- 6 Simister RJ, McLean MA, Barker GJ, Duncan JS. Proton magnetic resonance spectroscopy of malformations of cortical development causing epilepsy. *Epilepsy Res* 2007; **74**: 107-115 [PMID: 17379481 DOI: 10.1016/j.eplepsyres.2007.02.002]
- 7 Woermann FG, McLean MA, Bartlett PA, Barker GJ, Duncan JS. Quantitative short echo time proton magnetic resonance spectroscopic imaging study of malformations of cortical development causing epilepsy. *Brain* 2001; **124**: 427-436 [PMID: 11157569 DOI: 10.1093/brain/124.2.427]
- 8 Mueller SG, Laxer KD, Barakos JA, Cashdollar N, Flenniken DL, Vermathen P, Matson GB, Weiner MW. Metabolic characteristics of cortical malformations causing epilepsy. *J Neurol* 2005; **252**: 1082-1092 [PMID: 15868069 DOI: 10.1007/s00415-005-0819-7]
- 9 Andrade CS, Otaduy MC, Valente KD, Park EJ, Kanas AF, Silva Filho MR, Tsunemi MH, Leite CC. Widespread pH abnormalities in patients with malformations of cortical development and epilepsy: a phosphorus-31 brain MR spectroscopy study. *Brain Dev* 2014; **36**: 899-906 [PMID: 24485900 DOI: 10.1016/j.braindev.2013.12.010]
- 10 Janszky J, Ebner A, Kruse B, Mertens M, Jokeit H, Seitz RJ, Witte OW, Tuxhorn I, Woermann FG. Functional organization of the brain with malformations of cortical development. *Ann Neurol* 2003; **53**: 759-767 [PMID: 12783422 DOI: 10.1002/ana.10545]
- 11 Anderson AW, Zhong J, Petroff OA, Szafer A, Ransom BR, Prichard JW, Gore JC. Effects of osmotically driven cell volume changes on diffusion-weighted imaging of the rat optic nerve. *Magn Reson Med* 1996; **35**: 162-167 [PMID: 8622579 DOI: 10.1002/mrm.1910350206]
- 12 Rugg-Gunn FJ, Eriksson SH, Symms MR, Barker GJ, Duncan JS. Diffusion tensor imaging of cryptogenic and acquired partial epilepsies. *Brain* 2001; **124**: 627-636 [PMID: 11222461 DOI: 10.1093/brain/124.3.627]
- 13 Eriksson SH, Rugg-Gunn FJ, Symms MR, Barker GJ, Duncan JS. Diffusion tensor imaging in patients with epilepsy and malformations of cortical development. *Brain* 2001; **124**: 617-626 [PMID: 11222460 DOI: 10.1093/brain/124.3.617]
- 14 Flores-Sarnat L. Hemimegalencephaly: part 1. Genetic, clinical, and imaging aspects. *J Child Neurol* 2002; **17**: 373-384; discussion 384 [PMID: 12150586 DOI: 10.1177/088307380201700512]
- 15 Vurucu S, Battal B, Kocaoglu M, Akin R. Klippel-Trenaunay syndrome with hemimegalencephaly, retroperitoneal lymphangioma and double inferior vena cava. *Br J Radiol* 2009; **82**: e102-e104 [PMID: 19386952 DOI: 10.1259/bjr/36297676]
- 16 Blümcke I, Thom M, Aronica E, Armstrong DD, Vinters HV, Palmini A, Jacques TS, Avanzini G, Barkovich AJ, Battaglia G, Becker A, Cepeda C, Cendes F, Colombo N, Crino P, Cross JH, Delalande O, Dubeau F, Duncan J, Guerrini R, Kahane P, Mathern G, Najm I, Ozkara C, Raybaud C, Represa A, Roper SN, Salamon N, Schulze-Bonhage A, Tassi L, Vezzani A, Spreafico R. The clinicopathologic spectrum of focal cortical dysplasias: a consensus classification proposed by an ad hoc Task Force of the ILAE Diagnostic Methods Commission. *Epilepsia* 2011; **52**: 158-174 [PMID: 21219302 DOI: 10.1111/j.1528-1167.2010.02777.x]
- 17 Kabat J, Król P. Focal cortical dysplasia - review. *Pol J Radiol*

- 2012; **77**: 35-43 [PMID: 22844307 DOI: 10.12659/PJR.882968]
- 18 **Colombo N**, Salamon N, Raybaud C, Ozkara C, Barkovich AJ. Imaging of malformations of cortical development. *Epileptic Disord* 2009; **11**: 194-205 [PMID: 19720583 DOI: 10.1684/epd.2009.0262]
- 19 **Pang T**, Atefy R, Sheen V. Malformations of cortical development. *Neurologist* 2008; **14**: 181-191 [PMID: 18469675 DOI: 10.1097/NRL.0b013e31816606b9]
- 20 **Barkovich AJ**, Kuzniecky RI, Jackson GD, Guerrini R, Dobyns WB. A developmental and genetic classification for malformations of cortical development. *Neurology* 2005; **65**: 1873-1887 [PMID: 16192428 DOI: 10.1212/01.wnl.0000183747.05269.2d]
- 21 **Barkovich AJ**. Current concepts of polymicrogyria. *Neuroradiology* 2010; **52**: 479-487 [PMID: 20198472 DOI: 10.1007/s00234-009-0644-2]
- 22 **Barkovich AJ**, Hevner R, Guerrini R. Syndromes of bilateral symmetrical polymicrogyria. *AJNR Am J Neuroradiol* 1999; **20**: 1814-1821 [PMID: 10588102]
- 23 **Spalice A**, Parisi P, Nicita F, Pizzardi G, Del Balzo F, Iannetti P. Neuronal migration disorders: clinical, neuroradiologic and genetics aspects. *Acta Paediatr* 2009; **98**: 421-433 [PMID: 19120042 DOI: 10.1111/j.1651-2227.2008.01160.x]
- 24 **Granata T**, Freri E, Caccia C, Setola V, Taroni F, Battaglia G. Schizencephaly: clinical spectrum, epilepsy, and pathogenesis. *J Child Neurol* 2005; **20**: 313-318 [PMID: 15921232 DOI: 10.1177/08830738050200040801]
- 25 **Hayashi N**, Tsutsumi Y, Barkovich AJ. Morphological features and associated anomalies of schizencephaly in the clinical population: detailed analysis of MR images. *Neuroradiology* 2002; **44**: 418-427 [PMID: 12012128 DOI: 10.1007/s00234-001-0719-1]

P- Reviewer: Giovannetti G, Storto G
S- Editor: Ji FF **L- Editor:** A **E- Editor:** Jiao XK



Evaluation of primary adrenal insufficiency secondary to tuberculous adrenalitis with computed tomography and magnetic resonance imaging: Current status

Yu-Cheng Huang, Yu-Lian Tang, Xiao-Ming Zhang, Nan-Lin Zeng, Rui Li, Tian-Wu Chen

Yu-Cheng Huang, Yu-Lian Tang, Xiao-Ming Zhang, Nan-Lin Zeng, Rui Li, Tian-Wu Chen, Sichuan Key Laboratory of Medical Imaging, Department of Radiology, Affiliated Hospital of North Sichuan Medical College, Nanchong 637000, Sichuan Province, China

Author contributions: Huang YC and Chen TW wrote the paper; Tang YL, Zhang XM, Zeng NL and Li R performed the collected the data.

Conflict-of-interest statement: Authors declare no conflicts of interest for this article.

Open-Access: This article is an open-access article which was selected by an in-house editor and fully peer-reviewed by external reviewers. It is distributed in accordance with the Creative Commons Attribution Non Commercial (CC BY-NC 4.0) license, which permits others to distribute, remix, adapt, build upon this work non-commercially, and license their derivative works on different terms, provided the original work is properly cited and the use is non-commercial. See: <http://creativecommons.org/licenses/by-nc/4.0/>

Correspondence to: Tian-Wu Chen, MD, Sichuan Key Laboratory of Medical Imaging, Department of Radiology, Affiliated Hospital of North Sichuan Medical College, 63# Wenhua Road, Nanchong 637000, Sichuan Province, China. tianwuchen_nsmc@163.com
Telephone: +86-817-2262236
Fax: +86-817-2222856

Received: April 12, 2015

Peer-review started: April 13, 2015

First decision: August 15, 2015

Revised: August 25, 2015

Accepted: September 10, 2015

Article in press: September 16, 2015

Published online: October 28, 2015

Abstract

As one kind of infectious diseases of adrenal gland, adrenal tuberculosis can result in a life-threatening disorder which is called primary adrenal insufficiency (PAI) due to the destruction of adrenal cortex. Computed tomography (CT) and magnetic resonance imaging (MRI) play significant roles in the diagnosis of this etiology of PAI based on the CT and MRI appearances of the adrenal lesions. In this mini-review, we intend to study the CT and MRI features of adrenal tuberculosis, which could be helpful to both endocrinologist and radiologist to establish a definitive diagnosis for adrenal tuberculosis resulting in PAI.

Key words: Primary adrenal insufficiency; Tuberculosis; Adrenalitis; Computed tomography; Magnetic resonance imaging

© **The Author(s) 2015.** Published by Baishideng Publishing Group Inc. All rights reserved.

Core tip: Adrenal tuberculosis is an important cause of the primary adrenal insufficiency (PAI) due to the destruction of adrenal cortex. Computed tomography (CT) and magnetic resonance imaging (MRI) play vital roles in the diagnosis of this etiology of PAI based on the CT and MRI appearances of the adrenal lesions. We herein discuss the CT and MRI technique, manifestations, the role of CT and MRI in a definitive diagnosis for adrenal tuberculosis resulting in PAI.

Huang YC, Tang YL, Zhang XM, Zeng NL, Li R, Chen TW. Evaluation of primary adrenal insufficiency secondary to tuberculous adrenalitis with computed tomography and magnetic resonance

imaging: Current status. *World J Radiol* 2015; 7(10): 336-342
Available from: URL: <http://www.wjgnet.com/1949-8470/full/v7/i10/336.htm> DOI: <http://dx.doi.org/10.4329/wjr.v7.i10.336>

INTRODUCTION

Primary adrenal insufficiency (PAI), manifesting as clinically inadequate production or action of glucocorticoids, is a life-threatening disorder when at least 90 percent of adrenal cortex has been destroyed^[1,2]. As first depicted by Thomas Addison in 1855^[3], the clinical manifestation of adrenal insufficiency were characterized by weakness, malaise, nausea, fatigue, anorexia and abdominal pain, together with orthostatic hypotension, constipation, weight losing, salt craving and characteristic hyperpigmentation of the skin^[4-6]. The acute syndrome appears as a medical emergency since adrenal insufficiency may result in a severe hypotensive crisis and clouded sensorium^[7]. But most of the symptoms are not so specific that may delay diagnosis.

Adrenal tuberculosis has been regarded as an important cause of PAI since the first reports by Thomas Addison^[4,8]. During the past decades, incidence of adrenal tuberculosis has been greatly decreased due to the introduction of antituberculosis drugs. It is reported that PAI results from adrenal tuberculosis accounting for only 15%-20% patients in developed countries^[9]. However, adrenal tuberculosis is still the primary cause of PAI in developing countries^[10].

In the traditional diagnostic workup for adrenal insufficiency, basal detection of cortisol and adrenocorticotrophic hormone (ACTH) is sufficient for the diagnosis in most cases, but rarely the corticotropin test is required in primary failure^[11]. To confirm or rule out adrenal insufficiency, plasma cortisol can initially be measured between 8 and 9 am^[12]. The morning plasma cortisol concentrations of $\leq 3 \mu\text{g/dL}$ (83 nmol/L) are indicative of adrenal insufficiency, whereas concentrations of $\geq 19 \mu\text{g/dL}$ (525 nmol/L) rule out this disorder^[13,14]. The patients with plasma cortisol concentrations of 3-19 $\mu\text{g/dL}$ need the ACTH stimulation test. Additionally, basal plasma corticotropin should be measured in patients with possible PAI, and it can be found that plasma corticotropin concentrations invariably exceed 100 pg/mL (22 pmol/L), even though the plasma cortisol concentration is in the normal range^[1]. As for the ACTH stimulation test, the corticotrophin should be given intravenously or intramuscularly, and the serum cortisol level is usually measured before injection of 250 μg corticotrophin, and 30 or 60 min after this injection^[12,15]. Adrenal function is considered to be normal if the basal or the post-corticotropin plasma cortisol concentration is at least 18 $\mu\text{g/dL}$ (500 nmol/L), or at least 20 $\mu\text{g/dL}$ (550 nmol/L)^[12]. Most physicians use the highest plasma cortisol value before or after the injection of corticotropin as the criterion of normality and not the absolute increase in plasma cortisol after this injection.

With the laboratory diagnostic procedures, however, the causes of PAI caused by infectious diseases such as tuberculous adrenalitis cannot be recognized for appropriately essential therapy. Computed tomography (CT) and magnetic resonance imaging (MRI) play significant roles in evaluation of this etiology because the CT and MRI appearances of the underlying diseases depend not only on the pathologic nature but also on the duration of the illness and the type of treatment^[2,16,17]. Thus, we reviewed the CT and MRI features of tuberculous adrenalitis resulting in PAI for appropriate treatments.

CT TECHNIQUE

CT has been regarded as the modality of choice for identifying and characterizing tuberculous adrenalitis resulting in PAI^[18-22]. Prior to CT scan, opacification of the bowel should be carried out routinely with oral contrast materials, and 800-1000 mL of 1% solution of sodium diatrizoate is used as oral contrast material in our hospital. To show the adrenal tuberculosis, 3 mm helical collimation with the field of view targeted to the adrenal gland and 3 mm reconstruction interval was recommended for clinical examination^[18,23].

With the development of CT scanners, multidetector row CT (MDCT) has been used to depict the lesions of adrenal glands more and more frequently. In our institution, 16-row MDCT (Aquilion, Toshiba Medical Systems, Tokyo, Japan) has been used to detect the adrenal tuberculosis. Owing to the improvement of spatial resolution, small adrenal lesions can be detected on images of multiplanar reformation^[9]. Dual-energy CT was first utilized to evaluate the attenuation difference of adrenal lesions by Gupta *et al.*^[24].

There are two CT techniques including non-contrast and contrast-enhanced CT. Non-contrast CT scan can be performed to illustrate the calcified tissue. For well depicting tuberculous adrenalitis in the majority of patients with adrenal insufficiency, the non-contrast CT examination should be followed by a contrast enhanced study, which is performed 60-80 s after intravenously administering 80-100 mL of a contrast agent with 300 mg/mL of iodine at a rate of 3 mL/s by using a power injector.

MRI TECHNIQUE

MRI has been proven useful for evaluating the adrenal glands due to its advantages of superior contrast resolution and tissue characterization potential^[25-28]. Body coil is used for both excitation and reception of MR signal. Adrenal MRI should include T1-weighted axial images for showing the adrenal anatomy in detail, and T2-weighted axial images for showing the lesions^[29]. In our hospital, 1.5-T and 3.0-T MR scanners (Signa Excite; GE Medical System, Milwaukee, WI, United States) were used to detect the adrenal lesions, and adrenal MRI sequences include spin-echo or flash T1-

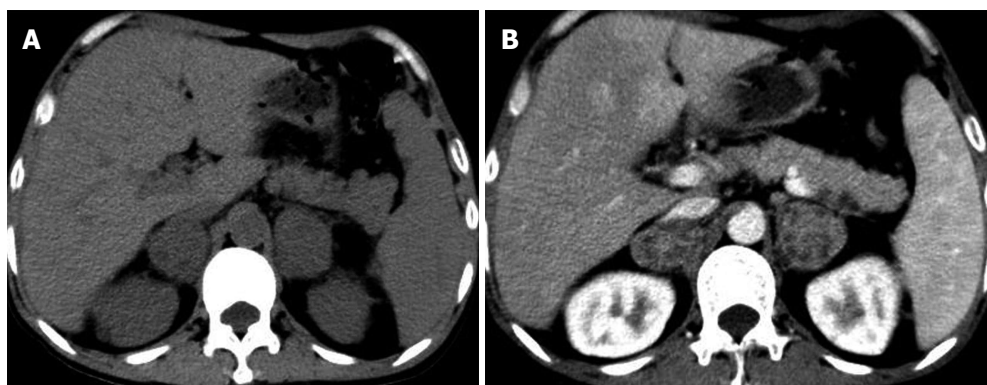


Figure 1 A 53-year-old man who has fatigue, pigmentation of skin and loss weight in last five months with primary adrenal insufficiency due to adrenal tuberculosis. The unenhanced (A) and contrast-enhanced (B) CT scans reveal the mass-like enlargement of the bilateral adrenals with multifocal peripheral enhancement. CT: Computed tomography.

weighted plain scan, and fast spin-echo T2-weighted scan. The adrenal MR images are acquired with a field of view of 35-45 cm, and 5-8 mm contiguous slice thickness. Enhanced T1-weighted images are acquired after intravenous administration of a bolus of 0.1 mmol/kg gadolinium diethylene triamine pentaacetic acid in our hospital. Because multiplanar imaging particularly including coronal section on all scanning series helps to detect extension of adrenal lesions into adjacent structures, the image planes are axial and coronal section on all scanning sequences at our institution. In addition, chemical-shift MRI with T1-weighted in-phase and out-of-phase gradient-echo pulse sequences and gadolinium-enhanced images is of great importance to evaluate the adrenal lesions^[30].

CT AND MRI MANIFESTATIONS OF ADRENAL TUBERCULOSIS

Adrenal tuberculosis occurs more commonly in bilateral glands (Figures 1-3) than in unilateral gland (Figure 4), and the occurrence of bilateral involvement is more than 80%^[2,9,23,31]. This predominant anatomic distribution may be explained by the reason that either of adrenal glands can be susceptible to infection by tubercle bacilli from the primary infection *via* hematogenous or lymph routes in equal incidence^[8]. The pathological changes of adrenal tuberculosis include tuberculous granuloma, caseous necrosis, fibrosis, cicatrix and calcification, and different CT and MR manifestations reflect the corresponding pathological changes.

Concerning on the adrenal contour, it varies during the courses of the adrenal tuberculosis. At early stage, the mass-like enlargement of the adrenals with tuberculosis can be frequently found on CT and MRI (Figures 1-4), but the contour of adrenal glands preserve^[2,9,23]. The radiologic appearances are pathologically based on the adrenals caseous necrosis area and tuberculous granuloma resulting from the destruction of the cortex by tuberculous mycobacteria^[32]. The mean course might

be approximately 3 years after the infection^[9,23].

At late stage, the enlarged tuberculous adrenal glands lessen or normalize pathologically in size or configuration due to the increase of fibrosis, fibrous cicatrix, and calcified tissue in the glands^[8,32,33]. When the continuous antituberculosis therapy is subsequently performed, the initially enlarged adrenal glands with smooth rounded contours become small with irregular margins (Figure 2) on follow-up CT and MRI^[8,9,23,32,34-37]. The adrenal glands become atrophic, and the pathological mechanism can be that the gland tissue is almost completely substituted with fibrous tissue or calcification^[2,35-37]. In general, small or atrophic adrenals indicate tuberculosis with long duration of adrenal insufficiency or quiescent adrenal tuberculosis, whereas enlarged adrenals suggest adrenal tuberculosis at early stage or active adrenal tuberculosis^[32,33,38-41].

As for adrenal calcification, it may be diffuse, localized or punctuated, and its incidence increases with the course of adrenal tuberculosis. The calcification, predominantly occurring at late stage of tuberculosis, cannot be well illustrated on MRI but on CT, and the incidence of calcification is more than one half when the diagnosis of adrenal tuberculosis is made^[33,41,42]. This manifestation may be due to the reason that the encapsulated granuloma becomes quiescent, and calcium salts deposit within the caseous regions at this stage^[9,23].

Another manifestation of adrenal tuberculosis is the density and enhancement on CT, or the signal intensity and enhancement on MRI at different stages. At early stage, the enlarged adrenals (Figures 1, 2 and 4) demonstrate central low density or homogeneous density on non-contrast CT scans, and peripheral enhancement with low density in the central area is observed on the contrast-enhanced scans in most of patients with adrenal tuberculosis^[9,23,42]. On MRI, the involved adrenals (Figure 3) appear as hypointense or isointense on T1-weighted images and hyperintense on T2-weighted images, and the glands with caseous

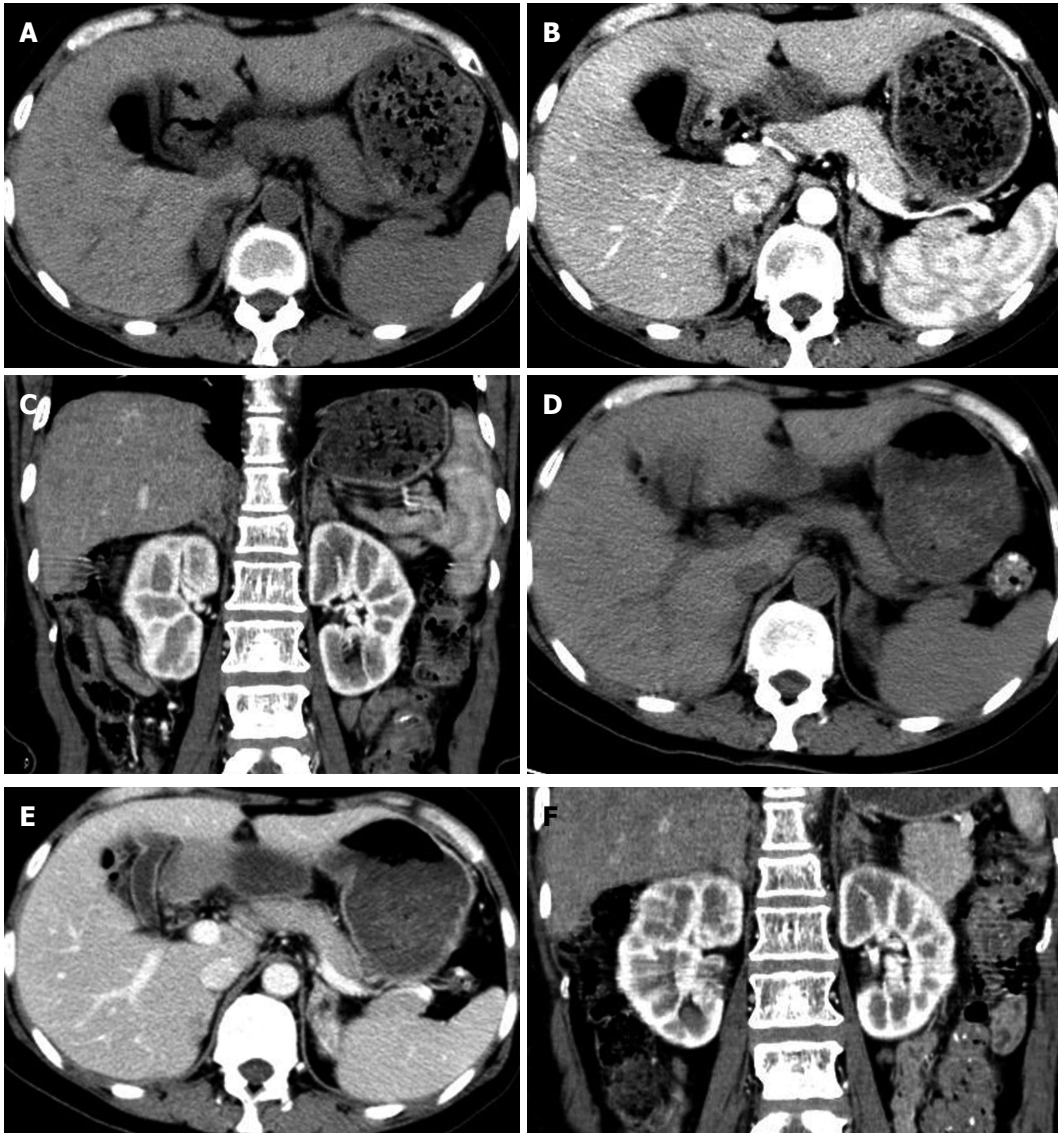


Figure 2 A 52-year-old woman who has anorexia, daytime somnolence and sweating in last three months with primary adrenal insufficiency due to adrenal tuberculosis. The unenhanced (A) and contrast-enhanced (B) CT scans reveal the mass-like enlargement of bilateral adrenals, but its contours are preserved with multifocal peripheral enhancement on axial (B) and coronary (C) reformed images. Three months after antituberculous therapy, the axial (D and E) and coronary (F) images demonstrate the initially enlarged adrenal glands become small with homogeneous density in the center, and decrease of probability of the presence of peripheral rim enhancement. CT: Computed tomography.

necrosis in the central area appear as peripheral rim enhancement on non-contrast CT^[2]. The enlarged adrenals without necrosis tissues in central zone display homogeneous enhancement on contrast-enhanced scans^[9]. The radiologic features reflect the pathologic feature of central caseous necrosis surrounded by fibrous tissue and granulomatous inflammatory tissue^[32,33,41,42].

If continuous antituberculosis therapy has been carried out, the adrenal lesions demonstrate homogeneous density (Figures 2D-F) or calcification in the center on CT scans, and the specific center with hypointense or isointense on T2 weighed images would appear on MRI due to a large amount of fibrous tissue, cicatrix, or calcification^[2,35-37]. When the lesions are completely substituted with fibrous tissue or calcification, the glands would show hypointense on all MR images^[2].

The probability of the presence of peripheral rim enhancement decreases on enhanced CT and MRI with the decrease of granuloma and caseating necrosis at late stage^[9,23]. In addition, contrast enhancement of adrenal tuberculosis could be quantitatively measured. As demonstrated by Ma *et al.*^[9], the difference in average density of the central zone of the enlarged adrenal glands between nonenhanced and enhanced CT scans is significantly less than that of peripheral zone (29 ± 2 HU vs 36 ± 11 HU).

Generally, the contrast-enhanced CT and MRI features of adrenal tuberculosis can provide information for the adrenal tuberculosis resulting in PAI, and might be useful for indicating the clinical duration of adrenal tuberculosis. However, some radiological features of adrenal tuberculosis could be similar with those of

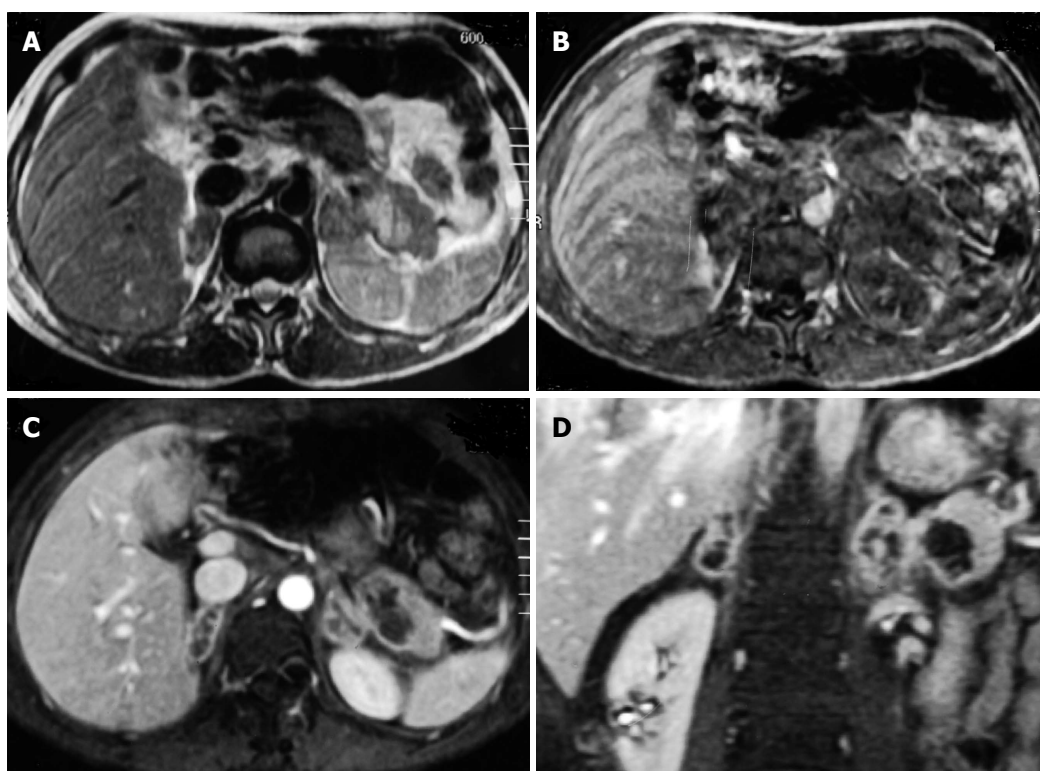


Figure 3 A 44-year-old man who has hypoglycemia and low blood pressure with primary adrenal insufficiency due to adrenal tuberculosis. MRI scans reveal the mass-like enlargement of bilateral adrenal glands on axial T1- weighted image (A) and T2-weighted image (B), but its contours are preserved with peripheral enhancement on contrast-enhanced axial (C) and coronal (D) T1-weighted image. MRI: Magnetic resonance imaging.

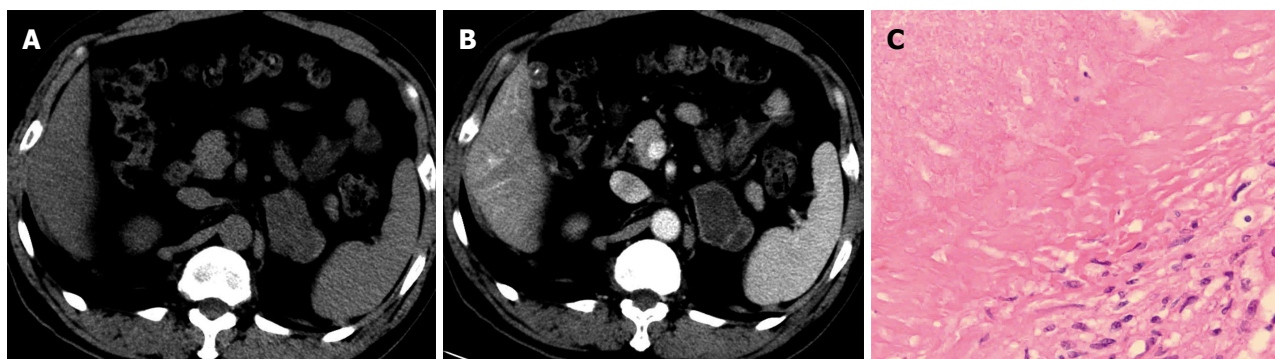


Figure 4 A 51-year-old man with pigmentation of skin and blood electrolyte abnormalities due to primary adrenal insufficiency due to adrenal tuberculosis. The unenhanced (A) and contrast-enhanced (B) CT scans illustrate the enlargement of the left adrenal gland with peripheral enhancement. This patient underwent adrenal pathology biopsy, and photomicrograph (C) shows central caseous necrosis surrounded by granulomatous inflammatory cells ($\times 40$). CT: Computed tomography.

adrenal fungal infections such as adrenal histoplasmosis. The diagnosis of adrenal tuberculosis should be considered in patients who has the CT and MRI features, and who has resided in an area where tuberculosis is not well controlled. Sometimes, biopsy is necessary for the diagnosis.

CONCLUSION

Adrenal tuberculosis can result in PAI. CT and MRI play important roles in the diagnosis of adrenal tuberculosis. Speed and availability of CT are of great importance to the diagnosis, and MRI can avoid the ionizing radiation

and perform multiparametric imaging and good spatial resolution. The radiological tools can well depict adrenal tuberculosis based on their pathologic nature and the duration of the illness, and the type of treatment. Understanding the imaging characteristics of adrenal tuberculosis is of great importance for correcting diagnosis and timely essential treatment of PAI secondary to adrenal tuberculosis.

REFERENCES

- 1 Oelkers W. Adrenal insufficiency. *N Engl J Med* 1996; **335**: 1206-1212 [PMID: 8815944 DOI: 10.1056/NEJM199610173351

- 607]
- 2 **Zhang XC**, Yang ZG, Li Y, Min PQ, Guo YK, Deng YP, Dong ZH. Addison's disease due to adrenal tuberculosis: MRI features. *Abdom Imaging* 2008; **33**: 689-694 [PMID: 18180983 DOI: 10.1007/s00261-007-9352-8]
- 3 **Addison T**. On the constitutional and local effects of disease of the supra-renal capsules (special ed 9th), 1855; Samuel Highley, London
- 4 **Løvås K**, Husebye ES. Addison's disease. *Lancet* 2005; **365**: 2058-2061 [PMID: 15950720 DOI: 10.1016/S0140-6736(05)66700-1]
- 5 **Kong MF**, Jeffcoate W. Eighty-six cases of Addison's disease. *Clin Endocrinol (Oxf)* 1994; **41**: 757-761 [PMID: 7889611 DOI: 10.1111/j.1365-2265.1994.tb02790.x]
- 6 **Nomura K**, Demura H, Saruta T. Addison's disease in Japan: characteristics and changes revealed in a nationwide survey. *Intern Med* 1994; **33**: 602-606 [PMID: 7827375 DOI: 10.2169/internalmedicine.33.602]
- 7 **Hahner S**, Loeffler M, Bleicken B, Drechsler C, Milovanovic D, Fassnacht M, Vetz M, Quinkler M, Allolio B. Epidemiology of adrenal crisis in chronic adrenal insufficiency: the need for new prevention strategies. *Eur J Endocrinol* 2010; **162**: 597-602 [PMID: 19955259 DOI: 10.1530/EJE-09-0884]
- 8 **Dunlop D**. Eighty-six cases of addison's disease. *Br Med J* 1963; **2**: 887-891 [PMID: 14067675 DOI: 10.1136/bmj.2.5362.887]
- 9 **Ma ES**, Yang ZG, Li Y, Guo YK, Deng YP, Zhang XC. Tuberculous Addison's disease: morphological and quantitative evaluation with multidetector-row CT. *Eur J Radiol* 2007; **62**: 352-358 [PMID: 17466476 DOI: 10.1016/j.ejrad.2006.12.012]
- 10 **Kinjo T**, Higuchi D, Oshiro Y, Nakamatsu Y, Fujita K, Nakamoto A, Owan I, Miyagi S, Kuba M, Fujita J. Addison's disease due to tuberculosis that required differentiation from SIADH. *J Infect Chemother* 2009; **15**: 239-242 [PMID: 19688243 DOI: 10.1007/s10156-009-0690-z]
- 11 **Schmidt IL**, Lahner H, Mann K, Petersenn S. Diagnosis of adrenal insufficiency: Evaluation of the corticotropin-releasing hormone test and Basal serum cortisol in comparison to the insulin tolerance test in patients with hypothalamic-pituitary-adrenal disease. *J Clin Endocrinol Metab* 2003; **88**: 4193-4198 [PMID: 12970286 DOI: 10.1210/jc.2002-021897]
- 12 **Grinspoon SK**, Biller BM. Clinical review 62: Laboratory assessment of adrenal insufficiency. *J Clin Endocrinol Metab* 1994; **79**: 923-931 [PMID: 7962298]
- 13 **Hägg E**, Asplund K, Lithner F. Value of basal plasma cortisol assays in the assessment of pituitary-adrenal insufficiency. *Clin Endocrinol (Oxf)* 1987; **26**: 221-226 [PMID: 3311477 DOI: 10.1111/j.1365-2265.1987.tb00780.x]
- 14 **Deutschbein T**, Unger N, Mann K, Petersenn S. Diagnosis of secondary adrenal insufficiency: unstimulated early morning cortisol in saliva and serum in comparison with the insulin tolerance test. *Horm Metab Res* 2009; **41**: 834-839 [PMID: 19585406 DOI: 10.1055/s-0029-1225630]
- 15 **Oelkers W**, Diederich S, Bähr V. Diagnosis and therapy surveillance in Addison's disease: rapid adrenocorticotropin (ACTH) test and measurement of plasma ACTH, renin activity, and aldosterone. *J Clin Endocrinol Metab* 1992; **75**: 259-264 [PMID: 1320051]
- 16 **Kawashima A**, Sandler CM, Fishman EK, Charnsangavej C, Yasumori K, Honda H, Ernst RD, Takahashi N, Raval BK, Masuda K, Goldman SM. Spectrum of CT findings in nonmalignant disease of the adrenal gland. *Radiographics* 1998; **18**: 393-412 [PMID: 9536486 DOI: 10.1148/radiographics.18.2.9536486]
- 17 **Charmandari E**, Nicolaides NC, Chrousos GP. Adrenal insufficiency. *Lancet* 2014; **383**: 2152-2167 [PMID: 24503135 DOI: 10.1016/S0140-6736(13)61684-0]
- 18 **Mayo-Smith WW**, Boland GW, Noto RB, Lee MJ. State-of-the-art adrenal imaging. *Radiographics* 2001; **21**: 995-1012 [PMID: 11452074 DOI: 10.1148/radiographics.21.4.g01j121995]
- 19 **Peña CS**, Boland GW, Hahn PF, Lee MJ, Mueller PR. Characterization of indeterminate (lipid-poor) adrenal masses: use of washout characteristics at contrast-enhanced CT. *Radiology* 2000; **217**: 798-802 [PMID: 11110946 DOI: 10.1148/radiology.217.3.r00dc29798]
- 20 **Arlt W**, Allolio B. Adrenal insufficiency. *Lancet* 2003; **361**: 1881-1893 [PMID: 12788587 DOI: 10.1016/S0140-6736(03)13492-7]
- 21 **Neary N**, Nieman L. Adrenal insufficiency: etiology, diagnosis and treatment. *Curr Opin Endocrinol Diabetes Obes* 2010; **17**: 217-223 [PMID: 20375886 DOI: 10.1097/MED.0b013e328338f608]
- 22 **Husebye E**, Løvås K. Pathogenesis of primary adrenal insufficiency. *Best Pract Res Clin Endocrinol Metab* 2009; **23**: 147-157 [PMID: 19500759 DOI: 10.1016/j.beem.2008.09.004]
- 23 **Guo YK**, Yang ZG, Li Y, Ma ES, Deng YP, Min PQ, Yin LL, Hu J, Zhang XC, Chen TW. Addison's disease due to adrenal tuberculosis: contrast-enhanced CT features and clinical duration correlation. *Eur J Radiol* 2007; **62**: 126-131 [PMID: 17182208 DOI: 10.1016/j.ejrad.2006.11.025]
- 24 **Gupta RT**, Ho LM, Marin D, Boll DT, Barnhart HX, Nelson RC. Dual-energy CT for characterization of adrenal nodules: initial experience. *AJR Am J Roentgenol* 2010; **194**: 1479-1483 [PMID: 20489086 DOI: 10.2214/AJR.09.3476]
- 25 **Gnannt R**, Fischer M, Goetti R, Karlo C, Leschka S, Alkadhi H. Dual-energy CT for characterization of the incidental adrenal mass: preliminary observations. *AJR Am J Roentgenol* 2012; **198**: 138-144 [PMID: 22194489 DOI: 10.2214/AJR.11.6957]
- 26 **Schultz CL**, Haaga JR, Fletcher BD, Alfidi RJ, Schultz MA. Magnetic resonance imaging of the adrenal glands: a comparison with computed tomography. *AJR Am J Roentgenol* 1984; **143**: 1235-1240 [PMID: 6333793 DOI: 10.2214/ajr.143.6.1235]
- 27 **Glazer GM**, Woolsey EJ, Borrello J, Francis IR, Aisen AM, Bookstein F, Amendola MA, Gross MD, Bree RL, Martel W. Adrenal tissue characterization using MR imaging. *Radiology* 1986; **158**: 73-79 [PMID: 3940402 DOI: 10.1148/radiology.158.1.3940402]
- 28 **Reinig JW**, Doppman JL, Dwyer AJ, Johnson AR, Knop RH. Adrenal masses differentiated by MR. *Radiology* 1986; **158**: 81-84 [PMID: 3940403 DOI: 10.1148/radiology.158.1.3940403]
- 29 **Outwater EK**, Siegelman ES, Huang AB, Birnbaum BA. Adrenal masses: correlation between CT attenuation value and chemical shift ratio at MR imaging with in-phase and opposed-phase sequences. *Radiology* 1996; **200**: 749-752 [PMID: 8756926 DOI: 10.1148/radiology.200.3.8756926]
- 30 **Woo S**, Cho JY, Kim SY, Kim SH. Adrenal adenoma and metastasis from clear cell renal cell carcinoma: can they be differentiated using standard MR techniques? *Acta Radiol* 2014; **55**: 1120-1128 [PMID: 24252816 DOI: 10.1177/0284185113512301]
- 31 **Bilbey JH**, McLoughlin RF, Kurkjian PS, Wilkins GE, Chan NH, Schmidt N, Singer J. MR imaging of adrenal masses: value of chemical-shift imaging for distinguishing adenomas from other tumors. *AJR Am J Roentgenol* 1995; **164**: 637-642 [PMID: 7863885 DOI: 10.2214/ajr.164.3.7863885]
- 32 **Efremidis SC**, Harsoulis F, Douma S, Zafiriadou E, Zamboulis C, Kouri A. Adrenal insufficiency with enlarged adrenals. *Abdom Imaging* 1996; **21**: 168-171 [PMID: 8661767 DOI: 10.1007/s002619900037]
- 33 **Vita JA**, Silverberg SJ, Golland RS, Austin JH, Knowlton AI. Clinical clues to the cause of Addison's disease. *Am J Med* 1985; **78**: 461-466 [PMID: 3976705 DOI: 10.1016/0002-9343(85)90339-0]
- 34 **Ammini AC**, Gupta R, Mukopadhyay C, Shah P, Sandhu MS, Vijayaraghavan M, Berry M. Computed tomography morphology of the adrenal glands of patients with Addison's disease. *Australas Radiol* 1996; **40**: 38-42 [PMID: 8838886 DOI: 10.1111/j.1440-1673.1996.tb00342.x]
- 35 **Fan ZM**, Zeng QY, Huo JW, Bai L, Liu ZS, Luo LF, Yang JC, Zhou XH. Macronodular multi-organs tuberculoma: CT and MR appearances. *J Gastroenterol* 1998; **33**: 285-288 [PMID: 9605964 DOI: 10.1007/s005350050085]
- 36 **Murata Y**, Yamada I, Sumiya Y, Shichijo Y, Suzuki Y. Abdominal macronodular tuberculomas: MR findings. *J Comput Assist Tomogr* 1996; **20**: 643-646 [PMID: 8708072 DOI: 10.1097/00004728-199607000-00027]
- 37 **Kawamori Y**, Matsui O, Kitagawa K, Kadoya M, Takashima

- T, Yamahana T. Macronodular tuberculoma of the liver: CT and MR findings. *AJR Am J Roentgenol* 1992; **158**: 311-313 [PMID: 1729789 DOI: 10.2214/ajr.158.2.1729789]
- 38 **Gülmez I**, Keleştimur F, Durak AC, Ozesmi M. Changes in the size of adrenal glands in acute pulmonary tuberculosis with therapy. *Endocr J* 1996; **43**: 573-576 [PMID: 8980899 DOI: 10.1507/endocrj.43.573]
- 39 **Doppman JL**, Gill JR, Nienhuis AW, Earll JM, Long JA. CT findings in Addison's disease. *J Comput Assist Tomogr* 1982; **6**: 757-761 [PMID: 7119194 DOI: 10.1097/00004728-198208000-00016]
- 40 **Villabona CM**, Sahun M, Ricart W, Serres X, Maroto A, Fernandez-Real JM, Gómez JM, Soler J. Tuberculous Addison's disease. Utility of CT in diagnosis and follow-up. *Eur J Radiol* 1993; **17**: 210-213 [PMID: 8293751 DOI: 10.1016/0720-048X(93)90106-W]
- 41 **Wang YX**, Chen CR, He GX, Tang AR. CT findings of adrenal glands in patients with tuberculous Addison's disease. *J Belge Radiol* 1998; **81**: 226-228 [PMID: 9880955]
- 42 **Yang ZG**, Guo YK, Li Y, Min PQ, Yu JQ, Ma ES. Differentiation between tuberculosis and primary tumors in the adrenal gland: evaluation with contrast-enhanced CT. *Eur Radiol* 2006; **16**: 2031-2036 [PMID: 16435135 DOI: 10.1007/s00330-005-0096-y]

P- Reviewer: Chu JP, Garcia-Elorriaga G,

Gumustas OG, Kumar J, Stanciu C

S- Editor: Qiu S **L- Editor:** A **E- Editor:** Jiao XK



Functional assessment of transplanted kidneys with magnetic resonance imaging

Yu-Ting Wang, Ying-Chun Li, Long-Lin Yin, Hong Pu, Jia-Yuan Chen

Yu-Ting Wang, Ying-Chun Li, Long-Lin Yin, Hong Pu, Jia-Yuan Chen, Department of Radiology, Sichuan Academy of Medical Sciences and Sichuan Provincial People's Hospital, Chengdu 610072, Sichuan Province, China

Author contributions: Wang YT and Chen JY developed the conception and designed the research; Wang YT, Li YC, Yin LL and Pu H performed the review of literature; Wang YT wrote the manuscript.

Supported by Scientific Research Subject of Health Department of Sichuan, China, No. 070045.

Conflict-of-interest statement: There is no conflict of interest associated with any of the authors contributed their efforts in this manuscript.

Open-Access: This article is an open-access article which was selected by an in-house editor and fully peer-reviewed by external reviewers. It is distributed in accordance with the Creative Commons Attribution Non Commercial (CC BY-NC 4.0) license, which permits others to distribute, remix, adapt, build upon this work non-commercially, and license their derivative works on different terms, provided the original work is properly cited and the use is non-commercial. See: <http://creativecommons.org/licenses/by-nc/4.0/>

Correspondence to: Yu-Ting Wang, MD, Physician of Radiology, Department of Radiology, Sichuan Academy of Medical Sciences and Sichuan Provincial People's Hospital, No. 32, Section 2, 1st Ring Road (West), Chengdu 610072, Sichuan Province, China. wangyuting_330@163.com
 Telephone: +86-28-87394280

Received: June 11, 2015

Peer-review started: June 15 2015

First decision: August 4, 2015

Revised: August 17, 2015

Accepted: September 7, 2015

Article in press: September 8, 2015

Published online: October 28, 2015

Abstract

Kidney transplantation has emerged as the treatment of

choice for many patients with end-stage renal disease, which is a significant cause of morbidity and mortality. Given the shortage of clinically available donor kidneys and the significant incidence of allograft dysfunction, a noninvasive and accurate assessment of the allograft renal function is critical for postoperative management. Prompt diagnosis of graft dysfunction facilitates clinical intervention of kidneys with salvageable function. New advances in magnetic resonance imaging (MRI) technology have enabled the calculation of various renal parameters that were previously not feasible to measure noninvasively. Diffusion-weighted imaging provides information on renal diffusion and perfusion simultaneously, with quantification by the apparent diffusion coefficient, the decrease of which reflects renal function impairment. Diffusion-tensor imaging accounts for the directionality of molecular motion and measures fractional anisotropy of the kidneys. Blood oxygen level-dependent MR evaluates intrarenal oxygen bioavailability, generating the parameter of R2* (reflecting the concentration of deoxyhemoglobin). A decrease in R2* could happen during acute rejection. MR nephro-urography/renography demonstrates structural data depicting urinary tract obstructions and functional data regarding the glomerular filtration and blood flow. MR angiography details the transplant vasculature and is particularly suitable for detecting vascular complications, with good correlation with digital subtraction angiography. Other functional MRI technologies, such as arterial spin labeling and MR spectroscopy, are showing additional promise. This review highlights MRI as a comprehensive modality to diagnose a variety of etiologies of graft dysfunction, including prerenal (*e.g.*, renal vasculature), renal (intrinsic causes) and postrenal (*e.g.*, obstruction of the collecting system) etiologies.

Key words: Magnetic resonance imaging; Diffusion-weighted imaging; Diffusion-tensor imaging; Kidney transplantation; Dysfunction; Magnetic resonance renography; Blood oxygen level-dependent; Magnetic resonance angiography; Functional evaluation

© The Author(s) 2015. Published by Baishideng Publishing Group Inc. All rights reserved.

Core tip: Kidney transplantation has been widely used clinically, and early detection of graft dysfunction with noninvasive imaging is crucial for postoperative management. Conventional imaging mainly focuses on morphology and has limited utility in functional aspects. Magnetic resonance imaging (MRI) has excellent soft-tissue contrast, and new technologies, such as diffusion-weighted imaging, diffusion-tensor imaging, blood oxygen level-dependent MRI, MR nephro-urography/renography, and MR angiography, provide more functional information and are therefore well suited to graft evaluation. This review illustrates the utility of functional MRI as a comprehensive modality to diagnose a variety of etiologies of graft dysfunction.

Wang YT, Li YC, Yin LL, Pu H, Chen JY. Functional assessment of transplanted kidneys with magnetic resonance imaging. *World J Radiol* 2015; 7(10): 343-349 Available from: URL: <http://www.wjgnet.com/1949-8470/full/v7/i10/343.htm> DOI: <http://dx.doi.org/10.4329/wjr.v7.i10.343>

BACKGROUND

Renal transplantation has been established as the preferred treatment for patients with end-stage renal diseases. It provides better a quality of life by sparing patients from lifelong dialysis and reduces morbidity and mortality. Early characterization and monitoring of dysfunction after renal transplantation are crucial to allow effective treatments and to improve the chance of a successful outcome^[1]. Despite continuously improving surgical techniques and immunosuppressive therapies, surgical and medical complications can still arise. After renal transplantation, at least one episode of acute allograft dysfunction occurs in approximately 30%-40% of patients. These dysfunctions have a variety of causes, including prerenal (e.g., renal vasculature), renal (mostly intrinsic causes) and postrenal (e.g., obstruction of the transplant collecting system) etiologies^[2,3].

The assessment of such large range of pathologies is difficult and relies heavily on invasive biopsies, with a risk of graft injury and loss^[4]. Noninvasive imaging evaluation of transplanted kidneys has been widely used and offers anatomic evaluation of possible complications; however, medical complications, such as acute and chronic rejection, acute tubular necrosis (ATN), and drug-related toxicity, remain diagnostic challenges^[5]. The utility of magnetic resonance imaging (MRI) in transplanted kidneys has been described for both anatomic and functional aspects, and it offers critical insights into the above-mentioned problems^[6-8]. In addition to the conventional MR sequences, new technologies, such as diffusion-weighted imaging (DWI) and diffusion-tensor imaging (DTI), blood oxygen

level-dependent (BOLD) imaging, nephro-urography, renography, and MR angiography (MRA), are being tested, and increasing amounts of clinical data are available. This article reviews the research progress of these technologies on the functional assessment of renal allograft and describes their specific clinical applications to diagnose various causes of graft dysfunction.

DWI AND DTI

Initially developed for the diagnosis of acute stroke, DWI has recently gained increasing importance in imaging beyond the brain for functional assessment^[9]. Any clinical MR unit can provide diffusion-weighted images by adding two equally large but opposite magnetic field gradients. Improved MR systems allows better magnetic field homogeneity, more effective fat suppression, fewer distortion artifacts and, probably most importantly, much stronger imaging gradients, therefore generating high-quality images with a sufficient signal-to-noise ratio^[5]. Compared to brain imaging, DWI in the lower abdomen is challenging due to motion-related artifacts. Optimization includes the reduction of echo times and geometric distortions, and nearly all examinations are performed by using echo planar imaging (EPI) sequences in the kidneys^[10-12]. For quantitative image analysis, DWI yields a total "apparent diffusion coefficient" (ADC_T) that provides information on diffusion and perfusion properties simultaneously if their contribution to total tissue diffusion can be separated. It is recommended that the ADCs of the medulla and cortex of the kidneys be analyzed separately if possible, due to their different intrinsic characteristics^[5].

In the kidneys, diffusion properties may be anisotropic because the main structures, such as vessels and tubules, exhibit a radial orientation, but DWI does not account for the directionality of molecular motion. The fractional anisotropy (F_A) of the kidneys can be assessed by DTI. The images can also be acquired with EPI sequence, and parametric ADC and F_A maps can be calculated online during image postprocessing^[13].

There currently are relatively limited data on the use of DWI in the assessment of transplanted kidneys. Thoeny *et al*^[10] investigated the DW imaging of transplanted kidneys in fifteen patients in stable condition and native kidneys in fifteen matched healthy volunteers. They measured ADC_T , an ADC reflecting pure diffusion (ADC_D) and the perfusion fraction (F_P). Compared with normal kidneys, renal allograft exhibited a lack of corticomedullary difference in the diffusion parameters. The authors claimed it was probably due either to the denervation of transplanted kidneys or to the secondary effects of immunosuppressive drugs. They also measured the within-subject parameters of repeated MRI, and coefficients of variation indicated that ADC was highly reproducible. In the same study, several examples were shown that focal hyperintense areas (corresponding to low ADC) might suggest acute rejection (AR) in pathological examinations.

Eisenberger *et al.*^[14] presented similar results on the lack of corticomedullary difference of transplanted kidneys using DWI. Moreover, they compared renal allografts with stable function and those with AR or ATN soon after transplantation, using histology sections from the biopsies as the reference. The results showed that the ADC_T values and, more remarkably, F_P were reduced in transplanted kidneys with AR and ATN, while ADC_D stayed relatively similar for all subjects. F_P values strongly decreased to less than 12% in the cortex and medulla of renal transplants with AR and ATN. The estimated glomerular filtration rate (eGFR) was shown to be significantly correlated with the F_P in the cortex and medulla, but not with ADC_T or ADC_D . Therefore, the authors proposed F_P as the most accurate indicator for allograft function assessment soon after transplant.

More recently, Kaul *et al.*^[15] compared DWI of renal allograft on the 7th day post-transplantation and corresponding kidney biopsy results. The ADC values were found to be slightly lower in the medulla compared with the cortex in transplanted kidneys with normal function. They also reported a significant reduction of ADC values in both the cortex and the medulla in allografts with abnormal function. More remarkably, such a reduction was correlated with the degree of rejection on the biopsies. Furthermore, the increase in ADC values was observed during the recovery from rejection, suggesting the usefulness of DWI for therapy monitoring after rejection episodes.

Lanzman *et al.*^[13] conducted DTI in addition to DWI in patients with kidney transplants. They employed eGFR to differentiate allografts into good or moderate function and impaired function. In functionally impaired renal allografts, both F_A and ADC of the renal medulla and cortex were significantly lower, and the corticomedullary difference in F_A values was also lower. The F_A of the medulla exhibited a high correlation with eGFR, while that of the cortex did not. In a more recent study conducted by Fan *et al.*^[16], similar results were reported, and the F_A of the medulla was proposed as a valuable indicator of allograft function. These data indicated that the results of DTI were generally concordant with DWI, while DTI might offer additional information on the differences between the renal medulla and cortex caused by anisotropy.

BOLD MRI

With the ability to measure intrarenal oxygenation, BOLD MRI has been used in native kidneys and has shown differences in medullary oxygenation during pathological conditions such as renal artery occlusion, water diuresis, and pharmacologic stimulation with Lasix, acetazolamide, and nitric oxide^[17,18]. Most published studies used a multiple gradient-recalled-echo sequence to perform BOLD MRI^[10,19,20]. This technique generates the parameter of $R2^*$, which is a measure of the rate of signal loss in a specific region and is related to the concentration of deoxyhemoglobin. Usually, $R2^*$ levels

are measured using the regions of interest (ROIs) tool. Experienced radiologists position certain numbers of ROIs in the cortical region and in the medullary region on the color $R2^*$ map.

Thoeny *et al.*^[10] compared BOLD images of the kidneys in patients with renal allografts and in healthy volunteers. Medullary $R2^*$ was observed to be significantly lower in the patients than in the volunteers. Moreover, coefficients of variation of repeated MRI showed that $R2^*$ was quite reproducible. This study investigated the correlation of parameters of DW imaging and BOLD imaging. In transplanted kidneys, $R2^*$ correlated negatively with ADC_T and ADC_D in the medulla.

Sadowski *et al.*^[19] also conducted BOLD MRI in patients who had received renal transplants. Twenty patients were included who had normal renal function, biopsy-proved ATN or AR. $R2^*$ values for the medulla were significantly lower in the AR group than the normal group and the ATN group. Using a certain threshold $R2^*$ value (18/s in this study), AR could be differentiated from normal function and ATN. $R2^*$ values for the cortex were higher in the ATN group than in the normal group and the AR group. More recently, Han *et al.*^[20] revealed similar results in a much larger patient group (110 patients). Sadowski *et al.*^[19] reported that the decreased $R2^*$ values in the medulla of kidneys with rejection could be due to changed hemodynamics and/or to reduced local oxygen consumption caused by decreased tubular function. These results established BOLD MRI as a promising tool to differentiate between AR and ATN.

MR NEPHRO-UROGRAPHY/RENOGRAPHY

MR nephro-urography/renography assessment of the renal allograft combines structural and functional data within a single imaging examination. While T2W images provide excellent anatomic information, post-contrast T1W 3D gradient-echo images have the capacity to provide functional data in addition to tissue enhancement. New advances in the quick acquisition of dynamic, postcontrast, time-resolved images and delayed postcontrast excretion urographic images have introduced comprehensive MR nephro-urography and renography, enabling quantitative measurements of renal function, including individual kidney GFR and renal blood flow, in postprocessing. More recently, multicompartmental kinetic modeling was applied in the postprocessing of MR renography, generating separate parameters for the vascular and tubular compartments^[21-24]. This model benefits from the use of the lowest possible concentration of gadolinium-chelate^[3].

To assess intrinsic causes of renal dysfunction, such as AR and ATN, Yamamoto *et al.*^[24] performed quantitative low-dose 3D MR renography on sixty patients with transplanted kidneys. The GFR and the mean transit time (MTT) of the tracer were calculated using a multicompartment renal model. GFR and MTT_k (MTT for the whole kidney) were significantly lower in the acute

Table 1 Main findings of recent studies exploring the use of magnetic resonance angiography

Ref.	Year	No. of Pt	Contrast	Criteria for artery stenosis	MRA findings	Reference and accuracy
Huber <i>et al</i> ^[28]	2001	41	Unclear ^a	> 0% as clinically significant	23 significant artery stenosis, 2 vein complications, 4 perfusion defects of the parenchyma	DSA; Se: 100%; Sp: 93%-97%
Gufler <i>et al</i> ^[33]	2008	63	Gd-DTPA	< 50%: mild; 50%-70%: moderate; > 70%: severe	Artery stenosis: 29 mild, 3 moderate, and 1 severe	DSA for severe stenosis, one overestimation
Lanzman <i>et al</i> ^[34]	2009	20	None (SSFP)	≥ 50% as clinically significant	6 significant artery stenosis	DSA; Se: 100%; Sp: 88%
Liu <i>et al</i> ^[30]	2009	13	None (SSFP)	≥ 50% as clinically significant	1 significant artery stenosis	Stenosis confirmed by DSA
Ismaeel <i>et al</i> ^[31]	2011	30	Unclear ^a	≥ 50% as clinically significant	15 significant artery stenosis	DSA; Se: 93.7%; Sp: 80%
Bashir <i>et al</i> ^[32]	2013	16	Ferumoxytol	Unclear	2 moderate to severe stenosis, 1 occlusion	Stenosis and occlusion confirmed by DSA
Hwang <i>et al</i> ^[11]	2013	144	Gadobutrol	< 50%: mild; 50%-70%: moderate; > 70%: severe	Artery stenosis: 10 mild, 5 moderate, and 8 severe; 17 renal parenchymal infarctions	Severe stenosis confirmed by DSA
Tang <i>et al</i> ^[29]	2014	75	None (SLEEK)	≥ 50% as clinically significant	14 artery stenosis (10 significant), other complications such as arteriovenous fistulas and pseudoaneurysms	Significant stenosis: DSA; positive predictive value: 91%

^aWith contrast, but unclear about the specific name. Pt: Patients; SSFP: Steady-state free precession; SLEEK: Spatial labeling with multiple inversion pulses; DSA: Digital subtraction angiography; Se: Sensitivity; Sp: Specificity; MRA: Magnetic resonance angiography.

dysfunction group than the normal function group. More specifically, the $MTT_{A/K}$ (fractional MTT of the tracer for the vascular compartment) was significantly higher in the AR group than in the normal function group or the ATN group. The $MTT_{T/K}$ (fractional MTT of the tracer for the tubular compartment) was significantly higher in the ATN group than in the normal function group or the AR group. The authors therefore claimed that this technique might help discriminate between AR and ATN. Researchers have also explored the use of other quantitative parameters, such as the medullary nephronal washout rate and the cortical arterial blood volume, but the results are still preliminary^[25].

To assess the postrenal etiology of renal allograft dysfunction, MR nephro-urography/renography offers functional information in addition to the exceptional soft-tissue contrast provided by standard MR images. Kalb *et al*^[3] has demonstrated how MR nephro-urography can guide clinical management with above-mentioned advantages. In addition to identifying anatomic variations, obstruction of transplant ureters, and fibrosis at certain anastomotic sites secondary to chronic ischemia, MR nephro-urography can enable precise measurement of GFR, thereby reflecting graft function.

MRA WITH OR WITHOUT CONTRAST

Vascular complications, such as artery stenosis, are relatively uncommon and are reported to occur in 5%-15% of transplanted kidneys, but they are a major cause of transplant loss, which usually necessitates resuming dialysis^[26,27]. Early and accurate diagnosis becomes critical because such complications are often correctable, and timely intervention can help salvage the graft kidney. Several studies have revealed the ability of

MRA to assess the renal parenchyma and peritransplant regions as well as vascular abnormalities^[1,28].

After conventional T1-weighted and T2-weighted sequences, an additional respiratory triggered 2D steady-state free precession (SSFP) sequence could be performed to visualize the vascular structure and generate reference images for planning the 3D contrast-enhanced MRA. A 3D gradient-echo sequence could then be initiated for angiography if contrast is used^[1,29].

Table 1 displays the main findings of the studies investigating the use of MRA for the assessment of transplanted kidneys^[1,28-34]. The primary strength of MRA is evaluating the stenosis of relevant arteries, and the results of these studies have shown a generally good correlation of MRA with digital subtraction angiography (DSA), which is the golden standard for vascular abnormalities. Other vascular complications, such as vein stenosis and arteriovenous fistulas, can also be detected; several studies have also reported the use of MRA to detect renal parenchymal infarctions and perfusion defects^[28,30].

There has been an ongoing discussion about the use of contrast agents. Early results have shown that time-of-flight MRA had inferior diagnostic effectiveness compared to contrast-enhanced MRA^[28]. In addition to conventional gadolinium chelate-based contrast agents, new contrasts claiming to be nonnephrotoxic, such as ferumoxytol, have been used in clinical trials. The initial findings of Bashir *et al*^[33] in renal transplant MRA using ferumoxytol have demonstrated excellent depiction of the transplant vasculature.

Recently, unenhanced MRA with advanced techniques, such as SSFP alone and spatial labeling with multiple inversion pulses, has made substantial progress and has been reported to be of comparable image quality and diagnostic accuracy with contrast-enhanced

MRA^[30,31]. However, the image quality of different artery segments might vary, as the image quality of the branches was observed to be inferior to that of the main arteries^[34].

OTHER FUNCTIONAL MRI TECHNIQUES

Arterial spin labeling (ASL) MRI was developed to measure tissue perfusion data and has been used extensively in the brain. Lanzman *et al.*^[35] conducted ASL MRI in 20 renal allograft recipients, divided into a good function group and an acute deterioration of renal function group. Quantitative measurement showed that cortical perfusion values were significantly reduced in transplanted kidneys with impaired function^[35]. Another study evaluated the reproducibility of ASL MRI in both native and transplanted kidneys. Intraclass correlation and coefficients of variation indicated that this technique was reproducible in the cortexes of native and transplanted kidneys, but that it demonstrated moderate to poor reproducibility for intravital and intervisit measures in the medulla^[36].

Studies have reported that chronic allograft dysfunction is accompanied by a decrease in the β -ATP/Pi ratio, a marker of kidney high-energy phosphate metabolism, as assessed by ³¹P-magnetic resonance spectroscopy (MRS), and that a relatively high β -ATP/Pi ratio (> 1.20 AU in one study) might indicate a good graft survival (probability > 3 years). Early improvement in the β -ATP/Pi ratio (within 6 mo) in renal transplant patients receiving short-term low-dose valsartan treatment can be detected by ³¹P-MRS^[37].

Magnetic resonance elastography (MRE) generates a quantitative measurement of tissue stiffness and has been widely used in the liver to assess the degree of fibrosis. Lee *et al.*^[38] performed MRE on 11 renal transplant patients and compared calculated the tissue stiffness value with histologic results. The mean stiffness value of patients with moderate interstitial fibrosis was higher than that of patients with mild or no interstitial fibrosis, but not significantly so. The authors suggested that multiple factors can influence renal stiffness^[38].

COMPARISON OF OTHER MODALITIES AND CLINICAL INDICATIONS

In evaluating transplanted kidneys, several imaging modalities are available for clinicians. The dysfunction of renal grafts is often clinically asymptomatic and presents only with an isolated increase in serum creatinine. To detect intrinsic etiologies, such as ATN or AR, color Doppler ultrasonography (US) is widely used because of its convenience and lack of radiation or toxic dye. However, it is user-dependent and its findings are often nonspecific for a final diagnosis or confirmation of normal function. Nuclear medicine (NM) imaging can be used to establish the flow, but its results can also be nonspecific to identify etiologies of dysfunction,

and it is time-consuming and not readily available^[8]. Functional MR technologies, such as DWI and DTI, could be recommended when patients have clinically suspicious intrinsic etiologies of graft dysfunction and negative or obscure results from US or NM imaging. Furthermore, these technologies have potential to monitor graft function during therapies. Quantitative measurements by BOLD MRI or 3D MR renography (especially when a multicompartment renal model is available) are worth considering to further differentiate between AR and ATN.

US is usually considered the first-line test to assess urologic obstructions, but the relatively poor anatomic detail it allows could lead to failure to identify the causes of the obstruction^[3,8]. Computed tomography (CT) can be used to detect nephrolithiasis-related obstructions, but it uses iodinated radiation and carries the risk of contrast nephropathy. MR nephro-urography can be recommended in such cases. With the exceptional soft-tissue contrast, MR nephro-urography may reveal causes such as anatomic variations and fibrosis at certain anastomotic sites while generating the precise value of GFR at the same time.

To evaluate vascular complications, US is generally used first, but it may be limited by the interposition of bowel gas between the transducer and the graft, and by issues of angulation and tortuosity caused by the irregular curvilinear anatomy of transplanted renal arteries. In addition, US cannot accurately visualize allograft artery stenosis in patients with high peak systolic velocities at the anastomosis^[1,8]. DSA is confirmatory and has the capacity of simultaneous interventions, but it is invasive and expensive. Computed tomographic angiography is valuable for evaluating graft vessels, but again, it uses iodinated contrast agents and exposes the patient to ionizing radiation. Gadolinium chelate-based contrast agents used in enhanced MRI are believed to be generally safer, and MRA without contrast with improved image quality and diagnostic accuracy has been proposed^[30,31,34]. Abundant evidence has shown the good correlation of MRA with DSA. Usually, patients with suspicion of transplant-related renal vascular complications, such as refractory hypertension and/or worsening graft function, elevated serum creatinine levels and nondiagnostic US findings are examined with MRA, which can assess renal parenchyma blood supply and the peritransplant region conditions in addition to the vascular abnormality.

MRI has limitations in clinical practices as well. It is less frequently available because, unlike US, the equipment is not portable, the cost is relatively high, and it requires specialized personnel who may not be available 24 h/d. Moreover, it carries the risk of nephrogenic systemic fibrosis in patients with a GFR lower than 30 mL/min per 1.73 m² in gadolinium-based studies^[8]. As with all medical procedures, a rational judgment must be applied to weigh the potential benefits against the risks.

CONCLUSION

To summarize, renal transplantation has been widely used clinically, and MRI is a noninvasive technique well suited for the assessment of renal allografts. Given the functional information provided by new technologies, MRI should be considered as a promising and powerful tool in the diagnostic workup for a variety of renal pathologic conditions, and it has the potential to significantly influence the postoperative management of kidney transplant patients. To further improve its diagnostic accuracy, a more comprehensive understanding of MRI, as well as knowledge of clinical situations, is recommended. The use of reproducible and representative quantitative parameters could be further explored, and clinical trials with larger sample sizes and solid references could offer critical clues.

ACKNOWLEDGMENTS

The authors thank Dr. Jonathan Fullner for editing part of the manuscript.

REFERENCES

- Hwang JK, Chun HJ, Kim JM, Kwon KH, Kim YK, Kim SD, Park SC, Choi BS, Kim JI, Yang CW, Kim YS, Moon IS. Contrast-enhanced magnetic resonance angiography in the early period after kidney transplantation. *Transplant Proc* 2013; **45**: 2925-2930 [PMID: 24157005 DOI: 10.1016/j.transproceed.2013.08.039]
- Chandraker A. Diagnostic techniques in the work-up of renal allograft dysfunction--an update. *Curr Opin Nephrol Hypertens* 1999; **8**: 723-728 [PMID: 10630820]
- Kalb B, Martin DR, Salman K, Sharma P, Votaw J, Larsen C. Kidney transplantation: structural and functional evaluation using MR Nephro-Urography. *J Magn Reson Imaging* 2008; **28**: 805-822 [PMID: 18821623 DOI: 10.1002/jmri.21562]
- Preda A, Van Dijk LC, Van Oostaijen JA, Pattynama PM. Complication rate and diagnostic yield of 515 consecutive ultrasound-guided biopsies of renal allografts and native kidneys using a 14-gauge Biopsy gun. *Eur Radiol* 2003; **13**: 527-530 [PMID: 12594555 DOI: 10.1007/s00330-002-1482-3]
- Thoeny HC, De Keyzer F. Diffusion-weighted MR imaging of native and transplanted kidneys. *Radiology* 2011; **259**: 25-38 [PMID: 21436095 DOI: 10.1148/radiol.10092419]
- Fang YC, Siegelman ES. Complications of renal transplantation: MR findings. *J Comput Assist Tomogr* 2001; **25**: 836-842 [PMID: 11711792]
- Browne RF, Tuite DJ. Imaging of the renal transplant: comparison of MRI with duplex sonography. *Abdom Imaging* 2006; **31**: 461-482 [PMID: 16447085 DOI: 10.1007/s00261-005-0394-5]
- Sharfuddin A. Renal relevant radiology: imaging in kidney transplantation. *Clin J Am Soc Nephrol* 2014; **9**: 416-429 [PMID: 24202132 DOI: 10.2215/CJN.02960313]
- Thoeny HC, De Keyzer F. Extracranial applications of diffusion-weighted magnetic resonance imaging. *Eur Radiol* 2007; **17**: 1385-1393 [PMID: 17206421 DOI: 10.1007/s00330-006-0547-0]
- Thoeny HC, Zumstein D, Simon-Zoula S, Eisenberger U, De Keyzer F, Hofmann L, Vock P, Boesch C, Frey FJ, Vermathen P. Functional evaluation of transplanted kidneys with diffusion-weighted and BOLD MR imaging: initial experience. *Radiology* 2006; **241**: 812-821 [PMID: 17114628 DOI: 10.1148/radiol.2413060103]
- Mürtz P, Flacke S, Träber F, van den Brink JS, Gieseke J, Schild HH. Abdomen: diffusion-weighted MR imaging with pulse-triggered single-shot sequences. *Radiology* 2002; **224**: 258-264 [PMID: 12091693 DOI: 10.1148/radiol.2241011117]
- Xu Y, Wang X, Jiang X. Relationship between the renal apparent diffusion coefficient and glomerular filtration rate: preliminary experience. *J Magn Reson Imaging* 2007; **26**: 678-681 [PMID: 17729335 DOI: 10.1002/jmri.20979]
- Lanzman RS, Ljimini A, Pentang G, Zgoura P, Zenginli H, Kröpil P, Heusch P, Schek J, Miese FR, Blondin D, Antoch G, Wittsack HJ. Kidney transplant: functional assessment with diffusion-tensor MR imaging at 3T. *Radiology* 2013; **266**: 218-225 [PMID: 23169797 DOI: 10.1148/radiol.12112522]
- Eisenberger U, Thoeny HC, Binser T, Gugger M, Frey FJ, Boesch C, Vermathen P. Evaluation of renal allograft function early after transplantation with diffusion-weighted MR imaging. *Eur Radiol* 2010; **20**: 1374-1383 [PMID: 20013274 DOI: 10.1007/s00330-009-1679-9]
- Kaul A, Sharma RK, Gupta RK, Lal H, Yadav A, Bhaduria D, Prasad N, Gupta A. Assessment of allograft function using diffusion-weighted magnetic resonance imaging in kidney transplant patients. *Saudi J Kidney Dis Transpl* 2014; **25**: 1143-1147 [PMID: 25394428]
- Fan WJ, Ren T, Li Q, Zuo PL, Long MM, Mo CB, Chen LH, Huang LX, Shen W. Assessment of renal allograft function early after transplantation with isotropic resolution diffusion tensor imaging. *Eur Radiol* 2015; Epub ahead of print [PMID: 26017738]
- Epstein FH, Veves A, Prasad PV. Effect of diabetes on renal medullary oxygenation during water diuresis. *Diabetes Care* 2002; **25**: 575-578 [PMID: 11874950]
- Juillard L, Lerman LO, Kruger DG, Haas JA, Rucker BC, Polzin JA, Riederer SJ, Romero JC. Blood oxygen level-dependent measurement of acute intra-renal ischemia. *Kidney Int* 2004; **65**: 944-950 [PMID: 14871414 DOI: 10.1111/j.1523-1755.2004.00469.x]
- Sadowski EA, Fain SB, Alford SK, Korosec FR, Fine J, Muehrer R, Djamali A, Hofmann RM, Becker BN, Grist TM. Assessment of acute renal transplant rejection with blood oxygen level-dependent MR imaging: initial experience. *Radiology* 2005; **236**: 911-919 [PMID: 16118170 DOI: 10.1148/radiol.2363041080]
- Han F, Xiao W, Xu Y, Wu J, Wang Q, Wang H, Zhang M, Chen J. The significance of BOLD MRI in differentiation between renal transplant rejection and acute tubular necrosis. *Nephrol Dial Transplant* 2008; **23**: 2666-2672 [PMID: 18308769 DOI: 10.1093/ndt/gfn064]
- Kalb B, Votaw JR, Salman K, Sharma P, Martin DR. Magnetic resonance nephrourography: current and developing techniques. *Radiol Clin North Am* 2008; **46**: 11-24, v [PMID: 18328877 DOI: 10.1016/j.rcl.2008.01.001]
- Lee VS, Rusinek H, Noz ME, Lee P, Raghavan M, Kramer EL. Dynamic three-dimensional MR renography for the measurement of single kidney function: initial experience. *Radiology* 2003; **227**: 289-294 [PMID: 12615998 DOI: 10.1148/radiol.2271020383]
- Martin DR, Sharma P, Salman K, Jones RA, Grattan-Smith JD, Mao H, Lauenstein TC, Burrow BK, Tudorascu DL, Votaw JR. Individual kidney blood flow measured with contrast-enhanced first-pass perfusion MR imaging. *Radiology* 2008; **246**: 241-248 [PMID: 18096538 DOI: 10.1148/radiol.2461062129]
- Yamamoto A, Zhang JL, Rusinek H, Chandarana H, Vivier PH, Babb JS, Diflo T, John DG, Benstein JA, Barisoni L, Stoffel DR, Lee VS. Quantitative evaluation of acute renal transplant dysfunction with low-dose three-dimensional MR renography. *Radiology* 2011; **260**: 781-789 [PMID: 21771953 DOI: 10.1148/radiol.11101664]
- de Priester JA, den Boer JA, Christiaans MH, Kessels AG, Giele EL, Hasman A, van Hooft HP, van Engelshoven JM. Automated quantitative evaluation of diseased and nondiseased renal transplants with MR renography. *J Magn Reson Imaging* 2003; **17**: 95-103 [PMID: 12500278 DOI: 10.1002/jmri.10217]
- Tarzamni MK, Argani H, Nurifar M, Nezami N. Vascular complication and Doppler ultrasonographic finding after renal transplantation. *Transplant Proc* 2007; **39**: 1098-1102 [PMID: 17524902 DOI: 10.1016/j.transproceed.2007.02.004]
- Dimitroulis D, Bokos J, Zavos G, Nikiteas N, Karidis NP, Katsaronis P, Kostakis A. Vascular complications in renal transp-

- lantation: a single-center experience in 1367 renal transplantations and review of the literature. *Transplant Proc* 2009; **41**: 1609-1614 [PMID: 19545690 DOI: 10.1016/j.transproceed.2009.02.077]
- 28 **Huber A**, Heuck A, Scheidler J, Holzknacht N, Baur A, Stangl M, Theodorakis J, Illner WD, Land W, Reiser M. Contrast-enhanced MR angiography in patients after kidney transplantation. *Eur Radiol* 2001; **11**: 2488-2495 [PMID: 11734946 DOI: 10.1007/s003300100992]
- 29 **Tang H**, Wang Z, Wang L, Hu X, Wang Q, Li Z, Li J, Meng X, Wang Y, Hu D. Depiction of transplant renal vascular anatomy and complications: unenhanced MR angiography by using spatial labeling with multiple inversion pulses. *Radiology* 2014; **271**: 879-887 [PMID: 24592960 DOI: 10.1148/radiol.14131800]
- 30 **Liu X**, Berg N, Sheehan J, Bi X, Weale P, Jerecic R, Carr J. Renal transplant: nonenhanced renal MR angiography with magnetization-prepared steady-state free precession. *Radiology* 2009; **251**: 535-542 [PMID: 19261926 DOI: 10.1148/radiol.2512081094]
- 31 **Ismaeel MM**, Abdel-Hamid A. Role of high resolution contrast-enhanced magnetic resonance angiography (HR CeMRA) in management of arterial complications of the renal transplant. *Eur J Radiol* 2011; **79**: e122-e127 [PMID: 21601400 DOI: 10.1016/j.ejrad.2011.04.039]
- 32 **Bashir MR**, Jaffe TA, Brennan TV, Patel UD, Ellis MJ. Renal transplant imaging using magnetic resonance angiography with a nonnephrotoxic contrast agent. *Transplantation* 2013; **96**: 91-96 [PMID: 23680931 DOI: 10.1097/TP.0b013e318295464c]
- 33 **Gufler H**, Weimer W, Neu K, Wagner S, Rau WS. Contrast enhanced MR angiography with parallel imaging in the early period after renal transplantation. *J Magn Reson Imaging* 2009; **29**: 909-916 [PMID: 19306426 DOI: 10.1002/jmri.21726]
- 34 **Lanzman RS**, Voiculescu A, Walther C, Ringelstein A, Bi X, Schmitt P, Freitag SM, Won S, Scherer A, Blondin D. ECG-gated nonenhanced 3D steady-state free precession MR angiography in assessment of transplant renal arteries: comparison with DSA. *Radiology* 2009; **252**: 914-921 [PMID: 19635833 DOI: 10.1148/radiol.2531082260]
- 35 **Lanzman RS**, Wittsack HJ, Martirosian P, Zgoura P, Bilk P, Kröpil P, Schick F, Voiculescu A, Blondin D. Quantification of renal allograft perfusion using arterial spin labeling MRI: initial results. *Eur Radiol* 2010; **20**: 1485-1491 [PMID: 19949799 DOI: 10.1007/s00330-009-1675-0]
- 36 **Artz NS**, Sadowski EA, Wentland AL, Djamali A, Grist TM, Seo S, Fain SB. Reproducibility of renal perfusion MR imaging in native and transplanted kidneys using non-contrast arterial spin labeling. *J Magn Reson Imaging* 2011; **33**: 1414-1421 [PMID: 21591011 DOI: 10.1002/jmri.22552]
- 37 **Fiorina P**, Bassi R, Gremizzi C, Vergani A, Caldara R, Mello A, Del Maschio A, De Cobelli F, Perseghin G, Secchi A. 31P-magnetic resonance spectroscopy (31P-MRS) detects early changes in kidney high-energy phosphate metabolism during a 6-month Valsartan treatment in diabetic and non-diabetic kidney-transplanted patients. *Acta Diabetol* 2012; **49** Suppl 1: S133-S139 [PMID: 22302190 DOI: 10.1007/s00592-012-0369-2]
- 38 **Lee CU**, Glockner JF, Glaser KJ, Yin M, Chen J, Kawashima A, Kim B, Kremers WK, Ehman RL, Gloor JM. MR elastography in renal transplant patients and correlation with renal allograft biopsy: a feasibility study. *Acad Radiol* 2012; **19**: 834-841 [PMID: 22503893 DOI: 10.1016/j.acra.2012.03.003]

P- Reviewer: Akoh JA, Logeswaran R,
Paraskevas K, Triantopoulou C
S- Editor: Ji FF **L- Editor:** A **E- Editor:** Jiao XK



Retrospective Cohort Study

Relevant incidental findings at abdominal multi-detector contrast-enhanced computed tomography: A collateral screening?

Luca Maria Sconfienza, Giovanni Mauri, Claudia Muzzupappa, Alessandro Poloni, Michele Bandirali, Anastassia Esseridou, Stefania Tritella, Francesco Secchi, Giovanni Di Leo, Francesco Sardanelli

Luca Maria Sconfienza, Giovanni Mauri, Michele Bandirali, Anastassia Esseridou, Stefania Tritella, Francesco Secchi, Giovanni Di Leo, Francesco Sardanelli, Servizio di Radiologia, IRCCS Policlinico San Donato, 20097 San Donato Milanese, Milano, Italy

Luca Maria Sconfienza, Francesco Secchi, Francesco Sardanelli, Dipartimento di Scienze Biomediche per la Salute, Università degli Studi di Milano, 20097 San Donato Milanese, Milano, Italy

Claudia Muzzupappa, Alessandro Poloni, Scuola di Specializzazione in Radiodiagnostica, Università degli Studi di Milano, 20122 Milano, Italy

Author contributions: Sconfienza LM, Mauri G, Di Leo G and Sardanelli F contributed to research pianification; Mauri G, Di Leo G and Sardanelli F contributed to statistical analysis; all authors contributed to data analysis, manuscript drafting and final approval.

Institutional review board statement: Institutional Review Board approval of IRCCS Ospedale San Raffaele, Milano, Italy was obtained.

Informed consent statement: Patients' informed consent was waived.

Conflict-of-interest statement: Authors have no conflict of interest to disclose related to the present paper.

Data sharing statement: Dataset is available from the corresponding author according to what is foreseen by the IRB.

Open-Access: This article is an open-access article which was selected by an in-house editor and fully peer-reviewed by external reviewers. It is distributed in accordance with the Creative Commons Attribution Non Commercial (CC BY-NC 4.0) license, which permits others to distribute, remix, adapt, build upon this work non-commercially, and license their derivative works on different terms, provided the original work is properly cited and

the use is non-commercial. See: <http://creativecommons.org/licenses/by-nc/4.0/>

Correspondence to: Luca Maria Sconfienza, MD, PhD, Servizio di Radiologia, IRCCS Policlinico San Donato, Piazza Malan 1, 20097 San Donato Milanese, Milano, Italy. io@lucasconfienza.it
Telephone: +39-02-52774468
Fax: +39-02-52774925

Received: May 16, 2015

Peer-review started: May 20, 2015

First decision: July 10, 2015

Revised: July 31, 2015

Accepted: August 20, 2015

Article in press: August 21, 2015

Published online: October 28, 2015

Abstract

AIM: To investigate the prevalence of relevant incidental findings (RIFs) detected during routine abdominal contrast-enhanced computed tomography (CeCT).

METHODS: We retrospectively evaluated the reports of a consecutive series of abdominal CeCT studies performed between January and May 2013. For each report, patients' age and sex, admission as inpatient or outpatient, clinical suspicion as indicated by the requesting physician, availability of a previous abdominal examination, and name of the reporting radiologist were recorded. Based on the clinical suspicion, the presence and features of any RIFs (if needing additional workup) was noted.

RESULTS: One thousand forty abdominal CeCT were performed in 949 patients (528 males, mean age 66 ±

14 years). No significant difference was found between inpatients and outpatients age and sex distribution ($P > 0.472$). RIFs were found in 195/1040 (18.8%) CeCT [inpatients = 108/470 (23.0%); outpatients = 87/570 (15.2%); $P = 0.002$]. RIFs were found in 30/440 (6.8%) CeCT with a previous exam and in 165/600 (27.5%) without a previous exam ($P < 0.001$). Radiologists' distribution between inpatients or outpatients was significantly different ($P < 0.001$). RIFs prevalence increased with aging, except for a peak in 40-49 year group. Most involved organs were kidneys, gallbladder, and lungs.

CONCLUSION: A RIF is detected in 1/5 patients undergoing abdominal CeCT. Risk of overdiagnosis should be taken into account.

Key words: Contrast-enhanced computed tomography; Abdomen; Incidental findings; Screening; Overdiagnosis

© **The Author(s) 2015.** Published by Baishideng Publishing Group Inc. All rights reserved.

Core tip: A relevant incidental finding (IF) is detected in one out of five patients undergoing abdominal contrast-enhanced computed tomography. Thus, in clinical practice, we daily perform unconscious collateral screening for a number of abdominal diseases. Notably, a problem still exists about how to deal with these findings, as their detection can be stressful and potentially harmful for patients, also contribute to increase in health care costs. On the one hand we have the risk of overdiagnosis, on the other hand there is a risk of legal issues for not having reported and suggested further work-up for these IFs.

Sconfienza LM, Mauri G, Muzzupappa C, Poloni A, Bandirali M, Esseridou A, Tritella S, Secchi F, Di Leo G, Sardanelli F. Relevant incidental findings at abdominal multi-detector contrast-enhanced computed tomography: A collateral screening? *World J Radiol* 2015; 7(10): 350-356 Available from: URL: <http://www.wjgnet.com/1949-8470/full/v7/i10/350.htm> DOI: <http://dx.doi.org/10.4329/wjr.v7.i10.350>

INTRODUCTION

Contrast-enhanced computed tomography (CeCT) has gained a crucial role in medical practice^[1]. With the increase of number and quality of CeCT examinations, a concurrent increase of unexpected (incidental) findings unrelated to clinical suspicion has occurred^[2]. Most of these incidental findings (IFs) are immediately recognized as benign or as anatomical variants and have no clinical relevance, but in a number of IFs additional workup is needed to reach a final diagnosis. This in turn generates anxiety for patients and additional costs for the healthcare systems^[3].

The discovery of an IF has been cited among the

causes of increased use of cross-sectional imaging and ionizing radiation exposure for medical reasons, being theoretically even detrimental for the patient^[1]. Balancing the benefit of an early detection of a disease with the risk of overdiagnosis is crucial from a societal viewpoint when a screening program is planned^[4]. Although some attempts to standardise the management of IFs have been made, in the clinical practice their management still vary widely between physicians and countries^[5].

Several studies have been devoted to assess the prevalence of IFs and their relevance^[6-12]. They have generally been performed to evaluate collateral findings detected during an imaging study dedicated to a single anatomical structure (e.g., IFs detected during CT colonography or cardiac CT/MRI, breast MRI, etc.)^[6-11] or performed in a specific clinical setting (e.g., IFs discovered during emergency abdominal CT)^[12]. Conversely, no data are available about relevant IFs that are occasionally detected in a series of consecutive patients undergoing abdominal CeCT.

The purpose of our work was to investigate the prevalence of relevant IFs detected during abdominal CeCT in the daily routine at our institution.

MATERIALS AND METHODS

Institutional Review Board approval of IRCCS Ospedale San Raffaele, Milano, Italy was obtained and patients' informed consent was waived. Our report is concerned with a retrospective evaluation of the reports of a consecutive series of abdominal CeCT performed at our institution between January and May 2014, including inpatients, outpatients, and patients coming from the emergency department. The last ones were considered as outpatients. CeCT examinations were performed using either a 16- or 64-slice CT systems (SOMATOM Emotion and Sensation, respectively; Siemens Medical, Erlangen, Germany) with oral administration of variable amount of diluted water-soluble iodinated contrast agent (Gastrografen, Bayer-Schering, Germany) and intravenous injection of iodinated contrast agent (Iomeron 350, Bracco, Milano, Italy) using different acquisition protocol according to the clinical suspicion. Electronic reports were retrieved from our radiology information system (RIS) (PolarIS, El.Co., Cairo Montenotte, Savona, Italy) and were reviewed in consensus by two radiology residents (CM and MB) with three years' experience in CeCT. For each report, they recorded patients' age and sex, his/her admission as inpatient or outpatient, the clinical suspicion as indicated by the requesting physician, and the name of the radiologist who signed the report. Based on the clinical suspicion, the report was searched to detect the presence of relevant IFs. IF was defined as "an incidentally discovered mass or lesion detected by abdominal CeCT performed for an unrelated reason"^[5]. IFs were considered as relevant if additional workup (other imaging tests, clinical evaluation, or follow-up) was suggested by the reporting

Table 1 Percentage of relevant incidental findings among inpatients and outpatients, with or without a previous exam *n* (%)

	Previous exam		<i>P</i>	Odds ratio (no/yes)
	Yes	No		
Inpatients	14/187 (7.5)	94/283 (33.2)	< 0.001	4.7
Outpatients	16/253 (6.3)	71/217 (22.4)	< 0.001	3.7
<i>p</i>	0.632	0.003		

P-values were calculated using the χ^2 test.

radiologist. If no specific note was included in the report, the two reviewers assessed in consensus the needing of additional workup. In case of disagreement, a staff radiologist with 10 years of experience in CeCT (LMS) addressed the issue.

For all patients, reviewers noted the presence of previous cross-sectional imaging exams (ultrasound, CT, or magnetic resonance imaging) performed within one year. If this information was already included in the report, patients were classified as provided with a previous examination. Thus, reviewers rated any newly reported IF as not already known. If the report did not include any information, previous exams were searched for in our RIS. Finally, if none of the two abovementioned criteria were applicable, patients were considered to be lacking of previous exams. For patients who underwent more than one abdominal CeCT in the considered period, the first exam was treated according to the abovementioned criteria, while the second and/or the third following exam was considered to have an available previous exam.

Relevant IFs were also stratified according to 10-year age groups and classified according to the organ involved.

Data and statistical analysis

Statistical analysis was performed by one of the authors (GDL) who has advanced statistical expertise. Data regarding the present paper may be shared upon request prior further Institutional Review Board Approval.

Age distribution between inpatients and outpatients subgroups was compared using the *U* Mann-Whitney test. Sex distribution between inpatients and outpatients, as well as relevant IFs distribution in our series was compared within different subgroups (inpatients, outpatients, patients with or without a previous exam) using the Chi-square test. Odds ratios were also calculated. All calculations were performed using SPSS Statistics v. 19 (SPSS, Chicago, IL, United States) and Excel (Microsoft Excel® 2010, Redmond, WA, United States). A *P*-value less than 0.05 was considered as significant.

RESULTS

In the considered period, 1040 abdominal CeCT were performed in 949 patients (528 males, 421 females,

Table 2 Number of inpatients and outpatients with or without a previous exam *n* (%)

	Previous exam		Yes/no
	Yes	No	
Inpatients	187/1040 (18.0)	283/1040 (27.2)	0.66
Outpatients	253/1040 (24.3)	317/1040 (30.5)	0.80
Inpatients/outpatients	0.74	0.89	<i>P</i> = 0.152

P-value was calculated using the χ^2 test.

mean age \pm standard deviation 66 ± 14 years); 75 patients underwent two CeCT examinations and eight patients underwent three CeCT examinations.

Four hundred seventy out of 1040 (45.2%) CeCT examinations were performed in 401 inpatients (228 males, 173 females; mean age 67 ± 15 years) and 570/1040 (54.8%) in 548 outpatients (300 males, 248 females; mean age 65 ± 12 years). Age and sex distribution was not significantly different between inpatients and outpatients (*P* = 0.472 and *P* = 0.717, respectively).

Overall, relevant IFs were found in 195/1040 (18.8%) CeCT, one IF per exam: 108/470 (23.0%) in inpatients and 87/570 (15.2%) in outpatients, the difference being statistically significant (*P* = 0.002).

A previous exam was available for 440/1040 (42.3%) CeCT examinations while it was not available for the remaining 600/1040 (57.7%). Relevant IFs were found in 30/440 (6.8%) CeCT with a previous exam and in 165/600 (27.5%) with no previous exam (*P* < 0.001). Subgroup analyses between inpatients and outpatients, with or without a previous exam are reported in Tables 1 and 2. No statistical difference was found regarding the number of patients with or without previous exams subdivided into inpatients and outpatients.

Exams were reported by nine different radiologists with three to 20 years experience in abdominal CeCT. The distribution of radiologists who reported CeCT exams of inpatients or outpatients was significantly different (*P* < 0.001). Full data are reported in Table 3.

Distribution of relevant IFs stratified according to 10-year age groups (total, inpatients, and outpatients) is shown in Table 4 and graphically represented in Figure 1.

Distribution of relevant IFs among involved organs is shown in Table 5. A list of the relevant IFs is reported in Table 6.

DISCUSSION

This study was performed to evaluate the prevalence of relevant IFs in a consecutive series of patients who underwent abdominal CeCT at our institution. Our study shows that relevant IFs are commonly encountered, being detected in about one fifth of patients undergoing abdominal CeCT.

Prevalence of IFs has been reported in literature

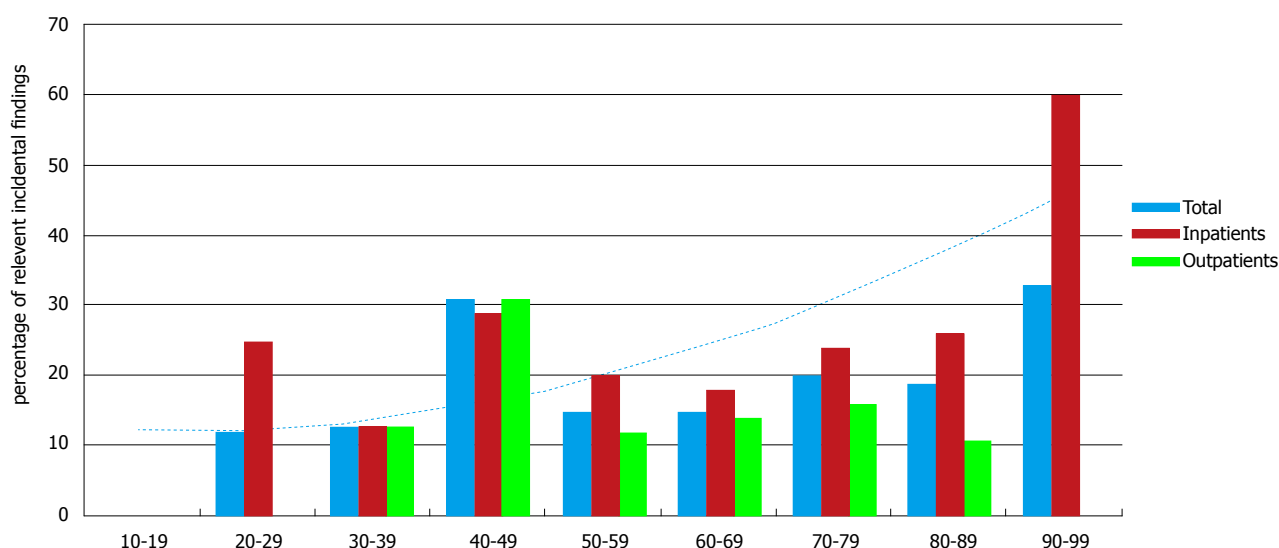


Figure 1 Relevant incidental findings stratified according to 10-year age groups subdivided between inpatients, outpatients and overall.

Table 3 Overall number of reports and relevant incidental findings per radiologist *n* (%)

Radiologist	Overall		Inpatients		Outpatients	
	Reports	Relevant IFs	Reports	Relevant IFs	Reports	Relevant IFs
A	69/1040 (6.6)	11/69 (16.0)	43/470 (9.1)	8/43 (18.6)	26/570 (4.6)	3/26 (11.5)
B	59/1040 (5.7)	11/59 (18.6)	21/470 (4.4)	3/21 (14.3)	38/570 (6.6)	8/38 (21.1)
C	164/1040 (15.8)	23/164 (14.0)	75/470 (16.0)	12/75 (16.0)	89/570 (15.6)	11/89 (12.4)
D	353/1040 (33.9)	81/353 (22.9)	145/470 (30.9)	41/145 (28.2)	208/570 (36.4)	40/208 (19.2)
E	160/1040 (15.4)	21/160 (13.1)	48/470 (10.2)	9/48 (18.7)	112/570 (19.6)	12/112 (10.7)
F	102/1040 (9.8)	12/102 (11.8)	70/470 (14.9)	10/70 (14.3)	32/570 (5.6)	2/32 (6.2)
G	8/1040 (0.8)	3/8 (37.5)	5/470 (1.1)	2/5 (40.0)	3/570 (0.5)	1/3 (33.3)
H	28/1040 (2.7)	8/28 (28.6)	11/470 (2.3)	4/11 (36.4)	17/570 (3.0)	4/17 (23.5)
I	97/1040 (9.3)	25/97 (25.8)	52/470 (11.1)	19/52 (36.5)	45/570 (7.9)	6/45 (13.3)
Total	1040/1040 (100.0)	195/1040 (18.8)	470/470 (100.0)	108/470 (23.0)	570/570 (100.0)	87/570 (15.3)

Comparison between relevant incidental finding rate in inpatients or in outpatients was calculated using the χ^2 test and resulted significantly different ($P < 0.001$). IFs: Incidental findings.

to vary from 3% to 58%^[6-12], depending on the study population, the organ or system involved, and on criteria used to classify IFs. Several papers are focused on the rate of IFs detected during CT exams aimed to the evaluation of a single organ. For example, extracolonic IFs are reported to be detected in up to 23% of patients undergoing CT colonography^[6,8] and this is nowadays considered one of the major issues regarding colon cancer screening with this technique. Dewey *et al*^[13] reported a 5% prevalence of relevant extra-cardiac IFs and a 10% prevalence of non-relevant IFs during coronary CT angiography in a cohort of 108 patients. However, Gil *et al*^[14] reported extra-cardiac IFs in 56% of their series, regardless to their severity. In the study of Law *et al*^[15], 56 out of 295 patients (19%) had extra-coronary IFs requiring clinical or radiological follow up. Other studies deal with IFs prevalence in a single organ. Rinaldi *et al*^[9] re-assessed the images of a series of abdominal CT exams to evaluate prevalence, reporting rates, and clinical implications of incidentally-discovered pulmonary nodules. In this retrospective case review, 39.1% of patients had lung nodules but only 8.4% of

them were mentioned in the report. O'Connor *et al*^[10] reported a 14% IFs prevalence in kidneys, while IFs prevalence in adrenal glands was reported to range between 3% and 7%^[16]. Some authors investigated IFs prevalence in a specific setting, such as patients who underwent abdominal CT in emergency. In this particular context, IFs prevalence has been reported between 15% and 35%^[12]. A recent literature review on 44 original studies on all imaging diagnostic modalities published between 1986 and 2007 reported a IFs mean prevalence of 23.6%^[2]. To our knowledge, no previous report investigated the overall prevalence of relevant IFs in a consecutive series of routine abdominal CeCT.

In our series, we found a significantly higher amount of relevant IFs in inpatients compared to outpatients. This result could be explained by the fact that CT exams performed in inpatients are generally requested with a focused clinical question (e.g., staging in a patient with colon cancer). As findings are considered as incidental solely when not related to the clinical suspicion, the narrower the clinical suspicion the higher the possibility to detect an unrelated finding^[2]. Conversely, clinical

Table 4 Relevant incidental findings stratified according to 10-year age groups subdivided between inpatients, outpatients, and overall *n* (%)

Age	Overall		Inpatients		Outpatients	
	CeCT	Relevant IFs	CeCT	Relevant IFs	CeCT	Relevant IFs
10-19	6/1040 (0.6)	0/6 (0.0)	3/470 (0.6)	0/3 (0.0)	3/570 (0.5)	0/3 (0.0)
20-29	17/1040 (1.7)	2/17 (11.8)	8/470 (1.7)	2/8 (25.0)	9/570 (1.6)	0/9 (0.0)
30-39	40/1040 (3.8)	5/40 (12.5)	8/470 (1.7)	1/8 (12.5)	32/570 (5.6)	4/32 (12.5)
40-49	88/1040 (8.5)	27/88 (30.6)	34/470 (7.2)	10/34 (29.4)	54/570 (9.4)	17/54 (31.5)
50-59	130/1040 (12.5)	20/130 (15.4)	55/470 (11.7)	11/55 (20.0)	75/570 (13.6)	9/75 (12.0)
60-69	260/1040 (25.0)	40/260 (15.4)	112/470 (23.8)	20/112 (17.8)	148/570 (26.0)	20/148 (13.5)
70-79	361/1040 (34.7)	73/361 (20.2)	173/470 (36.8)	42/173 (24.2)	188/570 (33.0)	31/188 (16.5)
80-89	129/1040 (12.4)	25/129 (19.4)	72/470 (15.3)	19/72 (26.4)	57/570 (10.0)	6/57 (10.5)
90-99	9/1040 (0.8)	3/9 (33.3)	5/470 (1.1)	3/5 (60.0)	4/570 (0.7)	0/4 (0.0)
Tot	1040/1040 (100)	195/1040 (18.8)	470/470 (100)	108/470 (23.0)	570/570 (100)	87/570 (15.2)

CeCT: Contrast-enhanced computed tomography; IFs: Incidental findings.

Table 5 Distribution of relevant incidental findings among involved organs *n* (%)

Anatomical site	Relevant IFs
Kidney	28/195 (14.4)
Gallbladder	27/195 (13.85)
Lung	24/195 (12.3)
Uterus	20/195 (10.3)
Adrenal gland	19/195 (9.7)
Vessels	19/195 (9.7)
Musculoskeletal	12/195 (6.2)
Ovary	12/195 (6.2)
Liver	7/195 (3.6)
Spleen	6/195 (3.1)
Prostate	6/195 (3.1)
Bowel	5/195 (2.6)
Bladder	4/195 (2.1)
Pancreas	3/195 (1.5)
Testicles	3/195 (1.5)

IFs: Incidental findings.

suspicion reported in outpatients' requests is usually more generic (e.g., abdominal pain), allowing for an easier correlation to a wide range of IFs, although this is not necessarily the rule. In our study, patients from emergency department were included in the outpatients group because they are often sent with a generic clinical suspicion, based on ill-defined clinical data and symptoms.

In our series, the only independent predictor of a relevant IF was the availability of a previous exam. In patients who had not performed a previous exam, the odds ratio calculation demonstrated a probability of detecting a relevant IF about five times greater than in those who had a previous exam available. This was expected, as IFs that had been already detected in previous exam have been currently considered as already known and thus excluded from our analysis.

We found significant difference in the distribution of radiologists who reported CeCT exams performed in inpatients or in outpatients. This data is partially due to statistical analysis of a large number of radiologists and a relatively small number of exams per each reader.

Table 6 Relevant incidental findings in 1040 contrast enhanced computer tomography examinations

IF	<i>n</i> %
Cholelithiasis	27 (2.6%)
Uterine lesion	20 (1.9%)
Adrenal mass	19 (1.8%)
Non-simple renal cyst	15 (1.4%)
Lung nodule	13 (1.3%)
Adnexal mass	12 (1.2%)
Kidney stones	10 (1.0%)
Pleural effusion	8 (0.8%)
Focal liver lesion	6 (0.6%)
Enlarged prostate	6 (0.6%)
Focal splenic lesion	5 (0.5%)
Abdominal aortic aneurysm	4 (0.4%)
Bladder wall thickening	4 (0.4%)
Aortic ectasia	4 (0.4%)
Inguinal hernia	4 (0.4%)
Focal pancreatic lesion	3 (0.3%)
Focal renal lesion	3 (0.3%)
Atheromasic aorta	3 (0.3%)
Iliac aneurysm	3 (0.3%)
Focal lesion of bones	3 (0.3%)
Lung consolidation	2 (0.2%)
Focal muscular lesion	2 (0.2%)
Appendicular enlargement	2 (0.2%)
Hydrocele testis	2 (0.2%)
Splenic artery aneurysm	1 (0.1%)
Mesenteric artery aneurysm	1 (0.1%)
Vertebral fracture	1 (0.1%)
Diverticulitis	1 (0.1%)
Ectasic portal vein	1 (0.1%)
Endoleak	1 (0.1%)
Emphysema	1 (0.1%)
Spinal disc herniation	1 (0.1%)
Colonic cancer	1 (0.1%)
Stasis liver	1 (0.1%)
Incisional hernia	1 (0.1%)
Femoral artery occlusion	1 (0.1%)
Splenomegaly	1 (0.1%)
Subocclusion	1 (0.1%)
Varicocele	1 (0.1%)
Total	195 (18.7%)

IF: Incidental finding.

However, this could somewhat represent an additional explanation of the difference of relevant IFs prevalence

between inpatients and outpatients.

Considering age group stratification (see Table 4), we found that relevant IFs increase with aging, as expected^[17]. An exception is represented by the 40-to-49 year group, in which relevant IFs prevalence was about one third. Patients included in such a group were lacking of a previous exam in 70% of cases, compared to the overall value of 57.7%. As the absence of a previous exam increase the possibility of relevant IFs detection, this data can somewhat explain the unusual prevalence peak in that age group.

Regarding the classification of relevant IFs according to the anatomical site, we note that the most involved organs were kidneys, gallbladder, and lungs. For renal lesions, there is no validated criteria - apart from follow-up - to differentiate solid benign from malignant lesions^[18]. This could partially explain the high incidence of relevant IFs, as for these lesions additional workup is frequently recommended. Regarding gallbladder, 10%-15% of occidental subjects will develop gallstones in their life. People with asymptomatic gallstones are likely to develop related problems in 1%-4% of cases, younger people being more at risk than elderly^[19]. Although prophylactic cholecistectomy is usually unnecessary, this procedure can be justified in young subjects that are more prone to develop acute pancreatitis related to small stones^[20]. This partially explains the high number of relevant IFs reported in our series, as additional workup (ultrasound follow-up or surgical evaluation) is usually suggested in these cases. In our series, we found 2.5% IFs related to lungs, considered as relevant in respect to previously published criteria^[21]. In a previous paper, Rinaldi *et al*^[9] reported an overall incidence of 39.1% of lung nodules visible on abdominal CeCT images, only 8.4% of them being described in radiologists' report. However, our values are not directly comparable to theirs, as we included only reported incidentally discovered lung nodules deserving additional workup.

Early diagnosis and detection of asymptomatic diseases have well known advantages, being also at the basis of screening programs. However, additional workup of relevant IFs can be responsible of tests and procedure that are often expensive - both for patients and healthcare systems - stressful, and sometimes potentially harmful for patients (e.g., invasive procedures or ionizing radiations exposure). Also, it can happen that IFs are so slow-progressing that will never cause symptoms or death. When this happens, the diagnosis might have been correct but is clinically irrelevant. This important concept is also known as overdiagnosis and it is a risk that should be always taken into account when dealing with screening tools and early diagnosis in general^[4].

Our study has some limitations. First, it was conducted at a single institution, so results may be not directly transferable to general population. Then, the retrospective nature of the study that was aimed solely to review radiological reports. Thus, our action

was limited to analyze findings that were included in those reports. Also, our results may be somewhat underestimated. Moreover, being able to access previous exams only when provided by patients themselves or when performed at our institution have surely affected the data of patients considered as lacking of a previous exam. Finally, we do not know whether additional work-up was really performed. Thus we could not evaluate the real impact of IFs on the healthcare system.

Summarizing, a relevant IF is detected in one out of five patients undergoing abdominal CeCT. Thus, in clinical practice, we daily perform unconscious collateral screening for a number of abdominal diseases. Notably, a problem still exists about how to deal with these findings, as their detection can be stressful and potentially harmful for patients, also contributing to raise health care costs. On the one hand we have the risk of overdiagnosis, on the other hand the risk of legal issues for not having reported and suggested further work-up for these IFs^[22].

COMMENTS

Background

Incidental findings (IFs) during contrast-enhanced computed tomography (CeCT) are increasingly being detected. This generates anxiety for patients and additional costs for the healthcare systems.

Research frontiers

The study is concerned with the evaluation of IFs during CeCT of the abdomen.

Innovations and breakthroughs

A relevant IF is detected in one out of five patients undergoing abdominal CeCT. Thus, in clinical practice, the authors daily perform unconscious collateral screening for a number of abdominal diseases.

Applications

A problem still exists about how to deal with these findings, as their detection can be stressful and potentially harmful for patients, also contribute to increase in health care costs. On the one hand we have the risk of overdiagnosis, on the other hand there is a risk of legal issues for not having reported and suggested further work-up for these IFs.

Terminology

Abdominal CE-CT: CeCT of the abdomen, a panoramic examination of the abdomen used to evaluate a wide range of pathologic conditions. IF: An incidentally discovered mass or lesion detected by abdominal CeCT performed for an unrelated reason.

Peer-review

The manuscript is well written.

REFERENCES

- 1 **Brenner DJ**, Hall EJ. Computed tomography--an increasing source of radiation exposure. *N Engl J Med* 2007; **357**: 2277-2284 [PMID: 18046031]
- 2 **Lumbreras B**, Donat L, Hernández-Aguado I. Incidental findings in imaging diagnostic tests: a systematic review. *Br J Radiol* 2010; **83**: 276-289 [PMID: 20335439 DOI: 10.1259/bjr/98067945]
- 3 **Berland LL**. Incidental extracolonic findings on CT colonography: the impending deluge and its implications. *J Am Coll Radiol* 2009;

- 6: 14-20 [PMID: 19111266 DOI: 10.1016/j.jacr.2008.06.018]
- 4 **Sardanelli F.** Evidence-based radiology and its relationship with quality. In Bruno MA, Abujudeh HH, eds. *Quality and safety in Radiology*. New York: Oxford University Press, 2009: 256-290
- 5 **Berland LL,** Silverman SG, Gore RM, Mayo-Smith WW, Megibow AJ, Yee J, Brink JA, Baker ME, Federle MP, Foley WD, Francis IR, Herts BR, Israel GM, Krinsky G, Platt JF, Shuman WP, Taylor AJ. Managing incidental findings on abdominal CT: white paper of the ACR incidental findings committee. *J Am Coll Radiol* 2010; **7**: 754-773 [PMID: 20889105 DOI: 10.1016/j.jacr.2010.06.013]
- 6 **Yee J,** Kumar NN, Godara S, Casamina JA, Hom R, Galdino G, Dell P, Liu D. Extracolonic abnormalities discovered incidentally at CT colonography in a male population. *Radiology* 2005; **236**: 519-526 [PMID: 16040909 DOI: 10.1148/radiol.2362040166]
- 7 **Veronesi G,** Bellomi M, Spaggiari L. The rate of incidental findings in lung cancer screening trials is not negligible. *Eur Radiol* 2008; **18**: 529 [PMID: 17994239 DOI: 10.1007/s00330-007-0797-5]
- 8 **Secchi F,** Lanza E, Cannà PM, Petrini M, Sconfienza LM, Sardanelli F. Noncardiac findings in clinical cardiac magnetic resonance: prevalence in 300 examinations after blind reassessment. *J Comput Assist Tomogr* 2013; **37**: 382-386 [PMID: 23674009 DOI: 10.1097/RCT.0b013e3182845bdb]
- 9 **Rinaldi MF,** Bartalena T, Giannelli G, Rinaldi G, Sverzellati N, Canini R, Gavelli G. Incidental lung nodules on CT examinations of the abdomen: prevalence and reporting rates in the PACS era. *Eur J Radiol* 2010; **74**: e84-e88 [PMID: 19446417 DOI: 10.1016/j.ejrad.2009.04.019]
- 10 **O'Connor SD,** Pickhardt PJ, Kim DH, Oliva MR, Silverman SG. Incidental finding of renal masses at unenhanced CT: prevalence and analysis of features for guiding management. *AJR Am J Roentgenol* 2011; **197**: 139-145 [PMID: 21701022 DOI: 10.2214/AJR.10.5920]
- 11 **Lazoura O,** Vassiou K, Kanavou T, Vlychou M, Arvanitis DL, Fezoulidis IV. Incidental non-cardiac findings of a coronary angiography with a 128-slice multi-detector CT scanner: should we only concentrate on the heart? *Korean J Radiol* 2010; **11**: 60-68 [PMID: 20046496 DOI: 10.3348/kjr.2010.11.1.60]
- 12 **Ekeh AP,** Walusimbi M, Brigham E, Woods RJ, McCarthy MC. The prevalence of incidental findings on abdominal computed tomography scans of trauma patients. *J Emerg Med* 2010; **38**: 484-489 [PMID: 19232878 DOI: 10.1016/j.jemermed.2008.11.019]
- 13 **Dewey M,** Schnapauff D, Teige F, Hamm B. Non-cardiac findings on coronary computed tomography and magnetic resonance imaging. *Eur Radiol* 2007; **17**: 2038-2043 [PMID: 17268800 DOI: 10.1007/s00330-006-0570-1]
- 14 **Gil BN,** Ran K, Tamar G, Shmueli F, Eli A. Prevalence of significant noncardiac findings on coronary multidetector computed tomography angiography in asymptomatic patients. *J Comput Assist Tomogr* 2007; **31**: 1-4 [PMID: 17259825 DOI: 10.1097/01.rct.0000233125.83184.33]
- 15 **Law YM,** Huang J, Chen K, Cheah FK, Chua T. Prevalence of significant extracoronary findings on multislice CT coronary angiography examinations and coronary artery calcium scoring examinations. *J Med Imaging Radiat Oncol* 2008; **52**: 49-56 [PMID: 18373827 DOI: 10.1111/j.1440-1673.2007.01911.x]
- 16 **National Institute of Health.** NIH state-of-the-science statement on management of the clinically inapparent adrenal mass ("incidentaloma"). *NIH Consens State Sci Statements* 2002; **19**: 1-25 [PMID: 14768652]
- 17 **Goldstein S.** The biology of aging. *N Engl J Med* 1971; **285**: 1120-1129 [PMID: 4937862 DOI: 10.1056/NEJM197111112852005]
- 18 **Lee SI,** Krishnaraj A, Chatterji M, Dreyer KJ, Thrall JH, Hahn PF. When does a radiologist's recommendation for follow-up result in high-cost imaging? *Radiology* 2012; **262**: 544-549 [PMID: 22084210 DOI: 10.1148/radiol.11111091]
- 19 **Sanders G,** Kingsnorth AN. Gallstones. *BMJ* 2007; **335**: 295-299 [PMID: 17690370 DOI: 10.1136/bmj.39267.452257.AD]
- 20 **Venneman NG,** Buskens E, Besselink MG, Stads S, Go PM, Bosscha K, van Berge-Henegouwen GP, van Erpecum KJ. Small gallstones are associated with increased risk of acute pancreatitis: potential benefits of prophylactic cholecystectomy? *Am J Gastroenterol* 2005; **100**: 2540-2550 [PMID: 16279912 DOI: 10.1111/j.1572-0241.2005.00317.x]
- 21 **MacMahon H,** Austin JH, Gamsu G, Herold CJ, Jett JR, Naidich DP, Patz EF, Swensen SJ. Guidelines for management of small pulmonary nodules detected on CT scans: a statement from the Fleischner Society. *Radiology* 2005; **237**: 395-400 [PMID: 16244247 DOI: 10.1148/radiol.2372041887]
- 22 **Berlin L.** Professionalism and disclosing errors. *AJR Am J Roentgenol* 2012; **198**: W315 [PMID: 22358031 DOI: 10.2214/AJR.10.5524]

P- Reviewer: Chu JP, Kumar J

S- Editor: Ji FF L- Editor: A E- Editor: Jiao XK



Delayed diagnosis of isolated alar ligament rupture: A case report

Robin A Kaufmann, Ingo Marzi, Thomas J Vogl

Robin A Kaufmann, Thomas J Vogl, Department of Diagnostic and Interventional Radiology, University Hospital Frankfurt, Goethe University, D-60590 Frankfurt am Main, Germany

Ingo Marzi, Department of Trauma, Hand and Reconstructive Surgery, University Hospital Frankfurt, Goethe University, D-60590 Frankfurt am Main, Germany

Author contributions: Kaufmann RA was mainly responsible for writing and researching the paper; Vogl TJ was the involved radiologist and Marzi I the traumatologist.

Institutional review board statement: Not applicable for case reports in our institution.

Informed consent statement: Patient gave informed consent to publication of case report.

Conflict-of-interest statement: No conflict of interest.

Open-Access: This article is an open-access article which was selected by an in-house editor and fully peer-reviewed by external reviewers. It is distributed in accordance with the Creative Commons Attribution Non Commercial (CC BY-NC 4.0) license, which permits others to distribute, remix, adapt, build upon this work non-commercially, and license their derivative works on different terms, provided the original work is properly cited and the use is non-commercial. See: <http://creativecommons.org/licenses/by-nc/4.0/>

Correspondence to: Robin A Kaufmann, MD, Department of Diagnostic and Interventional Radiology, University Hospital Frankfurt, Goethe University, Theodor-Stern-Kai 7, D-60590 Frankfurt am Main, Germany. robin.kaufmann@students.unibe.ch
Telephone: +49-69-63017277
Fax: +49-69-63017258

Received: March 30, 2015
Peer-review started: April 8, 2015
First decision: May 13, 2015
Revised: June 23, 2015
Accepted: June 30, 2015
Article in press: July 2, 2015

Published online: October 28, 2015

Abstract

Ligament disruptions at the craniovertebral junction are typically associated with atlantoaxial rotatory dislocation during upper cervical spine injuries and require external orthoses or surgical stabilization. Only in few patients isolated ruptures of the alar ligament have been reported. Here we present a further case, in which the diagnosis was initially obscured by a misleading clinical symptomatology but finally established six months following the trauma, demonstrating the value of contrast-enhanced high resolution 3 Tesla magnetic resonance imaging in identifying this particular lesion.

Key words: Alar ligament rupture; Cervical spine injury; Contrast-enhanced magnetic resonance imaging

© **The Author(s) 2015.** Published by Baishideng Publishing Group Inc. All rights reserved.

Core tip: Upper cervical spine injuries are common and bear a relevant medical and socioeconomic impact. While most of such lesions are related to atlantoaxial rotatory dislocation, thus far only few patients with isolated alar ligament ruptures have been reported. This particular trauma is a challenge to both clinicians and radiologists and diagnosis might thus be delayed. Here we present a further case of a young adult and discuss the value of sequential contrast-enhanced magnetic resonance imaging in establishing this diagnosis at a late stage and in the follow-up of a subsequently prolonged recovery.

Kaufmann RA, Marzi I, Vogl TJ. Delayed diagnosis of isolated alar ligament rupture: A case report. *World J Radiol* 2015; 7(10): 357-360 Available from: URL: <http://www.wjgnet.com/1949-8470/>

INTRODUCTION

Upper cervical spine injuries are common and mainly caused by car and sport accidents or falls. They frequently are associated with long-term impairment or work disability of involved individuals and bear a relevant medical and socioeconomic impact^[1-4]. Particularly, cases with hyperextension and rotation of the neck may eventually result in ligament ruptures, though this incident is not necessarily correlated with the intensity of the trauma^[5,6]. While most of such lesions are related to atlantoaxial rotatory dislocation, thus far only few patients with isolated alar ligament ruptures have been reported^[7]. Probably these cases are underdiagnosed, since they might be missed on initial presentation and only be identified in the context with persistent cervical instability. Here we present a case of a young adult and discuss the value of sequential contrast-enhanced magnetic resonance imaging (MRI) in establishing this diagnosis at a late stage and in the follow-up of a subsequently prolonged recovery.

CASE REPORT

A 25-year-old man was diagnosed with rupture of the tympanic membrane of the left ear following a blunt fist hit trauma to the left side of his head associated with a short period of retro- and ante-grade amnesia, hearing impairment and tinnitus. While topical membrane patching led to complete healing with reestablishment of hearing, ipsilateral tinnitus remained and was accompanied by intermittent occipital pain. Moreover, during the following weeks and after repetitive sport exercises including headstands the patient developed further symptoms such as projecting aching in both shoulders, neck stiffness, dysphagia, fasciculation predominantly in the left arm, paraesthesia along the thoracic spine, neuralgiform pain attacks in the chest, few episodes of unexplainable shivering without fever and some other vague symptoms. On repetitive neurological examination there was no evidence of any objective deficits apart from an impaired neck rotation to the left side. A plain MRI excluded cervical disc herniation and except a straightening of the cervical spine reported no otherwise pathology. Mobilization and physiotherapy was advised leading to further exacerbation of symptoms. After a chiropractic manoeuvre attempted by an orthopaedic surgeon the tinnitus was felt louder and of higher frequency. An additional osteopathic treatment with repetitive sessions of rotational overstretching of the cervical spine above the tolerable pain threshold further aggravated the symptomatology. Recalling the earlier blunt injury a traumatologist was finally consulted 6 mo after the initial event who disclosed a pathologic cervical hypermobility on rotating the neck to the

right site, which was considered highly suspicious of a ligament lesion within the atlantoaxial joint. At this time a computed tomography (CT) scan ruled out a fracture or atlanto-occipital dislocation but revealed a slight shift of the dens towards the right lateral mass of C-1 (Figure 1). An MRI (Magnetom Prisma 3T, Siemens Healthcare) confirmed loss of lordosis on sagittal plane while the contrast-enhanced axial T1-weighted sequences disclosed increased signal intensity within the apex of the dens as well as within the widened left lateral dens-atlas space indicative of edema. Moreover, the dark signal of the left alar ligament proved to be interrupted (Figure 2), whereas the tectorial membrane and transverse ligament as well as the spinal cord appeared intact. Taken together, the findings were suggestive of an isolated rupture of the left alar ligament.

Subsequently, the cervical spine was immobilized by means of a Philadelphia collar, leading to a partial relief of the symptoms. Follow-up MRI of the cervical spine 3 mo later still showed signal hyperintensity within the alar ligament and the apex of the dens while its deviation apparently almost had resolved. After allowing for less cervical immobilization using a soft collar the patient's complaint worsened again and a subsequent MRI two months later still confirmed hyperintense signalling of the involved ligament and dens. The Philadelphia collar was reintroduced and following another 3 mo of immobilization a 3rd MRI sequence showed marked improvement (Figure 3). The patient gained a progressively increasing range of neck motion in each plane and was nearly free of any discomfort except a feeling of cervical tension increasing during the day, sporadic periods of head and chest pain and persistent tinnitus of varying intensity.

DISCUSSION

Isolated unilateral alar ligament rupture is a diagnosis made by excluding associated dislocation, fracture, or disruption of other ligamentous structures in the craniovertebral junction. Only recently Wong *et al*^[7] emphasized the special anatomical and pathophysiological aspects of this particular trauma and the value of CT and MRI to confirm the diagnosis discussing a 9 years old girl and reviewing 6 additional cases from the literature aged between 5 and 21 years, all of which fully recovered after conservative immobilization therapy within 1 year^[7].

While cervical X-ray, CT and MRI (T2-weighted and STIR sequences) of spinal ligamentous and soft tissue trauma are normally initiated in an acute setting^[8,9], in some cases appropriate imaging of cervical injuries might be missed initially or performed with delay for a variety of reasons^[10-12]. Also in our patient an appropriate diagnostic work-up had finally been delayed for several months, since the initial trauma and symptoms were apparently considered inadequate for further imaging analysis. MRI studies of patients with suspected occult cervical injury are well established to detect ligamentous



Figure 1 Multidetector-computed tomography coronary construction. Verification of a relationship of dens axis, atlas and occipital condyles. Asymmetry of the denso-axial joint space between left and right (white arrows) with widening on the left side. No micro- or macro-fracture.

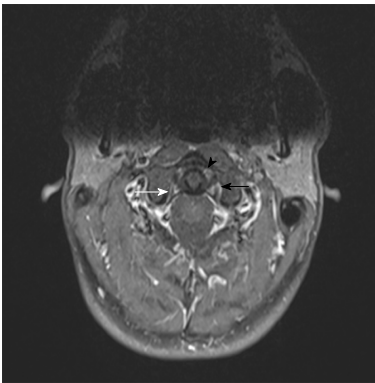


Figure 2 High resolution contrast-enhanced 3T magnetic resonance imaging, fat-saturated gradient echo sequence performed 6 mo following the trauma. In the contrast-enhanced T1w fat-suppressed magnetic resonance imaging sequence note the contrast enhancement in the periligamentous venous plexus (arrow head). On the left side lower than on the right side. No TS symmetry of the joint space left vs right side (black and white arrow).

injuries including the alar ligament^[13-15]. However, in the case presented here an earlier non contrast-enhanced MRI was performed in a private practice to check exclusively for cervical disc herniation as a potential cause of the unexplained symptoms and a ligament lesion was not suspected at that time. Only after subjective symptoms worsened and were possibly linked to the earlier trauma the potential lesion became evident after simply demonstrating contralateral hypermobility on physical testing.

For an optimal detection of ligamentous lesions, the strength of the MRI has been suggested to be at least 1.5 Tesla, which corresponds to half of the magnetic field strength used in our case for an optimal resolution. A slice thickness of 2 mm is reported to give excellent spatial resolution of the injured alar ligaments^[16]. Since T1-weighted images provide poor contrast resolution and thus less ability to differentiate small variations in signalling we in addition used a Gadolinium contrast enhanced imaging technique. We evaluated the unenhanced and enhanced images in comparison and could better stage the amount of ligamentous injury and an

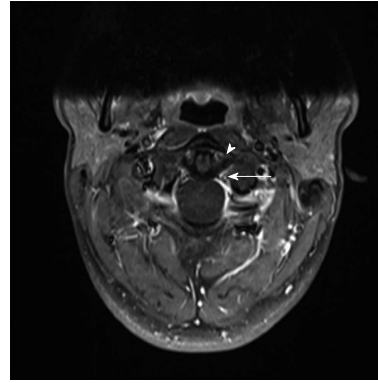


Figure 3 Follow-up magnetic resonance imaging. High resolution contrast-enhanced 3T magnetic resonance imaging, fat-saturated gradient echo sequence. After physical therapy stabilization. Note the clear contrast enhancement in the periligamentous venous plexus (arrow head) and the symmetric space evaluation (white arrow).

oedema of surrounding tissues.

On our final MRI after initiating the 12 mo immobilization therapy no relevant ligament or dens pathology could be documented. However, our patient still complaint of tinnitus and recurrent episodes of neck pressure, headaches and chest pain. Persisting symptoms following cervical injuries are well documented in the literature and seem likely if a healing after two years has not been achieved and more frequent in older individuals^[17,18]. Whether in our patient an instant diagnosis followed by immediate external orthoses or surgical therapy according to recent recommendations would have led to an entire and earlier relief of symptoms remains however hypothetical. In conclusion, we emphasize the value of contrast high resolution 3 Tesla MRI for the detection of ligamentous injuries at the craniovertebral junction^[19].

COMMENTS

Case characteristics

Patient presented with neck stiffness, dysphagia, fasciculation, paraesthesia and neuralgiform pain attacks.

Clinical diagnosis

Findings were suspicious of cervical ligament lesion.

Differential diagnosis

Spectrum of atlantoaxial rotatory dislocation.

Imaging diagnosis

3T Magnetic resonance imaging (MRI), fat-saturated gradient echo sequence (contrast-enhanced T1w fat-suppressed MRI sequence) showed a contrast enhancement in the periligamentous venous plexus with an asymmetry of the joint spaces.

Pathological diagnosis

Alar ligament rupture.

Treatment

Twelve months immobilization therapy.

Related reports

Wong ST, Ernest K, Fan G, Zovickian J, Pang D. Isolated unilateral rupture of the alar ligament. *J Neurosurg Pediatr* 2014; 13: 541-547.

Experiences and lessons

This particular trauma is a challenge and diagnosis might be delayed. We emphasize the value of contrast high resolution 3 Tesla MRI for the detection of ligamentous injuries at the craniocervical junction.

Peer-review

The authors present a case report on a delayed diagnosis of isolated alar ligament rupture and the added value of 3 Tesla MRI for the proper assessment. The paper is well written. Appropriate iconography. The purpose is well defined and it transmits properly the message becoming of potential interest for the readers.

REFERENCES

- 1 **Buitenhuis J**, de Jong PJ, Jaspers JP, Groothoff JW. Work disability after whiplash: a prospective cohort study. *Spine (Phila Pa 1976)* 2009; **34**: 262-267 [PMID: 19148041 DOI: 10.1097/BRS.0b013e3181913d07]
- 2 **Walton DM**, Macdermid JC, Giorgianni AA, Mascarenhas JC, West SC, Zammit CA. Risk factors for persistent problems following acute whiplash injury: update of a systematic review and meta-analysis. *J Orthop Sports Phys Ther* 2013; **43**: 31-43 [PMID: 23322093 DOI: 10.2519/jospt.2013.4507]
- 3 **McKinney MB**. [Treatment of dislocations of the cervical vertebrae in so-called "whiplash injuries"]. *Orthopade* 1994; **23**: 287-290 [PMID: 7970686]
- 4 **Grifka J**, Hedtmann A, Pape HG, Witte H, Bär HF. [Biomechanics of injury of the cervical spine]. *Orthopade* 1998; **27**: 802-812 [PMID: 9894234]
- 5 **Saternus KS**, Thrun C. [Traumatology of the alar ligaments]. *Aktuelle Traumatol* 1987; **17**: 214-218 [PMID: 2891250]
- 6 **Pfarrmann CW**, Binkert CA, Zanetti M, Boos N, Hodler J. Functional MR imaging of the craniocervical junction. Correlation with alar ligaments and occipito-atlantoaxial joint morphology: a study in 50 asymptomatic subjects. *Schweiz Med Wochenschr* 2000; **130**: 645-651 [PMID: 10846756]
- 7 **Wong ST**, Ernest K, Fan G, Zovickian J, Pang D. Isolated unilateral rupture of the alar ligament. *J Neurosurg Pediatr* 2014; **13**: 541-547 [PMID: 24679079 DOI: 10.3171/2014.2.PEDS13527]
- 8 **Dundamadappa SK**, Cauley KA. MR imaging of acute cervical spinal ligamentous and soft tissue trauma. *Emerg Radiol* 2012; **19**: 277-286 [PMID: 22398829 DOI: 10.1007/s10140-012-1033-4]
- 9 **Landi A**, Pietrantonio A, Marotta N, Mancarella C, Delfini R. Atlantoaxial rotatory dislocation (AARD) in pediatric age: MRI study on conservative treatment with Philadelphia collar--experience of nine consecutive cases. *Eur Spine J* 2012; **21** Suppl 1: S94-S99 [PMID: 22411035 DOI: 10.1007/s00586-012-2216-0]
- 10 **Gerrelts BD**, Petersen EU, Mabry J, Petersen SR. Delayed diagnosis of cervical spine injuries. *J Trauma* 1991; **31**: 1622-1626 [PMID: 1749033]
- 11 **Platzer P**, Hauswirth N, Jandl M, Chatwani S, Vecsei V, Gaebler C. Delayed or missed diagnosis of cervical spine injuries. *J Trauma* 2006; **61**: 150-155 [PMID: 16832263]
- 12 **O'Shaughnessy J**, Grenier JM, Stern PJ. A delayed diagnosis of bilateral facet dislocation of the cervical spine: a case report. *J Can Chiropr Assoc* 2014; **58**: 45-51 [PMID: 24587496]
- 13 **Geck MJ**, Yoo S, Wang JC. Assessment of cervical ligamentous injury in trauma patients using MRI. *J Spinal Disord* 2001; **14**: 371-377 [PMID: 11586135]
- 14 **Ackland HM**, Cameron PA, Varma DK, Fitt GJ, Cooper DJ, Wolfe R, Malham GM, Rosenfeld JV, Williamson OD, Liew SM. Cervical spine magnetic resonance imaging in alert, neurologically intact trauma patients with persistent midline tenderness and negative computed tomography results. *Ann Emerg Med* 2011; **58**: 521-530 [PMID: 21820209 DOI: 10.1016/j.annemergmed.2011.06.008]
- 15 **Wilmink JT**, Patijn J. MR imaging of alar ligament in whiplash-associated disorders: an observer study. *Neuroradiology* 2001; **43**: 859-863 [PMID: 11688704]
- 16 **Krakenes J**, Kaale BR, Moen G, Nordli H, Gilhus NE, Rorvik J. MRI assessment of the alar ligaments in the late stage of whiplash injury--a study of structural abnormalities and observer agreement. *Neuroradiology* 2002; **44**: 617-624 [PMID: 12136365]
- 17 **Gargan MF**, Bannister GC. Long-term prognosis of soft-tissue injuries of the neck. *J Bone Joint Surg Br* 1990; **72**: 901-903 [PMID: 2211780]
- 18 **Bunketorp L**, Nordholm L, Carlsson J. A descriptive analysis of disorders in patients 17 years following motor vehicle accidents. *Eur Spine J* 2002; **11**: 227-234 [PMID: 12107791]
- 19 **Joaquim AF**, Ghizoni E, Tedeschi H, Lawrence B, Brodke DS, Vaccaro AR, Patel AA. Upper cervical injuries - a rational approach to guide surgical management. *J Spinal Cord Med* 2014; **37**: 139-151 [PMID: 24559418 DOI: 10.1179/2045772313Y.0000000158]

P- Reviewer: Akcar N, Gumustas OG, Storto G, Sureka B

S- Editor: Ji FF L- Editor: A E- Editor: Jiao XK





Published by **Baishideng Publishing Group Inc**

8226 Regency Drive, Pleasanton, CA 94588, USA

Telephone: +1-925-223-8242

Fax: +1-925-223-8243

E-mail: bpgoffice@wjgnet.com

Help Desk: <http://www.wjgnet.com/esps/helpdesk.aspx>

<http://www.wjgnet.com>



World Journal of *Radiology*

World J Radiol 2015 November 28; 7(11): 361-420





Editorial Board

2014-2017

The *World Journal of Radiology* Editorial Board consists of 365 members, representing a team of worldwide experts in radiology. They are from 36 countries, including Afghanistan (1), Argentina (2), Australia (5), Austria (7), Belgium (2), Brazil (8), Canada (6), Chile (1), China (43), Croatia (1), Denmark (4), Egypt (6), France (5), Germany (22), Greece (10), India (12), Iran (6), Ireland (2), Israel (3), Italy (47), Japan (13), Netherlands (1), New Zealand (1), Pakistan (1), Poland (2), Portugal (1), Serbia (1), Singapore (3), Slovakia (1), South Korea (18), Spain (4), Sweden (2), Switzerland (4), Thailand (1), Turkey (26), United Kingdom (11), and United States (82).

EDITORS-IN-CHIEF

Kai U Juergens, *Bremen*
Edwin JR van Beek, *Edinburgh*
Thomas J Vogl, *Frankfurt*

GUEST EDITORIAL BOARD MEMBERS

Wing P Chan, *Taipei*
Chung-Huei Hsu, *Taipei*
Chin-Chang Huang, *Taipei*
Tsong-Long Hwang, *Taoyuan*
Jung-Lung Hsu, *Taipei*
Chia-Hung Kao, *Taichung*
Yu-Ting Kuo, *Tainan*
Hon-Man Liu, *Taipei*
Hui-Lung Liang, *Kaohsiung*
Chun Chung Lui, *Kaohsiung*
Sen-Wen Teng, *Taipei*
Yung-Liang (William) Wan, *Taoyuan*

MEMBERS OF THE EDITORIAL BOARD



Afghanistan

Takao Hiraki, *Okayama*



Argentina

Patricia Carrascosa, *Vicente Lopez*
Maria C Ziadi, *Rosario*



Australia

Lourens Bester, *Sydney*
Gemma A Figtree, *Sydney*



Austria

Herwig R Cerwenka, *Graz*
Gudrun M Feuchtnner, *Innsbruck*
Benjamin Henninger, *Innsbruck*
Rupert Lanzenberger, *Vienna*
Shu-Ren Li, *Vienna*
Veronika Schopf, *Vienna*
Tobias De Zordo, *Innsbruck*



Belgium

Steve Majerus, *Liege*
Kathelijne Peremans, *Merelbeke*



Brazil

Clerio F Azevedo, *Rio de Janeiro*
Patrícia P Alfredo, *São Paulo*
Eduardo FC Fleury, *São Paulo*
Edward Araujo Júnior, *São Paulo*
Wellington P Martins, *Ribeirao Preto*
Ricardo A Mesquita, *Belo Horizonte*
Vera MC Salemi, *São Paulo*
Claudia Szobot, *Porto Alegre*
Lilian YI Yamaga, *São Paulo*



Canada

Marie Arsalidou, *Toronto*
Otman A Basir, *Waterloo*

Tarik Zine Belhocine, *Toronto*
James Chow, *Toronto*
Tae K Kim, *Toronto*
Anastasia Oikonomou, *Toronto*



China

Hong-Wei Chen, *Wuxi*
Feng Chen, *Hangzhou*
Jian-Ping Chu, *Guangzhou*
Guo-Guang Fan, *Shenyang*
Bu-Lang Gao, *Shijiazhuang*
Qi-Yong Gong, *Chengdu*
Ying Han, *Beijing*
Xian-Li Lv, *Beijing*
Yi-Zhuo Li, *Guangzhou*
Xiang-Xi Meng, *Harbin*
Yun Peng, *Beijing*
Jun Shen, *Guangzhou*
Ze-Zhou Song, *Hangzhou*
Wai Kwong Tang, *Hong Kong*
Gang-Hua Tang, *Guangzhou*
Jie Tian, *Beijing*
Lu-Hua Wang, *Beijing*
Xiao-bing Wang, *Xi'an*
Yi-Gen Wu, *Nanjing*
Kai Wu, *Guangzhou*
Hui-Xiong Xu, *Shanghai*
Zuo-Zhang Yang, *Kunming*
Xiao-Dan Ye, *Shanghai*
David T Yew, *Hong Kong*
Ting-He Yu, *Chongqing*
Zheng Yuan, *Shanghai*
Min-Ming Zhang, *Hangzhou*
Yudong Zhang, *Nanjing*
Dong Zhang, *Chongqing*
Wen-Bin Zeng, *Changsha*

Yue-Qi Zhu, *Shanghai*



Croatia

Goran Kusec, *Osijek*



Denmark

Poul E Andersen, *Odense*

Lars J Petersen, *Aalborg*

Thomas Z Ramsøy, *Frederiksberg*

Morten Ziebell, *Copenhagen*



Egypt

Mohamed F Bazeed, *Mansoura*

Mohamed Abou El-Ghar, *Mansoura*

Reem HA Mohamed, *Cairo*

Mohamed R Nouh, *Alexandria*

Ahmed AKA Razek, *Mansoura*

Ashraf A Zytoon, *Shebin El-Koom*



France

Sabine F Bensamoun, *Compiègne*

Romarc Loffroy, *Dijon*

Stephanie Nougaret, *Montpellier*

Hassane Oudadesse, *Rennes*

Vincent Vinh-Hung, *Fort-de-France*



Germany

Henryk Barthel, *Leipzig*

Peter Bannas, *Hamburg*

Martin Beeres, *Frankfurt*

Ilja F Ciernik, *Dessau*

A Dimitrakopoulou-Strauss, *Heidelberg*

Peter A Fasching, *Erlangen*

Andreas G Schreyer, *Regensburg*

Philipp Heusch, *Duesseldorf*

Sonja M Kirchhoff, *Munich*

Sebastian Ley, *Munich*

Adel Maataoui, *Frankfurt am Main*

Stephan M Meckel, *Freiburg*

Hans W Muller, *Duesseldorf*

Kay Raum, *Berlin*

Dirk Rades, *Luebeck*

Marc-Ulrich Regier, *Hamburg*

Alexey Surov, *Halle*

Martin Walter, *Magdeburg*

Axel Wetter, *Essen*

Christoph Zilkens, *Düsseldorf*



Greece

Panagiotis Antoniou, *Thessaloniki*

Nikos Efthimiou, *Athens*

Dimitris Karnabatidis, *Patras*

George Latsios, *Athens*

Stylianios Megremis, *Iraklion*

Alexander D Rapidis, *Athens*

Kiki Theodorou, *Larissa*

Ioannis A Tsalafoutas, *Athens*

Evanthia E Tripoliti, *Ioannina*

Athina C Tsili, *Ioannina*



India

Ritesh Agarwal, *Chandigarh*

Chandan J Das, *New Delhi*

Prathamesh V Joshi, *Mumbai*

Naveen Kalra, *Chandigarh*

Chandrasekharan Kesavadas, *Trivandrum*

Jyoti Kumar, *New Delhi*

Atin Kumar, *New Delhi*

Kaushala P Mishra, *Allahabad*

Daya N Sharma, *New Delhi*

Binit Sureka, *New Delhi*

Sanjay Sharma, *New Delhi*

Raja R Yadav, *Allahabad*



Iran

Majid Assadi, *Bushehr*

SeyedReza Najafizadeh, *Tehran*

Mohammad Ali Oghabian, *Tehran*

Amir Reza Radmard, *Tehran*

Ramin Sadeghi, *Mashhad*

Hadi Rokni Yazdi, *Tehran*



Ireland

Tadhg Gleeson, *Wexford*

Frederik JAI Vernimmen, *Cork*



Israel

Dafna Ben Bashat, *Tel Aviv*

Amit Gefen, *Tel Aviv*

Tamar Sella, *Jerusalem*



Italy

Adriano Alippi, *Rome*

Dante Amelio, *Trento*

Michele Anzidei, *Rome*

Filippo F Angileri, *Messinas*

Stefano Arcangeli, *Rome*

Roberto Azzoni, *San Donato milanese*

Tommaso V Bartolotta, *Palermo*

Tommaso Bartalena, *Imola*

Livia Bernardin, *San Bonifacio*

Federico Boschi, *Verona*

Sergio Casciaro, *Lecce*

Emanuele Casciani, *Rome*

Musa M Can, *Napoli*

Alberto Cuocolo, *Napoli*

Michele Ferrara, *Coppito*

Mauro Feola, *Fossano*

Giampiero Francica, *Castel Volturno*

Luigi De Gennaro, *Rome*

Giulio Giovannetti, *Pisa*

Francesca Iacobellis, *Napoli*

Formato Invernizzi, *Monza Brianza*

Francesco Lassandro, *Naples*

Lorenzo Livi, *Florence*

Pier P Mainenti, *Napoli*

Laura Marzetti, *Chieti*

Giuseppe Malinverni, *Crescentino*

Enrica Milanese, *Turin*

Giovanni Morana, *Treviso*

Lorenzo Monti, *Milan*

Silvia D Morbelli, *Genoa*

Barbara Palumbo, *Perugia*

Cecilia Parazzini, *Milan*

Stefano Pergolizzi, *Messina*

Antonio Pinto, *Naples*

Camillo Porcaro, *Rome*

Carlo C Quattrocchi, *Rome*

Alberto Rebonato, *Perugia*

Giuseppe Rizzo, *Rome*

Roberto De Rosa, *Naples*

Domenico Rubello, *Rovigo*

Andrea Salvati, *Bari*

Sergio Sartori, *Ferrara*

Luca M Sconfienza, *Milano*

Giovanni Storto, *Rionero*

Nicola Sverzellati, *Parma*

Alberto S Tagliafico, *Genova*

Nicola Troisi, *Florence*



Japan

Yasuhiko Hori, *Chiba*

Hidetoshi Ikeda, *Koriyama*

Masahito Kawabori, *Sapporo*

Tamotsu Kamishima, *Sapporo*

Hiro Kiyosue, *Yufu*

Yasunori Minami, *Osaka-sayama*

Yasuhiro Morimoto, *Kitakyushu*

Satoru Murata, *Tokyo*

Shigeki Nagamachi, *Miyazaki*

Hiroshi Onishi, *Yamanashi*

Morio Sato, *Wakayama Shi*

Yoshito Tsushima, *Maebashi*

Masahiro Yanagawa, *Suita*



Netherlands

Willem Jan van Rooij, *Tilburg*



New Zealand

W Howell Round, *Hamilton*



Pakistan

Wazir Muhammad, *Abbottabad*



Poland

Maciej S Baglaj, *Wroclaw*

Piotr Czauderna, *Gdansk*



Portugal

Joao Manuel RS Tavares, *Porto*



Serbia

Olivera Ciraj-Bjelac, *Belgrade*



Singapore

Gopinathan Anil, *Singapore*

Terence KB Teo, *Singapore*

Cher Heng Tan, *Singapore*



Slovakia

Stefan Sivak, *Martin*



South Korea

Ki Seok Choo, *Busan*

Seung Hong Choi, *Seoul*

Dae-Seob Choi, *Jinju*

Hong-Seok Jang, *Seoul*

Yong Jeong, *Daejeon*

Chan Kyo Kim, *Seoul*

Se Hyung Kim, *Seoul*

Joong-Seok Kim, *Seoul*

Sang Eun Kim, *Seongnam*

Sung Joon Kwon, *Seoul*

Jeong Min Lee, *Seoul*

In Sook Lee, *Busan*

Noh Park, *Goyang*

Chang Min Park, *Seoul*

Sung Bin Park, *Seoul*

Deuk Jae Sung, *Seoul*

Choongsoo Shin, *Seoul*

Kwon-Ha Yoon, *Iksan*



Spain

Miguel A De Gregorio, *Zaragoza*

Antonio Luna, *Jaén*

Enrique Marco de Lucas, *Santander*

Fernando Ruiz Santiago, *Granada*



Sweden

Dmitry Grishenkov, *Stockholm*

Tie-Qiang Li, *Stockholm*



Switzerland

Nicolau Beckmann, *Basel*

Christian Boy, *Bern*

Giorgio Treglia, *Bellinzona*

Stephan Ulmer, *Kiel*



Thailand

Sirianong Namwongprom, *Chiang Mai*



Turkey

Kubilay Aydin, *Istanbul*

Ramazan Akdemir, *Sakarya*

Serhat Avcu, *Ankara*

Ayşe Aralasmak, *Istanbul*

Oktay Algin, *Ankara*

Nevbahar Akcar, *Meselik*

Bilal Battal, *Ankara*

Zulkif Bozgeyik, *Elazig*

Nazan Ciledag, *Aakara*

Fuldem Y Donmez, *Ankara*

Gulgun Engin, *Istanbul*

Ahmet Y Goktay, *Izmir*

Oguzhan G Gumustas, *Bursa*

Kaan Gunduz, *Ankara*

Pelin Ozcan Kara, *Mersin*

Kivanc Kamburoglu, *Ankara*

Ozgur Kilickesmez, *Istanbul*

Furuzan Numan, *Istanbul*

Cem Onal, *Adana*

Ozgur Oztekin, *Izmir*

Seda Ozbek (Boruban), *Konya*

Selda Sarikaya, *Zonguldak*

Figen Taser, *Kutahya*

Baran Tokar, *Eskisehir*

Ender Uysal, *Istanbul*

Ensar Yekeler, *Istanbul*



United Kingdom

Indran Davagnanam, *London*

M DC Valdés Hernández, *Edinburgh*

Alan Jackson, *Manchester*

Suneil Jain, *Belfast*

Long R Jiao, *London*

Miltiadis Krokidis, *Cambridge*

Pradesh Kumar, *Liverpool*

Peter D Kuzmich, *Derby*

Georgios Plataniotis, *Brighton*

Vanessa Sluming, *Liverpool*



United States

Garima Agrawal, *Saint Louis*

James R Brasic, *Baltimore*

Rajendra D Badgaiyan, *Buffalo*

Ulas Bagci, *Bethesda*

Anat Biegon, *Stony Brook*

Ramon Casanova, *Winston Salem*

Wenli Cai, *Boston*

Zheng Chang, *Durham*

Corey J Chakarun, *Long Beach*

Kai Chen, *Los Angeles*

Hyun-Soon Chong, *Chicago*

Marco Cura, *Dallas*

Ravi R Desai, *Bensalem*

Delia DeBuc, *Miami*

Carlo N De Cecco, *Charleston*

Timm-Michael L Dickfeld, *Baltimore*

Subba R Digumarthy, *Boston*

Huy M Do, *Stanford*

Todd A Faasse, *Grand Rapids*

Salomao Faintuch, *Boston*

Girish M Fatterpekar, *New York*

Dhakshinamoorthy Ganesan, *Houston*

Robert J Griffin, *Little Rock*

Andrew J Gunn, *Boston*

Sandeep S Hedgire, *Boston*

Timothy J Hoffman, *Columbia*

Mai-Lan Ho, *San Francisco*

Juebin Huang, *Jackson*

Abid Irshad, *Charleston*

Matilde Inglese, *New York*

El-Sayed H Ibrahim, *Jacksonville*

Paul R Julsrud, *Rochester*

Pamela T Johnson, *Baltimore*

Ming-Hung Kao, *Tempe*

Sunil Krishnan, *Houston*

Richard A Komoroski, *Cincinnati*

Sandi A Kwee, *Honolulu*

King Kim, *Ft. Lauderdale*

Guozheng Liu, *Worcester*

Yiyan Liu, *Newark*

Venkatesh Mani, *New York*

Lian-Sheng Ma, *Pleasanton*

Rachna Madan, *Boston*

Zeyad A Metwalli, *Houston*

Yilong Ma, *Manhasset*

Hui Mao, *Atlanta*

Feroze B Mohamed, *Philadelphia*

Gul Moonis, *Boston*

John L Noshier, *New Brunswick*

Rahmi Oklu, *Boston*

Aytekun Oto, *Chicago*

Bishnuhari Paudyal, *Philadelphia*

Rajul Pandya, *Youngstown*

Chong-Xian Pan, *Sacramento*

Jay J Pillai, *Baltimore*

Neal Prakash, *Duarte*

Reza Rahbar, *Boston*

Ali S Raja, *Boston*

Gustavo J Rodriguez, *El Paso*

David J Sahn, *Portland*

Steven Schild, *Scottsdale*

Ali R Sepahdari, *Los Angeles*

Li Shen, *Indianapolis*

JP Sheehan, *Charlottesville*

Atul B Shinagare, *Boston*

Sarabjeet Singh, *Boston*

Charles J Smith, *Columbia*

Kenji Suzuki, *Chicago*

Monvadi Srichai-Parsia, *Washington*

Sree H Tirumani, *Boston*

Hebert A Vargas, *New York*

Sachit Verma, *Philadelphia*

Yoichi Watanabe, *Minneapolis*

Li Wang, *Chapel Hill*

Carol C Wu, *Boston*

Shoujun Xu, *Houston*

Min Yao, *Cleveland*

Xiaofeng Yang, *Atlanta*

Qingbao Yu, *Albuquerque*

Aifeng Zhang, *Chicago*

Chao Zhou, *Bethlehem*

Hongming Zhuang, *Philadelphia*

**REVIEW**

- 361 Role of magnetic resonance imaging in the detection and characterization of solid pancreatic nodules: An update

Al Ansari N, Ramalho M, Semelka RC, Buonocore V, Gigli S, Maccioni F

MINIREVIEWS

- 375 Iliac vein compression syndrome: Clinical, imaging and pathologic findings
- 382 Application of positron emission tomography/computed tomography in radiation treatment planning for head and neck cancers

Brinegar KN, Sheth RA, Khademhosseini A, Bautista J, Oklu R

Awan MJ, Siddiqui F, Schwartz D, Yuan J, Machtay M, Yao M

ORIGINAL ARTICLE**Case Control Study**

- 394 Magnetic resonance imaging in assessment of stress urinary incontinence in women: Parameters differentiating urethral hypermobility and intrinsic sphincter deficiency
- 405 Partial correlation analyses of global diffusion tensor imaging-derived metrics in glioblastoma multiforme: Pilot study

Macura KJ, Thompson RE, Bluemke DA, Genadry R

Cortez-Conradis D, Rios C, Moreno-Jimenez S, Roldan-Valadez E

Observational Study

- 415 Pancreatic trauma: The role of computed tomography for guiding therapeutic approach

Moschetta M, Telegrafo M, Malagnino V, Mappa L, Stabile Ianora AA, Dabbicco D, Margari A, Angelelli G

ABOUT COVER

Editorial Board Member of *World Journal of Radiology*, Christoph Zilkens, MD, Surgeon, Department of Orthopaedic Surgery, University Hospital of Düsseldorf, 40225 Düsseldorf, Germany

AIM AND SCOPE

World Journal of Radiology (*World J Radiol*, *WJR*, online ISSN 1949-8470, DOI: 10.4329) is a peer-reviewed open access academic journal that aims to guide clinical practice and improve diagnostic and therapeutic skills of clinicians.

WJR covers topics concerning diagnostic radiology, radiation oncology, radiologic physics, neuroradiology, nuclear radiology, pediatric radiology, vascular/interventional radiology, medical imaging achieved by various modalities and related methods analysis. The current columns of *WJR* include editorial, frontier, diagnostic advances, therapeutics advances, field of vision, mini-reviews, review, topic highlight, medical ethics, original articles, case report, clinical case conference (clinicopathological conference), and autobiography.

We encourage authors to submit their manuscripts to *WJR*. We will give priority to manuscripts that are supported by major national and international foundations and those that are of great basic and clinical significance.

INDEXING/ABSTRACTING

World Journal of Radiology is now indexed in PubMed Central, PubMed, Digital Object Identifier, and Directory of Open Access Journals.

FLYLEAF

I-III Editorial Board

EDITORS FOR THIS ISSUE

Responsible Assistant Editor: *Xiang Li*
Responsible Electronic Editor: *Xiao-Kang Jiao*
Proofing Editor-in-Chief: *Lian-Sheng Ma*

Responsible Science Editor: *Xue-Mei Gong*
Proofing Editorial Office Director: *Xiu-Xia Song*

NAME OF JOURNAL
World Journal of Radiology

ISSN
ISSN 1949-8470 (online)

LAUNCH DATE
December 31, 2009

FREQUENCY
Monthly

EDITORS-IN-CHIEF
Kai U Juergens, MD, Associate Professor, MRT und PET/CT, Nuklearmedizin Bremen Mitte, ZEMODI - Zentrum für morphologische und molekulare Diagnostik, Bremen 28177, Germany

Edwin JR van Beek, MD, PhD, Professor, Clinical Research Imaging Centre and Department of Medical Radiology, University of Edinburgh, Edinburgh EH16 4TJ, United Kingdom

Thomas J Vogl, MD, Professor, Reader in Health Technology Assessment, Department of Diagnostic and Interventional Radiology, Johann Wolfgang

Goethe University of Frankfurt, Frankfurt 60590, Germany

EDITORIAL OFFICE
Jin-Lei Wang, Director
Xiu-Xia Song, Vice Director
World Journal of Radiology
Room 903, Building D, Ocean International Center, No. 62 Dongsihuan Zhonglu, Chaoyang District, Beijing 100025, China
Telephone: +86-10-59080039
Fax: +86-10-85381893
E-mail: editorialoffice@wjnet.com
Help Desk: <http://www.wjnet.com/esps/helpdesk.aspx>
<http://www.wjnet.com>

PUBLISHER
Baishideng Publishing Group Inc
8226 Regency Drive,
Pleasanton, CA 94588, USA
Telephone: +1-925-223-8242
Fax: +1-925-223-8243
E-mail: bpgoffice@wjnet.com
Help Desk: <http://www.wjnet.com/esps/helpdesk.aspx>
<http://www.wjnet.com>

PUBLICATION DATE
November 28, 2015

COPYRIGHT
© 2015 Baishideng Publishing Group Inc. Articles published by this Open-Access journal are distributed under the terms of the Creative Commons Attribution Non-commercial License, which permits use, distribution, and reproduction in any medium, provided the original work is properly cited, the use is non commercial and is otherwise in compliance with the license.

SPECIAL STATEMENT
All articles published in journals owned by the Baishideng Publishing Group (BPG) represent the views and opinions of their authors, and not the views, opinions or policies of the BPG, except where otherwise explicitly indicated.

INSTRUCTIONS TO AUTHORS
Full instructions are available online at http://www.wjnet.com/1949-8470/g_info_20100316162358.htm.

ONLINE SUBMISSION
<http://www.wjnet.com/esps/>

Role of magnetic resonance imaging in the detection and characterization of solid pancreatic nodules: An update

Najwa Al Ansari, Miguel Ramalho, Richard C Semelka, Valeria Buonocore, Silvia Gigli, Francesca Maccioni

Najwa Al Ansari, Valeria Buonocore, Silvia Gigli, Francesca Maccioni, Department of Radiological Sciences, Oncology and Pathology, Policlinico Umberto I Hospital Rome, Sapienza University of Rome, 00161 Rome, Italy

Miguel Ramalho, Department of Radiology, Hospital Garcia de Orta, 2801-951 Almada, Portugal

Miguel Ramalho, Richard C Semelka, Department of Radiology, University of North Carolina, Chapel Hill, NC 27599-7510, United States

Author contributions: All authors had contributed equally to this work in form of literature review, manuscript writing/editing, and figure collection/illustration/annotation/captioning.

Conflict-of-interest statement: There is no conflict of interest associated with any of the senior author or other co-authors contributed their efforts in this manuscript.

Open-Access: This article is an open-access article which was selected by an in-house editor and fully peer-reviewed by external reviewers. It is distributed in accordance with the Creative Commons Attribution Non Commercial (CC BY-NC 4.0) license, which permits others to distribute, remix, adapt, build upon this work non-commercially, and license their derivative works on different terms, provided the original work is properly cited and the use is non-commercial. See: <http://creativecommons.org/licenses/by-nc/4.0/>

Correspondence to: Richard C Semelka, MD, Professor, Department of Radiology, University of North Carolina, UNC at Chapel Hill CB 7510 - 2001 Old Clinic Bldg., Chapel Hill, NC 27599-7510, United States. richsem@med.unc.edu
Telephone: +1-919-9669676
Fax: +1-919-8437147

Received: April 27, 2015
Peer-review started: April 28, 2015
First decision: August 4, 2015
Revised: September 8, 2015
Accepted: October 1, 2015
Article in press: October 8, 2015
Published online: November 28, 2015

Abstract

Pancreatic ductal adenocarcinoma is the most common malignant tumor of the pancreas. The remaining pancreatic tumors are a diverse group of pancreatic neoplasms that comprises cystic pancreatic neoplasms, endocrine tumors and other uncommon pancreatic tumors. Due to the excellent soft tissue contrast resolution, magnetic resonance imaging (MRI) is frequently able to readily separate cystic from noncystic tumors. Cystic tumors are often easy to diagnose with MRI; however, noncystic non-adenocarcinoma tumors may show a wide spectrum of imaging features, which can potentially mimic ductal adenocarcinoma. MRI is a reliable technique for the characterization of pancreatic lesions. The implementation of novel motion-resistant pulse sequences and respiratory gating techniques, as well as the recognized benefits of MR cholangiopancreatography, make MRI a very accurate examination for the evaluation of pancreatic masses. MRI has the distinctive ability of non-invasive assessment of the pancreatic ducts, pancreatic parenchyma, neighbouring soft tissues, and vascular network in one examination. MRI can identify different characteristics of various solid pancreatic lesions, potentially allowing the differentiation of adenocarcinoma from other benign and malignant entities. In this review we describe the MRI protocols and MRI characteristics of various solid pancreatic lesions. Recognition of these characteristics may establish the right diagnosis or at least narrow the differential diagnosis, thus avoiding unnecessary tests or procedures and permitting better management.

Key words: Pancreatic nodules; Malignant; Lymphoma; Benign; Magnetic resonance imaging; Adenocarcinoma; Pancreas; Neuroendocrine; Solid pseudopapillary tumor; Metastases

© **The Author(s) 2015.** Published by Baishideng Publishing Group Inc. All rights reserved.

Core tip: In addition to pancreatic ductal adenocarcinoma

other solid pancreatic lesions occur. Less common solid primary pancreatic tumors and non-neoplastic disease processes that may be diagnosed with relatively high specificity employing magnetic resonance imaging (MRI). The radiologist must be familiar with their MRI appearance to correctly diagnose them, or suggest them in the differential diagnosis when appropriate, since it may change substantially the approach, prognosis and patient management.

Al Ansari N, Ramalho M, Semelka RC, Buonocore V, Gigli S, Maccioni F. Role of magnetic resonance imaging in the detection and characterization of solid pancreatic nodules: An update. *World J Radiol* 2015; 7(11): 361-374 Available from: URL: <http://www.wjgnet.com/1949-8470/full/v7/i11/361.htm> DOI: <http://dx.doi.org/10.4329/wjr.v7.i11.361>

INTRODUCTION

Pancreatic ductal adenocarcinoma is the most common malignant tumor of the pancreas, accounting for 85%-90% of all malignant pancreatic tumors and is the 4th most common cause of cancer death worldwide^[1]. The remaining 10%-15% of pancreatic tumors is a varied group of neoplasms that comprises cystic pancreatic neoplasms, endocrine tumors and other uncommon pancreatic tumors. Magnetic resonance imaging (MRI) is reliable for the characterization of solid and cystic pancreatic lesions. Due to the excellent soft-tissue contrast resolution, MRI is able to readily separate cystic from noncystic tumors. Cystic tumors are frequently easier to diagnose since they often possess typical imaging findings allowing an accurate and reliable prospective diagnosis. Noncystic noncarcinoma tumors may show a wide spectrum of imaging features, which most often are distinct from the features of ductal adenocarcinoma. Infrequently they may possess features that simulate carcinoma, and therefore clinical history and laboratory parameters are always important to be aware of. In this review we describe the typical MRI characteristics of various solid pancreatic lesions, which will aid in differentiation of adenocarcinoma from other benign and malignant entities. Recognition of these characteristics often may establish the right diagnosis or at least narrow the differential diagnosis, which will allow better patient management and avoid unnecessary tests or procedures.

We herein describe the typical MRI findings of ductal adenocarcinoma, of less common solid primary pancreatic tumors, and of non-neoplastic disease processes that may simulate ductal adenocarcinoma.

CLASSIFICATION OF PANCREATIC TUMORS

According to the World Health Organization classifi-

cation, pancreatic tumors are classified depending on the cell lineage they arise from. The tumors may have an epithelial or nonepithelial origin.

Tumors with epithelial origin include the exocrine pancreas: (1) ductal cells, including ductal adenocarcinoma with its different histopathological variants, and mucinous and serous cystic tumors; (2) acinar cells, including acinar cell carcinoma (ACC) and mixed acinar-endocrine carcinoma; or (3) uncertain origin, including solid pseudopapillary tumor (SPT) and pancreatoblastoma or the endocrine pancreas (functioning and nonfunctioning tumors).

The nonepithelial tumors include neoplasms such as primary lymphoma and tumors of mesenchymal cell origin (hemangioma, lymphangioma, sarcoma, lipoma, etc.).

There are also nonpancreatic tumor lesions in origin that might involve the pancreas, including malignant lesions such as metastasis or secondary lymphoma, and benign lesions such as intrapancreatic splenule.

MRI EVALUATION OF THE PANCREAS

MRI is a reliable technique for the characterization of pancreatic lesions. The implementation of novel motion-resistant pulse sequences and respiratory gating techniques, as well as the recognized benefits of MR cholangiopancreatography, make MRI a very accurate examination for the evaluation of pancreatic masses. MRI has the distinctive ability of non-invasive assessment of the pancreatic ducts, pancreatic parenchyma, neighbouring soft tissues, and vascular network in one examination.

MRI of the pancreas should be performed with state of the art scanners using high field strength (1.5T or 3T) units^[2-4] with phased-array torso coils and parallel imaging to maximize signal to noise ratio and permit for superior spatial resolution and faster acquisition times.

3T systems allow higher spatial resolution and provide the highest post-contrast imaging quality and temporal resolution of the pancreas, which is important when evaluating small focal pancreatic lesions^[4], and looking for vascular involvement or encasement.

The typical MRI protocol for the assessment of the pancreas commonly includes coronal and transverse T2-weighted single-shot echo train spin echo (SS-ETSE), transverse T2-weighted fat suppressed fast spin echo or SS-ETSE, transverse in-phase and out-of-phase T1-weighted spoiled gradient echo (GRE), and transverse T1-weighted fat suppressed three-dimensional (3D) GRE images, obtained before and after contrast injection during the late arterial, portal-venous and interstitial phases. Magnetic resonance cholangiopancreatography (MRCP) is routinely added to abdominal protocols to assess ductal obstruction, dilatation or luminal outline. This sequence combination provides comprehensive evaluation of a full range of pancreatic disease processes.

T2-weighted SS-ETSE sequences such as half-Fourier acquisition snapshot turbo spin-echo offer

anatomic display of the common bile duct (CBD) and pancreatic duct on coronal and transverse plane images. This sequence is important to evaluate fluid content, which most often allows clear separation of cystic and solid content lesions, as well as complications such as the assessment of the complexity of pancreatic fluid collections.

Pre- and post-contrast T1-weighted GRE sequences are typically obtained as a fat-suppressed 3D-GRE technique, allowing high-quality dynamic imaging of the pancreas. The main benefits of these sequences include the ability to obtain thinner slices (2-3 mm) and to perform multiplanar imaging, essential to assess and characterize focal pancreatic masses with < 1 cm in size and to evaluate diffuse pancreatic disease^[3,5-10].

3D MRCP images are obtained in an oblique coronal projection following the plane of the main pancreatic duct, with the complementary benefit of being able to generate multiplanar maximum intensity projection and volume rendering imaging. This approach delineates longer segments of the pancreatic duct. MRCP depicts well the biliary and pancreatic ducts allowing optimal evaluation of ductal contour and dilatation, as well as abnormal duct pathways^[7-9]. The combination of tissue imaging sequences and MRCP generate comprehensive information on pancreatic disease.

For the diagnosis of biliary disease, the secretin enhanced MRCP is routinely performed as part of the workup of patients with known or suspected pancreatic disease such as acute and chronic pancreatitis, congenital variants of the pancreaticoduodenal junction, and intraductal papillary mucinous neoplasms and follow-up of patients after pancreatectomy, in many centers. Secretin is well tolerated, and side effects are rarely seen^[11-13].

MRI is a non-ionizing cross-sectional imaging method with a safer intra-venous contrast profile in comparison to computed tomography (CT). This is especially important in patients at higher risk of radiation injury (*e.g.*, younger patients) especially those requiring repeated imaging follow-up.

Some gadolinium based contrast agents (GBCAs) are associated with nephrogenic systemic fibrosis. Avoidance of GBCAs exposure is the best approach for high-risk patients^[14] including patients with acute or advanced chronic kidney disease. Also, it has been reported that the incidence of immediate hypersensitivity reactions to MR GBCAs was 0.079%, and the recurrence rate of hypersensitivity reactions was 30% in patients with prior reactions^[15]. It is a very low percentage if we compare it to iodinated contrast media but however it should be considered.

New motion-resistant MRI techniques provide adequate images even in patients that are not able to suspend respiration^[16]. Preliminary studies demonstrated that in patients who are unable to suspend respiration, new imaging techniques for MRI, such as radial 3D-GRE acquired in a free breathing fashion, may be useful for pancreatic MR imaging and aid the radiologist in the

detection and characterization of pancreatic focal lesions.

Normal pancreatic parenchyma displays high T1 signal intensity due to the presence of aqueous protein^[3,4], which is accentuated on fat-suppressed GRE sequences. The normal pancreas typically shows uniform hyperintense enhancement on arterial phase images, fading overtime to become isointense to the liver on interstitial phase images (Figure 1)^[6,17].

In the elderly, the high T1 signal intensity of the pancreas may be diminished and be lesser than that of the liver, reflecting fibrosis resultant from the aging process^[5].

Pancreatic ductal adenocarcinoma

Ductal adenocarcinoma is the most common malignant pancreatic neoplasm and accounts for almost 90% of all malignant pancreatic tumors. Males are affected twice as often as women and the peak age of occurrence is in the 7th to 8th decades of life^[18]. At clinical presentation, 2/3 of patients have an advanced tumor stage. This may justify why pancreatic adenocarcinoma shows a poor prognosis, with a 5-year survival rate of 5%^[19]. Despite advances in patient management and new chemotherapy regimens, surgery remains the only curative treatment^[19].

The appearance of the typical ductal adenocarcinoma is an irregular, small focal solid mass (2-3 cm) without necrosis or hemorrhage. It is a heterogeneous and poorly enhancing mass with a tendency for local infiltration, including vascular encasement.

Near 60%-70% of ductal adenocarcinomas of the pancreas involve the pancreatic head, 10%-20% are found in the body and 5%-10% in the tail. Diffuse pancreatic involvement occurs in 5% of the cases^[20].

Spin-echo images are limited in the detection of pancreatic adenocarcinoma. On T2-weighted images, tumors are usually slightly hypointense relative to the background pancreatic parenchyma and consequently challenging to visualize. Ductal adenocarcinomas appear as low signal intensity lesions on noncontrast fat-suppressed T1-weighted images and usually well delineated from normal background pancreas, which is high in signal intensity^[17,21-24].

Detection of adenocarcinoma is better performed on the arterial phase images, where the lesion will enhance to a lesser degree than the adjacent background pancreas (Figures 2 and 3), due to the abundant fibrous stroma and scarce tumor vascularity^[23]. The increased volume of the extracellular space and the venous drainage of tumors compared to normal pancreatic tissue are responsible for the near isointense appearance of ductal adenocarcinoma on the interstitial phase^[23].

In general, large pancreatic tumors tend to persist low in signal intensity (Figure 2) on interstitial phase images, whereas the signal intensity of smaller tumors is more variable and may range from hypointense to minimally hyperintense on this phase (Figure 3).

Obstruction of the main pancreatic duct by the pancreatic adenocarcinoma, which may be seen even

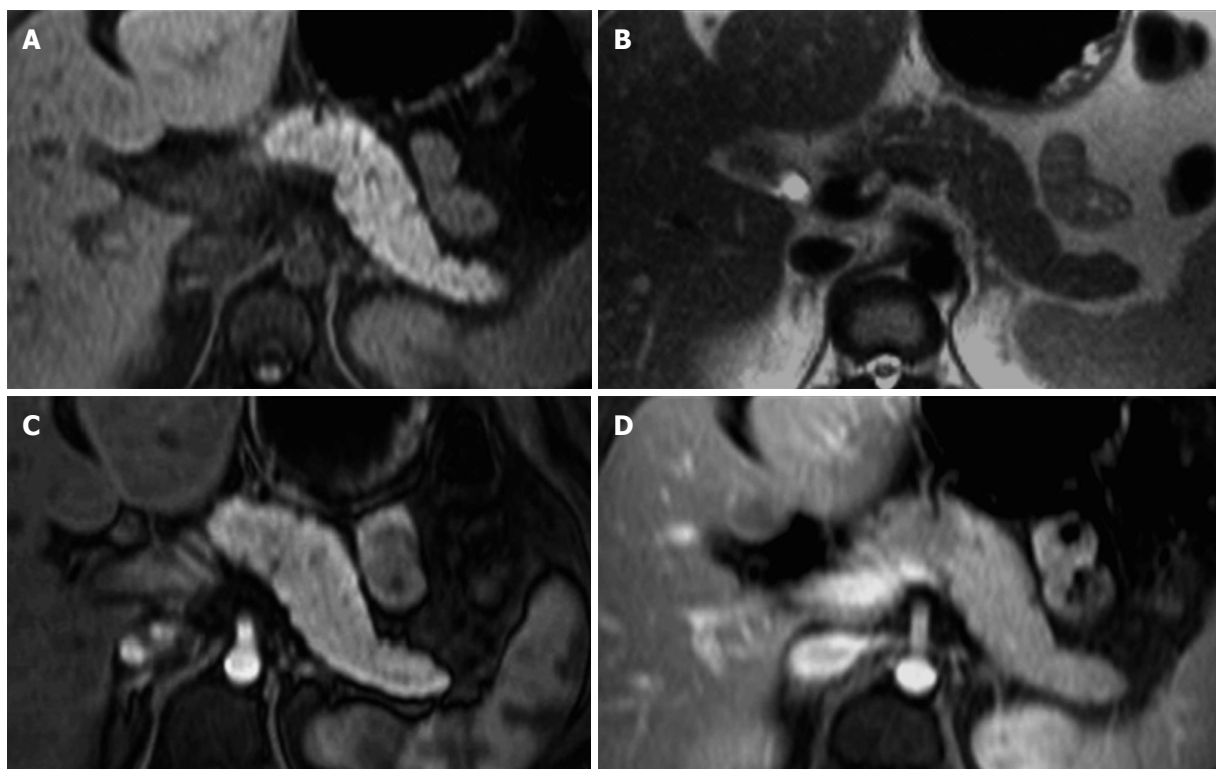


Figure 1 Normal pancreas. Axial T2-weighted SS-ETSE (A), pre-contrast fat-suppressed T1-weighted (B) GRE and post-gadolinium fat-suppressed T1-weighted gradient echo images acquired in the arterial (C) and venous (D) phases of enhancement. The normal pancreas is high in signal intensity on T1-weighted images (B) due to the presence of aqueous protein in the pancreatic acini. A uniform capillary blush is apparent on the immediate post-gadolinium image (C). T2-weighted sequences allow the depiction of the pancreatic duct. SS-ETSE: Single-shot echo train spin echo; GRE: Gradient echo.

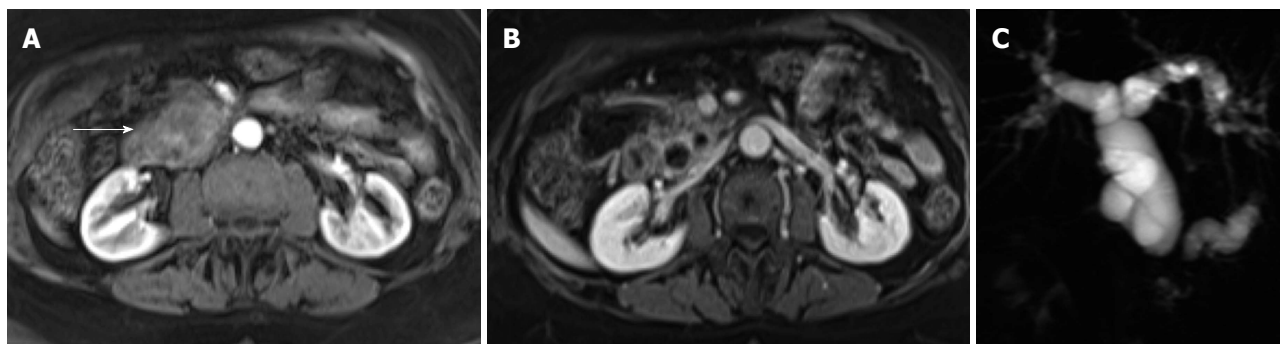


Figure 2 Pancreatic ductal adenocarcinoma. Axial post-gadolinium fat-suppressed T1-weighted images obtained in the arterial phase (A) and interstitial phase (B) image, and coronal maximum intensity projection image of MRCP (C). There is a hypovascular tumor arising in the pancreatic head (arrow, A) that obstructs the common bile duct and pancreatic duct (double duct sign). This sign is well depicted in the MRCP images (C). MRCP: Magnetic resonance cholangiopancreatography.

with small tumors, results in tumor-associated chronic pancreatitis. Many times, the pancreatic parenchyma distal to pancreatic adenocarcinoma is atrophic and low in signal intensity compared to normal pancreas, due to chronic inflammation, progressive fibrosis and diminished proteinaceous fluid of the gland^[23,24]. In these cases, depiction of the tumor is poor on noncontrast T1-weighted fat-suppressed images; nevertheless, arterial phase images are very helpful in the discrimination of the size and extent of pancreatic ductal adenocarcinomas, as tumors almost always enhance less than the adjacent chronically inflamed pancreas^[23,24]. These imaging characteristics along with substantial increase of CA 19.9

levels are unique to ductal adenocarcinoma and allow correct diagnosis with high accuracy.

Although it is non-specific, obstruction of the main pancreatic duct is one of the most important signs of ductal adenocarcinoma. The concurrent dilatation of the pancreatic and hepatic duct may frequently occurs when the pancreatic cancer develops in the cephalic region, thus depicting the so called "double duct sign", in some cases this may be the only sign, if the pancreatic tumor is very small. Possible differential diagnosis in this case includes an acute or chronic papillitis^[2,11] and the ampullary carcinoma^[25].

Regarding tumor resectability, radiologists should

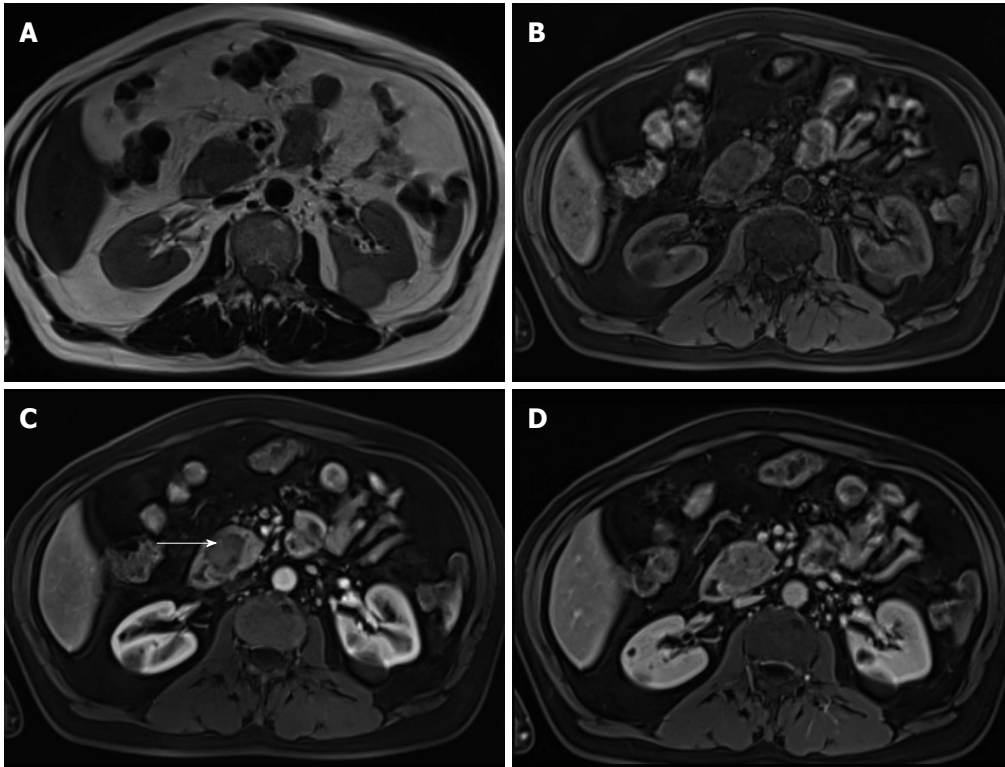


Figure 3 Pancreatic ductal adenocarcinoma. Axial T2-weighted single-shot echo train spin echo (A), pre-contrast fat-suppressed T1-weighted (B) gradient echo (GRE) and post-gadolinium fat-suppressed T1-weighted GRE images acquired in the arterial (C) and venous (D) phases of enhancement. There is a solid nodule in the head of the pancreas, which is more conspicuous in the pre-contrast and arterial phase T1-weighted images (B, arrow, C), consistent with ductal adenocarcinoma. Note that this lesion might be imperceptible on T2-weighted images (A) and venous phase images (D).

evaluate certain MRI findings and describe them in the MRI report: (1) distant metastases, frequently to the liver, peritoneum, lung and paraortic lymph nodes; (2) infiltration of neighboring structures, including stomach, colon, spleen; (3) invasion of the peripancreatic arteries, including celiac trunk, hepatic artery, superior mesenteric artery; and (4) invasion of the peripancreatic veins, including portal and superior mesenteric vein^[2,14,22,26].

State of the art MRI is suitable to detect and characterize focal ductal adenocarcinoma smaller than 1 cm^[2,21,22,27], which tend to appear as small non-contour-deforming pancreatic lesions. Detection of this early manifestation of disease is difficult or impossible to identify with multiphasic current-generation CT^[28,29].

Endoscopy ultrasound has been widely used in detection of clinically suspected pancreatic lesion; together with fine needle aspiration, it has been reported to be the best diagnostic method for small pancreatic neoplasms. Unfortunately this is an invasive and an operator-dependent-technique and is not yet widely used^[30].

It is very important to differentiate adenocarcinoma from other benign and malignant entities, because the clinical management and prognosis varies according to the type of pathology^[2,31]. Some lesions require surgery or imaging follow-up, whereas other lesions are clinically irrelevant, not requiring further evaluation and/or treatment.

BENIGN LESIONS THAT MAY SIMULATE DUCTAL ADENOCARCINOMA

Pancreatic lipomatosis

Pancreatic lipomatosis is a condition related to fatty infiltration/replacement of the pancreatic parenchyma, and is commonly seen in the elder, especially in obese patients. Involvement is normally diffuse but occasionally it may simulate a neoplastic lesion. The anterior aspect of the head of the pancreas is the most common location for pancreatic lipomatosis (Figure 4).

The absences of mass effect, ductal or vascular displacement are important findings to establish the correct diagnosis.

MRI is highly specific for the detection of fat^[32]. A moderate to marked signal loss in the out-of-phase relative to the in-phase images is distinctive of this condition (Figure 4)^[33]. Macroscopic fatty replacement of the pancreas will show high T1 and T2 signal intensity, and marked signal loss on fat-suppressed sequences^[32-34].

Acute pancreatitis

Acute pancreatitis is defined as an acute inflammatory condition typically presenting with abdominal pain and elevation in pancreatic enzymes secondary mainly to alcoholism or cholelithiasis.

MRI is more sensitive than CT, supporting the use of MRI in the evaluation of patients with a nonconclusive

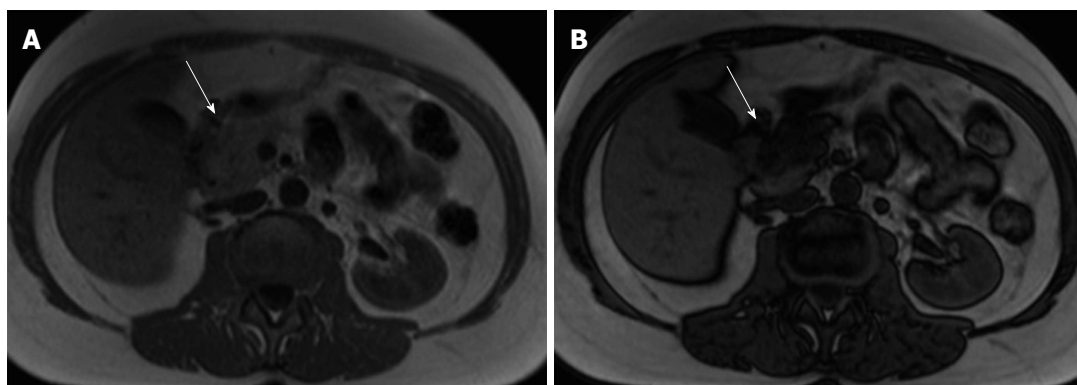


Figure 4 Pancreatic lipomatosis. Axial in-phase (A) and out-of-phase (B) T1-weighted GRE images. There is a focal fat infiltration in the region of the pancreatic head (arrows), only noticeable in the out-of-phase images, which is diagnostic for this entity. Focal fat infiltration is a benign condition that can simulate pancreatic adenocarcinoma especially on CT. GRE: Gradient echo; CT: Computed tomography.

CT or to differentiate pure inflammatory condition from neoplastic lesion of the pancreas.

The acutely inflamed pancreas shows either focal or diffuse enlargement of the parenchyma, with signal intensity comparable to that of normal pancreatic tissue in non-complicated mild to moderate pancreatitis. Peripancreatic fluid is an important sign visualized in acute pancreatitis, best displayed on fat-suppressed T2-weighted sequences, seen as high signal in a background of intermediate to low-signal pancreas and fat (Figure 5)^[2,35,36].

Chronic pancreatitis

Chronic pancreatitis is defined as a continuous or relapsing, chronic, inflammatory process of the pancreas, characterized by permanent morphologic changes and typically leads to diminishing of function. Distinction between focal pancreatitis and adenocarcinoma may be challenging because both entities may result in focal enlargement of the pancreatic head, atrophy of the tail of the pancreas and obliteration of the fat plane around the superior mesenteric artery. Ductal adenocarcinoma arising in the pancreatic head may cause obstruction of the CBD and pancreatic duct, with the MRCP appearance of a "double duct sign". This sign can be also appreciated, although less commonly, in patients with focal pancreatitis.

Focal chronic pancreatitis and adenocarcinoma may display comparable signal intensity changes of the enlarged region of pancreas on noncontrast T1- and T2-weighted images, including mild hypointensity on T1-weighted images and heterogeneous and mild hyperintensity on T2-weighted images.

On arterial phase images, focal chronic pancreatitis usually displays heterogeneous enhancement and may show signal voids from cysts and/or calcifications with no evidence of a definable mass. In this setting, the focally enlarged region of the pancreas preserve the glandular feathery texture, comparable to the remaining pancreas^[37]. Conversely, in ductal adenocarcinoma, the focally enlarged region of the pancreas loses its usual

anatomic detail.

Diffuse low T1 signal intensity and hypovascularity of the entire pancreas, including the region of focal enlargement, are distinctive for chronic pancreatitis. In the setting of ductal adenocarcinoma, the tumor enhances less than the adjacent chronically inflamed pancreatic parenchyma^[38].

Several features favor a diagnosis of focal pancreatitis, including: (1) non-dilated or smoothly tapering pancreatic and bile ducts coursing through the mass ("duct penetrating sign")^[38]; (2) parenchymal calcifications (seen as signal voids); (3) pancreatic duct beading and varying caliber; and (4) side branch dilatation. Instead, abrupt interruption of a smoothly dilated main pancreatic duct, minimal side-branch dilatation, upstream pancreatic atrophy and a high ratio of duct caliber to the pancreatic gland width are features typically observed in adenocarcinoma (Figure 2)^[39].

A previous investigation evaluated the accuracy of MRI in the differentiation between ductal adenocarcinoma and chronic pancreatitis, in patients with focal pancreatic mass^[37]; in this study, MR technique with the use of fat-suppressed T1-weighted 3D-GRE sequence was able to differentiate ductal adenocarcinoma from chronic pancreatitis with a sensitivity and specificity of 93% and 75%, respectively. The most critical finding for ductal adenocarcinoma of the pancreas was a relative delineation of the mass compared to the background pancreatic parenchyma. On the other hand, the most critical finding of chronic pancreatitis was an imprecise delineation with a mildly increased signal intensity and enhancement compared with the background pancreatic parenchyma on portal-venous phase images. These features reflect a more progressive enhancement of inflammatory tissue compared to ductal adenocarcinoma from arterial phase to portal-venous images. A further useful imaging feature is effacement of the fine, lobular architectural pattern of the pancreas in pancreatic adenocarcinoma^[37].

The encasement of the celiac axis, superior mesenteric artery, lymphadenopathy and liver metastases

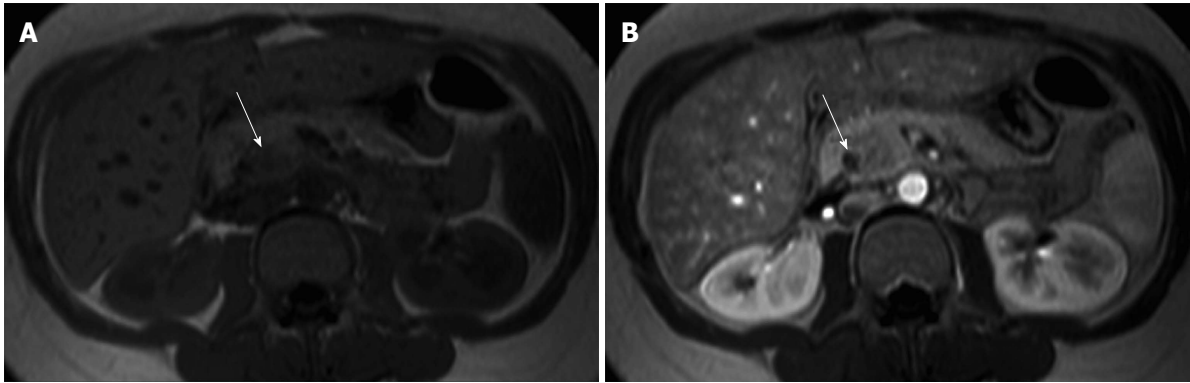


Figure 5 Acute pancreatitis. Axial in-phase (A) T1-weighted GRE image and arterial phase (B) fat-suppressed T1-weighted GRE image (B) in a patient with elevated amylase. There is a nodular area in the uncinate process showing mild T1-weighted hypointensity due to edema, however showing arterial enhancement (arrow, B) and with preservation of marbled pancreatic texture. This was compatible with focal acute pancreatitis. GRE: Gradient echo.

establish the diagnosis of ductal adenocarcinoma^[26,40], with liver metastases representing the definitive distinction.

OTHER SOLID PANCREATIC TUMORS WITH EPITHELIAL AND ENDOCRINE ORIGIN THAT MIGHT SIMULATE DUCTAL ADENOCARCINOMA

ACC

ACC is a rare primary tumor of the exocrine gland of the pancreas, and although acinar cells comprise most of the pancreatic parenchyma, ACC represents only 1% of all exocrine pancreatic cancers. Tumors generally occur between the fifth and seventh decades^[2]. It is defined as a carcinoma exhibiting pancreatic enzyme secretion by neoplastic exocrine cells, and its clinical presentation is usually related to either the local effects of the tumor or to metastases^[41]. Presenting symptoms are frequently nonspecific. "Lipase hypersecretion syndrome" is related to hypersecretion of lipase by the ACC, which may result in subcutaneous fat necrosis, bone infarcts, and polyarthritides^[42,43]. Hypoglycemia as a presenting symptom has also been observed in some patients.

These cancers are generally exophytic, oval or round, well marginated, and hypovascular. Small tumors are usually solid, whereas larger tumors almost invariably contain cystic areas representing regions of necrosis, hemorrhage, and occasionally amorphous intratumoral calcifications, seen as signal voids^[38,39].

These tumors are frequently uniformly or partially well-defined, with thin, enhancing capsules, and enhance less than the adjacent normal background pancreas^[38,39]. These tumors are predominantly low in signal intensity on T1-weighted images and iso- to moderately hyperintense on T2-weighted images.

ACC should always be considered when a large pancreatic mass with typical imaging is found a solid mass with variably sized central cystic areas or cystic

masses^[2,43-45]. The tumor marker CA 19.9, which is generally increased in pancreatic adenocarcinoma, is rarely elevated in ACC.

UNCERTAIN ORIGIN

SPT

SPT of the pancreas is an uncommon, low-grade epithelial malignancy of the exocrine pancreas that most often appears in young female patients^[2,20,46], and accounts for about 1% to 2% of all pancreatic tumors^[47].

This tumor is typically benign and is found mainly in young women between the 2nd and 3rd decades of life. This age presentation is rarely seen in ductal adenocarcinoma. This tumor shows a predilection for African-American and Asian women, despite rare cases having been reported in children and men. Malignant degeneration may occur, however most SPTs show benign behavior^[48,49]. Complete surgical removal is the treatment of choice. Metastasis is rare but local recurrence has been described. The prognosis is excellent after resection.

The mass occurs most frequently in the head or tail. SPT is often discovered incidentally and appears as a large well-demarcated and encapsulated pancreatic mass, surrounded by a marginal thick capsule and with variable relative amounts of intralesional solid, cystic and hemorrhagic components. The peripheral capsule is often present and seen on MRI, with an incidence of 95%-100%^[48]. Vascular encasement is exclusively seen in malignant types.

MR imaging characteristically shows a well-defined lesion with heterogeneous T1- and T2-weighted signal intensity, reflecting the complex nature of the mass. Regions of high T1 and low or inhomogeneous T2 signal intensity may be seen and are related with blood products and may help to differentiate SPTs from endocrine tumors, whose cystic components generally are not hemorrhagic and therefore not typically possessing moderately increased T1 signal intensity. Furthermore, the peripheral areas of SPTs are not

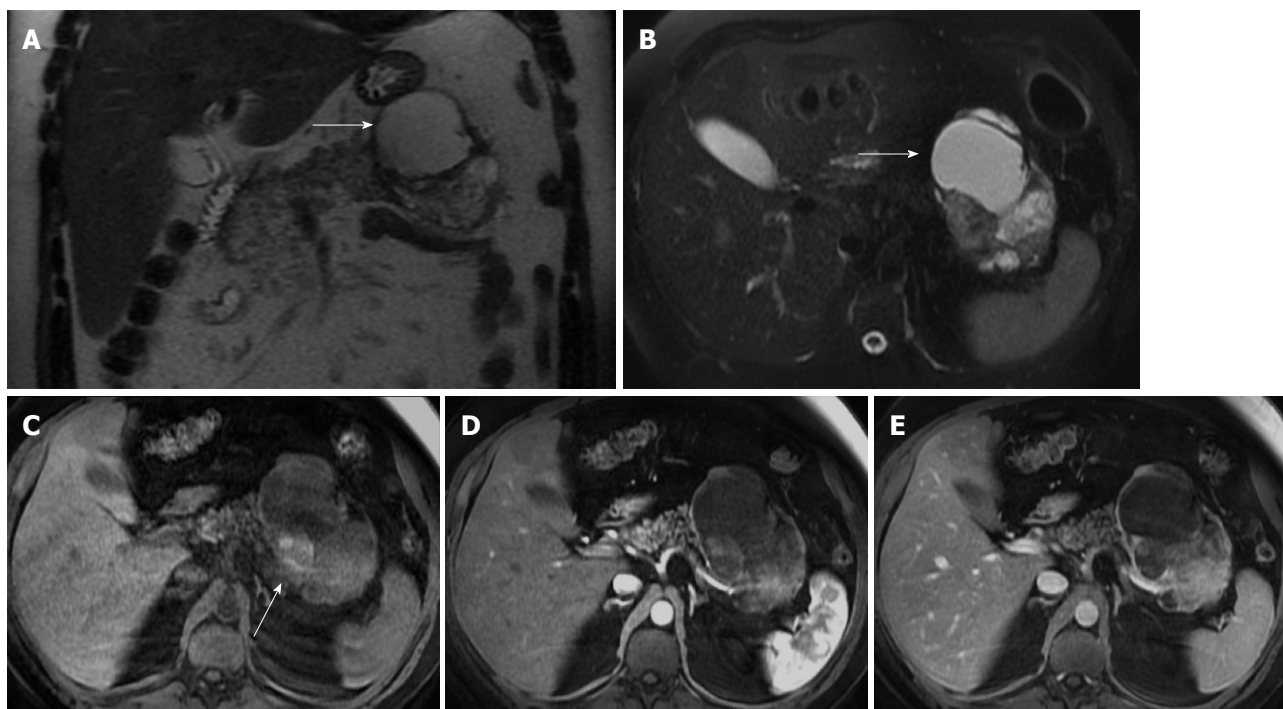


Figure 6 Solid pseudopapillary tumor. Coronal (A) and axial fat-suppressed (B) T2-weighted SS-ETSE, pre-contrast fat-suppressed T1-weighted (C) GRE and post-gadolinium fat-suppressed T1-weighted GRE images acquired in the arterial (D) and venous (E) phases of enhancement. A large well-demarcated and encapsulated mass is located in the tail and body of the pancreas. The mass shows heterogeneous signal intensity, with cystic (arrows, A and B) and hemorrhagic areas (arrow, C). The solid component of the lesion shows progressive enhancement over time. A mass with these characteristics, appearing in a young patient is most likely related with solid pseudopapillary tumor. SS-ETSE: Single-shot echo train spin echo; GRE: Gradient echo.

hypervascular, which is characteristically observed in islet cell tumors^[2,46,48,49] (Figure 6).

PANCREATIC NEUROENDOCRINE TUMORS

Pancreatic neuroendocrine tumors (NET) were previously called islet cell tumor, as it was believed that they derived from the islets of Langerhans. Recent evidence suggests that these tumors arise from pluripotential stem cells in the ductal epithelium^[50]. They account for 1%-2% of all pancreatic neoplasms. The majority NETs are sporadic, but association with syndromes such as with Wermer syndrome, neurofibromatosis type 1, von Hippel-Lindau syndrome, and tuberous sclerosis have been reported. NETs are classified into functioning and non-functioning tumors. Functioning tumors may clinically present with an endocrine malfunction subsequent to hormone secretion^[51]. The diagnosis of functioning NETs is almost always established biochemically, and the role of imaging is to depict the precise location of the tumor. Insulinomas and gastrinomas are the most common pancreatic NETs, followed by non-functional or untyped tumors.

Non-functional tumors account for 15%-20% of pancreatic NETs and tend to be symptomatic due to large tumor mass or metastatic disease. Functioning tumors manifest early in the course of disease when they are small, due to the clinical manifestations of

excessive hormone secretion.

Malignancy cannot be determined based on the histological appearance of pancreatic NETs, instead it is established by the coexistence of metastases or local invasion. The liver is the most affected organ for metastatic spread.

Insulinomas are usually benign tumors, whereas gastrinomas are malignant in nearly 60% of cases. Nonfunctioning tumors are malignant in most cases.

Tumor morphology is variable. Small tumors are usually solid and homogeneous, whereas larger tumors are usually heterogeneous with cystic degeneration and calcifications.

On MRI, NETs are moderately low T1 and intermediate to high signal intensity on T2-weighted fat-suppressed images^[52]. These tumors are typically highly hypervascular and therefore they enhance intensely on arterial/pancreatic phase after contrast administration. This distinctive feature must be interpreted cautiously, as although they may enhance more rapidly and avidly than the background pancreas, they may also appear iso-intense during the arterial phase, as the normal pancreatic parenchyma is also highly vascularized (Figure 7).

Insulinomas are usually seen as small tumors (< 2 cm), with intense and homogeneous enhancement on arterial phase images, whereas gastrinomas most commonly are larger lesions (3-4 cm approximately), with peripheral ring-like enhancement on arterial phase images^[2,53]. Gastrinomas generally occur in a

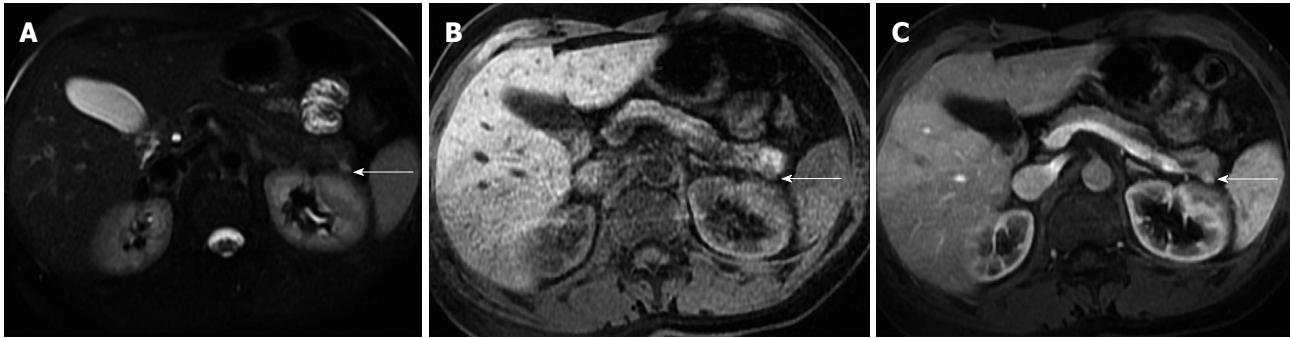


Figure 7 Pancreatic neuroendocrine tumor. Axial fat-suppressed T2-weighted SS-ETSE (A), pre-contrast fat-suppressed T1-weighted (B) GRE and arterial phase fat-suppressed T1-weighted GRE image (C). There is a small solid lesion in the tail of the pancreas (arrow, A-C), showing moderate signal intensity on T2-weighted images (arrow, A) and demonstrates marked enhancement in the arterial phase of enhancement (arrow, C). This was an insulinoma. SS-ETSE: Single-shot echo train spin echo; GRE: Gradient echo.

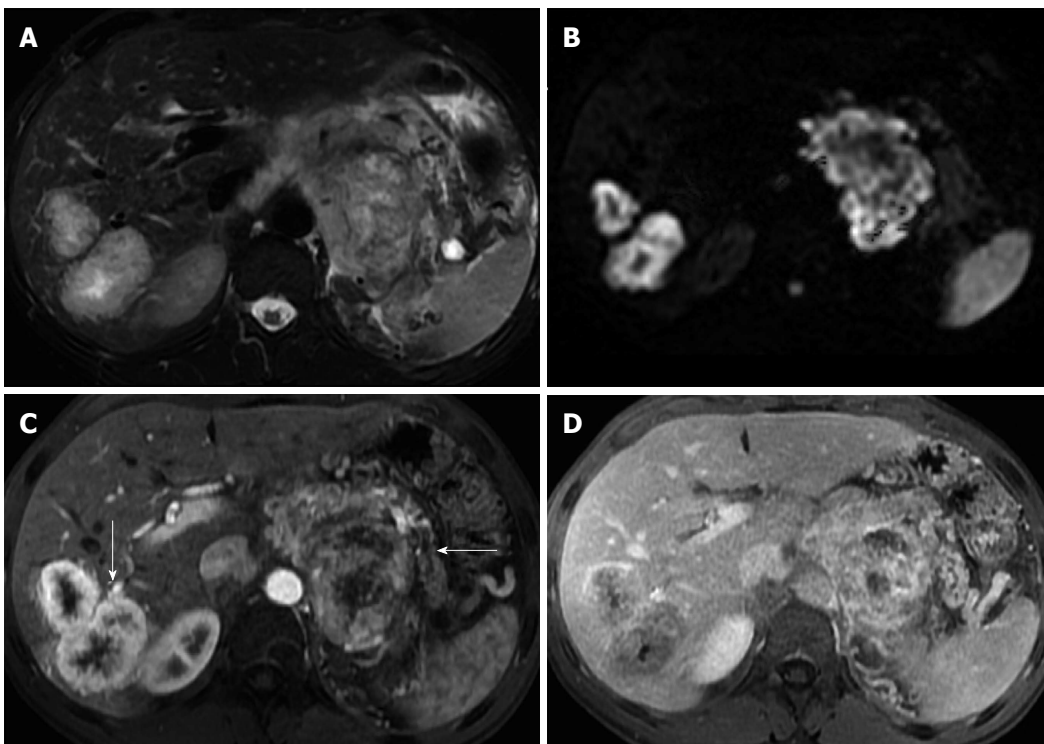


Figure 8 Pancreatic neuroendocrine tumor and liver metastases. Axial T2-weighted SS-ETSE (A), diffusion weighted images ($b = 500$) (B) and post-gadolinium fat-suppressed T1-weighted GRE images acquired in the arterial (C) and venous (D) phase of enhancement. A large mass is seen arising in the body and tail of the pancreas, showing moderate signal intensity on T2-weighted images (A) and restriction to diffusion (B). This lesion shows hypervascular characteristics (C). This mass was diagnosed as poorly differentiated neuroendocrine tumor. Note that the liver metastases show similar signal characteristics on T2- and diffusion-weighted images and demonstrate the characteristic arterial wash-in (arrow, C) and late washout (D) seen with neuroendocrine tumor metastases. SS-ETSE: Single-shot echo train spin echo; GRE: Gradient echo.

distinctive location, termed the gastrinoma triangle, bordered superiorly by the confluence of the cystic and CBDs; inferiorly, by the second and third portions of the duodenum; and medially, by the neck and body of the pancreas.

The likelihood of malignancy rises in parallel with tumor size, and tumors larger than 5 cm are frequently malignant. Even when malignant, these tumors are slow-growing and the prognosis is better than for ductal adenocarcinoma^[18,54]. Metastases to lymph nodes and solid organs may have an enhancement pattern similar

to that of the primary tumor (Figure 8).

It is essential to distinguish pancreatic NETs from other neoplasms, especially from ductal adenocarcinoma, as the prognosis and treatment options are usually substantially different for these two entities.

Features that discriminate most pancreatic NETs from pancreatic adenocarcinoma include the high T2 signal, increased homogeneous enhancement on arterial phase images, hypervascular liver metastases, and absence of pancreatic duct obstruction or vascular encasement^[53]. On the other hand, venous thrombosis, peritoneal, and

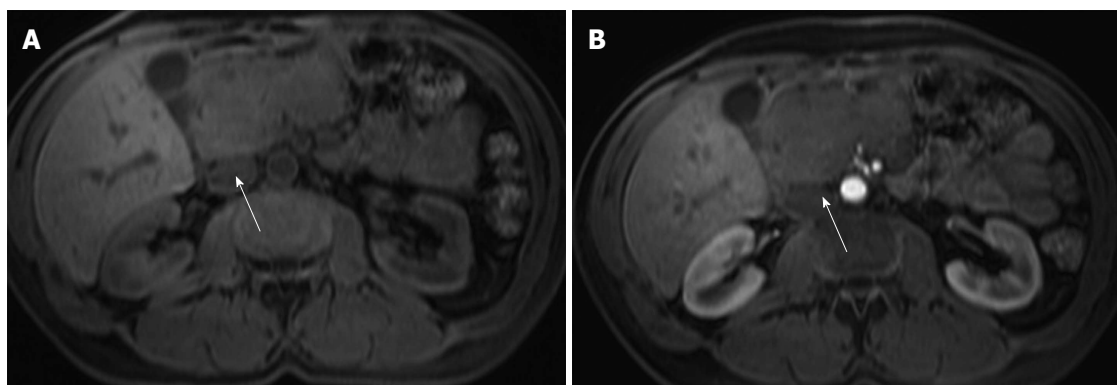


Figure 9 Pancreatic lymphoma. Pre-contrast fat-suppressed axial T1-weighted gradient - echo images (A) and acquired in the arterial phase after gadolinium injection (B). There is a large hypointense and hypovascular mass (arrows) localized in the pancreatic head, however showing no significant duct dilatation. There was evidence of enlarged lymph nodes. This mass was diagnosed as pancreatic lymphoma.

regional node enlargement are distinguishing features of pancreatic ductal adenocarcinoma, usually not seen in NETs.

MESENCHYMAL TUMORS

Mesenchymal neoplasms of the pancreas are rare, accounting for 1% to 2% of all pancreatic tumors^[55,56]. They derive from various connective tissue components and are classified according to their histologic origin.

Primary pancreatic lymphoma, although unusual, is the most common malignant mesenchymal tumor appearing in the pancreas. Benign mesenchymal adipose tissue tumors, such as lipomas or teratomas are extremely rare and show diagnostic features on MRI, with homogeneous encapsulated mature fat or with fat-fluid levels, respectively^[55,56]. Other mesenchymal tumors, such as lymphangiomas, leiomyoma, leiomyosarcoma, schwannoma, hemangioma, or hemangioendothelioma, have also been reported; however, they are exceedingly rare, appearing described only in the form of isolated case reports.

Pancreatic lymphoma

Non-Hodgkin lymphoma may involve peripancreatic lymph nodes or may directly infiltrate the pancreas. Peripancreatic lymph nodes show low to intermediate signal intensity on T1-weighted fat-suppressed images, which permit to be distinguished from the normal pancreas that shows high signal intensity^[57].

Primary pancreatic lymphoma is a rare entity, accounting for less than 2% of extranodal lymphomas and 0.5% of pancreatic tumors^[58].

Pancreatic lymphoma has a better prognosis than pancreatic ductal adenocarcinoma, as first-line treatment with chemotherapy is normally effective, allowing long-term disease regression or remission. Surgery is usually not required.

Two morphologic patterns are recognized: focal and diffuse form^[59]. The focal form occurs in the pancreatic head in 80% of the cases and may mimic

adenocarcinoma.

On MRI, lymphoma shows low T1 and intermediate T2 signal intensity. Several features may help discriminate pancreatic lymphoma from ductal adenocarcinoma such as the presence of a bulky confined tumor in the pancreatic head with absent or minimal main pancreatic duct dilatation, enlarged lymph nodes below the level of the renal vein, and a tendency to noninvasive tumor growth, which are characteristic for pancreatic lymphoma and atypical for pancreatic ductal adenocarcinoma (Figure 9). Vascular invasion is also less commonly seen in lymphoma^[2]. Additionally, CA 19.9 levels are usually not elevated in primary or secondary pancreatic lymphoma.

NONPANCREATIC TUMOR LESION

Metastases

Metastases to the pancreas may be the result of direct invasion or hematogenous spread. Direct invasion from stomach and transverse colon carcinoma and GIST tumors are rare, but the most common forms of direct extension.

Metastases derive most frequently from renal cell carcinoma and lung cancer followed by breast, colon, prostate and malignant melanoma.

Three morphological patterns of metastatic involvement of the pancreas have been described: solitary lesion (50%-70% of cases), multifocal (5%-10%), and diffuse (15%-44%)^[59].

Metastases generally show low T1 and mildly high T2 signal intensity. The enhancement of the majority of metastases follows a ring pattern, with a variable degree of enhancement depending on the angiogenic properties of the primary neoplasm (Figure 10)^[60].

Renal cancer metastases resemble the appearance of NETs. Melanocytic melanoma metastases may display high T1 signal due to the paramagnetic properties of melanin pigment.

Ductal obstruction is uncommon, even with larger tumors, which is an important feature distinguishing

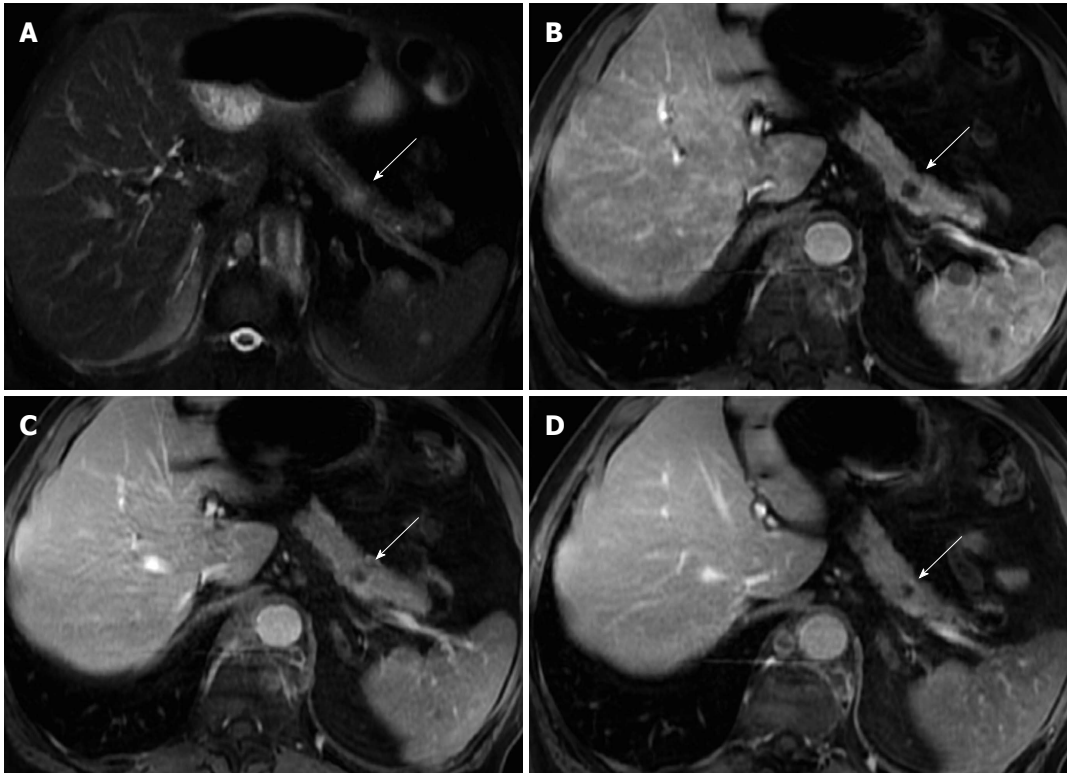


Figure 10 Solitary pancreatic metastasis. Axial T2-weighted SS-ETSE (A) and post-gadolinium fat-suppressed T1-weighted GRE images acquired in the arterial (B), venous (C) and interstitial (D) phases of enhancement. There is a nodular lesion in the pancreatic body showing moderate signal intensity on T2-weighted images (arrow, A) and showing hypovascular characteristics, with no pancreatic duct dilatation. These are typical features of a solitary pancreatic metastasis (arrows). Note additional splenic metastases (lung cancer). SS-ETSE: Single-shot echo train spin echo; GRE: Gradient echo.

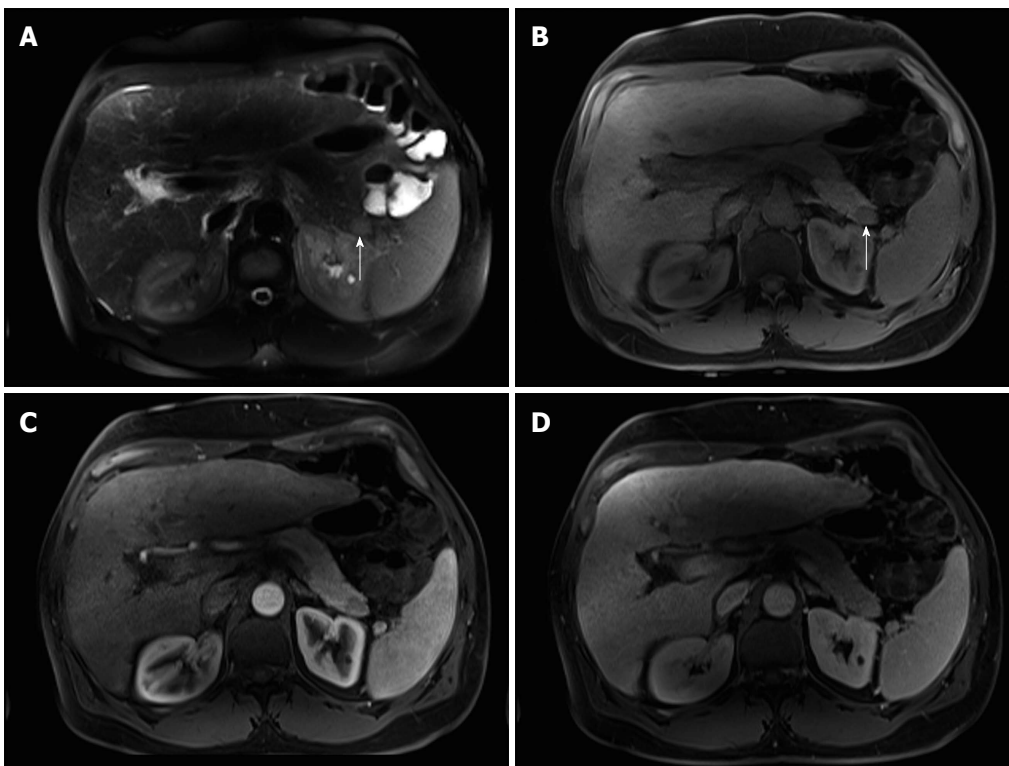


Figure 11 Intra-pancreatic splenule. Axial T2-weighted SS-ETSE (A), pre-contrast fat-suppressed T1-weighted (B) GRE and post-gadolinium fat-suppressed T1-weighted GRE images acquired in the arterial (C) and venous (D) phases of enhancement. There is a well-margined and lobulated round intra-pancreatic splenule (arrows, A and B) that shows isointense signal to the pancreas on T2- and T1-weighted images (A and B). This nodule is hypointense compared to the background pancreas on the precontrast T1-weighted image (B) and demonstrates lesser enhancement relative to the pancreas on the arterial phase (C) and hepatic venous phase (D). The enhancement pattern was homogenous on the postgadolinium images and similar to that of the pancreas. SS-ETSE: Single-shot echo train spin echo; GRE: Gradient echo.

from pancreatic ductal adenocarcinoma^[2,59].

INTRAPANCREATIC SPLENULE

The presence of accessory splenules may arise within the parenchyma of solid organs, notably the pancreas. Intrapancreatic splenule is a somewhat uncommon location for splenules. These lesions typically are < 2 cm in size and are located within 3 cm of the tip of the pancreatic tail^[55]. The presence of a well marginated rounded mass located in the distal tail of the pancreas with signal intensity features comparable to those of the spleen on all MR sequences suggests the diagnosis of intrapancreatic accessory spleen (Figure 11). A distinctive feature of these masses is that when greater than 2 cm they may exhibit serpiginous enhancement on arterial phase images, as typically seen in the spleen^[61]. Other entities may simulate the signal intensity and post-gadolinium enhancement features of intrapancreatic splenules, and DWI and SPIO-enhanced MRI can be used to characterize the lesion and to establish the definite diagnosis^[61,62].

CONCLUSION

In addition to pancreatic ductal adenocarcinoma other solid pancreatic lesions occur. Many of the above-described tumors may be diagnosed with relatively high specificity employing MRI. The radiologist must be familiar with their MRI appearance to correctly diagnose them, or suggest them in the differential diagnosis when appropriate, since it may change substantially the approach, prognosis and patient management. We have described specific features that may aid in the discrimination from ductal adenocarcinoma and establish the correct diagnosis.

REFERENCES

1. Jemal A, Siegel R, Ward E, Hao Y, Xu J, Murray T, Thun MJ. Cancer statistics, 2008. *CA Cancer J Clin* 2008; **58**: 71-96 [PMID: 18287387 DOI: 10.3322/CA.2007.0010]
2. Altun E, Elias Jr J, Armao D, Busakorn V, Semelka RC. Pancreas. 535-676. In: *Abdominal-Pelvic MRI*. 3rd edition. Semelka RC. editor. New Jersey: Wiley-Blackwell, 2010
3. Semelka RC, Ascher SM. MR imaging of the pancreas. *Radiology* 1993; **188**: 593-602 [PMID: 8351317 DOI: 10.1148/radiology.188.3.8351317]
4. Zapparo M, Semelka RC, Altun E, Tsurusaki M, Pamuklar E, Dale BM, Gasparetto EL, Elias J. 3.0-T MRI evaluation of patients with chronic liver diseases: initial observations. *Magn Reson Imaging* 2008; **26**: 650-660 [PMID: 18440749 DOI: 10.1016/j.mri.2008.01.037]
5. Mitchell DG, Vinitski S, Saponaro S, Tasciyan T, Burk DL, Rifkin MD. Liver and pancreas: improved spin-echo T1 contrast by shorter echo time and fat suppression at 1.5 T. *Radiology* 1991; **178**: 67-71 [PMID: 1984328 DOI: 10.1148/radiology.178.1.1984328]
6. Winston CB, Mitchell DG, Outwater EK, Ehrlich SM. Pancreatic signal intensity on T1-weighted fat saturation MR images: clinical correlation. *J Magn Reson Imaging* 1995; **5**: 267-271 [PMID: 7633102 DOI: 10.1002/jmri.1880050307]
7. Takehara Y, Ichijo K, Tooyama N, Kodaira N, Yamamoto H, Tatami M, Saito M, Watahiki H, Takahashi M. Breath-hold MR cholangiopancreatography with a long-echo-train fast spin-echo sequence and a surface coil in chronic pancreatitis. *Radiology* 1994; **192**: 73-78 [PMID: 8208969 DOI: 10.1148/radiology.192.1.8208969]
8. Bret PM, Reinhold C, Taourel P, Guibaud L, Atri M, Barkun AN. Pancreas divisum: evaluation with MR cholangiopancreatography. *Radiology* 1996; **199**: 99-103 [PMID: 8633179 DOI: 10.1148/radiology.199.1.8633179]
9. Soto JA, Barish MA, Yucel EK, Clarke P, Siegenberg D, Chuttani R, Ferrucci JT. Pancreatic duct: MR cholangiopancreatography with a three-dimensional fast spin-echo technique. *Radiology* 1995; **196**: 459-464 [PMID: 7617861 DOI: 10.1148/radiology.196.2.7617861]
10. Vachiranubhap B, Kim YH, Balci NC, Semelka RC. Magnetic resonance imaging of adenocarcinoma of the pancreas. *Top Magn Reson Imaging* 2009; **20**: 3-9 [PMID: 19687720 DOI: 10.1097/RMR.0b013e3181b48392]
11. Maccioni F, Martinelli M, Al Ansari N, Kagarmanova A, De Marco V, Zippi M, Marini M. Magnetic resonance cholangiography: past, present and future: a review. *Eur Rev Med Pharmacol Sci* 2010; **14**: 721-725 [PMID: 20707292]
12. Bian Y, Wang L, Chen C, Lu JP, Fan JB, Chen SY, Zhao BH. Quantification of pancreatic exocrine function of chronic pancreatitis with secretin-enhanced MRCP. *World J Gastroenterol* 2013; **19**: 7177-7182 [PMID: 24222963 DOI: 10.3748/wjg.v19.i41.7177]
13. Tirkes T, Sandrasegaran K, Sanyal R, Sherman S, Schmidt CM, Cote GA, Akisik F. Secretin-enhanced MR cholangiopancreatography: spectrum of findings. *Radiographics* 2013; **33**: 1889-1906 [PMID: 24224585 DOI: 10.1148/rg.337125014]
14. Perazella MA. Current status of gadolinium toxicity in patients with kidney disease. *Clin J Am Soc Nephrol* 2009; **4**: 461-469 [PMID: 19201920 DOI: 10.2215/CJN.06011108]
15. Jung JW, Kang HR, Kim MH, Lee W, Min KU, Han MH, Cho SH. Immediate hypersensitivity reaction to gadolinium-based MR contrast media. *Radiology* 2012; **264**: 414-422 [PMID: 22550309 DOI: 10.1148/radiol.12112025]
16. Azevedo RM, de Campos RO, Ramalho M, Herédia V, Dale BM, Semelka RC. Free-breathing 3D T1-weighted gradient-echo sequence with radial data sampling in abdominal MRI: preliminary observations. *AJR Am J Roentgenol* 2011; **197**: 650-657 [PMID: 21862807 DOI: 10.2214/AJR.10.5881]
17. Semelka RC, Kroeker MA, Shoenut JP, Kroeker R, Yaffe CS, Micflikier AB. Pancreatic disease: prospective comparison of CT, ERCP, and 1.5-T MR imaging with dynamic gadolinium enhancement and fat suppression. *Radiology* 1991; **181**: 785-791 [PMID: 1947098 DOI: 10.1148/radiology.181.3.1947098]
18. Mergo PJ, Helmlinger TK, Buetow PC, Helmlinger RC, Ros PR. Pancreatic neoplasms: MR imaging and pathologic correlation. *Radiographics* 1997; **17**: 281-301 [PMID: 9084072 DOI: 10.1148/radiographics.17.2.9084072]
19. Ros PR, Mortelé KJ. Imaging features of pancreatic neoplasms. *JBR-BTR* 2001; **84**: 239-249 [PMID: 11817475]
20. Low G, Panu A, Mollo N, Leen E. Multimodality imaging of neoplastic and nonneoplastic solid lesions of the pancreas. *Radiographics* 2011; **31**: 993-1015 [PMID: 21768235 DOI: 10.1148/rg.314105731]
21. Lee ES, Lee JM. Imaging diagnosis of pancreatic cancer: a state-of-the-art review. *World J Gastroenterol* 2014; **20**: 7864-7877 [PMID: 24976723 DOI: 10.3748/wjg.v20.i24.7864]
22. Benassai G, Mastrorilli M, Quarto G, Cappiello A, Giani U, Forestieri P, Mazzeo F. Factors influencing survival after resection for ductal adenocarcinoma of the head of the pancreas. *J Surg Oncol* 2000; **73**: 212-218 [PMID: 10797334 DOI: 10.1002/(SICI)1096-9098(200004)73:4<212::AID-JSO5>3.0.CO;2-D]
23. Gabata T, Matsui O, Kadoya M, Yoshikawa J, Miyayama S, Takashima T, Nagakawa T, Kayahara M, Nonomura A. Small pancreatic adenocarcinomas: efficacy of MR imaging with fat suppression and gadolinium enhancement. *Radiology* 1994; **193**: 683-688 [PMID: 7972808 DOI: 10.1148/radiology.193.3.7972808]
24. Semelka RC, Kelekis NL, Molina PL, Sharp TJ, Calvo B.

- Pancreatic masses with inconclusive findings on spiral CT: is there a role for MRI? *J Magn Reson Imaging* 1996; **6**: 585-588 [PMID: 8835950 DOI: 10.1002/jmri.1880060405]
- 25 **Ahualli J**. The double duct sign. *Radiology* 2007; **244**: 314-315 [PMID: 17581912 DOI: 10.1148/radiol.2441041978]
 - 26 **Clark LR**, Jaffe MH, Choyke PL, Grant EG, Zeman RK. Pancreatic imaging. *Radiol Clin North Am* 1985; **23**: 489-501 [PMID: 2997833]
 - 27 **Morgan KA**, Adams DB. Solid tumors of the body and tail of the pancreas. *Surg Clin North Am* 2010; **90**: 287-307 [PMID: 20362787 DOI: 10.1016/j.suc.2009.12.009]
 - 28 **Saisho H**, Yamaguchi T. Diagnostic imaging for pancreatic cancer: computed tomography, magnetic resonance imaging, and positron emission tomography. *Pancreas* 2004; **28**: 273-278 [PMID: 15084970 DOI: 10.1097/00006676-200404000-00011]
 - 29 **Vellet AD**, Romano W, Bach DB, Passi RB, Taves DH, Munk PL. Adenocarcinoma of the pancreatic ducts: comparative evaluation with CT and MR imaging at 1.5 T. *Radiology* 1992; **183**: 87-95 [PMID: 1312736 DOI: 10.1148/radiology.183.1.1312736]
 - 30 **Wang XY**, Yang F, Jin C, Fu DL. Utility of PET/CT in diagnosis, staging, assessment of resectability and metabolic response of pancreatic cancer. *World J Gastroenterol* 2014; **20**: 15580-15589 [PMID: 25400441 DOI: 10.3748/wjg.v20.i42.15580]
 - 31 **Adsay NV**, Basturk O, Klimstra DS, Klöppel G. Pancreatic pseudotumors: non-neoplastic solid lesions of the pancreas that clinically mimic pancreas cancer. *Semin Diagn Pathol* 2004; **21**: 260-267 [PMID: 16273945 DOI: 10.1053/j.semdp.2005.07.003]
 - 32 **Kim HJ**, Byun JH, Park SH, Shin YM, Kim PN, Ha HK, Lee MG. Focal fatty replacement of the pancreas: usefulness of chemical shift MRI. *AJR Am J Roentgenol* 2007; **188**: 429-432 [PMID: 17242252 DOI: 10.2214/AJR.05.1095]
 - 33 **Isserow JA**, Siegelman ES, Mammone J. Focal fatty infiltration of the pancreas: MR characterization with chemical shift imaging. *AJR Am J Roentgenol* 1999; **173**: 1263-1265 [PMID: 10541101 DOI: 10.2214/ajr.173.5.10541101]
 - 34 **Kawamoto S**, Siegelman SS, Bluemke DA, Hruban RH, Fishman EK. Focal fatty infiltration in the head of the pancreas: evaluation with multidetector computed tomography with multiplanar reformation imaging. *J Comput Assist Tomogr* 2009; **33**: 90-95 [PMID: 19188793 DOI: 10.1097/RCT.0b013e31815cfff0d]
 - 35 **Balthazar EJ**. CT diagnosis and staging of acute pancreatitis. *Radiol Clin North Am* 1989; **27**: 19-37 [PMID: 2642273]
 - 36 **Ichikawa T**, Sou H, Araki T, Arbab AS, Yoshikawa T, Ishigame K, Haradome H, Hachiya J. Duct-penetrating sign at MRCP: usefulness for differentiating inflammatory pancreatic mass from pancreatic carcinomas. *Radiology* 2001; **221**: 107-116 [PMID: 11568327 DOI: 10.1148/radiol.2211001157]
 - 37 **Kim JK**, Altun E, Elias J, Pamuklar E, Rivero H, Semelka RC. Focal pancreatic mass: distinction of pancreatic cancer from chronic pancreatitis using gadolinium-enhanced 3D-gradient-echo MRI. *J Magn Reson Imaging* 2007; **26**: 313-322 [PMID: 17610286 DOI: 10.1002/jmri.21010]
 - 38 **Semelka RC**, Shoenut JP, Kroeker MA, Micflikier AB. Chronic pancreatitis: MR imaging features before and after administration of gadopentetate dimeglumine. *J Magn Reson Imaging* 1993; **3**: 79-82 [PMID: 8428105 DOI: 10.1002/jmri.1880030114]
 - 39 **Siddiqi AJ**, Miller F. Chronic pancreatitis: ultrasound, computed tomography, and magnetic resonance imaging features. *Semin Ultrasound CT MR* 2007; **28**: 384-394 [PMID: 17970554 DOI: 10.1053/j.sult.2007.06.003]
 - 40 **Wittenberg J**, Simeone JF, Ferrucci JT, Mueller PR, vanSonnenberg E, Neff CC. Non-focal enlargement in pancreatic carcinoma. *Radiology* 1982; **144**: 131-135 [PMID: 7089244 DOI: 10.1148/radiology.144.1.7089244]
 - 41 **Chiou YY**, Chiang JH, Hwang JI, Yen CH, Tsay SH, Chang CY. Acinar cell carcinoma of the pancreas: clinical and computed tomography manifestations. *J Comput Assist Tomogr* 2004; **28**: 180-186 [PMID: 15091120 DOI: 10.1097/00004728-200403000-00005]
 - 42 **Khalili M**, Wax BN, Reed WP, Schuss A, Drexler S, Weston SR, Katz DS. Radiology-pathology conference. Acinar cell carcinoma of the pancreas. *Clin Imaging* 2006; **30**: 343-346 [PMID: 16919557 DOI: 10.1016/j.clinimag.2006.05.027]
 - 43 **Tatli S**, Mortelet KJ, Levy AD, Glickman JN, Ros PR, Banks PA, Silverman SG. CT and MRI features of pure acinar cell carcinoma of the pancreas in adults. *AJR Am J Roentgenol* 2005; **184**: 511-519 [PMID: 15671372 DOI: 10.2214/ajr.184.2.01840511]
 - 44 **Hsu MY**, Pan KT, Chu SY, Hung CF, Wu RC, Tseng JH. CT and MRI features of acinar cell carcinoma of the pancreas with pathological correlations. *Clin Radiol* 2010; **65**: 223-229 [PMID: 20152279 DOI: 10.1016/j.crad.2009.11.010]
 - 45 **Hu S**, Hu S, Wang M, Wu Z, Miao F. Clinical and CT imaging features of pancreatic acinar cell carcinoma. *Radiol Med* 2013; **118**: 723-731 [PMID: 23358813 DOI: 10.1007/s11547-012-0908-5]
 - 46 **Guerrache Y**, Soyer P, Dohan A, Faraoun SA, Laurent V, Tasu JP, Aubé C, Cazejust J, Boudiaf M, Hoeffel C. Solid-pseudopapillary tumor of the pancreas: MR imaging findings in 21 patients. *Clin Imaging* 2014; **38**: 475-482 [PMID: 24629792 DOI: 10.1016/j.clinimag.2014.01.015]
 - 47 **Ng KH**, Tan PH, Thng CH, Ooi LL. Solid pseudopapillary tumour of the pancreas. *ANZ J Surg* 2003; **73**: 410-415 [PMID: 12801340 DOI: 10.1046/j.1445-2197.2003.t01-1-02634.x]
 - 48 **Cooper JA**. Solid pseudopapillary tumor of the pancreas. *Radiographics* 2006; **26**: 1210 [PMID: 16848054 DOI: 10.1148/radiographics.26.4.0261210]
 - 49 **Kalb B**, Sarmiento JM, Kooby DA, Adsay NV, Martin DR. MR imaging of cystic lesions of the pancreas. *Radiographics* 2009; **29**: 1749-1765 [PMID: 19959519 DOI: 10.1148/rg.296095506]
 - 50 **Oberg K**, Eriksson B. Endocrine tumours of the pancreas. *Best Pract Res Clin Gastroenterol* 2005; **19**: 753-781 [PMID: 16253899 DOI: 10.1016/j.bpg.2005.06.002]
 - 51 **Mozell E**, Stenzel P, Woltering EA, Rösch J, O'Dorisio TM. Functional endocrine tumors of the pancreas: clinical presentation, diagnosis, and treatment. *Curr Probl Surg* 1990; **27**: 301-386 [PMID: 1973365 DOI: 10.1016/0011-3840(90)90025-Z]
 - 52 **Semelka RC**, Custodio CM, Cem Balci N, Woosley JT. Neuroendocrine tumors of the pancreas: spectrum of appearances on MRI. *J Magn Reson Imaging* 2000; **11**: 141-148 [PMID: 10713946 DOI: 10.1002/(SICI)1522-2586(200002)11:2<141::AID-JMRI10>3.0.CO;2-U]
 - 53 **Semelka RC**, Cumming MJ, Shoenut JP, Magro CM, Yaffe CS, Kroeker MA, Greenberg HM. Islet cell tumors: comparison of dynamic contrast-enhanced CT and MR imaging with dynamic gadolinium enhancement and fat suppression. *Radiology* 1993; **186**: 799-802 [PMID: 8381551 DOI: 10.1148/radiology.186.3.8381551]
 - 54 **Sheth S**, Hruban RK, Fishman EK. Helical CT of islet cell tumors of the pancreas: typical and atypical manifestations. *AJR Am J Roentgenol* 2002; **179**: 725-730 [PMID: 12185053 DOI: 10.2214/ajr.179.3.1790725]
 - 55 **Ferrozzi F**, Zuccoli G, Bova D, Calculli L. Mesenchymal tumors of the pancreas: CT findings. *J Comput Assist Tomogr* 2000; **24**: 622-627 [PMID: 10966199 DOI: 10.1097/00004728-200007000-00021]
 - 56 **Megibow AJ**, Francis IR. Unusual Pancreatic Neoplasms: Imaging. In: *Imaging of the Pancreas Cystic and Rare Tumors*. Carlo Procacci C, Megibow AJ, editors. Springer Berlin Heidelberg, 2003: 249-265
 - 57 **Zeman RK**, Schiebler M, Clark LR, Jaffe MH, Paushter DM, Grant EG, Choyke PL. The clinical and imaging spectrum of pancreaticoduodenal lymph node enlargement. *AJR Am J Roentgenol* 1985; **144**: 1223-1227 [PMID: 3890486 DOI: 10.2214/ajr.144.6.1223]
 - 58 **Zucca E**, Roggero E, Bertoni F, Cavalli F. Primary extranodal non-Hodgkin's lymphomas. Part 1: Gastrointestinal, cutaneous and genitourinary lymphomas. *Ann Oncol* 1997; **8**: 727-737 [PMID: 9332679 DOI: 10.1023/A:1008282818705]
 - 59 **Tsitouridis I**, Diamantopoulou A, Michaelides M, Arvanity M, Papaioannou S. Pancreatic metastases: CT and MRI findings. *Diagn Interv Radiol* 2010; **16**: 45-51 [PMID: 20027546 DOI: 10.4261/1305-3825.DIR.1996-08.1]
 - 60 **Al Ansari N**, Kim BS, Srirattanapong S, Semelka CT, Ramalho

- M, Altun E, Woosley JT, Calvo B, Semelka RC. Mass-forming cholangiocarcinoma and adenocarcinoma of unknown primary: can they be distinguished on liver MRI? *Abdom Imaging* 2014; **39**: 1228-1240 [PMID: 24929668 DOI: 10.1007/s00261-014-0172-3]
- 61 **Herédia V**, Altun E, Bilaj F, Ramalho M, Hyslop BW, Semelka RC. Gadolinium- and superparamagnetic-iron-oxide-enhanced MR findings of intrapancreatic accessory spleen in five patients. *Magn Reson Imaging* 2008; **26**: 1273-1278 [PMID: 18440173 DOI: 10.1016/j.mri.2008.02.008]
- 62 **Jang KM**, Kim SH, Lee SJ, Park MJ, Lee MH, Choi D. Differentiation of an intrapancreatic accessory spleen from a small (< 3-cm) solid pancreatic tumor: value of diffusion-weighted MR imaging. *Radiology* 2013; **266**: 159-167 [PMID: 23093681 DOI: 10.1148/radiol.12112765]

P- Reviewer: Aktas S

S- Editor: Ji FF **L- Editor:** A **E- Editor:** Jiao XK



Iliac vein compression syndrome: Clinical, imaging and pathologic findings

Katelyn N Brinegar, Rahul A Sheth, Ali Khademhosseini, Jemianne Bautista, Rahmi Oklu

Katelyn N Brinegar, Rahul A Sheth, Jemianne Bautista, Division of Interventional Radiology, Massachusetts General Hospital, Harvard Medical School, Boston, MA 02114, United States

Ali Khademhosseini, Harvard-MIT Division of Health Sciences and Technology, Cambridge, MA 02139, United States

Ali Khademhosseini, Wyss Institute for Biologically Inspired Engineering, Harvard University, Boston, MA 02115, United States

Ali Khademhosseini, Rahmi Oklu, Biomaterials Innovation Research Center, Department of Medicine, Brigham and Women's Hospital, Harvard Medical School, Boston, MA 02139, United States

Rahmi Oklu, Division of Interventional Radiology, Mayo Clinic, Scottsdale, AZ 85054, United States

Author contributions: Brinegar KN, Sheth RA, Khademhosseini A, Bautista J and Oklu R conceived the issues which formed the content of the manuscript and equally aided in its writing, editing, and revising.

Conflict-of-interest statement: The authors declared no conflicts of interest and have no financial disclosures.

Open-Access: This article is an open-access article which was selected by an in-house editor and fully peer-reviewed by external reviewers. It is distributed in accordance with the Creative Commons Attribution Non Commercial (CC BY-NC 4.0) license, which permits others to distribute, remix, adapt, build upon this work non-commercially, and license their derivative works on different terms, provided the original work is properly cited and the use is non-commercial. See: <http://creativecommons.org/licenses/by-nc/4.0/>

Correspondence to: Rahmi Oklu, MD, PhD, Division of Interventional Radiology, Mayo Clinic, 5777 E Mayo Blvd, Scottsdale, AZ 85054, United States. oklu.rahmi@mayo.edu
 Telephone: +1-480-3421650
 Fax: +1-480-3421650

Received: May 6, 2015
 Peer-review started: May 8, 2015
 First decision: July 10, 2015
 Revised: August 3, 2015

Accepted: September 10, 2015

Article in press: September 16, 2015

Published online: November 28, 2015

Abstract

May-Thurner syndrome (MTS) is the pathologic compression of the left common iliac vein by the right common iliac artery, resulting in left lower extremity pain, swelling, and deep venous thrombosis. Though this syndrome was first described in 1851, there are currently no standardized criteria to establish the diagnosis of MTS. Since MTS is treated by a wide array of specialties, including interventional radiology, vascular surgery, cardiology, and vascular medicine, the need for an established diagnostic criterion is imperative in order to reduce misdiagnosis and inappropriate treatment. Although MTS has historically been diagnosed by the presence of pathologic features, the use of dynamic imaging techniques has led to a more radiologic based diagnosis. Thus, imaging plays an integral part in screening patients for MTS, and the utility of a wide array of imaging modalities has been evaluated. Here, we summarize the historical aspects of the clinical features of this syndrome. We then provide a comprehensive assessment of the literature on the efficacy of imaging tools available to diagnose MTS. Lastly, we provide clinical pearls and recommendations to aid physicians in diagnosing the syndrome through the use of provocative measures.

Key words: May-Thurner; Thrombosis; Diagnostic; Iliac compression; Vascular; Imaging

© **The Author(s) 2015.** Published by Baishideng Publishing Group Inc. All rights reserved.

Core tip: There is currently no gold standard diagnostic criterion in iliac vein compression syndrome. Historically, the presence of pathologic factors has been the main component in diagnosis; however, imaging techniques

have led to a more radiologic-based diagnosis. This review details the clinical and radiologic challenges in the diagnosis of Iliac vein compression syndrome and presents clinical pearls that may help in deciding whether an endovascular intervention should be performed.

Brinegar KN, Sheth RA, Khademhosseini A, Bautista J, Oklu R. Iliac vein compression syndrome: Clinical, imaging and pathologic findings. *World J Radiol* 2015; 7(11): 375-381 Available from: URL: <http://www.wjgnet.com/1949-8470/full/v7/i11/375.htm> DOI: <http://dx.doi.org/10.4329/wjrv.7.i11.375>

INTRODUCTION

Iliac vein compression syndrome, also known as May-Thurner syndrome (MTS), is caused by both mechanical and physiologic factors; the chronic pulsatile compression of the left common iliac vein (LCIV) by the right common iliac artery (RCIA) stimulates the formation of fibrotic adhesions that can cause partial or complete iliac vein obstruction over time^[1,2]. The true incidence of MTS is not known. However, iliofemoral thrombosis is responsible for approximately 2%-3% of lower limb deep venous thrombosis (DVT) cases and approximately 50%-60% of left sided iliofemoral DVT cases exhibit iliac vein spurs resulting from extrinsic compression^[3-6]. Thus, MTS is a reasonably common occurrence and a greater level of clinical suspicion is necessary.

Although MTS has historically been diagnosed by the presence of pathologic features, the use of dynamic imaging techniques has led to a more radiologic based diagnosis. However, a diagnosis of MTS relies on both clinical and imaging findings because the presence of iliac vein compression alone is insufficient for a diagnosis. There are currently no standardized clinical or radiologic diagnostic protocols in place to aid in the identification of MTS. Since MTS is treated by a wide array of specialties, including interventional radiology, vascular surgery, cardiology, and vascular medicine, the need for an established diagnostic criterion is imperative in order to reduce misdiagnosis and inappropriate treatment. MTS patients generally do not respond well to conservative treatments; thus, early diagnosis and treatment is paramount in order to avoid complications such as iliofemoral DVT or venous insufficiency^[3,4]. This review will describe the clinical presentations of MTS and focus on the imaging modalities that have been used in aiding and confirming a diagnosis.

HISTORICAL BACKGROUND

In 1851, Virchow noted the first anatomical evidence for MTS when he observed an increased frequency of DVT in the left leg due to the compression of the left iliac vein between the overlying right iliac artery and the fifth lumbar vertebrae^[4]. In 1908, McMurrich

examined the iliac veins of 107 cadavers and observed that 29.9% had obstructions in the left iliac vein; he deemed that these obstructions were congenital in origin and were responsible for the increased incidence of left lower extremity (LLE) DVT^[7]. In 1943, Ehrlich and Krumbhaar found that out of 412 cadavers, 95 (23.8%) demonstrated obstructive lesions in the LCIV; the obstructions were comprised of collagen and elastin and were demonstrated to be acquired rather than congenital, as was previously thought^[8]. However, a comprehensive understanding of the anatomic variants of MTS was not established until 1957, with the work of May and Thurner.

May and Thurner, for whom the syndrome is named, found that 22% of 430 cadavers exhibited lesions in the LCIV; these lesions were described as "spurs" and were postulated to arise from the chronic compression of the LCIV by the RCIA. The spurs were categorized as central, lateral, or resulting in partial obliteration, based on location and size. Central spurs occur on the anteroposterior plane and split the lumina in two, lateral spurs occur along the sides of the LCIV, and partial obliteration results in the lumen being covered in a lattice of spurs and results in decreased venous flow^[7,8]. In 1965, Cockett *et al*^[9] further expounded the field by determining that patients with LCIV spurs could remain asymptomatic for a period of time due to the formation of venous collaterals. However, it was ruled that spur formation was an irreversible process, making early diagnosis integral for MTS patients.

ROLE OF CLINICAL PRESENTATION IN DIAGNOSIS

The clinical presentation and history of the patient are critical components in formulating a diagnosis of MTS. MTS is particularly prevalent in younger and middle aged women (mean age = 42), although it also affects men^[5]. Patients most commonly present with DVT, but may also present with LLE swelling, pain, venous claudication, ulcerations, nausea, and varicose veins. Rarer symptoms include phlebitis, phlegmasia alba dolens, phlegmasia cerulea dolens, and bilateral or right sided symptoms^[3,5-7,10]. MTS can present either acute or chronically; acute presentation of MTS is the sudden onset of left leg edema and is usually easier to diagnose, while the chronic phase of MTS is much more difficult to identify and requires a comprehensive investigation of patient history, physical examination, and diagnostic imaging studies^[7]. The clinical stages of MTS can be further delineated as being either Stage I, asymptomatic LCIV compression; stage II, the formation of an intraluminal spur; or Stage III, the occurrence of left iliac vein DVT^[11].

A patient history that reveals recurrent DVT, unexplained LLE edema, venous claudication, or varicosities should create suspicion for MTS as a cause. Additionally, physical examination that demonstrates LLE swelling,

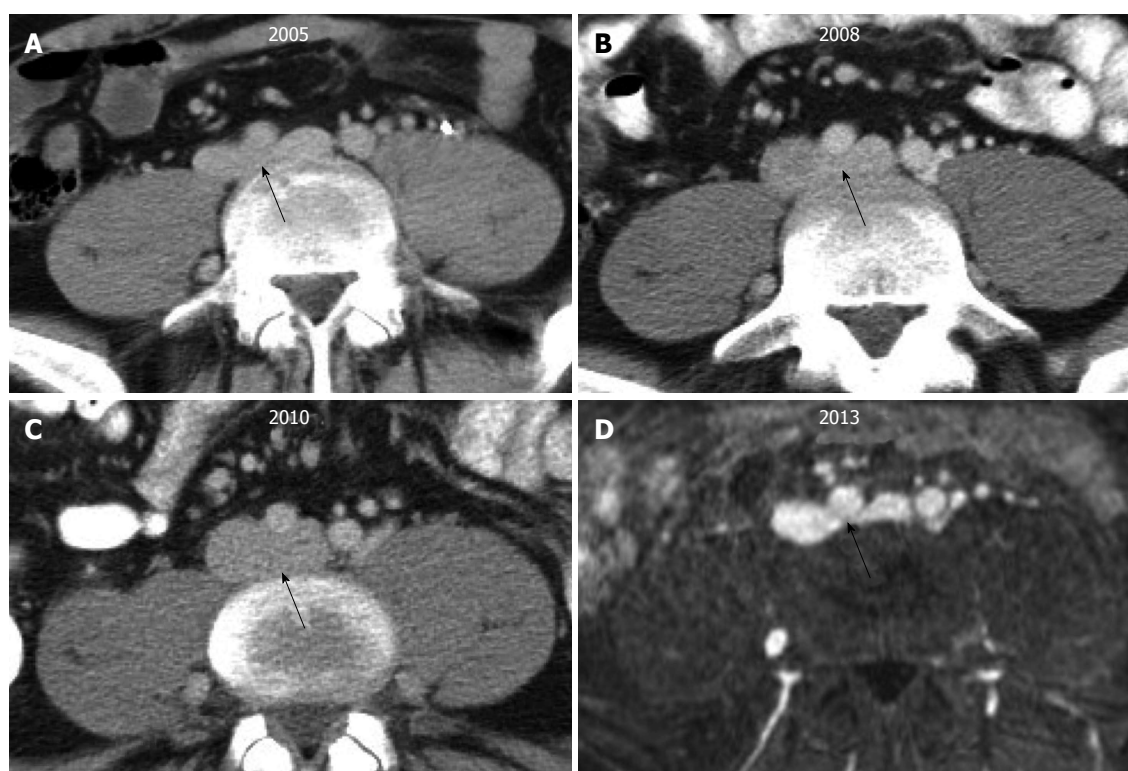


Figure 1 Transverse computed tomography and magnetic resonance images of the proximal left common iliac vein (black arrow) in a single patient across multiple time points illustrate the challenge of diagnosing May-Thurner syndrome. The degree of venous compression can vary substantially from one imaging study to another based upon the patient's volume status.

skin hyperpigmentation, varicose veins, telangiectasias, or evidence of ulceration in the ankle area are supportive of MTS^[7,12]. Iliofemoral thrombosis can also be a result of trauma, surgery, immobilization, recent catheterization, radiation and malignancies and all these explanations must be ruled out in order to diagnose MTS^[13]. Once differential diagnoses have been investigated, diagnostic imaging tests should be undertaken in order to confirm the presence of MTS anatomy and determine the best modality of treatment.

DIAGNOSTIC IMAGING CRITERION AND TECHNIQUES

Several studies have confirmed the presence of LCIV compression in an asymptomatic patient population; these suggest that LCIV compression is a normal anatomic variant and not necessarily a pathologic condition^[14-16]. Moreover, McDermott *et al.*^[1] found that the degree of LCIV compression in a single patient can vary over a short period of time (Figure 1); thus, the finding of May-Thurner anatomy in a single imaging study may just reflect the volume status of patient and may not be sufficient to suspect or confirm MTS^[1]. Although there is no established diagnostic imaging criterion for MTS, studies recommend that the imaging standard for appropriate diagnosis of MTS should exhibit persistent narrowing of the iliac vein due to the presence of permanent iliac spurs, regardless of patient positioning

during the imaging study. Thus, normal variant LCIV compression may be ruled out by placing the patient in prone position as such positioning may demonstrate a decrease in collateral flow or reveal normal iliac vein patency^[1]. A visualization of greater than 50% stenosis in the luminal diameter of the vein is considered an adequate indicator of LCIV compression related to MTS^[17]. An additional secondary indicator of MTS is the presence of venous collaterals, presence of intraluminal spurs, and changes in hemodynamic flow greater than 2 mmHg across the stenotic region with the patient in supine positioning^[1,4,17]. The MTS diagnostic imaging modalities include ultrasonography, pleythsmography, computed tomography (CT), magnetic resonance venography (MRV), ascending contrast venography, hemodynamic studies, and intravascular ultrasound (IVUS) (Figure 2). The advantages and disadvantages of each imaging technique in the diagnosis of MTS are discussed below.

Ultrasonography

Color Doppler ultrasonography (CDUS) is often the initial diagnostic modality in determining venous insufficiencies and DVT because it is noninvasive, bares no risk to the patient, is easy to perform, and is accurate in determining the location, severity, and cause of venous insufficiencies^[18]. Ultrasound can usually identify acute iliofemoral DVT, a common result of MTS^[7]. However, ultrasound has significant limitations in visualizing

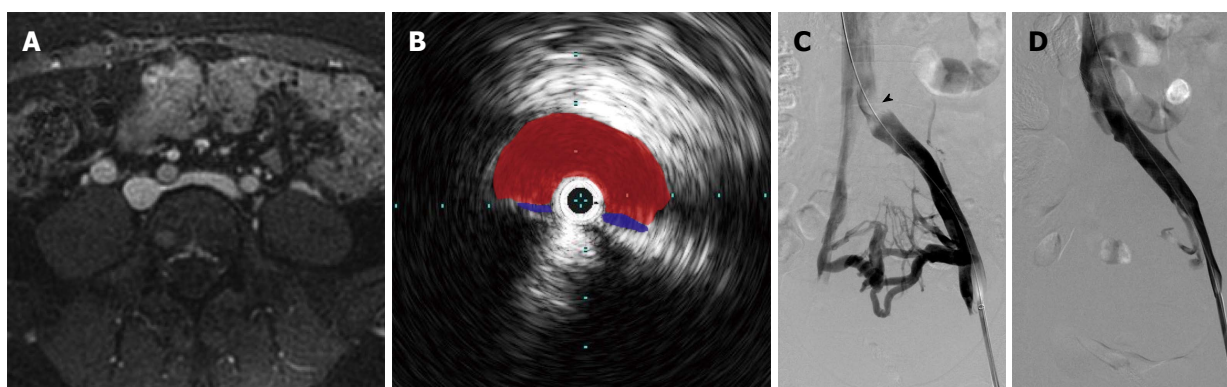


Figure 2 The appearance of May-Thurner syndrome on multiple imaging modalities from a single patient. A: Axial T1 fat-saturated magnetic resonance image following the administration of an intravascular contrast agent demonstrates > 50% narrowing of the left common iliac vein by the overlying right common iliac artery; B: Intravascular ultrasound with the transducer within the left common iliac vein (blue) demonstrates near complete obliteration of the vessel's lumen due to compression by the right common iliac artery (red); C: Digital subtraction angiography with contrast injection from a vascular sheath in the left external iliac vein demonstrates an obliquely oriented silhouette of the right common iliac artery compressing the left common iliac vein (arrowhead); multiple left-to-right pelvic collaterals are also present, signifying that the compression is hemodynamically significant; D: Following the placement of an uncovered stent, the compression is resolved, and there is no longer filling of the cross-pelvic collaterals.

abnormalities of the iliac veins because of the deep location of the veins in the pelvis; skilled sonographers are unable to visualize the iliac veins in approximately 20% of cases. Moreover, ultrasound does not reveal the specific anatomic characteristics of MTS such as iliac vein compression or intraluminal spurs^[4,18]. However, in a case report by Oğuzkurt *et al*^[3], a diagnosis of MTS was initially reached by transabdominal ultrasonography alone and later confirmed by CT, venography, and pressure measurements. Although transvaginal ultrasound can be used to determine the pathological reflux in the internal iliac veins in women, it does not allow for good imaging of the common iliac veins and is therefore not a very useful tool in the diagnosis of MTS^[19]. Overall, ultrasound is a useful mechanism for determining venous patency, but a negative study result does not rule out the possibility of MTS and therefore more imaging tests are needed in order to establish a diagnosis.

Pleythysmography

Air pleythysmography (APG) is a noninvasive test that can determine the degree of venous reflux and evaluate any proximal obstructions^[7]. Hurst *et al*^[5] utilized APG to determine the degree of iliac vein obstruction in 9 patients in order to confirm a suspected diagnosis of MTS. In all 9 cases, APG was unable to detect any iliac vein obstructions despite the presence of occlusions or stenosis in all patients. Hurst *et al*^[5] thus concluded that APG has a low sensitivity in confirming a diagnosis of MTS. Although APG can be useful in evaluating the severity of venous symptoms, it can be nondiagnostic due to the presence of collateral pathways and a lack of sufficient narrowing to impact the flow dynamics^[4,5]. Therefore, APG is not considered a routine diagnostic tool for MTS and more invasive tests are required in order to confirm a diagnosis of MTS.

CT

CT with intravenous contrast in a transverse plane has proven to be a useful modality in confirming the diagnosis of MTS^[14,18,20]. A CT examination of the abdomen or pelvis can rule out extrinsic reasons of compression as well as identify acute DVT and collateral pathways; however, a normal CT with 10-mm cuts cannot always establish a diagnosis of MTS because small iliac spurs are often too difficult to visualize and fibrosis can conceal the underlying vasculature^[7,8,21]. However, a CT analysis utilizing narrower cuts 3 to 5-mm can be sufficient enough to visualize the structural details that may be previously missed. Chung *et al*^[21] utilized spiral CT venography to evaluate iliac vein compression due to MTS in 27 out of 44 patients presenting with lower extremity DVT; Oguzkurt *et al*^[22] found that CT images in a transverse plane showed the compression of the LCIV by the LCIA in all 10 patients tested. Additionally, in a study conducted by Liu *et al*^[17], CT venography was found to have a high sensitivity and specificity in confirming MTS over other imaging modalities and that it can also distinguish between non-thrombotic and thrombotic MTS. The advantages of CT venography over CDUS or traditional venography include lack of operator dependence, clearer imaging of the pelvic veins, and a shorter exam time; however, the radiation dose is contraindicated in instances of pregnancy and large amount of contrast medium required for CT venography are contraindicated in patients with renal impairment^[22]. Overall, CT venography is a useful diagnostic tool in demonstrating iliac vein compression, although more studies are required in order to fully evaluate the sensitivity and specificity of CT images in diagnosing MTS.

MRV

Several studies have advocated that MRV is a suitable



Figure 3 Magnetic resonance venography with axial (A), sagittal (B), and coronal (C) reformatted images demonstrating May-Thurner syndrome anatomy with compression of the left common iliac vein (white arrowhead) by the right common iliac artery (black arrowhead).

imaging modality in diagnosing MTS (Figure 3)^[4-7,13]. In a case study by Wolpert *et al.*^[13], MRV was able to confirm a diagnosis of MTS in all 9 patients that presented with the condition; moreover, MRV was able to reveal the anatomic abnormalities of MTS as well as rule out the presence of DVT or pelvic masses. Additionally, Shebel *et al.*^[7] found that MRV was able to confirm the presence of nonocclusive iliac spurs (thus confirming a diagnosis of MTS) in 5 patients that had normal DUS results. The primary advantages of MRV in the diagnosis of MTS include its noninvasiveness, ability to analyze all pelvic structures, and lack of operator dependence^[13]. Additionally, MRV can estimate the degree of venous collateral flow, which greatly assists in the diagnosis of MTS^[23]. Lastly, MRV can be performed without contrast, which is beneficial to patients with contraindications such as contrast allergies or renal impairment^[8]. Conversely, the primary disadvantage of MRV in the diagnosis of MTS is that the vasculature above bifurcations has nonlaminar flow, which sometimes presents a confusing image^[13]. Additionally, MRV studies are expensive, take significant time to perform, and are hard to perform on severely ill patients^[18].

Although MRV is a beneficial diagnostic option, a single MRV study may not be sufficient enough to diagnose MTS; McDermott *et al.*^[11] found that the degree

of left iliac vein compression significantly differs in the same patient when undergoing repeated MRV imaging within a short period of time due to factors such as volume status or patient positioning^[1,8]. Because MTS is a chronic condition with the development of permanent adhesions and intraluminal spurs, the degree of left iliac vein compression should not change significantly over time or depend on patient positioning. Thus, the sole finding of MTS anatomy on one MRV study may not be sufficient enough to confirm a diagnosis of MTS and more imaging studies may be necessary in order to reach a definitive diagnosis.

Contrast venography/hemodynamic studies

Contrast venography has widely been considered the gold standard diagnostic modality for MTS and has been utilized to confirm a diagnosis of MTS in several studies^[5,6,12,24]. The procedure demonstrates the degree of iliac vein stenosis and can visualize any pelvic venous collaterals. Contrast dye must be injected in either the popliteal or femoral veins, as the standard method of dye injected into the dorsum of the foot is not adequate to fully visualize the iliac venous system^[7,8]. Venography also allows for hemodynamic evaluation of MTS through pressure gradient measurements; iliofemoral stenosis is considered significant with a measurement of greater than 2 mmHg at rest and greater than 3 mmHg during periods of exercise. However, a nondiagnostic result does not rule out MTS because the patient is tested while at rest; exercise is usually required to increase blood flow to demonstrate a significant pressure gradient^[4,7]. Although ascending venography almost always provides the evidence needed for a confirmed diagnosis of MTS, it is time consuming, invasive, cannot be performed in patients with widespread iliofemoral DVT and can result in post-procedural complications such as phlebitis^[18].

IVUS

IVUS, using either a 12.5-MHz or 20-MHz ultrasound transducer, can accurately determine LCIV vessel size and morphology, and can verify the presence of MTS anatomy^[10,25,26]. Knipp *et al.*^[6] utilized IVUS to confirm a diagnosis of MTS in 36 out of 58 patients; (62.1%) and defined the IVUS criteria for an MTS diagnosis as the lack of an evident venous lumen proximate to the IVUS catheter. In a small scale study conducted by Forauer *et al.*^[10], IVUS was not only used to confirm a diagnosis of MTS in all patients ($n = 16$), but information provided by the study was also found to influence the endovascular management of approximately 50% of the cases while also assisting with stent placement choice and accuracy. Moreover, in some studies, IVUS was found to have a higher success than venography in identifying obstructions^[27-29]. Overall, IVUS is a useful modality in the diagnosis of MTS, although more studies are needed to truly evaluate its advantages over other diagnostic techniques.

CLINICAL PEARLS TO IMPROVE MTS DIAGNOSIS

There are several clinical pearls that can be considered in the diagnosis of MTS. For instance, if ultrasound is possible and allows for visualization of the iliac veins, provocative maneuvers (*i.e.*, placing the patient in supine vs lateral positions or imaging during valsalva) may be performed to help demonstrate permanent vascular changes. These provocative maneuvers may also be used at the time of venography. Supine and prone CT or magnetic resonance imaging and cone beam CT at the time of venography may reveal the true state of common iliac vein. Additionally, due to the nil per os status for the procedure, the patient may be hypovolemic causing the IVC and iliac veins to easily flatten; in these cases, an IV bolus of 500-1000 cc of normal saline may be provided to the patient.

TREATMENT OPTIONS

Due to the mechanical nature of the obstruction, MTS patients generally do not respond well to conservative treatments^[4]. In the past, surgical management of MTS has resulted in variable outcomes, as it is correlated with a high morbidity rate and has varied success in reestablishing venous patency^[4,5]. Currently, the use of endovascular techniques in the treatment of MTS patients is considerably successful and carries less risk than invasive surgical treatments^[8]. Common endovascular treatment options include catheter-directed thrombolysis, angioplasty, and ultimately stent placement^[3,5,6,10,24]. Angioplasty has been found to be associated with low long-term patency rates, which indicates that the iliac vein compression may not be alleviated with solely the use of balloon angioplasty^[30]. Additionally, stent placement is often necessary; however, stents are also associated with poor long-term patency rates, thus making diagnostic accuracy even more critical in the treatment of MTS patients as the choice to stent should be not be chosen lightly^[8]. Overall, more studies are needed in order to fully evaluate the endovascular treatment that can provide the best outcome^[8].

CONCLUSION

Prompt diagnosis is critical in MTS patients in order to avoid potential complications and the permanent consequences of intraluminal spur development. Currently, there is no diagnostic criteria in place to confirm a diagnosis of MTS. Imaging techniques such as CT, IVUS, MRV, and ascending venography have been useful in verifying a diagnosis; conversely, ultrasonography and pleythysmography, while useful in evaluating DVT and venous obstructions, cannot effectively be used to diagnose MTS and are best used in conjunction with other imaging techniques. Overall, the identification of MTS relies on both clinical and image findings, and more

studies are needed in order to develop a comprehensive protocol for both.

REFERENCES

- 1 **McDermott S**, Oliveira G, Ergül E, Brazeau N, Wicky S, Oklu R. May-Thurner syndrome: can it be diagnosed by a single MR venography study? *Diagn Interv Radiol* 2013; **19**: 44-48 [PMID: 22801870 DOI: 10.4261/1305-3825.DIR.5939-12.1]
- 2 **Heijmen RH**, Bollen TL, Duyndam DA, Overtom TT, Van Den Berg JC, Moll FL. Endovascular venous stenting in May-Thurner syndrome. *J Cardiovasc Surg (Torino)* 2001; **42**: 83-87 [PMID: 11292912]
- 3 **Oğuzkurt L**, Ozkan U, Tercan F, Koç Z. Ultrasonographic diagnosis of iliac vein compression (May-Thurner) syndrome. *Diagn Interv Radiol* 2007; **13**: 152-155 [PMID: 17846991]
- 4 **O'Sullivan GJ**, Semba CP, Bittner CA, Kee ST, Razavi MK, Sze DY, Dake MD. Endovascular management of iliac vein compression (May-Thurner) syndrome. *J Vasc Interv Radiol* 2000; **11**: 823-836 [PMID: 10928517 DOI: 10.1016/S1051-0443(07)61796-5]
- 5 **Hurst DR**, Forauer AR, Bloom JR, Greenfield LJ, Wakefield TW, Williams DM. Diagnosis and endovascular treatment of ilio caval compression syndrome. *J Vasc Surg* 2001; **34**: 106-113 [PMID: 11436082 DOI: 10.1067/mva.2001.114213]
- 6 **Knipp BS**, Ferguson E, Williams DM, Dasika NJ, Cwikiel W, Henke PK, Wakefield TW. Factors associated with outcome after interventional treatment of symptomatic iliac vein compression syndrome. *J Vasc Surg* 2007; **46**: 743-749 [PMID: 17903652 DOI: 10.1016/j.jvs.2007.05.048]
- 7 **Shebel ND**, Whalen CC. Diagnosis and management of iliac vein compression syndrome. *J Vasc Nurs* 2005; **23**: 10-17; quiz 18-19 [PMID: 15741959 DOI: 10.1016/j.jvn.2004.12.001]
- 8 **Brazeau NF**, Harvey HB, Pinto EG, Deipolyi A, Hesketh RL, Oklu R. May-Thurner syndrome: diagnosis and management. *Vasa* 2013; **42**: 96-105 [PMID: 23485836 DOI: 10.1024/0301-1526/a000252]
- 9 **Cockett FB**, Thomas ML, Negus D. Iliac vein compression.-Its relation to iliofemoral thrombosis and the post-thrombotic syndrome. *Br Med J* 1967; **2**: 14-19 [PMID: 6020994 DOI: 10.1136/bmj.2.5543.14]
- 10 **Forauer AR**, Gemmete JJ, Dasika NL, Cho KJ, Williams DM. Intravascular ultrasound in the diagnosis and treatment of iliac vein compression (May-Thurner) syndrome. *J Vasc Interv Radiol* 2002; **13**: 523-527 [PMID: 11997362 DOI: 10.1016/S1051-0443(07)61535-8]
- 11 **Ibrahim W**, Al Safran Z, Hasan H, Zeid WA. Endovascular management of may-thurner syndrome. *Ann Vasc Dis* 2012; **5**: 217-221 [PMID: 23555515 DOI: 10.3400/avd.cr.12.00007]
- 12 **Patel NH**, Stookey KR, Ketcham DB, Cragg AH. Endovascular management of acute extensive iliofemoral deep venous thrombosis caused by May-Thurner syndrome. *J Vasc Interv Radiol* 2000; **11**: 1297-1302 [PMID: 11099239 DOI: 10.1016/S1051-0443(07)61304-9]
- 13 **Wolpert LM**, Rahmani O, Stein B, Gallagher JJ, Drezner AD. Magnetic resonance venography in the diagnosis and management of May-Thurner syndrome. *Vasc Endovascular Surg* 2002; **36**: 51-57 [PMID: 12704525 DOI: 10.1177/153857440203600109]
- 14 **Kibbe MR**, Ujiki M, Goodwin AL, Eskandari M, Yao J, Matsumura J. Iliac vein compression in an asymptomatic patient population. *J Vasc Surg* 2004; **39**: 937-943 [PMID: 15111841 DOI: 10.1016/j.jvs.2003.12.032]
- 15 **Moreland NC**, Ujiki M, Matsumura JS, Morasch MD, Eskandari MK, Pearce WH, Kibbe MR. Decreased incidence of left common iliac vein compression in patients with abdominal aortic aneurysms. *J Vasc Surg* 2006; **44**: 595-600 [PMID: 16950440 DOI: 10.1016/j.jvs.2006.05.046]
- 16 **Oğuzkurt L**, Ozkan U, Uluhan S, Koc Z, Tercan F. Compression of the left common iliac vein in asymptomatic subjects and patients with left iliofemoral deep vein thrombosis. *J Vasc Interv Radiol* 2008; **19**: 366-370; quiz 371 [PMID: 18295695 DOI: 10.1016/j.jvir.2007.09.007]

- 17 **Liu Z**, Gao N, Shen L, Yang J, Zhu Y, Li Z, Si Y. Endovascular treatment for symptomatic iliac vein compression syndrome: a prospective consecutive series of 48 patients. *Ann Vasc Surg* 2014; **28**: 695-704 [PMID: 24559785 DOI: 10.1016/j.avsg.2013.05.019]
- 18 **Lamba R**, Tanner DT, Sekhon S, McGahan JP, Corwin MT, Lall CG. Multidetector CT of vascular compression syndromes in the abdomen and pelvis. *Radiographics* 2014; **34**: 93-115 [PMID: 24428284 DOI: 10.1148/rg.341125010]
- 19 **Whiteley M**, Dos Santos S, Harrison C, Holdstock J, Lopez A. Transvaginal duplex ultrasonography appears to be the gold standard investigation for the haemodynamic evaluation of pelvic venous reflux in the ovarian and internal iliac veins in women. *Phlebology* 2014; Epub ahead of print [PMID: 25324278 DOI: 10.1177/0268355514554638]
- 20 **Zhu QH**, Zhou CY, Chen Y, Wang J, Mo HY, Luo MH, Huang W, Yu XF. Percutaneous manual aspiration thrombectomy followed by stenting for iliac vein compression syndrome with secondary acute isolated iliofemoral deep vein thrombosis: a prospective study of single-session endovascular protocol. *Eur J Vasc Endovasc Surg* 2014; **47**: 68-74 [PMID: 24183245 DOI: 10.1016/j.ejvs.2013.09.030]
- 21 **Chung JW**, Yoon CJ, Jung SI, Kim HC, Lee W, Kim YI, Jae HJ, Park JH. Acute iliofemoral deep vein thrombosis: evaluation of underlying anatomic abnormalities by spiral CT venography. *J Vasc Interv Radiol* 2004; **15**: 249-256 [PMID: 15028809 DOI: 10.1097/01.RV1.0000109402.52762.8D]
- 22 **Oguzkurt L**, Tercan F, Pourbagher MA, Kizilkilic O, Turkoz R, Boyvat F. Computed tomography findings in 10 cases of iliac vein compression (May-Thurner) syndrome. *Eur J Radiol* 2005; **55**: 421-425 [PMID: 16129251 DOI: 10.1016/j.ejrad.2004.11.002]
- 23 **Gurel K**, Gurel S, Karavas E, Buharaloglu Y, Daglar B. Direct contrast-enhanced MR venography in the diagnosis of May-Thurner syndrome. *Eur J Radiol* 2011; **80**: 533-536 [PMID: 20570076 DOI: 10.1016/j.ejrad.2010.04.033]
- 24 **Binkert CA**, Schoch E, Stuckmann G, Largiader J, Wigger P, Schoepke W, Zollikofer CL. Treatment of pelvic venous spur (May-Thurner syndrome) with self-expanding metallic endoprotheses. *Cardiovasc Intervent Radiol* 1998; **21**: 22-26 [PMID: 9473541 DOI: 10.1007/s002709900205]
- 25 **Ahmed HK**, Hagspiel KD. Intravascular ultrasonographic findings in May-Thurner syndrome (iliac vein compression syndrome). *J Ultrasound Med* 2001; **20**: 251-256 [PMID: 11270529]
- 26 **Canales JF**, Krajcer Z. Intravascular ultrasound guidance in treating May-Thurner syndrome. *Tex Heart Inst J* 2010; **37**: 496-497 [PMID: 20844634]
- 27 **McLafferty RB**. The role of intravascular ultrasound in venous thromboembolism. *Semin Intervent Radiol* 2012; **29**: 10-15 [PMID: 23450229 DOI: 10.1055/s-0032-1302446]
- 28 **Raju S**, Neglen P. High prevalence of nonthrombotic iliac vein lesions in chronic venous disease: a permissive role in pathogenicity. *J Vasc Surg* 2006; **44**: 136-143; discussion 144 [PMID: 16828437 DOI: 10.1016/j.jvs.2006.02.065]
- 29 **Neglén P**, Raju S. Intravascular ultrasound scan evaluation of the obstructed vein. *J Vasc Surg* 2002; **35**: 694-700 [PMID: 11932665 DOI: 10.1067/mva.2002.121127]
- 30 **Kim JY**, Choi D, Guk Ko Y, Park S, Jang Y, Lee do Y. Percutaneous treatment of deep vein thrombosis in May-Thurner syndrome. *Cardiovasc Intervent Radiol* 2006; **29**: 571-575 [PMID: 16502185 DOI: 10.1007/s00270-004-0165-7]

P- Reviewer: Chan WP, Chen F

S- Editor: Ji FF L- Editor: A E- Editor: Jiao XK



Application of positron emission tomography/computed tomography in radiation treatment planning for head and neck cancers

Musaddiq J Awan, Farzan Siddiqui, David Schwartz, Jiankui Yuan, Mitchell Machtay, Min Yao

Musaddiq J Awan, Jiankui Yuan, Mitchell Machtay, Min Yao, Department of Radiation Oncology, Case Comprehensive Cancer Center, University Hospitals and Case Western Reserve University School of Medicine, Cleveland, OH 44106, United States

Farzan Siddiqui, Department of Radiation Oncology, Henry Ford Health System, Detroit, MI 48202, United States

David Schwartz, Department of Radiation Oncology, University of Texas Southwestern Medical Center, Dallas, TX 75390, United States

Author contributions: Awan MJ, Siddiqui F and Yao M contributed equally to this work; Siddiqui F, Schwartz D and Yao M contributed to case examples; Yuan J contributed to the data collection and image process; Awan MJ, Siddiqui F, Schwartz D, Yuan J, Machtay M, and Yao M all contributed to writing and editing the paper.

Conflict-of-interest statement: The authors have no conflicts of interest to disclose related to the publication of this work.

Open-Access: This article is an open-access article which was selected by an in-house editor and fully peer-reviewed by external reviewers. It is distributed in accordance with the Creative Commons Attribution Non Commercial (CC BY-NC 4.0) license, which permits others to distribute, remix, adapt, build upon this work non-commercially, and license their derivative works on different terms, provided the original work is properly cited and the use is non-commercial. See: <http://creativecommons.org/licenses/by-nc/4.0/>

Correspondence to: Min Yao, MD, PhD, Professor, Department of Radiation Oncology, Case Comprehensive Cancer Center, University Hospitals and Case Western Reserve University School of Medicine, 11100 Euclid Avenue, Cleveland, OH 44106, United States. min.yao@uhhospitals.org
 Telephone: +1-216-8443103
 Fax: +1-216-8442005

Received: May 29, 2015
 Peer-review started: June 1, 2015

First decision: June 18, 2015
 Revised: July 8, 2015
 Accepted: September 16, 2015
 Article in press: September 18, 2015
 Published online: November 28, 2015

Abstract

18-fluorodeoxyglucose positron emission tomography/computed tomography (¹⁸FDG-PET/CT) provides significant information in multiple settings in the management of head and neck cancers (HNC). This article seeks to define the additional benefit of PET/CT as related to radiation treatment planning for squamous cell carcinomas (SCCs) of the head and neck through a review of relevant literature. By helping further define both primary and nodal volumes, radiation treatment planning can be improved using PET/CT. Special attention is paid to the independent benefit of PET/CT in targeting mucosal primaries as well as in detecting nodal metastases. The utility of PET/CT is also explored for treatment planning in the setting of SCC of unknown primary as PET/CT may help define a mucosal target volume by guiding biopsies for examination under anesthesia thus changing the treatment paradigm and limiting the extent of therapy. Implications of the use of PET/CT for proper target delineation in patients with artifact from dental procedures are discussed and the impact of dental artifact on CT-based PET attenuation correction is assessed. Finally, comment is made upon the role of PET/CT in the high-risk post-operative setting, particularly in the context of radiation dose escalation. Real case examples are used in these settings to elucidate the practical benefits of PET/CT as related to radiation treatment planning in HNCs.

Key words: Head and neck cancer; Radiation treatment planning; Computed tomography; Fluorodeoxyglucose positron emission tomography; Imaging

© The Author(s) 2015. Published by Baishideng Publishing Group Inc. All rights reserved.

Core tip: The 18-fluorodeoxyglucose positron emission tomography (¹⁸FDG-PET) scan has increasing clinical importance in the management of head and neck cancers. It has also proven useful in treatment planning for radiation therapy. PET scans have utility in tumor volume delineation, the identification of metastatic lymph nodes, the management of carcinoma of unknown primary, dental artifact reduction and high-risk post-operative radiation therapy. Many of these applications of ¹⁸FDG-PET scans are still in the preliminary stages of development and active investigations are ongoing to standardize these processes.

Awan MJ, Siddiqui F, Schwartz D, Yuan J, Machtay M, Yao M. Application of positron emission tomography/computed tomography in radiation treatment planning for head and neck cancers. *World J Radiol* 2015; 7(11): 382-393 Available from: URL: <http://www.wjgnet.com/1949-8470/full/v7/i11/382.htm> DOI: <http://dx.doi.org/10.4329/wjv7.i11.382>

INTRODUCTION

Head and neck cancer (HNC) is a significant cause of cancer morbidity and mortality worldwide. Approximately 650000 new HNC are diagnosed annually worldwide with approximately half of this number resulting in deaths^[1]. The majority of HNCs worldwide are squamous cell carcinomas (SCCs) related to tobacco abuse, however the incidence of head and neck SCCs resulting from infection with the human papilloma virus (HPV) is rising. The prognosis for HPV-negative (tobacco-related) cancers is inferior to that of HPV-positive cancers. Undoubtedly, radiation therapy plays a central role in the management of the majority of HNC patients and meticulous radiation treatment planning is required to ensure high rates of cure as well as in limiting toxicity. This is particularly important for HPV-positive oropharyngeal cancer patients as these patients are generally younger and with few co-morbidities and thus are expected to live longer with long-term radiation complications. Most HNCs present in a locally advanced stage and primary management takes one of the two courses: surgical resection with or without adjuvant radiation based upon pathologic features or definitive radiation therapy with or without concurrent chemotherapy saving surgery as a salvage option.

Modern radiation therapy is delivered using highly conformal technologies including three-dimensional conformal radiotherapy, intensity modulated radiation therapy (IMRT) and most recently IMRT with image guidance. Target delineation on treatment planning computed tomography (CT) scans is a central part of the treatment process in both cure and limiting toxicity. This is particularly important in the era of IMRT, in

which steep radiation dose falloff is achievable within millimeters.

A risk-stratified approach is taken in radiation treatment planning in HNCs. Areas of high-risk of disease spread and gross disease receive a high dose of radiation (usually 66-70 Gy). Other areas, including those of intermediate-risk of disease spread and grossly uninvolved nodal regions in which tumor recurrence may occur, receive lower doses of radiation (56-60 Gy and 50-56 Gy, respectively). Clinical data from physical examinations and diagnostic laryngoscopies, as well as pathologic data and multimodality imaging using CT, magnetic resonance imaging (MRI), ultrasound and positron emission tomography (PET) all contribute to the target delineation and treatment planning process. This article seeks to define the additional benefit of the utility of 18-fluorodeoxyglucose (¹⁸FDG) PET/CT scans in radiation treatment planning particularly as related to five areas: (1) Primary gross tumor and nodal volume (GTV) delineation; (2) Identification of involved metastatic lymph nodes; (3) Management of SCCs of unknown primary in the head and neck; (4) Utility in accounting for dental artifact; and (5) High-risk post-operative radiation (PORT).

DELINEATION OF THE PRIMARY AND NODAL GTV

¹⁸FDG-PET can help clarify the extent of primary tumor and eliminate unnecessary treatment volumes that may appear as abnormal on CT or MRI imaging. Significant variations have been noted in both primary tumor and lymph nodal volumes based on the diagnostic imaging modality(ies) used to define these. Iodinated-contrast-enhanced CT scans remain the imaging modality of choice due to their widespread availability in radiation oncology departments worldwide. Additionally, CT scans have a short image acquisition time and thus do not suffer from the image quality degradation that may result from longer acquisition times and normal breathing or swallowing motion. They provide sufficient anatomical details of the gross tumor and involved lymph nodes, provide electron density information for attenuation correction for treatment planning purposes, and require less end-user training for image interpretation relative to other modalities. Many reports have investigated the impact of additional PET imaging on primary and lymph nodal volume definition for radiation treatment planning purposes. Most of these reports have found major discrepancies between CT-based and PET-based volumes resulting in clinically significant implications for radiation therapy.

Studies assessing the addition of PET to CT-based planning

A number of studies have assessed the impact of the addition of PET in the manual segmentation of HNC GTVs. In an analysis of 12 HNC patients comparing CT

based GTV (GTV-CT) and PET based GTV (GTV-PET), the GTV increased or decreased by 25% or more because of PET in 17% and 33% of cases, respectively^[2]. In this report, the primary and nodal volumes were not assessed separately.

In another study, Heron *et al*^[3] did analyze the changes in primary and nodal volumes separately and noted a change in GTV delineation in 80% of cases with the use of PET scans. For the primary site, the GTV was larger in 14% and smaller in 66% of cases based on PET scans. Interestingly, for the abnormal lymph nodes, the volume was larger in 33% of cases and smaller in 14% of cases. The average ratio of GTVs for the CT-defined and PET-defined volumes was 3.1 (range, 0.3-23.6), whereas for abnormal nodes was 0.7 (range, 0-4). Hence, tumor volumes for the primaries were significantly larger as delineated on CT than on PET but not for nodal regions suggesting a larger benefit in delineating the primary tumor with the addition of PET.

A similar discrepancy between CT-GTV and PET-GTV was noted by Guido *et al*^[4]. Thirty-eight consecutive HNC patients underwent treatment planning CTs with intravenous contrast enhancement. A radiation oncologist defined all GTVs using both the PET/CT and CT scans. The CT-GTV was larger than PET-GTV in 92% cases. Unlike the previous study, no statistically significant difference was seen between these volumes for primary and nodal sites.

Variations in target delineation with the addition of PET/CT may also affect treatment planning. In a study of a group of 40 patients, Paulino *et al*^[5] noted changes in the PET-GTV in 37 cases (30 smaller, 7 larger). IMRT plans were generated based on the CT-based volumes and dosimetric analysis was performed to examine the adequacy of coverage for the PET-based volume in these IMRT plans. The volume of PET-GTV receiving at least 95% of the prescribed dose was 100% and 95%-99% in 20 and 10 cases, respectively. Thus, inadequate coverage (< 95% of the PET-GTV receiving the prescribed dose) was seen in 25% of cases.

A major reason for these variations in study results is the subjectivity associated with ¹⁸FDG-PET image interpretation and consequent user dependence on how the GTV is defined using PET images. The potential impact of interobserver and intraobserver variation was studied by Breen *et al*^[6]. Eight experienced observers (6 head and neck oncologists and 2 neuroradiologists) outlined the primary GTV for 10 patients. There was a very high agreement between and within observers on GTVs derived from contrast-enhanced CT scans. However, there was less reliability noted when PET/CT scans were used for outlining the GTV. In another similar analysis^[7], 4 physicians (2 neuroradiologists and 2 radiation oncologists) contoured GTVs in 16 patients on the basis of the CT alone, and then on PET/CT fusion. A high degree of variation was noted across physicians for the CT volumes ($P = 0.09$) and significant variation was seen for the PET/CT volumes ($P = 0.0002$). Observer variation in lymph nodal volume outlining was

not assessed in either of these studies.

Automated techniques of PET-GTV delineation

Due to limitations in how different experienced physicians define the GTVs for various cases it is very difficult to perform interinstitutional comparative studies and arrive at any meaningful conclusions on the utility of PET scans for head and neck treatment planning. To overcome these interobserver and intraobserver variations, many attempts have been made to automate the process of volume definition using PET scans. Various groups have attempted to describe "thresholding" or "segmentation" techniques to make the process more objective and eliminate or reduce the subjectivity associated with the use of PET imaging data.

Schinagl *et al*^[8] evaluated PET based GTVs derived using 5 different segmentation techniques: visual interpretation, applying an isocontour of a standardized uptake value (SUV) of 2.5, using a fixed threshold of 40% and 50% of the maximum signal intensity, and applying an adaptive threshold based on the signal-to-background ratio. Seventy-eight patients with Stages II-IV SCC of the head and neck were studied. The primary tumor was delineated on CT. The GTV method of applying an isocontour of a SUV of 2.5 failed to provide successful delineation in 45% of cases. However, the other segmentation methods resulted in PET-GTVs that were smaller than that seen on the CT scan. Additionally, the PET scans frequently showed tumor extension outside that seen on the CT scans. The authors concluded that none of the segmentation methods provided a satisfactory result.

In a subsequent publication, the authors used the same data set of 78 patients to assess whether PET scans could be used for target volume definition for metastatic lymph nodes in the head and neck region^[9]. On the CT scans, lymph nodes measuring 7-10 mm were labeled as "marginally enlarged" and those > 10 mm were "enlarged". Eight different PET segmentation methods were used to identify these nodes: visual interpretation, applying fixed thresholds at SUV of 2.5 and at 40% and 50% of the maximum signal intensity of the primary tumor and applying a variable threshold based on the signal-to-background ratio. Additionally, these same thresholds were acquired using the signal of the lymph node as the threshold reference. Based on the CT scan imaging, 208 lymph nodes were > 7 mm while 108 were >10 mm. A large percentage of these lymph nodes were not identified by the segmentation methods when normalized to the primary tumor PET-SUV. The results were better when the thresholds were set based on the lymph node SUV values. Due to these limitations, the authors concluded that until proper validation of ¹⁸FDG-PET based segmentation tools is done it should not be recommended for target volume definition of metastatic lymph nodes in routine clinical practice.

Another recent prospective study in 19 patients with 39 lesions used the signal-to-background ratio

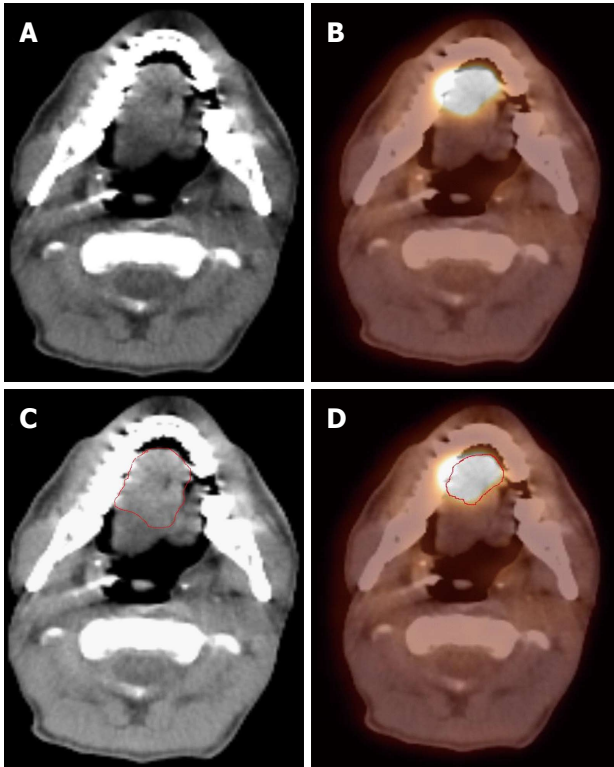


Figure 1 Positron emission tomography/computed tomography improves gross tumor and nodal volume delineation in a patient with oral tongue cancer. A: In the CT image, the tumor is difficult to separate from the soft tissues of the tongue; B: In the PET image, there is sharp demarcation of the primary tumor; C: The GTV is outlined in red based on CT scan; D: The GTV outlined in red based on ^{18}F FDG PET/CT is much smaller. ^{18}F FDG-PET/CT: 18 -fluorodeoxyglucose positron emission tomography/computed tomography; GTV: Gross tumor and nodal volume.

thresholding method to define tumor volumes. It concluded that methods that rely mainly on SUV_{max} for thresholding are very sensitive to partial volume effects and may provide unreliable results when applied on small lesions^[10]. Thus, automated thresholding and segmentation methods have not yet yielded promising results in PET-GTV delineation.

Pathologic correlation of PET-GTV volumes

Investigators have also evaluated the pathologic correlates to PET imaging findings in HNC patients. Daisne *et al.*^[11] compared delineation of tumor volumes on MRI, CT and PET in multiple patients with HNCs. Average PET-GTVs (20.3 cc) were smaller than those derived from MR (27.9 cc) or CT (32 cc). Additionally, PET-GTVs contained additional volume not delineated on either primary MR or CT images. For 9 patients with laryngeal cancer who underwent total laryngectomy after multi-modality imaging in this cohort, pathologic tumor volumes were significantly smaller than the estimated image volumes on all modalities studied. The average surgical specimen tumor volume measured 12.6 cc while tumor volume was measured as 16.3 cc, 20.8 cc and 23.8 cc on PET, CT and MRI images, respectively.

In a similar radio-pathologic correlative study,

Schinagl *et al.*^[12] identified 28 lymph nodes in 12 HNC patients and looked at the ability of various PET segmentation methods to predict pathologic size after lymph node dissection. Nodal volumes on CT scans and visual interpretation of PET scans showed good correlations with the pathological volume. The authors noted that ^{18}F FDG-PET scans are valuable for detection of lymph nodes for staging purposes but provide no additional information over CT scans for outlining radiotherapy target volumes.

Guidelines for the utility of PET/CT for GTV delineation

There is currently no consensus on the methods of auto-segmentation, volume definition and the overall utility of ^{18}F FDG-PET scans in RT of HNCs. This remains an active area of research and development. Currently, we use ^{18}F FDG-PET co-registered with the simulation CT images to identify the tumor, contour the GTV and subsequently modify the GTV volume with the CT images, especially with contrast-enhancing CT images. ^{18}F FDG-PET is especially helpful when it is difficult to separate the tumor from surrounding soft tissue and muscle in CT imaging, such as tumor in the oral tongue or oropharynx. Figure 1 shows a patient with oral tongue cancer, comparing CT vs PET. The GTV based on CT (Figure 1C) is much larger than that based on ^{18}F FDG-PET (Figure 1D).

^{18}F FDG-PET is also very helpful in identifying tumor extent that is not detectable on either CT or MR images. In particular, HNC patients often have synchronous second primaries. ^{18}F FDG-PET can help detect additional primary disease to be included in the high dose radiation field. Figure 2 shows a patient who presented with a right lateral oral tongue cancer. PET/CT revealed additional primary cancers in the soft palate and in the cervical esophagus (Figure 2A). Thus, the IMRT plan delivered 70 Gy to all of these primary tumors (Figure 2B-D).

IDENTIFICATION OF INVOLVED LYMPH NODES THAT ARE MISSED ON CT/MR

In addition to helping better delineate primary tumors, ^{18}F FDG-PET can clarify the involvement of metastatic lymph nodes in HNC patients. Standard CT and MR criteria for malignant cervical lymph nodes include size, shape, margins, and internal architecture, with size as the main criteria^[13]. These criteria for CT and MR may under- or over-diagnose lymph node involvement and nodal stage in patients, resulting in 20%-30% false positive and false negative results^[13]. The consequence of such errors may have a significant impact on treatment planning in HNC; in particular, small malignant lymph nodes may be under-dosed using CT or MRI criteria alone.

PET sensitivity and specificity for predicting involved nodes has been estimated at over 90%^[14]. Heron *et*

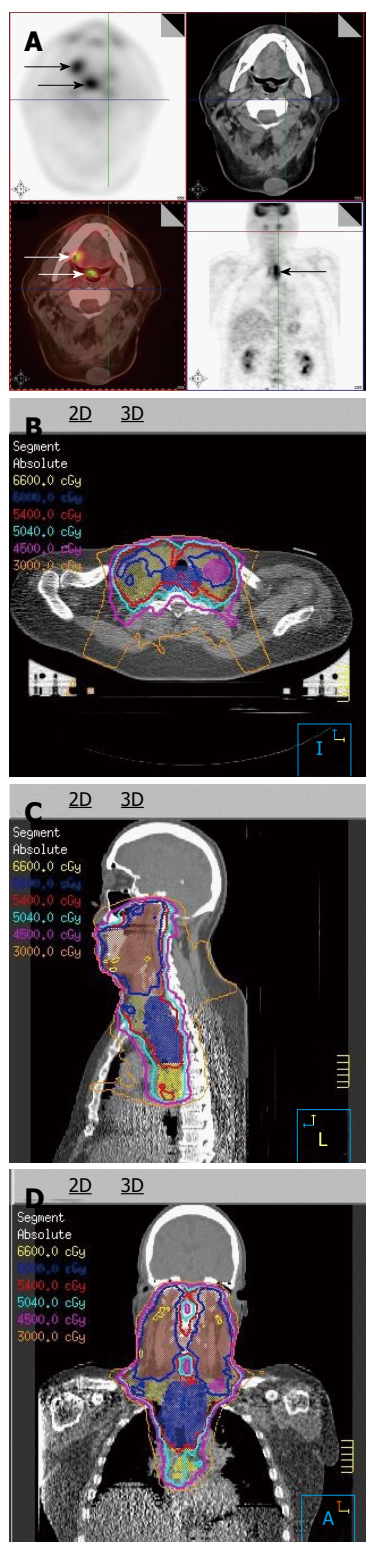


Figure 2 Positron emission tomography/computed tomography discovers multiple primaries in a patient with a right lateral tongue cancer. A: PET/CT images revealed that in addition to an oral tongue tumor, this patient had a primary tumor of the soft palate (inferior white arrow) as well as the cervical esophagus (black arrow); B-D: The IMRT plan for this patient demonstrates all three tumors covered in the high dose CTV. PET/CT: Positron emission tomography/computed tomography; IMRT: Intensity modulated radiation therapy.

a^[3] reported that the addition of ¹⁸FDG-PET to CT-

based treatment planning increased the number of abnormal nodes contoured in 5 of 21 (24%) patients in a small institutional study. In another study, Koshy *et al*^[15] reported significant changes in TNM staging affecting tumor volume delineation with the addition of ¹⁸FDG-PET to CT alone. Amongst a group of 36 patients in this study, 6 patients had a change in N-stage with the use of PET/CT relative to CT alone: 3 patients were upstaged including one to bilateral disease, while 3 other patients were downstaged to N0 disease. These changes in nodal staging are not trivial, as grossly involved nodal disease will receive radiation doses of up to 70 Gy, while node-negative disease may receive an elective radiation dose of 50-56 Gy or no radiation therapy at all.

In a prospective study by Schwartz *et al*^[16] evaluating the feasibility of PET/CT based treatment planning, 63 patients underwent PET/CT simulation and 20 patients underwent neck dissection after a PET/CT simulation. ¹⁸FDG-PET correctly identified all 17 diseased heminecks and 9 negative heminecks. Additionally, 26/27 pathologically involved nodal levels were identified with positive predictive value (PPV) and negative predictive values (NPV) for nodal staging at 98.5% and 96% respectively. This affirms the high level of accuracy by which ¹⁸FDG-PET can be used to assess nodal disease. Further, in comparing CT-based and PET/CT-based treatment planning, PET/CT-based planning directly improved parotid and laryngeal doses, thus theoretically sparing patients from long-term toxicities of xerostomia and dysphagia.

Figure 3 illustrates a patient with nasopharyngeal cancer. Initial staging by CT and MRI was T1N0, but an ¹⁸FDG-PET scan revealed a hypermetabolic level II lymph node which did not meet size criteria for malignancy by CT/MRI (Figure 3A-D). Fine needle aspiration (FNA) of this node confirmed metastatic disease. Thus, this lymph node was treated to a high dose of radiation (Figure 3E-H) and concurrent chemotherapy was indicated.

PET/CT has especially been helpful in detecting lymph nodes at a far distance from the primary tumor or in the contralateral neck, specifically when the lymph node has not reached size criteria by CT/MRI (Figure 4). ¹⁸FDG-PET is also very helpful in detecting involved lymph nodes in the lower neck in which CT visualization is hindered by complex muscular and vascular structures (Figure 5). Thus, additional highly suspicious nodes could be included in the high-dose dose field with the addition of ¹⁸FDG-PET.

Finally, well-lateralized tonsil cancer is often treated to the ipsilateral side to reduce toxicities. However, before subjecting the patient to ipsilateral radiation, it is prudent to rule out any contralateral suspicious nodes. Because of the highly sensitivity of ¹⁸FDG-PET to detect metastatic lymph nodes, it should be the best modality in selecting patients for this treatment (Figure 6).

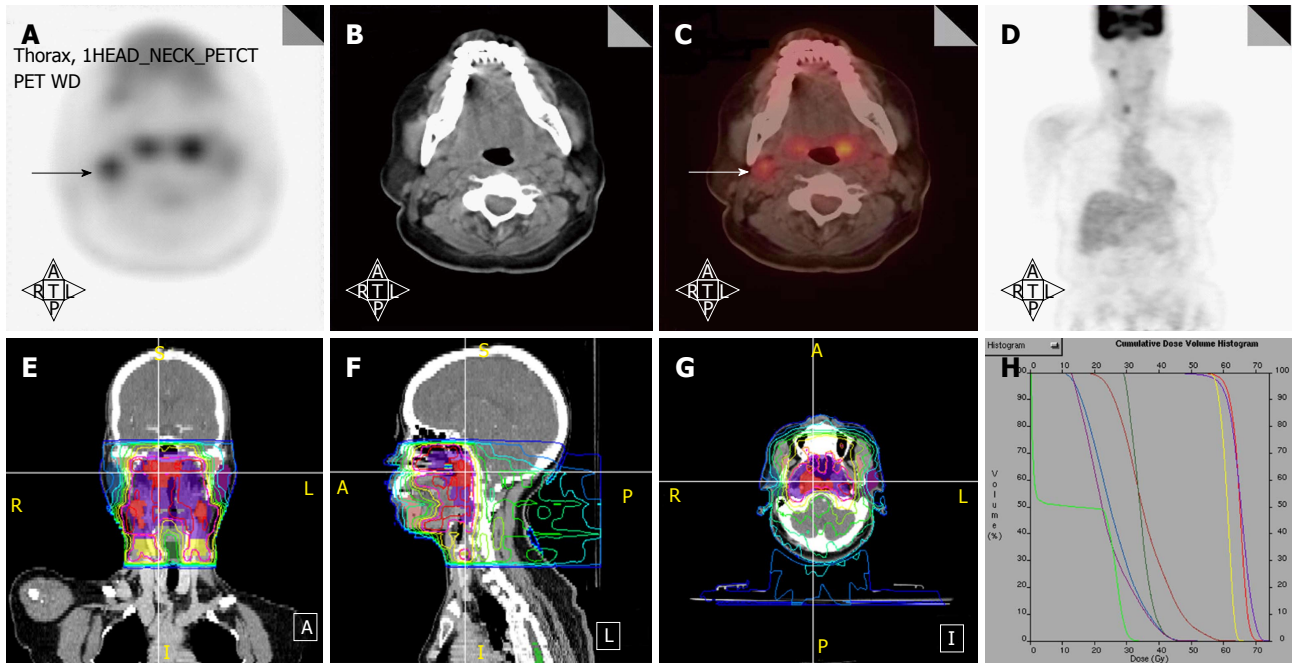


Figure 3 Positron emission tomography/computed tomography upstages a T1 nasopharyngeal cancer patient from N0 to N1. A-D: PET/CT images reveal that in addition to the T1 nasopharyngeal primary, there is increased FDG uptake in a level II node which was 1.0 cm in size (arrows). FNA of this node confirmed metastatic carcinoma. Thus, the patient was upstaged as T1N1 and treated with concurrent chemotherapy with IMRT; E-H: The IMRT plan for this patient treated the right level II node to a dose of 70 Gy. IMRT: Intensity modulated radiation therapy; PET/CT: Positron emission tomography/computed tomography; FDG: Fluorodeoxyglucose.

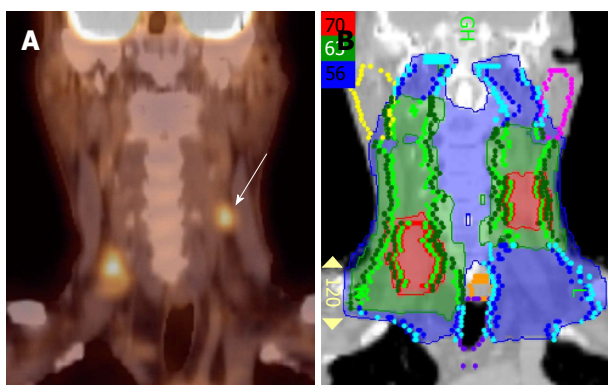


Figure 4 Positron emission tomography/computed tomography extends the high dose CTV contralaterally in a patient with a T2N2B base of tongue cancer. A: PET/CT reveals a contralateral level III node (white arrow), and thus, the patient was upstaged as T2N2C; B: An IMRT plan of this patient showing that this node was treated to 70 Gy and contralateral levels II and III were treated to 63 Gy. IMRT: Intensity modulated radiation therapy; PET/CT: Positron emission tomography/computed tomography.

UNKNOWN PRIMARY OF THE HEAD AND NECK

Between 2% and 9% of patients with HNC present with an enlarged cervical node without a definitive site of origin of the primary tumor by clinical examination and routine imaging studies^[17]. This entity is called HNC of unknown primary (HNCUP). As most HNCUPs are SCCs^[18], patients presenting with this entity undergo an examination under anesthesia (EUA) of the mucosal surface of the upper aerodigestive tract as well as

directed biopsies of the nasopharynx and oropharynx if no suspicious lesion is noted during EUA. Additionally, ipsilateral or bilateral tonsillectomies may be performed for diagnostic purposes. Approximately 50% of primaries are detected in this manner^[19].

PET/CT has been shown to be valuable in the work up and in identifying the primary tumor in patients with unknown primary. A systematic review of 16 studies of 302 patients by Rusthoven *et al.*^[20] validated the benefit of ¹⁸FDG-PET in HNCUP. The sensitivity, specificity and accuracy of ¹⁸FDG-PET in detecting unknown primary tumors were 88.3%, 74.9% and 78.8%. Additionally, ¹⁸FDG-PET detected 24.5% of primary tumors not apparent after traditional workup. The authors also noted that ¹⁸FDG-PET has a similar benefit in detecting additional occult nodal disease and metastases in the HNCUP population with a 15.9% and 11.2% detection rate, respectively.

In a prospective study, 20 patients with HNCUP underwent conventional workup prior to EUA^[21]. PET/CT was performed, and the surgeons performing EUA were blinded to the PET results. EUAs and traditional random biopsies were performed prior to the surgeon viewing the PET/CT. After EUA and biopsies, the surgeon was shown the PET/CT intraoperatively and further biopsies were obtained according to the ¹⁸FDG-PET results. PET/CT increased the detection of the primary site from 25% to 55%. This suggests that PET/CT directed biopsy is superior to traditional random biopsy in detecting a primary tumor.

Radiation treatment is the main treatment modality in HNCUP, but radiation volumes vary drastically

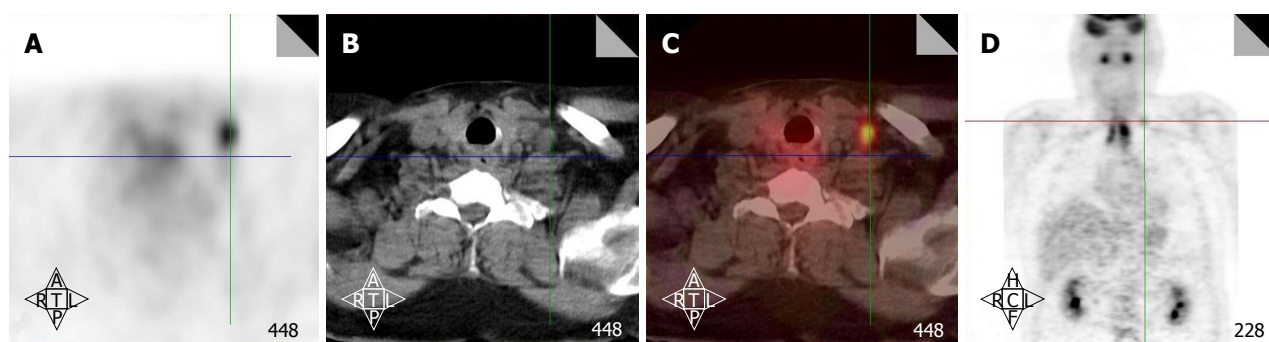


Figure 5 Positron emission tomography/computed tomography detects a low neck lymph node involved by metastasis. Increased FDG uptake in the low neck reveals a metastatic lymph node which would otherwise be difficult to detect because of the presence of muscular and vascular structures in this region of the neck (A-D). FDG: Fluorodeoxyglucose.

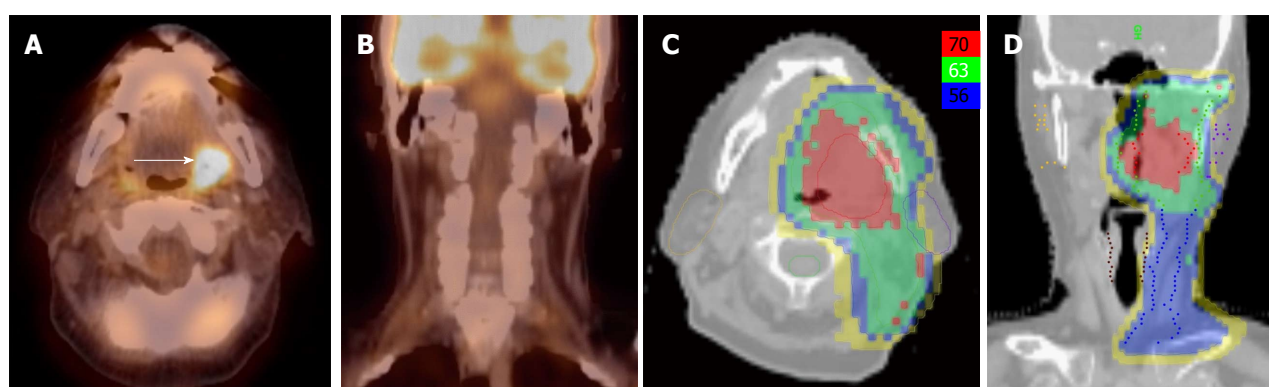


Figure 6 Positron emission tomography/computed tomography allows for unilateral tonsil cancer treatment in a patient with a T2N0 left tonsil cancer. A, B: PET/CT shows no evidence of lymph node metastasis in the contralateral (right) neck; C, D: An IMRT plan of the radiation treatment plan showing effective contralateral sparing. IMRT: Intensity modulated radiation therapy; PET/CT: Positron emission tomography/computed tomography.

between institutions and no standard has been defined. Radiation treatment may be directed to either the ipsilateral involved neck or to the bilateral neck, and may include pan-mucosal irradiation to areas that may harbor a microscopic primary tumor including the nasopharynx, oropharynx, larynx, and hypopharynx. Identifying the primary tumor is therefore critical and may allow tailoring the radiation volume according to the primary disease, thus avoiding high dose radiation to unnecessary areas and reducing toxicities of the treatment.

Figure 7 illustrates a patient who presented with multiple left neck nodes with FNA confirming SCC. Conventional workup including EUA and traditional biopsies failed to identify the primary tumor. PET/CT showed a hypermetabolic focus in the left base of tongue corresponding to the primary tumor. This patient was treated as a base of tongue cancer and thus other mucosal areas including the larynx and hypopharynx were spared from high dose radiation.

ACCOUNTING FOR DENTAL ARTIFACTS

Artifact from amalgam-based fillings and other dental procedures may significantly distort and hinder CT-based target delineation for primary tumors in HNCs.

Though artifact reduction techniques exist and have been used to improve the quality of CT-based target delineation and radiation treatment planning, many facilities may not have access to software to reduce dental artifacts on head and neck treatment planning CTs^[22].

CT-based attenuation correction is used to improve spatial resolution from PET imaging. Gamma rays produced after positron emission are affected by tissue heterogeneity, and utilizing CT data in addition to raw PET data improves spatial and quantitative accuracy of PET imaging^[23]. Multiple authors have addressed the issue of attenuation correction in the context of metallic dental artifact. A study by Kamel *et al*^[24] compared CT-based attenuation correction with Ge-68 PET-based attenuation correction in patients with metallic artifact and demonstrated quantitative value differences in regions of dental artifact raising the question of the impact of dental artifact on CT-based attenuation correction. Goerres *et al*^[25] confirmed that ¹⁸FDG-PET artifacts are indeed generated adjacent to dental artifact using CT-based correction using a similar methodology of Ge-68 PET-based attenuation correction. However, they also found that these artifacts demonstrated significantly lower ¹⁸FDG-uptake when compared to primary tumor, mitigating the clinical significance of these artifacts in

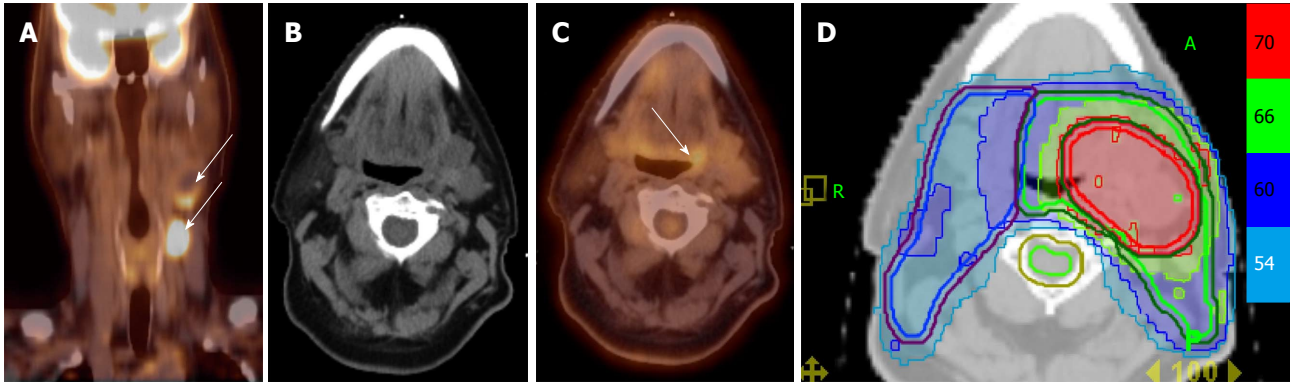


Figure 7 Positron emission tomography/computed tomography allows for detection for occult primary in a patient with multiple involved left neck nodes. A: PET/CT showing the initial presentation with multiple enlarged left neck nodes (white arrows); B: A conventional CT scan does not reveal a source of primary cancer; C: PET/CT demonstrated increased FDG uptake in the left base of tongue (white arrow) and a directed biopsy of this area revealed this as the primary site; D: IMRT treatment plan for this patient showing that the left base of tongue was included in the high-dose (70 Gy) volume while sparing uninvolved mucosal areas. IMRT: Intensity modulated radiation therapy; PET/CT: Positron emission tomography/computed tomography.

target delineation. Others have also demonstrated that irrespective of artifact reduction techniques, CT-based PET attenuation correction is robust as metallic artifacts do not propagate into the attenuation correction using CT imaging in HNC patients^[26].

As ¹⁸FDG-PET resolution is not significantly modified by dental artifact, it is practical to use ¹⁸FDG-PET to improve target delineation in this context. A study out of Korea compared tumor staging between CT alone, MRI alone, and PET/CT in 37 patients with dental artifact on CT and MRI^[27]. PET/CT had improved staging regardless of the presence of dental artifact, and had better specificity in ruling out involvement of the sublingual gland and floor of mouth. Comparing MRI-delineated primary tumor volume and PET-delineated primary tumor volume using an SUV cutoff of 2.5 with post-operative pathologic samples, demonstrated that MRI inferiorly predicted pathologic tumor size relative to PET/CT with an SUV cutoff of 2.5. Thus, PET/CT improved target definition in patients with dental artifact. A previous study also investigated the utility of PET/CT scans in oral cavity cancers comparing 69 patients with dental artifacts and 40 patients without such artifacts^[28]. The PET/CT scans detected more tumors as compared to CT scans (95% vs 75%). A regression equation was developed equating the pathologic volume of the tumors with the PET volume as defined by a SUV = 3.5.

Recently more algorithms have been developed to use PET/CT imaging in combination with MRI images to reduce the impact of the dental artifacts^[29-31].

UTILITY IN HIGH-RISK PORT

PORT for HNC can improve locoregional control and overall survival in patients with adverse pathologic features, including positive or close margins, extracapsular extension, perineural invasion, lymphovascular invasion, advanced tumor stage (T4), and advanced nodal stage (N2B or higher). Indications for PORT were validated in work by Peters *et al*^[32] and further stratified

by Ang *et al*^[33] at the MD Anderson Cancer Center. Randomized clinical trials from the Radiation Therapy Oncology Group and the European Organization for Research and Treatment of Cancer have shown that concurrent chemotherapy and radiation is significantly better than radiation alone in patients with high risk pathologic features; particularly those with extracapsular nodal extension or positive surgical margins. This was further validated by a pooled analysis of individual patient data from both trials^[34-36]. PORT should include the entire postoperative area to a dose between 57.6 and 60 Gy in 30 to 33 fractions. High-risk areas including areas of close or positive post-operative margins or extracapsular nodal extension may also benefit from radiation dose escalation in addition to the radio-sensitizing effect of concurrent chemotherapy^[37]. Radiation treatment to these high-risk areas is often escalated to 66 Gy.

Defining the radiation treatment targets is very challenging in the post-operative setting due to the anatomical changes after surgical resection and reconstruction especially in patients who have free flap reconstruction. Information including pre-operative imaging, pre-operative physical examination or endoscopy, surgical and pathologic findings, and post-operative imaging should be incorporated in target delineation in PORT and often requires a multidisciplinary approach with coordination between radiation oncologists, surgeons, radiologists, and pathologists. For patients who have pre-operative ¹⁸FDG-PET scans, registration of these PET images to postoperative simulation CT images can help to define the tumor beds which are often the high risk areas. Pre-operative PET/CT may be registered to the simulation CT using either rigid or deformable algorithms to provide guidance in assessing areas of high risk of recurrence^[38]. Through image registration, the radiation oncologist is able to directly correlate the pre-treatment disease volumes to the post-operative CT imaging, and delineate high-risk areas to be included in the high radiation dose field.

PORT is often delivered 4 to 6 wk after surgery when

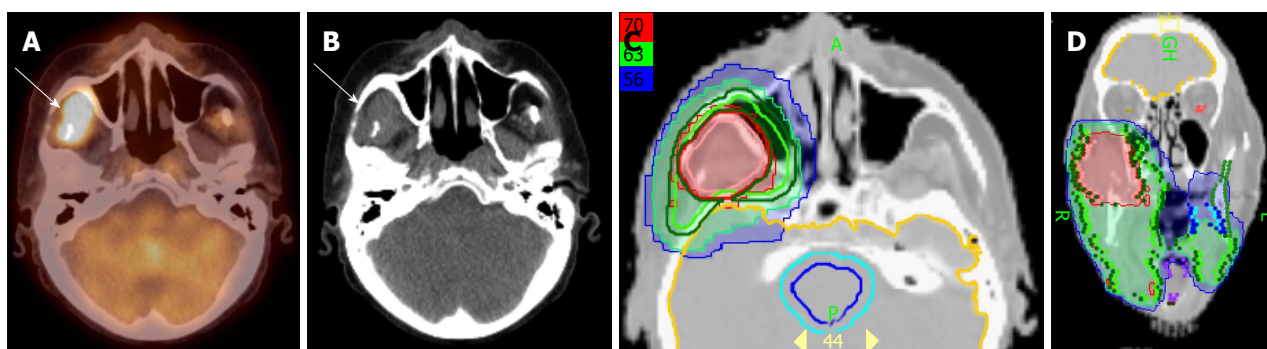


Figure 8 Positron emission tomography/computed tomography demonstrates tumor recurrence in a patient with a resected T4aN2b right buccal mucosa cancer prior to postoperative radiation. A-B: PET-CT obtained 50 d after surgery before postoperative radiation shows recurrent tumor (white arrow) in the infratemporal fossa; C-D: An IMRT treatment plan for this patient showing the recurrent tumor treated to a definitive radiation dose of 70 Gy rather than a typical postoperative radiation dose of 60 Gy. IMRT: Intensity modulated radiation therapy; PET/CT: Positron emission tomography/computed tomography.

the surgical wound is fully healed. Unfortunately, some patients with high-risk features may have recurrences even before starting PORT. Because of the anatomical distortion and fibrotic changes after surgery, and flap reconstruction, these recurrences are difficult to detect by physical examination and CT imaging. ^{18}F FDG-PET is an ideal imaging modality in this setting. Shintani *et al.*^[39] examined the utility of early post-operative pre-radiation PET/CT in HNCs. Among a cohort of 91 HNC patients, post-operative pre-radiation PET/CT performed at a median time of 28 d after surgery led to the discovery of 27 patients with suspicious findings on PET/CT. Of these, 24 patients (29% of the total cohort) underwent biopsy of these sites, with 11 biopsies positive for cancer. Treatment was changed in 14 patients (15.4%) with the addition of post-operative PET/CT: 4 underwent palliative care only, 6 had treatment to an extended volume, 1 received treatment to a higher dose, 2 underwent additional surgery and 2 received concurrent chemotherapy. Liao *et al.*^[40] also reported 29 patients who had a ^{18}F FDG-PET scan obtained before PORT. They found 7 patients with positive PET studies, 3 with distant metastases and 4 with local regional recurrences. For those who had locoregional disease detected by ^{18}F FDG-PET, the radiation volumes and radiation dose have to be changed, with higher doses delivered to the recurrent tumor. Thus, for patients with high-risk features or for those who have a prolonged interval from surgery to radiation, a post-surgery and pre-radiation ^{18}F FDG-PET will be valuable in treatment decision and radiation treatment planning.

Figure 8 illustrates a patient with initial stage T4AN2B right buccal mucosal cancer. He had surgery and radial forearm flap reconstruction. Due to the patient's non-compliance, he did not have radiation treatment planning until 50 d after surgery. A PET/CT was obtained at simulation that revealed tumor recurrence in the right masticator space and right infratemporal fossa region (Figure 8A and B). The recurrent tumor was not resectable and thus this was treated to 70 Gy rather than a traditional post-operative dose of 60 Gy. Figure 8C and D represents the IMRT plan for this

patient.

Both pre-operative and post-radiation PET/CT may also assist in predicting the likelihood of disease-free survival and locoregional recurrence after PORT. Kim *et al.*^[41] correlated multiple PET/CT derived imaging factors with areas of high likelihood of recurrence. Examining 100 patients with both pre-operative and post-operative post-radiation PET/CT, the authors found that a metabolic tumor volume defined as a pre-operative autosegmentation of SUV > 2.5 of more than 41 cc predicted for poorer disease-free survival. Additionally, post-radiation treatment SUV_{max} predicted for areas of locoregional recurrence. The authors suggested a post-treatment cutoff SUV value of 5.38 yielding a 93.7% NPV and a 66.7% positive predictive value. This may be used to select patients after postoperative radiation for further treatment interventions.

FUTURE DIRECTIONS

In addition to the routinely clinically available ^{18}F FDG substrate, many newer radioisotopes and radiotracers are being developed to image further functional characteristics of tumors including hypoxia, tumor proliferation, amino acid metabolism and presence of EGFR on tumor cells^[42]. Hypoxia is commonly noted in head and neck tumors including in the primary site and metastatic lymph nodes. This is commonly seen in HPV-positive cancers; tumors which often present with small primaries and large necrotic and hypoxic neck nodes. Identification of these hypoxic areas may allow for radiation dose escalation to hypoxic sub-regions of tumors. Hypoxia poses a major radiobiologic disadvantage and confers radioresistance to the tumor. Hypoxic cells are not killed in response to radiation therapy and may be responsible for treatment failure, either locally or as distant metastasis. A commonly used dose-prescription and dose-delivery technique is the "simultaneous integrated boost" method in which doses of 70 Gy are delivered to areas of gross disease while areas of intermediate-risk and low-risk of involvement by disease simultaneously receive 59.4 Gy to 63 Gy

and 56 Gy, respectively. Using the same technique it may be possible to further escalate the dose to the radio-resistant hypoxic regions in the same number of fractions while still meeting the dose constraints for surrounding normal tissue. Examples of radiopharmaceuticals being used to image the hypoxic portion of the tumor include ^{18}F -fluoromisonidazole, copper-diacetyl-bis (N4-methylthiosamincarbazone) (Cu-ATSM) and ^{18}F -fluoroazomycin arabinoside. The use of these agents has been described in literature^[43,44]. Another interesting possibility is the use of 3'-deoxy-3'-[^{18}F]-fluorothymidine, a PET tracer to noninvasively image tumor cell proliferation, and deliver higher doses to areas of the tumor showing higher degree of tumor growth^[45,46].

In addition to these newer substrates, there has also been an evolution in the imaging modalities with the development of simultaneous PET/MR imagers. These offer the advantages of high-quality soft tissue imaging from MR with whole-body and functional imaging from the PET component^[47-49]. The use of PET/MR in HNC patients has been recently described^[50,51].

Finally, improved acquisition technologies including time-of-flight PET (TOF-PET) and four-dimensional PET (4D-PET) are emerging. TOF-PET improves the signal-to-noise ratio in acquisition as well as reduces scanning time leading to improved image resolution^[52]. This may further improve the benefit of PET in target delineation of HNCs by reducing PET-GTVs. 4D-PET has primarily found clinical utility in lung cancers^[53], an entity in which tumor motion is more prominent than in HNCs. Though small relative to lung motion, organ motion does exist in the head and neck and an improvement in resolution and target delineation in HNCs by reducing artifacts may be expected with 4D-PET.

CONCLUSION

The widespread availability of PET imagers and clinical experience has increased considerably in the recent years. Although methodologies of how to use PET information with either ^{18}F FDG or new substrates in radiation therapy planning for HNCs are still under development, PET scans have changed our daily practice in management of these patients. Integrating tumor biology obtained from these images with advanced delivery techniques using IMRT and image-guided radiation therapy has the potential to significantly impact outcomes in HNCs.

REFERENCES

- 1 **Parkin DM**, Bray F, Ferlay J, Pisani P. Global cancer statistics, 2002. *CA Cancer J Clin* 2002; **55**: 74-108 [PMID: 15761078 DOI: 10.3322/canjclin.55.2.74]
- 2 **Ciernik IF**, Dizendorf E, Baumert BG, Reiner B, Burger C, Davis JB, Lütolf UM, Steinert HC, Von Schulthess GK. Radiation treatment planning with an integrated positron emission and computer tomography (PET/CT): a feasibility study. *Int J Radiat Oncol Biol Phys* 2003; **57**: 853-863 [PMID: 14529793 DOI: 10.1016/S0360-3016(03)00346-8]

- 3 **Heron DE**, Andrade RS, Flickinger J, Johnson J, Agarwala SS, Wu A, Kalnicki S, Avril N. Hybrid PET-CT simulation for radiation treatment planning in head-and-neck cancers: a brief technical report. *Int J Radiat Oncol Biol Phys* 2004; **60**: 1419-1424 [PMID: 15590173 DOI: 10.1016/j.ijrobp.2004.05.037]
- 4 **Guido A**, Fuccio L, Rombi B, Castellucci P, Cecconi A, Bunkheila F, Fuccio C, Spezi E, Angelini AL, Barbieri E. Combined 18F-FDG-PET/CT imaging in radiotherapy target delineation for head-and-neck cancer. *Int J Radiat Oncol Biol Phys* 2009; **73**: 759-763 [PMID: 18834671 DOI: 10.1016/j.ijrobp.2008.04.059]
- 5 **Paulino AC**, Koshy M, Howell R, Schuster D, Davis LW. Comparison of CT- and FDG-PET-defined gross tumor volume in intensity-modulated radiotherapy for head-and-neck cancer. *Int J Radiat Oncol Biol Phys* 2005; **61**: 1385-1392 [PMID: 15817341 DOI: 10.1016/j.ijrobp.2004.08.037]
- 6 **Breen SL**, Publicover J, De Silva S, Pond G, Brock K, O'Sullivan B, Cummings B, Dawson L, Keller A, Kim J, Ringash J, Yu E, Hendler A, Waldron J. Intraobserver and interobserver variability in GTV delineation on FDG-PET-CT images of head and neck cancers. *Int J Radiat Oncol Biol Phys* 2007; **68**: 763-770 [PMID: 17379435 DOI: 10.1016/j.ijrobp.2006.12.039]
- 7 **Anderson CM**, Sun W, Buatti JM, Maley JE, Policeni B, Mott SL, Bayouth JE. Interobserver and intermodality variability in GTV delineation on simulation CT, FDG-PET, and MR Images of Head and Neck Cancer. *Jacobs J Radiat Oncol* 2014; **1**: 006 [PMID: 25568889]
- 8 **Schinagl DA**, Vogel WV, Hoffmann AL, van Dalen JA, Oyen WJ, Kaanders JH. Comparison of five segmentation tools for 18F-fluoro-deoxy-glucose-positron emission tomography-based target volume definition in head and neck cancer. *Int J Radiat Oncol Biol Phys* 2007; **69**: 1282-1289 [PMID: 17967318 DOI: 10.1016/j.ijrobp.2007.07.2333]
- 9 **Schinagl DA**, Hoffmann AL, Vogel WV, van Dalen JA, Verstappen SM, Oyen WJ, Kaanders JH. Can FDG-PET assist in radiotherapy target volume definition of metastatic lymph nodes in head-and-neck cancer? *Radiother Oncol* 2009; **91**: 95-100 [PMID: 19285354 DOI: 10.1016/j.radonc.2009.02.007]
- 10 **Perez-Romasanta LA**, Bellon-Guardia M, Torres-Donaire J, Lozano-Martin E, Sanz-Martin M, Velasco-Jimenez J. Tumor volume delineation in head and neck cancer with 18-fluor-fluoro-deoxyglucose positron emission tomography: adaptive thresholding method applied to primary tumors and metastatic lymph nodes. *Clin Transl Oncol* 2013; **15**: 283-293 [PMID: 22865325 DOI: 10.1007/s12094-012-0914-z]
- 11 **Daisne JF**, Sibomana M, Bol A, Cosnard G, Lonnet M, Grégoire V. Evaluation of a multimodality image (CT, MRI and PET) coregistration procedure on phantom and head and neck cancer patients: accuracy, reproducibility and consistency. *Radiother Oncol* 2003; **69**: 237-245 [PMID: 14644482 DOI: 10.1016/j.radonc.2003.10.009]
- 12 **Schinagl DA**, Span PN, van den Hoogen FJ, Merckx MA, Slootweg PJ, Oyen WJ, Kaanders JH. Pathology-based validation of FDG PET segmentation tools for volume assessment of lymph node metastases from head and neck cancer. *Eur J Nucl Med Mol Imaging* 2013; **40**: 1828-1835 [PMID: 23942906 DOI: 10.1007/s00259-013-2513-9]
- 13 **Som PM**. Detection of metastasis in cervical lymph nodes: CT and MR criteria and differential diagnosis. *AJR Am J Roentgenol* 1992; **158**: 961-969 [PMID: 1566697 DOI: 10.2214/ajr.158.5.1566697]
- 14 **Adams S**, Baum RP, Stuckensen T, Bitter K, Hör G. Prospective comparison of 18F-FDG PET with conventional imaging modalities (CT, MRI, US) in lymph node staging of head and neck cancer. *Eur J Nucl Med* 1998; **25**: 1255-1260 [PMID: 9724374 DOI: 10.1007/s002590050293]
- 15 **Koshy M**, Paulino AC, Howell R, Schuster D, Halkar R, Davis LW. F-18 FDG PET-CT fusion in radiotherapy treatment planning for head and neck cancer. *Head Neck* 2005; **27**: 494-502 [PMID: 15772951 DOI: 10.1002/hed.20179]
- 16 **Schwartz DL**, Ford EC, Rajendran J, Yueh B, Coltrera MD, Virgin J, Anzai Y, Haynor D, Lewellen B, Mattes D, Kinahan P, Meyer J,

- Phillips M, Leblanc M, Krohn K, Eary J, Laramore GE. FDG-PET/CT-guided intensity modulated head and neck radiotherapy: a pilot investigation. *Head Neck* 2005; **27**: 478-487 [PMID: 15772953 DOI: 10.1002/hed.20177]
- 17 Jereczek-Fossa BA, Jassem J, Orecchia R. Cervical lymph node metastases of squamous cell carcinoma from an unknown primary. *Cancer Treat Rev* 2004; **30**: 153-164 [PMID: 15023433 DOI: 10.1016/j.ctrv.2003.10.001]
- 18 Grau C, Johansen LV, Jakobsen J, Geertsen P, Andersen E, Jensen BB. Cervical lymph node metastases from unknown primary tumours. Results from a national survey by the Danish Society for Head and Neck Oncology. *Radiother Oncol* 2000; **55**: 121-129 [PMID: 10799723 DOI: 10.1016/S0167-8140(00)00172-9]
- 19 Lee DJ, Rostock RA, Harris A, Kashima H, Johns M. Clinical evaluation of patients with metastatic squamous carcinoma of the neck with occult primary tumor. *South Med J* 1986; **79**: 979-983 [PMID: 3738594]
- 20 Rusthoven KE, Koshy M, Paulino AC. The role of fluorodeoxyglucose positron emission tomography in cervical lymph node metastases from an unknown primary tumor. *Cancer* 2004; **101**: 2641-2649 [PMID: 15517576 DOI: 10.1002/cncr.20687]
- 21 Rudmik L, Lau HY, Matthews TW, Bosch JD, Kloiber R, Molnar CP, Dort JC. Clinical utility of PET/CT in the evaluation of head and neck squamous cell carcinoma with an unknown primary: a prospective clinical trial. *Head Neck* 2011; **33**: 935-940 [PMID: 21674668 DOI: 10.1002/hed.21566]
- 22 Li H, Noel C, Chen H, Harold Li H, Low D, Moore K, Klahr P, Michalski J, Gay HA, Thorstad W, Mutic S. Clinical evaluation of a commercial orthopedic metal artifact reduction tool for CT simulations in radiation therapy. *Med Phys* 2012; **39**: 7507-7517 [PMID: 23231300 DOI: 10.1118/1.4762814]
- 23 Kinahan PE, Townsend DW, Beyer T, Sashin D. Attenuation correction for a combined 3D PET/CT scanner. *Med Phys* 1998; **25**: 2046-2053 [PMID: 9800714 DOI: 10.1118/1.598392]
- 24 Kamel EM, Burger C, Buck A, von Schulthess GK, Goerres GW. Impact of metallic dental implants on CT-based attenuation correction in a combined PET/CT scanner. *Eur Radiol* 2003; **13**: 724-728 [PMID: 12664109 DOI: 10.1007/s00330-002-1564-2]
- 25 Goerres GW, Schmid DT, Eyrych GK. Do hardware artefacts influence the performance of head and neck PET scans in patients with oral cavity squamous cell cancer? *Dentomaxillofac Radiol* 2003; **32**: 365-371 [PMID: 15070838 DOI: 10.1259/dmfr/77741718]
- 26 Nahmias C, Lemmens C, Paul D, Carlson E, Long M, Blodgett T, Nuyts J, Townsend D. Does reducing CT artifacts from dental implants influence the PET interpretation in PET/CT studies of oral cancer and head and neck cancer? *J Nucl Med* 2008; **49**: 1047-1052 [PMID: 18552154 DOI: 10.2967/jnumed.107.049858]
- 27 Hong HR, Jin S, Koo HJ, Roh JL, Kim JS, Cho KJ, Choi SH, Nam SY, Kim SY. Clinical values of (18) F-FDG PET/CT in oral cavity cancer with dental artifacts on CT or MRI. *J Surg Oncol* 2014; **110**: 696-701 [PMID: 24995957 DOI: 10.1002/jso.23691]
- 28 Baek CH, Chung MK, Son YI, Choi JY, Kim HJ, Yim YJ, Ko YH, Choi J, Cho JK, Jeong HS. Tumor volume assessment by 18F-FDG PET/CT in patients with oral cavity cancer with dental artifacts on CT or MR images. *J Nucl Med* 2008; **49**: 1422-1428 [PMID: 18703597 DOI: 10.2967/jnumed.108.051649]
- 29 Buchbender C, Hartung-Knemeyer V, Forsting M, Antoch G, Heusner TA. Positron emission tomography (PET) attenuation correction artefacts in PET/CT and PET/MRI. *Br J Radiol* 2013; **86**: 20120570 [PMID: 23580397 DOI: 10.1259/bjr.20120570]
- 30 Delso G, Wollenweber S, Lonn A, Wiesinger F, Veit-Haibach P. MR-driven metal artifact reduction in PET/CT. *Phys Med Biol* 2013; **58**: 2267-2280 [PMID: 23478566 DOI: 10.1088/0031-9155/58/7/2267]
- 31 Burger IA, Wurnig MC, Becker AS, Kenkel D, Delso G, Veit-Haibach P, Boss A. Hybrid PET/MR imaging: an algorithm to reduce metal artifacts from dental implants in Dixon-based attenuation map generation using a multiaquisition variable-resonance image combination sequence. *J Nucl Med* 2015; **56**: 93-97 [PMID: 25500830 DOI: 10.2967/jnumed.114.145862]
- 32 Peters LJ, Goepfert H, Ang KK, Byers RM, Maor MH, Guillaumondegui O, Morrison WH, Weber RS, Garden AS, Frankenthaler RA. Evaluation of the dose for postoperative radiation therapy of head and neck cancer: first report of a prospective randomized trial. *Int J Radiat Oncol Biol Phys* 1993; **26**: 3-11 [PMID: 8482629 DOI: 10.1016/0360-3016(93)90167-T]
- 33 Ang KK, Trotti A, Brown BW, Garden AS, Foote RL, Morrison WH, Geara FB, Klotch DW, Goepfert H, Peters LJ. Randomized trial addressing risk features and time factors of surgery plus radiotherapy in advanced head-and-neck cancer. *Int J Radiat Oncol Biol Phys* 2001; **51**: 571-578 [PMID: 11597795 DOI: 10.1016/S0360-3016(01)01690-X]
- 34 Bernier J, Dommene C, Ozsahin M, Matuszewska K, Lefebvre JL, Greiner RH, Giralt J, Maingon P, Rolland F, Bolla M, Cognetti F, Bourhis J, Kirkpatrick A, van Glabbeke M. Postoperative irradiation with or without concomitant chemotherapy for locally advanced head and neck cancer. *N Engl J Med* 2004; **350**: 1945-1952 [PMID: 15128894 DOI: 10.1056/NEJMoa032641]
- 35 Cooper JS, Pajak TF, Forastiere AA, Jacobs J, Campbell BH, Saxman SB, Kish JA, Kim HE, Cmelak AJ, Rotman M, Machtay M, Ensley JF, Chao KS, Schultz CJ, Lee N, Fu KK. Postoperative concurrent radiotherapy and chemotherapy for high-risk squamous-cell carcinoma of the head and neck. *N Engl J Med* 2004; **350**: 1937-1944 [PMID: 15128893 DOI: 10.1056/NEJMoa032646]
- 36 Bernier J, Cooper JS, Pajak TF, van Glabbeke M, Bourhis J, Forastiere A, Ozsahin EM, Jacobs JR, Jassem J, Ang KK, Lefebvre JL. Defining risk levels in locally advanced head and neck cancers: a comparative analysis of concurrent postoperative radiation plus chemotherapy trials of the EORTC (#22931) and RTOG (# 9501). *Head Neck* 2005; **27**: 843-850 [PMID: 16161069 DOI: 10.1002/hed.20279]
- 37 Grégoire V, Eisbruch A, Hamoir M, Levendag P. Proposal for the delineation of the nodal CTV in the node-positive and the post-operative neck. *Radiother Oncol* 2006; **79**: 15-20 [PMID: 16616387 DOI: 10.1016/j.radonc.2006.03.009]
- 38 Kovalchuk N, Jalisi S, Subramaniam RM, Truong MT. Deformable registration of preoperative PET/CT with postoperative radiation therapy planning CT in head and neck cancer. *Radiographics* 2012; **32**: 1329-1341 [PMID: 22977021 DOI: 10.1148/rg.325125008]
- 39 Shintani SA, Foote RL, Lowe VJ, Brown PD, Garces YI, Kasperbauer JL. Utility of PET/CT imaging performed early after surgical resection in the adjuvant treatment planning for head and neck cancer. *Int J Radiat Oncol Biol Phys* 2008; **70**: 322-329 [PMID: 17889447 DOI: 10.1016/j.ijrobp.2007.06.038]
- 40 Liao CT, Fan KH, Lin CY, Wang HM, Huang SF, Chen IH, Kang CJ, Ng SH, Hsueh C, Lee LY, Lin CH, Yen TC. Impact of a second FDG PET scan before adjuvant therapy for the early detection of residual/relapsing tumours in high-risk patients with oral cavity cancer and pathological extracapsular spread. *Eur J Nucl Med Mol Imaging* 2012; **39**: 944-955 [PMID: 22434050 DOI: 10.1007/s00259-012-2103-2]
- 41 Kim G, Kim YS, Han EJ, Yoo IeR, Song JH, Lee SN, Lee JH, Choi BO, Jang HS, Yoon SC. FDG-PET/CT as prognostic factor and surveillance tool for postoperative radiation recurrence in locally advanced head and neck cancer. *Radiat Oncol J* 2011; **29**: 243-251 [PMID: 22984677 DOI: 10.3857/roj.2011.29.4.243]
- 42 Wang TJC, Menda Y, Cheng SK, Wu CC, Lee NY. New Tracers PET in head and neck squamous cell carcinoma. *PET Clin* 2012; **7**: 431-441 [DOI: 10.1016/j.cpet.2012.06.009]
- 43 Chao KS, Bosch WR, Mutic S, Lewis JS, Dehdashti F, Mintun MA, Dempsey JF, Perez CA, Purdy JA, Welch MJ. A novel approach to overcome hypoxic tumor resistance: Cu-ATSM-guided intensity-modulated radiation therapy. *Int J Radiat Oncol Biol Phys* 2001; **49**: 1171-1182 [PMID: 11240261 DOI: 10.1016/S0360-3016(00)01433-4]
- 44 Servagi-Vernat S, Differding S, Hanin FX, Labar D, Bol A, Lee JA, Grégoire V. A prospective clinical study of ¹⁸F-FAZA PET-CT hypoxia imaging in head and neck squamous cell carcinoma before and during radiation therapy. *Eur J Nucl Med Mol Imaging* 2014; **41**: 1544-1552 [PMID: 24570097 DOI: 10.1007/s00259-014-

- 2730-x]
- 45 **Arens AI**, Troost EG, Hoeben BA, Grootjans W, Lee JA, Grégoire V, Hatt M, Visvikis D, Bussink J, Oyen WJ, Kaanders JH, Visser EP. Semiautomatic methods for segmentation of the proliferative tumour volume on sequential FLT PET/CT images in head and neck carcinomas and their relation to clinical outcome. *Eur J Nucl Med Mol Imaging* 2014; **41**: 915-924 [PMID: 24346414 DOI: 10.1007/s00259-013-2651-0]
 - 46 **Troost EG**, Bussink J, Hoffmann AL, Boerman OC, Oyen WJ, Kaanders JH. 18F-FLT PET/CT for early response monitoring and dose escalation in oropharyngeal tumors. *J Nucl Med* 2010; **51**: 866-874 [PMID: 20484426 DOI: 10.2967/jnumed.109.069310]
 - 47 **Berker Y**, Franke J, Salomon A, Palmowski M, Donker HC, Temur Y, Mottaghy FM, Kuhl C, Izquierdo-Garcia D, Fayad ZA, Kiessling F, Schulz V. MRI-based attenuation correction for hybrid PET/MRI systems: a 4-class tissue segmentation technique using a combined ultrashort-echo-time/Dixon MRI sequence. *J Nucl Med* 2012; **53**: 796-804 [PMID: 22505568 DOI: 10.2967/jnumed.111.092577]
 - 48 **Drzezga A**, Souvatzoglou M, Eiber M, Beer AJ, Fürst S, Martinez-Möller A, Nekolla SG, Ziegler S, Ganter C, Rummeny EJ, Schwaiger M. First clinical experience with integrated whole-body PET/MR: comparison to PET/CT in patients with oncologic diagnoses. *J Nucl Med* 2012; **53**: 845-855 [PMID: 22534830 DOI: 10.2967/jnumed.111.098608]
 - 49 **Keereman V**, Fierens Y, Broux T, De Deene Y, Lonnew M, Vandenberghe S. MRI-based attenuation correction for PET/MRI using ultrashort echo time sequences. *J Nucl Med* 2010; **51**: 812-818 [PMID: 20439508 DOI: 10.2967/jnumed.109.065425]
 - 50 **Covello M**, Cavaliere C, Aiello M, Cianelli MS, Mesolella M, Iorio B, Rossi A, Nicolai E. Simultaneous PET/MR head-neck cancer imaging: Preliminary clinical experience and multiparametric evaluation. *Eur J Radiol* 2015; **84**: 1269-1276 [PMID: 25958189 DOI: 10.1016/j.ejrad.2015.04.010]
 - 51 **Queiroz MA**, Huellner MW. PET/MR in cancers of the head and neck. *Semin Nucl Med* 2015; **45**: 248-265 [PMID: 25841279 DOI: 10.1053/j.semnuclmed.2014.12.005]
 - 52 **Surti S**. Update on time-of-flight PET imaging. *J Nucl Med* 2015; **56**: 98-105 [PMID: 25525181 DOI: 10.2967/jnumed.114.145029]
 - 53 **Chirindel A**, Adebahr S, Schuster D, Schimek-Jasch T, Schanne DH, Nemer U, Mix M, Meyer P, Grosu AL, Brunner T, Nestle U. Impact of 4D-(18)FDG-PET/CT imaging on target volume delineation in SBRT patients with central versus peripheral lung tumors. Multi-reader comparative study. *Radiother Oncol* 2015; **115**: 335-341 [PMID: 26116339 DOI: 10.1016/j.radonc.2015.05.019]

P- Reviewer: Chang Z, Gao BL

S- Editor: Tian YL **L- Editor:** A **E- Editor:** Jiao XK



Case Control Study

Magnetic resonance imaging in assessment of stress urinary incontinence in women: Parameters differentiating urethral hypermobility and intrinsic sphincter deficiency

Katarzyna Jadwiga Macura, Richard Eugene Thompson, David Alan Bluemke, Rene Genadry

Katarzyna Jadwiga Macura, The Russell H. Morgan Department of Radiology and Radiological Science, Johns Hopkins University, Baltimore, MD 21287, United States

Richard Eugene Thompson, Johns Hopkins Biostatistics Center, Baltimore, MD 21205, United States

David Alan Bluemke, National Institutes of Health Clinical Center, Bethesda, MD 20892, United States

Rene Genadry, University of Iowa Hospitals and Clinics, Iowa City, IA 52242, United States

Author contributions: Macura KJ, Bluemke DA and Genadry R contributed to the design of the study, acquisition of data, and interpretation of data; Thompson RE performed statistical analysis of data; Macura KJ and Genadry R drafted the article; Macura KJ, Thompson RE, Bluemke DA and Genadry R made critical review of the content of the manuscript and approved the final version of the article.

Supported by The Radiological Society of North America and the Society of Computed Body Tomography and Magnetic Resonance.

Institutional review board statement: The study was approved by the Johns Hopkins University Institutional Review Board.

Informed consent statement: The study was compliant with the Health Insurance Portability and Accountability Act. Study-specific written consent was obtained from all subjects.

Conflict-of-interest statement: The authors declare no conflicts of interest regarding this manuscript.

Data sharing statement: Participants did not give informed consent for data sharing and no additional data are available.

Open-Access: This article is an open-access article which was selected by an in-house editor and fully peer-reviewed by external reviewers. It is distributed in accordance with the Creative Commons Attribution Non Commercial (CC BY-NC 4.0) license, which permits others to distribute, remix, adapt, build upon this

work non-commercially, and license their derivative works on different terms, provided the original work is properly cited and the use is non-commercial. See: <http://creativecommons.org/licenses/by-nc/4.0/>

Correspondence to: Katarzyna Jadwiga Macura, MD, PhD, Professor of Radiology, The Russell H. Morgan Department of Radiology and Radiological Science, Johns Hopkins University, 601 N. Caroline Street, JHOC 3140C, Baltimore, MD 21287, United States. kmacura@jhmi.edu
Telephone: +1-410-9555391
Fax: +1-410-9557699

Received: June 30, 2015
Peer-review started: July 5, 2015
First decision: July 31, 2015
Revised: August 22, 2015
Accepted: September 29, 2015
Article in press: September 30, 2015
Published online: November 28, 2015

Abstract

AIM: To define the magnetic resonance imaging (MRI) parameters differentiating urethral hypermobility (UH) and intrinsic sphincter deficiency (ISD) in women with stress urinary incontinence (SUI).

METHODS: The static and dynamic MR images of 21 patients with SUI were correlated to urodynamic (UD) findings and compared to those of 10 continent controls. For the assessment of the urethra and integrity of the urethral support structures, we applied the high-resolution endocavitary MRI, such as intraurethral MRI, endovaginal or endorectal MRI. For the functional imaging of the urethral support, we performed dynamic MRI with the pelvic phased array coil. We assessed the following MRI parameters in both the patient and the

volunteer groups: (1) urethral angle; (2) bladder neck descent; (3) status of the periurethral ligaments, (4) vaginal shape; (5) urethral sphincter integrity, length and muscle thickness at mid urethra; (6) bladder neck funneling; (7) status of the puborectalis muscle; (8) pubo-vaginal distance. UD parameters were assessed in the patient study group as follows: (1) urethral mobility angle on Q-tip test; (2) Valsalva leak point pressure (VLPP) measured at 250 cc bladder volume; and (3) maximum urethral closure pressure (MUCP). The UH type of SUI was defined with the Q-tip test angle over 30 degrees, and VLPP pressure over 60 cm H₂O. The ISD incontinence was defined with MUCP pressure below 20 cm H₂O, and VLPP pressure less or equal to 60 cm H₂O. We considered the associations between the MRI and clinical data and UDs using a variety of statistical tools to include linear regression, multivariate logistic regression and receiver operating characteristic (ROC) analysis. All statistical analyses were performed using STATA version 9.0 (StataCorp LP, College Station, TX).

RESULTS: In the incontinent group, 52% have history of vaginal delivery trauma as compared to none in control group ($P < 0.001$). There was no difference between the continent volunteers and incontinent patients in body habitus as assessed by the body mass index. Pubovaginal distance and periurethral ligament disruption are significantly associated with incontinence; periurethral ligament symmetry reduces the odds of incontinence by 87%. Bladder neck funneling and length of the suprapubic urethral sphincter are significantly associated with the type of incontinence on UDs; funneling reduced the odds of pure UH by almost 95%; increasing suprapubic urethral sphincter length at rest is highly associated with UH. Both MRI variables result in a predictive model for UDs diagnosis (area under the ROC = 0.944).

CONCLUSION: MRI may play an important role in assessing the contribution of hypermobility and sphincteric dysfunction to the SUI in women when considering treatment options.

Key words: Magnetic resonance imaging; Stress urinary incontinence; Women; Urethra hypermobility; Intrinsic sphincter deficiency; Urodynamics; Dynamic magnetic resonance imaging

© **The Author(s) 2015.** Published by Baishideng Publishing Group Inc. All rights reserved.

Core tip: Magnetic resonance imaging (MRI) allows visualization of the female urethra and periurethral tissues relevant to stress urinary incontinence (SUI). The role of MRI in the specific diagnosis of SUI caused by urethral hypermobility (UH) and/or intrinsic sphincter deficiency (ISD) has not been documented. The purpose of this pilot study was to define the MRI parameters differentiating UH and ISD types of incontinence, and assess their ability to predict the type of SUI when urody-

namic (UD) results are used as a reference standard. Bladder neck funneling and length of the suprapubic urethral sphincter on MRI were significantly associated with the type of incontinence on UDs.

Macura KJ, Thompson RE, Bluemke DA, Genadry R. Magnetic resonance imaging in assessment of stress urinary incontinence in women: Parameters differentiating urethral hypermobility and intrinsic sphincter deficiency. *World J Radiol* 2015; 7(11): 394-404 Available from: URL: <http://www.wjgnet.com/1949-8470/full/v7/i11/394.htm> DOI: <http://dx.doi.org/10.4329/wjcr.v7.i11.394>

INTRODUCTION

Stress urinary incontinence (SUI) is the observation of involuntary urinary loss from the urethra synchronous with exertion, sneezing, or coughing. Urodynamic stress incontinence is noted during urodynamic testing and is defined as the involuntary leakage of urine during increases in abdominal pressure in the absence of a detrusor contraction. SUI is one of the most common conditions among women with a significant impact on the quality of life due to psychosocial and hygienic problems^[1]. Two main etiologic factors have been implicated in the urethral dysfunction leading to SUI, urethral hypermobility (UH) and intrinsic sphincter deficiency (ISD)^[2]. In UH, it is the weakness of pelvic floor support that results in a rotational descent of the vesical neck and urethra during increases in abdominal pressure with subsequent leakage. In ISD, there is malfunction of the urethral sphincter which leads to low urethral closure pressures^[3].

The type of urinary incontinence determines choice of surgical treatment, to prevent UH by repositioning the urethra into the pelvis to equalize pressure transmission between the bladder and urethra, and for women with low urethral resistance in ISD to increase the urethral closure pressures. Studies investigating the effects of UH and ISD on the outcome of the commonly performed procedures, such as transobturator tape (TOT) used to treat UH reported that the lack of UH as a contributing factor to SUI may be a risk factor for TOT failure^[4]. Also, Sand *et al*^[5] studied women who failed retropubic suspension and found a higher failure rate in those with ISD. It has been shown that SUI caused by ISD is the most challenging to treat; with failure rates as high as 54%^[6]. These failures were attributed to the correction of UH without concomitant increase of urethral closure pressures.

Traditionally, the diagnosis of SUI is made based on history, clinical exam and urodynamics (UDs) or videourodynamics. Urethral pressure profilometry [which allows to measure maximum urethral closure pressure (MUCP)] may be combined with videourodynamics. This indirect method has limitations, as only the physiologic effect of sphincteric dysfunction can be assessed,

without the evaluation of any morphological defects leading to SUI.

With its excellent soft tissue contrast and multiplanar acquisition, magnetic resonance imaging (MRI) allows visualization of the female urethra and periurethral tissues relevant to SUI^[7,8]. MRI findings related to SUI caused by UH and ISD in women have been described^[9]. Previous studies of MRI in female patients with SUI were focused on the assessment of lesions of the urethral support mechanism^[10], defects of the levator ani muscle^[11,12], and paravaginal fascia^[13], as well as on the kinematics of pelvic floor muscles function^[14].

To date, however, the role of MRI in the specific diagnosis of SUI caused by UH and/or ISD has not been documented. Therefore, the purpose of this pilot study was to define the MRI parameters differentiating UH and ISD types of incontinence, and assess their ability to predict the type of SUI with UD as a reference standard.

MATERIALS AND METHODS

Patient accrual and informed consent

The study was approved by the Institutional Review Board. The study was compliant with the Health Insurance Portability and Accountability Act. Study-specific written consent was obtained from all subjects. Patients were recruited from the Urogynecology clinic for this single-institution study, in which prospectively collected data from consecutive women who met the enrollment criteria and participated in the study were analyzed in a retrospective fashion. A target accrual of 20 patients with SUI and 10 volunteers was established for this pilot study. A total of 31 women were recruited. The inclusion criteria were as follows: (1) SUI documented on UD (for patients with SUI) or no clinical symptoms of SUI (for volunteers); (2) study-specific informed consent signed prior to study entry; (3) no contraindications to MRI. Subject exclusion criteria were as follows: (1) unable to give valid informed consent; (2) unable to undergo MR, e.g., patients with contra-indications to MR imaging; (3) latex allergy; (4) extraurethral incontinence and bladder abnormalities causing incontinence; (5) greater than grade II prolapse on clinical exam; (6) pregnancy and (7) metallic implant(s) that might compromise quality of MRI.

MR imaging technique

MRI was performed on 1.5 T magnet (Signa Excite, GE Medical Systems, Waukesha, WI). For the assessment of the urethra and integrity of the urethral support structures, we applied the high-resolution endocavitary MRI, such as intraurethral MRI, endovaginal or endorectal MRI. For the functional imaging of the urethral support, we performed dynamic MRI with the pelvic phased array coil.

Intraurethral MRI: The 14F endourethral coil (Surgi-Vision, Inc., Gaithersburg, MD) was inserted under

sterile conditions into the urethra. Both patient and volunteer groups underwent intraurethral MRI. All patients tolerated the procedure well and there were no complications from the coil placement. Patients were not pre-medicated with antibiotics. The imaging protocol included ultra-high resolution T2-weighted sequences in the axial and coronal planes (TR/TE 4000-6000 ms/90-120 ms, slice/spacing 2.5-3 mm/0-1 mm, FOV 6-10 cm centered on the urethra, matrix 256 × 256 ZIP interpolated to 512, NEX 6-8).

Endovaginal or endorectal MRI: The MRInnervu coil (Medrad, Indianola, PA) was placed in the vagina or rectum, depending on the patient's or volunteer's preference. The imaging protocol included T2-weighted fast spin echo (FSE) acquisition in three-plane with the field of view 10-14 cm and anatomical coverage between the symphysis pubis and coccyx. Imaging parameters were as follows: TR/TE 4000-6000 ms/90-120 ms, slice/space 3 mm/0-1 mm, matrix 256 × 192, NEX 3-4. The axial images were acquired in the oblique plane, perpendicular to the urethral axis. The frequency direction was AP to avoid endorectal/vaginal coil motion artifact over the urethra.

Pelvic MRI: Larger field of view imaging (20-30 cm) with the pelvic phased array coil was performed with the following parameters for the T2-weighted FSE images in axial and sagittal planes: TR/TE 4000-6000 ms/90-120 ms, slice/space 4-6 mm/0-1 mm, matrix 512 × 512, NEX 1-2. The dynamic pelvic floor imaging was performed in sagittal plane during rest and maximal strain with single shot fast spin echo (SSFSE) sequence TR/TE 15000/70 ms, slice/space 6 mm/2 mm, matrix 512 × 256, NEX 0.5; each image was acquired in 2 s, 10 images per sequence. At least two dynamic sequences were performed at maximal strain. Patients were asked to empty their bladder prior to the MRI, at the time of the dynamic evaluation they had their bladder at least half-full.

MRI interpretation

We assessed the following parameters in both the patient and the volunteer groups: (1) urethral angle; (2) bladder neck descent; (3) status of the periurethral ligaments; (4) vaginal shape; (5) urethral sphincter integrity, length and muscle thickness at mid urethra; (6) bladder neck funneling; (7) status of the puborectalis muscle (PRM); and (8) pubo-vaginal distance (PVD).

The urethral angle was defined as an angle between the patient body axis and the axis of the urethra, assessed at rest and during maximal strain. UH was diagnosed if the angle changed over 30 degrees between the rest and strain (as per definition of hypermobility)^[11]. The bladder neck descent was measured as a distance (cm) between its position at rest and strain in reference to the pubococcygeal line (PCL, a line drawn from the inferior margin of the pubic bone to the last coccygeal joint).

We assessed the integrity of the periurethral ligament that was seen in all patients. The periurethral ligament is the hypointense linear structure extending from PRM attachment on both sides of the pelvis and running in front of the urethra. The ligament status (intact/symmetric vs disrupted), as well as the site of disruption was evaluated. The ligament was judged as intact when the attachments were maintained and the ligament had a taut appearance and normal course. The ligament was deemed disrupted when there was a wavy/laxed appearance to the ligament, discontinuity of the ligament was present, or the attachment at PRM was lost.

The normal vaginal shape, assessed as an H-shaped contour on axial images, was deemed as a sign of the normal vaginolevator attachments. The loss of the H-shape vaginal morphology on axial images was interpreted as the presence of abnormal vaginolevator attachments (paravaginal defect) reflecting the loss of vaginal support. Laterality of the paravaginal defect was assessed. The PVD was measured as a distance between the posterior margin of the pubis and the anterior margin of the vagina at the mid urethra level (mid urethra defined at 50% of the sphincter length from the internal meatus).

The urethral sphincter length was measured at rest on the coronal and sagittal views, and a mean from both measurements was obtained as the total sphincter length. In addition to the total sphincter length, we assessed the functional length of the sphincter above the pelvic floor level (above the inferior pubic margin) and expressed it as a percentage of the total sphincter length. We evaluated the urethral sphincter muscle status for focal defects or signal changes within the sphincter. We measured the sphincter muscle thickness at the mid urethra level, for the anterior, lateral, and posterior urethral walls, separately for the striated and smooth muscle layers and for the total wall thickness.

We assessed the presence or absence of the bladder neck funneling, defined as an opening of the internal meatus of the urethral sphincter at rest or during strain.

The status of the PRM was evaluated at the mid urethra level. The muscle thickness (measured at mid length of the muscle), its length, and an angle between the PRM and an obturator internus muscle were assessed.

The anonymized MRI scans were reviewed on a PACS workstation (eFilm Workstation, Merge Healthcare, Milwaukee, WI) by two investigators (KJM with 10 years of experience in GU MRI and RG with 20 years of experience in urogynecology) blinded to the subject's status as a patient with SUI vs continent volunteer. The MRI parameters, as above, were assessed by consensus as to the presence of the finding, symmetry and/or severity. The review was performed at least 1 year post-imaging date, to avoid a memory bias as to the pelvic anatomy of the subjects. Data were entered into the Excel (Microsoft, Bellevue, WA) spreadsheet for subsequent transfer to the STATA 9.0 (StataCorp LP,

College Station, TX).

Urodynamics exam

The urodynamics exam was performed on a UD-2000 MMS (Medical Measurement System) using Millar Micro-tip 8F catheter transducers following a standard protocol: The patient empties her bladder and a post-void residual is measured. With the patient in the sitting position at 45°, and after the sensors have been zeroed to atmospheric pressure before insertion, a dual sensor catheter is inserted in the urethra with the proximal sensor in the bladder and the distal sensor positioned at the area of maximal urethral closure pressure (MUCP). A single sensor catheter is also inserted intravaginally to indirectly record intra-abdominal pressure. The detrusor pressure is monitored continually as an automatically subtracted pressure. An infusion of sterile water is instilled at a rate of 60 mL/min. Volume at first desire, strong desire and urge to urinate are recorded in standard fashion. After 250 mL have been instilled in the bladder a Valsalva leak point pressure (VLPP) is obtained. It is defined as the pressure increase leading to leakage in the absence of detrusor contraction. The subtracted nature of the pressure eliminates the effect of different pressures obtained with different types of catheters. Usually, the patient is asked to bear down maximally to determine the presence of incontinence and then incrementally to determine the lowest pressure leading to incontinence. In the absence of leakage with maximal Valsalva generated pressure, the patient was asked to cough maximally and incrementally for the same purpose. For this study group, a VLPP was obtained. The Q-tip test is obtained in the following manner. With the patient lying on the chair leveled with the horizontal, a sterile cotton-tipped swab is lubricated and placed in the urethra to the level of the urethrovaginal junction. With the patient at rest, the angle of the distal end of the swab is measured relative to the horizontal and recorded. The patient then is instructed to bear down to maximal Valsalva effort and the angle is measured again. The difference in the two angles is recorded as the Q-tip test angle.

Urodynamics parameters were assessed in the patient study group as follows: (1) urethral mobility angle on Q-tip test; (2) VLPP measured at 250 cc bladder volume; and (3) MUCP. The UH type of SUI was defined with the Q-tip test angle over 30 degrees, and VLPP pressure over 60 cm H₂O. The ISD incontinence was defined with MUCP pressure below 20 cm H₂O, and VLPP pressure less or equal to 60 cm H₂O. Out of 21 incontinent patients, 18 had a complete UD exam, 3 had incomplete exam that did not include the MUCP measurement. The volunteer group did not undergo the UD exam as volunteer women had no clinical symptoms of urinary incontinence and therefore were not subjected to the invasive UD workup.

Statistical analysis

As a primary analysis, we considered the statistical

associations between the MRI and clinical data with the binary outcome of incontinence (present/absent). Continuous variables were assessed using the two sample *t*-test with a two-sided alpha of 0.05. We used the χ^2 test and, when appropriate, the Fisher's exact test, for categorical and dichotomous data. As a secondary analysis, we looked at only the subset of women with the diagnosis of SUI. These analyses included an assessment of the correlation between the UD variables of MUCP and VLPP with the MRI data, as well as an investigation of the MRI variables that discriminated between women with a UD diagnosis of SUI due to pure UH vs a diagnosis of SUI with an ISD component (pure ISD or mixed UH/ISD). In the former analyses, we used the Pearson's correlation coefficient along with scatter plots and linear regression analyses. In the latter case, multivariate logistic regression models were created on the binary outcome of SUI with pure UH vs SUI with an ISD component using MRI and other clinical variables that at least trended toward statistical significance (e.g., *P* value < 0.1) in the univariate analyses. ROC analysis was then performed in order to assess the discriminative power of the MRI variables in the logistic regression models, and to obtain estimates of sensitivities, specificities, positive predictive values, and negative predictive values using the UD diagnosis as the reference standard. All statistical analyses were performed using STATA version 9.0 (StataCorp LP, College Station, TX) by a biomedical statistician.

RESULTS

Thirty one women recruited for this study were considered in the analysis, 21 with SUI and 10 volunteer controls. The characteristics of participants according to continent vs incontinent status are listed in Table 1.

When differences in clinical variables by incontinent status were considered, a history of obstetrical (OB) trauma was the only variable found to be statistically significant. Eleven of the 21 women with incontinence (52%) had a history of trauma during child birth (episiotomy, forceps delivery, perineal laceration) as compared to none of the control volunteer women (*P* < 0.001, Fisher's exact test). Incontinent women tended to be older with a mean (SD) age of 54.4 (11.8) years vs 45.1 (13.6) years for controls (*P* = 0.0610, *t*-test). There was no difference between the continent volunteers and incontinent patients in body habitus as assessed by the body mass index (BMI). Among the MRI variables, PVD and periurethral ligament disruption were found to be significantly associated with incontinence status (Table 1). Seven of the 10 control patients (70%) had intact, symmetric periurethral ligament, as opposed to only 4 of the 20 incontinent (20%) women (*P* = 0.015, Fisher's exact test) (Figures 1 and 2). When these variables were considered in a multivariable logistic regression model, we found that only periurethral ligament status was statistically associated with incontinence. Having intact periurethral

ligament reduced the odds of incontinence by 87% as compared to those who had periurethral disruption [Adjusted odds ratio 95%CI: 0.13 (0.018, 0.961), *P* = 0.046].

Among the subset of incontinent patients, we found an inverse correlation between bladder neck descent and MUCP that trended towards statistical significance (Pearson's correlation = -0.537, *P* = 0.089). When we looked at VLPP, only total urethral sphincter length trended to significance, giving a Pearson's correlation coefficient of 0.478 (*P* = 0.072) (Figures 3 and 4).

When we looked at the relationship of UD diagnosis in patients who had complete UD (SUI due to pure UH in 9 patients vs SUI with ISD component in 9 patients) and the MRI data, both bladder neck funneling (absent vs present) (Figure 5) and the functional suprapubic urethra sphincter length were found to be significantly associated with UD diagnosis. In the univariate logistic model, being positive for funneling reduced the odds of pure UH diagnosis by almost 95% as compared to no funneling [OR (95%CI) = 0.036 (0.003, 0.484), *P* = 0.012]. In contrast, increasing the suprapubic urethral sphincter length was highly associated with an UD diagnosis of UH [OR (95%CI) = 12.95 (1.17, 143.18), *P* = 0.037]. Both MRI variables considered in the multivariable logistic regression resulted in a highly predictive model for UD diagnosis (area under the ROC = 0.944); Figure 6 shows the ROC curve for this model, and Table 2 gives the corresponding predictive statistics and 95%CIs. The prediction statistics for this model were quite good, giving a 100% sensitivity and 88.9% specificity (Figure 7). Probability of UH diagnosis, alternative propensity scores, and covariate and outcome values are listed in Table 3. The predicted probability of UH at 0.529 cutoff was associated with suprapubic urethral sphincter length above 3.0 cm.

DISCUSSION

MRI allows the visualization of the urethra and its supporting structures with great detail, especially with a multi-coil MRI technique^[15,16], and also permits the evaluation of urethral mobility and bladder neck competence during strain and Valsalva. The importance of the integrity of the urethral attachments to the maintenance of continence is supported by our findings that the visualization of the periurethral ligament and assessment of its status leads to the prediction of incontinence. The majority of continent control patients (70%) in our study had intact, symmetric periurethral ligament, as opposed to only 20% of incontinent women. Having intact, symmetric periurethral ligament reduced the odds of incontinence by 87% as compared to those who had periurethral disruption. Similar results of distorted periurethral ligaments were found in 56% of the patients with SUI vs 13% of the women who were continent in the study by Kim *et al.*^[12], and also in a recent study by Tasali *et al.*^[10] where there was a significantly higher pubourethral

Table 1 Characteristics of participants according to continent *vs* incontinent status

Characteristics	Continent volunteers <i>n</i> = 10	Incontinent patients <i>n</i> = 21	<i>P</i> value
¹ Age (yr)	45.1 (13.6)	54.4 (11.8)	0.0610
² Race			
White	5 (50)	14 (67)	
Black	5 (50)	6 (29)	
Other	-	1 (4)	
¹ BMI index	29.98 (7.0)	29.95 (6.6)	0.9915
¹ Parity, <i>n</i> births	1.5 (1.2)	1.9 (1.2)	0.3329
² Vaginal, <i>n</i>	11 (65)	39 (90)	
² C-section, <i>n</i>	4 (24)	2 (5)	
² Nullipara, <i>n</i>	2 (12)	2 (5)	
² OB Trauma, <i>n</i>	0 (0)	11 (52)	< 0.001 ⁴
² Hormones, <i>n</i>	0 (0)	5 (24)	
² Hysterectomy, <i>n</i>	2 (2)	8 (38)	
³ Urethra wall thickness			
Ant total, mm	0.47 (0.43-0.50)	0.59 (0.33-0.84)	0.5161
Ant striated muscle, mm	0.17 (0.13-0.2)	0.21 (0.12-0.29)	0.5467
Ant smooth muscle, mm	0.30 (0.3-0.3)	0.38 (0.20-0.55)	0.5055
Post total, mm	0.40 (0.36-0.43)	0.39 (0.36-0.42)	0.7713
Post striated muscle, mm	0.11 (0.08-0.13)	0.09 (0.08-0.11)	0.3180
Post smooth muscle, mm	0.29 (0.26-0.31)	0.29 (0.27-0.32)	0.7952
³ Urethral sphincter length			
Total, cm	3.67 (3.45-3.88)	3.77 (3.47-4.06)	0.6432
Length, suprapubic, cm	3.03 (2.59-3.46)	2.95 (2.65-3.24)	0.7361
³ Urethra mobility angle	53 (19.6-86.6)	65 (50.1-80.2)	0.4116
³ Bladder neck descent			
Total, cm	1.98 (0.73-3.23)	2.56 (1.96-3.15)	0.3158
Rest, above PCL, cm	1.42 (0.43-2.41)	1.51 (1.16-1.85)	0.8195
Strain, below PCL, cm	0.56 (0.99-2.12)	1.05 (0.46-1.63)	0.4272
² Funneling, <i>n</i>	1 (10)	11 (52)	0.184
³ Retropubic distance to urethra, mm	5.2 (4.19-6.20)	5.0 (4.16-5.92)	0.8259
³ Pubo-vaginal distance			
Right, cm	1.81 (1.59-2.02)	1.59 (1.47-1.70)	0.0372
Left, cm	1.87 (1.72-2.01)	1.67 (1.53-1.79)	0.0475
² Normal vaginal shape, <i>n</i>	7 (70)	8 (40)	0.128
³ Puborectalis muscle thickness			
Right, mm	3.4 (2.6-4.1)	3.8 (1.8-3.0)	0.4903
Left, mm	3.9 (2.9-4.9)	4.7 (3.7-5.5)	0.2748
¹ Puborectalis muscle length			
Right, cm	1.81 (0.30)	1.59 (0.24)	0.037
Left, cm	1.87 (0.21)	1.67 (0.28)	0.048
³ Puborectalis angle			
Right, °	21 (17-24)	25 (21-28)	0.0781
Left, °	23 (19-27)	24 (19-28)	0.7323
² Periurethral ligament status			
Intact/symmetric, <i>n</i>	7 (70)	4 (20)	0.015 ⁴
Disrupted, <i>n</i>	3 (30)	16 (80)	

¹Data are presented as mean (standard deviation); ²Data are presented as number of cases (%); ³Data are presented as mean (95%CI); *P* value of *t*-test;

⁴Fisher's exact test. BMI: Body mass index; PCL: Pubococcygeal line; OB: Obstetric trauma to include episiotomy; Ant: Anterior; Post: Posterior.

ligament distortion and larger vesicourethral angle in women with SUI. In our study the PVD was also found to be significantly associated with incontinence status. Incontinent women had a shorter PVD than the control volunteers. Previous studies demonstrated that the volume of paravaginal fascia (connective tissue that contained venous plexus anterior to vagina) was reduced in patients with stress incontinence compared to reference continent subjects^[13], therefore our finding of shortening of the distance between the anterior vaginal wall and pubic wall in incontinent women may indirectly relate to diminishing volume of paravaginal tissue noted by deSouza *et al*^[13]. However, in the

study by Tasali *et al*^[10], authors documented lack of association between the dimension of the retropubic space and the SUI. Notably, in our study there was no difference in BMI between the incontinent patients and continent volunteers, therefore our results should not be influenced by the contribution of retropubic fat pad to the PVD in our study sample.

Contrary to findings by Kim *et al*^[12], Tasali *et al*^[10], and Morgan *et al*^[17], but in agreement with results from the study by Pontbriand-Drolet *et al*^[18], we did not find a statistically significant difference between the urethral sphincter striated muscle thickness in women with SUI *vs* that in the continent group. In our

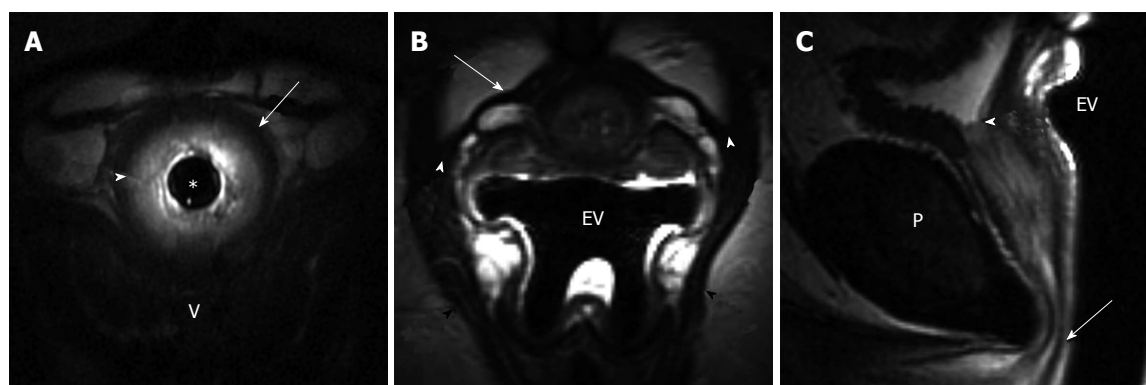


Figure 1 41-year-old woman post one vaginal delivery with episiotomy, body mass index: 46.7, with occasional stress urinary incontinence. A: Axial T2-weighted image of the mid urethra obtained with 14F endourethral MR coil (TR/TE 4816/68 ms) shows detailed depiction of the urethral sphincter with a hypointense outer layer of striated muscle (arrow) and inner hyperintense smooth muscle layer (arrowhead); B: Axial T2-weighted image at the mid urethra level obtained with endovaginal placement of MRInnervu coil (EV) (TR/TE 3000/92 ms) shows well-defined intact periurethral ligament (arrow) extending between the right and left puborectalis muscle (black arrowheads). Note symmetric, intact ligament attachment (white arrowheads); C: Sagittal T2-weighted image obtained with endovaginal placement of MRInnervu coil (EV) (TR/TE 4000/92 ms) shows normal resting position of the urethra, with distal end of urethral sphincter (arrow) at inferior pubis level (P). Note excellent coaptation of the mucosa at internal meatus/bladder neck level (arrowhead). V: Vagina.

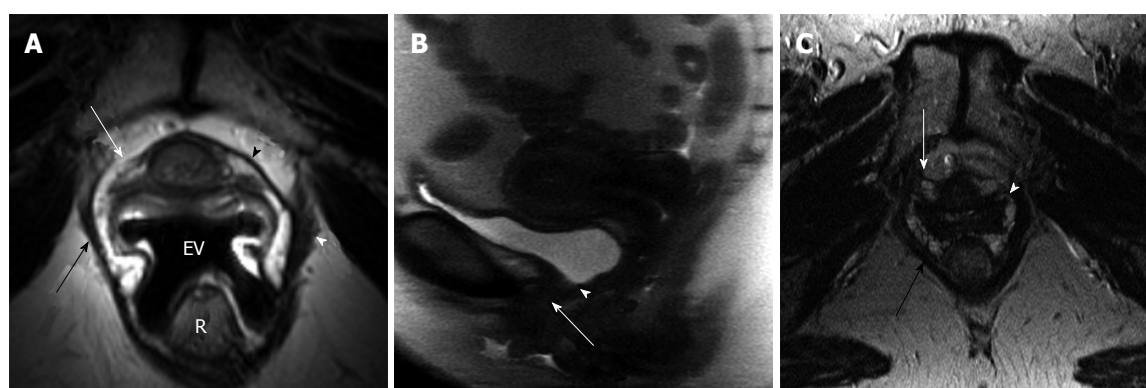


Figure 2 51-year-old woman post two uneventful vaginal deliveries, body mass index: 24.3. A: Axial oblique T2-weighted image at the mid urethra level (at 50% length from the internal meatus, about 1.2 cm), perpendicular to the axis of urethra, obtained with endovaginal placement of MRInnervu coil (EV) (TR/TE 3200/93 ms) shows disrupted attenuated right periurethral ligament (white arrow). Note intact left side of the periurethral ligament (black arrowhead) and its attachment to the puborectalis muscle (white arrowhead). Minimal asymmetric thinning of the right puborectalis muscle (black arrow); B: Sagittal SSFSE image (TR/TE 15000/78 ms) during strain shows hypermobility of the urethra (arrow). Note closure of bladder neck (arrowhead) during the urethral descent; C: Axial T2-weighted image of the pelvis at the level of mid urethra (at 50% from the internal meatus) obtained with pelvic coil (TR/TE 4666/85 ms) shows much less detail of the periurethral ligament compared to endovaginal MRI in A. It is difficult to appreciate the status of the ligament itself (white arrow) or its attachment (white arrowhead). Puborectalis muscle (black arrow) is well visualized. R: Rectum.

study, we performed precise measurements of the sphincter on images acquired with endourethral coil, both groups were comparable in body habitus and the mean age difference for incontinent patients and continent volunteers was less than a decade. It has been demonstrated that with aging, there is a decrease in the relative volume of urethral striated muscle and blood vessels^[19].

Urethral mobility is tested clinically with the Q test^[16]. Clinical Q test without visualization of urethral attachment defects may not be a reliable test, as continent women may also demonstrate hypermobility of the urethra. In our study groups there was an overlap between urethral mobility angles for continent women (mean 53 degrees) and incontinent women (mean 65 degrees) when assessed based on MRI. MRI is able to demonstrate not only the presence of hypermobility, but

also other associated findings. UH is often accompanied by moderate to severe bladder descent with anterior bulging of the vagina. Bladder neck descent can be quantified and its competence/coaptation can be assessed on MRI along with hypermobility. We found an inverse correlation between bladder neck strain and MUCP that supports the hypothesis that, with increased inferior translation of the bladder neck due to loosening of the bladder neck attachment, there is decreasing urethral closure pressure caused by loss of coaptation of the sphincter as it descends. We also noted a correlation approaching significance between the increasing total urethral sphincter length and increasing VLPP; the longer the sphincter, the higher the leak point pressure.

On MRI, urethral and bladder descent are assessed in reference to the level of the pelvic floor which can be defined by the PCL^[20-23]. Yang *et al.*^[21] demonstrated that

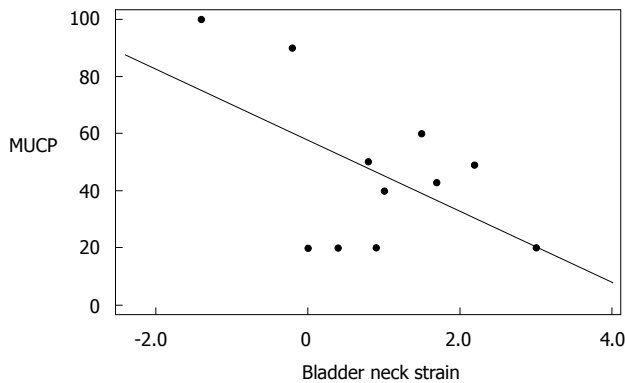


Figure 3 Scatter plot of maximum urethral closure pressure (cm H₂O) and bladder neck strain (distance in cm, traveled between position at rest and maximal strain) with fitted regression line (Pearson's correlation coefficient -0.537, $P = 0.089$). MUCP: Maximum urethral closure pressure.

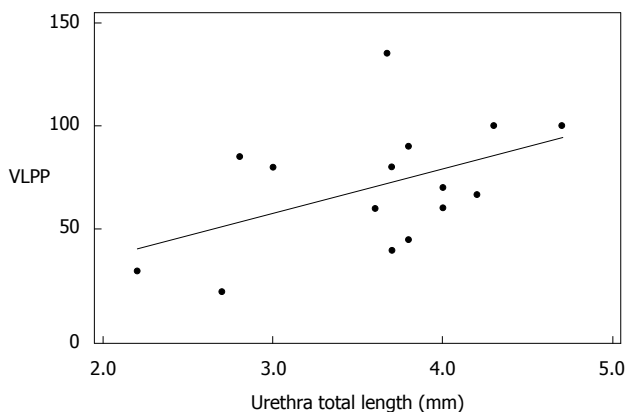


Figure 4 Scatter plot of valsalva leak point pressure (cm H₂O) and total urethra sphincter length (mm) with fitted regression line (Person's correlation coefficient 0.478, $P = 0.072$).

the normal vertical distance from PCL to the bladder base at strain should be no more than 1 cm below the line. In our study group, bladder neck descended to mean distance 0.56 cm below PCL in continent women during strain and 1.1 cm below PCL for incontinent women ($P = 0.43$).

Other findings associated with UH that can be detected on MRI are distortion of urethral support ligaments, either partial or complete. Partial defects include laxity, fluttering or focal attenuation of ligaments. Complete disruption shows a discontinuity of ligamentous fibers^[6,12]; mostly affected and reproducibly visualized on imaging is PEL and pubourethral ligaments^[10]. Findings are frequently accompanied by the abnormal vaginal configuration (loss of normal H-shape vaginal contour, or dropping vaginal fornix), best seen on axial images, and widening of the para-vaginal attachments. In our study group, normal vaginal shape was maintained in 70% of continent volunteers and 40% of incontinent women.

The levator ani muscle signal and integrity can be well evaluated on MR images, on axial and coronal T2-weighted images. Levator ani should be symmetric without defects or fraying. Abnormal signal in the levator

Table 2 Predictive value statistics and corresponding 95%CI for urethral hypermobility diagnosis for both suprapubic urethra sphincter length and bladder neck funneling (present/absent)

Urethral hypermobility diagnosis - suprapubic urethra sphincter length and bladder neck funneling ¹	Estimate 95%CI
Sensitivity	100.0% (66.4%, 100%) ²
Specificity	88.9% (51.8%, 99.7%)
Positive predictive value	90.0% (55.5%, 99.7%)
Negative predictive value	100.0% (63.1%, 100.0%) ²

A total of 18 incontinent women were included in the analysis. ¹ROC = 0.944; ²One-sided 97.5% CI.

Table 3 Probability of urethral hypermobility diagnosis, alternative propensity scores, and covariate and outcome values

Predicted probability of urethral hypermobility	Score	Funneling Y = 1, n = 0	Suprapubic urethral sphincter length (cm)	UH = 1 ISD/mixed = 0
0.008	-4.77	1	1.8	0
0.020	-3.84	1	2.1	0
0.027	-3.53	1	2.2	0
0.027	-3.53	1	2.2	0
0.065	-2.6	1	2.5	0
0.149	-1.67	1	2.8	0
0.193	-1.36	1	2.9	0
0.377	-0.43	1	3.2	0
0.529	0.19	1	3.4	1
0.587	0.38	0	2.3	1
0.605	0.5	1	3.5	1
0.659	0.69	0	2.4	1
0.925	2.55	0	3.0	1
0.925	2.55	0	3.0	0
0.969	3.48	0	3.3	1
0.969	3.48	0	3.3	1
0.969	3.48	0	3.3	1
0.996	5.65	0	4.0	1

UH: Urethral hypermobility; ISD: Intrinsic sphincter defects.

muscle, when compared to the obturator internus, and thinning can be observed in patients with stress incontinence and can be a result of fatty infiltration and atrophy as well as direct muscle injury^[24]. The normal thickness of the PRM is 5-6 mm^[25]. Interruption of the muscle fibers, lateral deviation of the muscle that is frequently associated with vaginal shape distortion on the affected side, can be observed. In our study group however, there was no difference between the thickness of PRM or the puborectalis angle between incontinent and continent women.

In patients with SUI, there are some imaging findings that are more likely to be associated with ISD, such as a short urethra, urethral muscle thinning, or bladder neck weakness demonstrated by funneling. Our results in incontinent women demonstrate that when the total urethral sphincter is shorter than 3.0 cm, or when the segment of urethral sphincter above

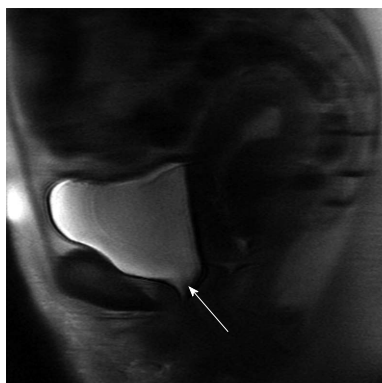


Figure 5 48-year-old woman post four vaginal deliveries, body mass index: 24.4. Sagittal SSFSE image (TR/TE 15000/78 ms) during strain shows funneling at the bladder neck level (arrow).

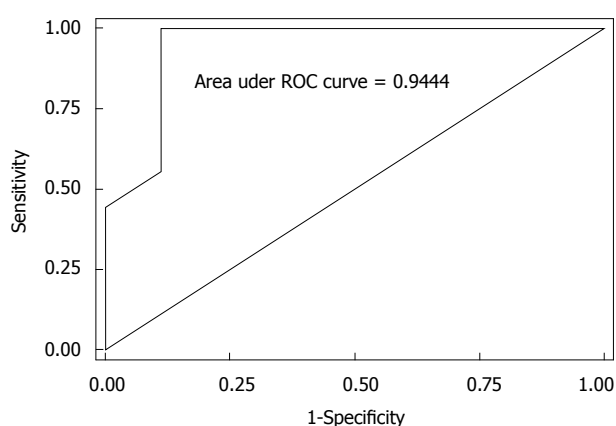


Figure 6 Receiver operating characteristic curve for the logistic model of urodynamics diagnosis regressed on bladder neck funneling and suprapubic urethral sphincter length.

the pelvic floor level is less than 3.0 cm, this decreased functional length of the urethra can lead to incontinence with urethral sphincter weakening associated with ISD on UD. Also, funneling at the bladder neck, which is the opening of the urethrovesical junction at rest or during strain, can be seen on MRI in patients with SUI. An open bladder neck and proximal urethra was shown to indicate an ISD^[26], however funneling can be also found in some postmenopausal continent women. In our study, funneling was seen in 52% of incontinent women and only in 1 (10%) continent volunteer. In a recent study by Pontbriand-Drolet *et al.*^[18] women with SUI symptoms were more likely to exhibit bladder neck funneling and a larger posterior urethrovesical angle at rest than both continent and mixed urinary incontinence women.

When we looked at the relationship of UD diagnosis (SUI with pure UH vs SUI with ISD component) and the MRI data, both bladder neck funneling and the suprapubic urethral sphincter length were found to be predictive of UD diagnosis; being positive for funneling on MRI reduced the odds of pure UH diagnosis on UD by almost 95% as compared to no funneling. Our

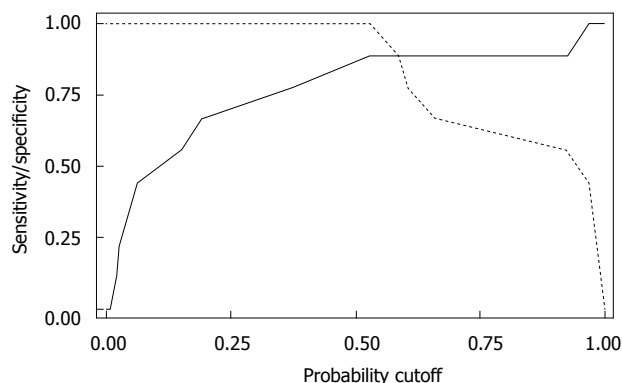


Figure 7 Plot of sensitivity (solid line) and specificity (dashed line) as a function of the probability cut points obtained from the logistic model of urodynamics diagnosis regressed on bladder neck funneling and suprapubic urethral sphincter length. The optimal probability cutoff point was determined to be 0.52.

results are consistent with previous reports showing that funneling predicts ISD, as it results from the weakness of the proximal sphincter^[26]. In contrast, increasing suprapubic urethral sphincter length was highly associated with a UD diagnosis of pure UH, as the dysfunction of the sphincter results from the inferior translation of the urethra that is poorly supported rather than from shortening or intrinsic weakness of the sphincter itself. Both variables considered in the multivariable logistic regression analyses resulted in a highly predictive model for UD diagnosis (area under the ROC = 0.944). The prediction statistics for this model was good, giving a 100% sensitivity and 88.9% specificity. However, due to a small size of the sample, the confidence intervals are large. A larger cohort study is needed to address these findings. Some patients may demonstrate imaging findings of both UH and ISD, as the ISD with bladder neck funneling may represent a secondary deficiency related to abnormal proximal urethral wall traction and shearing that can over time overcome the urethral coaptation such as in chronic hypermobility^[27,28].

A limitation of our study is a relatively small sample size for incontinent group as only 18 incontinent women had a complete UD exam to be included in the logistic regression model. Our study group patients were nearly-matched by age to within a decade. They were matched by BMI. However, there was a significant difference in the incidence of OB trauma, with 90% of incontinent patients reporting vaginal deliveries and 52% at least one incident of episiotomy, perineal laceration, or forceps delivery. No history of OB trauma was reported in the control group. This finding indirectly may relate to a known risk of pelvic floor injury during vaginal delivery as a cause of SUI. However, since the study sample was small, we were unable to control for individual types of injury to directly correlate the MRI findings with the severity of pelvic floor trauma. Another potential limitation of our study is imaging in the supine position, which is not a physiological position when patients

experience SUI. However, we performed dynamic pelvic floor strain imaging to allow assessment of the changes in the urethra that take place during increases of intra-abdominal pressures. Our study group was imaged with pelvic MRI that included three different imaging components, with intraurethral imaging and dynamic pelvic floor imaging performed in all patients, and endovaginal or endorectal imaging being performed based on patients' preference. This could have resulted in some measurements inconsistencies where endovaginal coil placement may have caused vaginal shape distortion.

In conclusion, our study demonstrated that there are specific morphological defects in women with SUI detectable on MRI that can be evaluated to differentiate incontinence related to the pure UH vs incontinence that has a component of ISD. Currently, MRI is usually considered in the diagnostic work-up of women who failed prior surgeries for incontinence or who have severe and complex pelvic organ prolapse. Further studies are needed to address the effects of aging, parity, pelvic floor injury, and hormonal status on SUI, in the context of specific anatomical defects related to SUI that can be observed and quantified on MR images, in order to evaluate the role of MRI in the assessment and treatment planning of women with SUI.

COMMENTS

Background

Anatomical defects related to stress urinary incontinence (SUI) can be observed and quantified with magnetic resonance imaging (MRI) and may contribute to diagnostic work-up and treatment planning of women with SUI.

Research frontiers

To date the role of MRI in the specific diagnosis of SUI caused by urethral hypermobility (UH) and/or intrinsic sphincter deficiency (ISD) has not been documented.

Innovations and breakthroughs

The results from this pilot study suggest that two MRI parameters, the bladder neck funneling and length of the suprapubic urethral sphincter on MRI can predict the UH and ISD types of incontinence when urodynamics results are used as a reference standard.

Applications

MRI may play a critical role in assessing the contribution of hypermobility and sphincteric dysfunction to the stress urinary incontinence in women when considering treatment options. Further studies are warranted to assess the potential added value of MRI to management strategy selection.

Peer-review

The authors performed an interesting pilot study aimed at the identification of MRI parameters differentiating UH and intrinsic sphincteric deficiency in women with SUI.

REFERENCES

- Abrams P, Blaivas JG, Stanton SL, Andersen JT. The standardisation of terminology of lower urinary tract function. The International Continence Society Committee on Standardisation of Terminology. *Scand J Urol Nephrol Suppl* 1988; **114**: 5-19 [PMID: 3201169]
- Blaivas JG, Romanzi LJ, Heritz DM. Urinary incontinence: pathophysiology, evaluation, treatment overview, and nonsurgical management. In: Walsh P, Retik A, Vaughan E, Wein A, editors. *Campbell's Urology*. Philadelphia: WB Saunders Co., 1997: 1007-1043
- McGuire EJ, Fitzpatrick CC, Wan J, Bloom D, Sanvordenker J, Ritchey M, Gormley EA. Clinical assessment of urethral sphincter function. *J Urol* 1993; **150**: 1452-1454 [PMID: 8411422]
- Haliloglu B, Karateke A, Coksuer H, Peker H, Cam C. The role of urethral hypermobility and intrinsic sphincteric deficiency on the outcome of transobturator tape procedure: a prospective study with 2-year follow-up. *Int Urogynecol J* 2010; **21**: 173-178 [PMID: 19802505 DOI: 10.1007/s00192-009-1010-y]
- Sand PK, Bowen LW, Panganiban R, Ostergard DR. The low pressure urethra as a factor in failed retropubic urethropepy. *Obstet Gynecol* 1987; **69**: 399-402 [PMID: 3822288]
- Shah SM, Gaunay GS. Treatment options for intrinsic sphincter deficiency. *Nat Rev Urol* 2012; **9**: 638-651 [PMID: 23027065 DOI: 10.1038/nrurol.2012.177]
- Macura KJ, Genadry RR. Female urinary incontinence: pathophysiology, methods of evaluation and role of MR imaging. *Abdom Imaging* 2008; **33**: 371-380 [PMID: 17610006 DOI: 10.1007/s00261-007-9257-6]
- el-Sayed RF, Morsy MM, el-Mashed SM, Abdel-Azim MS. Anatomy of the urethral supporting ligaments defined by dissection, histology, and MRI of female cadavers and MRI of healthy nulliparous women. *AJR Am J Roentgenol* 2007; **189**: 1145-1157 [PMID: 17954653 DOI: 10.2214/AJR.07.2215]
- Macura KJ, Genadry RR, Bluemke DA. MR imaging of the female urethra and supporting ligaments in assessment of urinary incontinence: spectrum of abnormalities. *Radiographics* 2006; **26**: 1135-1149 [PMID: 16844938 DOI: 10.1148/rg.264055133]
- Tasali N, Cubuk R, Sinanoğlu O, Sahin K, Saydam B. MRI in stress urinary incontinence: endovaginal MRI with an intracavitary coil and dynamic pelvic MRI. *Urol J* 2012; **9**: 397-404 [PMID: 22395838]
- Stoker J, Rociu E, Bosch JL, Messelink EJ, van der Hulst VP, Groenendijk AG, Eijkemans MJ, Laméris JS. High-resolution endovaginal MR imaging in stress urinary incontinence. *Eur Radiol* 2003; **13**: 2031-2037 [PMID: 12692675 DOI: 10.1007/s00330-003-1855-2]
- Kim JK, Kim YJ, Choo MS, Cho KS. The urethra and its supporting structures in women with stress urinary incontinence: MR imaging using an endovaginal coil. *AJR Am J Roentgenol* 2003; **180**: 1037-1044 [PMID: 12646452 DOI: 10.2214/ajr.180.4.1801037]
- deSouza NM, Daniels OJ, Williams AD, Gilderdale DJ, Abel PD. Female urinary genuine stress incontinence: anatomic considerations at MR imaging of the paravaginal fascia and urethra initial observations. *Radiology* 2002; **225**: 433-439 [PMID: 12409577 DOI: 10.1148/radiol.2252011347]
- Constantinou CE. Dynamics of female pelvic floor function using urodynamics, ultrasound and Magnetic Resonance Imaging (MRI). *Eur J Obstet Gynecol Reprod Biol* 2009; **144** Suppl 1: S159-S165 [PMID: 19303690 DOI: 10.1016/j.ejogrb.2009.02.021]
- Bergman A, McCarthy TA, Ballard CA, Yanai J. Role of the Q-tip test in evaluating stress urinary incontinence. *J Reprod Med* 1987; **32**: 273-275 [PMID: 3585870]
- Macura KJ, Genadry R, Borman TL, Mostwin JL, Lardo AC, Bluemke DA. Evaluation of the female urethra with intraurethral magnetic resonance imaging. *J Magn Reson Imaging* 2004; **20**: 153-159 [PMID: 15221821 DOI: 10.1002/jmri.20058]
- Morgan DM, Umek W, Guire K, Morgan HK, Garabrant A, DeLancey JO. Urethral sphincter morphology and function with and without stress incontinence. *J Urol* 2009; **182**: 203-209 [PMID: 19450822 DOI: 10.1016/j.juro.2009.02.129]
- Pontbriand-Drolet S, Tang A, Madill SJ, Tannenbaum C, Lemieux MC, Corcos J, Dumoulin C. Differences in pelvic floor morphology between continent, stress urinary incontinent, and mixed urinary incontinent elderly women: An MRI study. *Neurourol Urodyn* 2015; Epub ahead of print [PMID: 25727524 DOI: 10.1002/nau.22743]
- Carlike A, Davies I, Rigby A, Brocklehurst JC. Age changes in the human female urethra: a morphometric study. *J Urol* 1988; **139**:

- 532-535 [PMID: 3343739]
- 20 **Borghesi G**, Simonetti R, Goldman SM, Szejnfeld J, Srougi M, Ortiz V, Bruschini H. Magnetic resonance imaging urodynamics. Technique development and preliminary results. *Int Braz J Urol* 2006; **32**: 336-341; discussion 341 [PMID: 16813681 DOI: 10.1590/S1677-55382006000300015]
- 21 **Yang A**, Mostwin JL, Rosenshein NB, Zerhouni EA. Pelvic floor descent in women: dynamic evaluation with fast MR imaging and cinematic display. *Radiology* 1991; **179**: 25-33 [PMID: 2006286 DOI: 10.1148/radiology.179.1.2006286]
- 22 **Gufler H**, DeGregorio G, Allmann KH, Kundt G, Dohnicht S. Comparison of cystourethrography and dynamic MRI in bladder neck descent. *J Comput Assist Tomogr* 2000; **24**: 382-388 [PMID: 10864072 DOI: 10.1097/00004728-200005000-00005]
- 23 **Goh V**, Halligan S, Kaplan G, Healy JC, Bartram CI. Dynamic MR imaging of the pelvic floor in asymptomatic subjects. *AJR Am J Roentgenol* 2000; **174**: 661-666 [PMID: 10701605 DOI: 10.2214/ajr.174.3.1740661]
- 24 **Tunn R**, Paris S, Fischer W, Hamm B, Kuchinke J. Static magnetic resonance imaging of the pelvic floor muscle morphology in women with stress urinary incontinence and pelvic prolapse. *Neurourol Urodyn* 1998; **17**: 579-589 [PMID: 9829422 DOI: 10.1002/(SICI)1520-6777(1998)17:6<579::AID-NAU2>3.0.CO;2-R]
- 25 **Singh K**, Reid WM, Berger LA. Magnetic resonance imaging of normal levator ani anatomy and function. *Obstet Gynecol* 2002; **99**: 433-438 [PMID: 11864670 DOI: 10.1016/S0029-7844(01)01743-4]
- 26 **Mostwin JL**. Urinary incontinence. *J Urol* 1995; **153**: 352-353 [PMID: 7815581 DOI: 10.1097/00005392-199502000-00016]
- 27 **Mostwin JL**, Genadry R, Saunders R, Yang A. Stress incontinence observed with real time sonography and dynamic fastscan magnetic resonance imaging--insights into pathophysiology. *Scand J Urol Nephrol Suppl* 2001; **(207)**: 94-99; discussion 106-125 [PMID: 11409622 DOI: 10.1080/003655901750175033]
- 28 **Huang WC**, Yang JM. Bladder neck funneling on ultrasound cystourethrography in primary stress urinary incontinence: a sign associated with urethral hypermobility and intrinsic sphincter deficiency. *Urology* 2003; **61**: 936-941 [PMID: 12736011 DOI: 10.1016/S0090-4295(02)02558-X]

P- Reviewer: Francesco C, Tsai HH

S- Editor: Qiu S L- Editor: A E- Editor: Jiao XK



Case Control Study

Partial correlation analyses of global diffusion tensor imaging-derived metrics in glioblastoma multiforme: Pilot study

David Cortez-Conradis, Camilo Rios, Sergio Moreno-Jimenez, Ernesto Roldan-Valadez

David Cortez-Conradis, Magnetic Resonance Unit, Medica Sur Clinic and Foundation, Mexico City CP 14050, Mexico

Camilo Rios, Department of Neurochemistry, National Institute of Neurology and Neurosurgery, Mexico City CP 14269, Mexico

Sergio Moreno-Jimenez, Radioneurosurgery Unit, National Institute of Neurology and Neurosurgery, Mexico City CP 14269, Mexico

Ernesto Roldan-Valadez, Faculty of Health Sciences, Panamerican University, Mexico City CP 03920, Mexico

Ernesto Roldan-Valadez, Magnetic Resonance Unit, Medica Sur Clinic and Foundation, Puente de Piedra # 150, Col, Toriello Guerra, Deleg, Tlalpan, Mexico City CP 14050, Mexico

Author contributions: Roldan-Valadez E drafted the manuscript; all authors participated in the literature search, summary and interpretation; all authors edited and approved the final manuscript.

Supported by The Medica Sur Clinic and Foundation (in part); David Cortez-Conradis was research fellow at the MRI Unit of Medica Sur Clinic and Foundation from 2012 to 2014. Ernesto Roldan-Valadez was Coordinator of Research at the MRI Unit of Medica Sur Clinic and Foundation from 2010 to April 2015.

Institutional review board statement: The protocol for this study was previously accepted by the institutional review board of Medica Sur Clinic and Foundation (Project #2011-EXT-05).

Informed consent statement: Because this was a retrospective study using exclusively, quantitative parameter of MRI postprocessed images, the approved protocol included a waiver of informed consent statement.

Conflict-of-interest statement: The authors have no conflicts of interests to declare.

Data sharing statement: The dataset of this study is available from the corresponding author at Dryad repository.

Open-Access: This article is an open-access article which was selected by an in-house editor and fully peer-reviewed by external

reviewers. It is distributed in accordance with the Creative Commons Attribution Non Commercial (CC BY-NC 4.0) license, which permits others to distribute, remix, adapt, build upon this work non-commercially, and license their derivative works on different terms, provided the original work is properly cited and the use is non-commercial. See: <http://creativecommons.org/licenses/by-nc/4.0/>

Correspondence to: Ernesto Roldan-Valadez, MD, MSc, PhD, Magnetic Resonance Unit, Medica Sur Clinic and Foundation, Puente de Piedra # 150, Col, Toriello Guerra, Deleg, Tlalpan, Mexico City CP 14050, Mexico. ernest.rolدان@usa.net
Telephone: +52-55-54247230
Fax: +52-55-54244429

Received: April 20, 2015
Peer-review started: April 21, 2015
First decision: June 9, 2015
Revised: August 31, 2015
Accepted: October 12, 2015
Article in press: October 13, 2015
Published online: November 28, 2015

Abstract

AIM: To determine existing correlates among diffusion tensor imaging (DTI)-derived metrics in healthy brains and brains with glioblastoma multiforme (GBM).

METHODS: Case-control study using DTI data from brain magnetic resonance imaging of 34 controls (mean, 41.47; SD, \pm 21.94 years; range, 21-80 years) and 27 patients with GBM (mean, SD; 48.41 \pm 15.18 years; range, 18-78 years). Image postprocessing using FSL software calculated eleven tensor metrics: fractional (FA) and relative anisotropy; pure isotropic (p) and anisotropic diffusions (q), total magnitude of diffusion (L); linear (Cl), planar (Cp) and spherical tensors (Cs); mean (MD), axial (AD) and radial diffusivities (RD). Partial correlation analyses (controlling the effect of age

and gender) and multivariate Mancova were performed.

RESULTS: There was a normal distribution for all metrics. Comparing healthy brains *vs* brains with GBM, there were significant very strong bivariate correlations only depicted in GBM: [FA↔CI (+)], [FA↔q (+)], [p↔AD (+)], [AD↔MD (+)], and [MD↔RD (+)]. Among 56 pairs of bivariate correlations, only seven were significantly different. The diagnosis variable depicted a main effect [F-value (11, 23) = 11.842, $P \leq 0.001$], with partial eta squared = 0.850, meaning a large effect size; age showed a similar result. The age also had a significant influence as a covariate [F (11, 23) = 10.523, $P < 0.001$], with a large effect size (partial eta squared = 0.834).

CONCLUSION: DTI-derived metrics depict significant differences between healthy brains and brains with GBM, with specific magnitudes and correlations. This study provides reference data and makes a contribution to decrease the underlying empiricism in the use of DTI parameters in brain imaging.

Key words: Brain neoplasms; Diffusion tensor imaging; Magnetic resonance imaging; Software tools; Statistics as topic

© **The Author(s) 2015.** Published by Baishideng Publishing Group Inc. All rights reserved.

Core tip: Diffusion tensor imaging (DTI)-derived metrics depict specific magnitudes and correlations; and significant differences between healthy brains and brains with glioblastoma multiforme (GBM). For example, only 5 bivariate correlations in GBM depicted significant very strong association: [FA↔CI (+)], [FA↔q (+)], [p↔AD (+)], [D↔MD (+)], and [MD↔RD (+)]. Among 56 pairs of correlations, only seven were significantly different. Diagnosis showed a main effect [F-value (11, 23) = 11.842, $P \leq 0.001$], with a large effect size (partial eta squared = 0.850); a similar result was observed for age. This study makes a contribution to decrease the empiricism in the use of DTI parameters in brain imaging.

Cortez-Conradis D, Rios C, Moreno-Jimenez S, Roldan-Valadez E. Partial correlation analyses of global diffusion tensor imaging-derived metrics in glioblastoma multiforme: Pilot study. *World J Radiol* 2015; 7(11): 405-414 Available from: URL: <http://www.wjgnet.com/1949-8470/full/v7/i11/405.htm> DOI: <http://dx.doi.org/10.4329/wjr.v7.i11.405>

INTRODUCTION

In the last decade, advanced magnetic resonance (MR) techniques have been adopted for the diagnosis and follow-up of intra-axial brain tumors^[1], with a rising interest in novel diffusion tensor imaging (DTI)-derived

metrics showing clinical applicability either in a tumor-region assessment (ROIs measurements in the cystic cavity, enhancing rim, edema, and normal-appearing white matter regions)^[2-4]; or in a global approach (whole-brain selected values of DTI-derived biomarkers are able to assemble a predictive model for the diagnosis of glioblastoma multiforme)^[4].

Conventional MR evaluation of glial tumors reporting qualitative and quantitative findings in the T₁-w post gadolinium, Flair and T₂-w sequences represents a caveat in the pathologic and regional evaluation of astrocytomas grades II to IV, as evidence suggest these tumors should received a global instead of regional brain assessment: glial tumors can depict manifold regions with different histologic grading, conditioning that biopsies reviewed by the neuropathologist may not reflect higher malignancy degrees in supplemental tumor regions, which may lead to underrating pathology reports^[5]. There is a low correlation between visible margins of tumoral areas on conventional MR images with the true areas of tumor infiltration^[5] this is due to microscopic invasion of white matter (WM) regions^[6,7], extending dozens of millimeters from conspicuous areas of viable tumor^[8].

Several combinations of the terms of the diagonalized diffusion tensor, that is, the eigenvalues λ_1 , λ_2 , and λ_3 , have been reported as scalar measures of diffusion, such as: fractional (FA) and relative anisotropy (RA); pure isotropic (p) and anisotropic diffusions (q), total magnitude of diffusion (L); linear (CI), planar (Cp) and spherical tensors (Cs); mean (MD), axial (AD) and radial (RD) diffusivities^[2,3,9-11]; Table 1. However, to best of our knowledge, there is currently neither a clear understanding of the expected measurements among these variables, nor existing studies reporting their correlations; likewise there is a lack of consensus about which of the tensor metrics available should be used in the evaluation of brain tumors.

In this study we (1) used a global approach, that is, a single measure of the whole brain for each metric aimed to determine the normal limits (magnitudes) of previously reported DTI-derived tensor metrics in healthy brains and brains of patients with glioblastoma multiforme (GBM); (2) assessed the statistical significance between DTI values in these groups; and (3) analyzed the DTI-metrics correlates considering the influence of clinical diagnosis (healthy *vs* GBM brains).

MATERIALS AND METHODS

Subjects

Case-control study design; inclusion criteria considered preoperative brain MR examinations between January 2010 and September 2012 of patients with at first (suspected) diagnosis and later pathology confirmation of astrocytoma grade IV, GBM according to the World Health Organization. Exclusion criteria applied to corticosteroid or antibiotic treatment, lesions with areas

Table 1 Diffusion tensor imaging-derived tensor metric formulas

MD
$MD = D = (\lambda_1 + \lambda_2 + \lambda_3)/3$
FA
$FA = [(3/2) \times (q/L)]^{1/2}$
$= (3/2)^{1/2} \{[(\lambda_1 - D)^2 + (\lambda_2 - D)^2 + (\lambda_3 - D)^2] / (\lambda_1^2 + \lambda_2^2 + \lambda_3^2)\}^{1/2}$
RA
$RA = q/p = \{[(\lambda_1 - D)^2 + (\lambda_2 - D)^2 + (\lambda_3 - D)^2]^{1/2} / [3^{1/2}D]\}$
RD
$RD = (\lambda_2 + \lambda_3)/2$
AD
$AD = \lambda_1$
Cs
$Cs = 3\lambda_3 / (\lambda_1 + \lambda_2 + \lambda_3)$
p
$p = 3^{1/2}D = (\lambda_1 + \lambda_2 + \lambda_3)/3^{1/2}$
q
$q = [(\lambda_1 - D)^2 + (\lambda_2 - D)^2 + (\lambda_3 - D)^2]^{1/2}$
L
$L = (p^2 + q^2)^{1/2} = (\lambda_1^2 + \lambda_2^2 + \lambda_3^2)^{1/2}$
Cl
$Cl = (\lambda_1 - \lambda_2) / (\lambda_1 + \lambda_2 + \lambda_3)$
Cp
$Cp = 2(\lambda_2 - \lambda_3) / (\lambda_1 + \lambda_2 + \lambda_3)$

MD: Mean diffusivity; FA: Fractional anisotropy; RA: Relative anisotropy; RD: Radial diffusivity; AD: Axial diffusivity; Cs: Spherical tensor; p: Pure isotropic diffusion; q: Pure anisotropic diffusion; L: Total magnitude of the diffusion tensor; Cl: Linear tensor; Cp: Planar tensor.

related to calcification and/or haemorrhage and previous brain surgery. A control group included young and elderly healthy volunteers recruited among the enrolled interns and medical residents of the hospital as well as elderly subjects from our Geriatric unit. All volunteers received detailed health examinations; exclusion criteria considered major neurological, psychiatric, or cardiovascular diseases. A radiologist interpreted the MR images blinded to the patient's history. MR examinations with other structural abnormalities were excluded. The local Institutional Review Boards approved the study (Project #2011.044), patients and also volunteers gave "informed consent".

Brain image acquisition

MR sequences included conventional axial T₂-w imaging, axial FLAIR, axial SPGR, DWI and axial T₁-w imaging, using 0.1 mmol/kg of Magnevist (Schering, Berlin, Germany); healthy volunteers did not received endogenous contrast. DTI was performed using a SS SE EPI sequence. DTI sequence was acquired with 25 directions, a b-value of 1000 s/mm² and with b-value of 0 s/mm²; axial plane included 40 contiguous slices with 2.4 mm thickness, no intersection gap, TR 17000, TE 80 ms, with parallel imaging to reduce off-resonance artifacts (PI factor was 2); FOV 25 cm × 25 cm, and matrix size 128 × 128. Images were acquired using a 3T clinical scanner (GE Healthcare, HDxt Signa, Waukesha, WI, United States); and a 8-channels head coil (Invivo,

Gainesville city, Florida).

Image postprocessing and data analysis

The methodology for calculation of global DTI-derived tensor metrics has been recently described^[4]; each one of the eleven metrics in this study (Cl, Cp, Cs, RA, AD, RD, MD, FA, p, q, L) represent a single global measure of a whole-brain taking into account the higher (λ_1), medium (λ_2), and lower (λ_3) eigenvalues of DTI^[12].

Statistical analysis

Sample size: With the intention to run a Mancova analysis to investigate whether mean differences between healthy brains and brains of patients with GBM (combining different variables) occurred randomly, we followed Pallant's recommendation for sample size^[13], the absolute minimum of cases to have in each cell must equal at least the number of dependent variables; in our study, we had twenty-two cells (two levels of our independent variable: healthy brains/brains with GBM, and eleven dependent variables for each). The study was run in 34 controls and 27 patients; this numbers also follow the recommendation of Tabachnick and Fidell^[14], for whom a minimum of 20 cases in each cell should ensure a "robustness" analysis. Assumptions testing included normality, multicollinearity and homogeneity tests^[13,15]. We performed a partial correlation analysis to calculate association values between each pair of parameters. Considering the age range and the gender of the subjects in our study, this method allowed us to calculate correlations among tensor metrics without the effect of age and gender; independent analyses were carried out for each group (healthy brains vs brains with GBM). Each correlation coefficient was interpreted as very strong (at least of 0.8), moderately strong (0.6 up to 0.8), fair (0.3 up to 0.6) and poor (less than 0.3). Squaring *r*-values represented the coefficient of determination, the proportion of variance that each two compared variables had in common^[16]. We additionally tested the statistical significance of the difference between *r* coefficients from both groups by converting each pair of *r*-values into a standard *z* scores, then using the formula proposed by Pallant^[17]: Observed *Z* value ≤ -1.96 or ≥ 1.96 were considered statistically significantly different.

A two-way Mancova identified diagnosis and gender differences in tensor metrics measurements^[18]. The eleven tensor-metrics represented the dependent variables used; independent variables were the diagnosis and gender; the effect of age was controlled. The effect size was obtained using the Eta squared value^[19]: 0.01 to 0.06 represents small effect, 0.06 to 0.14 medium and > 0.14 shows a large effect^[20]. A *P*-value < 0.05 depicted a significant difference.

Software: All analyses were carried out using the IBM® SPSS® Statistics software (version 22.0.0.0 IBM Corporation; Armonk, NY).

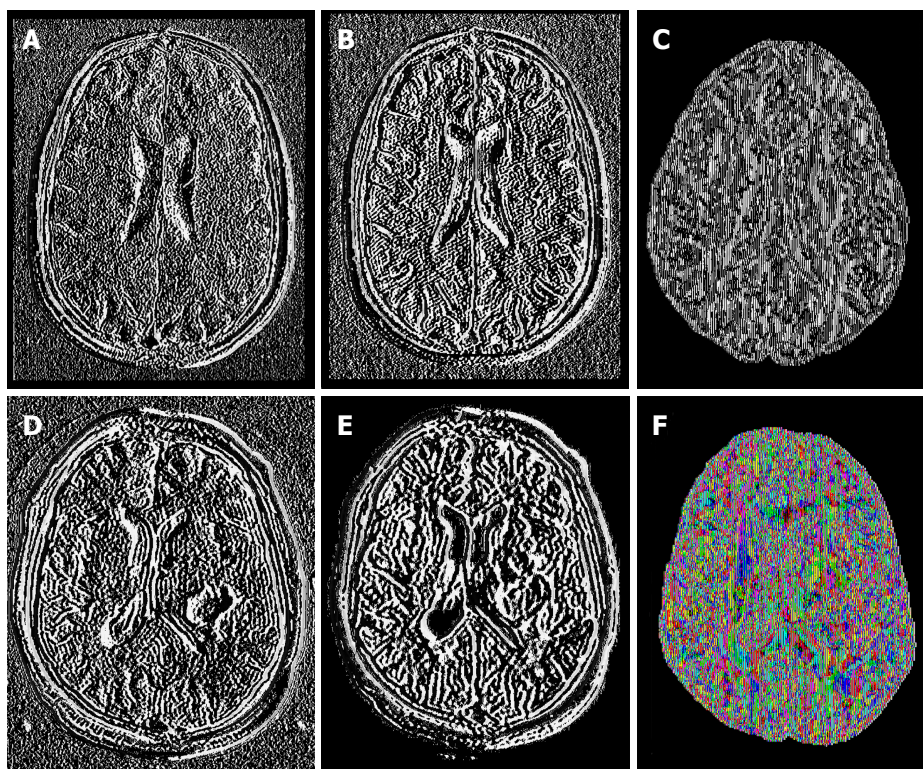


Figure 1 Example of some sequences and diffusion tensor imaging maps from healthy brains (upper row) and brains with glioblastoma multiforme (lower row): T1-postgadolinium images (A and D), Flair sequence (B and E); pure isotropic diffusion (C), color map of the V1-vector (F).

RESULTS

Demographic data and quantitative DTI tensor maps

The study was conducted in 61 subjects; 27 patients: 13 females (mean age 50.0 ± 15.4 years, range 31-73 years) and 14 males (mean age 46.93 ± 15.4 years, range 18-78 years); and 34 controls: 26 females (mean age 41.04 ± 22.3 years, range 21-80 years) and 8 males (mean age 42.88 ± 21.89 years, range 24-72 years). Tensor maps generated using the FSL software, added up to 671 tensor-metrics measurements. Figure 1 shows an example of some of the MR sequences and tensor-metric maps included in the data analyses.

Normality tests, magnitudes of means and SD

There was a normal distribution for all metrics. In order to understand the corresponding magnitudes of each DTI biomarker (previously not reported), we counted the number of decimal places to the right of the decimal point: five tensor metrics reported mean values within the tenths place: Cs, FA, RA, Cp and Cl; none tensor measurement fell in the hundredths place; five tensors values fell in the thousandths place: L, p, AD, MD and RD; and one tensor metrics had values in the ten thousandths place: q. Table 2 shows the means and SD ordered by descending means.

Partial correlation analyses

A scatterplot for each group showed no serious violation of the assumptions of linearity, homoscedasticity, and

outliers (Figure 2). In healthy brains, significant very strong bivariate correlations were observed for: [Cs↔RA (-)], [Cs↔Cp (-)], [Cs↔L (-)], [RA↔Cp (+)], [RA↔Cl (+)], [Cp↔Cl (+)], [L↔p (+)], [L↔AD (+)], [L↔MD (+)], [L↔RD (+)], [p↔MD (+)], [p↔RD (+)] and [MD↔RD (+)]; and moderately strong significant correlations were calculated for: [FA↔q (+)], [p↔AD (+)], [AD↔MD (+)] and [AD↔RD (+)].

In brains with GBM, the corresponding significant very strong bivariate correlations included: [Cs↔RA (-)], [Cs↔Cp (-)], [Cs↔L (-)], [FA↔Cl (+)], [FA↔q (+)], [RA↔Cp (+)], [RA↔Cl (+)], [Cp↔Cl (+)], [L↔p (+)], [L↔AD (+)], [L↔MD (+)], [p↔AD (+)], [p↔MD (+)], [p↔RD (+)], [AD↔MD (+)], and [MD↔RD (+)]; the moderately strong significant correlations were observed in: [Cl↔q (+)], [AD↔RD (+)] and [AD↔q (+)]. Table 3 present the correlations among the global tensor-metrics controlled for the effect of age and gender.

From the 55 pairs of bivariate correlations in each a group, statistical significances of the difference between r coefficients were observed in only seven pairs of variables: [Cs↔Cp], [FA↔Cl], [FA↔q], [RA↔q], [C↔q], [L↔p] and [L↔MD].

Mancova analysis

After adjusting for age, there was not interaction effect between the gender and clinical diagnosis [$F(11, 23) = 1.115$, $P = 0.394$]. There was not main affect of gender [$F(11, 23) = 2.060$, $P = 0.069$]; however, the main effect of diagnosis was statistically significant [$F(11, 23)$

Table 2 Means, SD and correlations (controlled for the effect of age and gender) in healthy brains

Tensor metric												Mean	SD
FA	Pearson's R	Cs										0.756690	0.032259
	P-value	FA										0.284317	0.018917
RA	Pearson's R	FA										0.224873	0.029523
	P-value	RA											
Cp	Pearson's R	RA										0.133346	0.017086
	P-value	Cp											
Cl	Pearson's R	Cp										0.111574	0.016583
	P-value	Cl											
L	Pearson's R	L										0.002275	0.000100
	P-value	L											
p	Pearson's R	p										0.002096	0.000087
	P-value	p											
AD	Pearson's R	AD										0.001553	0.000056
	P-value	AD											
MD	Pearson's R	MD										0.001210	0.000050
	P-value	MD											
RD	Pearson's R	RD										0.001046	0.000072
	P-value	RD											
q	Pearson's R	q										0.000445	0.000055
	P-value	q											

FA: Fractional anisotropy; RA: Relative anisotropy; Cp: Planar tensor; p: Pure isotropic diffusion; q: Pure anisotropic diffusion; L: Total magnitude of the diffusion tensor; Cl: Linear tensor; MD: Mean diffusivity; RD: Radial diffusivity; AD: Axial diffusivity.

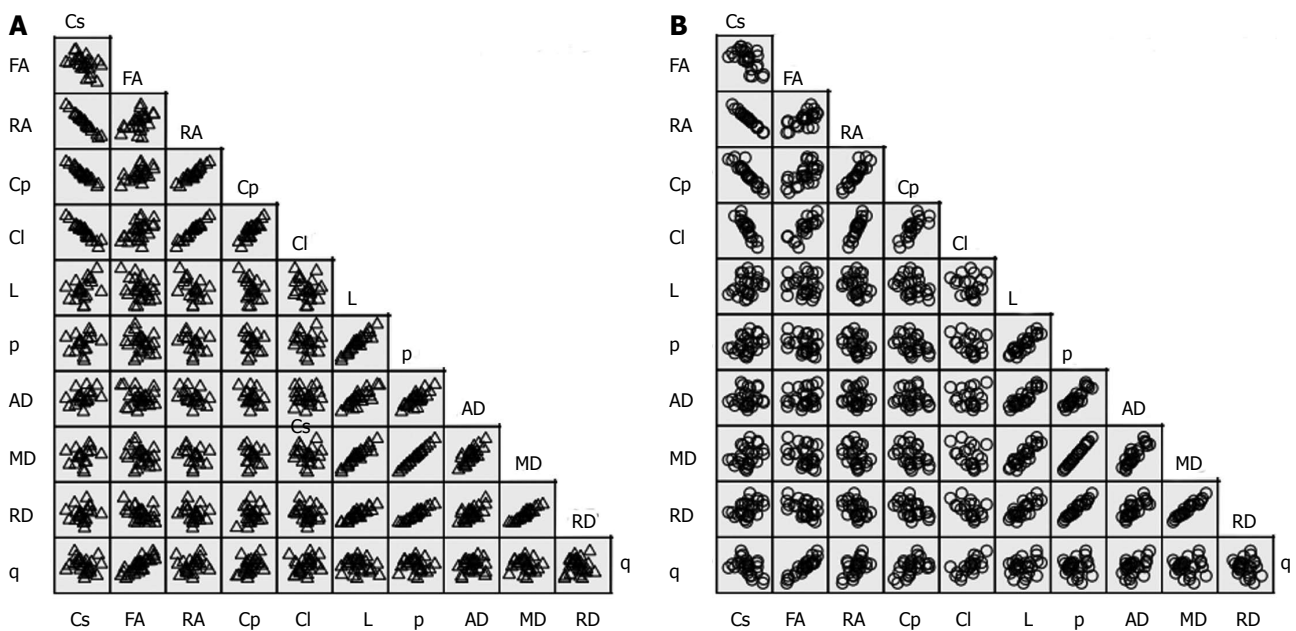


Figure 2 Scatter matrix of the variable's data grouped by diagnosis. A: Normal brains; B: Brains with GBM. MD: Mean diffusivity; FA: Fractional anisotropy; RA: Relative anisotropy; RD: Radial diffusivity; AD: Axial diffusivity; Cs: Spherical tensor; p: Pure isotropic diffusion; q: Pure anisotropic diffusion; L: Total magnitude of the diffusion tensor; Cl: Linear tensor; Cp: Planar tensor; GBM: Glioblastoma multiforme.

= 11.842, $P < 0.001$], corresponding to a large effect size (partial $\eta^2 = 0.850$). The age also had a significant influence as a covariate [$F(11, 23) = 10.523$, $P < 0.001$], and large effect size (partial $\eta^2 = 0.834$). Table 4 and Figure 3 depict the estimated marginal means; the age was controlled at the value of 43.92 years.

DISCUSSION

It is still not completely understood a priori which are the

magnitudes and associations among DTI measurements observed in the evaluation of brain tumors^[9]. The clinical relevance of these associations has been supported by several studies in the MR-DTI literature: Cs, Cp, Cl, FA and MD, have been related with brain abscesses, GBM and brain metastasis^[2]; p, q and L measurements have also been previously applied to the evaluation of GBM and brain metastasis^[3,21]; AD has been reported in encephalomyelitis of the spinal cord^[22], AD and RD have been correlated with brain development^[23], infantile

Table 3 Means, SD and correlations (controlled for the effect of age and gender) in brains with glioblastoma multiforme

Tensor metric										Mean	SD
FA	Pearson's R	Cs	-0.570							0.771562	0.066812
	P-value		0.003	FA						0.253531	0.028425
RA	Pearson's R	-1.000	0.592							0.201778	0.053287
	P-value	0.000	0.002	RA							
Cp	Pearson's R	-0.936	0.576	0.901						0.133265	0.043503
	P-value	0.000	0.003	0.000	Cp						
CI	Pearson's R	-0.904	0.819	0.969	0.803					0.098462	0.011929
	P-value	0.000	0.000	0.000	0.000	CI					
L	Pearson's R	0.096	0.151	0.009	-0.159	0.182				0.002111	0.000140
	P-value	0.648	0.472	0.967	0.446	0.469	L				
p	Pearson's R	0.156	-0.129	-0.094	-0.216	-0.177	0.834			0.001961	0.000123
	P-value	0.456	0.540	0.664	0.299	0.482	0.000	p			
AD	Pearson's R	-0.111	0.343	0.191	0.053	0.173	0.871	0.881		0.001397	0.000080
	P-value	0.596	0.094	0.372	0.803	0.492	0.000	0.000	AD		
MD	Pearson's R	0.154	-0.125	-0.090	-0.215	-0.173	0.837	1.000	0.883	0.001132	0.000071
	P-value	0.462	0.550	0.675	0.303	0.491	0.000	0.000	0.000	MD	
RD	Pearson's R	0.305	-0.411	-0.260	-0.360	-0.395	0.706	0.954	0.699	0.953	0.000999
	P-value	0.139	0.041	0.219	0.077	0.105	0.000	0.000	0.000	0.000	RD
q	Pearson's R	-0.484	0.928	0.539	0.466	0.736	0.430	0.187	0.629	0.191	-0.114
	P-value	0.014	0.000	0.007	0.019	0.001	0.032	0.371	0.001	0.361	0.588

MD: Mean diffusivity; FA: Fractional anisotropy; RA: Relative anisotropy; RD: Radial diffusivity; AD: Axial diffusivity; Cs: Spherical tensor; p: Pure isotropic diffusion; q: Pure anisotropic diffusion; L: Total magnitude of the diffusion tensor; CI: Linear tensor; Cp: Planar tensor.

Table 4 Estimated marginal means SE and CI of diffusion tensor imaging-derived tensor metrics (the effect of age was controlled at the value of 43.92 yr)

Tensor metric	Healthy brains				Brains with GBM			
	Mean	SE	95%CI		Mean	SE	95%CI	
			Lower	Upper			Lower	Upper
Cs	0.739511	0.009798	0.719577	0.759446	0.766043	0.007824	0.750126	0.781960
FA	0.290160	0.005721	0.278520	0.301799	0.255660	0.004568	0.246366	0.264954
RA	0.241025	0.008008	0.224734	0.257317	0.211498	0.006394	0.198490	0.224506
Cp	0.141366	0.007941	0.125210	0.157522	0.137961	0.006341	0.125061	0.150860
CI	0.119041	0.003243	0.112443	0.125638	0.099495	0.002589	0.094227	0.104763
L	0.002287	0.000029	0.002227	0.002347	0.002103	0.000024	0.002055	0.002151
p	0.002122	0.000027	0.002068	0.002177	0.001946	0.000021	0.001903	0.001990
AD	0.001558	0.000020	0.001518	0.001598	0.001395	0.000016	0.001363	0.001426
MD	0.001225	0.000015	0.001194	0.001257	0.001124	0.000012	0.001099	0.001149
RD	0.001059	0.000015	0.001029	0.001089	0.000988	0.000012	0.000964	0.001012
q	0.000454	0.000011	0.000432	0.000476	0.000371	0.000009	0.000354	0.000389

MD: Mean diffusivity; FA: Fractional anisotropy; RA: Relative anisotropy; RD: Radial diffusivity; AD: Axial diffusivity; Cs: Spherical tensor; p: Pure isotropic diffusion; q: Pure anisotropic diffusion; L: Total magnitude of the diffusion tensor; CI: Linear tensor; Cp: Planar tensor; GBM: Glioblastoma multiforme.

spasm^[24], amyotrophic lateral sclerosis^[25], schizophrenia^[26], and brain tumors^[27]; with only one recent study integrating a tumor-region diagnostic evaluation of 11 DTI-metrics^[4]. MD is understood as a synonym of the coefficient of diffusion in different space guidelines^[28]. FA measures the directional movement of water molecules in the brain^[29], it is an index of anisotropic diffusivity reflecting the integrity of myelinated axons^[30].

One advantage of using a global approach is that not the only the size of the viable tumor is included (enhanced regions with Gadolinium), but also the non-apparent regions that undergo microscopic infiltration (edema and increased-size regions). Additionally, by using a global approach, all the inhomogeneity nature

of GBM is included in a global measurement, a situation missed in a regional approach.

Some interesting associations are worthy to be noted: for example, there is no consensus of normal parameters between fractional anisotropy and mean diffusivity in a day-to-day basis^[3]; traditionally, MD and FA showed negative correlation with increased MD and decreased FA in high signal-intensity perilesional regions when compared with normal axonal areas^[31]; we observed a poor-negative non-significant correlation when controlling the effect of age and gender. One explanation might be that, different to MD that quantifies the degree of water molecules motion which is independent of myelinated axons; FA directly measures

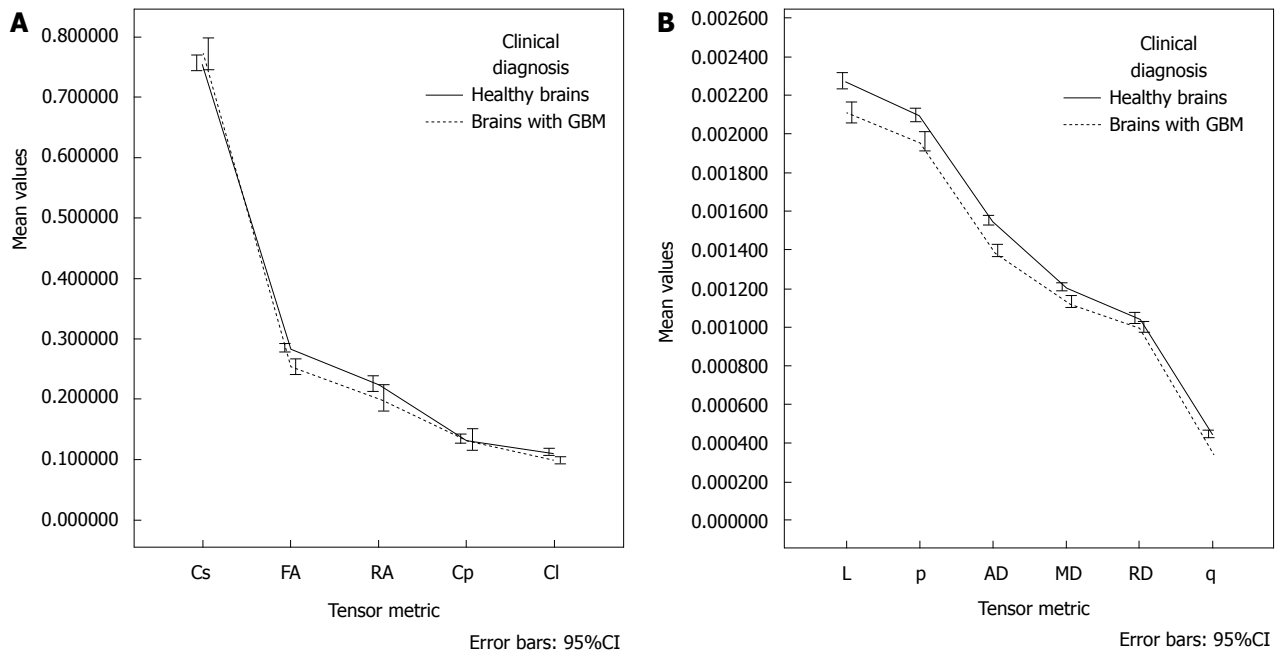


Figure 3 Graphs of the estimated marginal means for each tensor metric, the influence of age was controlled at the value of 43.92 years. MD: Mean diffusivity; FA: Fractional anisotropy; RA: Relative anisotropy; RD: Radial diffusivity; AD: Axial diffusivity; p: Pure isotropic diffusion; q: Pure anisotropic diffusion; L: Total magnitude of the diffusion tensor; Cl: Linear tensor; Cp: Planar tensor; GBM: Glioblastoma multiforme.

movement of water molecules along myelinated axons, it is a weighted anisotropic diffusion average^[10]. The absence of partial correlation analyses in previous reports could explain some conflicts of diffusivity and anisotropy values characterizing tumoral regions^[3,32]. For MD, the highest-significant correlation ($r = 1$) was observed with p and RD, a positive correlation between RD and MD have been previously observed in human brains^[33]. We found an inverse relationship between MD with Cp, which seems opposite to previously suggested direction measuring MD, FA and the shape tensor metrics (Cp, Cs, Cl) between tumoral brain tissue, metastasis and abscesses^[2]. FA's mechanisms of decreasing its value in brain tumors are still unclear: it might represent neuronal and axonal infiltration with widening of extracellular space^[32]; or tumoral substitution with decrement of extracellular space (this would explain the negative association between fractional anisotropy and tumoral cells)^[34]. The FA can also be calculated by dividing q over L^[9]; the q parameter could depict a comprehensive profile of brain tumor activity, in our study this parameter showed the highest-significant strength of correlation with FA ($r = 0.928$) in brains with GBM, it would seem an expected finding from its formula (ratio of q/L); however, our findings differ from other authors who observed no significant changes of q measurements in metastatic regions; this finding suggests that L instead of q, might be the main factor influencing the variability of FA. The inverse correlation between FA and RD observed in our study had been reported^[33], although there are not statements of the expected magnitudes among these correlations.

For most of the correlates observed in this study, there was a decrease in the strength of the linear

relationship after controlling the effect of age and gender. Poor correlations should be interpreted cautiously; in clinical settings these measurements might have the physiological implication to represent independent biological biomarkers. We do not have an explanation for the differences in the strength and directions of the observed correlations between normal and GBM brains, it is possible that the detailed info from the tumor may be obscured by the global measurement; the gender variable neither had interaction nor main effect in the observed measurements of DTI metrics; however, age did have a significant effect that should be controlled by researchers, as this variable could affect the p-value of the results.

As we mentioned in the results, there were some very strong, significant correlations observed only in brains with GBM (despite we use a global approach): [FA ↔ Cl (+)], [FA ↔ q (+)], [p ↔ AD (+)], [D ↔ MD (+)], and [MD ↔ RD (+)]; these findings were an indicator for us that, these parameters might be among the most useful for clinical diagnosis and/or treatment planning.

Comparing healthy brains vs brains with GBM, there were significant very strong bivariate correlations only depicted in GBM: [FA ↔ Cl (+)], [FA ↔ q (+)], [p ↔ AD (+)], [D ↔ MD (+)], and [MD ↔ RD (+)].

Our data might represent useful information for radiologist and/or bio imaging researchers trying to explain the relationships between tensor metrics to clinicians (neurologists, neurosurgeons, psychiatrist, neuro-oncologists, *etc.*) as well as in the preparation of prospective studies with clinical application. Further studies should address the significant differences we found in the correlations between healthy brains and brains with GBM, none of these results have been

previously reported. It will be interesting to know the data analyses from other research groups that help validate and support the clinical significance of the results presented in this study.

Several limitations in our study and factors that influence the clinical application of DTI-metrics need to be addressed: our decision to evaluate a single, global measure for each tensor-metric relationships came up from reports depicting absence of $P < 0.05$ differences in fractional anisotropy between enhanced and not enhanced tumoral areas^[35]; not significant differences between FA and MD measurements in tumor regions with distinct T₂-w signal-intensities^[36], and findings of increased variability of FA measurements among diverse brain areas^[3], making all them a patent lack of agreement between investigators. Also, some studies have evaluated only selected ROIs within the tumors, missing major components of viable tumor and perilesional infiltration zones; other studies reporting ROIs only of the whole viable tumor mass, excluded many times peritumoral regions, wasting the opportunity to identify areas of severe infiltration within axons^[3].

Although conventional sequences for the evaluation of GBM include the use of contrast enhancement agents (gadolinium), two situations could be observed in the managing assessment of these tumors: some regions of GBM could not depict enhancement because the tumor has not damaged enough the blood brain barrier, and second, there might be patients not able to receive gadolinium because chronic kidney failure; in both cases a global measurement of brain tissue would take into account non-evident abnormalities of the brain architecture.

Nowadays, there is still scarce evidence regarding the potential of these DTI biomarkers, for example, besides the clinical acceptance of FA; some studies have showed a significant increment of p (mean 68%) with evident decrement of q (mean 42%) in infiltrated axons^[37]. Also, some proved parameters, for example, the increase of RD as a marker of demyelination and axonal loss has not had generalization in its use^[33]. These facts reflect the limited acceptance of DTI by the medical community; it has not attained the same anatomic validation of structural myelin studies and so far does not discriminate individual tracts or complex functional linkages among synapses^[38]. DTI-derived tensor metrics intricacies to characterize brain tissue in health and disease might be affected among other variables by the quotient of extracellular to intracellular compartments; blood vessels density, abnormal accumulation of fluid in the interstitium, microscopic cysts, and the extracellular meshwork of proteins and carbohydrates that binds cells together^[39]. The clinical value of our findings has yet to be determined, and the biological impact of the different metrics should be explained in more detail in clinical journals.

In conclusion, a comprehensive understanding of the currently available DTI-derived parameters will help researchers in the decision of which one to include in

the diagnosis and treatment planning of brain tumors, researchers could know a priori expected relationships in a prospective analysis decreasing the underlying empiricism in this area. It is possible that several tensor metrics answer different questions; also, variations in DTI measures are not specific of one histologic type of tumor, which broaden the application of these biomarkers to a wider variety of intracranial pathologies. Given the increased availability of open source software in MRI units around the world, it is anticipated that measurements of DTI-derived tensor metrics may become a low-cost and common used approach.

COMMENTS

Background

In the last decade, advanced magnetic resonance techniques have adopted the use of diffusion tensor imaging (DTI)-derived metrics in the evaluation of glioblastoma multiforme. However, to best of our knowledge, there is currently neither a clear understanding of the expected measurements among these variables, nor existing studies reporting their correlations; likewise there is a lack of consensus about which of the tensor metrics available should be used in the evaluation of brain tumors.

Research frontiers

This study reports measurement of eleven DTI-derived tensor metrics which have only recently been described in the literature: fractional (FA) and relative anisotropy (RA); pure isotropic (p) and anisotropic diffusions (q), total magnitude of diffusion (L); linear (Cl), planar (Cp) and spherical tensors (Cs); mean (MD), axial (AD) and radial (RD) diffusivities.

Innovations and breakthroughs

Compared with previous studies, this report provides novel quantitative data of DTI-derived metrics in normal brains and brain with glioblastoma multiforme, its main aim is to decrease the underlying empiricism involving these parameters. Additionally, innovation is depicted in the use of a global approach (whole-brain) instead of the conventional tumor-region assessment; this approach warrants the inclusion of all tumor regions (ROIs measurements in the cystic cavity, enhancing rim, edema, and normal-appearing white matter regions).

Applications

Data in this study might represent useful information for radiologist and/or bio imaging researchers trying to explain the relationships between tensor metrics to clinicians (neurologists, neurosurgeons, psychiatrist, neuro-oncologists, etc.) as well as in the preparation of prospective studies with clinical application. The authors believed that the very strong, significant correlations observed only in brains with glioblastoma multiforme (GBM) (despite the authors use a global approach): [FA↔Cl (+)], [FA↔q (+)], [p↔AD (+)], [D↔MD (+)], and [MD↔RD (+)]; might be among the most useful parameters for clinical in diagnosis and/or treatment planning. Furthermore, the gender variable neither had interaction nor main effect in the observed measurements of DTI metrics; however, age did have a significant effect that should be controlled by researchers, as this variable could affect the *P*-value of the results. One advantage of using a global approach is that not the only the size of the viable tumor is included (enhanced regions with Gadolinium), but also the non-apparent regions that undergo microscopic infiltration (edema and increased-size regions). As this DTI-derived metrics do not require the use of a contrast agent (gadolinium), the proposed global approach takes into account non-evident abnormalities of the brain architecture which occurs in some regions of GBM without enhancement because the tumor has not damaged enough the blood brain barrier, and also, this approach can be used in patients not able to receive gadolinium because chronic kidney failure.

Terminology

The DTI-derived metrics reported in this study were calculated from the below

described formulas:

$$MD = D = (\lambda_1 + \lambda_2 + \lambda_3)/3$$

$$FA = [(3/2)(q/L)]^{1/2} = (3/2)^{1/2} \{[(\lambda_1 - D)^2 + (\lambda_2 - D)^2 + (\lambda_3 - D)^2]/(\lambda_1^2 + \lambda_2^2 + \lambda_3^2)\}^{1/2}$$

$$RA = q/p = \{[(\lambda_1 - D)^2 + (\lambda_2 - D)^2 + (\lambda_3 - D)^2]^{1/2}/[3^{1/2}D]\}$$

$$RD = (\lambda_2 + \lambda_3)/2$$

$$AD = \lambda_1$$

$$Cs = 3\lambda_3/(\lambda_1 + \lambda_2 + \lambda_3)$$

Pure Isotropic Diffusion (p)

$$p = 3^{1/2}D = (\lambda_1 + \lambda_2 + \lambda_3)/3^{1/2}$$

Pure Anisotropic Diffusion (q)

$$q = [(\lambda_1 - D)^2 + (\lambda_2 - D)^2 + (\lambda_3 - D)^2]^{1/2}$$

Total Magnitude of the Diffusion Tensor (L)

$$L = (p^2 + q^2)^{1/2} = (\lambda_1^2 + \lambda_2^2 + \lambda_3^2)^{1/2}$$

Linear Tensor (Cl)

$$Cl = (\lambda_1 - \lambda_2)/(\lambda_1 + \lambda_2 + \lambda_3)$$

Planar Tensor (Cp)

$$Cp = 2(\lambda_2 - \lambda_3)/(\lambda_1 + \lambda_2 + \lambda_3)$$

Peer-review

The authors studied the relationships of 11 DTI-derived tensor metrics between healthy brains and brains with GBM. They used a novel technique, *i.e.*, a single global measure of the whole brain for each metric rather than a conventional approach of measuring the entire tumor or some regions.

REFERENCES

- 1 **Young GS.** Advanced MRI of adult brain tumors. *Neurol Clin* 2007; **25**: 947-973, viii [PMID: 17964022 DOI: 10.1016/j.ncl.2007.07.010]
- 2 **Toh CH, Wei KC, Ng SH, Wan YL, Lin CP, Castillo M.** Differentiation of brain abscesses from necrotic glioblastomas and cystic metastatic brain tumors with diffusion tensor imaging. *AJNR Am J Neuroradiol* 2011; **32**: 1646-1651 [PMID: 21835939 DOI: 10.3174/ajnr.A2581]
- 3 **Wang W, Steward CE, Desmond PM.** Diffusion tensor imaging in glioblastoma multiforme and brain metastases: the role of p, q, L, and fractional anisotropy. *AJNR Am J Neuroradiol* 2009; **30**: 203-208 [PMID: 18842762 DOI: 10.3174/ajnr.A1303]
- 4 **Roldan-Valadez E, Rios C, Cortez-Conradis D, Favila R, Moreno-Jimenez S.** Global diffusion tensor imaging derived metrics differentiate glioblastoma multiforme vs. normal brains by using discriminant analysis: introduction of a novel whole-brain approach. *Radiol Oncol* 2014; **48**: 127-136 [PMID: 24991202 DOI: 10.2478/raon-2014-0004]
- 5 **Rees JH, Smirniotopoulos JG, Jones RV, Wong K.** Glioblastoma multiforme: radiologic-pathologic correlation. *Radiographics* 1996; **16**: 1413-1438; quiz 1462-1463 [PMID: 8946545]
- 6 **Scherer HJ.** A critical review: the pathology of cerebral gliomas. *J Neurol Psychiatry* 1940; **3**: 147-177 [PMID: 21610973]
- 7 **Johnson PC, Hunt SJ, Drayer BP.** Human cerebral gliomas: correlation of postmortem MR imaging and neuropathologic findings. *Radiology* 1989; **170**: 211-217 [PMID: 2535765]
- 8 **DeAngelis LM.** Brain tumors. *N Engl J Med* 2001; **344**: 114-123 [PMID: 11150363 DOI: 10.1056/NEJM200101113440207]
- 9 **Peña A, Green HA, Carpenter TA, Price SJ, Pickard JD, Gillard JH.** Enhanced visualization and quantification of magnetic resonance diffusion tensor imaging using the p: q tensor decomposition. *Br J Radiol* 2006; **79**: 101-109 [PMID: 16489190 DOI: 10.1259/bjr/24908512]
- 10 **Le Bihan D, Mangin JF, Poupon C, Clark CA, Pappata S, Molko N, Chabriat H.** Diffusion tensor imaging: concepts and applications. *J Magn Reson Imaging* 2001; **13**: 534-546 [PMID: 11276097]
- 11 **Koch K, Wagner G, Schachtzabel C, Schultz CC, Güllmar D, Reichenbach JR, Sauer H, Schlösser RG.** Neural activation and radial diffusivity in schizophrenia: combined fMRI and diffusion tensor imaging study. *Br J Psychiatry* 2011; **198**: 223-229 [PMID: 21357881 DOI: 10.1192/bjp.bp.110.081836]
- 12 **Tugcu B, Postalci LS, Gunaldi O, Tanriverdi O, Akdemir H.** Efficacy of clinical prognostic factors on survival in patients with glioblastoma. *Turk Neurosurg* 2010; **20**: 117-125 [PMID: 20401838 DOI: 10.5137/1019-5149.JTN.2461-09.4]
- 13 **Pallant J.** Multivariate analysis of variance. In: Pallant J, editor. *SPSS Survival Manual*. 4th ed. Crows Nest, NSW, Australia: Allen and Unwin, 2011: 283-296
- 14 **Tabachnick BG, Fidell LS.** Multivariate Normality. In: Tabachnick BG, Fidell LS, editors. *Using Multivariate Statistics*. 5th ed. 2007: 251
- 15 **Pallant J.** Assessing Normality. In: Pallant J, editor. *SPSS Survival Manual*. 4th ed. Crows Nest, NSW, Australia: Allen and Unwin, 2011: 59-64
- 16 **Chan YH.** Biostatistics 104: correlational analysis. *Singapore Med J* 2003; **44**: 614-619 [PMID: 14770254]
- 17 **Pallant J.** Testing the statistical significance of the difference between correlation coefficients. In: Pallant J, editor. *SPSS Survival Manual*. 4th ed. Crows Nest, NSW, Australia: Allen and Unwin, 2011: 139-141
- 18 **Pallant J.** Analysis of covariance. In: Pallant J, editor. *SPSS Survival Manual*. 4th ed. Crows Nest, NSW, Australia: Allen and Unwin, 2011: 297-318
- 19 **Pallant J.** Calculating effect size. In: Pallant J, editor. *SPSS Survival Manual*. 4th ed. Crows Nest, Australia: Allen and Unwin, 2011: 254-255
- 20 **Cohen JW.** Statistical power analysis for the behavioral sciences. 2nd ed. Hillsdale, NJ: Lawrence Erlbaum Associates, 1988: 284-287
- 21 **Price SJ, Jena R, Burnet NG, Hutchinson PJ, Dean AF, Peña A, Pickard JD, Carpenter TA, Gillard JH.** Improved delineation of glioma margins and regions of infiltration with the use of diffusion tensor imaging: an image-guided biopsy study. *AJNR Am J Neuroradiol* 2006; **27**: 1969-1974 [PMID: 17032877]
- 22 **Budde MD, Xie M, Cross AH, Song SK.** Axial diffusivity is the primary correlate of axonal injury in the experimental autoimmune encephalomyelitis spinal cord: a quantitative pixelwise analysis. *J Neurosci* 2009; **29**: 2805-2813 [PMID: 19261876 DOI: 10.1523/JNEUROSCI.4605-08.2009]
- 23 **Kumar R, Nguyen HD, Macey PM, Woo MA, Harper RM.** Regional brain axial and radial diffusivity changes during development. *J Neurosci Res* 2012; **90**: 346-355 [PMID: 21938736 DOI: 10.1002/jnr.22757]
- 24 **Simao GN, Zarei Mahmoodabadi S, Snead OC, Go C, Widjaja E.** Abnormal axial diffusivity in the deep gray nuclei and dorsal brain stem in infantile spasm treated with vigabatrin. *AJNR Am J Neuroradiol* 2011; **32**: 199-203 [PMID: 20801762 DOI: 10.3174/ajnr.A2224]
- 25 **Metwalli NS, Benatar M, Nair G, Usher S, Hu X, Carew JD.** Utility of axial and radial diffusivity from diffusion tensor MRI as markers of neurodegeneration in amyotrophic lateral sclerosis. *Brain Res* 2010; **1348**: 156-164 [PMID: 20513367 DOI: 10.1016/j.brainres.2010.05.067]
- 26 **Seal ML, Yücel M, Fornito A, Wood SJ, Harrison BJ, Walterfang M, Pell GS, Pantelis C.** Abnormal white matter microstructure in schizophrenia: a voxelwise analysis of axial and radial diffusivity. *Schizophr Res* 2008; **101**: 106-110 [PMID: 18262770 DOI: 10.1016/j.schres.2007.12.489]
- 27 **Chen F, Zhang X, Li M, Wang R, Wang HT, Zhu F, Lu DJ, Zhao H, Li JW, Xu Y, Zhu B, Zhang B.** Axial diffusivity and tensor shape as early markers to assess cerebral white matter damage caused by brain tumors using quantitative diffusion tensor tractography. *CNS Neurosci Ther* 2012; **18**: 667-673 [PMID: 22712656 DOI: 10.1111/j.1755-5949.2012.00354.x]
- 28 **Mori S, Barker PB.** Diffusion magnetic resonance imaging: its principle and applications. *Anat Rec* 1999; **257**: 102-109 [PMID: 10397783 DOI: 10.1002/(SICI)1097-0185(19990615)257:3<102::AID-AR7>3.0.CO;2-6]
- 29 **Lu S, Ahn D, Johnson G, Law M, Zagzag D, Grossman RI.** Diffusion-tensor MR imaging of intracranial neoplasia and associated peritumoral edema: introduction of the tumor infiltration index. *Radiology* 2004; **232**: 221-228 [PMID: 15220505 DOI: 10.1148/radiol.2321030653]

- 30 **Chenevert TL**, Brunberg JA, Pipe JG. Anisotropic diffusion in human white matter: demonstration with MR techniques in vivo. *Radiology* 1990; **177**: 401-405 [PMID: 2217776]
- 31 **Lu S**, Ahn D, Johnson G, Cha S. Peritumoral diffusion tensor imaging of high-grade gliomas and metastatic brain tumors. *AJNR Am J Neuroradiol* 2003; **24**: 937-941 [PMID: 12748097]
- 32 **Wieshmann UC**, Clark CA, Symms MR, Franconi F, Barker GJ, Shorvon SD. Reduced anisotropy of water diffusion in structural cerebral abnormalities demonstrated with diffusion tensor imaging. *Magn Reson Imaging* 1999; **17**: 1269-1274 [PMID: 10576712]
- 33 **Schmierer K**, Wheeler-Kingshott CA, Boulby PA, Scaravilli F, Altmann DR, Barker GJ, Tofts PS, Miller DH. Diffusion tensor imaging of post mortem multiple sclerosis brain. *Neuroimage* 2007; **35**: 467-477 [PMID: 17258908 DOI: 10.1016/j.neuroimage.2006.12.010]
- 34 **Stadlbauer A**, Ganslandt O, Buslei R, Hammen T, Gruber S, Moser E, Buchfelder M, Salomonowitz E, Nimsky C. Gliomas: histopathologic evaluation of changes in directionality and magnitude of water diffusion at diffusion-tensor MR imaging. *Radiology* 2006; **240**: 803-810 [PMID: 16926329 DOI: 10.1148/radiol.2403050937]
- 35 **Tsuchiya K**, Fujikawa A, Nakajima M, Honya K. Differentiation between solitary brain metastasis and high-grade glioma by diffusion tensor imaging. *Br J Radiol* 2005; **78**: 533-537 [PMID: 15900059 DOI: 10.1259/bjr/68749637]
- 36 **van Westen D**, Lätt J, Englund E, Brockstedt S, Larsson EM. Tumor extension in high-grade gliomas assessed with diffusion magnetic resonance imaging: values and lesion-to-brain ratios of apparent diffusion coefficient and fractional anisotropy. *Acta Radiol* 2006; **47**: 311-319 [PMID: 16613314]
- 37 **Price SJ**, Peña A, Burnet NG, Jena R, Green HA, Carpenter TA, Pickard JD, Gillard JH. Tissue signature characterisation of diffusion tensor abnormalities in cerebral gliomas. *Eur Radiol* 2004; **14**: 1909-1917 [PMID: 15221264 DOI: 10.1007/s00330-004-2381-6]
- 38 **Jones DK**. Studying connections in the living human brain with diffusion MRI. *Cortex* 2008; **44**: 936-952 [PMID: 18635164 DOI: 10.1016/j.cortex.2008.05.002]
- 39 **Brunberg JA**, Chenevert TL, McKeever PE, Ross DA, Junck LR, Muraszko KM, Dauser R, Pipe JG, Betley AT. In vivo MR determination of water diffusion coefficients and diffusion anisotropy: correlation with structural alteration in gliomas of the cerebral hemispheres. *AJNR Am J Neuroradiol* 1995; **16**: 361-371 [PMID: 7726086]

P- Reviewer: Chen F, Chu JP, Prakash N
S- Editor: Ji FF **L- Editor:** A **E- Editor:** Jiao XK



Observational Study

Pancreatic trauma: The role of computed tomography for guiding therapeutic approach

Marco Moschetta, Michele Telegrafo, Valeria Malagnino, Laura Mappa, Amato A Stabile Ianora, Dario Dabbicco, Antonio Margari, Giuseppe Angelelli

Marco Moschetta, Michele Telegrafo, Valeria Malagnino, Laura Mappa, Amato A Stabile Ianora, Giuseppe Angelelli, Interdisciplinary Department of Medicine, Section of Diagnostic Imaging, University of Bari Medical School, 70124 Bari, Italy

Dario Dabbicco, Antonio Margari, Department of Emergency and Organ Transplantation, University of Bari Medical School, 70124 Bari, Italy

Author contributions: Moschetta M, Telegrafo M, Malagnino V, Mappa L, Stabile Ianora AA, Dabbicco D, Margari A and Angelelli G contributed to study conception and design; Moschetta M, Telegrafo M and Malagnino V contributed to data acquisition, data analysis and interpretation, and writing of article; Moschetta M, Telegrafo M, Malagnino V, Mappa L, Stabile Ianora AA, Dabbicco D, Margari A and Angelelli G contributed to editing, reviewing and final approval of article.

Institutional review board statement: The study was approved by the local ethical committee.

Informed consent statement: Written informed consent for CT examinations was obtained in all cases.

Conflict-of-interest statement: All authors have no conflict of interests nor financial or personal relationships regarding this paper.

Data sharing statement: Patient data and full dataset are available from the corresponding author. The presented data are anonymised without the risk of identification.

Open-Access: This article is an open-access article which was selected by an in-house editor and fully peer-reviewed by external reviewers. It is distributed in accordance with the Creative Commons Attribution Non Commercial (CC BY-NC 4.0) license, which permits others to distribute, remix, adapt, build upon this work non-commercially, and license their derivative works on different terms, provided the original work is properly cited and the use is non-commercial. See: <http://creativecommons.org/licenses/by-nc/4.0/>

Correspondence to: Marco Moschetta, MD, Professor,

Interdisciplinary Department of Medicine, Section of Diagnostic Imaging, University of Bari Medical School, Piazza Giulio Cesare 11, 70124 Bari, Italy. marco.moschetta@gmail.com
 Telephone: +39-080-5478840
 Fax: +39-080-5592911

Received: May 14, 2015
 Peer-review started: May 19, 2015
 First decision: June 24, 2015
 Revised: September 10, 2015
 Accepted: October 12, 2015
 Article in press: October 13, 2015
 Published online: November 28, 2015

Abstract

AIM: To evaluate the role of computed tomography (CT) for diagnosing traumatic injuries of the pancreas and guiding the therapeutic approach.

METHODS: CT exams of 6740 patients admitted to our Emergency Department between May 2005 and January 2013 for abdominal trauma were retrospectively evaluated. Patients were identified through a search of our electronic archive system by using such terms as "pancreatic injury", "pancreatic contusion", "pancreatic laceration", "peri-pancreatic fluid", "pancreatic active bleeding". All CT examinations were performed before and after the intravenous injection of contrast material using a 16-slice multidetector row computed tomography scanner. The data sets were retrospectively analyzed by two radiologists in consensus searching for specific signs of pancreatic injury (parenchymal fracture and laceration, focal or diffuse pancreatic enlargement/edema, pancreatic hematoma, active bleeding, fluid between splenic vein and pancreas) and non-specific signs (inflammatory changes in peri-pancreatic fat and mesentery, fluid surrounding the superior mesenteric

artery, thickening of the left anterior renal fascia, pancreatic ductal dilatation, acute pseudocyst formation/peri-pancreatic fluid collection, fluid in the anterior and posterior pararenal spaces, fluid in transverse mesocolon and lesser sac, hemorrhage into peri-pancreatic fat, mesocolon and mesentery, extraperitoneal fluid, intra-peritoneal fluid).

RESULTS: One hundred and thirty-six/Six thousand seven hundred and forty (2%) patients showed CT signs of pancreatic trauma. Eight/one hundred and thirty-six (6%) patients underwent surgical treatment and the pancreatic injuries were confirmed in all cases. Only in 6/8 patients treated with surgical approach, pancreatic duct damage was suggested in the radiological reports and surgically confirmed in all cases. In 128/136 (94%) patients who underwent non-operative treatment CT images showed pancreatic edema in 97 patients, hematoma in 31 patients, fluid between splenic vein and pancreas in 113 patients. Non-specific CT signs of pancreatic injuries were represented by peri-pancreatic fat stranding and mesentery fluid in 89% of cases, thickening of the left anterior renal fascia in 65%, pancreatic ductal dilatation in 18%, acute pseudocyst/peri-pancreatic fluid collection in 57%, fluid in the pararenal spaces in 45%, fluid in transverse mesocolon and lesser sac in 29%, hemorrhage into peri-pancreatic fat, mesocolon and mesentery in 66%, extraperitoneal fluid in 66%, intra-peritoneal fluid in 41% cases.

CONCLUSION: CT represents an accurate tool for diagnosing pancreatic trauma, provides useful information to plan therapeutic approach with a detection rate of 75% for recognizing ductal lesions.

Key words: Trauma; Pancreas; Computed tomography; Imaging

© **The Author(s) 2015.** Published by Baishideng Publishing Group Inc. All rights reserved.

Core tip: Pancreatic trauma is associated with high morbidity and mortality especially in case of delayed diagnosis. Computed tomography (CT) represents an accurate imaging tool for recognizing direct and indirect signs of pancreatic trauma and provides useful information to plan therapeutic approach. Among the specific signs, the presence of fluid between the splenic vein and the pancreas represents the most common CT finding suggesting pancreatic injury and the potential of CT for detecting ductal lesions have improved as compared to previous studies, with a 75% detection rate.

Moschetta M, Telegrafo M, Malagnino V, Mappa L, Stabile Ianora AA, Dabbicco D, Margari A, Angelelli G. Pancreatic trauma: The role of computed tomography for guiding therapeutic approach. *World J Radiol* 2015; 7(11): 415-420 Available from: URL: <http://www.wjgnet.com/1949-8470/full/v7/i11/415.htm> DOI: <http://dx.doi.org/10.4329/wjcr.v7.i11.415>

INTRODUCTION

Pancreatic trauma incidence ranges between 0.2% and 12% and occurs mainly in penetrating injuries with higher prevalence in children and young adults^[1,2]. In case of blunt trauma, it is due to the impact of the organ against the adjacent vertebral column being the pancreatic body most commonly involved^[3-5].

In 90% of cases, pancreatic lesions are associated with traumatic injuries of other abdominal organs as liver, spleen, stomach and duodenum^[1,2].

Pancreatic trauma is associated with high morbidity and mortality especially in case of delayed diagnosis. In fact, the mortality ranges between 10% and 30% and is due to hemorrhagic lesions of the portal vein, splenic vein and inferior vena cava^[1,6-20]. The reported morbidity rate is about 30% and mainly associated with pancreatic duct damage, consisting of fistulas, recurrent pancreatitis, pseudocysts, abscess, blood collections, retroperitoneal bleeding and ductal stenosis^[6]. The diagnosis of early as late complications greatly increases the mortality rate which is mainly due to sepsis and multi-organ failure^[6]. Clinical symptoms and signs of pancreatic injuries are nonspecific and include fever, leukocytosis, and elevated serum amylase or lipase levels.

Computed tomography (CT) represents the imaging technique of choice in hemodynamically stable patients with abdominal trauma, with reported sensitivity and specificity values as high as 80% in detecting pancreatic injuries being able to establish the type and grading of the detected lesions^[8-14].

This study aims to evaluate the role of CT for diagnosing pancreatic injuries and guiding the choice of the therapeutic approach.

MATERIALS AND METHODS

Patients

CT exams of 6740 patients admitted to our Emergency Department between May 2005 and January 2013 for abdominal trauma were retrospectively evaluated. Patients were identified through a search of our electronic archive system by using such terms as "pancreatic injury", "pancreatic contusion", "pancreatic laceration", "peri-pancreatic fluid", "pancreatic active bleeding". The mean time between abdominal trauma and CT examination was about 1-2 h.

CT protocol

All patients were examined in an emergency setting. The CT scanner used was a 16-slice multidetector row CT (TSX - 101A - Aquilion 16, Toshiba Medical System, Tokyo, Japan). In all cases, scans were acquired before and after the intravenous injection of contrast material (120-140 mL injected at a rate of 3-3.5 mL/s), with image acquisition in the arterial phase, generally with a delay of 30-40 s from the beginning of contrast administration, in the portal venous phase, with a delay

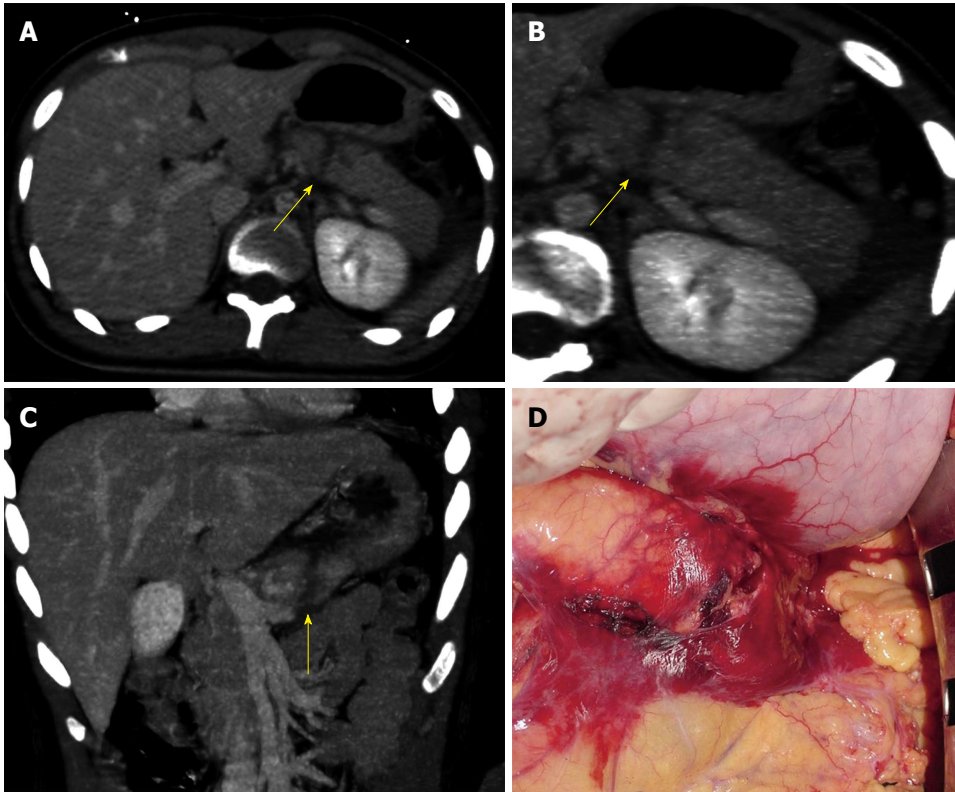


Figure 1 Computed tomography and intra-operative findings of pancreatic parenchymal fracture. A: CT image on axial plan showing a complete laceration of the pancreatic body appearing as a low-attenuation line oriented perpendicular to the long axis of the pancreas (arrow); B: CT image on axial plan showing a complete laceration of the pancreatic body appearing as a low-attenuation line oriented perpendicular to the long axis of the pancreas (arrow); C: CT image on coronal plan showing a complete laceration of the pancreatic body appearing as a low-attenuation line oriented perpendicular to the long axis of the pancreas (arrow); D: Intra-operative finding confirming the CT diagnosis of post-traumatic laceration of the pancreas. CT: Computed tomography.

of 60-90 s from the beginning of contrast-agent administration and in delayed phase with a delay of 120-180 s from the beginning of contrast-agent administration^[21].

Image interpretation

The data sets were retrospectively analyzed on a workstation (HP XW 6400) equipped with image reconstruction software (Vitrea 4.0, Vital Images, Minneapolis, MN, United States). Multi-planar, Maximum Intensity Projection and Minimum Intensity Projection reconstructions were used.

Two radiologists in consensus assessed all images. Post-processing duration time was approximately 15 min.

CT images were evaluated searching for specific signs of pancreatic injury: parenchymal fracture; laceration; pancreatic edema; hematoma; active bleeding; and fluid between splenic vein and pancreas.

On the other side, non-specific signs were also assessed: peri-pancreatic fat or mesentery stranding; mesenteric fluid; thickening of the left anterior renal fascia; pancreatic ductal dilatation; acute peri-pancreatic fluid collection; fluid in the pararenal spaces; fluid in transverse mesocolon and lesser sac; hemorrhage into peri-pancreatic fat, mesocolon and mesentery; extraperitoneal fluid; and intra-peritoneal fluid^[9,22]. Associated injuries to adjacent structures were also evaluated.

RESULTS

On the basis of CT findings, 136 out 6740 (2%) patients showed signs of traumatic injuries of the pancreas. In this group of patients, 90 patients were male and 46 were female with an average age of 45.4 ± 16.1 years (range: from 30 to 65 years old). Mechanism of injury was blunt motor vehicle collision in 70 patients, bicycle injury in 33, direct blow to the abdomen in 20, falls in 9 cases and sport related injury in 4 patients.

Eight out of 136 (6%) patients underwent surgical treatment within 8-12 h from the diagnosis and the pancreatic injuries were confirmed in all cases, represented by 3 cases of parenchymal fracture (Figure 1) and 5 of extensive lacerations. Pancreatic injuries involved the conjunction between the neck and the body of the pancreas in 4 cases. Three patients had pancreatic body injuries and one had pancreatic tail injury. A complete pancreatic fracture line was identified on CT images in all patients and was identified as a linear discontinuity of the glandular parenchyma extending from the anterior to the posterior surface.

In all patients, fluid between splenic vein and pancreas was found.

In 6 out 8 patients treated with surgical approach, pancreatic duct damage was suggested in the radiological reports and surgically confirmed in all cases. In the remaining 2 patients, CT did not suggest a ductal injury

but it was surgically detected.

One hundred and twenty-eight out of 136 (94%) patients underwent non-operative treatment and follow-up CT examination showed a resolution of the pathological findings. CT images showed pancreatic edema in 97 patients, hematoma in 31 patients, fluid between splenic vein and pancreas in 113 patients.

As regard with non-specific CT signs of pancreatic injuries, peri-pancreatic fat stranding and mesenteric fluid occurred in 122 out of 136 (89%) cases, thickening of the left anterior renal fascia in 88 out of 136 (65%), pancreatic ductal dilatation in 25 out of 136 (18%), acute pseudocyst/peri-pancreatic fluid collection in 78 out of 136 (57%), fluid in the pararenal spaces in 61 out of 136 (45%), fluid in transverse mesocolon and lesser sac in 40 out of 136 (29%), hemorrhage into peri-pancreatic fat, mesocolon and mesentery in 90 out of 136 (66%), extraperitoneal fluid in 90 out of 136 (66%), intra-peritoneal fluid in 56 out of 136 (41%) cases.

With regard to associated injuries to adjacent structures, in 27 out of 136 patients (20%) CT detected also extra-pancreatic findings represented by vertebral fracture ($n = 11$), liver contusion ($n = 6$), spleen contusion ($n = 4$), right kidney contusion ($n = 3$), small bowel injury ($n = 2$), left kidney contusion ($n = 1$).

DISCUSSION

CT represents the gold standard imaging technique for evaluating pancreatic trauma. Variable sensitivity and specificity values have been reported in the medical literature with an overall sensitivity in detecting all grades of pancreatic lesions of about 80%^[9]. The specific CT findings of pancreatic injury are represented by parenchymal contusion, laceration, hematoma, active extravasation of contrast medium and fracture. Contusions are defined as areas of diminished density without discontinuity at the surface of the gland, lacerations as low-attenuation lines perpendicular to the long axis of the pancreas and fractures as clear separations of parenchymal fragments^[9-11].

In our series specific CT signs of pancreatic trauma have been detected in all cases with the presence of fluid between the splenic vein and the pancreas being the most common and sensitive sign.

Lane *et al*^[12] reported that fluid between the splenic vein and the pancreas allows to identify a pancreatic trauma and it is detected in 90% of cases of pancreatic injury.

This data is also confirmed in our series. In fact, fluid between the splenic vein and the pancreas occurred in all cases treated with surgical approach and in 88% of patients treated conservatively, with an overall rate of 89% in our series.

On the other side, peri-pancreatic fat stranding, peri-pancreatic fluid collections represent the most common indirect CT signs of pancreatic trauma occurring in the 89% of cases in our series^[9-11].

The American Association for the Surgery of Trauma proposed a grading system mainly based on the site of pancreatic trauma and the integrity of the main pancreatic duct. In fact, a CT grading system has been established for supporting the surgical classification^[9,12-15]. Therefore, CT allows to establish a grading of pancreatic injuries by providing important information for management of the gland lesions. Grade I lesions include minor contusions or lacerations with no duct injury (less than 50% of the thickness pancreatic), Grade II major contusions or lacerations with no duct injury, Grade III transections or major lacerations with duct disruption in distal pancreas, Grade IV transections of proximal pancreas or major lacerations with associated injury to the ampulla of Vater, Grade V massive disruption of the pancreatic head. The lesions involving the pancreatic head have a mortality rate almost double (28%) as compared to the tail injuries (16%), because of the inferior vena cava, inferior mesenteric vein and portal vein involvement^[9,10,12-17].

Moreover, the most important prognostic factor is the destruction of the pancreatic duct which requires surgical or endoscopic treatment while the lesions which do not involve pancreatic duct can be treated by conservative treatment^[16,17]. The rupture of the pancreatic duct is reported to be poorly detectable with CT, even if parenchymal laceration affecting more than 50% of the thickness of the gland are associated with high risk of pancreatic duct damage^[18,19,23-25].

In fact, the main limitations of CT reported in the medical literature are represented by a low accuracy in detecting major ductal lesions which is reported to be about 43% and the underestimation of pancreatic injuries, especially in the first 12 h after the traumatic event. For this reason, a second CT examination is required within 24-48 h after admission in suspected pancreatic lesions in case of negative first CT^[1,9,13].

In fact, in patients with suspected pancreatic duct lesion magnetic resonance cholangiopancreatography (MRCP) or endoscopic retrograde colangiopancreatography (ERCP) are strongly suggested. The MRCP represents the gold standard in this cases and it is reported to have diagnostic accuracy of 100% for evaluating to evaluate pancreatic duct damage^[8]. However, ERCP allows direct imaging guided treatments. In fact, ERCP can guide surgical repair or can be used for stent placement. Many studies showed that mild pancreatic duct injuries may be treated with stent placement rather than surgical repair^[19,20,23,24].

In our series, CT detected a ductal injury in 75% of cases. This value seems to be higher than the one reported in the literature; however, further studies in this field with a larger number of enrolled patients are required in order to confirm this data.

Our study presents some limitations represented by the limited number of patient with pancreatic injuries and the related impossibility to apply statistical tests to evaluate our data; the absence of repeated CT examinations in our series in case of negative first CT

examination; the absence of MRI or ERCP evaluation in patient treated with conservative approach confirming pancreatic duct integrity; the lack of an inter-observer agreement evaluation; the retrospective type of the study and the lack of morbidity or mortality data in the current series.

In conclusion, CT represents an accurate imaging tool for recognizing direct and indirect signs of pancreatic trauma and provides useful information to plan therapeutic approach. Among the specific signs, the presence of fluid between the splenic vein and the pancreas represents the most common CT finding suggesting pancreatic injury and the potential of CT for detecting ductal lesions have improved as compared to previous studies, with a 75% detection rate.

COMMENTS

Background

Pancreatic trauma incidence ranges between 0.2% and 12% and is associated with high morbidity and mortality especially in case of delayed diagnosis. Computed tomography (CT) represents the imaging technique of choice in hemodynamically stable patients with abdominal trauma with reported sensitivity and specificity values as high as 80% in detecting pancreatic injuries being able to establish the type and grading of the detected lesions.

Research frontiers

The increasing trend of non-operative management, especially in blunt trauma and stable patients, and the consequences of delayed or missed diagnosis makes CT the imaging modality of choice for evaluating pancreatic lesions.

Innovations and breakthroughs

CT represents an accurate imaging tool for recognizing direct and indirect signs of pancreatic trauma and provides useful information to plan therapeutic approach. The potential of CT for detecting ductal lesions have improved as compared to previous studies, with a 75% detection rate.

Applications

CT allows the radiologist to recognize all findings suggestive of severe pancreatic injury and also to detect the main alterations suitable for surgical approach. Therefore, a diagnostic and prognostic role can be given to this imaging tool.

Peer-review

This is a very interesting study about the role of CT for diagnosis of pancreatic trauma, and as we know, pancreatic trauma is associated with high morbidity and mortality especially in case of delayed diagnosis. According to the result of this study, CT represents an accurate imaging tool for recognizing direct and indirect signs of pancreatic trauma, and provides useful information to plan therapeutic approach.

REFERENCES

- Gupta A, Stuhlfaut JW, Fleming KW, Lucey BC, Soto JA. Blunt trauma of the pancreas and biliary tract: a multimodality imaging approach to diagnosis. *Radiographics* 2004; **24**: 1381-1395 [PMID: 15371615]
- Holalkere NS, Soto J. Imaging of miscellaneous pancreatic pathology (trauma, transplant, infections, and deposition). *Radiol Clin North Am* 2012; **50**: 515-528 [PMID: 22560695 DOI: 10.1016/j.rcl.2012.03.011]
- Boffard KD, Brooks AJ. Pancreatic trauma--injuries to the pancreas and pancreatic duct. *Eur J Surg* 2000; **166**: 4-12 [PMID: 10688209]
- Rekhi S, Anderson SW, Rhea JT, Soto JA. Imaging of blunt pancreatic trauma. *Emerg Radiol* 2010; **17**: 13-19 [PMID: 19396480 DOI: 10.1007/s10140-009-0811-0]
- Madiba TE, Mokoena TR. Favourable prognosis after surgical drainage of gunshot, stab or blunt trauma of the pancreas. *Br J Surg* 1995; **82**: 1236-1239 [PMID: 7552005 DOI: 10.1002/bjs.1800820926]
- Bradley EL, Young PR, Chang MC, Allen JE, Baker CC, Meredith W, Reed L, Thomason M. Diagnosis and initial management of blunt pancreatic trauma: guidelines from a multiinstitutional review. *Ann Surg* 1998; **227**: 861-869 [PMID: 9637549 DOI: 10.1097/0000-0658-199806000-00009]
- Dawson AR, Webster CH, Howe HC, Theron EJ, Meiring L. Rupture of the head of the pancreas by blunt trauma. A case report. *S Afr Med J* 1985; **67**: 560-562 [PMID: 3992386]
- Wong YC, Wang LJ, Fang JF, Lin BC, Ng CJ, Chen RJ. Multidetector-row computed tomography (CT) of blunt pancreatic injuries: can contrast-enhanced multiphase CT detect pancreatic duct injuries? *J Trauma* 2008; **64**: 666-672 [PMID: 18332806 DOI: 10.1097/ta.0b013e31802c5ba0]
- Venkatesh SK, Wan JM. CT of blunt pancreatic trauma: a pictorial essay. *Eur J Radiol* 2008; **67**: 311-320 [PMID: 17709222 DOI: 10.1016/j.ejrad.2007.07.003]
- Phelan HA, Velmahos GC, Jurkovich GJ, Friese RS, Minei JP, Menaker JA, Philp A, Evans HL, Gunn ML, Eastman AL, Rowell SE, Allison CE, Barbosa RL, Norwood SH, Tabbara M, Dente CJ, Carrick MM, Wall MJ, Feeney J, O'Neill PJ, Srinivas G, Brown CV, Reifsnyder AC, Hassan MO, Albert S, Pascual JL, Strong M, Moore FO, Spain DA, Purtill MA, Edwards B, Strauss J, Durham RM, Duchesne JC, Greiffenstein P, Cothren CC. An evaluation of multidetector computed tomography in detecting pancreatic injury: results of a multicenter AAST study. *J Trauma* 2009; **66**: 641-646; discussion 646-647 [PMID: 19276732 DOI: 10.1097/ta.0b013e3181991a0e]
- Lee WJ, Foo NP, Lin HJ, Huang YC, Chen KT. The efficacy of four-slice helical CT in evaluating pancreatic trauma: a single institution experience. *J Trauma Manag Outcomes* 2011; **5**: 1 [PMID: 21214900 DOI: 10.1186/1752-2897-5-1]
- Lane MJ, Mindelzun RE, Sandhu JS, McCormick VD, Jeffrey RB. CT diagnosis of blunt pancreatic trauma: importance of detecting fluid between the pancreas and the splenic vein. *AJR Am J Roentgenol* 1994; **163**: 833-835 [PMID: 7503824 DOI: 10.2214/ajr.163.4.7503824]
- Teh SH, Sheppard BC, Mullins RJ, Schreiber MA, Mayberry JC. Diagnosis and management of blunt pancreatic ductal injury in the era of high-resolution computed axial tomography. *Am J Surg* 2007; **193**: 641-643; discussion 643 [PMID: 17434373 DOI: 10.1016/j.amjsurg.2006.12.024]
- Lahiri R, Bhattacharya S. Pancreatic trauma. *Ann R Coll Surg Engl* 2013; **95**: 241-245 [PMID: 23676806 DOI: 10.1308/003588413X13629960045913]
- Brandon JC, Fields PA, Evankovich C, Wilson G, Teplick SK. Pancreatic clefts by penetrating vessels: a potential diagnostic for pancreatic fracture on CT. *Emerg Radiol* 2000; **7**: 283-286 [DOI: 10.1007/pl00011842]
- DeGiannis E, Levy RD, Velmahos GC, Potokar T, Florizoone MG, Saadia R. Gunshot injuries of the head of the pancreas: conservative approach. *World J Surg* 1996; **20**: 68-71; discussion 72 [PMID: 8588416 DOI: 10.1007/s002689900012]
- Lewis G, Krige JE, Bornman PC, Terblanche J. Traumatic pancreatic pseudocysts. *Br J Surg* 1993; **80**: 89-93 [PMID: 8428304 DOI: 10.1002/bjs.1800800129]
- Wong YC, Wang LJ, Lin BC, Chen CJ, Lim KE, Chen RJ. CT grading of blunt pancreatic injuries: prediction of ductal disruption and surgical correlation. *J Comput Assist Tomogr* 1997; **21**: 246-250 [PMID: 9071293 DOI: 10.1097/00004728-199703000-00014]
- Linsenmaier U, Wirth S, Reiser M, Körner M. Diagnosis and classification of pancreatic and duodenal injuries in emergency radiology. *Radiographics* 2008; **28**: 1591-1602 [PMID: 18936023 DOI: 10.1148/rg.286085524]
- Yang L, Zhang XM, Xu XX, Tang W, Xiao B, Zeng NL. MR

- imaging for blunt pancreatic injury. *Eur J Radiol* 2010; **75**: e97-101 [PMID: 20056369 DOI: 10.1016/j.ejrad.2009.12.017]
- 21 **Moschetta M**, Stabile Ianora AA, Pedote P, Scardapane A, Angelelli G. Prognostic value of multidetector computed tomography in bowel infarction. *Radiol Med* 2009; **114**: 780-791 [PMID: 19551344 DOI: 10.1007/s11547-009-0422-6]
 - 22 **Daly KP**, Ho CP, Persson DL, Gay SB. Traumatic Retroperitoneal Injuries: Review of Multidetector CT Findings. *Radiographics* 2008; **28**: 1571-1590 [PMID: 18936022 DOI: 10.1148/rg.286075141]
 - 23 **Soto JA**, Alvarez O, Múnera F, Yepes NL, Sepúlveda ME, Pérez JM. Traumatic disruption of the pancreatic duct: diagnosis with MR pancreatography. *AJR Am J Roentgenol* 2001; **176**: 175-178 [PMID: 11133562 DOI: 10.2214/ajr.176.1.1760175]
 - 24 **Chinnery GE**, Krige JE, Kotze UK, Navsaria P, Nicol A. Surgical management and outcome of civilian gunshot injuries to the pancreas. *Br J Surg* 2012; **99** Suppl 1: 140-148 [PMID: 22441869]
 - 25 **Körner M**, Krötz MM, Degenhart C, Pfeifer KJ, Reiser MF, Linsenmaier U. Current Role of Emergency US in Patients with Major Trauma. *Radiographics* 2008; **28**: 225-242 [PMID: 18203940 DOI: 10.1148/rg.281075047]

P-Reviewer: Chen F, Fu DL, Kozarek R, Sureka B

S-Editor: Ji FF **L-Editor:** A **E-Editor:** Jiao XK





Published by **Baishideng Publishing Group Inc**

8226 Regency Drive, Pleasanton, CA 94588, USA

Telephone: +1-925-223-8242

Fax: +1-925-223-8243

E-mail: bpgoffice@wjgnet.com

Help Desk: <http://www.wjgnet.com/esps/helpdesk.aspx>

<http://www.wjgnet.com>



World Journal of *Radiology*

World J Radiol 2015 December 28; 7(12): 421-537





Editorial Board

2014-2017

The *World Journal of Radiology* Editorial Board consists of 365 members, representing a team of worldwide experts in radiology. They are from 36 countries, including Afghanistan (1), Argentina (2), Australia (5), Austria (7), Belgium (2), Brazil (8), Canada (6), Chile (1), China (43), Croatia (1), Denmark (4), Egypt (6), France (5), Germany (22), Greece (10), India (12), Iran (6), Ireland (2), Israel (3), Italy (47), Japan (13), Netherlands (1), New Zealand (1), Pakistan (1), Poland (2), Portugal (1), Serbia (1), Singapore (3), Slovakia (1), South Korea (18), Spain (4), Sweden (2), Switzerland (4), Thailand (1), Turkey (26), United Kingdom (11), and United States (82).

EDITORS-IN-CHIEF

Kai U Juergens, *Bremen*
Edwin JR van Beek, *Edinburgh*
Thomas J Vogl, *Frankfurt*

GUEST EDITORIAL BOARD MEMBERS

Wing P Chan, *Taipei*
Chung-Huei Hsu, *Taipei*
Chin-Chang Huang, *Taipei*
Tsong-Long Hwang, *Taoyuan*
Jung-Lung Hsu, *Taipei*
Chia-Hung Kao, *Taichung*
Yu-Ting Kuo, *Tainan*
Hon-Man Liu, *Taipei*
Hui-Lung Liang, *Kaohsiung*
Chun Chung Lui, *Kaohsiung*
Sen-Wen Teng, *Taipei*
Yung-Liang (William) Wan, *Taoyuan*

MEMBERS OF THE EDITORIAL BOARD



Afghanistan

Takao Hiraki, *Okayama*



Argentina

Patricia Carrascosa, *Vicente Lopez*
Maria C Ziadi, *Rosario*



Australia

Lourens Bester, *Sydney*
Gemma A Figtree, *Sydney*

Stuart M Grieve, *Sydney*
Wai-Kit Lee, *Fitzroy*
Prabhakar Ramachandran, *Melbourne*



Austria

Herwig R Cerwenka, *Graz*
Gudrun M Feuchtnner, *Innsbruck*
Benjamin Henninger, *Innsbruck*
Rupert Lanzenberger, *Vienna*
Shu-Ren Li, *Vienna*
Veronika Schopf, *Vienna*
Tobias De Zordo, *Innsbruck*



Belgium

Steve Majerus, *Liege*
Kathelijne Peremans, *Merelbeke*



Brazil

Clerio F Azevedo, *Rio de Janeiro*
Patrícia P Alfredo, *São Paulo*
Eduardo FC Fleury, *São Paulo*
Edward Araujo Júnior, *São Paulo*
Wellington P Martins, *Ribeirao Preto*
Ricardo A Mesquita, *Belo Horizonte*
Vera MC Salemi, *São Paulo*
Claudia Szobot, *Porto Alegre*
Lilian YI Yamaga, *São Paulo*



Canada

Marie Arsalidou, *Toronto*
Otman A Basir, *Waterloo*

Tarik Zine Belhocine, *Toronto*
James Chow, *Toronto*
Tae K Kim, *Toronto*
Anastasia Oikonomou, *Toronto*



China

Hong-Wei Chen, *Wuxi*
Feng Chen, *Hangzhou*
Jian-Ping Chu, *Guangzhou*
Guo-Guang Fan, *Shenyang*
Bu-Lang Gao, *Shijiazhuang*
Qi-Yong Gong, *Chengdu*
Ying Han, *Beijing*
Xian-Li Lv, *Beijing*
Yi-Zhuo Li, *Guangzhou*
Xiang-Xi Meng, *Harbin*
Yun Peng, *Beijing*
Jun Shen, *Guangzhou*
Ze-Zhou Song, *Hangzhou*
Wai Kwong Tang, *Hong Kong*
Gang-Hua Tang, *Guangzhou*
Jie Tian, *Beijing*
Lu-Hua Wang, *Beijing*
Xiao-bing Wang, *Xi'an*
Yi-Gen Wu, *Nanjing*
Kai Wu, *Guangzhou*
Hui-Xiong Xu, *Shanghai*
Zuo-Zhang Yang, *Kunming*
Xiao-Dan Ye, *Shanghai*
David T Yew, *Hong Kong*
Ting-He Yu, *Chongqing*
Zheng Yuan, *Shanghai*
Min-Ming Zhang, *Hangzhou*
Yudong Zhang, *Nanjing*
Dong Zhang, *Chongqing*
Wen-Bin Zeng, *Changsha*

Yue-Qi Zhu, *Shanghai*



Croatia

Goran Kusec, *Osijek*



Denmark

Poul E Andersen, *Odense*

Lars J Petersen, *Aalborg*

Thomas Z Ramsøy, *Frederiksberg*

Morten Ziebell, *Copenhagen*



Egypt

Mohamed F Bazeed, *Mansoura*

Mohamed Abou El-Ghar, *Mansoura*

Reem HA Mohamed, *Cairo*

Mohamed R Nouh, *Alexandria*

Ahmed AKA Razek, *Mansoura*

Ashraf A Zytoon, *Shebin El-Koom*



France

Sabine F Bensamoun, *Compiègne*

Romarc Loffroy, *Dijon*

Stephanie Nougaret, *Montpellier*

Hassane Oudadesse, *Rennes*

Vincent Vinh-Hung, *Fort-de-France*



Germany

Henryk Barthel, *Leipzig*

Peter Bannas, *Hamburg*

Martin Beeres, *Frankfurt*

Ilja F Ciernik, *Dessau*

A Dimitrakopoulou-Strauss, *Heidelberg*

Peter A Fasching, *Erlangen*

Andreas G Schreyer, *Regensburg*

Philipp Heusch, *Duesseldorf*

Sonja M Kirchhoff, *Munich*

Sebastian Ley, *Munich*

Adel Maataoui, *Frankfurt am Main*

Stephan M Meckel, *Freiburg*

Hans W Muller, *Duesseldorf*

Kay Raum, *Berlin*

Dirk Rades, *Luebeck*

Marc-Ulrich Regier, *Hamburg*

Alexey Surov, *Halle*

Martin Walter, *Magdeburg*

Axel Wetter, *Essen*

Christoph Zilkens, *Düsseldorf*



Greece

Panagiotis Antoniou, *Thessaloniki*

Nikos Efthimiou, *Athens*

Dimitris Karnabatidis, *Patras*

George Latsios, *Athens*

Stylianios Megremis, *Iraklion*

Alexander D Rapidis, *Athens*

Kiki Theodorou, *Larissa*

Ioannis A Tsalafoutas, *Athens*

Evanthia E Tripoliti, *Ioannina*

Athina C Tsili, *Ioannina*



India

Ritesh Agarwal, *Chandigarh*

Chandan J Das, *New Delhi*

Prathamesh V Joshi, *Mumbai*

Naveen Kalra, *Chandigarh*

Chandrasekharan Kesavadas, *Trivandrum*

Jyoti Kumar, *New Delhi*

Atin Kumar, *New Delhi*

Kaushala P Mishra, *Allahabad*

Daya N Sharma, *New Delhi*

Binit Sureka, *New Delhi*

Sanjay Sharma, *New Delhi*

Raja R Yadav, *Allahabad*



Iran

Majid Assadi, *Bushehr*

SeyedReza Najafizadeh, *Tehran*

Mohammad Ali Oghabian, *Tehran*

Amir Reza Radmard, *Tehran*

Ramin Sadeghi, *Mashhad*

Hadi Rokni Yazdi, *Tehran*



Ireland

Tadhg Gleeson, *Wexford*

Frederik JAI Vernimmen, *Cork*



Israel

Dafna Ben Bashat, *Tel Aviv*

Amit Gefen, *Tel Aviv*

Tamar Sella, *Jerusalem*



Italy

Adriano Alippi, *Rome*

Dante Amelio, *Trento*

Michele Anzidei, *Rome*

Filippo F Angileri, *Messinas*

Stefano Arcangeli, *Rome*

Roberto Azzoni, *San Donato milanese*

Tommaso V Bartolotta, *Palermo*

Tommaso Bartalena, *Imola*

Livia Bernardin, *San Bonifacio*

Federico Boschi, *Verona*

Sergio Casciaro, *Lecce*

Emanuele Casciani, *Rome*

Musa M Can, *Napoli*

Alberto Cuocolo, *Napoli*

Michele Ferrara, *Coppito*

Mauro Feola, *Fossano*

Giampiero Francica, *Castel Volturno*

Luigi De Gennaro, *Rome*

Giulio Giovannetti, *Pisa*

Francesca Iacobellis, *Napoli*

Formato Invernizzi, *Monza Brianza*

Francesco Lassandro, *Naples*

Lorenzo Livi, *Florence*

Pier P Mainenti, *Napoli*

Laura Marzetti, *Chieti*

Giuseppe Malinverni, *Crescentino*

Enrica Milanese, *Turin*

Giovanni Morana, *Treviso*

Lorenzo Monti, *Milan*

Silvia D Morbelli, *Genoa*

Barbara Palumbo, *Perugia*

Cecilia Parazzini, *Milan*

Stefano Pergolizzi, *Messina*

Antonio Pinto, *Naples*

Camillo Porcaro, *Rome*

Carlo C Quattrocchi, *Rome*

Alberto Rebonato, *Perugia*

Giuseppe Rizzo, *Rome*

Roberto De Rosa, *Naples*

Domenico Rubello, *Rovigo*

Andrea Salvati, *Bari*

Sergio Sartori, *Ferrara*

Luca M Sconfienza, *Milano*

Giovanni Storto, *Rionero*

Nicola Sverzellati, *Parma*

Alberto S Tagliafico, *Genova*

Nicola Troisi, *Florence*



Japan

Yasuhiko Hori, *Chiba*

Hidetoshi Ikeda, *Koriyama*

Masahito Kawabori, *Sapporo*

Tamotsu Kamishima, *Sapporo*

Hiro Kiyosue, *Yufu*

Yasunori Minami, *Osaka-sayama*

Yasuhiro Morimoto, *Kitakyushu*

Satoru Murata, *Tokyo*

Shigeki Nagamachi, *Miyazaki*

Hiroshi Onishi, *Yamanashi*

Morio Sato, *Wakayama Shi*

Yoshito Tsushima, *Maebashi*

Masahiro Yanagawa, *Suita*



Netherlands

Willem Jan van Rooij, *Tilburg*



New Zealand

W Howell Round, *Hamilton*



Pakistan

Wazir Muhammad, *Abbottabad*



Poland

Maciej S Baglaj, *Wroclaw*

Piotr Czauderna, *Gdansk*



Portugal

Joao Manuel RS Tavares, *Porto*



Serbia

Olivera Ciraj-Bjelac, *Belgrade*



Singapore

Gopinathan Anil, *Singapore*

Terence KB Teo, *Singapore*

Cher Heng Tan, *Singapore*



Slovakia

Stefan Sivak, *Martin*



South Korea

Ki Seok Choo, *Busan*

Seung Hong Choi, *Seoul*

Dae-Seob Choi, *Jinju*

Hong-Seok Jang, *Seoul*

Yong Jeong, *Daejeon*

Chan Kyo Kim, *Seoul*

Se Hyung Kim, *Seoul*

Joong-Seok Kim, *Seoul*

Sang Eun Kim, *Seongnam*

Sung Joon Kwon, *Seoul*

Jeong Min Lee, *Seoul*

In Sook Lee, *Busan*

Noh Park, *Goyang*

Chang Min Park, *Seoul*

Sung Bin Park, *Seoul*

Deuk Jae Sung, *Seoul*

Choongsoo Shin, *Seoul*

Kwon-Ha Yoon, *Iksan*



Spain

Miguel A De Gregorio, *Zaragoza*

Antonio Luna, *Jaén*

Enrique Marco de Lucas, *Santander*

Fernando Ruiz Santiago, *Granada*



Sweden

Dmitry Grishenkov, *Stockholm*

Tie-Qiang Li, *Stockholm*



Switzerland

Nicolau Beckmann, *Basel*

Christian Boy, *Bern*

Giorgio Treglia, *Bellinzona*

Stephan Ulmer, *Kiel*



Thailand

Sirianong Namwongprom, *Chiang Mai*



Turkey

Kubilay Aydin, *Istanbul*

Ramazan Akdemir, *Sakarya*

Serhat Avcu, *Ankara*

Ayşe Aralasmak, *Istanbul*

Oktay Algin, *Ankara*

Nevbahar Akcar, *Meselik*

Bilal Battal, *Ankara*

Zulkif Bozgeyik, *Elazig*

Nazan Ciledag, *Aakara*

Fuldem Y Donmez, *Ankara*

Gulgun Engin, *Istanbul*

Ahmet Y Goktay, *Izmir*

Oguzhan G Gumustas, *Bursa*

Kaan Gunduz, *Ankara*

Pelin Ozcan Kara, *Mersin*

Kivanc Kamburoglu, *Ankara*

Ozgur Kilickesmez, *Istanbul*

Furuzan Numan, *Istanbul*

Cem Onal, *Adana*

Ozgur Oztekin, *Izmir*

Seda Ozbek (Boruban), *Konya*

Selda Sarikaya, *Zonguldak*

Figen Taser, *Kutahya*

Baran Tokar, *Eskisehir*

Ender Uysal, *Istanbul*

Ensar Yekeler, *Istanbul*



United Kingdom

Indran Davagnanam, *London*

M DC Valdés Hernández, *Edinburgh*

Alan Jackson, *Manchester*

Suneil Jain, *Belfast*

Long R Jiao, *London*

Miltiadis Krokidis, *Cambridge*

Pradesh Kumar, *Liverpool*

Peter D Kuzmich, *Derby*

Georgios Plataniotis, *Brighton*

Vanessa Sluming, *Liverpool*



United States

Garima Agrawal, *Saint Louis*

James R Brasic, *Baltimore*

Rajendra D Badgaiyan, *Buffalo*

Ulas Bagci, *Bethesda*

Anat Biegon, *Stony Brook*

Ramon Casanova, *Winston Salem*

Wenli Cai, *Boston*

Zheng Chang, *Durham*

Corey J Chakarun, *Long Beach*

Kai Chen, *Los Angeles*

Hyun-Soon Chong, *Chicago*

Marco Cura, *Dallas*

Ravi R Desai, *Bensalem*

Delia DeBuc, *Miami*

Carlo N De Cecco, *Charleston*

Timm-Michael L Dickfeld, *Baltimore*

Subba R Digumarthy, *Boston*

Huy M Do, *Stanford*

Todd A Faasse, *Grand Rapids*

Salomao Faintuch, *Boston*

Girish M Fatterpekar, *New York*

Dhakshinamoorthy Ganesan, *Houston*

Robert J Griffin, *Little Rock*

Andrew J Gunn, *Boston*

Sandeep S Hedgire, *Boston*

Timothy J Hoffman, *Columbia*

Mai-Lan Ho, *San Francisco*

Juebin Huang, *Jackson*

Abid Irshad, *Charleston*

Matilde Inglese, *New York*

El-Sayed H Ibrahim, *Jacksonville*

Paul R Julsrud, *Rochester*

Pamela T Johnson, *Baltimore*

Ming-Hung Kao, *Tempe*

Sunil Krishnan, *Houston*

Richard A Komoroski, *Cincinnati*

Sandi A Kwee, *Honolulu*

King Kim, *Ft. Lauderdale*

Guozheng Liu, *Worcester*

Yiyan Liu, *Newark*

Venkatesh Mani, *New York*

Lian-Sheng Ma, *Pleasanton*

Rachna Madan, *Boston*

Zeyad A Metwalli, *Houston*

Yilong Ma, *Manhasset*

Hui Mao, *Atlanta*

Feroze B Mohamed, *Philadelphia*

Gul Moonis, *Boston*

John L Noshier, *New Brunswick*

Rahmi Oklu, *Boston*

Aytekun Oto, *Chicago*

Bishnuhari Paudyal, *Philadelphia*

Rajul Pandya, *Youngstown*

Chong-Xian Pan, *Sacramento*

Jay J Pillai, *Baltimore*

Neal Prakash, *Duarte*

Reza Rahbar, *Boston*

Ali S Raja, *Boston*

Gustavo J Rodriguez, *El Paso*

David J Sahn, *Portland*

Steven Schild, *Scottsdale*

Ali R Sepahdari, *Los Angeles*

Li Shen, *Indianapolis*

JP Sheehan, *Charlottesville*

Atul B Shinagare, *Boston*

Sarabjeet Singh, *Boston*

Charles J Smith, *Columbia*

Kenji Suzuki, *Chicago*

Monvadi Srichai-Parsia, *Washington*

Sree H Tirumani, *Boston*

Hebert A Vargas, *New York*

Sachit Verma, *Philadelphia*

Yoichi Watanabe, *Minneapolis*

Li Wang, *Chapel Hill*

Carol C Wu, *Boston*

Shoujun Xu, *Houston*

Min Yao, *Cleveland*

Xiaofeng Yang, *Atlanta*

Qingbao Yu, *Albuquerque*

Aifeng Zhang, *Chicago*

Chao Zhou, *Bethlehem*

Hongming Zhuang, *Philadelphia*

**EDITORIAL**

- 421 Future of cardiac computed tomography
De Cecco CN, Schoepf UJ

DIAGNOSTIC ADVANCES

- 424 Various diffusion magnetic resonance imaging techniques for pancreatic cancer
Tang MY, Zhang XM, Chen TW, Huang XH

REVIEW

- 438 Middle cerebellar peduncles: Magnetic resonance imaging and pathophysiologic correlate
Morales H, Tomsick T
- 448 Magnetic resonance imaging of the spinal marrow: Basic understanding of the normal marrow pattern and its variant
Nouh MR, Eid AF
- 459 Multi-detector computed tomography imaging of large airway pathology: A pictorial review
Jugpal TS, Garg A, Sethi GR, Daga MK, Kumar J

MINIREVIEWS

- 475 Amyloid positron emission tomography and cognitive reserve
Bauckneht M, Picco A, Nobili F, Morbelli S
- 484 Three-dimensional imaging of the uterus: The value of the coronal plane
Wong L, White N, Ramkrishna J, Araujo Júnior E, Meagher S, Da Silva Costa F

ORIGINAL ARTICLE**Retrospective Study**

- 494 Recovery of serum testosterone following neoadjuvant and adjuvant androgen deprivation therapy in men treated with prostate brachytherapy
Tsumura H, Satoh T, Ishiyama H, Hirano S, Tabata K, Kurosaka S, Matsumoto K, Fujita T, Kitano M, Baba S, Hayakawa K, Iwamura M
- 501 Common bile duct diameter in an asymptomatic population: A magnetic resonance imaging study
Peng R, Zhang L, Zhang XM, Chen TW, Yang L, Huang XH, Zhang ZM

Observational Study

- 509 Combined value of apparent diffusion coefficient-standardized uptake value max in evaluation of post-treated locally advanced rectal cancer

Ippolito D, Fior D, Trattenero C, De Ponti E, Drago S, Guerra L, Franzesi CT, Sironi S

Prospective Study

- 521 Cavernosal nerve functionality evaluation after magnetic resonance imaging-guided transurethral ultrasound treatment of the prostate

Sammet S, Partanen A, Yousuf A, Sammet CL, Ward EV, Wardrip C, Niekrasz M, Antic T, Razmaria A, Farahani K, Sokka S, Karczmar G, Oto A

SYSTEMATIC REVIEWS

- 531 Classifications of mandibular canal branching: A review of literature

Castro MAA, Lagravere-Vich MO, Amaral TMP, Abreu MHG, Mesquita RA

ABOUT COVER

Editorial Board Member of *World Journal of Radiology*, Gopinathan Anil, DNB, MD, Doctor, Department of Diagnostic Imaging, National University Hospital and Yong Loo Lin School of Medicine, Singapore 119074, Singapore

AIM AND SCOPE

World Journal of Radiology (*World J Radiol*, *WJR*, online ISSN 1949-8470, DOI: 10.4329) is a peer-reviewed open access academic journal that aims to guide clinical practice and improve diagnostic and therapeutic skills of clinicians.

WJR covers topics concerning diagnostic radiology, radiation oncology, radiologic physics, neuroradiology, nuclear radiology, pediatric radiology, vascular/interventional radiology, medical imaging achieved by various modalities and related methods analysis. The current columns of *WJR* include editorial, frontier, diagnostic advances, therapeutics advances, field of vision, mini-reviews, review, topic highlight, medical ethics, original articles, case report, clinical case conference (clinicopathological conference), and autobiography.

We encourage authors to submit their manuscripts to *WJR*. We will give priority to manuscripts that are supported by major national and international foundations and those that are of great basic and clinical significance.

INDEXING/ABSTRACTING

World Journal of Radiology is now indexed in PubMed Central, PubMed, Digital Object Identifier, and Directory of Open Access Journals.

FLYLEAF

I-III Editorial Board

EDITORS FOR THIS ISSUE

Responsible Assistant Editor: *Xiang Li*
Responsible Electronic Editor: *Huan-Liang Wu*
Proofing Editor-in-Chief: *Lian-Sheng Ma*

Responsible Science Editor: *Jin-Xin Kong*
Proofing Editorial Office Director: *Xiu-Xia Song*

NAME OF JOURNAL
World Journal of Radiology

ISSN
ISSN 1949-8470 (online)

LAUNCH DATE
December 31, 2009

FREQUENCY
Monthly

EDITORS-IN-CHIEF
Kai U Juergens, MD, Associate Professor, MRT und PET/CT, Nuklearmedizin Bremen Mitte, ZEMODI - Zentrum für morphologische und molekulare Diagnostik, Bremen 28177, Germany

Edwin JR van Beek, MD, PhD, Professor, Clinical Research Imaging Centre and Department of Medical Radiology, University of Edinburgh, Edinburgh EH16 4TJ, United Kingdom

Thomas J Vogl, MD, Professor, Reader in Health Technology Assessment, Department of Diagnostic and Interventional Radiology, Johann Wolfgang

Goethe University of Frankfurt, Frankfurt 60590, Germany

EDITORIAL OFFICE
Jin-Lei Wang, Director
Xiu-Xia Song, Vice Director
World Journal of Radiology
Room 903, Building D, Ocean International Center, No. 62 Dongsihuan Zhonglu, Chaoyang District, Beijing 100025, China
Telephone: +86-10-59080039
Fax: +86-10-85381893
E-mail: editorialoffice@wjnet.com
Help Desk: <http://www.wjnet.com/esps/helpdesk.aspx>
<http://www.wjnet.com>

PUBLISHER
Baishideng Publishing Group Inc
8226 Regency Drive,
Pleasanton, CA 94588, USA
Telephone: +1-925-223-8242
Fax: +1-925-223-8243
E-mail: bpgoffice@wjnet.com
Help Desk: <http://www.wjnet.com/esps/helpdesk.aspx>
<http://www.wjnet.com>

PUBLICATION DATE
December 28, 2015

COPYRIGHT
© 2015 Baishideng Publishing Group Inc. Articles published by this Open-Access journal are distributed under the terms of the Creative Commons Attribution Non-commercial License, which permits use, distribution, and reproduction in any medium, provided the original work is properly cited, the use is non commercial and is otherwise in compliance with the license.

SPECIAL STATEMENT
All articles published in journals owned by the Baishideng Publishing Group (BPG) represent the views and opinions of their authors, and not the views, opinions or policies of the BPG, except where otherwise explicitly indicated.

INSTRUCTIONS TO AUTHORS
Full instructions are available online at http://www.wjnet.com/1949-8470/g_info_20100316162358.htm.

ONLINE SUBMISSION
<http://www.wjnet.com/esps/>

Future of cardiac computed tomography

Carlo N De Cecco, U Joseph Schoepf

Carlo N De Cecco, U Joseph Schoepf, Division of Cardiovascular Imaging, Department of Radiology and Radiological Science, Medical University of South Carolina, Charleston, SC 29425, United States

U Joseph Schoepf, Division of Cardiology, Department of Medicine, Medical University of South Carolina, Charleston, SC 29425, United States

Author contributions: Both authors contributed to this manuscript.

Conflict-of-interest statement: Dr. Schoepf is a consultant for and/or receives research support from Bayer, Bracco, GE and Siemens. The other authors have no conflicts of interest to disclose.

Open-Access: This article is an open-access article which was selected by an in-house editor and fully peer-reviewed by external reviewers. It is distributed in accordance with the Creative Commons Attribution Non Commercial (CC BY-NC 4.0) license, which permits others to distribute, remix, adapt, build upon this work non-commercially, and license their derivative works on different terms, provided the original work is properly cited and the use is non-commercial. See: <http://creativecommons.org/licenses/by-nc/4.0/>

Correspondence to: Carlo Nicola De Cecco, MD, PhD, Division of Cardiovascular Imaging, Department of Radiology and Radiological Sciences, Medical University of South Carolina, 25 Courtenay Drive, MSC 226, Charleston, SC 29425, United States. dececco@musc.edu
 Telephone: +1-843-8763185
 Fax: +1-843-8763157

Received: June 8, 2015
 Peer-review started: June 10, 2015
 First decision: August 4, 2015
 Revised: September 17, 2015
 Accepted: October 16, 2015
 Article in press: October 19, 2015
 Published online: December 28, 2015

Abstract

Coronary computed tomography angiography (CCTA)

has become an integral tool in the noninvasive diagnostic workup of patients with suspected coronary artery disease in both elective and emergency settings. Today, it represents a mature technique providing accurate, non-invasive morphological assessment of the coronary arteries and atherosclerotic plaque burden. Iterative reconstruction algorithms, low kV imaging, and single-heart beat acquisitions hold promise to further reduce dose requirements and improve the safety and robustness of the technique in several circumstances including imaging of heavily calcified vessels, patients with morbid obesity or irregular heart rates, and assessment in the emergency setting. However, it has become clear over recent years that cardiac radiologists need to take further steps towards the development and integration of functional imaging with morphological CCTA assessment to truly provide a comprehensive evaluation of the heart. Computed tomography myocardial perfusion imaging, including both dynamic and static dual-energy approaches, has demonstrated the ability to directly assess and quantify myocardial ischemia with simultaneous CCTA acquisition with a reasonable contrast medium volume and radiation dose delivered to the patient. In order to promote CCTA in the clinical and research environments, radiologists should prepare to embrace the change from morphological to functional imaging, furnishing all the necessary resources and information to referring clinicians.

Key words: Coronary computed tomography angiography; Coronary computed myocardial perfusion imaging; Functional imaging; Coronary artery disease; Dynamic imaging; Dual energy coronary computed

© **The Author(s) 2015.** Published by Baishideng Publishing Group Inc. All rights reserved.

Core tip: Coronary computed tomography angiography (CCTA) represents a mature technique providing accurate, non-invasive morphological assessment of the coronary arteries and atherosclerotic plaque burden. Computed tomography myocardial perfusion imaging, including both dynamic and static dual-energy approaches, has

demonstrated the ability to directly assess and quantify myocardial ischemia with simultaneous CCTA acquisition. In order to promote CCTA in the clinical and research environments, radiologists should prepare to embrace the change from morphological to functional imaging.

De Cecco CN, Schoepf UJ. Future of cardiac computed tomography. *World J Radiol* 2015; 7(12): 421-423 Available from: URL: <http://www.wjgnet.com/1949-8470/full/v7/i12/421.htm> DOI: <http://dx.doi.org/10.4329/wjr.v7.i12.421>

In recent years, coronary computed tomography angiography (CCTA) has transitioned through the experimental and clinical validation stages to become an integral tool in the noninvasive diagnostic workup of patients with suspected coronary artery disease in both elective and emergency settings. Today, it represents a mature technique providing accurate, non-invasive morphological assessment of the coronary arteries and atherosclerotic plaque burden with a pooled sensitivity and specificity of 98% and 89%, respectively^[1]. Technical innovations are continuously improving diagnostic performance and decreasing the radiation dose and contrast medium volume necessary for this test. Iterative reconstruction algorithms, low kV imaging, and single-heart beat acquisitions hold promise to further reduce dose requirements and improve the safety and robustness of the technique in several circumstances including imaging of heavily calcified vessels, patients with morbid obesity or irregular heart rates, and assessment in the emergency setting. In parallel with the growth of CCTA, the cardiac radiologist has evolved from the role of a general thoracic radiologist with limited knowledge of cardiac pathophysiology to a specialist with vast expertise in cardiac disease and cutting edge imaging applications.

However, it has become clear over recent years that cardiac radiologists need to take further steps towards the development and integration of functional imaging with morphological CCTA assessment to truly provide a comprehensive evaluation of the heart. In fact, a growing body of evidence has shown that a purely anatomical evaluation of coronary stenosis does not adequately predict hemodynamic relevance and is thus suboptimal for guiding patient management, including the major FAME and COURAGE trials which validated the impact of functional tests in coronary revascularization^[2,3]. In response to this limitation, innovative computed tomography (CT) technology has allowed the derivation of functional data in addition to morphological assessment, providing comprehensive appraisal of both the anatomical and functional aspects of coronary heart disease with a single modality.

CT myocardial perfusion imaging, including both dynamic and static dual-energy approaches, has demonstrated the ability to directly assess and quantify myocardial ischemia with simultaneous CCTA

acquisition with a reasonable contrast medium volume and radiation dose delivered to the patient as long as the scanner technology is recent enough to meet such high technological requirements^[4]. The administration of a pharmacological stressor, including adenosine, regadenoson, dobutamine, or dipyridamole, to induce a hyperemic myocardium, could represent a potential challenge from a radiological point of view. However, as demonstrated in our department, a trained team composed of a radiologist, technologist, and nurse with the support of cardiologists or anesthesiologists can safely handle the administration of these drugs, especially in the case of regadenoson, a selective A2A receptor agonist with limited side effects and convenient administration.

In clinical settings where appropriate CT technology is not available or stress perfusion acquisitions cannot be easily performed, other options are available for the assessment of cardiac function^[5]. CT-based fractional flow reserve (FFR) allows the assessment of flow-limiting stenosis directly from CCTA datasets, without the use of stress agents, additional image acquisitions or contrast medium injections. However, CT-based FFR calculations require the use of dedicated third party off-site post-processing software, significantly increasing the cost and reporting time. In-house dedicated software is under development which could drastically increase the clinical availability and utilization of this technique. Other less advanced solutions in the diagnosis of significant coronary stenosis, including the lesion length/minimal luminal diameter or corrected coronary attenuation (CCO) can be directly calculated from the CCTA dataset without the need for any dedicated software and with sufficient efficacy^[6].

What role, then, should we expect CCTA to play in the standard clinical cardiovascular workup? As CT technology continues to increase the potential for functional assessment in CCTA, we believe the future of cardiac CT is bright.

The volume of CCTA examinations has increased exponentially over the last decade as the technique grew from a niche method performed in the research environment to a routinely used diagnostic test offered in most diagnostic imaging centers. As old scanners are replaced with more advanced versions, an increasing number of hospitals and private diagnostic centers will offer CCTA and it stands to reason that clinician demand will increase. In addition, the aforementioned technological improvements will bring CT-based functional analysis to clinical practice, echoing the rise of morphological CCTA assessment.

In order to promote CCTA in the clinical and research environments, radiologists should prepare to embrace the change from morphological to functional imaging, furnishing all the necessary resources and information to referring clinicians. We are confident in the continued development of this well-established but rapidly growing field and that any challenges to come will continue to promote the role of comprehensively trained cardiac

radiologists aware of their pivotal role in cardiac disease management.

REFERENCES

- 1 **De Cecco CN**, Meinel FG, Chiamida SA, Costello P, Bamberg F, Schoepf UJ. Coronary artery computed tomography scanning. *Circulation* 2014; **129**: 1341-1345 [PMID: 24664217 DOI: 10.1161/CIRCULATIONAHA.113.002835]
- 2 **Pijls NH**, Fearon WF, Tonino PA, Siebert U, Ikeno F, Bornschein B, van't Veer M, Klauss V, Manoharan G, Engström T, Oldroyd KG, Ver Lee PN, McCarthy PA, De Bruyne B. Fractional flow reserve versus angiography for guiding percutaneous coronary intervention in patients with multivessel coronary artery disease: 2-year follow-up of the FAME (Fractional Flow Reserve Versus Angiography for Multivessel Evaluation) study. *J Am Coll Cardiol* 2010; **56**: 177-184 [PMID: 20537493 DOI: 10.1016/j.jacc.2010.04.012]
- 3 **Shaw LJ**, Berman DS, Maron DJ, Mancini GB, Hayes SW, Hartigan PM, Weintraub WS, O'Rourke RA, Dada M, Spertus JA, Chaitman BR, Friedman J, Slomka P, Heller GV, Germano G, Gosselin G, Berger P, Kostuk WJ, Schwartz RG, Knudtson M, Veledar E, Bates ER, McCallister B, Teo KK, Boden WE. Optimal medical therapy with or without percutaneous coronary intervention to reduce ischemic burden: results from the Clinical Outcomes Utilizing Revascularization and Aggressive Drug Evaluation (COURAGE) trial nuclear substudy. *Circulation* 2008; **117**: 1283-1291 [PMID: 18268144 DOI: 10.1161/CIRCULATIONAHA.107.743963]
- 4 **Cannaò PM**, Schoepf UJ, Muscogiuri G, Wichmann JL, Fuller SR, Secchi F, Varga-Szemes A, De Cecco CN. Technical prerequisites and imaging protocols for dynamic and dual energy myocardial perfusion imaging. *Eur J Radiol* 2015; **84**: 2401-2410 [PMID: 25779223 DOI: 10.1016/j.ejrad.2015.02.010]
- 5 **De Cecco CN**, Varga-Szemes A, Meinel FG, Renker M, Schoepf UJ. Beyond stenosis detection: computed tomography approaches for determining the functional relevance of coronary artery disease. *Radiol Clin North Am* 2015; **53**: 317-334 [PMID: 25726997 DOI: 10.1016/j.rcl.2014.11.009]
- 6 **Wang R**, Renker M, Schoepf UJ, Wichmann JL, Fuller SR, Rier JD, Bayer RR, Steinberg DH, De Cecco CN, Baumann S. Diagnostic value of quantitative stenosis predictors with coronary CT angiography compared to invasive fractional flow reserve. *Eur J Radiol* 2015; **84**: 1509-1515 [PMID: 26022519 DOI: 10.1016/j.ejrad.2015.05.010]

P- Reviewer: Choe YH, Dogan OF **S- Editor:** Ji FF **L- Editor:** A
E- Editor: Wu HL



Various diffusion magnetic resonance imaging techniques for pancreatic cancer

Meng-Yue Tang, Xiao-Ming Zhang, Tian-Wu Chen, Xiao-Hua Huang

Meng-Yue Tang, Xiao-Ming Zhang, Tian-Wu Chen, Xiao-Hua Huang, Sichuan Key Laboratory of Medical Imaging, Department of Radiology, Affiliated Hospital of North Sichuan Medical College, Nanchong 637000, Sichuan Province, China

Author contributions: Tang MY, Zhang XM and Chen TW designed research; Tang MY and Huang XH performed research; Tang MY and Zhang XM contributed analytic tools; Tang MY, Zhang XM and Huang XH analyzed data; Tang MY, Zhang XM, Chen TW and Huang XH wrote the paper.

Supported by National Nature Science Foundation of China, No. 81271643.

Conflict-of-interest statement: Authors declare that there is no conflict of interests regarding the publication of this article.

Open-Access: This article is an open-access article which was selected by an in-house editor and fully peer-reviewed by external reviewers. It is distributed in accordance with the Creative Commons Attribution Non Commercial (CC BY-NC 4.0) license, which permits others to distribute, remix, adapt, build upon this work non-commercially, and license their derivative works on different terms, provided the original work is properly cited and the use is non-commercial. See: <http://creativecommons.org/licenses/by-nc/4.0/>

Correspondence to: Xiao-Ming Zhang, MD, PhD, Professor, Head, Sichuan Key Laboratory of Medical Imaging, Department of Radiology, Affiliated Hospital of North Sichuan Medical College, Wenhua Road 63, Nanchong 637000, Sichuan Province, China. cjr.zhxm@vip.163.com
 Telephone: +86-817-2262218
 Fax: +86-817-2222856

Received: May 15, 2015
 Peer-review started: May 20, 2015
 First decision: September 8, 2015
 Revised: September 15, 2015
 Accepted: November 13, 2015
 Article in press: November 17, 2015
 Published online: December 28, 2015

Abstract

Pancreatic cancer is one of the most common malignant

tumors and remains a treatment-refractory cancer with a poor prognosis. Currently, the diagnosis of pancreatic neoplasm depends mainly on imaging and which methods are conducive to detecting small lesions. Compared to the other techniques, magnetic resonance imaging (MRI) has irreplaceable advantages and can provide valuable information unattainable with other noninvasive or minimally invasive imaging techniques. Advances in MR hardware and pulse sequence design have particularly improved the quality and robustness of MRI of the pancreas. Diffusion MR imaging serves as one of the common functional MRI techniques and is the only technique that can be used to reflect the diffusion movement of water molecules *in vivo*. It is generally known that diffusion properties depend on the characterization of intrinsic features of tissue microdynamics and microstructure. With the improvement of the diffusion models, diffusion MR imaging techniques are increasingly varied, from the simplest and most commonly used technique to the more complex. In this review, the various diffusion MRI techniques for pancreatic cancer are discussed, including conventional diffusion weighted imaging (DWI), multi-b DWI based on intra-voxel incoherent motion theory, diffusion tensor imaging and diffusion kurtosis imaging. The principles, main parameters, advantages and limitations of these techniques, as well as future directions for pancreatic diffusion imaging are also discussed.

Key words: Pancreatic cancer; Magnetic resonance imaging; Diffusion; Diffusion weighted imaging; Diffusion tensor imaging; Diffusion kurtosis imaging

© **The Author(s) 2015.** Published by Baishideng Publishing Group Inc. All rights reserved.

Core tip: Magnetic resonance imaging (MRI) has irreplaceable advantages and can provide valuable information unattainable with other noninvasive or minimally invasive imaging techniques. Diffusion MR imaging serves as one of the common functional MRI

techniques and is the only technique that can be used to reflect the diffusion movement of water molecules *in vivo*. In this review, the various diffusion MR imaging techniques for pancreatic cancer will be discussed, including conventional diffusion weighted imaging (DWI), multi-b DWI based on intra-voxel incoherent motion theory, diffusion tensor imaging and diffusion kurtosis imaging.

Tang MY, Zhang XM, Chen TW, Huang XH. Various diffusion magnetic resonance imaging techniques for pancreatic cancer. *World J Radiol* 2015; 7(12): 424-437 Available from: URL: <http://www.wjgnet.com/1949-8470/full/v7/i12/424.htm> DOI: <http://dx.doi.org/10.4329/wjcr.v7.i12.424>

INTRODUCTION

Pancreatic cancer is one of the most common malignant tumors with a poor prognosis, of which the 5-year survival rate range is no more than 5%^[1] and as low as 0.4% to 2%^[2,3]. It is reported that there has been little improvement in survival rate over the past 30 years^[4]. Because the pancreas is deep-seated, there is a lack of apparent symptoms in early pancreatic cancer. In most cases, the tumor is diagnosed at an advanced stage, at which point, it does not benefit from radical surgery^[2]. The management of pancreatic cancer is still encountered as a significant and unresolved therapeutic challenge.

Currently, the diagnosis of pancreatic neoplasm depends mainly on the imaging, and which methods can be conducive to detecting small lesions. Despite the continuing advances in diagnostic techniques, the early precise diagnosis of pancreatic cancer remains unsatisfactory. Early detection followed by surgical resection offers hope for a cure and is the key to improving pancreatic cancer survival^[5]. Unfortunately, only 20% of patients are resectable at the time of diagnosis^[6]. Computed tomography (CT), Magnetic resonance imaging (MRI), transabdominal and endoscopic ultrasonography (US and EUS) and endoscopic retrograde cholangiopancreatography (ERCP) also play an important role in the diagnosis of pancreatic cancer^[7-10]. Among them, MRI has irreplaceable advantages, especially, the advances in MR hardware and pulse sequence design that have improved the quality and robustness of MRI of the pancreas. Today, MRI is an indispensable tool for pancreatic disorders and can provide valuable information unattainable with other noninvasive or minimally invasive imaging techniques^[11-13].

With the rapid development of the MRI, diffusion MR imaging, which is based on the microscopic mobility of water molecules in the tissues without contrast administration, is a promising technique that is widely applied in clinical practice. Diffusion MR imaging is also the only available method that can measure

the diffusion properties of tissues noninvasively and quantitatively^[14,15], such as the diffusion weighted imaging (DWI), and has been helpful for the detection and characterization of pancreatic conditions^[16,17]. The DWI technique serves as an excellent adjunct to routine abdominal MR imaging^[13], is noninvasive in contrast to EUS and ERCP, and does not employ ionizing radiation like CT^[18].

The changes in the composition and/or cellularity of tissues influences the random thermal diffusion of water molecules^[19]. Compared to normal pancreatic tissue, pancreatic cancer has a higher cell density, relatively smaller extracellular space and a different blood supply. Thus, the diffusion of molecules in the cancer would be different from that in the normal pancreatic tissue. DWI, one of the functional MRI techniques based on water molecule movement, can depict this change in diffusion and can quantitatively measure the parameters that can represent these diffusion properties. Thus, DWI can reflect biologic abnormalities at an early stage^[20].

In this review, the various diffusion MR imaging techniques for pancreatic cancer will be discussed, including DWI, multi-b DWI based on intra-voxel incoherent motion (IVIM) theory, diffusion tensor imaging (DTI) and diffusion kurtosis imaging (DKI). The principles, main parameters, advantages and limitations of each technique and the future directions for pancreatic diffusion imaging will also be discussed.

DWI FOR PANCREATIC CANCER

Conventional DWI

Single-shot spin-echo echo-planar (SE-EPI) sequence is the most widely applied in the DW MR imaging (Figure 1). Conventional DWI uses the 2 motion-probing bipolar gradients in 3 directions (x, y, z) and acquires the signal from the 3 directions. The final DW image is derived from the fusion of the 3 images. DWI exploits the random motion of water molecules in biologic tissues. The water molecules diffuse in 3 different compartments: The intracellular, the intravascular, and the interstitial compartment. The diffusion of water molecules depends on the interactions with cell membranes, tissue compartments, and intracellular content^[21]. Consequently, the diffusion of water in tissues reflects, to various degrees, a combination of tissue cellularity, tortuosity of extracellular spaces, integrity of cell membranes, and viscosity of fluids^[22].

DWI was originally described for the central nervous system^[23,24], which is particularly good for the diagnosis of ischemic stroke. In recent years, DWI has presented promising results in the diagnosis of some illnesses of the lower abdomen, such as those of the prostate^[25,26]. DWI of the upper abdomen has been a technical challenge due to respiration, bowel peristalsis, blood flow and long acquisition times^[18]. The implementation of ultrafast imaging techniques, such as parallel imaging, has made DWI (a combination of pulses and strong gradients) of the upper abdomen

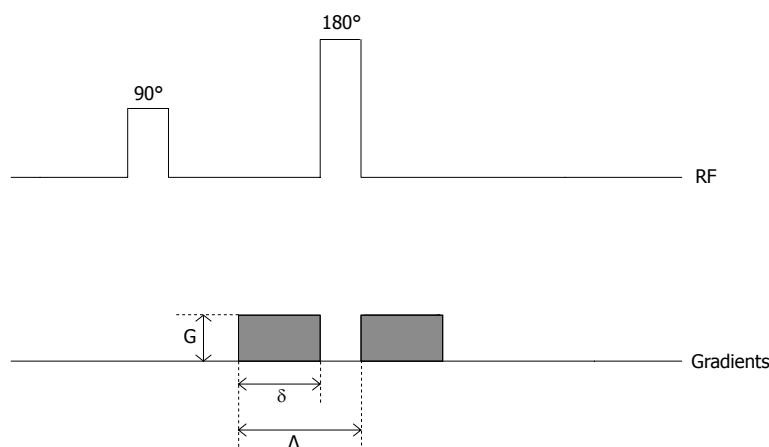


Figure 1 Diffusion weighted imaging sequence. Diffusion weighted imaging (DWI) applies the two motion-probing bipolar gradients on either side of the refocusing 180° pulse. The degree of diffusion weighting depends on the G (the amplitude of the gradients), δ (their duration) and Δ (the interval between gradients). This factor is quantitatively expressed by a parameter b , where $b = \gamma^2 G^2 \delta^2 (\Delta - \delta/3)$ and γ is a constant of the gyromagnetic ratio. Assuming that the water molecules in tissues are motionless, the effects of the two motion-probing bipolar gradients can cancel each other. Thus, for the free molecular diffusion of water molecules, the displacement can be depicted by the DWI. RF: Radio frequency.

a feasible option. It has also been found to be useful in the differentiation of malignancy from benign liver lesions^[27,28].

The three main parameters in the DWI are D value, b value and apparent diffusion coefficient (ADC) value. The D value is the diffusion parameter representing the free molecular diffusion and is defined as the average displacement by molecules in a certain direction, per unit of time. The D value can be affected by a variety of physiological factors, including respiration, perfusion, pulse and movement. The b value is referred to as the gradient factor, which can reflect the effect of the diffusion gradient. In the conventional DWI, the various b values can be selected. The low b value is applied more in water molecules with rapid movement or long diffusion distance, but the high b value is applied more in water molecules with slow movement or a short diffusion distance. Thus, the high b value is good for reducing the effect of the movement of water molecules due to perfusion^[29].

In vivo, there are many factors that can affect the diffusion movement of water molecules, including the b value, D value and T2 shine-through effect. The T2 shine-through effect occurs when tissue with a long T2 relaxation time is characterized by hyperintensity on DWI. The ADC results in standardizing by considering the above factors and would be used to reflect the state of diffusion of water molecules *in vivo*.

DWI, which can be used for the qualitative and quantitative assessment of tissue diffusivity, can be routinely applied in clinical practice^[16]. Recent studies indicate that DWI is also promising in pancreatic imaging^[30-34]. These popular research studies also reflect the value of DWI in the diagnosis of pancreatic cancer. Moreover, compared to the other techniques, the sensitivity and specificity for the diagnosis of pancreatic cancer is valuable. Kartalis *et al.*^[18] conducted research on the value of DWI for pancreatic cancer, and their

results showed that the qualitative DWI of pancreatic cancer has an accuracy of 96%; further, DWI has been shown to have high sensitivity (92%) and specificity (97%), consistent with the findings of Ichikawa *et al.*^[30] (96.2% and 98.6%, respectively). Furthermore, a recent study shows that the addition of DWI to conventional MR imaging improves the sensitivity of cancer detection^[35]. The sensitivity of DWI was close to that of dynamic gadolinium-enhanced MRI (97.7%), with a higher specificity (85.1%)^[36]. Compared to the multidetector CT, positron emission tomography with CT and transabdominal ultrasound, the sensitivity and specificity of DWI are higher^[18,37,38]. Although the sensitivity of EUS can reach 100%, it is invasive and has only 50% specificity^[39]. Thus, it does not have wide application in clinical practice.

DWI can provide information regarding the cellular density and properties of the extracellular matrix^[40,41]. The ADC values seem to reflect not only the underlying tissue microstructure but also the undirected movement of particles in the capillaries^[42]. The ADC value has been shown to be able to serve as a marker of cellularity^[41,43]. The ADC value in the normal pancreas has been reported to range from 1.0 to $2.0 \times 10^{-3} \text{ mm}^2/\text{s}$ ^[44]. Many studies have shown that the ADC value of pancreatic cancer is lower than that of the normal pancreas^[13,31,45-52]. There are three reasons that may explain these results^[53]. First, tumor cell growth is rapid with high cellularity. Second, tumor cell atypia and the richness of organelles are positively correlated in the pancreatic tumor cells, and the nucleus and organelles are bulkier than that of normal pancreas cells. Thus, to some extent, tumor cell growth may limit the diffusion of water molecules. Third, the decrease of extracellular space from dense cellularity and extracellular fibrosis may also account for the restricted water diffusion^[13,20,54-56]. However, Wang *et al.*^[54] reported that there is no significant difference in the ADC value between the normal pan-

creas and pancreatic cancer. These different results were most likely due to the application of different DWI experimental protocols and processing means^[57]. The most important factor is the choice of b value. Kim *et al.*^[58] conducted research to determine the effect of the magnitude of b values on the ADC. Their results showed that the calculated ADC value could be affected by the magnitude of the maximum b value and that the higher the maximum b value, the lower the ADC value.

Additionally, the diverse differentiation of pancreatic cancer can be differentiated using DWI. For example, poorly differentiated adenocarcinoma had significantly lower ADCs than those of well/moderately differentiated adenocarcinomas^[59].

Recently, DWI techniques have been shown not to be uniform, this controversial conclusion needs further study and differences in the sequence parameters and b values chosen may affect the ADC results. Future prospective studies are required to better determine the most appropriate use of the b value of pancreatic disease. Comparing different b values in a larger series of patients with malignant lesions would probably be of value; the quantification of the ADC of various lesions will be more accurate if feasible b values are used. The ADC values may have considerable overlap between the benign and malignant lesions, indicating that qualitative DWI seems to be more accurate than the quantitative analysis and can be used as an accurate method for the detection of pancreatic cancer^[18].

Multi-b DWI based on IVIM theory

The rapid development of DWI monoexponential and biexponential models, of which the theoretical basis of the techniques is that the diffusion of water molecules is characterized by a normal distribution, has been applied to abdominal imaging using DWI. The monoexponential model is the most commonly used in daily practice. However, the biexponential model, which is based on the IVIM theory that was introduced as a technique to reflect both perfusion and diffusion by Le Bihan *et al.*^[20] can account for separating tissue diffusivity and tissue microcapillary perfusion. The unique feature of the multi-b DWI based on IVIM is the application of the multiple b value (Figures 2-4), which can be used in biexponential models to calculate the IVIM-derived parameters.

Monoexponential models are based on an assumption that the diffusion occurs in a free and unrestricted environment in biologic tissue, that is to say, the distribution of displacements obeys Gaussian law. Biexponential models reflect a combination of tissue perfusion and tissue diffusivity effects. It is now generally accepted that when the b value is relatively low (0-200 s/mm²), the signal of ADC contains two parts; one is the diffusion of water molecules, and the other is the perfusion of water molecules in the capillary in local microcirculation. Further, the effect of perfusion is more sensitive. When the b value is relatively high (200-1000 s/mm²), the

attenuation of signal due to the effect of perfusion is slight, at this point, the signal of DWI only approximately reflects the diffusion of water molecules^[60]. This is a basic principle of conventional DWI and is the reason that the high b value was selected.

IVIM can accurately describe the relationship between signal attenuation and b values in the DWI and relatively obtain the parameters that present the effect of diffusion and perfusion in tissue.

Standard ADC value (or conventional ADC value) can be obtained from IVIM. Additionally, there are three main parameters in the IVIM, including D value, D* value and f value (perfusion fraction). D value is the true diffusion coefficient, also called the structural diffusion constant D value or slow ADC value, which reflects the tissue microstructure^[48] and is the actual diffusion effect of water molecules. The D* value, also referred as the pseudo diffusion coefficient, perfusion-related coefficient or fast ADC value, is the diffusion parameter due to the perfusion effect of the incoherent microcirculation within the voxel^[61]. The diffusion and perfusion can affect the signal intensity attenuation on DWI, and the proportion of the perfusion effect is defined as the perfusion fraction (Figure 4).

Diffusion-based IVIM has recently gained interest as a method to detect and characterize pancreatic lesions, and multi-b DWI based on IVIM theory shows very promising results and should be further investigated^[48,62]. The f values were reported to make a contribution to distinguishing between normal pancreatic parenchyma and pancreatic neoplasm^[45,49,50,63,64], and the f value proved to be the superior DWI-derived parameter for the differentiation of mass-forming pancreatitis and pancreatic carcinoma^[50].

Many studies indicated that the IVIM-derived parameter's f value was a superior parameter for differentiating pancreatic tumors from the normal pancreas compared to the conventional ADC values and that the f value is lower in pancreatic cancer^[48,51]. Lemke *et al.*^[63] conducted research to study the vascular contribution to the measured ADC value and to validate the IVIM theory; their results showed that the perfusion fraction f in the blood-suppressed pancreatic tissue decreased, possibly because the normal pancreas has a rich blood supply and will lead to a high f value. However, pancreatic cancer can destroy the normal pancreatic tissue and the vessel, and the decrease of vessel density may lead to the decreased f value, even if research shows that the f value in the IVIM-approach proved to be the best parameter for the differentiation between the normal pancreas and pancreatic cancer^[48,51].

Compared to the f value, there is relatively less research on D value and D* value in pancreatic tumors. The structural diffusion constant D value reflects the tissue microstructure. The value of the D value for pancreatic cancer is controversial. Lemke *et al.*^[48] found that the D value showed no significant difference in pancreatic carcinoma and the healthy pancreas. Concia

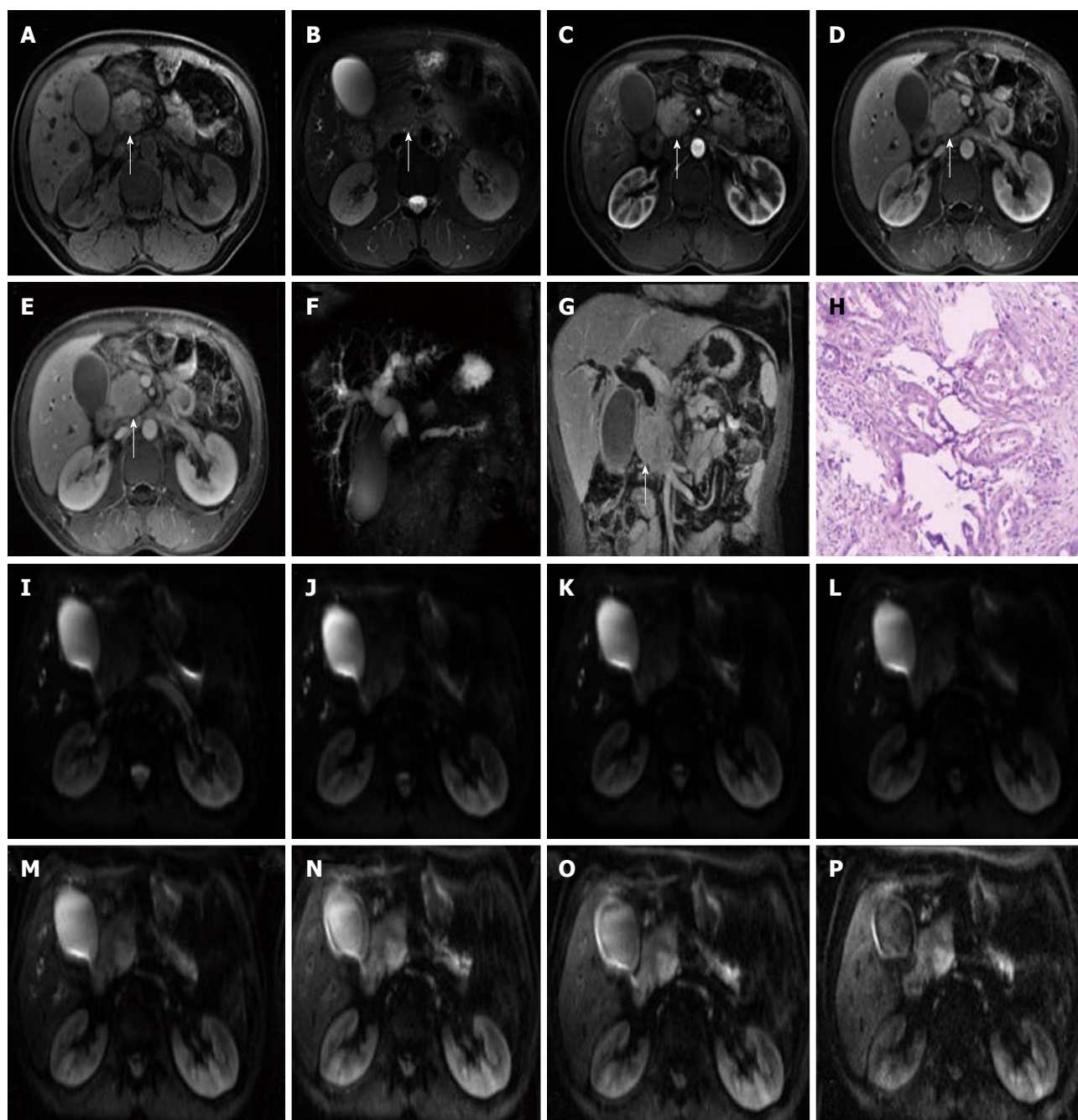


Figure 2 Images in a 47-year-old man with pancreatic moderately differentiated adenocarcinoma in the head of the pancreas (white arrows). A: Axial T1-weighted fat-suppressed gradient-echo MR image; B: Axial T2-weighted fat-suppressed fast spin-echo MR image; C-E and G: Axial and coronal slab three-dimensional liver acquisition with volume acceleration dynamic contrast-enhanced; F: MRCP shows the biliary obstruction; H: The pathology of the lesion is shown as pancreatic moderately differentiated adenocarcinoma; I-P: Multi-b DWI imaging ($b = 0, 50, 100, 300, 500, 800, 1000$ and 1500). MR: Magnetic resonance; DWI: Diffusion weighted imaging; MRCP: Magnetic resonance cholangiopancreatography.

et al.^[49] found that the D' value (D value was estimated by D' value) hardly differed in neuroendocrine pancreatic tumors and chronic pancreatitis. Klaus *et al.*^[50] reported that the D value cannot distinguish pancreatic carcinoma from mass-forming chronic pancreatitis. Klaus *et al.*^[42] reported that D value correlates with the histopathological grade of fibrosis in pancreatic lesions, which is the most characteristic histopathological feature of pancreatic carcinoma, compared with healthy pancreatic tissue, and concluded that D value can be

used to monitor novel therapy approaches that inhibit the formation of fibrosis. In 2014, Hwang *et al.*^[65] reported that the D value may be a better marker of cellularity than ADC. Until now, this was the only research on the D^* value in pancreatic cancer. In 2014, Kang *et al.*^[51] used IVIM-derived parameters for the differentiation of common pancreatic tumors and concluded that the D^* value and f values were more useful parameters in the differentiation of pancreatic adenocarcinomas from neuroendocrine tumors than were the ADC and D values.

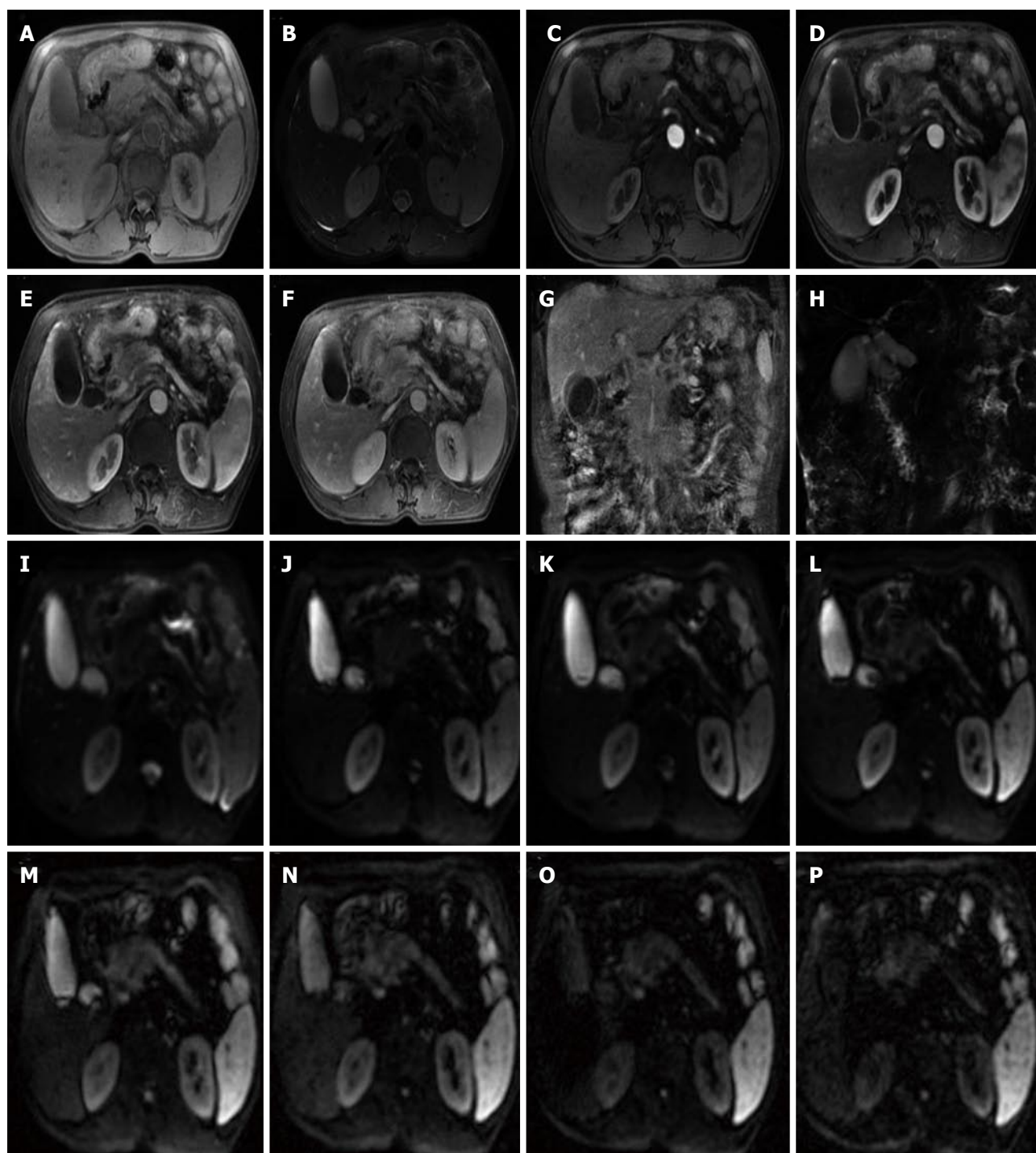


Figure 3 Images in a 63-year-old man with a focal lesion in the head of the pancreas. MR imaging suggests that it is a malignancy. A: Axial T1-weighted fat-suppressed gradient-echo MR image; B: Axial T2-weighted fat-suppressed fast spin-echo MR image; C-G: Axial and coronal slab three-dimensional liver acquisition with volume acceleration dynamic contrast-enhanced; H: MRCP shows the biliary obstruction; I-P: Multi-b DWI imaging ($b = 0, 50, 100, 300, 500, 800, 1000$ and 1500). MR: Magnetic resonance; DWI: Diffusion weighted imaging; MRCP: Magnetic resonance cholangiopancreatography.

DTI FOR PANCREATIC CANCER

The sequence of DTI is similar to that of the DWI, and both are a SE-EPI sequence. The DTI also applies the two motion-probing bipolar gradients on either side of the refocusing 180° pulse. The difference or the unique feature is that the DTI acquires images from multiple directions. Thus, in clinical practice, a minimum of 6

non-collinear images is needed, but 12 or more images are often collected to increase the accuracy of the measure (Figure 5, Figure 6Q and R).

The DTI based on the diffusion of water molecules is anisotropic, which can be illustrated by the fact that the diffusion can be greater in one direction than in other directions and is termed "anisotropic" due to some factors, such as cell membranes, fibers, and myelin^[66].

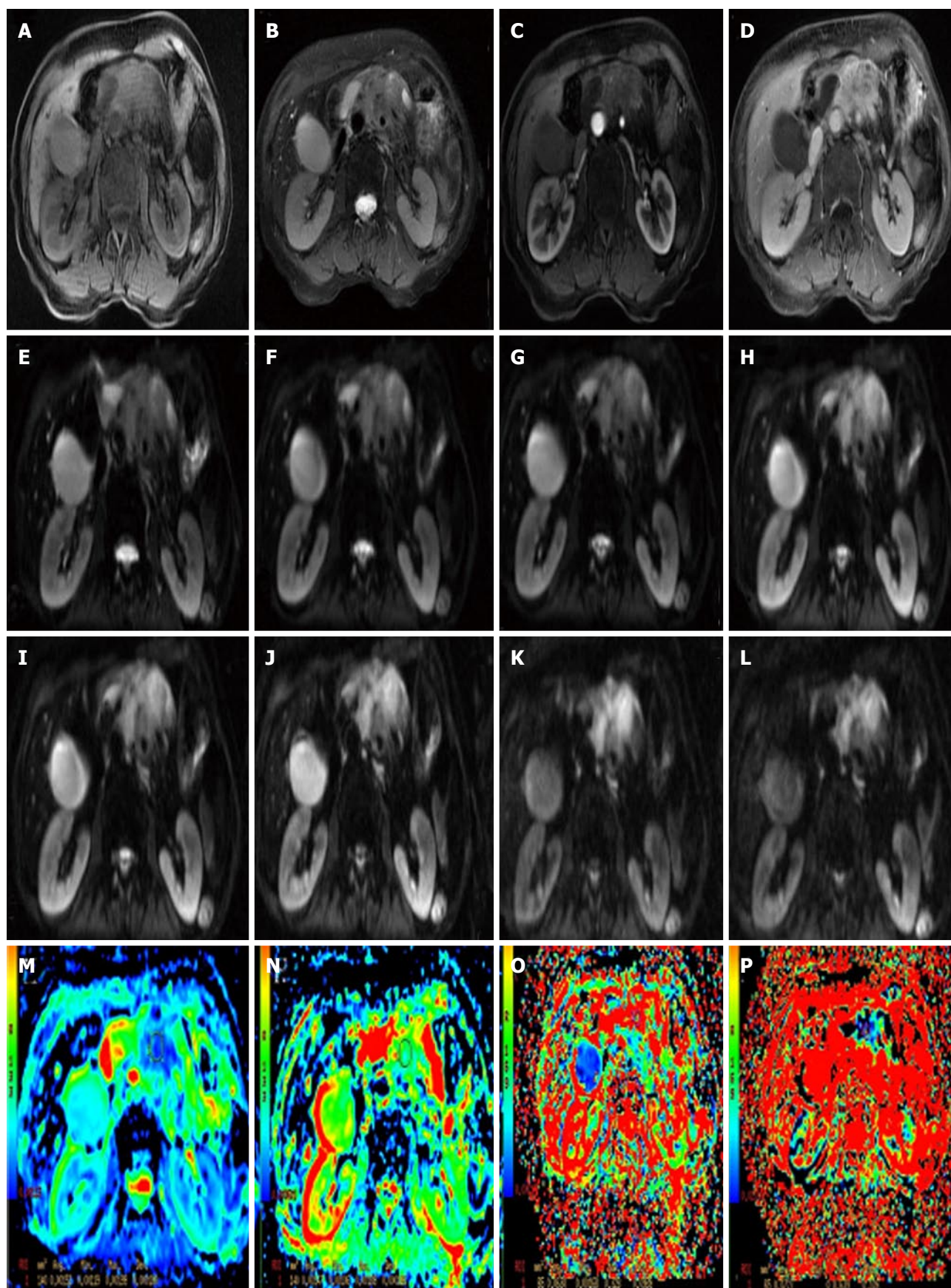


Figure 4 Images in a 65-year-old woman with a focal lesion in the neck of the pancreas. Magnetic resonance (MR) imaging suggests that it is a malignancy. A: Axial T1-weighted fat-suppressed gradient-echo MR image; B: Axial T2-weighted fat-suppressed fast spin-echo MR image; C and D: Axial slab three-dimensional liver acquisition with volume acceleration dynamic contrast-enhanced; E-L: Multi-b DWI ($b = 0, 50, 100, 300, 500, 800, 1000$ and 1500); M-P: Standard $ADC = 1.52 \times 10^{-3} \text{ mm}^2/\text{s}$, slow $ADC = 1.39 \times 10^{-3} \text{ mm}^2/\text{s}$, fast $ADC = 63 \times 10^{-3} \text{ mm}^2/\text{s}$ and $f = 7.2\%$ generated by the post-processing from the multi-b DWI. DWI: Diffusion weighted imaging; ADC: Apparent diffusion coefficient.

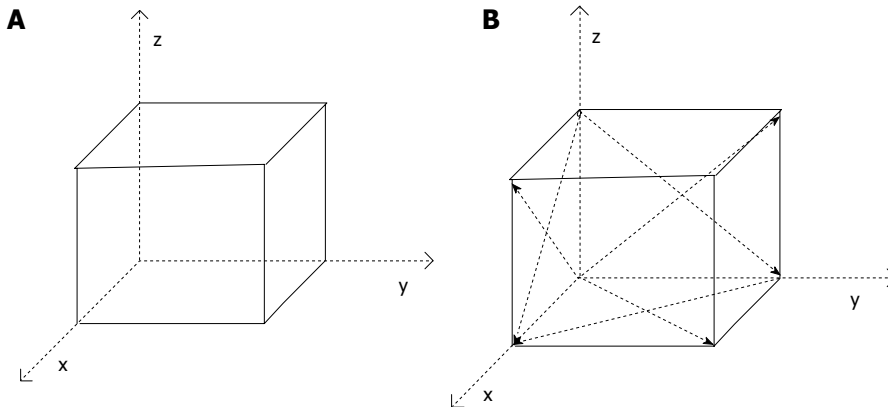


Figure 5 Conventional diffusion weighted imaging (A): The bipolar gradients in three directions; the diffusion tensor imaging bipolar gradients in the six non-collinear directions (solid black arrows) (B).

Conversely, without barriers, the random Brownian movement of water molecules is uniform in all directions or “isotropic”. In general, DWI experiments yield an average ADC over three orthogonal directions, ignoring the anisotropy of tissue in the diffusion process^[11,67]. Though the DTI model also assumes the diffusion distribution to be Gaussian, the same as the DWI, the DTI can measure the magnitude and directionality of water diffusion in tissue quantitatively^[66]. The “tensor” in DTI refers to a mathematical construct for representing the magnitude of directional water diffusion in a three-dimensional volume^[17].

DTI can not only reveal the degree of the restriction of water molecules in the diffusion movement but can also evaluate the different direction of diffusion. In a recently popular model, the DTI can provide some details on the microstructure of tissues that are not available in conventional imaging^[68-70]. The major advantages of DTI are that it can assess the directionality of the diffusion of water molecules in biological tissue^[71]. Thus, the DTI can evaluate more comprehensively and accurately the diffusion movement of water molecules in tissue. DTI also provides another non-invasive characterization of tissue microstructural properties *in vivo*^[68].

DTI can demonstrate the subtle abnormalities of some diseases, and degrees of anisotropy have been reported to correlate with the microstructural changes in neural tissues^[72,73] and even the peripheral nervous system^[70]. DTI is also applied in myocardial infarction^[74], prostate cancer^[75,76], kidneys^[77], liver^[78], breast cancer^[79], to name just a few. Indeed, it was reported that DTI would provide significant characterization of tissue microstructure and pathophysiology^[80-82]. Each voxel in a DTI data set contains vector information that reflects the directionality and magnitude of diffusion in the underlying tissue.

There are five main parameters in the DTI, including mean diffusivity (MD), three eigenvalues λ_1 , λ_2 , λ_3 , and fractional anisotropy (FA). MD is the average of the ADC in all directions and can represent the degree of diffusion. In theory, MD more truly reflects the water molecules’ diffusion ability than ADC, but in clinical

practice, the mean diffusivity is expressed as ADC. The FA represents the fraction of the magnitude of tensor that is due to anisotropic water diffusion^[83]. That is to say, FA represents the diversity of diffusion direction, which is calculated by the three above eigenvalues^[84].

In 2014, Nissan *et al.*^[57] used the DTI for patients with pancreatic-ductal-adenocarcinoma, and their results indicated that the parameters of DTI (λ_1 , λ_2 , λ_3 and the ADC value) were lower than the values of the corresponding diffusion coefficients in the distal normal pancreatic tissue of the patients^[57]; this outcome suggested that the fast diffusion component is dominated by the microcapillary perfusion process^[63]. The results were consistent with those of previous DWI studies reporting lower ADC values in pancreatic cancer attributed to their higher cellularity^[45-47].

DKI FOR PANCREATIC CANCER

The high b value is the most important feature of the DKI (Figure 6S and T). The DWI and IVIM are based on an assumption that the diffusion of water molecules obeys the normal distribution *in vivo*. However, Wu *et al.*^[85] reported that in biological tissue, complex cellular microstructures make water diffusion a highly hindered or restricted process, especially at high b values, where the distribution of displacements does not obey a Gaussian distribution. DKI was recently reported to be an extension to the Gaussian DT model^[14], and it has become more popular in recent years.

DKI uses the same pulse sequences as that of conventional DWI, but with b values that are somewhat larger than those usually selected^[86]. DKI is a straightforward extension of DTI, which requires only minor changes in data acquisition and processing^[87,88]. The theory of DKI is based on the above principles, which describes the non-Gaussian diffusion behavior in tissues^[14]. The literature has even reported that the DKI parameters, such as the radial or axial kurtosis, are more sensitive to brain physiology changes than the well-known DTI parameters in some white and gray matter structures^[14]. In the white and gray matter structures,

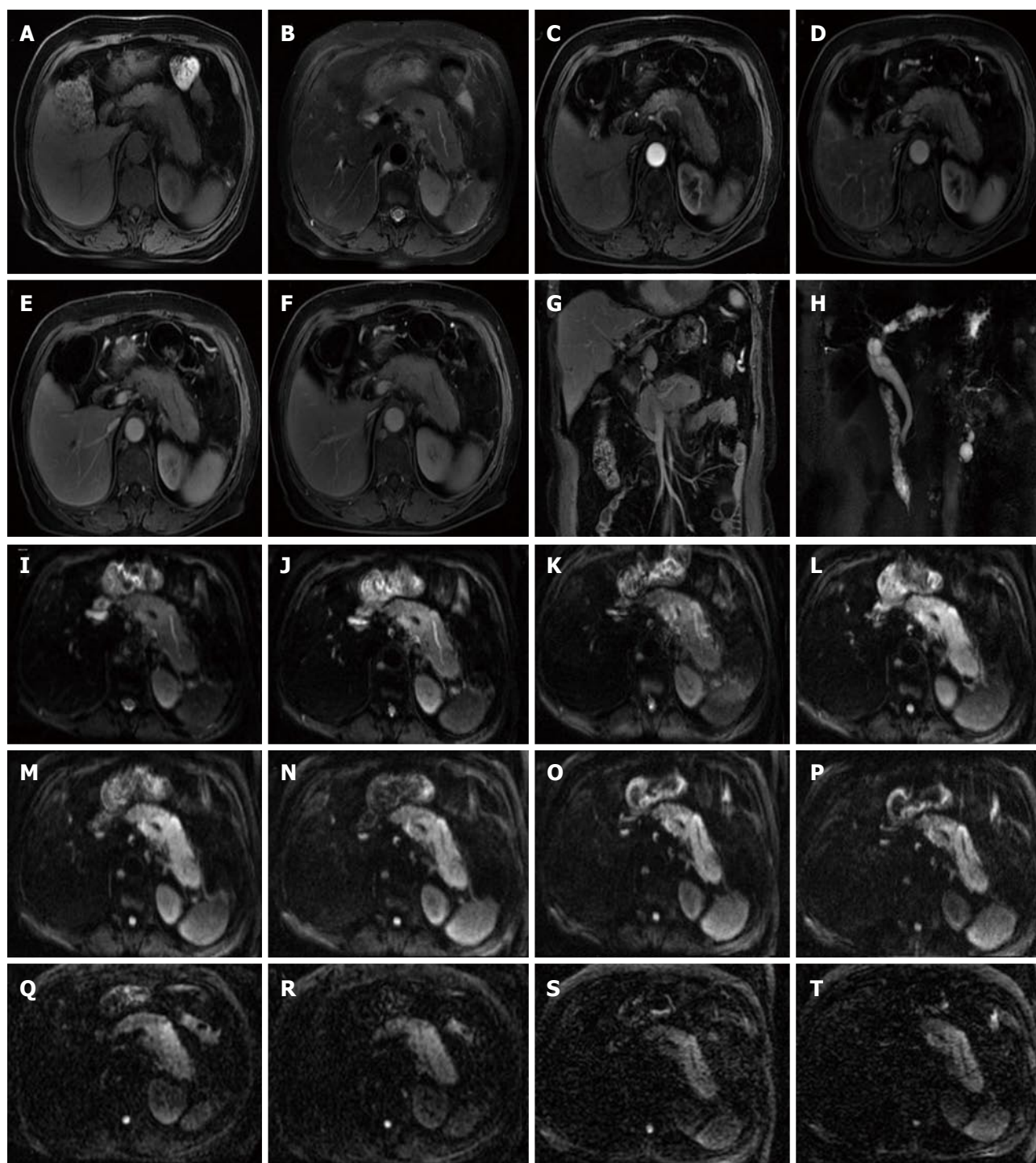


Figure 6 Images in a 52-year-old man with a focal lesion in the body and tail of the pancreas. MR imaging suggests that it is a malignancy. A: Axial T1-weighted fat-suppressed gradient-echo MR image; B: Axial T2-weighted fat-suppressed fast spin-echo MR image; C-G: Axial and coronal slab three-dimensional liver acquisition with volume acceleration dynamic contrast-enhanced; H: MRCP shows the dilated main pancreatic duct in the body and tail of pancreas; I-P: Multi-b DWI imaging ($b = 0, 50, 100, 300, 500, 800, 1000$ and 1500); DTI ($b = 500$ and 800) using 30 diffusion gradients directions; S and T: DKI ($b = 1500$ and 2000) using 30 diffusion gradients directions. MR: Magnetic resonance; DWI: Diffusion weighted imaging; DKI: Diffusion kurtosis imaging; MRCP: Magnetic resonance cholangiopancreatography.

the DKI shows a better detection and characterization of various changes^[89]. Hence, the DKI, which can measure the kurtosis excess of that distribution, allows for a more accurate description of the diffusion properties of neural tissues than the DTI model^[87].

In the model, DKI can obtain the parameters that can also be derived from DWI and DTI, such as ADC

and FA. Its main parameter is the mean kurtosis (MK). MK is a complex micro parameter that is associated with the complexity of the tissue structure. The high MK represents the more complex tissue structure^[14].

There is less research on DKI for pancreatic cancer. However, in 2012, Rosenkrantz *et al.*^[90] used DKI in prostate cancer, and their preliminary findings suggest

an increased value for DKI compared with that of standard DWI in prostate cancer assessment. In theory, the pancreatic cancer occurs with tumor cell invasion and the proliferation of interstitial cells and connective tissue. The change in the tissue structure leads to the change of MK value.

ADVANTAGES AND LIMITATIONS FOR THESE DIFFUSION MR IMAGING FOR PANCREATIC CANCER

In pancreatic cancer, tumor cell growth will lead to changes in cellularity, tumor cell atypia, organelles, and extracellular space. All of these factors can change the water molecules' movement and restrict water diffusion. Extending the diffusion MR imaging, the diffusion of water molecules can be described more accurately and comprehensively. The conventional DWI can reflect the diffusion in one direction. The multi-b value DWI is based on the IVIM theory, which is generated by the blood flow in the tortuous microcirculation of the normal pancreatic tissue^[51] and thus can reflect both perfusion and diffusion. The DTI can measure the magnitude and directionality of water diffusion in tissue quantitatively. DKI describes the non-Gaussian diffusion behavior in tissues.

However, we should be aware of the limitations of this technique: (1) Generally, in daily work, abdominal MRI suffers from interference and motional artifacts due to breathing^[91,92]; (2) The gradient eddy currents in the EPI protocols can lead to the B0 field inhomogeneity and susceptibility differences^[93,94]. Using a dielectric pad and a bellows belt for respiratory triggering can reduce geometrical distortions. DWI has been mostly acquired using single-shot echo planar imaging (ss EPI) to minimize motion-induced artifacts^[95]; and (3) the choice of b value can also limit the technique. Currently, the ADC of the pancreas still does not reach unanimity; some scholars think the ADC, which was derived from the low b value, presents only a small part of the diffusion movement, which leads to contamination of other forms of IVIM, such as perfusion in the capillary bed. The perfusion will affect the diffusion when the b value is low, even though it can characterize the anatomy and the details of the lesion^[55]. Finally, low b values result in increased ADC values^[19,20]. Conversely, Kim *et al.*^[58] indicated that the high b value can be useful in clinical practice. The high b value means that it needs a longer echo time (TE), implying that it will lead to decreasing the SNR and increasing artifacts. Poor image quality will affect observation^[18]. Using a high b value, the ADC value may be closer to the real state. In clinical practice, the choice of b value is controversial. As a compromise, a b value of 500 s/mm² was chosen^[18]; however, the higher b value of 1000 s/mm² has been reported as good for malignant abdominal tumors^[96] and the detection of pancreatic adenocarcinoma^[32,96].

The choice of b value to minimize motion artifacts and to improve the SNR in pancreas is very important. Higher b values may be more sensitive to reflect true diffusion^[30,97]. In clinical practice, taking the two factors into the consideration, a feasible b value can be selected depending on your purpose of study.

CONCLUSION

The proposed method may hold great promise for the non-invasive, non-contrast-enhanced imaging of pancreas lesions and may eventually become a screening tool for pancreatic cancer. MR is well suited to the quantitative and non-invasive measurement of diffusion. Diffusion MR imaging techniques are increasingly varied, from the simplest and most commonly used techniques to the more complex, such as from DWI to DKI. The diffusion MR imaging for pancreatic cancer revealed valuable advantages, such as high sensitivity and specificity. Moreover, diffusion MR imaging can aid in differentiating the different type of differentiation. These techniques go beyond traditional macrostructural volumetric methods and provide valuable information about underlying tissue integrity and organization at the microstructural and biochemical levels.

At present, a major issue with diffusion MR imaging is the lack of standardization of the protocol^[98]. The IVIM-derived parameters in pancreatic cancer are controversial. For example, it is unknown how fibrosis affects diffusion parameters^[42,52]. Further studies evaluating the behavior of IVIM-derived parameters in the diagnosis and treatment of pancreatic cancer are needed for standardization. One important point to bear in mind in future studies is that larger sample sizes, including imaging and histopathological workup are needed. The clinical report of utilization of the DTI and DKI in pancreatic cancer is still rare, and the potential of DTI to reveal the complex microstructure and physiology of the pancreas and detect pathological changes has not been investigated. Much work remains in solving the challenges inherent to tractography, which may certainly be a very promising technique that may be likely to contribute greatly to our understanding of nerve invasion.

In addition to the use of advanced DTI or DKI for pancreatic cancer, future advancements will come from continued study. Further standard diffusion MR imaging can benefit the accurate detection and staging of pancreatic cancer and provide the imaging evidence for clinical treatment.

REFERENCES

1. Vincent A, Herman J, Schulick R, Hruban RH, Goggins M. Pancreatic cancer. *Lancet* 2011; **378**: 607-620 [PMID: 21620466 DOI: 10.1016/S0140-6736(10)62307-0]
2. Krechler T, Horejs J, Ulrych J, Zeman M, Macásek J, Dusková J, Zák A. Current status of pancreatic cancer diagnosis. *Cas Lek Cesk*

- 2011; **150**: 587-593 [PMID: 22292339]
- 3 **Singh M**, Maitra A. Precursor lesions of pancreatic cancer: molecular pathology and clinical implications. *Pancreatol* 2007; **7**: 9-19 [PMID: 17449961 DOI: 10.1159/000101873]
- 4 **Siegel R**, Naishadham D, Jemal A. Cancer statistics, 2012. *CA Cancer J Clin* 2012; **62**: 10-29 [PMID: 22237781 DOI: 10.3322/caac.20138]
- 5 **Chari ST**, Kelly K, Hollingsworth MA, Thayer SP, Ahlquist DA, Andersen DK, Batra SK, Brentnall TA, Canto M, Cleeter DF, Firpo MA, Gambhir SS, Go VL, Hines OJ, Kenner BJ, Klimstra DS, Lerch MM, Levy MJ, Maitra A, Mulvihill SJ, Petersen GM, Rhim AD, Simeone DM, Srivastava S, Tanaka M, Vinik AI, Wong D. Early detection of sporadic pancreatic cancer: summative review. *Pancreas* 2015; **44**: 693-712 [PMID: 25931254 DOI: 10.1097/MPA.0000000000000368]
- 6 **Amedei A**, Niccolai E, Prisco D. Pancreatic cancer: role of the immune system in cancer progression and vaccine-based immunotherapy. *Hum Vaccin Immunother* 2014; **10**: 3354-3368 [PMID: 25483688 DOI: 10.4161/hv.34392]
- 7 **Li D**, Xie K, Wolff R, Abbruzzese JL. Pancreatic cancer. *Lancet* 2004; **363**: 1049-1057 [PMID: 15051286 DOI: 10.1016/S0140-6736(04)15841-8]
- 8 **Klimstra DS**, Pitman MB, Hruban RH. An algorithmic approach to the diagnosis of pancreatic neoplasms. *Arch Pathol Lab Med* 2009; **133**: 454-464 [PMID: 19260750 DOI: 10.1043/1543-2165-133.3.454]
- 9 **Jang SK**, Kim JH, Joo I, Jeon JH, Shin KS, Han JK, Choi BI. Differential diagnosis of pancreatic cancer from other solid tumours arising from the peripapillary area on MDCT. *Eur Radiol* 2015; **25**: 2880-2888 [PMID: 25916385 DOI: 10.1007/s00330-015-3721-4]
- 10 **Putzer D**, Jaschke W. Radiological evaluation of focal pancreatic lesions. *Dig Dis* 2015; **33**: 91-98 [PMID: 25531502 DOI: 10.1159/000366045]
- 11 **Heyn C**, Sue-Chue-Lam D, Jhaveri K, Haider MA. MRI of the pancreas: problem solving tool. *J Magn Reson Imaging* 2012; **36**: 1037-1051 [PMID: 23090915 DOI: 10.1002/jmri.23708]
- 12 **de la Santa LG**, Retortillo JA, Miguel AC, Klein LM. Radiology of pancreatic neoplasms: An update. *World J Gastrointest Oncol* 2014; **6**: 330-343 [PMID: 25232458 DOI: 10.4251/wjgo.v6.i9.330]
- 13 **O'Neill E**, Hammond N, Miller FH. MR imaging of the pancreas. *Radiol Clin North Am* 2014; **52**: 757-777 [PMID: 24889170 DOI: 10.1016/j.rcl.2014.02.006]
- 14 **Poot DH**, den Dekker AJ, Achten E, Verhoye M, Sijbers J. Optimal experimental design for diffusion kurtosis imaging. *IEEE Trans Med Imaging* 2010; **29**: 819-829 [PMID: 20199917 DOI: 10.1109/TMI.2009.2037915]
- 15 **Yao X**, Kuang T, Wu L, Feng H, Liu H, Cheng W, Rao S, Wang H, Zeng M. Optimization of MR diffusion-weighted imaging acquisitions for pancreatic cancer at 3.0T. *Magn Reson Imaging* 2014; **32**: 875-879 [PMID: 24848293 DOI: 10.1016/j.mri.2014.04.011]
- 16 **Barral M**, Taouli B, Guiu B, Koh DM, Luciani A, Manfredi R, Vilgrain V, Hoeffel C, Kanematsu M, Soyer P. Diffusion-weighted MR imaging of the pancreas: current status and recommendations. *Radiology* 2015; **274**: 45-63 [PMID: 25531479 DOI: 10.1148/radiol.14130778]
- 17 **Moseley M**, Bammer R, Illes J. Diffusion-tensor imaging of cognitive performance. *Brain Cogn* 2002; **50**: 396-413 [PMID: 12480486]
- 18 **Kartalis N**, Lindholm TL, Aspelin P, Permert J, Albiin N. Diffusion-weighted magnetic resonance imaging of pancreas tumours. *Eur Radiol* 2009; **19**: 1981-1990 [PMID: 19308414 DOI: 10.1007/s00330-009-1384-8]
- 19 **Ma C**, Li YJ, Pan CS, Wang H, Wang J, Chen SY, Lu JP. High resolution diffusion weighted magnetic resonance imaging of the pancreas using reduced field of view single-shot echo-planar imaging at 3 T. *Magn Reson Imaging* 2014; **32**: 125-131 [PMID: 24231348 DOI: 10.1016/j.mri.2013.10.005]
- 20 **Le Bihan D**, Breton E, Lallemand D, Aubin ML, Vignaud J, Laval-Jeantet M. Separation of diffusion and perfusion in intravoxel incoherent motion MR imaging. *Radiology* 1988; **168**: 497-505 [PMID: 3393671]
- 21 **Qayyum A**. Diffusion-weighted imaging in the abdomen and pelvis: concepts and applications. *Radiographics* 2009; **29**: 1797-1810 [PMID: 19959522 DOI: 10.1148/rg.296095521]
- 22 **Koh DM**, Collins DJ, Orton MR. Intravoxel incoherent motion in body diffusion-weighted MRI: reality and challenges. *AJR Am J Roentgenol* 2011; **196**: 1351-1361 [PMID: 21606299 DOI: 10.2214/AJR.10.5515]
- 23 **Le Bihan D**, Breton E, Lallemand D, Grenier P, Cabanis E, Laval-Jeantet M. MR imaging of intravoxel incoherent motions: application to diffusion and perfusion in neurologic disorders. *Radiology* 1986; **161**: 401-407 [PMID: 3763909 DOI: 10.1148/radiology.161.2.3763909]
- 24 **Robertson RL**, Glasier CM. Diffusion-weighted imaging of the brain in infants and children. *Pediatr Radiol* 2007; **37**: 749-768 [PMID: 17589837 DOI: 10.1007/s00247-007-0515-0]
- 25 **Morgan VA**, Kyriazi S, Ashley SE, DeSouza NM. Evaluation of the potential of diffusion-weighted imaging in prostate cancer detection. *Acta Radiol* 2007; **48**: 695-703 [PMID: 17611881 DOI: 10.1080/02841850701349257]
- 26 **Bittencourt LK**, Hausmann D, Sabaneeff N, Gasparetto EL, Barentsz JO. Multiparametric magnetic resonance imaging of the prostate: current concepts. *Radiol Bras* 2014; **47**: 292-300 [PMID: 25741104 DOI: 10.1590/0100-3984.2013.1863]
- 27 **Bruegel M**, Holzapfel K, Gaa J, Woertler K, Waldt S, Kiefer B, Stemmer A, Ganter C, Rummeny EJ. Characterization of focal liver lesions by ADC measurements using a respiratory triggered diffusion-weighted single-shot echo-planar MR imaging technique. *Eur Radiol* 2008; **18**: 477-485 [PMID: 17960390 DOI: 10.1007/s00330-007-0785-9]
- 28 **Gourtsoyianni S**, Papanikolaou N, Yarmenitis S, Maris T, Karantanias A, Gourtsoyiannis N. Respiratory gated diffusion-weighted imaging of the liver: value of apparent diffusion coefficient measurements in the differentiation between most commonly encountered benign and malignant focal liver lesions. *Eur Radiol* 2008; **18**: 486-492 [PMID: 17994317 DOI: 10.1007/s00330-007-0798-4]
- 29 **Szafer A**, Zhong J, Gore JC. Theoretical model for water diffusion in tissues. *Magn Reson Med* 1995; **33**: 697-712 [PMID: 7596275 DOI: 10.1002/mrm.1910330516]
- 30 **Ichikawa T**, Erturk SM, Motosugi U, Sou H, Iino H, Araki T, Fujii H. High-b value diffusion-weighted MRI for detecting pancreatic adenocarcinoma: preliminary results. *AJR Am J Roentgenol* 2007; **188**: 409-414 [PMID: 17242249 DOI: 10.2214/AJR.05.1918]
- 31 **Matsuki M**, Inada Y, Nakai G, Tatsugami F, Tanikake M, Narabayashi I, Masuda D, Arisaka Y, Takaori K, Tanigawa N. Diffusion-weighted MR imaging of pancreatic carcinoma. *Abdom Imaging* 2007; **32**: 481-483 [PMID: 17431713 DOI: 10.1007/s00261-007-9192-6]
- 32 **Takeuchi M**, Matsuzaki K, Kubo H, Nishitani H. High-b-value diffusion-weighted magnetic resonance imaging of pancreatic cancer and mass-forming chronic pancreatitis: preliminary results. *Acta Radiol* 2008; **49**: 383-386 [PMID: 18415779 DOI: 10.1080/02841850801895381]
- 33 **Jang KM**, Kim SH, Min JH, Lee SJ, Kang TW, Lim S, Choi D. Value of diffusion-weighted MRI for differentiating malignant from benign intraductal papillary mucinous neoplasms of the pancreas. *AJR Am J Roentgenol* 2014; **203**: 992-1000 [PMID: 25341136 DOI: 10.2214/AJR.13.11980]
- 34 **Lee NK**, Kim S, Kim DU, Seo HI, Kim HS, Jo HJ, Kim TU. Diffusion-weighted magnetic resonance imaging for non-neoplastic conditions in the hepatobiliary and pancreatic regions: pearls and potential pitfalls in imaging interpretation. *Abdom Imaging* 2015; **40**: 643-662 [PMID: 25216848 DOI: 10.1007/s00261-014-0235-5]
- 35 **Park MJ**, Kim YK, Choi SY, Rhim H, Lee WJ, Choi D. Preoperative detection of small pancreatic carcinoma: value of adding diffusion-weighted imaging to conventional MR imaging for improving confidence level. *Radiology* 2014; **273**: 433-443 [PMID: 24231348 DOI: 10.1016/j.mri.2013.10.005]

- 24991989 DOI: 10.1148/radiol.14132563]
- 36 **Birchard KR**, Semelka RC, Hyslop WB, Brown A, Armao D, Firat Z, Vaidean G. Suspected pancreatic cancer: evaluation by dynamic gadolinium-enhanced 3D gradient-echo MRI. *AJR Am J Roentgenol* 2005; **185**: 700-703 [PMID: 16120921 DOI: 10.2214/ajr.185.3.01850700]
 - 37 **Fletcher JG**, Wiersema MJ, Farrell MA, Fidler JL, Burgart LJ, Koyama T, Johnson CD, Stephens DH, Ward EM, Harmsen WS. Pancreatic malignancy: value of arterial, pancreatic, and hepatic phase imaging with multi-detector row CT. *Radiology* 2003; **229**: 81-90 [PMID: 14519871 DOI: 10.1148/radiol.2291020582]
 - 38 **Farma JM**, Santillan AA, Melis M, Walters J, Belinc D, Chen DT, Eikman EA, Malafa M. PET/CT fusion scan enhances CT staging in patients with pancreatic neoplasms. *Ann Surg Oncol* 2008; **15**: 2465-2471 [PMID: 18551347 DOI: 10.1245/s10434-008-9992-0]
 - 39 **Agarwal B**, Abu-Hamda E, Molke KL, Correa AM, Ho L. Endoscopic ultrasound-guided fine needle aspiration and multidetector spiral CT in the diagnosis of pancreatic cancer. *Am J Gastroenterol* 2004; **99**: 844-850 [PMID: 15128348 DOI: 10.1111/j.1572-0241.2004.04177.x]
 - 40 **Charles-Edwards EM**, deSouza NM. Diffusion-weighted magnetic resonance imaging and its application to cancer. *Cancer Imaging* 2006; **6**: 135-143 [PMID: 17015238 DOI: 10.1102/1470-7330.2006.0021]
 - 41 **Thoeny HC**, Ross BD. Predicting and monitoring cancer treatment response with diffusion-weighted MRI. *J Magn Reson Imaging* 2010; **32**: 2-16 [PMID: 20575076 DOI: 10.1002/jmri.22167]
 - 42 **Klauss M**, Gaida MM, Lemke A, Grünberg K, Simon D, Wente MN, Delorme S, Kauczor HU, Grenacher L, Stieltjes B. Fibrosis and pancreatic lesions: counterintuitive behavior of the diffusion imaging-derived structural diffusion coefficient d. *Invest Radiol* 2013; **48**: 129-133 [PMID: 23296083 DOI: 10.1097/RLI.0b013e31827ac0f1]
 - 43 **Schnapauff D**, Zeile M, Niederhagen MB, Fleige B, Tunn PU, Hamm B, Dudeck O. Diffusion-weighted echo-planar magnetic resonance imaging for the assessment of tumor cellularity in patients with soft-tissue sarcomas. *J Magn Reson Imaging* 2009; **29**: 1355-1359 [PMID: 19472392 DOI: 10.1002/jmri.21755]
 - 44 **Herrmann J**, Schoennagel BP, Roesch M, Busch JD, Derlin T, Doh LK, Petersen KU, Graessner J, Adam G, Habermann CR. Diffusion-weighted imaging of the healthy pancreas: ADC values are age and gender dependent. *J Magn Reson Imaging* 2013; **37**: 886-891 [PMID: 23086728 DOI: 10.1002/jmri.23871]
 - 45 **Lee SS**, Byun JH, Park BJ, Park SH, Kim N, Park B, Kim JK, Lee MG. Quantitative analysis of diffusion-weighted magnetic resonance imaging of the pancreas: usefulness in characterizing solid pancreatic masses. *J Magn Reson Imaging* 2008; **28**: 928-936 [PMID: 18821618 DOI: 10.1002/jmri.21508]
 - 46 **Fattahi R**, Balci NC, Perman WH, Hsueh EC, Alkaade S, Havlioglu N, Burton FR. Pancreatic diffusion-weighted imaging (DWI): comparison between mass-forming focal pancreatitis (FP), pancreatic cancer (PC), and normal pancreas. *J Magn Reson Imaging* 2009; **29**: 350-356 [PMID: 19161187 DOI: 10.1002/jmri.21651]
 - 47 **Fukukura Y**, Takumi K, Kamimura K, Shindo T, Kumagai Y, Tateyama A, Nakajo M. Pancreatic adenocarcinoma: variability of diffusion-weighted MR imaging findings. *Radiology* 2012; **263**: 732-740 [PMID: 22623694 DOI: 10.1148/radiol.120111222]
 - 48 **Lemke A**, Laun FB, Klauss M, Re TJ, Simon D, Delorme S, Schad LR, Stieltjes B. Differentiation of pancreas carcinoma from healthy pancreatic tissue using multiple b-values: comparison of apparent diffusion coefficient and intravoxel incoherent motion derived parameters. *Invest Radiol* 2009; **44**: 769-775 [PMID: 19838121 DOI: 10.1097/RLI.0b013e3181b62271]
 - 49 **Concia M**, Sprinkart AM, Penner AH, Brossart P, Gieseke J, Schild HH, Willinek WA, Mürtz P. Diffusion-weighted magnetic resonance imaging of the pancreas: diagnostic benefit from an intravoxel incoherent motion model-based 3 b-value analysis. *Invest Radiol* 2014; **49**: 93-100 [PMID: 24089021 DOI: 10.1097/RLI.0b013e3182a71cc3]
 - 50 **Klauss M**, Lemke A, Grünberg K, Simon D, Re TJ, Wente MN, Laun FB, Kauczor HU, Delorme S, Grenacher L, Stieltjes B. Intravoxel incoherent motion MRI for the differentiation between mass forming chronic pancreatitis and pancreatic carcinoma. *Invest Radiol* 2011; **46**: 57-63 [PMID: 21139505 DOI: 10.1097/RLI.0b013e3181fb3bf2]
 - 51 **Kang KM**, Lee JM, Yoon JH, Kiefer B, Han JK, Choi BI. Intravoxel incoherent motion diffusion-weighted MR imaging for characterization of focal pancreatic lesions. *Radiology* 2014; **270**: 444-453 [PMID: 24126370 DOI: 10.1148/radiol.13122712]
 - 52 **Muraoka N**, Uematsu H, Kimura H, Imamura Y, Fujiwara Y, Murakami M, Yamaguchi A, Itoh H. Apparent diffusion coefficient in pancreatic cancer: characterization and histopathological correlations. *J Magn Reson Imaging* 2008; **27**: 1302-1308 [PMID: 18504750 DOI: 10.1002/jmri.21340]
 - 53 **Sakuma H**, Nomura Y, Takeda K, Tagami T, Nakagawa T, Tamagawa Y, Ishii Y, Tsukamoto T. Adult and neonatal human brain: diffusional anisotropy and myelination with diffusion-weighted MR imaging. *Radiology* 1991; **180**: 229-233 [PMID: 2052700 DOI: 10.1148/radiology.180.1.2052700]
 - 54 **Wang Y**, Chen ZE, Nikolaidis P, McCarthy RJ, Merrick L, Sternick LA, Horowitz JM, Yaghamai V, Miller FH. Diffusion-weighted magnetic resonance imaging of pancreatic adenocarcinomas: association with histopathology and tumor grade. *J Magn Reson Imaging* 2011; **33**: 136-142 [PMID: 21182131 DOI: 10.1002/jmri.22414]
 - 55 **Padhani AR**, Liu G, Koh DM, Chenevert TL, Thoeny HC, Takahara T, Dzik-Jurasz A, Ross BD, Van Cauteren M, Collins D, Hammoud DA, Rustin GJ, Taouli B, Choyke PL. Diffusion-weighted magnetic resonance imaging as a cancer biomarker: consensus and recommendations. *Neoplasia* 2009; **11**: 102-125 [PMID: 19186405 DOI: 10.1593/neo.81328]
 - 56 **Wang Y**, Chen ZE, Yaghamai V, Nikolaidis P, McCarthy RJ, Merrick L, Miller FH. Diffusion-weighted MR imaging in pancreatic endocrine tumors correlated with histopathologic characteristics. *J Magn Reson Imaging* 2011; **33**: 1071-1079 [PMID: 21509863 DOI: 10.1002/jmri.22541]
 - 57 **Nissan N**, Golan T, Furman-Haran E, Apter S, Inbar Y, Ariche A, Bar-Zakay B, Goldes Y, Schvimer M, Grobgeld D, Degani H. Diffusion tensor magnetic resonance imaging of the pancreas. *PLoS One* 2014; **9**: e115783 [PMID: 25549366 DOI: 10.1371/journal.pone.0115783]
 - 58 **Kim T**, Murakami T, Takahashi S, Hori M, Tsuda K, Nakamura H. Diffusion-weighted single-shot echoplanar MR imaging for liver disease. *AJR Am J Roentgenol* 1999; **173**: 393-398 [PMID: 10430143 DOI: 10.2214/ajr.173.2.10430143]
 - 59 **Wang Y**, Miller FH, Chen ZE, Merrick L, Mortelet KJ, Hoff FL, Hammond NA, Yaghamai V, Nikolaidis P. Diffusion-weighted MR imaging of solid and cystic lesions of the pancreas. *Radiographics* 2011; **31**: E47-E64 [PMID: 21721197 DOI: 10.1148/rg.313105174]
 - 60 **Luciani A**, Vignaud A, Cavet M, Nhieu JT, Mallat A, Ruel L, Laurent A, Deux JF, Brugieres P, Rahmouni A. Liver cirrhosis: intravoxel incoherent motion MR imaging--pilot study. *Radiology* 2008; **249**: 891-899 [PMID: 19011186 DOI: 10.1148/radiol.2493080080]
 - 61 **Zhang JL**, Sigmund EE, Chandarana H, Rusinek H, Chen Q, Vivier PH, Taouli B, Lee VS. Variability of renal apparent diffusion coefficients: limitations of the monoexponential model for diffusion quantification. *Radiology* 2010; **254**: 783-792 [PMID: 20089719 DOI: 10.1148/radiol.09090891]
 - 62 **Grünberg K**, Grenacher L, Klauss M. Diffusion-weighted imaging of the pancreas. *Radiologe* 2011; **51**: 186-194 [PMID: 21305263 DOI: 10.1007/s00117-010-2059-9]
 - 63 **Lemke A**, Laun FB, Simon D, Stieltjes B, Schad LR. An in vivo verification of the intravoxel incoherent motion effect in diffusion-weighted imaging of the abdomen. *Magn Reson Med* 2010; **64**: 1580-1585 [PMID: 20665824 DOI: 10.1002/mrm.22565]
 - 64 **Re TJ**, Lemke A, Klauss M, Laun FB, Simon D, Grünberg K, Delorme S, Grenacher L, Manfredi R, Mucelli RP, Stieltjes B. Enhancing pancreatic adenocarcinoma delineation in diffusion derived intravoxel incoherent motion f-maps through automatic vessel and

- duct segmentation. *Magn Reson Med* 2011; **66**: 1327-1332 [PMID: 21437979 DOI: 10.1002/mrm.22931]
- 65 **Hwang EJ**, Lee JM, Yoon JH, Kim JH, Han JK, Choi BI, Lee KB, Jang JY, Kim SW, Nickel MD, Kiefer B. Intravoxel incoherent motion diffusion-weighted imaging of pancreatic neuroendocrine tumors: prediction of the histologic grade using pure diffusion coefficient and tumor size. *Invest Radiol* 2014; **49**: 396-402 [PMID: 24500090 DOI: 10.1097/RLI.000000000000028]
 - 66 **Wozniak JR**, Lim KO. Advances in white matter imaging: a review of in vivo magnetic resonance methodologies and their applicability to the study of development and aging. *Neurosci Biobehav Rev* 2006; **30**: 762-774 [PMID: 16890990 DOI: 10.1016/j.neubiorev.2006.06.003]
 - 67 **Fukuda Y**, Ohashi I, Hanafusa K, Nakagawa T, Ohtani S, An-naka Y, Hayashi T, Shibuya H. Anisotropic diffusion in kidney: apparent diffusion coefficient measurements for clinical use. *J Magn Reson Imaging* 2000; **11**: 156-160 [PMID: 10713948 DOI: 10.1002/(SICI)1522-2586(200002)11:2<156::AID-JMRI12>3.0.CO;2-8]
 - 68 **Basser PJ**, Pierpaoli C. Microstructural and physiological features of tissues elucidated by quantitative-diffusion-tensor MRI. *J Magn Reson B* 1996; **111**: 209-219 [PMID: 8661285 DOI: 10.1006/jmrb.1996.0086]
 - 69 **Le Bihan D**, Mangin JF, Poupon C, Clark CA, Pappata S, Molko N, Chabriat H. Diffusion tensor imaging: concepts and applications. *J Magn Reson Imaging* 2001; **13**: 534-546 [PMID: 11276097 DOI: 10.1002/jmri.1076]
 - 70 **Hagmann P**, Jonasson L, Maeder P, Thiran JP, Wedeen VJ, Meuli R. Understanding diffusion MR imaging techniques: from scalar diffusion-weighted imaging to diffusion tensor imaging and beyond. *Radiographics* 2006; **26** Suppl 1: S205-S223 [PMID: 17050517 DOI: 10.1148/rg.26si065510]
 - 71 **Basser PJ**, Mattiello J, LeBihan D. MR diffusion tensor spectroscopy and imaging. *Biophys J* 1994; **66**: 259-267 [PMID: 8130344 DOI: 10.1016/S0006-3495(94)80775-1]
 - 72 **Vandermosten M**, Boets B, Wouters J, Ghesquière P. A qualitative and quantitative review of diffusion tensor imaging studies in reading and dyslexia. *Neurosci Biobehav Rev* 2012; **36**: 1532-1552 [PMID: 22516793 DOI: 10.1016/j.neubiorev.2012.04.002]
 - 73 **Kuswanto CN**, Teh I, Lee TS, Sim K. Diffusion tensor imaging findings of white matter changes in first episode schizophrenia: a systematic review. *Clin Psychopharmacol Neurosci* 2012; **10**: 13-24 [PMID: 23429992 DOI: 10.9758/cpn.2012.10.1.13]
 - 74 **Wu MT**, Tseng WY, Su MY, Liu CP, Chiou KR, Wedeen VJ, Reese TG, Yang CF. Diffusion tensor magnetic resonance imaging mapping the fiber architecture remodeling in human myocardium after infarction: correlation with viability and wall motion. *Circulation* 2006; **114**: 1036-1045 [PMID: 16940196 DOI: 10.1161/CIRCULATIONAHA.105.545863]
 - 75 **Uribe CF**, Jones EC, Chang SD, Goldenberg SL, Reinsberg SA, Kozlowski P. In vivo 3T and ex vivo 7T diffusion tensor imaging of prostate cancer: Correlation with histology. *Magn Reson Imaging* 2015; **33**: 577-583 [PMID: 25721995 DOI: 10.1016/j.mri.2015.02.022]
 - 76 **Li L**, Margolis DJ, Deng M, Cai J, Yuan L, Feng Z, Min X, Hu Z, Hu D, Liu J, Wang L. Correlation of gleason scores with magnetic resonance diffusion tensor imaging in peripheral zone prostate cancer. *J Magn Reson Imaging* 2015; **42**: 460-467 [PMID: 25469909 DOI: 10.1002/jmri.24813]
 - 77 **Sigmund EE**, Vivier PH, Sui D, Lamparello NA, Tantillo K, Mikheev A, Rusinek H, Babb JS, Storey P, Lee VS, Chandarana H. Intravoxel incoherent motion and diffusion-tensor imaging in renal tissue under hydration and furosemide flow challenges. *Radiology* 2012; **263**: 758-769 [PMID: 22523327 DOI: 10.1148/radiol.12111327]
 - 78 **Taouli B**, Chouli M, Martin AJ, Qayyum A, Coakley FV, Vilgrain V. Chronic hepatitis: role of diffusion-weighted imaging and diffusion tensor imaging for the diagnosis of liver fibrosis and inflammation. *J Magn Reson Imaging* 2008; **28**: 89-95 [PMID: 18581382 DOI: 10.1002/jmri.21227]
 - 79 **Nissan N**, Furman-Haran E, Shapiro-Feinberg M, Grobgeld D, Degani H. Diffusion-tensor MR imaging of the breast: hormonal regulation. *Radiology* 2014; **271**: 672-680 [PMID: 24533873 DOI: 10.1148/radiol.14132084]
 - 80 **Cauley KA**, Filippi CG. Diffusion-tensor imaging of small nerve bundles: cranial nerves, peripheral nerves, distal spinal cord, and lumbar nerve roots--clinical applications. *AJR Am J Roentgenol* 2013; **201**: W326-W335 [PMID: 23883249 DOI: 10.2214/AJR.12.9230]
 - 81 **Jambawalikar S**, Baum J, Button T, Li H, Geronimo V, Gould ES. Diffusion tensor imaging of peripheral nerves. *Skeletal Radiol* 2010; **39**: 1073-1079 [PMID: 20593175 DOI: 10.1007/s00256-010-0974-5]
 - 82 **Lee JW**, Kim JH, Kang HS, Lee JS, Choi JY, Yeom JS, Kim HJ, Chung HW. Optimization of acquisition parameters of diffusion-tensor magnetic resonance imaging in the spinal cord. *Invest Radiol* 2006; **41**: 553-559 [PMID: 16772848 DOI: 10.1097/01.rli.0000221325.03899.48]
 - 83 **Masutani Y**, Aoki S, Abe O, Hayashi N, Otomo K. MR diffusion tensor imaging: recent advance and new techniques for diffusion tensor visualization. *Eur J Radiol* 2003; **46**: 53-66 [PMID: 12648802 DOI: 10.1016/S0720-048X(02)00328-5]
 - 84 **Basser PJ**, Pierpaoli C. Microstructural and physiological features of tissues elucidated by quantitative-diffusion-tensor MRI. 1996. *J Magn Reson* 2011; **213**: 560-570 [PMID: 22152371 DOI: 10.1016/j.jmr.2011.09.022]
 - 85 **Wu EX**, Cheung MM. MR diffusion kurtosis imaging for neural tissue characterization. *NMR Biomed* 2010; **23**: 836-848 [PMID: 20623793 DOI: 10.1002/nbm.1506]
 - 86 **Huang Y**, Chen X, Zhang Z, Yan L, Pan D, Liang C, Liu Z. MRI quantification of non-Gaussian water diffusion in normal human kidney: a diffusional kurtosis imaging study. *NMR Biomed* 2015; **28**: 154-161 [PMID: 25392938 DOI: 10.1002/nbm.3235]
 - 87 **Jensen JH**, Helpert JA, Ramani A, Lu H, Kaczynski K. Diffusional kurtosis imaging: the quantification of non-gaussian water diffusion by means of magnetic resonance imaging. *Magn Reson Med* 2005; **53**: 1432-1440 [PMID: 15906300 DOI: 10.1002/mrm.20508]
 - 88 **Lu H**, Jensen JH, Ramani A, Helpert JA. Three-dimensional characterization of non-gaussian water diffusion in humans using diffusion kurtosis imaging. *NMR Biomed* 2006; **19**: 236-247 [PMID: 16521095 DOI: 10.1002/nbm.1020]
 - 89 **Cheung MM**, Hui ES, Chan KC, Helpert JA, Qi L, Wu EX. Does diffusion kurtosis imaging lead to better neural tissue characterization? A rodent brain maturation study. *Neuroimage* 2009; **45**: 386-392 [PMID: 19150655 DOI: 10.1016/j.neuroimage.2008.12.018]
 - 90 **Rosenkrantz AB**, Sigmund EE, Johnson G, Babb JS, Mussi TC, Melamed J, Taneja SS, Lee VS, Jensen JH. Prostate cancer: feasibility and preliminary experience of a diffusional kurtosis model for detection and assessment of aggressiveness of peripheral zone cancer. *Radiology* 2012; **264**: 126-135 [PMID: 22550312 DOI: 10.1148/radiol.12112290]
 - 91 **Dietrich O**, Reiser MF, Schoenberg SO. Artifacts in 3-T MRI: physical background and reduction strategies. *Eur J Radiol* 2008; **65**: 29-35 [PMID: 18162353]
 - 92 **Riffel P**, Michaely HJ, Morelli JN, Pfeuffer J, Attenberger UI, Schoenberg SO, Haneder S. Zoomed EPI-DWI of the pancreas using two-dimensional spatially-selective radiofrequency excitation pulses. *PLoS One* 2014; **9**: e89468 [PMID: 24594702 DOI: 10.1371/journal.pone.0089468]
 - 93 **Dietrich O**, Biffar A, Baur-Melnyk A, Reiser MF. Technical aspects of MR diffusion imaging of the body. *Eur J Radiol* 2010; **76**: 314-322 [PMID: 20299172 DOI: 10.1016/j.ejrad.2010.02.018]
 - 94 **Jones DK**, Cercignani M. Twenty-five pitfalls in the analysis of diffusion MRI data. *NMR Biomed* 2010; **23**: 803-820 [PMID: 20886566 DOI: 10.1002/nbm.1543]
 - 95 **Yamada I**, Aung W, Himeno Y, Nakagawa T, Shibuya H. Diffusion coefficients in abdominal organs and hepatic lesions: evaluation with intravoxel incoherent motion echo-planar MR imaging. *Radiology* 1999; **210**: 617-623 [PMID: 10207458 DOI: 10.1148/

- radiology.210.3.r99fe17617]
- 96 **Tsushima Y**, Takano A, Taketomi-Takahashi A, Endo K. Body diffusion-weighted MR imaging using high b-value for malignant tumor screening: usefulness and necessity of referring to T2-weighted images and creating fusion images. *Acad Radiol* 2007; **14**: 643-650 [PMID: 17502253 DOI: 10.1016/j.acra.2007.02.006]
 - 97 **Huang WC**, Sheng J, Chen SY, Lu JP. Differentiation between pancreatic carcinoma and mass-forming chronic pancreatitis: usefulness of high b value diffusion-weighted imaging. *J Dig Dis* 2011; **12**: 401-408 [PMID: 21955434 DOI: 10.1111/j.1751-2980.2011.00517.x]
 - 98 **Sandrasegaran K**. Functional MR imaging of the abdomen. *Radiol Clin North Am* 2014; **52**: 883-903 [PMID: 24889176 DOI: 10.1016/j.rcl.2014.02.018]

P- Reviewer: Hayano K, Sugimura H **S- Editor:** Gong ZM
L- Editor: A **E- Editor:** Wu HL



Middle cerebellar peduncles: Magnetic resonance imaging and pathophysiologic correlate

Humberto Morales, Thomas Tomsick

Humberto Morales, Thomas Tomsick, Department of Neuroradiology, University of Cincinnati Medical Center, Cincinnati, OH 45267-0761, United States

Author contributions: All authors equally contributed to this paper.

Conflict-of-interest statement: The authors declare no source of funding or conflict of interest pertinent to this submitted manuscript.

Open-Access: This article is an open-access article which was selected by an in-house editor and fully peer-reviewed by external reviewers. It is distributed in accordance with the Creative Commons Attribution Non Commercial (CC BY-NC 4.0) license, which permits others to distribute, remix, adapt, build upon this work non-commercially, and license their derivative works on different terms, provided the original work is properly cited and the use is non-commercial. See: <http://creativecommons.org/licenses/by-nc/4.0/>

Correspondence to: Humberto Morales, MD, Assistant Professor of Radiology, Department of Neuroradiology, University of Cincinnati Medical Center, 234 Goodman Street, Cincinnati, OH 45267-0761, United States. moralehc@ucmail.uc.edu
Telephone: +1-513-5841584
Fax: +1-513-5849100

Received: July 22, 2015
Peer-review started: July 24, 2015
First decision: August 25, 2015
Revised: September 5, 2015
Accepted: October 23, 2015
Article in press: October 27, 2015
Published online: December 28, 2015

Abstract

We describe common and less common diseases that can cause magnetic resonance signal abnormalities of middle cerebellar peduncles (MCP), offering a systematic

approach correlating imaging findings with clinical clues and pathologic mechanisms. Myelin abnormalities, different types of edema or neurodegenerative processes, can cause areas of abnormal T2 signal, variable enhancement, and patterns of diffusivity of MCP. Pathologies such as demyelinating disorders or certain neurodegenerative entities (*e.g.*, multiple system atrophy or fragile X-associated tremor-ataxia syndrome) appear to have predilection for MCP. Careful evaluation of concomitant imaging findings in the brain or brainstem; and focused correlation with key clinical findings such as immunosuppression for progressive multifocal leukoencephalopathy; hypertension, post-transplant status or high dose chemotherapy for posterior reversible encephalopathy; electrolyte disorders for myelinolysis or suspected toxic-drug related encephalopathy; would yield an appropriate and accurate differential diagnosis in the majority of cases.

Key words: Middle cerebellar peduncle; Brachium pontis; Magnetic resonance imaging; Multiple sclerosis; Progressive multifocal leukoencephalopathy; Posterior reversible encephalopathy; Toxic encephalopathy

© The Author(s) 2015. Published by Baishideng Publishing Group Inc. All rights reserved.

Core tip: Though a few prior reviews have described pathologic processes involving the middle cerebellar peduncles (MCP), our paper offers not only an updated approach to include diffusion tensor imaging but also important correlations of imaging findings with anatomy, pathophysiologic insights and key clinical scenarios. Overall, this concise and comprehensive review is expected to help the readers not only to improve their approach to cases with MCP involvement, but also to increase awareness and understanding of pathologic processes increasingly seen in neuroimaging such as progressive multifocal leukoencephalopathy, posterior reversible encephalopathy and toxic encephalopathies.

Morales H, Tomsick T. Middle cerebellar peduncles: Magnetic resonance imaging and pathophysiologic correlate. *World J Radiol* 2015; 7(12): 438-447 Available from: URL: <http://www.wjgnet.com/1949-8470/full/v7/i12/438.htm> DOI: <http://dx.doi.org/10.4329/wjr.v7.i12.438>

INTRODUCTION

Pathologic processes can have predilection for specific anatomic locations. Our purpose is to describe not only common and less common entities, but also pathologic mechanisms causing magnetic resonance (MR) signal abnormalities of middle cerebellar peduncles (MCP). We provide a systematic approach narrowing differential diagnosis to help radiologists and clinicians.

ANATOMY AND CLINICAL CORRELATION

The MCP are the main afferent pathway to the cerebellum. MCP are composed by white matter fibers originated from the contralateral pontine nuclei (Figure 1). The pontine nuclei are intermediary gray matter scattered in the basis pons and part of the cortico-ponto-cerebellar pathway (closed loop communication between the cerebellum and pre-central /prefrontal cortex that control not only the action of motor tasks but also planning and initiation of movements)^[1]. The cerebellum has a high ratio of afferent/efferent pathways (40:1); with the small superior cerebellar peduncles (SCP) as the only efferent fibers, connecting the dentate nuclei to the cortex through the dentate-rubro-thalamic tracts (Figure 1C). In general, the cerebellar pathways decussate twice, one at the level of the pons (crossing pontine fibers) and other at the level of the inferior colliculi in the tegmentum (decussation of the SCP). Thus, clinical signs (*e.g.*, limb ataxia) are ipsilateral to MCP lesion. Difficulty walking (cerebellar ataxia), difficulty speaking (scanning speech) and in some cases vertigo and facial weakness are common clinical manifestation of MCP lesion.

INSIGHTS INTO PATHOLOGIC MECHANISMS

It is not surprising that demyelinating processes affect the MCP, composed of axons, oligodendrocytes and scattered glial cells. Demyelination can occur in the setting of immune-related entities such as MS or acute disseminated encephalomyelitis (ADEM), and is usually accompanied by perivascular inflammatory infiltrates (with areas of enhancement on MRI in some cases) (Figure 2). Demyelination can also occur secondary to infectious processes such as progressive multifocal leukoencephalopathy (PML) (Figures 3 and 4) or metabolic abnormalities such as osmotic demyelination syndrome (ODS) (Figure 5), usually not accompanied

by inflammatory changes (enhancement is not a characteristic feature on MR imaging). Vasogenic edema due to dys-regulation of small arteries can also cause increased T2 signal in the MCP, as is the case in posterior reversible encephalopathy (PRES) (Figure 6). However, the vascular dys-regulation and leaking edema might also be due to toxic states such as cyclosporine-related encephalopathy. Cytotoxic edema is characteristic of ischemia/infarction, a rare event in the MCP (Figure 7). Intra-myelinic edema appears to be the cause of areas of abnormal white matter signal in different entities. The edema can predominate between the myelin sheaths (potential extracellular space) or result from swelling of the oligodendrocytes, myelin sheaths or axons (intracellular compartment)^[2]. This type of edema might or might not be reversible and is the main pathologic mechanism in some toxic or myelinolytic states (Figure 8). White matter vacuolization/spongyform degeneration causes abnormal T2 signal in other toxic states (*e.g.*, chronic heroin inhalation). Damage to the axons (due to loss of antegrade or retrograde input) with subsequent myelin breakdown and end-stage gliosis/volume loss is the mechanism for wallerian degeneration (WD) (Figure 9). Myelin breakdown and white matter damage in leukodystrophies (LD) is caused by biochemical defects that interfere with myelin formation, maintenance, turnover, and catabolism (known as dysmyelination), leading to increased T2 signal and in some cases abnormal enhancement (*e.g.*, adrenoleukodystrophy) (Figure 10). Neurodegenerative processes affecting MCP have distinct mechanisms; in general, there is preferential loss of Purkinje cells, or gray matter nuclei in the brain stem in diseases such as multiple system atrophy (MSA-C, cerebellar variant), fragile X-associated tremor-ataxia syndrome (FXTAS) or some spino-cerebellar ataxias, leading to axonal loss and degeneration of the associated MCP fibers (Figure 11). Neoplastic processes are unusual in the MCP, though lymphoma or glial neoplasms can also involve them. Rare infectious or inflammatory pathologies, such as Lyme disease, *Listeria* rhombencephalitis, Whipple disease, neurosarcoid, vasculitis (*e.g.*, Bechet's), and the recently described CLIPPERS (chronic lymphocytic inflammation with pontine perivascular enhancement responsive to steroids) might also extend to MCP with variable imaging findings (usually enhancement accompany areas of increased T2 signal). Rarely, vascular malformations (Figure 12) can involve the MCP, in which case the recognition of their typical features is not challenging ("pop-corn" appearance for a cavernoma, or prominent flow voids for arteriovenous malformations).

PATHOLOGIC ENTITIES AND IMAGING FINDINGS

Demyelination

Cerebellar symptoms and signs are commonly seen in 50%-80% of multiple sclerosis (MS) patients. On

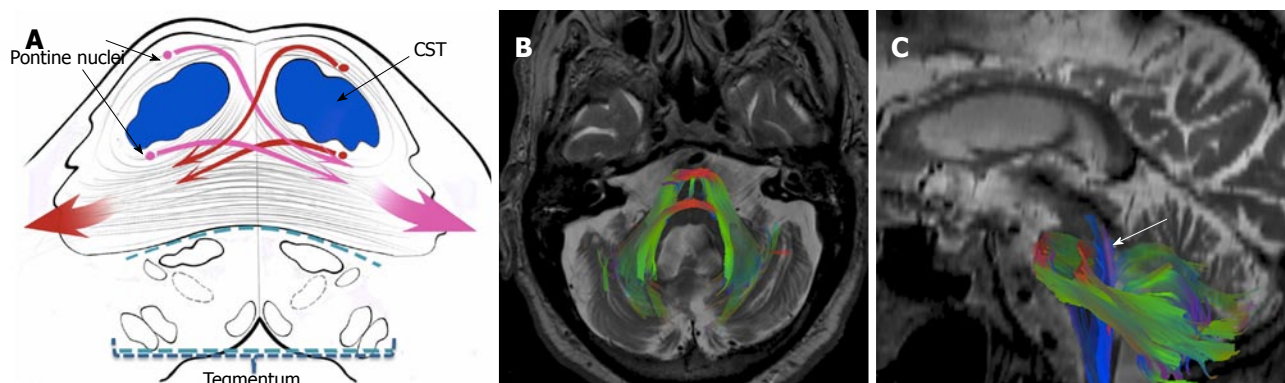


Figure 1 Anatomy of the middle cerebellar peduncles. A: Diagram shows the pontine crossing fibers (PCF) (red and pink long arrows) originating from the contralateral pontine nuclei and conforming the middle cerebellar peduncles (MCP) (only afferent fibers constitute MCP); B and C: Diffusion tensor imaging (DTI) tractography after seed ROIs placed in the bilateral MCP. Note the representation of the PCF (red on B). Here, we can envision the origin of well described signs on conventional T2 sequences such as the “hot cross bun sign” or “trident sign” where there is involvement of the PCF or central pons and sparing of the corticospinal tracts (CST) and tegmentum. Sagittal DTI (C) including the main efferent pathway (purple ascending fibers, arrow) through the pontine tegmentum and superior cerebellar peduncles which constitutes part of the dentate-rubro-thalamic tract. (DTI was acquired on a GE-3T Magnet, $b = 0$ and 1000 s/mm^2 with 25 directions; Brain Lab Software was used to fuse T2-WI with DTI acquisition; and tractography was performed using a tensor deflection algorithm). ROIs: Regions of interest.

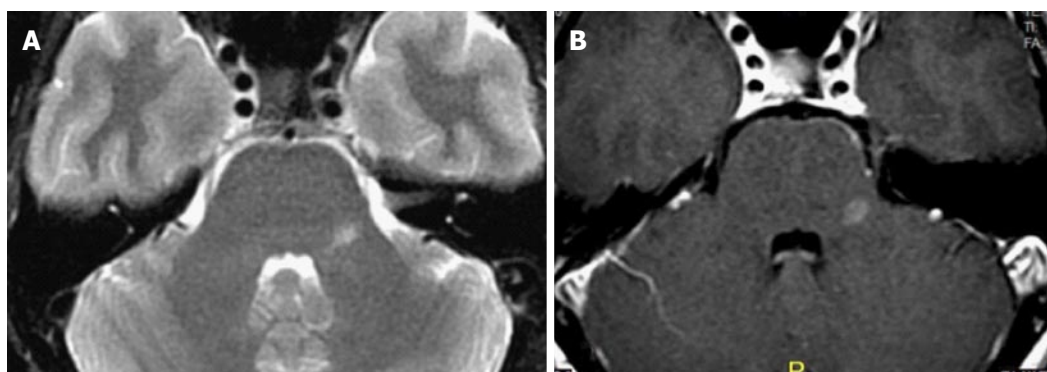


Figure 2 Multiple sclerosis. A 40-year-old female with 2 mo history of left facial pain/numbness and difficulty talking (scanning speech). Axial T2 (A) and axial post-contrast MR (B) images show isolated lesion in the left MCP. Due to suspicion for demyelinating disease MRI of the spine and CSF analysis was recommended. Additional lesion found in the thoracic cord (not shown) and CSF led to the diagnosis of MS. MCP: Middle cerebellar peduncles; CSF: Cerebrospinal fluid; MRI: Magnetic resonance imaging; MS: Multiple sclerosis.

conventional MRI, reported frequency of brainstem lesions and cerebellar lesions is 68% and 49%-88% respectively^[3].

Multifocal areas of demyelination, some times areas of cavitation characterize progressive multifocal leukoencephalopathy (PML), with scanty if any inflammatory-lymphocytic infiltrates. Posterior fossa involvement of JC virus (PML) has been reported in 58% of cases^[4], when present there is MCP involvement in 64%-100% of cases^[5]. There is increased recognition of the common involvement of posterior fossa by PML, with reported cases of isolated/restricted posterior fossa compromise^[6,7]. PML usually progresses relentlessly over a few months, resulting in increasing neurologic impairment, dementia, and eventually death. Treatment of the cause of the underlying immunosuppression can lead to remission of PML. However, white matter sequelae are seen in most cases^[8] (Figure 3). White matter lesions on PML should not enhance; if so, an infectious process, inflammatory reaction or neoplastic process should be considered.

Reconstitution of the immune system (*e.g.*, in the

treatment of AIDS with highly active antiretroviral therapy) occasionally causes a paradoxical inflammatory response in the CNS, also known as IRIS (immune reconstitution inflammatory syndrome). This response might or might not be associated with an infectious agent, as in the case of PML-IRIS (Figure 4). Enhancement is present in these cases.

Vascular/toxic

Involvement of the brainstem by posterior reversible encephalopathy (PRES) has been reported in 18% of cases^[9]. Isolated involvement of the brainstem or basal ganglia (no cortical or subcortical edema) can be seen in 4% of cases (central variant of PRES)^[10]. In fact, there is increased awareness of “atypical distribution patterns” of PRES; thus, involvement of the brainstem and MCP can actually be more common than expected (Figure 6)^[11].

Toxic/metabolic

ODS is a metabolic induced demyelination characteristically involving the central pons secondary to rapid

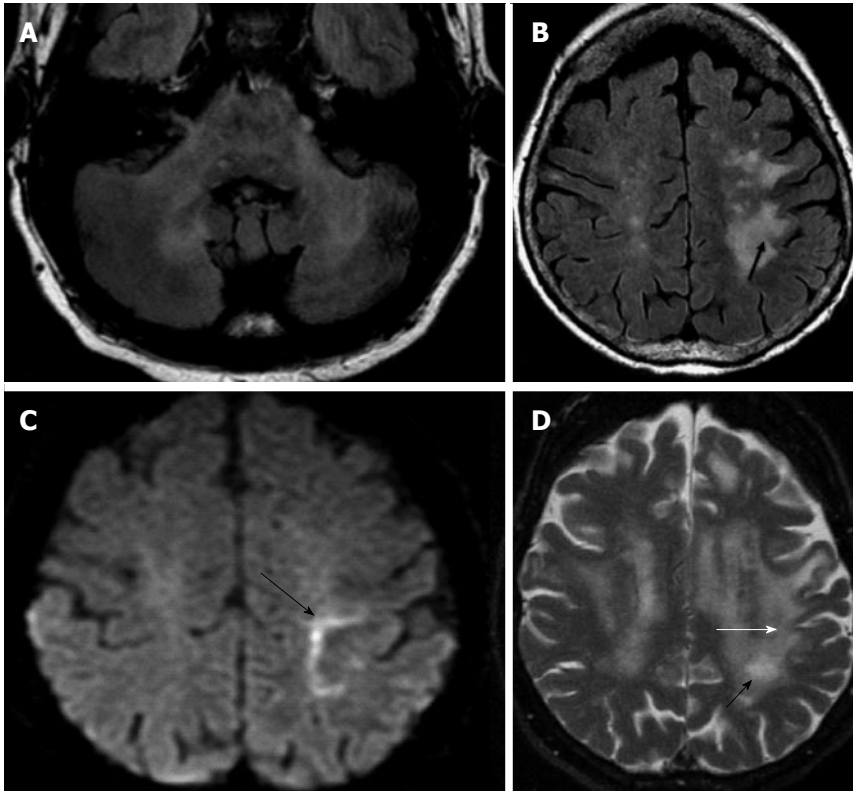


Figure 3 Progressive multifocal leukoencephalopathy. HIV patient with + JC virus on PCR-CSF. Bilateral involvement of MCP on axial FLAIR (A); with no enhancement (not shown); Axial FLAIR (B) and axial DWI (C) images show asymmetric confluent areas of increased signal in the subcortical WM with involvement of the u-fibers (arrow) and linear "edge" on DWI (arrow on C) consistent with advancing demyelinated edge; D: Three months f/u images better depict involvement of u-fibers (white arrow) as well as progression of WM disease with formation of small central cavitation/micro cyst, characteristic of PML (black arrow). PML: Progressive multifocal leukoencephalopathy; MCP: Middle cerebellar peduncles; CSF: Cerebrospinal fluid; DWI: Diffusion weighted-imaging; PCR: Polymerase chain reaction; HIV: Human immunodeficiency virus.

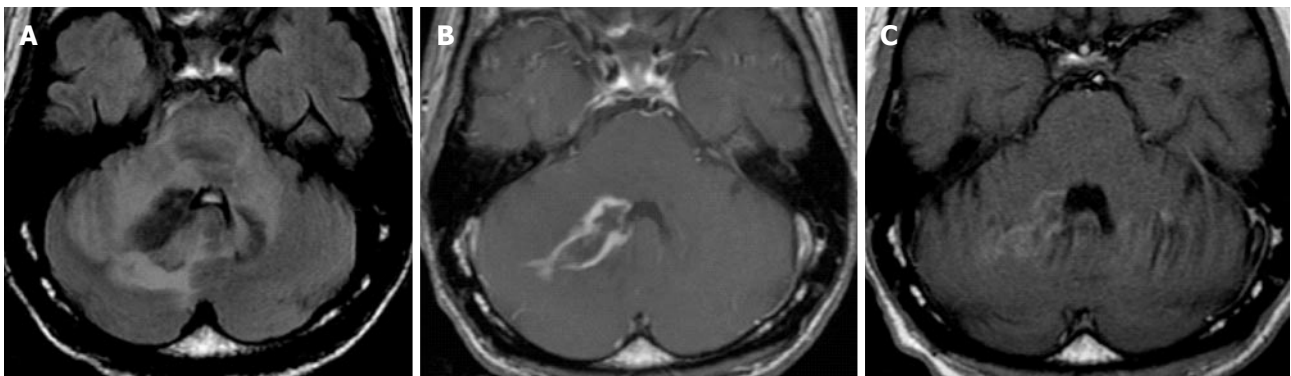


Figure 4 Immune reconstitution inflammatory syndrome and progressive multifocal leukoencephalopathy. HIV + JC virus, irregular antiretroviral therapy, with confusion and right sided weakness. Axial FLAIR (A) and axial post contrast (B) show abnormal signal in the bilateral MCP, greater on the right with associated enhancement; Axial post contrast (C) 2 mo after treatment with steroids and antiretroviral therapy show significant improvement of abnormal enhancement. IRIS might or might not be associated with an infectious process, in this case the abnormal enhancement in a patient with positive JC virus lead to the suspicious of a superimposed neoplastic process (lymphoma), other fungal or bacterial infection. Ultimately, the response to steroid gives the diagnosis of IRIS. IRIS: Immune reconstitution inflammatory syndrome; MCP: Middle cerebellar peduncles; HIV: Human immunodeficiency virus.

correction of hyponatremia (other disorders of the serum electrolyte such as hypernatremia could also cause it). The mechanism of demyelination is poorly understood. On imaging, there is usually preservation of the periphery of the pons and typically preservation of the corticospinal tracts ("trident sign") (Figure 5).

Toxic/drug induced involvement of the MCP has been reported after heroin inhalation ("chasing the

dragon"). The initial stage is characterized by diffuse leukoencephalopathy, presumably caused by excitotoxicity and in some cases difficult to distinguish from hypoxic-ischemic injury (though cortical involvement is also expected in the latter, potentially a characteristic to differentiate them) (Figure 8). This stage can be reversible or lead to a chronic form or spongiform leukoencephalopathy (typically involve the posterior brain



Figure 5 Osmotic demyelination syndrome. History of ethanol abuse and rapid correction of hyponatremia. A and B: Axial FLAIR images at two different levels of the pons show abnormal signal in the bilateral MCP as well as abnormal signal in the central pons with subtle “trident” appearance; C: Three months f/u demonstrate resolution of abnormal signal in the MCP and pons. ODS characteristically involve the central pons with sparing of the corticospinal tract, peripheral pons and tegmentum. In some acute cases, restricted diffusion is possible, differing from ischemic insult, which extends to the periphery of the pons with sparing of the midline (see Figure 9B). ODS: Osmotic demyelination syndrome; MCP: Middle cerebellar peduncles.

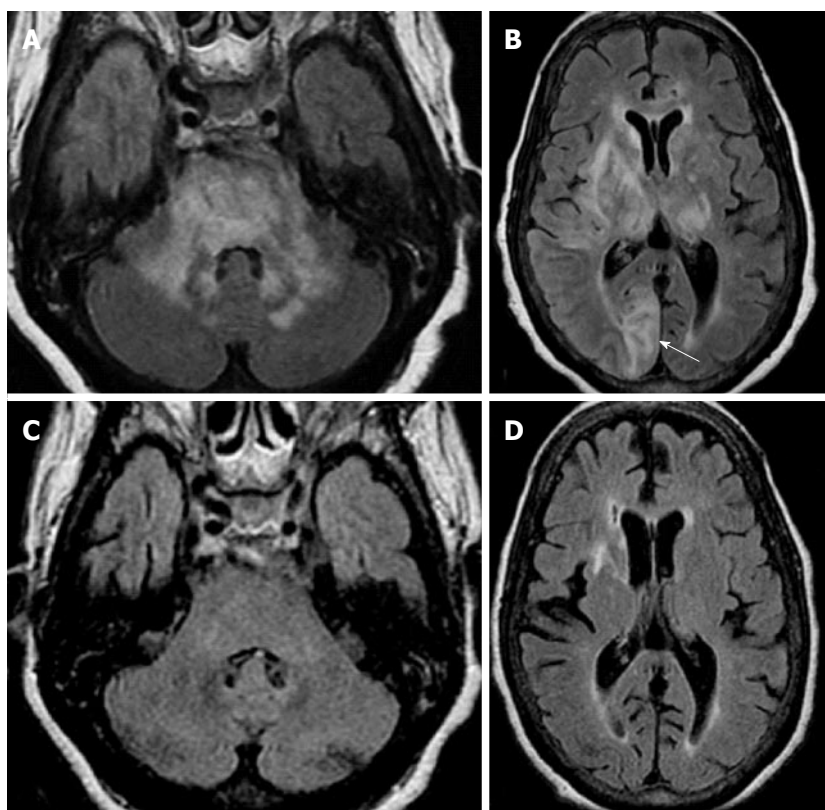


Figure 6 Posterior reversible encephalopathy. A and B: Axial FLAIR images in an hypertense encephalopathic patient show symmetric bilateral areas of abnormal signal in the MCP and pons. Concomitant involvement of supratentorial subcortical white matter in a “vasogenic type pattern” as well as cortical involvement (arrow on B) was noted; C and D: Three months f/u after control of hypertensive crisis show almost complete resolution of abnormal signal in MCP, pons and supratentorial regions to include the basal ganglia/thalami. Given the asymmetric distribution of supratentorial lesions, PML could be included in the differential. However, cortical involvement is not characteristic for PML. This case could be considered “atypical PRES” and proved by resolution of abnormal white matter disease (compare with Figure 3 where no resolution is noted). PRES: Posterior reversible encephalopathy; MCP: Middle cerebellar peduncles; PML: Progressive multifocal leucoencephalopathy.

white matter, midbrain and bilateral MCP)^[12]. Other toxic-drug-induced abnormalities, such as toluene or methotrexate toxicity, involving the cerebellum and MCP have also been reported^[13-15].

Preferential neuronal loss/volume loss of the putamen and caudate characterizes Wilson’s disease,

in some cases with late spongiform white matter changes^[8]. In the midbrain, abnormal signal in the tegmentum lead to the well described “panda sign”. Early work by King *et al*^[16] described 32% of cases with MCP involvement. It appears that signal changes on T2 are less conspicuous in long-standing disease^[16]

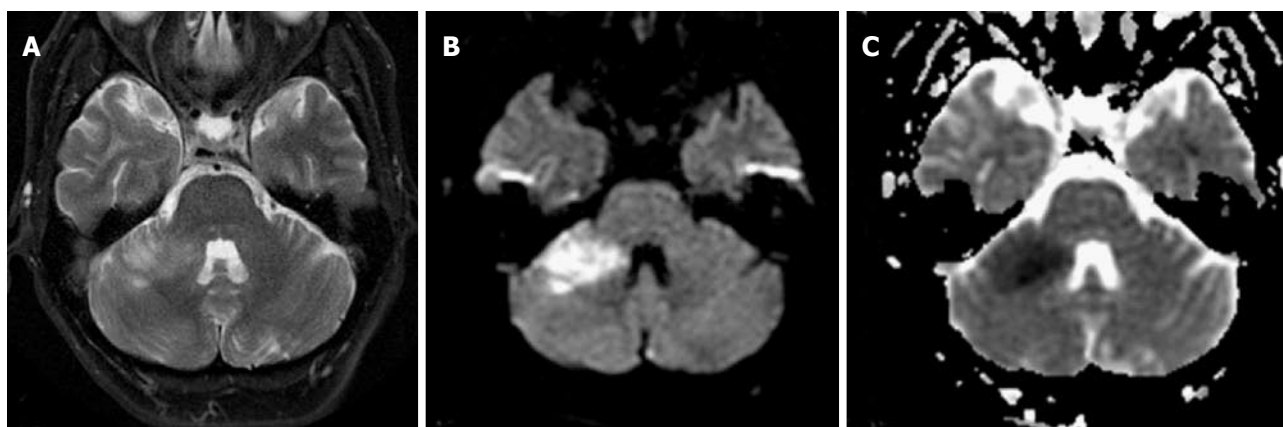


Figure 7 Anterior inferior cerebellar artery infarct. Patient with acute cerebellar ataxia and right-sided weakness. Axial T2 (A), DWI (B) and ADC maps (C) show well-defined area of high T2 signal and restricted diffusion consistent with ischemia. DWI: Diffusion weighted-imaging.

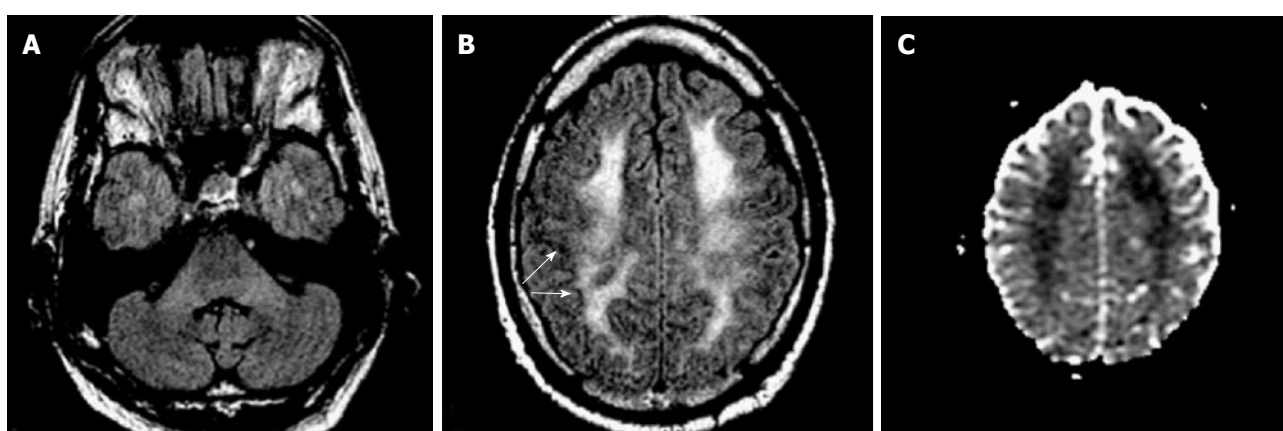


Figure 8 Acute heroin induced leukoencephalopathy (“chasing the dragon”). Twenty-year-old patient found down, history of recent heroin inhalation. A: Axial FLAIR shows subtle increased signal of MCP; Axial FLAIR (B) and ADC maps (C) show concomitant diffuse and confluent increased white matter signal and restricted diffusion with overall sparing of the subcortical u-fibers (arrows on B) and cortex. Though difficult to differentiate from hypoxic-ischemic event, the cortical sparing is more common in toxic leukoencephalopathies. Restricted diffusion has been described not only in the acute stage of toxic heroin inhalation, but in other hypoxic-toxic-metabolic states and could represent acute intramyelinic or excitotoxic edema, in some cases reversible. Evolution could lead to a chronic “chasing the dragon”, spongiform leukoencephalopathy, where the posterior white matter, pons and MCP are typically involved. MCP: Middle cerebellar peduncles.

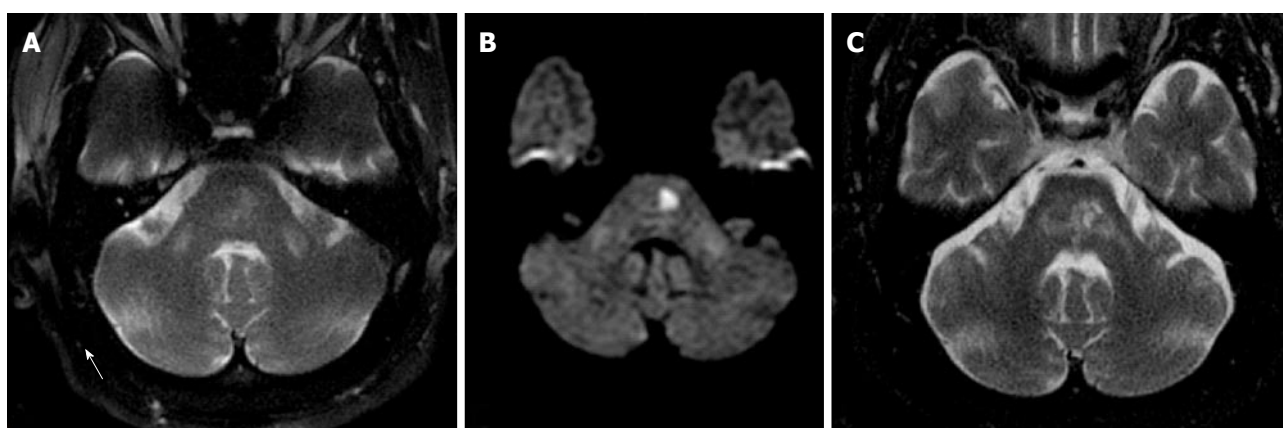


Figure 9 Wallerian degeneration of middle cerebellar peduncles. Axial T2 (A) and DWI (B) images show symmetric areas of abnormal signal in bilateral MCP as well as focal area of restricted diffusion in the left pons (note the characteristic spore of the midline due to occlusion of para-median branches of basilar artery); Axial T2 (C), 3 years f/u, shows evolution of lacunar infarction in the pons with resolution of abnormal signal in the right MCP and persistent abnormal signal and development of volume loss in the left MCP. Findings are consistent with WD of the MCP, with “acute” early changes in the bilateral MCP and subsequent left greater than right involvement on follow up (ipsilateral to infarct). WD: Wallerian degeneration; MCP: Middle cerebellar peduncles.

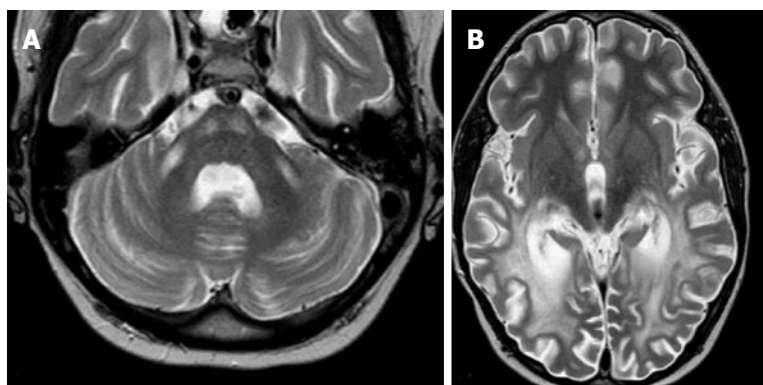


Figure 10 Adrenoleukodystrophy. A: Axial T2 image shows symmetric increased T2 signal in the MCP and bilateral corticospinal tracts; B: Axial T2 show concomitant symmetric and confluent white matter abnormal signal in bilateral occipito-parietal regions, typical for ADL. Note the preservation of subcortical u-fibers. Images courtesy of Dr. Lily Wang. ADL: Adrenoleukodystrophy; MCP: Middle cerebellar peduncles.

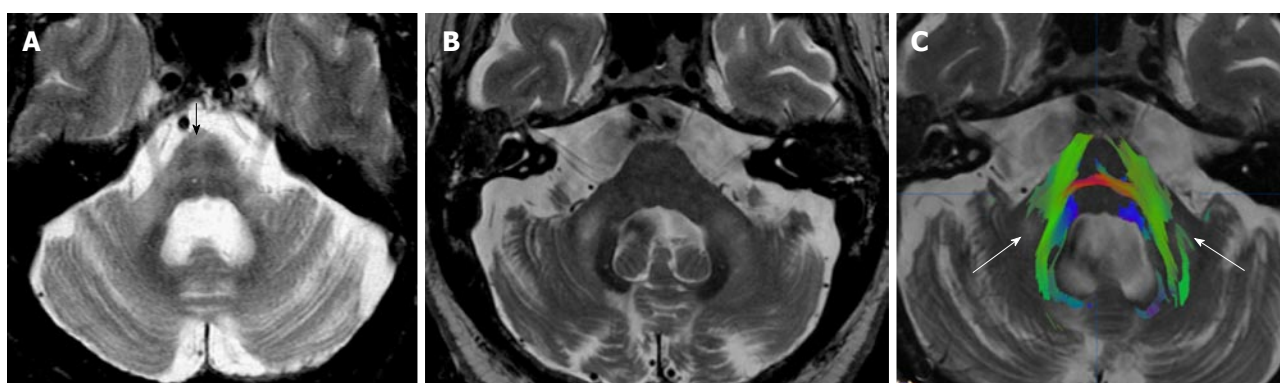


Figure 11 Multiple system atrophy C type and fragile-X associated tremor-ataxia syndrome. Axial T2 (A) in a patient with MSA-C show typical atrophy of the pons and MCP with degeneration of the pontine crossing fibers ("hot cross bun" sign, black arrow). There is also associated increased T2 signal of the MCP bilaterally. Axial T2 (B) and diffusion tensor imaging (DTI) tractography (C) in a patient with FXTAS show cerebellar volume loss and associated increased T2 signal and volume loss of MCP. Due to decreased fractional anisotropy (white arrows on C) there is lack of fibers in the areas of abnormal T2 signal. (DTI acquisition technique similar than Figure 1, please see figure for details). Image (B) courtesy of Dr. Andrew Duker. FXTAS: Fragile-X associated tremor-ataxia syndrome; MSA-C: Multiple system atrophy C type; MCP: Middle cerebellar peduncles.

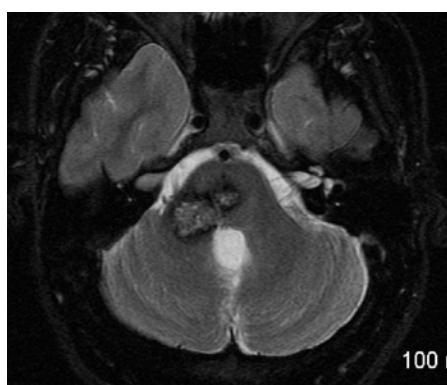


Figure 12 Cavernoma of middle cerebellar peduncle. Axial T2-WI shows contiguous lesions involving the pons and right MCP, with a typical mixed speckled hyper-intense and hypo-intense center and peripheral halo of hypo-intensity due to chronic hemosiderin deposition. MCP: Middle cerebellar peduncles.

and present in early or "active" forms of the disease; in some cases with concomitant restricted diffusion^[17]. In our experience involvement of the MCP by Wilson's is not a common finding.

Vascular/ischemic

MCP is supplied by the anterior inferior cerebellar artery (AICA) and in lesser degree by the superior cerebellar artery. Isolated AICA infarction (thromboembolic or secondary to severe atherosclerotic disease of basilar artery and branches) is an uncommon event. When it occurs, characteristic restricted diffusion is seen in the involved cerebellar peduncle (Figure 7).

WD in the MCP can occur in the setting of pontine ischemia or hemorrhage (Figure 9). Increased T2 signal caused by gliosis would correspond to the third of four stages in the evolution of WD, as described by Kuhn *et al.*^[18]. This stage should occur 10-14 wk after axonal injury/loss of antegrade input. Interestingly, increased signal on diffusion weighted-imaging (DWI) in the cortico-spinal tract (CST) have been reported in approximately 20% of cases of MCA/ACA infarcts as early as 72 h^[19]. Similarly, restricted diffusion in the CST has been reported at 48 h after MCA ischemia in the pediatric population^[20] and in the bilateral MCP at 3-4 wk after acute pontine insult^[21-24]. In all cases the changes are attributed to early WD. Certainly, they

represent different phases in the development of WD and should not be misinterpreted as ischemic insults.

Degenerative

MSA is a sporadic neurodegenerative disorder characterized clinically by any combination of parkinsonian, autonomic, cerebellar or pyramidal signs. The abundant presence of glial cytoplasmic inclusions in all clinical subtypes of MSA led to the recognition that Shy-Drager syndrome, striatonigral degeneration, and sporadic olivopontocerebellar atrophy are one disease characterized by neuronal multisystem degeneration with unique oligodendroglial inclusion pathology^[25].

Preferential neuronal loss of the cerebellum, pons and olivary nucleus with subsequent MCP degeneration characterizes the MSA-C subtype (where cerebellar ataxia is the main motor feature)^[8]. Abnormal T2 signal of MCP has been reported in 43% of cases of MSA-C^[26]. Concomitant volume loss is the rule (Figure 11A)^[27].

FXTAS is a genetic disorder with overexpression of the fragile-X mental retardation 1 gene (*FMR1*); it is most common in males and associated with progressive ataxia as the individual age. Though there are abnormal inclusions in the neurons and cortical atrophy, there is predominant loss of Purkinje cells with cerebellar axonal degeneration^[8,28]. Interestingly, in some series, as much as 82% of cases demonstrated increased T2 signal in the MCP (Figure 11B) (called as the "MCP sign", which as we described here, is not an specific sign)^[28].

LD

LD are inherited metabolic disorders in which biochemical defects interfere with myelin formation. Usually, LD are associated with peroxisomal (*e.g.*, adrenoleukodystrophy) or lysosomal defects (*e.g.*, metachromatic LD). LD can affect the MCP. However, there is concomitant, usually symmetric involvement of the supratentorial white matter, with sparing of subcortical u-fibers (Figure 10). Few LD, such as Canavan's or Pelizaeus-Merzbacher disease, compromise the subcortical u-fibers^[8].

Infectious

ADEM or rhombencephalitis can affect MCP. In most cases, the cause of ADEM or rhombencephalitis is not known; however an association with recent systemic infectious process or vaccination is described. Most common associated virus is varicella, mumps, measles, rubella or rotavirus. Rarely, bacterial infections such as Lyme disease, *Listeria* or Whipple can affect the posterior fossa and compromise the MCP^[29,30].

DWI AND DIFFUSION TENSOR IMAGING

As discussed, other conditions besides ischemic/cytotoxic edema can cause restriction diffusion (*e.g.*, intra-myelinic edema) (Figure 8). Some acute toxic states can show white matter restricted diffusion^[31,32]. In fact, the signal changes in these conditions could be reversible^[32]. Early WD and early stages of metabolic

diseases such as Wilson's disease can also be associated with areas of restricted diffusion^[17,20,21,33]. Overall, the mechanism of restricted diffusion in the "non-ischemic" cases is debatable. In addition to the mentioned intra-myelinic edema; acute white matter vacuolization or other types of excitotoxic edema could be postulated.

The use of diffusion tensor imaging (DTI) for prediction of neurologic deficits or for differential diagnosis is in continuous research. Fractional anisotropy (FA) measurements by DTI have proved involvement of the cerebellar peduncles by MS (even in the absence of T2 signal changes). Decreased FA in the MCP of MS patients as compared with controls is also correlated with motor deficits^[34]. Decreased FA early in the course of WD appears to predict neurologic deficits^[35]. DTI in the MCP has also been used to differentiate neurodegenerative diseases such as MSA-C from other cerebellar degenerative ataxias or Parkinson-like syndromes (Figure 11C)^[36].

OTHER ADVANCED IMAGING TECHNIQUES

MR spectroscopy (MRS) evaluates the biochemical signature in normal and abnormal brain parenchyma. Multiple metabolites to include N-acetyl-aspartate (NAA - marker of neuronal tissue), choline (Cho - membrane turnover), myo-Inositol (glial tissue), lipids (necrosis) and lactate (hypoxia) are altered in different pathologic processes. Very few studies of MRS in the MCP have assessed changes in neurodegenerative diseases, particularly MSA-C^[37]. They demonstrated decreased NAA in correlation with known decreased of neuronal/axonal tissue. In demyelinating processes, in addition to decreased NAA, an increase in Cho can also be demonstrated particularly in cases of acute demyelination (usually attributed to active myelin breakdown or increased macrophages in acute demyelinating plaques)^[7,38,39]. In other pathophysiologic processes, such as ischemia, an increase in lactate might be expected^[38,40].

MR perfusion is expecting to be altered in different pathologic processes involving the MCP. MR Perfusion, in conjunction with MRS and particularly DWI, is an important indicator of hypoxia, cell density and necrosis. Decreased perfusion on SPECT imaging has been demonstrated in MSA-C including the cerebellum and peduncles^[41-43]. Demyelinating or ischemic processes usually show decreased perfusion as compared with other pathologic processes such as tumors^[40,44,45].

Clinical clues

Given the improvement in the management of chronic infectious (*e.g.*, HIV) or immune-mediated diseases (*e.g.*, rituximab on MS or rheumatoid arthritis patients), patients in chronic immune-suppression states are not uncommon. In these populations, JC virus infection/reactivation (PML) should be high in the differential

when confronting abnormal MCP signal. A post-transplant patient have also a particular risk for PRES and in less degree ODS. Other known associations for PRES includes not only hypertension but also high dose chemotherapy. Concomitant or recent history of fever should raise suspicion for infectious or post infectious process (ADEM or rhombencephalitis). In the pediatric population, a leukodystrophy should be excluded. In a young encephalopathic patient, high suspicion for toxic/illicit drug use is warranted. Other toxic leukoencephalopathies, such as cyclosporine or methotrexate, should also be correlated clinically. After exclusion of relative common acquired causes of ataxia such as alcohol/anti-epileptic drugs (where cerebellar vermian atrophy predominates rather than MCP involvement), a progressive ataxic syndrome should raise suspicion for a degenerative process such as MSA-C or FXTAS (where areas of increased T2 signal in the MCP are common).

Imaging clues

As previously discussed, the involvement of the MCP or posterior fossa can be isolated (Figure 2). However, usually there is concomitant involvement of the pons or supratentorial white matter. The distribution and characteristic of the concomitant involvement can help in the differential. There is usually involvement of subcortical u-fibers in demyelinating diseases, particularly PML. To the contrary, the subcortical u-fibers are spared in other leukoencephalopathies such as toxic/metabolic entities or most LD^[8]. Additionally, the involvement is usually symmetric in these cases. Vasogenic edema pattern with not only involvement of the subcortical white matter but also the adjacent cortex should rise suspicion for PRES. Restricted diffusion is characteristic of an acute ischemic process, however it can be the result of early WD, the acute phase of ODS or toxic leukoencephalopathies. In these cases, restricted diffusion is usually bilateral. Volume loss characterizes not only neurodegenerative disorders such as MSA-C and FXTAS, but also the late stage of WD.

CONCLUSION

Pathologic entities such as demyelinating disorders and certain neurodegenerative diseases have predilection for the MCP. When approaching abnormal T2 signal in the MCP, entities such as MS, PML, PRES, and certain toxic/metabolic or neurodegenerative states should be entertained. Careful evaluation of concomitant imaging findings described, in conjunction with focused correlation with key clinical findings discussed; would yield an appropriate and accurate differential diagnosis in the majority of cases.

ACKNOWLEDGEMENTS

The authors would like to thanks Dr. Angelo Rutty, Perea Hospital - Puerto Rico, for his wonderful contribution

with the anatomic drawing presented in Figure 1. Previously presented exhibit at the Annual Meeting of the American Society of Neuroradiology, Chicago, 2015.

REFERENCES

- 1 **Ramnani N.** The primate cortico-cerebellar system: anatomy and function. *Nat Rev Neurosci* 2006; **7**: 511-522 [PMID: 16791141 DOI: 10.1038/nrn1953]
- 2 **Moritani T,** Smoker WR, Sato Y, Numaguchi Y, Westesson PL. Diffusion-weighted imaging of acute excitotoxic brain injury. *AJNR Am J Neuroradiol* 2005; **26**: 216-228 [PMID: 15709116]
- 3 **Ormerod IE,** Miller DH, McDonald WI, du Boulay EP, Rudge P, Kendall BE, Moseley IF, Johnson G, Tofts PS, Halliday AM. The role of NMR imaging in the assessment of multiple sclerosis and isolated neurological lesions. A quantitative study. *Brain* 1987; **110** (Pt 6): 1579-1616 [PMID: 3427402]
- 4 **Post MJ,** Yiannoutsos C, Simpson D, Booss J, Clifford DB, Cohen B, McArthur JC, Hall CD. Progressive multifocal leukoencephalopathy in AIDS: are there any MR findings useful to patient management and predictive of patient survival? AIDS Clinical Trials Group, 243 Team. *AJNR Am J Neuroradiol* 1999; **20**: 1896-1906 [PMID: 10588116]
- 5 **Bag AK,** Curé JK, Chapman PR, Roberson GH, Shah R. JC virus infection of the brain. *AJNR Am J Neuroradiol* 2010; **31**: 1564-1576 [PMID: 20299430 DOI: 10.3174/ajnr.A2035]
- 6 **Gonçalves FG,** Lamb L, Del Carpio-O'Donovan R. Progressive multifocal leukoencephalopathy restricted to the posterior fossa in a patient with systemic lupus erythematosus. *Braz J Infect Dis* 2011; **15**: 609-612 [PMID: 22218525]
- 7 **Horger M,** Beschoner R, Beck R, Nägele T, Schulze M, Ernemann U, Heckl S. Common and uncommon imaging findings in progressive multifocal leukoencephalopathy (PML) with differential diagnostic considerations. *Clin Neurol Neurosurg* 2012; **114**: 1123-1130 [PMID: 22771304 DOI: 10.1016/j.clineuro.2012.06.018]
- 8 **Ellison D,** Love S, Chimelli L, Harding BN, Lowe J, Vinters HV. Neuropathology: A Reference Text of CNS Pathology (2nd edition). MOSBY, Elsevier Ltd, 2004: 879 [DOI: 10.1111/j.1365-2990.2004.00620.x]
- 9 **Bartynski WS,** Boardman JF. Distinct imaging patterns and lesion distribution in posterior reversible encephalopathy syndrome. *AJNR Am J Neuroradiol* 2007; **28**: 1320-1327 [PMID: 17698535 DOI: 10.3174/ajnr.A0549]
- 10 **McKinney AM,** Jagadeesan BD, Truwit CL. Central-variant posterior reversible encephalopathy syndrome: brainstem or basal ganglia involvement lacking cortical or subcortical cerebral edema. *AJR Am J Roentgenol* 2013; **201**: 631-638 [PMID: 23971457 DOI: 10.2214/AJR.12.9677]
- 11 **McKinney AM,** Short J, Truwit CL, McKinney ZJ, Kozak OS, SantaCruz KS, Teksam M. Posterior reversible encephalopathy syndrome: incidence of atypical regions of involvement and imaging findings. *AJR Am J Roentgenol* 2007; **189**: 904-912 [PMID: 17885064 DOI: 10.2214/AJR.07.2024]
- 12 **Geibprasert S,** Gallucci M, Krings T. Addictive illegal drugs: structural neuroimaging. *AJNR Am J Neuroradiol* 2010; **31**: 803-808 [PMID: 19875473 DOI: 10.3174/ajnr.A1811]
- 13 **Okamoto K,** Tokiguchi S, Furusawa T, Ishikawa K, Quardery AF, Shinbo S, Sasai K. MR features of diseases involving bilateral middle cerebellar peduncles. *AJNR Am J Neuroradiol* 2003; **24**: 1946-1954 [PMID: 14625215]
- 14 **Uchino A,** Sawada A, Takase Y, Kudo S. Symmetrical lesions of the middle cerebellar peduncle: MR imaging and differential diagnosis. *Magn Reson Med Sci* 2004; **3**: 133-140 [PMID: 16093630]
- 15 **Arora A,** Neema M, Stankiewicz J, Guss ZD, Guss JG, Prockop L, Bakshi R. Neuroimaging of toxic and metabolic disorders. *Semin Neurol* 2008; **28**: 495-510 [PMID: 18843577 DOI: 10.1055/s-0028-1083684]
- 16 **King AD,** Walshe JM, Kendall BE, Chinn RJ, Paley MN, Wilkinson ID, Halligan S, Hall-Craggs MA. Cranial MR imaging in Wilson's

- s disease. *AJR Am J Roentgenol* 1996; **167**: 1579-1584 [PMID: 8956601 DOI: 10.2214/ajr.167.6.8956601]
- 17 **Sener RN**. Diffusion MR imaging changes associated with Wilson disease. *AJNR Am J Neuroradiol* 2003; **24**: 965-967 [PMID: 12748103]
- 18 **Kuhn MJ**, Johnson KA, Davis KR. Wallerian degeneration: evaluation with MR imaging. *Radiology* 1988; **168**: 199-202 [PMID: 3380957 DOI: 10.1148/radiology.168.1.3380957]
- 19 **Castillo M**, Mukherji SK. Early abnormalities related to postinfarction Wallerian degeneration: evaluation with MR diffusion-weighted imaging. *J Comput Assist Tomogr* 1999; **23**: 1004-1007 [PMID: 10589585]
- 20 **Bekiesinska-Figatowska M**, Duczkowski M, Madzik J, Uliasz M, Zawadka A, Baszczeska J. Diffusion-Weighted Imaging of the Early Phase of Wallerian Degeneration. A Report of two Pediatric Cases and Literature Review. *Neuroradiol J* 2012; **25**: 657-664 [PMID: 24029177]
- 21 **De Simone T**, Regna-Gladin C, Carriero MR, Farina L, Savoiardo M. Wallerian degeneration of the pontocerebellar fibers. *AJNR Am J Neuroradiol* 2005; **26**: 1062-1065 [PMID: 15891160]
- 22 **Fitzek C**, Fitzek S, Stoeter P. Bilateral Wallerian degeneration of the medial cerebellar peduncles after ponto-mesencephalic infarction. *Eur J Radiol* 2004; **49**: 198-203 [PMID: 14962648 DOI: 10.1016/S0720-048X(03)00132-3]
- 23 **Küker W**, Schmidt F, Heckl S, Nägele T, Herrlinger U. Bilateral Wallerian degeneration of the middle cerebellar peduncles due to paramedian pontine infarction: MRI findings. *Neuroradiology* 2004; **46**: 896-899 [PMID: 15526095 DOI: 10.1007/s00234-004-1287-y]
- 24 **Gala F**, Becker A, Pfeiffer M, Kollias S. Acute Wallerian degeneration of middle cerebellar peduncles due to basilar artery thrombosis. *Indian J Radiol Imaging* 2013; **23**: 164-167 [PMID: 24082483 DOI: 10.4103/0971-3026.116581]
- 25 **Wenning GK**, Colosimo C, Geser F, Poewe W. Multiple system atrophy. *Lancet Neurol* 2004; **3**: 93-103 [PMID: 14747001]
- 26 **Naka H**, Ohshita T, Murata Y, Imon Y, Mimori Y, Nakamura S. Characteristic MRI findings in multiple system atrophy: comparison of the three subtypes. *Neuroradiology* 2002; **44**: 204-209 [PMID: 11942373]
- 27 **Nicoletti G**, Fera F, Condino F, Auteri W, Gallo O, Pugliese P, Arabia G, Morgante L, Barone P, Zappia M, Quattrone A. MR imaging of middle cerebellar peduncle width: differentiation of multiple system atrophy from Parkinson disease. *Radiology* 2006; **239**: 825-830 [PMID: 16714464 DOI: 10.1148/radiol.2393050459]
- 28 **Tassone F**, Berry-Kravis EM. Fragile X-associated tremor ataxia syndrome (FXTAS). New York, London: Springer, 2010
- 29 **Guzmán-De-Villoria JA**, Ferreira-Argüelles C, Fernández-García P. Differential diagnosis of T2 hyperintense brainstem lesions: Part 2. Diffuse lesions. *Semin Ultrasound CT MR* 2010; **31**: 260-274 [PMID: 20483393 DOI: 10.1053/j.sult.2010.03.002]
- 30 **Black DF**, Aksamit AJ, Morris JM. MR imaging of central nervous system Whipple disease: a 15-year review. *AJNR Am J Neuroradiol* 2010; **31**: 1493-1497 [PMID: 20395395 DOI: 10.3174/ajnr.A2089]
- 31 **Rollins N**, Winick N, Bash R, Booth T. Acute methotrexate neurotoxicity: findings on diffusion-weighted imaging and correlation with clinical outcome. *AJNR Am J Neuroradiol* 2004; **25**: 1688-1695 [PMID: 15569732]
- 32 **McKinney AM**, Kieffer SA, Paylor RT, SantaCruz KS, Kendi A, Lucato L. Acute toxic leukoencephalopathy: potential for reversibility clinically and on MRI with diffusion-weighted and FLAIR imaging. *AJR Am J Roentgenol* 2009; **193**: 192-206 [PMID: 19542414 DOI: 10.2214/AJR.08.1176]
- 33 **Musson R**, Romanowski C. Restricted diffusion in Wallerian degeneration of the middle cerebellar peduncles following pontine infarction. *Pol J Radiol* 2010; **75**: 38-43 [PMID: 22802803]
- 34 **Anderson VM**, Wheeler-Kingshott CA, Abdel-Aziz K, Miller DH, Toosy A, Thompson AJ, Ciccarelli O. A comprehensive assessment of cerebellar damage in multiple sclerosis using diffusion tractography and volumetric analysis. *Mult Scler* 2011; **17**: 1079-1087 [PMID: 21511688 DOI: 10.1177/1352458511403528]
- 35 **Liang Z**, Zeng J, Zhang C, Liu S, Ling X, Wang F, Ling L, Hou Q, Xing S, Pei Z. Progression of pathological changes in the middle cerebellar peduncle by diffusion tensor imaging correlates with lesser motor gains after pontine infarction. *Neurorehabil Neural Repair* 2009; **23**: 692-698 [PMID: 19244384 DOI: 10.1177/1545968308331142]
- 36 **Prakash N**, Hageman N, Hua X, Toga AW, Perlman SL, Salamon N. Patterns of fractional anisotropy changes in white matter of cerebellar peduncles distinguish spinocerebellar ataxia-1 from multiple system atrophy and other ataxia syndromes. *Neuroimage* 2009; **47** Suppl 2: T72-T81 [PMID: 19446636 DOI: 10.1016/j.neuroimage.2009.05.013]
- 37 **Terakawa H**, Abe K, Watanabe Y, Nakamura M, Fujita N, Hirabuki N, Yanagihara T. Proton magnetic resonance spectroscopy (1H MRS) in patients with sporadic cerebellar degeneration. *J Neuroimaging* 1999; **9**: 72-77 [PMID: 10208103]
- 38 **Oz G**, Alger JR, Barker PB, Bartha R, Bizzi A, Boesch C, Bolan PJ, Brindle KM, Cudalbu C, Dinçer A, Dydak U, Emir UE, Frahm J, González RG, Gruber S, Gruetter R, Gupta RK, Heerschap A, Henning A, Hetherington HP, Howe FA, Hüppi PS, Hurd RE, Kantarci K, Klomp DW, Kreis R, Kruiskamp MJ, Leach MO, Lin AP, Luijten PR, Marjańska M, Maudsley AA, Meyerhoff DJ, Mountford CE, Nelson SJ, Pamir MN, Pan JW, Peet AC, Poptani H, Posse S, Pouwels PJ, Ratai EM, Ross BD, Scheenen TW, Schuster C, Smith IC, Soher BJ, Tkáč I, Vigneron DB, Kauppinen RA. Clinical proton MR spectroscopy in central nervous system disorders. *Radiology* 2014; **270**: 658-679 [PMID: 24568703 DOI: 10.1148/radiol.13130531]
- 39 **Shah R**, Bag AK, Chapman PR, Curé JK. Imaging manifestations of progressive multifocal leukoencephalopathy. *Clin Radiol* 2010; **65**: 431-439 [PMID: 20451009 DOI: 10.1016/j.crad.2010.03.001]
- 40 **Chu WJ**, Mason GF, Pan JW, Hetherington HP, Liu HG, San Pedro EC, Mountz JM. Regional cerebral blood flow and magnetic resonance spectroscopic imaging findings in diaschisis from stroke. *Stroke* 2002; **33**: 1243-1248 [PMID: 11988598]
- 41 **Miyoshi F**, Kanasaki Y, Shinohara Y, Fujii S, Kaminou T, Tanabe Y, Ogawa T. Significance of combined use of MRI and perfusion SPECT for evaluation of multiple system atrophy, cerebellar type. *Acta Radiol* 2015 Aug 7; Epub ahead of print [PMID: 26253930 DOI: 10.1177/0284185115598810]
- 42 **Cilia R**, Marotta G, Benti R, Pezzoli G, Antonini A. Brain SPECT imaging in multiple system atrophy. *J Neural Transm (Vienna)* 2005; **112**: 1635-1645 [PMID: 16284908 DOI: 10.1007/s00702-005-0382-5]
- 43 **Matsuda H**, Imabayashi E, Kuji I, Seto A, Ito K, Kikuta D, Yamada M, Shimano Y, Sato N. Evaluation of both perfusion and atrophy in multiple system atrophy of the cerebellar type using brain SPECT alone. *BMC Med Imaging* 2010; **10**: 17 [PMID: 20701753 DOI: 10.1186/1471-2342-10-17]
- 44 **Song SS**. Advanced imaging in acute ischemic stroke. *Semin Neurol* 2013; **33**: 436-440 [PMID: 24504605 DOI: 10.1055/s-0033-1364214]
- 45 **Fayed-Miguel N**, Morales-Ramos H, Modrego-Pardo PJ. Magnetic resonance imaging with spectroscopy, perfusion and cerebral diffusion in the diagnosis of brain tumours. *Rev Neurol* 2006; **42**: 735-742 [PMID: 16775800]

P- Reviewer: Li YZ, Shen J, Sijens PE S- Editor: Ji FF
L- Editor: A E- Editor: Wu HL



Magnetic resonance imaging of the spinal marrow: Basic understanding of the normal marrow pattern and its variant

Mohamed Ragab Nouh, Ahmed Fathi Eid

Mohamed Ragab Nouh, Faculty of Medicine, Alexandria University, Alexandria 21563, Egypt

Ahmed Fathi Eid, National Guard hospital, Al Ehsa 31982, Eastern Province, Saudi Arabia

Author contributions: Nouh MR had the idea of the manuscript, reviewed the literature, drafted the manuscript and supplied some of the figures; Eid AF supplied some of the figures, critically reviewed the manuscript; Both authors approved the manuscript in its current final form.

Conflict-of-interest statement: The authors declare no conflict of interest.

Open-Access: This article is an open-access article which was selected by an in-house editor and fully peer-reviewed by external reviewers. It is distributed in accordance with the Creative Commons Attribution Non Commercial (CC BY-NC 4.0) license, which permits others to distribute, remix, adapt, build upon this work non-commercially, and license their derivative works on different terms, provided the original work is properly cited and the use is non-commercial. See: <http://creativecommons.org/licenses/by-nc/4.0/>

Correspondence to: Mohamed Ragab Nouh, MD, Assistant Professor of radiology and clinical imaging, Faculty of Medicine, Alexandria University, 1 Kolyat El-Teb Street, Mahata El-Ramel, Alexandria 21563, Egypt. mrabab73@yahoo.com
Telephone: +20-111-6590365

Received: June 2, 2015

Peer-review started: June 5, 2015

First decision: August 8, 2015

Revised: September 29, 2015

Accepted: October 23, 2015

Article in press: October 27, 2015

Published online: December 28, 2015

Abstract

For now, magnetic resonance (MR) is the best non-invasive imaging modality to evaluate vertebral bone marrow thanks to its inherent soft-tissue contrast and

non-ionizing nature. A daily challenging scenario for every radiologist interpreting MR of the vertebral column is discerning the diseased from normal marrow. This requires the radiologist to be acquainted with the used MR techniques to judge the spinal marrow as well as its normal MR variants. Conventional sequences used basically to image marrow include T1W, fat-suppressed T2W and short tau inversion recovery (STIR) imaging provides gross morphological data. Interestingly, using non-routine MR sequences; such as opposed phase, diffusion weighted, MR spectroscopy and contrast-enhanced imaging; may elucidate the nature of bone marrow heterogeneities; by inferring cellular and chemical composition; and adding new functional prospects. Recalling the normal composition of bone marrow elements and the physiologic processes of spinal marrow conversion and reconversion eases basic understanding of spinal marrow imaging. Additionally, orientation with some common variants seen during spinal marrow MR imaging as hemangiomas and bone islands is a must. Moreover, awareness of the age-associated bone marrow changes as well as changes accompanying different variations of the subject's health state is essential for radiologists to avoid overrating normal MR marrow patterns as pathologic states and mitigate unnecessary further work-up.

Key words: Magnetic resonance imaging; Normal; Spinal; Marrow; Variants

© **The Author(s) 2015.** Published by Baishideng Publishing Group Inc. All rights reserved.

Core tip: Magnetic resonance (MR) remains the ideal noninvasive imaging modality to evaluate vertebral bone marrow. Radiologists have to be aware by age-associated bone marrow changes as well as changes accompanying different variations of the subject's health state. Moreover, acquaintance with the used MR techniques, their privileges and limitations, in evaluation of spinal marrow is a prime requirement for radiologist to discern the normal spinal marrow as well as its

variants from diseased one.

Nouh MR, Eid AF. Magnetic resonance imaging of the spinal marrow: Basic understanding of the normal marrow pattern and its variant. *World J Radiol* 2015; 7(12): 448-458 Available from: URL: <http://www.wjgnet.com/1949-8470/full/v7/i12/448.htm> DOI: <http://dx.doi.org/10.4329/wjr.v7.i12.448>

INTRODUCTION

The spine is the largest store of bone marrow in the body^[1,2]. Addressing bone marrow signal pattern is an integral part of the spinal magnetic resonance (MR) imaging evaluation. By far, magnetic resonance imaging (MRI) is the best imaging modality to depict bone marrow thanks to its inherent soft-tissue contrast and non-ionizing nature^[3-5].

Bone marrow is a dynamic organ with continued changes occurring with increased age and increased hematopoietic needs in different environmental and health states^[4,6]. Similarly, it is the target of a lot of pathologic processes that results in altered signal intensity or heterogenous signal pattern on MR imaging. A daily challenging scenario for every radiologist interpreting MR of the spine is to discern the diseased from normal marrow. This requires the radiologist to be acquainted with normal MR patterns of the spinal bone marrow, its chronological conversion, and its different common variants. This review starts with a brief discussion of the composition and physiology of the spinal marrow, followed by a concise discussion on the common MR sequences used to evaluate the spinal marrow. In the latter section the normal spinal marrow MR patterns and common variants are displayed.

Spinal bone marrow buildup and physiology

Imaging-wise, the spinal bone marrow is a mix of cellular elements enclosed within a cortical bone shell; the vertebral body. These cellular elements are enmeshed within the medullary bony trabeculae; predominantly vertically oriented; that provide both structural support and storage of minerals as calcium and phosphate; thicker in the lumbar region^[2,5,6]. There are two types of bone marrow in the spine: the red marrow, named after its richness in hemoglobin in erythrocytes lineage and is richly vascular; and the yellow marrow, named after abundant carotenoid bodies in its fat cells and is scarily vascular^[7]. Either marrow type, whether red or yellow, is composed of a blend of fat, water and proteins in different proportions (Table 1). The 3 components vary in volume with normal growth and in response to different stimuli. Hence, their proportions are the main determinants of spinal marrow MR signal characteristics^[8-10]. The nutrition of spinal marrow is derived from ambient sinusoids branching from nutrient vessels piercing the vertebral cortices and drained *via* the Batson's venous

Table 1 Vertebral bone marrow chemical composition and cellular buildup

Marrow phenotype	Chemical composition	Cellular components
Red marrow	40%-60% lipids	60% hematopoietic cells
	30%-40% water	40% fat cells
	10%-20% proteins	
Yellow marrow	80% lipids	95% fat cells
	15% water	5% hematopoietic cells
	5% proteins	

plexus emerging from the posterior vertebral bodies' cortices. Nerves accompany this vascular network and few lymph nodes can be identified within the vertebral marrow^[7]. The function of bone marrow is to provide different blood cell lineages involved in tissue nutrition, oxygenation and body's immune reactions^[7].

Spinal marrow conversion

At birth, the whole spinal marrow is metabolically active (hematopoietic/red marrow). This pattern gradually, and in orderly fashion, turns into a less metabolically active (fat/yellow) marrow with growing up. This temporal physiologic phenomenon is known as normal marrow conversion and concludes around age of 25-30 years^[2,6,11,12]. As in other skeletal region, the pattern of spinal marrow conversion is centripetal starting in the subcortical and subendplates regions and going to the center of vertebral body^[8]. At all times, both red and yellow marrow are spinal marrow cohabitant yet the prevalent type is used to address the type of marrow in focus^[2,4,12]. Moreover, a peculiar character of the spinal marrow is the persistence of red marrow over all ages, especially in the lumbar region^[1]. Consequently, heterogeneity of the spinal marrow is a normal phenomenon, especially in adolescence and middle age. Focal areas of red marrow may be a challenge to disclose its nature in some clinical scenarios and mandates making use of different MR pulse sequences to disclose its nature.

Spinal marrow reconversion

During lifetime, various physiologic and pathologic states require increased tissue demands for more oxygen and hemoglobin. The metabolically inactive fat marrow dynamically repopulates into the metabolically active red type, capable of responding to tissues' needs of oxygen in a process named marrow reconversion^[5,6,13,14].

It could be in response to physiologic stimuli as in obesity, cigarette smokers and heavy training athletes; or pathologic conditions as chronic hemolytic anemias and marrow replacing disorders^[2,13,14].

In contrast to the orderly fashion of normal marrow conversion, reconversion is a patchy and an asymmetrical process where areas of red marrow are embedded within the surrounding yellow marrow^[15]. That is why recognition of this physiologic phenomenon is mandatory to rule out underlying myeloproliferative

disorder on MR imaging.

MRI technique for the spinal marrow

Routine evaluation of spinal marrow will include spin echo T1 and T2W pulse sequences in the sagittal plane. Some institutes add short tau inversion recovery (STIR) sequences in the sagittal plane as a routine. The author's prefer to use the STIR in the coronal plane to discourse the neutral axis and its meningeal sleeves, especially in cervical and lumbar regions, abnormalities of the facets and sacroiliac joints and exploration of accidental extra-spinal pathologies not apparent on routine sagittal and axial planes. Any suspicious bone marrow lesion on the routine planes could be ascertained on this additional coronal STIR image. Axial planes will be advantageous in labeling presence of extra-medullary extensions and neural axis involvement by any marrow pathology.

Routine MR sequences for spinal bone marrow imaging

T1-weighted imaging: Both red and fat marrows contain lipid and water with various proportions. The red marrow appears as low signal due to its higher water content on T1W images yet it has to be higher than that of intervertebral discs and paraspinal muscles^[16]. On the contrary, a high lipid content of yellow marrow returns high signal intensity comparable to that of subcutaneous fat on T1W images^[16]. This makes T1W the money's worth sequence of MR screening of bone marrow^[3,17,18].

T2-weighted imaging: The signal returning from both water and fat are high yet signal returning from red marrow is slightly lower than that of yellow marrow^[19]. So, the ability of T2-sequence to differentiate marrow hyperplasia from marrow lesions is limited without the use of fat suppression especially on the fast spin echo (FSE) acquisitions^[10,20]. This mandates the use of fat-suppression for better utility of T2 FSE used in clinical imaging of the spines. On fat suppression T2W sequences the red marrow will be of slightly higher signal than muscle while the yellow marrow has signal lower than it^[6,10].

STIR sequence: It enhances the difference in longitudinal relaxation of fat and water on T1W imaging. A non-selective 180° inversion pulse applied at specified inversion time followed by refocusing 90 pulse can cancel any signal from fat and the returning signal will be of the non-fatty components, *e.g.*, water^[10,21]. This enhances contrast of bone marrow lesions within the suppressed background. The main drawback of STIR imaging, that it suppresses any signal other than fat as hematomas and gadolinium enhancement^[22].

Problem-solving MR sequences for spinal bone marrow imaging

Chemical-shift imaging: Chemical-shift or opposed phase imaging relies on the fact that water and fat have different resonance frequencies so that when they are resonating aligned their signal is summed (in-phase

imaging) while when they are opposed (out-phase imaging) their signals are subtracted with subsequent signal drop^[23]. As fat and water intermix in both types of marrow, the signal of red marrow will not significantly drop in out phase while that of yellow marrow will^[23]. However, this is not absolute and a cut off value of 20% signal drop has postulated^[24].

The main value of opposed phase imaging is to rule out neoplastic replacement of the marrow. Metastatic and infiltrative marrow neoplasia will destroy normal marrow and retain high water content with resultant high-signal on out-phase imaging^[23]. This has proved beneficiary in differentiation neoplastic and osteoporotic fractures^[25,26].

However, false negative results can rise from fat-containing metastasis (*e.g.*, from renal cell carcinoma) and false positive results can results from marrow fibrosis as well as susceptibility artifacts accompanying marrow hematomas and sclerotic metastasis^[25,27]. This may necessitate marrow biopsy for histopathologic confirmation.

Diffusion-weighted imaging

Diffusion imaging addresses the free mobility of protons in a specific tissue^[28]. This could be qualitative^[29], *i.e.*, bull eying or quantitative^[30] using the apparent diffusion coefficient (ADC). It is a sound fast sequence that can comprehend functional aspects of the examined tissues in addition to the available routine morphologic sequences. Normal marrow that is rich in protons will show free diffusion and high ADC values (*i.e.*, high signal intensity on both the diffusion image and ADC map)^[31,32]. Contrarily, in metastatic lesions with densely packed cells and in cytotoxic edematous cells following trauma lower ADC values are seen (*i.e.*, high signal intensity on the diffusion image and low signal on ADC map)^[31,32]. However, studies on the use of diffusion weighted imaging of the marrow are controversial and it should be interpreted in line with the routine marrow sequences^[31,33].

Currently, common clinical musculoskeletal applications of diffusion weighted imaging of the spine are differencing osteoporotic fractures and neoplastic vertebral body collapse^[34], differentiation of infective and degenerative sub-endplates changes^[35] and follow-up treatment response of neoplastic marrow lesions^[36].

Contrast-enhanced marrow imaging

Contrast enhancement is used to depict marrow lesions. The normal spinal marrow may show mild homogenous contrast enhancement in neonates and pediatrics due to abundant blood flow, prominent extravascular space and rich diverse cellularity^[17,37]. This progressively become imperceptible as a function of age and increased fatty marrow content^[38]. In normal adults spinal marrow doesn't show perceptible enhancement following administration of gadolinium based T1W agents^[17,37,38].

Dynamic contrast studies of the spinal marrow had been used to diagnose and follow-up myelo-proli-

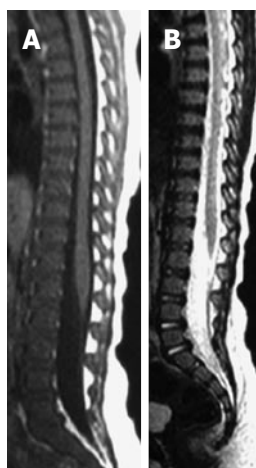


Figure 1 Sagittal T1W (A) and T2W (B) images of 2-year-old boy showing low-signal of the spinal marrow just barely brighter than intervertebral discs on T1W images due to richness in red marrow.

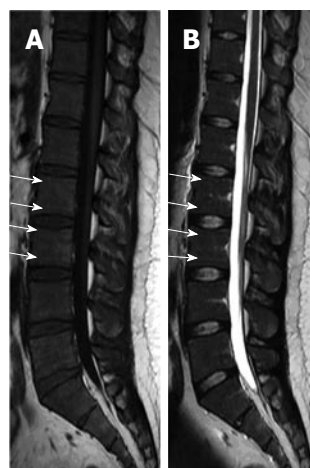


Figure 2 Sagittal T1W (A) and T2W (B) images of 25-year-old male showing linear high-signal of the normal fat marrow at the sub-endplate zones (white arrows) at LV2 through LV5 levels. Note also, linear focal fat depositions along the basi-vertebral veins posteriorly.

ferative disorders^[39]. Following rapid IV gadolinium-based contrast agent administration, the changes in longitudinal relaxation of vertebral marrow are measured and signal time intensity curve is reproduced. Various parameters have been used like maximum intensity, slope of the curve and contrast washout^[40]. Normal vertebral marrow shows decreased maximal enhancement, slope of enhancement and washout indices with increased age and fat marrow content^[38,41]. However, dynamic contrast-enhanced studies have not been widely used in clinical practices.

Another less commonly used class of MR contrast agents affect the T2- or T2* imaging characteristics. These contrast agents, *e.g.*, ultra small particles iron oxides are engulfed by the hematopoietic cells of the normal bone marrow, produce local field inhomogeneities with resultant suppression of normal bone marrow^[42]. This results in increased conspicuity of marrow lesion that will not take these agents. They are used to differentiate infiltrative marrow lesions from reactive marrow hyperplasia^[43]. Also they can differentiate bone metastasis from infection^[44].

Proton MR spectroscopy

MR spectroscopy is a non-invasive method of quantification of fat content of the marrow and evaluation of its chemical composition^[45]. A single or multi-voxel method can be used to assess one or more vertebral bodies and the fat content is expressed as a percentage (due to multiple lipid peaks) not an absolute value^[46,47]. Previous reports emphasized age and sex related physiologic changes of the fat content of the spinal bone marrow^[48,49].

However, it is not widely used clinically as same information could be achieved by the above used tools.

MRI appearance of the normal spinal bone marrow

As mentioned earlier, the bone marrow is a mix of red and yellow marrow supported by a trabecular marrow network. The trabecular marrow appears as a mesh of

linear intermingled low signal intensities within both red and yellow marrow on all pulse sequences, especially prominent on the gradient recalled one. The trabecular marrow changes have little effects on the spinal marrow MR signal, if present.

Actually, the relative ratio of fat and water is the main determinant for the MR signal of spinal bone marrow as well as the used MR pulse sequence^[1,4,5,9,13,50,51].

On T1W images, the vertebral fat marrow is high-signal intensity similar to subcutaneous fat in adults^[2,5,6]. However, at birth all spinal marrow is of the red type with high water content resulting in low signal intensity of the vertebral bodies even relative to the intervertebral discs and muscles on T1W images (Figure 1)^[14,52]. After that, gradual increased amount of fat cells, especially at the sub-endplates region and anterior part of the vertebral body (Figure 2), in the marrow results into the adulthood heterogeneous vertebral marrow pattern (Figure 3)^[52].

On T2W images, fatty marrow exhibits signal intensity near to that of the subcutaneous fat^[2,6,10,17,18,53]. So use of fat suppression on fast/turbo spin echo T2 imaging is a must for better clinical utility of T2W sequence.

On fat-suppressed T2W and STIR images (Figure 3), the red marrow emits an intermediate signal slightly higher than adjacent paravertebral muscles against the black background of suppressed fatty marrow. However, it is far less intense compared to pathologic lesions with high cellular and water contents^[10].

Following intravenous gadolinium-based contrast media administration, the red marrow; predominantly in children and young adolescents; shows appreciable visual enhancement and increased quantitative parameters on MR dynamic contrast studies inferring its abundant vascularity, well perfusion and increased metabolic activity. However, this SI increased has to be less than 35% by the age of 35 years^[54]. On the other

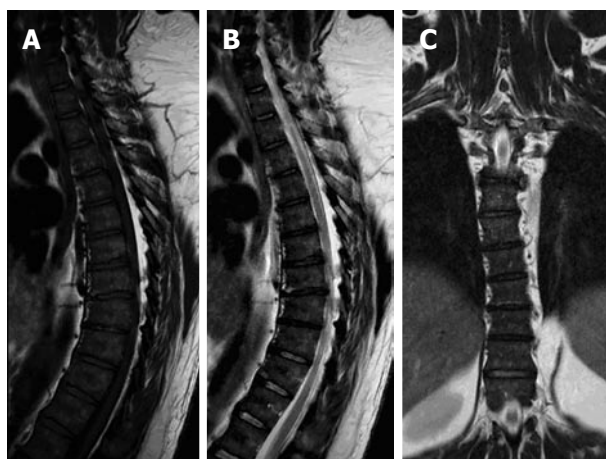


Figure 3 Sagittal T1W (A), T2W (B) and coronal STIR (C) images of the dorsal spines of a 60-year-old male with mild scoliotic deformity of the mid dorsal region. The figure shows heterogeneous vertebral marrow with predominantly T1W high-signal and T2W intermediate signal meanwhile, the whole marrow did not exhibit abnormal signal on STIR images. STIR: Short tau inversion recovery.

hand, this enhancement pattern is hardly perceptible in the fat marrow, in adults^[37,38,55,56].

On chemical-shift imaging, the red marrow shows no remarkable signal drop on the out-phase image thanks to its near equal contents of both water and fat protons^[57]. However, some signal drop may be seen in the yellow marrow (less than 20%) yet it is far less than malignant destructive processes^[25].

On DWI, the normal red marrow shows intermediate signal that does not show lost signal on the corresponding ADC map.

Common variant of the normal spinal marrow on MR imaging

As bone marrow is a dynamic organ with the normal processes of conversion and reconversion in response to various environmental and health stresses, and spines are the largest marrow reservoir of our body, heterogeneity of vertebral marrow MR signal is a common finding in daily clinical MR examinations. Additionally, this is more complicated by age- and sex-related variations as fat marrow is higher in men than women^[49,58] and water content is higher in females child-bearing age^[59].

In the same vertebral body of an adult, bone marrow is homogeneously distributed with more abundance of the cellular red-marrow (50% of the spinal marrow by age of 70 years) near the endplates and anterior portion of the vertebral body while fat marrow is abundant around the basi-vertebral vein^[2,60].

These spatial and sex-related changes are common between individuals of the same age group. However, it is important to recognize that these variations have to be homogenous between vertebral bodies of the same subject^[54].

Spinal marrow heterogeneities' may be seen in all



Figure 4 Sagittal T1W (A) and T2W (B) images of 24-year-old male showing linear high-signal intensities along the course of basi-vertebral veins with near ending of normal marrow conversion into the mature/fat type.

spinal regions but it is more common in the lumbar spines^[1,6,9]. These changes could be in a focal or diffuse pattern, produced by either yellow or red marrow variant distributions^[6,54,61,62].

LOCALIZED NORMAL VARIANTS

Focal T1W hyper-intensities

Basi-vertebral vein fat: On T1W and T2W imaging, areas of focal fat deposition are commonly seen in the posterior elements of the vertebrae as well as areas of high vascularity with active processes of conversion and reconversion. This will include the sub-endplates and subcortical zones and around the basivertebral vein (Figure 4)^[5,32,60].

Vertebral-end plate degenerative changes: Progressive degenerative changes of the vertebral endplates are not uncommon findings on spinal MR (Figure 5)^[63]. Modic and colleagues described band-like sub-end plate marrow changes that exhibit water-like (low T1W and high T2W) MR signal for type-I, fat-like (high T1W and T2W signals) for type-II, and calcium-like (low T1W and T2W signals) for type-III Modic changes^[64]. Recognition of associated disc dehydration and presence of intra-discal gas precludes underlying pathologies, *e.g.*, discitis.

Focal fatty marrow islands (Focal fatty metaplasia): A developmental variation of the bone marrow conversion process is the localized aggregates of areas of fat marrow. It can occur in any vertebral level yet it is a common variant in the lumbar spines (Figure 6) and lateral sacral ala of males than females; an area where sex-related marrow changes are important as age-related changes as proved by chemical-shift imaging and spectroscopic data^[49,65]. It can take the eye of an inexperienced interpreter if seen in the turbo-spin echo



Figure 5 Sagittal T1W (A) and T2W (B) images of 53-year-old male showing LV4 lower end plate irregularities with subjacent Type-II Modic changes with high-T1W and T2W signal. Note adjacent LV4-5 disc desiccations.

T2W images. However, recognizing its high signal on T1W images and vanishing on fat-suppressed images will disclose its nature. Their corresponding radiographs and CT examinations will show preserved trabecular and cortical bone. They are not uncommon finding on daily spinal MR evaluations and should not raise clinical awkward.

HAEMANGIOMA

Histologically, hemangiomas are developmental vascular malformations consist of endothelial lined, thin-walled, blood-filled vessels and sinuses, containing and supported by fat and interspersed among the longitudinally oriented trabeculae of bones^[66]. They are common in vertebral bodies than posterior elements. Hemangiomas are not exceedingly uncommon finding in MR studies of the spines. They are commonly asymptomatic and multiple. On T2W images as well as STIR images, typical hemangiomas have high-signal intensity due to slow flow in vascular channels^[67]. Its benign nature is ascertained by corresponding high-signal intensity on T1W images due to its abundant fat content (Figure 7)^[67]. Some atypical patterns of hemangioma may mimic more worrisome neoplastic lesions on MR imaging (Figure 8). Commonly, the intervening thickened trabeculae exhibits linear low-signal intensity on all pulse sequences^[68]. Spinal hemangiomas shows variable patterns of enhancement and can be confused for serious bony lesions^[69]. Radiography (Figure 8) and CT can help to solve such confusing situations by showing prominent trabeculae with the pathognomonic polka-dot sign (Figure 8) on axial images^[70,71].

Focal T1W hypo-intensities

Vertebral enostosis: Enostosis (or bone island) is a common imaging finding on all imaging modalities assessing skeletal parts, especially the spine with an

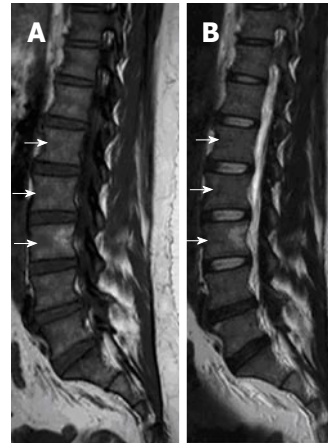


Figure 6 Sagittal T1W (A) and T2W (B) images of 41-year-old female showing LV3 patch of high-signal intensity (unchanged on serial magnetic resonance follow-up; not shown) on both T1W and T2W with fuzzy margins, proved to focal fatty metaplasia. Note areas of low signal intensity under the anterior cortex of multiple adjacent vertebral bodies (short white arrows) corresponding to focal nodules of red marrow.

incidence of about 14%. It is thought as a benign osseous hamartoma of developmental origin^[72]. It is composed of cortical bone layers embedded within the surrounding vertebral marrow cavity and it is usually endosteal surface based. It is common in the mid-dorsal and lumbar regions, although it can occur anywhere. It has low signal on all MR pulse sequences^[72]. However, a previous report described a rare pattern of peripheral rim of high-signal intensity on STIR images making it difficult to differentiate from sclerotic metastasis^[73]. However, correlation with radiography and CT will help to disclose the lesion's nature.

Focal nodular hyperplasia of the red marrow

Bone marrow hyperplasia is an aberrance of normal marrow conversion-reconversion process with abundance of red marrow^[74,75]. Mild regional forms can be seen in endurance athletes, obese subjects and heavy smokers^[15,76]. A more pronounced form can show up in some hematologic disorders (*e.g.*, Hemolytic anemias) and malignancies as well as patients treated with granulocyte colony stimulating factors (GCSF) used to relieve marrow suppression associated with chemotherapeutic regimens^[77,78].

Rarely a localized focal form can be seen in the spinal (Figure 6) and pelvic marrow. On MR imaging these areas follow the signal criteria of normal red marrow, *i.e.*, low signal intensity on T1W images, intermediate or no signal increase on T2W, Fat-suppressed and STIR imaging. On gadolinium administration faint or no enhancement is observed. Sometimes, these focal lesions can show increased signal intensity on T2 FSE sequences. This is contradictory to high T2W signal and contrast enhancement seen in neoplastic cases^[74,75,79].

Presences within areas rich in red marrow (sub-cortical and around basi-vertebral vein), elongated shape of the lesions, presence of central high-spot on T1W

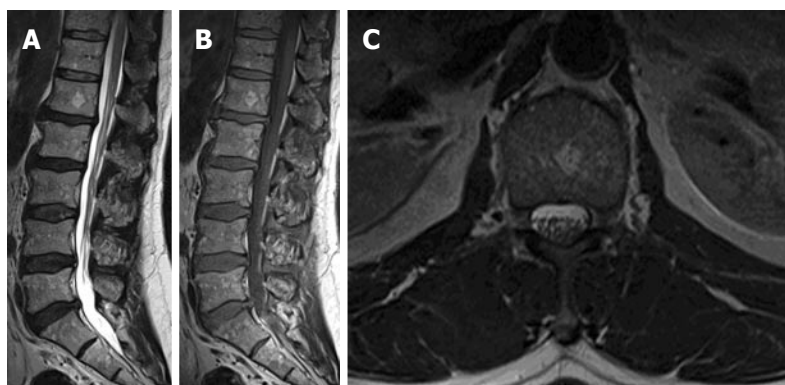


Figure 7 Sagittal T1W (A), T2W (B) and axial T2W images of 63-year-old osteoporotic female showing heterogeneous lumbar vertebral marrow signal with diffuse increased high-signal intensities due to higher fat content. There is a focal round patch of increased signal on both T1 and T2 weighting in LV1 body with small punctuate areas of low signal intensities; seen unchanged from previous 2 magnetic resonance examinations (not shown here) confirmed to be a small typical vertebral hemangioma.

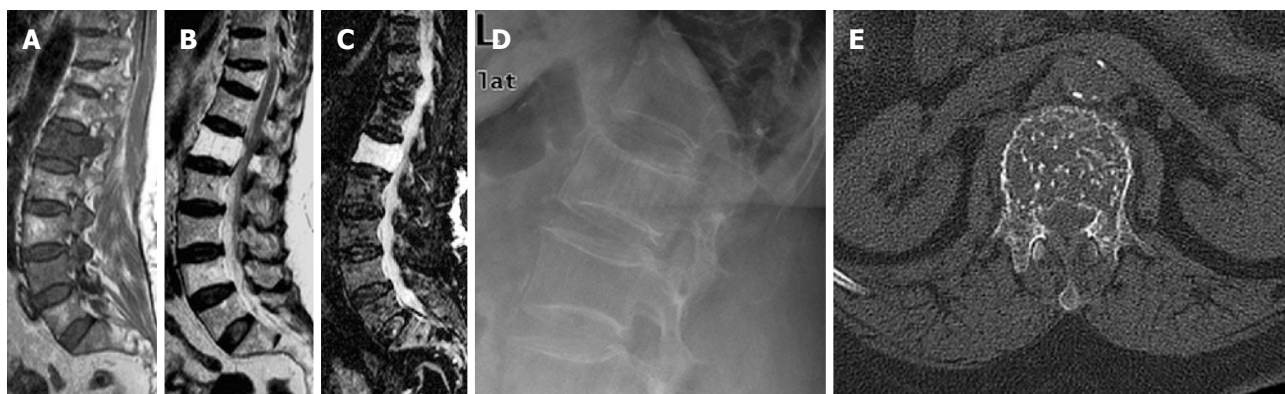


Figure 8 Sagittal T1W (A), T2W (B) and STIR (C) images of 65-year-old female showing L1 vertebral body atypical hemangioma with diffuse low signal intensity on T1W image and high-signal intensity on T2W and STIR images presented on a background of lumbar spondylotic changes. Note also, DV11 old porotic wedging. Companion imaging showed prominent trabecular pattern on focused radiography (D) and CT (E) of the LV1 with characteristic polka-dot sign. STIR: Short tau inversion recovery.

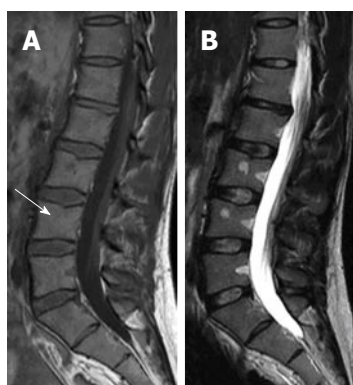


Figure 9 Sagittal T1W (A) and T2W (B) images of 33-year-old male showing focal geographic low signal intensity patches targeting LV3 and LV4 bodies centers as well as around basi-vertebral veins. These patches still of high-signal intensity on T2W image. Note, the central fat spot (white arrow) and fuzzy margins of LV4 lesion inferring benignity features are consistent with focal nodular marrow reconversion.

images (Figure 9), fuzzy margins are predictors of their benignity^[1,3]. On corresponding radiographs and CT studies, radiolucency, geographic nature and absence of

cortical disruption will ascertain their benign nature.

Benign notochordal cell tumors

Benign notochordal cell tumors are increasingly recognized intraosseous; presumably; benign lesions of notochordal remnants^[80]. Its reported incidence in autopsies reaches 20% of divus and vertebral bodies^[81]. They are incidental finding on radiologic and histologic examinations and have to be distinguished from chordomas to save inadvertent extensive surgeries^[82]. These lesions were found to emit homogenous low- to iso-signal intensity on T1W images and high-signal on T2W images with no enhancement on MR contrast studies^[82,83]. Lesions that are sizable enough to be picked on CT and radiographs are sclerotic in nature. However, topographic features of the lesion, *i.e.*, intravertebral, preserved trabecular pattern and non-enhancement following MR contrast administration, are equally important to rule the possibility of chordoma; the extremely malignant spectrum of notochordal cell lineage^[82,83]. A recent report described malignant, transformation into chordoma of L1 vertebral body supporting the postulation of a relation of

the two entities^[84]. MR imaging is the best modality to address and followup these lesions.

Diffuse normal variants

Diffuse hematopoietic marrow hyperplasia: Diffuse hematopoietic marrow hyperplasia is an exaggeration of the normal marrow reconversion discussed in an earlier section. It can occur in response to different physiologic stimuli as discussed before. Moreover, it is increasingly recognized in patients under chemo- and radio-therapeutic regimens whom are treated with GCSF to lessen the associated bone marrow suppression^[85,86].

It can be confused with diffuse marrow infiltrative processes in the vertebral marrow thanks to both red and fat marrow cohabitation. As a rule of thumb, marrow hyperplasia exhibits a signal similar to that of red marrow. The vertebral hyperplastic marrow shows low signal on T1W images that may be even lower than adjacent intervertebral discs^[1,6,13,14,87,88]. It may show mild to moderate enhancement following IV gadolinium administration^[86]. However, the signal is relatively higher than paravertebral muscles on STIR and fat-saturated T2 imaging^[1,6,13,14,87,88]. In chronic hemoglobinopathies, low signal may be seen on T2W images due to chronic hemosidine deposition^[5]. Problem-solving MR sequences may be utilized in some difficult cases.

Fat conversion of the marrow

Under certain conditions, there may be premature conversion of red marrow into the fat type with increased MR signal compared to the age and sex matched subjects. This can be seen in subjects with hypercortisolism (whether endogenous or exogenous) and in some feeding disorders as anorexia nervosa^[89]. This supposed to be mediated *via* hormonal effects on the preferential differentiation of bone marrow progenitor cells^[90]. It has to be considered as a normal variation of the bone marrow for the health status of those subjects and not a pathologic marrow disease.

Serous conversion of the marrow

In conditions of severe systemic illness associated with loss body fat stores, *e.g.*, malignant cachexia, AIDS, anorexia nervosa or even following severe infections in pediatrics, a rare phenomenon of serous or gelatinous transformation of the bone marrow may commence in either diffuse or focal forms^[91]. It starts in peripheral skeleton yet it eventually reaches the axial skeleton. Pathologically; it is characterized by paucicellular marrow including both fat and hematopoietic cells which become embedded in hyaluronic acid-rich extracellular gelatinous substances^[91,92]. These pathologic changes are recognized on MR as fat-poor marrow, which emits water-like signal on all pulse sequences, *i.e.*, low on T1W and high on T2W and STIR sequences^[3,93]. Visual loss of normal fat stores of the subcutis and inter-tissues fascial spaces will raise this suspicion^[93,94]. On 18FDG PET/CT it may show increased tracer uptake^[95].

CONCLUSION

MR is the gold standard noninvasive imaging modality to evaluate vertebral bone marrow. Conventional sequences used basically to image marrow include T1W, fat-suppressed T2W and STIR imaging provides gross morphological data. Moreover, non-routine MR sequences may elucidate the nature of bone marrow heterogeneities; by inferring cellular and chemical composition; and adding new functional prospects. Awareness of the age-related bone marrow changes as well as changes accompanying different variations of the subject's health state is essential for radiologists. This will avoid overrating normal MR marrow patterns as pathologic states and avoid unnecessary further work-up.

ACKNOWLEDGMENTS

The authors would thank to Dr. Osamah Al Atyah, anesthesia and ICU Consultant, Hussein Al Ali Hospital, Al Ehsa, Saudi Arabia, for his critical linguistic revision of the final manuscript.

REFERENCES

- 1 **Alyas F**, Saifuddin A, Connell D. MR imaging evaluation of the bone marrow and marrow infiltrative disorders of the lumbar spine. *Magn Reson Imaging Clin N Am* 2007; **15**: 199-219, vi [PMID: 17599640]
- 2 **Murphy DT**, Moynagh MR, Eustace SJ, Kavanagh EC. Bone marrow. *Magn Reson Imaging Clin N Am* 2010; **18**: 727-735 [PMID: 21111977 DOI: 10.1016/j.mric.2010.07.003]
- 3 **Vande Berg BC**, Lecouvet FE, Michaux L, Ferrant A, Maldague B, Malghem J. Magnetic resonance imaging of the bone marrow in hematological malignancies. *Eur Radiol* 1998; **8**: 1335-1344 [PMID: 9853210 DOI: 10.1007/s003300050548]
- 4 **Strong PN**, Goerke J, Oberg SG, Kelly RB. beta-Bungarotoxin, a pre-synaptic toxin with enzymatic activity. *Proc Natl Acad Sci USA* 1976; **73**: 178-182 [PMID: 1749 DOI: 10.1007/s00256-007-0309-3]
- 5 **Tall MA**, Thompson AK, Vertinsky T, Palka PS. MR imaging of the spinal bone marrow. *Magn Reson Imaging Clin N Am* 2007; **15**: 175-198, vi [PMID: 17599639 DOI: 10.1016/j.mric.2007.01.001]
- 6 **Vande Berg BC**, Malghem J, Lecouvet FE, Maldague B. Magnetic resonance imaging of the normal bone marrow. *Skeletal Radiol* 1998; **27**: 471-483 [PMID: 9809875]
- 7 **Riley RS**, Williams D, Ross M, Zhao S, Chesney A, Clark BD, Ben-Ezra JM. Bone marrow aspirate and biopsy: a pathologist's perspective. II. interpretation of the bone marrow aspirate and biopsy. *J Clin Lab Anal* 2009; **23**: 259-307 [PMID: 19774631 DOI: 10.1002/jcla.20305]
- 8 **Vande Berg BC**, Malghem J, Lecouvet FE, Maldague B. Normal bone marrow: dynamic aspects in magnetic resonance imaging. *J Radiol* 2001; **82**: 127-135 [PMID: 11428207]
- 9 **Vande Berg BC**, Lecouvet FE, Galant C, Simoni P, Malghem J. Normal variants of the bone marrow at MR imaging of the spine. *Semin Musculoskelet Radiol* 2009; **13**: 87-96 [PMID: 19455471 DOI: 10.1055/s-0029-1220879]
- 10 **Shah LM**, Hanrahan CJ. MRI of spinal bone marrow: part I, techniques and normal age-related appearances. *AJR Am J Roentgenol* 2011; **197**: 1298-1308 [PMID: 22109283 DOI: 10.2214/AJR.11.7005]
- 11 **Kricun ME**. Red-yellow marrow conversion: its effect on the location of some solitary bone lesions. *Skeletal Radiol* 1985; **14**: 10-19 [PMID: 3895447]
- 12 **Rosen CJ**, Ackert-Bicknell C, Rodriguez JP, Pino AM. Marrow fat

- and the bone microenvironment: developmental, functional, and pathological implications. *Crit Rev Eukaryot Gene Expr* 2009; **19**: 108-124 [DOI: 10.1615/CritRevEukaryotGeneExpr.v19.i2.20]
- 13 **Malkiewicz A**, Dziedzic M. Bone marrow reconversion - imaging of physiological changes in bone marrow. *Pol J Radiol* 2012; **77**: 45-50 [PMID: 23269936]
- 14 **Guillerman RP**. Marrow: red, yellow and bad. *Pediatr Radiol* 2013; **43** Suppl 1: S181-S192 [PMID: 23478934 DOI: 10.1007/s00247-012-2582-0]
- 15 **Poulton TB**, Murphy WD, Duerk JL, Chapek CC, Feiglin DH. Bone marrow reconversion in adults who are smokers: MR Imaging findings. *AJR Am J Roentgenol* 1993; **161**: 1217-1221 [PMID: 8249729]
- 16 **Carroll KW**, Feller JF, Tirman PF. Useful internal standards for distinguishing infiltrative marrow pathology from hematopoietic marrow at MRI. *J Magn Reson Imaging* 1997; **7**: 394-398 [PMID: 9090597]
- 17 **Vogler JB**, Murphy WA. Bone marrow imaging. *Radiology* 1988; **168**: 679-693 [PMID: 3043546]
- 18 **Long SS**, Yablon CM, Eisenberg RL. Bone marrow signal alteration in the spine and sacrum. *AJR Am J Roentgenol* 2010; **195**: W178-W200 [PMID: 20729415 DOI: 10.2214/AJR.09.4134]
- 19 **Levine CD**, Schweitzer ME, Ehrlich SM. Pelvic marrow in adults. *Skeletal Radiol* 1994; **23**: 343-347 [PMID: 7939832]
- 20 **Silva JR**, Hayashi D, Yonenaga T, Fukuda K, Genant HK, Lin C. MRI of bone marrow abnormalities in hematological malignancies. *Diagn Interv Radiol Ank Turk* 2013; **19**: 393-3999 [DOI: 10.5152/dir.2013.067]
- 21 **Mirowitz SA**, Apicella P, Reinus WR, Hammerman AM. MR imaging of bone marrow lesions: relative conspicuousness on T1-weighted, fat-suppressed T2-weighted, and STIR images. *AJR Am J Roentgenol* 1994; **162**: 215-221 [DOI: 10.2214/ajr.162.1.8273669]
- 22 **Bydder GM**, Steiner RE, Blumgart LH, Khenia S, Young IR. MR imaging of the liver using short T1 inversion recovery sequences. *J Comput Assist Tomogr* 1985; **9**: 1084-1089 [PMID: 4056142]
- 23 **Disler DG**, McCauley TR, Ratner LM, Kesack CD, Cooper JA. In-phase and out-of-phase MR imaging of bone marrow: prediction of neoplasia based on the detection of coexistent fat and water. *AJR Am J Roentgenol* 1997; **169**: 1439-1447 [DOI: 10.2214/ajr.169.5.9353477]
- 24 **Zajick DC**, Morrison WB, Schweitzer ME, Parellada JA, Carrino JA. Benign and malignant processes: normal values and differentiation with chemical shift MR imaging in vertebral marrow. *Radiology* 2005; **237**: 590-596 [PMID: 16244268 DOI: 10.1148/radiol.2372040990]
- 25 **Erlly WK**, Oh ES, Outwater EK. The utility of in-phase/opposed-phase imaging in differentiating malignancy from acute benign compression fractures of the spine. *AJNR Am J Neuroradiol* 2006; **27**: 1183-1188 [PMID: 16775260]
- 26 **Ragab Y**, Emad Y, Gheita T, Mansour M, Abou-Zeid A, Ferrari S, Rasker JJ. Differentiation of osteoporotic and neoplastic vertebral fractures by chemical shift {in-phase and out-of phase} MR imaging. *Eur J Radiol* 2009; **72**: 125-133 [PMID: 18672340 DOI: 10.1016/j.ejrad.2008.06.019]
- 27 **Swartz PG**, Roberts CC. Radiological reasoning: bone marrow changes on MRI. *AJR Am J Roentgenol* 2009; **193**: S1-4, Quiz S5-9 [PMID: 19696238 DOI: 10.2214/AJR.09.7069]
- 28 **Dietrich O**, Biffar A, Reiser MF, Baur-Melnyk A. Diffusion-weighted imaging of bone marrow. *Semin Musculoskelet Radiol* 2009; **13**: 134-144 [PMID: 19455476 DOI: 10.1055/s-0029-1220884]
- 29 **Lichy MP**, Aschoff P, Plathow C, Stemmer A, Horger W, Mueller-Horvat C, Steidle G, Horger M, Schafer J, Eschmann SM, Kiefer B, Claussen CD, Pfannenberger C, Schlemmer HP. Tumor detection by diffusion-weighted MRI and ADC-mapping--initial clinical experiences in comparison to PET-CT. *Invest Radiol* 2007; **42**: 605-613 [PMID: 17700275 DOI: 10.1097/RLI.0b013e31804ff4d9]
- 30 **Costa FM**, Ferreira EC, Vianna EM. Diffusion-weighted magnetic resonance imaging for the evaluation of musculoskeletal tumors. *Magn Reson Imaging Clin N Am* 2011; **19**: 159-180 [PMID: 21129640 DOI: 10.1016/j.mric.2010.10.007]
- 31 **Baur A**, Huber A, Dürr HR, Nikolaou K, Stäbler A, Deimling M, Reiser M. Differentiation of benign osteoporotic and neoplastic vertebral compression fractures with a diffusion-weighted, steady-state free precession sequence. *Rofo* 2002; **174**: 70-75 [PMID: 11793288 DOI: 10.1055/s-2002-19534]
- 32 **Biffar A**, Baur-Melnyk A, Schmidt GP, Reiser MF, Dietrich O. Multiparameter MRI assessment of normal-appearing and diseased vertebral bone marrow. *Eur Radiol* 2010; **20**: 2679-2689 [DOI: 10.1016/j.ejrad.2010.03.011]
- 33 **Castillo M**, Arbelaez A, Smith JK, Fisher LL. Diffusion-weighted MR imaging offers no advantage over routine noncontrast MR imaging in the detection of vertebral metastases. *AJNR Am J Neuroradiol* 2000; **21**: 948-953 [PMID: 10815675]
- 34 **Karchevsky M**, Babb JS, Schweitzer ME. Can diffusion-weighted imaging be used to differentiate benign from pathologic fractures? A meta-analysis. *Skeletal Radiol* 2008; **37**: 791-795 [PMID: 18551290 DOI: 10.1007/s00256-008-0503-y]
- 35 **Eguchi Y**, Ohtori S, Yamashita M, Yamauchi K, Suzuki M, Orita S, Kamoda H, Arai G, Ishikawa T, Miyagi M, Ochiai N, Kishida S, Masuda Y, Ochi S, Kikawa T, Takaso M, Aoki Y, Inoue G, Toyone T, Takahashi K. Diffusion magnetic resonance imaging to differentiate degenerative from infectious endplate abnormalities in the lumbar spine. *Spine (Phila Pa 1976)* 2011; **36**: E198-E202 [PMID: 21099738 DOI: 10.1097/BRS.0b013e3181d5ff05]
- 36 **Padhani AR**, Koh DM, Collins DJ. Whole-body diffusion-weighted MR imaging in cancer: current status and research directions. *Radiology* 2011; **261**: 700-718 [PMID: 22095994 DOI: 10.1148/radiol.11110474]
- 37 **Baur A**, Stäbler A, Bartl R, Lamerz R, Scheidler J, Reiser M. MRI gadolinium enhancement of bone marrow: age-related changes in normals and in diffuse neoplastic infiltration. *Skeletal Radiol* 1997; **26**: 414-418 [PMID: 9259099]
- 38 **Montazel JL**, Divine M, Lepage E, Kobeiter H, Breil S, Rahmouni A. Normal Spinal Bone Marrow in Adults: Dynamic Gadolinium-enhanced MR Imaging1. *Radiol* 2003; **229**: 703-709 [DOI: 10.1148/radiol.2293020747]
- 39 **Rahmouni A**, Montazel JL, Divine M, Lepage E, Belhadj K, Gaulard P, Bouanane M, Golli M, Kobeiter H. Bone marrow with diffuse tumor infiltration in patients with lymphoproliferative diseases: dynamic gadolinium-enhanced MR imaging. *Radiology* 2003; **229**: 710-717 [PMID: 14593191 DOI: 10.1148/radiol.2293020748]
- 40 **Erlemann R**, Reiser M, Peters PE, Wuisman P, Niendorf HP, Kunze V. Time-dependent changes in signal intensity in neoplastic and inflammatory lesions of the musculoskeletal system following intravenous administration of Gd-DTPA. *Radiologe* 1988; **28**: 269-276 [PMID: 3399673]
- 41 **Griffith JF**, Yeung DK, Antonio GE, Lee FK, Hong AW, Wong SY, Lau EM, Leung PC. Vertebral bone mineral density, marrow perfusion, and fat content in healthy men and men with osteoporosis: dynamic contrast-enhanced MR imaging and MR spectroscopy. *Radiology* 2005; **236**: 945-951 [PMID: 16055699 DOI: 10.1148/radiol.2363041425]
- 42 **Simon GH**, Raatschen HJ, Wendland MF, von Vopelius-Feldt J, Fu Y, Chen MH, Daldrup-Link HE. Ultrasmall superparamagnetic iron-oxide-enhanced MR imaging of normal bone marrow in rodents: original research original research. *Acad Radiol* 2005; **12**: 1190-1197 [PMID: 16099684 DOI: 10.1016/j.acra.2005.05.014]
- 43 **Daldrup-Link HE**, Rummeny EJ, Ihssen B, Kienast J, Link TM. Iron-oxide-enhanced MR imaging of bone marrow in patients with non-Hodgkin's lymphoma: differentiation between tumor infiltration and hypercellular bone marrow. *Eur Radiol* 2002; **12**: 1557-1566 [PMID: 12042968 DOI: 10.1007/s00330-001-1270-5]
- 44 **Fukuda Y**, Ando K, Ishikura R, Kotoura N, Tsuda N, Kato N, Yoshiya S, Nakao N. Superparamagnetic iron oxide (SPIO) MRI contrast agent for bone marrow imaging: differentiating bone metastasis and osteomyelitis. *Magn Reson Med Sci* 2006; **5**: 191-196 [PMID: 17332709]
- 45 **Hu HH**, Kan HE. Quantitative proton MR techniques for measuring

- fat. *NMR Biomed* 2013; **26**: 1609-1629 [PMID: 24123229 DOI: 10.1002/nbm.3025]
- 46 **Li X**, Kuo D, Schafer AL, Porzig A, Link TM, Black D, Schwartz AV. Quantification of vertebral bone marrow fat content using 3 Tesla MR spectroscopy: reproducibility, vertebral variation, and applications in osteoporosis. *J Magn Reson Imaging* 2011; **33**: 974-979 [PMID: 21448966 DOI: 10.1002/nbm.3025]
- 47 **Schwartz AV**, Sigurdsson S, Hue TF, Lang TF, Harris TB, Rosen CJ, Vittinghoff E, Siggeirsdottir K, Sigurdsson G, Oskarsdottir D, Shet K, Palermo L, Gudnason V, Li X. Vertebral bone marrow fat associated with lower trabecular BMD and prevalent vertebral fracture in older adults. *J Clin Endocrinol Metab* 2013; **98**: 2294-2300 [PMID: 23553860 DOI: 10.1210/jc.2012-3949]
- 48 **Jung CM**, Kugel H, Schulte O, Heindel W. [Proton-MR spectroscopy of the spinal bone marrow. An analysis of physiological signal behavior]. *Radiologe* 2000; **40**: 694-699 [PMID: 11006939]
- 49 **Kugel H**, Jung C, Schulte O, Heindel W. Age- and sex-specific differences in the 1H-spectrum of vertebral bone marrow. *J Magn Reson Imaging* 2001; **13**: 263-268 [PMID: 11169833]
- 50 **Panicek DM**, Schwartz LH. MR Imaging of Bone Marrow in Patients with Musculoskeletal Tumors. *Sarcoma* 1999; **3**: 37-41 [PMID: 18521263]
- 51 **Vanel D**, Dromain C, Tardivon A. MRI of bone marrow disorders. *Eur Radiol* 2000; **10**: 224-229 [PMID: 10663751]
- 52 **Foster K**, Chapman S, Johnson K. MRI of the marrow in the paediatric skeleton. *Clin Radiol* 2004; **59**: 651-673 [PMID: 15262540 DOI: 10.1016/j.crad.2004.02.001]
- 53 **Hilfiker P**, Zanetti M, Debatin JF, McKinnon G, Hodler J. Fast spin-echo inversion-recovery imaging versus fast T2-weighted spin-echo imaging in bone marrow abnormalities. *Invest Radiol* 1995; **30**: 110-114 [PMID: 7654279]
- 54 **Vande Berg BC**, Lecouvet FE, Galant C, Maldague BE, Malghem J. Normal variants and frequent marrow alterations that simulate bone marrow lesions at MR imaging. *Radiol Clin North Am* 2005; **43**: 761-770, ix [PMID: 15893536 DOI: 10.1016/j.rcl.2005.01.007]
- 55 **Bollow M**, Knauf W, Korfel A, Taupitz M, Schilling A, Wolf KJ, Hamm B. Initial experience with dynamic MR imaging in evaluation of normal bone marrow versus malignant bone marrow infiltrations in humans. *J Magn Reson Imaging* 1997; **7**: 241-250 [PMID: 9039623]
- 56 **Biffar A**, Dietrich O, Sourbron S, Duerr HR, Reiser MF, Baur-Melnyk A. Diffusion and perfusion imaging of bone marrow. *Eur J Radiol* 2010; **76**: 323-328 [PMID: 20381277 DOI: 10.1016/j.ejrad.2010.03.011]
- 57 **Blebea JS**, Houseni M, Torigian DA, Fan C, Mavi A, Zhuge Y, Iwanaga T, Mishra S, Udupa J, Zhuang J, Gopal R, Alavi A. Structural and functional imaging of normal bone marrow and evaluation of its age-related changes. *Semin Nucl Med* 2007; **37**: 185-194 [PMID: 17418151 DOI: 10.1053/j.semnucmed.2007.01.002]
- 58 **Mitchell DG**, Rao VM, Dalinka M, Spritzer CE, Axel L, Geftter W, Kricun M, Steinberg ME, Kressel HY. Hematopoietic and fatty bone marrow distribution in the normal and ischemic hip: new observations with 1.5-T MR imaging. *Radiology* 1986; **161**: 199-202 [PMID: 3763867 DOI: 10.1148/radiology.161.1.3763867]
- 59 **Ishijima H**, Ishizaka H, Horikoshi H, Sakurai M. Water fraction of lumbar vertebral bone marrow estimated from chemical shift misregistration on MR imaging: normal variations with age and sex. *AJR Am J Roentgenol* 1996; **167**: 355-358 [PMID: 8686603 DOI: 10.2214/ajr.167.2.8686603]
- 60 **Ricci C**, Cova M, Kang YS, Yang A, Rahmouni A, Scott WW, Zerhouni EA. Normal age-related patterns of cellular and fatty bone marrow distribution in the axial skeleton: MR imaging study. *Radiology* 1990; **177**: 83-88 [PMID: 2399343 DOI: 10.1148/radiology.177.1.2399343]
- 61 **Hajek PC**, Baker LL, Goobar JE, Sartoris DJ, Hesselink JR, Haghighi P, Resnick D. Focal fat deposition in axial bone marrow: MR characteristics. *Radiology* 1987; **162**: 245-249 [PMID: 3786770 DOI: 10.1148/radiology.162.1.3786770]
- 62 **Baur A**, Dietrich O, Reiser M. Diffusion-weighted imaging of bone marrow: current status. *Eur Radiol* 2003; **13**: 1699-1708 [PMID: 12759770 DOI: 10.1007/s00330-003-1873-0]
- 63 **Kuisma M**, Karppinen J, Niinimäki J, Kurunlahti M, Haapea M, Vanharanta H, Tervonen O. A three-year follow-up of lumbar spine endplate (Modic) changes. *Spine (Phila Pa 1976)* 2006; **31**: 1714-1718 [PMID: 16816768 DOI: 10.1097/01.brs.0000224167.18483.14]
- 64 **Modic MT**, Steinberg PM, Ross JS, Masaryk TJ, Carter JR. Degenerative disk disease: assessment of changes in vertebral body marrow with MR imaging. *Radiology* 1988; **166**: 193-199 [PMID: 3336678 DOI: 10.1148/radiology.166.1.3336678]
- 65 **Duda SH**, Laniado M, Schick F, Strayle M, Claussen CD. Normal bone marrow in the sacrum of young adults: differences between the sexes seen on chemical-shift MR imaging. *AJR Am J Roentgenol* 1995; **164**: 935-940 [PMID: 7726052 DOI: 10.2214/ajr.164.4.7726052]
- 66 **Hart JL**, Edgar MA, Gardner JM. Vascular tumors of bone. *Semin Diagn Pathol* 2014; **31**: 30-38 [PMID: 24680180 DOI: 10.1053/j.semdp.2014.01.003]
- 67 **Baudrez V**, Galant C, Vande Berg BC. Benign vertebral hemangioma: MR-histological correlation. *Skeletal Radiol* 2001; **30**: 442-446 [PMID: 11479749 DOI: 10.1007/s0025610300442]
- 68 **Ross JS**, Masaryk TJ, Modic MT, Carter JR, Mapstone T, Dengel FH. Vertebral hemangiomas: MR imaging. *Radiology* 1987; **165**: 165-169 [PMID: 3628764 DOI: 10.1148/radiology.165.1.3628764]
- 69 **Rodallec MH**, Feydy A, Larousserie F, Anract P, Campagna R, Babinet A, Zins M, Drapé JL. Diagnostic imaging of solitary tumors of the spine: what to do and say. *Radiographics* 2008; **28**: 1019-1041 [PMID: 18635627 DOI: 10.1148/rg.284075156]
- 70 **Laredo JD**, Reizine D, Bard M, Merland JJ. Vertebral hemangiomas: radiologic evaluation. *Radiology* 1986; **161**: 183-189 [PMID: 3763864 DOI: 10.1148/radiology.161.1.3763864]
- 71 **Persaud T**. The polka-dot sign. *Radiology* 2008; **246**: 980-981 [PMID: 18309021 DOI: 10.1148/radiol.2463050903]
- 72 **Murphy MD**, Andrews CL, Flemming DJ, Temple HT, Smith WS, Smirniotopoulos JG. From the archives of the AFIP. Primary tumors of the spine: radiologic pathologic correlation. *Radiographics* 1996; **16**: 1131-1158 [PMID: 8888395 DOI: 10.1148/radiographics.16.5.8888395]
- 73 Proceedings of UK Radiological Congress 1997. The British Institute of Radiology, 1997; 150. Available from: URL: <http://www.birpublications.org/doi/abs/10.1259/conf-pukrc.1997> [DOI: 10.1259/conf-pukrc.1997]
- 74 **Bordalo-Rodrigues M**, Galant C, Lonnew M, Clause D, Vande Berg BC. Focal nodular hyperplasia of the hematopoietic marrow simulating vertebral metastasis on FDG positron emission tomography. *AJR Am J Roentgenol* 2003; **180**: 669-671 [PMID: 12591672 DOI: 10.2214/ajr.180.3.1800669]
- 75 **Detti B**. A Case of Focal Haematopoietic Hyperplasia of a Vertebral Body and Review of the Modern Literature. *J Nucl Med Radiat Ther* 2013; **4**: In press [DOI: 10.4172/2155-9619.1000151]
- 76 **Deutsch AL**, Mink JH, Rosenfelt FP, Waxman AD. Incidental detection of hematopoietic hyperplasia on routine knee MR imaging. *AJR Am J Roentgenol* 1989; **152**: 333-336 [PMID: 2783510 DOI: 10.2214/ajr.152.2.333]
- 77 **Hollinger EF**, Alibazoglu H, Ali A, Green A, Lamonica G. Hematopoietic cytokine-mediated FDG uptake simulates the appearance of diffuse metastatic disease on whole-body PET imaging. *Clin Nucl Med* 1998; **23**: 93-98 [PMID: 9481497 DOI: 10.1097/00003072-199802000-00007]
- 78 **Stähler A**, Doma AB, Baur A, Krüger A, Reiser MF. Reactive bone marrow changes in infectious spondylitis: quantitative assessment with MR imaging. *Radiology* 2000; **217**: 863-868 [PMID: 11110955 DOI: 10.1148/radiology.217.3.r00dc23863]
- 79 **Steiner RM**, Mitchell DG, Rao VM, Schweitzer ME. Magnetic resonance imaging of diffuse bone marrow disease. *Radiol Clin North Am* 1993; **31**: 383-409 [PMID: 8446756]
- 80 **Amer HZ**, Hameed M. Intraosseous benign notochordal cell tumor. *Arch Pathol Lab Med* 2010; **134**: 283-288 [PMID: 20121620 DOI: 10.1043/1543-2165-134.2.283]
- 81 **Yamaguchi T**, Suzuki S, Ishiwa H, Shimizu K, Ueda Y. Benign notochordal cell tumors: A comparative histological study of benign

- notochordal cell tumors, classic chordomas, and notochordal vestiges of fetal intervertebral discs. *Am J Surg Pathol* 2004; **28**: 756-761 [PMID: 15166667]
- 82 **Yamaguchi T**, Iwata J, Sugihara S, McCarthy EF, Karita M, Murakami H, Kawahara N, Tsuchiya H, Tomita K. Distinguishing benign notochordal cell tumors from vertebral chordoma. *Skeletal Radiol* 2008; **37**: 291-299 [PMID: 18188556 DOI: 10.1007/s00256-007-0435-y]
 - 83 **Nishiguchi T**, Mochizuki K, Ohsawa M, Inoue T, Kageyama K, Suzuki A, Takami T, Miki Y. Differentiating benign notochordal cell tumors from chordomas: radiographic features on MRI, CT, and tomography. *AJR Am J Roentgenol* 2011; **196**: 644-650 [PMID: 21343509 DOI: 10.2214/AJR.10.4460]
 - 84 **Nishiguchi T**, Mochizuki K, Tsujio T, Nishita T, Inoue Y. Lumbar vertebral chordoma arising from an intraosseous benign notochordal cell tumour: radiological findings and histopathological description with a good clinical outcome. *Br J Radiol* 2010; **83**: e49-e53 [PMID: 20197427 DOI: 10.1259/bjr/63846600]
 - 85 **Altehoefer C**, Bertz H, Ghanem NA, Langer M. Extent and time course of morphological changes of bone marrow induced by granulocyte-colony stimulating factor as assessed by magnetic resonance imaging of healthy blood stem cell donors. *J Magn Reson Imaging* 2001; **14**: 141-146 [PMID: 11477672]
 - 86 **Ciray I**, Lindman H, Aström GK, Wanders A, Bergh J, Ahlström HK. Effect of granulocyte colony-stimulating factor (G-CSF)-supported chemotherapy on MR imaging of normal red bone marrow in breast cancer patients with focal bone metastases. *Acta Radiol* 2003; **44**: 472-484 [PMID: 14510752]
 - 87 **Caldemeyer KS**, Smith RR, Harris A, Williams T, Huang Y, Eckert GJ, Slemenda CW. Hematopoietic bone marrow hyperplasia: correlation of spinal MR findings, hematologic parameters, and bone mineral density in endurance athletes. *Radiology* 1996; **198**: 503-508 [PMID: 8596857 DOI: 10.1148/radiology.198.2.8596857]
 - 88 **Hanrahan CJ**, Shah LM. MRI of spinal bone marrow: part 2, T1-weighted imaging-based differential diagnosis. *AJR Am J Roentgenol* 2011; **197**: 1309-1321 [PMID: 22109284 DOI: 10.2214/AJR.11.7420]
 - 89 **Geiser F**, Mürtz P, Lutterbey G, Träber F, Block W, Imbierowicz K, Schilling G, Schild H, Liedtke R. Magnetic resonance spectroscopic and relaxometric determination of bone marrow changes in anorexia nervosa. *Psychosom Med* 2001; **63**: 631-637 [PMID: 11485117 DOI: 10.1097/00006842-200107000-00016]
 - 90 **Gimble JM**, Zvonic S, Floyd ZE, Kassem M, Nuttall ME. Playing with bone and fat. *J Cell Biochem* 2006; **98**: 251-266 [PMID: 16479589 DOI: 10.1002/jcb.20777]
 - 91 **Jain R**, Singh ZN, Khurana N, Singh T. Gelatinous transformation of bone marrow: a study of 43 cases. *Indian J Pathol Microbiol* 2005; **48**: 1-3 [PMID: 16758772]
 - 92 **Ecklund K**, Vajapeyam S, Feldman HA, Buzney CD, Mulkern RV, Kleinman PK. Bone marrow changes in adolescent girls with anorexia nervosa. *J Bone Miner Res* 2010; **25**: 298-304 [DOI: 10.1359/jbmr.090805]
 - 93 **García AI**, Milinkovic A, Tomás X, Rios J, Pérez I, Vidal-Sicart S, Pomés J, Del Amo M, Mallolas J. MRI signal changes of the bone marrow in HIV-infected patients with lipodystrophy: correlation with clinical parameters. *Skeletal Radiol* 2011; **40**: 1295-1301 [PMID: 21479859 DOI: 10.1007/s00256-011-1147-x]
 - 94 **Tins B**, Cassar-Pullicino V. Marrow changes in anorexia nervosa masking the presence of stress fractures on MR imaging. *Skeletal Radiol* 2006; **35**: 857-860 [DOI: 10.1007/s00256-005-0053-5]
 - 95 **Chong A**, Song HC, Oh JR, Ha JM, Min JJ, Bom HS, Choi YD, Lee JS. Gelatinous degeneration of the bone marrow mimicking osseous metastasis on 18F-FDG PET/CT. *Clin Nucl Med* 2012; **37**: 798-800 [PMID: 22785516 DOI: 10.1097/RLU.0b013e31825ae455]

P- Reviewer: Anil G, Gao BL, Shen J, Sureka B **S- Editor:** Qiu S
L- Editor: A **E- Editor:** Wu HL



Multi-detector computed tomography imaging of large airway pathology: A pictorial review

Tejeshwar Singh Jugpal, Anju Garg, Gulshan Rai Sethi, Mradul Kumar Daga, Jyoti Kumar

Tejeshwar Singh Jugpal, Anju Garg, Jyoti Kumar, Department of Radiodiagnosis, Maulana Azad Medical College and associated Lok Nayak Hospital, New Delhi 110002, India

Gulshan Rai Sethi, Department of Pediatrics, Maulana Azad Medical College and associated Lok Nayak Hospital, New Delhi 110002, India

Mradul Kumar Daga, Department of Medicine, Maulana Azad Medical College and associated Lok Nayak Hospital, New Delhi 110002, India

Author contributions: Jugpal TS substantially contributed towards the conception of study and drafting the article; Garg A and Kumar J analysed the data and critically revised to assess intellectual content in the article; Sethi GR and Daga MK contributed data for study.

Conflict-of-interest statement: Authors declare no conflict of interests for this article.

Open-Access: This article is an open-access article which was selected by an in-house editor and fully peer-reviewed by external reviewers. It is distributed in accordance with the Creative Commons Attribution Non Commercial (CC BY-NC 4.0) license, which permits others to distribute, remix, adapt, build upon this work non-commercially, and license their derivative works on different terms, provided the original work is properly cited and the use is non-commercial. See: <http://creativecommons.org/licenses/by-nc/4.0/>

Correspondence to: Jyoti Kumar, MD, Professor, Department of Radiodiagnosis, Maulana Azad Medical College and associated Lok Nayak Hospital, New Delhi 110002, India. drjyotikumar@gmail.com
Telephone: +91-99-68604361

Received: May 24, 2015

Peer-review started: May 25, 2015

First decision: August 3, 2015

Revised: October 23, 2015

Accepted: November 13, 2015

Article in press: November 17, 2015

Published online: December 28, 2015

Abstract

The tracheobronchial tree is a musculo-cartilagenous framework which acts as a conduit to aerate the lungs and consequently the entire body. A large spectrum of pathological conditions can involve the trachea and bronchial airways. These may be congenital anomalies, infections, post-intubation airway injuries, foreign body aspiration or neoplasms involving the airway. Appropriate management of airway disease requires an early and accurate diagnosis. In this pictorial essay review, we will comprehensively describe the various airway pathologies and their imaging findings by multi-detector computed tomography.

Key words: Multi detector computed tomography; Trachea; Bronchial tree; Airway abnormality; Virtual bronchoscopy

© **The Author(s) 2015.** Published by Baishideng Publishing Group Inc. All rights reserved.

Core tip: There is a wide range of lesions affecting the airway and patients with airway pathology usually present late during the course of disease. Multi-detector computed tomography (MDCT) has become the mainstay investigation modality as it provides detailed information about the airway and its surrounding structures with high spatial resolution. Therefore it is prudent to know the various pathology affecting airway and its appearance on MDCT.

Jugpal TS, Garg A, Sethi GR, Daga MK, Kumar J. Multi-detector computed tomography imaging of large airway pathology: A pictorial review. *World J Radiol* 2015; 7(12): 459-474 Available from: URL: <http://www.wjgnet.com/1949-8470/full/v7/i12/459.htm> DOI: <http://dx.doi.org/10.4329/wjr.v7.i12.459>

INTRODUCTION

The introduction of multi-detector computed tomo-

graphy (MDCT) technology over the past decade has tremendously revolutionized imaging of airway^[1,2]. Modern MDCT scanners have markedly increased the speed of data collection and cranio-caudal volume coverage enabling them to acquire thin-section, high spatial resolution images of the entire airway. These scanners can reconstruct images of varying slice thickness and in multiple planes from the acquired axial images^[3-5].

The advancements in computer technology aid in processing the data sets acquired by the MDCT scanners to reconstruct the bronchial tree in three dimensions^[6]. The developed computer software generates 3D view of the airway which provides clinically acceptable information with real time visualization of the entire tracheobronchial airway.

IMAGING TECHNIQUE

Thin slice axial images are acquired in a single breath hold. The imaging protocol that is used in our department for adults includes a tube voltage of 120 kV, tube current of 300 mA, 0.6 mm × 128 slices, a pitch of 1.5 with a matrix size of 512 × 512. For children, the tube voltage is reduced to 80 kV and tube current is altered to 110 mA.

Administration of contrast is generally not required for assessment of airway. However it is used in suspected cases of extraluminal compressive lesions to delineate the various mediastinal vascular structures and for suspected neoplastic etiology. Non-ionic iodinated contrast medium may be given using a dose of 1 mL/kg for adults and 1.5 mL/kg for children through peripheral venous access route.

Image reconstruction

The cross-sectional images are then transferred to a separate graphic computer. Reconstruction is done using standard visualization software. The acquired near isotropic data is used to generate multiplanar reformations (MPRs), minimum intensity projections (MinIPs) and volume rendered images for 3D reconstruction.

Two basic methods of 3D imaging are currently employed in airway reconstruction including external rendering and internal rendering. The external rendering of the airway shows its external surface and is also called computed tomography (CT) tracheo-bronchography. Internal rendering or virtual bronchoscopy (VB) allows navigation through the internal airway lumen of airway using the "fly through" virtual endoscopy CT software. The airway reconstructed by VB closely resemble those seen on conventional bronchoscopy^[7-9]. However, VB can evaluate the airway distal to a high grade stenosis which is not possible on fiberoptic bronchoscopy.

NORMAL ANATOMY

Trachea

Trachea is a tubular structure extending from the level

of the cricoid cartilage (6th cervical vertebral level) to the carina (5th thoracic vertebral level). Trachea is made up of multiple C shaped cartilages^[10]. It measures 10 to 11 cm in length^[10]. The trachea is divided into extra- and intra-thoracic parts. The extrathoracic part extends from the level of inferior border of cricoid upto the thoracic inlet. The intrathoracic portion extends from the thoracic inlet to the carina. The normal tracheal diameter in men ranges from 13 to 25 mm in the coronal dimension and 13 to 27 mm in the sagittal dimension^[11,12]. In women, trachea is smaller and its dimension range from 10 to 21 mm in the coronal plane and 10 to 23 mm in the sagittal plane^[11,12]. The posterior portion of the tracheal wall, lying between the open ends of the tracheal cartilages, is a thin fibromuscular membrane termed the posterior tracheal membrane. The cross section of trachea has marked variability in appearance, which may appear round, oval or horse shoe shaped. The posterior tracheal membrane may appear convex posteriorly, flat or convex anteriorly.

Carina

Trachea divides at the level of sternal angle (4th-5th dorsal vertebral levels) at the carina into the right and left mainstem bronchi^[11]. The normal carinal angle ranges between 70°-100°.

Mainstem, lobar and segmental bronchi

The mainstem bronchi extend infero-laterally from the carina into the pulmonary hila. At the pulmonary hila, they branch further to form the bronchial tree within the pulmonary parenchyma. The mainstem bronchi divide into lobar bronchi. There are 3 lobar bronchi on right side and 2 on left side. The lobar bronchi further divides into segmental and subsegmental bronchi. There are approximately 23 generations of branching till the bronchi form the alveoli^[13]. The segmental bronchi are accompanied by segmental arteries that form a broncho-pulmonary segment.

The bronchi on MDCT appear as small circular lucencies on axial scans. Bronchi that course obliquely to the axial plane are more difficult to evaluate on axial scans and therefore require MPRs images and MinIP images (Figure 1). VB also provides the intraluminal view (Figure 2).

PATHOLOGY

The pathological conditions affecting airway vary from innocuous to sinister. To add to the diagnostic dilemma, identification of tracheal disease is notoriously difficult. Patients become symptomatic very late in the natural history of diseases affecting the airway. Patients with tracheobronchial pathology can present with breathlessness, persistent cough, stridor, recurrent cyanotic episodes and haemoptysis in varying severity, depending upon the degree of airway involvement. These may cause sudden deterioration of the patient's clinical condition. Therefore rapid and accurate diagnosis is imperative to reduce morbidity and mortality.

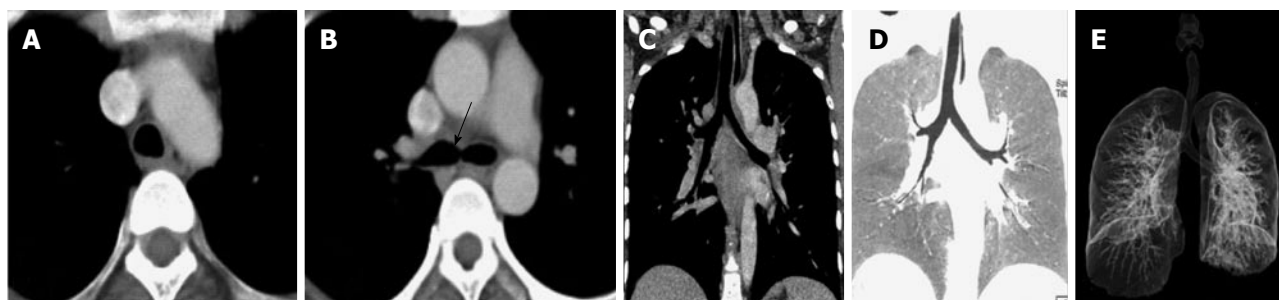


Figure 1 Normal airway. Axial image at the level of arch of aorta (A) shows a typical inverted U shaped trachea with thin fibromuscular membrane in posterior portion lying between open ends of tracheal cartilages. Axial image (B) at the level of carina (arrow) shows dichotomous branching of trachea at its distal end into right and left main bronchi. Coronal MPR image (C) shows trachea and mainstem bronchi as uniform tubular structures in midline within the mediastinum. Coronal reconstructed MinIP image (D) shows trachea and its bronchial branches as tubular air containing structures continuous from thoracic inlet till its divisions into the lung parenchyma. Volume rendered image (E) is the external rendered image showing 3-dimensional display of external surface of the airway and lung parenchyma. MPR: Multiplanar reformation; MinIP: Minimum intensity projection.

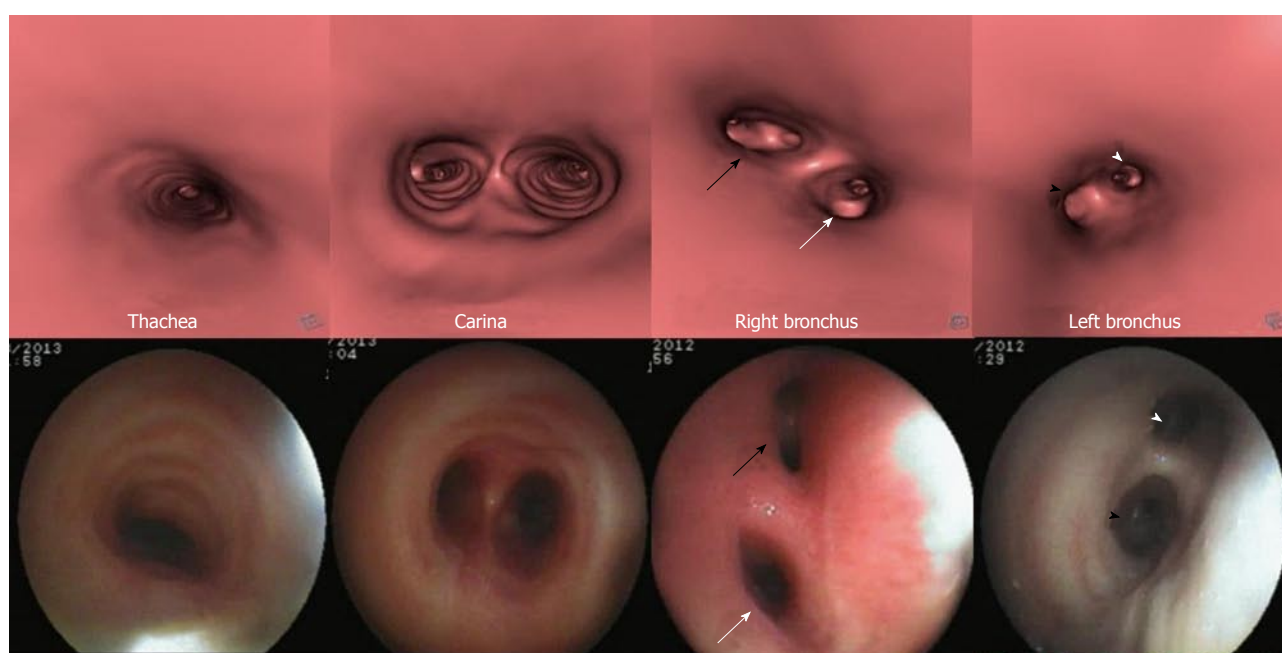


Figure 2 Virtual bronchoscopy of normal airway. Virtual bronchoscopy or internal rendered images reconstructed using dedicated “fly through” software at the level of trachea, carina, right and left main bronchus (top row) with corresponding appearance on fiberoptic bronchoscopy (bottom row). The division of right bronchus into upper lobe (white arrow) and bronchus intermedius (black arrow) and division of left main bronchus into upper (black arrowhead) and lower lobe bronchus (white arrowhead) is seen.

For descriptive purposes, the lesions affecting airway may be broadly classified as focal and diffuse lesions^[14]. A lesion is characterized as focal when it affects a single short segment of airway, whereas it is characterized as diffuse if it involves either long segment of airway or when multiple lesions are detected.

FOCAL AIRWAY LESIONS

Intrinsic focal lesions

Tracheobronchial neoplasm: Tracheobronchial neoplasm is one of the commonest focal lesion involving the airway^[15]. Tracheobronchial involvement by a malignant process can be both primary and secondary. Mostly airway is secondarily invaded by primary neoplasms arising from adjacent organs. Trachea is in close

approximation with various organs in its extrathoracic and intrathoracic course. Therefore primary malignancy of adjacent organs like lung, esophagus or thyroid can invade the tracheobronchial tree.

Primary lung carcinoma is a disease with a very high mortality rate worldwide and commonly involves the airway. The main histopathological types include: adenocarcinoma, squamous cell carcinoma (SCC), small cell carcinoma and large cell carcinoma of which SCC and small cell carcinoma are most common types originating from the central airway^[16,17]. SCC has an intraluminal growth pattern that can cause airway obstruction leading to pulmonary atelectasis or lobar collapse (Figure 3)^[16]. Bronchial obstruction is much less common with small cell carcinoma than with SCC. The most common imaging finding seen in small cell

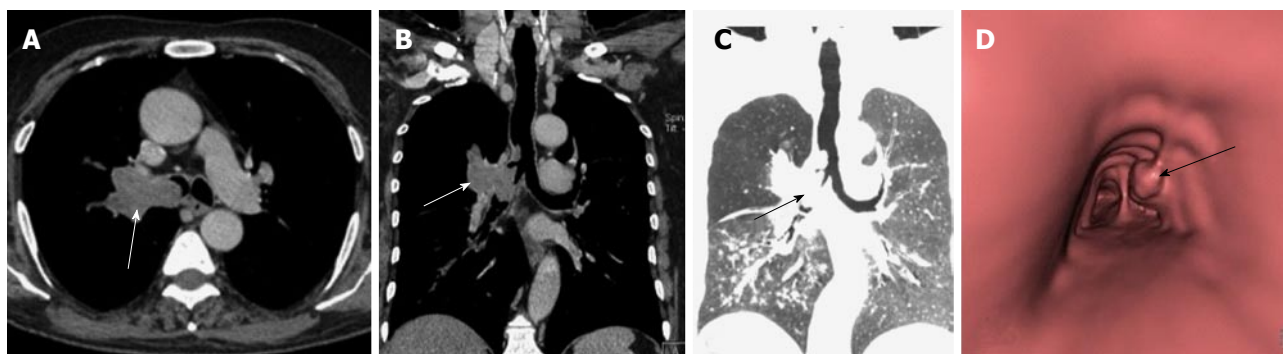


Figure 3 Squamous cell lung carcinoma. Contrast enhanced axial (A) and coronal MPR (B) images show enhancing soft tissue mass in right perihilar region with intraluminal extension of growth into the right mainstem bronchus and lower trachea (arrow). Coronal MinIP image (C) shows attenuation of right mainstem bronchus with a polypoidal growth extending into lower trachea (arrow). Virtual bronchoscopy (D) shows an irregular polypoidal intraluminal mass in lower trachea (arrow). MPR: Multiplanar reformation; MinIP: Minimum intensity projection.

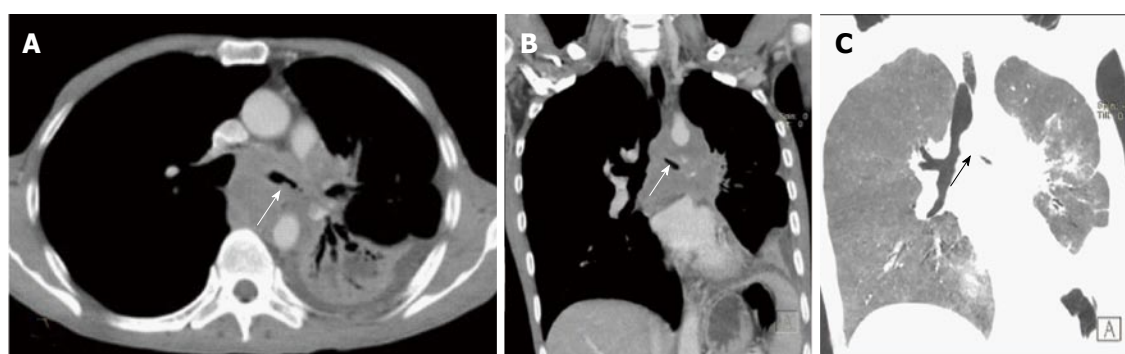


Figure 4 Small cell lung cancer. Axial (A) and coronal MPR (B) images show heterogeneously enhancing mass lesion encasing and attenuating left main bronchus and its lower division with mediastinal invasion and associated collapse-consolidation of left lower lobe. Coronal MinIP image (C) shows attenuated left main bronchus (arrow). MPR: Multiplanar reformation; MinIP: Minimum intensity projection.

carcinoma is that of extensive hilar or mediastinal lymphadenopathy (Figure 4)^[18].

Primary tracheal neoplasm can also occur but are very rare. Majority of the primary tracheal neoplasms in adults are malignant with common histopathological patterns comprising of SCC, adenoid cystic carcinoma, carcinoid, mucoepidermoid carcinoma, and papilloma. SCC is the most common tracheal tumor and is more common in men^[19]. It is highly associated with cigarette smoking and is histologically identical to lung SCC^[14]. SCC appears as a polypoid intraluminal lesion generally in the lower third of trachea. It typically has irregular margins as it arises from the surface epithelium. It may invade mediastinum by direct extension or lymphatic spread (Figure 5)^[20]. The second common cell type is adenoid cystic carcinoma (ACC) which occurs in younger patients with equal sex distribution. ACC arises within the submucosal glands and therefore has a smooth outline (Figure 6)^[21]. The mucosal covering of the lesion rarely ulcerates in contrast to SCC. Lymphadenopathy and metastases are also uncommon^[22].

Benign tumors of the airway include endobronchial carcinoid, hamartoma and papillomas. Endobronchial carcinoids are the most common airway tumors in adolescents and young adults. They generally arise within the central bronchi causing cough, hemoptysis,

and airway obstruction^[23]. They appear as an intensely enhancing endobronchial or hilar masses with post obstructive features like atelectasis or air trapping^[23]. About one-fourth of these tumors can also show calcification on CT^[24].

Respiratory papilloma is caused by human papilloma virus infection of the upper airway. The infection is usually acquired during birth or rarely through oro-genital sexual route. The tracheo-laryngeal form of papilloma is the commonest form and occurs in 2%-17% cases^[25]. Respiratory papilloma is a benign endoluminal lesion that commonly involves larynx, trachea and the mainstem bronchi. It is a well circumscribed polypoid lesion which does not extend across the wall of trachea or bronchi (Figure 7)^[25]. Respiratory papillomas can occur at multiple sites along the airway. VB can show the entire extent of the disease without the risk of downstream spread, which can be a problem with conventional bronchoscopy. Papillomas can cause airway obstruction and lead to post obstructive changes like atelectasis, pneumonia or pneumothorax. The most serious long term complication is malignant degeneration of papilloma to SCC^[26].

MDCT acquired after contrast administration is currently the standard imaging modality to diagnose and stage central airway tumors. Axial images along

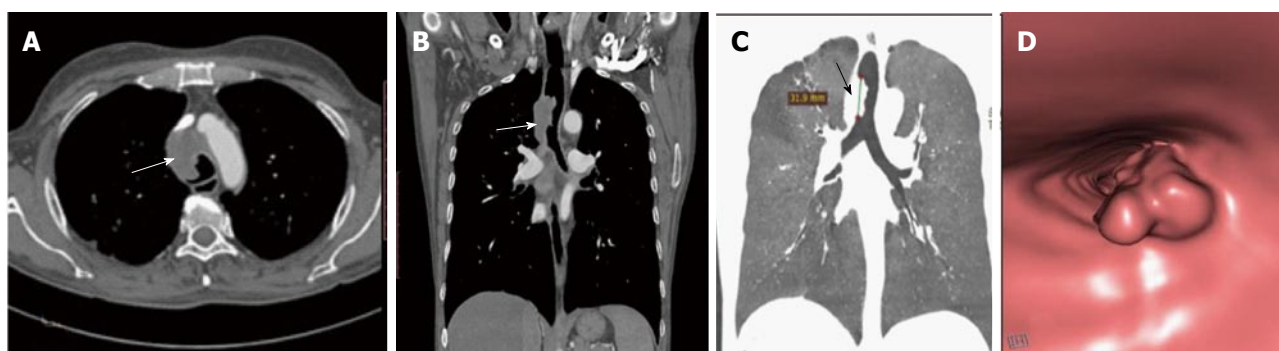


Figure 5 Squamous cell carcinoma of trachea. Axial (A) and coronal MPR (B) images show eccentric soft tissue mass with irregular surface involving trachea (arrow in B) with mediastinal extension (arrow in A). Coronal MinIP (C) shows partial attenuation of mid tracheal lumen involving a length of 3.19 cm (arrow). Virtual bronchoscopy (D) shows this mass lesion as irregular intraluminal growth along the right wall of trachea causing tracheal luminal narrowing. MPR: Multiplanar reformation; MinIP: Minimum intensity projection.

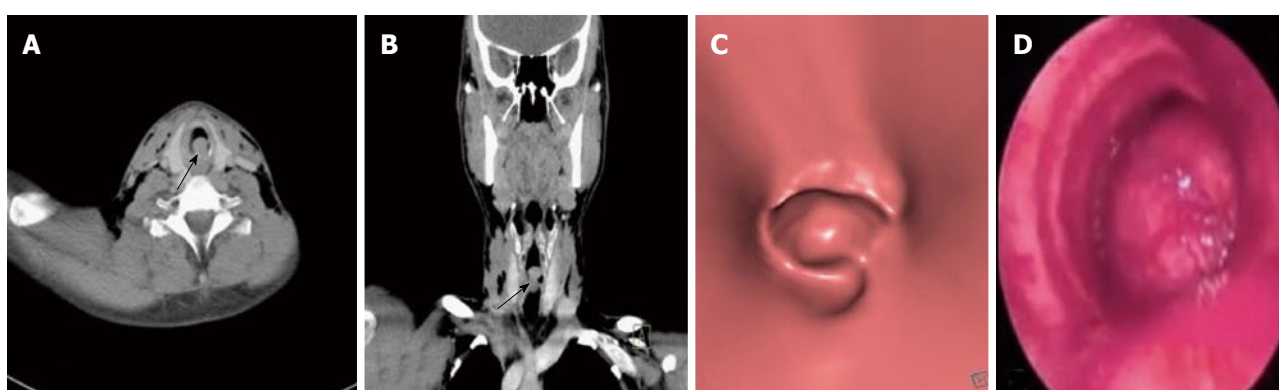


Figure 6 Adenoid cystic carcinoma of trachea. Axial (A) and coronal MPR (B) images show polypoidal mass with smooth outline within the trachea in subglottic region causing near complete attenuation of the airway (arrow). Virtual bronchoscopy (C) shows intraluminal smooth mass within trachea similar to that seen on conventional bronchoscopy (D). MPR: Multiplanar reformation.

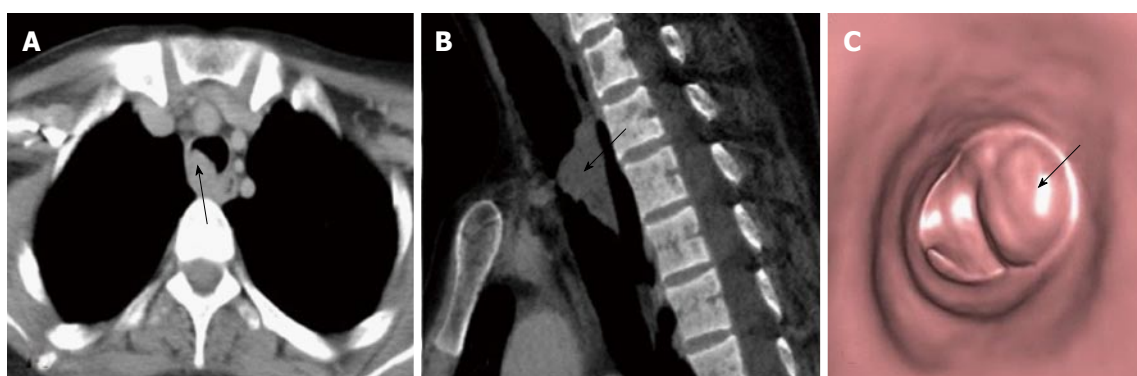


Figure 7 Respiratory papilloma. Axial (A) and sagittal MPR (B) images show a smooth polypoidal soft tissue mass arising from the postero-lateral wall of trachea (arrow). Virtual bronchoscopy (C) shows the intraluminal mass lesion with smooth surface (arrow). MPR: Multiplanar reformation.

with reconstructed MPR and 3D images provide comprehensive information about the involvement of airway by the tumor and its relationship with adjacent structures. MDCT can also detect associated lymph nodal spread and metastases (both intra-pulmonary and distant sites), thereby altering tumor staging. VB images provide an intraluminal view of the tumor involving the airway. These also score over conventional bronchoscopy due to their inability to evaluate the

airway distal to a high grade narrowing or complete obstruction. This can have a significant impact on patient management as palliative stent placement in the airway can be offered to patients with proximal occlusive lesion and patent distal airway.

Post tracheostomy complications: Prolonged tracheal intubation and tracheostomy can cause airway complications. Tracheal stenosis is a frequently encoun-

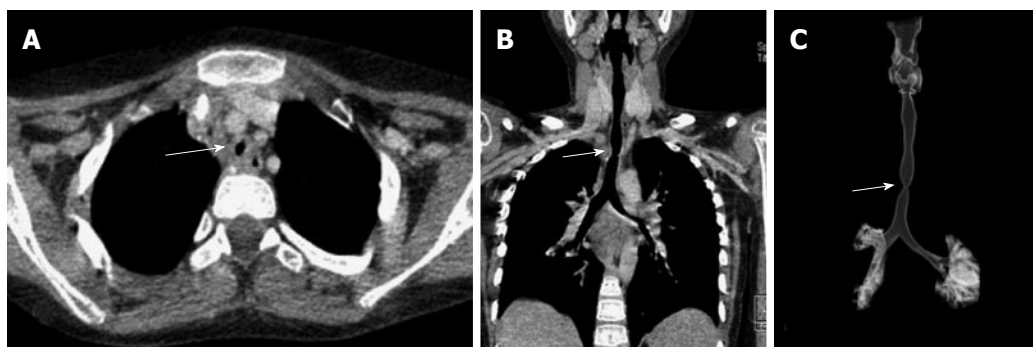


Figure 8 Post intubation tracheal stenosis. Axial (A), coronal MPR (B) and VRT (C) images show a focal short segment concentric narrowing of tracheal lumen giving an "hourglass" configuration better appreciated on coronal images. MPR: Multiplanar reformation; VRT: Volume rendering technique.

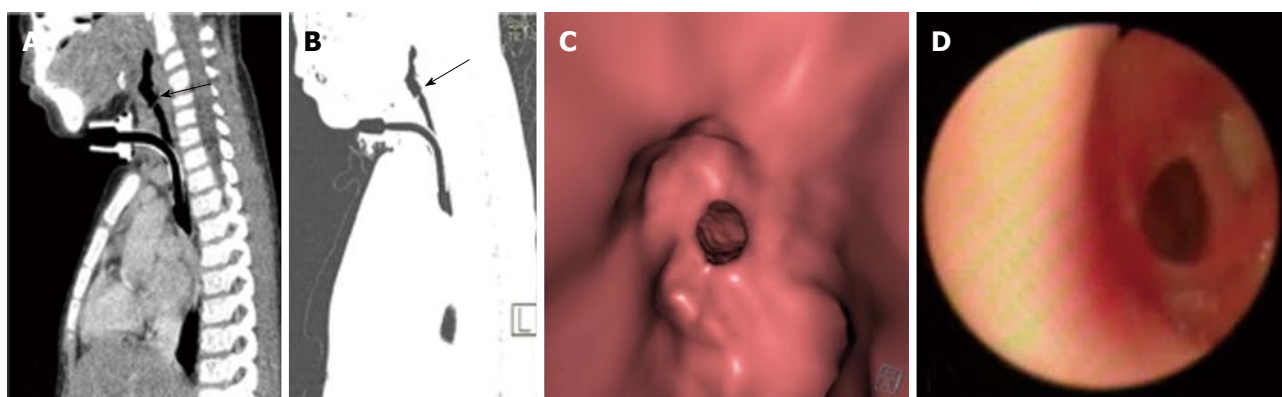


Figure 9 Tracheal membrane. Sagittal MPR (A) and sagittal MinIP (B) images show a partially occluding thin membrane in subglottic airway (arrow). Note made of tracheostomy tube insitu. Virtual bronchoscopy (C) shows circumferential membrane causing narrowing of airway lumen with similar finding confirmed on fiberoptic bronchoscopy. MPR: Multiplanar reformation; MinIP: Minimum intensity projection.

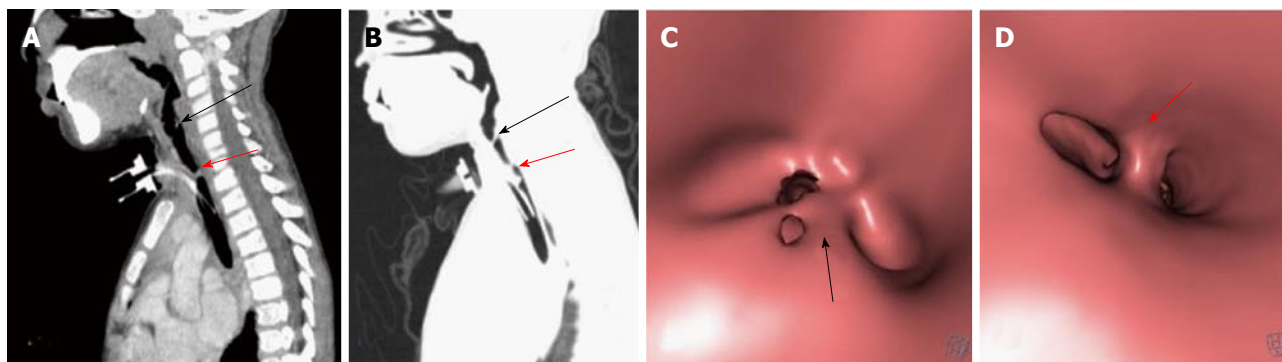


Figure 10 Post intubation mucosal synechiae. Sagittal MPR (A) and MinIP (B) images show thin membrane like adhesions within the airway at subglottic (black arrow) and upper tracheal (red arrow) levels extending across the airway lumen and compromising its patency suggestive of synechiae formation. The corresponding appearance of these synechiae are very well demonstrated on virtual bronchoscopy (C and D). MPR: Multiplanar reformation; MinIP: Minimum intensity projection.

tered entity in these patients. The stenosis generally occur at two sites: At the level of endotracheal tube cuff which is most common site and at the stoma site. The high pressure of the endotracheal tube balloon causes mucosal injury of tracheal wall. This leads to tissue scarring and ultimately tracheal stenosis.

The most common CT finding in post intubation stenosis is a localized area of narrowing of tracheal lumen^[27,28]. This focal circumferential narrowing generally produces a characteristic hourglass configuration (Figure

8). Less common findings include a thin membrane projecting into the tracheal lumen (Figure 9). Due to mucosal injury there can also be formation of multiple mucosal synechiae compromising the tracheal lumen (Figure 10).

MDCT with multi planar reformats and VB provides information regarding the stenosis, *i.e.*, grade of stenosis, distance of stenotic segment from the vocal cord and length of the stenotic segment. These findings give a detailed road map to the surgeons before the

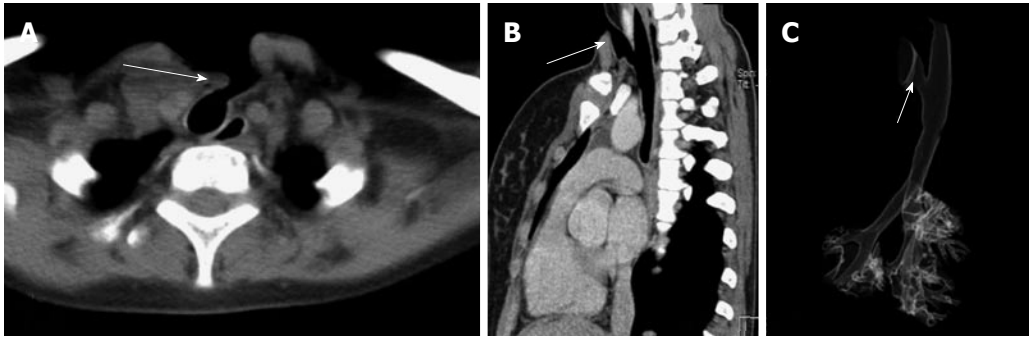


Figure 11 Post tracheostomy tracheo-cutaneous fistula. Axial (A) and oblique sagittal MPR (B) images show the fistula as an abnormal tract extending from antero-lateral wall of upper trachea to the skin surface (arrow). This fistulous tract is very well demonstrated on VRT image (C, arrow). MPR: Multiplanar reformation; VRT: Volume rendering technique.

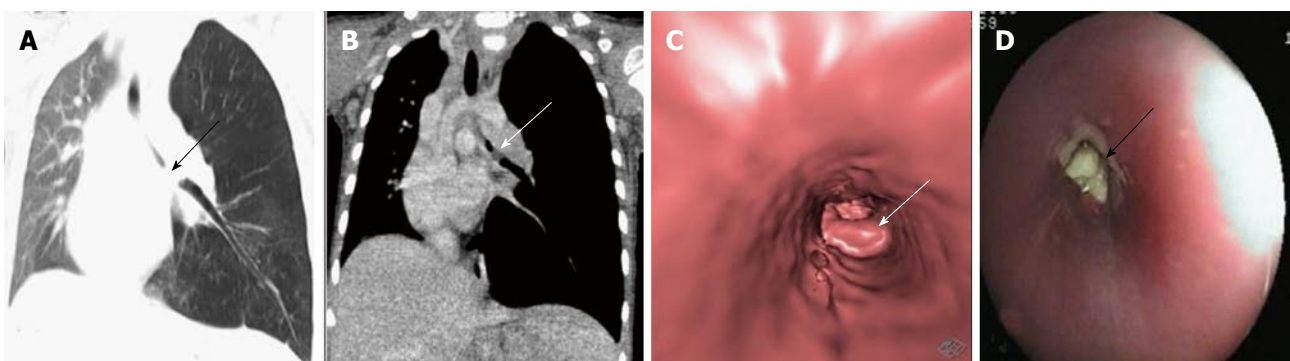


Figure 12 Foreign body aspiration. Coronal MPR images of thorax in lung settings (A) and mediastinal window settings (B) reveal soft tissue density attenuating left main bronchus (arrow) with associated hyperinflation of left lung. Virtual bronchoscopy (C) shows obstruction of left main bronchus with lobulated surface confirmed to be endobronchial foreign body (arrow) on conventional bronchoscopy (D). MPR: Multiplanar reformation.

patient is taken up for surgery. The MPR and volume rendering technique images are helpful in appreciating the vertical length of the lesion more precisely.

Other complication like diverticulum at the stoma site and tracheocutaneous fistula can also develop after tracheostomy. MDCT can accurately demonstrate the location, dimension and tract of the fistula which has an implication on the surgical management of these patients (Figure 11).

Foreign body aspiration: Foreign body aspiration is generally encountered in young children (aged between 6 mo to 5 years) and is a frequent cause of morbidity and mortality^[29,30]. Foreign body aspiration is potentially life threatening if not recognised early and appropriately treated. Any child with acute stridor should always be evaluated for potential aspiration of foreign body. However, patients with chronically impacted foreign body are difficult to diagnose. They usually present with recurrent wheezing and radiographs if obtained may show pulmonary infiltrates, bronchiectatic changes or lung abscess^[31]. Aspiration of organic vegetative objects is more dangerous as these swell with bronchial secretions and cause progressively increasing airway obstruction. Allergic and chemical bronchitis is also a frequent complication of aspiration of organic foreign

body^[32].

In suspected cases of foreign body aspiration, obtaining radiographs in both inspiratory and expiratory phases can be helpful. Decubitus view and fluoroscopic assessment can also be performed to look for features of airway obstruction like hyperinflation. However, radiographs are normal in around one-third of these cases and nearly 90% of these foreign bodies are radiolucent^[33]. Therefore, the advantage of MDCT in evaluating these cases lies in the fact that it can detect both radioopaque and radiolucent foreign bodies (like plastic and organic food items). The aspirated radiolucent objects usually appear as non-enhancing soft tissue structure within the airway causing partial or complete airway obstruction (Figure 12). CT also help in identifying ancillary post obstructive findings like hyperinflation, lobar atelectasis or complete lung collapse (Figure 13)^[34].

Broncholithiasis: The presence of calcific/ossific material within the bronchial lumen is called broncholithiasis. It is most commonly associated with erosion of the airway by a calcified lymph node caused by long-standing foci of granulomatous lymphadenitis like tubercular infection which can then extrude into the lumen of the bronchus. Other rarer causes include *in-situ* calcification of chronically aspirated foreign body

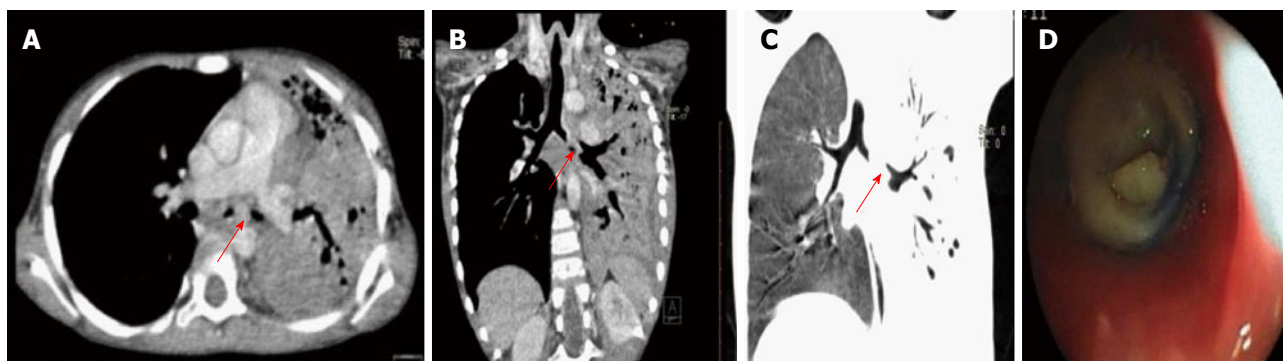


Figure 13 Chronic foreign body aspiration. Axial (A) and oblique coronal MPR (B) images reveal soft tissue density partially occluding the left main bronchus (arrow) with consolidation of left lung and associated bronchiectatic changes. Coronal MinIP image (C) shows attenuation of left main bronchus (arrow) with collapse of left lung. Endobronchial foreign body within left main bronchus was confirmed to be a small piece of plastic on conventional bronchoscopy (D). MPR: Multiplanar reformation; MinIP: Minimum intensity projection.

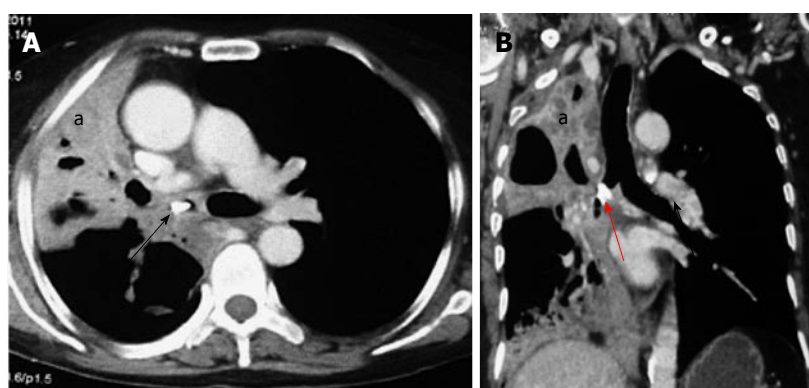


Figure 14 Broncholith. Axial (A) and coronal MPR (B) images show a hyperdense calcific density within the right main bronchus (arrow) with collapse-consolidation and bronchiectasis in the right lung (a). MPR: multiplanar reformation.

or even migration of calcified pleural plaque into the bronchus^[35]. CT has high spatial resolution and superior ability to depict calcification. Therefore it provides useful information in the evaluation of suspected case of broncholithiasis. The presence of endobronchial or peribronchial calcified nodule is highly suggestive of broncholithiasis. It can also show features of bronchial obstruction like atelectasis, obstructive pneumonitis or bronchiectasis (Figure 14).

Tracheal wall pathology

Post traumatic tracheal rent: Tracheo-bronchial injuries are rare but they can occur in motor-vehicle accidents with trauma to the thoracic cavity. The injury predominantly involves the posterior membranous wall of intrathoracic trachea. The injury occurs due to sudden increase in the intra-airway pressure against a closed glottis at the time of injury^[36].

MDCT depicts the site of injury as a focal or circumferential defect in tracheal wall, deformed tracheal contour or fistulous communication with adjacent structures (Figure 15)^[36]. Other non-specific signs include pneumo-mediastinum, pneumo-thorax and non-resolving subcutaneous emphysema. Tracheo-bronchial injury is an emergency and early diagnosis

with immediate surgical repair is necessary to reduce morbidity and mortality in such patients.

Tracheo-esophageal fistula: Esophageal atresia and tracheoesophageal fistula are a group of congenital anomalies involving the structures arising from primitive foregut. They occur due to an unknown intrauterine insult during the normal process of separation of primitive foregut into trachea and esophagus. (Figure 15)^[37]. Tracheo-esophageal fistula can be an isolated anomaly or a part of VACTERL complex (vertebral, anal, cardiac, tracheal, esophageal, renal, and limb anomalies)^[38].

However current usefulness of pre-operative CT in cases of tracheoesophageal fistula is controversial. It provides limited information about the fistulous tract as compared to endoscopy. Thus, the use of CT scan is not routinely recommended in the management of tracheoesophageal atresia.

Extrinsic focal lesions

Vascular compression: Anomalous mediastinal vessels (aorta and pulmonary arteries) are important causes of compression of the trachea. Although a majority of these patients are asymptomatic, vascular

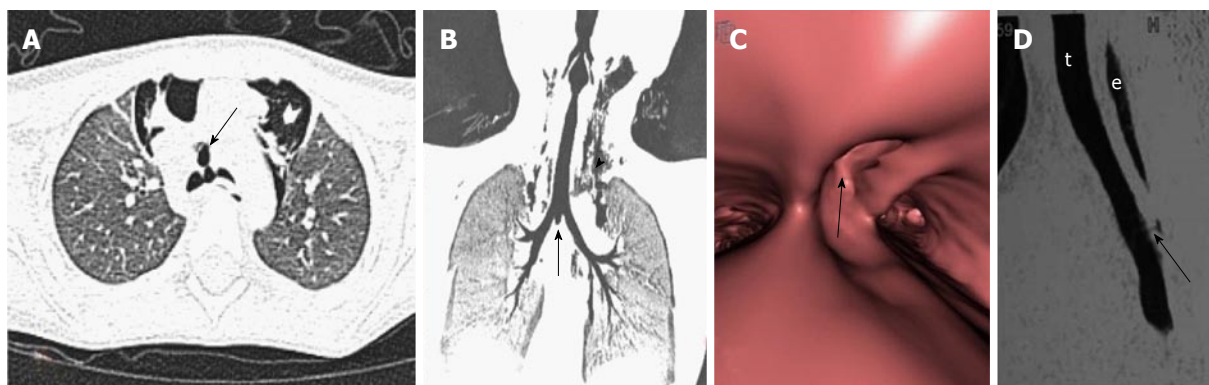


Figure 15 Airway wall pathology. Traumatic tracheal rent-Axial (A) and oblique coronal MiniP (B) images show a focal air containing outpouching at the level of carina in midline projecting antero-inferiorly (arrows). Virtual bronchoscopy (C) shows a focal defect within the wall of trachea at the level of carina (arrow). Note made of marked subcutaneous emphysema (arrowhead in B). Tracheo-esophageal fistula-sagittal MPR image (D) of another case shows a thin faint air containing tract (arrow) extending from esophagus (e) to trachea (t). MPR: Multiplanar reformation; MiniP: Minimum intensity projection.

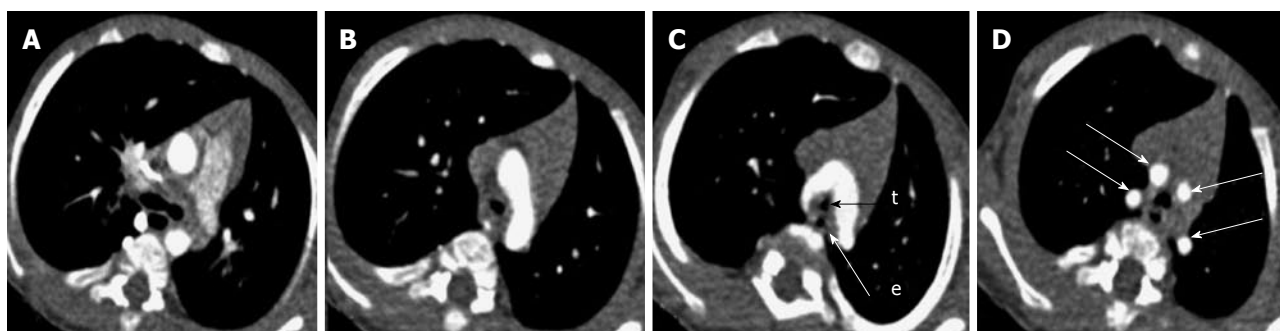


Figure 16 Double aortic arch. Serial axial images (A-D) of thorax (in caudo-cranial direction) reveal 2 aortic arches encircling and compressing trachea (t) and esophagus (e). Ipsilateral subclavian and common carotid arteries arise from each arch giving a characteristic "4-vessel sign" (arrows in D).

compression of the airway have been observed in 13%-26% of children who undergo bronchoscopy for persistent wheezing, stridor and apnea^[39]. The vascular anomalies that present with airway compression include double aortic arch, anomalous course of innominate artery and pulmonary artery sling.

Double aortic arch is a vascular anomaly that occurs due to non regression of right aortic arch during intrauterine development. There is persistence of both right and left aortic arches, which form a vascular ring encircling and compressing esophagus and trachea. Each arch gives off two branches - the common carotid and subclavian arteries supplying ipsilateral sides of the body giving the characteristic "four vessel sign" (Figure 16). In most of the cases the right sided arch is higher and is larger in diameter. However they can also be in the same plane or the right sided arch may even be lower in location. Sometimes one of the arches may be replaced by a fibrous cord with absent luminal patency^[40].

The innominate artery can sometimes have an anomalous course and originate at a point farther along the arch than is normal; when it does so, it winds around the anterior surface of the trachea as it courses upward and to the right. If this vessel is large and taut, it can compress the trachea to a serious degree (Figure

17).

Left pulmonary artery sling is a rare anomaly characterized by abnormal origin and course of left pulmonary artery. The left pulmonary artery has an anomalous origin from right pulmonary artery and courses between trachea and esophagus before entering the left hilum (Figure 18). It is thought to result from a failure of formation of the 6th aortic arch. Nearly half of the infants born with this condition present with symptoms of airway compression at birth. At one month of age, approximately 65% of the children develop stridor of varying degree^[41].

Bronchogenic cyst: Bronchogenic cysts are intra-thoracic cystic developmental lesions caused by abnormal antenatal budding of the tracheobronchial tree^[42,43]. These are included under the broad spectrum of foregut duplication cysts that also includes neurenteric cysts and enteric cysts. Bronchogenic cysts are typically located in the middle mediastinum with subcarinal region being the most common site followed by right paratracheal location^[44]. Rarely, they can also occur as intra-pulmonary lesions most of which are located in the lower lobes^[44]. Small bronchogenic cysts are usually asymptomatic; however large lesions can cause mass effect on adjacent structures like the airway

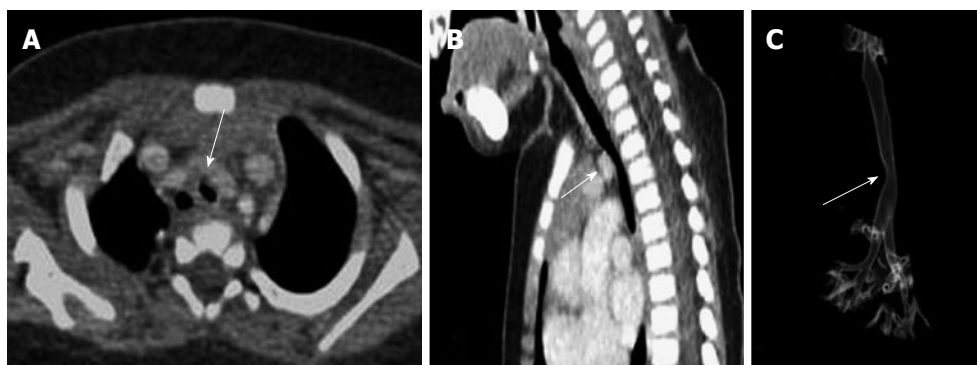


Figure 17 Innominate artery compression. Contrast enhanced axial (A) and sagittal MPR (B) images show extraluminal compression of trachea by anomalous course of innominate artery winding around the anterior wall of trachea (arrow). 3D VRT image (C) shows smooth indentation on the tracheal air column (arrow). MPR: Multiplanar reformation; VRT: Volume rendering technique.



Figure 18 Left pulmonary artery sling. Contrast enhanced axial (A) and sagittal MPR (B) images reveal aberrant course of left pulmonary artery between trachea and esophagus (arrow) causing tracheal compression and vascular indentation on esophagus. Note made of left superior vena cava (a). Virtual bronchoscopy (C) shows an eccentric impression causing focal narrowing of the tracheal lumen (arrow). MPR: Multiplanar reformation.

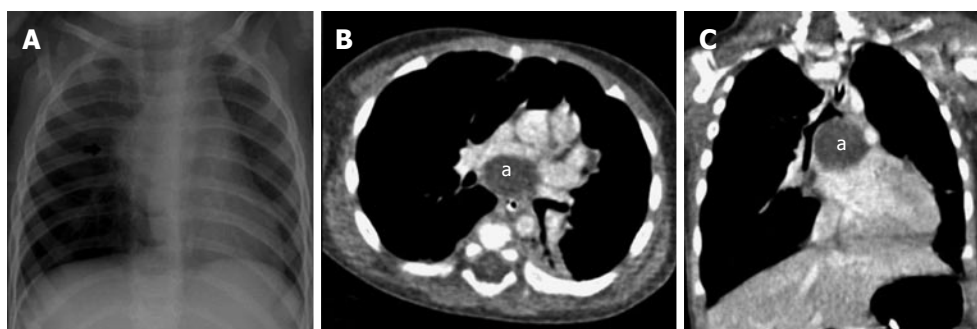


Figure 19 Subcarinal bronchogenic cyst. Frontal radiograph of chest (A) reveals mediastinal widening (arrow). Contrast enhanced axial (B) and coronal MPR (C) images reveal well defined non-enhancing homogenous fluid attenuation lesion in subcarinal location (a) narrowing the bronchial divisions with resultant subsegmental atelectasis in left lower lobe. MPR: Multiplanar reformation.

or esophagus causing respiratory distress and feeding difficulty respectively^[43,44].

Bronchogenic cysts are usually single and show characteristic MDCT appearance of a well-circumscribed round or oval lesion with homogenous fluid attenuation (Figures 19 and 20). On contrast administration, they usually do not enhance or show minimal peripheral rim enhancement. The presence of thick walls, solid component, calcification or septations is unusual. If they cause substantial mass effect on adjacent airways post obstructive features like hyperinflation or lung collapse

may also occur. Bronchogenic cysts can sometimes appear as an air containing cystic lesion if a fistulous communication develop with the airway (Figure 21).

Impacted esophageal foreign body: Foreign body ingestion with impaction within the oesophagus can rarely cause compression on the airway. Such cases are rarely encountered however may be seen especially in very young children who have a compliant airway which gets compressed extraluminally leading to airway compromise and post obstructive pulmonary changes

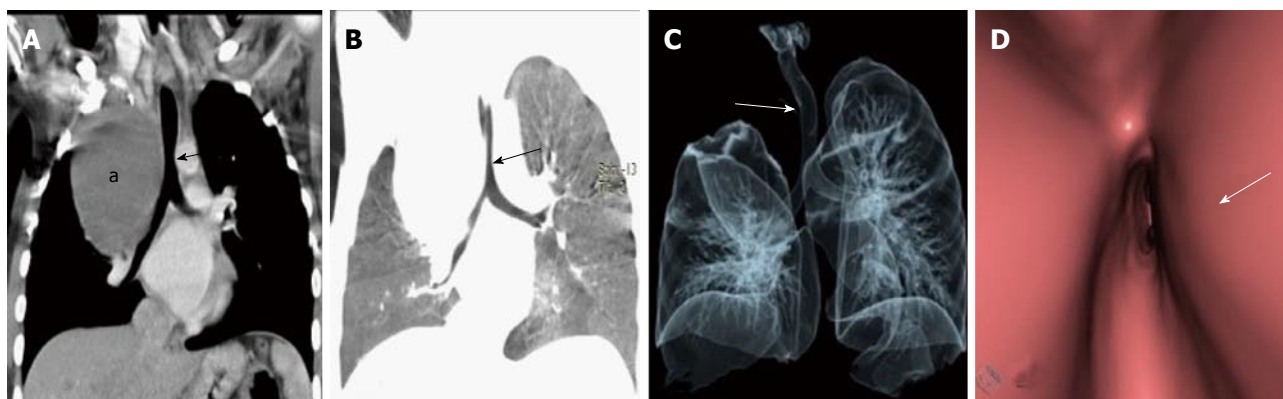


Figure 20 Paratracheal bronchogenic cyst. Coronal MPR image (A) shows large well defined non enhancing fluid attenuation lesion (a) in right paratracheal location with mass effect on adjacent trachea causing tracheal luminal attenuation (arrow). Coronal MinIP (B) and VRT (C) images show extrinsic mass effect on the airway (arrow) and right lung. Virtual bronchoscopy (D) clearly demonstrates the smooth extraluminal compression along the right wall of trachea causing luminal compromise. MPR: multiplanar reformation; MinIP: Minimum intensity projection; VRT: Volume rendering technique.

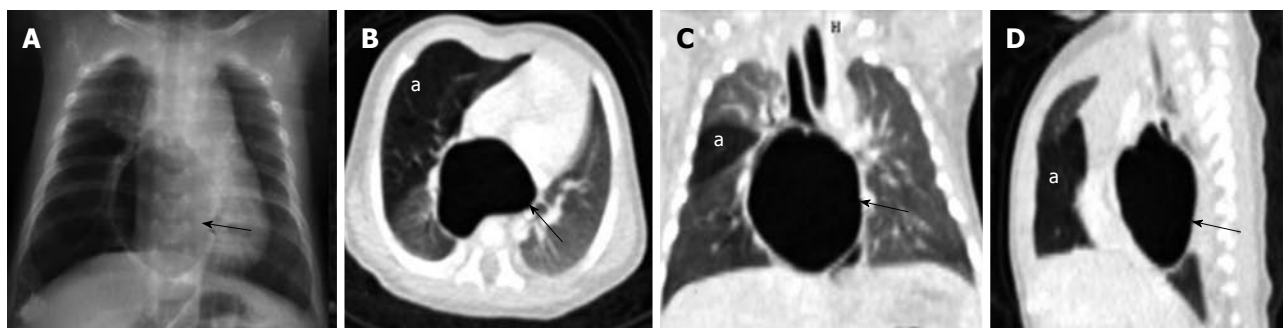


Figure 21 Bronchogenic cyst. Frontal radiograph of chest (A) shows a well-defined air filled cystic lesion in the retrocardiac location. Axial (B), coronal (C) and sagittal (D) MPR images show a large well defined homogenous air containing lesion (arrow) with carinal widening. The lesion is causing partial airway obstruction seen as air trapping in right middle lobe (a). MPR: Multiplanar reformation.

like atelectasis, consolidation and collapse (Figure 22)^[45,46].

Lymphadenopathy: The mediastinum and pulmonary hila have a rich network of lymphatic tissues. These can enlarge due to various disease conditions including infective aetiologies like tuberculosis, histoplasmosis and malignant conditions like lymphoma and small cell lung cancer^[47]. These may obstruct the airway to cause post obstructive pulmonary changes like atelectasis and collapse (Figure 23). Enlarged lymph nodes may also erode and infiltrate into the adjacent tracheal and bronchial wall leading to focal discontinuity of the airway wall (Figure 24). MDCT clearly depicts the cause of compression as enlarged lymph nodes and may also characterize primary pathology leading to lymphadenopathy.

DIFFUSE AIRWAY LESIONS

Saber-sheath trachea

Saber-sheath trachea is an abnormal morphological appearance of trachea seen in association with chronic obstructive pulmonary disease (COPD). It is seen

almost exclusively in men and is characterized by reduced transverse and increased sagittal diameter of intrathoracic trachea (Figure 25). The sagittal-to-coronal diameter ratio is greater than 2^[48]. The extra-thoracic trachea is not affected. Repeated injury to the airway from chronic coughing in patients with COPD is the probable cause. These changes initially begin at the thoracic inlet but can progress to involve the entire intrathoracic trachea over time. Other smoking-related conditions may be present such as emphysema and respiratory bronchiolitis^[49].

Tracheo-bronchomegaly

This is also referred to as Mounier-Kuhn syndrome. There is dilatation of the central airway with the mucosa projecting between the cartilaginous rings forming multiple diverticulae. This gives a characteristic corrugated appearance of trachea and mainstem bronchi (Figure 26). This entity is seen in patients with recurrent respiratory infections in their 3rd and 4th decade resulting in thinning of the muscularis mucosa of airway^[50]. Mounier-Kuhn syndrome is characterized by tracheal diameter of more than 3 cm and mainstem bronchi diameters of greater than 2.4 cm^[50,51].

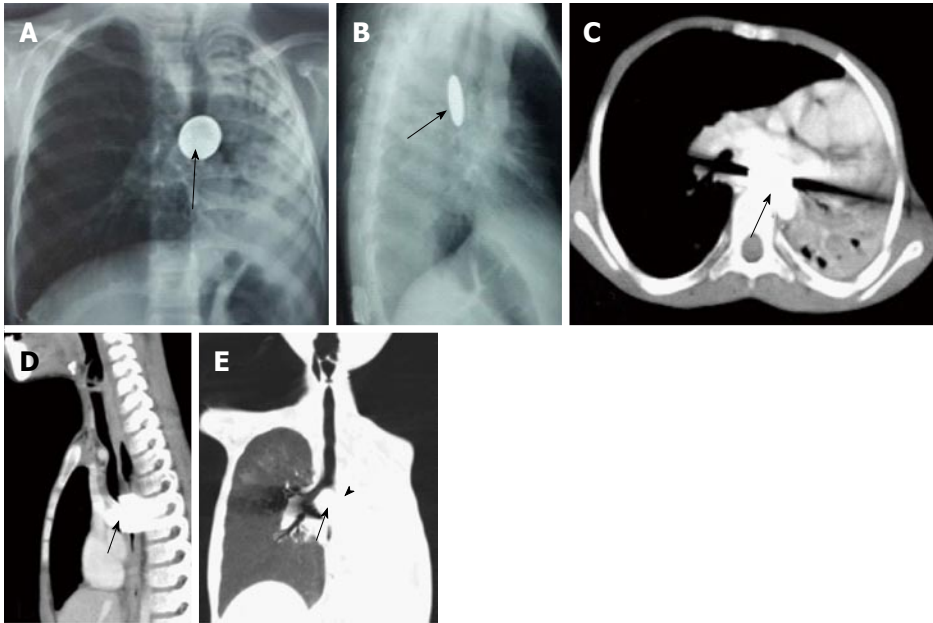


Figure 22 Impacted esophageal foreign body compressing airway. Frontal (A) and lateral (B) radiographs of chest reveal a well-defined round radio-opaque foreign body in the esophagus at the level of carina (arrows) with associated volume loss of left lung. Contrast enhanced axial (C) and sagittal (D) MPR images show a hyperdense foreign body giving streak artefacts impacted within the esophagus (arrow). Coronal MinIP image (E) shows near complete occlusion of left main bronchus (arrowhead) by the impacted esophageal foreign body (arrow) with collapse of left lung. MPR: Multiplanar reformation; MinIP: Minimum intensity projection.

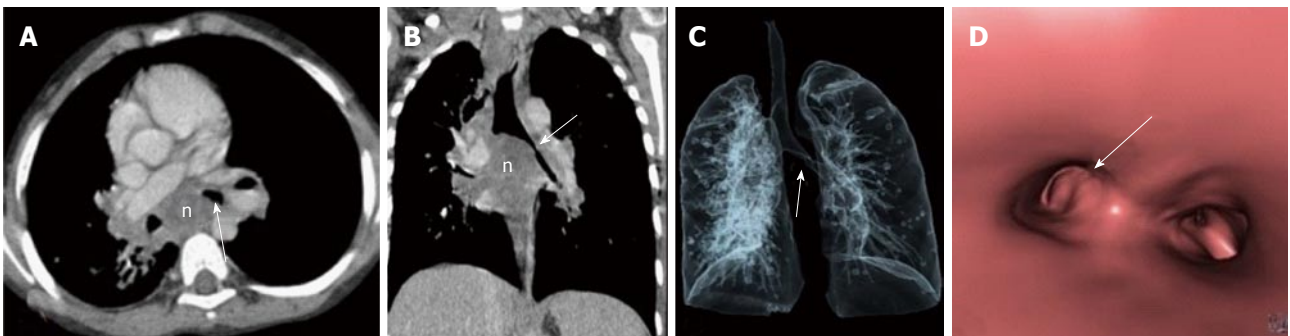


Figure 23 Enlarged tubercular lymph nodes compressing airway. Contrast enhanced axial (A) and coronal MPR (B) images show enlarged necrotic lymph nodal mass (n) in subcarinal station causing carinal widening and compression of left main bronchus (arrow). VRT (C) and virtual bronchoscopy (D) images also show compression of left main bronchus (arrow). MPR: Multiplanar reformation; VRT: Volume rendering technique.

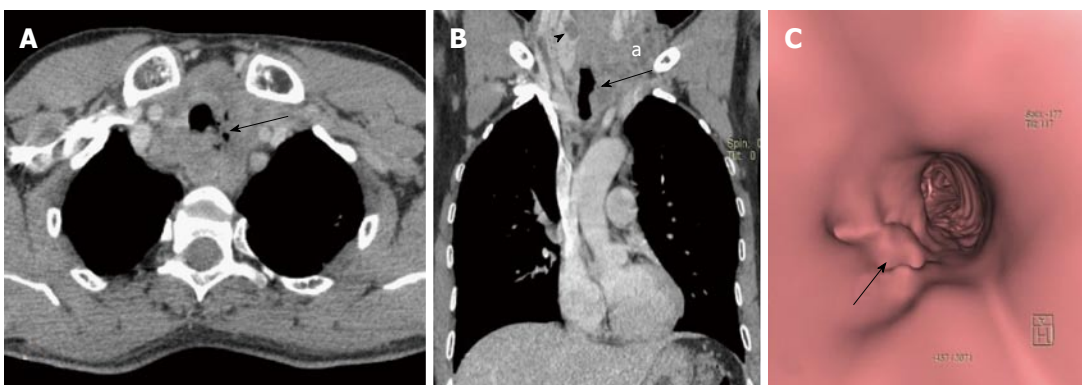


Figure 24 Paratracheal erosive malignant lymph nodes. Contrast enhanced axial (A) and coronal MPR (B) images show enlarged necrotic paratracheal lymph nodes eroding adjacent airway and showing foci of air within. There is a hypodense mass lesion (arrowhead in B) in right lobe of thyroid (patient was a known case of metastatic papillary thyroid carcinoma). Enlarged necrotic left lower jugular lymph nodes (a in B) also noted. Virtual bronchoscopy (C) shows focal area of irregularity along left lateral tracheal wall (arrow). MPR: Multiplanar reformation.

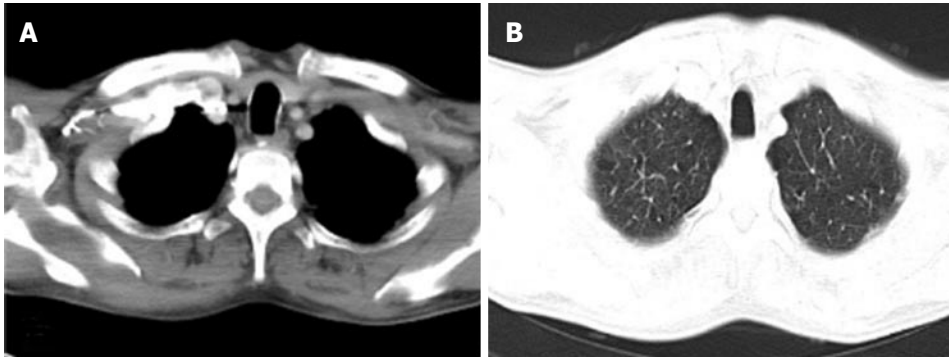


Figure 25 Saber-sheath trachea. In a 70-year old male with chronic obstructive pulmonary disease, axial images of thorax in mediastinal (A) and lung (B) window settings show increase in antero-posterior diameter of the trachea with narrowing of the transverse diameter. The sagittal to transverse diameter ratio measured 2.13:1.

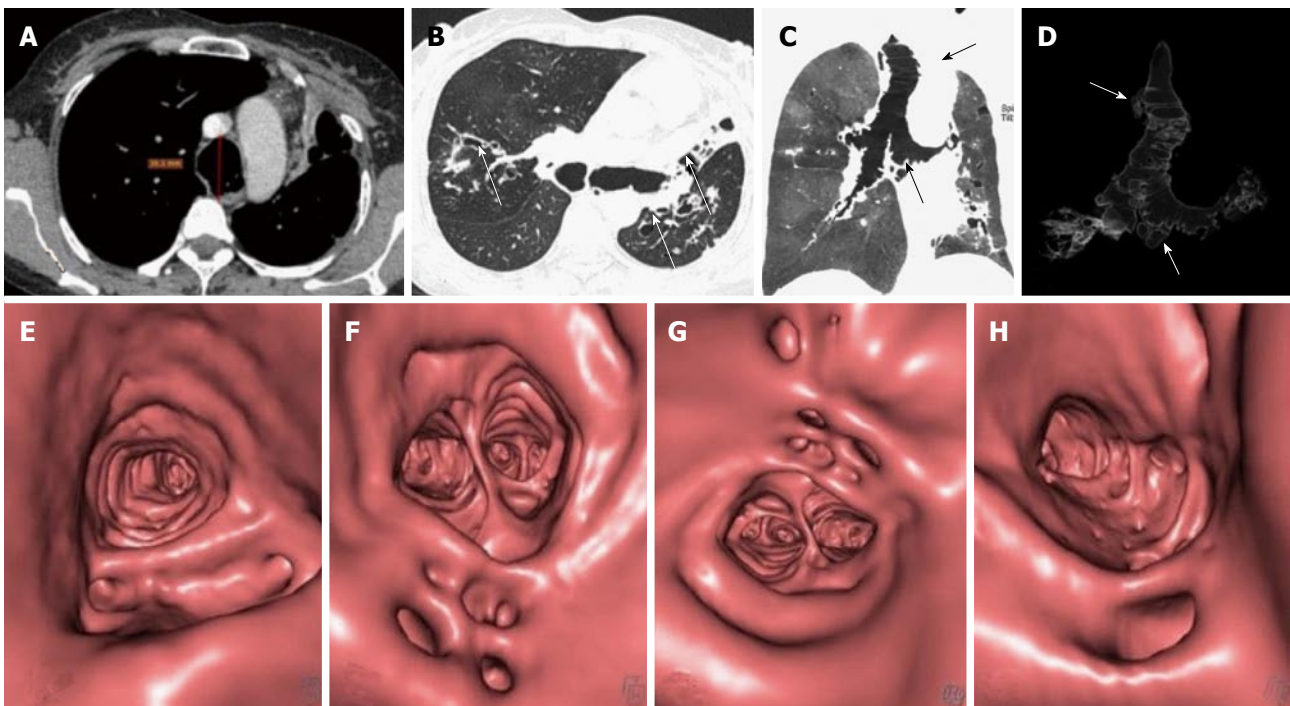


Figure 26 Mounier Kuhn syndrome. Axial images (A and B) show dilated trachea-AP diameter 3.6 cm at level of aortic arch (A) with dilated bronchi (B) and diverticula formation. Bronchiectasis is seen in bilateral upper and left lower lobes with collapse of lingula (arrow in B). Coronal MinIP (C) and VRT (D) images show tracheo-bronchomegaly with diffuse scattered diverticulosis (arrows). Virtual bronchoscopy also shows diffusely scattered defects in the walls of upper trachea (E), carina (F), right (G) and left (H) main bronchi. MinIP: Minimum intensity projection; VRT: Volume rendering technique.

Tracheobronchopathia osteochondroplastica

Tracheobronchopathia osteochondroplastica is a rare, benign condition involving the trachea, and possibly major bronchi. The disease is characterised by diffuse nodularities, or polyps consisting of cartilaginous and/or osseous metaplastic tissue involving tracheal cartilaginous wall with sparing of membranous posterior wall (Figure 27)^[52]. The nodules are 1 to 3 mm in diameter and may cause narrowing and rigidity of the trachea and bronchi. The majority of people remain asymptomatic throughout their lives unless severe airway stenosis develops, in which case patients may experience symptoms such as dyspnoea, hoarseness, persistent and often productive cough, haemoptysis and recurrent or slowly resolving pneumonia^[53].

MISCELLANEOUS DEVELOPMENTAL ANOMALIES

Tracheal bronchus/displaced bronchus

The term tracheal bronchus was initially used for a right upper lobe bronchus originating from trachea by Sandifort in 1785. However, currently the term is applied for a variety of anomalous bronchi that supply the upper lobe or its apical segment. The anomalous bronchi may originate from trachea or main bronchi (Figure 28)^[38]. Patients are usually asymptomatic. However, in patients presenting with persistent/recurrent pneumonia or atelectasis of the upper lobe, a possibility of tracheal bronchus should be kept in mind.

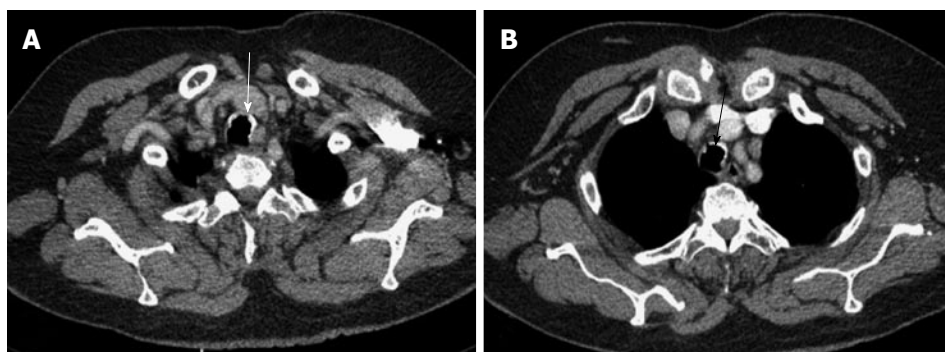


Figure 27 Tracheobronchopathia osteochondrodisplastica. Axial images of thorax (A and B) show irregular nodular thickening with foci of calcification involving the anterior and lateral walls of trachea (arrows). There is characteristic sparing of the posterior tracheal membrane.

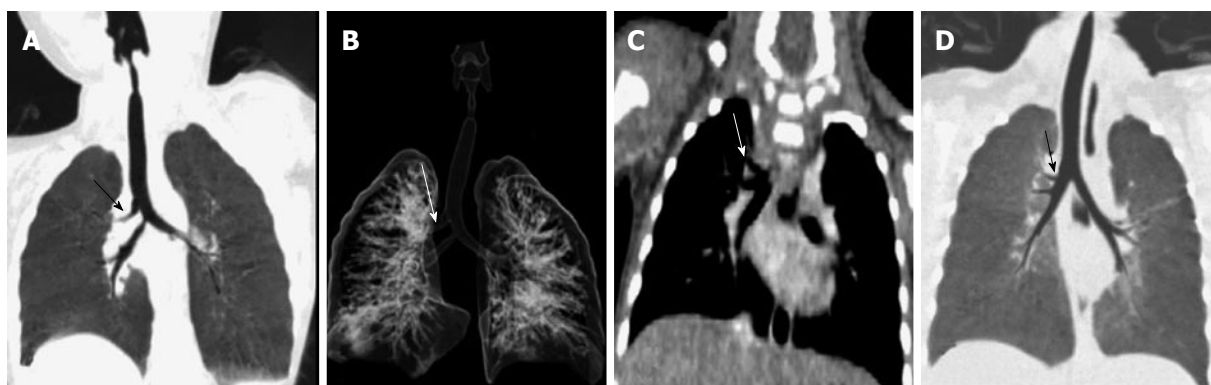


Figure 28 Displaced bronchus. Case 1: Coronal MinIP (A) and VRT (B) images show anomalous origin of right upper lobe bronchus from trachea-"Pig bronchus/bronchus suis" (arrow). Case 2: Coronal MPR (C) and MinIP (D) images show anomalous origin of the right apical segment bronchus from right main bronchus (arrow). MPR: Multiplanar reformation; MinIP: Minimum intensity projection; VRT: Volume rendering technique.

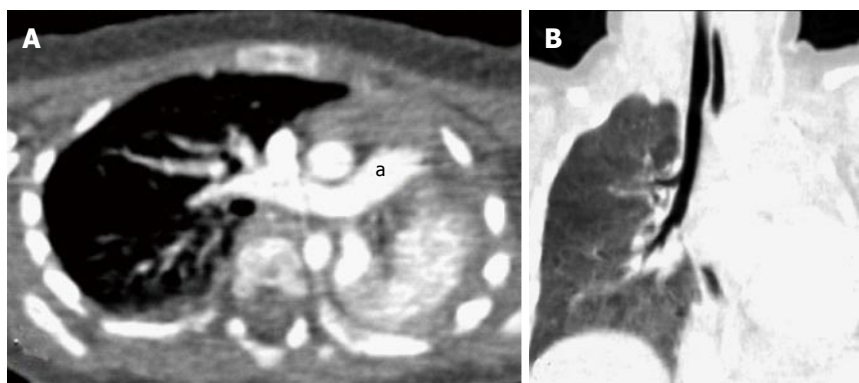


Figure 29 Bronchial agenesis. Axial (A) and coronal MinIP (B) images show absent left lung with left sided mediastinal shift and volume loss. Main pulmonary artery (a) continues as right pulmonary artery with absent left pulmonary artery. There is also associated absence of left main bronchus. MinIP: Minimum intensity projection.

Bronchial agenesis

Bronchial agenesis is always associated with congenital absence of lung, *i.e.*, pulmonary agenesis and absence of its vascular supply^[54]. Bilateral lung agenesis is always fatal in antenatal or immediate postnatal period. Infants with unilateral agenesis usually survive, but they may have associated congenital heart disease, trachea-esophageal atresia, spinal and renal anomalies^[39]. These neonates usually present with respiratory distress. They can also be discovered incidentally in older children and

adults. MDCT is the modality of choice as it can easily diagnose the absence of lung parenchyma, bronchus and pulmonary vessels (Figure 29).

CONCLUSION

MDCT is a rapid and non-invasive investigation for evaluation of patients with suspected airway pathology. It is highly accurate in evaluating intraluminal obstruction, extraluminal vascular anomalies and airway wall

defects. The entire extra luminal anatomy anatomy is clearly delineated and any associated finding within the mediastinum or lung parenchyma is also clearly depicted. Therefore, it provides a comprehensive information about the extent of disease process including the luminal and extraluminal components. In addition, VB can also help access sites beyond a proximal stenosis which cannot be seen on conventional bronchoscopy due to the inability of bronchoscope to negotiate through a proximal occlusive lesion. Therefore MDCT has an immense potential to emerge as a non-invasive, rapidly reproducible investigation tool which can provide information about primary airway disease as well as extra-luminal pathologies affecting the airway.

REFERENCES

- Burke AJ, Vining DJ, McGuirt WF, Postma G, Browne JD. Evaluation of airway obstruction using virtual endoscopy. *Laryngoscope* 2000; **110**: 23-29 [PMID: 10646710 DOI: 10.1097/00005537-200001000-00005]
- Stern RL, Cline HE, Johnson GA, Ravin CE. Three-dimensional imaging of the thoracic cavity. *Invest Radiol* 1989; **24**: 282-288 [PMID: 2745007 DOI: 10.1097/00004424-198904000-00005]
- Hu H, He HD, Foley WD, Fox SH. Four multidetector-row helical CT: image quality and volume coverage speed. *Radiology* 2000; **215**: 55-62 [PMID: 10751468 DOI: 10.1148/radiology.215.1.r00ap3755]
- Rydborg J, Buckwalter KA, Caldemeyer KS, Phillips MD, Conces DJ, Aisen AM, Persohn SA, Kopecky KK. Multisecton CT: scanning techniques and clinical applications. *Radiographics* 2000; **20**: 1787-1806 [PMID: 11112829 DOI: 10.1148/radiographics.20.6.g00nv071787]
- Ravenel JG, McAdams HP, Remy-Jardin M, Remy J. Multidimensional imaging of the thorax: practical applications. *J Thorac Imaging* 2001; **16**: 269-281 [PMID: 11685092 DOI: 10.1097/00005382-200110000-00008]
- Boiselle PM, Reynolds KF, Ernst A. Multiplanar and three-dimensional imaging of the central airways with multidetector CT. *AJR Am J Roentgenol* 2002; **179**: 301-308 [PMID: 12130424 DOI: 10.2214/ajr.179.2.1790301]
- Remy-Jardin M, Remy J, Artaud D, Fribourg M, Naili A. Tracheobronchial tree: assessment with volume rendering--technical aspects. *Radiology* 1998; **208**: 393-398 [PMID: 9680565 DOI: 10.1148/radiology.208.2.9680565]
- Higgins WE, Ramaswamy K, Swift RD, McLennan G, Hoffman EA. Virtual bronchoscopy for three--dimensional pulmonary image assessment: state of the art and future needs. *Radiographics* 1998; **18**: 761-778 [PMID: 9599397 DOI: 10.1148/radiographics.18.3.9599397]
- Kay CL, Evangelou HA. A review of the technical and clinical aspects of virtual endoscopy. *Endoscopy* 1996; **28**: 768-775 [PMID: 9007432 DOI: 10.1055/s-2007-1005603]
- Holbert JM, Strollo DC. Imaging of the normal trachea. *J Thorac Imaging* 1995; **10**: 171-179 [PMID: 7674430 DOI: 10.1097/00005382-199522000-00003]
- Boiselle PM, Lee KS, Ernst A. Multidetector CT of the central airways. *J Thorac Imaging* 2005; **20**: 186-195 [PMID: 16077334 DOI: 10.1097/01.rti.0000171624.84951.f2]
- Gamsu G, Webb WR. Computed tomography of the trachea: normal and abnormal. *AJR Am J Roentgenol* 1982; **139**: 321-326 [PMID: 6979885 DOI: 10.2214/ajr.139.2.321]
- Naidich DP, Webb WR. Introduction to imaging methodology and airway anatomy. In: Naidich DP, Webb WR, Grenier PA, Gefter WB, Harkin TJ, editor. *Imaging of the Airways Functional and Radiologic Correlations*. Philadelphia: Lippincott Williams and Wilkins, 2005: 1-28
- Ngo AV, Walker CM, Chung JH, Takasugi JE, Stern EJ, Kanne JP, Reddy GP, Godwin JD. Tumors and tumorlike conditions of the large airways. *AJR Am J Roentgenol* 2013; **201**: 301-313 [PMID: 23883210 DOI: 10.2214/AJR.12.9043]
- Jemal A, Siegel R, Xu J, Ward E. Cancer statistics, 2010. *CA Cancer J Clin* 2010; **60**: 277-300 [PMID: 20610543 DOI: 10.3322/caac.20073]
- Hartman TE, Tazelaar HD, Swensen SJ, Müller NL. Cigarette smoking: CT and pathologic findings of associated pulmonary diseases. *Radiographics* 1997; **17**: 377-390 [PMID: 9084079 DOI: 10.1148/radiographics.17.2.9084079]
- Travis WD. Pathology of lung cancer. *Clin Chest Med* 2002; **23**: 65-81, viii [PMID: 11901921 DOI: 10.1016/S0272-5231(03)00061-3]
- Pearlberg JL, Sandler MA, Lewis JW, Beute GH, Alpern MB. Small-cell bronchogenic carcinoma: CT evaluation. *AJR Am J Roentgenol* 1988; **150**: 265-268 [PMID: 2827450 DOI: 10.2214/ajr.150.2.265]
- Rady PL, Schnadig VJ, Weiss RL, Hughes TK, Tyring SK. Malignant transformation of recurrent respiratory papillomatosis associated with integrated human papillomavirus type 11 DNA and mutation of p53. *Laryngoscope* 1998; **108**: 735-740 [PMID: 9591556 DOI: 10.1097/00005537-199805000-00021]
- Park CM, Goo JM, Lee HJ, Kim MA, Lee CH, Kang MJ. Tumors in the tracheobronchial tree: CT and FDG PET features. *Radiographics* 2009; **29**: 55-71 [PMID: 19168836 DOI: 10.1148/r.291085126]
- Jeong SY, Lee KS, Han J, Kim BT, Kim TS, Shim YM, Kim J. Integrated PET/CT of salivary gland type carcinoma of the lung in 12 patients. *AJR Am J Roentgenol* 2007; **189**: 1407-1413 [PMID: 18029878 DOI: 10.2214/AJR.07.2652]
- Hartman TE, Primack SL, Lee KS, Swensen SJ, Müller NL. CT of bronchial and bronchiolar diseases. *Radiographics* 1994; **14**: 991-1003 [PMID: 7991828 DOI: 10.1148/radiographics.14.5.7991828]
- Gustafsson BI, Kidd M, Chan A, Malfetheriner MV, Modlin IM. Bronchopulmonary neuroendocrine tumors. *Cancer* 2008; **113**: 5-21 [PMID: 18473355 DOI: 10.1002/cncr.23542]
- Marom EM, Goodman PC, McAdams HP. Focal abnormalities of the trachea and main bronchi. *AJR Am J Roentgenol* 2001; **176**: 707-711 [PMID: 11222209 DOI: 10.2214/ajr.176.3.1760707]
- Chang CH, Wang HC, Wu MT, Lu JY. Virtual bronchoscopy for diagnosis of recurrent respiratory papillomatosis. *J Formos Med Assoc* 2006; **105**: 508-511 [PMID: 16801040]
- Kozower BD, Javidan-Nejad C, Lewis JS, Safdar S, Cooper JD, Patterson GA. Clinical-pathologic conference in general thoracic surgery: malignant transformation of recurrent respiratory papillomatosis. *J Thorac Cardiovasc Surg* 2005; **130**: 1190-1193 [PMID: 16214538 DOI: 10.1016/j.jtcvs.2005.06.036]
- Taha MS, Mostafa BE, Fahmy M, Ghaffar MK, Ghany EA. Spiral CT virtual bronchoscopy with multiplanar reformatting in the evaluation of post-intubation tracheal stenosis: comparison between endoscopic, radiological and surgical findings. *Eur Arch Otorhinolaryngol* 2009; **266**: 863-866 [PMID: 19002699 DOI: 10.1007/s00405-008-0854-y]
- Lee KS, Yoon JH, Kim TK, Kim JS, Chung MP, Kwon OJ. Evaluation of tracheobronchial disease with helical CT with multiplanar and three-dimensional reconstruction: correlation with bronchoscopy. *Radiographics* 1997; **17**: 555-567; discussion 568-570 [PMID: 9153696 DOI: 10.1148/radiographics.17.3.9153696]
- Koşucu P, Ahmetoğlu A, Koramaz I, Orhan F, Özdemir O, Dinç H, Okten A, Gümele HR. Low-dose MDCT and virtual bronchoscopy in pediatric patients with foreign body aspiration. *AJR Am J Roentgenol* 2004; **183**: 1771-1777 [PMID: 15547227 DOI: 10.2214/ajr.183.6.01831771]
- Applegate KE, Dardinger JT, Lieber ML, Herts BR, Davros WJ, Obuchowski NA, Maneker A. Spiral CT scanning technique in the detection of aspiration of LEGO foreign bodies. *Pediatr Radiol* 2001; **31**: 836-840 [PMID: 11727016 DOI: 10.1007/s002470100001]
- Karakoç F, Karadağ B, Akbenlioglu C, Ersu R, Yildizeli B, Yüksel

- M, Dağlı E. Foreign body aspiration: what is the outcome? *Pediatr Pulmonol* 2002; **34**: 30-36 [PMID: 12112794 DOI: 10.1002/ppul.10094]
- 32 **Khan MF**, Herzog C, Ackermann H, Wagner TO, Maataoui A, Harth M, Abolmaali ND, Jacobi V, Vogl TJ. Virtual endoscopy of the tracheo-bronchial system: sub-millimeter collimation with the 16-row multidetector scanner. *Eur Radiol* 2004; **14**: 1400-1405 [PMID: 15133710 DOI: 10.1007/s00330-004-2325-1]
- 33 **Slim MS**, Yacoubian HD. Complications of foreign bodies in the tracheobronchial tree. *Arch Surg* 1966; **92**: 388-393 [PMID: 5906833 DOI: 10.1001/archsurg.1966.01320210068013]
- 34 **Zerella JT**, Dimler M, McGill LC, Pippus KJ. Foreign body aspiration in children: value of radiography and complications of bronchoscopy. *J Pediatr Surg* 1998; **33**: 1651-1654 [PMID: 9856887 DOI: 10.1016/S0022-3468(98)90601-7]
- 35 **Seo JB**, Song KS, Lee JS, Goo JM, Kim HY, Song JW, Lee IS, Lim TH. Broncholithiasis: review of the causes with radiologic-pathologic correlation. *Radiographics* 2002; **22** Spec No: S199-S213 [PMID: 12376611 DOI: 10.1148/radiographics.22.suppl_1.g02oc07s199]
- 36 **Moriwaki Y**, Sugiyama M, Matsuda G, Toyoda H, Kosuge T, Uchida K, Fukuyama H, Iwashita M, Morimura N, Suzuki J, Yamamoto T, Suzuki N. Usefulness of the 3-dimensionally reconstructed computed tomography imaging for diagnosis of the site of tracheal injury (3D-tracheography). *World J Surg* 2005; **29**: 102-105 [PMID: 15599743 DOI: 10.1007/s00268-004-7433-1]
- 37 **Turner A**, Gavel G, Coutts J. Vascular rings--presentation, investigation and outcome. *Eur J Pediatr* 2005; **164**: 266-270 [PMID: 15666159 DOI: 10.1007/s00431-004-1607-6]
- 38 **Berrocal T**, Madrid C, Novo S, Gutiérrez J, Arjonilla A, Gómez-León N. Congenital anomalies of the tracheobronchial tree, lung, and mediastinum: embryology, radiology, and pathology. *Radiographics* 2004; **24**: e17 [PMID: 14610245 DOI: 10.1148/rg.e17]
- 39 **Lee EY**, Boisselle PM, Cleveland RH. Multidetector CT evaluation of congenital lung anomalies. *Radiology* 2008; **247**: 632-648 [PMID: 18487532 DOI: 10.1148/radiol.2473062124]
- 40 **Kimura-Hayama ET**, Meléndez G, Mendizábal AL, Meave-González A, Zambrana GF, Corona-Villalobos CP. Uncommon congenital and acquired aortic diseases: role of multidetector CT angiography. *Radiographics* 2010; **30**: 79-98 [PMID: 20083587 DOI: 10.1148/rg.301095061]
- 41 **Schanker HM**, Rachelefsky G, Siegel S, Katz R, Spector S, Rohr A, Rodriquez C, Woloshin K, Papanek PJ. Immediate and delayed type hypersensitivity to malathion. *Ann Allergy* 1992; **69**: 526-528 [PMID: 1471787]
- 42 **Aktoğlu S**, Yuncu G, Halilçolar H, Ermete S, Buduneli T. Bronchogenic cysts: clinicopathological presentation and treatment. *Eur Respir J* 1996; **9**: 2017-2021 [PMID: 8902460 DOI: 10.1183/09031936.96.09102017]
- 43 **McAdams HP**, Kirejczyk WM, Rosado-de-Christenson ML, Matsumoto S. Bronchogenic cyst: imaging features with clinical and histopathologic correlation. *Radiology* 2000; **217**: 441-446 [PMID: 11058643 DOI: 10.1148/radiology.217.2.r00nv19441]
- 44 **Williams HJ**, Johnson KJ. Imaging of congenital cystic lung lesions. *Paediatr Respir Rev* 2002; **3**: 120-127 [PMID: 12297058 DOI: 10.1016/S1526-0550(02)00006-9]
- 45 **Torres de Amorim e Silva CJ**, Fink AM. Case 137: Pneumonia and bronchiectasis secondary to unrecognized peanut impaction. *Radiology* 2008; **248**: 1080-1082 [PMID: 18710997 DOI: 10.1148/radiol.2483050725]
- 46 **Urkin J**, Bar-David Y. Respiratory distress secondary to esophageal foreign body: a case report. *ScientificWorldJournal* 2006; **6**: 16-19 [PMID: 16432624 DOI: 10.1100/tsw.2006.08]
- 47 **Edlavitch SA**, Crow R, Burke GL, Huber J, Prineas R, Blackburn H. The effect of the number of electrocardiograms analyzed on cardiovascular disease surveillance: the Minnesota Heart Survey (MHS). *J Clin Epidemiol* 1990; **43**: 93-99 [PMID: 2319286 DOI: 10.1002/ppul.22728]
- 48 **Grenier PA**, Beigelman-Aubry C, Brillet PY. Nonneoplastic tracheal and bronchial stenoses. *Radiol Clin North Am* 2009; **47**: 243-260 [PMID: 19249454 DOI: 10.1016/j.rcl.2008.11.011]
- 49 **Trigaux JP**, Hermes G, Dubois P, Van Beers B, Delaunois L, Jamart J. CT of saber-sheath trachea. Correlation with clinical, chest radiographic and functional findings. *Acta Radiol* 1994; **35**: 247-250 [PMID: 8192961 DOI: 10.1177/028418519403500310]
- 50 **Shin MS**, Jackson RM, Ho KJ. Tracheobronchomegaly (Mounier-Kuhn syndrome): CT diagnosis. *AJR Am J Roentgenol* 1988; **150**: 777-779 [PMID: 3258088 DOI: 10.2214/ajr.150.4.777]
- 51 **Jain P**, Dave M, Singh DP, Kumawat DC, Babel CS. Mounier-Kuhn syndrome. *Indian J Chest Dis Allied Sci* 2002; **44**: 195-198 [PMID: 12206481]
- 52 **Chroneou A**, Zias N, Gonzalez AV, Beamis JF. Tracheobronchopathia osteochondroplastica. An underrecognized entity? *Monaldi Arch Chest Dis* 2008; **69**: 65-69 [PMID: 18837419]
- 53 **Zack JR**, Rozenshtein A. Tracheobronchopathia osteochondroplastica: report of three cases. *J Comput Assist Tomogr* 2002; **26**: 33-36 [PMID: 11801902 DOI: 10.1097/00004728-200201000-00006]
- 54 **Ghaye B**, Szapiro D, Fanchamps JM, Dondelinger RF. Congenital bronchial abnormalities revisited. *Radiographics* 2001; **21**: 105-119 [PMID: 11158647 DOI: 10.1148/radiographics.21.1.g01ja06105]

P- Reviewer: Chow J, Yazdi HR S- Editor: Gong ZM L- Editor: A
E- Editor: Wu HL



Amyloid positron emission tomography and cognitive reserve

Matteo Bauckneht, Agnese Picco, Flavio Nobili, Silvia Morbelli

Matteo Bauckneht, Silvia Morbelli, Nuclear Medicine Unit, Department of Health Science, University of Genoa and IRCCS AOU San Martino-IST, 16132 Genoa, Italy

Agnese Picco, Flavio Nobili, Clinical Neurology Unit, Department of Neuroscience, University of Genoa and IRCCS AOU San Martino-IST, 16132 Genoa, Italy

Author contributions: Morbelli S designed the review; Bauckneht M performed literature search and draft the manuscript; Picco A, Nobili F and Morbelli S made critical revisions related to important intellectual content of the manuscript; Morbelli S have given final approval of the version of the article to be published; all authors read and approved the final manuscript.

Conflict-of-interest statement: The authors have no conflict of interest to declare.

Open-Access: This article is an open-access article which was selected by an in-house editor and fully peer-reviewed by external reviewers. It is distributed in accordance with the Creative Commons Attribution Non Commercial (CC BY-NC 4.0) license, which permits others to distribute, remix, adapt, build upon this work non-commercially, and license their derivative works on different terms, provided the original work is properly cited and the use is non-commercial. See: <http://creativecommons.org/licenses/by-nc/4.0/>

Correspondence to: Silvia Morbelli, MD, PhD, Nuclear Medicine Unit, Department of Health Science, University of Genoa and IRCCS AOU San Martino-IST, Largo R. Benzi 10, 16132 Genoa, Italy. silviadaniela.morbelli@hsanmartino.it
Telephone: +39-10-5552027
Fax: +39-10-5556911

Received: July 28, 2015
Peer-review started: July 29, 2015
First decision: August 14, 2015
Revised: September 1, 2015
Accepted: October 16, 2015
Article in press: October 19, 2015
Published online: December 28, 2015

Abstract

Alzheimer's disease (AD) is characterized by a non-linear progressive course and several aspects influence the relationship between cerebral amount of AD pathology and the clinical expression of the disease. Brain cognitive reserve (CR) refers to the hypothesized capacity of an adult brain to cope with brain damage in order to minimize symptomatology. CR phenomenon contributed to explain the disjunction between the degree of neurodegeneration and the clinical phenotype of AD. The possibility to track brain amyloidosis ($A\beta$) *in vivo* has huge relevance for AD diagnosis and new therapeutic approaches. The clinical repercussions of positron emission tomography (PET)-assessed $A\beta$ load are certainly mediated by CR thus potentially hampering the prognostic meaning of amyloid PET in selected groups of patients. Similarly, amyloid PET and cerebrospinal fluid amyloidosis biomarkers have recently provided new evidence for CR. The present review discusses the concept of CR in the framework of available neuroimaging studies and specifically deals with the reciprocal influences between amyloid PET and CR in AD patients and with the potential consequent interventional strategies for AD.

Key words: Cognitive reserve; Amyloid positron emission tomography; Mild cognitive impairment; Alzheimer disease; Brain

© The Author(s) 2015. Published by Baishideng Publishing Group Inc. All rights reserved.

Core tip: Given the large population of aging individuals and the consequent huge, progressive Alzheimer's disease (AD)-related healthcare costs, it is critical to find effective therapeutic strategies to mitigate the AD cognitive dysfunction. Accordingly, understanding the neurobiological mechanisms underlying cognitive reserve (CR) is of utmost importance. Instead, Amyloid

positron emission tomography (PET) has recently improved our knowledge in the field of CR. The present review discusses the concept of CR in the framework of available neuroimaging studies and specifically deals with the reciprocal influences between Amyloid PET and CR in AD patients and with the potential consequent interventional strategies for AD.

Bauckneht M, Picco A, Nobili F, Morbelli S. Amyloid positron emission tomography and cognitive reserve. *World J Radiol* 2015; 7(12): 475-483 Available from: URL: <http://www.wjgnet.com/1949-8470/full/v7/i12/475.htm> DOI: <http://dx.doi.org/10.4329/wjcr.v7.i12.475>

INTRODUCTION

Alzheimer's disease (AD) is the most common neurodegenerative cause of dementia and affects around 10% of individuals over age 65 and up to 40% of individuals over age 85^[1]. In 2010 it has been estimated that 4.7 million individuals aged 65 years or older were affected by AD in the United States with the total number of people with AD dementia projected to be 13.8 million in 2050^[1]. AD is characterized by a progressive deterioration in memory and other cognitive abilities as well as in capability for independent living. The course of AD is variable^[2], but symptoms tend to develop over the same general steps: Mild cognitive impairment (MCI) (which in typical forms begin with episodic memory impairment), slow, progressive affection of other cognitive domains and, eventually, dementia^[3]. Amyloid deposition and tau pathology (neurofibrillary tangles) within the cerebral cortex are the neuropathological hallmarks of AD^[4]. Several lines of evidence, demonstrated that AD is characterized by a non-linear progressive course and that several aspects may influence the relationship between cerebral amount of AD pathology and its clinical expression^[3,5,6]. In fact, it has been shown that at least 20% of elderly people who are cognitively normal before death show postmortem findings sufficient to fulfill neuropathological criteria for AD^[7,8]. On the other hand, several studies showed that biological factors such as the age of onset and the expression of Apolipoprotein E genotype, can be associated with a faster cognitive decline^[9,10]. Similarly, increasing evidence has highlighted the role of oxidative stress in AD, because of the increased production of reactive oxygen species and the influence of oxidative stress on brain energy metabolism^[11].

Accordingly clinical expression of AD is critically affected by the resilience of the individual brain to molecular mechanisms and neuropathology^[12]. These complex mechanisms have been historically referred to as Brain Cognitive Reserve phenomenon (CR^[13]). CR refers to the hypothesized capacity of an adult brain to cope with brain damage in order to minimize symptomatology^[13]. Individuals with high reserve are

thought to have either higher number of neurons and synapses ("brain reserve"), and/or a better ability to put in place alternative strategies or compensatory mechanisms ("cognitive reserve") than individuals with low reserve^[12,14]. Therefore, CR phenomenon may also at least partially explain the disjunction between the degree of neurodegeneration and the clinical phenotype of AD.

In this framework it has been hypothesized that not only duration of formal education, but also the quality of performance throughout the years can influence CR and the general brain reaction to AD pathology in clinical terms^[12]. First evidence for CR date back to the 80's, when neuropathological studies highlighted the existence of subgroups of cognitively intact subjects matching criteria for AD at autopsy^[7]. In the following decades, structural [magnetic resonance imaging (MRI)] and functional (MRI, SPECT and PET) studies have confirmed the existence of CR and allowed a better comprehension and anatomical localization of this phenomenon. In more recent years, the availability of new molecular probes sensitive to amyloid-beta (A β) deposition have allowed the *in vivo* demonstration of amyloid load by means of PET (Amy-PET)^[15-18]. The possibility to track A β pathology *in vivo* has huge relevance for AD diagnosis and clinical trials. The oldest and more extensively studied PET tracer for Amy-PET is the Carbon11 labeled pittsburgh compound B (PiB)^[15]. More recently three fluorine18 labeled compounds have been developed. Following multicenter phase 3 trials, they were all approved both in the United States and Europe to *in vivo* image amyloid plaques^[18-20]. Accordingly, appropriate use criteria have been now proposed for the use of Amy-PET^[21]. Although obtaining *in vivo* information about the presence of amyloid pathology allowed a greater accuracy in the work up of patients with suspected AD, the clinical repercussions of PET-assessed A β load are certainly mediated by CR. In fact CR can potentially hamper the prognostic meaning of Amy-PET at least in selected groups of patients. On the other side CR phenomenon itself has gained renovated interest from the possibility of knowing and *in vivo* localizing A β load by means of PET thus providing further evidence for a more etiopathological effect of CR^[22,23]. Therefore on the one side, Amy-PET [and cerebrospinal fluid (CSF) amyloidosis biomarkers] provide new evidence for CR, on the other side, CR has clinical and pathophysiological repercussion for the study of AD, especially now, in the era of brain amyloidosis biomarkers. The present review discusses the concept of CR in the framework of available neuroimaging studies and specifically deals with the reciprocal influences between Amy-PET and CR in AD patients and with the potential consequent interventional strategies for AD.

CONCEPT OF COGNITIVE RESERVE: PIONEERING STUDIES

Historically the first model proposed to explain CR

was referred to quantitative measures of head circumference, brain size^[24], and synaptic or neuronal count^[25]. According to this approach, individuals with more neurons required more brain damage to reach a threshold of clinically evident dementia (passive model of CR). However, since the first studies on CR, subjects with either greater brain size, quantities of neurons or synapses were demonstrated to have different epidemiological/demographic features that can be responsible for CR and thus can serve as proxies for reserve. These factors include measures of educational attainment and socioeconomic status, such as income or occupational attainment. Similarly, physical activity and cognitive activity even during midlife have been associated with a reduced risk of AD^[26,27]. However, since the first studies education has probably been the most widely used proxy for CR. In fact level of education is relatively easy to ascertain. Moreover, proposed model fitted to the epidemiological evidence that higher incidence of AD and other dementia was observed among elder populations with low levels of education^[27]. However, this epidemiological approach lacks of anatomic localization and produces only indirect (based on neuropsychology) evidence about brain functional damage and networking^[28].

CONTRIBUTION OF NEUROIMAGING TO THE UNDERSTANDING OF CR

Due to these limitations many groups turned to functional neuroimaging approach, which is able to provide a more precise proxy measure about CR *in vivo*, thus allowing a more comprehensive understanding and localization of this phenomenon. In fact, while neuropsychological test results are influenced by the cognitive ability of the patient and his/her motivation to perform the tests, the imaging-assessed brain impairment more closely reflects the underlying brain damage (*i.e.*, neurodegeneration). In this line, functional neuroimaging supported the idea that even when neurodegeneration is higher in educated individuals, the clinical phenotype of AD may be similar to those in patients with lower education and less pathology^[14]. Based on this integrated approach, CR can be defined as the difference between an individual's expected (based on neuroimaging) and actual (assessed by neuropsychology) cognitive performance.

To elucidate these mechanisms, several imaging studies have originally used resting regional cerebral blood flow (rCBF) PET measurement as a surrogate of AD pathology^[29]. In these studies correlation between rCBF on one side and education and life-time activities score on the other was tested and an inverse correlation with rCBF in temporal-parietal-occipital areas was demonstrated in AD patients^[29].

Similar results were obtained by means of 3D MRI analysis demonstrating that education increases regional cortical thickness in healthy controls, while it

is inversely correlated with regional cortical thicknesses in temporal, parietal and occipital regions in AD patients^[30]. Finally, FDG-PET studies demonstrated that reserve mechanism are already at work in patients with amnesic mild cognitive impairment (aMCI) and prodromal Alzheimer's disease (pAD) patients^[14,31]. In fact, even in this early stages, AD patients with higher education showed more severe and extended "posterior" AD typical brain hypometabolism with respect to poorly educated patients expressing the same level of cognitive symptoms^[14,31]. This means that in early stage of disease CR may have meaningful repercussions for the clinical diagnosis of AD as highly educated prodromal AD patients can clinically hide the disease for a longer period of time. Accordingly, new lines of research focused on the mechanism(s) specifically allowing highly educated AD to cope with their greater brain damage. These mechanisms, evaluated by means of functional MRI and H215O PET activation studies as well with resting FDG PET, allowed to develop the so-called "active model" of CR^[29,32]. As CR allows maintenance of effective function across a wide range of activities despite the presence of brain pathology, it can be hypothesized that a specific network (or multiple integrated networks) are able to sustain CR and thus patients' cognitive function and independent activities of daily living^[33,34]. To investigate this hypothesis, Stern's group^[35] carried out a fMRI study by scanning young and elder subjects while performing two different tasks underlying two different cognitive domains and activations were regressed onto putative CR variables. A common network was actually identified including bilateral superior and medial frontal gyri thus suggesting a central role of the frontal cortex in CR-mediating mechanism^[35]. Another possible strategy to identify a specific CR network is the so-called metabolic connectivity analysis of brain ¹⁸F-FDG PET studies^[36]. In fact by calculating correlation coefficients -or pattern of intercorrelations- between values of FDG uptake, it is possible to estimate the functional association between cerebral areas^[36]. Therefore interregional correlations of metabolic glucose rates can be regarded in terms of "traffic (metabolic-functional connectivity) in the anatomical 'roads' present in the brain" which, by contrast, can be investigated by other neuroimaging methods such as diffusion tensor imaging^[37,38]. Morbelli *et al.*^[14] investigated functional mechanisms underlying CR in 64 early stage AD patients and 90 healthy controls who underwent brain ¹⁸F-FDG PET. Highly and poorly educated subjects were compared bidirectionally and with age and education-matched controls. It was indeed demonstrated that although AD-typical damage is more prominent in highly educated subjects, highly educated pAD have also a relatively higher metabolic levels with respect to poorly educated patients in the right inferior, middle, and superior frontal gyri with respect to less educated AD subjects.

These regions, which corresponded to the right

dorsolateral prefrontal cortex (DLFC), were then included as covariates in the subsequent metabolic connectivity analysis in highly and poorly educated AD patients. As the results, in highly educated AD patients, metabolism of the DLFC correlated significantly with that of several cortical areas in both hemispheres, while it was basically only auto correlated in poorly educated AD. Accordingly this metabolic connectivity analysis supports the existence of a network mediating CR and is anatomically consistent with a crucial role of lateral frontal cortex in CR-mediating mechanism. However, all these analyses did not completely elucidate whether these functional networks are due to preserved functional connections that are physiologically present in more educated subjects (*i.e.*, the brain reserve component of cognitive reserve) or to the recruitment of alternative neural networks able to support cognitive function just in the presence of disease related damage elsewhere (*i.e.*, the brain compensation component of cognitive reserve)^[33]. To specifically address this aspect, the same analysis was extended to the control groups and demonstrated that the large bilateral fronto-temporal-limbic metabolic network related to CR was actually present and topographically similar in highly educated controls. However this network was quantitatively less pronounced with respect to highly educated AD patients thus demonstrating that CR in early AD patients with a high level of education is a result of both neural reserve and neural compensation^[14]. The importance of reinforcement in brain connectivity in healthy elders was further confirmed in a multimodal imaging study involving 36 healthy elders presenting normal cognition and a negative florbetapir-PET scan^[39]. In fact, seed connectivity analyses of resting state fMRI showed that education was positively related to the magnitude of functional connectivity between the anterior cingulate cortex and the hippocampus as well as the inferior frontal lobe, posterior cingulate cortex and angular gyrus.

IMPLICATION OF CR FOR CLINICAL USE AMYLOID IMAGING

Amy-PET offers great promise to facilitate the evaluation of patients in a clinical setting, to improve our understanding of AD pathophysiology and to advance the development of effective therapy.

In vivo PET studies have shown an increased uptake of amyloid ligand 11C-labeled Pittsburgh Compound B ([11C]PIB) and fluorinated Amy-PET tracers in AD and mild cognitive impairment patients, especially in the frontal, parietal, and temporal cortices and in the posterior cingulate, which indicates an increased amyloid accumulation in these areas^[40,41]. However, in agreement with reports that significant A β deposits can be found in the brain of cognitively normal elderly individuals at autopsy, Amy-PET studies revealed that 20%-40% of cognitively unimpaired individuals over

the age of 65 years can have brain uptake above a predetermined threshold for AD in at least one region of interest^[42,43]. This evidence can be at least partially linked to CR phenomenon. In fact it was further demonstrated that even in patients with AD, the well-known greater posterior hypometabolism present in highly educated pAD is paralleled by a greater Amy-PET tracer's uptake especially in the ventrolateral frontal cortex^[44]. While only longitudinal evaluation of Amy-PET positive cognitively normal subjects can allow to access their long term outcome, this evidence have important diagnostic repercussion. In fact as CR is influenced by several (often measurable) epidemiological and social factors, these factors could be taken into account to support the final diagnosis of probable AD by means of Amy-PET or CSF amyloidosis biomarkers. Kemppainen *et al.*^[44] tested this hypothesis by assessing whether factors thought to influence the association of AD pathology and dementia help to accurately identify dementia of the Alzheimer type when considered together with Amy-PET. They generated receiver operating characteristic curves to compare the predictive accuracy of using Amy-PET alone or Amy-PET together with the above mentioned factors with the aim to tell apart AD patients from subjects with normal cognition. In this study, factors reported to influence associations between AD pathology and dementia demonstrated to improve the predictive accuracy of amyloid imaging for the identification of symptomatic AD. In fact, if a scan is performed and found positive (*i.e.*, in depressed patients with concurrent cognitive impairment), the risk of incidental brain amyloidosis must be taken into consideration when defining probable diagnosis and planning subsequent management^[45]. In this scenario high prognostic value of Amy-PET is present in case of a negative scan thus virtually excluding AD and encouraging a more vigorous evaluation of alternative diagnoses and treatment (for example when differential diagnosis was defined with respect to depression)^[45]. By contrast to exclude the presence of "incidental" positivity of Amy-PET the use of different biomarkers (*i.e.*, biomarkers of neurodegeneration) can be proposed to support a diagnosis of AD. In fact glucose hypometabolism as assessed by means of ¹⁸F-FDG PET as well as brain atrophy are more directly associated with neurodegeneration and thus with concurrent cognitive function^[46]. Noteworthy, if CR phenomenon is at work, PET-assessed hypometabolism might be markedly reduced even in presence of a mild cognitive impairment. The validity of this approach have been recently confirmed by a large retrospective multicenter study showing that, in clinical setting, the combined use of both amyloid and neuronal injury markers offers the most accurate prognosis in MCI patients^[47]. Besides underlying the importance of integrating Amy-PET with neurodegeneration biomarkers, the issue of positive Amy-PET in cognitive normal subjects further supports the need of a standardized approach

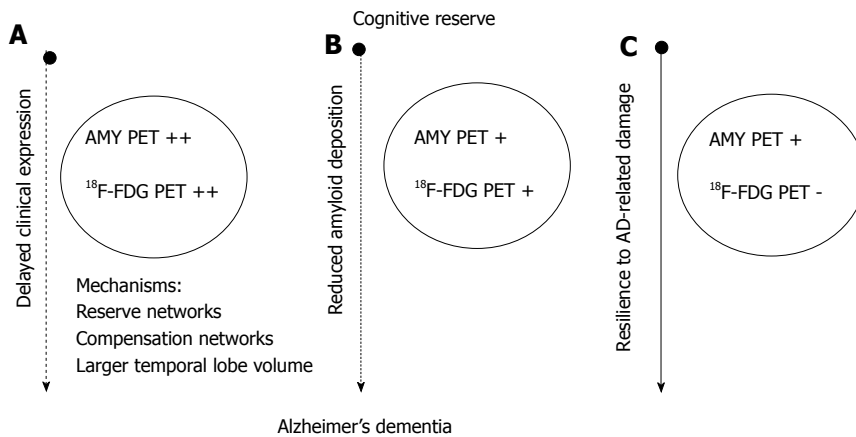


Figure 1 Schematic representation of the possible mechanisms mediating the effect of cognitive reserve on the onset of Alzheimer's dementia and corresponding expected results on ^{18}F -FDG and amyloid positron emission tomography. According to hypothesis (A) cognitive reserve (CR) would simply delay the clinical expression of the disease. In fact despite amyloid positron emission tomography (PET) and FDG PET marked positivity patients are able to delay symptoms thanks to compensative functional networks and/or structural features such as larger temporal lobe volume^[44,51]. Hypothesis (B) admits an opposite scenario in which, CR would prevent/delay amyloid deposition and Alzheimer's dementia (AD) pathology and thus neuronal damage and dementia onset^[17]. Finally hypothesis (C) could coexist with either of the first two and would explain the effect of CR as a sort of brain resilience despite AD pathology thus allowing a relatively preserved ^{18}F -FDG PET scan for a longer period of time^[59]. Amy-PET: Amyloid PET; ++: Markedly positive scan; +: Positive scan; -: Negative/relatively preserved scan.

to Amy-PET quantification. In fact, to date there's still considerable variability in the numbers reported as quantitative outcome measures of tracer retention. Many international efforts are ongoing to address the problem of Amy-PET quantification^[48]. Besides the increased accuracy and consistency potentially provided by tracer binding quantification, a further possible benefit would be related to the possibility of defining three ranges of amyloid deposition: (1) the amyloid-negative range; (2) the "AD-like" range; and (3) the "just-positive" range^[48,49]. A greater comprehension of this latter range may be of interest to better differentiated "incidental" amyloid load from amyloid load in the AD-like range in cognitively intact subjects with greater CR.

IMPLICATION OF AMYLOID IMAGING FOR COMPREHENSION OF CR

Many implications have been derived from CR for the clinical use of Amy-PET. Similarly, CR has gained new evidence and new interest from the availability of Amy-PET. As mentioned, patients with mild AD dementia and higher education (*i.e.*, 15 or more years of education) were found to have higher uptake of amyloid PET tracers in the frontal cortex compared with patients with lower education (*i.e.*, 6 years of education)^[6]. These results confirm that highly educated individuals manifest mild AD later on in the clinical course of the disease when more A β pathology is present thus supporting CR hypothesis.

However the availability of this information during life and the possibility to correlate this finding with other biomarkers have provided novel evidence for CR. This information can be relevant for AD model approach and biomarkers cascade in more comprehensive way. In fact, Chételat *et al.*^[50] correlated Amy-PET and brain structure

data and cognitive performance in subjects with and without memory complaints. They demonstrated that Amy-PET positive subjects without memory complaints had larger temporal lobes and better verbal learning performance than Amy-PET negative controls. On the opposite, Amy-PET positive subjects with subjective memory complaints had smaller regional brain volumes and worse global cognition than Amy-PET with memory complaints. Altogether these findings allow to propose a general model of interpretation. In fact the larger temporal lobes may have been crucial for Amy-PET positive subjects to maintain their cognitive ability while Amy-PET positive subjects with memory complaints might originally have less gray matter than those without memory complaints, and therefore had less CR^[50,51] (Figure 1). Accordingly the availability of Amy-PET and this multi-biomarker approach provided *in vivo* evidence that improving brain structure (*i.e.*, through cognitive or physical activity) may help compensate for AD related damage.

NEW PERSPECTIVE ON AMYLOID PET AND CR

Given the large population of aging individuals and the consequent huge, progressive AD-related Healthcare Costs, it is critical to find effective therapeutic strategies to mitigate the AD cognitive dysfunction. Understanding the neurobiological mechanisms underlying CR is thus of utmost importance. First studies trying to simulate, measure and possibly influence the effect of CR on AD were performed in animal models. Environmental enrichment paradigms has been developed in rodents by manipulating the complexity of their social, cognitive, and sensorial environments^[52]. These models are ideal to experimentally measure the effect of environmental

stimulation on cognitive reserve. In addition, previous studies demonstrated that environmental enrichment triggers structural and biochemical modification on neurons^[53], stimulates hippocampal neurogenesis in adult animals^[54] and attenuate cognitive decline in transgenic models of familial AD^[55]. Animal models may also serve to better define the specific age and time-frame in which exposure to environmental enrichment can still trigger functional compensation and mitigate memory dysfunction. Finally, the effect of environmental stimulation on neuropathological hallmarks of AD can be assessed *ex vivo* for example in mouse model of the disease. In this framework, Verret *et al.*^[22] examined whether exposure of a Tg2576 transgenic mouse model of AD to environmental enrichment at a specific period during the amyloidogenic process favored the establishment of a cognitive reserve. They demonstrated that environmental stimulation during early adulthood of mice - before amyloidogenesis has started - reduced the severity of AD-related cognitive deficits more efficiently than exposure later in life, when the pathology is already present. More importantly they highlighted *ex vivo* that, early-life environmental stimulation, slightly reduced forebrain surface covered by amyloid plaques (while not significantly impact remodeling in the hippocampus). These findings may open new scenarios related to the effect of CR in AD patients as they might suggest that cognitive activity may even modify amyloid deposition, rather than just compensating for it^[51]. Amy-PET and CSF biomarkers may allow to test this hypothesis *in vivo* in humans. In this framework, Landau *et al.*^[17] aimed to assess the association between lifestyle practices (cognitive and physical activity) and β -amyloid deposition, measured with positron emission tomography using carbon [11C]PIB, in healthy elderly. Greater participation in cognitively stimulating activities across the lifespan, but particularly in early and middle life, was associated with reduced [11C]PIB uptake (taken into account age, sex, and education). Moreover, among older controls, those who were more involved in cognitively stimulating activities across the lifespan (especially during young and middle age) had brain amyloid levels comparable to young controls, while those who were poorly cognitively active had amyloid levels similar to AD patients. Other studies reported that CR-related factors such as physical exercise correlated with less A β accumulation, however results are not always consistent. In fact in some cases those effects reached significance only in ApoE4 carriers^[56] and in other studies no evidence was highlighted concerning an effect of lifetime cognitive stimulation on the level of A β accumulation regardless of ApoE genotype^[57].

Accordingly is still a matter of debate if cognitive/physical stimulation can really modify the underlying pathology of AD or if CR just gives a resilience to it (as in the original definition of CR^[13]). However even in this latter case the availability of amyloidosis and neurodegeneration AD biomarkers can further clarify

and possibly localize mechanism of resistance to AD-related damage. In other words: Should we just define CR as the use of pre-existing and/or compensative network or can we hypothesized that brains/neurons in subjects with higher CR may be less damaged by AD-related pathology and thus may demonstrate less neurodegeneration? A first answer to this question has been provided by Almeida *et al.*^[58] who aimed to measure whether cognitive reserve could weaken the relationship between age and AD biomarker levels. A cross-sectional cohort of 268 individuals (211 cognitively normal and 57 cognitively impaired subjects; average age 62 years) was evaluated with respect to A β 42, t-tau, and p-tau immunoassays. The authors found that the difference in CSF phosphorylated tau (p-tau) and total tau (t-tau) between younger and older people was larger in subgroup of subjects with less than 16 years of education than it was in the subgroups with at least 16 years of schooling. These findings suggest that education could attenuate age-related increment in CSF p-tau and t-tau and might suggest a more general effect on age-related neurodegeneration. However, although raising interesting possibility and stimulating new interventional strategies in AD patients, this evidence need to be further tested especially with respect to its relevance for the future onset of dementia. In the next future, the availability not only of Amy-PET but also of Tau imaging (and thus the possibility to quantify and anatomically localize neurodegeneration^[59]) will allow to track and localize the pathological biomarkers cascade of AD in earlier stage of the illness (Figure 1). In fact, given models in which molecular pathologic changes (β -amyloid deposition) may temporarily precede neurodegeneration by a substantial of time period^[60], evaluation of just one of these two types of biomarkers do not allow to direct measure resilience to AD-related damage. Once entity, time-frame and individual peculiarity of this resilience will be identified, a more precise model of CR and its consequences on AD clinics will be defined thus finally elucidating (and selecting patients) for CR-related interventional approaches.

REFERENCES

- 1 **Hebert LE**, Weuve J, Scherr PA, Evans DA. Alzheimer disease in the United States (2010-2050) estimated using the 2010 census. *Neurology* 2013; **80**: 1778-1783 [PMID: 23390181 DOI: 10.1212/WNL.0b013e31828726f5]
- 2 **Tschanz JT**, Corcoran CD, Schwartz S, Treiber K, Green RC, Norton MC, Mielke MM, Piercy K, Steinberg M, Rabins PV, Leoutsakos JM, Welsh-Bohmer KA, Breitner JC, Lyketsos CG. Progression of cognitive, functional, and neuropsychiatric symptom domains in a population cohort with Alzheimer dementia: the Cache County Dementia Progression study. *Am J Geriatr Psychiatry* 2011; **19**: 532-542 [PMID: 21606896 DOI: 10.1097/JGP.0b013e3181faec23]
- 3 **Grober E**, Hall CB, Lipton RB, Zonderman AB, Resnick SM, Kawas C. Memory impairment, executive dysfunction, and intellectual decline in preclinical Alzheimer's disease. *J Int Neuropsychol Soc* 2008; **14**: 266-278 [PMID: 18282324 DOI: 10.1017/S1355617708080302]
- 4 **Hardy J**, Selkoe DJ. The amyloid hypothesis of Alzheimer's

- disease: progress and problems on the road to therapeutics. *Science* 2002; **297**: 353-356 [PMID: 12130773]
- 5 **Cummings JL**, Vinters HV, Cole GM, Khachaturian ZS. Alzheimer's disease: etiologies, pathophysiology, cognitive reserve, and treatment opportunities. *Neurology* 1998; **51**: S2-S17; discussion S65-S67 [PMID: 9674758]
 - 6 **Mungas D**, Reed BR, Jagust WJ, DeCarli C, Mack WJ, Kramer JH, Weiner MW, Schuff N, Chui HC. Volumetric MRI predicts rate of cognitive decline related to AD and cerebrovascular disease. *Neurology* 2002; **59**: 867-873 [PMID: 12297568]
 - 7 **Katzman R**, Terry R, DeTeresa R, Brown T, Davies P, Fuld P, Renbing X, Peck A. Clinical, pathological, and neurochemical changes in dementia: a subgroup with preserved mental status and numerous neocortical plaques. *Ann Neurol* 1988; **23**: 138-144 [PMID: 2897823]
 - 8 **Bennett DA**, Schneider JA, Arvanitakis Z, Kelly JF, Aggarwal NT, Shah RC, Wilson RS. Neuropathology of older persons without cognitive impairment from two community-based studies. *Neurology* 2006; **66**: 1837-1844 [PMID: 16801647]
 - 9 **Kim EJ**, Cho SS, Jeong Y, Park KC, Kang SJ, Kang E, Kim SE, Lee KH, Na DL. Glucose metabolism in early onset versus late onset Alzheimer's disease: an SPM analysis of 120 patients. *Brain* 2005; **128**: 1790-1801 [PMID: 15888536]
 - 10 **Mosconi L**, Perani D, Sorbi S, Herholz K, Nacmias B, Holthoff V, Salmon E, Baron JC, De Cristofaro MT, Padovani A, Borroni B, Franceschi M, Bracco L, Pupi A. MCI conversion to dementia and the APOE genotype: a prediction study with FDG-PET. *Neurology* 2004; **63**: 2332-2340 [PMID: 15623696]
 - 11 **Picco A**, Polidori MC, Ferrara M, Cecchetti R, Amaldi D, Baglioni M, Morbelli S, Bastiani P, Bossert I, Fiorucci G, Brugnolo A, Dottorini ME, Nobili F, Mecocci P. Plasma antioxidants and brain glucose metabolism in elderly subjects with cognitive complaints. *Eur J Nucl Med Mol Imaging* 2014; **41**: 764-775 [PMID: 24297504 DOI: 10.1007/s00259-013-2638-x]
 - 12 **Ewers M**, Frisoni GB, Teipel SJ, Grinberg LT, Amaro E, Heinsen H, Thompson PM, Hampel H. Staging Alzheimer's disease progression with multimodality neuroimaging. *Prog Neurobiol* 2011; **95**: 535-546 [PMID: 21718750 DOI: 10.1016/j.pneurobio.2011.06.004]
 - 13 **Stern Y**. What is cognitive reserve? Theory and research application of the reserve concept. *J Int Neuropsychol Soc* 2002; **8**: 448-460 [PMID: 11939702]
 - 14 **Morbelli S**, Perneckzy R, Drzezga A, Frisoni GB, Caroli A, van Berckel BN, Ossenkoppele R, Guedj E, Didic M, Brugnolo A, Naseri M, Sambucetti G, Pagani M, Nobili F. Metabolic networks underlying cognitive reserve in prodromal Alzheimer disease: a European Alzheimer disease consortium project. *J Nucl Med* 2013; **54**: 894-902 [PMID: 23591639 DOI: 10.2967/jnumed.112.113928]
 - 15 **Klunk WE**, Engler H, Nordberg A, Wang Y, Blomqvist G, Holt DP, Bergström M, Savitcheva I, Huang GF, Estrada S, Ausén B, Debnath ML, Barletta J, Price JC, Sandell J, Lopresti BJ, Wall A, Koivisto P, Antoni G, Mathis CA, Långström B. Imaging brain amyloid in Alzheimer's disease with Pittsburgh Compound-B. *Ann Neurol* 2004; **55**: 306-319 [PMID: 14991808]
 - 16 **Villemagne VL**, Mulligan RS, Pejoska S, Ong K, Jones G, O'Keefe G, Chan JG, Young K, Tochon-Danguy H, Masters CL, Rowe CC. Comparison of 11C-PiB and 18F-florbetaben for A β imaging in ageing and Alzheimer's disease. *Eur J Nucl Med Mol Imaging* 2012; **39**: 983-989 [PMID: 22398958 DOI: 10.1007/s00259-012-2088-x]
 - 17 **Landau SM**, Marks SM, Mormino EC, Rabinovici GD, Oh H, O'Neil JP, Wilson RS, Jagust WJ. Association of lifetime cognitive engagement and low β -amyloid deposition. *Arch Neurol* 2012; **69**: 623-629 [PMID: 22271235]
 - 18 **Curtis C**, Gamez JE, Singh U, Sadowsky CH, Villena T, Sabbagh MN, Beach TG, Duara R, Fleisher AS, Frey KA, Walker Z, Hunjan A, Holmes C, Escovar YM, Vera CX, Agronin ME, Ross J, Bozoki A, Akinola M, Shi J, Vandenberghe R, Ikonovic MD, Sherwin PF, Grachev ID, Farrar G, Smith AP, Buckley CJ, McLain R, Salloway S. Phase 3 trial of flutemetamol labeled with radioactive fluorine 18 imaging and neuritic plaque density. *JAMA Neurol* 2015; **72**: 287-294 [PMID: 25622185 DOI: 10.1001/jamaneurol.2014.4144]
 - 19 **Clark CM**, Schneider JA, Bedell BJ, Beach TG, Bilker WB, Mintun MA, Pontecorvo MJ, Hefti F, Carpenter AP, Flitter ML, Krautkramer MJ, Kung HF, Coleman RE, Doraiswamy PM, Fleisher AS, Sabbagh MN, Sadowsky CH, Reiman EP, Zehntner SP, Skovronsky DM. Use of florbetapir-PET for imaging beta-amyloid pathology. *JAMA* 2011; **305**: 275-283 [PMID: 21245183 DOI: 10.1001/jama.2010.2008]
 - 20 **Sabri O**, Sabbagh MN, Seibyl J, Barthel H, Akatsu H, Ouchi Y, Senda K, Murayama S, Ishii K, Takao M, Beach TG, Rowe CC, Leverenz JB, Ghetti B, Ironside JW, Catafau AM, Stephens AW, Mueller A, Koglin N, Hoffmann A, Roth K, Reiningner C, Schulz-Schaeffer WJ. Florbetaben PET imaging to detect amyloid beta plaques in Alzheimer's disease: phase 3 study. *Alzheimers Dement* 2015; **11**: 964-974 [PMID: 25824567 DOI: 10.1016/j.jalz.2015.02.004]
 - 21 **Johnson KA**, Minoshima S, Bohnen NI, Donohoe KJ, Foster NL, Herscovitch P, Karlawish JH, Rowe CC, Hedrick S, Pappas V, Carrillo MC, Hartley DM. Update on appropriate use criteria for amyloid PET imaging: dementia experts, mild cognitive impairment, and education. Amyloid Imaging Task Force of the Alzheimer's Association and Society for Nuclear Medicine and Molecular Imaging. *Alzheimers Dement* 2013; **9**: e106-e109 [PMID: 23809369 DOI: 10.1016/j.jalz.2013.06.001]
 - 22 **Verret L**, Krezymon A, Halley H, Trouche S, Zerwas M, Lazouret M, Lassalle JM, Rampon C. Transient enriched housing before amyloidosis onset sustains cognitive improvement in Tg2576 mice. *Neurobiol Aging* 2013; **34**: 211-225 [PMID: 22727275 DOI: 10.1016/j.neurobiolaging.2012.05.013]
 - 23 **Landau SM**, Lu M, Joshi AD, Pontecorvo M, Mintun MA, Trojanowski JQ, Shaw LM, Jagust WJ. Comparing positron emission tomography imaging and cerebrospinal fluid measurements of β -amyloid. *Ann Neurol* 2013; **74**: 826-836 [PMID: 23536396 DOI: 10.1002/ana.23908]
 - 24 **Katzman R**. Education and the prevalence of dementia and Alzheimer's disease. *Neurology* 1993; **43**: 13-20 [PMID: 8423876]
 - 25 **Yodlowski EH**, Mortimer JT. The relationship between receptor occlusion and the frequency sweep electromyogram during competitive neuromuscular blockade. *Anesthesiology* 1981; **54**: 23-28 [PMID: 6257148]
 - 26 **Friedland RP**, Fritsch T, Smyth KA, Koss E, Lerner AJ, Chen CH, Petot GJ, Debanne SM. Patients with Alzheimer's disease have reduced activities in midlife compared with healthy control-group members. *Proc Natl Acad Sci USA* 2001; **98**: 3440-3445 [PMID: 11248097]
 - 27 **Stern Y**, Gurland B, Tatemichi TK, Tang MX, Wilder D, Mayeux R. Influence of education and occupation on the incidence of Alzheimer's disease. *JAMA* 1994; **271**: 1004-1010 [PMID: 8139057]
 - 28 **Reed BR**, Mungas D, Farias ST, Harvey D, Beckett L, Widaman K, Hinton L, DeCarli C. Measuring cognitive reserve based on the decomposition of episodic memory variance. *Brain* 2010; **133**: 2196-2209 [PMID: 20591858 DOI: 10.1093/brain/awq154]
 - 29 **Scarmeas N**, Zarahn E, Anderson KE, Habeck CG, Hilton J, Flynn J, Marder KS, Bell KL, Sackeim HA, Van Heertum RL, Moeller JR, Stern Y. Association of life activities with cerebral blood flow in Alzheimer disease: implications for the cognitive reserve hypothesis. *Arch Neurol* 2003; **60**: 359-365 [PMID: 12633147]
 - 30 **Liu Y**, Julkunen V, Paajanen T, Westman E, Wahlund LO, Aitken A, Sobow T, Mecocci P, Tsolaki M, Vellas B, Muehlboeck S, Spenger C, Lovestone S, Simmons A, Soininen H. Education increases reserve against Alzheimer's disease—evidence from structural MRI analysis. *Neuroradiology* 2012; **54**: 929-938 [PMID: 22246242 DOI: 10.1007/s00234-012-1005-0]
 - 31 **Garibotto V**, Borroni B, Kalbe E, Herholz K, Salmon E, Holthoff V, Sorbi S, Cappa SF, Padovani A, Fazio F, Perani D. Education and occupation as proxies for reserve in aMCI converters and AD: FDG-PET evidence. *Neurology* 2008; **71**: 1342-1349 [PMID: 18936426 DOI: 10.1212/01.wnl.0000327670.62378.c0]

- 32 **Springer MV**, McIntosh AR, Winocur G, Grady CL. The relation between brain activity during memory tasks and years of education in young and older adults. *Neuropsychology* 2005; **19**: 181-192 [PMID: 15769202]
- 33 **Stern Y**. Cognitive reserve. *Neuropsychologia* 2009; **47**: 2015-2028 [PMID: 19467352 DOI: 10.1016/j.neuropsychologia.2009.03.004]
- 34 **Morbelli S**, Nobili F. Cognitive reserve and clinical expression of Alzheimer's disease: evidence and implications for brain PET imaging. *Am J Nucl Med Mol Imaging* 2014; **4**: 239-247 [PMID: 24795838]
- 35 **Stern Y**, Zarahn E, Habeck C, Holtzer R, Rakitin BC, Kumar A, Flynn J, Steffener J, Brown T. A common neural network for cognitive reserve in verbal and object working memory in young but not old. *Cereb Cortex* 2008; **18**: 959-967 [PMID: 17675368]
- 36 **Morbelli S**, Arnaldi D, Capitanio S, Picco A, Buschiazzo A, Nobili F. Resting metabolic connectivity in Alzheimer's disease. *Clin Transl Imaging* 2013; **1**: 271-278 [DOI: 10.1007/s40336-013-0027-x]
- 37 **Lee DS**, Kang H, Kim H, Park H, Oh JS, Lee JS, Lee MC. Metabolic connectivity by interregional correlation analysis using statistical parametric mapping (SPM) and FDG brain PET; methodological development and patterns of metabolic connectivity in adults. *Eur J Nucl Med Mol Imaging* 2008; **35**: 1681-1691 [PMID: 18491089 DOI: 10.1007/s00259-008-0808-z]
- 38 **Morbelli S**, Drzezga A, Pernecky R, Frisoni GB, Caroli A, van Berckel BN, Ossenkoppele R, Guedj E, Didic M, Brugnolo A, Sambucetti G, Pagani M, Salmon E, Nobili F. Resting metabolic connectivity in prodromal Alzheimer's disease. A European Alzheimer Disease Consortium (EADC) project. *Neurobiol Aging* 2012; **33**: 2533-2550 [PMID: 22365486 DOI: 10.1016/j.neurobiologia.2012.01.005]
- 39 **Arenaza-Urquijo EM**, Landeau B, La Joie R, Mevel K, Mézenge F, Perrotin A, Desgranges B, Bartrés-Faz D, Eustache F, Chételat G. Relationships between years of education and gray matter volume, metabolism and functional connectivity in healthy elders. *Neuroimage* 2013; **83**: 450-457 [PMID: 23796547 DOI: 10.1016/j.neuroimage.2013.06.053]
- 40 **Kemppainen NM**, Aalto S, Wilson IA, Någren K, Helin S, Brück A, Oikonen V, Kailajärvi M, Scheinin M, Viitanen M, Parkkola R, Rinne JO. Voxel-based analysis of PET amyloid ligand [11C]PIB uptake in Alzheimer disease. *Neurology* 2006; **67**: 1575-1580 [PMID: 16971697]
- 41 **Kemppainen NM**, Aalto S, Wilson IA, Någren K, Helin S, Brück A, Oikonen V, Kailajärvi M, Scheinin M, Viitanen M, Parkkola R, Rinne JO. PET amyloid ligand [11C]PIB uptake is increased in mild cognitive impairment. *Neurology* 2007; **68**: 1603-1606 [PMID: 17485647 DOI: 10.1212/01.wnl.0000260969.94695.56]
- 42 **Aizenstein HJ**, Nebes RD, Saxton JA, Price JC, Mathis CA, Tsopelas ND, Ziolk SK, James JA, Snitz BE, Houck PR, Bi W, Cohen AD, Lopresti BJ, DeKosky ST, Halligan EM, Klunk WE. Frequent amyloid deposition without significant cognitive impairment among the elderly. *Arch Neurol* 2008; **65**: 1509-1517 [PMID: 19001171 DOI: 10.1001/archneur.65.11.1509]
- 43 **Lister-Jones J**, Pontecorvo MJ, Clark C, Joshi AD, Mintun MA, Zhang W, Lim N, Zhuang Z, Golding G, Choi SR, Benedum TE, Kennedy P, Hefti F, Carpenter AP, Kung HF, Skovronsky DM. Florbetapir f-18: a histopathologically validated Beta-amyloid positron emission tomography imaging agent. *Semin Nucl Med* 2011; **41**: 300-304 [PMID: 21624563 DOI: 10.1053/j.semnucmed.2011.03.001]
- 44 **Kemppainen NM**, Aalto S, Karrasch M, Någren K, Savisto N, Oikonen V, Viitanen M, Parkkola R, Rinne JO. Cognitive reserve hypothesis: Pittsburgh Compound B and fluorodeoxyglucose positron emission tomography in relation to education in mild Alzheimer's disease. *Ann Neurol* 2008; **63**: 112-118 [PMID: 18023012]
- 45 **Rowe CC**, Villemagne VL. Brain amyloid imaging. *J Nucl Med Technol* 2013; **41**: 11-18 [PMID: 23396994 DOI: 10.2967/jnumed.110.076315]
- 46 **Ossenkoppele R**, van der Flier WM, Verfaillie SC, Vrenken H, Versteeg A, van Schijndel RA, Sikkes SA, Twisk J, Adriaanse SM, Zwan MD, Boellaard R, Windhorst AD, Barkhof F, Scheltens P, Lammertsma AA, van Berckel BN. Long-term effects of amyloid, hypometabolism, and atrophy on neuropsychological functions. *Neurology* 2014; **82**: 1768-1775 [PMID: 24748672 DOI: 10.1212/WNL.0000000000000432]
- 47 **Vos SJ**, Verhey F, Frölich L, Kornhuber J, Wiltfang J, Maier W, Peters O, Rütger E, Nobili F, Morbelli S, Frisoni GB, Drzezga A, Didic M, van Berckel BN, Simmons A, Soininen H, Kłoszewska I, Mecocci P, Tsolaki M, Vellas B, Lovestone S, Muscio C, Herukka SK, Salmon E, Bastin C, Wallin A, Nordlund A, de Mendonça A, Silva D, Santana I, Lemos R, Engelborghs S, Van der Mussele S, Freund-Levi Y, Wallin ÅK, Hampel H, van der Flier W, Scheltens P, Visser PJ. Prevalence and prognosis of Alzheimer's disease at the mild cognitive impairment stage. *Brain* 2015; **138**: 1327-1338 [PMID: 25693589 DOI: 10.1093/brain/awv029]
- 48 **Klunk WE**, Koeppe RA, Price JC, Benzinger TL, Devous MD, Jagust WJ, Johnson KA, Mathis CA, Minhas D, Pontecorvo MJ, Rowe CC, Skovronsky DM, Mintun MA. The Centiloid Project: standardizing quantitative amyloid plaque estimation by PET. *Alzheimers Dement* 2015; **11**: 1-15.e1-1-15.e4 [PMID: 25443857 DOI: 10.1016/j.jalz.2014.07.003]
- 49 **Mormino EC**, Brandel MG, Madison CM, Rabinovici GD, Marks S, Baker SL, Jagust WJ. Not quite PIB-positive, not quite PIB-negative: slight PIB elevations in elderly normal control subjects are biologically relevant. *Neuroimage* 2012; **59**: 1152-1160 [PMID: 21884802 DOI: 10.1016/j.neuroimage.2011.07.098]
- 50 **Chételat G**, Villemagne VL, Pike KE, Baron JC, Bourgeat P, Jones G, Faux NG, Ellis KA, Salvado O, Szeoke C, Martins RN, Ames D, Masters CL, Rowe CC. Larger temporal volume in elderly with high versus low beta-amyloid deposition. *Brain* 2010; **133**: 3349-3358 [PMID: 20739349 DOI: 10.1093/brain/awq187]
- 51 **Braskie MN**, Thompson PM. Understanding cognitive deficits in Alzheimer's disease based on neuroimaging findings. *Trends Cogn Sci* 2013; **17**: 510-516 [PMID: 24029445 DOI: 10.1016/j.tics.2013.08.007]
- 52 **Nithianantharajah J**, Hannan AJ. Enriched environments, experience-dependent plasticity and disorders of the nervous system. *Nat Rev Neurosci* 2006; **7**: 697-709 [PMID: 16924259]
- 53 **Escorihuela RM**, Fernández-Teruel A, Tobeña A, Vivas NM, Marmol F, Badia A, Dierssen M. Early environmental stimulation produces long-lasting changes on beta-adrenoceptor transduction system. *Neurobiol Learn Mem* 1995; **64**: 49-57 [PMID: 7582812]
- 54 **van Praag H**, Kempermann G, Gage FH. Running increases cell proliferation and neurogenesis in the adult mouse dentate gyrus. *Nat Neurosci* 1999; **2**: 266-270 [PMID: 10195220]
- 55 **Costa DA**, Cracchiolo JR, Bachstetter AD, Hughes TF, Bales KR, Paul SM, Mervis RF, Arendash GW, Potter H. Enrichment improves cognition in AD mice by amyloid-related and unrelated mechanisms. *Neurobiol Aging* 2007; **28**: 831-844 [PMID: 16730391]
- 56 **Head D**, Bugg JM, Goate AM, Fagan AM, Mintun MA, Benzinger T, Holtzman DM, Morris JC. Exercise Engagement as a Moderator of the Effects of APOE Genotype on Amyloid Deposition. *Arch Neurol* 2012; **69**: 636-643 [PMID: 22232206]
- 57 **Vemuri P**, Lesnick TG, Przybelski SA, Machulda M, Knopman DS, Mielke MM, Roberts RO, Geda YE, Rocca WA, Petersen RC, Jack CR. Association of lifetime intellectual enrichment with cognitive decline in the older population. *JAMA Neurol* 2014; **71**: 1017-1024 [PMID: 25054282 DOI: 10.1001/jamaneurol.2014.963]
- 58 **Almeida RP**, Schultz SA, Austin BP, Boots EA, Dowling NM, Gleason CE, Bendlin BB, Sager MA, Hermann BP, Zetterberg H, Carlsson CM, Johnson SC, Asthana S, Okonkwo OC. Effect of Cognitive Reserve on Age-Related Changes in Cerebrospinal Fluid Biomarkers of Alzheimer Disease. *JAMA Neurol* 2015; **72**: 699-706 [PMID: 25893879 DOI: 10.1001/jamaneurol.2015.0098]
- 59 **Cook CN**, Murray ME, Petrucelli L. Understanding biomarkers of neurodegeneration: Novel approaches to detecting tau pathology. *Nat Med* 2015; **21**: 219-220 [PMID: 25742457 DOI: 10.1038/

nm.3809]
60 **Jack CR**, Knopman DS, Jagust WJ, Shaw LM, Aisen PS, Weiner
MW, Petersen RC, Trojanowski JQ. Hypothetical model of

dynamic biomarkers of the Alzheimer's pathological cascade.
Lancet Neurol 2010; **9**: 119-128 [PMID: 20083042 DOI: 10.1016/
S1474-4422(09)70299-6]

P- Reviewer: Gupta SK, Vinh-Hung V **S- Editor:** Tian YL
L- Editor: A **E- Editor:** Wu HL



Three-dimensional imaging of the uterus: The value of the coronal plane

Lufee Wong, Nikki White, Jayshree Ramkrishna, Edward Araujo Júnior, Simon Meagher, Fabricio Da Silva Costa

Lufee Wong, Nikki White, Jayshree Ramkrishna, Simon Meagher, Fabricio Da Silva Costa, Monash Ultrasound for Women, Clayton, Victoria 3168, Australia

Lufee Wong, Department of Obstetrics and Gynaecology, Monash Medical Centre, Southern Health, Clayton, Victoria 3168, Australia

Edward Araujo Júnior, Department of Obstetrics, Paulista School of Medicine - Federal University of São Paulo (EPM-UNIFESP), São Paulo, CEP 05303-000, Brazil

Author contributions: Wong L performed the research; White N, Ramkrishna J, Meagher S and Da Silva Costa F contributed to the images; Wong L and Da Silva Costa F wrote the manuscript; Araujo Júnior E reviewed the manuscript.

Conflict-of-interest statement: The authors declare no conflict of interest.

Open-Access: This article is an open-access article which was selected by an in-house editor and fully peer-reviewed by external reviewers. It is distributed in accordance with the Creative Commons Attribution Non Commercial (CC BY-NC 4.0) license, which permits others to distribute, remix, adapt, build upon this work non-commercially, and license their derivative works on different terms, provided the original work is properly cited and the use is non-commercial. See: <http://creativecommons.org/licenses/by-nc/4.0/>

Correspondence to: Edward Araujo Júnior, PhD, Professor, Department of Obstetrics, Paulista School of Medicine - Federal University of São Paulo (EPM-UNIFESP), Rua Belchior de Azevedo, 156, apto. 111 Torre Vitoria, São Paulo, CEP 05303-000, Brazil. araujojred@terra.com.br
Telephone: +55-11-37965944
Fax: +55-11-37965944

Received: July 9, 2015
Peer-review started: July 14, 2015
First decision: August 25, 2015
Revised: October 10, 2015
Accepted: November 3, 2015
Article in press: November 4, 2015
Published online: December 28, 2015

Abstract

Advent in three-dimensional (3D) imaging technology has seen 3D ultrasound establish itself as a useful adjunct complementary to traditional two-dimensional imaging of the female pelvis. This advantage largely arises from its ability to reconstruct the coronal plane of the uterus, which allows further delineation of many gynecological disorders. 3D imaging of the uterus is now the preferred imaging modality for assessing congenital uterine anomalies and intrauterine device localization. Newer indications include the diagnosis of adenomyosis. It can also add invaluable information to delineate other endometrial and myometrial pathology such as fibroids and endometrial polyps.

Key words: Three-dimensional ultrasound; Coronal view; Pelvis; Uterus; Uterine anomalies

© **The Author(s) 2015.** Published by Baishideng Publishing Group Inc. All rights reserved.

Core tip: Three-dimensional ultrasound imaging of the female pelvis is a useful adjunct to conventional two-dimensional imaging. By acquiring a set volume which is stored, volumetric acquisitions allow the offline review, manipulation and analysis of saved images to obtain the maximum information from a study. Recent literature has suggested this imaging approach is rapidly realizing widespread use in the assessment of a variety of gynecological disorders including uterine anomalies, intrauterine device localization, endometrial disorders and fibroids. Recent advances have also suggested it may be useful in diagnosing disorders of the endometrial-myometrial interface, such as adenomyosis.

Wong L, White N, Ramkrishna J, Araujo Júnior E, Meagher S, Da Silva Costa F. Three-dimensional imaging of the uterus: The value of the coronal plane. *World J Radiol* 2015; 7(12): 484-493 Available from: URL: <http://www.wjgnet.com/1949-8470/full/v7/i12/484.htm> DOI: <http://dx.doi.org/10.4329/wjr.v7.i12.484>

INTRODUCTION

Three-dimensional (3D) ultrasound imaging of the female pelvis is a useful adjunct to conventional two-dimensional (2D) imaging. By acquiring a set volume which is stored, volumetric acquisitions allow the offline review, manipulation and analysis of saved images to obtain the maximum information from a study. Recent literature has suggested this imaging approach is rapidly realizing widespread use in the assessment of a variety of gynecological disorders including uterine anomalies, intrauterine device (IUD) localization, endometrial disorders and fibroids^[1]. Recent advances have also suggested it may be useful in diagnosing disorders of the endometrial-myometrial interface, such as adenomyosis^[2].

While 2D imaging provides information through axial and sagittal planes, it is limited by accessibility to assess pathology in the coronal plane. One of the main advantages of 3D imaging of the uterus, on the other hand, is the capacity to reconstruct the coronal plane. Particularly when the 2D imaging is abnormal, it offers the ability to better define some uterine anomalies. Andreotti *et al*^[3] reported that out of 49 patients with abnormal findings on 2D ultrasound, 3D ultrasound provided additional information in 26 (53%) of these patients. These included uterine anomalies, improved endometrium delineation, more accurate visualization of endometrial polyps, fibroids and location of IUD. In another study, Benacerraf *et al*^[4] showed 3D ultrasound provided additional information in 16 out of 66 patients. When 2D imaging is normal, it is a less useful adjunct but still offers the ability to occasionally detect unsuspected anomalies in some circumstances, such as arcuate uteri. The improved visualization with 3D ultrasound is particularly evident when the endometrium thickness is greater than 5 mm, since there is greater contrast with the more hypoechoic myometrium^[4].

This article aims to illustrate the applicability of 3D imaging of the uterus, particularly some of the newer advances of 3D imaging in the assessment of myometrial disorders.

OBTAINING A 3D CORONAL IMAGE OF THE UTERUS

Volume acquisition for 3D ultrasound requires specialized ultrasound systems and transducers. A transvaginal, compared to the transabdominal, approach is generally preferred, due to the higher frequency of the probe and the proximity to the pelvic organs, which improve image resolution^[1]. An adequately enlarged mid-sagittal or transverse section of the uterine body is obtained, although a mid-sagittal plane is preferred since under optimal circumstances, this allows the visualization of the entire length of the endometrial cavity as well as the endocervical canal. Depending on the machine, an automatic or manual sweep is performed to obtain a

Table 1 Steps for the application of the “Z-rotation” technique

Step 1: Position the reference marker/dot at the level of the mid-cavity over the endometrial stripe in the sagittal plane (Figure 1A)
Step 2: Use the Z rotation to align the long axis of the endometrial stripe along the horizontal axis in the sagittal plane of the uterus
Step 3: Position the reference marker/dot at the level of the of the midcavity over the endometrial stripe in the transverse plane (Figure 1B)
Step 4: Use the Z rotation to align the endometrial stripe with the horizontal axis in the transverse plane of the uterus
Step 5: Following step 4, the coronal plane of the uterus will be displayed in plane C (Figure 1C); use the Z rotation on plane C to display the midcoronal plane in the conventional orientation (Figure 1D)

Data from “The Z Technique: an easy approach to the display of the midcoronal plane of the uterus in volume sonography”. *J Ultrasound Med* 2006; 25: 607-612.

volume of the region of interest. Upon acquisition of the 3D volume, examination of the volume is performed in the standardized multi-planar view by adjusting the slice through the three orthogonal planes separately (Figure 1). This standardized multi-planar view reduces inter-observer variation and may be achieved by the “Z-rotation” technique (Table 1)^[5-7]. This information could be stored, which allows the user to manipulate and analyze the images offline. This may also facilitate the retrospective analysis of these images to give a second opinion by another examiner if required^[1].

Multiple features for image optimization and post-processing functions are available, including surface rendering and volume contrast imaging (VCI) (Figure 2). VCI increases the contrast of images by refining the slices through the images. This improves depth perception and thus improves the visualization of finer detail. This is particularly useful for improving assessment of the junctional zone (JZ)^[2,8]. Rendering is a technique that mimics the concept of placing a “drape” over the organ of interest. It is particularly applicable to visualizing the surface, such as over the external serosal contour of the uterus. However, the disadvantage of this method is that while the surface display is optimized, the sonographic information within the object is not displayed^[9].

LIMITATIONS OF 3D ULTRASOUND OF THE UTERUS

Like 2D ultrasound, 3D ultrasound is subject to the same limitations of ultrasound physics. One of the main underlying prerequisites to a quality 3D image is a good 2D image. Volume acquisition in 3D imaging relies on reconstruction of a series of images processed during a sweep with a single elevation focus where the resolution of images beyond the focal zone is diminished^[1]. Hence, it is quintessential that imaging settings are optimized to enhance 3D imaging. Artifacts in 3D reconstructions can be less readily recognizable and have the potential to distort an image enough to alter the diagnosis. In

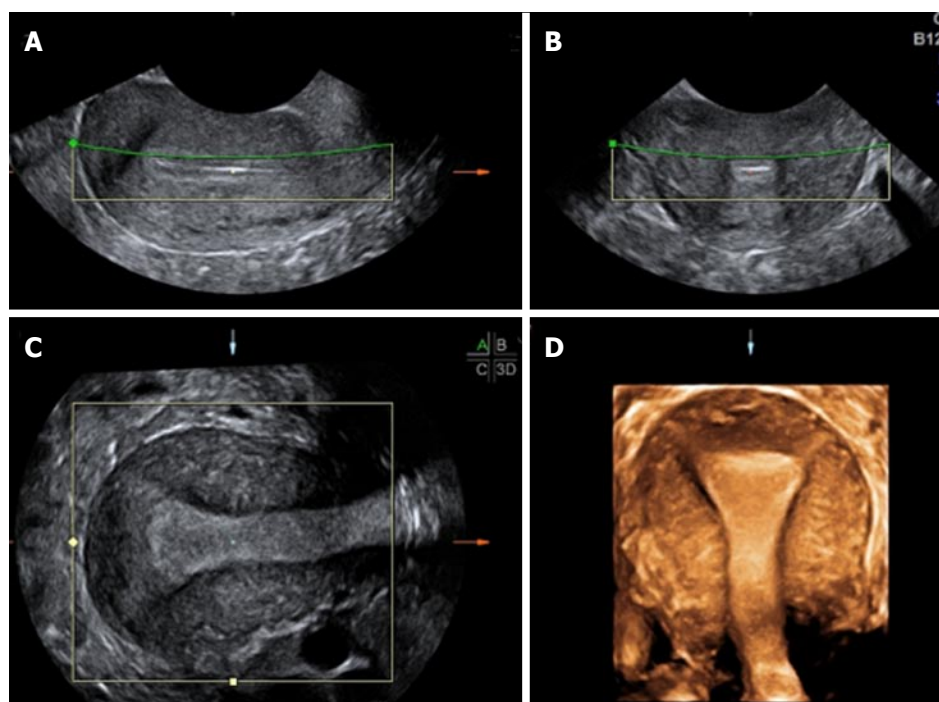


Figure 1 Multiplanar and rendering modes of the uterus. Multiplanar reconstructions from 3D ultrasound show a normal uterus in sagittal (A), transverse (B) and true coronal (C) planes. Surface rendering reconstructed image in a coronal plane of the uterus demonstrating a normal uterine fundal contour (D). 3D: Three-dimensional.

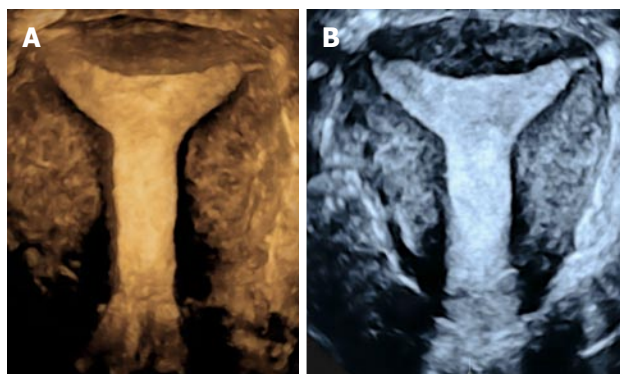


Figure 2 Examples of post-processing functions include surface render and volume contrast imaging. A: Three-dimensional (3D) ultrasound with surface rendering of a normal uterus in the coronal plane; B: 3D ultrasound with volume contrast imaging of the same uterus.

fact, artifacts can be compounded within a volume and not be immediately apparent. Thus, it is important to review the image in the acquisition plane to identify these artifacts^[6]. Another potential disadvantage is the considerable “learning curve” associated with the manipulation of 3D ultrasound by the examiner. Various settings, which are machine-dependent, are available to the operator and optimizing the image through the manipulation of settings require training and time^[1]. Machines and probes with 3D capability often come at an additional cost, which may limit its availability and accessibility although it is likely that with increasing popularity and acceptance, this will be less prohibitive since it also has proven cost effectiveness^[10].

PRACTICAL APPLICATIONS

Mullerian duct anomalies

Congenital uterine anomalies are associated with an increased risk of infertility, recurrent miscarriages and other obstetric complications. It is estimated to have a prevalence of 17% in the population with recurrent miscarriages, compared to 6% in the general population^[11]. Following a proposed classification by Buttram *et al*^[12] of Mullerian duct anomalies in 1979, the American Society for Reproductive Medicine (formerly the American Fertility Society) subsequently adapted this classification for use in 1988, and this remains the most widely accepted over the last 25 years^[12,13]. Traditionally, screening for uterine cavity anomalies has relied on hysterosalpingography, an image modality that is disadvantaged by potential contrast medium hypersensitivity and radiation exposure. If an anomaly was suspected, further investigations involving a hysteroscopy was considered the gold standard for diagnosing uterine cavity shape anomalies under direct vision, and laparoscopy could be used to assess the external fundal contour. The advances in magnetic resonance imaging (MRI), has increasingly gained popularity as an alternative modality for diagnosing congenital uterine anomalies since it has the potential to illustrate both the uterine cavity as well as external fundal contour. However, widespread uptake of MRI has been limited by its higher cost and lower patient acceptance. As 3D ultrasound gained validity, there has been shown to be a high degree of concordance between 3D ultrasound and MRI in defining uterine

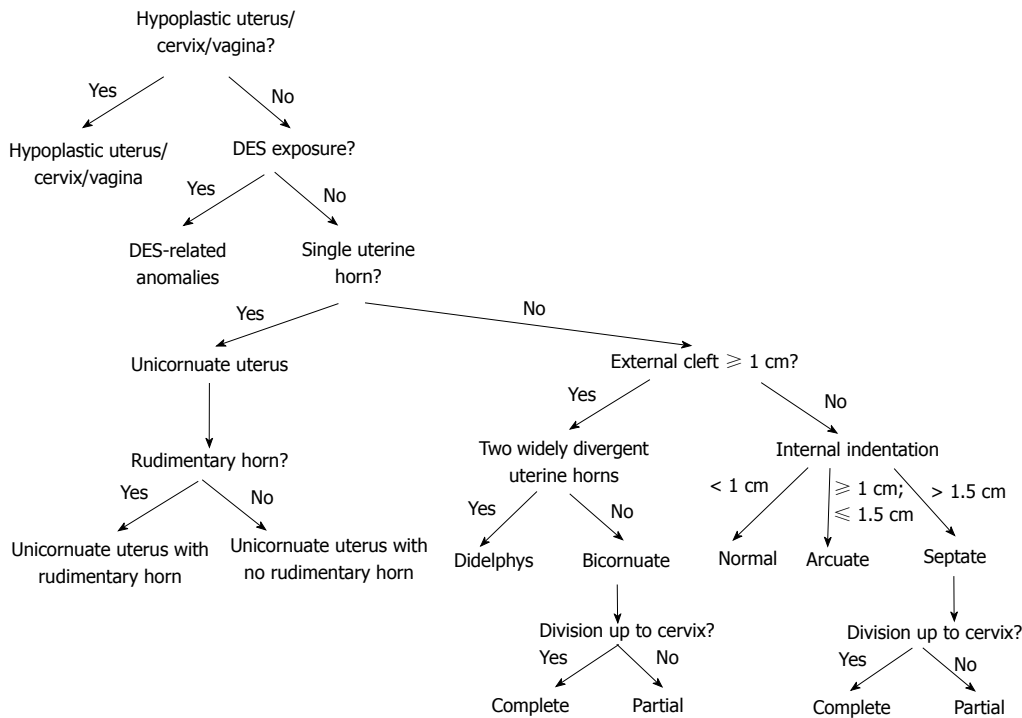


Figure 3 Algorithm for distinguishing between Mullerian duct anomalies. Modified to include morphology criteria by Ludwin *et al.*^[17], Bermejo *et al.*^[14] and Salim *et al.*^[17,18].

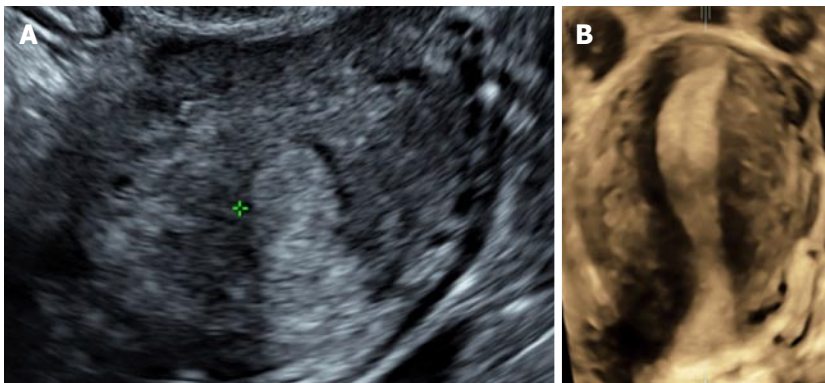


Figure 4 Unicornuate uterus with no rudimentary horn. A: Transverse 2D ultrasound image shows a single endometrial cavity; B: Coronal 3D (with VCI) ultrasound image of the unicornuate uterus showing a single uterine horn with no divergence of the endometrium towards both ostia and absence of a rudimentary horn. 3D: Three-dimensional; 2D: Two-dimensional; VCI: Volume contrast imaging.

anomalies^[14]. While 2D transvaginal ultrasonography has an accurate diagnosis rate of 60%-82% for uterine malformation depending on different studies, 3D ultrasound was superior with a diagnostic accuracy of 88%-100%^[15,16].

Uterine anomalies can be broadly classified into 3 broad categories: Fusion (didelphys and bicornuate uteri), septal resorption (arcuate and septate uteri) and hypoplasia/agenesis abnormalities. In 2D sonography, these abnormalities can present with a common feature: 2 endometrial cavities are seen. To distinguish between these various abnormalities, a coronal plane would be useful in demonstrating their distinguishing features. Although there are no universally-accepted criteria for the classification of Mullerian duct anomalies, Ludwin

et al.^[17], Bermejo *et al.*^[14] and Salim *et al.*^[18,19] described distinguishing features involving the external cleft of the fundal contour and internal cavity indentation, measured from a horizontal line drawn across the two uterine horns of the uterine cavity. Using this criterion, an algorithm for distinguishing between uterine anomalies is proposed (Figure 3). Hypoplastic uterus, cervix, vagina can be related to the Mayer-Rokitansky-Kuster-Hauser syndrome whereby the uterus, cervix and vagina are hypoplastic or absent. The classic anomaly associated with Diethylstilboestrol exposure is the T-shaped uterus which includes a widened lower uterine segment, a hypoplastic uterus, and a narrowed fundal endometrial cavity. A single uterine horn distinguishes a unicornuate uterus from the remaining ano-

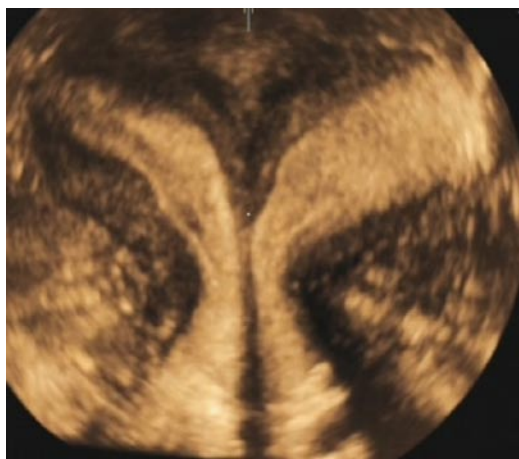


Figure 5 Uterine didelphys. Coronal 3D ultrasound image of a didelphys uterus show two widely divergent uterine horns separated by a deep external cleft ≥ 1 cm. 3D: Three-dimensional.

malies, although a rudimentary horn can sometimes be present (Figure 4). The distinguishing feature of fusion anomalies (didelphys or bicornuate uteri) from resorption anomalies is the external contour. Should the external cleft be greater than or equal to 1 cm, the degree of separation of the two horns will distinguish an uterine didelphys (Figure 5) from a bicornuate uterus (Figure 6). Uterine didelphys has 2 widely separated uterine horns, while a bicornuate uterus has a single uterine body with internal indentation greater than or equal to 1.5 cm. In the event that the external cleft is less than 1 cm, the depth of internal indentation will distinguish the septate (greater than 1.5 cm) (Figure 7) from the arcuate (between 1 and 1.5 cm) (Figure 8), and from normal uteri (less than 1 cm). Note that normal uteri can have either a straight or convex contour, or an external contour of less than 1 cm (Figure 3).

In several series, arcuate uteri was the commonest anomaly detected in 3D ultrasound when 2D ultrasound was normal^[3,4]. While arcuate uteri is generally thought to be a normal variant with no reproductive consequences, there is some limited evidence that arcuate uteri can be associated with recurrent fetal loss^[20]. It is particularly important to distinguish a septate uterus from fusion abnormalities since a septate uterus is amenable to hysteroscopic septoplasty to respect the residual septum while surgery is not an option for fusion abnormalities.

While septate and fusion anomalies are usually recognized on 2D ultrasound due to the presence of 2 uterine cavities, a unicornuate uterus (Figure 4) is more likely to be undetected given that the presence of a rudimentary horn can be very small and be masked by surrounding bowel. This anomaly has potentially severe consequences since besides the associations with miscarriage and premature delivery, the rudimentary horn can harbor a developing pregnancy and result in late uterine rupture and potentially life-threatening consequences^[21].

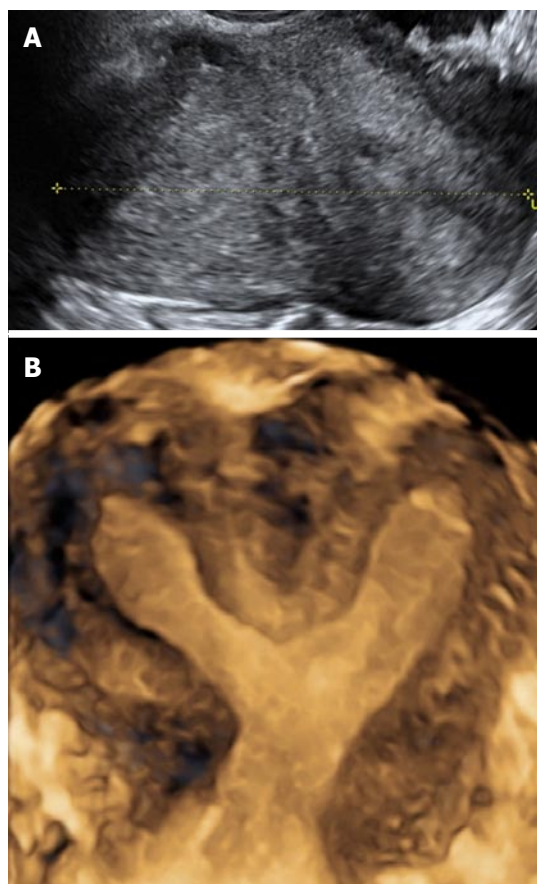


Figure 6 Bicornuate uterus. A: Transverse 2D ultrasound image of a bicornuate uterus showing the presence of 2 endometrial cavities; B: Coronal 3D ultrasound image of a bicornuate uterus showing external cleft ≥ 1 cm and internal indentation ≥ 1.5 cm. Note the presence of fundal soft tissue separating the 2 uterine cavities, which distinguishes it from uterine didelphys. 3D: Three-dimensional; 2D: Two-dimensional.

IUDs

While 2D transvaginal sonography has traditionally been used to assess the placement of IUDs, it is not able to demonstrate the entire IUD. 3D reconstructions in the coronal plane have the added advantage of demonstrating the complete IUD including shaft and arms. Lee *et al.*^[22] reported that by using the coronal plane, simultaneous visualization of the TCu380A IUD in its entirety was possible in 95% of 96 cases, while keeping examination time to a minimum. This can improve the detection rate of IUDs that have embedded in the myometrium since this can be a significant source of pelvic pain and abnormal bleeding for patients post IUD insertion (Figure 9)^[23]. When assessing for IUD location, it should not extend past the endometrial cavity into the myometrium or cervix.

Fibroids and endometrial polyps

Fibroids are benign smooth muscle tumors of the uterus. While they are commonly asymptomatic, they can result in heavy menstrual bleeding, particularly when they are submucosal and distort the endometrial cavity (Figure 10)^[24]. However, while fibroids can be

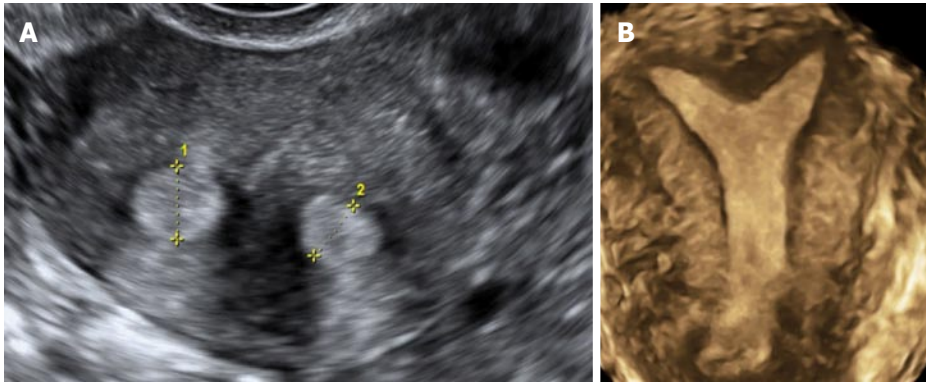


Figure 7 Septate uterus. A: Transverse 2D ultrasound image of a septate uterus showing the presence of 2 endometrial cavities; B: Coronal 3D ultrasound image of a partial septate uterus with the external cleft < 1 cm but internal indentation > 1.5 cm. 3D: Three-dimensional; 2D: Two-dimensional.

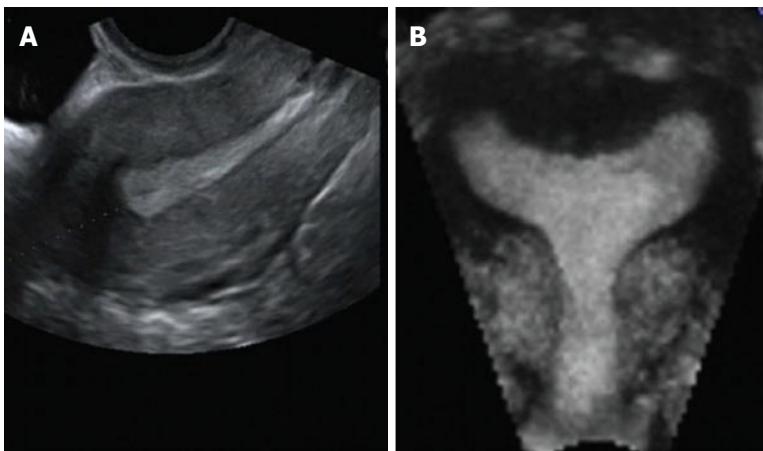


Figure 8 Arcuate uterus. A: Sagittal 2D ultrasound image of an arcuate uterus; B: Coronal 3D ultrasound image of an arcuate uterus with a smooth external contour and internal indentation ≥ 1 cm but ≤ 1.5 cm. 3D: Three-dimensional; 2D: Two-dimensional.

assessed on standard 2D imaging, their exact location in relation to the endometrial cavity and serosal contour can be difficult to determine due to shadowing artifacts. These difficulties can be overcome on a coronal plane since it allows the demonstration of the exact location of the fibroids, such as cavity distortion by submucosal fibroids and the planning of management options. Benacerraf *et al.*^[4] demonstrated that the 3D coronal view was useful in more accurately determining the specific location of fibroids (*i.e.*, submucous vs intramural) in 24% of patients using the coronal view.

Endometrial polyps are benign growths that are generally rounded, well-circumscribed echogenic masses seen within the endometrial cavity. Accurate imaging in 2D generally relies on the demonstration of a feeding vessel on color Doppler as demonstrated in Figure 11. As an adjunct, a coronal 3D imaging provides an opportunity to delineate the polyp more accurately since nearly the entire endometrial cavity can be seen in the same plane. However, the importance of the surrounding contrasting endometrium must not be overlooked. Indeed, Benacerraf *et al.*^[4] demonstrated that the width of the endometrium was an important predictor of whether the reconstructed coronal view

would be helpful. Endometrium thickness of greater than 5 mm allowed a more confident diagnosis compared to patients whose endometrium was less than 5 mm^[4].

Adenomyosis

Myometrial disorders are increasingly recognized as a cause for infertility and miscarriages, as well as subsequent obstetric complications^[25,26]. The endometrium and the myometrial JZ, which is a highly-specialized inner third of the myometrium that together with its overlying endometrium, are key areas fundamental to the process of implantation and subsequent placentation. Consequently, any endometrial or myometrial disorders in the uterus that disrupt the transformation of these layers in early pregnancy can potentially interfere with the implantation and subsequent placentation, leading to various complications, such as miscarriage, pre-eclampsia and fetal growth restriction (Figure 12)^[25]. Changes in the JZ have been thought to explain the pathogenesis behind why myometrial disorders such as adenomyosis can contribute to infertility^[26].

Adenomyosis refers to the presence of ectopic endometrial glands and stroma within the myometrium, and

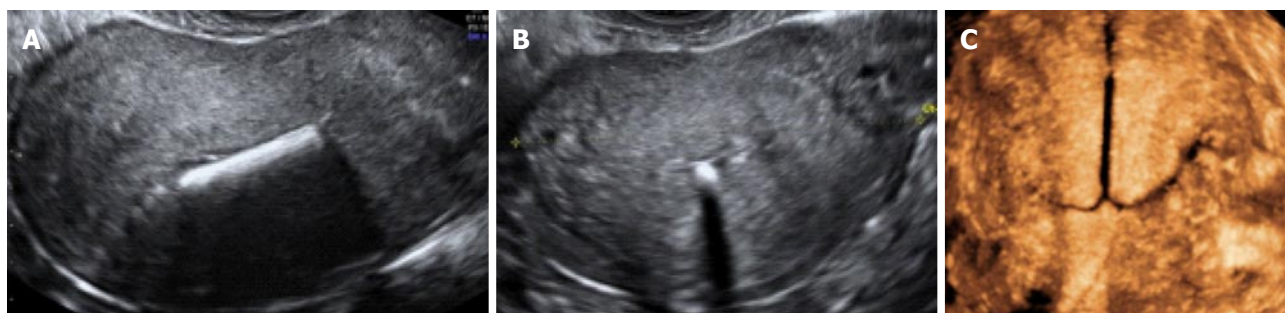


Figure 9 Malposition of an intrauterine device. Sagittal (A) and transverse (B) 2D ultrasound image showing the shaft within the endometrial cavity; C: Coronal 3D ultrasound image showing the IUD lying inverted with both arms embedded within the myometrium. 3D: Three-dimensional; 2D: Two-dimensional; IUD: Intrauterine device.

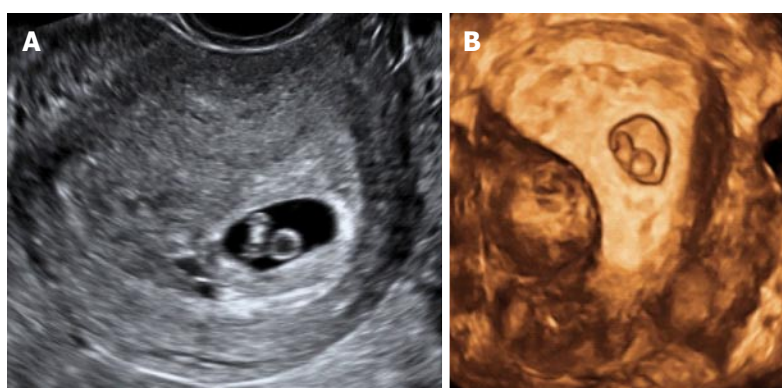


Figure 10 Intramural fibroid with an intrauterine pregnancy. A: Transverse 2D ultrasound image showing an intrauterine gestation sac positioned towards the left endometrial cavity; B: 3D coronal ultrasound image showing an intramural fibroid distorting the endometrial cavity, thus deviating the intrauterine pregnancy towards the left endometrial cavity. 3D: Three-dimensional; 2D: Two-dimensional.

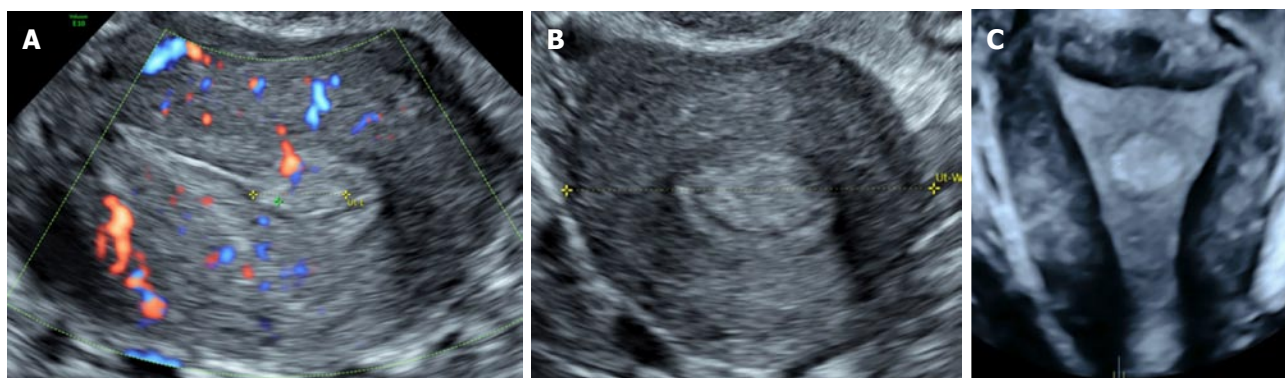


Figure 11 Endometrial polyp. A: Sagittal 2D ultrasound image of an endometrial polyp as identified by a vascular pedicle; B: Transverse 2D ultrasound image of the echogenic endometrial polyp; C: 3D coronal (VCI) ultrasound image showing the endometrial polyp better delineated as an echogenic mass. 3D: Three-dimensional; 2D: Two-dimensional; VCI: Volume contrast imaging.

is often classified as either diffuse or focal^[27]. Rarely, it can present as a large adenomyotic cyst^[28]. In assessing for changes due to adenomyosis, assessment of both the myometrium, as well as the JZ, are important features of diagnosing adenomyosis. In fact, in a recent consensus statement^[28] describing ultrasound features of myometrial pathology, ultrasound features considered to be typical of adenomyosis include asymmetrical thickening, cysts, hyperechoic islands, fan shaped shadowing, echogenic subendometrial lines and buds,

translesional vascularity, irregular JZ and interrupted JZ. While most of these features can be demonstrated on 2D ultrasound or colour Doppler, 3D ultrasound can be particularly useful for assessing the JZ in the coronal plane.

The JZ may be regular, irregular, interrupted, not visible, not assessable, or may manifest more than one feature, as classified by a recent consensus^[28]. Although detailed morphological assessment and measurement of the JZ is currently predominantly for research pur-

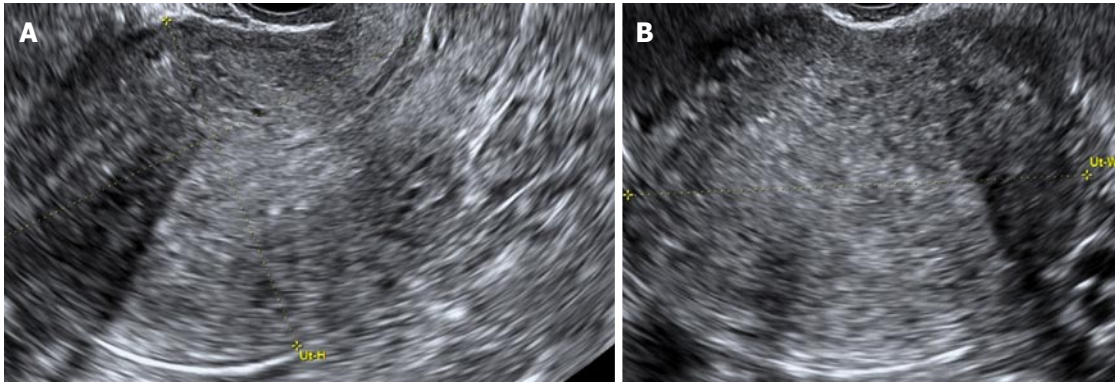


Figure 12 Adenomyosis with loss of the endometrial-myometrial junction. Sagittal (A) and transverse (B) 2D ultrasound images show the classic "venetian blind" shadowing of diffuse adenomyosis with loss of the endometrial-myometrial junction; B: 3D coronal ultrasound image (with VCI) showing the irregular endometrial-myometrial junction. Note the left lateral intramural fibroid. 3D: Three-dimensional; 2D: Two-dimensional; VCI: Volume contrast imaging.

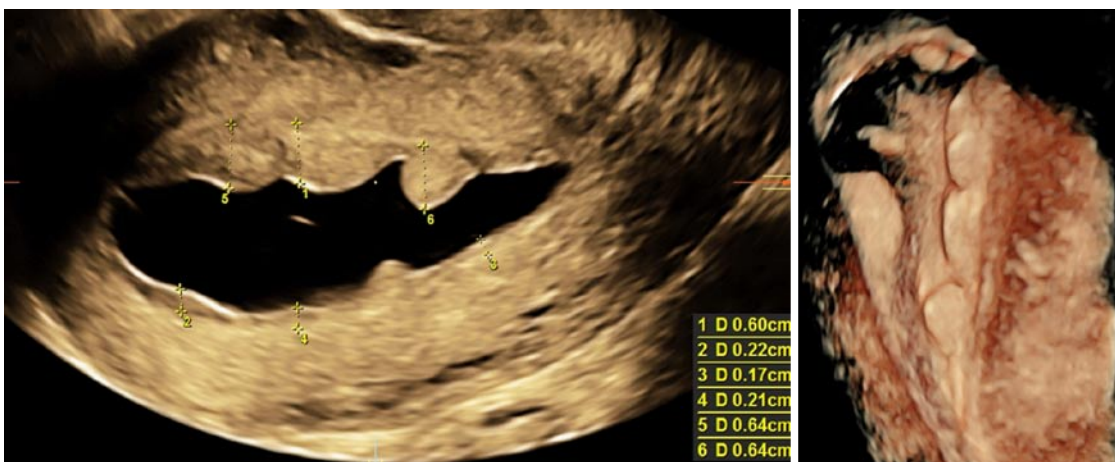


Figure 13 Saline infusion sonohysterography. A: 3D (VCI) A-plane image showing a thickened polypoid anterior endometrium upon distension with saline; B: 3D coronal image showing delineation of the polypoid endometrium on SIS. SIS: Saline infusion sonohysterography; 3D: Three-dimensional; VCI: Volume contrast imaging.

poses, broadly categorizing the JZ as either normal, or abnormal (irregular/interrupted), or not visible/not assessable will give an indication of the likelihood of JZ disorders^[28].

Both MRI and 3D ultrasonography have been used to diagnose adenomyosis. In a systematic review by Champaneria *et al.*^[29] comparing the accuracy of the two imaging modalities, both TVUS and MRI were shown to have sufficiently high diagnostic accuracy although the study did not distinguish between 2D and 3D ultrasound. As on T2-weighted MR images, the JZ on 3D ultrasound appear as hypoechoic zone underlying the endometrium. 3D reconstruction of coronal sections of the uterine cavity has made it possible to assess minor changes in the lateral and fundal aspects of the JZ, which are impossible to delineate using standard 2D ultrasound. In additional, processing modalities such as VCI further enhance visualization of the hypoechoic JZ in comparison to that using 2D imaging^[2,30,31]. Thus, 3D technology has made it possible to accurately assess and grade changes in the JZ architecture such as thickening, disruption and protrusion of the endometrium in to

the inner myometrium. Exacoustos *et al.*^[2] correlated 2D and 3D transvaginal ultrasound imaging with histopathological features of adenomyosis in a total of 72 premenopausal patients. The most specific 2D-transvaginal ultrasound feature for the diagnosis of adenomyosis was presence of myometrial cysts (98% specificity; 78% accuracy), whereas a heterogeneous myometrium was most sensitive (88% sensitivity; 75% accuracy). On 3D-transvaginal ultrasound, the best markers were JZ difference ≥ 4 mm and JZ infiltration and distortion (both 88% sensitivity; 85% and 82% accuracy, respectively)^[2].

Uterine synechiae

Uterine synechiae or adhesions have a significant adverse effect on fertility. 2D ultrasound may present a diagnostic clue to adhesions within the endometrial cavity through the presence of bands seen within the endometrial echo, particularly with the aid of sonohysterography. However, the true narrowing or "bands" adherent across the cavity is usually well delineated on the coronal plane on 3D imaging. Knopman *et al.*^[32] demonstrated that the

sensitivity of detection with 3D ultrasound was higher compared to hysterosalpingogram and that 3D ultrasound predicted adhesions and cavity damage with greater accuracy than hysterosalpingogram in patients with suspected Asherman's syndrome.

3D reconstructions with saline-instilled sonohysterography

Saline-instilled sonohysterography (SIS) involves injection of sterile saline into the endometrial cavity via a catheter (Figure 13). The main purpose is to allow for assessment of the endometrial cavity for possible distortion of the endometrial cavity due to submucosal fibroids or endometrial polyps, congenital uterine anomalies or synechiae after distension of the cavity. Besides 2D SIS, 3D SIS to assess this data in the coronal plane is also helpful. 3D SIS may have the advantages over 2D SIS because by injection of saline, it will enhance the contrast of the endometrial-myometrial junction. It will also allow the collection of volume data which can then be manipulated and analysed offline, hence potentially decreasing the time taken to perform the study^[1].

CONCLUSION

Advent in 3D imaging technology has seen 3D ultrasound establish itself as a useful adjunct complementary to traditional 2D imaging of the female pelvis. This advantage largely arises from its ability to reconstruct the coronal plane of the uterus, which allows further delineation of many gynecological disorders. 3D imaging of the uterus is now the preferred imaging modality for assessing congenital uterine anomalies and IUD localization. Newer indications include the diagnosis of adenomyosis. It can also add invaluable information to delineate other endometrial and myometrial pathology such as fibroids and endometrial polyps.

REFERENCES

- 1 Andreotti RF, Fleischer AC. Practical applications of 3D sonography in gynecologic imaging. *Radiol Clin North Am* 2014; **52**: 1201-1213 [PMID: 25444101 DOI: 10.1016/j.rcl.2014.07.001]
- 2 Exacoustos C, Brienza L, Di Giovanni A, Szabolcs B, Romanini ME, Zupi E, Arduini D. Adenomyosis: three-dimensional sonographic findings of the junctional zone and correlation with histology. *Ultrasound Obstet Gynecol* 2011; **37**: 471-479 [PMID: 21433167 DOI: 10.1002/uog.8900]
- 3 Andreotti RF, Fleischer AC, Mason LE. Three-dimensional sonography of the endometrium and adjacent myometrium: preliminary observations. *J Ultrasound Med* 2006; **25**: 1313-1319 [PMID: 16998104]
- 4 Benacerraf BR, Shipp TD, Bromley B. Which patients benefit from a 3D reconstructed coronal view of the uterus added to standard routine 2D pelvic sonography? *AJR Am J Roentgenol* 2008; **190**: 626-629 [PMID: 18287431 DOI: 10.2214/AJR.07.2632]
- 5 Martins WP, Raine-Fenning NJ, Leite SP, Ferriani RA, Natri CO. A standardized measurement technique may improve the reliability of measurements of endometrial thickness and volume. *Ultrasound Obstet Gynecol* 2011; **38**: 107-115 [PMID: 21465609 DOI: 10.1002/uog.9016]
- 6 Armstrong L, Fleischer A, Andreotti R. Three-dimensional volumetric sonography in gynecology: an overview of clinical applications. *Radiol Clin North Am* 2013; **51**: 1035-1047 [PMID: 24210443 DOI: 10.1016/j.rcl.2013.07.005]
- 7 Abuhamad AZ, Singleton S, Zhao Y, Bocca S. The Z technique: an easy approach to the display of the mid-coronal plane of the uterus in volume sonography. *J Ultrasound Med* 2006; **25**: 607-612 [PMID: 16632784]
- 8 Exacoustos C, Luciano D, Corbett B, De Felice G, Di Felicianantonio M, Luciano A, Zupi E. The uterine junctional zone: a 3-dimensional ultrasound study of patients with endometriosis. *Am J Obstet Gynecol* 2013; **209**: 248.e1-248.e7 [PMID: 23770466 DOI: 10.1016/j.ajog.2013.06.006]
- 9 Steiner H, Staudach A, Spitzer D, Schaffer H. Three-dimensional ultrasound in obstetrics and gynaecology: technique, possibilities and limitations. *Hum Reprod* 1994; **9**: 1773-1778 [PMID: 7836537]
- 10 Bocca SM, Oehninger S, Stadtmayer L, Agard J, Duran EH, Sarhan A, Horton S, Abuhamad AZ. A study of the cost, accuracy, and benefits of 3-dimensional sonography compared with hysterosalpingography in women with uterine abnormalities. *J Ultrasound Med* 2012; **31**: 81-85 [PMID: 22215773]
- 11 Saravolos SH, Cocksedge KA, Li TC. Prevalence and diagnosis of congenital uterine anomalies in women with reproductive failure: a critical appraisal. *Hum Reprod Update* 2008; **14**: 415-429 [PMID: 18539641 DOI: 10.1093/humupd/dmn018]
- 12 Buttram VC, Gibbons WE. Müllerian anomalies: a proposed classification. (An analysis of 144 cases). *Fertil Steril* 1979; **32**: 40-46 [PMID: 456629]
- 13 The American Fertility Society classifications of adnexal adhesions, distal tubal occlusion, tubal occlusion secondary to tubal ligation, tubal pregnancies, müllerian anomalies and intrauterine adhesions. *Fertil Steril* 1988; **49**: 944-955 [PMID: 3371491]
- 14 Bermejo C, Martínez Ten P, Cantarero R, Díaz D, Pérez Pedregosa J, Barrón E, Labrador E, Ruiz López L. Three-dimensional ultrasound in the diagnosis of Müllerian duct anomalies and concordance with magnetic resonance imaging. *Ultrasound Obstet Gynecol* 2010; **35**: 593-601 [PMID: 20052665 DOI: 10.1002/uog.7551]
- 15 Ghi T, Casadio P, Kuleva M, Perrone AM, Savelli L, Giunchi S, Meriggiola MC, Gubbini G, Pili G, Pelusi C, Pelusi G. Accuracy of three-dimensional ultrasound in diagnosis and classification of congenital uterine anomalies. *Fertil Steril* 2009; **92**: 808-813 [PMID: 18692833 DOI: 10.1016/j.fertnstert.2008.05.086]
- 16 Moini A, Mohammadi S, Hosseini R, Eslami B, Ahmadi F. Accuracy of 3-dimensional sonography for diagnosis and classification of congenital uterine anomalies. *J Ultrasound Med* 2013; **32**: 923-927 [PMID: 23716512 DOI: 10.7863/ultra.32.6.923]
- 17 Ludwin A, Ludwin I. Comparison of the ESHRE-ESGE and ASRM classifications of Müllerian duct anomalies in everyday practice. *Hum Reprod* 2015; **30**: 569-580 [PMID: 25534461 DOI: 10.1093/humrep/deu344]
- 18 Salim R, Regan L, Woelfer B, Backos M, Jurkovic D. A comparative study of the morphology of congenital uterine anomalies in women with and without a history of recurrent first trimester miscarriage. *Hum Reprod* 2003; **18**: 162-166 [PMID: 12525460]
- 19 Salim R, Woelfer B, Backos M, Regan L, Jurkovic D. Reproducibility of three-dimensional ultrasound diagnosis of congenital uterine anomalies. *Ultrasound Obstet Gynecol* 2003; **21**: 578-582 [PMID: 12808675 DOI: 10.1002/uog.127]
- 20 Woelfer B, Salim R, Banerjee S, Elson J, Regan L, Jurkovic D. Reproductive outcomes in women with congenital uterine anomalies detected by three-dimensional ultrasound screening. *Obstet Gynecol* 2001; **98**: 1099-1103 [PMID: 11755560]
- 21 Jurkovic D, Mavrelis D. Catch me if you scan: ultrasound diagnosis of ectopic pregnancy. *Ultrasound Obstet Gynecol* 2007; **30**: 1-7 [PMID: 17587215 DOI: 10.1002/uog.4077]
- 22 Lee A, Eppel W, Sam C, Kratochwil A, Deutinger J, Bernaschek G. Intrauterine device localization by three-dimensional transvaginal sonography. *Ultrasound Obstet Gynecol* 1997; **10**: 289-292 [PMID: 9383883 DOI: 10.1046/j.1469-0705.1997.10040289.x]
- 23 Benacerraf BR, Shipp TD, Bromley B. Three-dimensional ultrasound

- detection of abnormally located intrauterine contraceptive devices which are a source of pelvic pain and abnormal bleeding. *Ultrasound Obstet Gynecol* 2009; **34**: 110-115 [PMID: 19565532 DOI: 10.1002/uog.6421]
- 24 **Sehgal N**, Haskins AL. The mechanism of uterine bleeding in the presence of fibromyomas. *Am Surg* 1960; **26**: 21-23 [PMID: 14444585]
 - 25 **Brosens I**, Derwig I, Brosens J, Fusi L, Benagiano G, Pijnenborg R. The enigmatic uterine junctional zone: the missing link between reproductive disorders and major obstetrical disorders? *Hum Reprod* 2010; **25**: 569-574 [PMID: 20085913 DOI: 10.1093/humrep/dep474]
 - 26 **Campo S**, Campo V, Benagiano G. Adenomyosis and infertility. *Reprod Biomed Online* 2012; **24**: 35-46 [PMID: 22116070 DOI: 10.1016/j.rbmo.2011.10.003]
 - 27 **Meredith SM**, Sanchez-Ramos L, Kaunitz AM. Diagnostic accuracy of transvaginal sonography for the diagnosis of adenomyosis: systematic review and metaanalysis. *Am J Obstet Gynecol* 2009; **201**: 107.e1-107.e6 [PMID: 19398089 DOI: 10.1016/j.ajog.2009.03.021]
 - 28 **Van den Bosch T**, Dueholm M, Leone FP, Valentin L, Rasmussen CK, Votino A, Van Schoubroeck D, Landolfo C, Installé AJ, Guerriero S, Exacoustos C, Gordts S, Benacerraf B, D'Hooghe T, De Moor B, Brölmann H, Goldstein S, Epstein E, Bourne T, Timmerman D. Terms, definitions and measurements to describe sonographic features of myometrium and uterine masses: a consensus opinion from the Morphological Uterus Sonographic Assessment (MUSA) group. *Ultrasound Obstet Gynecol* 2015; **46**: 284-298 [PMID: 25652685 DOI: 10.1002/uog.14806]
 - 29 **Champaneria R**, Abedin P, Daniels J, Balogun M, Khan KS. Ultrasound scan and magnetic resonance imaging for the diagnosis of adenomyosis: systematic review comparing test accuracy. *Acta Obstet Gynecol Scand* 2010; **89**: 1374-1384 [PMID: 20932128 DOI: 10.3109/00016349.2010.512061]
 - 30 **Abdallah Y**, Naji O, Saso S, Pexsters A, Stalder C, Sur S, Raine-Fenning N, Timmerman D, Brosens JJ, Bourne T. Ultrasound assessment of the peri-implantation uterus: a review. *Ultrasound Obstet Gynecol* 2012; **39**: 612-619 [PMID: 21910147 DOI: 10.1002/uog.10098]
 - 31 **Naftalin J**, Jurkovic D. The endometrial-myometrial junction: a fresh look at a busy crossing. *Ultrasound Obstet Gynecol* 2009; **34**: 1-11 [PMID: 19565525 DOI: 10.1002/uog.6432]
 - 32 **Knopman J**, Copperman AB. Value of 3D ultrasound in the management of suspected Asherman's syndrome. *J Reprod Med* 2007; **52**: 1016-1022 [PMID: 18161399]

P- Reviewer: Peitsidis P, Tirumani SH **S- Editor:** Ji FF **L- Editor:** A
E- Editor: Wu HL



Retrospective Study

Recovery of serum testosterone following neoadjuvant and adjuvant androgen deprivation therapy in men treated with prostate brachytherapy

Hideyasu Tsumura, Takefumi Satoh, Hiromichi Ishiyama, Shuhei Hirano, Ken-ichi Tabata, Shinji Kurosaka, Kazumasa Matsumoto, Tetsuo Fujita, Masashi Kitano, Shiro Baba, Kazushige Hayakawa, Masatsugu Iwamura

Hideyasu Tsumura, Takefumi Satoh, Shuhei Hirano, Ken-ichi Tabata, Shinji Kurosaka, Kazumasa Matsumoto, Tetsuo Fujita, Shiro Baba, Masatsugu Iwamura, Department of Urology, Kitasato University School of Medicine, Sagami-hara 252-0374, Japan

Hiromichi Ishiyama, Masashi Kitano, Kazushige Hayakawa, Department of Radiation Oncology, Kitasato University School of Medicine, Sagami-hara 252-0374, Japan

Author contributions: Tsumura H performed the majority of the work including collecting, analyzing, and interpreting the data and writing the report; Ishiyama H, Hirano S, Kurosaka S and Kitano M contributed to collecting the data; Tabata K, Matsumoto K and Fujita T were participated in analyzing and interpreting the data; Satoh T, Baba S, Hayakawa K and Iwamura M designed and coordinated the study.

Institutional review board statement: The study was reviewed and approved by the Institutional Review Board of Kitasato University School of Medicine and Kitasato University Hospital (B14-21).

Informed consent statement: This retrospective study was performed under IRB approval, all data is de-identified for statistical analysis. Therefore, we think that a waiver of informed consent may be justifiable under this situation.

Conflict-of-interest statement: Dr. Tsumura received honoraria for lecture fees from Nihon Medi-Physics Co, Ltd. Astellas Pharma Inc, and Takeda Pharmaceutical Co, Ltd. Drs Satoh, Ishiyama and Hayakawa received honoraria for lecture fees from Medicon Co, Ltd, and Nihon Medi-Physics Co, Ltd.

Data sharing statement: No additional data are available.

Open-Access: This article is an open-access article which was selected by an in-house editor and fully peer-reviewed by external reviewers. It is distributed in accordance with the Creative Commons Attribution Non Commercial (CC BY-NC 4.0) license, which permits others to distribute, remix, adapt, build upon this

work non-commercially, and license their derivative works on different terms, provided the original work is properly cited and the use is non-commercial. See: <http://creativecommons.org/licenses/by-nc/4.0/>

Correspondence to: Hideyasu Tsumura, MD, Department of Urology, Kitasato University School of Medicine, 1-15-1 Kitasato Minami-ku, Sagami-hara 252-0374, Japan. tsumura@med.kitasato-u.ac.jp
Telephone: +81-42-7789091
Fax: +81-42-7789374

Received: May 8, 2015
Peer-review started: May 9, 2015
First decision: July 27, 2015
Revised: August 13, 2015
Accepted: October 12, 2015
Article in press: October 12, 2015
Published online: December 28, 2015

Abstract

AIM: To investigate the time course of testosterone (T) recovery after cessation of androgen deprivation therapy (ADT) in patients treated with brachytherapy.

METHODS: One-hundred and seventy-four patients treated between June 1999 and February 2009 were studied. Patients were divided into a short-term usage group (≤ 12 mo, $n = 91$) and a long-term usage group (≥ 36 mo, $n = 83$) according to the duration of gonadotropin-releasing hormone agonist therapy. Median follow-up was 29 mo in the short-term group and was 60 mo in the long-term group.

RESULTS: Cumulative incidence rates of T recovery to normal and supracastrate levels at 24 mo after cessation

were 28.8% and 74.6%, respectively, in the long-term usage group, whereas these values were 96.4% and 98.8% in the short-term usage group. T recovery to normal and supracastrate levels occurred significantly more rapidly in the short-term than in the long-term usage group ($P < 0.001$ and $P < 0.001$, respectively). Five years after cessation, 22.6% of patients maintained a castrate T level in the long-term usage group. On multivariate analysis, lower T levels (< 10 ng/dL) at cessation of ADT was significantly associated with prolonged T recovery to supracastrate levels in the long-term usage group ($P = 0.002$).

CONCLUSION: Lower T levels at cessation of ADT were associated with prolonged T recovery in the long-term usage group. Five years after cessation of long-term ADT, approximately one-fifth of patients still had castrate T levels. When determining the therapeutic effect, especially biochemical control, we should consider this delay in T recovery.

Key words: Androgen deprivation; Gonadotropin-releasing hormone agonist; Prostate brachytherapy; Prostate cancer; Testosterone

© The Author(s) 2015. Published by Baishideng Publishing Group Inc. All rights reserved.

Core tip: We evaluated the time course of testosterone recovery and the prognostic factors associated with prolonged testosterone recovery after the cessation of long-term (≥ 36 mo) androgen deprivation therapy in patients treated with brachytherapy. Five years after cessation, 22.6% of patients maintained a castrate testosterone level. We should consider this delay when determining therapeutic effects. Lower testosterone levels at cessation were significantly associated with prolonged testosterone recovery.

Tsumura H, Satoh T, Ishiyama H, Hirano S, Tabata K, Kurosaka S, Matsumoto K, Fujita T, Kitano M, Baba S, Hayakawa K, Iwamura M. Recovery of serum testosterone following neoadjuvant and adjuvant androgen deprivation therapy in men treated with prostate brachytherapy. *World J Radiol* 2015; 7(12): 494-500 Available from: URL: <http://www.wjgnet.com/1949-8470/full/v7/i12/494.htm> DOI: <http://dx.doi.org/10.4329/wjrr.v7.i12.494>

INTRODUCTION

Gonadotropin-releasing hormone (GnRH) agonists are widely used in various radiotherapies for the management of prostate cancer. The intended purpose and duration of hormonal therapy vary depending on the local extent of the cancer and the type of radiotherapy^[1-3]. According to several randomized controlled studies, the use of 6 to 36 mo of hormonal therapy with external beam radiotherapy (EBRT)

contributed to overall survival or cancer-specific survival in men with locally advanced or localized unfavorable-risk prostate cancer compared with radiotherapy alone^[4-7]. After the cessation of androgen deprivation therapy (ADT), serum testosterone (T) levels usually recover from castrate levels to normal levels. However, some patients maintain the castrate T levels for several years after cessation, especially if hormonal manipulation is used for prolonged periods. In these cases, clinicians cannot assess whether radiotherapy controls prostate-specific antigen (PSA) levels because there is a possibility that prolonged effects of ADT simply control the disease. Thus, clinicians should assess the recovery of T levels after cessation of ADT when they interpret PSA relapse-free survival rates. Although some studies have documented the time course of recovery of T levels after cessation of long-term ADT, these studies were intended for patients who had received less than 36 mo of continuous GnRH agonist therapy or who were observed for shorter follow-up periods^[8,9].

In this retrospective study, we estimated the time course of recovery of T levels after cessation of long-term use (≥ 36 mo) of ADT and short-term use (≤ 12 mo) of ADT in patients treated with prostate brachytherapy. In addition, the factors associated with T recovery were analyzed to determine which patients have the potential for prolonged time until recovery to supracastrate and/or normal T levels after cessation of ADT.

MATERIALS AND METHODS

Patients

There were 216 candidates for this study who received either ¹⁹²Ir high-dose rate (HDR) brachytherapy or ¹²⁵I permanent low-dose rate (LDR) brachytherapy for prostate cancer with neoadjuvant hormonal therapy (NHT) or adjuvant hormonal therapy (AHT) using GnRH agonists between June 1999 and February 2009 at our institution. Patients were divided into two groups according to the duration of GnRH agonist therapy: short-term (neoadjuvant) usage group (duration 3 to 12 mo) and long-term (neoadjuvant and adjuvant) usage group (≥ 36 mo). A normal level of T and a castrate T level were defined as ≥ 207 ng/dL and ≤ 50 ng/dL, respectively. A T level of > 50 ng/dL was defined as a supracastrate level. Both supracastrate and normal levels were used for the definition of T recovery.

The T level of each patient was measured 1 mo before the cessation of GnRH agonist therapy (baseline levels) and until it recovered to a normal level. A follow-up examination after the cessation of ADT was scheduled every 3 mo for the first year, and then every 6 mo thereafter. Patients were removed from the study if PSA failure was observed during AHT because they needed to continue the administration of GnRH agonist therapy to maintain the castrate T level. All patients underwent a complete history and physical examination at the time of brachytherapy, including

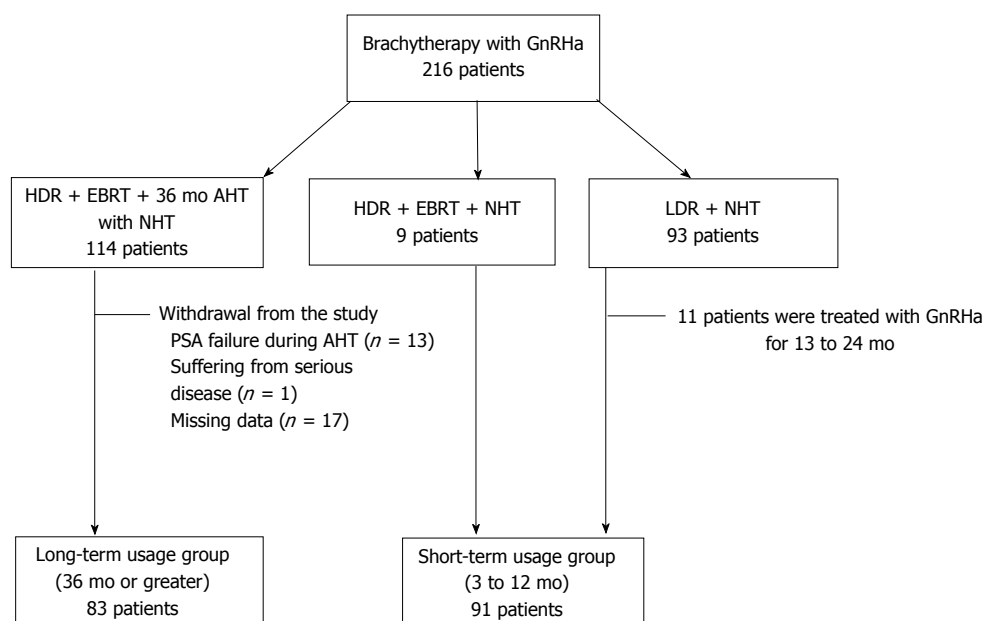


Figure 1 Characteristics of the 216 candidates considered for the study. GnRHa: Gonadotropin-releasing hormone agonist therapy; HDR: High-dose rate brachytherapy; EBRT: External beam radiotherapy; AHT: Adjuvant hormonal therapy; NHT: Neoadjuvant hormonal therapy; LDR: Low-dose rate brachytherapy; PSA: Prostate-specific antigen.

body mass index and the presence or absence of diabetes and hypertension. ADT consisted of GnRH agonist as a 1-mo or 3-mo formulation with or without an oral anti-androgen. Either flutamide (375 mg/d) or bicalutamide (80 mg) was used as the nonsteroidal anti-androgen agent. Either goserelin (3.6 or 10.8 mg) or leuporelin (3.75 or 11.25 mg) was administered as the GnRH agonist. Serum T levels were measured by immunoradiometric assay. Approval was granted by the ethics committee of our institution. Median follow-up times from cessation were 29 and 60 mo for the short-term and long-term groups, respectively.

LDR brachytherapy and hormonal therapy

Patients with low-risk or intermediate-risk prostate cancer were candidates for LDR brachytherapy. The prescribed dose to the periphery of the prostate was 145 Gy using a prostate implant technique that was described previously^[10,11]. Patients who had large glands or who were at intermediate risk were treated with combined androgen blockade for 3 to 12 mo as NHT. Neither EBRT nor AHT was administered.

HDR brachytherapy and hormonal therapy

We previously mentioned about our protocol and procedure for HDR brachytherapy and hormonal therapy in high-risk prostate cancer^[12,13]. Briefly, the mean dose to 90% of the planning target volume was 6.3 Gy/fraction of ¹⁹²Ir HDR brachytherapy. After five fractions of HDR treatment, EBRT with 10 fractions of 3 Gy was administered. Patients received EBRT using a dynamic-arc conformal technique, administered with high-energy photons comprising 10-MV X-rays. The radiation field was limited to the prostate gland with

or without proximal seminal vesicles with a 7-mm leaf margin using multileaf collimators. Testicular dose was not computed. All patients initially underwent 6 mo or more of neoadjuvant ADT. In patients who had high-risk cancer, adjuvant ADT was continued for 36 mo after EBRT. Low-risk or intermediate-risk patients were treated without adjuvant ADT. D'Amico criteria were used for risk group stratification^[14].

Statistical analysis

The Kaplan-Meier method was used to estimate the cumulative incidence of T recovery. A Log-Rank test was performed to compare these estimates. Multivariate Cox regression models were created based on the covariates that were significant in univariate analysis. Differences were regarded as statistically significant at $P < 0.05$. Analyses were performed using SPSS version 11.0 for Windows (SPSS, Inc., Chicago, IL, United States), GraphPad Prism, version 5 (GraphPad Software, Inc., CA, United States), and Microsoft Excel (Microsoft, Redmond, WA, United States).

RESULTS

Patient characteristics

Figure 1 provides the characteristics of the 216 patients who were candidates for the present study. Data for the 174 who were eligible for inclusion in the efficacy analysis were analyzed, and 42 patients (19.4%) were removed for reasons detailed in Figure 1: PSA failure during AHT ($n = 13$), severe disease ($n = 1$), missing data ($n = 17$), and ADT duration deviation from study protocol ($n = 11$). All patients reached castrate T levels at cessation of ADT. Table 1 shows the patient

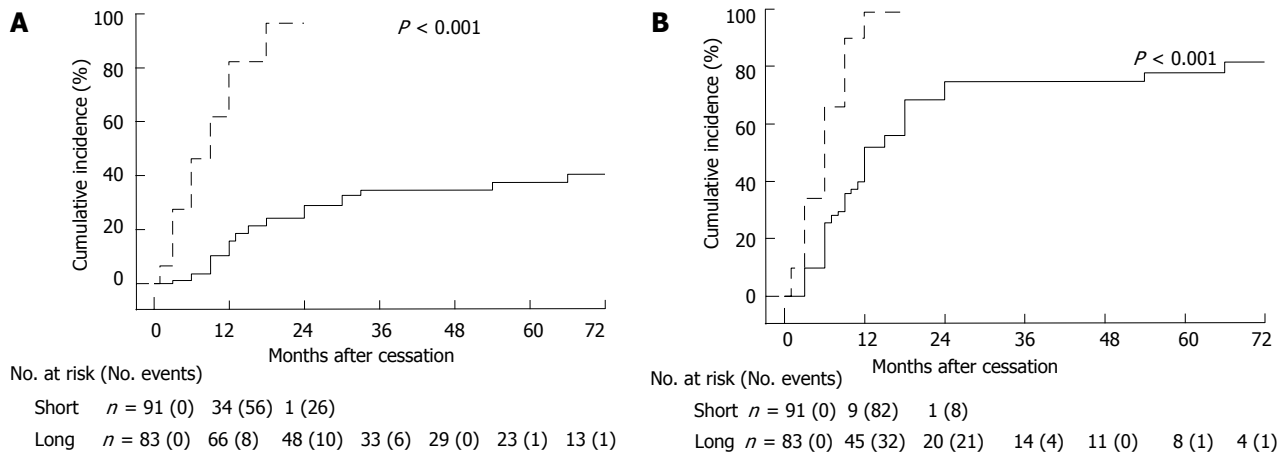


Figure 2 Cumulative incidence of testosterone recovery to normal levels (A) and supracastrate levels (B) according to duration of gonadotropin-releasing hormone agonist therapy. Significance ($P < 0.05$) was determined according to a Log-Rank test.

Table 1 Patient background data

	Short-term usage group ($n = 91$)		Long-term usage Group ($n = 83$)	
	Median	Range	Median	Range
Age at cessation (yr)	69	54-78	73	53-90
Body mass index	24.1	18.6-32.5	24.3	17.1-32.5
Duration of GnRHa (mo)	6	3-12	47	36-66
Follow-up duration from cessation of GnRHa (mo)	29	3-52	60	3-94
	<i>n</i>	%	<i>n</i>	%
Diabetes, yes	10	10.9	8	9.6
Hypertension, yes	36	39.5	33	39.7

GnRHa: Gonadotropin-releasing hormone agonist therapy.

background data for the short-term and long-term usage groups ($n = 91$ and $n = 83$, respectively).

Cumulative incidence of T recovery

We compared the cumulative incidence of T recovery to normal levels (Figure 2A) and to supracastrate levels (Figure 2B) between the short-term and long-term usage groups. A Log-Rank test showed that T recovery to normal levels occurred significantly more rapidly in the short-term than in the long-term usage group (HR = 9.180; 95%CI: 5.883-14.32; $P < 0.001$). T recovery to supracastrate levels also occurred significantly more rapidly in the short-term than in the long-term usage group (HR = 5.051; 95%CI: 3.346-7.624; $P < 0.001$). Cumulative incidences of T recovery to normal and supracastrate levels at 24 mo after cessation were 28.8% and 74.6%, respectively, in the long-term usage group, whereas these values were 96.4% and 98.8% in the short-term usage group. Five years after cessation, 22.6% of patients maintained a castrate T level in the

Table 2 Univariate and multivariate analyses of factors associated with testosterone recovery to supracastrate levels in the long-term usage group

Factor	Univariate analysis			Multivariate analysis		
	HR	95%CI	P value	HR	95%CI	P value
At brachytherapy						
Body mass index						
< 25	1.249	0.733-2.130	0.413	-	-	-
≥ 25	1.000	(reference)		-	-	-
Diabetes						
No	1.262	0.505-3.156	0.687	-	-	-
Yes	1.000	(reference)		-	-	-
Hypertension						
No	0.959	0.572-1.608	0.873	-	-	-
Yes	1.000	(reference)		-	-	-
At cessation						
Age						
< 73 yr	1.98	1.182-3.317	0.009	2.020	1.190-3.429	0.009
≥ 73 yr	1.000	(reference)		1.000	(reference)	
T level at baseline ¹						
< 10 ng/dL	1.000	(reference)		1.000	(reference)	
≥ 10 ng/dL	2.261	1.316-3.883	0.003	2.327	1.354-4.000	0.002
Drug formulation						
Duration of activity						
1 mo	1.000	(reference)		-	-	-
3 mo	1.419	0.821-2.454	0.209	-	-	-
Material						
Goserelin	0.973	0.579-1.635	0.917	-	-	-
Leuprorelin	1.000	(reference)		-	-	-

¹Testosterone level at baseline was measured 1 mo before the cessation of androgen deprivation therapy. Statistical significance was assessed at $P < 0.05$. T: Testosterone.

long-term usage group.

Factors associated with T recovery

Table 2 provides the univariate and multivariate results of factors that may influence T recovery to supracastrate levels in the long-term usage group. Age 73 years or older at cessation ($n = 47$; 57%) was significantly associated with slower recovery to supracastrate levels in the long-term usage group (multivariate analysis, $P = 0.009$). T level < 10 ng/dL at baseline ($n = 39$; 47%)

was also significantly associated with slower recovery to supracastrate levels in this group (multivariate analysis, $P = 0.002$). Both age 73 years or older at cessation and T level < 10 ng/dL at baseline were also significantly associated with slower recovery to normal levels in the long-term usage group on multivariate analysis ($P = 0.005$ and $P = 0.001$, respectively). There were no significant factors associated with slower T recovery in the short-term usage group (data not shown).

Influence of different GnRH agonist agents on T recovery

To examine the influence of different GnRH agonist agents on T recovery in the long-term usage group, patients were divided into two groups according to drug material: Goserelin ($n = 34$; 41%) and leuporelin ($n = 49$; 59%). Patients were also divided into two groups according to the duration of drug activity: 1-mo formulation ($n = 34$; 41%) and 3-mo formulation ($n = 35$; 42%). Fourteen patients (17%) were switched from the 1-mo formulation to the 3-mo formulation for various reasons and were removed from this analysis. There was no significant difference regarding the time course of T recovery to supracastrate levels between goserelin and leuporelin (univariate analysis, $P = 0.917$). The 1-mo formulation was not significantly associated with more rapid recovery to supracastrate levels, nor was the 3-mo formulation (univariate analysis, $P = 0.209$).

DISCUSSION

In the present study, we estimated the time course of recovery of T levels after cessation of long-term use (≥ 36 mo) of ADT in high-risk prostate cancer patients treated with brachytherapy. More than half the patients who received long-term ADT did not experience recovery to normal T levels at 5 years after cessation. In addition, approximately one-fifth of the patients who received long-term ADT still had castration levels at 5 years after cessation. In these cases, we have difficulty judging whether cure is attributable to radiotherapy, to sustained castration, or to both.

Several studies showed that the longer the ADT treatment, the more time that was required for T recovery^[8,15-17]; some studies reported prolonged sustainment of castrate T levels after cessation of long-term ADT. Giberti *et al.*^[18] performed testicular biopsies in seven patients who received long-term ADT. This revealed impaired Leydig cell masses with tubular derangement and fibrosis. The findings suggested that long-term ADT induces not only functional inhibition of testicular androgenesis but also anatomical testicular damage that is likely irreversible. We previously investigated the changes in serum T and luteinizing hormone (LH) levels after withdrawal of long-term ADT in patents with intermittent endocrine therapy. Patients who maintained castrate T levels after long-term follow-up had above-normal LH levels^[16]. This indicated that the feedback system of the hypothalamo-pituitary

responded normally to the low levels of T after cessation. Thus, the prolonged sustainment of castrate T levels after cessation of long-term ADT may be attributable to the testicular damage, which is likely irreversible.

Shahidi *et al.*^[19] reported serum T levels were restored to normal levels in the majority of patients (88%) after short-term (3 to 6 mo) GnRH agonist administration and radiotherapy. Murthy *et al.*^[20] found that T was maintained at normal levels 5 years after the combination of a short course of GnRH agonist therapy (median, 97 d; range, 28-167 d) and EBRT. Our findings also suggest that the suppression of T levels after short-term ADT is reversible, because the majority of men who underwent prostate brachytherapy had T that recovered to normal levels. Although prolonged sustainment of castrate T levels after cessation of ADT is of little concern for the short-term usage group (≤ 12 mo), this sustainment occurred in approximately 20% of patients in the long-term usage group (≥ 36 mo) in the present study. Yoon *et al.*^[9] reported that approximately 10% of patients maintained castrate T levels after cessation of long-term use (2 years) of ADT. The rates of prolonged sustainment have a tendency to increase with the duration of the use of ADT. The longer the ADT treatment, the more patients were unlikely to recover from castrate T levels. The use of more than 2 years of ADT is likely to increase the incidence of this prolonged sustainment of castrate T levels.

The prolonged sustainment of castrate T levels not only could affect the biochemical control rates in patients treated with prostate radiotherapy but also could maintain the adverse long-term effects in patients. This could put some men at risk for cardiovascular events, diabetes, and osteoporotic fracture^[21-23]. Fracture rates increased with increasing cumulative GnRH dose. The osteoporotic fracture caused by long-term ADT could affect the prognosis in prostate cancer patients, and the mortality rate doubled for men experiencing a fracture after their diagnosis compared with that for men who did not experience a fracture^[24]. Thus, the management of bone health and T recovery is important in those patients^[21,25].

In accordance with our findings, previous studies reported that older age was a significant factor associated with slower T recovery when GnRH agonist therapy was used for at least 24 mo^[9,17,26]. The production of T decreases with age^[27,28]. This decline might also be related to later T recovery in older men treated with long-term ADT^[9].

The present study has certain shortcomings. Previous studies suggested the impact of scatter radiation on T levels and Leydig cell function in men treated with EBRT^[29,30]. It is still unclear how HDR or LDR brachytherapy influences T levels. Thus, the cumulative incidence of T recovery might be incommensurable among men undergoing different kinds of radiotherapy. Unlike previous studies^[9,17], we could not evaluate the impact of pre-ADT T levels on T recovery because some patients had already received ADT when

they began treatment at our institution. In addition, we did not investigate how the prolonged sustainment of castrate T levels had an impact on patient quality of life. However, the present study is the first to find that a lower T level at cessation of ADT (≤ 10 ng/dL) is one significant factor that affected the slower T recovery to supracastrate levels in patients treated with long-term GnRH agonist therapy.

In men treated with long-term ADT, 22.6% of the patients maintained castrate T levels at 5 years after cessation. When determining the therapeutic effects, especially biochemical control, we should consider this delay in time to T recovery. Older age (73 years or older) and lower T levels (< 10 ng/dL) at ADT cessation were significantly associated with slower T recovery to supracastrate levels in men treated with long-term ADT.

COMMENTS

Background

Some patients maintain the castrate testosterone (T) levels for several years after cessation of androgen deprivation therapy (ADT), especially if hormonal manipulation is used for prolonged periods. In these cases, clinicians cannot assess whether radiotherapy controls prostate-specific antigen (PSA) levels because there is a possibility that prolonged effects of ADT simply control the disease. Thus, clinicians should assess the recovery of T levels after cessation of ADT when they interpret PSA relapse-free survival rates.

Research frontiers

Some studies have documented the time course of recovery of T levels after cessation of long-term ADT. These studies were intended for patients who had received less than 36 mo of continuous gonadotropin-releasing hormone (GnRH) agonist therapy. The present study is the first to evaluate the time course of recovery of T levels after cessation of ≥ 36 mo use of ADT.

Innovations and breakthroughs

Previous studies reported that older age was a significant factor associated with slower T recovery when GnRH agonist therapy was used for at least 24 mo. The present study is the first to find that a lower T level at cessation of ADT (≤ 10 ng/dL) is one significant factor that affected the slower T recovery to supracastrate levels in patients treated with long-term GnRH agonist therapy.

Applications

Five years after cessation of long-term ADT (≥ 36 mo), approximately one-fifth of patients still had castrate T levels. When determining the therapeutic effect of radiotherapy, especially biochemical control, researchers should consider this delay in T recovery.

Terminology

ADT: Prostate cancer usually requires androgen hormones such as T. GnRH agonists are widely used as ADT for the management of prostate cancer. GnRH agonists reduce the levels of serum T.

Peer-review

Very well written paper and the authors provided the important and clear message that GnRHa hormone therapy might cause long lasting androgen suppression.

REFERENCES

- 1 **Monroe AT**, Faricy PO, Jennings SB, Biggers RD, Gibbs GL, Poddada AV. High-dose-rate brachytherapy for large prostate volumes (& gt; or =50cc)-Uncompromised dosimetric coverage and

- acceptable toxicity. *Brachytherapy* 2008; **7**: 7-11 [PMID: 18299109 DOI: 10.1016/j.brachy.2007.10.005]
- 2 **Bittner N**, Merrick GS, Butler WM, Galbreath RW, Lief J, Adamovich E, Wallner KE. Long-term outcome for very high-risk prostate cancer treated primarily with a triple modality approach to include permanent interstitial brachytherapy. *Brachytherapy* 2012; **11**: 250-255 [PMID: 22436516 DOI: 10.1016/j.brachy.2012.02.002]
- 3 **Zumsteg ZS**, Spratt DE, Pei X, Yamada Y, Kalikstein A, Kuk D, Zhang Z, Zelefsky MJ. Short-term androgen-deprivation therapy improves prostate cancer-specific mortality in intermediate-risk prostate cancer patients undergoing dose-escalated external beam radiation therapy. *Int J Radiat Oncol Biol Phys* 2013; **85**: 1012-1017 [PMID: 22981709 DOI: 10.1016/j.ijrobp.2012.07.2374]
- 4 **Bolla M**, Collette L, Blank L, Warde P, Dubois JB, Mirimanoff RO, Storme G, Bernier J, Kuten A, Sternberg C, Mattelaer J, Lopez Torecilla J, Pfeffer JR, Lino Cutajar C, Zurlo A, Pierart M. Long-term results with immediate androgen suppression and external irradiation in patients with locally advanced prostate cancer (an EORTC study): a phase III randomised trial. *Lancet* 2002; **360**: 103-106 [PMID: 12126818]
- 5 **Horwitz EM**, Bae K, Hanks GE, Porter A, Grignon DJ, Brereton HD, Venkatesan V, Lawton CA, Rosenthal SA, Sandler HM, Shipley WU. Ten-year follow-up of radiation therapy oncology group protocol 92-02: a phase III trial of the duration of elective androgen deprivation in locally advanced prostate cancer. *J Clin Oncol* 2008; **26**: 2497-2504 [PMID: 18413638 DOI: 10.1200/JCO.2007.14.9021]
- 6 **Denham JW**, Steigler A, Lamb DS, Joseph D, Mameghan H, Turner S, Matthews J, Franklin I, Atkinson C, North J, Poulsen M, Christie D, Spry NA, Tai KH, Wynne C, Duchesne G, Kovacev O, D'Este C. Short-term androgen deprivation and radiotherapy for locally advanced prostate cancer: results from the Trans-Tasman Radiation Oncology Group 96.01 randomised controlled trial. *Lancet Oncol* 2005; **6**: 841-850 [PMID: 16257791 DOI: 10.1016/S1470-2045(05)70348-X]
- 7 **D'Amico AV**, Chen MH, Renshaw AA, Loffredo M, Kantoff PW. Androgen suppression and radiation vs radiation alone for prostate cancer: a randomized trial. *JAMA* 2008; **299**: 289-295 [PMID: 18212313 DOI: 10.1001/jama.299.3.289]
- 8 **Pickles T**, Agranovich A, Berthelet E, Duncan GG, Keyes M, Kwan W, McKenzie MR, Morris WJ. Testosterone recovery following prolonged adjuvant androgen ablation for prostate carcinoma. *Cancer* 2002; **94**: 362-367 [PMID: 11900222 DOI: 10.1002/cncr.10219]
- 9 **Yoon FH**, Gardner SL, Danjoux C, Morton G, Cheung P, Choo R. Testosterone recovery after prolonged androgen suppression in patients with prostate cancer. *J Urol* 2008; **180**: 1438-1443; discussion 1443-1444 [PMID: 18710743 DOI: 10.1016/j.juro.2008.06.029]
- 10 **Ishiyama H**, Kitano M, Satoh T, Niibe Y, Uemae M, Fujita T, Baba S, Hayakawa K. Difference in rectal dosimetry between pre-plan and post-implant analysis in transperineal interstitial brachytherapy for prostate cancer. *Radiother Oncol* 2006; **78**: 194-198 [PMID: 16414135 DOI: 10.1016/j.radonc.2005.12.008]
- 11 **Sekiguchi A**, Ishiyama H, Satoh T, Tabata K, Komori S, Tsumura H, Kawakami S, Soda I, Iwamura M, Hayakawa K. 125Iodine monotherapy for Japanese men with low- and intermediate-risk prostate cancer: outcomes after 5 years of follow-up. *J Radiat Res* 2014; **55**: 328-333 [PMID: 24105711 DOI: 10.1093/jrr/rrt113]
- 12 **Ishiyama H**, Kitano M, Satoh T, Kotani S, Uemae M, Matsumoto K, Okusa H, Tabata K, Baba S, Hayakawa K. Genitourinary toxicity after high-dose-rate (HDR) brachytherapy combined with Hypofractionated External beam radiotherapy for localized prostate cancer: an analysis to determine the correlation between dose-volume histogram parameters in HDR brachytherapy and severity of toxicity. *Int J Radiat Oncol Biol Phys* 2009; **75**: 23-28 [PMID: 19243900 DOI: 10.1016/j.ijrobp.2008.11.006]
- 13 **Ishiyama H**, Satoh T, Kitano M, Tabata K, Komori S, Ikeda M, Soda I, Kurosaka S, Sekiguchi A, Kimura M, Kawakami S, Iwamura M, Hayakawa K. High-dose-rate brachytherapy and hypofractionated external beam radiotherapy combined with long-

- term hormonal therapy for high-risk and very high-risk prostate cancer: outcomes after 5-year follow-up. *J Radiat Res* 2014; **55**: 509-517 [PMID: 24222312 DOI: 10.1093/jrr/rrt128]
- 14 **D'Amico AV**, Whittington R, Malkowicz SB, Schultz D, Blank K, Broderick GA, Tomaszewski JE, Renshaw AA, Kaplan I, Beard CJ, Wein A. Biochemical outcome after radical prostatectomy, external beam radiation therapy, or interstitial radiation therapy for clinically localized prostate cancer. *JAMA* 1998; **280**: 969-974 [PMID: 9749478]
- 15 **Nejat RJ**, Rashid HH, Bagiella E, Katz AE, Benson MC. A prospective analysis of time to normalization of serum testosterone after withdrawal of androgen deprivation therapy. *J Urol* 2000; **164**: 1891-1894 [PMID: 11061874]
- 16 **Egawa S**, Okusa H, Matsumoto K, Suyama K, Baba S. Changes in prostate-specific antigen and hormone levels following withdrawal of prolonged androgen ablation for prostate cancer. *Prostate Cancer Prostatic Dis* 2003; **6**: 245-249 [PMID: 12970730 DOI: 10.1038/sj.pcan.4500675]
- 17 **Kaku H**, Saika T, Tsushima T, Ebara S, Senoh T, Yamato T, Nasu Y, Kumon H. Time course of serum testosterone and luteinizing hormone levels after cessation of long-term luteinizing hormone-releasing hormone agonist treatment in patients with prostate cancer. *Prostate* 2006; **66**: 439-444 [PMID: 16329145 DOI: 10.1002/pros.20341]
- 18 **Giberti C**, Barreca T, Martorana G, Truini M, Franceschini R, Rolandi E, Giuliani L. Hormonal pattern and testicular histology in patients with prostatic cancer after long-term treatment with a gonadotropin-releasing hormone agonist analogue. *Eur Urol* 1988; **15**: 125-127 [PMID: 2975220]
- 19 **Shahidi M**, Norman AR, Gadd J, Huddart RA, Horwich A, Dearnaley DP. Recovery of serum testosterone, LH and FSH levels following neoadjuvant hormone cyoreduction and radical radiotherapy in localized prostate cancer. *Clin Oncol (R Coll Radiol)* 2001; **13**: 291-295 [PMID: 11554629 DOI: 10.1007/s001740170058]
- 20 **Murthy V**, Norman AR, Barbachano Y, Parker CC, Dearnaley DP. Long-term effects of a short course of neoadjuvant luteinizing hormone-releasing hormone analogue and radical radiotherapy on the hormonal profile in patients with localized prostate cancer. *BJU Int* 2007; **99**: 1380-1382 [PMID: 17537213 DOI: 10.1111/j.1464-410X.2007.06843.x]
- 21 **Zhumkhawala AA**, Gleason JM, Cheetham TC, Niu F, Loo RK, Dell RM, Jacobsen SJ, Chien GW. Osteoporosis management program decreases incidence of hip fracture in patients with prostate cancer receiving androgen deprivation therapy. *Urology* 2013; **81**: 1010-1015 [PMID: 23490521 DOI: 10.1016/j.urology.2012.11.066]
- 22 **Keating NL**, O'Malley AJ, Smith MR. Diabetes and cardiovascular disease during androgen deprivation therapy for prostate cancer. *J Clin Oncol* 2006; **24**: 4448-4456 [PMID: 16983113 DOI: 10.1200/JCO.2006.06.2497]
- 23 **Keating NL**, O'Malley A, Freedland SJ, Smith MR. Diabetes and cardiovascular disease during androgen deprivation therapy: observational study of veterans with prostate cancer. *J Natl Cancer Inst* 2012; **104**: 1518-1523 [PMID: 23210129]
- 24 **Beebe-Dimmer JL**, Cetin K, Shahinian V, Morgenstern H, Yee C, Schwartz KL, Acquavella J. Timing of androgen deprivation therapy use and fracture risk among elderly men with prostate cancer in the United States. *Pharmacoepidemiol Drug Saf* 2012; **21**: 70-78 [PMID: 22114014 DOI: 10.1002/pds.2258]
- 25 **Skolarus TA**, Caram MV, Shahinian VB. Androgen-deprivation-associated bone disease. *Curr Opin Urol* 2014; **24**: 601-607 [PMID: 25144145 DOI: 10.1097/MOU.0000000000000101]
- 26 **Wilke DR**, Parker C, Andonowski A, Tsuji D, Catton C, Gospodarowicz M, Warde P. Testosterone and erectile function recovery after radiotherapy and long-term androgen deprivation with luteinizing hormone-releasing hormone agonists. *BJU Int* 2006; **97**: 963-968 [PMID: 16542340 DOI: 10.1111/j.1464-410X.2006.06066.x]
- 27 **Plymate SR**, Tenover JS, Bremner WJ. Circadian variation in testosterone, sex hormone-binding globulin, and calculated non-sex hormone-binding globulin bound testosterone in healthy young and elderly men. *J Androl* 1989; **10**: 366-371 [PMID: 2592266]
- 28 **Morley JE**, Kaiser FE, Perry HM, Patrick P, Morley PM, Stauber PM, Vellas B, Baumgartner RN, Garry PJ. Longitudinal changes in testosterone, luteinizing hormone, and follicle-stimulating hormone in healthy older men. *Metabolism* 1997; **46**: 410-413 [PMID: 9109845 DOI: 10.1016/S0026-0495(97)90057-3]
- 29 **Izard MA**. Leydig cell function and radiation: a review of the literature. *Radiother Oncol* 1995; **34**: 1-8 [PMID: 7792393]
- 30 **Zagars GK**, Pollack A. Serum testosterone levels after external beam radiation for clinically localized prostate cancer. *Int J Radiat Oncol Biol Phys* 1997; **39**: 85-89 [PMID: 9300743]

P- Reviewer: Vinh-Hung V S- Editor: Tian YL L- Editor: A
E- Editor: Wu HL



Retrospective Study

Common bile duct diameter in an asymptomatic population: A magnetic resonance imaging study

Rong Peng, Ling Zhang, Xiao-Ming Zhang, Tian-Wu Chen, Lin Yang, Xiao-Hua Huang, Ze-Ming Zhang

Rong Peng, Ling Zhang, Ze-Ming Zhang, Department of Radiology, Medical Imaging Center, Panzhihua Central Hospital, Panzhihua 617000, Sichuan Province, China

Xiao-Ming Zhang, Tian-Wu Chen, Lin Yang, Xiao-Hua Huang, Sichuan Key Laboratory of Medical Imaging, Department of Radiology, Affiliated Hospital of North Sichuan Medical College, Nanchong 637000, Sichuan Province, China

Author contributions: Peng R and Zhang XM contributed equally to this work; Peng R, Zhang L, Zhang XM, Chen TW, Yang L, Huang XH and Zhang ZM designed research; Peng R, Zhang L and Zhang XM performed research; Peng R, Chen TW and Zhang ZM analyzed the data; Peng R and Zhang XM wrote the paper.

Institutional review board statement: This study was reviewed and approved by Ethics Committee of Affiliated Hospital of North Sichuan Medical College.

Informed consent statement: Through consideration by the Ethics Committee, the experimental design and the program of the study will not cause harm and risk to the subjects. Due to the retrospective nature of this study and the actual medical condition of Nanchong, it's difficult to get informed consent from all patients involved in the study. The data collected were analyzed anonymously. So Ethics Committee of our Hospital waived the need for written informed consent from the all participants.

Conflict-of-interest statement: We have no financial relationships to disclose.

Data sharing statement: No additional data are available.

Open-Access: This article is an open-access article which was selected by an in-house editor and fully peer-reviewed by external reviewers. It is distributed in accordance with the Creative Commons Attribution Non Commercial (CC BY-NC 4.0) license, which permits others to distribute, remix, adapt, build upon this work non-commercially, and license their derivative works on different terms, provided the original work is properly cited and the use is non-commercial. See: <http://creativecommons.org/licenses/by-nc/4.0/>

Correspondence to: Xiao-Ming Zhang, MD, PhD, Sichuan Key Laboratory of Medical Imaging, Department of Radiology, Affiliated Hospital of North Sichuan Medical College, Wenhua Road 63, Nanchong 637000, Sichuan Province, China. cjr.zhxm@vip.163.com
Telephone: +86-817-2262218
Fax: +86-817-2222856

Received: June 12, 2015

Peer-review started: June 15, 2015

First decision: October 21, 2015

Revised: November 11, 2015

Accepted: December 8, 2015

Article in press: December 11, 2015

Published online: December 28, 2015

Abstract

AIM: To measure the common bile duct (CBD) diameter by magnetic resonance cholangiopancreatography (MRCP) in a large asymptomatic population and analyze its some affecting factors.

METHODS: This study included 862 asymptomatic subjects who underwent MRCP. The CBD diameter was measured at its widest visible portion on regular end-expiration MRCP for all subjects. Among these 862 subjects, 221 volunteers also underwent end-inspiration MRCP to study the effect of respiration on the CBD diameter. The age, sex, respiration, body length, body weight, body mass index (BMI), portal vein diameter (PVD), length of the extrahepatic duct and CBD, cystic junction radial orientation and location were recorded. The subjects were divided into 7 groups according to age. All of the above factors were compared with the CBD diameter on end-expiration MRCP.

RESULTS: Among the 862 subjects, the CBD diameter was 4.13 ± 1.11 mm (range, 1.76-9.45 mm) and

was correlated with age ($r = 0.484$; $P < 0.05$), with a dilation of 0.033 mm per year. The upper limit of the 95% reference range was 5.95 mm, resulting in a reasonable upper limit of 6 mm for the asymptomatic population. Respiration and other factors, including sex, body length, body weight, BMI, PVD, length of the extrahepatic duct and CBD, cystic junction radial orientation and location, were not related to the CBD diameter.

CONCLUSION: We established a reference range for the CBD diameter on MRCP for an asymptomatic population. The CBD diameter is correlated with age. Respiration did not affect the non-dilated CBD diameter.

Key words: Adult; Biliary tract; Common bile duct; Magnetic resonance imaging

© The Author(s) 2015. Published by Baishideng Publishing Group Inc. All rights reserved.

Core tip: We measured the common bile duct (CBD) diameter by magnetic resonance cholangiopancreatography (MRCP) for a large asymptomatic population and suggested the normal upper limit of the duct be set at 6 mm on MRCP. The CBD diameter was correlated with age, and gradually dilates 0.033 mm per year. Respiration didn't effect on the non-dilated CBD diameter on MRCP. The significant changes of CBD diameter between inspiration and expiration may suggest a dilation of CBD.

Peng R, Zhang L, Zhang XM, Chen TW, Yang L, Huang XH, Zhang ZM. Common bile duct diameter in an asymptomatic population: A magnetic resonance imaging study. *World J Radiol* 2015; 7(12): 501-508 Available from: URL: <http://www.wjgnet.com/1949-8470/full/v7/i12/501.htm> DOI: <http://dx.doi.org/10.4329/wjcr.v7.i12.501>

INTRODUCTION

A dilated common bile duct (CBD) suggests obstructive causes, which may require invasive imaging or remedial procedures^[1]. However, an accurate reference range for CBD size remains debatable^[1-9]. Thus, to determine whether a spontaneous abnormality or atypical dilation is important, there needs to be a reference range such that CBD diameters exceeding the upper limit can be classified as abnormal.

With the widespread use of cross-sectional imaging and improvements in cross-sectional imaging technology, the diameter of the CBD is being detected incidentally with increasing frequency when using ultrasound, computed tomography (CT) and magnetic resonance cholangiopancreatography (MRCP)^[1-9]. MRCP is a technique that uses T2 sequence magnetic resonance imagery to perform a noninvasive evaluation of the anatomy and pathology of the pancreatobiliary

system^[10]. MRCP can be used to measure the diameter of the CBD^[11]. MRCP is the principal diagnostic modality that determines whether endoscopic retrograde cholangiopancreatography is needed, particularly when ultrasound findings are equivocal^[12]. Chen *et al*^[1] measured the normal CBD diameter in 187 patients by MRCP and found that the CBD diameter was significantly correlated only with age.

The diameter of the CBD changes in response to various factors, including age^[1-3], cholecystectomy^[2,3], measurement location^[4], respiration^[5], and body mass index (BMI, which was calculated as weight in kilograms divided by the square of height in meters)^[3]. For some of these factors, such as age and gender, the effect on the CBD is not clear. More than 30 years ago, Wu *et al*^[6] utilized ultrasound to determine that the CBD diameter increases by 1 mm every decade. Later, other studies supported this observation^[1-4,9]. However, Horrow *et al*^[7] obtained controversial results by ultrasound; they found that age was not associated with the size of the extrahepatic bile duct in 258 asymptomatic adults. Some studies^[1,3,8] have suggested that gender has no significant effect on CBD diameter by ultrasound and MRCP, but Matcuk *et al*^[9] reported that the extrahepatic bile duct was larger in females after performing an ultrasound on 1484 normal individuals. There has been only one study^[3] concerning the effect of BMI on the CBD diameter. The anomalous junction of the cystic duct with the common bile duct may cause stagnation of bile^[13]. Cystic duct anatomic variants (such as the cystic junction radial orientation variant) can be a source of confusion during surgery if unrecognized^[14]. Low-junction patients with a short CBD experience several complications, including congenital dilation of the cystic duct^[13]. Choledochocoele is a cystic or diverticular dilatation of the lower bile duct and is sometimes associated with cholangitis or pancreatitis^[15]. To the best of our knowledge, there is no report concerning the relationship between the diameter and length of the extrahepatic duct and the CBD, the cystic junction radial orientation or the cystic junction location.

The purpose of our study was to evaluate the CBD diameter in a large cohort of asymptomatic patients using MRCP and to determine the normal size range of the CBD in this population. In addition, this study aimed to determine the effects of age, sex, respiration, body length, body weight, BMI, portal vein diameter (PVD), extrahepatic duct and CBD length, cystic junction radial orientation and cystic junction location on the CBD diameter as measured by MRI.

MATERIALS AND METHODS

Patients

This retrospective study was approved by our institutional review board. Patient informed consent was waived. During the period of January 2010 to March 2014, we recruited all the patients who underwent an abdominal MRI in our hospital for our study. We recorded

the age, sex, medical history, list of medications, total serum cholesterol, liver function tests, and hepatitis status of each patient. In addition, body length, body weight and BMI were recorded for the volunteers.

The following search criteria were used: (1) normal abdomen; (2) hepatic cysts; (3) hepatic or splenic hemangiomas; and (4) renal cysts.

The exclusion criteria were the following: (1) pre-existing hepatobiliary and pancreatic surgery; (2) intra- or retroperitoneal tumors, inflammation or hemorrhagic diseases; (3) biliary tract stones; (4) cholecystitis; (5) cirrhosis of the liver; (6) ascites; (7) abnormal liver function tests (total bilirubin, aspartate aminotransferase, alanine aminotransferase); (8) current use of medication that causes relaxation of smooth muscle (*e.g.*, calcium blockers and papaverine hydrochloride); and (9) abnormal total serum cholesterol.

We identified 5792 patients who underwent abdominal MR imaging at our hospital. Of these patients, 167 were excluded because of artifacts. A total of 4763 patients met the exclusion criteria and were not included in the study. The final study cohort consisted of 862 consecutive patients, including 450 male and 412 female patients aged 5 to 87 years (mean age \pm SD, 46.10 ± 16.38 years). Among these 862 people, 221 were volunteers, including 108 males and 113 females aged 17 to 80 years (mean age \pm SD, 37.80 ± 17.77 years).

The patients were divided into 7 groups according to their age: Group I, ≤ 20 years; Group II, 21-30 years; Group III, 31-40 years; Group IV, 41-50 years; Group V, 51-60 years; Group VI, 61-70 years; and Group VII, > 70 years.

The patients were divided into normal weight (BMI $< 25 \text{ kg/m}^2$), overweight ($25 \text{ kg/m}^2 \leq \text{BMI} < 28 \text{ kg/m}^2$) and obesity ($\text{BMI} \geq 28 \text{ kg/m}^2$) groups according to their BMI^[16,17].

MR imaging technique

MR imaging was performed on the patients after an overnight fast of at least 8 h prior to the MR examination. All the examinations were performed with a 1.5-T MR scanner with 38 mT/M gradients and a 120 mT/M-per-second slope (Signa Excite; GE Medical Systems, Milwaukee, WI, United States) using a phased-array torso-pelvis coil. The imaging sequences, including two-dimensional coronal and axial single-shot fast spin-echo (SSFSE) T2-weighted imaging, axial respiratory gating fast-recovery fast-spin echo (FRFSE) T2-weighted imaging with fat suppression, fast-spoiled gradient-echo T1-weighted imaging with fat suppression, axial spoiled dual gradient-echo T1-weighted in- and out-of-phase MR imaging, axial slab three-dimensional (3D) spoiled gradient-echo dynamic contrast-enhanced MR imaging with fat suppression, and SSFSE radial series slab MRCP, were performed when all the patients were at the end of expiration and were holding their breath. End-expiration MRCP was considered conventional MRCP

for each patient. The volunteers also underwent MRCP at the end of inspiration.

Coronal and axial SSFSE T2-weighted images were obtained during breath-holding with the following parameters: echo time (TE) = 90-100 ms; 2 s between slice acquisitions; section thickness = 5 mm; intersection gap = 0.5 mm; matrix = 384×224 ; one-half signal acquired; and field of view (FOV) = $33 \text{ cm} \times 33 \text{ cm}$. FRFSE T2-weighted images were obtained with the following parameters: repetition time (TR) ms/TE ms = 10000-12000/90-100, with TR determined by the frequency of respiration; section thickness = 5 mm; intersection gap = 0.5 mm; matrix = 256×192 ; number of signals acquired (NSA) = 3; and FOV = $34 \text{ cm} \times 34 \text{ cm}$. The acquisitions were completed in approximately 3-4 min.

Radial oblique slab SSFSE images were obtained for end-expiration and end-inspiration MRCP with the following parameters: TE = 1300 ms; 6 s between image acquisitions; section thickness = 40 mm; matrix = 384×224 ; one-half signal acquired; and FOV = $30 \text{ cm} \times 30 \text{ cm}$.

All of the other routine sequences mentioned above were not used in the analysis presented in this article; thus, we have not listed the parameters for those sequences.

It took approximately 30 min to complete all of the non-contrast MRI sequences and 35 min to complete the contrast-enhanced MR imaging.

MR image analysis

The original MRI data were loaded onto a workstation (GE, AW 4.1, Sun Microsystems, Palo Alto, CA, United States) for review. Two observers (with 4 and 6 years of experience interpreting abdominal MR images) retrospectively and individually reviewed the coronal and transverse T2-weighted and MRCP images to evaluate the CBD.

The widest diameter of the CBD was measured by placing an electronic caliper perpendicular to the long axis at the widest visible portion of the CBD on end-expiration MRCP for all the patients (Figure 1A). To study the effect of breath on the diameter of the CBD, the volunteers also underwent end-inspiration MRCP. The measurements on end-inspiration MRCP were taken at the same location as those on end-expiration. Because the CBD frequently exhibits a tortuous or serpentine course, the length of the extrahepatic bile duct is the sum of the length from the hepatic hilum to the tortuous portion and from the tortuous portion to the ampulla (Figure 1B). Similarly, the length of the CBD is the sum of the length from the cystic duct insertion to the tortuous portion and from the tortuous portion to the ampulla (Figure 1C). The anteroposterior diameters of the portal vein were measured by placing the electronic caliper at the splenic veins into the portal vein on T2-weighted images (Figure 1D). The radial orientation of the cystic junction was defined as lateral (insertion diagonally from the right), medial (insertion into the left

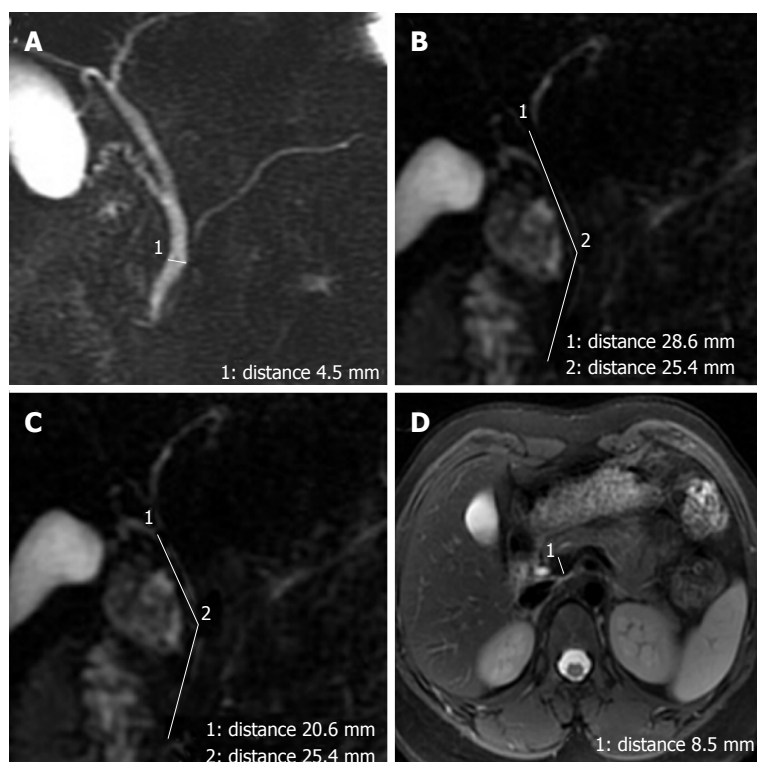


Figure 1 The measurement method. A: Measurement of the common bile duct (CBD) diameter by placing an electronic caliper at the widest visible portion of the CBD on magnetic resonance cholangiopancreatography (MRCP); B: Measurement of the length of the extrahepatic bile duct on MRCP. It is the sum of the length from the hepatic hilum to the tortuous portion and from the tortuous portion to the ampulla; C: Measurement of the length of the CBD on MRCP. It is the sum of the length from the cystic duct insertion to the tortuous portion and from the tortuous portion to the ampulla; D: Measurement of the portal vein anteroposterior diameters by placing the electronic caliper at the splenic veins into the portal vein on T2-weighted images.

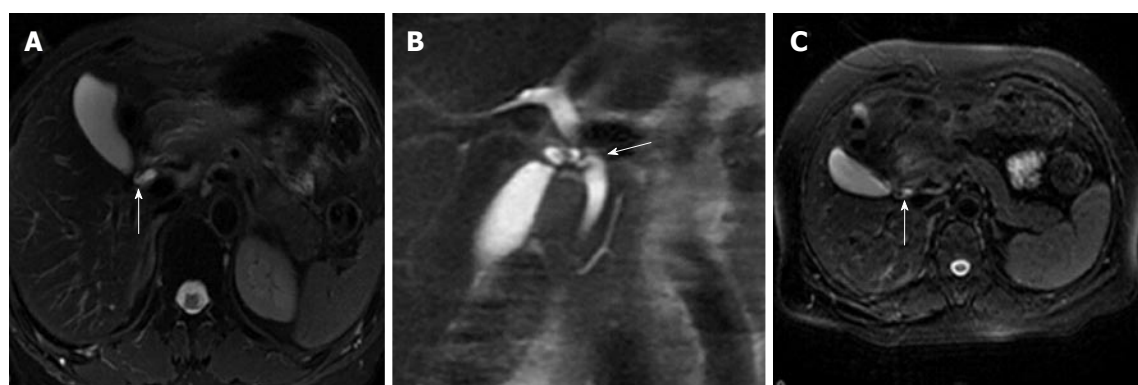


Figure 2 The cystic junction radial orientation. An FRFSE T2-weighted image (A) shows lateral insertion of the cystic duct (arrow). A coronal SSFSE T2-weighted image (B) shows medial insertion of the cystic duct (arrow). An FRFSE T2-weighted image (C) shows posteroanterior insertion of the cystic duct (arrow). SSFSE: Single-shot fast spin-echo; FRFSE: Fast-recovery fast-spin echo.

side of the common hepatic duct), or posteroanterior (overlap of the junction with the bile duct in the postero-anterior view)^[14] (Figure 2). Proximal, middle and low insertion of the cystic duct into the bile duct was defined when the cystic junction was detected in the proximal, middle or distal third, respectively, of the bile duct between the hepatic hilum and the ampulla of Vater (Figure 3).

Statistical analysis

Data derived from the MR images were expressed as the average of the two observers' findings. Any

discrepancies in the discrete data were discussed by the two observers until a consensus was reached.

The inter-rater agreement for the prevalence of the cystic junction radial orientation and cystic junction location was assessed using the kappa (κ) statistic. This statistic is generally interpreted as follows: A κ value equal to or greater than 0.81 indicates very good agreement, a κ value ranging from 0.80 to 0.61 indicates good agreement, a kappa value ranging from 0.60 to 0.41 indicates moderate agreement, and a κ value of less than 0.41 indicates poor agreement.

The results of the CBD diameter, body length, body

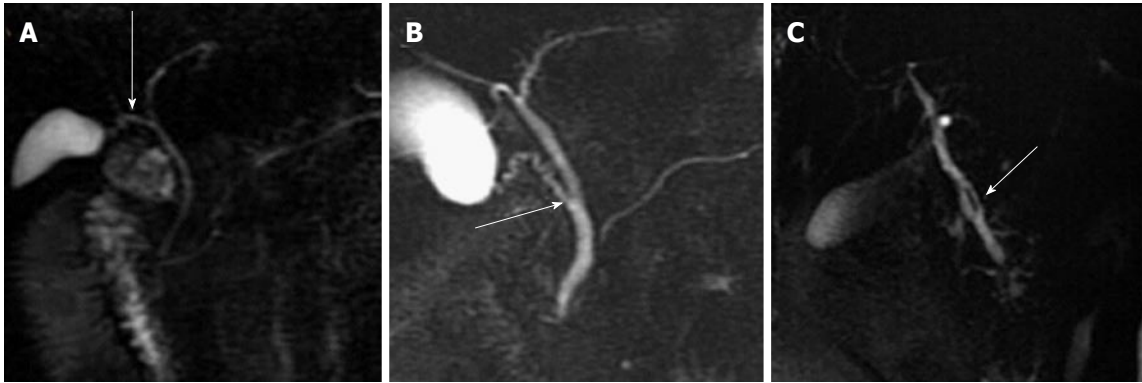


Figure 3 The cystic junction location. Magnetic resonance cholangiopancreatography shows proximal (A), middle (B) and distal (C) third conjunction of the cystic duct with the common bile duct (arrow).

Table 1 Common bile duct diameters in each age group

Group number	Age (yr)	Patient number	Common bile duct diameter Mean \pm SD (mm)
I	≤ 20	42	3.23 ± 0.77
II	21-30	123	3.45 ± 0.67
III	31-40	137	3.80 ± 0.97
IV	41-50	234	4.01 ± 0.89
V	51-60	155	4.50 ± 1.11
VI	61-70	113	4.83 ± 1.18
VII	> 70	58	5.12 ± 1.10

weight, BMI, PVD, and extrahepatic duct and CBD length were expressed as the mean \pm SD. The upper limit of the 95% reference range for the CBD diameter was defined as the mean + 1.64 SD.

The independent *t* test was used to compare the CBD diameter between patients younger and older than 60 years and between genders. CBD diameters were analyzed based on age, body length, body weight, PVD, and extrahepatic duct and CBD length using Pearson correlations. The CBD diameters in the end-inspiration and end-expiration phases were analyzed using paired *t* tests. Analysis of variance (ANOVA) was used to compare the diameter by BMI, cystic junction radial orientation and cystic junction location. Linear regressions were used to confirm the relationships between the CBD diameters and age.

The data analysis was performed using Statistical Package for Social Sciences (SPSS) for Windows (Version 13.0, Chicago, IL, United States). *P* values ≤ 0.05 were considered statistically significant.

RESULTS

Agreement between the two radiologists was good regarding the prevalence of the cystic junction location ($\kappa = 0.79$) and moderate concerning the prevalence of the cystic junction radial orientation ($\kappa = 0.53$).

Among the 862 subjects, the mean diameter of the CBD on end-expiration MRCP was 4.13 ± 1.11 mm (1.76-9.45 mm). There was a significant correlation between the CBD diameter and age ($r = 0.484$, $P <$

0.05; Figure 4). According to the linear periodic model, the regression equation for diameter was as follows: $0.033 \times \text{age} + 2.624$. Thus, the duct gradually dilated by 0.033 mm per year. Table 1 lists the mean CBD diameters of the subjects in each group. The upper limit of the 95% reference range for the CBD diameter was 5.95 mm, resulting in the reasonable upper limit of 6 mm for the asymptomatic population. The CBD diameter in people older than 61 years of age (4.93 ± 1.15 mm) was significantly different than that in subjects younger than 60 years of age (3.93 ± 0.99 mm; $t = -11.364$, $P = 0.000$).

In the cohort of 862 subjects, the mean CBD diameter in females was slightly larger than that in males (4.18 ± 1.09 mm vs 4.09 ± 1.13 mm), although this difference was not statistically significant ($t = -1.252$, $P = 0.211$).

Among the 221 volunteers, the mean CBD diameter was slightly larger on end-inspiration MRCP (3.90 ± 0.96 mm) than on end-expiration MRCP (3.88 ± 0.96 mm), but the difference was not statistically significant ($t = -0.896$, $P = 0.371$) (Figure 5).

In the cohort of 221 volunteers, the normal weight subjects (83.7%; 185/221) had a CBD diameter of 3.85 ± 0.95 mm, the overweight subjects (14.5%; 32/221) had a CBD diameter of 4.09 ± 1.00 mm, and the obese subjects (1.8%; 4/221) had a CBD diameter of 3.61 ± 1.14 mm. The CBD diameters are not significantly different among the normal weight, overweight and obese groups ($F = 1.034$, $P = 0.357$).

In the 221 volunteers, the mean CBD diameters were not significantly related to body length or body weight (Table 2). In the 862 subjects, the mean CBD diameters were not significantly related to the PVD, extrahepatic bile duct length or CBD length (Table 2).

Based on the different cystic junction radical orientations, subjects (74.8%; 645/862) with a lateral junction had a CBD diameter of 4.09 ± 1.10 mm, subjects with a medial junction (7.9%; 68/862) had a CBD diameter of 4.25 ± 1.30 mm, and subjects with a posteroanterior junction (17.3%; 149/862) had a CBD diameter of 4.24 ± 1.03 mm. The CBD diameters were not significantly different between the subjects grouped based on cystic

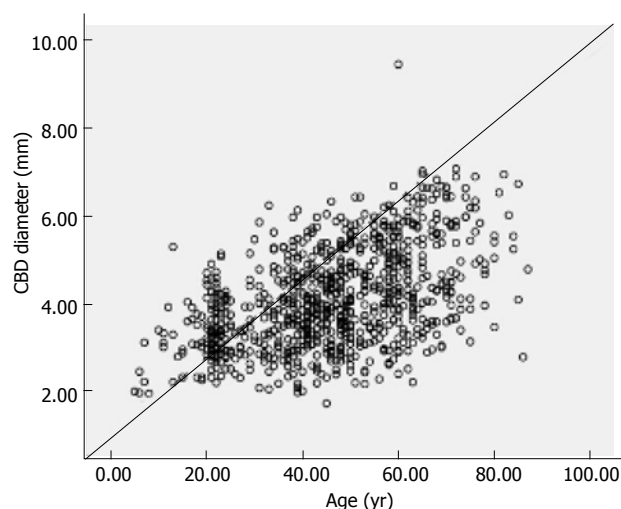


Figure 4 Pearson correlation between the diameter of the common bile duct and age ($r = 0.484$, $P = 0.000$).

junction radial orientation ($F = 1.559$, $P = 0.211$). Based on the cystic junction location, subjects with a proximal insertion (23.5%; 203/862) had a CBD diameter of 4.04 ± 1.17 mm, subjects with a middle insertion (73.8%; 636/862) had a CBD diameter of 4.30 ± 1.08 mm, and subjects with a low insertion (2.7%; 23/862) had a CBD diameter of 4.16 ± 1.08 mm. The CBD diameters were not significantly different among the groups based on cystic junction location ($F = 1.683$, $P = 0.186$).

DISCUSSION

In this study, we found that the mean diameter of the CBD on end-expiration MRCP was 4.13 ± 1.11 mm, with a range of 1.76 to 9.45 mm. The CBD diameters were significantly different between patients younger and older than 60 years of age ($P < 0.05$). The CBD diameter was correlated with age ($r = 0.484$; $P < 0.05$) and gradually dilated 0.033 mm per year. We suggest that the normal upper limit of the duct should be set at 6 mm. The CBD diameters were not significantly related to gender, body length, body weight, BMI, PVD, the length of the extrahepatic duct or the CBD, the cystic junction radial orientation or location. Respiration did not affect the non-dilated CBD diameter. Our results established a reference range for the CBD diameter on MRCP in an asymptomatic population that will be useful for evaluating suspected biliary tract disease.

Previous studies have shown that the mean diameter of the CBD is between 3.4 and 7.39 mm, with a range of 1.0 to 15.0 mm^[1,2,4-8,18,19], and our results were well within the reported range. In our study, the upper limit of the 95% reference range for the CBD diameter was 5.95 mm, and the upper limit was 6 mm; these values are comparable to those from ultrasound^[4] and CT^[2]. The upper limit in our study was lower than that reported by Chen *et al.*^[1], possibly because of the larger

Table 2 Pearson correlation coefficients between the common bile duct diameters and their relationship to different parameters

	Patient number	Mean \pm SD	R value	P value
Body length (m)	221	1.60 \pm 0.07	-0.067	0.325
Body weight (kg)	221	57.01 \pm 9.17	0.041	0.548
Portal vein diameter (mm)	862	8.79 \pm 0.91	0.034	0.318
Length of the extrahepatic bile duct (mm)	862	63.75 \pm 9.07	0.045	0.185
Length of the CBD (mm)	862	47.53 \pm 10.44	0.003	0.922

CBD: Common bile duct.

population and wider age range in our study.

A few reports have considered the important age-dependent variations in the CBD diameter^[1-4,6,8,9,18,19]. Some studies have revealed a slight increase in duct diameter with advancing age^[6,9]. It has also been shown that the CBD diameter is directly proportional to age after patients were divided into two groups with 65 years as the cut-off age^[1]. Park *et al.*^[18] reported that the CBD diameter by CT in people older than 51 years of age was significantly different than that in subjects younger than 50 years of age. Additionally, Kaim *et al.*^[19] reported that the CBD diameter in asymptomatic elderly subjects (> 75 years) was considerably higher compared with the recommended borderline values in the ultrasound literature. However, Horrow *et al.*^[7] found no increase in the size of the extrahepatic bile duct with increasing age in an adult population, and their data do not support the rule of a 1-mm-per-decade increase in the size of the bile duct by ultrasound. In this study, we found that the CBD diameter increases with age and gradually dilates 0.033 mm per year. CBD diameters are significantly different between patients who are younger or older than 60 years of age, perhaps because longitudinal smooth muscle bands and their intervening connective tissue fragments with increasing age accompanied by the loss of the reticulo-endothelial network of the ductal wall^[20], resulting in age-related biliary dilatation of the CBD.

Some previous studies have reported that gender has no significant effect on the CBD diameter^[1,3,8]. However, Matcuk *et al.*^[9] found that the extrahepatic bile duct increases with female sex by ultrasound. Our studies support the notion that gender has no significant effect on the CBD diameter.

Wachsberg^[5] demonstrated that the maximal bile duct measurement can increase during deep inspiration by ultrasonography. However, their study included thirty subjects with a maximal anteroposterior CBD diameter of 5 mm or greater, some of whom presented with biliary obstruction. An MRCP study^[21] found that the mean maximal diameter of the extrahepatic bile duct was significantly larger on end-inspiratory MRCP in the group of subjects with an extrahepatic bile duct diameter of less than 10 mm. However, their study included 102 patients

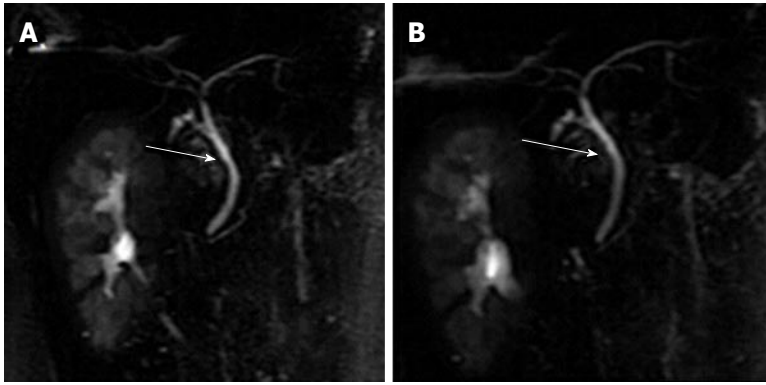


Figure 5 Deep respiratory magnetic resonance cholangiopancreatography obtained in a 32-year-old female volunteer. Breath-hold magnetic resonance cholangiopancreatography obtained during end-expiration (A) or end-inspiration (B) provides an overview of the common bile duct (arrow). There is no obvious change in the common bile duct diameter.

with suspected biliary abnormalities by ultrasonography or computed tomography. Our results showed that the mean CBD diameters between end-inspiratory MRCP and end-expiratory MRCP were not statistically different. Our study is unique in that MRCP was used to evaluate the effect of respiration on the "normal" diameter of the CBD. Our results indicate that respiration does not affect the non-dilated CBD diameter. We speculate that the significant changes in the CBD diameter between inspiration and expiration^[5,21] may suggest dilation of the CBD.

Previous studies have suggested that body length and body weight have no significant effect on the CBD diameter^[3,8]. Our studies support these observations. Daradkeh *et al*^[3] reported that the CBD diameter was correlated with BMI by ultrasound. In this study, we found that BMI had no significant effect on the CBD diameter, perhaps because ultrasound has limitations regarding overweight persons^[22]. In our study, 14% (32/221) of the patients were overweight, and 1.8% (4/221) were obese. Ultrasound may have certain limitations in measuring the CBD diameter in these 15.8% of the patients, thereby resulting in measureable differences.

In our study, we also found that the PVD was not associated with the CBD diameter on MRCP, a finding that is similar to that reported by Chen *et al*^[1].

The most common or "normal" way of entry (up to 65%) involves draining the cystic duct from the right lateral position^[23]; however, in other series, a lateral junction was observed in only 31.8% of the cases^[14]. In our study, lateral insertion of the cystic duct was detected in 74.8% of the cases, whereas medial and posteroanterior insertions accounted for the remainder. Our study of the cystic junction radial orientation supports the report by Turner *et al*^[23]. The cystic duct usually joins the common hepatic duct about halfway between the porta hepatis and the ampulla of Vater (in 75% of cases)^[23]. We found that the cystic duct joins the common hepatic duct about halfway between the porta hepatis and the ampulla of Vater in 73.8% of cases, a rate similar to that reported by Turner *et al*^[23]. We found

no relationships among the diameter and length of the extrahepatic duct, length of the CBD, cystic junction radial orientation or cystic junction location.

There are some limitations to this retrospective study. First, the variation in the depth of individual patient inspiration may have affected the length and maximal diameter of the extrahepatic bile duct during respiratory MRCP, although all of the patients were instructed before the examinations to take a deep breath or to completely exhale. Second, there were only a few patients older than 70 (6.7%) or younger than 20 (4.9%) years. This may have introduced bias regarding the imaging review and analysis.

In conclusion, in this study, we established a reference range for the CBD diameter on MRCP for an asymptomatic population. The CBD diameter is correlated with age, and its normal upper limit can be set at 6 mm. Respiration and other factors, such as gender, body length, body weight, BMI, PVD, extrahepatic duct and CBD length, and the cystic junction radial orientation and location, do not affect the non-dilated CBD diameter. The significant changes in the CBD diameter between inspiration and expiration may suggest dilation of the CBD. This is a useful reference for evaluating suspected biliary tract disease.

COMMENTS

Background

A dilated common bile duct (CBD) suggests obstructive. An accurate reference range for CBD size remains debatable. Magnetic resonance cholangiopancreatography (MRCP) can be used to measure the diameter of the CBD.

Research frontiers

An accurate reference for CBD size on imaging.

Innovations and breakthroughs

To measurement the CBD diameter in a large cohort of asymptomatic patients (862) using MRCP.

Applications

The CBD diameter is correlated with age, and its normal upper limit can be set at 6 mm. Respiration and other factors, such as gender, body length, body weight,

body mass index, portal vein diameter, extrahepatic duct and CBD length, and the cystic junction radial orientation and location, do not affect the non-dilated CBD diameter.

Peer-review

This work is alright to publish. However, more relationships of diameter other than age should be presented. Relationships of diameter and say, gender, patient weight and height are suggested.

REFERENCES

- 1 **Chen T**, Hung CR, Huang AC, Lii JM, Chen RC. The diameter of the common bile duct in an asymptomatic Taiwanese population: measurement by magnetic resonance cholangiopancreatography. *J Chin Med Assoc* 2012; **75**: 384-388 [PMID: 22901722 DOI: 10.1016/j.jcma.2012.06.002]
- 2 **Senturk S**, Miroglu TC, Bilici A, Gumus H, Tekin RC, Ekici F, Tekbas G. Diameters of the common bile duct in adults and postcholecystectomy patients: a study with 64-slice CT. *Eur J Radiol* 2012; **81**: 39-42 [PMID: 21144686 DOI: 10.1016/j.ejrad.2010.11.007]
- 3 **Daradkeh S**, Tarawneh E, Al-Hadidy A. Factors affecting common bile duct diameter. *Hepatogastroenterology* 2005; **52**: 1659-1661 [PMID: 16334751]
- 4 **Bowie JD**. What is the upper limit of normal for the common bile duct on ultrasound: how much do you want it to be? *Am J Gastroenterol* 2000; **95**: 897-900 [PMID: 10763933]
- 5 **Wachsbarg RH**. Respiratory variation of extrahepatic bile duct diameter during ultrasonography. *J Ultrasound Med* 1994; **13**: 617-621 [PMID: 7933030]
- 6 **Wu CC**, Ho YH, Chen CY. Effect of aging on common bile duct diameter: a real-time ultrasonographic study. *J Clin Ultrasound* 1984; **12**: 473-478 [PMID: 6436325]
- 7 **Horrow MM**, Horrow JC, Niakosari A, Kirby CL, Rosenberg HK. Is age associated with size of adult extrahepatic bile duct: sonographic study. *Radiology* 2001; **221**: 411-414 [PMID: 11687684]
- 8 **Mahour GH**, Wakim KG, Ferris DO. The common bile duct in man: its diameter and circumference. *Ann Surg* 1967; **165**: 415-419 [PMID: 6019316]
- 9 **Matcuk GR**, Grant EG, Ralls PW. Ultrasound measurements of the bile ducts and gallbladder: normal ranges and effects of age, sex, cholecystectomy, and pathologic states. *Ultrasound Q* 2014; **30**: 41-48 [PMID: 24901778 DOI: 10.1097/RUQ.0b013e3182a80c98]
- 10 **Uysal F**, Obuz F, Uçar A, Seçil M, Igci E, Dicle O. Anatomic variations of the intrahepatic bile ducts: analysis of magnetic resonance cholangiopancreatography in 1011 consecutive patients. *Digestion* 2014; **89**: 194-200 [PMID: 24732700 DOI: 10.1159/000358558]
- 11 **Chiu NC**, Chiou YY. Role of MRCP in the measurement of the CBD diameter. *J Chin Med Assoc* 2012; **75**: 423-424 [PMID: 22989536 DOI: 10.1016/j.jcma.2012.06.013]
- 12 **Shanmugam V**, Beattie GC, Yule SR, Reid W, Loudon MA. Is magnetic resonance cholangiopancreatography the new gold standard in biliary imaging? *Br J Radiol* 2005; **78**: 888-893 [PMID: 16177010]
- 13 **Uetsuji S**, Okuda Y, Komada H, Yamamura M, Kamiyama Y. Clinical evaluation of a low junction of the cystic duct. *Scand J Gastroenterol* 1993; **28**: 85-88 [PMID: 8430277]
- 14 **Tsitouridis I**, Lazaraki G, Papastergiou C, Pagalos E, Germanidis G. Low conjunction of the cystic duct with the common bile duct: does it correlate with the formation of common bile duct stones? *Surg Endosc* 2007; **21**: 48-52 [PMID: 16960679]
- 15 **Kamisawa T**, Yoshiike M, Egawa N, Tsuruta K, Okamoto A, Matsukawa M. Classification of choledochocoele. *Hepatogastroenterology* 2005; **52**: 29-32 [PMID: 15782987]
- 16 **Salas-Salvadó J**, Rubio MA, Barbany M, Moreno B. SEEDO 2007 Consensus for the evaluation of overweight and obesity and the establishment of therapeutic intervention criteria. *Med Clin (Barc)* 2007; **128**: 184-196; quiz 1 p following 200 [PMID: 17298782]
- 17 **Adeboye B**, Bermanno G, Rolland C. Obesity and its health impact in Africa: a systematic review. *Cardiovasc J Afr* 2012; **23**: 512-521 [PMID: 23108519 DOI: 10.5830/CVJA-2012-040]
- 18 **Park JS**, Lee DH, Jeong S, Cho SG. Determination of Diameter and Angulation of the Normal Common Bile Duct using Multidetector Computed Tomography. *Gut Liver* 2009; **3**: 306-310 [PMID: 20431765 DOI: 10.5009/gnl.2009.3.4.306]
- 19 **Kaim A**, Steinke K, Frank M, Enriquez R, Kirsch E, Bongartz G, Steinbrich W. Diameter of the common bile duct in the elderly patient: measurement by ultrasound. *Eur Radiol* 1998; **8**: 1413-1415 [PMID: 9853225]
- 20 **Kialian GP**, Aznaurian AV. The age-related characteristics of the muscular layer of the common bile duct in man. *Morfologija* 1995; **108**: 10-12 [PMID: 7550906]
- 21 **Ito K**, Shimizu A, Tanabe M, Matsunaga N. Respiratory variation of the extrahepatic bile duct: evaluation with deep inspiratory and expiratory MRCP. *Magn Reson Imaging* 2012; **30**: 579-582 [PMID: 22387023 DOI: 10.1016/j.mri.2011.12.024]
- 22 **Ongofa N**, Sissoko F, Ouologuem I, Béréte S, Diop AK, Sidibé S, Touré M, Kéita AD, Koumaré AK. The size of the bile duct by echograph. A study. *Morphologie* 2012; **96**: 7-11 [PMID: 22445527 DOI: 10.1016/j.morpho.2012.01.003]
- 23 **Turner MA**, Fulcher AS. The cystic duct: normal anatomy and disease processes. *Radiographics* 2001; **21**: 3-22; questionnaire 288-294 [PMID: 11158640]

P- Reviewer: Chow J S- Editor: Wang JL L- Editor: A
E- Editor: Wu HL



Observational Study

Combined value of apparent diffusion coefficient-standardized uptake value max in evaluation of post-treated locally advanced rectal cancer

Davide Ippolito, Davide Fior, Chiara Trattenero, Elena De Ponti, Silvia Drago, Luca Guerra, Cammillo Talei Franzesi, Sandro Sironi

Davide Ippolito, Davide Fior, Chiara Trattenero, Elena De Ponti, Silvia Drago, Luca Guerra, Cammillo Talei Franzesi, Sandro Sironi, School of Medicine, University of Milano-Bicocca, 20126 Milan, Italy

Davide Ippolito, Davide Fior, Chiara Trattenero, Silvia Drago, Cammillo Talei Franzesi, Sandro Sironi, Department of Diagnostic Radiology, H S.Gerardo Monza, 20052 Milan, Italy

Luca Guerra, Department of Nuclear Medicine and PET Unit-Molecular Bioimaging Centre, San Gerardo Hospital, 20052 Monza, Italy

Elena De Ponti, Department of Medical Physics, San Gerardo Hospital, 20052 Monza, Italy

Author contributions: Ippolito D was the guarantor of integrity of entire study and contributed to study concepts; Ippolito D, Fior D and Trattenero C contributed to study design; Drago S and Franzesi CT contributed to literature research; Ippolito D and Guerra L contributed to clinical studies; Ippolito D, Fior D and Guerra L contributed to data acquisition; Ippolito D, Fior D, Trattenero C and De Ponti E contributed to data analysis/interpretation; De Ponti E contributed to statistical analysis; Ippolito D, Fior D, Trattenero C and Drago S contributed to manuscript preparation; Ippolito D and Sironi S contributed to manuscript definition of intellectual content and manuscript editing; all the authors contributed to manuscript revision/review; Ippolito D gave the manuscript final version approval.

Institutional review board statement: No ethical approval is needed, because the used data have been generated as part of the routine work of our organization.

Informed consent statement: This prospective study was approved by our institutional review board, and informed consent was obtained from all patients.

Conflict-of-interest statement: No Conflict-of-interest. Authors declare no competing financial interests in relation to the work described.

Data sharing statement: No additional data are available.

Open-Access: This article is an open-access article which was selected by an in-house editor and fully peer-reviewed by external reviewers. It is distributed in accordance with the Creative Commons Attribution Non Commercial (CC BY-NC 4.0) license, which permits others to distribute, remix, adapt, build upon this work non-commercially, and license their derivative works on different terms, provided the original work is properly cited and the use is non-commercial. See: <http://creativecommons.org/licenses/by-nc/4.0/>

Correspondence to: Davide Ippolito, MD, Department of Diagnostic Radiology, H S.Gerardo Monza, Via Pergolesi 11, 20052 Milan, Italy. davide.atena@tiscalinet.it
Fax: +39-039-2333463

Received: January 25, 2015

Peer-review started: January 26, 2015

First decision: March 6, 2015

Revised: July 1, 2015

Accepted: November 3, 2015

Article in press: November 4, 2015

Published online: December 28, 2015

Abstract

AIM: To assess the clinical diagnostic value of functional imaging, combining quantitative parameters of apparent diffusion coefficient (ADC) and standardized uptake value (SUV)max, before and after chemo-radiation therapy, in prediction of tumor response of patients with rectal cancer, related to tumor regression grade at histology.

METHODS: A total of 31 patients with biopsy proven diagnosis of rectal carcinoma were enrolled in our study. All patients underwent a whole body ¹⁸FDG positron emission tomography (PET)/computed tomography

(CT) scan and a pelvic magnetic resonance (MR) examination including diffusion weighted (DW) imaging for staging (PET1, RM1) and after completion (6.6 wk) of neoadjuvant treatment (PET2, RM2). Subsequently all patients underwent total mesorectal excision and the histological results were compared with imaging findings. The MR scanning, performed on 1.5 T magnet (Philips, Achieva), included T2-weighted multiplanar imaging and in addition DW images with b-value of 0 and 1000 mm²/s. On PET/CT the SUVmax of the rectal lesion were calculated in PET1 and PET2. The percentage decrease of SUVmax (Δ SUV) and ADC (Δ ADC) values from baseline to presurgical scan were assessed and correlated with pathologic response classified as tumor regression grade (Mandard's criteria; TRG1 = complete regression, TRG5 = no regression).

RESULTS: After completion of therapy, all the patients were submitted to surgery. According to the Mandard's criteria, 22 tumors showed complete (TRG1) or subtotal regression (TRG2) and were classified as responders; 9 tumors were classified as non responders (TRG3, 4 and 5). Considering all patients the mean values of SUVmax in PET 1 was higher than the mean value of SUVmax in PET 2 ($P < 0.001$), whereas the mean ADC values was lower in RM1 than RM2 ($P < 0.001$), with a Δ SUV and Δ ADC respectively of 60.2% and 66.8%. The best predictors for TRG response were SUV2 (threshold of 4.4) and ADC2 (1.29×10^{-3} mm²/s) with high sensitivity and specificity. Combining in a single analysis both the obtained median value, the positive predictive value, in predicting the different group category response in related to TRG system, presented R² of 0.95.

CONCLUSION: The functional imaging combining ADC and SUVmax in a single analysis permits to detect changes in cellular tissue structures useful for the assessment of tumour response after the neoadjuvant therapy in rectal cancer, increasing the sensitivity in correct depiction of treatment response than either method alone.

Key words: Advanced rectal cancer; Functional imaging; FDG-PET/CT; Magnetic resonance imaging; Apparent diffusion coefficient; Neoadjuvant treatment; Tumor regression grade

© The Author(s) 2015. Published by Baishideng Publishing Group Inc. All rights reserved.

Core tip: In our study we evaluated the combination of changes of glucose metabolism values expressed as SUVmax and the changes of apparent diffusion coefficient (ADC map) values, before and after neoadjuvant therapy, in patients with advanced rectal cancer in order to predict, *in vivo*, the therapy response. The importance of this work consist of the possibility to offer, in the era of positron emission tomography (PET)/magnetic resonance imaging scanner, a new advanced tool that allows the non-invasive evaluation of response to neoadjuvant chemotherapy treatment in patients with

rectal cancer, by adding quantitative value information on diffusion weighted images and on PET/computed tomography imaging.

Ippolito D, Fior D, Trattenero C, De Ponti E, Drago S, Guerra L, Franzesi CT, Sironi S. Combined value of apparent diffusion coefficient-standardized uptake value max in evaluation of post-treated locally advanced rectal cancer. *World J Radiol* 2015; 7(12): 509-520 Available from: URL: <http://www.wjgnet.com/1949-8470/full/v7/i12/509.htm> DOI: <http://dx.doi.org/10.4329/wjrv.7.i12.509>

INTRODUCTION

The use of pre-operative chemoradiation treatment (CRT) induces downsizing and downstaging of primary rectal tumors, yielding a pathologic complete response (pCR) in up to 24% of patients^[1]. A pCR is known to be associated with a favourable oncologic outcome, in regard to both recurrence and patients survival^[2].

The trend in treatment of rectal cancer, although is still controversial, to date is toward a more conservative approach in patients identified as complete responders after CRT. Generally, a pCR is determined with histopathologic examination after surgery, but, if the determination of CR before surgery may influence the subsequent treatment decision, an accurate clinical assessment of response becomes essential^[3-5].

Recently, diffusion weighted magnetic resonance imaging (DW-MR) after CRT has demonstrated to be more valuable than standard morphologic MR study in differentiation between a pCR and the presence of residual disease. On DW images, the viable neoplastic remnants are more easily defined, since they appear hyperintense in comparison to the low signal intensity (SI) of the surroundings not neoplastic tissues^[6,7]. Promising results have been shown with quantitative DW imaging analysis by quantifying the apparent diffusion coefficient (ADC) in the evaluation of treatment response to CRT in patients having rectal cancer^[8-14].

Even positron emission tomography (PET)/computed tomography (CT) has been suggested to be an accurate imaging modality in the staging of newly diagnosed or in detection of recurrent rectal cancer. Furthermore, qualitative and quantitative assessment of fluoro-deoxyglucose-PET provide helpful information regarding treatment response and prognosis of patients with rectal cancer^[15,16].

Both DWI imaging and PET-CT imaging have been used separately in different fields of tumor evaluation, such as detection, characterization and CRT response assessment. As both ADC and standardized uptake value (SUV) have been associated with biological behaviour and treatment response in various tumors types a correlation between SUV values, which reflect metabolic activity and ADC values which reflect cellular density might be found^[17].

To date, there have been few comparative studies between ADC and SUVmax to evaluate the tumour response to preoperative CRT in locally advanced rectal cancer (LARC). The aim of this study was, along with brief review of literature, to evaluate the accuracy of combined ADC and SUVmax values in prediction of tumor regression grade (TRG) complete responders in LARC patients, using histological tumor regression grade as standard reference.

MATERIALS AND METHODS

Patients

Between June 2009 and April 2012, 53 consecutive patients with diagnosis of rectal cancer were considered for eligibility. Inclusion criteria were: (1) histopathologically proved rectal adenocarcinoma (0 to 15 cm from anal verge, by means of endoscopic biopsy); (2) LARC staged by baseline MR imaging examination (\geq T3 or positive lymph nodes); (3) absence of distant metastases; (4) neoadjuvant preoperative CRT. The exclusion criteria were: (1) previous CRT for primary rectal carcinoma or tumour in other organ; (2) contraindication to MR imaging study; (3) premature discontinuation of CRT; (4) delayed (more than 8 mo after CRT) or cancelled surgery; and (5) discontinued or non-diagnostic MR imaging examinations during therapy.

A total of 31 patients (22 men and 9 women, mean age of 64.5 years with a range of 42-80) met the study criteria.

This prospective study was approved by our institutional review board, and informed consent was obtained from all patients.

MR acquisition protocol

The baseline MR imaging examination (MR1) was performed within a mean of 4.8 wk (I-III quartile: 3.8-6.3 wk) before the treatment for tumour staging, while the second study (MR2) was performed within a mean of 6.6 wk (I-III quartile: 5.3-7.7 wk) after the completion of CRT and before surgery. MRI was performed using a 1.5 T magnet (Philips, Achieva 1.5 T, The Netherlands). The patients were positioned supine and feet first, and scan was performed by using a five-channel high resolution phased-array body coil.

The standard protocol included multiplanar T2- TSE-weighted sequences without fat suppression, applying the following parameters: Repetition time msec/echo time msec 4750/120; slice thickness: 3 mm; slices: 18; matrix: 256 \times 256; number of signal acquired (NSA): 4; axial TSE T1-weighted axial sequence Turbo Spin-Echo (TSE) T1-weighted (slice thickness: 3 mm; slice: 20; gap: 3 mm; TR: 612 ms; TE: 14 ms; flip angle: 90°; Field of View (FOV): 180; RFOV: 85; matrix: 272 \times 320; NSA: 4.

The images were obtained in three different planes: sagittal, coronal and transverse, with the latter two

orientations angled perpendicularly to the long axis of the tumour according to sagittal images. At the end of the examination, DW images using a Multi-slice Spin Echo Eco-planar Single Shot (SE-EPI-SSH) sequence were obtained in the axial plane with the following parameters: Repetition time msec/echo time 3000/74; slice thickness: 6 mm; slices: 12; matrix: 240 \times 256; NSA: 4; b values of 0 and 1000 mm²/s; time: 1.30 min; SENSE factor 1.5.

No intravenous contrast medium was injected as part of our routine acquisition protocol for rectal cancer evaluation, according to recent guidelines about clinical management of rectal cancer patients with MRI (recommendations from ESGAR, 2012).

MR image analysis

MR images were analyzed and ADC measurements were made by one radiologist experienced in abdominal radiology (DI), and who was blinded to the therapeutic response and to the histological results (Figures 1 and 2).

On post-CRT ADC maps, the region of interest (ROIs) were manually drawn on the basis of visual analysis of focal areas of residual high SI on the high-b-value images within the location of the primary tumour site, by comparing pre-CRT examination if needed. When no remaining high SI area could be depicted on the post-CRT DW images, the ROIs were drawn on the rectal wall at the former location of the primary tumour, using pre-CRT DW and T2W images as reference. The lesions were manually contoured along their edge avoiding vessels distortion areas, vessels and motion artefacts. Then, the mean and standard deviation of the ADC values were automatically calculated.

The size of ROI of one section was not less than 20 voxels. Diffusion-weighted images were of diagnostic quality in all patients, and no patients were excluded from the study.

In order to determine percentage variation of ADC before and after CRT, the ADC values in the MR1 (ADC 1) and MR2 (ADC 2) were used also to define delta ADC (Δ ADC) as follows: Δ ADC = [(ADC2 - ADC1)/ADC2] \times 100.

¹⁸F-FDG-PET/CT imaging technique

All patients were investigated by FDG-PET/CT prior to the onset of CRT (PET1) and 4 wk after the completion of the pre-operative treatment (PET2). All studies were performed on a PET scanner coupled with a 8-detector rows CT scanner (Discovery ST - GE Healthcare, Milwaukee, WI, United States), thus allowing one step acquisition of co-registered PET and CT images. According to the acquisition protocol, patients fasted for at least 6 h before the intravenous administration of 3.7 MBq/kg body weight of ¹⁸F-FDG. Blood glucose levels were checked before tracer administration and patients with glucose level above 170 mg/dL were excluded from the study. All patients were orally hydrated (500 mL of water) during the FDG uptake period and were

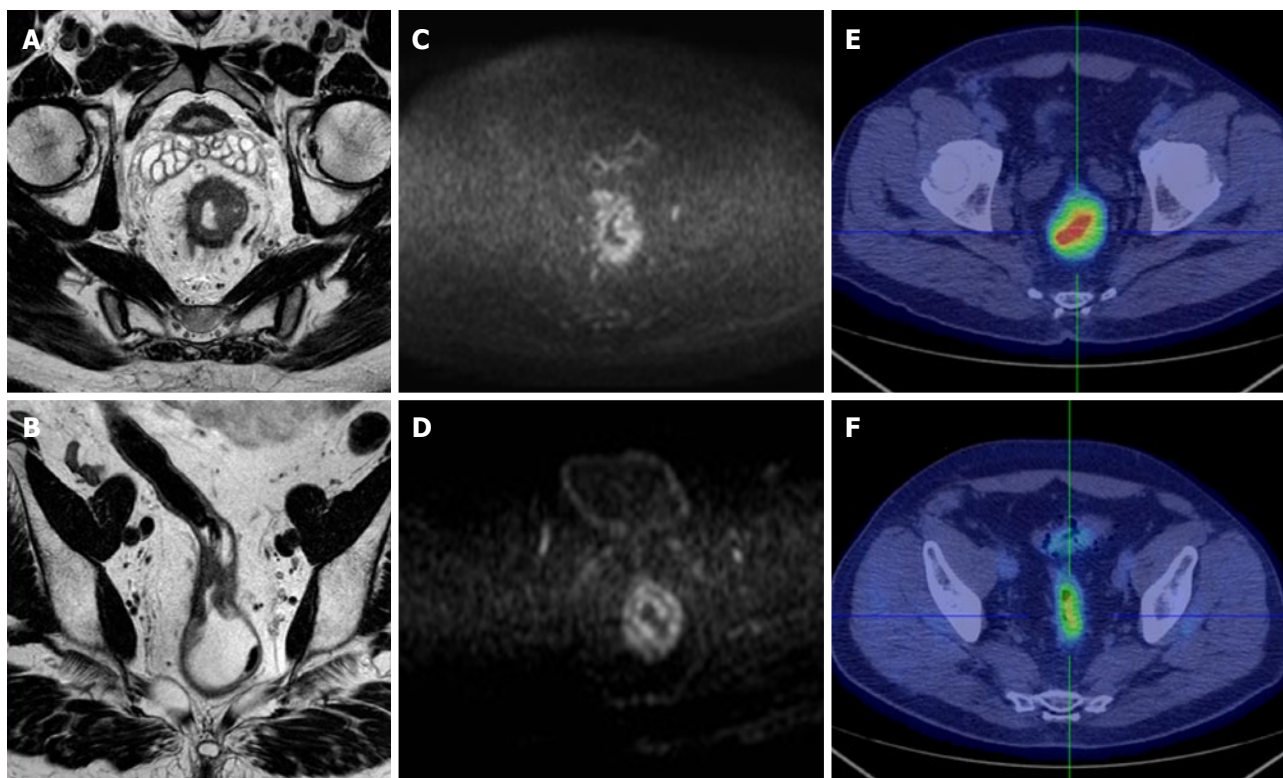


Figure 1 A 72-year-old man with pathologically proven proximal rectal cancer, classified as non-responder after chemoradiation treatment. A: Pre-CRT T2-weighted axial MR image shows a circumferential pathological rectal mass, with largest thickening from 12 to 6 o'clock position, narrowing rectal lumen and with corresponding mesorectal fat spread around; B: Post-CRT T2-weighted axial MR image shows incomplete decrease in rectal wall thickening, with irregular and inhomogeneous neoplastic tissue still determining lumen narrow; C: Pre-CRT DWI image shows the presence of hyperintense area at the corresponding level of tumor mass (ADC: $0.63 \times 10^{-3} \text{ mm}^2/\text{s}$); D: Post-CRT DWI image demonstrated partial response, with focal hyperintense area still detectable (ADC: $1.25 \times 10^{-3} \text{ mm}^2/\text{s}$); E: Pre-CRT axial pelvic scan examination image demonstrates a significant radiotracer uptake in the right rectum, corresponding tumor region (SUVmax: 19.4); F: The partial metabolic response is also confirmed by CRT PET/CT scans, in particular a significant tumor uptake is still present (SUVmax: 4.3). CRT: Chemoradiation treatment; DWI: Diffusion weighted imaging; ADC: Apparent diffusion coefficient; SUV: Standardized uptake value.

asked to empty their bladder before positioning for the scan. Sixty \pm ten minutes after the trace injection, PET/CT study was performed. Unenhanced low-dose CT (LD-CT) was acquired first with the following parameters: 120 kV, 60 mA, gantry rotation time of 0.8 s, section thickness of 3.75 mm and pitch of 1.65. PET emission scanning was performed immediately after LD-CT, with the same coverage volume. All PET studies were acquired in 3D mode, with acquisition time of 3 min per FOV. Images were reconstructed with ordered subsets expectation-maximization algorithm, 128×128 matrix size, attenuation, random, and scatter correction. Attenuation correction was performed on the basis of CT scan data. The CT pixel values measured in hounsfield units were transformed into linear attenuation coefficients for the 511-keV energy radiation. CT and PET images were then matched and fused into transaxial, coronal, and sagittal images.

Image analysis and quantification of PET data

PET, CT, and fused PET/CT images were displayed on Xeleris workstation (GE Medical Systems, Milwaukee, WI). Images were interpreted by one experienced nuclear medicine physicians (LG) without knowledge of clinical and histological data, but only of the presence

of primary rectal cancer. Lesion uptake was identified as an area of pathologically increased ^{18}F -FDG uptake, excluding causes of nonspecific or physiologic accumulation of the radio-tracer (Figures 1 and 2). ROIs were drawn over the region of pathological uptake on the baseline scan (PET1) for the calculation of SUV1. At subsequent PET/CT (PET2) images were co-registered with the baseline study by means of the anatomical CT and the ROIs were drawn in the same positions of PET1 in order to calculate SUV2. SUV values were calculated using the maximum activity values within each ROI on the transaxial slices, normalized to the injected dose and patient's body weight, as per ADC values. The SUVmax values in the PET1 (SUV1) and PET2 (SUV2) were used to define ΔSUV in percentage as follows: $\Delta\text{SUV1} = [(\text{SUV1} - \text{SUV2})/\text{SUV1}] \times 100$.

Histopathologic evaluation and TRG definition

Pathologic response was evaluated on resected specimens by a pathologist, with 15-year experience in gastrointestinal pathology. Each specimen was fixed in 10% buffered formalin for at least 48 h and inked. Serial transversal tissue blocks were cut at 5 mm intervals from the distal portion. Each block, consisting of full thickness of the rectal wall and the mesorectum,

Table 1 Summarizing table of mean values of standardized uptake value and apparent diffusion coefficient, before and after chemoradiation treatment, and their variation in the overall patients

Variable	Mean \pm SD	P value (Wilcoxon paired)
SUV1	16.3 \pm 8.6	< 0.0001
SUV2	4.5 \pm 2.1	
Δ SUV (%)	66.8 \pm 20.4	
ADC1	0.83 \pm 0.15	
ADC2	1.33 \pm 0.13	
Δ ADC (%)	60.2 \pm 23.2	

ADC: Apparent diffusion coefficient; SUV: Standardized uptake value.

was embedded in paraffin. Whole-mount sections were obtained and stained with hematoxylin and eosin. The TRG definition of Mandard *et al.*^[18] was adopted for clinical response classification. Patients with TRG1-2 scores were considered as responders, while patients with TRG3-5 were classified as non-responders.

Statistical analysis

Mean and SD of the SUV1, SUV2, ADC1 and ADC2 were calculated and the comparison between SUV1 and SUV2, and between ADC1 and ADC2 was done with Wilcoxon paired test (Table 1). The comparison of the same quantitative parameter was also performed between histopathologic responders and non responders patients with the non parametric Mann-Whitney *U* test (Table 2). The correlation between histological TRG in the resected specimen and the ADC and SUVmax values assessed before and after surgery was analysed with the Pearson correlation test. Multivariate regression model was evaluated including those parameters with significant correlation in univariate regression analysis (Figure 3). The final model incorporated ADC and SUVmax values measured after surgery (ADCpost - SUVpost). Model predictions of histological tumour regression were also compared with true patients' TRG and investigated with scatter diagram (Figure 4).

Receiver operating characteristic (ROC) analysis was performed to define the best accuracy of the metabolic parameters in predicting the response to treatment.

The sensitivity, specificity and overall diagnostic accuracy for each item were calculated under the optimal cut-off value.

Stata software 9.0 (Stata Corporation, College Station, Texas, United States) was used for performing statistical analysis and a *P* < 0.05 was deemed as statistical significant.

RESULTS

All patients underwent surgical excision within 8-10 wk after CRT completion, *i.e.*, low anterior resection (*n* = 24), abdominoperineal resection (*n* = 6) and extended resection (*n* = 1). The surgical approach was established considering the clinical response to CRT defined at conventional restaging.

Table 2 Responders (TRG1-2) vs non responders (TRG3-5)

Variable	Responders (Mean \pm SD)	Not responders (Mean \pm SD)	P value (Mann-Whitney <i>U</i> test)
SUV1	15.1 \pm 8.0	19.5 \pm 9.8	0.151
SUV2	3.6 \pm 1.4	6.6 \pm 2.1	0.0009
Δ SUV (%)	68.5 \pm 23.2	62.8 \pm 10.5	0.151
ADC1	0.88 \pm 0.19	0.78 \pm 0.09	0.076
ADC2	1.47 \pm 0.22	1.19 \pm 0.2	0.009
Δ ADC (%)	72.6 \pm 27.1	55.5 \pm 18.5	0.0078

Mann-Whitney *U* test was used to calculate and compare obtained values between SUV1 and SUV2 and between ADC1 and ADC2. ADC: Apparent diffusion coefficient; SUV: Standardized uptake value.

ADC values analysis

In the whole sample of 31 patients, the mean tumor ADC before CRT in the responder group of 22 patients was $0.88 \times 10^{-3} \text{ mm}^2/\text{s}$; while in the non-responder group (9 patients) was $0.78 \times 10^{-3} \text{ mm}^2/\text{s}$. After CRT, the mean tumour ADC in the down-staged group was $1.47 \times 10^{-3} \text{ mm}^2/\text{s}$, while in the nondown-staged group was $1.19 \times 10^{-3} \text{ mm}^2/\text{s}$. Δ ADC showed to be statistically relevant between responders and non responders (*P* = 0.0078), as shown in Table 2.

The regression analysis in comparing the ability of post-CRT ADC, Δ ADC values in the identification of response to CRT demonstrates an optimal cut-off point of 1.294 for post-CRT measures [sensitivity = 86.4%, specificity = 66.7%, positive predictive value (PPV) = 86.4%, negative predictive value (NPV) = 66.7%], 0.500 for Δ ADC (sensitivity = 63.4%, specificity = 66.7%, PPV = 82.4%, NPV = 42.9%).

SUVmax analysis

The mean SUVmax and Δ SUV values of the rectal lesion for each PET/CT study are reported (Tables 1 and 2). SUV1 was found significantly higher than SUV2 (*P* < 0.0001). Figure 3 shows the results of univariate and multivariate linear regression analysis comparing metabolic parameters to TRG groups. In the univariate analysis, a statistically significant correlation was found for SUV2 (*P* = 0.009) with TRG (Table 2).

Considering the TRG1-2 patients as responder and TRG3-5 patients as non-responder, the highest accuracy in defining the response to treatment was obtained with a SUV2 cut-off value of 4.4. With this threshold, metabolic response evaluation was true positive in 17 patients, true negative in 8 patients, false positive in 1 patients and false negative in 5 patients, obtaining sensitivity, specificity, accuracy, PPV and NPV of 77.3%, 88.9%, 80.7%, 94.4% and 61.5%, respectively.

DISCUSSION

Recently, a more conservative treatment has been advocated in patients with rectal cancer showing a good or a complete response to neoadjuvant treatments. The

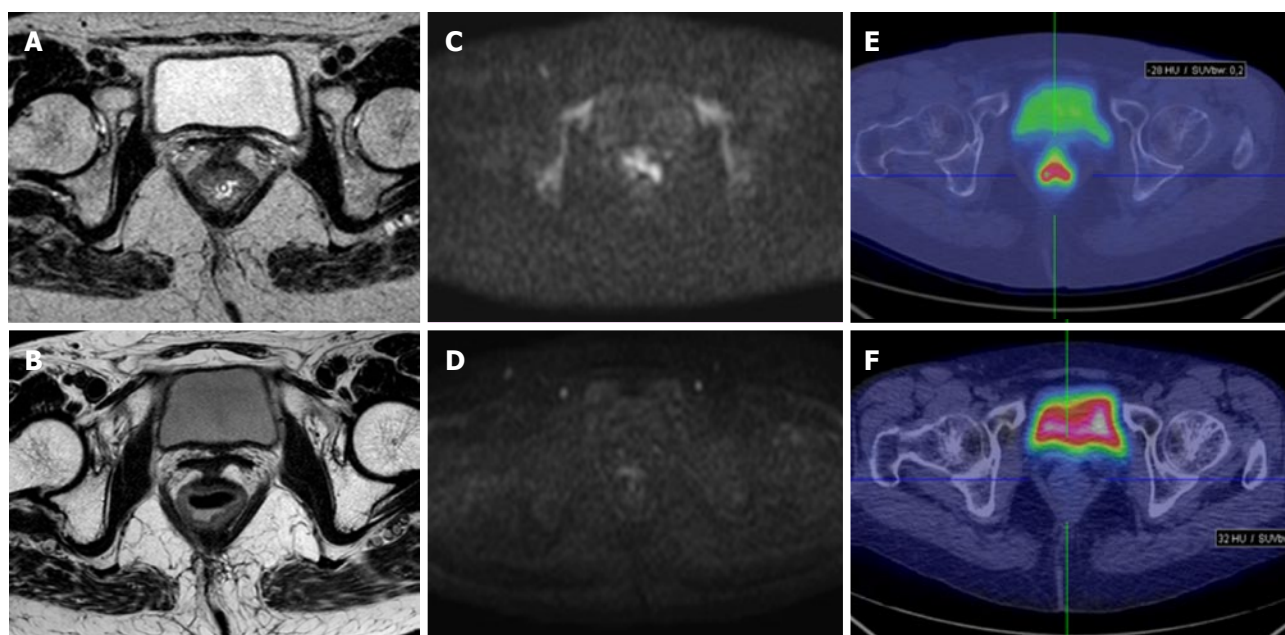


Figure 2 A 63-year-old woman with pathologically proven cancer in low rectum. It was difficult to evaluate correctly the response after CRT treatment by using only the T2 morphological information. After the additional reading of DWI images, the radiologist changed his evaluation and correctly classified the patient as responder. A: Pre-CRT T2-weighted axial MR image shows a ulcerative narrowing rectal neoplastic lesion from 11 to 3 o'clock position; B: Post-CRT T2-weighted axial MR image shows a residual homogeneous rectal wall thickening, isointense and not clearly definable as fibrotic tissue; C: Pre-CRT axial DWI image shows a focal hyperintense area in the corresponding site of rectal mass (ADC: $0.84 \times 10^{-3} \text{ mm}^2/\text{s}$); D: Post-CRT axial DWI shows no residual hyperintense signal in the corresponding site of rectal wall (ADC: $1.39 \times 10^{-3} \text{ mm}^2/\text{s}$); E: Pre-CRT axial pelvic scan of PET/CT examination image demonstrated a significant focal radiotracer uptake in correspondence of rectal mass (SUVmax: 9.3); F: Post-CRT axial pelvic scan of PET/CT examination image shows no significant uptake (SUVmax: 2.6). CRT: Chemoradiation treatment; DWI: Diffusion weighted imaging; ADC: Apparent diffusion coefficient; SUV: Standardized uptake value.

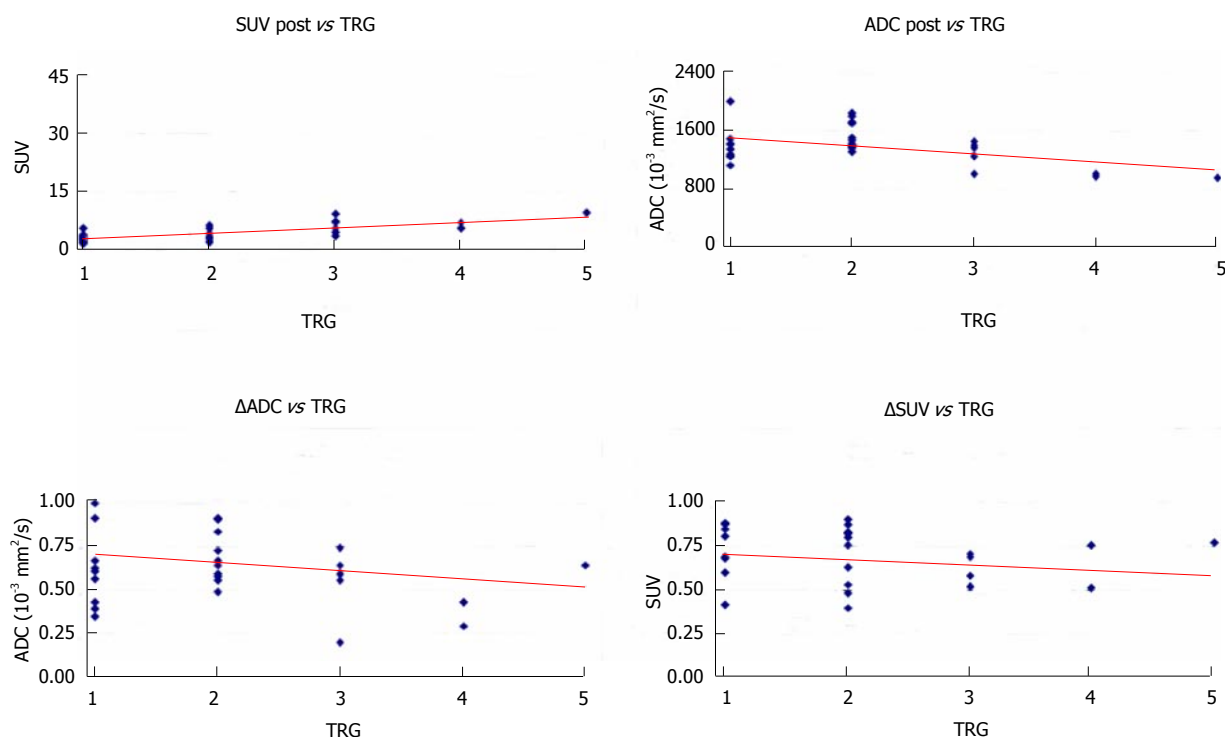


Figure 3 Univariate linear regression analysis comparing mean standardized uptake value post and apparent diffusion coefficient post with tumor regression grade. ADC: Apparent diffusion coefficient; SUV: Standardized uptake value; TRG: Tumor regression grade.

selection of true responders is essential and the role of imaging for restaging after CRT has been the subject of several recent studies, suggesting that neither MRI nor

endorectal ultrasound or FDG-PET are enough accurate for identifying the true complete responders, with an overall PPV ranging from 17% to 50%^[6,19-23].

Table 3 Overview of studies analysing mean standardized uptake value and delta standardized uptake value values of the rectal lesion for each PET/CT study

Ref.	No. of patients	Mean SUV 1	Mean SUV 2	Mean SUV 3	Sn (%)	Sp (%)	Late cut-off (%)	Sn (%)	Sp (%)	Delta SUV 1 R (%)	Delta SUV 1 NR (%)	Delta SUV 2 R (%)	Delta SUV 2 NR (%)
Bampo <i>et al</i> ^[31]	30	17.5		7.1								73.1	50.2
Cascini <i>et al</i> ^[24]	33	11.2	6	2.7	100	87				62	28		
Guerra <i>et al</i> ^[46]	31	16.3	8.1	4.3	63.2	55.6	60	77.3	55.6	51	43.1	68.5	62.8
Hermann <i>et al</i> ^[26]	28	9.5	5.2	3.1	74	50	45	63	100				
Janssen <i>et al</i> ^[25]	46	16.4	13										
Lambrecht <i>et al</i> ^[28]	22				100	75	76	100	75	59	25	90	63
Rosenberg <i>et al</i> ^[27]	30	9.5	5.5	3.5	74	70	57.5	79	70	44.3	29.6	66	48.3
Shanmugan <i>et al</i> ^[29]	70	10.8		3.8			63	60	84			74	56
Sun <i>et al</i> ^[30]	35	14.7		7.9								57.8	

R: Responders; NR: Non responders; SUV: Standardized uptake value; Sn: Sensibility; Sp: Specificity.

The correlation between therapy-related changes in FDG uptake and tumour response in rectal cancer has been previously reported by several groups. Despite the differences in study set-up, scan type, pathological and metabolic evaluation, the final metabolic response to CRT in rectal cancer with FDG-PET/CT have been demonstrated to correlate with the histopathological response and therefore to be a useful method for early assessment of treatment efficacy in rectal cancer. The different studies provided similar cut-off values, however the above mentioned differences make a direct comparison of the results not possible (Table 3).

Cascini *et al*^[24] showed that early responder patients, evaluated with PET/CT 12 d after the beginning of therapy, had a higher decrease of SUV than non-responder patients (62% vs 28%, respectively; $P < 0.0001$). Conversely, the pre-surgical PET data did not demonstrate any statistically significant correlation between mean SUV late change and TRG findings ($P = 0.2$) obtaining a low correlation between overall changes and the TRG ($P = 0.63$).

Also Janssen *et al*^[25] found an early significant decrease of the metabolic activity after the first week of CRT, both in SUVmean and SUVmax, that decreased from respectively 8.5 ± 2.8 (range: 4.0-15.1) and 16.4 ± 5.8 (range: 7.0-28.1) to 6.9 ± 2.2 (range: 4.3-12.7) ($P < 0.001$) and 13.0 ± 4.8 (range: 7.6-27.4) ($P < 0.001$) after the first week of combined treatment. More recently Herrmann *et al*^[26] found in 28 patients a decrease of mean SUV uptake from 9.5 at baseline to 5.5 ($P < 0.001$) 14 d after the onset of preoperative radiochemotherapy and in the third PET scan (4 wk after completion of treatment), mean SUV decreased to 3.1 ($P < 0.001$).

Rosenberg *et al*^[27] did not obtain the same result but reported that the percentage of early SUV reduction tended to be higher (44.3%) in responders than in non-responder patients (29.6%; $P = 0.085$). However after the completion of therapy, the reduction of FDG uptake was 66% in histopathologically responding tumors and 48.3% in non responding tumors ($P = 0.040$).

Similarly also Lambrecht *et al*^[28] found, during CRT, a mean reduction in SUVmax of 59% in patients

with histopathological complete response vs a mean reduction of SUVmax of 25% in patients without complete response ($P = 0.0036$). Additionally, 5 wk after the completion of CRT, a 90% SUVmax reduction in the first group vs 63% in second group ($P = 0.013$) was found.

Shanmugan *et al*^[29] recently evaluated seventy patients that underwent pre- and post-CRT PET/CT followed by surgery and found that patients with pCR had a lower median post-CRT SUV compared with those without (2.7 vs 4.5, $P = 0.01$). Median SUV decrease was 63% (7.5%-95.5%) and predicted pCR ($P = 0.002$); the authors concluded that post-treatment SUV and %SUV decrease correlate with pCR.

Similar results were found by Sun *et al*^[30] in a study group of 53 patients diagnosed with clinical T3- 4 and/or N+ rectal cancer and treated with CRT followed by radical surgery after 6-8 wk. A PET/CT scan was performed before (PET/CT1) beginning of treatment and a second scan (PET/CT2) was performed within 1 wk after the completion of CRT. Thirty-five out of 53 patients also underwent a third (PET/CT3) scan within 1 wk before surgery. When patients were regrouped as having a pCR and a non-pCR significant differences were found in the percentage difference between PET/CT1 and PET/CT3 in SUVmax [$(\Delta\% \text{ SUVmax}(1-3); 69.17\% \text{ vs } 57.77\%)$].

Also Bampo *et al*^[31] evaluated the possible predictive role of late FDG-PET/CT for the assessment of pathological response in locally advanced rectal cancer following neoadjuvant chemoradiation in 30 patients; significant differences in late SUV value and response index were observed between complete and non-complete pathological responder ($P = 0.0006$ and 0.03). Furthermore, with receiver operating characteristic curve analysis, a SUV threshold of 5.4% had 81% sensitivity and 100% specificity, with 90% overall accuracy.

Nevertheless the optimal timing of the post-treatment PET scan, for a proper assessment of early response to CRT, is still unclear. Radiation-induced reduction in glucose intake occurs due to cell loss, which is a prolonged effect^[32]. However, this can be confounded by two transient processes that occur soon after radio-

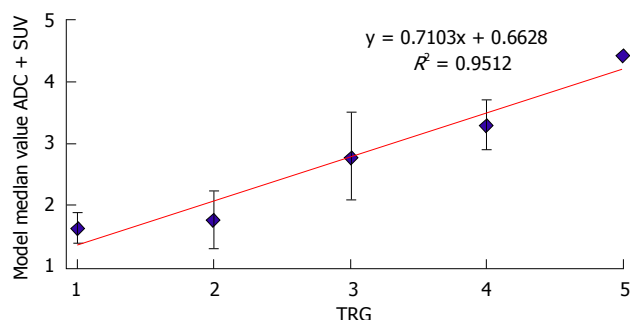


Figure 4 Univariate linear regression analysis of combined model with median value of standardized uptake value post and apparent diffusion coefficient post, in comparison with tumor regression grade. ADC: Apparent diffusion coefficient; SUV: Standardized uptake value; TRG: Tumor regression grade.

chemotherapy. The first is defined as “stunning” of tumor cells and can lead to a transient reduction in glucose metabolism, increasing false negative results^[33]. The second one is the possible increase in FDG uptake due to radiogenic inflammatory processes after radiotherapy and can lead to false positive results^[34]. Increasing time interval between neoadjuvant treatment and PET scan should theoretically lead to a more accurate evaluation. Alternatively, ¹⁸F-FLT PET has been tested to minimize the influence of radiation-induced inflammation^[35]. In previous animal studies, FLT uptake has been shown to be in inflamed tissue as compared with FDG. However, it has not shown to be a valid tool for a proper CRT response assessment in rectal cancer patients^[36].

In Lambrecht *et al.*^[28] study ROC curve analysis identified a threshold value for Δ SUVmax of 40%, for differentiating patients with a complete response after 2 wk, with a sensitivity of 100%, but a specificity of 75% and a PPV of 60%. Similarly using a threshold for Δ SUVmax of 76% after CRT and before surgery, is possible to identify complete responders with a sensitivity of 100%, a specificity of 75% and a PPV of 60%.

Considering our results, ROC curves analysis have shown that SUV2 has the best accuracy (80.7%) in predicting response to neoadjuvant treatment with a threshold value of 4.4. Interestingly, to note that in our study the PPV of SUV2 in predicting response was very high (94.4%) suggesting more conservative surgical approaches only in patients with evidence of lower glucose uptake at the end of neoadjuvant treatment.

While evaluating the correlation between the changes of ADC before and after CRT we found that before CRT, the mean tumour ADC in the responder group was $(0.88 \pm 0.19) \times 10^{-3} \text{ mm}^2/\text{s}$, while that in the non-responder group was $(0.78 \pm 0.09) \times 10^{-3} \text{ mm}^2/\text{s}$. At the end of combined chemoradiation therapy the mean tumor ADC value for responder patients was $(1.47 \pm 0.22) \times 10^{-3} \text{ mm}^2/\text{s}$. For non-responder patients the mean ADC value after therapy was $(1.19 \pm 0.20) \times 10^{-3} \text{ mm}^2/\text{s}$.

Our results are in line with the previously published by Jung *et al.*^[37]. Before neoadjuvant CRT, the mean

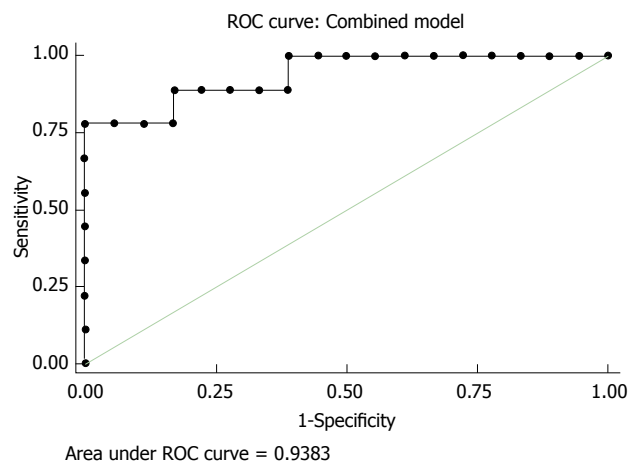


Figure 5 Receiver operating characteristic curve of combined model with median value of standardized uptake value post and apparent diffusion coefficient post, in comparison with tumor regression grade. ROC: Receiver operating characteristic.

ADC of responders and non-responders were $(0.93 \pm 0.09) \times 10^{-3} \text{ mm}^2/\text{s}$ and $(1.03 \pm 0.08) \times 10^{-3} \text{ mm}^2/\text{s}$, respectively. After neoadjuvant CRT the mean post-CRT ADC in responders was higher than in non-responders ($P = 0.009$), being respectively $(1.29 \pm 0.13) \times 10^{-3} \text{ mm}^2/\text{s}$ and $(1.18 \pm 0.08) \times 10^{-3} \text{ mm}^2/\text{s}$. Using a post-CRT ADC of $1.18 \times 10^{-3} \text{ mm}^2/\text{s}$ as cut-off value for discriminate between the responders and non-responders, the highest accuracy (77.1%) was obtained, with the following diagnostic predictive values: Sensitivity 91.3%, specificity 50.0%, positive predictive value 77.8%, and negative predictive value 75.0%.

Similarly Kim *et al.*^[6] reported that the mean ADC after CRT in the responders group $[(1.62 \pm 0.36) \times 10^{-3} \text{ mm}^2/\text{s}]$ differed significantly from the one in the non-responders group $[(1.04 \pm 0.24) \times 10^{-3} \text{ mm}^2/\text{s}]$. Moreover, when an ADC value of $1.20 \times 10^{-3} \text{ mm}^2/\text{s}$ was used as cut-off, the authors obtained an accuracy of 85% with the following diagnostic predictive values: sensitivity 100%, specificity 79%, positive predictive value 65%, and negative predictive value 100%.

Recently, other studies^[38-40] revealed similar data. Ha *et al.*^[38] comparing the mean post-CRT ADC for the RC group vs the non-CR group $[(1.33 \pm 0.25) \times 10^{-3} \text{ mm}^2/\text{s}$ vs $(1.13 \pm 0.32) \times 10^{-3} \text{ mm}^2/\text{s}]$ found a significant increased ($P = 0.001$) of ADC value. When a post-CRT ADC of $1.20 \times 10^{-3} \text{ mm}^2/\text{s}$ was used as a cut-off value for discriminating CR, the accuracy was 67%, sensitivity was 52.1%, specificity of 80.8%, positive predictive value of 71.4%, and negative predictive value of 64.6%.

Even the best timing to perform the follow-up MR study for the assessment of response to CRT is still debated. Some Authors performed the diffusion-MR also during the first 15 d of the combined treatment. Sun *et al.*^[12] evaluated the ADC only one week after the beginning of CRT. Before CRT the mean tumour ADC value in the down-staged group was lower than that in

Table 4 Overview of studies analysing mean apparent diffusion coefficient and delta apparent diffusion coefficient values of the rectal lesion for each MR study

Ref.	n of patients	Pre ADC mean R	Pre ADC mean NR	Post ADC mean R	Post ADC mean NR	ROC curve (highest accuracy)
Ippolito <i>et al</i> ^[45]	30	0.88 ± 0.19	0.78 ± 0.09	1.47 ± 0.22	1.19 ± 0.20	1.28 (80%)
Kim <i>et al</i> ^[41]	34	0.90 ± 0.06	0.94 ± 0.03			
Jung <i>et al</i> ^[37]	35	0.93 ± 0.09	1.03 ± 0.08	1.29 ± 0.13	1.18 ± 0.08	1.18 (77.1%)
Kim <i>et al</i> ^[6]	40			1.62 ± 0.36	1.04 ± 0.24	1.20 (85%)
Curvo Semedo <i>et al</i> ^[43]	50	1.07 ± 0.15	1.10 ± 0.19	1.39 ± 0.24	1.45 ± 0.28	1.41 (53%)
Ha <i>et al</i> ^[38]	100	0.59 ± 0.29	0.49 ± 0.22	1.33 ± 0.25	1.13 ± 0.32	1.20 (67%)
Genovesi ^[44]	28	1.01 ± 0.06	1.29 ± 0.02	1.79 ± 0.51	1.37 ± 0.43	29.5 (91.3%)
Cai <i>et al</i> ^[39]	15	0.659	0.885	0.713	1.027	
Birlik <i>et al</i> ^[40]	43	0.66 ± 0.10	0.72 ± 0.14	1.22 ± 0.26	0.95 ± 0.20	1.20 (60%)

R: Responders; NR: Non responders; ADC: Apparent diffusion coefficient.

the nondown-staged group ($1.07 \times 10^{-3} \text{ mm}^2/\text{s} \pm 0.13$ vs $1.19 \times 10^{-3} \text{ mm}^2/\text{s} \pm 0.15$, $F = 6.91$, $P = 0.013$). At the end of the first week, the mean tumour ADC increased significantly to $1.32 \times 10^{-3} \text{ mm}^2/\text{s} \pm 0.16$ ($F = 37.63$, $P < 0.001$) in the down-staged group, while there was no significant ADC value increase in the nondown-staged group ($F = 1.18$, $P = 0.291$).

Also Kim *et al*^[41] reported that the mean percentage of tumour ADC change in the responder group after 2 wk of CRT was higher in comparison with that of the non-responder group, even if not statistically significant. Seierstad *et al*^[42] found an increase in tumour ADC values on day 11 after the beginning of CRT.

Cai *et al*^[39] obtained an increase in the mean tumour ADC during the course of neoadjuvant CRT, especially at the 2th week ($P = 0.004$), with a significant increase in the mean ADC at the 2th week of neoadjuvant therapy in the T down-stage and tumour regression group ($P = 0.011$; 0.004). They also found a strong negative correlation between the mean pretreatment tumour ADC and tumour regression after neoadjuvant CRT ($P = 0.0021$).

Hypotizing that disrupted membranes increase the extracellular volume since they demonstrated higher permeability, Authors concluded that the ADC values changes in this early phase of CRT are probably the result of irreparable radiation induced DNA damage. However considering the variability among the results obtained in the recent literature (Table 4), actual evidence suggests that DWI-MR performed early after the beginning of therapy could not provide accurate and reproducible results for the evaluation of early tumour response to CRT. Hence the attention should be focused on ADC values obtained after the end of the treatment.

As well as for SUV values, in order to evaluate the prognostic value of pretreatment MR, several authors assessed^[6,7,38-40,43,44] the pre-CRT ADC, obtaining controversial results. Curvo-Semedo *et al*^[43] demonstrated that lower pre-CRT ADC values were associated with a more aggressive tumour profile: in their study mean ADCs were significantly different for mesorectal fascia tumour free (MRF) vs MRF-invaded ($P = 0.013$), mrN0 vs mrNp ($P = 0.011$), and for the different

tumour differentiation grades at histology ($P = 0.025$). Particularly tumours with involved MRFs, nodal-positive disease and those of less differentiated showed lower ADC values. Furthermore, a significant positive correlation ($r = 0.374$; $P = 0.019$) between ADC values and the distance of the tumour from the MRF was found.

Jung *et al*^[37] recently reported that the mean pre-CRT ADC obtained with a 3 Tesla MR of responders was lower than that of non-responders ($P = 0.034$). Other authors^[39,40], obtained similar results with 1.5 T MR. For instance, in the study of Birlik *et al*^[40], before CRT the mean tumour ADC in the responder group was significantly lower than that in the nonresponder group ($P < 0.001$).

Other authors, however, reported that pre-treatment ADC values were not statistically different for responders and non-responders and that may be limited in predicting treatment outcome^[6,38,41,44,45]. For instance, Kim *et al*^[41] reported that, predicting the treatment outcome based on TRG, there were no significant differences among responder and non-responder groups when comparing pre-CRT ADCs and early tumour ADC increase rates: As the tumour responds to treatment, ADC values will probably rise at first, due the initial disruption of cell membranes, and then decrease at the end of the treatment, for the post-irradiation ingrowth of fibrosis restricting water mobility.

Considering these results and according to recent literature, the best reproducibility was obtained by studies that evaluated a post-treatment cut-off value of ADC and SUV; being the most promising and precise way of applying functional techniques in the clinical practice.

Moreover, as evaluated in our series of patients, combining in a single analysis the mathematical model of median values of ADC and of SUV values, the power of both functional technique improves, gaining a strictly and significant relationship with TRG system staging by linear regression analysis with R^2 of 0.95 (Figure 5).

In the era of PET/MRI scanner, the future approach should be represented by the combination of PET imaging with MRI not only to increase anatomical resolution but also for cell and molecular imaging, improving

the accuracy in the assessment of tumour response. Moreover, the synchronous acquisition of both technique is critical in order to avoid differences in patient position, organ motion, and tumor growth.

In conclusion, the combined functional analysis of MRI and PET imaging, by the quantitative analysis of ADC map on DW-MR imaging and glucose uptake by ^{18}F -FDG-PET, can contribute to the management of patients with locally advanced rectal cancer increasing the overall accuracy and sensitivity for treatment response evaluation in one step, since they permit to detect changes in cellular tissue structures useful in prediction the different group category response in relation to TRG system.

COMMENTS

Background

The treatment of locally advanced rectal cancer has shifted in recent years toward a more conservative policy for patients identified as complete responders after chemoradiation treatment (CRT). Therefore the determination of CR before surgery would influence the subsequent treatment choice, an accurate clinical assessment of response becomes essential. Conventional imaging modalities cannot distinguish fibrosis or scar from viable tumour cells in residual masses after chemoradiotherapy; therefore, these methods have a negligible impact on the prediction of pathologic findings. For these reasons, in recent years, the functional imaging studies are increasingly being conducted to add information about changes in tumour pathophysiology.

Research frontiers

^{18}F fluorodeoxyglucose positron emission tomography (^{18}F -FDG PET) is a non-invasive tool to detect tumour metabolic activity and can be used to assess changes in tumour glucose metabolism after a CRT treatment. The semiquantitative assessment of glucose metabolism by evaluating the standardized uptake value (SUV) has been shown to have clinical relevance in several tumour types, since a strong relationship between ^{18}F -FDG SUV changes and pathological response has been proved in different types of cancer. DW-MRI enables noninvasive characterization of biologic tissues on the basis of their water diffusion properties (Brownian motion) microcirculation. Due to the restricted motion of water molecules, the diffusion coefficients obtained by quantitative DWI differ from the free diffusion values and are called apparent diffusion coefficients (ADC), and it can be measured. ADCs tend to decrease with increased tissue cellularity or cell density. Conversely, the cell density may be indicative of tumor aggressiveness; increased metastatic capacity of tumors with high cellularity.

Innovations and breakthroughs

The importance of this work consist of the possibility to offer, in the era of PET/MRI scanner, a new advanced quantitative tool that allows the non-invasive evaluation of response to neoadjuvant chemotherapy treatment in patients with rectal cancer, by adding quantitative value information on DW images and on PET/CT imaging, combined in a single analysis. Moreover in this manuscript the authors reviewed and commented the recent literature findings on this field by using the two different techniques modalities [*i.e.*, PET/CT and magnetic resonance imaging (MRI)].

Applications

Considering the variability among the results obtained in the recent literature, in rectal cancer post-therapy imaging assessment, the actual evidence suggests that DWI-MR and PET/CT performed early after the beginning of therapy could not provide accurate and reproducible results for the evaluation of early tumour response to CRT. Hence the attention should be focused on functional quantitative evaluation of ADC and SUVmax obtained after the end of the treatment.

Terminology

DWI: Diffusion MRI (or dMRI) is a MRI method which allows the mapping of the diffusion process of molecules, mainly water, in biological tissues, *in vivo* and non-invasively. Molecular diffusion in tissues is not free, but reflects interactions with many obstacles, such as macromolecules, fibers, and membranes. Water molecule diffusion patterns can therefore reveal microscopic details about tissue architecture, either normal or in a diseased state. ADC is a measure of the magnitude of diffusion (of water molecules) within tissue, and is commonly clinically calculated using MRI with diffusion weighted imaging, the extent of tissue cellularity and the presence of intact cell membrane help determine the impedance of water molecule diffusion. This impedance of water molecules diffusion can be quantitatively assessed using the ADC value. This assessment can be done using different b values *via* changing gradient amplitude. ADC values are calculated automatically by the software and then displayed as a parametric map that reflects the degree of diffusion of water molecules through different tissues. Then, by use of a dedicated workstation, ADC measurements are recorded for a given region by drawing regions of interest (ROIs) on the ADC map. SUVmax: The SUV is often used in PET imaging for a simple semiquantitative analysis. Its use is particularly common in the analysis of ^{18}F -FDG images of cancer patients. It can also be used with other PET agents especially when no arterial input function is available for more detailed pharmacokinetic modeling. The SUV represents the ratio of the image derived radioactivity concentration found in a selected part of the body at a certain time point, and as reference the radioactivity concentration in the hypothetical case of an even distribution of the injected radioactivity across the whole body.

Peer-review

This study is well designed and well described. The conclusion that MRI and PET imaging including the quantitative analysis of ADC map on DW-MR imaging and glucose uptake by ^{18}F -FDG-PET can contribute to the management of patients with locally advanced rectal cancer is helpful in clinical practice.

REFERENCES

- 1 **Curvo-Semedo L**, Lambregts DM, Maas M, Thywissen T, Mehsen RT, Lammering G, Beets GL, Caseiro-Alves F, Beets-Tan RG. Rectal cancer: assessment of complete response to preoperative combined radiation therapy with chemotherapy--conventional MR volumetry versus diffusion-weighted MR imaging. *Radiology* 2011; **260**: 734-743 [PMID: 21673229 DOI: 10.1148/radiol.11102467]
- 2 **Maas M**, Nelemans PJ, Valentini V, Das P, Rödel C, Kuo LJ, Calvo FA, García-Aguilar J, Glynn-Jones R, Haustermans K, Mohiuddin M, Pucciarelli S, Small W, Suárez J, Theodoropoulos G, Biondo S, Beets-Tan RG, Beets GL. Long-term outcome in patients with a pathological complete response after chemoradiation for rectal cancer: a pooled analysis of individual patient data. *Lancet Oncol* 2010; **11**: 835-844 [PMID: 20692872 DOI: 10.1016/S1470-2045(10)70172-8]
- 3 **Bujko K**, Kepka L, Nowacki MP. Chemoradiotherapy alone for rectal cancer: a word of caution. *Lancet Oncol* 2007; **8**: 860-862; author reply 862-863 [PMID: 17913654]
- 4 **O'Neill BD**, Brown G, Heald RJ, Cunningham D, Tait DM. Chemoradiotherapy alone for rectal cancer: a word of caution--author's reply [Letter]. *Lancet Oncol* 2007; **8**: 662-863
- 5 **O'Neill BD**, Brown G, Heald RJ, Cunningham D, Tait DM. Non-operative treatment after neoadjuvant chemoradiotherapy for rectal cancer. *Lancet Oncol* 2007; **8**: 625-633 [PMID: 17613424]
- 6 **Kim SH**, Lee JM, Hong SH, Kim GH, Lee JY, Han JK, Choi BI. Locally advanced rectal cancer: added value of diffusion-weighted MR imaging in the evaluation of tumor response to neoadjuvant chemo- and radiation therapy. *Radiology* 2009; **253**: 116-125 [PMID: 19789256 DOI: 10.1148/radiol.2532090027]
- 7 **Lambregts DM**, Vandecaveye V, Barbaro B, Bakers FC, Lambrecht M, Maas M, Haustermans K, Valentini V, Beets GL, Beets-Tan RG. Diffusion-weighted MRI for selection of complete responders after chemoradiation for locally advanced rectal cancer: a multicenter study. *Ann Surg Oncol* 2011; **18**: 2224-2231 [PMID: 21347783]
- 8 **Kim SH**, Lee JY, Lee JM, Han JK, Choi BI. Apparent diffusion

- coefficient for evaluating tumour response to neoadjuvant chemoradiation therapy for locally advanced rectal cancer. *Eur Radiol* 2011; **21**: 987-995 [PMID: 20978768 DOI: 10.1007/s00330-010-1989-y]
- 9 **Hein PA**, Kremser C, Judmaier W, Griebel J, Pfeiffer KP, Kreczy A, Hug EB, Lukas P, DeVries AF. Diffusion-weighted magnetic resonance imaging for monitoring diffusion changes in rectal carcinoma during combined, preoperative chemoradiation: preliminary results of a prospective study. *Eur J Radiol* 2003; **45**: 214-222 [PMID: 12595106]
 - 10 **DeVries AF**, Kremser C, Hein PA, Griebel J, Kreczy A, Ofner D, Pfeiffer KP, Lukas P, Judmaier W. Tumor microcirculation and diffusion predict therapy outcome for primary rectal carcinoma. *Int J Radiat Oncol Biol Phys* 2003; **56**: 958-965 [PMID: 12829130]
 - 11 **Kremser C**, Judmaier W, Hein P, Griebel J, Lukas P, de Vries A. Preliminary results on the influence of chemoradiation on apparent diffusion coefficients of primary rectal carcinoma measured by magnetic resonance imaging. *Strahlenther Onkol* 2003; **179**: 641-649 [PMID: 14628131]
 - 12 **Sun YS**, Zhang XP, Tang L, Ji JF, Gu J, Cai Y, Zhang XY. Locally advanced rectal carcinoma treated with preoperative chemotherapy and radiation therapy: preliminary analysis of diffusion-weighted MR imaging for early detection of tumor histopathologic downstaging. *Radiology* 2010; **254**: 170-178 [PMID: 20019139 DOI: 10.1148/radiol.2541082230]
 - 13 **Dzik-Jurasz A**, Domenig C, George M, Wolber J, Padhani A, Brown G, Doran S. Diffusion MRI for prediction of response of rectal cancer to chemoradiation. *Lancet* 2002; **360**: 307-308 [PMID: 12147376]
 - 14 **Roth Y**, Tichler T, Kostenich G, Ruiz-Cabello J, Maier SE, Cohen JS, Orenstein A, Mardor Y. High-b-value diffusion-weighted MR imaging for pretreatment prediction and early monitoring of tumor response to therapy in mice. *Radiology* 2004; **232**: 685-692 [PMID: 15215551]
 - 15 **Amthauer H**, Denecke T, Rau B, Hildebrandt B, Hünnerbein M, Ruf J, Schneider U, Gutberlet M, Schlag PM, Felix R, Wust P. Response prediction by FDG-PET after neoadjuvant radiochemotherapy and combined regional hyperthermia of rectal cancer: correlation with endorectal ultrasound and histopathology. *Eur J Nucl Med Mol Imaging* 2004; **31**: 811-819 [PMID: 14762698]
 - 16 **Kalff V**, Duong C, Drummond EG, Matthews JP, Hicks RJ. Findings on 18F-FDG PET scans after neoadjuvant chemoradiation provides prognostic stratification in patients with locally advanced rectal carcinoma subsequently treated by radical surgery. *J Nucl Med* 2006; **47**: 14-22 [PMID: 16391182]
 - 17 **Gu J**, Khong PL, Wang S, Chan Q, Law W, Zhang J. Quantitative assessment of diffusion-weighted MR imaging in patients with primary rectal cancer: correlation with FDG-PET/CT. *Mol Imaging Biol* 2011; **13**: 1020-1028 [PMID: 20872077 DOI: 10.1007/s11307-010-0433-7]
 - 18 **Mandard AM**, Dalibard F, Mandard JC, Marnay J, Henry-Amar M, Petiot JF, Roussel A, Jacob JH, Segol P, Samama G. Pathologic assessment of tumor regression after preoperative chemoradiotherapy of esophageal carcinoma. Clinicopathologic correlations. *Cancer* 1994; **73**: 2680-2686 [PMID: 8194005]
 - 19 **Janssen MH**, Ollers MC, Riedl RG, van den Bogaard J, Buijsen J, van Stiphout RG, Aerts HJ, Lambin P, Lammering G. Accurate prediction of pathological rectal tumor response after two weeks of preoperative radiochemotherapy using (18)F-fluorodeoxyglucose-positron emission tomography-computed tomography imaging. *Int J Radiat Oncol Biol Phys* 2010; **77**: 392-399 [PMID: 19646825 DOI: 10.1016/j.ijrobp.2009.04.030]
 - 20 **Capirci C**, Rubello D, Chierichetti F, Crepaldi G, Carpi A, Nicolini A, Mandoliti G, Polico C. Restaging after neoadjuvant chemoradiotherapy for rectal adenocarcinoma: role of F18-FDG PET. *Biomed Pharmacother* 2004; **58**: 451-457 [PMID: 15464875]
 - 21 **Kristiansen C**, Loft A, Berthelsen AK, Graff J, Lindebjerg J, Bisgaard C, Jakobsen A. PET/CT and histopathologic response to preoperative chemoradiation therapy in locally advanced rectal cancer. *Dis Colon Rectum* 2008; **51**: 21-25 [PMID: 17975715]
 - 22 **Suppiah A**, Hunter IA, Cowley J, Garimella V, Cast J, Hartley JE, Monson JR. Magnetic resonance imaging accuracy in assessing tumour down-staging following chemoradiation in rectal cancer. *Colorectal Dis* 2009; **11**: 249-253 [PMID: 18513192 DOI: 10.1111/j.1463-1318.2008.01593.x]
 - 23 **Vanagunas A**, Lin DE, Stryker SJ. Accuracy of endoscopic ultrasound for restaging rectal cancer following neoadjuvant chemoradiation therapy. *Am J Gastroenterol* 2004; **99**: 109-112 [PMID: 14687151]
 - 24 **Cascini GL**, Avallone A, Delrio P, Guida C, Tatangelo F, Marone P, Aloj L, De Martinis F, Comella P, Parisi V, Lastoria S. 18F-FDG PET is an early predictor of pathologic tumor response to preoperative radiochemotherapy in locally advanced rectal cancer. *J Nucl Med* 2006; **47**: 1241-1248 [PMID: 16883000]
 - 25 **Janssen MH**, Ollers MC, van Stiphout RG, Buijsen J, van den Bogaard J, de Ruyscher D, Lambin P, Lammering G. Evaluation of early metabolic responses in rectal cancer during combined radiochemotherapy or radiotherapy alone: sequential FDG-PET-CT findings. *Radiother Oncol* 2010; **94**: 151-155 [PMID: 20116114 DOI: 10.1016/j.radonc.2009.12.033]
 - 26 **Herrmann K**, Bundschuh RA, Rosenberg R, Schmidt S, Praus C, Souvatzoglou M, Becker K, Schuster T, Essler M, Wieder HA, Friess H, Ziegler SI, Schwaiger M, Krause BJ. Comparison of different SUV-based methods for response prediction to neoadjuvant radiochemotherapy in locally advanced rectal cancer by FDG-PET and MRI. *Mol Imaging Biol* 2011; **13**: 1011-1019 [PMID: 20936364 DOI: 10.1007/s11307-010-0383-0]
 - 27 **Rosenberg R**, Herrmann K, Gertler R, Künzli B, Essler M, Lordick F, Becker K, Schuster T, Geinitz H, Maak M, Schwaiger M, Siewert JR, Krause B. The predictive value of metabolic response to preoperative radiochemotherapy in locally advanced rectal cancer measured by PET/CT. *Int J Colorectal Dis* 2009; **24**: 191-200 [PMID: 19050900 DOI: 10.1007/s00384-008-0616-8]
 - 28 **Lambrecht M**, Deroose C, Roels S, Vandecaveye V, Penninckx F, Sagaert X, van Cutsem E, de Keyser F, Haustermans K. The use of FDG-PET/CT and diffusion-weighted magnetic resonance imaging for response prediction before, during and after preoperative chemoradiotherapy for rectal cancer. *Acta Oncol* 2010; **49**: 956-963 [PMID: 20586658 DOI: 10.3109/0284186X.2010.498439]
 - 29 **Shanmugan S**, Arrangoiz R, Nitzkowski JR, Yu JQ, Li T, Cooper H, Konski A, Farma JM, Sigurdson ER. Predicting pathological response to neoadjuvant chemoradiotherapy in locally advanced rectal cancer using 18FDG-PET/CT. *Ann Surg Oncol* 2012; **19**: 2178-2185 [PMID: 22395978 DOI: 10.1245/s10434-012-2248-z]
 - 30 **Sun W**, Xu J, Hu W, Zhang Z, Shen W. The role of sequential 18(F)-FDG PET/CT in predicting tumour response after preoperative chemoradiation for rectal cancer. *Colorectal Dis* 2013; **15**: e231-e238 [PMID: 23384167 DOI: 10.1111/codi.12165]
 - 31 **Bampo C**, Alessi A, Fantini S, Bertarelli G, de Braud F, Bombardieri E, Valvo F, Crippa F, Di Bartolomeo M, Mariani L, Milione M, Biondani P, Avuzzi B, Chiruzzi C, Pietrantonio F. Is the standardized uptake value of FDG-PET/CT predictive of pathological complete response in locally advanced rectal cancer treated with capecitabine-based neoadjuvant chemoradiation? *Oncology* 2013; **84**: 191-199 [PMID: 23328390 DOI: 10.1159/000345601]
 - 32 **Schiepers C**, Haustermans K, Geboes K, Filez L, Bormans G, Penninckx F. The effect of preoperative radiation therapy on glucose utilization and cell kinetics in patients with primary rectal carcinoma. *Cancer* 1999; **85**: 803-811 [PMID: 10091757]
 - 33 **Denecke T**, Rau B, Hoffmann KT, Hildebrandt B, Ruf J, Gutberlet M, Hünnerbein M, Felix R, Wust P, Amthauer H. Comparison of CT, MRI and FDG-PET in response prediction of patients with locally advanced rectal cancer after multimodal preoperative therapy: is there a benefit in using functional imaging? *Eur Radiol* 2005; **15**: 1658-1666 [PMID: 15806369]
 - 34 **Haberkorn U**, Strauss LG, Dimitrakopoulou A, Engenhart R, Oberdorfer F, Ostertag H, Romahn J, van Kaick G. PET studies of fluorodeoxyglucose metabolism in patients with recurrent colorectal tumors receiving radiotherapy. *J Nucl Med* 1991; **32**: 1485-1490 [PMID: 1714497]

- 35 **van Waarde A**, Cobben DC, Suurmeijer AJ, Maas B, Vaalburg W, de Vries EF, Jager PL, Hoekstra HJ, Elsinga PH. Selectivity of 18F-FLT and 18F-FDG for differentiating tumor from inflammation in a rodent model. *J Nucl Med* 2004; **45**: 695-700 [PMID: 15073267]
- 36 **Wieder HA**, Geinitz H, Rosenberg R, Lordick F, Becker K, Stahl A, Rummeny E, Siewert JR, Schwaiger M, Stollfuss J. PET imaging with [18F]3'-deoxy-3'-fluorothymidine for prediction of response to neoadjuvant treatment in patients with rectal cancer. *Eur J Nucl Med Mol Imaging* 2007; **34**: 878-883 [PMID: 17195074]
- 37 **Jung SH**, Heo SH, Kim JW, Jeong YY, Shin SS, Soung MG, Kim HR, Kang HK. Predicting response to neoadjuvant chemoradiation therapy in locally advanced rectal cancer: diffusion-weighted 3 Tesla MR imaging. *J Magn Reson Imaging* 2012; **35**: 110-116 [PMID: 21989997 DOI: 10.1002/jmri.22749]
- 38 **Ha HI**, Kim AY, Yu CS, Park SH, Ha HK. Locally advanced rectal cancer: diffusion-weighted MR tumour volumetry and the apparent diffusion coefficient for evaluating complete remission after preoperative chemoradiation therapy. *Eur Radiol* 2013; **23**: 3345-3353 [PMID: 23812242 DOI: 10.1007/s00330-013-2936-5]
- 39 **Cai G**, Xu Y, Zhu J, Gu WL, Zhang S, Ma XJ, Cai SJ, Zhang Z. Diffusion-weighted magnetic resonance imaging for predicting the response of rectal cancer to neoadjuvant concurrent chemoradiation. *World J Gastroenterol* 2013; **19**: 5520-5527 [PMID: 24023496 DOI: 10.3748/wjg.v19.i33.5520]
- 40 **Birlik B**, Obuz F, Elibol FD, Celik AO, Sokmen S, Terzi C, Sagol O, Sarioglu S, Gorken I, Oztup I. Diffusion-weighted MRI and MR-volumetry--in the evaluation of tumor response after preoperative chemoradiotherapy in patients with locally advanced rectal cancer. *Magn Reson Imaging* 2015; **33**: 201-212 [PMID: 25460330 DOI: 10.1016/j.mri.2014.08.041]
- 41 **Kim YC**, Lim JS, Keum KC, Kim KA, Myoung S, Shin SJ, Kim MJ, Kim NK, Suh J, Kim KW. Comparison of diffusion-weighted MRI and MR volumetry in the evaluation of early treatment outcomes after preoperative chemoradiotherapy for locally advanced rectal cancer. *J Magn Reson Imaging* 2011; **34**: 570-576 [PMID: 21751285 DOI: 10.1002/jmri.22696]
- 42 **Seierstad T**, Folkvord S, Roe K, Flatmark K, Skretting A, Olsen DR. Early changes in apparent diffusion coefficient predict the quantitative antitumoral activity of capecitabine, oxaliplatin, and irradiation in HT29 xenografts in athymic nude mice. *Neoplasia* 2007; **9**: 392-400 [PMID: 17534444]
- 43 **Curvo-Semedo L**, Lambregts DM, Maas M, Beets GL, Caseiro-Alves F, Beets-Tan RG. Diffusion-weighted MRI in rectal cancer: apparent diffusion coefficient as a potential noninvasive marker of tumor aggressiveness. *J Magn Reson Imaging* 2012; **35**: 1365-1371 [PMID: 22271382 DOI: 10.1002/jmri.23589]
- 44 **Genovesi D**, Filippone A, Ausili Cefaro G, Trignani M, Vinciguerra A, Augurio A, Di Tommaso M, Borzillo V, Sabatino F, Innocenti P, Liberatore E, Colecchia G, Tartaro A, Cotroneo AR. Diffusion-weighted magnetic resonance for prediction of response after neoadjuvant chemoradiation therapy for locally advanced rectal cancer: preliminary results of a monoinstitutional prospective study. *Eur J Surg Oncol* 2013; **39**: 1071-1078 [PMID: 23953231 DOI: 10.1016/j.ejso.2013.07.090]
- 45 **Ippolito D**, Monguzzi L, Guerra L, Deponti E, Gardani G, Messa C, Sironi S. Response to neoadjuvant therapy in locally advanced rectal cancer: assessment with diffusion-weighted MR imaging and 18FDG PET/CT. *Abdom Imaging* 2012; **37**: 1032-1040 [PMID: 22270580 DOI: 10.1007/s00261-011-9839-1]
- 46 **Guerra L**, Niespolo R, Di Pisa G, Ippolito D, De Ponti E, Terrevazzi S, Bovo G, Sironi S, Gardani G, Messa C. Change in glucose metabolism measured by 18F-FDG PET/CT as a predictor of histopathologic response to neoadjuvant treatment in rectal cancer. *Abdom Imaging* 2011; **36**: 38-45 [PMID: 20033405 DOI: 10.1007/s00261-009-9594-8]

P- Reviewer: Shen J, Yazdi HR **S- Editor:** Song XX **L- Editor:** A
E- Editor: Wu HL



Prospective Study

Cavernosal nerve functionality evaluation after magnetic resonance imaging-guided transurethral ultrasound treatment of the prostate

Steffen Sammet, Ari Partanen, Ambereen Yousuf, Christina L Sammet, Emily V Ward, Craig Wardrip, Marek Niekrasz, Tatjana Antic, Aria Razmaria, Keyvan Farahani, Shunmugavelu Sokka, Gregory Karczmar, Aytekin Oto

Steffen Sammet, Ambereen Yousuf, Emily V Ward, Gregory Karczmar, Aytekin Oto, Department of Radiology, University of Chicago, Chicago, IL 60615, United States

Steffen Sammet, Gregory Karczmar, Committee on Medical Physics, University of Chicago, Chicago, IL 60615, United States

Ari Partanen, Shunmugavelu Sokka, Philips, Andover, MA 01810, United States

Christina L Sammet, Department of Medical Imaging, Lurie Children's Hospital, Chicago, IL 60611, United States

Craig Wardrip, Marek Niekrasz, Aria Razmaria, Department of Surgery, University of Chicago, Chicago, IL 60615, United States

Tatjana Antic, Department of Pathology, University of Chicago, Chicago, IL 60615, United States

Keyvan Farahani, National Cancer Institute, Bethesda, MD 60615, United States

Author contributions: Sammet S, Partanen A, Yousuf A, Farahani K, Sokka S, Karczmar G and Oto A designed the research; Sammet S, Partanen A, Karczmar G and Oto A developed the MRI protocols; Sammet S, Partanen A and Oto A performed the MRI and therapeutic ultrasound experiments; Antic T performed the histological analysis and the histological/radiological comparison; Oto A performed the radiological image analysis and the histological/radiological comparison; Sammet S, Wardrip C, Niekrasz M and Razmaria A monitored the animals during therapeutic ultrasound treatment and performed surgeries; Sammet S, Partanen A, Yousuf A, Ward EV, Sammet CL, and Oto A wrote the paper.

Supported by The National Cancer Institute Education and Career Development program R25 Cancer Nanotechnology in Imaging and Radiotherapy (5R25CA132822-04) in part; the Cancer Research Foundation; the University of Chicago Comprehensive Cancer Center; and Philips Healthcare.

Institutional review board statement: The study was reviewed and approved by the University of Chicago Institutional Animal Care and Use Committee.

Clinical trial registration statement: This study is not a registered clinical trial.

Informed consent statement: This study did not involve human subjects and therefore did not require informed consent.

Conflict-of-interest statement: Steffen Sammet, MD, PhD has received research funding from Philips Healthcare and fees as a consultant for Guerbet SA. Ari Partanen, PhD is an employee of Philips Healthcare. Shunmugavelu Sokka, PhD is an employee of Philips Healthcare. Aytekin Oto, MD has received research funding from Philips Healthcare and fees as a consultant for Guerbet SA.

Data sharing statement: No additional data are available.

Open-Access: This article is an open-access article which was selected by an in-house editor and fully peer-reviewed by external reviewers. It is distributed in accordance with the Creative Commons Attribution Non Commercial (CC BY-NC 4.0) license, which permits others to distribute, remix, adapt, build upon this work non-commercially, and license their derivative works on different terms, provided the original work is properly cited and the use is non-commercial. See: <http://creativecommons.org/licenses/by-nc/4.0/>

Correspondence to: Steffen Sammet, MD, PhD, DABR, FAMP, Associate Professor and Director of Clinical MR Physics, Department of Radiology, University of Chicago, 5841 South Maryland Avenue, MC2026, Chicago, IL 60615, United States. ssammet@uchicago.edu
 Telephone: +1-773-7023162
 Fax: +1-773-7021161

Received: February 7, 2015
Peer-review started: February 8, 2015
First decision: May 19, 2015

Revised: October 19, 2015

Accepted: November 24, 2015

Article in press: November 25, 2015

Published online: December 28, 2015

Abstract

AIM: To evaluate the feasibility of using therapeutic ultrasound as an alternative treatment option for organ-confined prostate cancer.

METHODS: In this study, a trans-urethral therapeutic ultrasound applicator in combination with 3T magnetic resonance imaging (MRI) guidance was used for real-time multi-planar MRI-based temperature monitoring and temperature feedback control of prostatic tissue thermal ablation *in vivo*. We evaluated the feasibility and safety of MRI-guided trans-urethral ultrasound to effectively and accurately ablate prostate tissue while minimizing the damage to surrounding tissues in eight canine prostates. MRI was used to plan sonications, monitor temperature changes during therapy, and to evaluate treatment outcome. Real-time temperature and thermal dose maps were calculated using the proton resonance frequency shift technique and were displayed as two-dimensional color-coded overlays on top of the anatomical images. After ultrasound treatment, an evaluation of the integrity of cavernosal nerves was performed during prostatectomy with a nerve stimulator that measured tumescence response quantitatively and indicated intact cavernous nerve functionality. Planned sonication volumes were visually correlated to MRI ablation volumes and corresponding histo-pathological sections after prostatectomy.

RESULTS: A total of 16 sonications were performed in 8 canines. MR images acquired before ultrasound treatment were used to localize the prostate and to prescribe sonication targets in all canines. Temperature elevations corresponded within 1 degree of the targeted sonication angle, as well as with the width and length of the active transducer elements. The ultrasound treatment procedures were automatically interrupted when the temperature in the target zone reached 56 °C. In all canines erectile responses were evaluated with a cavernous nerve stimulator post-treatment and showed a tumescence response after stimulation with an electric current. These results indicated intact cavernous nerve functionality. In all specimens, regions of thermal ablation were limited to areas within the prostate capsule and no damage was observed in periprostatic tissues. Additionally, a visual analysis of the ablation zones on contrast-enhanced MR images acquired post ultrasound treatment correlated excellent with the ablation zones on thermal dose maps. All of the ablation zones received a consensus score of 3 (excellent) for the location and size of the correlation between the histologic ablation zone and MRI based ablation zone. During the prostatectomy and histologic examination, no damage was noted in the bladder or rectum.

CONCLUSION: Trans-urethral ultrasound treatment of the prostate with MRI guidance has potential to safely, reliably, and accurately ablate prostatic regions, while minimizing the morbidities associated with conventional whole-gland resection or therapy.

Key words: Ultrasound therapy; Thermal tissue ablation; Prostate; Magnetic resonance imaging guided therapy; Intra-operative; Histology; Validation

© **The Author(s)** 2015. Published by Baishideng Publishing Group Inc. All rights reserved.

Core tip: Therapeutic ultrasound is a promising treatment modality for minimally invasive thermal ablation of tissue. This study assessed a novel trans-urethral ultrasound therapy device with magnetic resonance imaging (MRI) guidance to ablate canine prostate tissue *in vivo*. Real-time temperature monitoring and thermotherapy feedback control was performed in a clinical 3T whole-body MR scanner. Post-treatment evaluation of cavernous nerve functionality was performed with a nerve stimulator. Treatment accuracy was assessed by correlation of treatment planning, thermal dose maps, and histopathological results. Regions of thermal ablation were limited to areas within the prostate capsule and no damage was observed in adjacent anatomical structures. These results indicate that MRI-guided transurethral ultrasound therapy can accurately ablate prostatic regions with minimal damage to surrounding tissue.

Sammet S, Partanen A, Yousuf A, Sammet CL, Ward EV, Wardrip C, Niekrasz M, Antic T, Razmaria A, Farahani K, Sokka S, Karczmar G, Oto A. Cavernosal nerve functionality evaluation after magnetic resonance imaging-guided transurethral ultrasound treatment of the prostate. *World J Radiol* 2015; 7(12): 521-530 Available from: URL: <http://www.wjgnet.com/1949-8470/full/v7/i12/521.htm> DOI: <http://dx.doi.org/10.4329/wjr.v7.i12.521>

INTRODUCTION

Cancer of the prostate is one of the most frequent malignant diseases and among the primary reasons of male cancer deaths in the United States^[1]. Over-treatment is described as an unnecessary aggressive treatment of prostate cancer (Pca) including prostatectomy and radiation therapy and can lead to complications. The overtreatment of Pca is an important public health problem occurring in about 30%-40% of the cases^[2]. Therefore, there is a need for the development of precise focal Pca treatment approaches to preserve continence and potency^[3,4].

Ultrasound therapy is a novel, minimally invasive treatment option where an ultrasound transducer emits ultrasound waves with high acoustic intensities into the target regions. The deposited acoustic energy leads to temperature elevation and tissue destruction when the temperature exceeds $\geq 56^{\circ}\text{C}$ within the focal area;

a phenomenon defined as thermo-ablation^[4-8]. The ultrasound treatment can be guided with diagnostic ultrasound (US) or magnetic resonance imaging (MRI). MRI is superior to diagnostic US due to its ability to better detect real-time temperature changes in multiple planes. High resolution anatomical imaging sequences with superior soft tissues contrast and physiological protocols such as diffusion and perfusion MRI allow to evaluate the extent of tissue destruction post-ablation^[9-11]. A combination of therapeutic ultrasound and MR guidance is particularly beneficial for focal and regional therapy of Pca^[8]. Preliminary clinical trials utilizing trans-rectal and trans-urethral ultrasound for focal ablation of Pca have reported feasibility of these techniques^[6,12]. One of the important unwanted side effects of whole gland treatment is erectile dysfunction. Even though focal therapy is expected to be safer in this regard, there is limited data in the literature to support this hypothesis.

This study utilized a novel transurethral ultrasound therapy system to ablate canine prostate tissue *in vivo* while simultaneously monitoring tissue temperature with multi-planar MRI. This dual modality system can assess temperature in real-time and is equipped with temperature feedback control^[13]. The goal was *in vivo* evaluation of possible side-effects of this transurethral ultrasound therapy device. In addition to rectal damage, we specifically assessed the post-treatment functionality of the cavernosal nerves by analyzing the tumescence response qualitatively and quantitatively with a nerve stimulator during prostatectomy.

MATERIALS AND METHODS

Animals

In this Institutional Animal Care and Use Committee (IACUC) approved (University of Chicago, IACUC protocol number: 72317) MRI guided ultrasound treatment study, 8 canines (age range: 6 to 57 mo, average age: 26 mo; weight range 24 to 35.8 kg average weight: 27.9 kg) were treated with therapeutic ultrasound. All procedures took place in facilities that are United States Department of Agriculture registered, and AAALAC International (Association for Assessment and Accreditation of Laboratory Animal Care) accredited.

Pre-treatment procedures

A perineal urethrostomy was performed at least one week before the ultrasound treatment in all canines to better accommodate the ultrasound applicator in the incurvated penile urethra of the canines. A cephalic IV catheter was placed to induce anesthesia with either Propofol (5.5 mg/kg) or a combination of Buprenex (9 µg/kg), ketamine (3 mg/kg) and Dexdomitor (15 µg/kg) followed by an endotracheal intubation of the canines. A continuous inhalation of isoflurane (2%-4%) maintained the anesthesia during ultrasound treatment and subsequent MR imaging. A 6-French Foley catheter was inserted for bladder voiding until treatment. A 20-French rectal tube was placed before

the ultrasound treatment to release gases from the rectum. The ultrasound applicator was manually carefully forwarded in the penile urethra to the prostate and the correct position within the prostate was verified with MR imaging. Experienced veterinarians and veterinary technologists monitored each canine throughout the procedure continuously. Monitoring included an electrocardiogram, blood pressure, blood oxygenation, in- and expired gases and physiological saline infusion.

MRI-guided ultrasound therapy system

A transurethral MR-guided ultrasound therapy prototype system (Philips, Vantaa, Finland) was utilized for administration of the ultrasound treatment on a clinical 3T MRI system (Achieva, Philips Healthcare, Best, The Netherlands). The ultrasound therapy system included a therapy workstation to plan and control the treatment, a radio-frequency generator, a water-cooled trans-urethral ultrasound system [5 mm (15 French) diameter] with eight transducer elements (4 mm × 5 mm/element) (Figure 1) and a motor to rotate the system (Figure 2). A clinical 8-channel cardiac receiver MR coil (Philips Healthcare, Best, The Netherlands) was used for MR imaging (Figure 3). The coil consisted of a 4-element anterior and a 4-element posterior part and was immobilized with straps around the canine and on the patient table (Figure 4).

Ultrasound treatment was performed at a frequency of 6.0 MHz in continuous wave mode. The motor rotated the applicator around its long axis and the ultrasound propagated through a 25 µm polyester membrane into the prostate tissue. Aqueous ultrasound gel was used to improve acoustic coupling. The urethras of the canines were cooled by pumping degassed water that circulated along the membrane and the transducer elements. Ablation depths from the urethra and ablation volumes were controlled by regulating the number of active transducer elements, output power of each element and the duration of sonication.

Ultrasound therapy planning, real-time MR thermometry, and post-therapy evaluation

MRI was used to localize the targets, plan ultrasound exposures, and to provide real-time intraprocedural temperature-monitoring during sonications. MRI images were also used to assess treatment outcome. Cumulative equivalent minutes at 43 °C (CEM₄₃) were used as a metric to quantify thermal tissue damage. Thermal doses in excess of 240 CEM₄₃ were defined as ablative exposures^[14]. MRI treatment planning included two-dimensional multi-slice T₂-weighted Turbo Spin Echo sequences in coronal, sagittal, and axial orientations. Seven slices were acquired in each dynamic in all orientations. Temporal resolution was 4.1 s/8 slices with spatial resolution of 1.5 mm × 1.5 mm in-plane and a 5 mm slice thickness. The MRI-guided ultrasound planning software allows the MRI slices to be automatically aligned with the ultrasound beam to monitor temperatures and to calculate thermal doses in the target region as



Figure 1 Trans-urethral ultrasound therapy probe. Rigid, water-cooled trans-urethral ultrasound applicator with 5 mm (15 French) diameter and eight transducer elements (4 mm x 5 mm/element).



Figure 2 Magnetic resonance imaging-compatible ultrasound therapy device. Set-up of the trans-urethral ultrasound applicator on the MRI patient table with control cables, and motor unit to control the rotation of the ultrasound transducer. MRI: Magnetic resonance imaging.

well as in the peri-prostatic tissues. The MRI-based proton resonance frequency shift (PRFS = 0.0094 ppm/°C) method was used to calculate temperatures and thermal dose maps in real-time^[15]. Color-coded temperature and thermal dose maps were displayed on top of anatomical MR images and updated in real time. Baseline temperature drift was accounted for by normalizing average apparent temperature changes in tissues outside the heated volumes.

Following ultrasound treatment, an axial T₂-weighted sequence was acquired in the same locations and orientation as the pre-treatment sequence. Diffusion weighted MR images (DWI) were acquired before a T₁-weighted fast-field echo sequence was used to monitor the inflow of an FDA approved gadolinium-chelate MRI contrast agent (Multihance, Bracco Diagnostics, 0.1 mmol/kg). The use of DWI and contrast-enhanced T₁-weighted MRI to visualize necrotic tissue were validated in previous studies^[16,17].

Feedback control of thermal ablation

Before thermal ablations, a test-sonication ($P_{ac} = 1.1$ W of one active element, $t = 12$ s) was performed to verify sufficient acoustic coupling, the correct angle of the



Figure 3 Equipment integration for magnetic resonance imaging-guided ultrasound therapy. Frontal oblique view of the 3T Philips MRI scanner with an 8-channel cardiac MR coil on the anterior part of the scanner table and ultrasound transducer on the posterior part of scanner table. MRI: Magnetic resonance imaging.

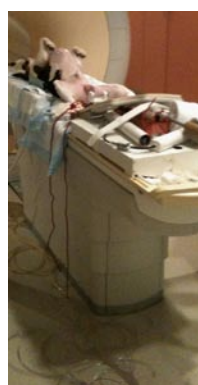


Figure 4 Canine positioning for magnetic resonance imaging-guided ultrasound therapy. Positioning of a canine in supine orientation on the patient table and preparation for the placement of the transurethral ultrasound transducer in the canine prostate.

ultrasound transducer and the location of the heated volume. The rotation angle of the ultrasound transducer was modified with the control software if necessary to reach the target volume precisely, and a sonication was performed. A cool down period (> 5 min) was applied to allow the sonicated prostatic tissue to return to its baseline temperature. In each canine prostate this procedure was repeated in two discrete locations.

Treatment volumes were selected in different locations of the prostate and MRI-based temperature monitoring was used in each ablation location. A temperature feedback control volume of 5 voxels was selected at radial distances of 1.3 to 1.9 cm from the applicator. The acoustic power level ranged from 1.1 to 1.8 W per transducer element and it was kept constant during all independent treatments. The software stopped the sonications automatically once the mean temperature reached 56 °C in the control volume^[18].

Evaluation of the integrity of cavernosal nerves post-treatment

Following the procedure, during the prostatectomy to



Figure 5 The CaverMap Surgical Aid nerve stimulator control unit. Device control unit with connectors for the stimulation needle, display of the applied current in mA, and light-emitting diode display (blue and red) to visualize tumescence response on an ordinal scale.

harvest the prostate, CaverMap Surgical Aid (Blue Torch Corporation, Norwood, MA) was used intra-operatively to identify and map the integrity of cavernosal nerves responsible for potency (Figure 5)^[19]. The CaverMap Surgical Aid includes a nerve stimulator and an erectile response detection system. The CaverMap Surgical Aid has three major components: (1) A control unit with the electronics, connectors for the probe handle and disposable kit and a user interface to control the system; (2) A sterile and reusable probe handle for controlling the device during surgeries; and (3) A disposable kit including a probe tip that can be attached to the probe handle and a tumescence sensor. The electrical current is emitted by the probe tip.

The system applies a mild electrical stimulation for a measured tumescence response. The probe tip was inserted in close proximity to the cavernous nerves (Figures 6 and 7). A biphasic current pulse train with pulse duration of 800 μ s and a current of 8 mA to 20 mA was applied for stimulation. The current was automatically increased every 20 s from 8 to 20 mA. Stimulating the cavernous nerves with the CaverMap Surgical Aid leads to an erectile response that can be measured in penile circumference changes in the tumescence sensor loop that is placed around the canine's penis. Stimulation with the probe tip produces a small erectile response that leads to an increased penile circumference. The integrity and functionality of the cavernous nerves after ultrasound therapy was evaluated by measuring erectile responses quantitatively by analyzing relative penile circumference changes with the tumescence sensor loop. Circumference changes of the sensor loop produced a change in the electric resistance in the mercury filled sensor. Tumescence changes of 0.5% produce a audible signal and a change of light-emitting diode scale (Figure 8).

Once an erectile response was measured, in a certain location of the neurovascular bundle, the position of stimulation was recorded and the probe tip was moved to another location^[20].

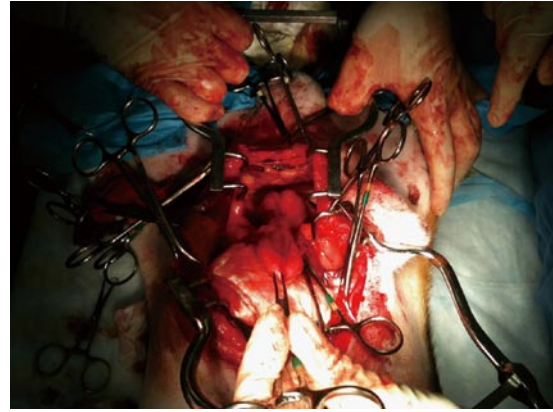


Figure 6 Surgical preparation of the canine prostate for nerve stimulation of the cavernosal nerves.

Post-treatment procedures

Following treatment, post-treatment imaging, and caver-mapping, canines were euthanized by injecting 150 mg/kg sodium pentobarbital IV followed by a prostatectomy. Potential thermal damage to periprostatic anatomical structures (e.g., rectal wall, bladder wall) were also resected (Figure 9) for a detailed histological analysis (Figure 10).

Histopathological analysis

Following prostatectomies, the specimens were fixed in 10% formalin. The prostates were then sliced at 5 mm thickness parallel to the MRI axial slices and submitted for further processing. The processed paraffin blocks were cut at 4 μ m and stained with haematoxylin and eosin stain. The immunohistochemical stain cytokeratin 8 (CK8) was used to analyze cell viability^[21,22]. Photographs of the histological sections show visible lesions from the ultrasound treatment (Figure 10).

Ultrasound therapy analysis

The ultrasound therapy console allows the measurement of the mean temperature, the maximum temperature, and a calculation of thermal dose (> 240 CEM₄₃) volumes by using the Sapareto-Dewey equation^[23].

An experienced genitourinary pathologist and a radiologist then visually correlated thermal dose (> 240 CEM₄₃) volumes, non-perfused volumes on immediate post-ablation contrast-enhanced MR images with whole-mount sections of the prostate. In each case, the correlation between MRI and pathology for location and size of the ablation zone was separately scored on a consensus scale of 3 (no correlation: 1; modest correlation: 2; and excellent correlation: 3).

RESULTS

MRI

MRI was performed in this study to plan the ultrasound treatment and to monitor temperature changes (Figure 11). The canine prostate was identified in the pre-treatment MR images and target locations were prescribed

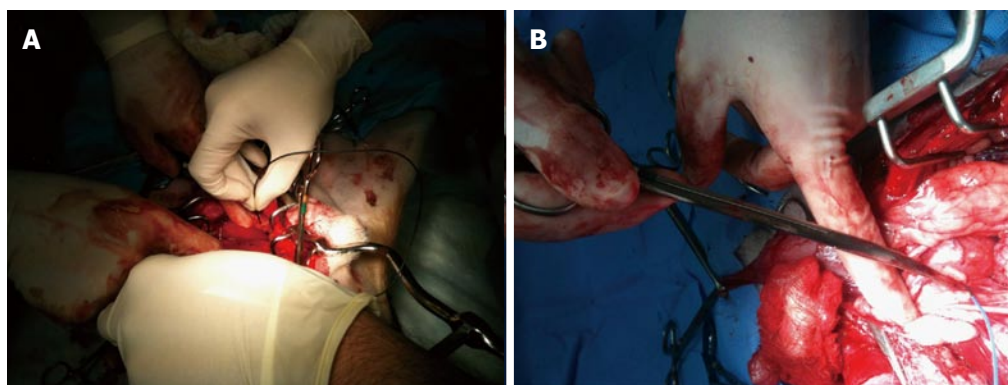


Figure 7 Placement of the CaverMap Surgical Aid nerve stimulator (A and B). Intraoperative placement of the stimulation needle of the CaverMap Surgical Aid nerve stimulator close to the cavernosal nerves of the canine prostate.



Figure 8 The CaverMap Surgical Aid nerve stimulator display. Control unit and display of the CaverMap Surgical Aid nerve stimulator to measure tumescence response on an ordinal scale intraoperatively. Below the digital display are the connectors for the probe handle, the tumescence sensor, and the lead for connecting the tumescence sensor to the control unit. The electric current for stimulation is emitted by the probe tip.

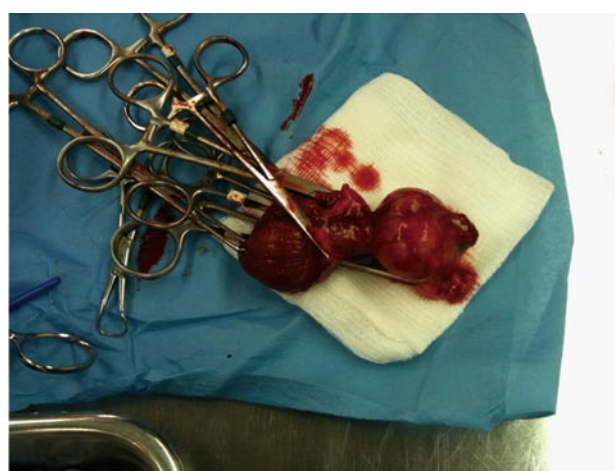


Figure 9 Explanted canine prostate and bladder after prostatectomy.

(Figure 11A, Figure 12A and B). Temperature elevations (Figure 11B and C) were in alignment of the direction of the transducer elements and corresponded to the element length and width. Figure 11D shows a corresponding histological slide of the canine prostate in haematoxylin and eosin staining to evaluate ultrasound treatment effects.

Feedback control of thermal ablation

A total of 16 sonications were performed in 8 canines. The ultrasound treatment procedures were automatically interrupted when the temperature in the target zone reached 56 °C. The MRI-guided transurethral ultrasound therapy system provided multi-planar thermal maps of the prostate and periprostatic tissues, allowing for well-prescribed and controlled ablation of the selected targets.

Example temperature elevations in direction of the ultrasound beam propagation at the end of a sonication are shown in Figure 11B and C. The time period to

reach the target mean temperature of 56 °C within the control volume was 1-3 min, and depended on the local tissue characteristics, control point distance, number of active elements, and acoustic power. The ultrasound treatment was stopped after reaching the target temperature. Tissue temperature dropped to their baseline values after approximately 5 min.

Thermal dose estimation, MR image evaluation, and histopathological evaluation

An exemplary T₂-weighted planning image, contrast-enhanced MR-image, temperature maps, and thermal dose maps are displayed in Figure 12. Contrast-enhanced-images were acquired in all canines after ultrasound treatment for visualization of non-perfused tissue (Figure 12G). Thermal dose assessments in the ablation zones are displayed in Figure 12E and F. In all specimens, regions of thermal ablation were limited to areas within the prostate capsule and no damage was observed in peri-prostatic tissues (Table 1).

In all canines erectile responses were evaluated with a cavernous nerve stimulator in average 5 d (range 0 to 15 d) post-treatment and showed tumescence responses ≥ 2 on an ordinal scale ranging from + 2 to

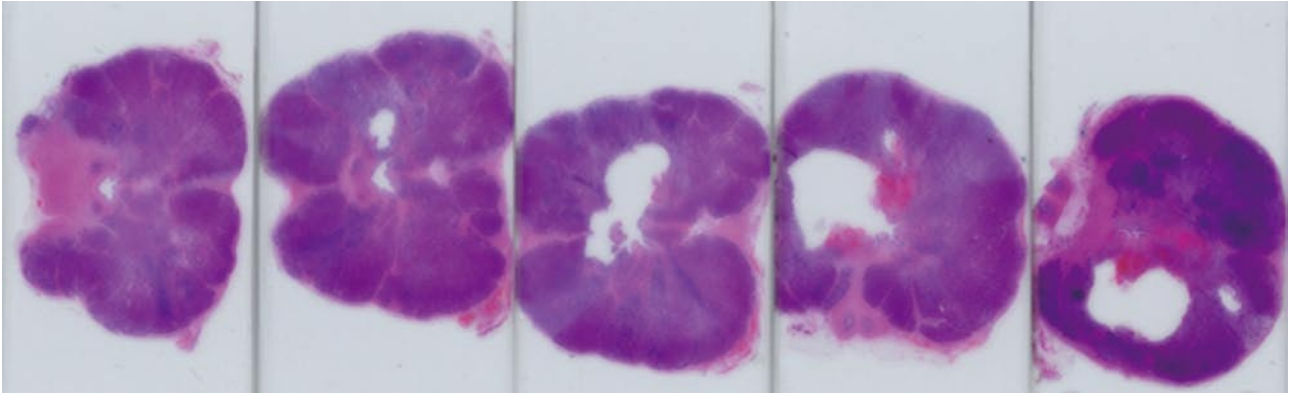


Figure 10 Histology of treated canine prostate. Series of histological slides of a canine prostate after H and E staining show ultrasound ablation zones and hemorrhage.

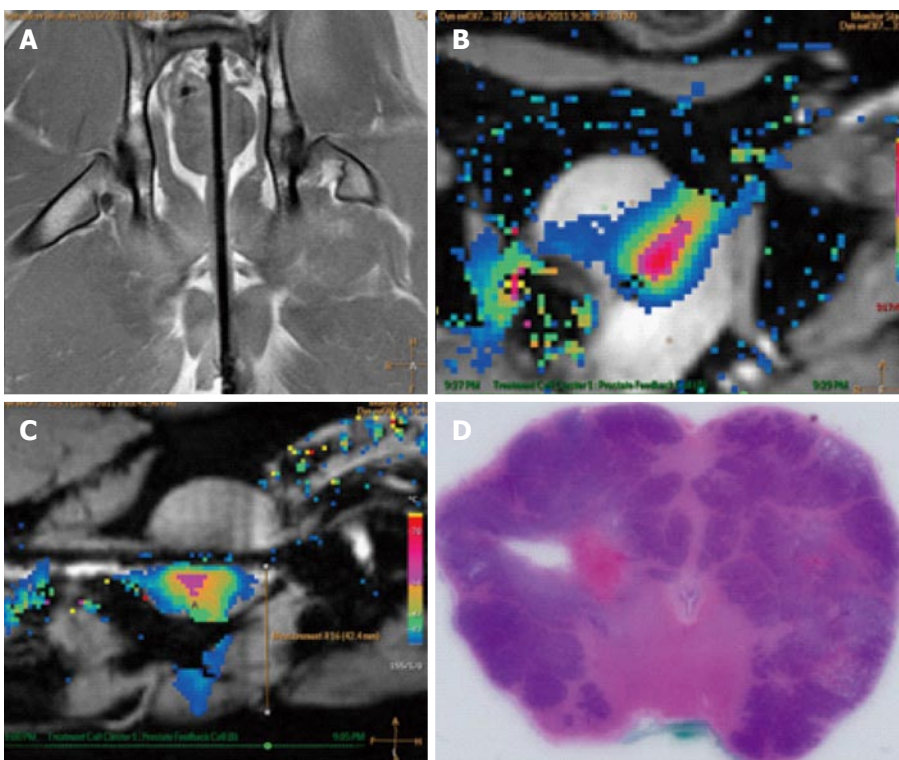


Figure 11 Example images of planning, treatment, and histological outcome. A: Coronal MR image of the intra-urethral catheter placement in the canine prostate for treatment planning with the canine in supine position: The ultrasound applicator is forwarded in the penile urethra to the prostate; B: Color-coded axial temperature map overlaid on the corresponding anatomical MR image demonstrates the typical temperature distribution post ultrasound treatment. Proton Resonance Frequency Shift measurements with a FFE-EPI imaging sequence were used for temperature monitoring and control; C: Sagittal temperature map during ultrasound treatment; D: Histological slide of the canine prostate in haematoxylin and eosin staining to evaluate ultrasound treatment effects. MR: Magnetic resonance; FFE: Fast-field echo.

+ 4 after a stimulation with a maximum current of 14 mA (Table 1). These results indicated intact cavernous nerve functionality.

Additionally, a visual analysis of the ablation zones on contrast-enhanced MR images acquired post ultrasound treatment correlated excellent with the ablation zones on thermal dose maps. All of the ablation zones received a consensus score of 3 (excellent) for the location and size of the correlation between the histologic ablation zone and MRI based ablation zone during the review of the lesions by a genitourinary pathologist and radiologist (Table 1). During the prostatectomy and

histologic examination, no damage was noted in the bladder or rectum.

DISCUSSION

Image guided focal therapy of prostate cancer is a promising new technology that may provide high efficacy with reduced treatment-related morbidity. Focal therapy options to treat prostate cancer are laser ablation, electroporation, cryotherapy and ultrasound therapy^[4]. Focal ultrasound therapy delivers ablative hyperthermia to the prostate and may be efficacious in

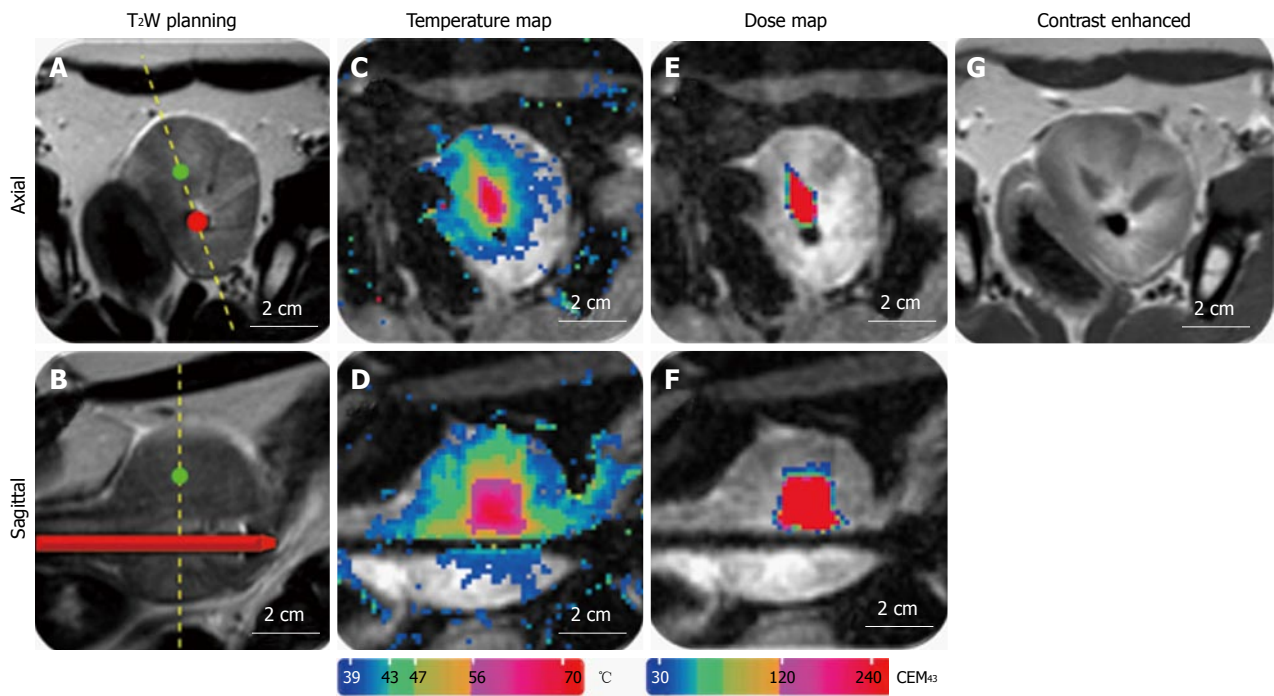


Figure 12 Representative images of magnetic resonance imaging-guidance. A: T₂-weighted image for positioning and treatment planning in axial and sagittal orientation (B); C: MR temperature map during ultrasound treatment in axial and sagittal orientation (D); E: MR dose map during ultrasound treatment in axial and sagittal orientation (F); G: Contrast enhanced T₁-weighted image after ultrasound treatment. MR: Magnetic resonance.

Table 1 Intra- and post-surgical evaluations after the treatment of eight canine prostates <i>in vivo</i> with magnetic resonance imaging-guided ultrasound therapy: Tumescence response on an ordinal scale, assessment of thermal damage to peri-prostatic tissues, and correlation between magnetic resonance imaging, thermal dose (> 240 CEM ₄₃) volumes and pathology for location and size of the ablation zone			
Canine	Tumescence response	Inspection of peri-prostatic tissues	Correlation between MRI, thermal dose (> 240 CEM ₄₃) volumes and pathology for location and size of the ablation zone (no correlation: 1; modest correlation: 2; and excellent correlation: 3)
1	3	No damage	3
2	4	No damage	3
3	3	No damage	3
4	2	No damage	3
5	4	No damage	3
6	2	No damage	3
7	3	No damage	3
8	3	No damage	3

MRI: Magnetic resonance imaging.

the treatment of prostate cancer^[4]. Multiple clinical trials have demonstrated the value of high intensity focused ultrasound to treat cancer^[6,12,24,25].

Ultrasound therapy

Trans-rectal ultrasound therapy has been successfully applied as a focal prostate cancer treatment before^[4,6,12], but limitations of trans-rectal ultrasound, imaging and trans-rectal biopsies have also been demonstrated^[26].

It has been documented that multi-parametric MRI is superior to trans-rectal biopsy for detection of prostate carcinoma^[27] with high specificity and sensitivity^[28]. The combined use of multi-parametric MRI with trans-urethral ultrasound therapy could improve diagnosis and clinical outcomes in prostate cancer^[13].

The results of this canine study demonstrate the feasibility of MR-guided trans-urethral ultrasound for the treatment of prostatic tissue. Our results suggest that focused ultrasound has sufficient spatial accuracy and precision to safely apply treatment of prostate tissue without damaging the neurovascular bundle or the surrounding organs. The nerves around the prostate responsible for erection remained functionally and anatomically intact following ultrasound treatment. We also demonstrated with MRI-based temperature monitoring that temperatures sufficient for ablation in target zones can be achieved while avoiding substantial increases in temperature in adjacent critical anatomical areas. Target locations in this study were located in different zones of the prostate and adequate depth of sonication could be achieved within the prostate. The ability to target diseased tissue in the prostate while avoiding thermal damage to periprostatic structure (especially to the neurovascular bundles) will be critical to the success of future clinical transurethral ultrasound ablation studies.

Although these pre-clinical results are promising, further investigations are needed to optimize trans-urethral MR-guided ultrasound therapy for use in humans with prostate cancer. In our feasibility study we chose not to rotate the applicator during ultrasound exposures.

Future experiments could explore the system's capability for regional or whole prostate treatments using this feature^[29,30]. In particular, modifying the transducer orientation while sonicating may shorten the time it takes to treat the tissue^[29,31]. Moreover, studies that employ a more flexible ultrasound applicator could facilitate urethral placement and improve tolerance of the therapy. Future research should also investigate the potential of this thermoablative therapy for the management of benign prostatic hypertrophy.

This study evaluated feasibility and precision of MRI-guided transurethral ultrasound in prostatic tissue *in vivo* and was therefore limited by not assessing the short-term or long-term outcomes of the therapy. As our canine subjects were cancer-free, we did not have a physiological target region. We instead defined a target region, applied only one ablation in this region, and assessed for correlation between planned targets and treatment. This may not adequately simulate clinical practice where several ablations may be required to treat the cancerous lesions. This study was also limited in its use of pre-pubertal canines. We recommend post-pubertal canines for future pre-clinical ultrasound therapy studies of the prostate to assure large enough prostate sizes for treatment of multiple locations.

In summary, a promising new dual-modality device which combines MRI guidance with a trans-urethral ultrasound therapy probe was able to precisely ablate canine prostate tissue while simultaneously providing accurate thermal maps of the prostate and periprostatic tissue. Real-time, multi-planar temperature mapping equipped with feed-back control allowed for well-targeted ablation of prescribed lesions. There was no impact of ablation on the function of the neurovascular bundle or surrounding organs such as rectum and bladder. Functionality of the cavernosal nerves after trans-urethral ultrasound therapy was confirmed with a nerve stimulator measuring the tumescence response. Results of the feasibility study reported here indicate that future research into the efficacy and functional outcomes of ultrasound therapy for prostate cancer should be explored.

ACKNOWLEDGMENTS

We would like to thank our MRI technologists Peters S and Jamison E as well as the certified veterinary technicians Vosicky J, Bruner M, Peterson K, McGrath J, and Zamora M for their outstanding support of this study and Dr. Mustafi D for providing degassed water.

COMMENTS

Background

Cancer of the prostate is one of the most common malignant diseases and among the leading reasons of male cancer deaths in the United States. There is a need for the development of precise focal Pca treatment approaches to preserve continence and potency. Ultrasound therapy is a novel, minimally invasive treatment option where an ultrasound probe emits a high intensity beam that can be used to destroy or "ablate" cancerous tissue. This study

evaluated possible side-effects of prostate tissue ablation *in vivo* with an magnetic resonance imaging (MRI) guided transurethral ultrasound therapy system.

Research frontiers

In this study, an MRI guided transurethral ultrasound therapy system was tested in dogs. The authors evaluated the feasibility and safety of MRI-guided trans-urethral ultrasound to effectively and accurately ablate prostate tissue while minimizing the damage to surrounding tissues in canine prostates. In addition to assessing rectal and bladder damage, the authors specifically assessed the post-treatment functionality of the nerves by analyzing their response qualitatively and quantitatively with a nerve stimulator.

Innovations and breakthroughs

In this study, MRI was performed for treatment planning, ultrasound guidance and post-treatment evaluation in all canines. Prostate tissue was successfully ablated with the MRI-guided ultrasound therapy unit and regions of thermal ablation were limited to areas within the prostate capsule and no damage was observed in tissues surrounding the prostate. In all canines erectile responses were evaluated with a nerve stimulator post-treatment and indicated intact nerve functionality. No damage was noted in the bladder and rectum.

Applications

Image guided focal ultrasound therapy could help to treat prostate cancer with fewer side effects than standard treatment methods. The authors' results in a canine model suggest that MRI-guided trans-urethral focal ultrasound treatment is a safe and accurate approach to ablate prostatic tissue without damaging the neurovascular bundle and surrounding organs.

Terminology

Thermo-ablation: Energy absorption to increase in temperature for tissue destruction when the temperature exceeds $\geq 56^{\circ}\text{C}$ within the focal area. Thermocoagulation: The use of heat to bring about localized destruction and congealing of tissue. Transurethral: A medical procedure performed via the urethra. Neurovascular bundle: The nerves, arteries, veins and lymphatics that travel together in the body, specifically in this article, around the prostate. Cavernous Nerve: The nerves that facilitate penile erection.

Peer-review

This article is very good.

REFERENCES

- 1 **American Cancer Society.** Cancer Facts & Figures 2014. Atlanta: American Cancer Society, 2014. accessed 2014 Jun 12. Available from: URL: <http://www.cancer.org/acs/groups/content/@research/documents/webcontent/acspc-042151.pdf>
- 2 **Klotz L.** Prostate cancer overdiagnosis and overtreatment. *Curr Opin Endocrinol Diabetes Obes* 2013; **20**: 204-209 [PMID: 23609043 DOI: 10.1097/MED.0b013e328360332a]
- 3 **Hoang AN, Volkin D, Yerram NK, Vourganti S, Nix J, Linehan WM, Wood B, Pinto PA.** Image guidance in the focal treatment of prostate cancer. *Curr Opin Urol* 2012; **22**: 328-335 [PMID: 22647649 DOI: 10.1097/MOU.0b013e32835482cc]
- 4 **Lindner U, Trachtenberg J, Lawrentschuk N.** Focal therapy in prostate cancer: modalities, findings and future considerations. *Nat Rev Urol* 2010; **7**: 562-571 [PMID: 20842187 DOI: 10.1038/nrurol.2010.142]
- 5 **Hildebrandt B, Wust P, Ahlers O, Dieing A, Sreenivasa G, Kerner T, Felix R, Riess H.** The cellular and molecular basis of hyperthermia. *Crit Rev Oncol Hematol* 2002; **43**: 33-56 [PMID: 12098606]
- 6 **Ahmed HU, Freeman A, Kirkham A, Sahu M, Scott R, Allen C, Van der Meulen J, Emberton M.** Focal therapy for localized prostate cancer: a phase I/II trial. *J Urol* 2011; **185**: 1246-1254 [PMID: 21334018 DOI: 10.1016/j.juro.2010.11.079]
- 7 **Lindner U, Lawrentschuk N, Weersink RA, Davidson SR, Raz O, Hlasny E, Langer DL, Gertner MR, Van der Kwast T, Haider MA, Trachtenberg J.** Focal laser ablation for prostate cancer followed by radical prostatectomy: validation of focal therapy and imaging

- accuracy. *Eur Urol* 2010; **57**: 1111-1114 [PMID: 20346578]
- 8 **Lukka H**, Waldron T, Chin J, Mayhew L, Warde P, Winquist E, Rodrigues G, Shayegan B. High-intensity focused ultrasound for prostate cancer: a systematic review. *Clin Oncol (R Coll Radiol)* 2011; **23**: 117-127 [PMID: 20932728 DOI: 10.1016/j.clon.2010.09.002]
- 9 **Soylu FN**, Eggenner S, Oto A. Local staging of prostate cancer with MRI. *Diagn Interv Radiol* 2012; **18**: 365-373 [PMID: 22399364 DOI: 10.4261/1305-3825.DIR.4970-11.2]
- 10 **Jia G**, Abaza R, Williams JD, Zynger DL, Zhou J, Shah ZK, Patel M, Sammet S, Wei L, Bahnson RR, Knopp MV. Amide proton transfer MR imaging of prostate cancer: a preliminary study. *J Magn Reson Imaging* 2011; **33**: 647-654 [PMID: 21563248 DOI: 10.1002/jmri.22480]
- 11 **Wang S**, Peng Y, Medved M, Yousuf AN, Ivancevic MK, Karademir I, Jiang Y, Antic T, Sammet S, Oto A, Karczmar GS. Hybrid multidimensional T(2) and diffusion-weighted MRI for prostate cancer detection. *J Magn Reson Imaging* 2014; **39**: 781-788 [PMID: 23908146 DOI: 10.1002/jmri.24212]
- 12 **Ahmed HU**, Hindley RG, Dickinson L, Freeman A, Kirkham AP, Sahu M, Scott R, Allen C, Van der Meulen J, Emberton M. Focal therapy for localised unifocal and multifocal prostate cancer: a prospective development study. *Lancet Oncol* 2012; **13**: 622-632 [PMID: 22512844]
- 13 **Partanen A**, Yerram NK, Trivedi H, Dreher MR, Oila J, Hoang AN, Volkin D, Nix J, Turkbey B, Bernardo M, Haines DC, Benjamin CJ, Linehan WM, Choyke P, Wood BJ, Ehnholm GJ, Venkatesan AM, Pinto PA. Magnetic resonance imaging (MRI)-guided transurethral ultrasound therapy of the prostate: a preclinical study with radiological and pathological correlation using customised MRI-based moulds. *BJU Int* 2013; **112**: 508-516 [PMID: 23746198 DOI: 10.1111/bju.12126]
- 14 **Meshorer A**, Prionas SD, Fajardo LF, Meyer JL, Hahn GM, Martinez AA. The effects of hyperthermia on normal mesenchymal tissues. Application of a histologic grading system. *Arch Pathol Lab Med* 1983; **107**: 328-334 [PMID: 6687797]
- 15 **Ishihara Y**, Calderon A, Watanabe H, Okamoto K, Suzuki Y, Kuroda K, Suzuki Y. A precise and fast temperature mapping using water proton chemical shift. *Magn Reson Med* 1995; **34**: 814-823 [PMID: 8598808]
- 16 **Chen J**, Daniel BL, Diederich CJ, Bouley DM, van den Bosch MA, Kinsey AM, Sommer G, Pauly KB. Monitoring prostate thermal therapy with diffusion-weighted MRI. *Magn Reson Med* 2008; **59**: 1365-1372 [PMID: 18506801 DOI: 10.1002/mrm.21589]
- 17 **Jacobs MA**, Herskovits EH, Kim HS. Uterine fibroids: diffusion-weighted MR imaging for monitoring therapy with focused ultrasound surgery--preliminary study. *Radiology* 2005; **236**: 196-203 [PMID: 15987974 DOI: 10.1148/radiol.2361040312]
- 18 **Chopra R**, Tang K, Burtnyk M, Boyes A, Sugar L, Appu S, Klotz L, Bronskill M. Analysis of the spatial and temporal accuracy of heating in the prostate gland using transurethral ultrasound therapy and active MR temperature feedback. *Phys Med Biol* 2009; **54**: 2615-2633 [PMID: 19351975 DOI: 10.1088/0031-9155/54/9/002]
- 19 **Kim HL**, Mhoon DA, Brendler CB. Does the CaverMap device help preserve potency? *Curr Urol Rep* 2001; **2**: 214-217 [PMID: 12084267]
- 20 **Walsh PC**, Marschke P, Catalona WJ, Lepor H, Martin S, Myers RP, Steiner MS. Efficacy of first-generation Cavermap to verify location and function of cavernous nerves during radical prostatectomy: a multi-institutional evaluation by experienced surgeons. *Urology* 2001; **57**: 491-494 [PMID: 11248626]
- 21 **Makin CA**, Bobrow LG, Bodmer WF. Monoclonal antibody to cytokeratin for use in routine histopathology. *J Clin Pathol* 1984; **37**: 975-983 [PMID: 6206100]
- 22 **Van Leenders GJ**, Beerlage HP, Ruijter ET, de la Rosette JJ, van de Kaa CA. Histopathological changes associated with high intensity focused ultrasound (HIFU) treatment for localised adenocarcinoma of the prostate. *J Clin Pathol* 2000; **53**: 391-394 [PMID: 10889823]
- 23 **Sapareto SA**, Dewey WC. Thermal dose determination in cancer therapy. *Int J Radiat Oncol Biol Phys* 1984; **10**: 787-800 [PMID: 6547421]
- 24 **Foster RS**, Bihlre R, Sanghvi N, Fry F, Kopecky K, Regan J, Eble J, Hennige C, Hennige LV, Donohue JP. Production of prostatic lesions in canines using transrectally administered high-intensity focused ultrasound. *Eur Urol* 1993; **23**: 330-336 [PMID: 7683997]
- 25 **Gelet A**, Chapelon JY, Margonari J, Theillere Y, Gorry F, Cathignol D, Blanc E. Prostatic tissue destruction by high-intensity focused ultrasound: experimentation on canine prostate. *J Endourol* 1993; **7**: 249-253 [PMID: 8358423]
- 26 **Hwang SI**, Lee HJ. The future perspectives in transrectal prostate ultrasound guided biopsy. *Prostate Int* 2014; **2**: 153-160 [PMID: 25599070 DOI: 10.12954/PI.14062]
- 27 **Sciarra A**, Barentsz J, Bjartell A, Eastham J, Hricak H, Panebianco V, Witjes JA. Advances in magnetic resonance imaging: how they are changing the management of prostate cancer. *Eur Urol* 2011; **59**: 962-977 [PMID: 21367519 DOI: 10.1016/j.eururo.2011.02.034]
- 28 **Turkbey B**, Pinto PA, Mani H, Bernardo M, Pang Y, McKinney YL, Khurana K, Ravizzini GC, Albert PS, Merino MJ, Choyke PL. Prostate cancer: value of multiparametric MR imaging at 3 T for detection--histopathologic correlation. *Radiology* 2010; **255**: 89-99 [PMID: 20308447 DOI: 10.1148/radiol.09090475]
- 29 **Chopra R**, Colquhoun A, Burtnyk M, N'djin WA, Kobelevskiy I, Boyes A, Siddiqui K, Foster H, Sugar L, Haider MA, Bronskill M, Klotz L. MR imaging-controlled transurethral ultrasound therapy for conformal treatment of prostate tissue: initial feasibility in humans. *Radiology* 2012; **265**: 303-313 [PMID: 22929332 DOI: 10.1148/radiol.12112263]
- 30 **Diederich CJ**, Stafford RJ, Nau WH, Burdette EC, Price RE, Hazle JD. Transurethral ultrasound applicators with directional heating patterns for prostate thermal therapy: in vivo evaluation using magnetic resonance thermometry. *Med Phys* 2004; **31**: 405-413 [PMID: 15000627]
- 31 **Siddiqui K**, Chopra R, Vedula S, Sugar L, Haider M, Boyes A, Musquera M, Bronskill M, Klotz L. MRI-guided transurethral ultrasound therapy of the prostate gland using real-time thermal mapping: initial studies. *Urology* 2010; **76**: 1506-1511 [PMID: 20709381 DOI: 10.1016/j.urology.2010.04.046]

P- Reviewer: Soria F S- Editor: Ji FF L- Editor: A
E- Editor: Wu HL



Classifications of mandibular canal branching: A review of literature

Mauricio Augusto Aquino Castro, Manuel Oscar Lagravere-Vich, Tânia Mara Pimenta Amaral, Mauro Henrique Guimaraes Abreu, Ricardo Alves Mesquita

Mauricio Augusto Aquino Castro, Tânia Mara Pimenta Amaral, Ricardo Alves Mesquita, Department of Oral Surgery and Pathology, School of Dentistry, Federal University of Minas Gerais, Belo Horizonte MG 253 31270-901, Brazil

Manuel Oscar Lagravere-Vich, Graduate Orthodontic Program, University of Alberta, University of Alberta, Edmonton T6G1C9, Canada

Mauro Henrique Guimaraes Abreu, Department of Social and Preventive Dentistry, School of Dentistry, Federal University of Minas Gerais, Belo Horizonte MG 253 31270-901, Brazil

Author contributions: Castro MAA, Lagravere-Vich MO, Amaral TMP, Abreu MHG and Mesquita RA contributed equally to this work; all authors read and approved the final manuscript.

Supported by Grants from National Council for Scientific Technological Development (CNPq, #309209/2010-2).

Conflict-of-interest statement: All the authors declare that they have no competing interests.

Data sharing statement: The technical appendix and dataset are available from the corresponding author at ramesquita@ufmg.br.

Open-Access: This article is an open-access article which was selected by an in-house editor and fully peer-reviewed by external reviewers. It is distributed in accordance with the Creative Commons Attribution Non Commercial (CC BY-NC 4.0) license, which permits others to distribute, remix, adapt, build upon this work non-commercially, and license their derivative works on different terms, provided the original work is properly cited and the use is non-commercial. See: <http://creativecommons.org/licenses/by-nc/4.0/>

Correspondence to: Ricardo Alves Mesquita, PhD, Department of Oral Surgery and Pathology, School of Dentistry, Federal University of Minas Gerais, Av. Antonio Carlos, 6627, Pampulha, Belo Horizonte MG 253 31270-010, Brazil. ramesquita@ufmg.br
 Telephone: +55-31-34092499
 Fax: +55-31-34092430

Received: May 29, 2015
 Peer-review started: June 1, 2015
 First decision: August 4, 2015
 Revised: October 20, 2015
 Accepted: November 3, 2015
 Article in press: November 4, 2015
 Published online: December 28, 2015

Abstract

AIM: To gather existing radiographic classifications of mandibular canals branching, considering the criteria on which these were based.

METHODS: The search for studies on mandibular canals based on imaging exams included literature reviews, epidemiological studies of prevalence, descriptive studies, or case reports. An electronic search in the MEDLINE (OvidSP), PubMed, EMBASE (OvidSP), Web of Science (Thompson Reuters), and Scopus (Elsevier) databases was performed, as well as a manual evaluation of the references of the selected articles. Combinations of key words were placed in each database. No restrictions were imposed regarding the year of publication or language. References collected in duplicate were removed by the authors. A table was drawn up, containing the included studies and respective interest data.

RESULTS: Six classifications of mandibular canals branching were selected for the present literature review. Four were based on two-dimensional radiographic exams, and two were performed based on three-dimensional tomographic exams. Three-dimensional classifications were determined based on the analysis found in the least number of exams, comparatively to two-dimensional studies. The prevalence of mandibular canal branching varied from 0% to 38.75% in the works based on two-dimensional exams, while those found in

three-dimensional exams ranged from 15.6% to 65%. The studies were mostly referred to branches that began in the mandibular ramus. Just one classification considered the branches that began in the mandibular body region.

CONCLUSION: Three-dimensional exams appear to be the best method to view mandibular canal branching. Further studies are warranted to determine its true prevalence and questions concerning to associations.

Key words: Inferior alveolar nerve; Mandibular canal; Bifid mandibular canal; Dental radiography; Cone-beam computed tomography

© **The Author(s) 2015.** Published by Baishideng Publishing Group Inc. All rights reserved.

Core tip: The identification of the mandibular canal and its branching are important for the planning of dental procedures. Due to the limitations of the two-dimensional exams, the three-dimensional view of the structures provided by computed tomography (CT) exams allowed for greater sensitivity for the detection and evaluation of mandibular canals. Nevertheless, some studies performed with CT exams continued to use the classifications based on two-dimensional exams. Given the variability of information on this aspect, this study aimed to gather existing information in an attempt to provide researchers and clinical professionals with a stronger basis for their studies and procedures.

Castro MAA, Lagravere-Vich MO, Amaral TMP, Abreu MHG, Mesquita RA. Classifications of mandibular canal branching: A review of literature. *World J Radiol* 2015; 7(12): 531-537 Available from: URL: <http://www.wjgnet.com/1949-8470/full/v7/i12/531.htm> DOI: <http://dx.doi.org/10.4329/wjr.v7.i12.531>

INTRODUCTION

Mandibular canals are intraosseous ducts, normally unique in each hemimandible. These begin in the mandibular foramen, located in the lingual surfaces of the mandibular bodies and stretch until they emerge in the mental foramen, in a vestibular direction in the pre-molar region. Located inside of these canals is the inferior alveolar neurovascular bundle, the largest ramus of the mandibular division of the trigeminal nerve, responsible for the innervation of the posterior teeth, of the surrounding bone structure, and of the mucosa of the tongue coating of the posterior region^[1].

The identification of the mandibular canal is important for the planning of a wide range of dental procedures, especially surgical procedures. The insertion of implants, extraction of impacted teeth, surgical planning of biopsies, enucleations of pathologies, orthognathic surgeries, and the defining of differential diagnoses are

only a few examples of the clinical importance of its localization^[2-7]. The occurrence of anatomical branching in mandibular canals constitutes a complicating factor and requires care for the proper planning of such cases in order to avoid inferior alveolar neurovascular bundle lesions.

As this study treats intraosseous anatomic structures, imaging exams are recognized as the main diagnostic resource for their localization and evaluation. The radiographic study of human fetal mandibles, performed by Chávez-Lomeli *et al.*^[8], detected that bifid or trifid canals are the main anatomical branching of the mandibular canals. For this reason, radiographic classifications were developed according to conventional exams. These systems considered their origins, localization, aspect, and direction as core criteria^[1,9-12]. Due to the limitation inherent to the two-dimensional exams, Langlais *et al.*^[11] contemplated the possibility of the existence of undetected or undescribed canals.

The three-dimensional view of the structures provided by computed tomography (CT) exams allowed for greater sensitivity for the detection and evaluation of mandibular canals, in addition to the three-dimensional classification of the mandibular canal. CT studies have presented different prevalence levels and other types of mandibular canal branches (Figure 1)^[13-15]. Nevertheless, some studies performed with CT exams continued to use the classification of the variation of mandibular canals based on two-dimensional exams^[14,16].

Bearing this finding in mind, the present review seeks to list the classifications and descriptions of the branching of existing mandibular canals, considering the applied diagnostic resources and the criteria on which these were based. Given the variability of information on this aspect, as well as the prevalence and classification, this study aimed to gather existing information in an attempt to provide researchers and clinical professionals with a stronger basis for their studies and procedures.

MATERIALS AND METHODS

Eligibility criteria

This literature review proposed the search for radiographic studies on mandibular canals in humans, based on conventional and digital two-dimensional exams and on CT exams. This work included literature reviews, epidemiological studies of prevalence, descriptive studies, or case reports. No letters to the editor, animal studies, abstracts, or personal opinions were included.

Sources

This study performed an electronic search in the PubMed, Embase, Web of Science (Thompson Reuters), and Scopus (Elsevier) databases. The references of the selected articles were also manually evaluated to detect relevant studies that might have been lost in the electronic search. A complementary search was also conducted using Google Search and Google Scholar



Figure 1 White arrow showing the origin of a mandibular canal branch in the mandibular body found by Rouas *et al*^[13] (2007) on a computed tomography exam.

search tools.

Research strategy

Combinations of key words were placed in each database, using the following key words: Mandible, mandibular nerve, inferior alveolar nerve, mandibular canal, bifid mandibular canal, bifid canals, radiography, panoramic radiography, cone-beam computed tomography, dental implant, and anatomic variation. No restrictions were imposed regarding the year of publication or language. References collected in duplicate were removed by the authors.

Study selection

After having removed the duplicates, the abstracts of all of the chosen articles were read to verify the appropriateness of the theme. The main objective was to find articles that defined the classification of mandibular canal branching. After having selected the articles that met the eligibility criteria, these were read in full and incorporated into the present review.

Synthesis of the collected data

A table of the included studies was drawn up, containing the following data: Authors' names, year of publication, sample size, exam per image used in each study, prevalence of mandibular canal branching, and description of the defined classification, including the name adopted for the branches, the frequency of each type, the location of origin, aspect, direction, and end location.

RESULTS

Six radiographic classifications of the branching in mandibular canals were selected for the present literature review (Table 1)^[1,9-12,14,15].

Within the listed classification, four were defined by evaluating the canals and their branching in two-dimensional radiographic exams^[1,9-12], and two were performed based on three-dimensional CT exams.

Two of the classifications based on two-dimensional evaluations also conducted dissections of the anatomical parts^[10,12].

The classifications based on two-dimensional exams were carried out by analyzing the samples with the highest number of exams (9717 in total, with an average of 2429.25 exams). Nortjé *et al*^[1,9] evaluated 3612 panoramic radiographs, while Langlais *et al*^[11] evaluated 6000 exams. Three-dimensional classifications were determined based on the analysis found in the least number of exams (374 in total, with an average of 187 CT exams).

The prevalence of the mandibular canal branching varied from 0% to 38.75% in the works based on two-dimensional exams, with an average of 10.15%. The prevalence of branches found in CT exams ranged from 15.6% to 65%, with an average of 40.3%.

Only the classification defined by Kieser *et al*^[12] considered the branches that began in the mandibular body. All others referred to those initiated in the mandibular ramus.

DISCUSSION

Radiographic studies of the prevalence branching in mandibular canals presents variability, ranging from 0.08%^[17] to 38.75%^[10] when based on two-dimensional exams, and from 15.6%^[14] to 65%^[15]. This variability is related to the use of different methods, including panoramic radiographic evaluations and CT exams.

Claeys *et al*^[18] warned that, although panoramic radiographs offer diagnostic conditions, the recognition of the branching in mandibular canals is rare. The authors defined that the cross-sectional cuts of the mandibular bodies, made possible through CT exams, were the best method to identify and locate their route. In an attempt to establish a more efficient method, capable of detecting the real prevalence and localization of these alterations, the CT exam has truly sparked great progress and has proven to be better as regards the limitations presented by the panoramic radiographs^[3,15,19]. For this reason, it is recommended as the method of choice for the planning of a wide range of surgical procedures in dentistry^[20].

However, the comparison among the methods reaches beyond that referent to the absolute prevalence of the occurrence of anatomical branching in mandibular canals. The comparison of the prevalence of different types of canals detected in panoramic radiographs and in the three-dimensional exams is of outmost importance due to the highest and lowest clinical significance that each type can represent. Furthermore, this comparison is made more difficult by the lack of a standardization of the classifications adopted in the different studies. The classification of the branches detected through tomographic exams (Figure 2)^[15,16,21,22], though similar to those from two-dimensional exams, presented some differences and some new criteria^[1,10-12].

Table 1 Classifications of mandibular canal branching (1971-2010)

Ref.	Exam	Sample	Prevalence (mandibular canal branching)	Classification	Frequency of the types	Region of origin	Aspect	Direction	Local of termination
Carter <i>et al</i> ^[10] (1971)	Unilateral radiographs and dissection	80	38.75%	Type I	61.25%	Ramus region, from a single Mandibular Foramen	Single large structure with very short dental branches	Superior to the tips of molars roots	Mental arborization
				Type II	13.75% (types 1 or 2)	Ramus region, from a single Mandibular Foramen	Substantially lower down, with dental branches given off more posteriorly, longer and oblique	Oblique, toward the tips of molars roots	Mental arborization
				Type III	25% (types 2 or 3)	Ramus region, from a single Mandibular Foramen	Two large branches initiated posteriorly	Uppers like alveolar branches	Upper to the tips of the roots; Lower to mental forame
Nortjé <i>et al</i> ^[11] (1977)	Panoramic radiographs	3612	0.9	Type Ia	30.3% of duplication cases	Ramus region, from a single Mandibular Foramen	Two canals of a similar width (lower slightly narrower)	Inferior narrower	
				Type Ib		Ramus region, from a single Mandibular Foramen	Double (Superior narrower)	Anterior	
				Type II		Ramus region, from a single Mandibular Foramen	Duplo (Superior shorter)	Anterior	Superior: toward 2 nd and 3 rd molars and inferior: toward mental foramen
				Type III		Ramus region, from separated Mandibular Foramens	Double (Join in the molars region)	Anterior	Molars region
Nortjé <i>et al</i> ^[9] (1977)		3612		Type IV		Ramus region, from a single Mandibular Foramen	Double (Superior narrower than the main canal)	Anterior	Ramus region
Langlais <i>et al</i> ^[11] (1985)	Radiografias panorámicas convencionalis	6000	0.95	Type I	38.6%	Ramus region, from a single Mandibular Foramen	Double (Superior shorter)	Anterior	3 rd molar and adjacente region
				Type II	54.4%	Ramus region, from a single Mandibular Foramen	Double (Joining anteriorly)	Anterior	Ramus or mandibular body regions
				Type III	3.5%	Ramus region, from a single Mandibular Foramen	Double (Combination of types II and III)	Anterior	Ramus, retromolar ou 3 rd molar regions
				Type IV	3.5%	Ramus region, from separated Mandibular Foramens	Double (Joining anteriorly)	Inferior	Ramus region

Kieser <i>et al</i> ^[12] (2005)	Oclusal and unilateral radiographs and dissection	107 mandibles (25 radiographic exams)	0%	Type I (detected by mean of dissections and radiographs)		Ramus region, from a single Mandibular Foramen	Single, without branches	Anterior	Mental foramen region
				Type II (detectado em dissecações)		Mandibular body region	Series of individual branches	Superior	Alveolar process (Edentulous mandibles)
				Type III (detectado em dissecações)		Molars region	Molar plexus	Superior	Molar region (Edentulous mandibles)
				Type IV (detectado em dissecações)		Distal and proximal regions	Distal and proximal plexus	Distal plexus forward. Proximal plexus toward superior	Alveolar process (Edentulous mandibles)
Naitoh <i>et al</i> ^[13] (2009)	CBCT	122	65%	Type I Retromolar	29.8%	Ramus region	Superior	Superior	Retromolar region
				Type II Dental Canal (3° molar)	7%	Ramus region	Superior	Anterior	Root Apex of the third molar
				Type II Dental Canal (2° molar)	1.8%	Ramus region	Superior	Anterior	Root Apex of the second molar
				Type III Forward Canal (with confluence)	4.5%	Ramus region	Superior (Joining to the main canal)	Anterior	Mandibular body
				Type III Forward Canal (without confluence)	55.3%	Ramus region	Superior	Anterior	Mandibular body
				Type IV Buccal or lingual canal	1.8%	Ramus region	Lateral	Inferior (Buccal or lingual)	Ramus region
				Less than 50% of the diameter of the main canal	51%		Narrower (Less than 50% of the diameter of the main canal)		
				Equal or bigger than 50% of the diameter of the main canal	49%		Equal or bigger than 50% of the diameter of the main canal		
Kuribayashi <i>et al</i> ^[14] (2010)	CBCT	301 unilateral exams from 252 patients	15.60%						

CBCT: Cone beam computed tomography.

In one three-dimensional exam, Kuribayashi *et al*^[14], although they had defined an additional classification criterion by evaluating the diameter of the branches of the mandibular canals in relation to the main canal, primarily used the two-dimensional classification set forth by Nortjé *et al*^[11] for detected canals. Their results pointed towards a greater prevalence of mandibular canal branching when compared to that found by Nortjé *et al*^[11]. Moreover, when compared to the diverse types of branches, a difference could also be observed regarding the most prevalent type of canal. While Nortjé *et al*^[11] found greater prevalence for type I bifid canals (78.8%), Kuribayashi *et al*^[14] found a greater prevalence of type II branches (13.2%).

Likewise, Correr *et al*^[16] used the two-dimensional classification, as defined by Langlais *et al*^[11], for a tomographic evaluation of mandibular canal branching. It was not possible to compare the prevalence of these studies, given that the samples evaluated by Correr *et al*^[16] consisted, in its totality, of previously diagnosed exams referent to the occurrence of branches. However, as regards the proportion among the different types of branches, differences were observed. The type I standard was the most commonly detected in tomographic exams (72.6%), followed by the type II (19.3%), whereas the types I and II were detected in 38.6% and 54.4% of the panoramic radiographs, respectively. No type IV branches were detected in the scans.

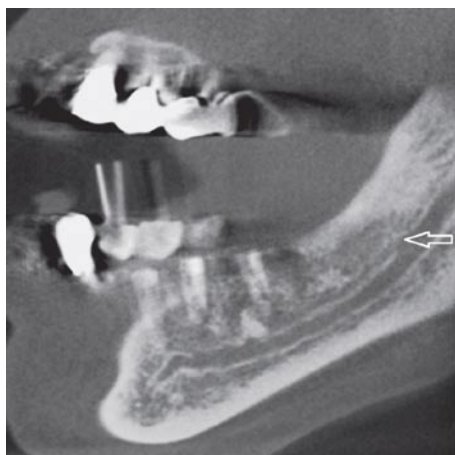


Figure 2 Cone beam computed tomography exam with a white arrow pointing the origin of a forward canal without confluence, bifurcated from the main mandibular canal in the ramus region, and classified as type 3 by Naitoh *et al*^[15] (2009).

These results reveal the existence of differences in the diagnostic accuracy of the methods. Nevertheless, the analysis of the different two- and three-dimensional classifications calls attention to some other relevant differences. As regards the evaluation of the diameters of the branches referent to the main canals^[14], this can contribute to the greater or lesser relevance of the findings. While higher caliber branches may represent a greater risk of injury, one must also bear in mind that the branches of a lesser volume may be referent to nutrient canals, such as that found in the dissections performed by Carter and Keen^[10].

Another aspect to be considered refers to the direction of the branches. Whereas the two-dimensional classification includes the description of the direction only in the anteroposterior and superoinferior directions, the three-dimensional classification set forth by Naitoh *et al*^[15] is also concerned with the situation of the branches in the vestibular-lingual direction. This is an important factor to be considered in the surgical planning of cases^[2,6,23,24] thus contributing to improvements in the definition of the localization of the surgical access route as well as better estimations of the risk of injury to the surrounding anatomical structures.

In conclusion, the detection of mandibular canal branching is important to determine the proper conduct to be taken with patients with dental problems, and imaging exams represent the standard method to view these alterations. Three-dimensional exams appear to be the best method, however, further studies are warranted to determine the true prevalence these alterations, some possible associated factor, and other such questions concerning three-dimensional systems.

COMMENTS

Background

Mandibular canals are intraosseous ducts that contain the inferior alveolar neurovascular bundle, responsible for the innervation of the posterior teeth

and of the surrounding structures of the posterior region. The identification of the mandibular canal is important for the planning of a wide range of dental surgical procedures. The occurrence of mandibular canals branching constitutes a complicating factor and requires care for the proper planning of the procedures in order to avoid neurovascular lesions. The present review seeks to list the classifications and descriptions of the mandibular canal branching, considering the applied diagnostic resources and the criteria on which these were based. Given the variability of information on this aspect, this study aimed to gather existing information in an attempt to provide researchers and clinical professionals with a stronger basis for their studies and procedures.

Research frontiers

Bifid or trifid canals are the main anatomical branching of the mandibular canals, according Ch  vez-Lomeli *et al* (1996). As the mandibular canals are intraosseous anatomic structures, imaging exams are recognized as the main diagnostic resource for their localization and evaluation. Radiographic classifications were mainly developed according to conventional exams. Due to the limitation of the two-dimensional exams, Langlais *et al* (1985) contemplated the possibility of the existence of undescribed canals.

Innovations and breakthroughs

The three-dimensional view of the structures provided by computed tomography (CT) exams allowed for greater sensitivity for the detection and evaluation of mandibular canals, in addition to the three-dimensional classification of the mandibular canal. CT studies have presented different prevalence levels and other types of mandibular canal branches. Nevertheless, some studies performed with CT exams continued to use the classification of the variation of mandibular canals based on two-dimensional exams.

Applications

This review suggests that three-dimensional exams appear to be the best method to view mandibular canal branching. Further studies are warranted to determine its true prevalence, new classifications and questions concerning to associations.

Terminology

Both cone beam computed tomography and CT exams were equally referred as the generic term CT in this study. These types of three-dimensional exams have greater sensitivity for the detection of mandibular canal branching in comparison to two-dimensional exams and a comparative evaluation of the sensitivity of these methods was not a goal of this review.

Peer-review

In this paper the authors conducted an internet based search on the different radiographic classifications as regards the identification of the mandibular canal and its branching. The review is concise and well written one.

REFERENCES

- 1 **Nortj   CJ**, Farman AG, Grotepass FW. Variations in the normal anatomy of the inferior dental (mandibular) canal: a retrospective study of panoramic radiographs from 3612 routine dental patients. *Br J Oral Surg* 1977; **15**: 55-63 [PMID: 268217 DOI: 10.1016/0007-117X(77)90008-7]
- 2 **Juodzb  lys G**, Wang HL, Sab  lys G. Injury of the Inferior Alveolar Nerve during Implant Placement: a Literature Review. *J Oral Maxillofac Res* 2011; **2**: e1 [PMID: 24421983 DOI: 10.5037/jomr.2011.2101]
- 3 **Kim TS**, Caruso JM, Christensen H, Torabinejad M. A comparison of cone-beam computed tomography and direct measurement in the examination of the mandibular canal and adjacent structures. *J Endod* 2010; **36**: 1191-1194 [PMID: 20630297 DOI: 10.1016/j.joen.2010.03.028]
- 4 **Hori M**, Sato T, Kaneko K, Okaue M, Matsumoto M, Sato H, Tanaka H. Neurosensory function and implant survival rate following implant placement with nerve transpositioning: a case study. *J Oral Sci* 2001; **43**: 139-144 [PMID: 11515599 DOI: 10.2334/josn.43.139]
- 5 **Gonz  lez-Santana H**, Pe  narrocha-Di  go M, Guarinos-Carb  

- J, Balaguer-Martínez J. Pain and inflammation in 41 patients following the placement of 131 dental implants. *Med Oral Patol Oral Cir Bucal* 2005; **10**: 258-263 [PMID: 15876971]
- 6 **Mizbah K**, Gerlach N, Maal TJ, Bergé SJ, Meijer GJ. The clinical relevance of bifid and trifid mandibular canals. *Oral Maxillofac Surg* 2012; **16**: 147-151 [PMID: 21698363 DOI: 10.1007/s10006-011-0278-5]
- 7 **Simonton JD**, Azevedo B, Schindler WG, Hargreaves KM. Age- and gender-related differences in the position of the inferior alveolar nerve by using cone beam computed tomography. *J Endod* 2009; **35**: 944-949 [PMID: 19567312 DOI: 10.1016/j.joen.2009.04.032]
- 8 **Chávez-Lomeli ME**, Mansilla Lory J, Pompa JA, Kjaer I. The human mandibular canal arises from three separate canals innervating different tooth groups. *J Dent Res* 1996; **75**: 1540-1544 [PMID: 8906121 DOI: 10.1177/00220345960750080401]
- 9 **Nortjé CJ**, Farman AG, de V Joubert JJ. The radiographic appearance of the inferior dental canal: an additional variation. *Br J Oral Surg* 1977; **15**: 171-172 [PMID: 271020 DOI: 10.1016/0007-117X(77)90050-6]
- 10 **Carter RB**, Keen EN. The intramandibular course of the inferior alveolar nerve. *J Anat* 1971; **108**: 433-440 [PMID: 5575310]
- 11 **Langlais RP**, Broadus R, Glass BJ. Bifid mandibular canals in panoramic radiographs. *J Am Dent Assoc* 1985; **110**: 923-926 [PMID: 3860553 DOI: 10.14219/jada.archive.1985.0033]
- 12 **Kieser J**, Kieser D, Hauman T. The course and distribution of the inferior alveolar nerve in the edentulous mandible. *J Craniofac Surg* 2005; **16**: 6-9 [PMID: 15699637 DOI: 10.1097/00001665-200501000-00003]
- 13 **Rouas P**, Nancy J, Bar D. Identification of double mandibular canals: literature review and three case reports with CT scans and cone beam CT. *Dentomaxillofac Radiol* 2007; **36**: 34-38 [PMID: 17329586 DOI: 10.1259/dmfr/27374727]
- 14 **Kuribayashi A**, Watanabe H, Imaizumi A, Tantanapornkul W, Katakami K, Kurabayashi T. Bifid mandibular canals: cone beam computed tomography evaluation. *Dentomaxillofac Radiol* 2010; **39**: 235-239 [PMID: 20395465 DOI: 10.1259/dmfr/66254780]
- 15 **Naitoh M**, Nakahara K, Hiraiwa Y, Aimiya H, Gotoh K, Ariji E. Observation of buccal foramen in mandibular body using cone-beam computed tomography. *Okajimas Folia Anat Jpn* 2009; **86**: 25-29 [PMID: 19522303]
- 16 **Correr GM**, Iwanko D, Leonardi DP, Ulbrich LM, Araújo MR, Deliberador TM. Classification of bifid mandibular canals using cone beam computed tomography. *Braz Oral Res* 2013; **27**: 510-516 [PMID: 24346049 DOI: 10.1590/S1806-83242013000600011]
- 17 **Grover PS**, Lorton L. Bifid mandibular nerve as a possible cause of inadequate anesthesia in the mandible. *J Oral Maxillofac Surg* 1983; **41**: 177-179 [PMID: 6572228 DOI: 10.1016/0278-2391(83)90076-9]
- 18 **Claeys V**, Wackens G. Bifid mandibular canal: literature review and case report. *Dentomaxillofac Radiol* 2005; **34**: 55-58 [PMID: 15709108 DOI: 10.1259/dmfr/23146121]
- 19 **Muñelo-Lorenzo J**, Suárez-Quintanilla JA, Fernández-Alonso A, Marsillas-Rascado S, Suárez-Cunqueiro MM. Descriptive study of the bifid mandibular canals and retromolar foramina: cone beam CT vs panoramic radiography. *Dentomaxillofac Radiol* 2014; **43**: 20140090 [PMID: 24785820 DOI: 10.1259/dmfr.20140090]
- 20 **Tyndall DA**, Price JB, Tetradis S, Ganz SD, Hildebolt C, Scarfe WC. Position statement of the American Academy of Oral and Maxillofacial Radiology on selection criteria for the use of radiology in dental implantology with emphasis on cone beam computed tomography. *Oral Surg Oral Med Oral Pathol Oral Radiol* 2012; **113**: 817-826 [PMID: 22668710 DOI: 10.1016/j.oooo.2012.03.005]
- 21 **Orhan AI**, Orhan K, Aksoy S, Özgül O, Horasan S, Arslan A, Kocyigit D. Evaluation of perimandibular neurovascularization with accessory mental foramina using cone-beam computed tomography in children. *J Craniofac Surg* 2013; **24**: e365-e369 [PMID: 23851871 DOI: 10.1097/SCS.0b013e3182902f49]
- 22 **Kang JH**, Lee KS, Oh MG, Choi HY, Lee SR, Oh SH, Choi YJ, Kim GT, Choi YS, Hwang EH. The incidence and configuration of the bifid mandibular canal in Koreans by using cone-beam computed tomography. *Imaging Sci Dent* 2014; **44**: 53-60 [PMID: 24701459 DOI: 10.5624/isd.2014.44.1.53]
- 23 **Tay AB**, Zuniga JR. Clinical characteristics of trigeminal nerve injury referrals to a university centre. *Int J Oral Maxillofac Surg* 2007; **36**: 922-927 [PMID: 17875382 DOI: 10.1016/j.ijom.2007.03.012]
- 24 **Miller CS**, Nummikowski PV, Barnett DA, Langlais RP. Cross-sectional tomography. A diagnostic technique for determining the buccolingual relationship of impacted mandibular third molars and the inferior alveolar neurovascular bundle. *Oral Surg Oral Med Oral Pathol* 1990; **70**: 791-797 [PMID: 2263343 DOI: 10.1016/0030-4220(90)90023-L]

P- Reviewer: Abdel-Salam OME, Stoetzer M **S- Editor:** Ji FF

L- Editor: A **E- Editor:** Wu HL





Published by **Baishideng Publishing Group Inc**

8226 Regency Drive, Pleasanton, CA 94588, USA

Telephone: +1-925-223-8242

Fax: +1-925-223-8243

E-mail: bpgoffice@wjgnet.com

Help Desk: <http://www.wjgnet.com/esps/helpdesk.aspx>

<http://www.wjgnet.com>

